Water Science and Technology Library

Chandra Shekhar Jha
Ashish Pandey
V. M. Chowdary
Vijay Singh *Editors*

Geospatial Technologies for Resources Planning and Management

Springer

Water Science and Technology Library

Volume 115

The aim of the *Water Science and Technology Library* is to provide a forum for dissemination of the state-of-the-art of topics of current interest in the area of water science and technology. This is accomplished through publication of reference books and monographs, authored or edited. Occasionally also proceedings volumes are accepted for publication in the series. *Water Science and Technology Library* encompasses a wide range of topics dealing with science as well as socio-economic aspects of water, environment, and ecology. Both the water quantity and quality issues are relevant and are embraced by *Water Science and Technology Library*. The emphasis may be on either the scientific content, or techniques of solution, or both. There is increasing emphasis these days on processes and *Water Science and Technology Library* is committed to promoting this emphasis by publishing books emphasizing scientific discussions of physical, chemical, and/or biological aspects of water resources. Likewise, current or emerging solution techniques receive high priority. Interdisciplinary coverage is encouraged. Case studies contributing to our knowledge of water science and technology are also embraced by the series. Innovative ideas and novel techniques are of particular interest.

Comments or suggestions for future volumes are welcomed.

Vijay P. Singh, Department of Biological and Agricultural Engineering & Zachry Department of Civil and Environment Engineering, Texas A&M University, USA
Email: vsingh@tamu.edu

All contributions to an edited volume should undergo standard peer review to ensure high scientific quality, while monographs should also be reviewed by at least two experts in the field.

Manuscripts that have undergone successful review should then be prepared according to the Publisher's guidelines manuscripts: https://www.springer.com/gp/authors-editors/book-authors-editors/book-manuscript-guidelines

More information about this series at https://link.springer.com/bookseries/6689

Chandra Shekhar Jha · Ashish Pandey ·
V. M. Chowdary · Vijay Singh
Editors

Geospatial Technologies for Resources Planning and Management

Springer

Editors
Chandra Shekhar Jha
National Remote Sensing Centre
Hyderabad, Telangana, India

V. M. Chowdary
Government of India
MNCFC, DA&FW
New Delhi, Delhi, India

Ashish Pandey
Department of Water Resources
Development and Management
Indian Institute of Technology Roorkee
Roorkee, Uttarakhand, India

Vijay Singh
College Station, TX, USA

ISSN 0921-092X ISSN 1872-4663 (electronic)
Water Science and Technology Library
ISBN 978-3-030-98980-4 ISBN 978-3-030-98981-1 (eBook)
https://doi.org/10.1007/978-3-030-98981-1

This Springer imprint is published by the registered company Springer Nature Switzerland AG
The registered company address is: Gewerbestrasse 11, 6330 Cham, Switzerland

Contents

Chapter 1
Geospatial Technology for Geomorphology Mapping and Its Applications

G. Sreenivasan and C. S. Jha

Abstract Geomorphology, which is the scientific study of landforms, provides us with an understanding of the variety of surface and sub-surface processes that have been active on the earth's surface and have carved the variety of landforms. Geomorphology, along with ancillary information on geology, soil, vegetation, and hydrology have wide range of societal applications in various fields for developmental planning. Satellite-based geospatial technology is being used for the last five decades for carrying out geomorphological mapping and its applications. The synoptic and temporal capability of satellite remote sensing can be effectively used to depict the morphography, morphogenesis, and morphochronology of different landforms. Remote sensing is effective in providing rapid and systematic geomorphological mapping at low cost, enables change detection and mapping of landforms in dynamic landscapes at different scales and for different purposes. The advancements in geospatial technology in terms of high and very high-resolution satellite data both in optical and microwave domains, availability of high-resolution DEMs, and new data-driven techniques and algorithms of remote sensing data analysis have brought newer vistas in landform mapping, geomorphic process analysis, and its applications. Geomorphology is considered an important input for disaster risk reduction and is used widely in hazard zonation for floods and landslides. Geomorphology mapping has applications in the area of geoengineering for site assessment before undertaking any major structures such as dams, and road or railway line alignments. Geomorphological guides are one of the indicator zones for occurrence of minerals and are also useful in oil and gas exploration. They also have an important role in demarcation of hydro-geomorphic units and associated ground water potential zones. It is one of the primary inputs for coastal zone management. Geomorphic anomalies are also being widely used in archaeological and anthropological studies. Currently, imprints of geomorphic processes on any landscape are used for studying the climate change. This chapter discusses role of geospatial technology in geomorphological mapping,

G. Sreenivasan (✉)
Regional Remote Sensing Centre—Central, NRSC, ISRO, Nagpur, India
e-mail: sreenu_v@yahoo.com

C. S. Jha
Regional Centers, National Remote Sensing Centre, ISRO, Hyderabad, India

C. S. Jha et al. (eds.), *Geospatial Technologies for Resources Planning and Management*, Water Science and Technology Library 115,
https://doi.org/10.1007/978-3-030-98981-1_1

advanced techniques of mapping, different classification schemas, and some major applications of geomorphology.

Keywords Geomorphology · Landforms · Remote sensing · Classification schema · Geomorphology applications · Disaster risk reduction · Geoengineering · Palaeodrainage · Hydrogeomorphology · Geomorphic anomalies

1.1 Introduction

Earth is a dynamic planet and is continually evolving since geological past. Combination of actions by various agents such as wind, water, ice, etc. modifies the earth's surface. The present-day topography of the earth is carved out by these various processes. Geomorphology is the science dealing with the morphology of the terrain forms, their relief, and the processes that carve these forms on the earth's surface (Gregory and Lewin 2017; Lopatin and Zhirov 2017; Merriam-Webster 2021). The term Geomorphology is derived from the Greek words 'ge' meaning earth, 'morphe' meaning form, and 'logos' meaning discourse or study (Gregory and Goudie, 2011; Gregory and Lewin 2017). Geomorphology focuses on the classification of the different landforms with respect to their shape, origin, evolution, and dynamics. The geomorphic processes are either endogenic (related to tectonic, volcanic, or isostatic) or exogenic (related to external agents like wind, water, ice, etc.) (Hauber et al. 2018).

The understanding of geomorphology of an area is important for several geoengineering and developmental planning applications. This is an important planning input in addition to the information on geology, soils, hydrology, and land use. The application of geomorphology is especially well valued in the areas of disaster risk reduction, mineral exploration, groundwater prospecting, water conservation planning, pedology, land resources development, watershed management, archaeological exploration, coastal zone management, regulation zoning, urban planning, etc. Dynamics of landforms is also an important aspect to be studied. Apart from changes that happen due to endogenic and exogenic factors, changes occurring due to anthropogenic impact and climate change are very significant. Therefore, geomorphology is also an important input for environmental management and the study of environmental changes happening due to global climate change and its impact such as global warming (Slaymaker et al. 2015). Present-day, the study of geomorphology deals not only with mapping the different landforms and studying their genesis in terms of the processes that acted in carving these landforms, but it also deals with studying the present-day processes and landform changes and development of landscapes that impact a large number of environmental issues and their mitigation.

In this chapter, we discuss the utilization of geospatial technology for mapping geomorphology and its advancements and the different classification schemas. Finally, major geospatial applications of the geomorphology are discussed with few case studies.

1.2 Geomorphology Mapping

Geomorphological mapping, in a traditional way, has evolved from field mapping about a century back (Knight et al. 2011). While geomorphology dates back to Ancient Greece period, the early modern geomorphology started evolving at the end of 18th Century (Paul and Montgomery 2020). The 'cycle of erosion' model of broad-scale landscape evolution was developed by William Morris Davis during this time, popularly known as 'Davisian theory', which was later modified by Walther Penck (Oldroyd and Grapes 2008). During this time and further into the 19th Century the European Geomorphologists from Germany, Poland, Switzerland, and France did extensive mapping of geomorphology. Emphasis was given to the geomorphological process in large-scale mapping, whereas morpho-structure was given prominence in mapping carried out on medium to small-scale by countries like Russia (Verstappen, 2011). An empirical system of mapping landforms based on the slopes and flats was brought in by geomorphologists in Britain. In Australia, the Geomorphology mapping was used for resources management, wherein, a landform was considered as the functional unit of a landscape and each unit was dominated by a land area that had a similar genesis and also depicts similar topography, soils, and vegetation pattern. The quantitative and process-based geomorphology started evolving during the middle of the 20th Century, which finally lead toward the contemporary geomorphology dwelling upon the form-process relationship models (Mukhopadhyay 2003).

Though the essence of geomorphological processes is emphasized in geomorphology mapping, the importance of the form, terrain configuration, and the underlying structure is considered important for geomorphological mapping (Verstappen 2011). Thus, landforms are also considered as the distinct cartographic forms which are portrayal of the terrain structure. The inherent advantages of Remote sensing technology giving the synoptic view of the terrain in different wavelength bands, beyond visible, forms an effective tool for studying the terrain forms and their association with the surrounding ecosystem, thus giving an understanding of the processes that have acted. These advantages have led geomorphologists to use this technology in mapping. Morphochronology is another important factor embedded in geomorphology, which brings in the factor of time in the formation of landforms and their dynamics. Remote sensing, by virtue of its repetitive coverage, has an advantage in studying these dynamics of landforms.

A new era of geomorphology mapping thus began with the advent of remote sensing from aerial and space platforms. While the aerial photos have been used in studying terrain forms since the World War II times, the space remote sensing-based geomorphological mapping started during 1970s after the launch of Landsat-1, formerly known as Earth Resources Technology Satellite—ERTS-1 (Napieralski et al. 2013; Srivastav et al. 2021). Subsequent availability of large number of Remote Sensing Satellites both by India and other countries, advancements in the spatial and spectral domains, and also advancements in digital image processing techniques, led to more systematic geomorphological mapping by many countries at different scales.

Scale of mapping has an impact on the way we perceive and describe a landform. Landforms at different scales, will in a way, describe large landforms seen at a smaller scale to small landforms (which are constituents of larger landforms) seen at large scales. For example, a pediment-Inselberg-Complex is a large landform usually mapped at a smaller scale, whereas the Inselbergs which are smaller features can be mapped at a large-scale. Thus, remote sensing satellites, by virtue of providing satellite images at different spatial resolutions, will help us in providing the required technology for carrying out geomorphological mapping using a hierarchical system describing landforms at different levels (GSI and NRSC 2010).

1.3 Role of Geospatial Technology in Geomorphology Mapping

The geospatial technology mainly constitutes of the Remote Sensing, Geographical Information System (GIS), and Global Positioning System (GPS). Remote sensing, which employs electromagnetic radiation (EMR) to acquire information about the earth's surface features from aerial or satellite platforms, mainly works on the principle of interaction of electromagnetic energy with the material on the earth's surface. The spectral response patterns generated from the interaction of EMR with earth's surface aid in the detection, identification, and analysis of earth's surface material.

Geospatial technology has been deeply linked with study of geomorphology since the advent of these technologies during mid-twentieth Century. Since then, these technologies have been extensively used in many geomorphological studies for mapping, analysis, and measurement of the geomorphological forms and processes. With the continual advancements in the geospatial tools and techniques, especially the remote sensing image processing and photogrammetric techniques, and also availability of the Digital Elevation Models (DEMs) from space, the quantification of landforms and detection of geomorphic changes has become possible. In this section, the role of geospatial technology, including the conventional methods, digital techniques, and advanced methods of mapping are discussed.

1.3.1 Conventional Techniques of Photo Interpretation

The use of remote sensing technology for geomorphology mapping initiated with visual interpretation of aerial photographs. Landform mapping from aerial photographs was done using both qualitative interpretation as well as quantitative stereoscopic methods to measure the landforms by 3-D visualization, which was possible by viewing two aerial photos of the terrain from two different vantage points simultaneously. The qualitative interpretation usually required distinguishing and identification of the terrain/relief features, drainage, and cultural features, and

knowledge of the geomorphology to analyze the relief features and drainage patterns for interpreting different landform features. Some mapping techniques depended on using other data like topographic maps and identifying and demarcating boundaries of landforms using contour lines for bringing out the actual relief. As aerial photographs are having inherently high spatial resolution, large-scale geomorphic maps features were extracted and depicted in the maps. However, the large spatial resolution is compensated by the small area coverage and thus preparation of local area maps. Bringing aerial photographs onto a georeferenced framework was also a very cumbersome exercise. Therefore, the initial efforts of interpreting aerial photographs for preparing geomorphological maps were limited to local areas and lacked the regional perspective to the geomorphological mapping. Especially, mapping large area features like mountains and large rivers and associated landforms required large number of aerial photographs to be stitched, which was time-consuming and expensive. The aerial photographs also had the limitation of not being able to image the earth's surface in many numbers of spectral bands.

The limitations of the aerial photographs in geomorphological mapping were quickly overcome by the advent of the satellite platforms for remote sensing. The conventional techniques of remote sensing imagery interpretation for mapping geomorphology used hardcopy photos or satellite images, which were printed after applying required photo/image corrections and enhancements. Visual interpretation of images requires keen observation and understanding of the basic elements of photo interpretation, viz., tone, color, texture, pattern, shape, size, shadow, association, location of the feature, and the height or depth and related aspects. These elements of visual interpretation are already well described and understood by remote sensing professionals (Jenson 2007; Asokan et al. 2020). Though for interpreting any feature on a photo or imagery use of all these elements is not possible at all times, a combined use of at least some of these will guide an experienced interpreter to arrive at a fairly correct conclusion about the feature or form. Additionally, for mapping geomorphology through visual interpretation, knowledge of other terrain features such as drainage patterns, the geology of the area, and the climatic environment are important to arrive at the correct understanding of the geomorphic process and interpretation of the landform.

1.3.2 Analysis and Information Extraction from Digital Remote Sensing Data

The development of the advanced computational techniques and image processing algorithms made a revolutionary change in remote sensing techniques as well. Remote sensing progressed from use of hard copy images to processing of digital data. This had advantages for information extraction from remote sensing images by applying corrections to the raw image data for improving the radiometry of the

images, geometric correction of the images for tying them precisely to any geographical point on the earth's surface, applying area-specific enhancements to images and generation of mosaics of large areas for preparing seamless databases.

As a part of radiometric corrections, pixel digital value is converted to at-sensor radiance by subtraction of the atmospheric contribution, topographic normalization, and sensor calibration. The calibration of images has an important impact on the information extraction from the images by giving a correct spectral response pattern for proper identification and classification of the earth's surface features and forms (Sreenivasan and Krishna Murthy 2018). Further, it will allow comparison of any feature's continuity from one image to another, especially when we use large number of images taken over different time periods for mapping geomorphology over a large study area. This calibration is also important when we are monitoring geomorphological changes over a long period of time. By doing geometric correction, the systematic and nonsystematic distortions and relief displacement is corrected and will result in adding the map projections and ground coordinate system with a local or global ellipsoid.

The image enhancement is an important step in processing digital remote sensing images before we can start mapping the geomorphology. It improves the quality of the image and information content from the original images and brings out landform information hidden in the data. The most commonly used digital image processing tasks include contrast enhancement, edge enhancement, spatial filtering, band combinations, principal component analysis, and band ratios (Haldar 2018; Sreenivasan and Krishna Murthy 2018). Contrast enhancement expands the gray levels in the original data and brings about better contrast between closely resembling features and the background. For instance, the boundaries between the pediplain and pediments, and the paleochannel features which are difficult to discern in original data will get enhanced after applying contrast stretch to the satellite images, and enable extraction of these features in a more precise way. Spatial filtering and edge enhancement are more commonly used for sharpening the boundaries of features and enhancing linear features like lineaments and structures, which have controlled the formation of the geomorphic forms.

Band combinations are more pertinent when using multi-spectral data involving number of bands and diverse information content being provided by image at each wavelength band. The usually used band combination is standardized and is called False Color Composite (FCC) which has combination of Infrared, Red, and Green image bands given the colors of Red, Green, and Blue in the RGB color model, and has been extensively used for landform identification and mapping (Fig. 1.1). FCC is considered standard as it has been found to give the maximum information of the earth's surface features compared to the natural color composites (Haldar 2018). This is also because the land cover is prominently brought out in the standard FCC. The geomorphology has a significant influence on the land cover pattern of an area and is an important guiding factor in differentiating landforms.

However, band combinations with other image bands including Shortwave Infrared (SWIR), have given better information for specific landforms. A good example of this is the mapping of fluvial landforms such as flood plains, meander

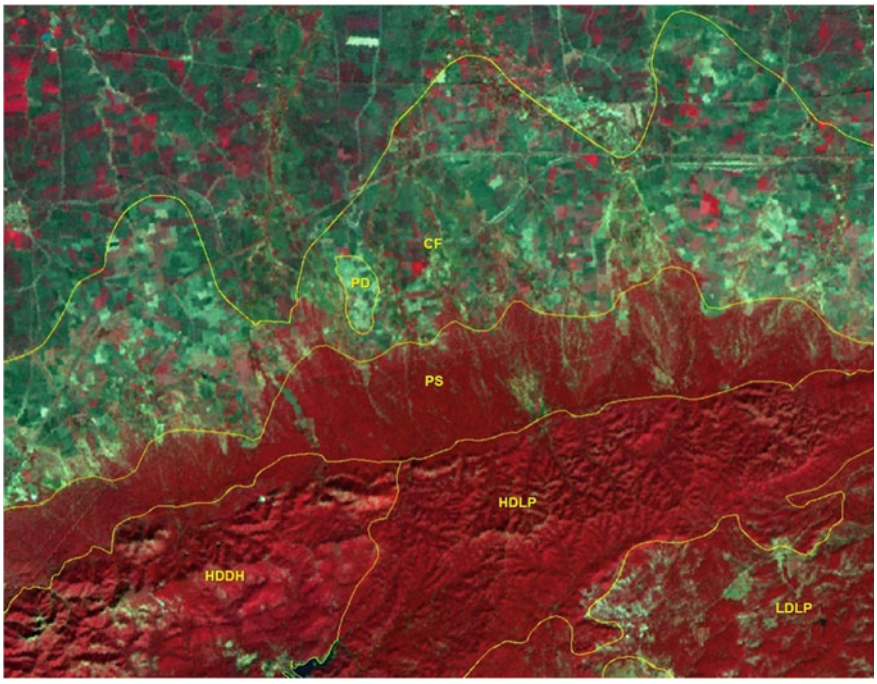

Fig. 1.1 Interpretation of denudational landforms from an area in Hoshangabad district of Madhya Pradesh from a standard False-color composite (FCC) derived from IRS-P6 LISS-III sensor with RGB: IR, R, G. The landform labels are: CF-colluvial fan, PS-piedmont slope, PD-pediment, HDDH-highly dissected denudational hill, HDLP-highly dissected lower plateau, LDLP-low dissected lower plateau

scars, and point bars (Fig. 1.2). The reason for better contrast of the fluvial landforms in the color composite images with SWIR as one of the bands is that these landforms usually contain more moisture than background, and get highlighted by contrastingly darker tones because of extreme absorption in SWIR wavelength in the presence of water content (Tian and Philpot 2015).

Image enhancements such as principal component analysis (PCA), and the color composites generated from the first few principal components (PC) bring out perceptible contrast in landforms, depending on the terrain and geomorphic landscape being mapped. An example of a PCA generated and the color composite of first, second and third PC in RGB for mapping the Quaternary geomorphic units is shown in Fig. 1.3. Good differentiation of alluvial fans formed over the different periods is contrastingly brought out in the images. This helped in detailed mapping of the different alluvial fans formed in the region, and this could further be an important input for morpho-chronological sequencing of the alluvial fans.

The selection of the right season of satellite data is very important in geomorphological mapping as this has a bearing on the interpretability of the landform features. The selection of the right season satellite data is dependent on several factors, like

Fig. 1.2 Use of SWIR band in deriving a color composite highlights the fluvial landforms along the Tawa river in Madhya Pradesh. The color composite is derived using SWIR, IR, and Red bands were given to RGB. The landform labels are: PB-point bar, NL-Natural levee

the target landforms, the topography of area, and the land cover pattern. Though it is a well-accepted practice to use summer season data for interpreting geomorphic features, it may not be always true.

In general, it is observed that certain landforms are better discernable on a particular season data, whereas some landforms get subdued. Some landforms may be better discernable using data of summer season, for e.g., the palaeochannels, whereas some other landforms may be better discernable using winter season data, for e.g., the denudational landforms, as demonstrated by the example shown in Fig. 1.4. Therefore, it is desirable to use multi-temporal satellite images spanning across two or more seasons of the year to derive complimentary information, which may be missing in a single dataset.

After image enhancement, the extraction of geomorphology information is done using various techniques ranging from manual on-screen digitization using the GIS software to semi-automatic and automatic techniques using rule-based classifiers. Though more research is now toward quantitative geomorphology, however, for preparing operational and baseline geomorphological maps for large areas, we still

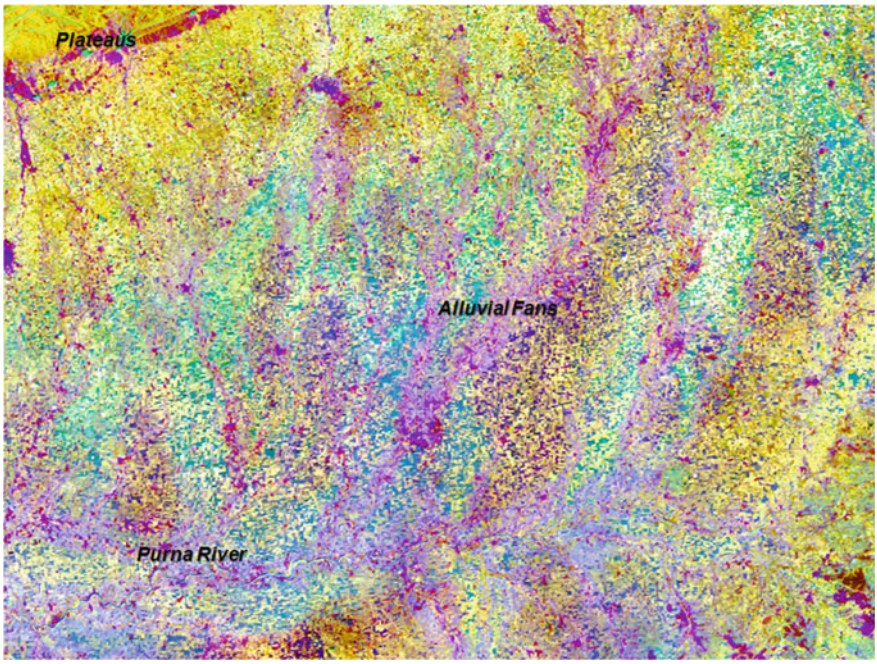

Fig. 1.3 Principal component analysis and the combination of the PC1, PC2, and PC3 in a color composite help in differentiation of alluvial fans formed over the different periods and is an input for morpho-chronological sequencing of the alluvial fans

continue to adopt on-screen interpretation of the landforms from satellite data, considering and integrating additional information derived from other terrain and natural resources datasets (GSI and NRSC 2010; Kumar et al. 2013; GSI 2014; Gnanachandrasamy et al. 2018; Sreenivasan and Krishna Murthy 2018). This process involves loading enhanced satellite images on the computer screens in any GIS package and carrying out digitization using the GIS tools. The interpreter is expected to have knowledge of geomorphology and skills in remote sensing image interpretation. The advantage of this approach is that the professional can use all his experience and intuitive knowledge about the area and modulate the information extraction accordingly.

Additional ancillary information including geology, geological structures, terrain, slope, drainage, and land use and cover in the form of GIS layers is usually overlaid for analysis and improvising the geomorphology mapping. Use of any supplementary data, such as geophysical data, will provide additional information on surface and sub-surface form, composition, and structure and will help in better deciphering the landforms and processes. Use of advanced techniques like object-based image analysis and machine learning-based classifiers are also being attempted. A broad process flow for preparation of geomorphological maps is given in Fig. 1.5. Description of advanced methods of geomorphology mapping is given in the further sections.

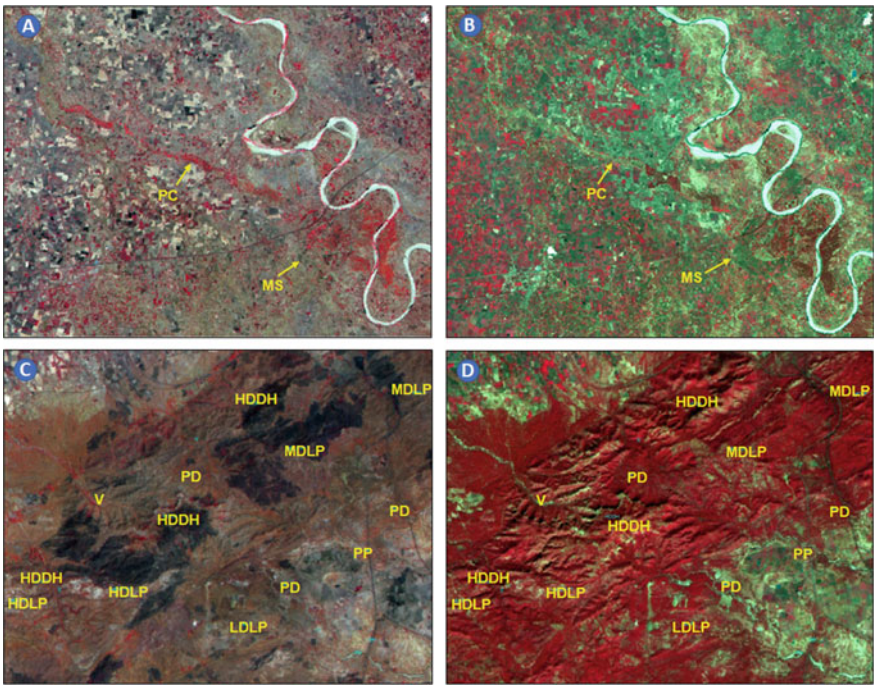

Fig. 1.4 Influence of time-period of satellite data on the interpretability of the landforms. The palaeochannel (PC) is seen very conspicuously in the satellite image of IRS Resourcesat LISS-III sensor of April month (A), whereas it is not interpretable in the satellite data of the same sensor acquired in December month (B). The meander scar (MS) is better interpreted in data acquired in December (B) than in the April (A). Similarly, the denudational landforms viz., highly dissected denudational hills (HDDH), highly dissected lower plateaus (HDLP), moderately dissected lower plateau (MDLP), low dissected lower plateau (LDLP), valley (V), pediment (PD), and pediplain (PP) are not interpretable from the satellite image of IRS Resourcesat LISS-III sensor of April month (C), whereas these landforms and the details like dissection pattern are very clearly visible in the satellite data acquired in December month (D)

1.3.2.1 Optical Remote Sensing

The remote sensing in optical region includes satellite data imaged in the visible and infrared regions, including SWIR and Thermal Infrared (TIR) wavelength regions. Presently, optical remote sensing data is available from a number of satellites and sensors, with varied spectral and spatial capabilities suitable for mapping geomorphology. The selection of the type of satellite/sensor data for mapping geomorphology can be made based on the type of terrain and features being mapped and the required scale of mapping. Satellite images having spatial resolutions from ~1 to ~188 m have been extensively used for mapping geomorphology at various scales of mapping ranging from 1:2 Million scales to 1:10,000 scale. For regional-scale geomorphological map preparation low spatial resolution data from ~188 to ~70 m

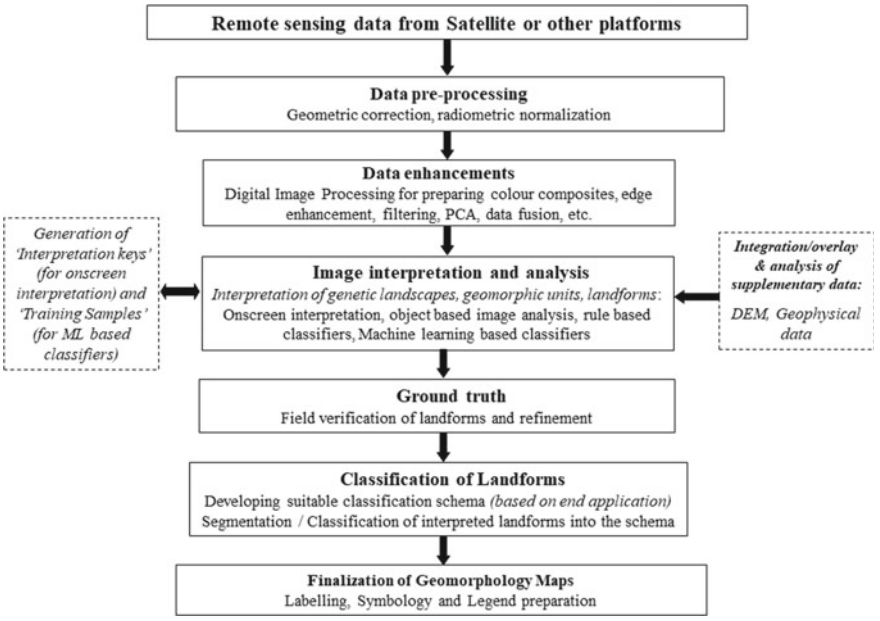

Fig. 1.5 Process flow for preparation of geomorphological maps using integrated geospatial technology

is ideal, and for preparing moderate scale maps satellite data with ~23 to ~10 m is useful, whereas satellite data of ~6 to ~1 m is ideal for detailed landform mapping for a small area for the purposes of micro-level developmental planning (Sreenivasan and Krishna Murthy 2018).

Indian Remote Sensing Satellite (IRS) provides Earth Observation remote sensing data at different spatial, spectral, and temporal resolutions with spectral dimensions covering entire EMR in the Optical region with a series of satellites starting from IRS-1A to the recent Resourcesat-2A and Cartosat series of satellite (Jaiswal and Bhatawdekar 2018) (Table 1.1). These satellite sensors provide images with spatial resolutions ranging from 1 km to better than 1 m, and radiometric resolution ranging from 7 to 12 bits. With flexible imaging capabilities, these data have been extensively used for geomorphology mapping at regional level to village level for detailed landform mapping. Additionally, a number of satellite sensors from other space-faring nations of the world are available for geomorphological mapping, providing remote sensing data at varied spatial and temporal resolutions (Table 1.1).

The spectral variability from visible, near-infrared to shortwave infrared has been fully exploited for different types of landforms detection. The selection of spectral bands for geomorphological mapping depends on the morphogenetic regime that is being mapped. Though usually the Green and Red wavelengths in the visible region, and the near-infrared wavelengths in infrared region of the EMR are suitable to map landforms sculpted due to most processes, certain wavelength bands are useful

Table 1.1 Optical remote sensing satellites-sensors available for geomorphology studies

Satellites	Sensor	Spatial resolution (in meters)	Revisit time (days)	Scales of geomorphology mapping
RESOURCESAT-1/2, IRS-1C/IRS-1D	LISS-III	23.5	5	1:50,000
RESOURCESAT-1/2	LISS-IV	5.8	5	1:25,000–1:15,000
RESOURCESAT-1/2	AWiFS	56	5	1:250,000
CARTOSAT-3	MX	1.12	–	1:5000–1:3000
CARTOSAT-2C, D, E, F	HRMX	~2.0	4	1:10,000–1:5000
CARTOSAT-1	PAN	2.5	5	1:10,000–1:5000
LANDSAT-9	OLI-2	30	16	1:50,000
LANDSAT-9	TIRS-2	100		1:500,000–1:250,000
LANDSAT-8	OLI-1	100	16	1:250,000
LANDSAT-8	TIRS-1	30	16	1:250,000
SENTINEL-3	OLCI	300	2–4	1:500,000–1:10,00,000
SENTINEL-2A/2B	MSI	10–20	5	1:50,000–1:20,000
SPOT-7	PAN	1.5	1–5	1:10,000–1:3000
SPOT-7	MS	6.0	1–5	1:25,000–1:12,000
PLANET LAB SKYSAT-C	MS	0.5	5	1:5000–1:2000
PLEIADES NEO-3/4	MS	1.2	Daily	1:5000–1:3000
PLEIADES 1A/1B	MS	2.0	Daily	1:8000–1:4000
KOMPSAT-3A	MS	2.2	1.4	1:10,000–1:5000
KOMPSAT-3	MS	2.8	1.4	1:15,000–1:10,000
WORLDVIEW-4/3	MS	1.24	<1	1:10,000–1:3000
WORLDVIEW-4/3	SWIR	3.70	<1	1:20,000–1:10,000
RAPID EYE	MS	6.5	1–5.5	
TERRA-ASTER	VNIR	15	16	1:50,000–1:25,000
TERRA-ASTER	SWIR	30	16	1:50,000
TERRA-ASTER	TIR	90	16	1:250,000
CBERS-4	MUXCam	20	26	1:50,000
CBERS-4	IRS	40	26	1:250,000–1:50,000
CBERS-4	WFI	64	5	1:250,000–1:150,000
SUPER VIEW-1	MS	2.0	2	1:8000–1:4000
QUICKBIRD	MS	2.62	1–3.5	1:10,000–1:5000
GEOEYE-1	MS	1.84	3	1:10,000–1:4000
GAOFEN-2	MS	3.2	5	1:20,000–1:10,000

(continued)

Table 1.1 (continued)

Satellites	Sensor	Spatial resolution (in meters)	Revisit time (days)	Scales of geomorphology mapping
TRIPLESAT	MS	3.2	Daily	1:20,000–1:10,000
IRS-1C/IRS-1D	PAN	5.8	5	1:25,000–1:12,000
LANDSAT-7	ETM + (V, NIR)	30	16	1:100,000–1:50,000
LANDSAT-7	ETM + (TIR)	60	16	1:250,000–1:150,000
IKONOS	MS	3.28	3–5	1:20,000–1:10,000
SPOT-5	MS-NIR/SWIR	10 (NIR)/20 (SWIR)	2–3	1:25,000–1:15,000
LANDSAT-4 & 5	TM (V, NIR)	30	16	1:100,000–1:50,000
LANDSAT-4 & 5	TM (TIR)	120	16	1:500,000–1:250,000
IRS-1A/IRS-1B	LISS-I	72.5	22	1:250,000–1:150,000
IRS-1A/IRS-1B	LISS-II	36.25	22	1:100,000–1:50,000
LANDSAT-1,2,3,4,5	MSS	60	18	1:250,000–1:150,000

for landforms formed due to specific agents and processes. For instance, shortwave infrared and mid-infrared in a combination with other bands are more suitable for mapping fluvial landforms, whereas, the thermal infrared may be of specific aid in mapping active volcanic landforms.

The temporal nature of satellite remote sensing is exploited in studying the dynamics of geomorphic processes and the resultant landforms. Each satellite sensor has a specific revisit period. As a virtue of this capability, the same site is imaged after a fixed time-period. Presently satellites are available with temporal resolution ranging from 1 to 22 days (Jaiswal and Bhatawdekar 2018). This enables monitoring of any change that is happening on the earth's surface. The time scale of change for different landforms vary, and range from tens and hundreds of years for denudational and depositional landforms to just few days for landforms formed due to endogenic processes like volcanism, diastrophism, and the events caused by their impacts like earthquakes, landslides, and change in river courses, and the natural disasters like floods and cyclones.

1.3.2.2 Radar Remote Sensing

The microwave region of the EMR provides additional advantages for remote sensing of geomorphology. Active sensors like Synthetic Aperture Radar (SAR) are more widely used for geomorphological mapping due to their high spatial resolution compared to the passive microwave sensors.

Apart from the general advantages of all-weather imaging, which is beneficial for all-natural resources applications, geomorphological studies especially benefit from the side-looking geometry of the Synthetic Aperture Radar (SAR) sensors and

also the sub-surface penetration capability of the SAR signals. The sensitiveness of radar backscatter signal to surface roughness, slope and relief, and moisture (dielectric constant) also are advantageous to geomorphologists in studying landforms, as these inherent properties of radar indirectly give information on the terrain structure and physical properties of surface material. These significantly indicate the type of processes the terrain has undergone in the past that led to the sculpting of the present landforms. The relief and slope, which are very important to perceive and label a landform are not directly sensed from the optical satellite images, whereas in the SAR images the side-looking geometry brings in the shadow effect, due to which the relative differences in relief and slope of the terrain gets clearly highlighted. Therefore, many times SAR data fused with optical data may be more useful in bringing out better contrast of geomorphic forms, than using only optical data of the same area (Fig. 1.6).

The sub-surface penetration capability of the radar is a function of frequency of the radar signal. The larger wavelength bands like L-band (15–30 cm) and P-band (30–100 cm) have better penetration to shallow depth-dependent on the dryness of the sub-stratum. Several active microwave remote sensing satellites are presently available like RISAT series from India, ALOS from Japan, ENVISAT and Sentinel-1 from European Union, Radarsat from Canada, Terra-SAR, and TanDEM-X from Germany, and KOMPSAT-5 from South Korea. Except ALOS all other satellites are C-Band or X-band SAR. Even though the penetration capability of C-band SAR is limited, still it has been used for geomorphology mapping as a standalone as well as complementary dataset along with the optical remote sensing data. SAR has been more advantageously exploited in geomorphology for mapping the shallow buried features such as paleochannels of lost river systems (Gupta et al. 2011). The penetration capability of SAR helps as well in mapping shallow buried pediments, and relict valleys in arid terrains (Fig. 1.7).

1.3.2.3 Digital Elevation Models

The terrain topographical information is important requirement for mapping geomorphology. In the initial days of the geomorphological mapping using satellite data, topographical information available from topographic contour maps was used as a reference dataset. Interpretation of remote sensing images for geomorphological classification is usually descriptive, while quantitative measurements, usually called morphometry, were added through field surveys. But with the development of the Digital Elevation Models (DEMs) and availability of GIS Spatial Analyst tools, DEMs are being directly used for analysis of terrain morphometric conditions, which directly benefits the geomorphic form and process study.

The first Digital Elevation Models (DEM), generated using the topographical maps derived through survey techniques, were available during 1970s. The first satellite-derived digital elevation data was available by the year 2000 with the availability of Shuttle Radar Topography Mission (SRTM) DEM. Presently there are various types of DEM's available from space platforms (Mudd 2020) developed

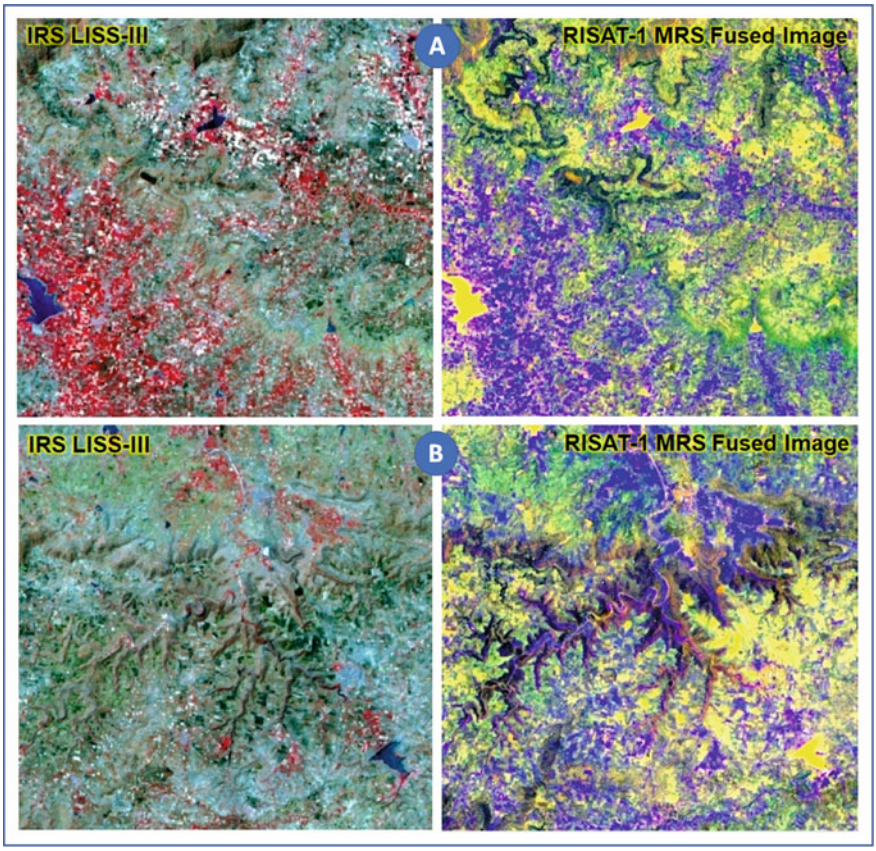

Fig. 1.6 Comparison of the landform interpretation from optical and microwave SAR satellite data. (A) The plateaus, plateaus margins, and scarps are better seen in the RISAT-1 MRS SAR data fused with multi-spectral optical data than the optical data alone from IRS LISS-III sensor. (B) The dissection pattern in the plateaus is more clearly highlighted in the RISAT-1 MRS fused microwave SAR data than in the IRS LISS-III image

through either optical stereoscopic data through photogrammetric techniques or through radar data through interferometric techniques. CartoDEM of 10 m resolution from ISRO, ASTER DEM of 30 m resolution jointly by Japan and USA, ALOS World 3D (AW3D and AW3D30) of 5 and 30 m resolution from JAXA, TanDEM-X of 12 m resolution from DLR Germany, MERIT DEM which is a combination of SRTM and AW3D30 of 30 m resolution are a few global DEMs useful for geomorphological studies (Mudd 2020).

The basic information used from the DEM in mapping landforms are the derivatives of DEM, viz., slope, aspect, and curvature. These are used for analyzing the morphometric conditions and dividing the land into discrete surface forms for quantitative depiction of land topography, which led to the development of the field

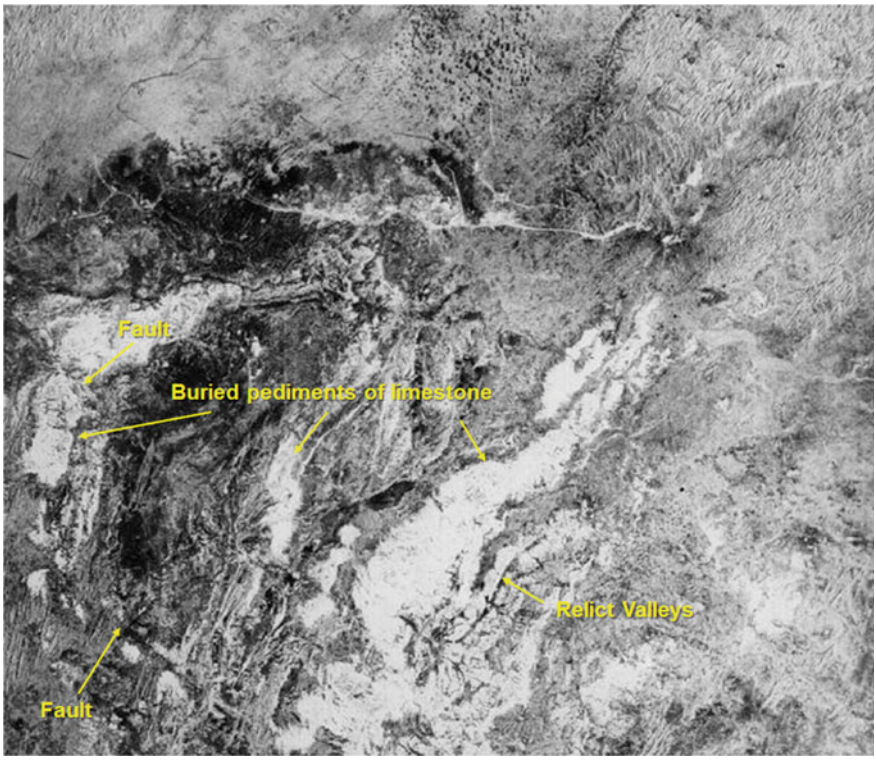

Fig. 1.7 Sub-surface penetration capability of SAR helps in bringing out shallow buried landforms. Here the buried pediments and sub-surface relict valleys in arid Thar Desert region are brought out conspicuously in the ALOS PALSAR L-band SAR data due to the penetration capability of the SAR

of geomorphometry (Napieralski et al. 2013). The landform morphometry data is mainly used for quantitative analysis of size and shape of the landforms, which helps in delimitation of the landscapes at higher level formed under a specific process, for example, the large fluvial landscapes, into smaller homogeneous land features which are then grouped together into landforms (Evans 2012).

Morphometric analysis of landforms using high-resolution DEMs is more applied aspect, than simply mapping the landforms, and has practical applications in several other areas. Geomorphometry of glacial cirque, for instance, could provide indications on the paleoenvironment and paleoclimate during the glaciation period during which the cirque has developed (Barr and Spagnolo 2015), and also be useful for hydrological modeling and natural hazard management (Mudd 2020). DEM is also utilized in geomorphological mapping as a DTM model for visualization of the terrain in 3D perspective for better assessment of the morphology of the landforms (Fig. 1.8), which would help in visualizing the landforms in 3D perspective, that will

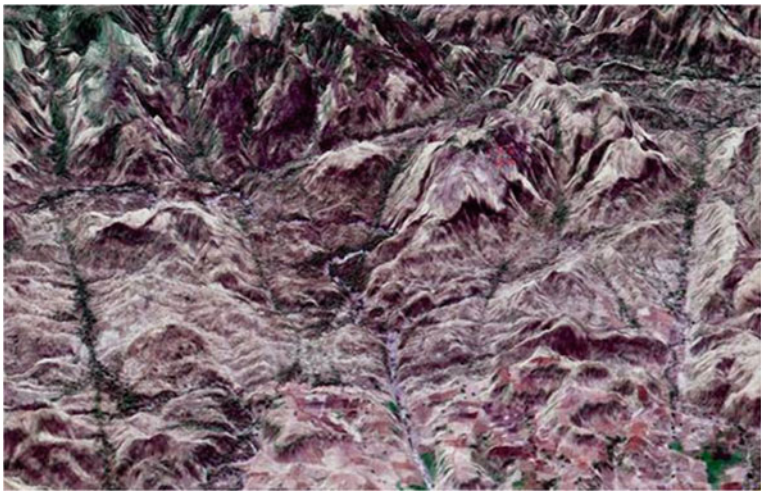

Fig. 1.8 Digital terrain model of an area in Amravati district, Maharashtra. The geomorphic forms, viz., the plateaus and constituent mesas and buttes, along with the structural controls, are better highlighted in the DTM

help in better identification of landforms and preparing geomorphology maps with better thematic accuracy.

1.3.3 Advanced Methods of Geomorphology Mapping

Geomorphology mapping from remote sensing has always been a challenging task. The visual interpretation of satellite images by referring to large number of other ancillary information layers on terrain characteristics, hydrology, land cover, vegetation, soils, geology, structures, etc. has been cumbersome and highly time-consuming job. It also involves an element of subjectivity, which depends on the knowledge and skill of the professional who is carrying out the mapping. Another aspect that needs consideration is that the landform boundaries are not discrete, but are mostly transitional, this is more so for landforms in plains than in mountainous terrain (Eisank et al. 2010; Napieralski et al. 2013). These challenges and limitations are now being overcome with the advancements in remote sensing technology and image analysis techniques. These include availability of very high-resolution image datasets and DEMs from satellite, UAV platform, and LiDAR technology; and image analysis techniques such as object-based classifiers, machine learning algorithms, and data-driven approaches for semi-automatic and automatic mapping of geomorphology.

With the availability of different resolution DEMs, more efforts are presently seen to exploit the terrain segmentation using object-based classifiers. The terrain factors are optimized using other parameters like texture metrics which go as input

to rule-based classifiers or decision tree classifiers (Na et al. 2021). The LiDAR is the other technology that is being used for tectonic geomorphological analysis and specifically geomorphometry of micro-geomorphic units. Specifically, the DTM that is generated from LiDAR and other optical and radar remote sensing datasets are useful in precisely limiting the boundaries of geomorphic units (Bufalini et al. 2021), which otherwise are arbitrary if they are drawn from mere remote sensing image interpretation in the optical or microwave domains.

Another comprehensive tool for geomorphological applications that provides hyper-scale three-dimensional (3D) landform models is the structure from motion (SfM) photogrammetry, which is an amalgamation of techniques from photogrammetry and computer vision (Eltner and Sofia 2020). SfM provides very high-resolution topographic dataset with high temporal frequency and accuracies comparable to airborne laser scanners, and thus gives detailed topographic characterization of the surface to the extent of distinguishing micro-geomorphic forms such as granite tors (Kasprzak et al. 2018; Eltner and Sofia 2020). The very high-resolution images from satellite and UAV platforms, high-resolution DEMs from LiDAR, optical and radar data, and SfM technologies separately or in combination are useful for automatic detection and morphological analysis of many other micro-geomorphic forms and processes, for instance, gully formation, their evolution, and monitoring for estimation of their sediment budget and susceptibility mapping (Arabameri et al. 2020; Niculiță et al. 2020), quantifying landform changes (Chirico et al. 2021), mapping coastal landforms and their dynamics (Medjkane et al. 2018; Taddia et al. 2019; Yulianto et al. 2019; Singh et al. 2020b), mapping glacial geomorphology (Benjamin et al. 2018). In the fluvial geomorphology domain, the Airborne Laser Topo Bathymetry (ALTB) has emerged as a new tool for high-resolution mapping of the 3D channel geometry, and erosion and sedimentation mapping, though ALTB is still not an operational remote sensing technique for regular geomorphological analysis (Laguea and Feldmann 2020).

Scale of landforms is an important parameter in selecting the appropriate datasets and classification approaches, which would bring in better accuracies in the final classified maps. Wavelet decomposition techniques such as Discrete wavelet transform (DWT) method are applied on DEMs for discretizing the terrain texture and further classifying the landforms using machine learning-based classifiers like Random Forest (Xu et al. 2021). These automatic landform classification techniques are able to bring in more accurate landform classification giving appropriate consideration to the scale of the landforms.

Recently, data-driven algorithms such as Direct Sampling and Random Forest (RF) are successfully utilized for semi-automatic regional-scale geomorphological mapping, especially for mountainous areas (Giaccone et al. 2021), where elevation and relief are important factors in defining the landform morphology. In addition to RF, other Machine Learning (ML) algorithms such as Support Vector Machines (SVM), Logistic Regression (LR) and Boosted Regression Trees (BRT), genetic algorithm (GA), extreme gradient boosting machine (XGBoost), and ensemble of ML algorithms are utilized for different applied aspects of geomorphology, for instance, landslide and debris flow susceptibility modeling (Pham et al. 2018; Kavzoglu et al

2019; Sahin et al. 2020; Xiong et al. 2020), and mapping gully erosion susceptibility (Arabameri et al. 2021).

Advancement in geospatial technology has also brought in new tools and methods for studying dynamics of landforms and monitoring landforms changes. The changes in landforms due to geomorphic processes may be very minor in scale most of the time, and therefore it had always been a challenge to detect and analyze these minor changes. The capability to measure and monitor surface topographical changes at different spatial and temporal scales has improved with the availability of advanced geospatial techniques such as Differential Interferometric Synthetic Aperture Radar (DInSAR), LiDAR and its elevation products, Differential Global Positioning System (DGPS), and UAV photogrammetry and SfM (Gutiérrez and Soldati 2018; Abdelkareem et al. 2020; Fedele et al. 2021). These techniques have been successfully used for geomorphic dynamics of volcanic fumaroles (Fedele et al. 2021), desert landforms (Abdelkareem et al. 2020), and coastal geomorphology (Medjkane et al. 2018; Godfrey et al. 2020).

The present trend is combining multi-source datasets including remote sensing images from satellite and UAV platforms, data from geophysical surveys such as Electrical Resistivity Tomography (ERT) and DEMs, through geospatial modeling and ensemble of Artificial Intelligence (AI) and Machine Learning (ML) algorithms for achieving mapping, monitoring and modeling of geomorphological landforms and processes (Metelka et al. 2018; Kasprzak et al. 2019; Chirico et al. 2021).

Though these advancements in geospatial technology have leapfrogged geomorphology mapping into more of an analytical and quantitative science, it is important to note that the traditional satellite image interpretation still remains the fundamental technique, due to the fact that geomorphology requires more intricate unraveling of the local details considering the connections with contiguous geomorphic ecosystems, for building a holistic form-structure-process relationship in a regional perspective, especially so for undertaking operational programs.

1.4 Classification Schemas

Development of geomorphological mapping in different countries followed systems of categorizing landforms considering mainly parameters such as morphology, morpho-structure morphogenesis, and morphochronology. The simplest form of landform classification used the morphology, which considered the form or shape of the landforms, and was based on descriptive morpho-graphic features. With the development of the modern concepts of geomorphology, the emphasis on including process or genesis of the landforms in detailed geomorphological maps took a place in the classification systems, whereas the morpho-structure was considered at the highest level of the classification in the small-scale geomorphology maps (Verstappen 2011).

The initial efforts of standardization of geomorphological maps were put by International Geographical Union (IGU) Commission on Geomorphological Survey and Mapping and detailed geomorphological mapping and legend for the International Geomorphological Map for medium scale geomorphological maps were published by a joint consortium of Italy, Poland, Russia, Italy, Germany, Canada, Netherlands, Switzerland, and Britain (Hayden 1986). These standards had emphasized the morpho-structure at the highest level as the basis of the geomorphological classification.

Later on, several geomorphological classification systems evolved. Some geomorphology classification systems were developed for addressing specific geomorphic landscapes, for instance, geomorphic classification for "fluvial geomorphic landscapes" specifically targeting the rivers and streams (Kondolf et al. 2016; Horacio et al. 2017); "standardized geomorphic classification for seafloors" (Goes et al. 2019; Sowers et al. 2020), classification of wetlands (Grenfell et al. 2019). While some other geomorphic classifications systems were developed aiming specific applications, for instance, characterizing forest ecological map units, groundwater prospects identification, landslide hazard zonation, river system management, digital soil mapping, to name a few. One such geomorphic classification was developed during 1995–1998 by the USDA Forest Service. The main purpose of this classification system was to link the ecological unit as well as the aquatic units with the "National Hierarchical Framework" of USDA (United States Forest Service 1998). This classification system considered four components, viz., "Geomorphic Process, Landform, Morphometry and Geomorphic Generation". Another geomorphologic classification system has been developed aimed at "geopedologic mapping" and "digital soil mapping". In this classification system, the "geoforms" are hierarchically structured into six nested levels, giving emphasis to structure of the landscape and morphogenic agents (Zinck 2016).

In India, few attempts have been made to bring out a regional classification system addressing all the aspects of the landform evolution initially by Geological Survey of India (GSI) and later by ISRO (GSI and NRSC, 2010; GSI 2014; Srivastav et al. 2021). The geomorphological mapping carried out by ISRO under the Integrated Mission for Sustainable development (IMSD) during 1992–1996 adopted the hydrogeomorphic-based classification approach (NRSA 1995). The mapping schema lay prominence on identification of landform units with end utility of the maps for groundwater exploration. The legend of these maps depicted structure and lithology apart from the geomorphic units and landforms. The schema was based on the origin of the landforms and the processes were arranged in chronological sequence. This classification schema was further modified under the National Natural Resources Information System (NRIS) program initiated by ISRO during 1998 (Shah and Thakkar 2008). This program developed a geomorphological classification schema that put geomorphic units at the first level, landform at the second, and form based on morpho-structure at the third level. The system is conceptualized in a way to regroup the landform classes at different levels for easy upscaling or generalization.

Another effort for developing a national-level geomorphic classification was made under the Rajiv Gandhi National Drinking Water Mission, which was for the specific

application of applying geomorphology for groundwater prospect zones mapping. This classification system categorized the landforms into 116 types considering morphology, weathering, erosion, and dissection (Das et al. 2021). The classification system considered the broad physiography at the first level categorizing the landscape into hills, plateaus, piedmont zones, plains, and valleys. At the second level, the geomorphic unit is considered which is segmentation of the units at first level based on the form, structure, and process, for example, plains at the first level are segmented into eolian plains, flood plains, alluvial plains, etc. At the third level, the units are further categorized into landforms considering the amount of weathering or deposition, or dissection.

A national classification system was developed by GSI, specifically, targeting the Quaternary Geology and Geomorphology of the entire country (GSI and NRSC 2010). The mapping addressed all major river basins of the country. The classification schema was genetic in nature and had geomorphic units and landform units at first and second levels.

Though several geomorphological classification systems in the country partly tried to include the process and genesis of landforms in the schema, however, the first national-level genetic classification system for geomorphological mapping in India was prepared by Geological Survey of India (GSI), the national nodal agency which carries out geological mapping in India, for preparing the geomorphological maps of India on 1:2 M scale. Later, the National Natural Resources Management System (NNRMS) of ISRO under the Standing Committee on Geology and Mineral Resources (NNRMS SCG), discussed the importance of a common standardized national-level genetic geomorphological classification system, and an inter-agency working group of national-level organizations involved in geological and geomorphological studies was constituted to finalize a comprehensive genetic geomorphological classification schema covering all geological provinces of the country (Srivastav et al. 2021). During 2009, the 14th NNRMS SCG meeting of ISRO and 44th Central Geological Planning Board (CGPB) meeting of GSI approved the proposal of national-level geomorphological mapping at 1:50,000 scale using the newly developed comprehensive genetic hierarchical system of landform classification (GSI and NRSC 2010). The genetic aspect is addressed at the first level of this classification system, the broad morphology (geomorphic form) is addressed at the second level and the landform is addressed at the third level. This classification system has categorized the landforms into 11 genetic classes at the highest level and comprises 417 landforms at the lowest level (NRSC 2012a; Singh et al. 2015).

The significant aspect of most of these classification schemas is that they follow a hierarchical system, with broad level to detailed level of landforms representation, thus providing the flexibility to collapse classes at the lower levels to higher levels for regionalization of the geomorphology maps.

1.5 Applications of Geomorphology Mapping

The science of geomorphology has been strongly linked with various applied fields of geology, mineral exploration, geoengineering, hydrology, soil sciences, natural resources management, disaster management, and many more. Since ages geomorphology is being used, directly or indirectly, as an important scientific input integrated with inputs from other fields such as geology, hydrology, soil science, ecology, biological sciences, etc. in providing solutions to several pragmatic problems faced by the society, for example, for Disaster Risk Reduction (DRR), and for planning and management of natural resources and infrastructure. The applications of Geomorphology have now evolved as a separate field called the "Applied Geomorphology" which mainly deals with the applications of geomorphology to the society (Meitzen 2017).

In the following sub-sections, some of the major applications of geomorphology are discussed.

1.5.1 Applications of Geomorphology in Disaster Risk Reduction

Disaster Risk Reduction (DRR) is defined as the "concept and practice of reducing disaster risks through systematic efforts to analyze and manage the causes of disasters, including through reduced exposure to hazards, decreased vulnerability of people and property, sustainable management of land and the environment, and improved preparedness for adverse events" (ISSAT 2020). DRR is sometimes interchangeably used with Disaster Risk Management. Sendai Framework for Disaster Risk Reduction 2015–2030 clearly states the goal and importance of DRR which includes implementation of technological measures for preventing and reducing the disaster hazard and increasing preparedness for response and recovery (UNISDR 2018).

Most of the natural hazards are linked to the exogenic and endogenic processes prevalent on the earth's surface and within, therefore having a strong link with geomorphology. Thus, understanding and management of most natural hazards require knowledge of the landforms or the processes that have acted or presently acting in formation of these landforms. For instance, the occurrence of floods, which are the most prevalent natural hazard all over the world, are affected by the river channel morphology, the geomorphology of the flood plains, and the overall basin morphology. Many times, the local geomorphology plays a major role in causing seasonal floods in some rivers. A study was carried out for assessing seasonal flooding in Shivnath River in Rajnandgaon district of Chhattisgarh state. These floods unusually affected a localized stretch of the Shivnath River. It was observed that elevation profile of the area did not play any significant role in causing these floods as the entire area was almost plain with not much variation in the relief. Interpretation of the high-resolution satellite data and geospatial integration showed that specific

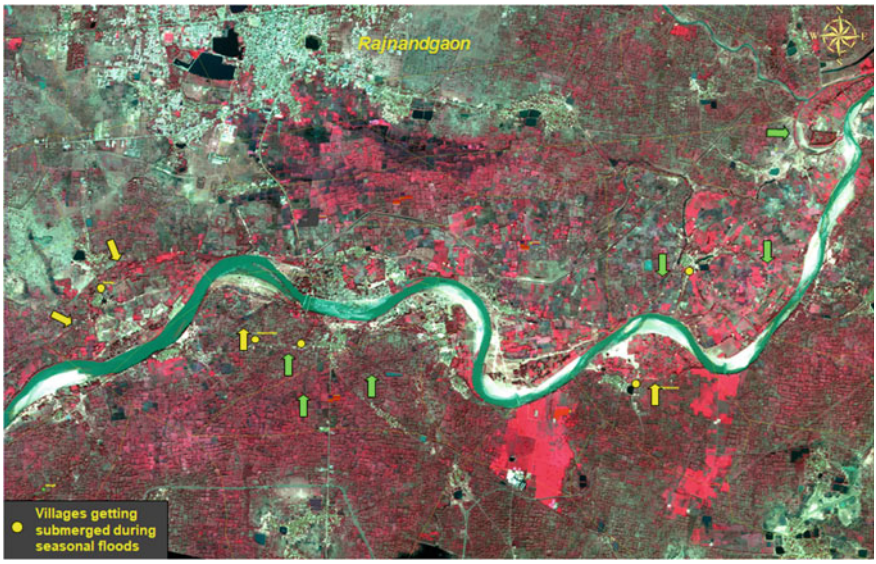

Fig. 1.9 Analysis of the seasonal floods along the Shivnath River in Rajnandgaon district of Chhattisgarh. The fluvial landforms, viz., the meander scars, shown by the yellow-colored arrows and the palaeochannels, shown by the green arrows have caused localized floods along these tracts due to heavy seasonal rainfall leading to the submergence of villages

landform features such as palaeochannels (PC) and cut-off meanders (CM), and the channel morphology in this part of the river were leading to flooding during the peak monsoon period (Fig. 1.9). The villages located on these cut-off meanders and palaeochannels were getting inundated due to floods regularly. But the field conditions never indicated presence of PC and CM, until the multi-spectral satellite image could decipher these features. These geomorphological studies helped in suggesting mitigation measures to the district administration in controlling the occurrence of floods in the future.

Flood hazard zone maps are an important tool for flood risk preparedness. These provide geospatial advisories on most likely areas that could get affected during floods. The high-resolution topographic information goes as an essential input for preparing flood hazard maps. High-resolution satellite data-derived river configuration and bank erosion time series products are highly useful for river engineering studies for mitigating floods.

Geomorphology has a critical role in landslide process and therefore is essential input for preparedness and mitigation of landslides. Geomorphology is one of the critical parameters in the landslide hazard modeling, for preparing landslide hazard zone maps showing landslide-prone areas as well as in preparing mitigation action plans for taking corrective measures against landslides. The landslide hazard zone mapping using the geospatial techniques carried out by NRSC, ISRO in collaboration with other national-level institutes is an excellent application of geomorphology for

landslide hazard zonation mapping along the major tourist and pilgrim routes in the states of Uttarakhand and Himachal Pradesh states (NRSC 2012b). The landslide hazard maps thus prepared are hosted on ISRO-NRSC Bhuvan portal (https://bhuvan-app1.nrsc.gov.in/bhuvandisaster/#landslide), an example of which is shown in Fig. 1.10.

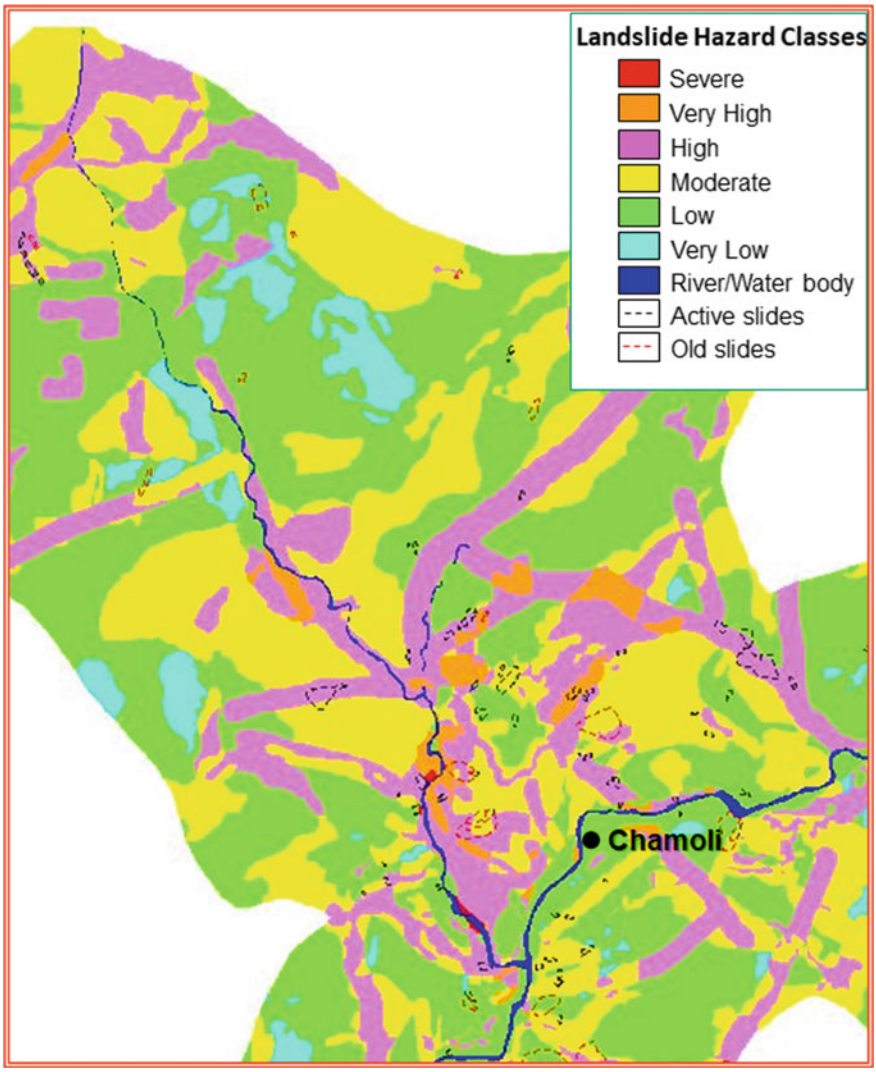

Fig. 1.10 Landslide hazard susceptibility map for part of the Rishikesh-Rudraprayag-Chamoli-Badrinath sector of the pilgrimage and tourist routes in the Himalayas prepared using geospatial modeling of multi-thematic information including geomorphology and terrain data. *Source* https://bhuvan-app1.nrsc.gov.in/disaster/disaster.php?id=landslide_monitor

Fourteen terrain factors, including causative and triggering factors, were modeled using AHP techniques to derive landslide hazard (susceptibility) maps. Geomorphology, slope angle, aspect, and morphology were the important factors apart from lithology and rock weathering, geological structures, drainage, land use-cover, and soil parameters. These maps have an immense utility for governmental and non-governmental agencies for disaster preparedness. Apart from use in preparation of landslide hazard maps, geomorphology is useful in analyzing past landslides, evaluating debris flows to characterize the rheology of the flow material based on the surface morphology studies, analyzing the study of boulder morphology, and understanding the weathering, and chronology which would help in assessing the probable period by which these boulders will detach and flow down the slope (Kellar et al. 2020).

1.5.2 Geoengineering Applications

Engineers consider a holistic and inclusive approach considering the geology (includes lithology as well as structures), geomorphology, and soil properties for site assessment for any geoengineering project. Study of landforms in a project site will supply several critical information on the processes that have acted on the site and provide information on the much-required terrain aspects like elevation profile, slope, and the broad idea on the composition of the surface and sub-surface material. In a way, geomorphology offers the baseline information, which will guide the geo-engineers for taking up any further detailed site-specific studies. According to Hearn (2019), geomorphological assessment in geoengineering is useful in providing three major functions, viz., first, understanding of sub-surface ground conditions, second, influence of geomorphological processes such as fluvial processes, and third, impact of the landform dynamics due to natural or anthropogenic processes on the geoengineering projects. Several geoengineering applications apply geomorphology in this perspective.

Study of patterns of landform change is especially an important aspect for many engineering mega-projects. Identification of active landslides and slope instabilities could be possible by study of time series high-resolution remote sensing images from satellite and UAV platforms, and using the high-resolution DEMs generated either through optical stereo photogrammetry or through LiDAR (Keller et al. 2020).

River channel morphological studies, involving study of river planform, cross-sections, and their dynamics, are an important input for planning, designing, and maintaining water resources projects requiring construction of river engineering structures such as bridges, dams, and reservoirs, and channel construction for diversion of surplus waters. The river morphological studies can give solutions to unique problems such as changes in river courses, severe erosion of banks by hill streams, development of natural cut-off in meandering streams, morphological changes in a river due to changes in its base level, etc. encountered during the engineering planning of river-linking projects. A major project on inter-linking of rivers has been taken up

in India to link Indian rivers by a network of reservoirs and canals with the purpose of proper management of water resources, to enhance irrigation and groundwater recharge, reduce incessant floods in some parts of the country and droughts in other parts. The National Water Development Agency (NWDA) in India has taken up planning of River Link Projects across the country considering major inputs from river morphological studies. An example of one such application is the river morphological studies carried out for Par-Tapi-Narmada link project, which envisages diversion of surplus water available in the west-flowing rivers between Par and Tapi of south Gujarat and neighboring Maharashtra for utilization of water in the drought-prone Saurashtra and Kutch regions of North Gujarat (Bothale 2013). Under this study, river morphology mapping and analysis have been carried out for Par, Auranga, Ambika, and Purna rivers to study the river planform, tortuosity, sinuosity, analysis of meanders, and thalweg. The meander dynamics indicated 29 prominent meanders, and the morphological studies showed that these rivers developed most of these meanders in the initial phase due to structural control, but depicted few meanders after reaching planes (Fig. 1.11) The hypsometric analysis indicated mature stage of these rivers basins. The rivers did not show any change in planform during the period of 1975–2010 owing to hard rock through which the rivers flow. The study results illustrated the possible potential changes that would take place in the hydrology and its potential impact on the geomorphology and ecology of the area.

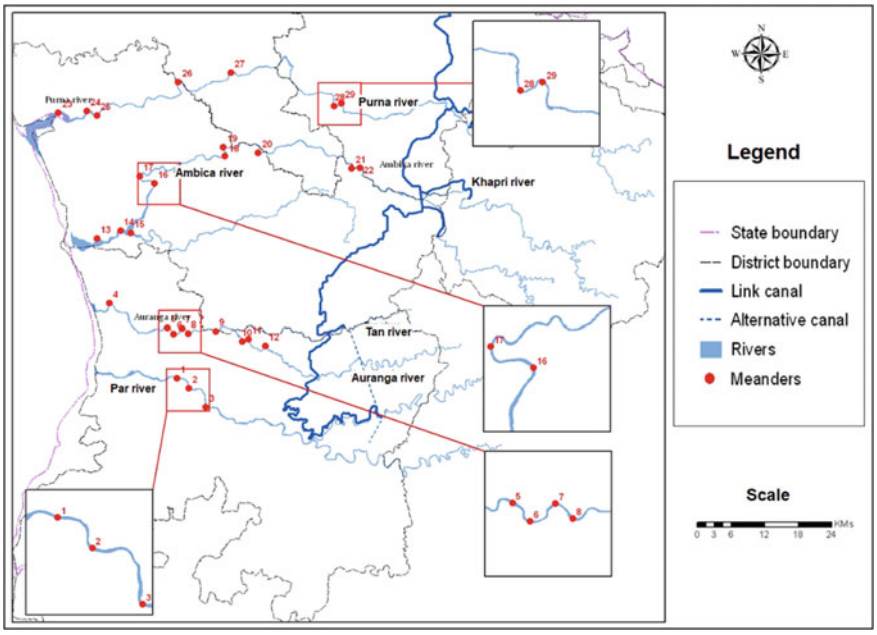

Fig. 1.11 Meander dynamics mapped used multi-temporal satellite data as a part of River morphology studies for Par-Tapi-Narmada river link project. *Source* Bothale (2013)

Engineering planning for new road and railway line alignment is a complex problem requiring through analysis of the terrain. Most roads and railway line alignments follow stipulated criteria to follow suitable gradients and also look into the aspect of terrain stability. This brings up the primary requirement for identifying the high topographic forms such as hills and plateaus using high-resolution remote sensing data and their morphometric analysis through use of DEMs. This information is mainly used for excluding such areas if possible, and if not possible, then for making analysis on the volume of cut and fill, or assessing the length of tunnels, if they need to be constructed.

These terrain-geomorphic analyses have a great bearing on the safety and sustainability of the proposed roads and railway lines, and also effects the cost of the entire project. For this, geomorphological studies conducted using multi-temporal high-resolution satellite data will help in identifying and mapping specific problematic areas with frequent mass movements and landslides, areas with karst landforms, fluvial landscapes with highly dynamic river courses prone to frequent changes in stream courses. The maps thus generated can be used in the geospatial modeling for rule-based exclusion of these areas for delineating suitable alignments for roads and railway lines. Detailed studies on geomorphic history will also aid in analysis of the surface materials and their properties.

The study carried out for railway line alignment in Akot–Amlakhurd Railway Section of South-Central Railway (SCR) in states of Maharashtra and Madhya Pradesh is a good example of using terrain-geomorphic information in such projects. Figure 1.12 is an output of integrated geospatial modeling using inputs from detailed terrain-geomorphic and geo-structural analysis showing one of the suitable alignments out of many alternate alignments for the Akot–Amlakhurd Railway Section. The work was carried out under a study for Akola–Khandwa Guage Conversion Project of SCR (Prakasa Rao and Sreenivasan 2012). Similar application of geomorphological studies is also implemented for deriving the best suitable road route for connecting Dumro and Same basti in the state of Arunachal Pradesh (Singh et al. 2019). The geomorphology and the terrain information has been used for mapping mass movements and landslide hazardous zones and used as the criteria in the road route alignment.

Apart from above-mentioned geoengineering applications, other applications of geomorphology in geoengineering include analysis for dam construction sites, selection of sites for hydro-power, coastal engineering, etc.

1.5.3 Geomorphology for Mineral Exploration Applications

Mineral deposits are generally associated with unique geo-structural environments, which leave a conspicuous imprint on the surface in the form of specific morphological expressions. The study of landscape characteristics may indicate the large geological structures which control the occurrence of mineral deposits. Some mineral deposits are directly associated with specific types of landforms, for instance, the

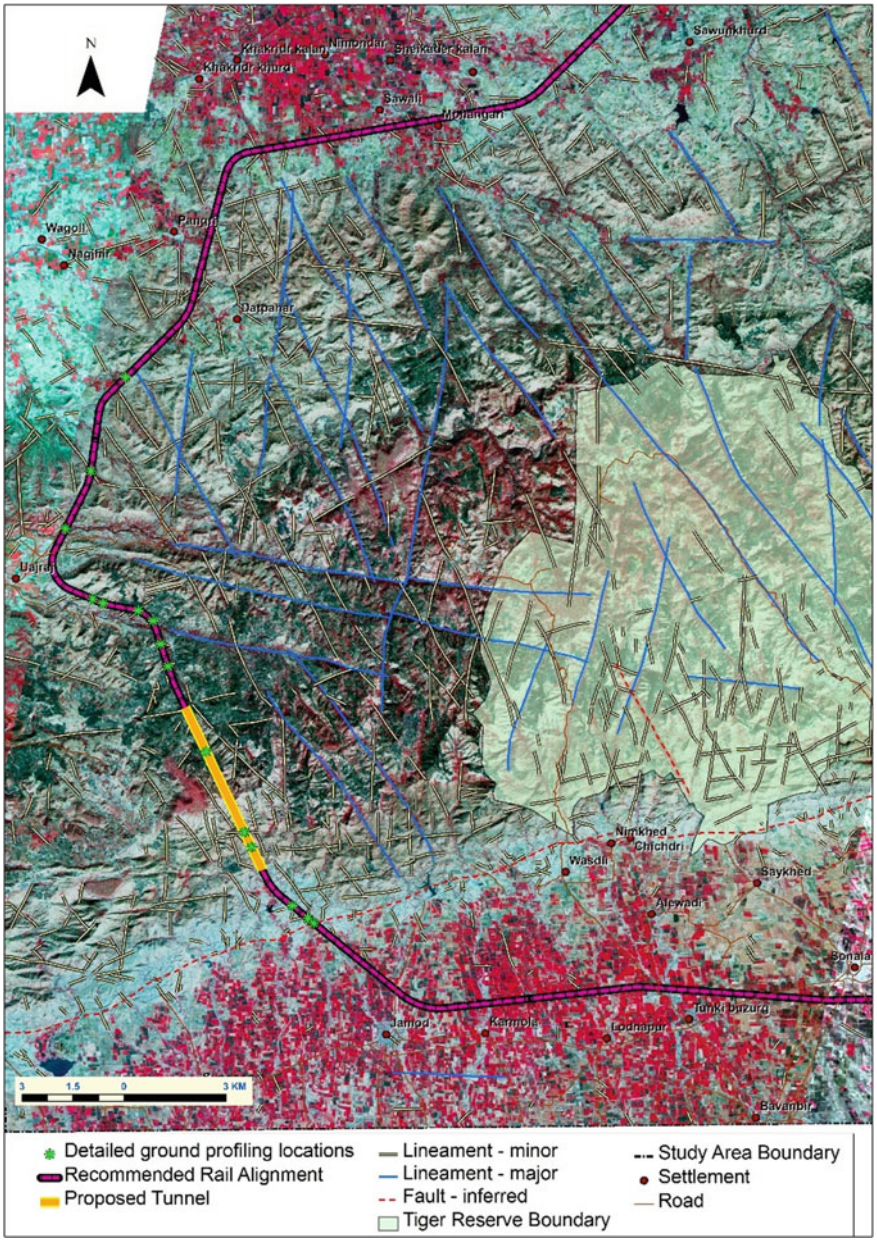

Fig. 1.12 Output of integrated geospatial modeling using inputs from detailed terrain-geomorphic and geo-structural analysis showing one of the suitable alignments out of many alternate alignments for the Akot–Amlakhurd Railway Section in part of Maharashtra-Madhya Pradesh

residual bauxite deposits are mostly associated with residual capping on plateaus, and therefore these landforms may form an indication for narrowing down the area as a first step in mineral exploration of these deposits.

Understanding regolith is important for mineral exploration in regions where no bed rock is exposed. Knowing the distribution of these regolith landform units and their origin is crucial for any kind of successful geological mineral exploration work (Metelka et al. 2018). Regolith geomorphic units could be prospective zones for mineral deposits of nickel, cobalt, chromium, tin, gold, copper, and rare earth elements. Regolith landform mapping and understanding the processes that formed these landforms is important during the initial steps of mineral exploration, where usually narrowing down to prospective area and target identification for further detailed delineation of ore deposits happens (González-Álvarez et al. 2016).

According to Chardon et al. (2018) landform-regolith mapping and palaeo-landscape studies can guide in the mineral exploration for interpreting geochemical anomalies on pediments, identifying the source of regolith material in case of transported regoliths, and probing for the ore beneath the pediments. However, integration of geomorphology with other datasets on geochemistry and geophysics is required for more detailed analysis of the landscape geochemistry and the processes involved in the geochemical dispersion.

Some ore bodies are expressed as topographic forms due to outcrops of gossans or landforms such as fault scarps formed due to geological structures. Some ore deposits, like gold deposits, may be associated with large quartz veins and reefs. These quartz reefs are expressed as ridges due to their resistance to weathering compared to the background rocks. Geomorphology mapping brings out these positive topographic indicators of the ore deposits.

The geomorphic anomalies useful in mineral exploration may be categorized into micro or mega in scale. Micro-geomorphic anomalies have great significance in exploration of some mineral deposits. An excellent example of use of micro-geomorphic anomaly is seen in case of diamond exploration. Specific micro-geomorphic anomaly is an important parameter, along with other lithological-structural data, for geospatial modeling to delineate probable zones for occurrence of kimberlite pipes hosting the diamonds. Especially with the availability of high-resolution satellite images, it has become possible to easily identify and map these micro-geomorphic anomalies, which are termed circular anomalies. The importance of these micro-geomorphological anomalies has been demonstrated in identification of potential zones for kimberlites in the Panna and Tikamgarh area of Madhya Pradesh state (Sreenivasan 2011) (Fig. 1.13). The potential zone maps derived from the geospatial modeling using the micro-geomorphic anomalies along with other litho-structural information are useful guides for carrying out detailed field geochemical sampling for diamond prospecting.

There are certain other micro-anomalies, which are not to be called direct geomorphic anomalies but are most of the time related to specific landform features. An example of this is the hydrocarbon micro-seepage, which has greater probability of occurrence in swamp landforms (Januadi Putra et al. 2018).

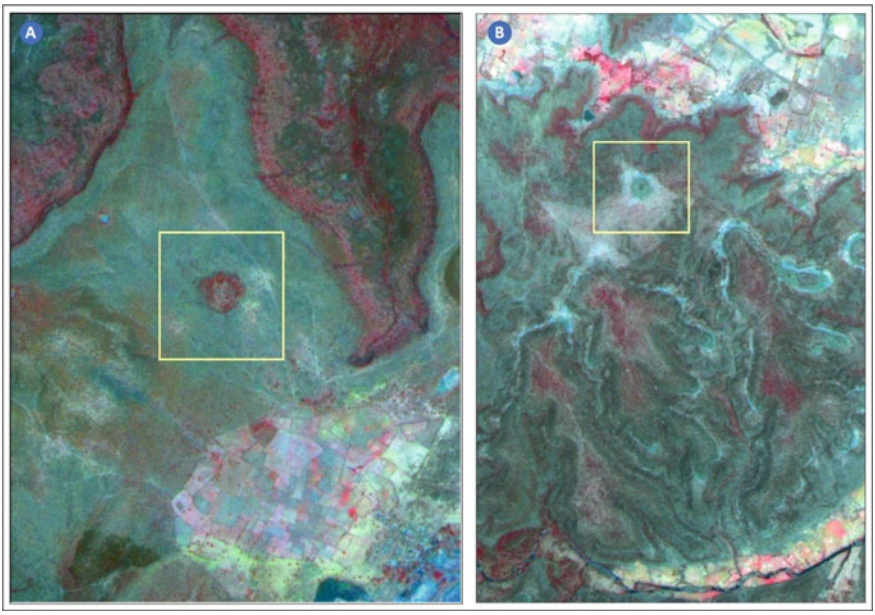

Fig. 1.13 Micro-geomorphological anomaly (circular anomaly) observed on IRS high-resolution satellite in Panna area of Madhya Pradesh. (A) Circular anomaly (within yellow box) of a verified kimberlite pipe (B) Circular anomaly (within yellow box) in a virgin mineral prospecting area indicating probable kimberlite pipe

Mega scale geomorphic anomalies are used extensively in deciphering large subsurface geological structures for identification of traps which are potential areas for hydrocarbon (oil and gas) deposits (Mazumdar et al. 2018). These geomorphology maps depicting the mega geomorphic anomalies form the baseline information in case of hydrocarbon exploration for identifying favorable zones for exploration through geophysical surveys like seismic and other techniques. In some cases, the seismic geomorphology anomalies indicating bowl-shaped geometry give a lead for identifying potential areas for hydrocarbon occurrence in off-shore areas (Chenin et al. 2021).

The geomorphological processes have an important role in formation of placer mineral deposits. Placer deposit is an accretion of valuable minerals by the process of gravity separation from specific primary host rocks by the geomorphological processes of weathering, erosion, movement, and accumulation in favorable zones. Understanding these geomorphological processes and the resulting landforms have led to discovery of some of the important placer mineral deposits of the world. Placers are formed of heavy minerals and those which resist weathering. Placer deposits could be alluvial or fluvial, i.e., formed due to fluvial transportation; colluvial, those formed by transportation by gravity and deposited on slopes and piedmonts; coastal or beach placers found to occur on sea beaches or on the shores of large inland lakes; aeolian formed due to wind action of deflation, concentration and

accumulation; or eluvial, those weathered materials that get deposited at the point of formation (Haldar 2018; Harald 2018). Placer deposits are commonly formed of minerals such as gold, gemstones like diamond, rutile, monazite, and zircon, platinum group minerals (most commonly platinum, rhodium, iridium, and palladium), cassiterite, wolframite pyrite, magnetite, and ilmenite. India has some of the major beach placer deposits such as Manavalkurichi, Kudiraimozhi in Tamil Nadu, Chavara in Kerala, Kakinada in Andhra Pradesh, Gopalpur, Rushikulya, Chatrapur in Orrisa, and Ratnagiri in Maharashtra (Rao et al. 2018; Mohapatra et al. 2019; Singh et al. 2020a). Palaeo-drainages are is also a potential source for placer mineral deposits, the mineral resources potential mainly depending on the dimension of the landforms and their provenance. Uranium mineral deposits, in some cases, are associated with the paleochannel landforms (Keeling 2007; Rao et al. 2015).

The study of sub-marine geomorphology plays significant role in the exploration of minerals in the seafloor. Several valuable minerals are associated with the oceans such as Manganese nodule deposits and massive sulfide deposits (Peukert et al. 2018). Sea floor morphological analysis helps assessment of the extent and thickness of the sub-marine mineral deposits, and also favorability of the terrain for mining.

1.5.4 Application of Geomorphology in Groundwater Exploration

The occurrence and movement of groundwater in the sub-surface is mainly controlled by many terrain parameters including the geology, viz., the type of lithology and geological structures, the geomorphology, and the hydrological characteristics of a terrain. Though the conventional technique of groundwater exploration usually happened through field surveys, and later through ground geophysical surveys, with the advent of the space remote sensing, techniques for targeting groundwater and finding prospective sites have developed into a new application. Especially, the hydrogeomorphology approach for groundwater exploration evolved and became popular with use of remote sensing-based groundwater targeting techniques.

Hydrogeomorphology approach brings in a relation between geomorphic-landform processes, the geological-lithology, and the hydrology-surface and sub-surface water. Though lithology—the sub-surface rock formations—give information on the porosity and permeability, quantifying and using these parameters for direct mapping of groundwater potential zones has limitations and involves extensive field surveys and laboratory analysis. Apart from this, by merely using the lithological information, we miss out on vital information on the weathering and the active geomorphic processes that have acted on the primary litho-units and modified its primary water-bearing aquifer parameters. Another factor that is overlooked in the lithological approach is the terrain slope conditions, which is very essential parameter controlling the flow of surface water and recharging of groundwater aquifers. It is also important to consider that, many times the sub-surface rock formation has

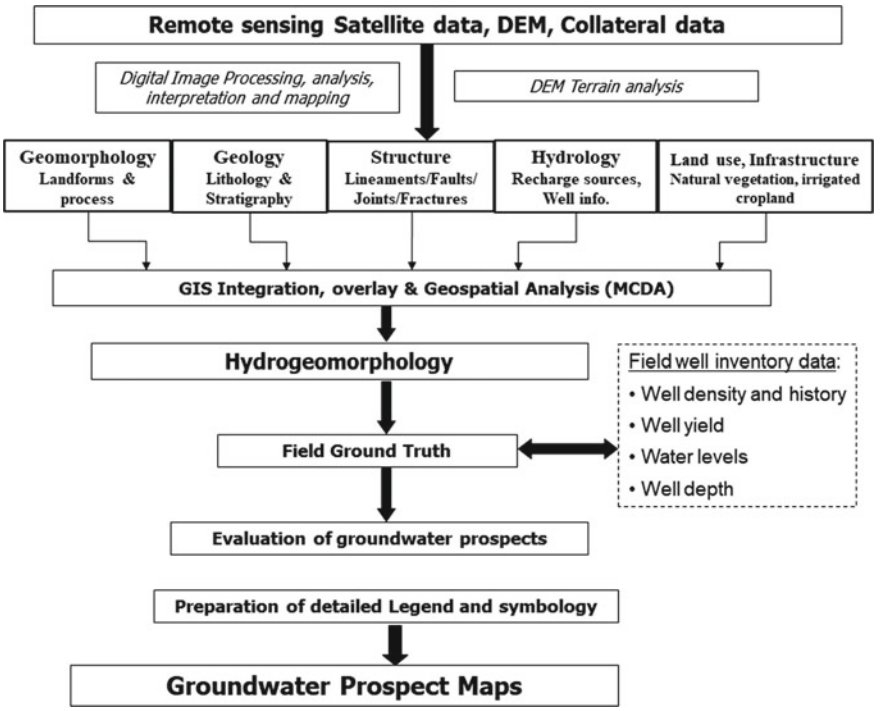

Fig. 1.14 Broad process of hydrogeomorphology approach for groundwater prospecting

the potential to hold groundwater, but the surface hydrology lacks in providing the source of water for percolation to the sub-surface. All these arguments are overcome by considering the interdisciplinary hydro-geo-morphological approach of ground water exploration. The broad process of hydrogeomorphology approach for groundwater prospecting is given in Fig. 1.14. Several studies have been carried out for groundwater exploration using integrated geospatial technology, and geomorphology has always been an indispensable parameter used in most of these applications (Silwal and Pathak 2018; Oyedele 2019; Shah and Lone 2019; Anbarasu et al. 2020; Avtar et al. 2020.

The most versatile application for the hydrogeomorphology-based groundwater targeting completed recently is the national-level groundwater prospects mapping for entire India. The work is carried out under the Rajiv Gandhi National Drinking Water Mission (RGNDWM) by NRSC, ISRO for the erstwhile Department of Drinking Water and Sanitation (DDWS) under the Ministry of Rural Development (MoRD), Govt. of India (presently under the Ministry of Jal Shakti) (Das et al. 2021).

In this work, the hydrogeomorphic units have been derived by systematic integration of the thematic layers on geomorphology, lithology, geological structures, hydrology, and base features interpreted from digital IRS satellite data. The hydrogeomorphic units delineated have been evaluated for their groundwater prospects

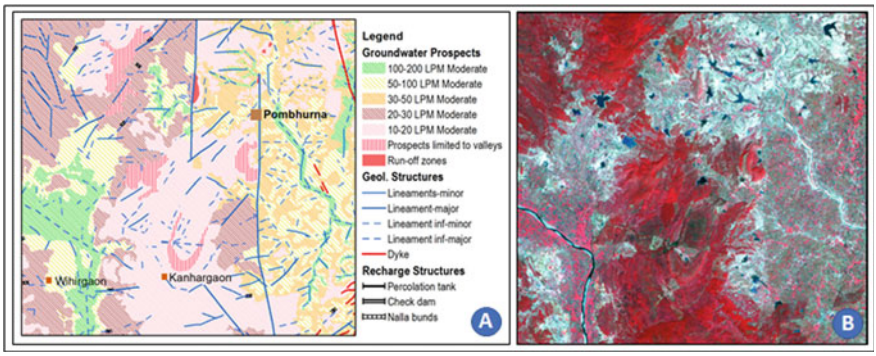

Fig. 1.15 Example of groundwater prospect map prepared using hydrogeomorphology approach. (A) Groundwater prospect map for part of Chandrapur district of Maharashtra (B) IRS LISS-III satellite image of the corresponding area

by integrating well inventory data on well yield, depth, and water levels collected from various field sources. The hydrogeomorphic units have been further utilized for suggesting sites for groundwater recharge by estimation and analysis of the recharge conditions, considering terrain conditions, and analysis of the hydrology for the availability and adequacy of surface water either in the form of overland flow or base flow for harvesting. The project accomplished preparation of a total of 4898 groundwater prospects maps on 1:50,000 scale in different phases during 1999–2014 period for the entire country. These maps are used by the state government line departments for identifying relatively better groundwater prospect zones in the vicinity of the villages for conducting ground vertical electrical soundings for pinpointing sits for drilling wells and identifying sites for construction of groundwater recharge structures. A sample groundwater prospect map prepared using this approach is given in Fig. 1.15. The groundwater prospects maps for the entire country are available on the Bhuvan portal of ISRO (https://www.isro.gov.in/earth-observation/bhuvan-bhujal).

Development of new drinking water sources or augmentation of the existing reliable drinking water sources to provide long-term sustainability of water supply system is an important requirement in the light of the climate change, changing pattern of monsoon, and degradation of existing land and water resources. Programs such as Jal Jeevan Mission of the government of India with a plan to provide safe and adequate drinking water by 2024 to all households in rural India is an important initiative in consideration of these aspects. Large-scale geomorphological database will be highly useful in achieving the goals set in these government programs. With the availability of the very-high-resolution remote sensing data from the satellite and UAV platforms, updating the geomorphology to large-scale maps (1:10,000–1:5,000 scale) providing more detailed geomorphic information is now being taken up. These maps along with detailed geo-structural maps are facilitating the preparation of large-scale groundwater potential zone maps at village level, and also providing specific sites for taking up groundwater recharge structures. These maps will be highly useful in

preparing village-level water security plans for long-term sustainability of the water resources to the villages.

1.5.5 Palaeodrainage Studies

Palaeodrainage study is a specific application of geomorphology which refers to identification and mapping of palaeo-rivers or stream network that flowed in past but presently is buried by fluvial or aeolian deposits. The term palaeodrainage is sometimes used interchangeably with other terms like palaeochannels or palaeo-rivers. The geotectonic, geomorphological, and climatic processes have led to the loss of many large river networks that were active during the past in different parts of the world. Many of these palaeodrainage networks are seen in semi-arid and arid ecosystems, where climate along with other geomorphological processes has played a major role in carving these networks.

The study of palaeodrainage has wide applications in the field of palaeoenvironmental science, mineral exploration of placer deposits, groundwater exploration, archaeology, preservation of culture and heritage, and development of eco-tourism. Seeing the importance of the palaeodrainage networks, many studies have been carried out across the world by geologists and geomorphologists for deciphering and mapping the lost-rivers using remote sensing technology, for example, palaeochannels in Western Namibia of Africa (Paillou et al. 2020); Eastern Lybia (Paillou 2017); Mauritanian coast of Western Sahara (Skonieczny et al. 2015); Libiyan Desert (Francke 2016); western Mauritania (Paillou 2017) and others. As the palaeodrainage network is not visible on the surface, therefore the multi-spectral capability of remote sensing has played a major role in deciphering the palaeochannels, while other techniques like geophysical surveys, Ground Penetrating Radar, radiometric dating, etc. have been used for evidence building and verification of the palaeodrainage mapped from remote sensing data.

Several studies on palaeodrainage network in the Northwest India has been carried out by ISRO and many other organizations (CAZRI, CGWB, GSI, ONGC, BARC, and others). The palaeodrainage network in Northwest India has been famously linked by many to the lost Sarasvati River (Valdiya and Chatterjee 2018). Significant work on mapping this palaeodrainage network using integrated geospatial techniques has been carried out by ISRO (Gupta et al. 2003, 2011; Bhadra et al. 2009; Sharma et al. 2014; Sreenivasan et al. 2021). This was the first holistic study for mapping entire palaeo-Sarasvati river network in the Northwest India using integrated space-based remote sensing techniques and ground-based techniques. The study brought out entire course and network of the large river between the foothills of the Siwalik Hills and the Rann of Kachchh covering major part of the palaeo-Sarasvati basin covering almost 2 million sq km (Fig. 1.16).

The study analyzed multi-sensor, multi-temporal, multi-spectral, and multi-spatial remote sensing datasets (from Indian Remote Sensing satellites sensors and satellites of other countries including WiFS, AWiFS, LISS III, LISS IV, Landsat TM/ETM,

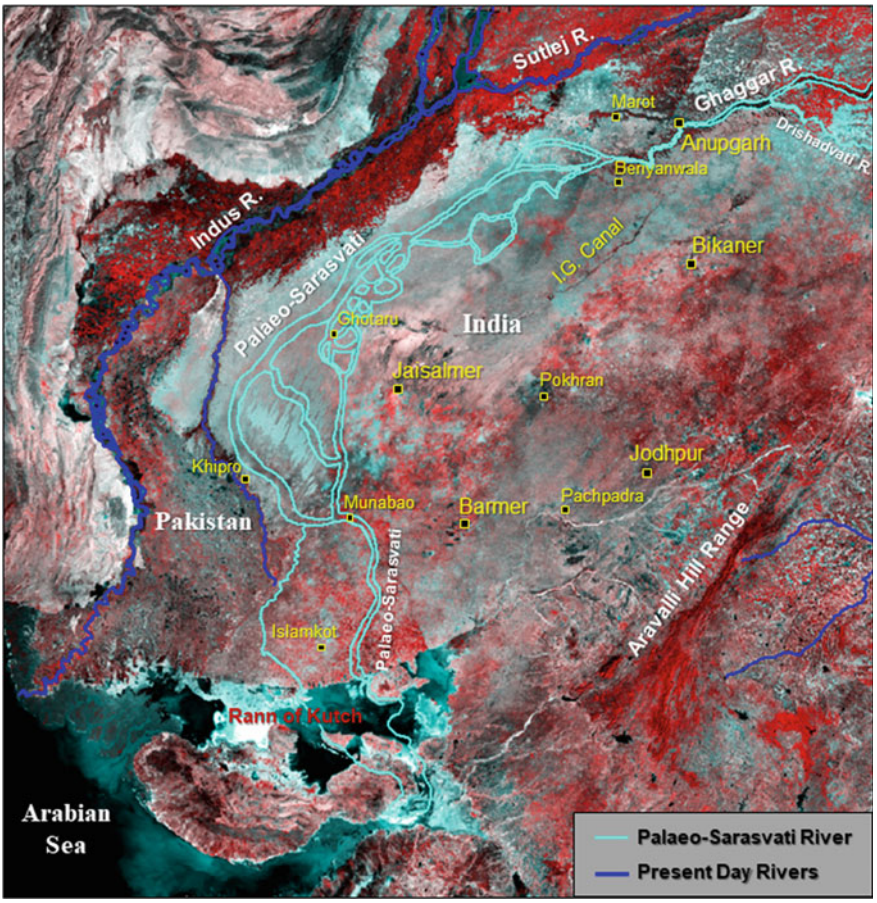

Fig. 1.16 Map of the palaeo-river Sarasvati in the Northwest India prepared using integrated geospatial techniques. *Source* Sreenivasan et al. (2021)

RISAT-1, and ALOS-PALSAR) through specific digital image enhancement techniques such as piecewise histogram stretch and arithmetic data merging, apart from other techniques like band combinations and principal component analysis. Unique signatures of the palaeochannels have been deciphered and integrated from large number of satellite image datasets for delineation of the palaeo-river course. The unique geomorphic signatures included distinct sinusoidal morphological patterns, drainage like patterns in darker tones due to presence of moisture (compared to the background dry aeolian material), vegetation anomalies in curvilinear channel pattern, meanders, and oxbow lakes like forms without presence of any active channels and the unique corncob shaped micro-geomorphic anomaly (Fig. 1.17). The course has been validated using various ground-based evidence including archaeological sites, ground exploratory drilling, hydrogeological analysis, sedimentary data

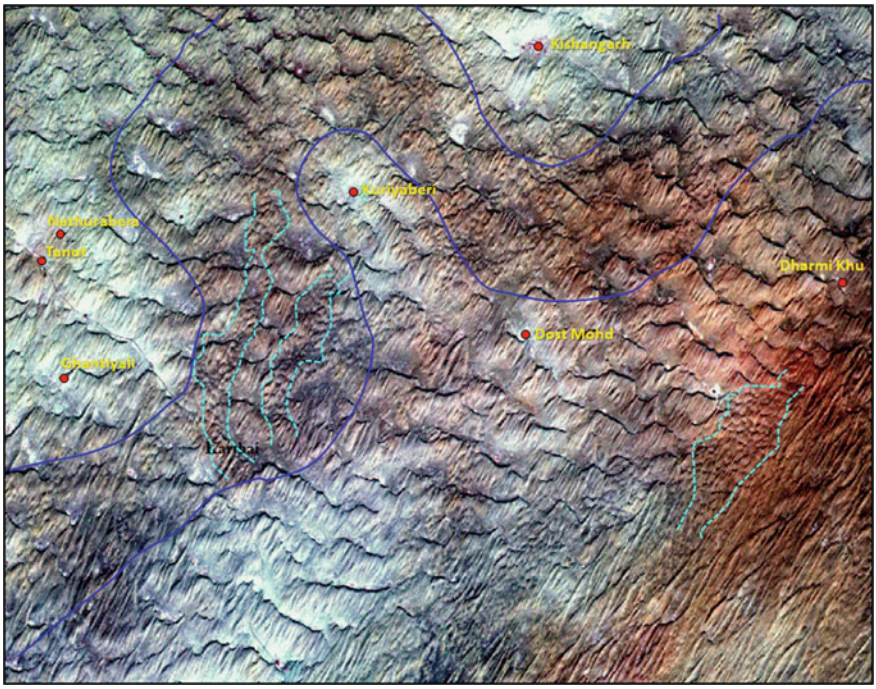

Fig. 1.17 "Corncob" micro-geomorphological anomalies (enclosed within dashed lines in cyan color) along the Palaeo Sarasvati River main-channel (enclosed within blue lines), which is one of the many conspicuous geomorphic signatures interpreted for mapping the palaeodrainage in the Northwest India

analysis, groundwater quality data along the paleochannels, dating of groundwater, and study of the "old maps of India".

The results of the palaeodrainage studies in Northwest India have several practical applications, some of which are already being exploited, whereas some have potential for taking up in future. Providing potable quality drinking water in the water-scarce Thar Desert region; delineation of new aquifers along paleochannels and their recharging; exploring for new archaeological sites and development of cultural heritage associated with mythological Sarasvati River; and exploring for placer deposits are a few potential applications.

The palaeodrainage studies of Sarasvati river system led to research by many groups for understanding the morpho-tectonics that the region has undergone in the past, and reconstructing the palaeo-environment of the period during which the river system was active. One model according to this analysis indicated that, formation or reactivation of an NNW–SSE trending "Yamuna Tear Fault" tore apart the Siwalik Hills which led to the displacement of the western fault block southwards relative to the eastern block and caused raising of the western block up by 20–30 m (Valdiya 2016). This caused blockage of the eastern branch of the Himalayan Sarasvati river

(the Tons river), leading to southwards deflection of this river through the greatly weakened fault zone and descending onto the plains to ultimately join the Yamuna, which later joins Ganga river at the Prayagraj (erstwhile Allahabad city) in Uttar Pradesh state of Northern India, to form the popularly known "Triveni Sangam". Later another tectonic event caused the western branch of the Himalayan Sarasvati river (the Satluj river) to deflect west at Ropar causing total deprivation of flow to the great Himalayan Sarasvati river (Valdiya 2016).

Similar palaeodrainage studies in other parts of the world also developed a good understanding of the tectonics of a region, the crustal deformation processes and the resultant river captures and flow reversals of major rivers, for example, the palaeo-Red River system of East Asia (Zhang et al. 2019). Palaeodrainage studies also helped in reconstructing the palaeo-environment and palaeo-hydrology of the palaeo-river basins as in case of southern Nefud desert of Northern Saudi Arabia (Breeze et al. 2015; Orengo and Petrie 2017).

1.5.6 Other Applications of Geomorphology

Apart from the major applications of geomorphology discussed in the above sub-sections, there are several other interdisciplinary applications of geomorphology, a few of which are briefly dealt with here.

The application of geomorphology in soil sciences is well appreciated. Geology and geomorphology impact the soil formation process, and to a great extent determine what type and composition would be the soils. The geomorphic parameters, viz., the morphometry, and morphography control the soil distribution units, whereas the morphogenesis and morphochronology control the soil formation processes. Therefore, all these four parameters of geomorphology are useful in soil mapping and delineation of soil units by providing information on relief, parent material, and age of the soils (Zinck et al. 2016). Soils vary in each geomorphic unit further modified by the climate, hydrology, and terrain slope conditions. Hence, geomorphology mapping is the first step in soil mapping. The geomorphic units delineated based on the processes provide the first level soil boundaries in soil map. The field survey for soil profiling also considers the geomorphic landscapes as the reference units. Therefore, geomorphology maps are critical base maps for soil mapping and survey.

Soil erosion studies are presently using geomorphology inputs to calculate soil erosion and sediment balances. In a method called "geomorphic change detection" difference of DEMs is computed to characterize topographic surfaces at different time periods, and assess the geomorphological changes in terrain surface. These inputs are used in a model to compare soil volume loss (Balaguer-Puig et al. 2018).

Geomorphology plays a significant role in coastal zone management applications. With long coastlines and major cities now located on the sea coast both in India and many other countries across the world, the importance of coastal zone management has ever increased for safeguarding the population living in the coastal towns and

villages, the marine life, as well as preserving the coastal ecosystem in an environmental perspective. Coastal zone is a very sensitive region for the reason that this is a triple junction of the ecosystem where land, ocean, and atmosphere interactions take place. Coastal geomorphology, which deals with the study of geomorphic units and landforms formed due to the actions of waves, tides, and fluvial systems connecting the coast, is an important applied field for management of coastal zones. Coastal zones are highly dynamic in nature, and that is a reason why study of geomorphic dynamics of the coasts is very important in applications of coastal zone management. The remote sensing, with the present availability of data of high spatial resolution and temporal frequency, is the most ideal technique for monitoring the coastal dynamics.

The coastal zones are continually impacted by the geomorphic processes of erosion, sediment transport, deposition, and sea-level changes. These processes continuously modify the coastline and the landforms. The analysis of shoreline changes and preparation of shoreline change maps on a regular basis helps in knowing the areas under continual erosion and those which are relatively stable. This is an essential information in planning any infrastructure within or nearer to the coasts (Nayak 2017). The maps of shoreline changes are also important for planning effective coastal protection measures for mitigation of natural hazards. Shoreline change and coastal landform maps were prepared by ISRO and are available at https://www.vedas.sac.gov.in. The long-time changes in shorelines due to geomorphological processes of erosion and accretion, along with many other parameters such as climatological data, predicted long-term sea-level rise and coastal topographical data on elevation and slopes has been applied for preparing coastal vulnerability maps for entire Indian coast (Kumar et al. 2010; Nayak 2017). These maps are being used as baseline information for coastal management during the cyclone and tsunami-like disasters.

Geomorphology has been applied in the field of anthropology and archaeology since decades for studying patterns of human settlements, the reasons for their migration, and for exploring new archaeological sites and related cultural features. There is a synchronous relationship between the earth's surface processes and the human settlement pattern. The human settlements have always developed considering fundamental factors such as availability of natural resources for survival, especially the water; and safety of the people from natural hazards. Both these factors are related to the geomorphic processes, which have been always very dynamic in nature. Many recorded episodes of migration of people were due to deprivation of the existing water resources or sometimes due to geohazards, for e.g., coastal inundation. The study of the present and past geomorphic processes will be helpful in analyzing such migration patterns.

Landforms mapping and analysis will help in identification of areas of high archaeological value (Biscione et al. 2018). Most of the ancient settlements have been found to occur near water sources like major rivers or coastal shorelines. Many of the discovered Harappan civilization towns have been found along the banks of the ancient rivers. Therefore, mapping paleo-fluvial landforms such as palaeochannels may help in exploration of new archaeological sites. For instance, the studies carried out on mapping palaeo-Saraswati in the Northwest India and the geospatial digital database

prepared under this work have provided new potential areas to archaeologist's for exploration (Gupta et al. 2011; Valdiya and Chatterjee 2018). The spatial analysis in GIS by overlay of the landform maps and the point database of available archaeological sites has also brought out the relationships between the palaeochannels and the already explored and proven archaeological sites (Gupta et al. 2001; Sharma et al. 2014; Sreenivasan et al. 2021). Archaeologists are also benefited by following geomorphic anomalies such as mound-like structures having specific spectral characteristics interpreted using high-resolution satellite digital data. These geomorphic anomalies may indicate buried ancient structures. The archaeological exploration in a virgin area is usually supported by first finding such geomorphic anomalies for conducting preliminary surveys for discovering an ancient site/monument, and later conducting more detailed surveys through GPR or other geophysical methods.

Preservation and conservation of archaeological monuments is another area where geomorphology may help, especially for monuments located in such landscapes which are prone to highly dynamic geomorphic processes. Like the natural landscapes, the monuments are also subject to the processes of weathering and erosion by natural agents of water and wind (Pope et al. 2002). Therefore, study of spatial and temporal variation of these processes may provide valuable information about how much impact these processes will have on the dilapidation of these monuments, which may help in preparation of more scientific management plans for preservation of these monuments.

Currently, the most important applied area of geomorphology is studying climate change, which incidentally is the most critical problem faced by the world today. The study of geomorphological processes and their imprints left on the earth's surface in the form of landforms and landscapes will provide valuable information on the changing climate. One such example is already provided in the previous section of this chapter while discussing the palaeodrainage studies. Palaeodrainage, in fact, is the best example of a geomorphic form and process, which helps us in understanding the climate that prevailed in the past and how it has changed to the present-day climate. The geospatial studies of the geomorphic units, and processes linked to these units, will enable building proxy records of climate, which will help in demonstrating variability of climate in short periods of decades to long periods of thousands of years (Keller et al. 2020). Examples of such geomorphic processes include the fluvial processes, wherein, a short-time and frequent change in river courses may indicate catastrophic flooding events which may be the impact of changing rainfall pattern due to climate change; or glacial processes, wherein presence of landforms like glacial cirques indicate former glaciation and detailed analysis of these landforms can provide vital information on the past temperatures, precipitation patterns, and wind directions (Barr and Spagnolo 2015). The study of dynamics of the landform changes may demonstrate the response of the landform to the past climate change, and this can give us an understanding of how it may respond to the future climate change that may be likely of greater dimension than in the past (Harrison et al. 2019).

1.6 Conclusions and Future Outlook

With advancements in geospatial techniques of remote sensing and allied techniques such as geographical information sciences, geomorphology mapping has evolved over the last few decades. The progression of remote sensing sensors from providing coarse spatial resolution to very fine resolutions, availability of high to very high-resolution DEMs from space and UAV platforms, and development of new data-driven techniques and algorithms of remote sensing data analysis has enabled mapping of smaller landforms, and capture more details of larger landforms, and is transforming the spatial analysis of geomorphic processes—progressing from qualitative to analytical and quantitative.

Application of geomorphology has made a great progress in several areas of interdisciplinary sciences. Many of these applications are very relevant in solving the intricate problems of society, serving the various areas of developmental planning, and is contributing to the national development. These include important areas of disaster risk reduction; geoengineering infrastructure development; groundwater development, conservation, and management; identification of potential zones for valuable minerals; discovering lost-rivers and new archaeological sites; coastal zone management, and several others.

As the baseline information of geomorphology on medium scales (1:50,000) is already available, the future of geomorphology is toward building large-scale geomorphology database of the country. It is more pertinent to address the dynamic landscapes initially and map them frequently on larger scales (1:10,000–1:5000). Research has already initiated toward more analytical aspects of geomorphology, though with smaller strides. The future will be more of analytical geomorphology with numerical analysis of the forms and processes, and their dynamics. Presently, geomorphology is less applied in crucial global problems such as climate change and other important areas of national importance like archaeology and culture. More awareness and growth of these applications of geomorphology in future is envisaged.

Acknowledgements The authors thankfully acknowledge the teams of scientists from NRSC and its Regional Centres who were associated with some of the works cited here. All literature cited in the text has been duly referenced and is duly acknowledged.

References

Abdelkareem M, Gaber A, Abdalla F, El-Din GK (2020) Use of optical and radar remote sensing satellites for identifying and monitoring active/inactive landforms in the driest desert in Saudi Arabia. Geomorphology 362:2020. https://doi.org/10.1016/j.geomorph.2020.107197

Anbarasu S, Brindha K, Elango L (2020) Multi-influencing factor method for delineation of groundwater potential zones using remote sensing and GIS techniques in the western part of Perambalur district, southern India. Earth Sci Inform 13:317–332. https://doi.org/10.1007/s12145-019-00426-8

Arabameri A, Blaschke T, Pradhan B, Pourghasemi HR, Tiefenbacher JP, Bui DT (2020) Evaluation of recent advanced soft computing techniques for gully erosion susceptibility mapping: a comparative study. Sensors 2020(20):335. https://doi.org/10.3390/s20020335

Arabameri A, Pal SC, Costache R, Saha A, Rezaie F, Danesh AS, Pradhan B, Lee S, Hoang ND (2021) Prediction of gully erosion susceptibility mapping using novel ensemble machine learning algorithms. Geomat Nat Haz Risk 12(1):469–498. https://doi.org/10.1080/19475705.2021.1880977

Asokan A, Anitha J, Ciobanu M, Gabor A, Naaji A, Hemanth DJ (2020) Image processing techniques for analysis of satellite images for historical maps classification—an overview. Appl Sci 10:4207. https://doi.org/10.3390/app10124207

Avtar R, Komolafe AA, Kouser A, Singh D, Yunus AP, Dou J, Kumar P, Gupta RD, Johnson BA, Minh HVT, Aggarwal AK, Kurniawan TA (2020) Assessing sustainable development prospects through remote sensing: a review. Remote Sens Appl Soc Environ 20:2020. https://doi.org/10.1016/j.rsase.2020.100402

Balaguer-Puig M, Marqués-Mateu Á, Lerma JL, Ibáñez-Asensio S (2018) Quantifying small-magnitude soil erosion: Geomorphic change detection at plot scale. Land Degrad Dev 29:825–834.https://doi.org/10.1002/ldr.2826

Barr ID, Spagnolo M (2015) Glacial cirques as paleoenvironmental indicators: their potential and limitations. Earth Sci Rev 151:48–78

Benjamin MP, Chandler BMP, Lovell H, Boston CM, Lukas S et al (2018) Glacial geomorphological mapping: a review of approaches and frameworks for best practice. Earth Sci Rev 185:806–846https://doi.org/10.1016/j.earscirev.2018.07.015

Bhadra BK, Gupta AK, Sharma JR (2009) Saraswati Nadi in Haryana and its linkage with the Vedic Saraswati River— Integrated study based on satellite images and ground-based information. J Geol Soc India 73:273–288

Biscione M, Danese M, Masini N (2018) A framework for cultural heritage management and research: the Cancellara case study. J Maps 14(2):576–582. https://doi.org/10.1080/17445647.2018.1517699

Bierman PR, Montgomery DR (2020) A brief history of geomorphology. In: Key concepts in geomorphology. Macmillan Higher Education, 2nd edn

Bothale RV (2013) Par-Tapi-Narmada Link Project—Morphological studies using remote sensing and GIS. Technical report no. NRSC-RC-Mar-2007-TR-615, Regional Remote Sensing Service Centre-Central, National Remote Sensing Centre, ISRO, Nagpur, India, p 71

Breeze PS, Drake NA, Groucutt HS, Parton A, Jennings RP, White TS et al (2015) Remote sensing and GIS techniques for reconstructing Arabian palaeohydrology and identifying archaeological sites. Quatern Int 382(2015):98–119. https://doi.org/10.1016/j.quaint.2015.01.022

Bufalini M, Materazzi M, Amicis MD, Pambianchi G (2021) From traditional to modern 'full coverage' geomorphological mapping: a study case in the Chienti river basin (Marche region, central Italy). J Maps 17(3):17–28. https://doi.org/10.1080/17445647.2021.1904020

Chardon D, Grimaud JL, Beauvais A, Bamba O (2018) West African lateritic pediments: landform-regolith evolution processes and mineral exploration pitfalls. Earth Sci Rev 179(2018):124–146. https://doi.org/10.1016/j.earscirev.2018.02.009

Chenin J, Silver C, Bedle H (2021) Seismic geomorphology anomalies within a Pliocene deepwater channel complex in the Taranaki Basin, offshore New Zealand. Interpretation 9:C1–C10. https://doi.org/10.1190/INT-2020-0037.1

Chirico PG, Bergstresser SE, DeWitt JD, Alessi MA (2021) Geomorphological mapping and anthropogenic landform change in an urbanizing watershed using structure-from-motion photogrammetry and geospatial modeling techniques. J Maps 17(4):241–252. https://doi.org/10.1080/17445647.2020.1746419

Das IC, Kumar KV, Rajasekhar D et al (2021) IRS-1C satellite data utilization for groundwater prospects mapping for the entire country under national rural drinking water program (NRDWP): a state of the art initiative. J Indian Soc Remote Sens 49:111–120. https://doi.org/10.1007/s12524-021-01308-7

Eltner A, Sofia G (2020) Structure from motion photogrammetric technique. In: Tarolli P, Mudd SM (eds) Developments in Earth surface processes, vol 23. Elsevier, Pages 1–24. https://doi.org/10.1016/B978-0-444-64177-9.00001-1

Eisank C, Dragut L, Gotz J, Blaschke T (2010) Developing a semantic model of glacial landforms for object-based terrain classification–the example of glacial cirques. In: Addink E, Van Coillie FMB (eds), GEOBIA 2010—geographic object-based image analysis. Ghent University, Ghent, Belgium, ISPRSXXXVIII-4/C7 Archives

Evans IS (2012) Geomorphometry and landform mapping: what is a landform? Geomorphology 137(1):94–106. https://doi.org/10.1016/j.geomorph.2010.09.029

Fedele A, Somma R, Troise C, Holmberg K, De Natale G, Matano F (2021) Time-lapse landform monitoring in the Pisciarelli (Campi Flegrei-Italy) Fumarole Field Using UAV photogrammetry. Remote Sens 2021(13):118. https://doi.org/10.3390/rs13010118

Francke J (2016) Mapping paleochannels in the Libyan Sahara with ground penetrating radar. In: International conference on ground penetrating radar (GPR), Hong Kong. https://doi.org/10.1109/ICGPR.2016.7572655

Giaccone E, Oriani F, Tonini M, Lambiel C, Mariéthoz G (2021) Using data-driven algorithms for semi-automated geomorphological mapping. Stoch Environ Res Risk Assess. https://doi.org/10.1007/s00477-021-02062-5

Gnanachandrasamy G, Zhou Y, Bagyaraj M, Venkatramanan S, Ramkumar T, Wang S (2018) Remote sensing and GIS based groundwater potential zone mapping in Ariyalur District, Tamil Nadu. J Geol Soc India 92;484–490. https://doi.org/10.1007/s12594-018-1046-z

Godfrey S, Cooper J, Bezombes F, Plater A (2020) Monitoring coastal morphology: the potential of low-cost fixed array action cameras for 3Dreconstruction. Earth Surf. Process Landforms 45:2478–2494. https://doi.org/10.1002/esp.4892

Goes ER, Brown CJ, Araújo TC (2019) Geomorphological classification of the benthic structures on a tropical continental shelf. Front Mar Sci 6:47. https://doi.org/10.3389/fmars.2019.00047

González-Álvarez I, Boni M, Anand RR (2016) Mineral exploration in regolith-dominated terrains: global considerations and challenges. Ore Geol Rev 73(2016):375–379

Gregory KJ, Goudie A (2011) Introduction to the discipline of geomorphology. In: Gregory KJ, Goudie AS (eds), The SAGE handbook of geomorphology. SAGE Publications. https://doi.org/10.4135/9781446201053.n1

Gregory KJ, Lewin J (2017) Introduction: concepts and geomorphology. In: The basics of geomorphology: key concepts. SAGE Publications. https://doi.org/10.4135/9781473909984.n1

Grenfell S, Grenfell M, Ellery W, Job N, Walters D (2019) A genetic geomorphic classification system for Southern African Palustrine Wetlands: global implications for the management of Wetlands in Drylands. Front Environ Sci 7:174. https://doi.org/10.3389/fenvs.2019.00174

GSI and NRSC (2010) Manual for national geomorphological and lineament mapping on 1:50,000 scale. Document No. NRSC-RS&GISAAERG-G&GD-FEB 10-TR149, National Remote Sensing Centre (NRSC), Hyderabad, India (prepared jointly by Geological Survey of India, GSI and NRSC)

GSI (2014) National geomorphological and lineament Mapping at 1:50,000 scale using satellite data. Unpublished Report, Geological Survey of India (GSI) (FS 2009–2014)

Gupta AK, Sreenivasan G, Sharma JR (2001) An attempt towards establishing interrelationship between palaeo-drainage courses and the archaeological sites found in the Sarasvati River basin, western Rajasthan. NNRMS Bulletin, No. 26, June 2001, pp 14–23

Gupta AK, Sreenivasan G, Sharma JR, Srivastava KS (2003) Confirming the presence of palaeochannels in western parts of Jaisalmer district, Rajasthan through integration of space and ground methods. Proc Indian Acad Sci 69A(2):231–239

Gupta AK, Sharma JR, Sreenivasan G (2011) Using satellite imagery to reveal the course of an extinct river below the Thar Desert in the Indo-Pak region. Int J Remote Sens 32(18):5197–5216. https://doi.org/10.1080/01431161.2010.495093

Gutiérrez F, Soldati M (2018) Landforms. In: Bobrowsky PT, Marker B (eds) Encyclopedia of engineering geology. Encyclopedia of earth sciences series. Springer, Cham. https://doi.org/10.1007/978-3-319-73568-9_181

Haldar SK (2018) Mineral exploration—principals and applications, 2nd edn. Elsevier Inc., Amsterdam

Harald DG (2018) Gems and placers—a genetic relationship par excellence. Minerals 8:470. https://doi.org/10.3390/min8100470

Harrison S, Mighall T, Stainforth DA et al (2019) Uncertainty in geomorphological responses to climate change. Clim Change 156:69–86. https://doi.org/10.1007/s10584-019-02520-8

Hauber E, Mège D, Platz T, Brož P (2018) Endogenic processes. In: Rossi A, van Gasselt S (eds) Planetary geology. Springer Praxis Books. Springer, Cham. https://doi.org/10.1007/978-3-319-65179-8_8

Hayden RS (1986) Geomorphology mapping. In: Short NM, Blair Jr R (eds), Geomorphology from space-a global overview of regional landforms, NASA SP (Series)-486, National aeronautics and space administration, scientific and technical information branch, Washington, DC, 1986, pp 637–656

Hearn G (2019) Geomorphology in engineering geological mapping and modelling. Bull Eng Geol Environ 78:723–742. https://doi.org/10.1007/s10064-017-1166-5

Horacio J, Ollero A, Pérez-Alberti A (2017) Geomorphic classification of rivers: a new methodology applied in an Atlantic Region (Galicia, NW Iberian Peninsula). Environ Earth Sci 76:746. https://doi.org/10.1007/s12665-017-7072-0

ISSAT (2020) Disaster risk reduction, preparedness and relief & the security sector. Technical Note, The International Security Sector Advisory Team, DCAF- Geneva Centre for Security Sector Governance, Geneva, https://issat.dcaf.ch/Learn/SSR-in-Practice/Thematics-in-Practice/Disaster-Risk-Response-and-SSR. Accessed on 23 Nov 2021

Jaiswal RK, Bhatawdekar S (2018) Indian earth observation program. In: Liang S (eds), Comprehensive remote sensing. Elsevier, 2018, Pages 280–298. https://doi.org/10.1016/B978-0-12-409548-9.10321-5

Putra J, Supriatna MI, Asriningum W (2018) Hydrocarbon Microseepage potential area exploration using sentinel 2 Imagery. E3S Web Conf 73:03021. https://doi.org/10.1051/e3sconf/20187303021

Jenson JR (2007) Remote sensing of the environment, 2nd edn. Pearson Prentice Hall

Kasprzak M, Jancewicz K, Michniewicz A (2018) UAV and SfM in detailed geomorphological mapping of granite tors: an example of Starościńskie Skały (Sudetes, SW Poland). Pure Appl Geophys 175:3193–3207. https://doi.org/10.1007/s00024-017-1730-8

Kasprzak M, Jancewicz K, Różycka M, Kotwicka W, Migoń P (2019) Geomorphology- and geophysics-based recognition of stages of deep-seated slope deformation (Sudetes, SW Poland). Eng Geol 260:2019. https://doi.org/10.1016/j.enggeo.2019.105230

Kavzoglu T, Colkesen I, Sahin EK (2019) Machine learning techniques in landslide susceptibility mapping: a survey and a case study. In: Pradhan S, Vishal V, Singh T (eds) Landslides: theory, practice and modelling. Advances in natural and technological hazards research, vol 50. Springer, Cham. https://doi.org/10.1007/978-3-319-77377-3_13

Keeling JL (2007) Cainozoic palaeochannel-hosted uranium and current exploration methods, South Australia. MESA J 46:34–39

Keller E, Adamaitis C, Alessio P, Anderson S, Goto E, Gray S, Gurrola L, Morell K (2020) Applications in geomorphology. Geomorphology 366. https://doi.org/10.1016/j.geomorph.2019.04.001

Knight J, Mitchell WA, Rose J (2011) Geomorphological field mapping. In: Smith MJ, Paron P, Griffiths JS (eds), Developments in earth surface processes, vol 15. Elsevier, pp 151–187. https://doi.org/10.1016/B978-0-444-53446-0.00006-9

Kondolf GM, Piégay H, Schmitt L, Montgomery DR (2016) Geomorphic classification of rivers and streams. In: Mathias Kondolf G, Piégay H (eds), Tools in fluvial geomorphology. Wiley, pp 133–158

Kumar KV, Mathew J, Martha TR, Guha A, Govindha Raj BK, Majumdar R, Roy PS (2013) Remote sensing applications using IRS data in geosciences. NNRMS Bull 37:116–122

Kumar TS, Mahendra RS, Nayak S, Radhakrishnan K, Sahu KC (2010) Coastal vulnerability assessment for Orissa coast, east coast of India. J Coastal Res 26(3):523–534

Laguea D, Feldmann B (2020) Topo-bathymetric airborne LiDAR for fluvial-geomorphology analysis. In: Tarolli P, Mudd SM (eds) Remote sensing of geomorphology. Developments in earth surface processes, book series, vol 23. Elsevier, pp 25–54. https://doi.org/10.1016/B978-0-444-64177-9.00002-3

Lopatin DV, Zhirov AI (2017) Geomorphology in the system of earth sciences. Geogr Nat Resour 38(4):313–318

Mazumdar S, Adhikari K, Mitra DS, Mahapatra S, Pangtey KKS (2018) Delineation of subtle and obscure structures in West Bengal Shelf: a remote sensing and GIS-based parallel approach. Curr Sci 115(5):874–885

Medjkane M, Maquaire O, Costa ST, Roulland T, Letortu P, Fauchard C, Antoine R, Davidson R (2018) High-resolution monitoring of complex coastal morphology changes: cross-efficiency of SfM and TLS-based survey (Vaches-Noires cliffs, Normandy, France). Landslides 15:1097–1108.https://doi.org/10.1007/s10346-017-0942-4

Meitzen KM (2017) Applied geomorphology. In Richardson D, Castree N, Goodchild MF, Kobayashi A, Liu W, Marston RA (eds) International encyclopedia of geography: people, the earth, environment and technology. https://doi.org/10.1002/9781118786352.wbieg0144

Merriam-Webster (2021) Geomorphology. In Merriam-Webster.com dictionary. https://www.merriam-webster.com/dictionary/geomorphology, Retrieved Nov 19 2021

Metelka V, Baratoux L, Jessell MW, Barth A, Ježek J, Naba S (2018) Automated regolith landform mapping using airborne geophysics and remote sensing data, Burkina Faso, West Africa. Remote Sens Environ 204(2018):964–978. https://doi.org/10.1016/j.rse.2017.08.004

Mohapatra R, Nayak B, Mangaraj M, Akella V, Behera P (2019) Mineralogical Characterisation of Beach Placers at Kantiaghar in Ganjam District Odisha. J Geol Soc India 93.https://doi.org/10.1007/s12594-019-1150-8

Mudd SM (2020) Topographic data from satellites. In: Tarolli P, Mudd SM (eds) Remote sensing of geomorphology. Developments in earth surface processes, Book series, vol 23. Elsevier, pp 91–128. https://doi.org/10.1016/B978-0-444-64177-9.00004-7

Mukhopadhyay SC (2003) Contemporary geomorphology: context and rationale. Natl Geogr J India 49(1):13–20

Na J, Ding H, Zhao W, Liu K, Tang G, Pfeifer N (20210 Object-based large-scale terrain classification combined with segmentation optimization and terrain features: a case study in China Trans GIS. https://doi.org/10.1111/tgis.12795

Napieralski J, Barr I, Kamp U, Kervyn M (2013) Remote sensing and GIScience in geomorphological mapping. In: Shroder J, Bishop MP (eds) Treatise on geomorphology, remote sensing and gioscience in geomorphology, vol 3. Academic Press, San Diego, CA, pp 187–227

Nayak S (2017) Coastal zone management in India—present status and future needs. Geo-Spatial Inf Sci 20(2):174–183. https://doi.org/10.1080/10095020.2017.1333715

Niculiță M, Mihai Ciprian Mărgărint MC, Tarolli P (2020) Using UAV and LiDAR data for gully geomorphic changes monitoring. In: Tarolli P, Mudd SM (eds) Developments in earth surface processes, vol 23. Elsevier, pp 271–315. https://doi.org/10.1016/B978-0-444-64177-9.00010-2

NRSA (1995) Integrated Mission for sustainable development (IMSD)—Technical Guidelines. National Remote Sensing Agency, Hyderabad

NRSC (2012a) Manual for geomorphological and lineament mapping (Web Version). Document No. NRSC-RSAA-ERG-G&GD-SEP'12-TR-445, National Remote Sensing Centre (NRSC), Hyderabad, India, pp 1–28

NRSC (2012b) Landslide hazard zonation mapping in Uttarakhand and Himachal Pradesh States (Web Version). Document No. NRSC-RSAA-ERG-G&GD-OCT'12-TR-449, National Remote Sensing Centre (NRSC), October 2012, Hyderabad, India, pp 1–7

Oldroyd DR, Grapes RH (2008) Contributions to the history of geomorphology and quaternary geology: an introduction. In: Grapes RH, Oldroyd D, GrigelisR A (eds), History of geomorphology and quaternary geology. Geological society, vol 301, London, Special Publications, pp 1–17.

Orengo HA, Petrie CA (2017) Large-scale, multi-temporal remote sensing of Palaeo-River Networks: a case study from Northwest India and its implications for the indus civilisation. Remote Sens 2017(9):735. https://doi.org/10.3390/rs9070735

Oyedele AA (2019) Use of remote sensing and GIS techniques for groundwater exploration in the basement complex terrain of Ado-Ekiti, SW Nigeria. Appl Water Sci 9:51. https://doi.org/10.1007/s13201-019-0917-9

Paillou P (2017) Mapping Palaeohydrography in deserts: contribution from space-borne imaging radar. Water 9:194. https://doi.org/10.3390/w9030194

Paillou P, Lopez S, Marais E, Scipal K (2020) Mapping Paleohydrology of the Ephemeral Kuiseb River, Namibia, from Radar remote sensing. Water 12:1441. https://doi.org/10.3390/w12051441

Peukert A, Petersen S, Greinert J, Charlot F (2018) Seabed mining. In: Micallef A, Krastel S, Savini A (eds) Submarine geomorphology. Springer Geology. Springer, Cham. https://doi.org/10.1007/978-3-319-57852-1_24

Pham BT, Bui DT, Prakash I (2018) Landslide susceptibility modelling using different advanced decision trees methods. Civ Eng Environ Syst 35(1–4):139–157. https://doi.org/10.1080/10286608.2019.1568418

Pope GA, Meierding TC, Paradise TR (2002) Geomorphology's role in the study of weathering of cultural stone. Geomorphology 47(2–4):211–225. https://doi.org/10.1016/S0169-555X(02)00098-3

Prakasa Rao DS, Sreenivasan G (2012) DEM generation and geological interpretation for proposed detour alignment of railway line between Amlakhurd-Akot Stations of Akola- Khandwa Guage Conversion Project of South-Central Railway. Technical Report No. NRSC-RC-Oct-2012-TR-626, Regional Remote Sensing Centre-Central, NRSC, ISRO, Nagpur, India, p 46

Rao AY, Vijay Raj K, Yadav OP, Nanda LK, Rai AK, Parihar PS (2015) Uranium-bearing magnesian-calcrete in surficial environment from Khemasar, Churu district, Rajasthan, India. Curr Sci V.108:8:1540–1544

Rao JM, Raju UPN, Rao GR, Mounika KSS (2018) Beach placer deposits of India, their distribution, mineralogy and sustainable-mining with reference to placer ilmenite. Int J Sci Res V.7:5. https://doi.org/10.21275/ART20182614

Sahin EK, Colkesen I, Acmali SS, Akgun A, Aydinoglu AC (2020) Developing comprehensive geocomputation tools for landslide susceptibility mapping: LSM tool pack. Comput Geosci 144.https://doi.org/10.1016/j.cageo.2020.104592

Shah PB, Thakkar NJ (2008) Geo-spatial metadata services-ISRO's initiative. Int Arch Photogram Remote Sens Spatial Inf Sci, vol XXXVII, Part B4, pp 667–674

Shah RA, Lone SA (2019) Hydrogeomorphological mapping using geospatial techniques for assessing the groundwater potential of Rambiara river basin, western Himalayas. Appl Water Sci 9:64. https://doi.org/10.1007/s13201-019-0941-9

Sharma JR, Bhadra BK, Gupta AK, Sreenivasan G (2014) River Saraswati: an integrated study based on remote sensing and GIS techniques. Technical report, RRSC-W, NRSC, ISRO, p 59

Silwal CB, Pathak D (2018) Review on practices and state of the art methods on delineation of ground water potential using GIS and remote sensing. Bull Depart Geol 20:7–20. https://doi.org/10.3126/bdg.v20i0.20717

Singh S, Guha A, Kumar VK, Bardhan S, Lesslie A, Kumar MV, Chatterjee A (2015) Satellite based mapping and morphogenetic analysis of the landforms in the tertiary fold belts of parts of Tripura, India. Geocarto Int V.30. https://doi.org/10.1080/10106049.2015.1013064

Singh MS, Saikhom V, Raju PLN, Prasad SS (2019) Route alignment planning in hilly terrain using geospatial technology: a case study in parts of Arunachal Pradesh India. J Geomatics 13(2):195–202

Singh R, Venkatesh AS, Sudhakar C, Sethy SN, Prasad Babu K (2020a) Exploration for strategic placer mineral deposits in a fluctuating shoreline: Depositional environment and mineralogical characterization of the NE Odisha coast placers, India. Ore Geol Rev 127:2020. https://doi.org/10.1016/j.oregeorev.2020.103850

Singh S, Kumar KV, Jagannadha Rao M (2020b) Utilization of LiDAR DTM for systematic improvement in mapping and classification of coastal micro-geomorphology. J Indian Soc Remote Sens 48:805–816. https://doi.org/10.1007/s12524-020-01114-7

Skonieczny C, Paillou P, Bory A, Bayon G, Biscara L, Crosta X et al (2015) African humid periods triggered the reactivation of a large river system in Western Sahara. Nat Commun 6(1). https://doi.org/10.1038/ncomms9751

Slaymaker O, Spencer T, Embleton-Hamann C (2015) Geomorphology and global environmental change. Cambridge University Presshttps://doi.org/10.1017/CBO9780511627057

Sowers DC, Giuseppe M, Mayer LA, Paul J, Gardner JV, Armstrong AA (2020) Standardized geomorphic classification of seafloor within the United States Atlantic Canyons and continental margin. Front Mar Sci 7(2020):1–18. https://doi.org/10.3389/fmars.2020.00009

Sreenivasan G (2011) Remote sensing studies for diamond exploration in Tikamgarh RP Area, Madhya Pradesh. Technical Report no. NRSC-RC-Nov-2011-TR-623, Regional Remote Sensing Centre (RRSC), NRSC, ISRO, Nagpur, India, p 38

Sreenivasan G, Gupta AK, Sharma JR (2021) Exploration for Saraswati River in Thar Desert Region—Integrated approach through space based remote sensing technology and ground data analysis. In: Sharma M, Joshi S (eds) 'Dwi roopa Saraswati—The Saraswati: tracing the glory of Indian culture and civilization. Published by Indira Gandhi National Centre for Arts, Ministry of Culture, New Delhi, pp 156–176

Sreenivasan G, Krishna Murthy YVN (2018) Remote sensing and GIS applications in micro level planning. In: Reddy GPO, Singh SK (eds), Geospatial technologies in land resources mapping, monitoring and management, geotechnologies and the environment 21. Springer International Publishing AG, part of Springer Nature. https://doi.org/10.1007/978-3-319-78711-4_29

Srivastav SK, Chatterjee RS, Kapoor D, Sreenivasan G, Parthasaradhy EVR (2021) Use of IRS-1C and its follow-on missions for geological applications: a review. J Indian Soc Remote Sens 49:121–149.https://doi.org/10.1007/s12524-020-01284-4

Taddia Y, Corbau C, Zambello E, Pellegrinelli A (2019) UAVs for structure-from-motion coastal monitoring: a case study to assess the evolution of embryo dunes over a two-year time frame in the Po River Delta, Italy. Sensors 2019(19):1717. https://doi.org/10.3390/s19071717

Tian J, Philpot DW (2015) Relationship between surface soil water content, evaporation rate, and water absorption band depths in SWIR reflectance spectra. Remote Sens Environ 169:280–289. https://doi.org/10.1016/j.rse.2015.08.007

UNISDR (2018) UNISDR Annual Report 2017. http://www.unisdr.org. Accessed on: 23 Nov 2021

United States Forest Service, Geomorphology Working Group, Haskins DM, Correll CS, Foster R.A, Chatoian JM, Fincher JM, et al (1998) A geomorphic classification system. USDA Forest Service

Valdiya KS (2016) Prehistoric River Saraswati: geological appraisal and social aspects. Springer Publications, Cham, Switzerland, p 136

Valdiya K, Chatterjee R (2018) Review and assessment of the Palaeochannels of North West India by an Expert Committee. In: Bhujal Manthan-2, aquifer mapping and ground water management—conference proceedings, central ground water board ministry of water resources, RD & GR Government of India, 29th November, 2016 Vigyan Bhawan, New Delhi

Verstappen HT (2011) Old and new trends in geomorphological and landform mapping. In: Smith MJ, Paron P, Griffiths JS (eds), Geomorphological Mapping—methods and applications, developments in earth surface processes, vol 15, pp 13–38. https://doi.org/10.1016/B978-0-444-53446-0.00002-1

Xiong K, Adhikari BR, Stamatopoulos CA, Zhan Y, Wu S, Dong Z, Di B (2020) Comparison of different machine learning methods for debris flow susceptibility mapping: a case study in the Sichuan Province, China. Remote Sens 2020(12):295. https://doi.org/10.3390/rs12020295

Xu Y, Zhang S, Li J, Liu H, Zhu H (2021) Extracting Terrain texture features for landform classification using wavelet decomposition. ISPRS Int J Geo-Inf 2021(10):658. https://doi.org/10.3390/ijgi10100658

Yulianto F, Suwarsono MT, Khomarudin MR (2019) Analysis of the dynamics of coastal landform change based on the integration of remote sensing and GIS techniques: Implications for tidal flooding impact in Pekalongan, Central Java, Indonesia. Quaestiones Geographicae 38(3):17–29. Bogucki Wydawnictwo Naukowe, Poznań

Zhang P, Najman Y, Mei L, Millar I, Sobel ER, Carter A, Barfod D, Dhuime B, Garzanti E, Govin G, Vezzoli G, Hu X (2019) Palaeodrainage evolution of the large rivers of East Asia, and Himalayan-Tibet tectonics. Earth Sci Rev 192:601–630. https://doi.org/10.1016/j.earscirev.2019.02.003

Zinck JA (2016) The Geomorphic landscape: classification of geoforms. In: Zinck JA, Metternicht G, Bocco G, Del Valle HF (eds), Geopedology: an integration of geomorphology and pedology for soil and landscape studies. Springer International Publishing. https://doi.org/10.1007/978-3-319-19159-1_7

Zinck JA, Metternicht G, Del Valle HF, Bocco G (2016) Chapter-1 presentation. In: Zinck JA, Metternicht G, Bocco G, Del Valle HF (eds) Geopedology: an integration of geomorphology and pedology for soil and landscape studies. Springer International Publishing. https://doi.org/10.1007/978-3-319-19159-1_7

Chapter 2
Water Resource Management Studies at Micro Level Using Geospatial Technologies

S. Rama Subramoniam, Sudha Ravindranath, Shivukumar Rakkasagi, and R. Hebbar

Abstract Water availability for different purposes, particularly for irrigation and domestic use, is of immense importance in the near future for both rural and urban areas. The per capita availability of water is decreasing at a higher rate due to the impact of climate change and the ever-increasing population. Hence, it becomes necessary to utilize water resources in a judicious way, ensuring maximum benefits with minimal waste. The need for local participation in water management and attending to local needs makes the Panchayats ideally suited to tackle water scarcity problems. In this current context of the growing importance of Panchayats as vehicles of programme implementation, local panchayats can assume high responsibility and play an important role in localized planning for assessment of water resources and management within the Panchayat. The water management scenario is designed and influenced by a set of linked physicals, biological, and socio-economic factors such as surface water hydrology, groundwater hydrology, climate, soils topography, land use, water quality, ecosystems, demographics, institutional arrangements and infrastructure. In this book chapter, an effort has been made for evaluation of the present status of availability, demand and development possibilities with regard to the water resources at Gram-Panchayat/Watershed/Micro level. Indlawadi Gram-Panchayat, Anekal Taluk is selected for this study. Water resources assessment has been prepared using high resolution-merged satellite (LISS IV + Cartosat) data, Survey of India Toposheets and existing literature in conjunction with Ground-truth and created various resource layers on a 1:10,000 scale. The rainfall data for a

S. R. Subramoniam (✉) · R. Hebbar
Regional Remote Sensing Centre-South, NRSC, ISRO, Bengaluru, Karnataka, India
e-mail: ramasubramoniam_s@nrsc.gov.in

R. Hebbar
e-mail: hebbar_kr@nrsc.gov.in

S. Ravindranath
Head Applications, Regional Remote Sensing Centre-South, NRSC, ISRO, Bengaluru, Karnataka, India
e-mail: ravindranath_s@nrsc.gov.in

S. Rakkasagi
Discipline of Civil Engineering, Indian Institute of Technology Indore, Indore, India

C. S. Jha et al. (eds.), *Geospatial Technologies for Resources Planning and Management*, Water Science and Technology Library 115,
https://doi.org/10.1007/978-3-030-98981-1_2

period of 38 years (1981–2018) is used to understand the variability of rainfall of the selected Taluka of study area. Average annual rainfall is 838.36 mm and Soil Conservation Services (SCS) Model is used for estimating runoff. Analytic Hierarchy Process (AHP) technique has been performed utilizing various thematic layers generated using satellite data to determine the most suitable water conservation sites and develop action plans such as check dams, farm ponds, rainwater harvesting, recharge pits/wells and percolation tanks, etc. and proper maintenance of the stored water and water flow. The water requirement for domestic and agricultural crops is calculated based on the population and crops grown. This information is very useful for farmers to decide the crops/plantations suitable for the region. Systematic approach using geospatial techniques with ground measurements paves the way for sustainable planning of water resources management.

Keywords Water resources · Geospatial technology · AHP · Water conservation

2.1 Introduction

Water resource management refers to all the competing demands for water and seeks to allocate water on an equitable basis to satisfy all uses and demands (Dongardive 2018, Zeinolabedinia and Esmaeilyb 2015). In the current scenario, there is an urgent need for re-designing and re-building our villages for their overall upliftment. Keeping this in mind, this study is carried out for micro-level planning and development of water resources using remote sensing and GIS technology (Pandey and Tripathi 2020). The responsibility of water resources management in India is primarily entrusted to state governments (Pandit and Biswas 2019). The central government provides financial support to state governments for implementing national-level policies and projects (Abdel Rahman 2016, Ahmad and Verma 2016, 2017, Ahmed 2019, Bamne et al. 2014). The state governments have multiple institutions and administrative departments such as those for water, irrigation, public works, gram (village) panchayat, and other regulatory authorities to manage water resources. Panchayat Raj institutions are responsible for the administration, maintenance, operation, and implementation of projects related to water resource management. Actions related to local policymaking and fund allocations are performed by the Zilla (district) and Taluk (subdivision) panchayat, whereas the implementations, monitoring and operations of projects are performed by taluk (block) and gram (village) panchayats (Hutchings et al. 2017). In India, water resource management projects occur in a grouped and illogical manner, often at the discretion of certain individuals or institutions. Hence there is a need to examine and evaluate the National Water Policy strategies (Pani et al. 2021, Bandara 2006, Batchelor 2013, Central Ground Water Board 2007).

2.2 Critical Review of Recent Water Resources Management Studies

There is a major policy concern in India especially the effects of growing water availability to weaker section of the society. This study describes the efficiency of both macro-level policies for conservation of rainwater as well as micro-level sustainable management of traditional water bodies by local community (Chowdhury and Behera 2021). Historically, the water bodies have played a significant role in promoting livelihood activities by maintaining an all-round socio-ecological balance in rural human settlements (Reddy and Behera 2009). These century-old water infrastructures were developed and maintained by rulers with the active participation of local communities for harvesting and storing rainwater and subsequently using it for irrigation, domestic uses, and recharging groundwater throughout the year (Ariza et al. 2007, García et al. 2008, Kota et al. 2017, Kristvik 2015, Kumar et al. 1997, Lele et al. 2013, Murry 2013, Murthy 2003, Nyatuame et al. 2014, Ouma and Tateishi 2014, Rajendran et al. 2016, Rao et al. 1996, Sethupathi et al. 2012, Sharma et al. 2015, Shashikumar et al. 2018). In addition, these water infrastructures also help control floods and combat the adverse effects of prolonged droughts. In India, these traditional water bodies provide livelihood security to millions of poor people living especially in fragile semi-arid regions (Reddy and Behera 2009). Village-level local organizations and institutions perform several important functions relating to the management of water systems. These functions include the maintenance of the physical structure of the water bodies, controlling and monitoring the uses of resources, and their equitable distribution among legitimate members (Chowdhury and Behera 2021; Shyam et al. 2021; Taloor et al. 2019; and Sood et al. 2021;.

In the study, Srivastava and Chinnasamy (2021) examined water scarcity issues regarding drinking and irrigation in few villages of the Sahyadri region in Maharashtra. The study recommended a scientific investigation of different component of water resources to arrive at better management policies. There is a need for water management and monitoring plans at region level. Mondal and Sahoo (2021) carried out a study which aims to evaluate block-wise temporal changes of groundwater storage under the terrestrial water storage in Howrah District, West Bengal, India, using Catchment Land Surface Model (CLSM) from the Global Land Data Assimilation System (GLDAS-2).

In saline monsoon dominant regions, shallow groundwater management interventions by the community has proved to be important management solutions. Local chauka system has been adopted in Laporiya village in the semi-arid Salt Lake region of Rajasthan state which was formerly degraded socio-ecological system (Sethupathi et al. 2012).

2.3 Micro Level Water Resources Management at Indlawadi Gram-Panchayat

Water is essential for human well-being and environmental sustainability. Water resources play a crucial role in the sustainable development of a state. The Ministry of Water Resources of India is responsible for the conservation, management, and development of water. In order to achieve this, the Panchayats play a crucial role, and Panchayats are constitutionally mandated to perform various functions that facilitate water resources assessment. The need for local participation in water management and attending to local needs makes the Panchayats ideally suited to tackle water scarcity problems within the Panchayat. In this current context of the growing importance of Panchayats as vehicles of programme implementation, local Panchayats can assume high responsibility and important role in localized planning for water resources assessment and management within the panchayat. In the present study, an effort has been made to study the present status of availability, demand, and development possibilities with regard to the water resources in Indlawadi Gram-Panchayat, Anekal Taluk, Bengaluru Urban District.

2.3.1 Study Area

The Indlawadi GP is ecologically susceptible area and has better scope for water conservation activities. There are around 16 lakes that are all going dry. The Indlawadi GP area is about 4360 ha consisting of 22 villages. The total numbers of households in Indlawadi Gram-Panchayat are 1757 with a total population of 11,058 people. The geographical area of Indlawadi Gram-Panchayat is 4345.043 ha (Fig. 2.1). Every 10 years, there will be 4–5 years of drought. Groundwater quality is good and is suitable for growing agronomic and horticultural crops. Availability of water is below normal and rainfall is highly uncertain and varies spatially. The majority of the population is engaged in agriculture, and major crops grown are Millets, Vegetables, Flowers and Mango plantations. The topography of Anekal region is an uneven landscape with an intermingling of hills and valleys, and bare rocky outcrops rise to about 120–150 ft above ground level.

For present study, the daily rainfall data for a period of 38 years (1981–2018) is used to understand the variability of rainfall of the selected Taluka of study area. Average annual rainfall is calculated to be 838.36 mm and Soil Conservation Services (SCS) Model known as Curve Number (CN) method is used for estimating runoff. Also, the water requirement for domestic and agricultural crops is calculated based on the population and crops grown. This is very useful for the farmer to understand the suitability of crops to be grown in his fields.

The identification of suitable locations for water conservation and storage sites was made with the help of remote sensing and GIS techniques. In the present study, the identification of suitable locations in Indlawadi Gram-Panchayat, Anekal Taluk

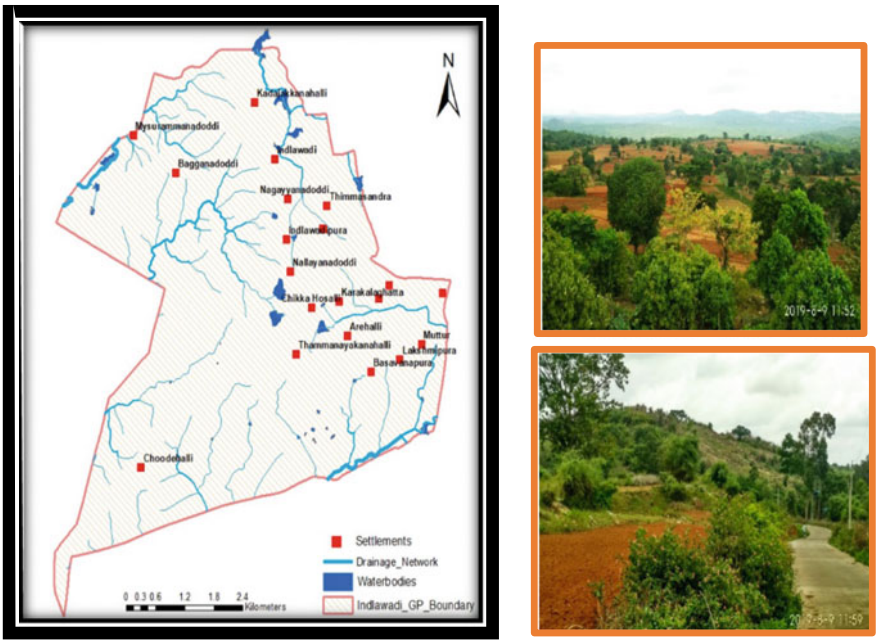

Fig. 2.1 Location map of Indlawadi GP, Bengaluru Urban district, Karnataka

(mainly falling in Arkavathi River catchment of Cauvery Basin and small part falling in South Pennar river catchment of Ponnaiyar Basin) based on the Analytic Hierarchy Process (AHP) technique is being employed considering all the thematic layers and their different classes to find the appropriate sites for water conservation. This mapping helps to create the action plan in selecting potential sites for water conservation and storage structures such as check dams, farm bunds, rainwater harvesting, recharge pits/wells and percolation tanks, etc. and proper maintenance of the stored water and water flow. Geospatial technique are useful for planning and decision making on number and type of water conservation structures to efficiently use the funds available with the Indlawadi GP. These techniques enable us to assess water resources available and plan management strategies in a short span of time and effective manner.

2.3.2 Rainfall Analysis

The climate of Bengaluru is classified as tropical wet and seasonally dry. Bengaluru rural district receives rainfall from both Pre-monsoon, South West monsoon and North East monsoon. However maximum rainfall is received during south west monsoon. It experiences humid to semi-arid climatic conditions. The rainfall pattern

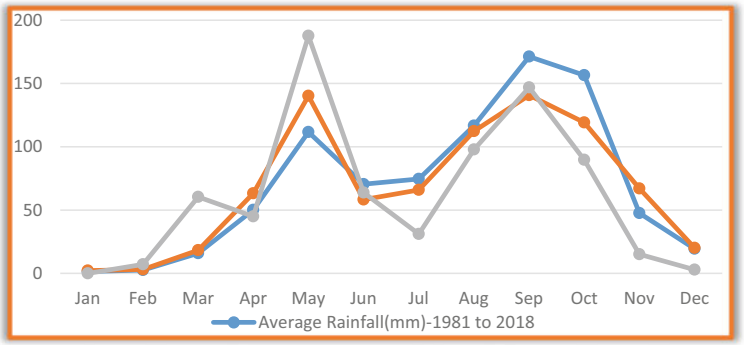

Fig. 2.2 Average rainfall variation curves for different periods

of the Bengaluru rural district is studied by considering rainfall of all the five taluks from 1981 to 2018. The annual rainfall of Anekal taluk is the minimum among all the taluks and is about 838.36 mm. Maximum Temperature (monthly mean maximum) of 38.10 °C is observed in April/May and Minimum Temperature (monthly mean minimum) of 8.30 °C is observed in December/January. Similarly, Minimum Relative Humidity (mean monthly) of 44% (min) is observed in March and Maximum Relative Humidity of 85% (max) is observed in October. Generally, wind flows are observed mostly in easterly and westerly predominant directions. Rainfall data collected from KSNDMC, Bengaluru are used for runoff estimation (Fig. 2.2).

2.3.3 Water Requirement Demand for Indlawadi GP

Important parameters such as climate, culture, food habits, work and working conditions, level and type of development, and physiology determine the requirement of water.

2.3.4 Domestic Water Requirement

Domestic consumption includes water requirements primarily for drinking, cooking, bathing, washing of clothes and utensils and flushing of toilets. As per the manual on Water supply and Treatment, published by Central Public Health & Environmental Engineering Organization (CPHEEO), Ministry of Housing and Urban Affairs, New Delhi, the per capita rate of water supply per day has been considered net at consumer point 135 lpcd for domestic & non-domestic needs. The Bureau of Indian Standards recommends a minimum water supply of 200 L per capita per day (lpcd). An amount of 150–200 lpcd is recommended for bigger cities with full flushing system by

BIS. The Indlawadi GP is in the sub-urban area, which is still developing into a modern urban locality with the inclusive commercial & industrial development with a complete flushing system.

Hence, the per capita rate of water supply per day has been considered for our study area is 185 lpcd for domestic purpose. The estimated water requirement for the Indlawadi Gram-Panchayat for the current population, i.e., 11,058 is 2.045 Million Litres per day and 746.70 Million Litres per year.

2.3.5 Irrigation Water Requirement of Field Crops

Irrigation Water Demand" is total amount of water required by crop from the sowing time to harvesting time. The irrigation demand depends on the cropping pattern, type of soil, climate etc.

2.3.6 Satellite Data and Ancillary Data

The study was carried out by collecting data from both primary and secondary sources. The following table shows the different data sets used in the study.

LISS IV + CARTOSAT1 high resolution merged imagery is used in the preparation of the thematic layers for the Indlawadi Gram-Panchayat. In the present study, the slope map was prepared using the digital elevation model (DEM) and slope generation tools in ArcGIS software. The SRTM DEM data is used for Slope and Flow Accumulation processes in AHP analysis for site suitability of water conservation locations. The Survey of India Toposheet essentially contains base information on Roads, Railways, Settlements, Canals, Rivers, Drainages, etc. Figure 2.3 shows the LISS IV + CARTOSAT high resolution merged imagery used in the present study.

2.3.7 Ground Truth/Field Data Collection

Ground-truth generally refers to the data collected in the field about the different surface features. Ground-truth is usually carried-out in 10–15% of the study area, and involves taking geographic coordinates of features to understand how it is represented on remote sensing data.

Information on the drainage, bore well locations and its depths (No. of bore wells, yield of bore well etc.) was collected. The major tree species found in the forest region of the study area are Eucalyptus, Sandalwood, Bamboo and Syzygium cumini. The land use pattern, soil type, hydro geological properties, recharge pits, ponds, crops grown were also checked during the visit. GPS waypoints along with important field photographs of different LULC classes were captured. Based on the field survey,

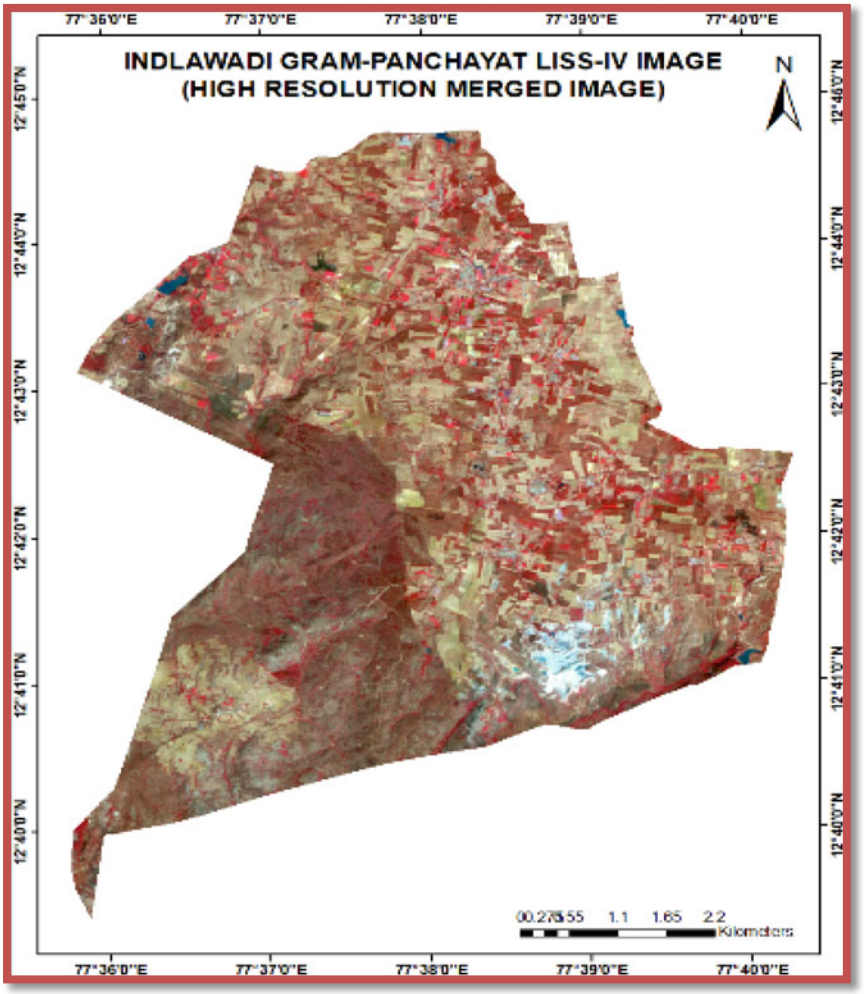

Fig. 2.3 Indlawadi GP high resolution image

the identification of water conservation and storage structures were also carried-out based on the IMSD/Integrated survey (NRSC) guidelines.

2.4 Thematic Map Generation

Preparation of required database is the prerequisite for undertaking preparation of thematic layers using visual interpretation. Thematic maps required for the present study were generated using high resolution satellite datasets (LISS IV + CARTOSAT

Merged). The methodology for generation of thematic maps involved selection and procurement of optimum satellite datasets, orthorectification of satellite data, ground-truth collection, and analysis/interpretation of satellite data.

Orthorectification is the process of removing the geometric distortion which are integral part of satellite imagery caused by sensor orientation, topographic relief displacement and errors associated with satellite imagery. Input datasets were orthorectified using 8–10 uniformly distributed ground control points (GCPs) and available Carto-1 DEM. The existing Cartosat-1 orthorectified database was used as reference and individual LISS-IV scenes were orthorectified using RPCs, 8–10 GCPs and DEM, employing projective transformation. Thus, ortho-rectified satellite datasets were generated with UTM projection and WGS 84 spheroid which were visually interpreted to generate thematic layers, viz., LULC, Soil texture, Drainage, Lineaments, Geomorphology and Roads layers are digitized. Slope map is prepared using SRTM DEM data. Layers are generated and digitized in by using high resolution merged LISS IV data, Survey of India Topo-sheets, DEM data and existing literatures in conjunction with ground-truth data.

2.4.1 Drainage Network and Lakes/Water-Bodies Layer

Water-bodies were delineated based on the visual interpretation of high resolution (LISS IV + CARTOSAT) merged data. Drainage map was digitized from Survey of India Topo-sheets in GIS environment and it was updated by using the high-resolution satellite data. Based on the drainage pattern, the stream ordering was carried-out. Stream order ranges from 1st to 4th order. The drainage map is as shown in Fig. 2.4. Indlawadi Gram-Panchayat, Anekal Taluk drains mainly in to Arkavathi River of Cauvery Basin and a small portion of Indlawadi panchayat drains in to South Pennar river of Ponnaiyar Basin. The drainage network shows how the channel water flows through and reach the lakes/tanks as sources. The layer is very essential for preparing water conservation plans showing type of structures and their location on the map. Flow accumulation of a linear stream network is indicated by drainage order. There were around 16 lakes that were going dry with each passing year. It is observed that there are few tanks and less drainage density in the study area, hence, there is enough scope to plan and implement the rainwater harvesting structures and improve the availability of water for drinking & agriculture/horticulture/agroforestry development in the study area.

2.4.2 Land Use/Land Cover (LU/LC) Layer

LU/LC layer is prepared by visual interpretation of high resolution merged data and assigning level II classification system. All the classes occurring in the area were categorized and the polygons are properly coded, and attribute data were entered.

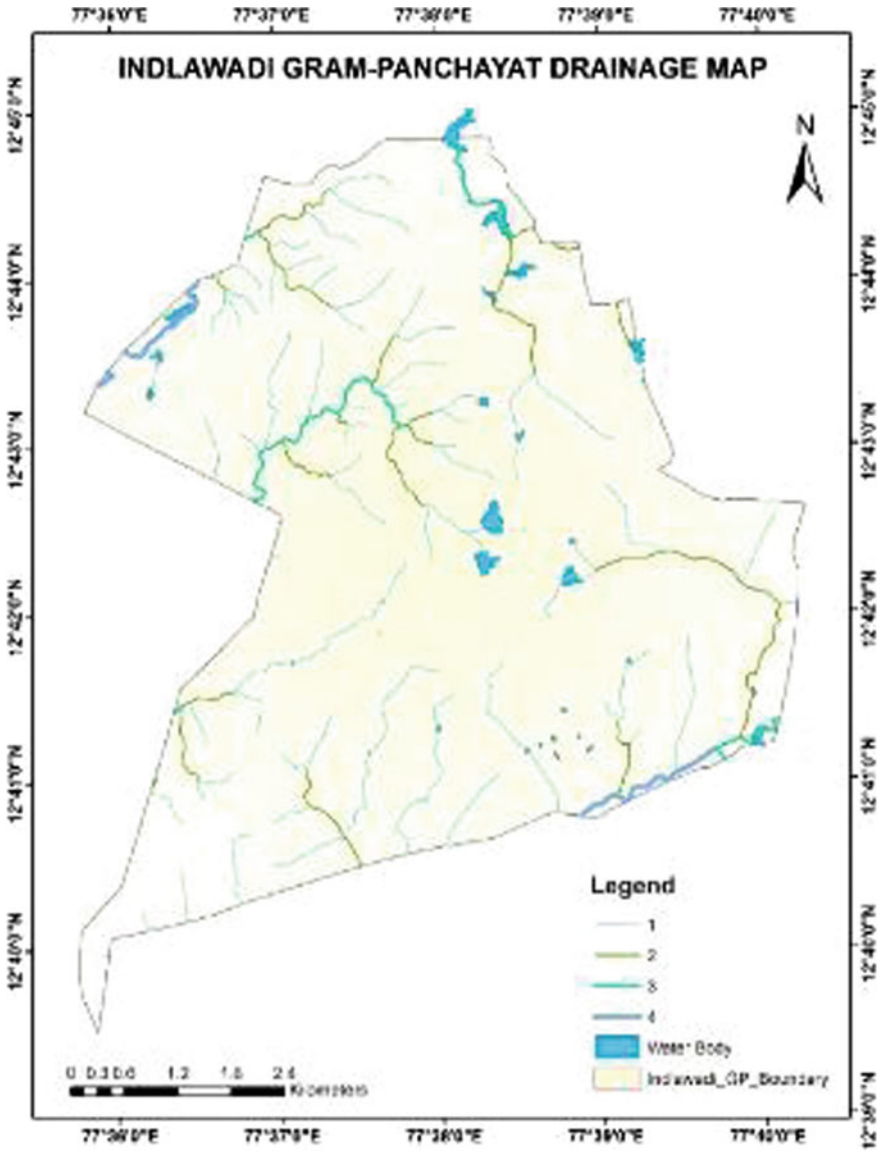

Fig. 2.4 Water-bodies and drainage map

The LULC categories were verified with ground-truth data collected. LU/LC map generated is shown in Fig. 2.5, and the area covered by each class is tabulated in Table 2.1. It is observed that the dominant area is covered by Agriculture land (46.98%). The major crops grown are Millet, Vegetables, Flowers, and Mango plantation. South-west part of the study area is covered by deciduous forest (23.53%). The major trees

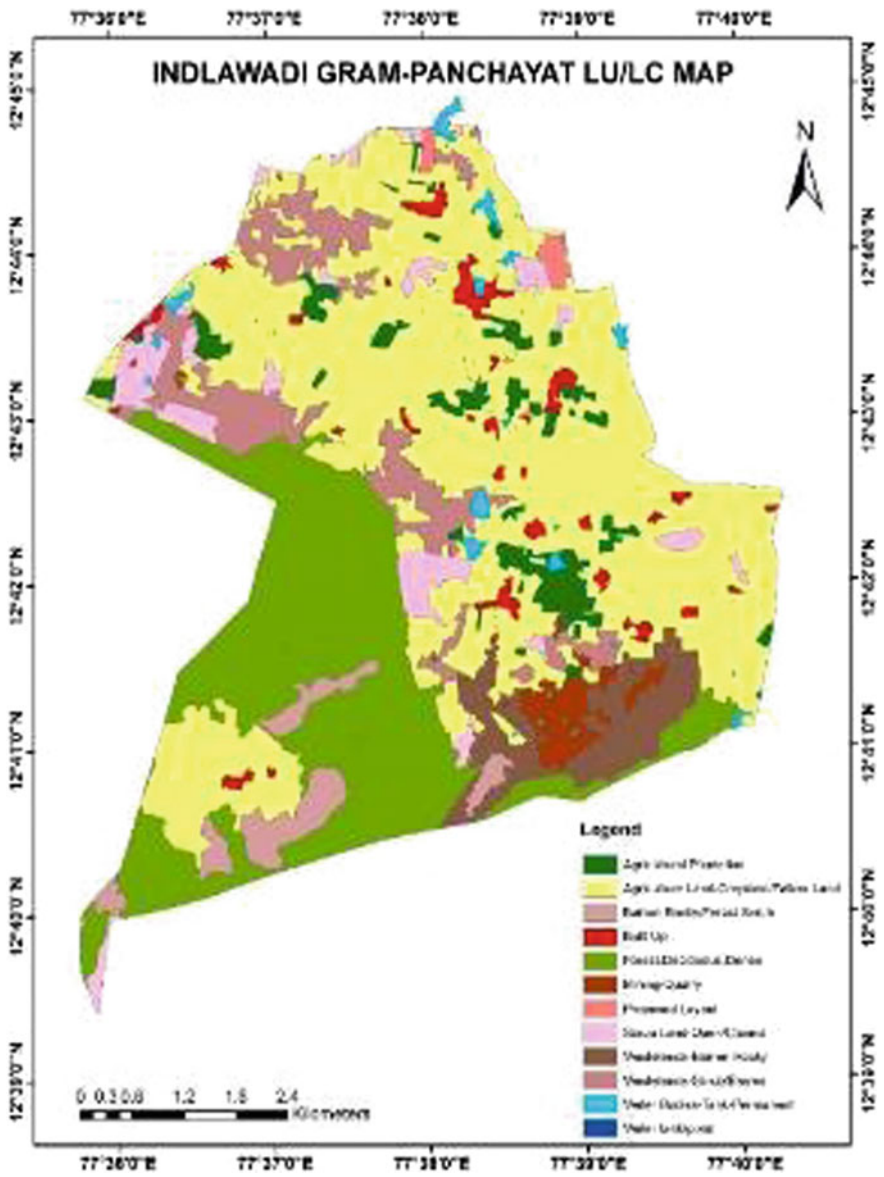

Fig. 2.5 Land use/land cover map

Table 2.1 Details of data source

Sl. No	Data	Data source
1	DEM	SRTM, USGS
2	LISS-IV	Resourcesat-2
3	Topo-sheet	SOI
4	GroundWater Prospect Layer	www.bhuvan.nrsc.gov.in
5	Soil map	1:50 K (NRIS)
6	Rainfall data	KSNDMC, Bengaluru
7	Road network layer	OSM
8	Village boundary shapefile	NRSC

Table 2.2 Land use/land cover statistics of the study area

Class	Area_Sqm	% Area
Agricultural plantation	1,595,644.82	3.67
Agriculture land-cropland/fallow land	20,412,311.70	46.98
Barren rocky/forest scrub	1,286,096.71	2.96
Built up	938,573.96	2.16
Forest-deciduous-dense	10,223,458.8	23.53
Mining/quarry	886,855.75	2.04
Poly sheeting green house	65,873.64	0.15
Proposed layout	231,318.06	0.53
Scrub land-open/closed	1,878,566.3	4.32
Wastelands-barren rocky	2,109,117.86	4.85
Wastelands-scrub/barren	3,364,352.96	7.74
Water bodies-tank-permanent	451,720.46	1.04
Water pond-farm pond	6543.82	0.02

found in the forest are Eucalyptus, Sandalwood, Bamboo and Syzygium cumini. Mining area is seen toward southern part of the study area, which covers 2.04% of total area. Wasteland and Scrubland are the other classes which cover an area of 7.74% and 4.32% respectively (Table 2.2).

2.4.3 Soil Map

Soil map of the study area has been prepared from the NRSC 1:50 K soil map and updated based on ground-truth. 3 soil textural classes are found in study area viz., Gravelly sandy loam, Gravelly sandy loam/Forest soil and Gravelly silty loam soil

(Fig. 2.6). It is observed that Gravelly sandy loam, Gravelly sandy loam/Forest soil and Gravelly silty loam soil have covered about 57%, 32%, and 11% respectively of total study area. The dominant area is covered by Gravelly sandy loam soil at most part of the study area which has agricultural lands. South-west part of the GP is

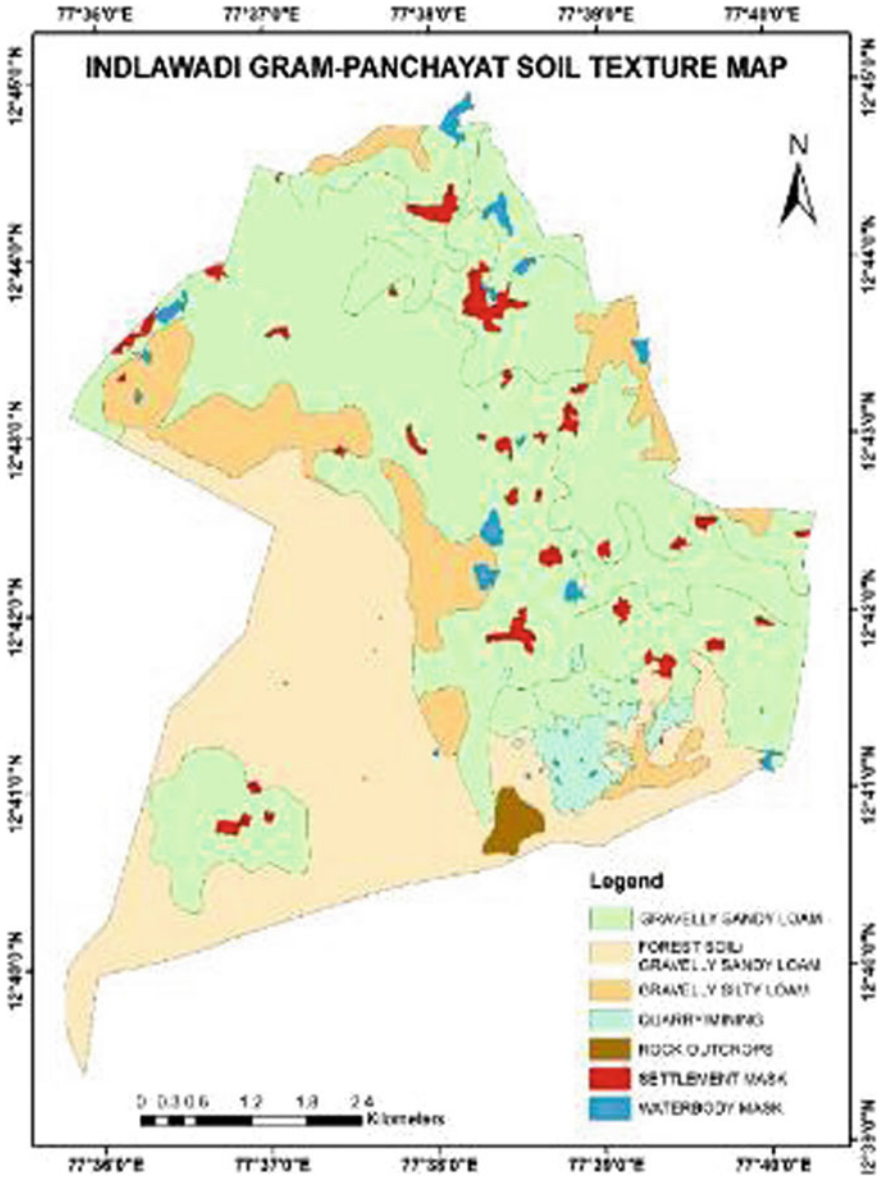

Fig. 2.6 Soil map

covered by Forest soil with deciduous forest. Valley contains the Gravelly silty loam soil which has highly suitable conservation structures.

2.4.4 Slope Map

A slope map was generated from SRTM DEM, which was divided into five classes. The varying degree of slope indicates different levels of erosion of soil/land. The slope of the GP ranges from 0 to 27.10%. The slope map indicates five classes in percentages, viz., level (0–1) nearly level (1–3), gentle slope (3–5), moderate slope (5–10) and steep slope (10–15). A low-water infiltration is observed in high slope and steeper terrain, while a lower slope represents flat terrain and high possibility of infiltration. Slope plays an important role in the suitability of water conservation sites. The central and northern part of the study area have very gentle slope which permit less runoff and have very good potential for groundwater and suitable for water conservation structures. On the other hand, there is an increase in a slope toward the southern and southwest part of the study area. Areas with steep slopes facilitate high runoff and have poor potential for groundwater.

2.4.5 Geomorphology and Ground Water Prospect Layer

Geomorphology is the scientific study of the origin and evolution of *topographic* and *bathymetric* features created by physical, chemical or biological processes operating at or near the Earth's surface. Some of the factors which controls the movement of groundwater are lithology, geomorphology, geological structures and recharge conditions etc. The distribution of hydro geomorphic units is the derivative of above factors. The analysis of hydro geological characteristics of the hydro geomorphic units provides the groundwater prospects in the study area in the form of depth, type and yield range of the wells.

Geomorphology Map: Geomorphology map is prepared by visual interpreting the high-resolution merged data and SOI Topo-sheets. All the landforms occurring in the area are mapped and depicted in Fig. 2.7.

Lineament map: Using the existing structural map and high resolution image the structural features have been updated. The structural features include faults and fractures, which indicates movement of groundwater in the form of channels and barriers. These features were represented as line. Lineaments, particularly joints or fractures and their intersection are potential sites for exploration of groundwater.

Areas with higher lineament density and nearly level slope makes the zone ideal for groundwater infiltration and therefore have good potential for groundwater development.

Ground Water Prospect Map: Groundwater prospects map of Indlawadi Gram-Panchayat is derived from the Bhuvan portal. Geomorphologically, the area of the GP

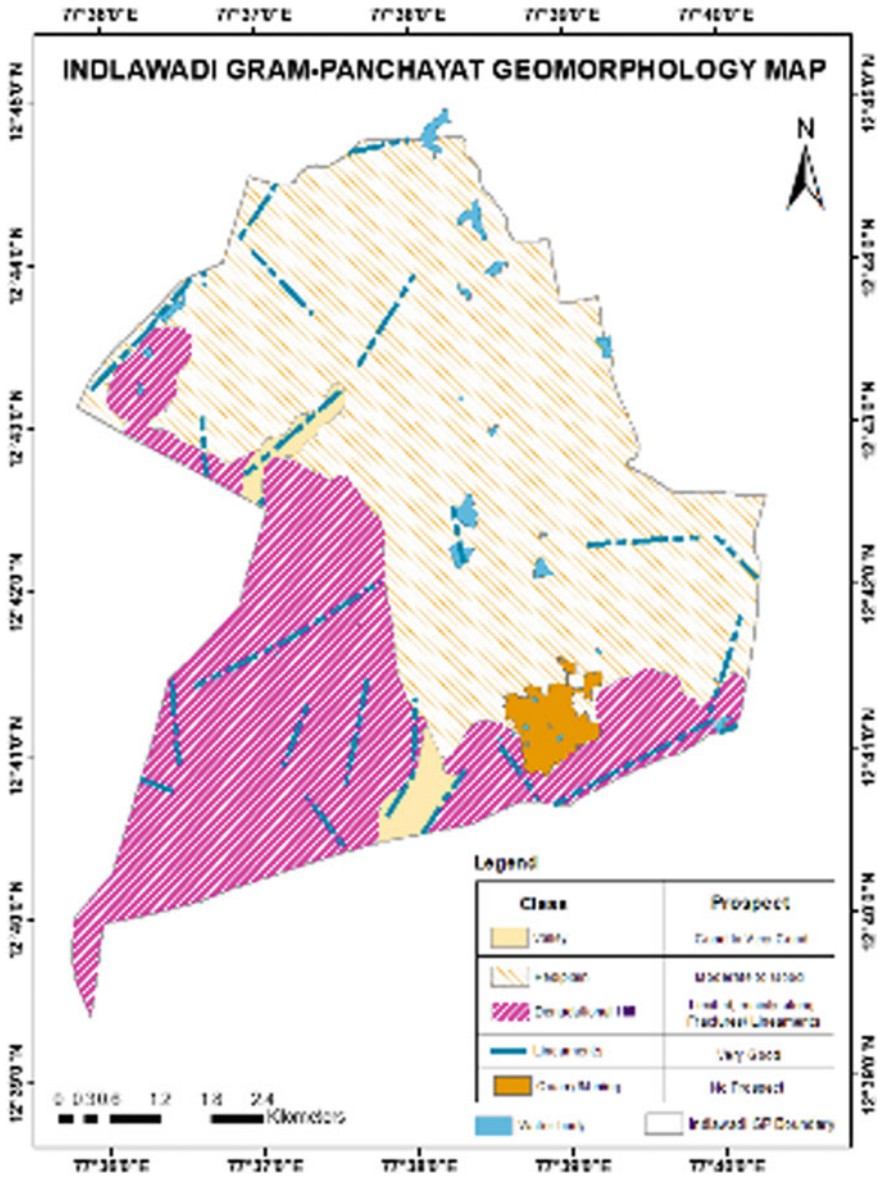

Fig. 2.7 Geomorphology and ground water prospect

and its surroundings is mainly comprised of pediplains, denudational hill, occasional rock outcrops, and shallow valleys. The depth range of wells varies from 70–80 to 130–140 m. The pediplains form major part of the Indlawadi Gram-Panchayat is underlain by gneisses and granites. The yield range varies from 20–30 to 400–500 LPM and fracture-controlled valley fills are suitable for groundwater development like recharge pits and percolation ponds/tanks due to extensive development utilization of GW for irrigation purposes. The pediplains-shallow (PPS) zones are suitable for groundwater development with moderate prospects. To have sustained yield from wells, it is essential to recharge groundwater with suitable structures like recharge pits and percolation ponds/tanks.

2.5 Runoff Potential

To assess the Runoff potential, SCS Curve number (CN) approach is adopted. This map is prepared to determine the potential or actual runoff in the GP. Hydrologic soil group (HSG) and land use determine the CN. The CN ranges from 0 to 100 with 0 value indicating no runoff condition while a value of 100 representing rainfall is equal to runoff. Low runoff is indicated by CN range of 26–50 and moderate runoff indicated by CN range of 50–75 and high runoff (CN of 75–100). Runoff estimation using both Rational and SCN curve methods are computed and the total runoff works out to be 23.303 MCM and 22.995 MCM respectively. Both the values are close to each other. The study shows that the south-west part of the study area generates high surface runoff and most of the western part is endowed with dense forests.

2.5.1 Runoff Estimation Using Rational Method

The geographical area of Indlawadi Gram-Panchayat is 43450434.90 m^2 and considering the fact that 838.361 mm is the average annual rain fall in Anekal taluk; if the infiltration (is around 20%) is taken in to account, the quantum of possible runoff could be estimated as follows:

$$\text{Average Annual Rain fall} = 838.361 \text{ mm (38 years average)}$$

$$\text{Area of the site} = 43450434.90\,\text{m}^2$$

$$\text{Potential Runoff} = 43450434.90\,\text{m}^2 \times 0.838\,\text{m} \times 0.80 = 29129171.557\,\text{m}^3 = 29.129\,\text{MCM}$$

$$\text{Evapotranspiration losses (20\%)} = 0.2 \times 29129171.557\,\text{m}^3$$

$$= 5825834.331\,\text{m}^3 = 5.825\,\text{MCM}$$

$$\text{Surface Runoff} = 29129171.557\,\text{m}^3 \times 0.80$$
$$= 23303337.245\,\text{m}^3 = 23.303\,\text{MCM}$$

2.5.2 Run-Off Estimation Using SCS Curve Number

Runoff estimation is also carried-out by the SCS Curve Number method. The soil present in the study area is Gravelly sandy loam, Gravelly silty loam, and Forest soil. The type of soil and land use/land cover is used to determine the Curve Number. The product of area, rainfall and runoff coefficient yields the amount of discharge/runoff.

Runoff estimation is also carried-out by Rational Method is 23.303 MCM and runoff estimation carried-out by the SCS Curve Number method is 24.59 MCM. The runoff estimation using both the methods are close to each other. The study shows that the south-west part of the study area having high surface runoff and most of this part is endowed with dense forests. The runoff potential can be harvested through the Artificial Recharge by constructing the Nala Bunds and Farm ponds at suitable sites.

2.5.3 AHP Analysis

Analytic Hierarchy Process (AHP) is one of multi criteria decision-making method adopted in this study. The procedure of AHP include identifying a hierarchy of objectives, criteria and alternatives; pairwise comparison of criteria; an integration with result from pairwise comparison as relative importance over all levels of hierarchy. AHP is applied to determine the priority of each parameter over one another and is expressed in terms of percentile. Relative importance is derived from all the 8 parameters.

Based on literature review of previous work, data availability and conditions of Indlawadi Gram-Panchayat, 8 criteria were considered as main factors which includes drainage density with respect to stream order (200 m buffer), precipitation amount of previous year. i.e. 2018 computed using Thiessen polygon approach, Topographic conditions (Slope), Soil texture, LU/LC, Flow accumulation, Lineaments (100 m buffer) and Geomorphology layer.

Four major criteria have been considered for selecting the suitable sites for water storage structures as per the Integrated Mission for Sustainable Development (IMSD) guidelines The slope should be less than 15%; the land use may be barren, shrub land, and river bed; the infiltration rate of the soil should be less and the type of soil should be sandy clay loam (IMSD 1995; Padmavathy et al. 1993).

2.5.4 *Generated Layers for AHP Analysis*

The Drainage density (200 m Buffer), Rainfall (Thiessen polygon), Lineaments (100 m Buffer) layers are generated to analyze the AHP method. Flow accumulation vector map was also prepared using SRTM DEM data.

A suitability map for water conservation sites in Indlawadi Gram-Panchayat is shown in Fig. 2.8 and a histogram showing area and percentage of different suitability levels which is depicted in Fig. 2.9.

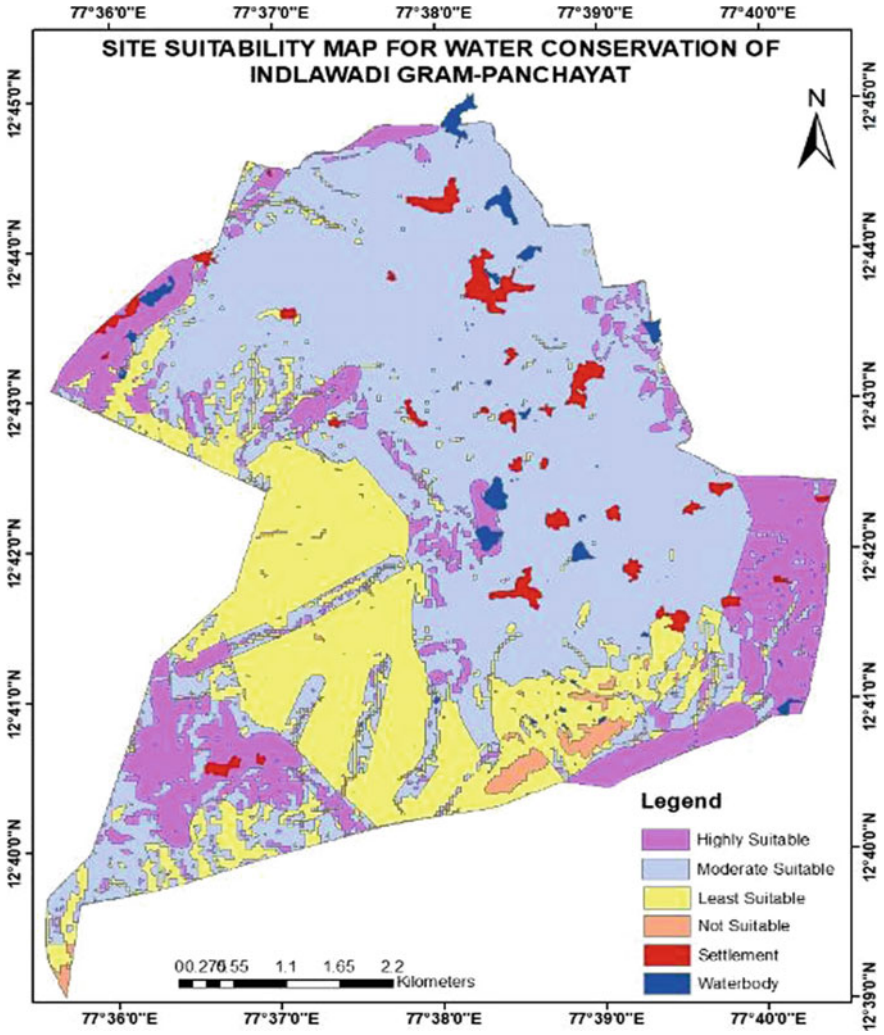

Fig. 2.8 Suitability map for water conservation sites in Indlawadi Gram-Panchayat

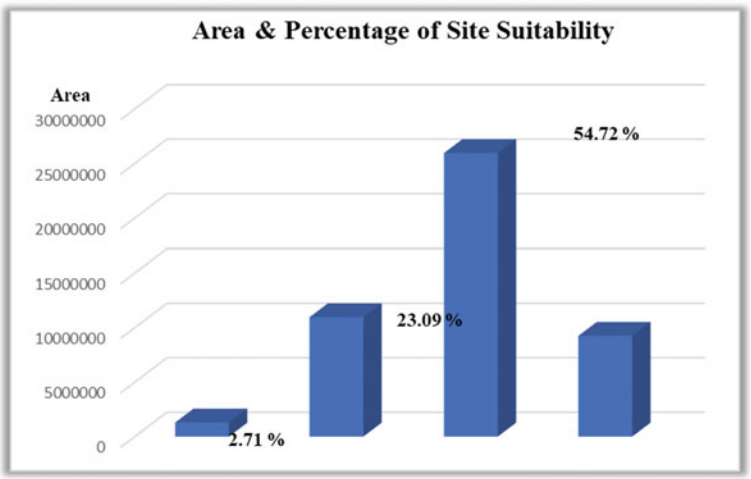

Fig. 2.9 Area and percentage of suitability levels

When the selected sites will be utilized for water conservation, it will increase the available water resources in the Gram-Panchayat. This will lead to socio-economic development of Indlawadi GP. Before constructing any structures, it is needed to conduct a fieldwork to investigate the suitability of soil and the sub-surface layers for its stability to hold water conserving and storage structures. Some of the following investigations needs to be conducted to validate the outcomes of this analysis:

- To prevent the selection of sites located in other land uses of high socio-economic and cultural values there is a need to survey the selected sites.
- Along with survey, a geophysical investigation is needed to study the sub-surface layers within the study area. This investigation will help in determining whether these layers are suitable to establish water conservation schemes.
- The textural suitability of soils within the study area has to be validated by conducting soil sampling from various locations within the study area to identify the suitable areas.
- Estimation of runoff that could be utilized in these sites needs to be done by demarcating watersheds around the selected sites.

2.6 Generation of Comprehensive Developmental Plans

There is an urgent action required for with respect to water resources management and conservation. Many factors viz., increasing population, more water-intensive agricultural practices, increasing rainfall variability, and water pollution are resulting in obstruction to poverty eradication and sustainable development of rural areas. Floods and droughts are yet another dimension to water which results in huge financial

and materialistic losses across the world. The climate variability is causing extreme conditions with respect to water resources scenario across the globe. A projection of 40% shortfall in water availability is projected by 2030 if the world continues on its current path of water usage.

Some of the recommendations such as artificial recharge methods, rainwater harvesting, drip and micro irrigation etc., are suggested to avoid over exploitation of groundwater resources in Gram-Panchayat. Comprehensive Developmental Plan addresses steps to be taken in order to achieve overall sustainable development of a region. Based on the resource's information and requirement of people in the Indlawadi GP, plan is generated to address the issues of shortage of drinking water in problematic villages, improvement of water resources for crop/vegetable/floriculture/agro-horticulture and development of under-utilized and wastelands.

2.6.1 Water Resources Assessment Action Plan

Conservation and sustainable management practices requires sound ecological principles to manage the natural resources to ensure sustainability. Rainwater harvesting is seen as a viable alternative to augment water resources within in Gram-Panchayat. Rainwater harvesting in the site has two components viz., harvesting the roof water and the other, harvesting the surface runoff. In addition, treated waste water is an important source of water.

2.6.2 Roof Water Harvesting to Meet the Drinking Water Requirement of Villages

Roof water from the buildings and other paved areas can be collected and stored in sumps for reuse in the water deficit villages, and also for recharging the bore wells after filtering (using pebble, charcoal, sand beds). It would be advantageous to plan this activity while constructing the new building to collect as much roof water as possible and further for diverting this water to the sumps nearby and the bore wells, after necessary filtering. Designs in this regard need to be worked out separately, taking into consideration of the roof area, rainfall, slope, etc.

Roof water could be harvested by connecting the pipes and bringing the rainwater to a common pipe and then to sumps (size depends on roof area and requirement) after passing through filter beds. This water can be used for flushing, gardening, washing, etc. For the new buildings under construction, harvesting roof water, through sumps, and recharging borewells could be planned.

Some of the common suggestions for groundwater recharge and rainwater harvesting in the villages to be adopted.

- Depth to water levels during pre and post rainy seasons of all existing bore wells are to be monitored at regular intervals
- All existing bore wells to be directly recharged (after filtering the roof water)
- Existing drain/waterways should be cleaned & maintained and linked
- Direct recharging of bore wells will help in recharging depleted fractures and fissures to have sustainable yield from bore wells.

2.6.3 Surface Water Harvesting

All pits/percolation ponds, check dams, dugout ponds (existing and the planned new ones) together will hold a considerable quantity of rainwater for recharging the groundwater. Further, the rainwater from the study area could be diverted during the rainy season to the large covered underground/Ground Level Reservoirs/storage tanks (GLR), located on elevated locations in water deficit villages and then transported to overhead tanks through pumping for water distribution in the villages. From these GLRs, water could be used for gardening and other purposes through gravity. Storing water in the GLRs will avoid loss due to evaporation. For all the tanks, silt filters could be constructed to prevent silting of the tanks. This will also ensure that the water stored in the GLRs is free of silt.

2.6.4 Use of Water from Other Sources

Efforts need to be made to reduce the supply of water through the tanker water supply to problematic village by finding/adopting alternate methods. Exploration of additional external sources to meet both drinking & irrigation needs to be explored. Over-exploitation of groundwater sources can be reduced by setting up of small STPs in villages and using recycled water for other uses like gardening, industrial cooling, flushing, etc. Viable option to minimize load on freshwater supply is by adopting dual water supply systems in the village areas where potable and non-potable water are supplied separately.

2.6.5 Water Resources Development Action Plan

To increase water supply to croplands, horticulture and nurseries, groundwater exploration is suggested which is not fully exploited in the close vicinity of villages. Measures need to be taken to store the water as well as allow water to percolate into the ground by holding the water in water harvesting structures as much as possible. In certain parts of the GP, the surface runoff could be diverted to the dugout ponds, recharge pits and diversion channels. The stream channels could also be de-silted,

widened, and the sides strengthened and linked properly. Trees/plants can also be planted on the sides of these channels.

2.6.6 Water Resources Action Plan Consists of the Following Proposed Structures/Measures

Check Dams

Small barriers or dams constructed of stone, bagged sand or gravel, or other durable material across a stream/drainage. The creation of check dams is helpful for micro-irrigation as well as underground water recharge. Check dams were proposed on the 2nd and 3rd order streams with less than 5% slope along the foot hills. The chain of such check dams along the stream helps in storing rainwater which can be subsequently used for irrigation and replenishing the groundwater. Tentatively about, 11 suitable check dam sites are identified and shown in Fig. 2.10.

Rejuvenation/Restoration/Desilting of Tanks

The Rejuvenation/Restoration/Desilting of tanks is suggested for all bigger tanks which are partially filled with silt. During the fieldwork as well as during the interpretation of the high-resolution image it was observed that some of tanks were silted. Lakes and tanks have a larger ecological and biological role by regulating runoff, reduce erosion and act as a sink for recharging groundwater. Figure 2.10 shows the proposed or existing six tanks/lakes identified for Rejuvenation/Restoration/Disiltation in Indlawadi GP.

Drip irrigation

Drip irrigation systems are generally recommended for plantation and vegetable crops growing in this regions for optimum water usage especially in summer season. A well laid out, drip irrigation can save up to 80% more water than conventional irrigation methods along with increase in the crop yield and production.

Farm Ponds

Storing Water in small to medium sized Farm Ponds was observed in the study area during fieldwork close to villages. Polythene sheets were used to reduce the seepage/infiltration losses. Many farms rely on municipal water or wells (groundwater), while some have built their own ponds to capture and store rainfall for use throughout the year. Adequately managed ponds can also help to minimize their impact on the surrounding watershed. This practice may be further encouraged to sustain horticulture, flori-culture and vegetable growing in the Indlawadi GP.

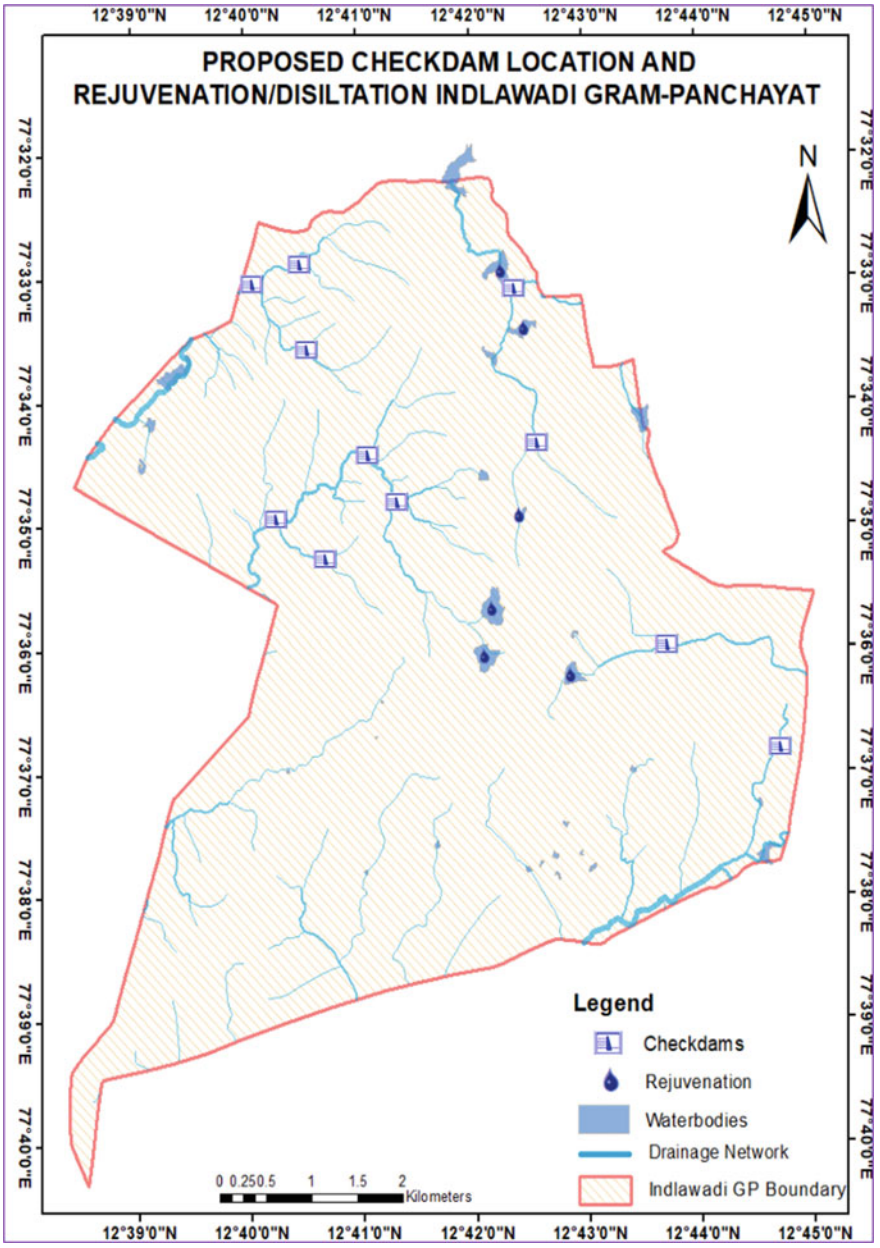

Fig. 2.10 Proposed check-dams locations and tanks/lakes for rejuvenation/restoration for Indlawadi GP

2.7 Recommendations and Suggestions for Improving Water Resources in Indlawadi GP

Based on site specific scientific investigation, it is recommended to construct structures like dug and bore wells, recharge pits/trenches, percolation tanks, check dams, sub surface dykes, point recharge structures for artificial recharge of groundwater. In the present study, using AHP techniques, the suitable areas for artificial recharge has been demarcated. It is well known that, waterbodies have many purposes viz., irrigation, recharging, maintaining the groundwater table as well as reduce erosion by controlling runoff, trap for collecting sediment etc., hence, suggested measures, if implemented for rejuvenation of tanks and lakes in the study area, will definitely build up groundwater resources. Drip irrigation and farm pond (Bottom covered with polythene sheets to prevent infiltration) techniques are already in practice. These techniques with advanced agricultural practices should be encouraged to reduce pressure on depleting groundwater sources. Exploration of additional external sources for both drinking and irrigation needs to be carried out. Setting-up of small STPs and using recycled water for secondary uses through major village municipal supply will definitely help to reduce exploitation of groundwater sources. Collective action on conservation of water would go a long way in increasing the groundwater resources. A two way separate water supply system at GP level for potable and non-potable water will minimize the pressure on fresh water supply. There is a need for active participation by the citizens and also the recommendations have to be implemented by making the public aware of the need for these measures in conserving water.

Acknowledgements We would like to thank the Director, National Remote Sensing Centre, Chief General Manager, RCs, National Remote Sensing Centre for their encouragement and support for this study. We also express our sincere thanks to the staff of Regional Remote Sensing Centre (South) for their useful discussions and special thanks to Dr. Ganesha Raj, Former General Manager, RC-South and Dr. K. S. Ramesh, Former Head, RC-South for their constant guidance and support.

References

Abdel Rahman A (2016) The use of AHP within GIS in selecting potential sites for water harvesting sites in the Azraq Basin—Jordan. J Geogr Inf Syst 8:73–88. http://www.scirp.org/journal/jgis. https://doi.org/10.4236/jgis.2016.81008

Ahmad I, Verma MK (2017) GIS based analytic hierarchy process in determination of suitable site for water storage. Euro Water 60:139–146, 2017. © 2017 E.W. Publications

Ahmad I, Verma MK (2016) Site suitability mapping for water storage structures using remote sensing & GIS for Sheonath Basin in Chhattisgarh State. Int J Appl Eng Res 11(6):4155–4160

Ahmed A (2019) Water governance in India: evidence on water law, policy, and administration from Eight Indian States. Water 11:2071. https://doi.org/10.3390/w11102071

Ariza P, Galán E, Serrano T, Reyes-García V (2007) Water tanks as ecosystems. Local ecosystemic perception for integral management of water tanks in Tamil Nadu, South India. Perifèria Rev d'investigació i Form. en Antropol. 7:1. https://doi.org/10.5565/rev/periferia.178

Bamne Y, Patil KA, Vikhe SD (2014) Selection of appropriate sites for structures of water harvesting in a watershed using remote sensing and GIS. Int J Emerg Technol Adv Eng 4(11):270–275
Bandara KMPS (2006) Assessing irrigation performance by using remote sensing. ISBN: 90-8504-406-5 ITC Dissertation number 134
James Batchelor (2013) Using GIS and SWAT analysis to assess water scarcity and WASH services levels in rural Andhra Pradesh
Central Ground Water Board (2007) Manual on artificial recharge of ground water. Ministry of Water Resources, Government of India, New Delhi
Chowdhury K, Behera B (2021) Institutional dynamics and water resource management: the case of traditional water bodies in West Bengal, India. Int J Water Resour Dev, 1–25. https://doi.org/10.1080/07900627.2021.1916448
Dongardive et al (2018) Water resources planning for the micro watersheds using geospatial techniques. Int J Chem Stud
García A, Sainz A, Revilla JA, Álvarez C, Juanes JA, Puente A (2008) Surface water resources assessment in scarcely gauged basins in the north of Spain. J Hydrol 356:312–326. https://doi.org/10.1016/j.jhydrol.2008.04.019
Hutchings P, Richard F, Smits S, Mekala S (2017) Community management of rural water supply. Routledge, London, New York: Earthscan from Routledge, 2017|Series. https://doi.org/10.4324/9781315313337
IMSD (1995) Integrated mission for sustainable development: technical guidelines. NRSA, Hyderabad, India, 1–27. LULC, Bhuvan (ISRO)—bhuvan.nrsc.gov.in/gis/thematic/index.php
Kota N, Ramudu N, Ravikumar S, Suresh M (2017) Hydrogeomorphological Mapping upto cadastral level, by using high resolution satellite data in Gokaphaslwada watershed, Doulthabad Mandal, Mahabubnagar District. IOSR J Appl Geol Geophys (IOSR-JAGG) 5(1):46–51. e-ISSN: 2321–0990, p-ISSN: 2321–0982. Ver. II, www.iosrjournals.org
Birthe Riisnes Erle Kristvik (2015) Hydrological assessment of water resources in Bergen. Master of Science in Civil and Environmental Engineering Submission date: 10 June 2015
Kumar P, Tiwari KN, Pal DK (1997) Establishing SCS runoff curve number from IRS digital database. J Indian Soc Remote Sens 19(4):246–251
Lele S, Srinivasan V, Jamwal P, Thomas BK, Eswar M, Zuhail TM (2013) Water Management in Arkavathy Basin: A situation analysis. Environment and development discussion paper No. 1 March 2013. Ashoka Trust for Research in Ecology and the Environment
Mondal BK, Sahoo S (2021) Evaluation of spatiotemporal dynamics of water storage changes at block level for sustainable water management in Howrah District of West Bengal. Environ Dev Sustain. https://doi.org/10.1007/s10668-021-01838-7
Murry B (2013) Geospatial modeling for assessing ground water resources: a study in Dimapur Area. Thesis submitted to the Andhra University, Visakhapatnam, NE India
Murthy VVN (2003) Land and water management engineering. Kalyani Publishers, New Delhi
Nyatuame M, Owusu-Gyimah V, Ampiaw F (2014) Statistical analysis of rainfall trend for Volta Region in Ghana. Int J Atmos Sci 67(2):1–11
Ouma YO, Tateishi R (2014) Urban flood vulnerability and risk mapping using integrated multi-parametric AHP and GIS: methodological overview and case study assessment. Water 6:1515–1545. https://doi.org/10.3390/w6061515
Padmavathy AS, Ganesha Raj K, Yogarajan N, Thangavel P (1993) Check dam site selection using GIS approach. Adv Space Res 13(11):123–127
Pandey S, Tripathi G (2020) Development of a smart Village through micro-level planning using geospatial techniques—a case study of Jangal Aurahi Village of Gorakhpur District. In: Sustainable development practices using geoinformatics. Wiley, pp 85–109. https://doi.org/10.1002/9781119687160.ch6
Pandit C, Biswas AK (2019) India's National Water Policy: 'feel good' document, nothing more. Int J Water Resour Dev 35:1015–1028. https://doi.org/10.1080/07900627.2019.1576509

Pani A, Ghatak I, Mishra P (2021) Understanding the water conservation and management in India: an integrated study. Sustain Water Resour Manag 7:77. https://doi.org/10.1007/s40899-021-00556-2

Rajendran V, Venkatasubramani R, Vijayakumar G (2016) Rainfall variation and frequency analysis study in Dharmapuri district (India), India. J Geo Mar Sci 45(11):1560–1565

Rao KV, Bhattacharya AK, Mishra K (1996) Runoff estimation by curve number method- case studies. J Soil Water Conserv 40:1–7

Reddy VR, Behera B (2009) The economic and ecological impacts of tank restoration in South India. Eur J Dev Res 21:112–136. https://doi.org/10.1057/ejdr.2008.12

Sethupathi AS, Lakshmi Narasimhan C, Vasanthamohan (2012) Evaluation of hydrogeomorphological landforms and lineaments using GIS and Remote Sensing techniques in Bargur—Mathur subwatersheds, Ponnaiyar River basin, India. Int J Geomatics Geosci 3(1). ISSN 0976-4380

Sharma SK, Kansal ML, Tyagi A (2015) Resource assessment and strategic planning for improvement of water supply to Shimla city in India using geo-spatial techniques. Egypt J Remote Sens Space Sci 18:85–97. https://doi.org/10.1016/j.ejrs.2015.04.001

Shashikumar BN, Garg V, Nikam BR (2018) Analytical hierarchy process for identification of suitable water harvesting site in geospatial environment. In: ISPRS annals of the photogrammetry, remote sensing and spatial information sciences, volume IV-5, 2018 ISPRS TC V Mid-term Symposium "Geospatial Technology—Pixel to People", 20–23 Nov 2018, Dehradun, India

Shyam GM, Taloor AK, Sudhanshu SSK, Kanga S (2021) Sustainable water management using rainfall-runoff modeling: a geospatial approach. Groundw Sustain Dev 15:100676.https://doi.org/10.1016/j.gsd.2021.100676

Sood V, Gusain HS, Gupta S, Taloor AK, Singh S (2021) Detection of snow/ice cover changes using subpixel-based change detection approach over Chhota-Shigri glacier, Western Himalaya, India. Quat Int 575–576:204–212. https://doi.org/10.1016/j.quaint.2020.05.016

Srivastava A, Chinnasamy P (2021) Developing village-level water management plans against extreme climatic events in Maharashtra (India)—a case study approach, pp 615–635. https://doi.org/10.1007/978-3-030-76008-3_27

Taloor AK, Kotlia BS, Jasrotia AS, Kumar A, Alam A, Ali S, Kouser B, Garg PK, Kumar R, Singh AK, Singh B, Jasrotia R (2019) Tectono-climatic influence on landscape changes in the glaciated Durung Drung basin, Zanskar Himalaya, India: a geospatial approach. Quat Int 507:262–273. https://doi.org/10.1016/j.quaint.2018.09.030

Zeinolabedinia M, Esmaeilyb A (2015) Groundwater potential assessment using geographic information systems and AHP method (Case Study: Baft City, Kerman, Iran). The international archives of the photogrammetry, remote sensing and spatial information sciences, vol XL-1/W5, International conference on sensors & models in remote sensing & photogrammetry, pp 23–25 Nov 2015, Kish Island, Iran

Chapter 3
Long-Term Analysis of River Migration Pattern Using Geospatial Techniques—A Case Study of Upper Part of the Ganga River, India

Vinod K. Sharma, Abhishek Mishra, V. M. Chowdary, and C. S. Jha

Abstract Dynamic changes in river basin cause river bank shifting, change in river channel patterns, river width and course direction. It may cause due to natural phenomena like flood or by construction of man-made structures like dams, barrages. Study of river migration patterns is of much importance and needs historical river course information. Remote sensing satellite data provides synoptic and temporal coverage useful for change analysis. Geospatial techniques integrated with remote sensing data, have potential to carry out river migration studies. Manual analysis of satellite data is a time-consuming process and subjected to human induced errors. This study focuses on different methods, including online cloud-based geospatial analytic platforms for river bank changes using temporal satellite data. A case study of identification of long-term river migration patterns, on Ganga River between Bhimgoda barrage, Haridwar, Uttarakhand, India to Luv-Kush Barrage, Kanpur, Uttar Pradesh, India is attempted. Automated procedures analyzing satellite data from 1975 to 2020, are successfully utilized to calculate morphometric parameter for identifying river migration. Meandering of Ganga River is observed after construction of Narora barrage and Bijnor barrage. Increasing trend in meandering and braiding indices between 0.21 and 0.43 during the study period are observed during the period 1975–2020.

Keywords Remote sensing · River migration · River meandering · Sinuosity index and braiding index

V. K. Sharma (✉)
Regional Remote Sensing Center North, National Remote Sensing Center, New Delhi, India
e-mail: vinod_sharma@nrsc.gov.in

A. Mishra · V. M. Chowdary
Amity Institute of Geoinformatics and Remote Sensing, Amity University, Noida, UP, India

C. S. Jha
Regional Remote Sensing Centre, National Remote Sensing Centre, Hyderabad, India

C. S. Jha et al. (eds.), *Geospatial Technologies for Resources Planning and Management*, Water Science and Technology Library 115,
https://doi.org/10.1007/978-3-030-98981-1_3

3.1 Introduction

Rivers are an important source of water that play an important role in human life. It's a natural waterway that flows across landscape from higher elevation to lower elevation (Sinha and Ghosh 2012). River Ganga is one of the important Indian rivers originating from Himalayan mountains and flows nearly 2525 km distance through Indo Gangetic plains of Uttar Pradesh, Bihar and West Bengal, before joining the Bay of Bengal. Yamuna and Ramganga are the two important tributaries of River Ganga, while Padma and Bhagirathi-Holly are key tributaries. Frequent flooding, shifting of river channels and soil erosion are some of the commonly seen issues in the Indo-Gangetic basin.

River ganga from Gaumukh to Haridwar is called as upper Ganga region, which flows through steep surface having rich biodiversity and fragile ecosystem. Region from Haridwar to Varanasi called as middle Ganga region and has plain region characterized by wide river bed and flood plains. River meandering in plain region is mostly happened, due to human interventions that include diversion for agricultural and industrial activities. Flooding due to sediment deposition is observed in the Varanasi to Ganga Sagar region that leads to channel path changes. River Ganga shows geographic diversity while flowing from upper to lower Ganga region, that exhibits river bank erosion and thereby sediment transportation and deposition along river section. Central water and power research station (CWPRS 2016) briefly explained the aggrading and degrading processes in Ganga River from Bhimgoda Barrage Uttarakhand to Luv-Kush Barrage, Uttar Pradesh. River bank erosion, channel shifting due to sediment deposition or by flooding are considered as geomorphological processes. Pati et al. (2008) studied bank erosion of Majuli island in Brahamputra river using temporal satellite data. Studies on River Ganga and its tributaries indicated erosion and siltation processes from middle Ganga region to lower Ganga region (Thakur et al. 2012). In general, longitudinal profile of major rivers may be straight, meandering or braided channels. However, rivers having straight river channels are rare, they always have meandering and braided channels. Meandering channel creates *S* shape and has alternating bends. Rivers with unstable banks and wide plains are having braided channels. It can be categorized and identified based on multiple channels creating islands in between the river. Researchers have successfully assessed the morphological changes across main rivers including Bhagirathi River and Padma River (Panda and Bandypadhya 2010; Reza 2011) using satellite datasets. Aerial photographs and Landsat images with temporal resolution (1976, 1979 and 1983) were used for identifying average lateral channel erosion rates over Manu and Amazon rivers of Peru at analysis scale of ~100 km (Puhakka et al. 1992; Salo et al. 1986). Landsat and Sentinel satellite imagery for the period 1972–2017 were analyzed over Po di Pilla mouths, Po River delta of Italy for analysis of delta progradation process (Ninfo et al. 2018). Researchers used remote sensing data for computation of morphometric parameters viz., sinuosity, tortuosity and braiding indices, that helps to understand the changes caused by fluvial action of rivers. For

large river systems, satellite remote sensing images are the only way to successfully observe and quantify planimetric morphology (Gilvear and Bryant 2016). Time series analysis of satellite data is helpful in understanding the fluvial changes and river migration pattern over a time. Time series analysis of satellite data for a longer period necessitates data downloading either from providers' websites or FTPs (File Transfer Protocol), which requires good bandwidth and space. Further, selection of cloud free data consumes lot of time. Automation of satellite data analysis can overcome the challenges of analysis of multi-temporal satellite images over larger river systems and can save time. COTS (Commercial – off The Shelf) software's and geospatial analysis skills are required for analysis of satellite data. Manual analysis of satellite datasets for computation of morphometric parameters and river migration is time-consuming process and needs special skills, which is subjected to human induced errors. Data driven semi-automated algorithms were used for geomorphological mapping and landform classification (Giaccone et al. 2021; Giano et al. 2020). Modeling techniques were also successfully utilized for Geomorphological mapping process (Chirico et al. 2021).

Recent advances in technologies have increased the computational power by many folds, while traditional methods of storing the data have been replaced by cloud-based systems, offering on demand resource availability. Online platforms like Google Earth Engine (GEE) facilitate analysis of satellite imageries for different applications (Gorelick et al. 2017). Geospatial analysis power of online platforms has been successfully used for seasonal water bodies extraction (Wang et al. 2018) and surface water spatial extents (Deng et al. 2019). A hybrid approach that integrates digital image processing techniques and online geospatial platforms helps to compute morphometric parameters and identify river migration pattern in an efficient manner. Manual downloading, organizing and geoprocessing of satellite datasets can be minimized by using online processing platform, thereby reducing the high computational and storage requirements.

This study focused on the use of remote sensing satellite data and techniques for studying river migration patterns. Morphometric parameters namely sinuosity, tortuosity and braiding indices were computed using temporal satellite datasets, which help to understand the changes and to identify the patterns. A case study of river Ganga stretch situated between Bhimgoda Barrage (Haridwar, Uttarakhand) and Luv-Kush (Kanpur, Uttar Pradesh) (having an approx. length of 942 km) is carried out to identify the changes for the period 1975–2020 using the morphometric parameters. A hybrid approach that includes online geoprocessing platform (GEE) was used for flood layer generation and to study river migration patterns.

3.2 Role of Remote Sensing in River Migration Studies

Remote Sensing data obtained from aerial surveys and satellites have increasingly been used by researchers for river geomorphic studies. Advancements in spatial and spectral resolutions of remote sensing data have increased capabilities for earth

surface analysis. It offers advantage of better capability to study the spectral responses over the electromagnetic spectrum to distinguish various features, which remain undetected using data obtained through traditional field data collection methods. It is an important source of information for the areas, where ground-based surveys are not feasible (Sui and Maggio 1999). Potential of remote sensing techniques was used globally for river studies (Zaji et al. 2018; Sichangi et al. 2018; Sun et al. 2020). Wide range of remote sensing sensors viz., Landsat (1972 onwards), Indian Remote Sensing (IRS, 1988 onwards) and SPOT (1986 onwards) are providing temporal satellite datasets that are useful for fluvial landform change analysis (Table 3.1). Temporal satellite data, preferably over 20 to 30 years are needed for carrying out the detailed change analysis study. River channel width is an important criterion for choosing the remote sensing sensor for analysis. Larger rivers with more than 200 m width can be easily studied by using medium and high-resolution satellite data (Ramasamy et al. 1991), whereas for very small rivers (less than 20 m width), very high-resolution satellite data or aerial surveys data is needed.

Recently, Unmanned Aerial Vehicle photogrammetry is also used for fluvial geomorphology studies (Gracchi et al. 2021). Identification of morphological changes in Roia River (Ventimiglia, Italy) is carried out using UAV aerial data of 2018 and 2019 covering 12 km of river stretch. Comparison of DTMs (Digital Terrain Models) and orthophotos were carried out to obtain the changes over the study area.

Approximation of fluvial landform change detection using manual GIS (Geographic Information System) analysis involves collection of input satellite data, extraction of study area from the input images and basic image preprocessing. Image

Table 3.1 High and medium resolution satellite datasets for geomorphological

Applications					
Sensor	Band information	Spatial resolution (m)	Temporal resolution (days)	Data availability since	Agency
Landsat	4–9	15–80	16	1972	NASA
IRS	4	5.8–70	5–24	1988	ISRO
SPOT	4–5	2.5–20	26	1986	ESA
ASTER	14	15–90	16	1999	NASA
Sentinel-2 MSI	13	10–60	5	2015	ESA
Cartosat	4	0.25–2.5	5	2005	ISRO
IKONOS	5	1–4	1–3	1999	DigitalGlobe
QuickBird	5	0.61–2.24	2–3	2001	DigitalGlobe
WorldView	4–17	0.31–0.40	1–4	2007	NASA
RapidEye	5	5	1–6	2008	Planet Lab
PRISMA	Spectral bands from 400–2500 nm	30	29	2019	NASA

processing includes ortho correction meant for removal of the internal and external distortions. Further, the ortho-corrected and georeferenced images need to be classified and Normalized Difference Water Index (NDWI) is to be computed. Channel geometry also needs to be calculated for change detection analysis (Biswas et al. 2021). Parameters like River sinuosity also can be computed by identifying the possibility for change and ability of system to recover from disturbance based on the landform change analysis (Fryirs 2017). Manual analysis of multiple inputs demands lot of time and expertise. Semi-automated procedures, object-based analysis methods and data driven approaches are suggested, to perform faster landform analysis (Klingseisen et al. 2008; Anders et al. 2011; Stout and Belmont 2014; Giaccone et al. 2021). Both manual and semi-automated methods demand manual river bank delineation, causing uncertainty and are always subjected to errors. To minimize the human involvement in the change analysis process, fully automated frameworks are essential, saving the time and efforts.

Artificial Intelligence-based techniques are showing promising results in various fields and have potential to be used for change detection analysis. Utilization of machine learning techniques and aerial survey data is attempted for feature detection in fluvial environment (Pontoglio 2021). Supervised machine learning demands huge labeled training datasets and unsupervised machine learning algorithms demand high computation. Recent technological advancements in the field of cloud-based computing, big data and virtualization enabled to process huge datasets efficiently at faster speed. Envisaging online cloud-based platforms for remote sensing applications that include identification of river migration and its patterns can be very useful.

3.3 Zonation for River Migration Studies

3.3.1 Erosion Buffer

Migration of river and migration rates for a given river segment for the study period is computed by generation of Erosion Buffer (EB) around the river segment. To identify the change caused by the manmade structures like barrages and dams, analysis needs to be carried out for the period, that signifies before and after construction of the manmade structures (FEMA 1999; Washington 2004; Thatcher et al. 2009).

3.3.2 Historical Migration Zone (HMR)

Time series satellite data over the study area is divided into different time periods. In each phase, satellite images are overlaid onto each other and a new layer is generated

by considering all the river channel stretches for generation of a composite zone, known as HMR (Thatcher et al. 2009).

3.3.3 Avulsion Potential Zone (APZ)

APZ is mapped based on channel migration zoning (CMZ), where CMZ for a given river segment is computed by summation of the historic migration zone and erosion buffer. The APZ is generated by digitization of the river channel bend ways using satellite images (Cheng 2016).

3.3.4 Disconnected Migration Area (DMA)

DMA may be defined as an area or zone where the river bank protection measures are restricting the river channel migration (Thatcher et al. 2009). It is extracted by CMZ zone behind the protected river bank.

3.4 Geospatial Analytics Platforms

Online geoprocessing and geospatial analytics on cloud-based platforms facilitate users to process time series geospatial data for information extraction without any additional computational hardware, software and data management logistics. Open-source technologies are successfully used to develop online geospatial analytics platforms like Vedas (https://vedas.sac.gov.in/), Bhuvan geo platform (https://bhuvan.nrsc.gov.in/) and Google Earth Engine (https://earthengine.google.com/).

Vedas, provides an online geospatial platform for online processing of geospatial datasets derived over land, mainly collected using Indian sensors. Web analytics tools for vegetation monitoring, new and renewable energy, urban sprawl information system, hydrological applications, cryosphere application and air quality monitoring are available for usage over Indian region. Bhuvan Geo platform is providing online geospatial services for G governance applications, environmental applications and for Disaster management. Online tools for flood management (Sharma et al. 2017, 2018) are developed onto Bhuvan platform for managing natural disasters over India.

Google Earth Engine provides an online access of up-to-date remote sensing databases to users associated with scientific and academic fields. It also provides APIs (Application Programmable Interfaces) to develop the code in JavaScript and Python for spatial and temporal analysis (Gorelick et al. 2017; Google 2022; Sharma et al. 2022). Online geoprocessing platforms have potential for processing remote sensing satellite data for river migration studies and pattern analysis.

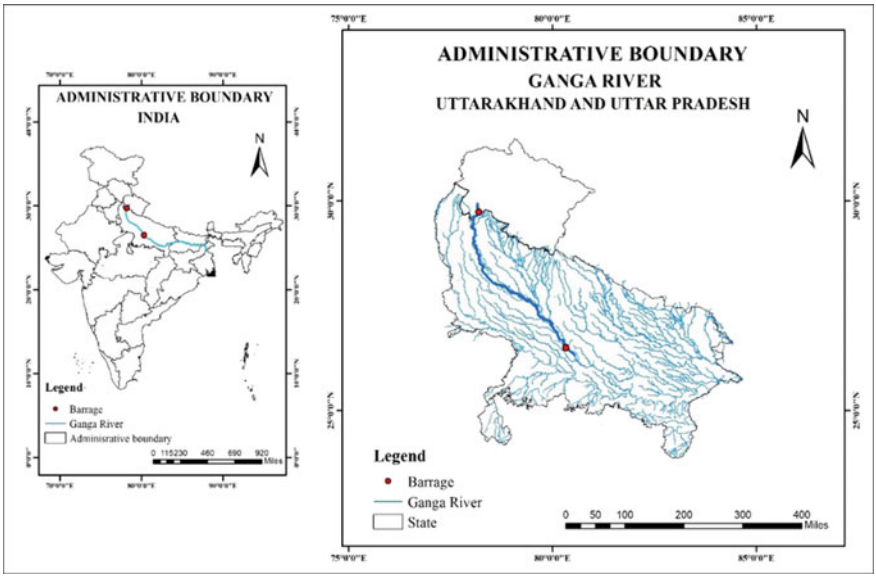

Fig. 3.1 Location map of the study river stretch in the Ganga basin

3.5 Materials and Methods

3.5.1 Study Area

River stretch between Bhimgoda Barrage (Haridwar, Uttarakhand) and Luv-Kush Barrage (Kanpur, Uttar Pradesh) was chosen as study area for this study. Geographically, situated between 29°57′23″N 78°10′49″E and 80.3164°E longitudes and 29°57′23″N and 26.5068°N (Fig. 3.1). Mean annual rainfall of study region is nearly 1100 mm. River Ganga enters the plains near Haridwar after originating from Himalayas and crosses through number of barrages situated at Bhimgoda, Bijnor, Narora and Kanpur in the study river segment. River Ganga is the largest basin in India and traverses a distance of nearly 1450 km between Uttarakhand and Uttar Pradesh states, with a catchment area of 294,410 km^2. It exhibits braided, meandering and anastomosing patterns in the catchment area (CWPRS 2016).

3.5.2 Remote Sensing Satellite Data Processing and Analysis

Remote sensing satellite data of past 45 years for the study area was analyzed to identify the trend in the Ganga River migration pattern between Bhimgoda Barrage

Table 3.2 Satellite datasets used for river migration analysis

Satellite	Sensor	Period	Spatial resolution (m)
Landsat 1	MSS	1975	60
Landsat 3	MSS	1980	60
Landsat 4	TM	1985	30
Landsat 5	TM	1990, 1995, 2000	30
Landsat 7	ETM	2005, 2010	30
Landsat 8	OLI	2015, 2020	30

(Haridwar, Uttarakhand) and Luv-Kush Barrage (Kanpur, Uttar Pradesh). Details of satellite datasets used in this study are given in Table 3.2.

Recent days, Google Earth Engine (GEE) is found to be quite useful for meeting the current needs, associated with remote sensing satellite data analysis in open-source domain. It is based on Java script and python-based API's (Application Programmable Interface), which facilitate users with computational resources needed for processing satellite datasets. It helps to customize and access the large up to date remote sensing satellite data. It is also useful in the spatiotemporal analysis of satellite data (Gorelick et al. 2017).

Cloud free optical datasets of Landsat satellite at 5-year interval are used to identify the changes during non-monsoon season. Landsat satellite image attribute (CLOUD_COVER), providing information of cloudiness percentage is used to choose the cloud free images over the study area.

GEE is a unique platform on web, that helps to visualize and analyze the Landsat images since July, 1972. Available datasets can be visualized onto the online spatial viewer and best suitable cloud free data can be chosen for further analysis, thus saving efforts and time. On the contrary, manual analysis demands downloading and processing of satellite datasets, which is computationally cumbersome. In the manual analysis, all the satellite datasets have to be georeferenced where, SOI (Survey of India) toposheets and ground control points can be used to georeferenced the images over Indian region. Further, it has to be reprojected (like UTM projection) for further analysis. This time-consuming pre-processing analysis can be minimized by using the GEE platform. Multi-temporal Landsat images with different spatial resolutions (Table 3.2) are resampled to 30 m, corresponding to other input layers. In this study, significant planform change was carried out on yearly basis using mosaicked satellite data for the entire study river stretch. Once the pre-processing is completed, the Ganga River bank lines are extracted by vectorizing, from the satellite data corresponding to different years namely 1975, 1980, 1985, 1990, 1995, 2001, 2005, 2010, 2015 and 2020.

In general, green and NIR bands of electromagnetic spectrum are of great help for delineation of water feature, where it can clearly distinguish from other features like agriculture and plantation. Waterbodies absorb the NIR band radiation. MIR &

SWIR spectral bands of Landsat 7 exhibit the similar characteristics and easily classify the water feature. Water feature is classified using NDWI (Normalized Difference Water Index) (McFeeters 1996) and MNDWI (Modified Normalized Difference Water Index) (Xu 2006) and the equations are given below.

$$\text{NDWI} = (\text{Green}--\text{NIR})/(\text{Green} + \text{NIR}) \tag{3.1}$$

$$\text{MNDWI} = (\text{Green}--\text{SWIR})/(\text{Green} + \text{SWIR}) \tag{3.2}$$

Conditioning factors are applied, to improve the water mask layer. Slope, aspect and LULC (Land Use Land Cover) are used to minimize the false polygon of water. Once the river bank lines corresponding to different years are extracted from satellite data, deviations in river banks were identified using overlay analysis. River center line i.e., the center part of the river from its bank is an important parameter, which describes the planform changes over time. Manual image processing method (Zhang and Suen 1984) and automated methods (Medial axis algorithm of GEE) can be used to determine the river centerline. Li et al. (2019) has successfully employed GEE platform for identification of river center line using GEE platform and similar concept is adopted in this study.

3.5.3 River Migration Analysis

Meandering indices and braiding index were computed to study the changes in planform and river migration over the study river Ganga. An attempt was also made to establish a relation between planform change and flooding in this study. Decadal flood layers for the period 2010–2020 pertaining to the part of Uttar Pradesh state (plain region) were analyzed and correlated with change in river planform to study the effect of floods on river migration.

3.5.3.1 River Shift

River shifting is a geomorphological process that involves lateral migration of alluvial river channel across its floodplain. Rivers adopt meandering courses in the great plains due to prevailing level topography and gentle slopes, swing in their valleys and often change their course during floods due to increased quantity of water, where the streams try to straighten in their courses. Meandering in river streams is mainly caused by the bank erosion and deposition over time, while in braided streams, river shift is caused by sediment transport. Satellite datasets of 1975, 1980, 1985, 1990, 1995, 2001, 2005, 2010, 2015 and 2020 were overlaid and analyzed to identify the shift in the river course.

3.5.3.2 Sinuosity Index

The sinuosity index may be defined as the distance measured between two points. If the difference is computed on the stream along the thalweg and divided by the valley length between the two points, it is termed as sinuosity ration (Krishnau and Gopinath 2015). Thus, sinuosity ratio (SR) helps to identify channel meandering. If SR of a river channel is greater than or equal to 1.5, the channel can be categorized as meandering channel (Leopold and Wolman 1957).

River sinuosity can be computed with a centerline method (Zhang and Suen 1984). River mean width, its connectivity and river sinuosity can be computed and analyzed to obtain annual river planform variations. GEE provides the functionality to compute the 3 planform parameters, where sinuosity index computed using GEE and Mean sinuosity index derived from End Point Rate (EPR) and Linear Regression Rate (LRR) highlights the advantages of online platform for carrying out river related studies. The EPR technique integrated with remote sensing satellite data is accurate and reliable approach used for computation of shoreline change analysis (Sebat and Salloum 2018). LRR has potential to study more than 2 shorelines and is determined by fitting a least-square regression line to all shoreline points for a particular transects (Salghuna and Bharathvaj 2015).

$$\begin{aligned}\text{Sinuosity} = \{&(\text{Number of pixels associated with straight line})/\\ &(\text{Number of pixels associated with center line})\}\end{aligned} \tag{3.3}$$

In this study, potential of both methods is used to compute the sinuosity index.

3.5.3.3 Braiding Index

A river is said to be braided if a river channel consists of network of smaller channels, separated by temporary island. CWPRS (2016) has proposed an updated formula for computation of the braiding index (BI).

Braid index (BI) is calculated by dividing the total channel length, including all active secondary channels (ΣL_S), by the main channel length (ΣL_M) based on the centerline of the channels (Kuo et al. 2017).

$$\text{Braiding Index} = (\Sigma L_S + \Sigma L_M)/\Sigma L_M \tag{3.4}$$

3.6 Results Ad Discussion

Multi-temporal post-monsoon satellite images are studied to analyze the long-term river migration pattern over the study area and observed change in river morphology

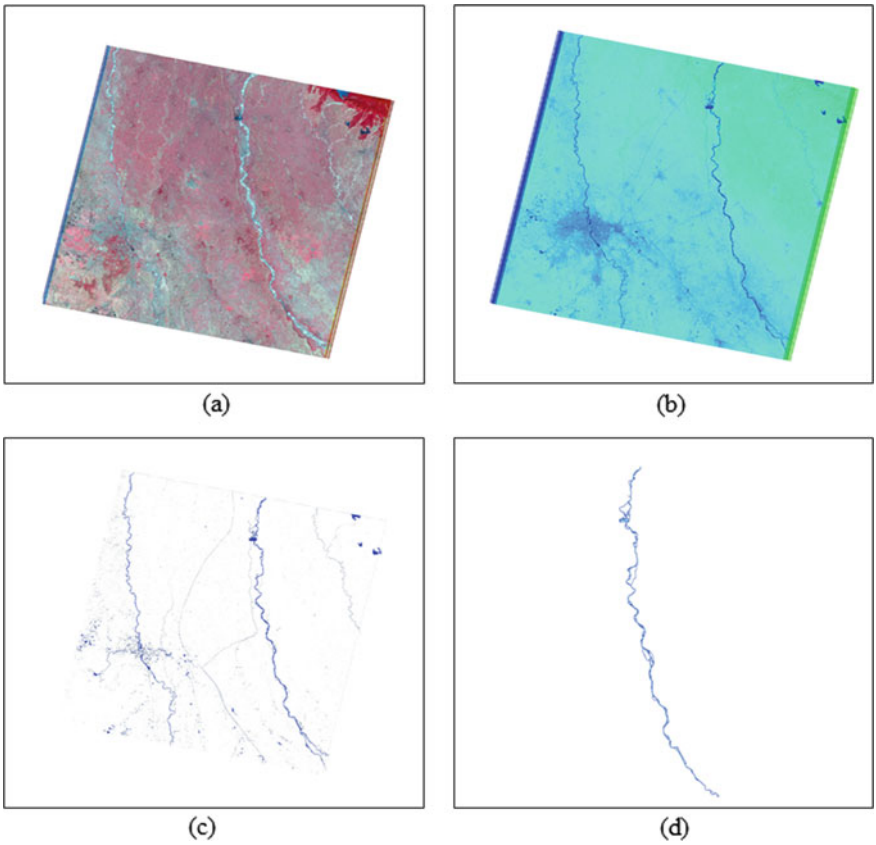

Fig. 3.2 River line extraction using MNDWI **a** Landsat 7 imagery over study area, **b** MNDWI output, **c** Water mask layer after conditioning factor, **d** Final River line

of Ganga River. Sinuosity index was computed using two approaches namely, (i) Mean sinuosity index derived from End Point Rate and Linear Regression Rate, (ii) Sinuosity index derived using GEE, by rationing pixels associated with straight line and pixels associated with centerline (Tobón-Marín and Cañón Barriga 2020).

Sinuosity index was computed from the extracted river lines of each year. River line extraction using MNDWI on input Landsat image is shown in Fig. 3.2.

3.6.1 River Migration Analysis Using End Point Rate and Linear Regression Rate

The study area from Bhimgoda barrage to Luv-Kush Barrage was divided into 4 river segments, namely (i) Bhimgoda barrage to Gongli Khadar, (ii) Gongli Khadar to

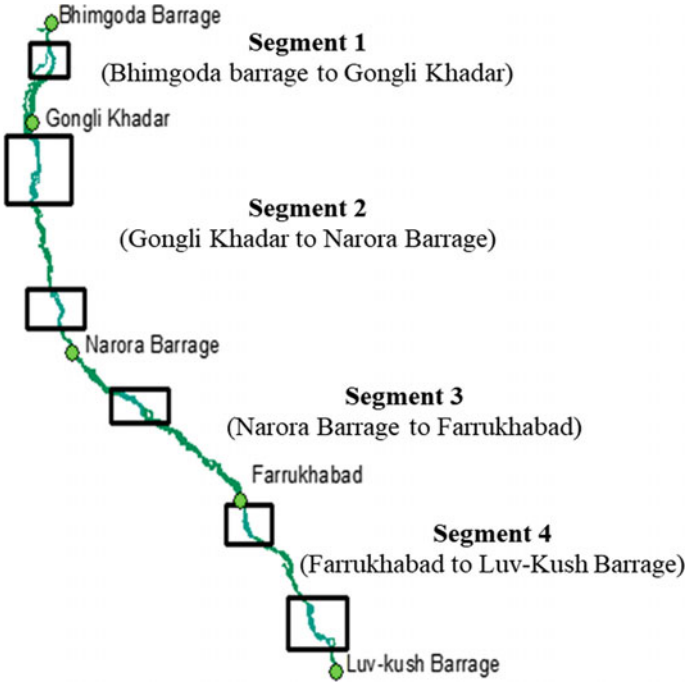

Fig. 3.3 Segmentation of study area between Bhimgoda and Luv-Kush barrage for generation of end point rate and linear regression rate

Narora barrage, (iii) Narora barage to Farukhabad, and (iv) Farukhabad to Luv-Kush Barrage for analysis purpose (Fig. 3.3).

River bank lines derived using the temporal satellite datasets for the years 1975 to 2020 were analyzed for computation of End point rate. It is calculated by considering the distance of shoreline movement and the time elapsed in between the earliest and latest measurements. The study river stretch is divided into four segments and 1214 transects for computational ease and effective analysis. These four segments were analyzed for three time periods namely (i) 1975–1995, (ii) 1995–2020 and (iii) 1975–2020 (Table 3.3). Zone A, in 1995–2020 period observed high Mean Erosion/Accretion of 26.42 m, whereas zone D during 1975–1995 observed maximum accretion of 367.67 m. Erosion values for the 3 periods vary from −10 to 895 m. Values of erosion & accretion computations are shown in Table 3.3.

Analysis of linear regression rates with respect to transects for shorter, medium and longer durations to determine change statistics is shown in Figs. 3.4 and 3.5.

Linear regression rates for Study period 2 (1995 to 2020) indicated that the average rate of stream is 26.42 m, which is higher as compared to other time periods. Highest accretion rates were observed during the period 1975–1995 for segment 4, which indicated decreasing trend after 2006 that may be attributed to construction of new barrage.

Table 3.3 Erosion and Accretion computations for short term, medium term and long term over study area

	River bank shift rates (m/year)											
	Period (1975–1995)				Period (1995–2020)				Period (1975–2020)			
Terms	Zone A	Zone B	Zone C	Zone D	Zone A	Zone B	Zone C	Zone D	Zone A	Zone B	Zone C	Zone D
No of Transects	189	321	391	304	189	321	391	304	189	321	391	304
Mean Erosion/ Accretion	5.034	−26.67	−9.14	−6.38	26.42	5.218	25.40	18.84	0.11	−20.53	−2.12	−9.28
Max. Accretion	240.67	140.74	137.12	367.67	250.48	199.13	144.58	127.82	112.25	85.08	317.37	128.07
Min. Accretion	1.09	0.22	0.006	0.32	0.19	0.68	0.76	0.01	1.01	0.11	0.07	0.65
Max. Erosion	−101.46	−259.4	−256.26	−253.43	−103.48	−33.78	−152.15	−10.01	−143.5	−347.19	−895.5	−268.57
Min. Erosion	−0.74	−1.44	−0.24	−0.32	−0.79	−0.32	−0.05	−0.84	−0.21	−0.05	−0.24	−0.12
Mean Accretion	61.49	44.01	41.94	47.268	55.25	35.51	53.39	37.10	36.09	15.91	34.09	30.32
Mean Erosion	-35.001	-66.25	-71.56	-55.95	-26.21	-32.99	-41.53	-27.12	-40.126	-36.32	-38.34	-35.76

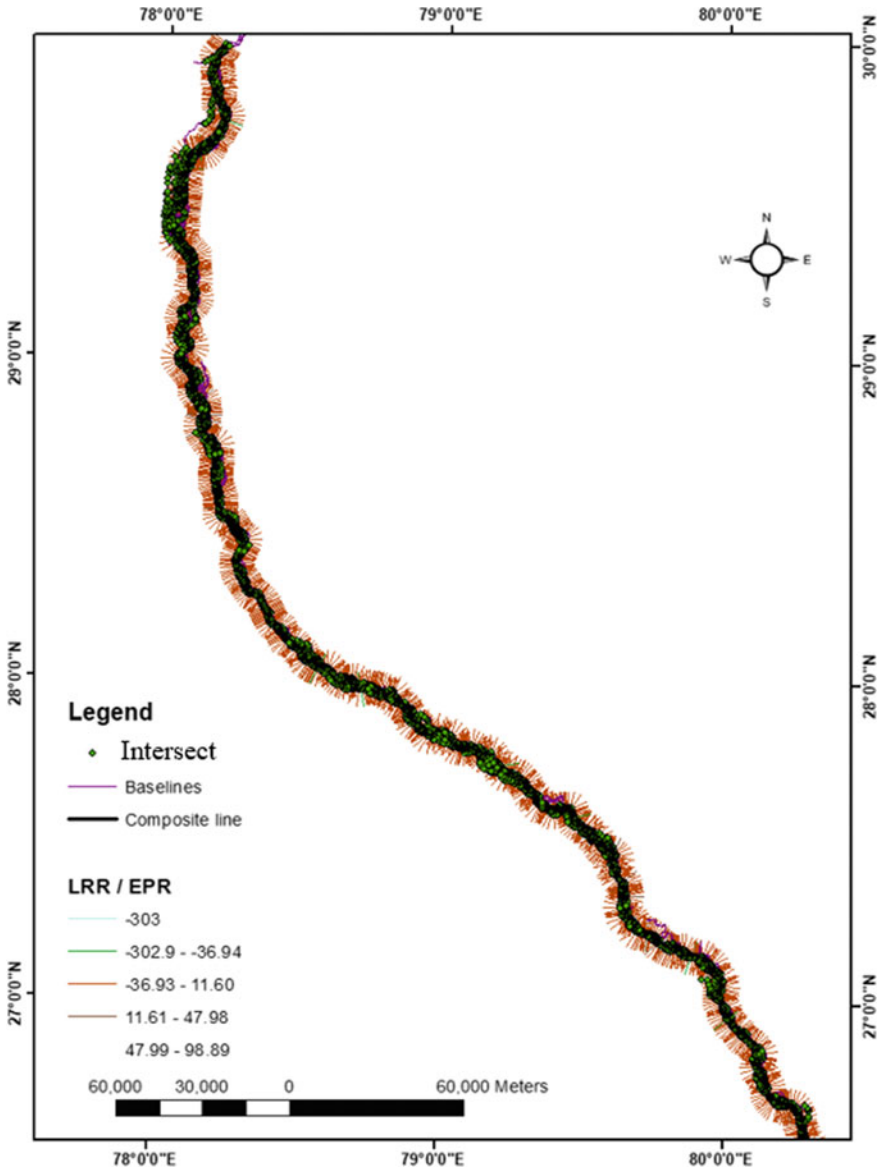

Fig. 3.4 Linear regression rate computed over study area

3.6.2 Sinuosity Index Derived Using Centerline Method

Changes in river surface area is very much essential in river plain form study. Shifting in the river bank line is the major indicator of river bed shift or change in river width.

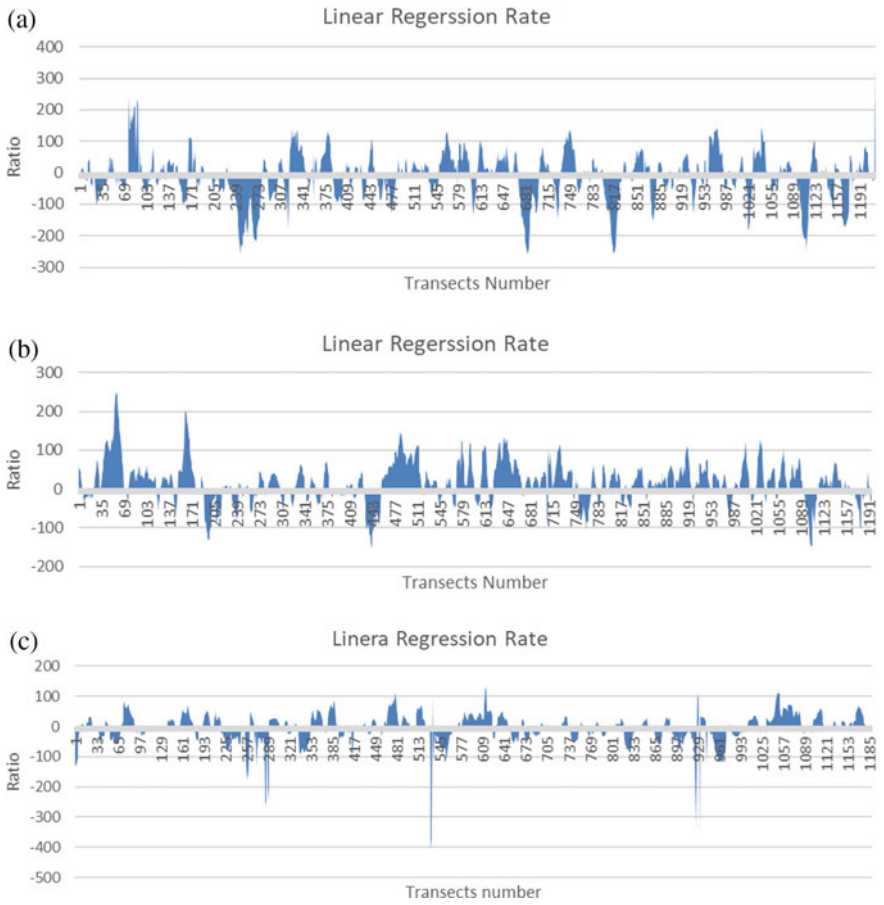

Fig. 3.5 Linear regression rate with respect to transects. **a** Study period 1 (1975 to 1995) **b** Study period 2 (1995 to 2020) and **c** Study period 3 (1975 to 2020)

Study of temporal satellite images indicated changes in the river bank line in upper and middle Gangetic plain during year 1975 to 2020. Sinuosity index derived using centerline method over the study area ranges between 1.26 and 1.39 (Table 3.4). Sinuosity index is an indicator of river meandering where <1.05 value indicates straight river pattern, 1.05 to 1.3 indicates sinuous pattern and above 1.3 indicates river meandering. Observed sinuosity index values in the study area for different years indicated meandering pattern.

Table 3.4 Sinuosity index computed for the period 1975–2020 at 5-year interval

Year	Sinousity index
1975	1.26
1980	1.26
1985	1.33
1990	1.27
1995	1.30
2000	1.30
2005	1.39
2010	1.37
2015	1.36
2020	1.33

3.6.3 Meandering Index

Meandering index, computed for the study area (Bhimgoda to Luv-Kush Barrage) indicated an increasing trend of 1.26 to 1.35 for the period 1975–2020 (Fig. 3.6), that can be attributed to construction of barrage. River change and shift in mainstream channel at upper and middle part is also observed. Sedimentation and siltation might have increased the braiding of Ganga River near Narora and Luv-Kush Barrage. Diversion of river flows through network of canals also might have affected the river flows in the upstream.

3.6.4 Analysis of River Migration Pattern

River migration over the study area was analyzed for different time periods namely (i) 1990–2000 (ii) 2000–2010 and (iii) 2010–2020 (Figs. 3.7a–c). Significant shift was observed during these study periods over study area, which clearly indicated that the construction of man-made structures is affecting the river flow and contributed to river migration.

3.6.5 Fluvial Landform Changes

River Ganga between Bhimgoda Barrage at Haridwar, Uttarakhand to Luv-Kush, Kanpur, Uttar Pradesh was analyzed using multi-temporal satellite datasets for understanding the fluvial landform changes. Migration of river was observed over the study area during the period 1975–2020. Shift in the river course was observed near Luv-Kush Barrage with a mean accretion of 367.67 m and mean erosion of −10.146 m during the period 1975–1995. Change in the stream capacity is one of the important

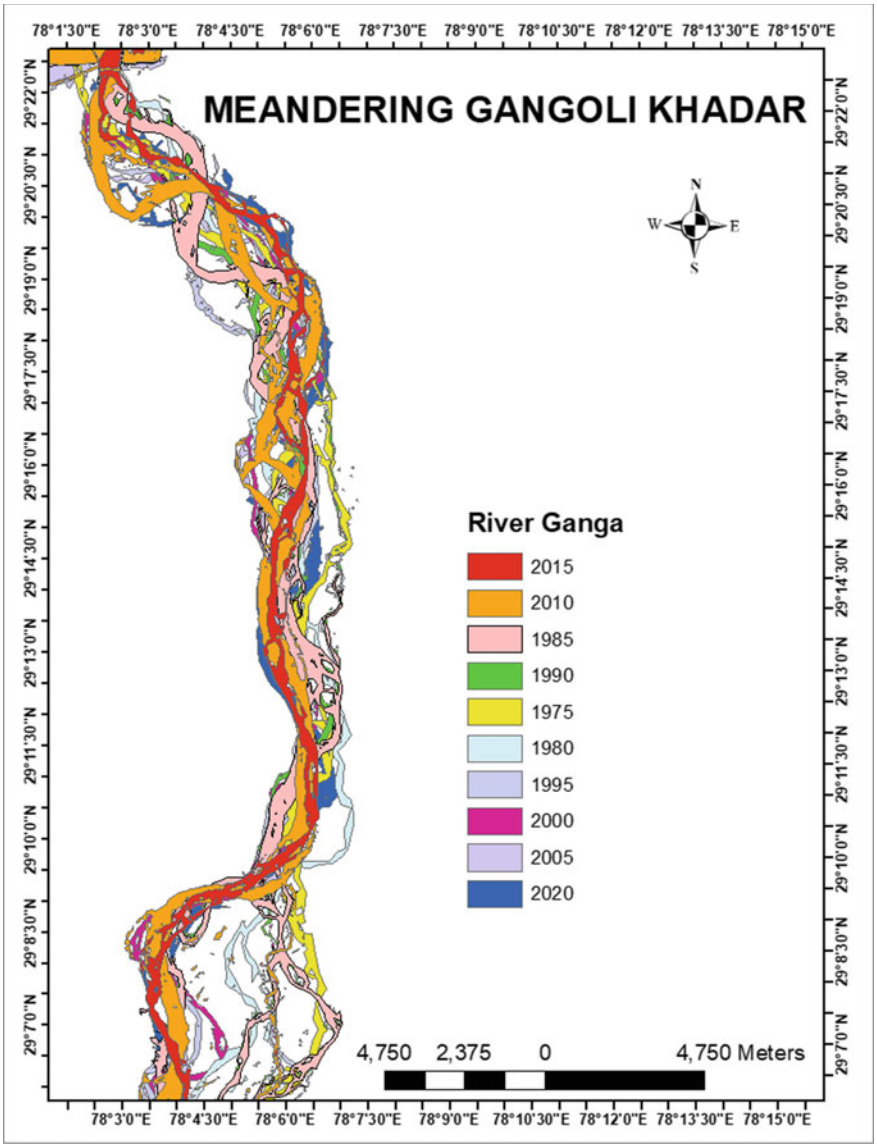

Fig. 3.6 Meandering of river Ganga near Gangoli Khadar

driving factors for river meandering. Stream discharge and expansion of human settlements due to urbanization in the segment 3 (Narora barrage to Farrukhabad) have influenced the river pattern. This led to high accretion and erosion for the period 1995–2020. Construction of new barrages and structures during this period regulated the stream flow thereby causing extended migration pattern. A hybrid approach

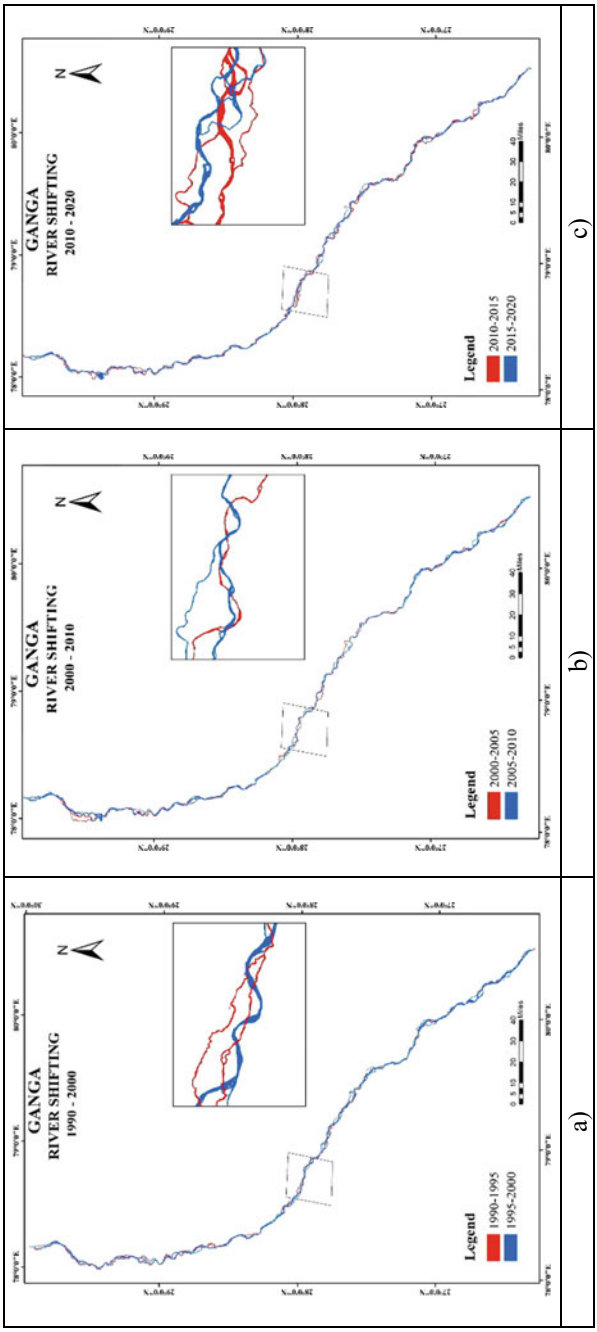

Fig. 3.7 Decadal River migration patterns during the periods: **a** 1990–2000, **b** 2000–2010 and **c** 2010–2020

that includes both automated procedures and digital image processing techniques was envisaged for computation of morphometric parameters in an efficient manner. These parameters were successfully used to analyze and to identify the river migration patterns over the study area for the period 1975–2020.

3.7 Summary

Historical remote sensing satellite datasets provides a framework for river migration patterns identification and river management planning. Geographic information system integrated with satellite imageries accurately measures morphometric parameter, that are vital for carrying out studies related to fluvial environments and its management. Recent advancements in storage and computational facilities, provide opportunities to utilize online platforms for carrying out the studies related to river migration. Cloud-based online geospatial analytic platform and automated procedures are successfully utilized in analysis and identification of river migration patterns for the upper part of the Ganga River, India. River migration change on Ganga River between Bhimgoda barrage, Haridwar, Uttarakhand, India to Luv-Kush Barrage, Kanpur, Uttar Pradesh, India is studied, using satellite images acquired between 1975 and 2020. Results indicated a considerable shift in the river course near downstream of Bhimgoda Barrage and in segment 3 (Narora barrage to Farrukhabad). Channel sinuosity computed over the river study indicated change in river width. Diversion of water into canals, construction of dams and barrages causes considerable decrease in the discharge rate for Ganga River near Haridwar and Narora barrage, causing shift in river channels. Patterns of River migration using historical satellite datasets are successfully studied and various indices (sinuosity and braiding index) are computed using geospatial techniques, which indicated shift in the river course during the period 1975–2020. Shifting of these river channels could be attributed to human interventions and constructions.

Acknowledgements Organizations ISRO, USGS and Google Earth Engine are gratefully acknowledged for accessibility to the various data sets needed for execution of this study. We sincerely thank NRSC for providing resources to carry out this study.

References

Anders NS, Seijmonsbergen AC, Bouten W (2011) Segmentation optimization and stratified object-based analysis for semi-automated geomorphological mapping. Remote Sens Environ 115(12):2976–2985

Biswas RN, Islam MN, Islam MN, Shawon SS (2021) Modeling on approximation of fluvial landform change impact on morphodynamics at Madhumati river basin in Bangladesh. Model Earth Syst Environ 7(1):71–93

Boothroyd RJ, Williams RD, Hoey TB, Barrett B, Prasojo OA (2021) Applications of Google earth engine in fluvial geomorphology for detecting river channel change. Wiley Interdisc Rev: Water 8(1):e21496

Cheng NS (2016) Comparison of sediment-pickup rates over plane bed and dunes. J Hydraul Eng 142(12):04016057

Chirico PG, Bergstresser SE, DeWitt JD, Alessi MA (2021) Geomorphological mapping and anthropogenic landform change in an urbanizing watershed using structure-from-motion photogrammetry and geospatial modeling techniques. J Maps 17(4):241–252

CWPRS (2016) Report of the committee constituted for preparation of guidelines for works on Desiltation from Bhimgoda (Uttrakhand) to Farakka (West Bengal), India

Deng Y, Jiang W, Tang Z, Ling Z, Wu Z (2019) Long-term changes of open-surface water bodies in the Yangtze river basin based on the Google earth engine cloud platform. Remote Sens 11(19):2213

FEMA (1999) River erosion hazard areas—mapping feasibility study: federal emergency management agency, technical services division, Hazards Study Branch

Fryirs KA (2017) River sensitivity: a lost foundation concept in fluvial geomorphology. Earth Surf Proc Land 42(1):55–70

Giaccone E, Luoto M, Vittoz P, Guisan A, Mariéthoz G, Lambiel C (2019) Influence of microclimate and geomorphological factors on alpine vegetation in the Western Swiss Alps. Earth Surf Proc Land 44(15):3093–3107

Giaccone E, Oriani F, Tonini M, Lambiel C Mariéthoz G (2021) Using data-driven algorithms for semi-automated geomorphological mapping. Stoch Environ Res Risk Assess 1–17

Giano SI, Danese M, Gioia D, Pescatore E, Siervo V, Bentivenga M (July 2020) Tools for semi-automated landform classification: a comparison in the basilicata region (Southern Italy). In: International conference on computational science and its applications. Springer, Cham, pp 709–722

Gilvear D, Bryant R (2016) Analysis of remotely sensed data for fluvial geomorphology and river science. Tools Fluvial Geomorphol 103–132

Google (2022) Google earth engine. Retrieved from https://earthengine.google.com/

Gorelick N, Hancher M, Dixon M, Ilyushchenko S, Thau D, Moore R (2017) Google earth engine: planetary-scale geospatial analysis for everyone. Remote Sens Environ 202:18–27

Gracchi T, Rossi G, Stefanelli CT, Tanteri L, Pozzani R, Moretti S (2021) Tracking the evolution of riverbed morphology on the basis of UAV photogrammetry. Remote Sens 13(4):829

Klingseisen B, Metternicht G, Paulus G (2008) Geomorphometric landscape analysis using a semi-automated GIS-approach. Environ Model Softw 23(1):109–121

Krishnau A, Gopinath G (2015) Sinuosity analysis using geographic information system (GIS): case study of a tropical river basin. Int J Earth Sci 8(2):0974–5904

Kuo CW, Chen CF, Chen SC, Yang TC, Chen CW (2017) Channel planform dynamics monitoring and channel stability assessment in two sediment-rich rivers in Taiwan. Water 9(2):84

Leopold LB, Wolman MG (1957) River channel patters: braided, meandering, straight, physiographic and hydraulic studies of rivers. U.S. Government Printing Office, Washington

Li Q, Lan H, Zhao X, Wu Y (2019) River centerline extraction using the multiple direction integration algorithm for mixed and pure water pixels. GIScience Remote Sens 56(2):256–281

McFeeters SK (1996) The use of the normalized difference water index (NDWI) in the delineation of open water features. Int J Remote Sens 17(7):1425–1432

Ninfo A, Ciavola P, Billi P (2018) The Po delta is restarting progradation: geomorphological evolution based on a 47-years earth observation dataset. Sci Rep 8(1):1–6

Panda S, Bandyopadhyay J (2010) Morphodynamic changes of Bhagirathi river at Murshidabad district using geoinformatics. J Geogr Inf Syst 3:85–97

Pati JK, Lal J, Prakash K, Bhusan R (2008) Spatio-temporal shift of western bank of the Ganga river, Allahabad city and its implications. J Indian Soc Remote Sens 36(3):289–297

Pontoglio E, Dabove P, Grasso N, Lingua AM (2021) Automatic features detection in a fluvial environment through machine learning techniques based on UAVs multispectral data. Remote Sens 13(19):3983

Puhakka M, Kalliola R, Rajasilta M, Salo J (1992) River types, site evolution and successional vegetation patterns in Peruvian Amazonia. J Biogeogr 651–665

Ramasamy SM, Bakliwal PC, Verma RP (1991) Remote sensing and river migration in Western India. Title Remote Sens 12(12):2597–2609

Reza I (2011) Tracking the morphological change of a river extent of Bangladesh using satellite images in ArcGIS. City Reg Planning Depart 1/11

Salghuna NN, Bharathvaj SA (17 March 2015) Shoreline change analysis for northern part of the coromandel coast

Salo J, Kalliola R, Häkkinen I, Mäkinen Y, Niemelä P, Puhakka M, Coley PD (1986) River dynamics and the diversity of Amazon lowland forest. Nature 322(6076):254–258

Sebat M, Salloum J (2018) Estimate the rate of shoreline change using the statistical analysis technique (Epr). Business It 8(1):59–65. https://doi.org/10.14311/bit.2018.01.07

Sharma VK, Mishra N, Shukla AK, Yadav A, Rao GS, Bhanumurthy V (2017) Satellite data planning for flood mapping activities based on high rainfall events generated using TRMM, GEFS and disaster news. Ann GIS 23(2):131–140

Sharma VK, Mishra N, Bhatt CM, Rao GS, Bhanumurthy V (2018) An open source framework for publishing flood inundation extent libraries in a Web GIS environment using open source technologies. Int J Cartography 4(1):65–77

Sharma VK, Azad RK, Chowdary VM, Jha CS (2022) Delineation of frequently flooded areas using remote sensing: a case study in part of Indo-Gangetic basin. In: Geospatial technologies for land and water resources management. Springer, Cham, pp 505–530

Sichangi AW, Wang L, Hu Z (2018) Estimation of river discharge solely from remote-sensing derived data: an initial study over the Yangtze river. Remote Sens 10(9):1385

Sinha R, Ghosh S (2012) Understanding dynamics of large rivers aided by satellite remote sensing: a case study from lower Ganga plains, India. Geocarto Int 27(3):207–219

Stout JC, Belmont P (2014) TerEx Toolbox for semi-automated selection of fluvial terrace and floodplain features from lidar. Earth Surf Proc Land 39(5):569–580

Sui DZ, Maggio RC (1999) Integrating GIS with hydrological modeling: practices, problems, and prospects. Comput Environ Urban Syst 23(1):33–51

Sun W, Shan J, Wang Z, Wang L, Lu D, Jin Z, Yu K (2020) Geospatial analysis of urban expansion using remote sensing methods and data: a case study of Yangtze river delta. China. Complexity

Thakur PK, Laha C, Aggarwal SP (2012) River bank erosion hazard study of river Ganga, upstream of Farakka barrage using remote sensing and GIS. Nat Hazards 61(3):967–987

Thatcher T, Swindell B, Boyd K (2009) Yellowstone river channel migration zone mapping. DTM Consulting, Inc , and Applied Geomorphology. Inc.: Bozeman, MT. https://ftpgeoinfo.msl.mt.gov/Documents/Projects/Channel_Migration_Zones/Yellowstone20090413Report.pdf. Accessed 28 Apr 2021

Thatcher T, Swindell B, Boyd K (2016) Yellowstone river channel migration zone mapping. Yellowstone river conservation district council

Tobón-Marín A, Cañón Barriga J (2020) Analysis of changes in rivers planforms using google earth engine. Int J Remote Sens 41(22):8654–8681

Wang X, Xie S, Zhang X, Chen C, Guo H, Du J, Duan Z (2018) A robust multi-band water index (MBWI) for automated extraction of surface water from Landsat 8 OLI imagery. Int J Appl Earth Obs Geoinf 68:73–91

Washington DNR (2004) Standard methods for identifying bankfull channel features and channel migration zones, Washington department of natural resources forest board manual, 2004, Section 2: p 69. http://file.dnr.wa.gov/publications/fp_board_manual_section02.pdf. Accessed on 28 Jan 2021

Xu H (2006) Modification of normalised difference water index (NDWI) to enhance open water features in remotely sensed imagery. Int J Remote Sens 27(14):3025–3033

Zaji AH, Bonakdari H, Gharabaghi B (2018) Remote sensing satellite data preparation for simulating and forecasting river discharge. IEEE Trans Geosci Remote Sens 56(6):3432–3441
Zhang TY, Suen CY (1984) A fast parallel algorithm for thinning digital patterns. Commun ACM 27(3):236–239. https://doi.org/10.1145/357994.358023

Chapter 4
Space-Borne Scatterometers for Understanding the Large-Scale Land Hydrological Processes

Praveen Kumar Gupta, Ashish Pandey, Deen Dayal, Rohit Pradhan, R. P. Singh, and A. Misra

Abstract This chapter is aimed to provide insight into various hydrological processes and capabilities of scatterometers for hydrological applications. Space-borne scatterometers are active microwave radar instruments that measure the normalized radar cross-section or backscatter of the surface. A separate measurement of the noise-only power is also measured to determine backscatter and estimate brightness temperatures. These sensors mainly operate in Ku (13.5 GHz) and C (5.3 GHz) band frequencies. Sensors are designed primarily for operational ocean applications, especially for estimating wind speed and directions in oceans using ocean surface roughness. The spatial resolution is coarse, but the scanning geometry provides multiple observations of the target, and overlapping orbits provide scope to improve spatial resolution using signal and image processing techniques. Therefore, recently these active radar sensors have also been used for land hydrological applications to address the sub-catchment scale hydrological processes such as soil moisture, inundation, runoff, etc. using the dielectric property of the surface. Microwave radiations, sensitive to moisture in the soil, are being utilized at sub-catchment scales as a proxy to estimate the river/reservoir water levels, river discharge, identification of irrigated areas, drought events, releases to the canal, and other hydrological water fluxes using advanced techniques such as machine learning and, through assimilation in hydrological and hydrodynamic models. Also, along with microwave signals, the scatterometer provides brightness temperatures which are used to map the major inundation at global scales. The advantage of a scatterometer lies in its ability to provide high temporal observations of 1–2 days at global scales, which becomes

P. K. Gupta · R. Pradhan · R. P. Singh · A. Misra
Space Applications Centre, Indian Space Research Organisation, Ahmedabad, Gujarat 380015, India

A. Pandey · D. Dayal (✉)
Department of Water Resources Development and Management, Indian Institute of Technology Roorkee, Roorkee, Uttarakhand 247667, India
e-mail: ddayal@wr.iitr.ac.in

C. S. Jha et al. (eds.), *Geospatial Technologies for Resources Planning and Management*, Water Science and Technology Library 115,
https://doi.org/10.1007/978-3-030-98981-1_4

essential for near to real-time hydrological applications. Scatterometers provide valuable operational monitoring tools of terrestrial hydrology and, with different configurations, can be used to get an advanced insight into earth surface hydrological processes and long-term change.

Keywords Scatterometers · Microwave radiations · Hydrological processes · River discharge · Flood inundation

4.1 Introduction

The "Remote Sensing Age" offers new and attractive opportunities to hydrologists for obtaining hydrologically relevant information at a low cost. With the successful launch of various satellites, researchers gained a valuable new source of space-based observations for studying hydrologic systems and processes (Schultz 1988; Birkett et al. 2002). With the advent of remote sensing, hydrologists could make detailed assessments of water-resource conditions, which was previously difficult due to lack of detailed spatial information (Pietroniro and Prowse 2002; Schmugge et al. 2002). Moreover, hydrologic models were extensively revised to make even more efficient use of this new form of information (Schultz 1988) obtained from orbital/airborne remote sensing. Such work has continued to expand as the number of satellite and airborne platforms has multiplied, and their spatial resolution, global coverage, and orbital frequency have increased.

Land surface features such as snow cover, surface water areas, land use, surface temperature, etc. have been observed using visible and infrared imaging sensors for many years (Schmugge et al. 2002). However, the fact that these instruments rely on atmospheric conditions is a huge disadvantage. Cloud cover, water vapor, and aerosols can disrupt the signals, resulting in limited information about the land surface. Furthermore, these sensors rely on the sun to illuminate the land surface and cannot provide data at night, except for thermal infrared sensors. On the other hand, remote sensing instruments working in the microwave range of the electromagnetic spectrum can be operated day and night and are less affected by atmospheric conditions (Engman 1991). This has resulted in a significant amount of research and development in microwave remote sensing.

Microwave remote sensing offers emerging capabilities to monitor global hydrological processes (Engman 1991). Instruments like scatterometers have been recognized as a useful tool to monitor the water fluxes at high temporal resolution well suited for macro-scale hydrological applications (Wagner et al. 1999; Scipal et al. 2005; Meier et al. 2011; Dayal et al. 2021). The spatial coverage offered by satellite scatterometry is far superior to in-situ measurements. It enables the scatterometers to provide data to investigate the global weather patterns and impact on global ocean circulation models, monitor storm intensities, improve meteorological forecasts, facilitate climate prediction, and much more (Stoffelen 1998; Wen and Su 2003; Sood et al. 2020). Although scatterometers have been mainly used in ocean

applications (wind velocity and wind direction), it also has some unique hydrological applications over the land surface. In addition to introducing the basics of scatterometry, this article will provide examples of satellite scatterometer applications in the field of hydrology. The study also shows how further advancements in the technique can be expected to yield even better results in the future.

4.2 Scatterometer Background

Scatterometers are side-looking radar sensors designed to measure the radar backscatter coefficient (σ°) of the observed surfaces. Wind retrieval across oceans was the major goal of space-borne scatterometers (Stoffelen 1998). Although, backscattered signal measured by scatterometers contains substantial information of the underlying area when they operate over land (Ulaby et al. 1982). Moreover, scatterometers have widely been used for various ocean and land applications since their inception. In the field of hydrology, scatterometers have been used, directly or indirectly, for the estimation of surface soil moisture (Wagner et al. 1999; Wen and Su 2003; Bartalis et al. 2007; Naeimi et al. 2009), river water levels, and discharge (Scipal et al. 2005; Meier et al. 2011; Dayal et al. 2021), snow cover monitoring (Nghiem and Tsai 2001; Brown et al. 2007; Foster et al. 2011; Sood et al. 2020; Singh et al. 2021a, b), crop monitoring (Kim et al. 2000; Oza et al. 2008; Lim et al. 2008), and estimation of leaf area index (Prevot et al. 1993).

Scatterometry has a long history which began in World War II when radar measurements over oceans were corrupted due to sea clutter or noise, and the cause was unknown at that time (Liu 2002). The noise in the radar signal was discovered to be the radar's response to the winds over the ocean only in the 1960s. The first scatterometer flew in 1973 and 1974 as part of the Skylab missions, establishing that space-borne scatterometers were possible. Then in 1978, the Seasat-a Satellite Scatterometer (SASS) demonstrated that precise wind velocity data could be taken from space. In the 1990s, a single beam scatterometer onboard European Remote Sensing Satellites (ERS-1 and ERS-2) was launched by European Space Agency (ESA). The NASA Scatterometer (NSCAT) was the first dual-swath Ku-band scatterometer to fly since Seasat and was launched in 1996. Subsequently, a number of scatterometer missions (SeaWinds onboard QuikSCAT and ADEOS II in 1999 and 2002, respectively; ASCAT onboard Metop-A, B and C in 2002, 2012, and 2018, respectively; OSCAT onboard Oceansat-2 in 2009; HSCAT onboard HY-2A and 2B in 2011 and 2018, respectively; RapidSCAT onboard ISS in 2014; SCATSAT-1 in 2016; SCAT onboard CFOSAT in 2018) have been launched. A brief description of the scatterometer missions is provided in Table 4.1.

Table 4.1 Past and present Scatterometer missions

Scatterometer/mission	Country	year	Frequency	Scanning characteristics	Spatial resolution
SeaSat-A	USA	1978	14.6 GHz	Two-sided double swath	50 km
ERS-1	Europe	1991	5.3	One-sided single swath	50 km
ERS-2	Europe	1997	5.3	One-sided single swath	50 km
NSCAT	USA	1996	13.4	Two-sided double swath	25 km
QSCAT	USA	2006	13.4 GHz	Conical scan one wide swath	25 km
METOP-A	Europe	2006	5.25 GHz	Two-sided double swath	50 km
Oceansat-2	India	2009	13.5 GHz	Conical scan one wide swath	25 km
HY-2A	China	2011	13.4 GHz	Conical scan one wide swath	25 km
METOP-B	Europe	2012	5.25 GHz	Two-sided double swath	50 km
HY-2B	China	2015	13.4 GHz	Conical scan one wide swath	25 km
SCATSAT-1	India	2016	13.5 GHz	Conical scan one wide swath	25 km
FY-3E	China	2016	5.25 GHz & 13.5 GHz	Conical scan one wide swath	25 km
Meteor-M N3	Russia	2017	13.4 GHz	Conical scan one wide swath	25 km
METOP-C	Europe	2017	5.25 GHz	Two-sided double swath	50 km
CFOSAT	China/France	2018	13.4 GHz	Conical scan one wide swath	25 km
Hai Yang-2C	China	2021	13.4 GHz	Conical scan one wide swath	25 m

4.3 Applications of Scatterometers

Scatterometers are radar-based devices that have been designed to monitor wind speed and direction for ocean applications. Since their launch, wind retrieval has been a routine application, but many researchers have found the potential to use the scatterometer data in other land applications. In this study, the potential applications of scatterometer data in the field of hydrology and water resources have been presented.

4.3.1 Estimation of Surface Soil Moisture

Soil moisture is the core of the system that controls the hydrological interactions between soil, vegetation, and climate forcing and plays a key role in governing the water and energy balance between the land surface and atmosphere (Entekhabi 1995). It has applicability in various fields such as flood forecasting (Koster et al. 2010; Brocca et al. 2011), numerical weather prediction (Scipal et al. 2008), and climate and agricultural modeling (Potopová et al. 2020). Satellite sensors such as scatterometers and radars operating in the microwave region of the electromagnetic spectrum can monitor soil moisture at various scales. Apart from their original use as an ocean monitoring instrument, there is considerable evidence that scatterometers can be used to assess soil moisture over land (Wagner et al. 1999; Naeimi et al. 2009). Since microwaves have a high sensitivity to the water content in the soil, scatterometers provide a reasonably direct way to assess it from a physical standpoint. This is especially true in the low-frequency domain (1–15 GHz), where the scatterometers work.

To retrieve soil moisture from scatterometer observations, most approaches use inversion methods based on physical approximations of the scattering process (Pulliainen et al. 1998; Woodhouse and Hoekman 2000; Magagi and Kerr 2001; Jarlan et al. 2002). They typically use simple bare soil backscattering models (Oh et al. 1992; Fung et al. 1992) and vegetation models (Attema and Ulaby 1978; Mougin et al. 1995). Major problems of these retrieval concepts appear to be their physical validity at large scales and their parameterization (Grippa and Woodhouse 2002). Wagner et al. (1999) presented a possible solution to these problems by utilizing the unique sensor design of the ERS/METOP scatterometers and a change detection method which will further be referred to as the TU-Wien model. Several studies have shown that if enough long-term data is available, the change detection technique can overcome some drawbacks of physical-based inversion models. From a mathematical point of view, the change detection algorithm is easy and simple compared to other physical, empirical, and semi-empirical modeling approaches (Wagner et al. 1999). The potential of using such methods has been demonstrated by researchers in their studies (Moeremans and Dautrebande 2000; Quesney et al. 2000; Le Hégarat-Mascle et al. 2002). The TU-Wien model subtracts a reference backscatter value from the vegetated land surface under dry soil conditions from the actual backscatter measurement to account for roughness and heterogeneous land cover. Further, the vegetation-sensitive signature of the multi-incidence angle observations is used to account for the effects of plant growth and decay. Finally, soil moisture is determined by normalizing net backscatter measurements to dry/wet benchmarks, yielding a relative estimate. Equation (4.1) represents the methodology to retrieve the surface soil moisture considering the lowest and highest value of backscatter:

$$\mathrm{SM}_t = \frac{\sigma^\circ(t, \theta_{\mathrm{ref}}) - \sigma^\circ_{\mathrm{dry}}(\theta_{\mathrm{ref}})}{\sigma^\circ_{\mathrm{wet}}(\theta_{\mathrm{ref}}) - \sigma^\circ_{\mathrm{dry}}(\theta_{\mathrm{ref}})} \tag{4.1}$$

where SM_t is a relative measure (or degree of saturation) of the surface soil moisture, $\sigma^{\circ}(t, \theta_{\text{ref}})$ is the backscatter coefficient (measured in decibels, dB) at time t, and reference angle θ_{ref}, $\sigma^{\circ}_{\text{dry}}(\theta_{\text{ref}})$ is the backscatter coefficient in dry condition (long-term lowest value of backscatter), $\sigma^{\circ}_{\text{wet}}(\theta_{\text{ref}})$ is the backscatter coefficient in wet conditions (long-term highest value of backscatter). All these backscattering (σ°) values are measured at a reference incidence angle of 40°.

Since scatterometers measure soil moisture up to a few centimeters below the soil surface, it is reasonable to believe that the time series of surface wetness observations provide insight into the wetting and drying trend of the moisture in the soil profile. This is because weather patterns influence the moisture content of the soil profile over few days to weeks, which are represented in the SM series. Because the changes in moisture content in the soil profile are significantly smaller than in the uppermost layer, it seemed reasonable to use a filter that smooths the SM series to reproduce the trend in deep soil layers. Wagner et al. (1999) proposed a simple approach based on an exponential filter to link intermittent surface estimates to profile soil moisture content (Eq. 4.2).

$$\text{SWI}(t_n) = \frac{\sum_i^n \text{SM}(t_i) e^{-\left(\frac{t_n - t_i}{T}\right)}}{\sum_i^n e^{-\left(\frac{t_n - t_i}{T}\right)}} \tag{4.2}$$

where $\text{SWI}(t_n)$ is the Soil Water Index at time t_n and $\text{SM}(t_i)$ is the surface soil moisture retrieved from scatterometer data at time t_i. T represents the time scale of soil moisture variation in units of the day. The SWI is calculated if at least one scatterometer measurement in the time interval $[t - T, t]$ and at least three measurements in the interval $[\text{t} - 5\ T, t]$ are available.

The positive feedback of the TU-Wien model motivated the implementation of an operational near-real-time METOP ASCAT processor at EUMETSAT's H-SAF project. Here, we present an example (Fig. 4.1) of scatterometer-based soil moisture product (H-SAF's H-113 product) for the Betwa river basin in India. From the figure, we can observe the seasonal and spatial variation in the soil moisture over the basin. The soil moisture during the monsoon season (June to September), especially in July, August, and September, is high since the rainfall is concentrated in these months, resulting in higher values over the region.

4.3.2 Estimation of Rainfall

For every hydrological study, precipitation is the most important climatic variable. The most accurate source of rainfall data has always been direct measurements using rain gauges, and acquiring the observed precipitation, whether real-time or historical, has proven to be rather difficult. The discontinuity in the recorded observations is a significant restriction in the usefulness of gauge-based observations. In this regard, satellite-based precipitation products (SPPs) play a crucial role in improving the

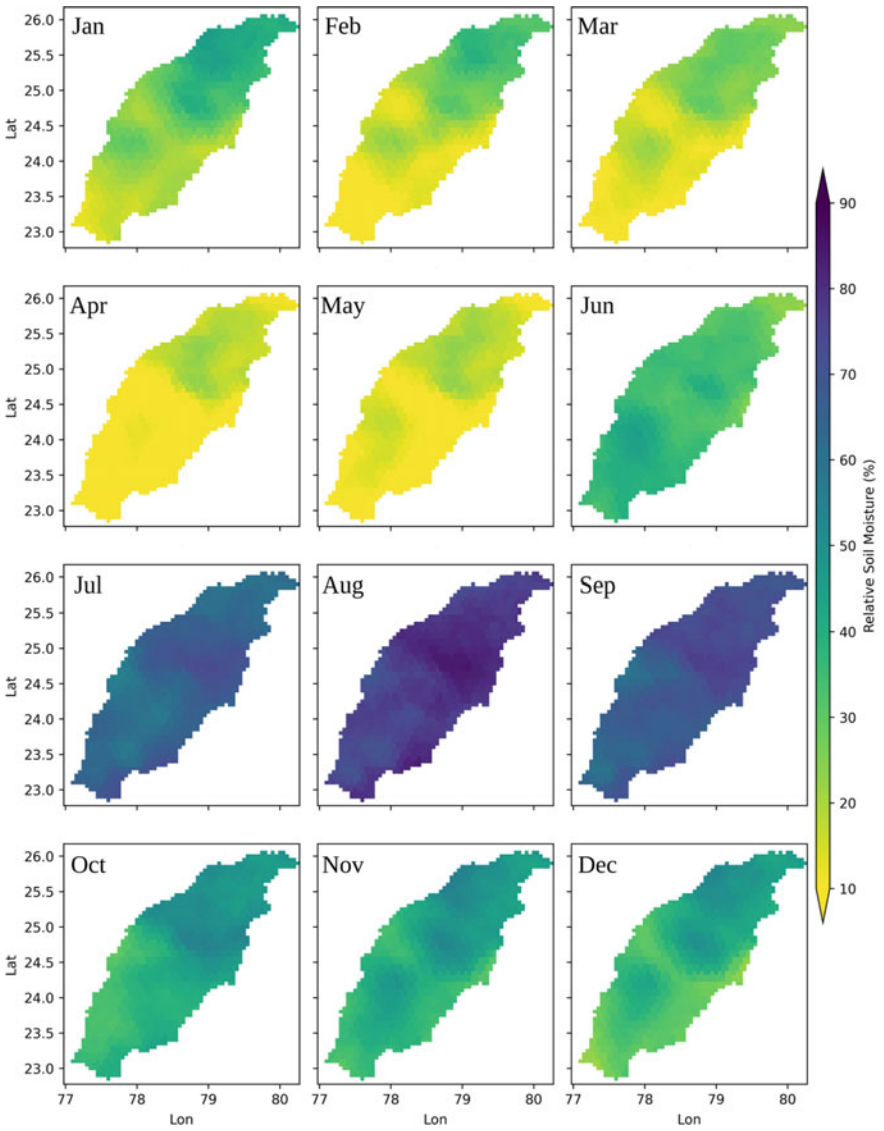

Fig. 4.1 Long-term monthly variation of ASCAT derived soil moisture over Betwa river basin, India

current hydrologic prediction capabilities (Dayal et al. 2021) as they come with a high spatiotemporal resolution and global coverage addressing the issues of sparse and missing data. There are numerous SPPs available in the open-source domain that has been used for hydrological applications (Himanshu et al. 2017; Dayal et al. 2021; Guptha et al. 2021; Santos et al. 2021).

Studies have demonstrated that the scatterometer-based soil moisture observations have been used to estimate the rainfall (Brocca et al. 2013, 2014, 2019; Wagner et al. 2013). A bottom-up approach (SM2RAIN) has been employed to ASCAT retrieved soil moisture to create an SM2RAIN-ASCAT rainfall dataset (Brocca et al. 2019). The SM2RAIN algorithm is based on the soil water balance equation (Eq. 4.3) and uses in-situ or satellite-based soil moisture data to estimate the amount of water entering the soil.

$$nZ\frac{dS(t)}{dt} = p(t) - g(t) - sr(t) - e(t) \tag{4.3}$$

where n, Z, S, t, p, sr, g, and e are soil porosity, soil layer depth, relative soil moisture, time, rainfall, surface runoff, subsurface runoff, and actual evapotranspiration, respectively. The SM2RAIN-ASCAT rainfall product has been demonstrated to be very good at detecting daily rainfall events (Dayal et al., 2022). Moreover, this works well with low rainfall events, but it under accounts for the high rainfall events (Dayal et al. 2022).

4.3.3 Estimation of River Discharge

Estimating surface runoff or river discharge from a scatterometer is not a direct but rather an indirect approach. Scipal et al. (2005) made the first such attempt, which investigated the potential to apply scatterometer data for river discharge estimation. They used the basin water index (BWI), or the averaged wetness condition over the basin, derived from scatterometer retrieved SWI, as a proxy to model the river discharge. Equation (4.4) represent the formula for deriving the BWI from scatterometer-based SWI.

$$\mathrm{BWI} = \frac{\sum_{i=1}^{n} \mathrm{SWI}_i(t)}{n} \tag{4.4}$$

where n is the number of pixels in the basin. Equation (4.4) assumes that all points in the river basin are equally important for runoff generation (Scipal et al. 2005; Meier et al. 2011). In this approach, the location of each pixel within the watershed area with respect to the gauging site was not considered. From the study carried out by Scipal et al. (2005), it was found that BWI is well correlated with the observed discharge. Based on this, a relationship between BWI and observed discharge was developed, and those were found to be logarithmic in nature.

Meier et al. (2011) utilized the scatterometer-derived BWI in their conceptual model. In their study, they observed that the discharge variations are small for low values of BWI. As the value of BWI exceeds 0.5 to 0.6, the variation suddenly increases. This necessitates the incorporation of other parameters to model the

discharge. According to the research, discharge is decoupled from the soil moisture as the soil approaches complete saturation, and decoupling is mainly caused by rainfall. Therefore, they included the rainfall data in their study, which is more realistic. They employed simple water balance equations (Eq. 4.5–Eq. 4.10) in their model, in which it is assumed that a portion of the rainfall is routed to the surface runoff and the remainder to the subsurface runoff, depending on the BWI value. If the BWI value is 1, all the rainfall amount is routed to the surface runoff, whereas BWI value 0 indicates the entire rainfall amount goes to the subsurface. The measured change in BWI is used to model the change in subsurface storage.

$$I_{GW} = k_1 A R(t)[1 - \mathrm{BWI}(t)] \tag{4.5}$$

$$\frac{\Delta S_S(t)}{\Delta t} = k_1 A R(t) - I_{GW} - k_2 S_S(t-1) \tag{4.6}$$

$$\frac{\Delta S_{GW}(t)}{\Delta t} = \max[I_{GW} + k_3\{\mathrm{BWI}(t) - \mathrm{BWI}(t-1)\}; 0] - k_4 S_{GW}(t-1) \tag{4.7}$$

$$Q_S(t) = k_2 S_S(t-1) \tag{4.8}$$

$$Q_{GW}(t) = k_4 S_{GW}(t-1) \tag{4.9}$$

$$Q(t) = Q_S(t - \Delta\tau_S) + Q_{GW}(t - \Delta\tau_{GW}) \tag{4.10}$$

where I_{GW} is the direct infiltration of rainfall to the subsurface storage, A is the area of the catchment, R is the average rainfall in the catchment, k_i are the model parameters, S_S and S_{GW} are the surfaces and the subsurface storage volumes, respectively, τ_S and τ_{GW} are time lags (mostly dependent on the size of the catchments) for surface and subsurface discharge routing, respectively. A detailed description of the model can be found in Meier et al. (2011).

Gupta et al. (2019) analyzed the potential of OSCAT and SCATSAT-1 retrieved backscatter and brightness temperature for estimating the water level and discharge of the river. The relationship between OSCAT derived BWI and river water levels was observed to follow a power function ($y = ax^b + c$). Figure 4.2 represents model functions for Satrapur (Godavari River) and Dhubri (Brahmaputra River) gauging sites. Similar model functions were developed for more gauging sites in different river basins, and those model functions were applied over the SCATSAT-1 derived BWI to estimate the river water levels (Fig. 4.3).

Further, Dayal et al. (2021) applied the concept of Scipal et al. (2005) in a machine learning framework to estimate the streamflow of six river basins of India. They found that BWI followed the trend of discharge (Fig. 4.4). Based on this, they build

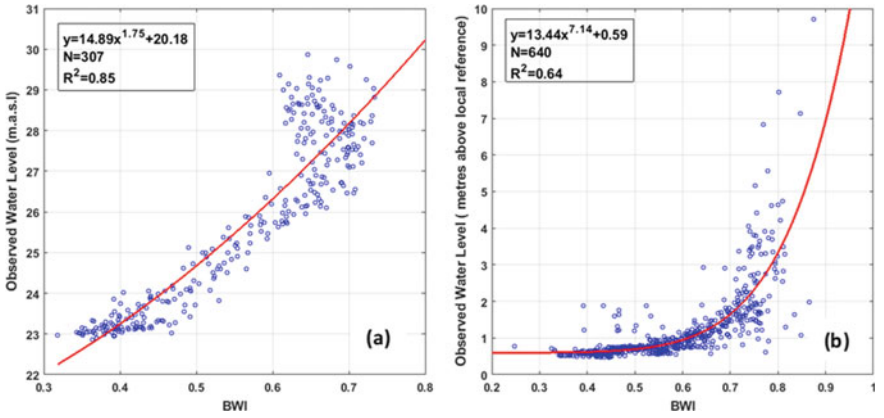

Fig. 4.2 Model functions for two gauging sites **a** Dhubri in the downstream Brahmaputra river and **b** Satrapur in upstream Godavari river

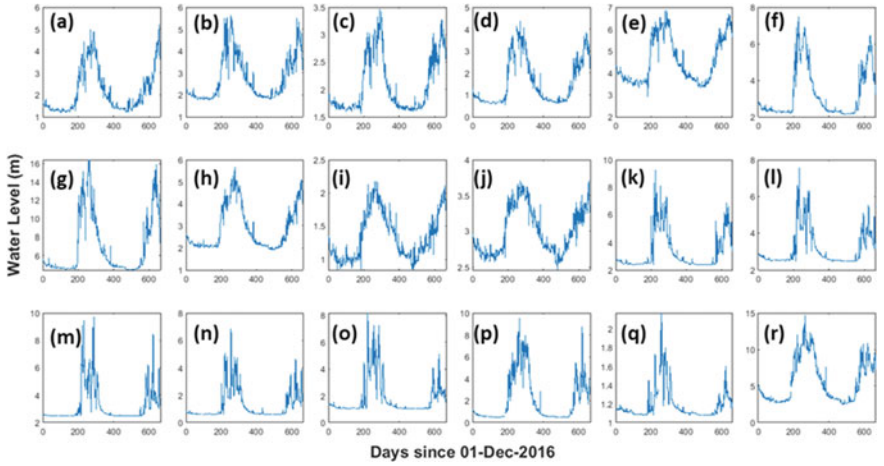

Fig. 4.3 Water level retrieved over 18 virtual gauging stations using SCATSAT-1 backscatter data (01–12-2016 to 22–12-2017) **a** Aditypor **b** Ghatsila **c** Tilga **d** Panposh **e** Gomali **f** Basantpur **g** Tikarapara **h** Kantamal **i** Purushottampur **j** Kashinagar **k** Hoshangabad **l** Mandleshwar **m** Burhanpur **n** Satrapur **o** PG Penganga **p** Pathagudem **q** Mancherial and **r** Polavaram

two different models using an ensemble learning technique (Random Forest). The methodology for the same is presented in Fig. 4.5.

Dayal et al. (2021) have also compared the results of BWI-based models with the classical rainfall-runoff model and Global Flood Awareness System (GloFAS). They found that the BWI-runoff model performed well, but classical rainfall-runoff outperformed the same. However, the BWI-rainfall-runoff model outperformed the

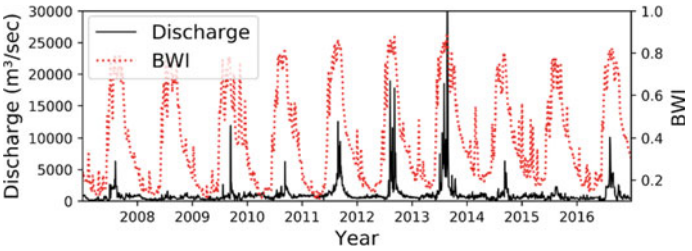

Fig. 4.4 Timeseries of ASCAT derived BWI and discharge at Mandleshwar gauging site of Narmada river basin

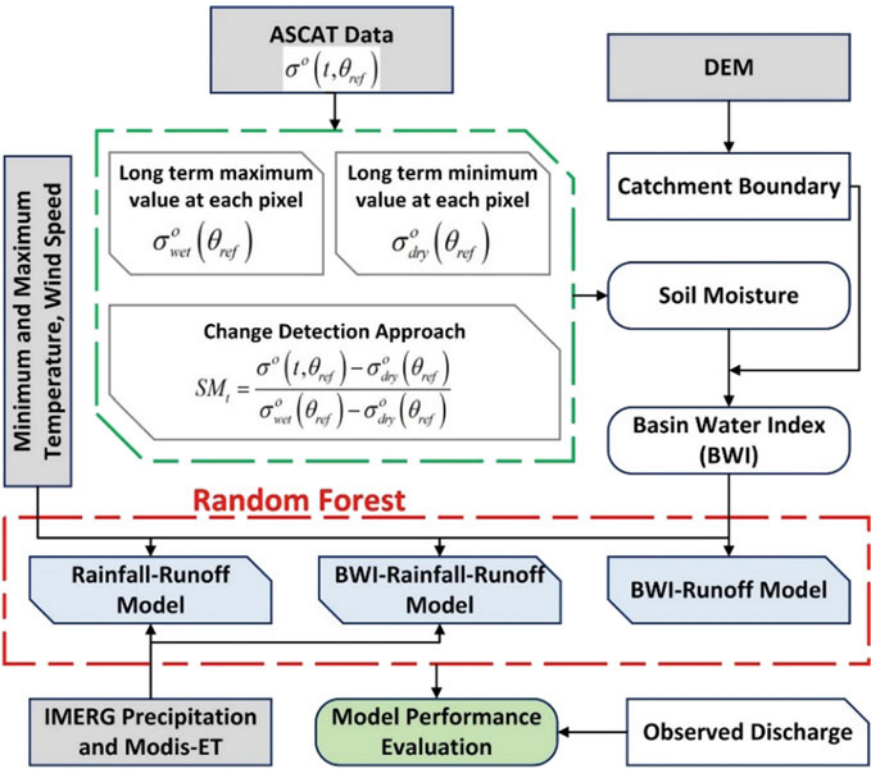

Fig. 4.5 Methodology flowchart adopted by Dayal et al. (2021)

classical rainfall-runoff model. A time series plot for the developed models over Narmada river basin has been presented in Fig. 4.6.

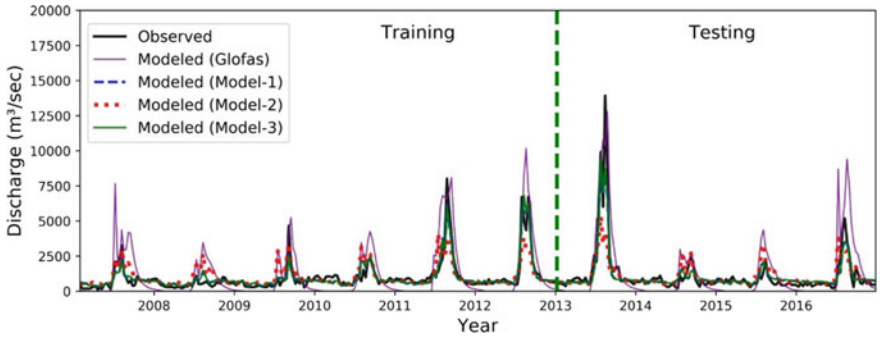

Fig. 4.6 Time series plot of observed and modeled streamflow from BWI-based models (Model-1: BWI-runoff model; Model-3: BWI-rainfall-runoff model), GloFAS, and classical rainfall-runoff model (Model-2) for Mandleshwar

4.3.4 Water Level Estimation in a Forested Catchment

Here, we present a case study of water level retrieval for a small, forested catchment in Gir National Park (NP), Gujarat. The SWI and BWI estimation technique from SCATSAT-1 data is similar as presented earlier. Since SCATSAT-1 operates in Ku band, its signal can be influenced by the forest canopy. However, Gir National Park is a deciduous forest region, so we can expect some signal of surface soil moisture being obtained from the backscatter signal. To test this hypothesis, a radar type of water level recorder was placed along a small catchment in one of the streams of Gir NP (Fig. 4.7). A steep exponential curve between BWI and water level was observed (Fig. 4.8), unique to forested regions. With the onset of rainfall, forests initially do not generate any runoff as they can capture moisture by infiltration. As the wet season progresses and soil tends to saturate, runoff increases exponentially, and a sudden increase in water level is observed. For the post-monsoon period a linear relationship between observed water level and BWI is observed (Fig. 4.9).

4.3.5 Estimation of Reservoir Water Level

The study of the relationship between BWI and reservoir level is different from the river discharge estimation. In the case of the reservoir, water accumulated till the end of monsoon season and thereafter it is released as per the irrigation and other requirements. Hence two separate models need to be developed for both periods, i.e., one model for the period of July to November and another one for December to June. The first step in this is to obtain the cumulative BWI time series. For the preparation of the cumulative BWI time series, the BWI needs to be added until the end of the November month starting from July of each year and thereafter subtracted daily values until June.

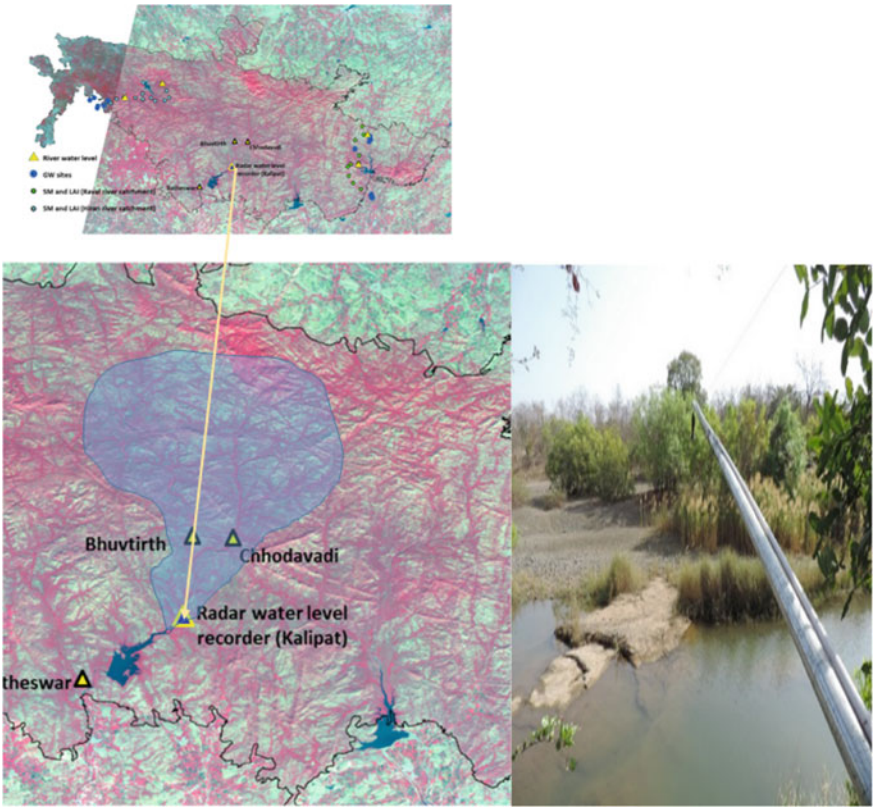

Fig. 4.7 Sensor installed over a stream (Gir national park) measuring water level in the forested catchment

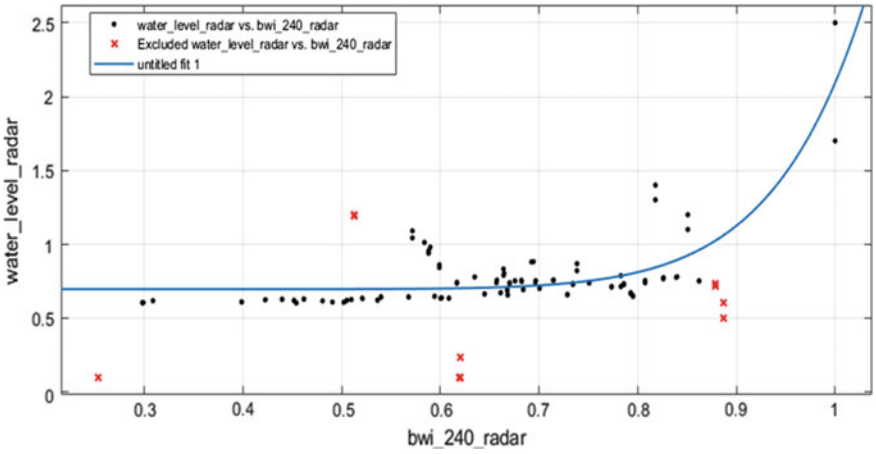

Fig. 4.8 BWI versus water level relationship for the selected catchment during the monsoon period

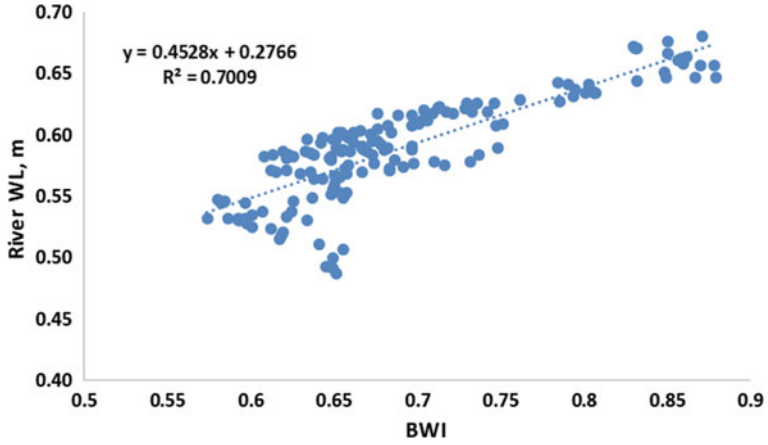

Fig. 4.9 BWI versus water level relationship for the selected catchment during the post-monsoon period

In connection with this, a case study for the Ukai reservoir has been carried out. Cumulative BWI has been plotted against the water level for the period of July to November of the year 2013 in Fig. 4.10. From the scatterplots, it can be observed that there is a nonlinear relationship between ASCAT derived cumulative BWI and water level. The second-order polynomial model functions have been fitted, and based on the developed models, water level of the reservoir was computed. The developed models have been validated using the model efficiency parameters. The results showed that the scatterometer observations performed well to estimate water levels in the reservoirs.

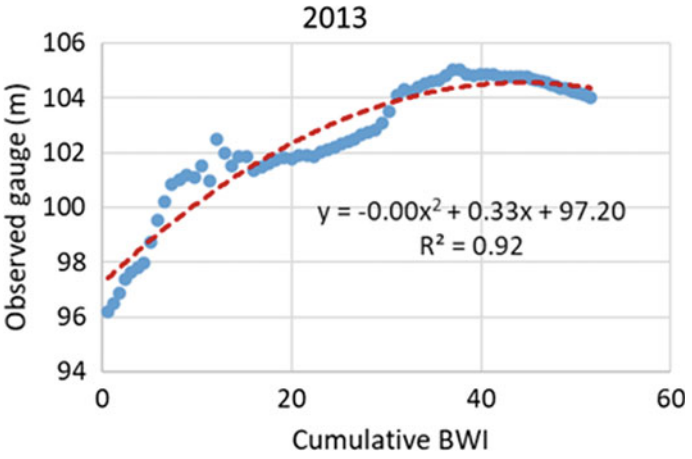

Fig. 4.10 Scatterplot between cumulative BWI and observed water level for Ukai reservoir of India

4.3.6 *Identification of Irrigation, Canal, and River Releases Using BWI*

A case study for the identification of irrigation using scatterometer data is carried out for the Ganga river basin. A unique observation from the BWI-water level relationship for the Kanpur gauging site of the upper Ganga basin was the stark difference between the two variables (BWI and water level) for the post-monsoon period (Fig. 4.11). The BWI increased without any rainfall, indicating an anthropogenic influence of irrigation on the backscatter signal. These differences between surface soil moisture and water level downstream can directly indicate water being used for irrigation through canal releases from the river in the catchment. SWI maps can also represent the regions where the farmers have initiated irrigation. For the catchment upstream to the Kanpur site, SWI maps for the post-monsoon period are shown in Fig. 4.12. Also,

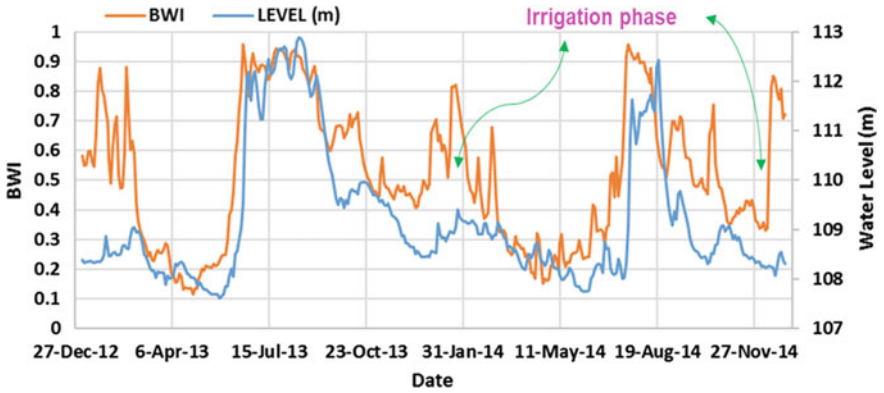

Fig. 4.11 Time series plot of BWI and observed water level at Kanpur site of Ganga river basin

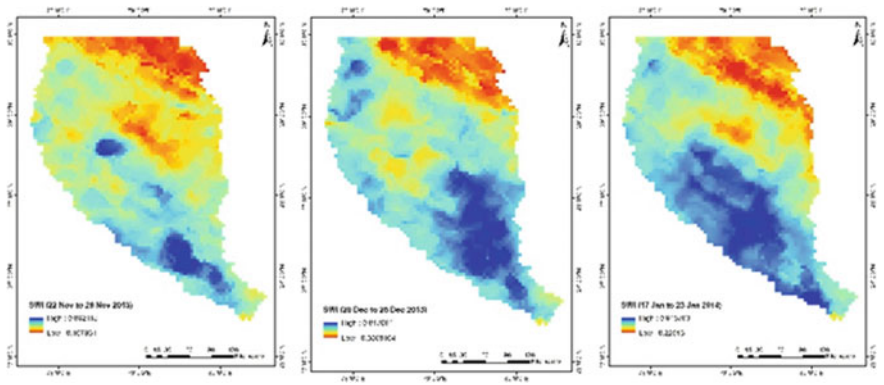

Fig. 4.12 Soil moisture maps of the basin for Rabi (winter) season

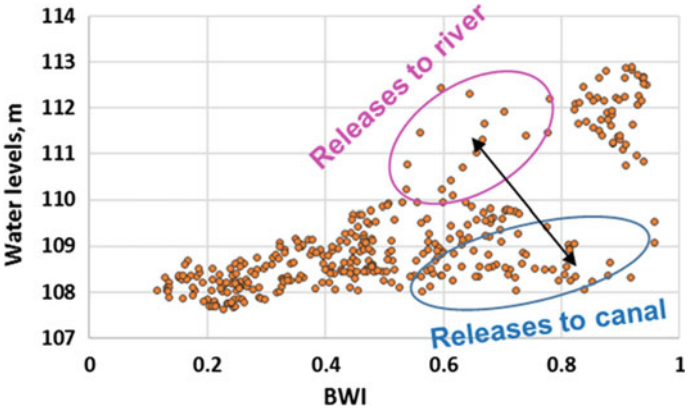

Fig. 4.13 Scatterplot indicating water release to canals and river

due to heavy rain upstream, barrages approach their danger level, which prompts the release of water from barrages to the main river for flood control/dam protection. Hence, causing a sudden rise in the river water levels downstream, but not picked by BWI (Fig. 4.13).

4.3.7 Estimation of Irrigation Water Amount

The majority of irrigation databases are based on statistical surveys or merely irrigation-equipped regions (Siebert et al. 2015; Salmon et al. 2015) and are usually valid for a single or multi-year period. Large inaccuracies and subjective judgments may cause these datasets to fail to represent the spatiotemporal dynamics of irrigated regions (Deines et al. 2017). In this regard, visible and optical remote sensing has been widely employed to estimate irrigated areas as an alternative (Ozdogan et al. 2010). While locating irrigated regions has received much attention, quantifying the amount of water utilized for irrigation is significantly more difficult (Brocca et al. 2018). Technical limits, such as the deployment of monitoring systems, and economic constraints, such as the cost of water and non-legal consumptions, make it difficult to determine the real water volume utilized for irrigation.

Brocca et al. (2018) exploited the satellite soil moisture information from scatterometer data to quantify the amount of water applied for irrigation. To estimate the total volume of water entering the soil, Brocca et al. (2018) constructed an adapted version of the SM2RAIN method. The SM2RAIN-derived water flux in irrigated areas comprises rainfall plus irrigation, and by removing the rainfall signal (e.g., obtained from rain gauge observations), they could quantify the amount of water applied for irrigation. The same approach was further used by Jalilvand et al. (2019), who obtained good agreement with ground-based irrigation data in a semi-arid region in Iran. An alternative method, but based on the same premise, i.e., that soil moisture

predictions from land surface models do not contain irrigated water, whereas satellite soil moisture retrievals do, was proposed by Zaussinger et al. (2019), who estimated the irrigation water use over the Contiguous United States from coarse-resolution ASCAT data. This approaches the aggregated deviation between the modeled and satellite-observed soil moisture climatology as an irrigation water use estimate.

4.3.8 Mapping of Inundated Zones

When the soil surface is completely inundated by water, the emissivity decreases, causing the reduction in Brightness Temperature (BT) measured in microwave frequencies. The decrease of BT in horizontal polarization is greater compared to that in vertical polarization (Ulaby et al. 1978). This property of water can be utilized to detect surface inundation. Many studies have demonstrated the potential of using high-resolution Synthetic Aperture Radar (SAR) data to map the extent of surface flooding (Brakenridge et al. 1994, 1998; Gstaiger et al. 2012; Townsend and Foster 2002). SAR sensors have an excellent spatial resolution (of the order of a few meters) but lack the necessary temporal resolution to monitor flood events efficiently. Scatterometers can cover large swaths and provide 1–2 day repetivity with coarser spatial resolution. This offers a unique opportunity to continuously monitor flood events at a catchment scale and obtain valuable information about the affected regions and the duration of flooding. Brakenridge et al. (2003) used the SeaWinds scatterometer on QuikSCAT to develop a flood detection algorithm using the backscatter polarization ratio. Based on the microwave radiative transfer equation, the microwave index was first proposed by Pampaloni and Paloscia (1985). Many researchers have demonstrated the relationship between Microwave Polarization Difference Index (MPDI) and various soil and vegetation parameters. Singh and Dadhwal (2003) used MPDI to monitor crop growth, whereas Owe et al. (2001) used MPDI to retrieve surface soil moisture. It is defined as the normalized difference of Brightness temperature in V and H polarizations at a given frequency (Eq. 4.11).

$$\text{MPDI} = \frac{T_{bV} - T_{bH}}{T_{bV} + T_{bH}} \tag{4.11}$$

where T_{bV} and T_{bH} are the brightness temperatures in V and H polarization, respectively. One major requirement of this equation to be valid is that the incidence angle must be the same for HH and VV beams. However, this is not the case with OSCAT/SCATSAT-1. Hence, angle normalized product is essential for performing these calculations by removing the dependency on incidence angle (Naeimi et al. 2013). Li et al. (2013) analyzed MPDI over different land cover types in northeast China over the 6 AMSR-E frequencies. Since there are no space-borne radiometers available at 13.6 GHz, the analysis by Li et al. (2013) provides a good approximation of expected MPDI values over different land covers.

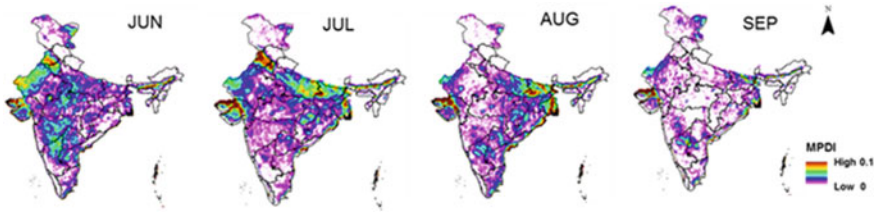

Fig. 4.14 SCATSAT-1 derived mean monthly MPDI

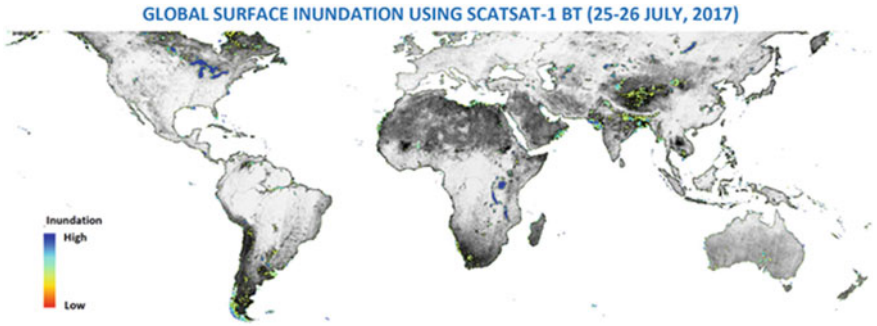

Fig. 4.15 Global surface inundation for 21–25 July 2017 using SCATSAT-1

SCATSAT-1 provides brightness temperature data at 13.6 GHz (Ku band) in horizontal and vertical polarization, and the same has been used to detect inundated pixels. SCATSAT-1 L4 BT product in H and V polarization at 0.02° spatial resolution for descending orbits are used to compute MPDI over land pixels (Fig. 4.14). Regions with an elevation greater than 1500 m were excluded from the analysis due to the effects of rough surfaces on MPDI. Pixels near the coast were masked to remove the effect of the sea in the data. Based on analysis by Li et al. (2013), an appropriate threshold of MPDI >0.05 was used to obtain inundated pixels. To determine the intensity of flooding within a detected pixel, a flood index was developed which uses a linear relation with BT in *H* polarization such that lower BT gives higher flood index. The range of flood index was set from 0 (no flooding) to 1 (completely flooded pixel). The algorithm has been used to produce the global surface inundation map from SCATSAT-1 data (Fig. 4.15).

4.3.9 Monitoring of Drought

Drought is one of the costliest and damaging natural disasters, resulting in reduced agricultural productivity, water scarcity, and severe heat waves (Hatfield et al. 2011; Hoerling et al. 2013). In response, drought plans are being created worldwide, with

a special emphasis on thorough drought monitoring (Hayes et al. 2011). As part of drought monitoring, precipitation is the most commonly used climatic variable (Anshuka et al. 2019). On the other hand, soil moisture is frequently utilized to indicate moisture stress and agricultural drought (Quiring and Papkyriakou 2003). In connection with this, a scatterometer provides precipitation data (Brocca et al. 2013, 2019) and soil moisture at high temporal resolution (Wagner et al. 1999; Naeimi et al. 2009) and shows high potential for drought monitoring at a global scale. Soil moisture retrieved from active microwave sensors can be used to characterize critical drought factors such as the severity, frequency, and spatial extent of soil moisture deficiency. Several studies have utilized the scatterometer retrieved soil moisture product to compute soil moisture-based indicators for drought monitoring (Carrão et al. 2016; Jung et al. 2020; Potopová et al. 2020; Trnka et al. 2020). Koohi et al. (2021) used a scatterometer-based rainfall product (SM2RAIN-ASCAT product) to detect drought events in Iran. They have also suggested that these products could be very promising for application in data-scarce regions for drought monitoring.

4.3.10 Monitoring of Snow Cover

Regular monitoring and mapping of the snow cover area are crucial for managing natural resources and determining the impact of climate change on snow cover. However, estimating the snow cover area in inaccessible locations is one of the most challenging tasks (Mishra et al. 2009). Optical sensors have been used to map the snow cover so far (Jain et al. 2008) but in general, those are influenced by cloud cover and susceptible to interference from environmental factors. In this regard, the researchers have made numerous efforts to map the snow cover using microwave data (Nghiem and Tsai 2001; Tedesco and Miller 2007). Several studies have demonstrated that microwave-based scatterometer sensors may be used to get snow cover information (Hillard et al. 2003; Oza et al. 2011; Barrand et al. 2013; Bothale et al. 2015).

Previous research has shown the potential to use the Ku-band scatterometer data in a variety of applications, including snowmelt estimation from QuikSCAT and OSCAT (Bothale et al. 2015), understanding variations in ice sheets using QuikSCAT (Oza et al. 2011), spatiotemporal variations on snow properties (King et al. 2015), assessing the cryospheric parameters and mapping the snow-covered area using SCATSAT-1 (Nikam et al. 2017; Oza et al. 2019; Singh et al. 2019), snowpack changes using POLSCAT (Oza et al. 2019; Singh et al. 2019). The high temporal resolution of the space-borne scatterometers has been the major advantage over other datasets for their applicability in snow cover monitoring.

4.4 Summary

Scatterometry is an established technique that has demonstrated its ability to provide oceanic wind speeds with exceptional precision and global coverage. Scatterometers are a type of radar sensor designed initially for ocean applications, but scientists have applied them for other land applications over time. Scatterometers currently in orbit or planned for the future, promise a continuous long-term global observation that will benefit hydro-climatic research. Scatterometers' sensitivity to the dielectric properties of the soil water, and vegetation open the way to monitor the moisture content in the soil surface and vegetation. In connection with this, studies carried out by researchers over more than three decades have made it possible to develop some operational products of soil moisture and rainfall, which got tremendous response among the meteorological community.

In recent years, scatterometers have been used by many researchers for understanding the catchment scale hydrological processes. The long time series by scatterometers represents a valuable dataset for analyzing the long-term variability in hydrological components at a large scale. In this study, we have discussed the potential applications of scatterometer data in the field of hydrology and water resources. We have also presented some case studies on the same. Based on our observations, we have listed below some key highlights about the scatterometers and their applications:

(1) Space agencies have launched several scatterometer missions due to their potential applicability in various fields.
(2) The sensitivity of the scatterometer measurements to soil moisture has been a crucial component in using this data for monitoring the land surface as part of numerous meteorological and hydrological applications.
(3) C-band scatterometers have widely been used for the estimation of surface soil moisture, and some operational soil moisture products with good temporal resolution (revisit time of 1 or 2 days) are also available at a global scale.
(4) Scatterometers have been used for the estimation of rainfall. A bottom-up approach named SM2RAIN has been applied to scatterometer-based soil moisture products for developing the operational rainfall product.
(5) Some studies have found the applicability of scatterometer-based wetness product (SWI) to estimate river water level or discharge. Soil wetness products have also been used in the hydrological model in the data assimilation framework.
(6) It has also been demonstrated that the scatterometer data may help to estimate the river water level or discharge of the forested catchment. Although, more research is needed in this regard.
(7) Scatterometer data have found their applicability in estimating the reservoir water levels.
(8) Scatterometer data has also been used for the identification of irrigated areas as well as for the quantification of irrigation water amount.
(9) Scatterometer data can potentially map the flooded zones using brightness temperatures as demonstrated in the studies.

(10) With a short revisit time (daily/weekly), it is possible to monitor the snow-covered area on a global scale.
(11) Scatterometer-derived soil moisture and rainfall estimates are helpful for drought monitoring at regional and continental scales because of their global coverage and long-term records.

One of the main advantages of space-borne scatterometers is that they can provide continuous coverage over broad geographic areas and do not have the same restrictions as their multispectral counterparts in terms of light availability and cloud coverage. However, the capacity of these sensors to penetrate deep soil strata is limited. Future advances in scatterometry are expected to make this technology even more useful in investigating hydrological systems and a variety of other exploratory uses in water resources.

Acknowledgements This study is a part of the project ISR-1075-WRC sponsored by the Space Applications Centre, ISRO, Ahmedabad, for which the authors are very thankful to the organization. The resources and facilities provided by the Indian Institute of Technology Roorkee are acknowledged.

References

Anshuka A, van Ogtrop FF, Vervoort RW (2019) Drought forecasting through statistical models using standardised precipitation index: a systematic review and meta-regression analysis. Nat Hazards 97(2):955–977

Attema EPW, Ulaby FT (1978) Vegetation modeled as a water cloud. Radio Sci 13(2):357–364

Barrand NE, Vaughan DG, Steiner N, Tedesco M, Kuipers Munneke P, Van Den Broeke MR, Hosking JS (2013) Trends in Antarctic Peninsula surface melting conditions from observations and regional climate modeling. J Geophys Res Earth Surf 118(1):315–330

Bartalis Z, Wagner W, Naeimi V, Hasenauer S, Scipal K, Bonekamp H, Figa J, Anderson C (2007) Initial soil moisture retrievals from the METOP-A advanced scatterometer (ASCAT). Geophys Res Lett 34(20)

Birkett CM, Mertes LAK, Dunne T, Costa MH, Jasinski MJ (2002) Surface water dynamics in the Amazon basin: application of satellite radar altimetry. J Geophys Res: Atmos 107(D20):LBA-26

Bothale RV, Rao PVN, Dutt CBS, Dadhwal VK (2015) Detection of snow melt and freezing in Himalaya using OSCAT data. J Earth Syst Sci 124(1):101–113

Brakenridge GR, Knox JC, Paylor ED, Magilligan FJ (1994) Radar remote sensing aids study of the great flood of 1993. EOS Trans Am Geophys Union 75(45):521–527

Brakenridge GR, Tracy BT, Knox JC (1998) Orbital SAR remote sensing of a river flood wave. Int J Remote Sens 19(7):1439–1445

Brakenridge GR, Anderson E, Nghiem SV, Caquard S, Shabaneh TB (2003) Flood warnings, flood disaster assessments, and flood hazard reduction: the roles of orbital remote sensing

Brocca L, Moramarco T, Melone F, Wagner W, Hasenauer S, Hahn S (2011) Assimilation of surface- and root-zone ASCAT soil moisture products into rainfall–runoff modeling. IEEE Trans Geosci Remote Sens 50(7):2542–2555

Brocca L, Moramarco T, Melone F, Wagner W (2013) A new method for rainfall estimation through soil moisture observations. Geophys Res Lett 40(5):853–858

Brocca L, Ciabatta L, Massari C, Moramarco T, Hahn S, Hasenauer S, Kidd R, Dorigo W, Wagner W, Levizzani V (2014) Soil as a natural rain gauge: estimating global rainfall from satellite soil moisture data. J Geophys Res: Atmos 119(9):5128–5141

Brocca L, Tarpanelli A, Filippucci P, Dorigo W, Zaussinger F, Gruber A, Fernández-Prieto D (2018) How much water is used for irrigation? A new approach exploiting coarse resolution satellite soil moisture products. Int J Appl Earth Obs Geoinf 73:752–766

Brocca L, Filippucci P, Hahn S, Ciabatta L, Massari C, Camici S, Schüller L, Bojkov B, Wagner W (2019) SM2RAIN–ASCAT (2007–2018): global daily satellite rainfall data from ASCAT soil moisture observations. Earth Syst Sci Data 11(4):1583–1601

Brown R, Derksen C, Wang L (2007) Assessment of spring snow cover duration variability over northern Canada from satellite datasets. Remote Sens Environ 111(2–3):367–381

Carrão H, Russo S, Sepulcre-Canto G, Barbosa P (2016) An empirical standardized soil moisture index for agricultural drought assessment from remotely sensed data. Int J Appl Earth Obs Geoinf 48:74–84

Dayal D, Gupta PK, Pandey A (2021) Streamflow estimation using satellite-retrieved water fluxes and machine learning technique over monsoon-dominated catchments of India. Hydrol Sci J 66(4):656–671

Dayal D, Singh G, Pandey A, Gupta PK (2022) Performance evaluation of SM2RAIN-ASCAT rainfall product over an agricultural watershed of India. In: Geospatial technologies for land and water resources management. Springer, Cham, pp 223–236

Deines JM, Kendall AD, Hyndman DW (2017) Annual irrigation dynamics in the US Northern high plains derived from landsat satellite data. Geophys Res Lett 44(18):9350–9360

Engman ET (1991) Applications of microwave remote sensing of soil moisture for water resources and agriculture. Remote Sens Environ 35(2–3):213–226

Entekhabi D (1995) Recent advances in land-atmosphere interaction research. Rev Geophys 33(S2):995–1003

Foster JL, Hall DK, Eylander JB, Riggs GA, Nghiem SV, Tedesco M, Kim E, Montesano PM, Kelly RE, Casey KA, Choudhury B (2011) A blended global snow product using visible, passive microwave and scatterometer satellite data. Int J Remote Sens 32(5):1371–1395

Fung AK, Li Z, Chen KS (1992) Backscattering from a randomly rough dielectric surface. IEEE Trans Geosci Remote Sens 30(2):356–369

Grippa M, Woodhouse IH (2002) Validation of surface scattering models across large footprints for global scatterometer applications. IEEE Trans Geosci Remote Sens 40(10):2229–2233

Gstaiger V, Huth J, Gebhardt S, Wehrmann T, Kuenzer C (2012) Multi-sensoral and automated derivation of inundated areas using TerraSAR-X and ENVISAT ASAR data. Int J Remote Sens 33(22):7291–7304

Guptha GC, Swain S, Al-Ansari N, Taloor AK, Dayal D (2021) Evaluation of an urban drainage system and its resilience using remote sensing and GIS. Remote Sens Appl: Soc Environ 23100601–10. https://doi.org/1016/j.rsase.2021.100601

Gupta PK, Pradhan R, Singh RP, Misra A (2019) Scatterometry for land hydrology science and its applications. Curr Sci 117(6):1014–1021

Hatfield JL, Boote KJ, Kimball BA, Ziska LH, Izaurralde RC, Ort DR, Thomson AM, Wolfe D (2011) Climate impacts on agriculture: implications for crop production

Hayes M, Svoboda M, Wall N, Widhalm M (2011) The Lincoln declaration on drought indices: universal meteorological drought index recommended. Bull Am Meteor Soc 92(4):485–488

Hillard U, Sridhar V, Lettenmaier DP, McDonald KC (2003) Assessing snowmelt dynamics with NASA scatterometer (NSCAT) data and a hydrologic process model. Remote Sens Environ 86(1):52–69

Himanshu SK, Pandey A, Yadav B (2017) Assessing the applicability of TMPA-3B42V7 precipitation dataset in wavelet-support vector machine approach for suspended sediment load prediction. J Hydrol 550:103–117

Hoerling M, Kumar A, Dole R, Nielsen-Gammon JW, Eischeid J, Perlwitz J, Quan XW, Zhang T, Pegion P, Chen M (2013) Anatomy of an extreme event. J Clim 26(9):2811–2832

Jain SK, Goswami A, Saraf AK (2008) Accuracy assessment of MODIS, NOAA and IRS data in snow cover mapping under Himalayan conditions. Int J Remote Sens 29(20):5863–5878
Jalilvand E, Tajrishy M, Hashemi SAGZ, Brocca L (2019) Quantification of irrigation water using remote sensing of soil moisture in a semi-arid region. Remote Sens Environ 231:111226
Jarlan L, Mazzega P, Mougin E (2002) Retrieval of land surface parameters in the Sahel from ERS wind scatterometer data: a brute force method. IEEE Trans Geosci Remote Sens 40(9):2056–2062
Jung HC, Kang DH, Kim E, Getirana A, Yoon Y, Kumar S, Peters-lidard CD, Hwang E (2020) Towards a soil moisture drought monitoring system for South Korea. J Hydrol 589:125176
Kim S, Kim B, Kong Y, Kim YS (2000) Radar backscattering measurements of rice crop using X-band scatterometer. IEEE Trans Geosci Remote Sens 38(3):1467–1471
King J, Kelly R, Kasurak A, Duguay C, Gunn G, Rutter N, Watts T, Derksen C (2015) Spatio-temporal influence of tundra snow properties on Ku-band (17.2 GHz) backscatter. J Glaciol 61(226):267–279
Koohi S, Azizian A, Brocca L (2021) Spatiotemporal drought monitoring using bottom-up precipitation dataset (SM2RAIN-ASCAT) over different regions of Iran. Sci Total Environ 779:146535
Koster RD, Mahanama SP, Livneh B, Lettenmaier DP, Reichle RH (2010) Skill in streamflow forecasts derived from large-scale estimates of soil moisture and snow. Nat Geosci 3(9):613–616
Le Hégarat-Mascle S, Zribi M, Alem F, Weisse A, Loumagne C (2002) Soil moisture estimation from ERS/SAR data: toward an operational methodology. IEEE Trans Geosci Remote Sens 40(12):2647–2658
Li YY, Zhao K, Zheng XM, Ren JH (2013) Analysis of microwave polarization difference index characteristics about different vegetation types in northeast of China. In: International conference on remote sensing, environment and transportation engineering
Lim KS, Koo V, Ewe HT (2008) Multi-angular scatterometer measurements for various stages of rice growth. Prog Electromagnet Res 83:385–396
Liu WT (2002) Progress in scatterometer application. J Oceanogr 58(1):121–136
Magagi RD, Kerr YH (2001) Estimating surface soil moisture and soil roughness over semiarid areas from the use of the copolarization ratio. Remote Sens Environ 75(3):432–445
Meier P, Frömelt A, Kinzelbach W (2011) Hydrological real-time modelling in the Zambezi river basin using satellite-based soil moisture and rainfall data. Hydrol Earth Syst Sci 15(3):999–1008
Mishra VD, Sharma JK, Singh KK, Thakur NK, Kumar M (2009) Assessment of different topographic corrections in AWiFS satellite imagery of Himalaya terrain. J Earth Syst Sci 118(1):11–26
Moeremans B, Dautrebande S (2000) Soil moisture evaluation by means of multi-temporal ERS SAR PRI images and interferometric coherence. J Hydrol 234(3–4):162–169
Mougin E, Seena DL, Rambal S, Gaston A, Hiernaux P (1995) A regional Sahelian grassland model to be coupled with multispectral satellite data. I: model description and validation. Remote Sens Environ 52(3):181–193
Naeimi V, Scipal K, Bartalis Z, Hasenauer S, Wagner W (2009) An improved soil moisture retrieval algorithm for ERS and METOP scatterometer observations. IEEE Trans Geosci Remote Sens 47(7):1999–2013
Naeimi V, Leinenkugel P, Sabel D, Wagner W, Apel H, Kuenzer C (2013) Evaluation of soil moisture retrieval from the ERS and Metop scatterometers in the lower Mekong basin. Remote Sens 5(4):1603–1623
Nghiem SV, Tsai WY (2001) Global snow cover monitoring with space-borne K/sub u/-band scatterometer. IEEE Trans Geosci Remote Sens 39(10):2118–2134
Nikam BR, Garg V, Gupta PK, Thakur PK, Kumar AS, Chouksey A, Aggarwal SP, Dhote P, Purohit S (2017) Satellite-based mapping and monitoring of heavy snowfall in North Western Himalaya and its hydrologic consequences. Curr Sci 2328–2334
Oh Y, Sarabandi K, Ulaby FT (1992) An empirical model and an inversion technique for radar scattering from bare soil surfaces. IEEE Trans Geosci Remote Sens 30(2):370–381

Owe M, de Jeu R, Walker J (2001) A methodology for surface soil moisture and vegetation optical depth retrieval using the microwave polarization difference index. IEEE Trans Geosci Remote Sens 39(8):1643–1654

Oza SR, Panigrahy S, Parihar JS (2008) Concurrent use of active and passive microwave remote sensing data for monitoring of rice crop. Int J Appl Earth Obs Geoinf 10(3):296–304

Oza SR, Singh RKK, Vyas NK, Sarkar A (2011) Study of inter-annual variations in surface melting over Amery Ice Shelf, East Antarctica, using space-borne scatterometer data. J Earth Syst Sci 120(2):329–336

Oza SR, Bothale RV, Rajak DR, Jayaprasad P, Maity S, Thakur PK, Tripathi N, Chouksey A, Bahuguna IM (2019) Assessment of cryospheric parameters over the Himalaya and Antarctic regions using SCATSAT-1 enhanced resolution data. Curr Sci 117(6):1002–1013

Ozdogan M, Yang Y, Allez G, Cervantes C (2010) Remote sensing of irrigated agriculture: opportunities and challenges. Remote Sens 2(9):2274–2304

Pampaloni P, Paloscia S (1985) Experimental relationships between microwave emission and vegetation features. Int J Remote Sens 6(2):315–323

Pietroniro A, Prowse TD (2002) Applications of remote sensing in hydrology. Hydrol Process 16(8):1537–1541

Potopová V, Trnka M, Hamouz P, Soukup J, Castraveț T (2020) Statistical modelling of drought-related yield losses using soil moisture-vegetation remote sensing and multiscalar indices in the south-eastern Europe. Agric Water Manag 236:106168

Prevot L, Champion I, Guyot G (1993) Estimating surface soil moisture and leaf area index of a wheat canopy using a dual-frequency (C and X bands) scatterometer. Remote Sens Environ 46(3):331–339

Pulliainen JT, Manninen T, Hallikainen MT (1998) Application of ERS-1 wind scatterometer data to soil frost and soil moisture monitoring in boreal forest zone. IEEE Trans Geosci Remote Sens 36(3):849–863

Quesney A, Le Hégarat-Mascle S, Taconet O, Vidal-Madjar D, Wigneron JP, Loumagne C, Normand M (2000) Estimation of watershed soil moisture index from ERS/SAR data. Remote Sens Environ 72(3):290–303

Quiring SM, Papakryiakou TN (2003) An evaluation of agricultural drought indices for the Canadian prairies. Agric for Meteorol 118(1–2):49–62

Salmon JM, Friedl MA, Frolking S, Wisser D, Douglas EM (2015) Global rain-fed, irrigated, and paddy croplands: a new high resolution map derived from remote sensing, crop inventories and climate data. Int J Appl Earth Obs Geoinf 38:321–334

Santos CAG, Neto RMB, do Nascimento TVM, da Silva RM, Mishra M, Frade TG (2021) Geospatial drought severity analysis based on PERSIANN-CDR-estimated rainfall data for Odisha state in India (1983–2018). Sci Total Environ 750:141258

Schmugge TJ, Kustas WP, Ritchie JC, Jackson TJ, Rango A (2002) Remote sensing in hydrology. Adv Water Resour 25(8–12):1367–1385

Schultz GA (1988) Remote sensing in hydrology. J Hydrol 100(1–3):239–265

Scipal K, Scheffler C, Wagner W (2005) Soil moisture-runoff relation at the catchment scale as observed with coarse resolution microwave remote sensing. Hydrol Earth Syst Sci 9(3):173–183

Scipal K, Drusch M, Wagner W (2008) Assimilation of a ERS scatterometer derived soil moisture index in the ECMWF numerical weather prediction system. Adv Water Resour 31(8):1101–1112

Siebert S, Kummu M, Porkka M, Döll P, Ramankutty N, Scanlon BR (2015) A global data set of the extent of irrigated land from 1900 to 2005. Hydrol Earth Syst Sci 19(3):1521–1545

Singh RP, Dadhwal VK (2003) Comparison of space-based microwave polarization difference index and normalized difference vegetation index for crop growth monitoring. Indian J Radio Space Phys 32:193–197

Singh RK, Singh KN, Maisnam M, Jayaprasad P, Maity S (2019) Observing Larsen C ice-shelf using ISRO's SCATSAT-1 data. Polar Sci 19:57–68

Singh S, Tiwari RK, Sood V, Prashar S (2021a) Unsupervised snow cover classification using dual-polarized SCATSAT-1 satellite data. In: Soft computing and signal processing. Springer, Singapore, pp 627–635

Singh S, Tiwari RK, Sood V, Gusain HS, Prashar S (2021b) Image-Fusion of Ku-band based SCATSAT-1 and MODIS data for cloud-free change detection over Western Himalayas. IEEE transactions on geoscience and remote sensing

Sood V, Gusain HS, Gupta S, Singh S, Kaur S (2020) Evaluation of SCATSAT-1 data for snow cover area mapping over a part of Western Himalayas. Adv Space Res 66(11):2556–2567

Stoffelen A (1998) Toward the true near-surface wind speed: error modeling and calibration using triple collocation. J Geophys Res: Oceans 103(C4):7755–7766

Tedesco M, Miller J (2007) Observations and statistical analysis of combined active—passive microwave space-borne data and snow depth at large spatial scales. Remote Sens Environ 111(2–3):382–397

Townsend PA, Foster JR (2002) Assessing flooding and vegetation structure in forested wetlands using Radarsat SAR imagery. In: IEEE international geoscience and remote sensing symposium, vol 2. IEEE, pp 1171–1173

Trnka M, Hlavinka P, Možný M, Semerádová D, Štěpánek P, Balek J, Bartošová L, Zahradníček P, Bláhová M, Skalák P, Farda A, Žalud Z (2020) Czech Drought Monitor System for monitoring and forecasting agricultural drought and drought impacts. Int J Climatol 40(14):5941–5958

Ulaby FT, Batlivala PP, Dobson MC (1978) Microwave backscatter dependence on surface roughness, soil moisture, and soil texture: part I-bare soil. IEEE Trans Geosci Electron 16(4):286–295

Ulaby FT, Kouyate F, Fung AK, Sieber AJ (1982) A backscatter model for a randomly perturbed periodic surface. IEEE Trans Geosci Remote Sens 4:518–528

Wagner W, Lemoine G, Rott H (1999) A method for estimating soil moisture from ERS scatterometer and soil data. Remote Sens Environ 70(2):191–207

Wagner W, Hahn S, Kidd R, Melzer T, Bartalis Z, Hasenauer S, Figa J, De Rosnay P, Jann A, Schneider S, Komma J, Rubel F (2013) The ASCAT soil moisture product: a review of its specifications, validation results, and emerging applications. Meteorol Z 22(1):5–33

Wen J, Su Z (2003) A time series based method for estimating relative soil moisture with ERS wind scatterometer data. Geophys Res Lett 30(7)

Woodhouse IH, Hoekman DH (2000) Determining land-surface parameters from the ERS wind scatterometer. IEEE Trans Geosci Remote Sens 38(1):126–140

Zaussinger F, Dorigo W, Gruber A, Tarpanelli A, Filippucci P, Brocca L (2019) Estimating irrigation water use over the contiguous United States by combining satellite and reanalysis soil moisture data. Hydrol Earth Syst Sci 23(2):897–923

Chapter 5
Delineation and Monitoring of Wetlands Using Time Series Earth Observation Data and Machine Learning Algorithm: A Case Study in Upper Ganga River Stretch

Akash Goyal, M. Upreti, V. M. Chowdary, and C. S. Jha

Abstract Wetlands are unique and valuable ecosystems and are the traditional zones between land and water. They are considered to be one of the most important resources on the earth. The rapid loss of wetlands during the past decades necessitates continuous monitoring of wetlands with respect to its hydrological changes, vegetation, soil etc. The Ramsar Convention of wetland conservation plays a significant role in outlining the internationally important wetlands and the efficient measures for their protection. The present study focused on the delineation and monitoring of wetlands situated in the upper Ganga River stretch, a potential Ramsar site in Uttar Pradesh using Sentinel 2A and Landsat satellite images. Periodical monitoring and change analysis of Ramsar wetland and its environment was studied at decadal scale during the period 1991 to 2019. Machine learning-based classification approach Random Forest classifier was used for extraction of surface water bodies and wetland classification. The overall accuracy and overall kappa coefficient of the classified data is nearly 80% or above in all the years of study, while kappa coefficient ranges between 0.77 and 0.92 for all study years. Further, seasonal turbidity of water was assessed temporally based on the spectral index such as Normalized Differential Turbidity Index using satellite data. The sewage discharge between Anupsahar and Narora towns, industrial activities, non-point source pollution of runoff due to fertilizers and pesticides are some of the important factors that led to increased turbidity levels.

A. Goyal (✉)
Regional Remote Sensing Centre-North, New Delhi, India
e-mail: akash_g@nrsc.gov.in

M. Upreti
Department of Geoinformatics, Central University of Jharkhand, Ranchi, India

V. M. Chowdary
Mahalanobis National Crop Forecast Centre, New Delhi, India

C. S. Jha
National Remote Sensing Centre, Hyderabad, India

C. S. Jha et al. (eds.), *Geospatial Technologies for Resources Planning and Management*, Water Science and Technology Library 115,
https://doi.org/10.1007/978-3-030-98981-1_5

Further, intensive agricultural practices at the riverbank side and cultivation in the riverbed areas also act a major cause for wetland loss or degradation in the study area.

Keywords Wetland · Optical · Ramsar site · Machine learning · Random forest classifier · Change detection · Turbidity · Classification · NDTI

5.1 Introduction

Wetlands are the most productive ecosystems in the world and cover nearly 7 million ha. of the earth (Wania et al. 2013). The varying characteristics of wetlands are mainly concerned to size, hydrological conditions, vegetation and its geographical location. The Ramsar Convention of Wetland Conservation defined wetlands as the "areas of marsh, fen, peatland or water, weather natural or artificial, permanent or temporary, with water that is static or flowing, fresh, brackish or salt, including areas of marine water, the depth of which at low tide does not exceed six meters" (Ramsar Convention Secretariat 2016; Ramsar Convention 1971, Article 1.1). Wetland being an important environmental ecosystem providing benefits for irrigated agriculture, flood protection, species habitation, etc. is also the most threatened one for the past decades. The Assessment Report of the Intergovernmental Science-Policy on Biodiversity and Ecosystem services reported that nearly 75% of the land area is degraded among which wetlands have been the hardest hit with the loss of 87% globally in the last 300 years. Protection and continuous monitoring of wetlands have become one of the major issues for natural resource management and mitigation of climate change (Guo et al. 2017; Gallant 2015; Bates et al. 2008). Monitoring of wetland ecosystems at different spatio-temporal scales requires continuous data on local, regional and global level, which can be obtained through satellite-based earth observation in an effective manner (Rebelo et al. 2008). With technological advancements, there is a growing scope for study of earth resources using geospatial technologies. Various remote sensing approaches envisage satellite data acquired from different platforms viz., aerial photography, multispectral sensors, hyperspectral sensors, Synthetic Aperture Radar (SAR) and other microwave systems for wetland mapping and monitoring for conservation purposes along with the implementation of machine learning techniques like Random forest (RF), Support Vector Machine (SVM), etc. for automation of land cover classification (Mahdavi et al. 2018; Ghosh and Das 2020). Studies on ecosystem sustenance like phytoremediation of wetlands in order to keep the wetland pollution free and response of wetlands to anthropogenic activities that are responsible for degradation were studied in the past (Garg and Joshi 2015; Galbraith et al. 2005). Remote sensing-based approaches are proved to be helpful for developing management strategies by the public and private authorities (Mayer and Lopez 2011). The multispectral data that includes near and shortwave infrared bands are well suited for wetland mapping, ecosystem analysis and also for identifying the plant and hydrological conditions (Chavez et al. 2009).

The identification, extraction or classification of riverine wetlands is itself a challenge and requires a proper hierarchical system based on its hydro-geomorphic characteristics (Sinha et al. 2017). One of the well-known classification systems that was adopted by the Ramsar secretariat refers to multilevel classification scheme characterized with nearly 40 to 55 wetland types (Cowardian et al. 2005). Murthy et al. (2013) proposed the wetland classification system for the National Wetland Inventory Project for Indian conditions with the inclusion of wetland classes as per the Ramsar definition of wetlands. Machine learning-based classification algorithm, i.e. Random Forest has a high potential and ability to model the complex class signatures as well as can accept variety of predictor datasets in a non-parametric distribution, which helps to explore the complexities faced while mapping and classifying the resources like wetland (Maxwell et al. 2018; Bangira et al. 2019). Relative performance of Random Forest algorithm for satellite data classification indicated 10% higher accuracy as compared to support vector machine and maximum likelihood classification algorithms (Akar and Güngör 2012) and provides feasible solutions for automated extraction and classification of waterbodies (Bangira et al. 2019).

A three-level-based classification scheme for extraction of surface water bodies and wetlands either natural or artificial in nature helps to relate the environmental conditions developed around the wetland with respect to the land use changes (Khan et al. 2013). Riverine wetlands are susceptible to the sediments washed down from the agricultural fields, sand beds, sewage waste etc. and show high turbidity alongside the river. The water clarity levels can be predicted and analyzed using water-based spectral indices i.e. Normalized Difference Turbidity Index (Dam 2020). Thus, the satellite-based monitoring of wetlands has become essential due to their unsustainable, overutilization, as well as rapid changes in the land use pattern with the increasing demand to develop the framework for sustainable management of resources. The present study demonstrates the exploitation of satellite-based temporal data and machine learning algorithms for delineation of Brijghat-Narora riverine wetland and temporal changes occurred over this wetland situated in the upper Ganga river stretch.

5.2 Study Area

The Upper Ganga River stretch from Brijghat to Narora a potential Ramsar Site in Uttar Pradesh with an area of 26,590 ha is selected for the present study. The study area was declared as Ramsar site no.1574 on November 8th, 2005 the only river/stream wetland type in India based on Criterion 2 and 5 of the Ramsar Convention (Murthy et al. 2013). The site is bounded by four districts Hapur in north west, Bulandshahr in south west, Amroha in north east and Badaun in south east. It supports the threatened ecological communities listed in the Convention on International Trade in Endangered Species of Wild Fauna and Flora (CITIES), International Union for Conservation of Nature (IUCN) Redbook as endangered (Ramsar 2005) and supports 20,000 or more water birds regularly.

Table 5.1 Satellite datasets used

Satellite	Data acquisition year/months				Spatial resolution
	1991	1999	2009	2019	
Sentinel 2A	Nil	Nil	Nil	April & Oct	10 m
Landsat 8/5	May& Dec	April & Dec	May & Nov	April & Dec	30 m

5.3 Satellite Data Used

The Landsat-8 OLI/TIRS and Landsat-4/5 TM seasonal datasets with 30 m spatial resolution are acquired for the years 1991, 1999, 2009 and 2019 from USGS earth explorer for delineation of surface water bodies and wetlands. Sentinel 2A images with 10 m spatial resolution for the year 2019 are used to draw comparison among the datasets varying in spatial resolution for wetland delineation based on area statistics and accuracies. Details of the satellite data used in this study are given Table 5.1.

5.4 Methodology

The workflow of the present study that includes processing and classification of sentinel 2A and Landsat seasonal datasets for wetland studies is given in Fig. 5.1. Initially, Optical remote sensing data was atmospherically and radiometrically corrected as a first step. The random forest classifier (Breiman 2001) was used for three level classification of wetlands using training data from the area of interest. Subsequently, band rationing technique was used for analyzing the turbidity levels of the river.

5.4.1 Pre-processing Data

Temporal data of Landsat 5 and 8 and Sentinel 2A with cloud cover less than 10% are pre-processed using Semi-automatic classification plugin in QGIS software. The Dark Object Subtraction (DOS) atmospheric correction, a simple stretch function converting from raw or Top of the Atmosphere (TOA) Digital Numbers (DNs) to reflectance values (Congedo 2016). The DOS corrected images are consistently sharper in contrast between wetland and non-wetland features. Multiple spectral bands (red, green, blue, NIR and SWIR) are stacked to constitute a single image i.e. false color composite (FCC), which is used for wetland classification. The study area boundary with a 12 km buffer is used for sub-setting the area of interest from the entire satellite scene.

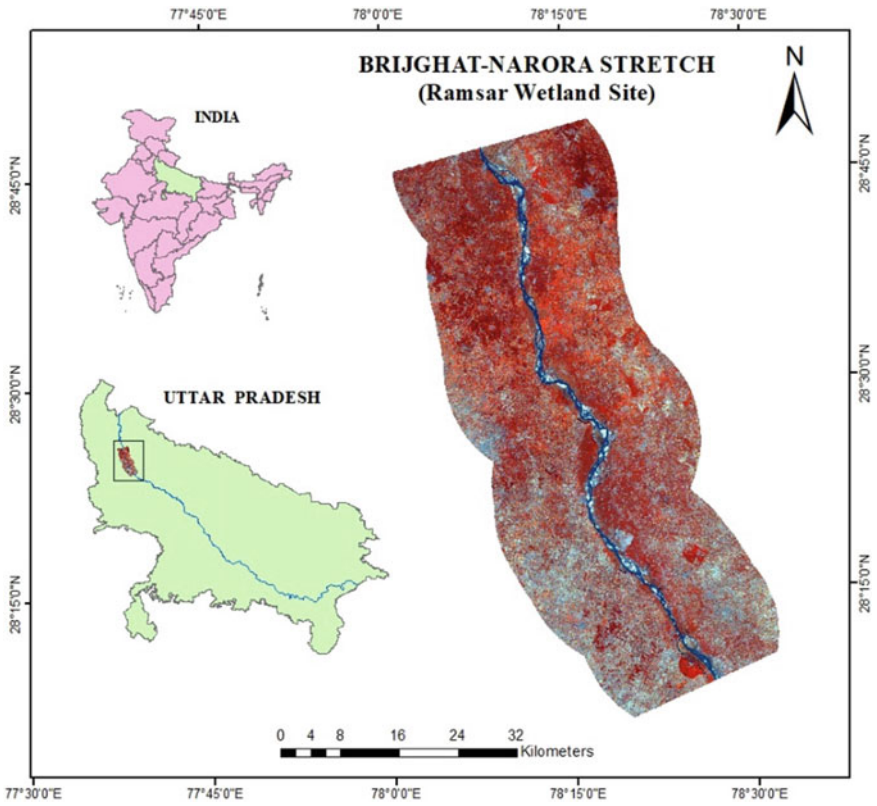

Fig. 5.1 Study area map of wetland site

5.4.2 Classification

The assessment for wetland classification and monitoring should be carried out in a systematic way. A hierarchical classification system representing three levels helps in the overall understanding of the wetland environment. Prior to that a general classification of the surface water was carried out as an important aspect of wetland ecology. Satellite images are classified into three levels as shown in Fig. 5.2. Level one classification is performed to distinguish between surface water and non-water features and to delineate the general wetland boundary of the study area. The output of level one is used as an input for level two with the help of Model Builder in ArcGIS that classifies the extracted pre- and post-monsoon surface water into seasonal and permanent water bodies or wetlands in the study area. Level three classification of wetlands is carried out using the classification system suggested by Murthy et al. (2013), where wetlands are classified as lakes, waterlogged and riverine wetlands. The study area is the only river/stream type wetland in the country that is found adjacent to the river or within the channel fed by river water acting as a major source

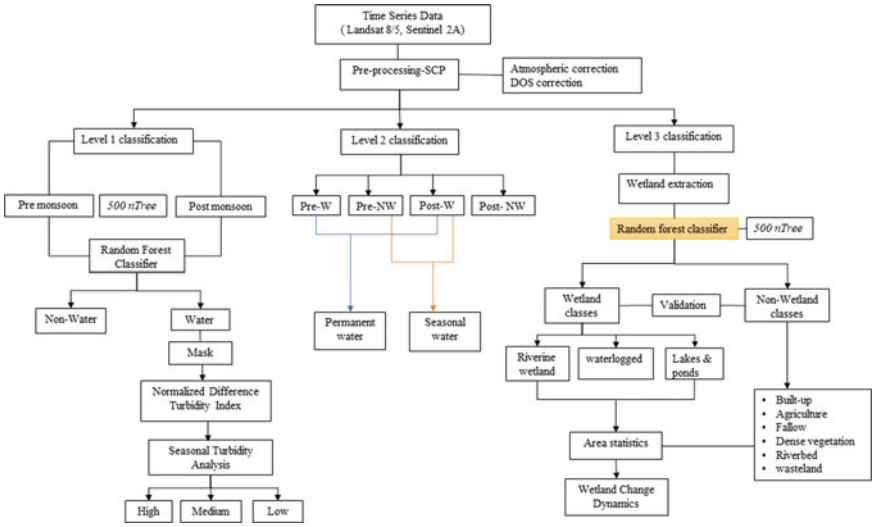

Fig. 5.2 Workflow for wet land classification with turbidity status using remote sensing

of water. This necessitates wetland classification in three levels. The non-wetland feature includes the remaining land cover classes such as agricultural land, built up and wasteland etc.

5.4.2.1 Random Forest Classification

Random Forest Classifier (Breiman 2001), a robust classification technique that works efficiently on large databases with the ability to handle thousands of variables as input and do not require scaling or normalization while giving estimates on the variables that are more important in the classification (Rodriguez-Galiano et al. 2012). It is a machine learning method for supervised classification that creates multiple decision trees from randomly selected subsets of the training data samples for classification (Belgiu and Drăgu 2016). The pre- and post-monsoon season satellite data for the study area are used as the input while sample polygons indicative of wetlands are used as vector training data in the classifier, which extract the underlying pixel values from the satellite images. The classification was performed with 200 training samples for level 1 while 300 samples for level 3. The most commonly recommended *nTree* parameter to set in the classifier is 500 (Belgiu and Drăgu 2016) and the number of samples was set to 5000 for each classification that is the number of pixels within the training polygons selected randomly. Before setting the number of trees, a trial classification was performed on 100, 200 and 500 trees to identify optimum number of trees. The output of the classification is further used for periodic change analysis.

5.4.2.2 Training Data

The training data are prepared using the optical data with special reference to Google earth and visual interpretation of satellite imageries. The ground validated wetland Atlas prepared under National Wetland Inventory project was also considered as an important reference source while preparing the training datasets (Murthy et al. 2013). Nearly 100 samples each for water and non-water classes for level-1 and total 300 samples for level-3 classification were prepared. Special attention was given while identifying training samples for wetlands considering the presence of vegetation, water and marsh-like conditions that contributed to the development of wetland. For the validation purpose, nearly 100 reference data for each year are collected using the multispectral satellite and google earth images for computing accuracy and kappa statistics.

5.4.3 Turbidity Analysis

The ratio of Green and Red spectral bands was used for computing the Normalized Difference Turbidity Index (NDTI) that quantifies seasonal water clarity in the study area. The spectral reflectance values of red and green bands having wavelengths of 0.61–0.68 μm (red) and 0.5–0.59 μm (green) are used to estimate the turbidity levels (Bid and Siddique 2019). The reflectance in red is more than green due to the reflectance of the suspended particles in the turbid water bodies (Islam and Sado 2006). The NDTI values vary from −0.2 to 0.0 for clear water whereas it ranges from 0.0 to 0.2 for moderately turbid water and values greater than + 0.25 indicate high turbidity. The Landsat time series data was used for computing the water clarity of the upper Ganga river stretch and surrounding water bodies in order to evaluate the effects over the wetlands in the region. The turbidity levels can be shown with respect to hue as high (blue), medium (green to bluish green) and low (yellow to red) for better visualization and analysis. NDTI computed using spectral bands of green and red is computed and reclassified as low, medium and high, where higher value indicates high concentration of suspended sediments. NDTI is computed as given below:

$$\text{NDTI} = (\text{Red band} - -\text{Green band})/(\text{Red band} + \text{Green band})$$

5.5 Results and Discussion

The study primarily focuses on the identification, extraction, classification and monitoring of wetlands in Brijghat-Narora stretch of the upper Ganga river basin. The level 1 classification was carried out in order to extract the surface water differentiating

Table 5.2 Water spread area from level 1 classification data

Landsat	Water spread (area ha)		Non-water (area ha)	
Year	Pre-monsoon	Post-monsoon	Pre-monsoon	Post-monsoon
1991	4991.58	5890.05	275,419.98	274,476.42
1999	4750.11	5771.07	275,661.45	275,652.09
2009	4206.51	4123.98	276,205.05	276,287.58
2019	4910.04	5291.73	275,424.39	275,119.83
Sentinel 2A				
2019	5088.44	5293.7	275,093.54	274,888.28

from non-water features in the study area for the years 1991, 1999, 2009 and 2019 delineating a general wetland boundary. The statistical analysis of presence of surface water is shown in Table 5.2. Analysis indicated that area under water bodies during study years in the post-monsoon season ranges between 4123.98 ha and 5890 ha.

A slight difference in area of waterbodies in the pre-monsoon can be seen in both the data sets for the same year, 2019 as the area in pre-monsoon is computed for sentinel 2 is 5088.4 ha which is more than the area computed with Landsat i.e. 4910.04 ha.

Level 2 classification laid emphasis over the characterization of surface water bodies in the study area as seasonal or permanent (Figs. 5.3 and 5.4). Permanent water corresponds to the presence of water that is mostly retained throughout the year with slight variations, while seasonal water is defined as the water that undergoes frequent drying phase and last only up to one season. Once the water bodies are delineated from the satellite data during both seasons, extracted waterbodies were further classified into either seasonal or permanent water bodies using a logical criteria set in the ArcGIS model builder. The water present during both pre- and post-monsoon seasons were classified as permanent water while water present in either pre- or post-monsoon period is classified as seasonal (Pre-W + Post-NW) or (Pre-NW + Post-W). Analysis indicated that permanent water shows slow decline from 1991 to 2009 and increased up to 780.48 ha in 2019. Permanent water shows inverse fluctuating pattern with increase of 1105.87 ha from1991 to 1999 and then declined in 2009 which later shows steady increase in the year 2019.

Level 3 classification is performed for extraction and classification of wetlands in the selected study Ramsar site. The upper Ganga Brijghat-Narora stretch is characterized with the presence of riverine type of wetland which is constituted with the river or stream channels or stagnant water bodies normally found adjacent to the river or the areas. The radiometrically and atmospherically corrected images are given as input into the random forest classifier with 300 training vectors for each year. The output is reclassified into 10 classes corresponding to wetlands and non-wetlands. The need for classifying the non-wetland classes is to minimize the possibility of misclassification as wetlands that are characterized with complex spectral signatures. Further, this also helps to comprehend the influence of other land cover features over the wetland degradation with regard to the changing pattern of land use.

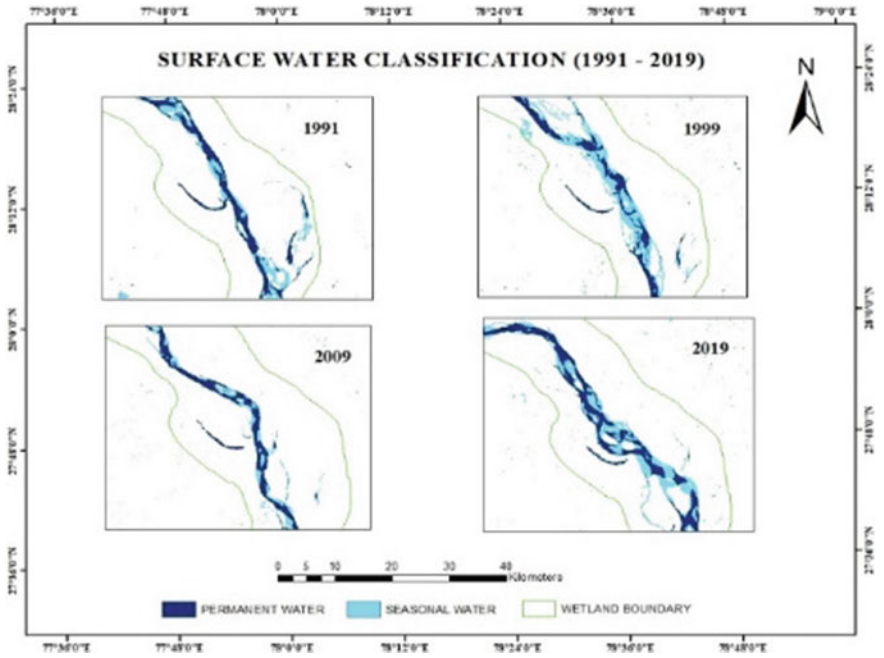

Fig. 5.3 Level 2 classification of surface water bodies

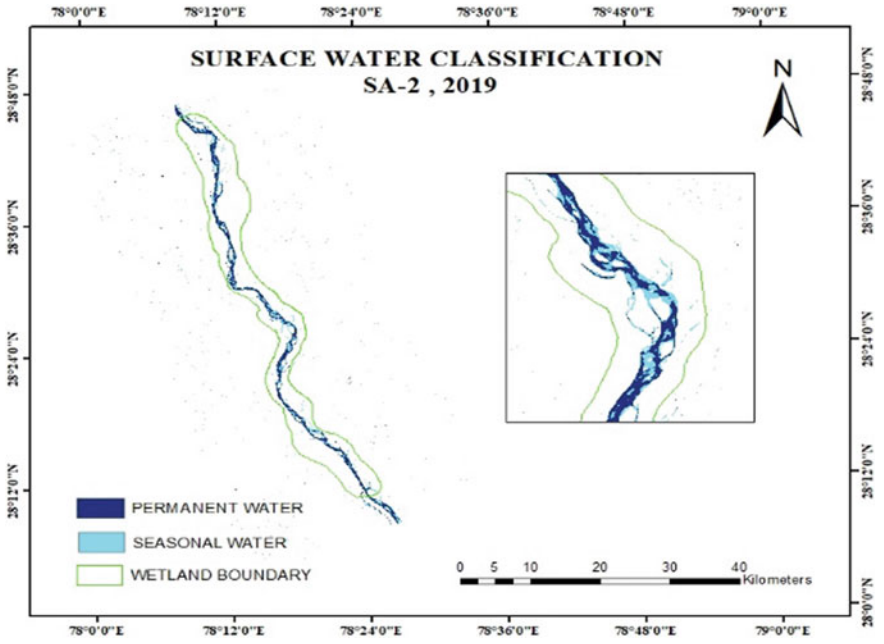

Fig. 5.4 Level 2 classification of surface water bodies using Sentinel 2A

Wetland map of the study area with Level 3 classification with 13 classes is shown as Fig. 5.5. In the inset of Fig. 5.5, A represents riverine type of wetland, B depicts waterlogged and C is for lakes and ponds. The similar areas are enlarged and shown for the years 1991 to 2019 as well as for sentinel 2A 2019 image along with the wetland boundary.

5.5.1 Accuracy Assessment of Wetland Delineation

The accuracy for level 3 classification is performed for both the datasets (Table 5.3). The overall accuracy and overall kappa coefficient of the classified data is nearly 80% or above in all the years of study, while kappa coefficient ranges between 0.77 and 0.92 for all study years.

The accuracy of 2019 for sentinel 2A classified image is 92% as compared to 84% with Landsat 2019 image, which may be attributed to higher resolution data. High resolution Sentinel data facilitated better identification of features visually thereby ensuring better training data. Although this data is available in open source domain, but its availability since 2015 is a major limitation for long-term analysis. Random forest-based classification ensured higher accuracy as it operates on large number of uncorrelated trees (models) for better prediction.

5.5.2 Temporal Dynamics and Change Analysis

The output of level 3 classified data is used for monitoring the decadal changes in wetlands during the period 1991 to 2019. The upper Ganga wetland was declared as a Ramsar site in the year 2005 based on the criteria drawn by the convention. However, the existence of wetlands prior to 2005 was also studied. Temporal analysis of wetland and non-wetland features during the period 1991–2019 was presented in Table 5.4, Results indicated degradation of wetlands along with the positive and negative impacts over the study period.

Riverine wetlands indicated 7% increase in the area from 1991 to 1999 whereas reduction by −66% was observed from 1999 to 2009 followed by reduction of −40% by the year 2019. In case of lakes and ponds, declining trend was observed during the period 1991–2019 (Fig. 5.6).

Area under waterlogged condition indicated an increase of 9% during the period 1991 to 1999. Subsequently, n reduction of waterlogged area by −55% during the period 1999–2009 and increase of 9% during the period 2009–2019 was observed. Further, analysis indicated increase of agricultural and wetland area in the study area.

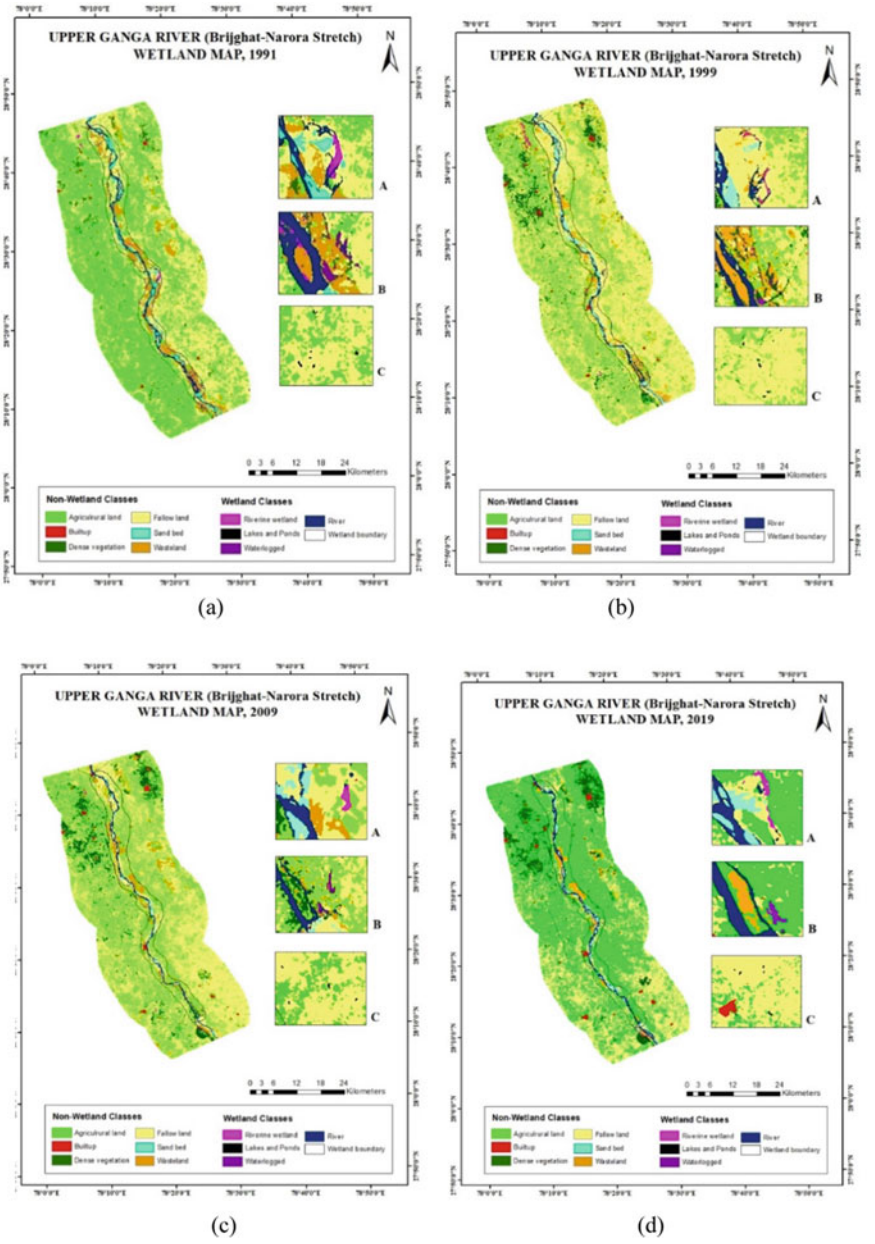

Fig. 5.5 **a**, **b**, **c**, **d**, **e** Level 3 classification of wetlands form the year 1991–2019

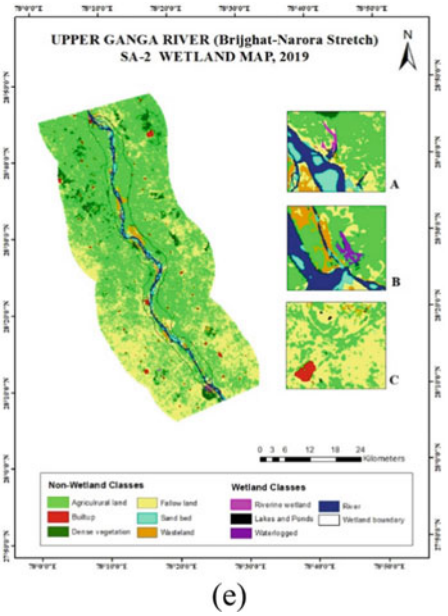

(e)

Fig. 5.5 (continued)

Table 5.3 Accuracy assessment of wetland delineation

Landsat (8/5)		
year	Overall accuracy (%)	Overall Kappa
1991	85.18	0.83
1999	79.36	0.77
2009	86.44	0.84
2019	84.39	0.82
Sentinel 2A		
2019	92.94	0.92

5.5.3 Seasonal Turbidity Analysis

The study area is dominated with agricultural, industrial and other anthropogenic practices that contributed to the river contamination thereby ultimately degrading the quality of riverine wetlands. Turbidity maps at decadal scale generated during both pre- and post-monsoon seasons for different years were shown as Figs. 5.7, 5.8, 5.9 and 5.10. The inset maps are representing the upper, middle and lower stretches of the river within the study wetland boundary. The higher NDTI values indicated higher turbidity values in the study area.

Analysis indicated that the turbidity level during pre-monsoon period is mostly low to medium during all the study years, it is medium to high during post-monsoon

Table 5.4 Wetland Level 3 classification statistics

Year	1991	1999	2009	2019
Wetland classes	(Area, ha)			
Lake/pond	186.3	177.21	80.01	53.55
Riverine wetland	396.18	424.8	143.55	85.85
Waterlogged	210.87	230.13	102.87	112.32
River/canal	5352.66	4239.99	3903.48	5180.85
Non-wetland classes	(Area, ha)			
Agriculture	110,951.4	75,365.82	104,104	112,938.7
Fallow	77,636.79	106,126	82,151.82	72,141.53
Built up	986.94	1236.51	1277.1	2166.48
Dense vegetation	3758.13	11,455.85	12,598.02	13,880.88
Riverbed	3018.6	2861.37	1292.31	2071.26
Wasteland	10,374.75	10,760.04	7203.96	4259.97

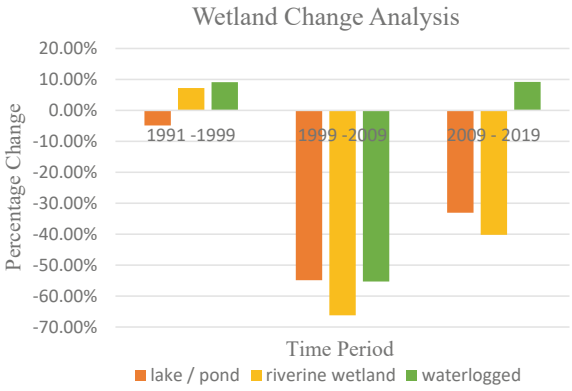

Fig. 5.6 Wetland change analysis during the period 1991–2019

season. Higher turbidity levels are attributed to soil erosion in the catchment of the study region, which if neglected might lead to siltation of wetlands.

The Brijghat-Narora Ramsar wetland site has many ecological, economic and social values, which is why it is considered as a potential wetland. Inspite of its great importance, it is also subjected to various threats that may act as driving factors for the wetland degradation (Ramsar 2005). The sewage discharge between Anupsahar and Narora towns, industrial activities, non-point source pollution of runoff due to fertilizers and pesticides are some of the important factors that led to increased turbidity levels. Intensive agricultural practices at the riverbank side and cultivation in the riverbed areas also act a major cause for wetland loss or degradation. These are some of the common threats to the river and the wetlands of the study area. Further, species supported by wetlands are also facing the threats from poaching, hunting etc. (WII-GACMC 2017). With the increasing threats to the wetlands Several conservation

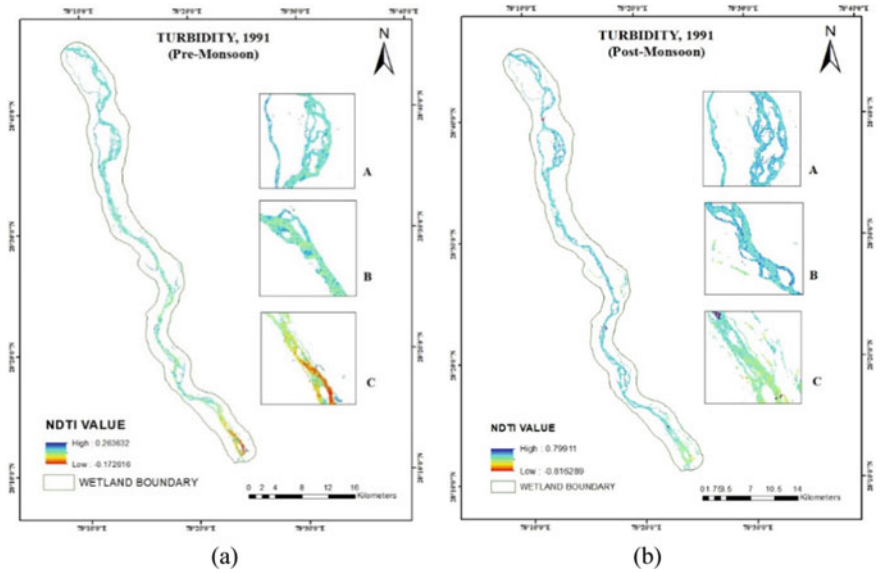

Fig. 5.7 Turbidity levels during pre- and post-monsoon seasons (1991)

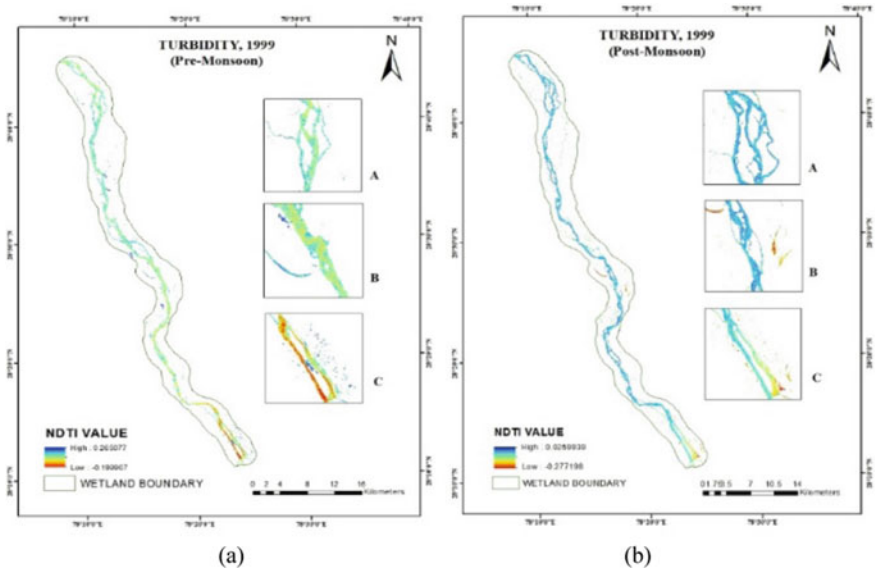

Fig. 5.8 Turbidity levels during pre- and post-monsoon seasons (1999)

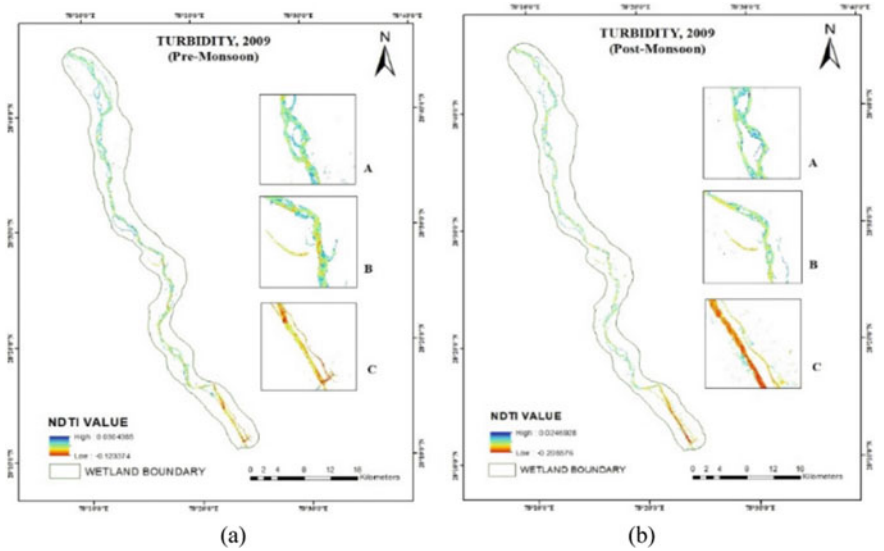

Fig. 5.9 Turbidity levels during pre- and post-monsoon seasons (2009)

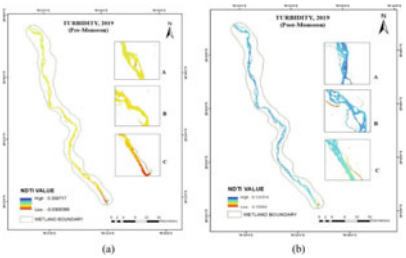

Fig. 5.10 Turbidity levels during pre- and post-monsoon seasons (2019)

and management measures such as domestic sewage treatment plant near Anupsahar were initiated by the government and private organizations (Ramsar 2005). The active partnership and participation of World Wide Fund for nature (WWF), the government has banned commercial fishing in both the bank stretch of the area.

5.6 Conclusions

The study wetland, Brijghat -Narora stretch of upper Ganga river, one of 37 Ramsar wetland sites in India is selected as a case study area in this study. The study area is the only river stream type wetland and wetlands were delineated in a systematic way using temporal satellite data for the years 1991, 1999, 2009, 2019. The Machine learning-based classification algorithm i.e. Random Forest algorithm was

used for multi-level classification in order to extract and classify surface water bodies, wetlands and other land cover classes and also to monitor the decadal change in wetlands. The riverine, waterlogged and lakes and ponds as major wetland types are classified in level 3. Spectral index, NDTI was useful for analysis of turbidity status in the study wetland. Temporal analysis indicated that the lakes and ponds are depleting throughout the study years while increase of riverine wetland in 1999 was observed followed by a negative trend till 2019. Similarly, decline in the water-logged areas was observed only during 1999 to 2009. Overall analysis indicated transformation of wetlands either to agricultural or wastelands in the study area. The water clarity of the river is computed based on the NDTI index method from 1991 to 2019 concluding high turbidity in post-monsoon as compared to pre-monsoon due to incoming suspended sediments, sewage from industries and agricultural effluents. Thus, the increasing threats over the wetlands led the Government of India to take up collaborative initiatives with other institutions like worldwide fund for nature, State wetland authorities, NGOs etc. for the conservation of wetlands. The wetland rule, 2017 by Govt. of India indicated the complete autonomy to the states for the formation of State wetland authority that can help in the preparation of efficient plans and management strategies toward to promote the wetland conservation in flood plain areas similar to the study area (WWF-NMCG 2019).

References

Akar Ö, Güngör O (2012) Classification of multispectral images using Random Forest algorithm. J Geodesy Geoinformation 1(2):105–112. https://doi.org/10.9733/jgg.241212.1

Bangira T, Alfieri SM, Menenti M, van Niekerk A (2019) Comparing thresholding with machine learning classifiers for mapping complex water. Remote Sens 11(11). https://doi.org/10.3390/rs11111351

Bates BC, Kundzewicz ZW, Wu S, Palutikof JP (eds) (2008) Climate change and water. Technical paper of the intergovernmental panel on climate change. IPCC Secretariat, Geneva, p 210

Belgiu M, Drăgu L (2016) Random forest in remote sensing: a review of applications and future directions. ISPRS J Photogrammetry Remote Sens 114:24–31. https://doi.org/10.1016/j.isprsjprs.2016.01.011

Bid S, Siddique G (2019) Identification of seasonal variation of water turbidity using NDTI method in Panchet Hill Dam, India. Model Earth Syst Environ 5:1179–1200. https://doi.org/10.1007/s40808-019-00609-8

Breiman L (2001) Random forest. Mach Learn 45:5–32. https://doi.org/10.1023/A:1010933404324

Chavez BL, Riordan K, Powell R, Miller N, Nowels M (2009) Improving wetland characterization with multi-sensor, multi-temporal SAR and optical/infrared data fusion. Adv Geosci Remote Sens. https://doi.org/10.5772/8327

Congedo L (2016) Semi-automatic classification plugin documentation. Release 4(0.1):29

Cowardin LM, Carter V, Golet FC, Laroe ET (2005) Classification of wetlands and deepwater habitats of the United States. Water Encycl https://doi.org/10.1002/047147844x.sw2162

Dam PH (2020) Identification of seasonal variation of water turbidity using NDTI method in Identification of seasonal variation of water turbidity using NDTI method in Panchet Hill Dam. Modeling Earth Systems and Environment, India. https://doi.org/10.1007/s40808-019-00609-8

Galbraith H, Amerasinghe P, Huber-Lee A (2005) The effects of agricultural irrigation on wetland ecosystems in developing countries: a literature review. Agriculture 1–30

Gallant AL (2015) The challenges of remote monitoring of wetlands. Remote Sens 7:10938–10950. https://doi.org/10.3390/rs70810938

Garg A, Joshi B (2015) Ecosystem sustenance of upper Ganga Ramsar site through phytoremediation. Geophytology 45(2):175–180

Ghosh S, Das A (2020) Wetland conversion risk assessment of East Kolkata Wetland: a Ramsar site using random forest and support vector machine model. J Cleaner Prod 275:123475. https://doi.org/10.1016/j.jclepro.2020.123475

Guo M, Li J, Sheng C, Xu J, Wu L (2017) A review of wetland remote sensing. Sensors (basel, Switzerland) 17(4):777. https://doi.org/10.3390/s17040777

Islam M, Sado K (2006) Analyses of ASTER and Spectroradiometer data with in-situ measurements for turbidity and transparency study of lake Abashri. Int J Geoinf 2:31–45

Khan MS, Islamia JM, Islamia JM (2013) Quantifying land use land cover change along upper Ganga river (Brijghat to Narora Stretch). Using Landsat TM Geogr 60(2)

Mahdavi S, Salehi B, Granger J, Amani M, Brisco B, Huang W (2018) Remote sensing for wetland classification: a comprehensive review. Giscience Remote Sens 55(5):623–658. https://doi.org/10.1080/15481603.2017.1419602

Maxwell AE, Warner TA, Fang F (2018) Implementation of machine-learning classification in remote sensing: an applied review sensing: an applied review. Int J Remote Sens 39(9):2784–2817. https://doi.org/10.1080/01431161.2018.1433343

Mayer A, Lopez R (2011) Use of remote sensing to support forest and wetlands policies in the USA. Remote Sens 3:1211–1233

Murthy TVR, Patel JG, Panigrahy S, Parihar JS (2013) National wetland atlas: wetlands of international importance under Ramsar convention. SAC/EPSA/ABHG/NWIA/ATLAS/38/2013, Space Applications Centre (ISRO). Ahmedabad, India, pp 230–246

Ramsar Convention Secretariat (2016) An introduction to the convention on wetlands, 7th ed. (previously The Ramsar Convention Manual). Gland, Switzerland, p 107

Ramsar (2005) Information sheet on Ramsar wetlands—upper Ganga River. Ramsar, 1–14. Retrieved from https://rsis.ramsar.org/RISapp/files/RISrep/IN1574RIS.pdf

Rebelo L-M, Finlayson M, Nagabhatla N (2008) Remote sensing and GIS for wetland inventory, mapping and change analysis. J Environ Manag 90:2144–2153. https://doi.org/10.1016/j.jenvman.2007.06.027

Rodriguez-Galiano VF, Ghimire B, Rogan J, Chica-Olmo M, Rigol-Sanchez JP (2012) An assessment of the effectiveness of a random forest classifier for land-cover classification. ISPRS J Photogrammetry Remote Sens 67(1):93–104. https://doi.org/10.1016/j.isprsjprs.2011.11.002

Sinha R, Saxena S, Singh M (2017) Protocols for riverine wetland mapping and classification using remote sensing and GIS. Current Sci 112(7):1544–1552. https://doi.org/10.18520/cs/v112/i07/1544-1552

Wania R, Melton JR, Hodson EL, Poulter B, Ringeval B, Spahni R, Bohn T, Avis CA, Chen G, Eliseev AV, Hopcroft PO, Kaplan JO (2013) Present state of global wetland extent and wetland methane modelling: methodology of a model inter-comparison project (WETCHIMP). Geoscientific Model Dev 6:617–641. https://doi.org/10.5194/gmd-6-617-2013

WII-GACMC (2017) Aquatic Fauna of Ganga river: status and conservation. Ganga aqualife conservation monitoring centre. Wildlife Institute of India, Dehradun.

WWF-NMCG (2019) Conserving wetlands in the Ganga basin, Recommendations From the national workshop contents. World wild fund for nature-India & national mission for clean Ganga, p 12–47

Chapter 6
Geospatial Analysis of Glacial Lake Outburst Flood (GLOF)

Manish Rawat, Ashish Pandey, and Praveen Kumar Gupta

Abstract The Himalayan region is a fragile ecosystem with a steep landscape where natural disasters such as the Glacial Lake Outburst Floods (GLOFs) event have been frequently observed that cause significant damage in valleys downstream areas. GLOF is one of the major unexpected serious hazards that can release a large volume of water with debris cover in a very short interval of time that caused loss of lives, properties, and severe damage to downstream infrastructures. In the present study, lake-terminating South Lhonak lake (Lat 27° 54′ 41.88″ N and Long 88° 11′ 44.65″ E) is located at an altitude of 5205 m above mean sea level (a.s.l.) in the Teesta basin, Sikkim has been identified as highest potentially dangerous glacial lake based on the criteria of area, elevation, slope, distance from the glacier and volume of water held, with maximum surface area 1.39 km^2 acquired on October 2020. Spatio-temporal analysis of the glacial lake using Landsat 5 and Landsat-8 satellite imagery shows that the glacial lake has been grown from 0.48 to 1.39 km^2 over the past 30 years. The depth of South Lhonak glacial lake is 39.54 m which has been calculated by using Huggle's formula. This study evaluates the one-dimensional hydrodynamic modeling for GLOF simulation at different downstream sites from the glacial lake. The HEC-GeoRAS has been used for the creation of river geodatabase. Consequently, simulation was carried out using HECRAS model at multiple sections along the river. The GLOF scenario was revealed due to overtopping failure of the frontal moraine, producing peak discharge, and releasing water volume of 54.96×10^6 m^3. The result of this study reveals that the predicted peak discharges of the lake have been estimated for breach widths of 30, 40, and 60 m, and breach formation time has also been considered as 40, 30, and 20 min, respectively. The estimated flood peak was

M. Rawat (✉) · A. Pandey
Department of Water Resources Development & Management, Indian Institute of Technology Roorkee, Roorkee, Uttarakhand 247667, India
e-mail: rawat1992manish@gmail.com

A. Pandey
e-mail: ashish.pandey@wr.iitr.ac.in

P. K. Gupta
Space Application Centre, Indian Space Research Organisation, Ahmedabad, India
e-mail: pkgupta@sac.isro.gov.in

C. S. Jha et al. (eds.), *Geospatial Technologies for Resources Planning and Management*, Water Science and Technology Library 115,
https://doi.org/10.1007/978-3-030-98981-1_6

14,658.60 m^3/s at the GLOF site, and the same got mitigated to 11,978.77 m^3/s at the downstream end, respectively. The study's findings will aid in the formulation of risk management plans and risk reduction strategies in the event of a GLOF hazard.

Keywords South Lhonak lake · Glacial Lake outburst floods · HEC-RAS model · HEC-GeoRAS · River cross-section · Flood hydrograph

6.1 Introduction

The global climate variability during the first half of the twentieth century had a significant impact on the glacier lifecycle in the Himalayan region, resulting in several glaciers are melting rapidly and forming a large number of glacial lakes. The formation of different types of glacial lakes in the Himalayan region can be interpreted as a caution of glacier mass balance changes. The formation of glacial lakes occurs when the glaciers retreat (Sakai 2012; Zhang et al. 2015; Ahmed et al. 2021). The retreating and melting rate of glaciers are faster than ever, causing rapid accumulation of ice and snow on the glacier, this results in a prompt increase in the volume of the glacial lakes. Most of high altitude glacial lakes are surrounded by moraine dam which is formed by loose unconsolidated material deposited by the retreating glacier which can be burst suddenly, leading to discharge of huge volume of water with debris causing potentially devastating hazards that may destroy the livelihood and other infrastructure and this may also destroy the serene beauty of the Himalayan region. The water availability in Himalayan glaciers has the potential to serve India's vast population in the future decades (Bajracharya et al. 2007).

The Himalayas are not only the world's highest mountain range, but they also comprise the greatest freshwater reservoirs in the form of glacial snow and ice, but due to the effect of global warming, glaciers in the Himalayan region are melting rapidly, and the rate at which Himalayan glaciers are receding provides a compelling indication of climate change. In the last 200 years, the Gangotri glacier in the northern Himalayan region of India has retreated 2 km (Bhambri et al. 2012).

The Himalayan glaciers are known to be one of the most susceptible regions to the adverse effects of climate change. The Himalayan is a fragile ecosystem with a steep landscape prone to natural calamities such as landslides, avalanche, and glacial lake outbursts flood have been frequently observed (Singh et al. 2006). The resulting flood can devastate settlements and infrastructure in low-lying areas. The Himalayan glaciers employed a substantial effect on high terrain hydrology and provided water resources supporting the ecological life system in central Asia. Recent studies have shown that most of the Himalayan glaciers are under intensive shrinkage, offering the most negative glacier mass balance and indicating the most significant reduction in length of the glacier (Cogley 2006; Gardelle et al. 2013). The continuous retreating and thinning of glaciers, leaving the debris mass at the end of the glacier and that end moraine exposed may lead to the creation of new glacial lakes (Costa and Schuster 1998; Emmer 2017; Harrison et al. 2018; Mergili et al. 2021) thereby increasing

the risk of the downstream region to glacial lake outburst flood. The establishment of glacial lakes at higher altitudes growths the risk of catastrophic GLOF events in low-lying areas. This kind of flood event is frequently accompanied by dam breach formation and leads to moraine dam failure (Richardson and Reynolds 2000; Worni et al. 2014). GLOF represents a catastrophic event in the Himalayan glaciers and poses a potential risk to the downstream hydro-project power plant due to the extreme river flow. GLOF phenomenon is related to various flow characteristics in both spatial and temporal scales (Westby et al. 2014).

There are multiple inventories of glacial lakes, and state wide hazard evaluations are available for Sikkim Himalaya (Mool et al. 2003; Raj et al. 2013; Worni et al. 2013; Aggarwal et al. 2016, 2017; Sattar et al. 2019). Mool et al. (2003) described the first glacial lake inventory, where mapping 266 lakes with a total area having 20.2 km^2, out of 266 lakes, only14 lakes have been identified as potentially dangerous. South Lhonak glacier has become one of the fastest receding glaciers in the Teesta basin; Sikkim and the accompanying proglacial lakes have grown to be the most rapid rate in the state (Aggarwal et al. 2017). In the last few years, the Hindu Kush Himalaya region has been witnessing multiple GLOF events that often result in catastrophic flooding downstream, with major geomorphic and socioeconomic impacts and livelihoods. Glaciers thinning and retreating phenomenon has been found in most provinces of the Hindu Kush Himalaya (HKH) (Bolch et al. 2012), which has resulted in the creation of numerous new glacial lakes. Most of the glacial lakes have been situated at the snout or ablation zone of the glacier, which is dammed by the end or lateral moraine, where there is the highest risk of breaching. These kind of lakes might be potentially dangerous and carry a huge volume of water. To analyze the potential threats from such lakes, it is essential to identification and mapping of such glacial lakes that have been categorized based on the number frequency of lakes of different areas and different elevations.

Regular monitoring of the glacial lakes is essential to prevent the GLOF hazard and assess the damage that may occur in the near future time. Remote sensing and GIS could play an important role in the identification of potentially dangerous lakes and proper monitoring of the GLOF events in real-time. The monitoring of glacial lakes has been carried out by using multi-temporal Landsat imagery and microwave remote sensing-based altimetry data (Thakur et al. 2021). One-dimensional hydrodynamic models were studied to analyze the GLOF event in the Himalayan region (Jain et al. 2012; Thakur et al. 2019).

In previous research, the inventory of glacial lakes was monitored and found to increase due to climate change and glaciers retreating (Reynolds 2000; Ageta et al. 2000; Benn et al. 2000). A semi-automatic water body extraction method based on the normalized difference water index (NDWI) was employed on Imja Glacial Lake by Bolch et al. (2008).

Remote sensing techniques combined with a flood simulation model can assist in identifying and preventing damage to downstream communities and infrastructure. The study's assessment analyzes the potential dangerous glacial lake using remote sensing technology coupled with HEC-RAS one-dimensional unsteady flow hydrodynamic modeling. This study incorporates (i) To estimate the volume of the glacial

lake using Huggel formulas, (ii) to evaluate different lateral moraine breach scenarios based on varying breach formation time and breach width, producing breach hydrographs, (iii) one-dimensional unsteady flow hydrodynamic mathematical modeling has been used to assess the potential threat of glacial lake, (iv) also study of flow hydraulic of potential GLOF and its downstream impact at different sites along the river and creation of flood inundation map using HEC-RAS model and GIS, including prediction of flow depth, flow velocity, flood travel time, and peak discharge due to GLOF hazard.

6.2 Study Area

The South Lhonak glacial lake, which is located in the North-western parts of Sikkim, is one of the Himalaya's fastest-growing glacial lakes. The South Lhonak glacial lake (Lat 27° 54′ 41.88″ N and Long 88° 11′ 44.65″ E) is situated at an altitude of 5205 m a.s.l. in the Teesta basin, Sikkim. The lake is entirely blocked by moraine-dammed, which is susceptible in the perspective of GLOF. In the present study, Glacial Lake's outburst flood risk assessment has been carried out in the South Lhonak glacial lake. A temporal examination of the glacial lake using Landsat 5 and Landsat-8 satellite imagery shows that the lake has been grown from 0.48 km^2 to 1.39 km^2 in the last 30 years. The maximum lake depth is 39.54 m, and it stores 54.96×10^6 m^3 of water. The GLOFs wave has been routed from the glacial lake up to 20 km stretch, as shown in Fig. 6.1.

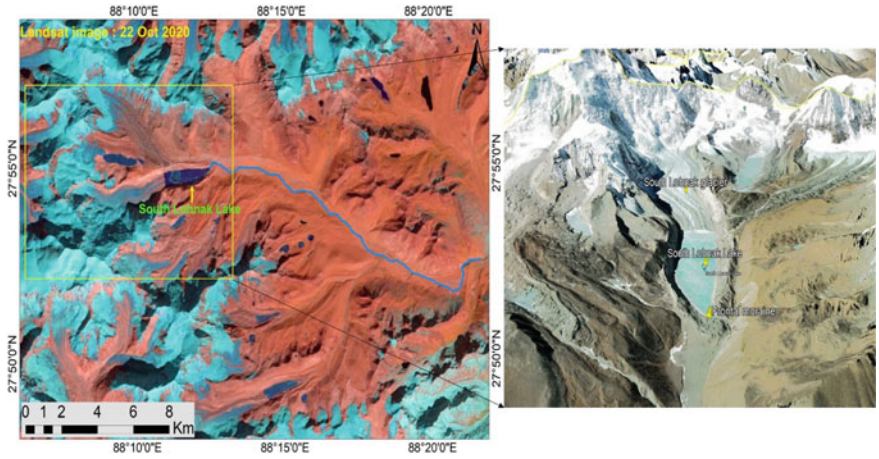

Fig. 6.1 The study area for GLOF

6.3 Dataset and Methodology

The data required to accomplish GLOF modeling are satellite imagery and SRTM 30 m DEM. To carry out GLOF modeling, glacial lake's analysis has been done by using HEC-RAS 1D hydrodynamic model and remote sensing techniques, and GIS. Time series of Landsat imagery has been used to identify potential lake sites and monitor the spatial and temporal variation in the lake area. Figure 6.3 gives the time series of Landsat images that show change detection in the glacial lake area from 1990 to 2020. Table 6.1 shows satellite data used in this study for identification of glacial lake area changes. After the analysis of temporal variation in satellite imagery, we have found that a glacial lake is formed at lower ablation zones of the mother glacier, which shows the breaching evidence, and the area of the lake keep growing as the continuous glacier retreat. Therefore, South Lhonak glacial lake has been found the most hazardous lake with its maximum area of 1.39 km^2, therefore, it has been selected for GLOF study. Figure 6.2 depicts the overall methodology adopted in this study.

The Manning coefficient for hilly terrain has a steep slope with no vegetation, gravel, cobbles, boulder, and bushes on the banks ranging from 0.03 to 0.07 (HEC-RAS Manual HEC 2010). In the present study, Manning coefficient has been taken from 0.04 to 0.10 as an input in the HEC-RAS model.

6.3.1 Hydraulic Analysis Using HEC-RAS

HEC-RAS is the most significant hydraulic model used for glacial hazard studies (Klimes et al. 2011). It is a user-friendly, reliable model that has the dynamic capability of performing complex flow simulations in the design, management, and operation of river systems.

In this study, HEC-RAS one-dimensional unsteady flow hydrodynamic mathematical modeling has been used to simulate the GLOF occurrence of the South Lhonak glacial lake in Teesta Basin to evaluate the downstream flood wave due to potential GLOF. The model is based on one-dimensional St. Venant equations performing flood scenarios caused by the Glacial lake outburst event. For unsteady flow simulation, the hydraulic model requires two basic inputs data for flow analyses: geometric and flow data. The pre-processing of the geometric data is done by HECGeoRAS. The geometric data includes all the layers related to river cross-sectional station, elevation data, river centerline, bank stations, and flow paths. This

Table 6.1 Satellite data used in this study for mapping of glacial lake area changes

Date of acquisition	Sensor	Spatial resolution (m)
21 September 1990	Landsat 4-5TM	30
22 October 2020	Landsat 8 OLI	30

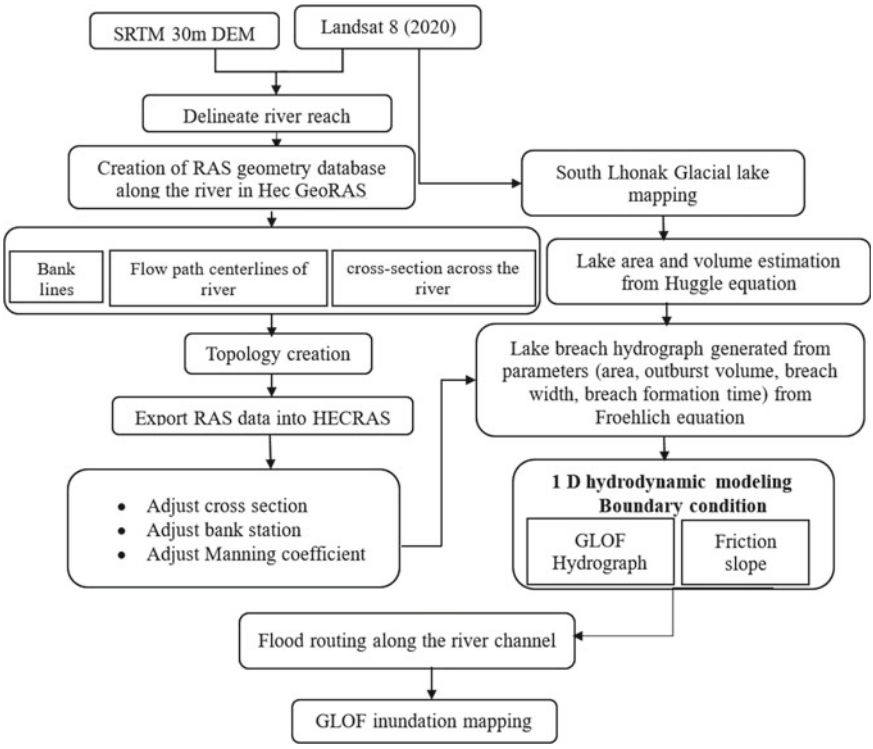

Fig. 6.2 Flowchart of methodology

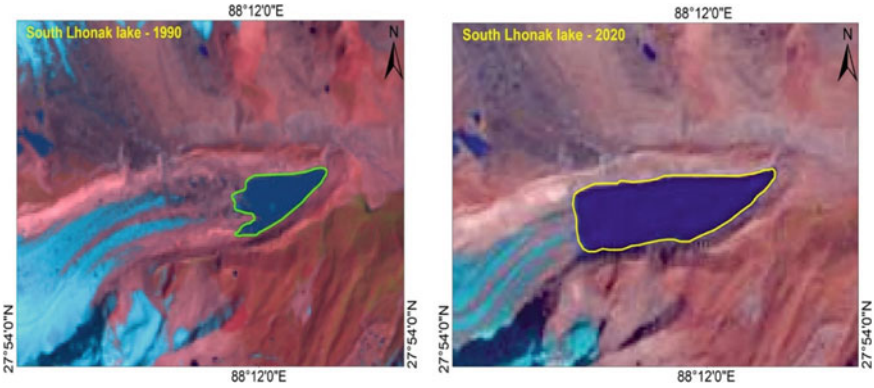

Fig. 6.3 Images showing growth of glacial lake area from 1990 to 2020

was accomplished by creating a vector layer of the streamline and flow paths along the stream at a distance of 1 km. The created geometric layers were imported into HEC-RAS for unsteady flow simulation. The other input data needed for GLOF modeling is flow data which requires upstream and downstream boundary conditions. The dam breach hydrograph is typically used for upstream boundary conditions and downstream boundary conditions considered as a channel bed slope. In this study, the glacial lake has been characterized as a dam failure structure with a certain crest length and elevation above the invert level. Its breach dimensions were specified as a simulation time series and considered the corresponding lake was taken into account. An inline structure known as the Latero-frontal moraine that is entered at the lower elevation of the lake. The failure catastrophe is modeled by breaching the inline structure before performing a dam break analysis. For the upper boundary, the glacial lake was considered a reservoir in the model by its elevation-storage relationship. The elevation-storage volume is generated based on the total volume and maximum depth obtained from the Huggel formulas. SRTM DEM has been used to generate a TIN terrain model for 1-D hydrodynamic modeling. From the terrain, the minimum elevation of the lake was obtained. The storage capacity at a minimum elevation of the lake is zero, and at maximum elevation, the total volume of the lake is obtained. Based on these two parameters, the elevation-storage capacity for the lake has been generated. These parameters are the inputs required by the empirical equations that estimate the peak outflow and failure time of the moraine dam breach event. The Froehlich model requires fewer input parameters for dam break analysis to estimate peak breach outflow hydrography.

In this study, unsteady flow data analysis was performed for calculating flood inundation water depths, flow velocity, and flood peak discharge at various sections downstream of the river flow.

6.3.2 Hazard Assessment of South Lhonak Lake

Glacial Lake volume releases a large amount of water and debris-covered involved in a GLOF. There is no assessment available to estimate glacial lakes volume in high altitude rugged terrain in the Himalayan region. However, Huggel et al. (2002, 2004) provided an empirical equation for calculating glacial lake volume in the Swiss Alps region. Due to unavailable bathymetric data of potentially vulnerable glacial lakes, they develop an empirical relationship based on the area to estimate the volume of glacial lakes. There are several empirical relationships, but the equation developed by Huggel is most extensively applied in earlier GLOF hazard studies where bathymetric surveying data were not available. The volume of the lake in this study was estimated by Huggel et al.'s (2002) equation:

$$V = 0.104\, A^{1.42} \tag{6.1}$$

where V is the volume of the glacial lake (m^3) and A is the lake area (m^2). Using Eq. 6.1, the lake's volume was estimated to be 54.96×10^6 m^3.

In any dam breach event, estimation of dam breach characteristics is essential to predict the breach outflow hydrograph. This study employs the 1 HD modeling to evaluate the lake outburst hydrograph for the GLOF simulation. GLOF occurs when glacial meltwater cannot freely flow downward, resulting in new glacial lakes. These water bodies are trapped by the natural dam made by loose glacial moraine called moraine dam. These moraine dams cannot hold a large volume of water due to the water's pressure on the upstream face of dam that exceeds the stabilizing forces like soil shear and cohesion, resulting in overtopping failure of the moraine dam. The main breach characteristics that are required as an input of dam breach parameters such as breach width and breach formation time have been estimated by employing the empirical equations proposed by Froehlich:

$$B_w = 0.180 K_o (V_w)^{0.32} (h_b)^{0.19} \tag{6.2}$$

$$T_f = 0.002 (V_w)^{0.53} (h_b)^{0.9} \tag{6.3}$$

where B_w and V_w in Eqs. 6.2 and 6.3 are the breach width (m) and lake volume (m^3), h_b and T_f is the height of breach (m) and breach formation time (h) respectively. Here, the lake volume calculated using Eq. (6.1) shows the breach width (B_w) as a function of the volume of the reservoir (V_w) and height of breach (h_b). Similarly, Eq. (6.3) determines the breach formation time (T_f) based on the same parameters.

The present study, developed various dam breach scenarios based on varying breach width and breach formation time for producing peak discharge from glacial lakes to evaluate a potential GLOF event. The failure mechanism as an overtopping is considered in breach scenarios.

6.4 Results and Discussion

6.4.1 Growth of Glacial Lake

Majority of the glacial lakes in the high mountainous himalayan region are in contact with mother glaciers but due to constantly increasing of hydraulic pressure on unconsolidated and loose moraine material forming the dam like structure surrounding the lakes, that is considered as an important factor leading to a GLOF event. According to the previous study carried out by ICIMOD (2011), a total of 1104 glacial lakes have been reported in the Sikkim Himalayas, compared to 266 glacial lakes in 2004 having an area > 0.01 km^2. Based on the satellite imagery, it has been observed that South Lhonak lake in the Teesta Basin of Sikkim has shown discernible increase in the last 30 years (Sharma et al. 2018; Aggarwal et al. 2017). It has been identified as

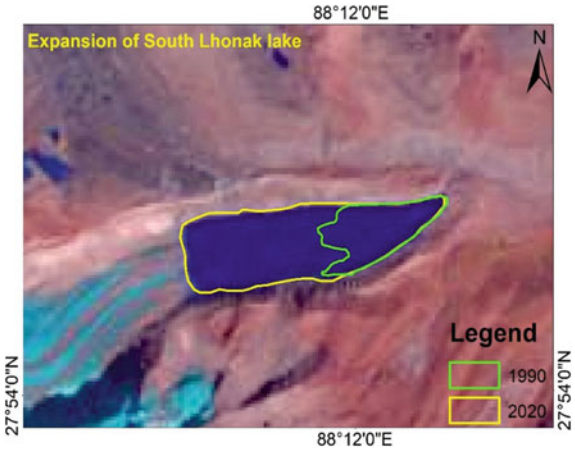

Fig. 6.4 Glacial Lake areal expansion in three decadal period

Table 6.2 Glacial lake area changes

Year	Area (km^2)
1990	0.48
2020	1.39

one of the most dangerous lakes with a high risk of outburst (Raj et al. 2013; Worni et al. 2014). The lake's area increased from 0.48 km^2 in 1990 to 1.39 km^2 in 2020. The expansion of the glacial lake area is shown in Fig. 6.4. The change in lake area from 1990 to 2020 is given in Table 6.2.

6.4.2 Assessment and Simulation of GLOF

GLOF simulation has been carried out for the South Lhonak lake in the Teesta basin, with a maximum lake area 1.39 km^2 in October 2020. The altitude of the lake is 5205 m. The volume and depth of the lake are calculated using Eq. 6.1, and it comes out to be 54.96×10^6 m^3 and 39.54 m. A dam-break hydrodynamic simulation model was performed to assess a GLOF occurrence in the glacial lake.

As seen from Landsat imagery, it was found that this unstable moraine-dammed glacial lake is positioned at the snout of the mother glacier known as South Lhonak glacier, which has been retreating rapidly in the past few decades that reflect glacial lake has been expanding. Therefore, it has been chosen for the GLOF study. The flood routing from the glacial lake to the downstream end (length 20 km) has been characterized in the model by varying numbers of river cross-sections derived from SRTM DEM that has been given as an input in the HEC-RAS model shown in Fig. 6.5. Wang et al. (2012) examined impact of DEM data on GLOF modeling in Tibet and concluded that, whereas flood inundation extent and flow depths are affected

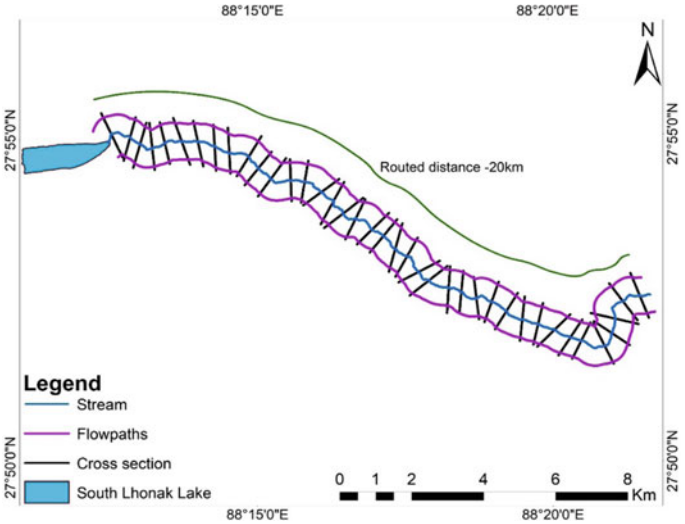

Fig. 6.5 River Network model setup for GLOF study of South Lhonak glacial Lake

by the adapted DEM, the level of deviation has little significance when predicting peak-discharge floods. Figure 6.6 depicts the cross-sectional profiles plotted over the streamflow across the downstream section.

The hydrodynamic model is intimately connected to flow discharge and water level. The South Lhonak moraine-breach was simulated to estimate the breach hydrograph, further routed along the downstream channel from the lake. The resulting GLOF wave due to breach of the frontal moraine dam has been propagated in the downstream area is simulated using the 1-D unsteady flow HEC-RAS model. The breach simulations have been executed to analyze the unsteady flow hydrodynamic model to input the dam-breach parameters (breach width and breach formation time). Therefore, to estimate the breach hydrograph, possible varying breach width (B_w) and breach failure time (T_f) of the lake was considered for different worst-case scenarios, in which breach widths of 30, 40, and 60 m and breach formation time has considered being as 40, 30 and 20 min, respectively.

Hydrodynamic modeling applied in the Himalayan region is generally associated with fraught and uncertainty because there is lack of information about the various properties of moraine and breach formation process. In GLOF event, numerous empirical relationship has been established to evaluate peak flows (Costa and Schuster 1988; Huggel et al. 2002). The initial flow hydrograph is a function of two important parameters i.e., breach width (B_w) and the breach formation period (T_f). B_w and T_f are dependent upon many factors, such as geometry, internal structure of the moraine dam, and the type and magnitude of the traumatic event (Kougkoulos et al. 2018).

Figure 6.7a–c show that nine scenarios of 1-D breach hydrograph were performed with varying breach width (B_w) and breach formation time (T_f). The results of these

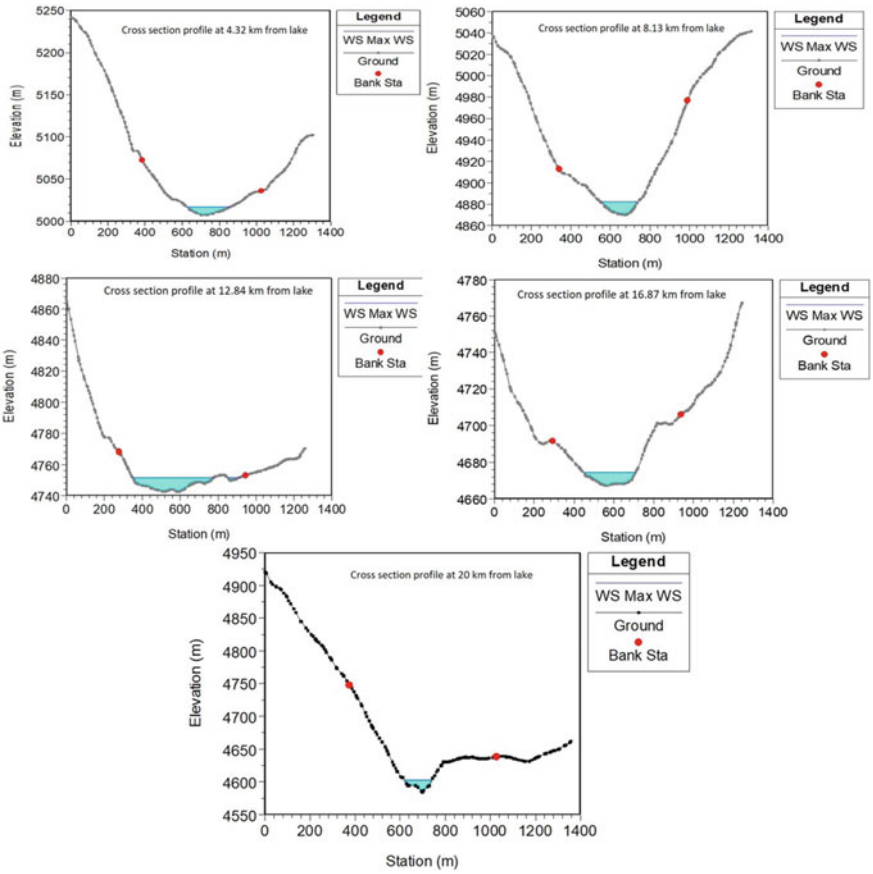

Fig. 6.6 Cross-sectional profiles with water surface levels at various sections across the river

scenarios are given in Table 6.3. We have considered nine scenarios with varied B_w = 60 m, B_w = 40 m, and B_w = 30 m with a constant T_f. These different scenarios were evaluated, and breach hydrograph was estimated.

It is inferred from this study, among the nine different breach scenarios, GLOF breach hydrograph for 40 m B_w and 30 min T_f, produced peak discharge of 14,658.6 m^3/s has been considered as an input for upstream boundary condition, generates flood routing at different sites along the river flow path, which gives different peak flood hydrographs and other significant flood wave parameters like flow depth, flow velocity, and flood peak arrival time.

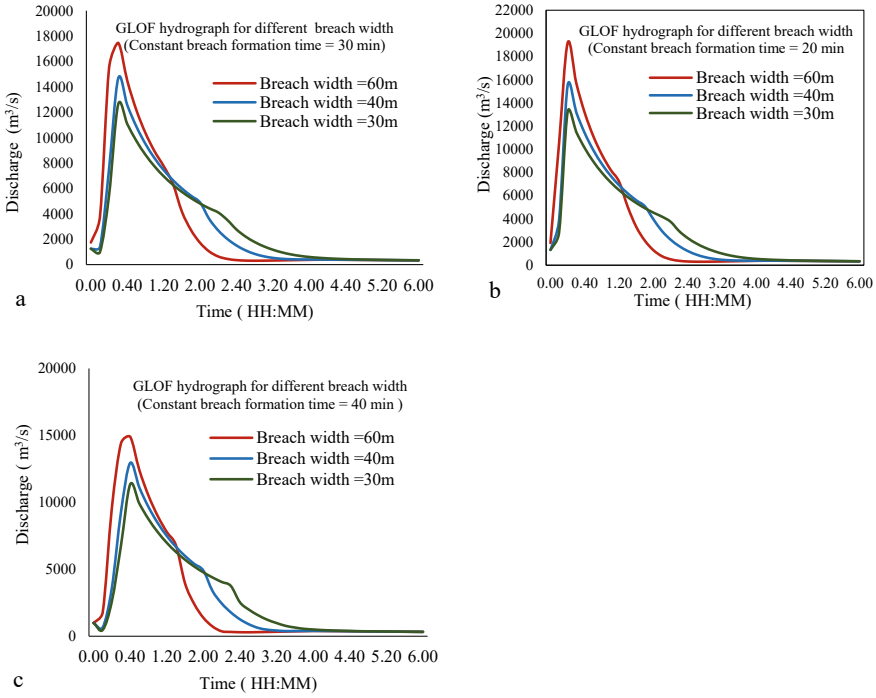

Fig. 6.7 **a, b, c** Showing peak discharge obtained for varied B_w keeping the T_f constant

6.4.3 Assessment of GLOF Hydrograph at Downstream Sites

The assessment of the different magnitude of flood peak hydrographs at various cross-sections across the river is shown in Figs. 6.8, 6.9, 6.10, 6.11 and 6.12. In this study, attenuated flood peak hydrographs have been evaluated at five different locations at a distance of 4.32, 8.13, 12.84, 16.87, and 20 km downstream from the lake. The estimated flood peak was 14,658.60 m^3/s at the GLOF site, and the same got mitigated to 11,978.77 m^3/s at the downstream outlet, respectively. The flood peak arrival time from lake to the outlet at a distance of 20 km is about 1 h 20 min. This reflects that the downstream river reach is relatively wide with a gentle slope compared to that narrow valley of upstream glacial area. As a result, flood water spreads across a floodplain resulting in a gradual decrease of peak discharge as it proceeds downstream from the lake, as shown in Table 6.4. In 2013, one of the largest GLOF events in the Chorabari lake in Kedarnath region of Uttarakhand, which is a part of the North-Western Himalayas was triggered by hydraulic pressure caused by massive precipitation and accelerated dam failure, resulting in devastation in a stretch of 18 km downstream along the river, with 6000 lives lost and a substantial quantity of property damage (NRSC 2016).

Table 6.3 Breach parameters like breach width (m) and breach formation time (minutes) for the different GLOF scenarios; Simulated peak flood (m^3/s) of the breach hydrographs

Failure mode- overtopping									
	Scenario 1	Scenario 2	Scenario 3	Scenario 4	Scenario 5	Scenario 6	Scenario 7	Scenario 8	Scenario 9
Breach width (m)	60	40	30	60	40	30	60	40	30
Breach time (minutes)	20	20	20	30	30	30	40	40	40
Peak discharge (m^3/s)	19,178.73	15,512.6	13,235.73	17,464.62	14,658.6	12,619.42	14,403.21	12,938.85	11,333.93

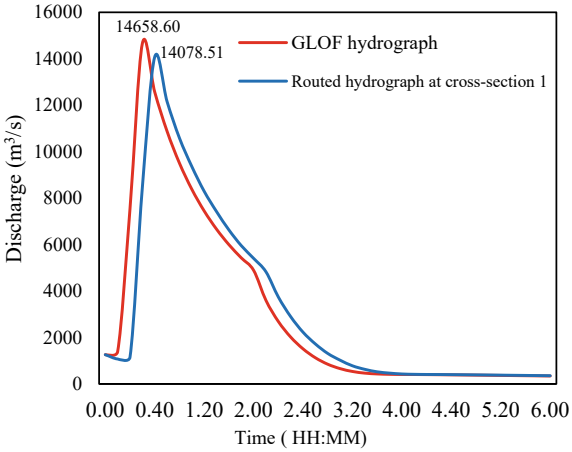

Fig. 6.8 GLOF hydrograph at site 1

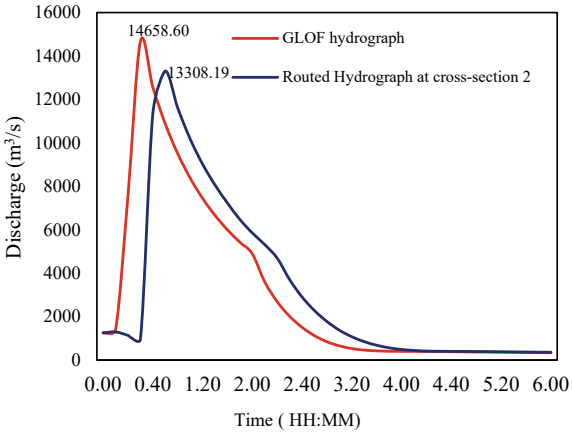

Fig. 6.9 GLOF hydrograph at site 2

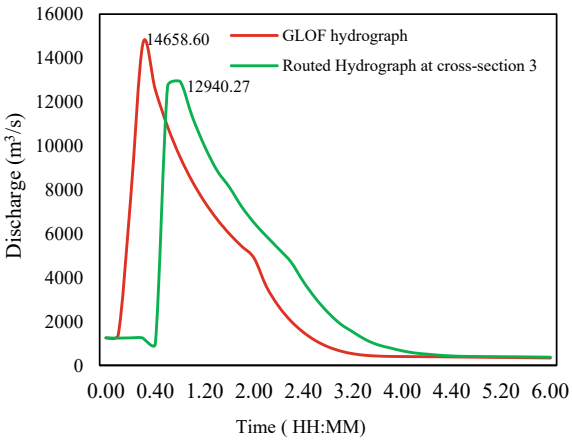

Fig. 6.10 GLOF hydrograph at site 3

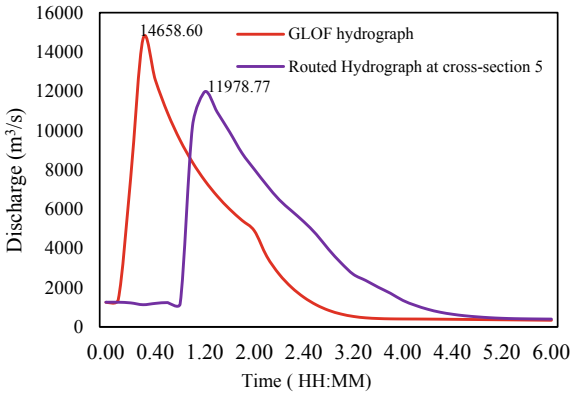

Fig. 6.11 GLOF hydrograph at site 4

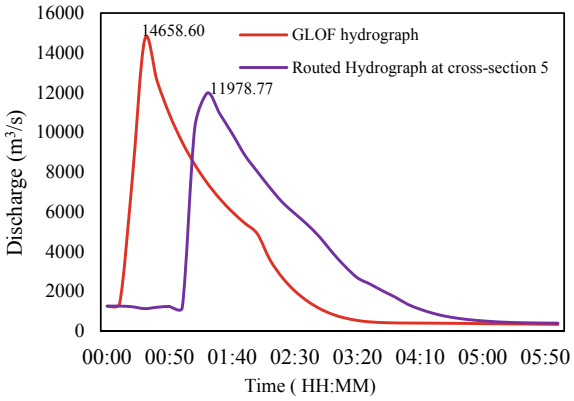

Fig. 6.12 GLOF hydrograph at site 5

High intensity of rainfall or snowmelt could cause a rise in the water level of glacial lakes, resulting in lake overflow or moraine collapse (Emmer and& Cochachin 2013). However, temperature patterns and geological characteristics of lake type may provide useful information about external trigger causes of GLOF condition. In the Himalayan region, it has been found that, at least one GLOF event occurs every 3–10 years (Bajracharya et al. 2008), but with increasing temperatures and more climate variability, the frequency of GLOF events is predicted to rise in the coming decades. A hydrodynamic model has been performed to compute peak discharges and flood heights and simulate GLOF repercussions on the downstream section.

Table 6.4 Routed Peak flood and time of peak at different downstream locations along the flow path due to GLOF event

Sites	Distance from Lake (km)	Peak flood (m^3/s)	Volume (1000 m^3)	Channel elevation (m)	Water surface elevation (m)	Depth (m)	Velocity (m/s)	Flood peak arrival time (HH:MM)
Cross section 1	4.32	14,078.51	77,748.76	5007.5	5017.28	9.78	9.91	00:40
Cross section 2	8.13	13,308.19	78,856.02	4870.09	4882.15	12.06	9.26	00:50
Cross section 3	12.84	12,940.27	81,020.58	4730.94	4738.74	7.8	7.09	01:00
Cross section 4	16.87	12,470.94	82,738.52	4644.54	4657.26	12.72	2.89	01:10
Cross section 5	20	11,978.77	82,960.86	4584.57	4603.43	18.86	9.62	01:20

6.4.4 Inundation Simulation

In the present study, one-dimensional unsteady flow routing has been performed from the lake up to the route of 20 km downstream. The flood hydrograph at just downstream of the lake and different sites across the river are shown from Figs. 6.8, 6.9, 6.10, 6.11 and 6.12. The total flood peak at the GLOF site from the lake is 14658.62 m^3/s, and the flood peak at the outlet site is 11978.77 m3/s, and flood peak arrival time from the lake site to the outlet at a distance of 20 km is 01 h 20 min, respectively. The maximum flow depth and flow velocity along the flow path are 22.42 m and 11.29 m/s. Figures 6.13 and 6.14 show the spatial inundation map of flow depth and flow velocity along the river flow path from the South Lhonak lake to the routing stretch up to 20 km. The estimated flood depth and flow velocity in the downstream section varies depending upon the morphology of the river channel.

The figures and tabular data were generated using the finding of one-dimensional flow analysis. They include profiles of the expected peak flood levels and an estimation of the time from the commencement of the breach to the moment the location begins. They have profiles of the predicted peak flood levels and an estimation of the time from the commencement of the breach to the moment the location begins to be inundated. More hazard reference values such as flow depth, flow velocity, water surface elevation, and flood peak arrival time are shown in Table 6.4 for the downstream locations. The flood had created deep canyons, wiped the vegetation in riverbed, rocks, deposited debris and sediments along the river's course (Byers et al. 2019).

The analysis shows that the flood routing varies gradually decreases along with the downstream of lakes. Inundation maps shown in the figures illustrate the areas subject to flooding from a GLOF.

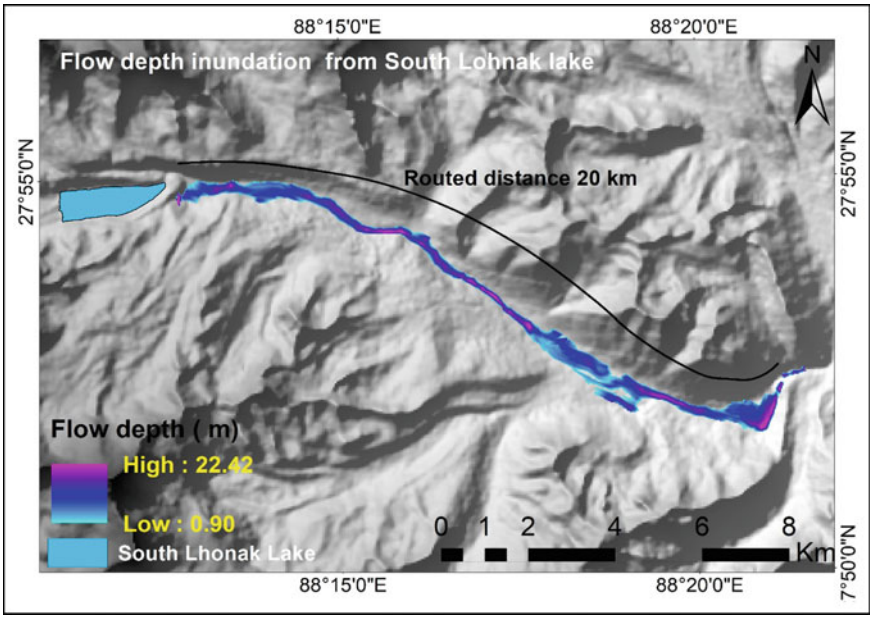

Fig. 6.13 Flow depth inundation map showing from glacial lake to the downstream valley

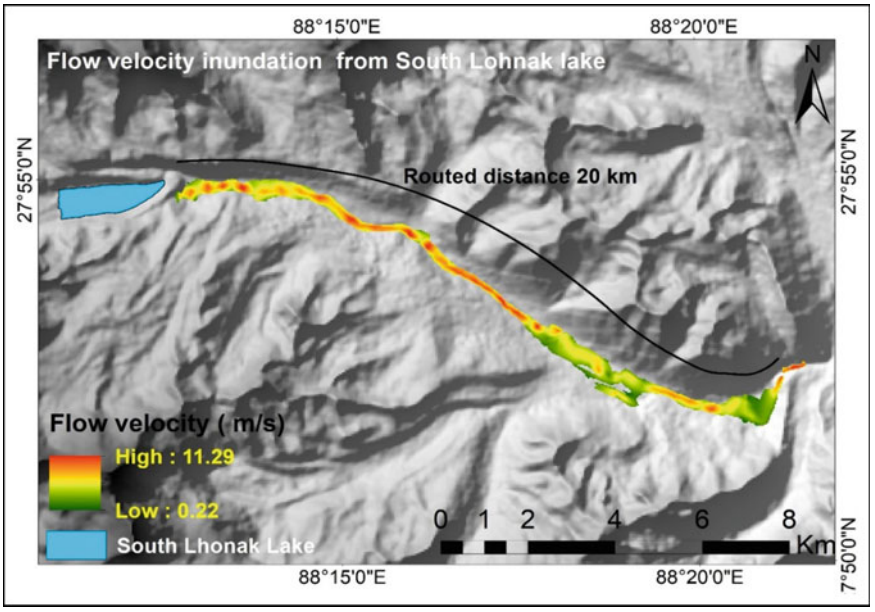

Fig. 6.14 Flow velocity inundation map showing from glacial lake to the downstream valley

6.5 Conclusions

The current study was conducted with the GLOF condition of the South Lhonak lake in the Teesta Basin, Sikkim. The glacial lake area expanded by approximately three times within the past 30 years. The lake was 0.48 km^2 in 1990 and 1.39 km^2 in 2020. In this study, cross-section details from the DGPS survey were not accessible due to rugged terrain with high altitudes. Hence, HEC-GeoRAS was used for automatic extraction of river cross-sections from an SRTM DEM, and these cross-sections were modified before being used in an HEC-RAS 1D unsteady flow hydraulic model. The breach of moraine dams leads to the sudden discharge of a huge volume of glacial lake water known as GLOF. For the simulation of GLOF outburst and flood propagation scenarios, the current methodology used dam-break and hydrodynamic models. The dam breach hydrograph was used as an input parameter in HEC-RAS to simulate the GLOF propagation in the downstream section. The estimated flood peak was 14,658.60 m^3/s at the GLOF site, and the same got mitigated to 11,978.77 m^3/s at the downstream end. The GLOF hazard findings are promising for prospective hydrodynamic modeling studies in India, particularly in the glacierized basins of himalayas. HEC-RAS, a one-dimensional hydrodynamic model, would be very beneficial for GLOF modeling or flood control studies, as well as the design of hydraulic engineering structures. One of the key actions identified for the country is the monitoring of GLOF and disaster risk mitigation (Ministry of Environment 2010). Monitoring and assessment is further suggested for medium and low outburst-prone lakes, However, it remains a major challenge to enhance and intensify regional collaboration and coordination in order to manage, preserve, and protect the diverse and fragile ecosystems (SAARC 2014). The study's outcomes will aid in formulating risk management plans and risk reduction strategies in the event of a GLOF hazard (Clague and Evans 2000, Haritashya et al. 2018, Kaser et al. 2006).

Acknowledgements I am thankful for the Department of Water Resources Development and Management (WRD&M), IIT Roorkee for providing facilities to carry out this research work.

References

Ageta Y, Iwata S, Yabuki H, Naito N, Sakai A, Narama C, Karma T (2000) Expansion of glacier lakes in recent decades in the Bhutan Himalayas. In: Debris-covered glaciers, proceedings of a workshop held in Seattle, Washington, USA, Sept 2000. International Association of Hydrological Sciences, Wallingford, pp 165–175

Aggarwal A, Jain SK, Lohani AK, Jain N (2016) Glacial lake outburst flood risk assessment using combined approaches of remote sensing, GIS and dam break modelling. Geomat Nat Haz Risk 7(1):18–36

Aggarwal S, Rai SC, Thakur PK, Emmer A (2017) Inventory and recently increasing GLOF susceptibility of glacial lakes in Sikkim, Eastern Himalaya. Geomorphology 295:39–54

Ahmed R, Wani GF, Ahmad ST, Sahana M, Singh H, Ahmed P (2021) A review of glacial lake expansion and associated glacial lake outburst floods in the Himalayan Region. Earth Syst Environ, pp 1–14

Bajracharya SR, Mool PK, Shrestha BR (2007) Impact of climate change on Himalayan glaciers and glacial lakes: case studies on GLOF and associated hazards in Nepal and Bhutan. International Centre for Integrated Mountain Development (ICIMOD)

Bajracharya SR, Mool PK, Shrestha BR (2008) Global climate change and melting of Himalayan glaciers. In: Ranade PS (ed) Melting glaciers and rising sea levels: impacts and implications. Hyderabad, Icfai University Press

Benn D, Wiseman S, Warren C (2000) Rapid growth of a supraglacial lake, Ngozumpa Glacier, Khumbu Himal Nepal. Debris-Covered Glaciers. IAHS 264:177–186

Bhambri R, Bolch T, Kawishwar P, Dobhal DP, Srivastava D, Pratap B (2012) Heterogeneity in Glacier response from 1973 to 2011 in the Shyok valley, Karakoram, India. Cryosphere Discuss 6:3049–3078

Byers AC, Rounce DR, Shugar DH, Lala JM, Byers EA, Regmi D (2019) A rockfall-induced glacial lake outburst flood, Upper Barun Valley Nepal. Landslides 16(3):533–549

Clague JJ, Evans SG (2000) A review of catastrophic drainage of moraine-dammed lakes in British Columbia. Quatern Sci Rev 19(17–18):1763–1783

Costa JE, Schuster RL (1988) The formation and failure of natural dams. Geol Soc Am Bull 100 (7):1054–1068

Emmer A (2017) Geomorphologically effective floods from moraine-dammed lakes in the Cordillera Blanca, Peru. Quatern Sci Rev 177:220–234

Emmer A, Cochachin A (2013) The causes and mechanisms of moraine-dammed lake failures in the cordillera blanca, North American Cordillera, and Himalayas. Acta Univ Carolinae Geogr 48:5–15

Gardelle J, Berthier E, Arnaud Y, Kääb A (2013) Region-wide glacier mass balances over the Pamir-Karakoram-Himalaya during 1999–2011. Cryosphere 7(4):1263–1286

Haritashya UK, Kargel JS, Shugar DH, Leonard GJ, Strattman K, Watson CS, Shean D, Harrison S, Mandli KT, Regmi D (2018) Evolution and controls of large glacial lakes in the Nepal Himalaya. Remote Sens 10(5):798

Huggel C, Kääb A, Haeberli W, Teysseire P, Paul F (2002) Remote sensing based assessment of hazards from glacier lake outbursts: a case study in the Swiss Alps. Can Geotech J 39:316–330

Huggel C, Haeberli W, Kääb A, Bieri D, Richardson S (2004) An assessment procedure for glacial hazards in the Swiss Alps. Can Geotech J 41(6):1068–1083

ICIMOD (2011) Glacial lakes and glacial lake outburst floods in Nepal. Kathmandu, Nepal, Kathmandu

Jain SK, Lohani AK, Singh RD, Chaudhary A, Thakural L (2012) Glacial lakes and glacial lake outburst flood in a Himalayan basin using remote sensing and GIS. Nat Hazards 62(3):887–899

Kaser G, Cogley JG, Dyurgerov MB, Meier MF, Ohmura A (2006) Mass balance of glaciers and ice caps: cConsensus estimates for 1961–2004. Geophys Res Lett 33(19)

Kougkoulos I, Cook SJ, Edwards LA, Clarke LJ, Symeonakis E, Dortch JM, Nesbitt K (2018) Modelling glacial lake outburst flood impacts in the Bolivian Andes. Nat Hazards 94(3):1415–1438

Mergili M, Vilca O, Emmer A, Frey H, Huggel C (2021) The glacial lake outburst flood process chain at Lake Salkantaycocha (Cordillera Vilcabamba, Peru). Landslides 18(6):2211–2223

Ministry of Environment (2010) National adaptation programme of action to climate change. Government of Nepal, Ministry of Environment, Kathmandu

Mool PK, Bajracharya SR, Shrestha B, Joshi SP, Roohi R, Ashraf A, Naz R, Hussain SA, Chaudhry MH (2003) Inventory of Glaciers, Glacial Lakes and the Identification of Potential Glacial Lake Outburst Floods (GLOFs) Affected by Global Warming in the Mountains of Himalayan Region: Tista Basin, Sikkim Himalaya, India. Unpublished project report, with database on CD-ROM, prepared for APN and ICIMOD, Kathmandu

Raj BK, Kumar VK, Remya SN (2013) Remote sensing-based inventory of glacial lakes in Sikkim Himalaya: semi-automated approach using satellite data. Geomatics Nat Haz Risk 4(3):241–253
Reynolds JM (2000) On the formation of supraglacial lakes on debris-covered glaciers. IAHS Publ 264:153–161
Richardson SD, Reynolds JM (2000) An overview of glacial hazards in the Himalayas. Quatern Int 65:31–47
SAARC (2014) Area of cooperation: environment, climate change and natural disasters. Maldives
Sakai A (2012) Glacial lakes in the Himalayas: a review on formation and expansion processes. Glob Environ Res 16(2011):23–30
Sattar A, Goswami A, Kulkarni AV (2019) Application of 1D and 2D hydrodynamic modeling to study glacial lake outburst flood (GLOF) and its impact on a hydropower station in Central Himalaya. Nat Hazards 97(2):535–553
Sharma RK, Pradhan P, Sharma NP, Shrestha DG (2018) Remote sensing and in situ-based assessment of rapidly growing South Lhonak glacial lake in eastern Himalaya, India. Natural Hazards, pp 1–17
Thakur PK, Aggarwal SP, Dhote P, Nikam BR, Garg V, Bhatt CM, Chouksey A, Jha A (2019) Hydrometeorological hazards mapping, monitoring and modelling. In: Remote sensing of Northwest Himalayan ecosystems. Springer, Singapore, pp 139–169
Thakur PK, Garg V, Kalura P, Agrawal B, Sharma V, Mohapatra M, Kalia M, Aggarwal SP, Calmant S, Ghosh S, Dhote PR, Sharma R, Chauhan, P (2021) Water level status of Indian reservoirs: aA synoptic view from altimeter observations. Adv Space Res 68(2):619–640
Wang W, Yang X, Yao T (2012) Evaluation of ASTER GDEM and SRTM and their suitability in hydraulic modelling of a glacial lake outburst flood in southeast Tibet. Hydrol Process 26(2):213–225
Westoby MJ, Glasser NF, Brasington J, Hambrey MJ, Quincey DJ, Reynolds JM (2014) Modelling outburst floods from moraine-dammed glacial lakes. Earth Sci Rev 134:137–159
Worni R, Huggel C, Stoffel M (2013) Glacial lakes in the Indian Himalayas—from an area-wide glacial lake inventory to on-site and modeling based risk assessment of critical glacial lakes. Sci Total Environ 468:S71–S84
Worni R, Huggel C, Clague JJ, Schaub Y, Stoffel M (2014) Coupling glacial lake impact, dam breach, and flood processes: a modeling perspective. Geomorphology 224:161–176
Zhang G, Yao T, Xie H, Wang W, Yang W (2015) An inventory of glacial lakes in the Third Pole region and their changes in response to global warming. Glob Planet Change 131:148–157

Chapter 7
Investigating Soil Erosion Status of Baitarani River Basin Using RUSLE and Geospatial Techniques

Dhananjay Paswan Das and Uday Pratap Singh Bhadoriya

Abstract Soil erosion is a severe environmental threat accelerated due to anthropogenic activities such as agricultural and industrial intensification. Soil erosion status information of a watershed or basin using soil loss models can be helpful for planning and conservation measures. The present study used Revised Universal Soil Loss Equation (RUSLE) along with the geospatial techniques to estimate the soil loss in the Baitarani basin located in the eastern India. The Baitarani basin, having a drainage area of 14,218 km^2. The parameters of RUSLE model for Baitarani River basin were estimated using IMD rainfall data and remote sensing data (LULC, soil map, DEM). Results highlight the areas which require prioritization whilst implementing the soil conservation and management measures to reduce the soil erosion in the Baitarani Basin. The estimated thematic inputs vary spatially across the basin. The computed annual soil erosion of BRB varies from 0.02 to 206.57 t ha^{-1}/yr. Analysis showed that 94% of the BRB area have soil loss less 5 t ha^{-1}/yr i.e., slight erosion whereas, only 0.1% area is under very severe soil loss (>80t ha^{-1}/yr) category. Also, it is evident from the results that 1.2%, 0.33%, and 0.06% area of BRB is under high, very high, and severe erosion respectively. The findings of this study may help the planners to focus on the erosion prone regions whilst practically implementing soil conservation practices to check regional soil erosion.

Keywords GIS · RUSLE · Remote sensing · Soil erosion

D. P. Das
Department of Water Resource Development & Management, Indian Institute of Technology Roorkee, Roorkee, Uttarakhand 247667, India

U. P. S. Bhadoriya (✉)
Agricultural and Food Engineering Department, Indian Institute of Technology Kharagpur, Kharagpur, West Bengal 721302, India
e-mail: udaybhadoriya@iitkgp.ac.in

C. S. Jha et al. (eds.), *Geospatial Technologies for Resources Planning and Management*, Water Science and Technology Library 115,
https://doi.org/10.1007/978-3-030-98981-1_7

7.1 Introduction

Soil erosion is a severe environmental threat, caused by water or wind agents, leading to loss of top surface soil enriched with useful nutrients and organic matter. Further, exposure of more impermeable subsoil layer, thereafter, causes increment in runoff and subsequently, reduces the water amount accessible to crops/plants. Soil erosion and its consequent, land degradation poses significant problems worldwide, thus, various studies are performed to model the soil erosion process (Dabral et al. 2008; Eniyew et al. 2021; Fayas et al. 2019; Ganasri and Ramesh 2016; Masroor et al. 2021). In mainland India, almost 45% (130 million hectares) of area comes under degraded land affected by heavy soil erosion, desert, water logging, and wastelands (Kothyari 1996). Therefore, soil erosion mapping of a watershed or basin in India is of utmost importance.

Scientific management plans with the help of ground soil surveys can assess the magnitude and extent of soil erosion hazards on regional levels (Kothyari et al. 1994), however, these are costly and tedious. On the other hand, modelling erosion process is a readily available method to estimate soil erosion or sediment yield by using various observed or satellite derived inputs. Further, soil erosion simulation models are used to analyse and manage land and water resources at basin scale. Universal Soil Loss Equation (USLE) model, developed by Wischmeier and Smith in 1965 is the most widely known empirical model for assessing the sheet and rill erosion. USLE was primarily developed for estimating soil erosion in agricultural land with gentle slope. However, modifications or corrections are performed in USLE with time, such as modified (MUSLE) and revised (RUSLE) versions (Wischmeier and Smith 1978; Remortel Van et al. 2001) are still being applied in various regions for soil loss estimation. RUSLE model can predict the soil erosion potential based on the consistent spatial resolution to effectively identify the soil loss in space and time over a large area. After that GIS may be used to extract and further assess the locations to determine the role of individual drivers contributing to the soil erosion potential. However, uncertainty in RUSLE prediction arises due to the multiple scale and sources of the available inputs. Pandey et al. 2021a, b analysed ASTER, SRTM, and Cartosat DEMs with various grid resolutions and found that the Cartosat DEM with a 200 m grid was the best combination to estimate soil erosion.

Soil erosion models are classified into three categories (1) empirical (2) conceptual (3) physically-based (Jha and Paudel 2010). Different soil erosion models represent the physical process with varying level of complexity. USLE and its modifications come under empirical/conceptual model group. Water erosion prediction project (WEPP) model is a process-based, continuous simulation erosion prediction model (Laflen et al. 1991; Pandey et al. 2009). SWAT (Soil water assessment tool) is another widely used model for hydrological and sediment modelling (Arnold et al. 1993; Pandey and Palmate 2019; Pandey et al. 2021a, b). MIKE SHE (Systeme Hydrologique Europeen) is, further, a comprehensive distributed and physically-based soil erosion model. Some other models such as AGNPS (agricultural non-point

source pollution; Young et al. 1989), ANSWERS (areal non-point source watershed environment response simulation; Beasley et al. 1980) are also used by many researchers.

The combined use of soil erosion models, ground observed data and remote sensing (RS) data with the geospatial techniques and geographic information system (GIS) is of the interest future studies (Biddoccu et al. 2020; Boussadia-Omari et al. 2021; Eniyew et al. 2021; Fayas et al. 2019; Ganasri and Ramesh 2016; Gitas et al. 2009; Masroor et al. 2021). Thus, keeping the above-mentioned conditions in view, the study attempts to use the potential of geospatial techniques along with Revised Universal Soil Loss Equation (RUSLE) to estimate soil loss across the Baitarani River Basin located in the eastern India.

7.2 Study Area

The Baitarani River, having a total catchment area of 14,218 km^2, is an important peninsular river flowing the eastern part of India and finally, joining the Bay of Bengal. Major portion of its catchment area lies in the state of Orissa and a small region of the upper reach falls in Jharkhand. The Baitarani River basin (BRB) lies between longitudes 85° 10′ E–87° 03′ E and latitudes 20° 35′ N–22° 15′ N (Fig. 7.1). Gonasika/Guptaganga (refers to as cow nose shaped) hills is the origin of the Baitarani River. The river is flashy in nature and flood occurs regularly causing loss of life and livelihood to the inhabitants of the nearby area the river. It has a total length of 355 km, with a considerable fall in elevation from 367 m at Champua to 28 m at Anandpur. BRB is adjacent to the Brahmani basin on the South and West, the Subarnarekha basin on the North, the Burhabalang and the Bay of Bengal on the east. Daily air temperature in basin varies from 6 °C in winter and 48.5 °C in summer. Annual rainfall is 1187 mm and almost 80% of this rainfall is contributed by south-west monsoon.

7.3 Data Processing and Thematic Layers Generations

To prepare the thematic layers of the required model inputs various data were collected as shown in Table 7.1. The data were preprocessed by using GIS. Land use and land cover (LULC) of the basin have eight major classes as shown in Fig. 7.2. Tree cover class covers the maximum area (43.8%) whereas Herbaceous Wetland has minimum area (0.13%). The study area has three main soil texture classes i.e., Loam, Sandy Loam, and Sandy clay loam as shown in Fig. 7.3. Sandy clay loam occupies majority of the area (44.4%). Figure 7.4 presents the extent of spatial variation of average annual rainfall in the basin. The middle part of the basin shows higher annual

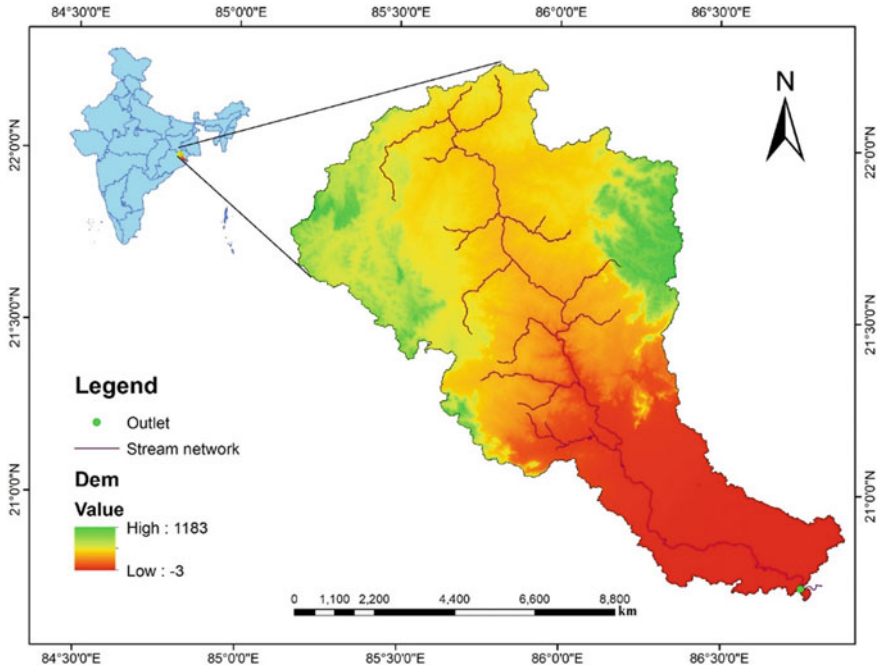

Fig. 7.1 Location of the study area along with the stream network and DEM

Table 7.1 Information about the data used in the study

Sl. No	Input data	Resolution	Source
1	SRTM DEM	30 m	USGS Earth explorer
2	Soil map	1 km * 1 km	FAO soil map
3	LANSAT 8 image	30 m	USGS Earth explorer
4	LULC map	10 m	https://esa-worldcover.org/en/data-access
5	Rainfall data	0.25 * 0.25°	India Meteorological Department (IMD)

rainfall as compared to other parts. Interpolation or resampling of thematic layers is carried out using 'Kriging' method. The slope of the study area mainly is below 4.49°, around 69% of area (Fig. 7.5).

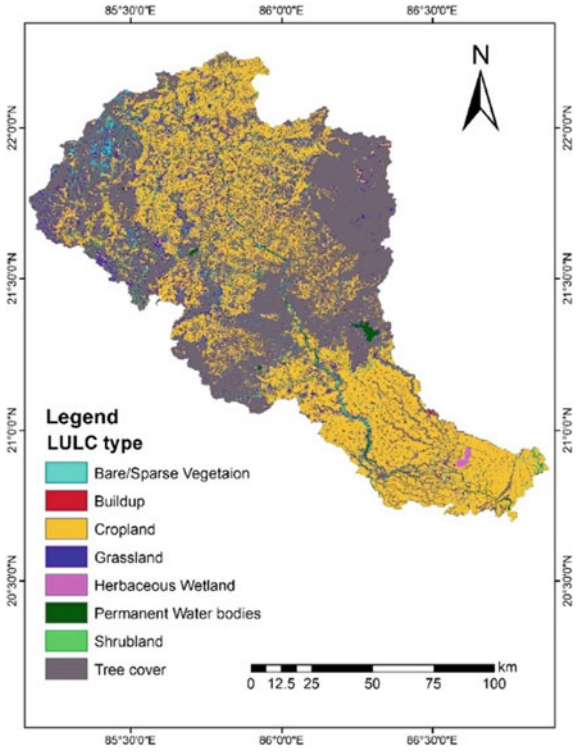

Fig. 7.2 Land use and land cover (LULC) of BRB

7.4 Methodology

7.4.1 Estimation of Average Annual Soil Loss

RUSLE (Wischmeier and Smith 1978), commonly used method to predict long-term soil erosion from a region under various crop and field management practices. The computed soil erosion only includes the sheet or inter-rill and rill erosion. RUSLE is a conceptual and empirical erosion prediction model which can be used at both regional and large scales. Here, the fundamental equation and variables of RUSLE are the same, however, there have been significant modifications in its factors. For this study, RUSLE is applied to estimate average annual soil loss. RUSLE parameters are extensively available through existing databases. In absence of such databases or to improve the results, these parameters can also be obtained by processing satellite images (Remote sensing) and DEM. Processing may include preparation of supervised or unsupervised LULC from satellite images, slope and aspect estimation from DEM. These thematic layers could be further processed or overlay to other RUSLE inputs easily in ArcGIS. The major limitation of this procedure is that it cannot model the routing process of sediments through the streams, thus, its applicability is

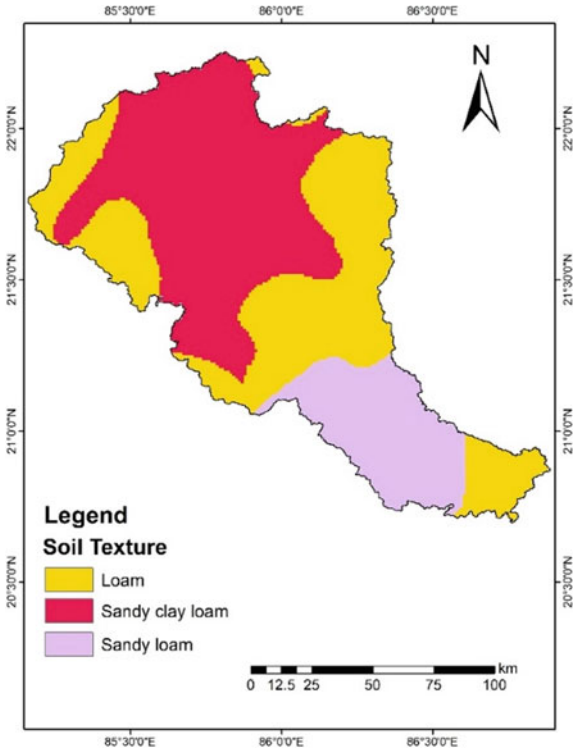

Fig. 7.3 Soil texture classes of BRB

restricted to small regions. Thus, applications of this model to larger watersheds are limited (Nearing et al. 2005). In this study, RUSLE is applied to the Baitarani River basin by using the ArcGIS 10.5 software representing the basin as square grids of 1 km × 1 km and thus, computing soil erosion for each cell. Numerically, RUSLE is written as follows.

$$A = R \times K \times L \times S \times C \times P \tag{7.1}$$

where A is estimated average annual soil loss per unit of area (units are relative to the units of K and time period of R-factor estimation; ton per hectare per year), R is rainfall-runoff erosivity factor (MJ mmha^{-1} h^{-1}) per year; K is soil erodibility factor (t ha^{-1} MJ mm^{-1}), L is slope length factor; S is slope steepness factor, C is cover management factor, P is conservation practice factor. C, P, and LS do not have units.

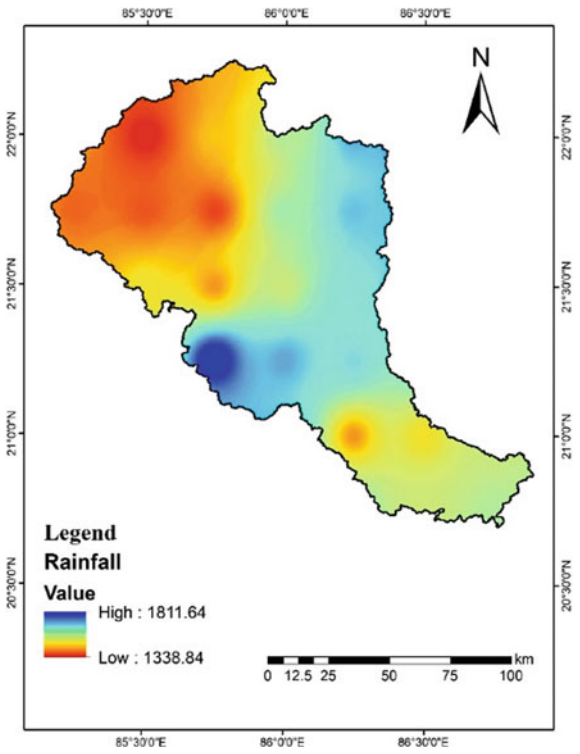

Fig. 7.4 Spatial variation of average annual rainfall in the BRB

7.4.2 Preparation of RUSLE Model Database

The methodology to carry out the analysis work in this study is shown in the Fig. 7.6. Here, all five input factors of RUSLE are estimated individually and thereafter, combined to estimate the spatial annual soil erosion status of BRB.

7.4.2.1 Rainfall Erosivity Factor (*R*)

Rainfall erosivity factor (*R*) corresponds to the potential of rainfall intensity on soil erosion. Long-term records of precipitation data are required for its calculation. R-factor represents or includes the effect of two most important characteristics of rainfall event viz. rainfall magnitude and maximum fall rate occurred during a defined time period. This also includes the impact of falling raindrops and produced runoff volume and rate. Often, rainfall intensity data, if available, is used to calculate the R-factor. Here, we used daily rainfall data of BRB from 2010 to 2020, converted to monthly scale, is used to calculate the *R*-factor by using Eq. (7.2).

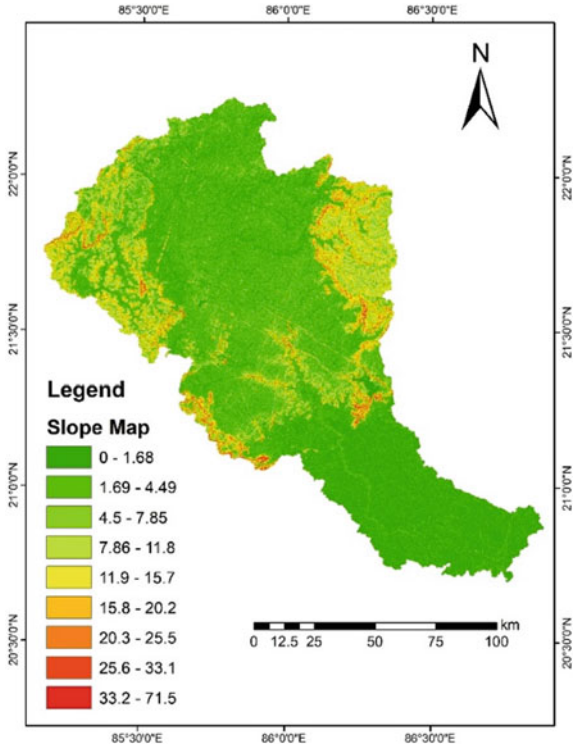

Fig. 7.5 Variation of slope of the BRB

$$R = \sum_{1}^{12} 1.735 * 10^{\left(1.5 \log_{10}\left(\frac{P_i}{P}\right) - 0.08188\right)} \tag{7.2}$$

where R is a rainfall erosivity factor in MJ mm ha^{-1} h^{-1} per year, P_i is monthly rainfall in mm, P is an annual rainfall in mm.

7.4.2.2 Soil Erodibility Factor (K)

Soil erodibility factor (K) represents the surface soil's erodibility potential through detachment and transportation, under the impact of rainfall and generated streamflow. K-factor is estimated based on the soil textures, physical, and chemical properties of the top soil layer. Thus, K values may be referred to as the rate of soil loss per rainfall-runoff erosivity (R) index.

Equation (7.3) can be used to calculate K-factor by using following properties of soil: soil texture, % silt plus very fine sand, % sand, % organic matter, soil structure, and permeability. Heavy soils, because of resistance to detachment, have low K-factor values. Sandy soils also have low K-factor but because of sediment transportation

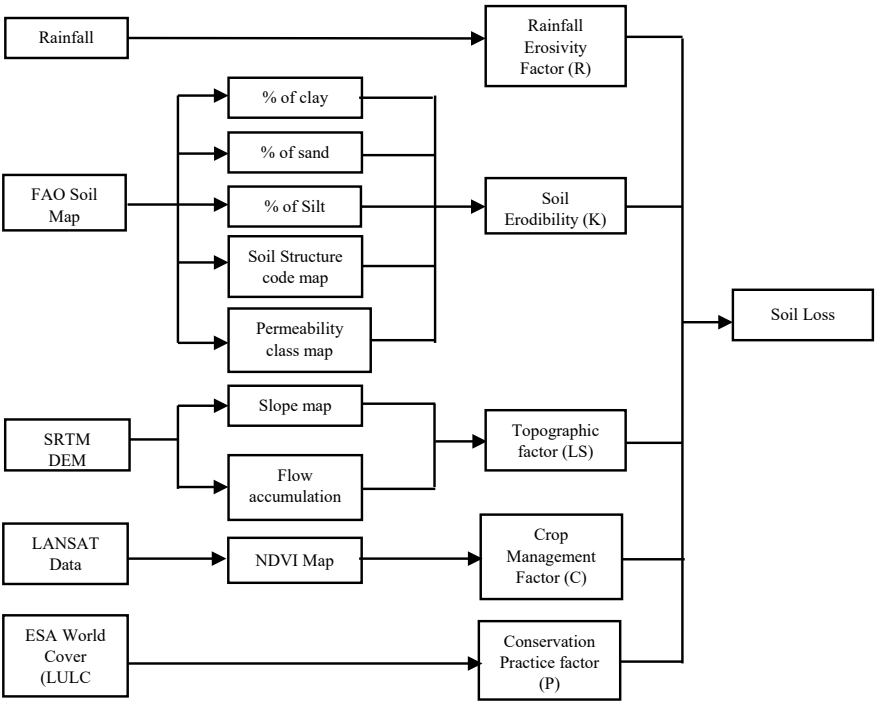

Fig. 7.6 Flow chart of the process followed to estimate soil erosion in the study

capacity of runoff is reduced due to more infiltration. Moderate to high K values are obtained in silt loam soils because the soil particles detachment and infiltration rate varies between moderate to low. Generally, silt soils due to their easily erodible soil crust have the highest K values.

$$K = 27.66 * m^{1.14} * 10^{-8} * (12 - a) + 0.0043 * (b - 2) + 0.0033 * (c - 3) \quad (7.3)$$

where, m = silt (%) + very fine sand (%) * (100-Clay (%)), a = organic matter (%), b = structure code (1-very structured or particulate, 2-fairly structured, 3-slightly structured, 4-solid), c = profile permeability code (1-rapid, 2-moderate to rapid,3-moderate, 4-moderate to slow, 5-slow, 6-very slow).

7.4.2.3 Topographic (LS) Factor

Slope length and steepness, representing the topographical characteristics of area, highly influence the soil detachment and transportation capacity of runoff or overland flow. High length and steepness increase the sediment movement or soil erosion

and make the area erosion prone. LS-factor highly governs the transportation mechanism of the soil erosion process. First, slope length factor (L) is estimated using the following equation:

$$L = \frac{\left(A_{ij-in} + D^2\right)^{m+1} - A_{ij-in}^{m+1}}{D^{m+2} * X_{ij}^{m} * 22.13^{m}} \tag{7.4}$$

where, $L_{i,j}$ is slope length factor having coordinates (i, j), $A_{i,j\text{-in}}$ is contributing area (m^2) at the inlet of the corresponding grid having coordinates (i, j), and m is the exponent of slope length factor.

Thereafter, slope steepness factor (S) is calculated using the following equations:

$$S = 10 \sin\theta + 0.03 \quad \text{if} \quad (S \geq 9\%) \tag{7.5}$$

$$S = 16.8 \sin\theta - 0.50 \quad \text{if} \quad (S \geq 9\%) \tag{7.6}$$

The L and S factors are combinedly known as the topographic (LS) factor representing the behaviour of topographic impacts on the soil erosion processes.

7.4.2.4 Cover Management Factor (*C*)

C-factor refers to the crop management conditions of the region or field. Values of *C*-factor for all Indian crop conditions are not available in literature and thus required regional computation. The presence of trees or plant covers or vegetation helps to reduce soil particles movement in forest or cultivated regions. This canopy affect varies seasonally with monsoonal climate or crop characteristics. *C*-factor's seasonal variation related to multiple factors such as precipitation, evapotranspiration, agricultural management practices, crop types etc. *C*-factor incorporates the role of crop management alternatives which can also be compared by changing the corresponding *C*-factor. Near zero values of *C*-factor refer to as a beat or well-protected ground cover whereas 1 represents the barren/fallow land. In this study, spatial map of *C*-factor of the study area is prepared on the basis of NDVI map by using Eqs. (7.7) and (7.8). NDVI map was prepared using the downloaded Landsat 8 image covering the study area.

$$\text{NDVI} = \frac{(\text{NIR} - \text{Red})}{(\text{NIR} + \text{Red})} \tag{7.7}$$

where, NDVI = Normalized difference vegetation index, NIR = reflectance from NIR band, Red = reflectance from red band

$$c = \exp\left[-\alpha * \frac{\text{NDVI}}{\beta - \text{NDVI}}\right] \tag{7.8}$$

7.4.2.5 Conservation Practice Factor (*P*)

Conservation practice factor (*P*), in RUSLE model, accounts for the comparison of soil loss in a support practice field to the straight-row farming up and down the slope when no such practice is carried out. It represents the beneficial influence of crop support practices performed in the field. Control practices reduce the runoff rate and volume, alter drainage patterns and hydraulic force on soil particle and thus, consequently, decrease soil detachment and transportation. *P*-factor of a region is allowed to vary between 0 and 1, where the close to zero values represent good conservation practices and the values near to 1 indicate unsatisfactory or poor conservation practices.

7.5 Results and Discussion

7.5.1 Estimation of RUSLE Inputs

The RUSLE parameters are estimated using the procedure mentioned above and their details are mentioned below.

7.5.1.1 Rainfall Erosivity Factor (*R*)

R factor is estimated for 2010–2020 and its values and annual rainfall information are shown in Table 7.2. The highest *R* is obtained in 2013 i.e., 5600.56 whereas 2036.52 is the lowest value. To estimate annual soil loss, mean *R* is calculated for 2010–2020 as shown in Fig. 7.7. *R* ranges between 2881 and 4614 and spatially varies across the basin. Upper basin shows lower *R* values as compared to lower basin. The southern parts of lower basin, especially, show higher R values.

7.5.1.2 Soil Erodibility Factor (*K*)

Figure 7.8 presents the map of the spatial averaged soil erodibility factor (*K*) estimated using the soil characteristics information. Six distinct classes of *K* are obtained in the basin ranging from 0.124 to 0.160. Class with *K* of 0.143 covers majority of the area (44.41). Overall, low and moderate values of *K* suggest low susceptibility of soil particles to get eroded.

Table 7.2 Estimates of the annual rainfall and annual rainfall erosivity factor (*R*)

Year	Annual rainfall (mm)	Annual *R*
2010	1146.42	2036.52
2011	1835.08	5925.90
2012	1265.02	2789.67
2013	1945.14	5600.56
2014	1599.07	4396.05
2015	1222.36	3756.12
2016	1405.14	2861.01
2017	1410.80	2820.96
2018	1779.51	3531.83
2019	1573.10	2647.94
2020	1707.60	4499.07
Average	1535.40	3715.06

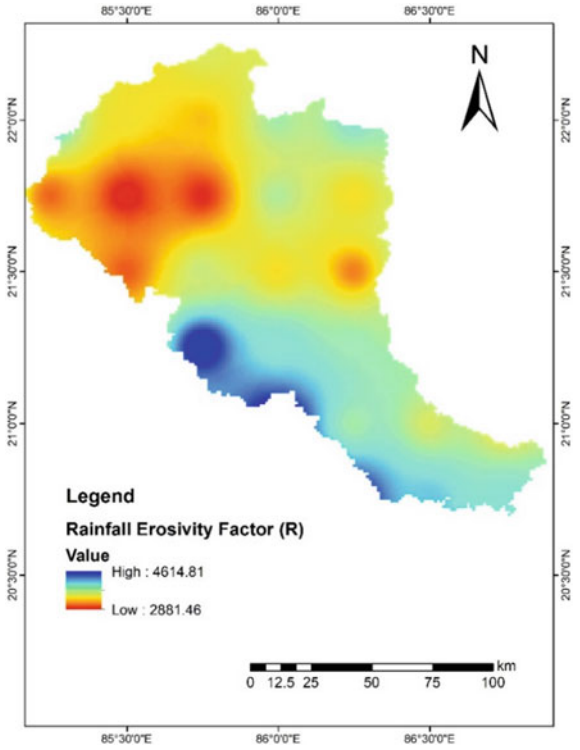

Fig. 7.7 Estimated rainfall erosivity factor (*R*) of BRB

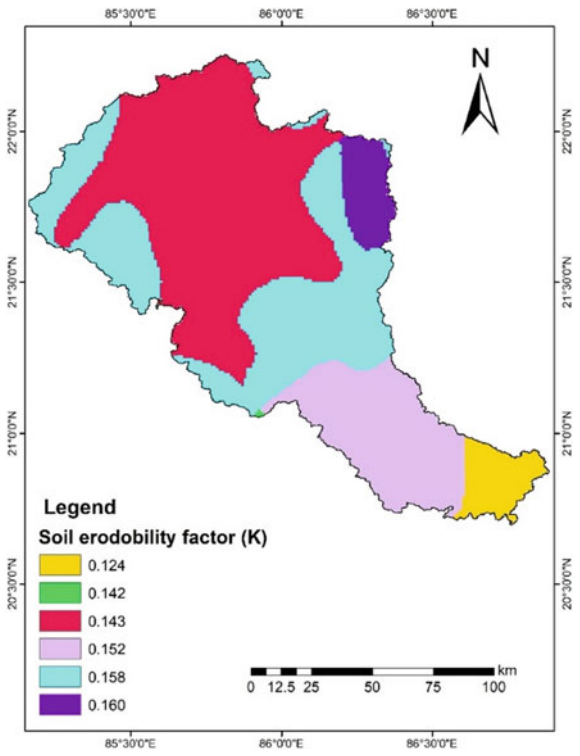

Fig. 7.8 Estimated soil erodibility factor (*K*) of BRB

7.5.1.3 Topographic Factor (LS)

To obtain spatial map of topographic factor (LS) as shown in Fig. 7.9, first, the slope length (*L*) map is prepared by analysing DEM using ArcGIS. Similarly, slope steepness (*S*) map is prepared. Thereafter, by multiplying both *L* and *S* spatial maps LS factor map of BRB is estimated. LS-factor ranges between 0.03 and 30.5. Majority of the area, especially lower basin, shows LS-factor in the range of 0.03–0.5.

7.5.1.4 Crop Cover Management Factor (*C*)

Figure 7.10 presents the crop cover management factor (*C*-factor) estimated using the NDVI map of the study area. Here, the lowest *C*-factor value is 0.13 and the highest is obtained as 1.

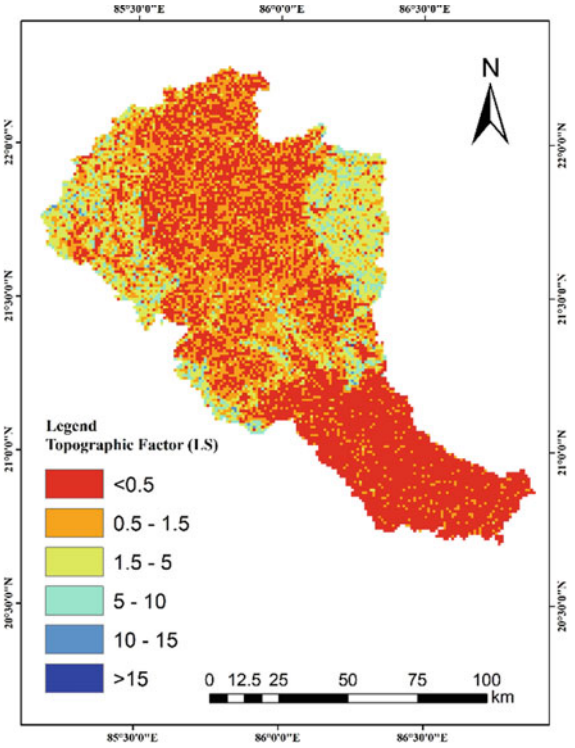

Fig. 7.9 Estimated topographic factor (LS) of BRB

7.5.1.5 Conservation Practice Factor (*P*)

The crop practice factor is estimated using the LULC map of the study area and based on the information from previous studies (Singh et al. 1981, 1992; Rao 1981). The *P*-factor map obtained (Fig. 7.11) has seven distinct values based on the various LULC classes present in the basin.

7.5.2 Annual Soil Loss Estimation

Lastly, using the above estimated spatial maps of all the required parameters of RUSLE, the average annual soil loss is computed using the RUSLE equation as shown in Fig. 7.12. Before estimating the soil loss, all the spatial maps were interpolated or resampled to 1 km × 1 km scale to maintain consistency for soil loss computation. The estimated annual soil erosion of BRB ranges between 0.02 and 206.57 t ha^{-1}/yr. Results show that most of the region (94%) of the total basin area have slight annual soil loss (<5 t ha^{-1}/yr). On the other hand, very severe soil loss (> 80t ha^{-1}/yr) is obtained in only 0.01% area. The results also reveal that 1.2%, 0.33%, and 0.06%

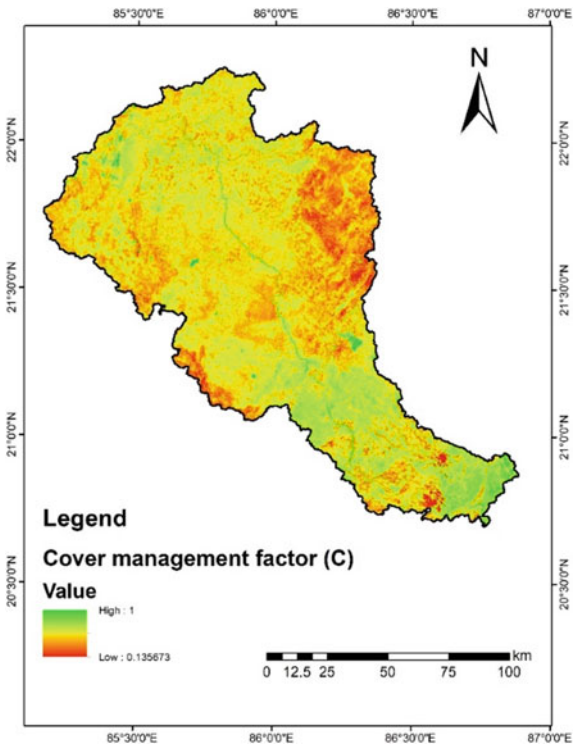

Fig. 7.10 Estimated crop cover management factor (*C*) of BRB

area of BRB is under high, very high, and severe erosion respectively. Further details are given in Table 7.3.

7.6 Conclusion

Local soil conservation project works require prior planning at catchment or basin scale. Therefore, basin scale soil erosion assessment is a general step before initiating or executing such works. In this study, RUSLE methodology integrated with geospatial techniques of GIS was used to determine the spatial extent as well as magnitude of soil erosion prone regions in the Baitarani River basin. Limitation of conventional soil loss estimation techniques restricts their employment in large areas. Modern geospatial techniques incorporated in the GIS can overcome their limitations and give reliable estimates of soil loss rate. Various studies across the world have used geospatial techniques along with RUSLE to aid the formation of proper soil conservation and management strategies of a river basin. In this study, we assessed the potential soil loss per year of a subtropical basin, Baitarani River basin, in India. All the required inputs of RUSLE were, first, individually estimated using GIS techniques. *R*-factor varies spatially between 2881 and 4614 in the basin, with upper basin showing relatively less *R* in comparison to lower basin. *K*-factor showed

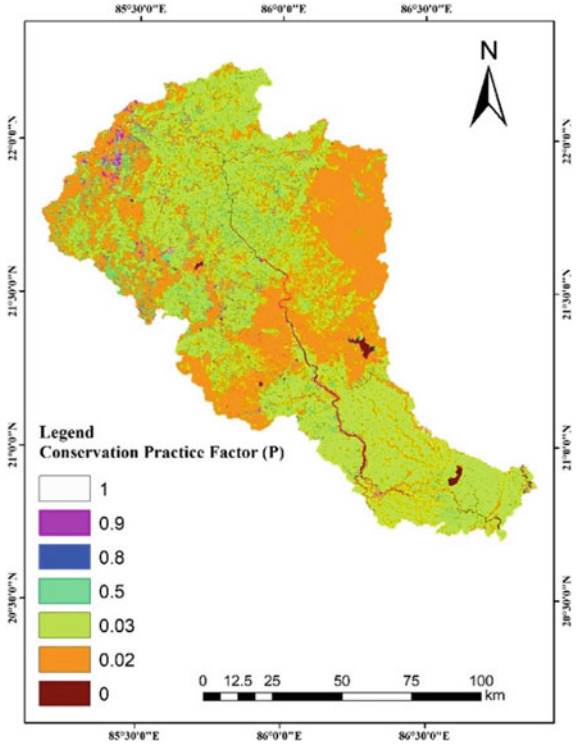

Fig. 7.11 Estimated conservation practice factor (*P*) of study area

six different values; out of which 0.143 covers most of the area (44.41%). Most area shows LS-factor in the range of 0.03–0.5. The lowest value of *C*-factor obtained was 0.13. The computed annual soil erosion of BRB varies from as low as 0.02 t ha-1/yr to as high as 206.57 t ha^{-1}/yr. Results show that 94% of the BRB area have soil loss less than 5 t ha^{-1}/yr i.e., slight erosion. Furthermore, results indicate that 1.2%, 0.33%, and 0.06% area of BRB is under high, very high, and severe erosion, respectively and thus are of utmost importance for planners and decision-makers. Soil conservation plans in the erosion prone regions of BRB require immediate action and should be prioritized accordingly. Thus, outcomes of the present study may support or help the land and water resources planners to take appropriate measures so as to reduce soil erosion in the potentially severe areas.

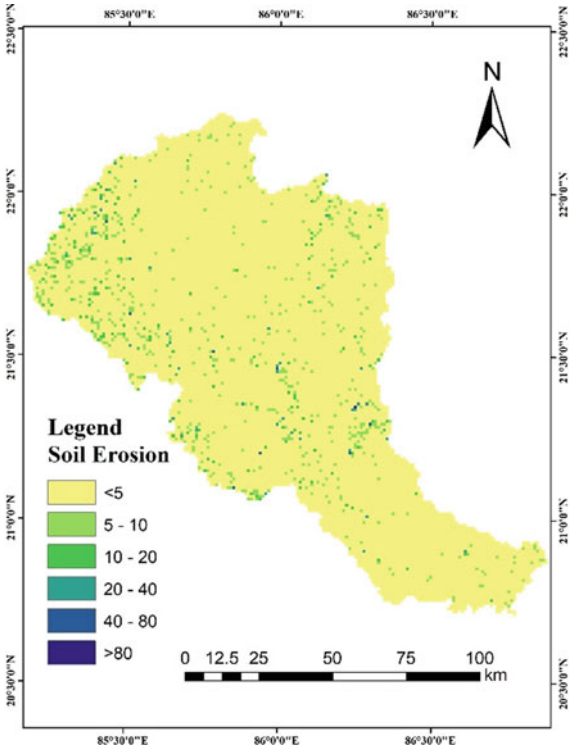

Fig. 7.12 Estimated average annual soil loss (*P*) of BRB

Table 7.3 Details of BRB area under various soil loss categories

Sl. No	Soil erosion	Class	Area (km^2)	Area percentage
1	<5	Slight	13,350.49	93.90
2	5–10	Moderate	640.07	4.50
3	10–20	High	171.11	1.20
4	20–40	Very high	46.57	0.33
5	40–80	Severe	8.66	0.06
6	>80	Very severe	1.08	0.01

Acknowledgements Authors would like to thank the India Meteorological Department, FAO, USGS, and ESA for providing the rainfall data, soil map, satellite images, and LULC, respectively.

References

Arnold JG, Allen PM, Bernhardt G (1993) A comprehensive surface-groundwater flow model. J Hydrol 142:47–69

Beasley DB, Huggins LF, Monke EJ (1980) ANSWERS: a model for watershed planning. Trans ASAE 23(4):938–944

Biddoccu M, Guzmán G, Capello G, Thielke T, Strauss P, Winter S, Zaller JG, Nicolai A, Cluzeau D, Popescu D, Bunea C, Hoble A, Cavallo E, Gómez JA (2020) Evaluation of soil erosion risk and identification of soil cover and management factor (C) for RUSLE in European vineyards with different soil management. Int Soil Water Conserv Res 8:337–353

Boussadia-Omari L, Ouillon S, Hirche A, Salamani M, Guettouche MS, Ihaddaden A, Nedjraoui D (2021) Contribution of phytoecological data to spatialize soil erosion: application of the RUSLE model in the Algerian atlas. Int Soil Water Conserv Res 9:502–519

Dabral PP, Baithuri N, Pandey A (2008) Soil erosion assessment in a Hilly catchment of North Eastern India using USLE, GIS and remote sensing. Water Resour Manage 22:1783–1798

Eniyew S, Teshome M, Sisay E, Bezabih T (2021) Integrating RUSLE model with remote sensing and GIS for evaluation soil erosion in Telkwonz Watershed, Northwestern Ethiopia. Remote Sens Appl Soc Environ 24:100623

Fayas CM, Abeysingha NS, Nirmanee KGS, Samaratunga D, Mallawatantri A (2019) Soil loss estimation using rusle model to prioritize erosion control in KELANI river basin in Sri Lanka. Int Soil Water Conserv Res 7:130–137

Ganasri BP, Ramesh H (2016) Assessment of soil erosion by RUSLE model using remote sensing and GIS—a case study of Nethravathi Basin. Geosci Front 7:953–961

Gitas LZ, Kostas D, Chara M, Silleos GN, Karydas CG (2009) Multi-temporal soil erosion risk assessment in N.Chalkidiki using a modified USLE raster model. EARSeL eProc 8:40e52

Jha MK, Paudel RC (2010) Erosion predictions by empirical models in a mountainous watershed in Nepal. J Spat Hydrol 10(1):89e102

Kothyari UC, Tewari AK, Singh R (1994) Prediction of sediment yield. J Irrigg Drain Eng ASCE 120(6):1122e1131

Kothyari UC (1996) Erosion and sediment problems in India. In: Proceedings of the Exeter symposium on erosion and sediment yield: global and regional perspectives July 1996, pp 531e540. IAHS Publ. No. 236

Laflen JM, Lane JL, Foster GR (1991) WEPP—a new generation of erosion prediction technology. J Soil Water Conserv 46(1):34–38

Masroor M, Sajjad H, Rehman S, Singh R, Hibjur Rahaman M, Sahana M, Ahmed R, Avtar R (2021) Analysing the relationship between drought and soil erosion using vegetation health index and RUSLE models in Godavari Middle Sub-basin, India. Geosci Front 101312

Nearing MA, Jetten V, Baffaut C, Cerdan O, Couturier A, Hernandez M, Le Bissonnais Y, Nichols MH, Nunes JP, Renschler CS, Souche're V, van Oost K (2005) Modeling response of soil erosion and runoff to changes in precipitation and cover. Catena 61:131e154

Pandey A, Chowdary VM, Mal BC, Billib M (2009) Application of the WEPP model for prioritization and evaluation of best management practices in an Indian watershed. Hydrol Process 23:2997–3005

Pandey A, Palmate SS (2019) Assessing future water–sediment interaction and critical area prioritization at sub-watershed level for sustainable management. Paddy Water Environ 17:373–382

Pandey A, Bishal KC, Kalura P, Chowdary VM, Jha CS, Cerdà A (2021a) A soil water assessment tool (swat) modeling approach to prioritize soil conservation management in river basin critical areas coupled with future climate scenario analysis. Air Soil Water Res 14117862212110213

Pandey A, Gautam AK, Chowdary VM, Jha CS, Cerdà A (2021b) Uncertainty assessment in soil erosion modelling using RUSLE, multisource and multiresolution DEMs. J Indian Soc Remote Sens 49:1689–1707

Remortel Van R, Hamilton M, Hickey R (2001) Estimating the LS factor for RUSLE through iterative slope length processing of digital elevation data. Cartography 30(1):27e35

Rao YP (1981) Evaluation of cropping management factor in Universal Soil Loss Equation under natural rainfall conditions of Kharagpur, India. In: Proceedings of Southeast Asian regional symposium on problems of soil erosion and sedimentation, Asian Institute of Technology, Bangkok, pp 241–254

Singh G, Babu R, Chandra S (1981) Soil loss prediction research in India. Dehradun, India: Indian Council of Agricultural Research, Bulletin of Central Soil and Water Conservation Research and Training Institute (No. T-12/D-9)

Singh G, Babu R, Narain P, Bhushan LS, Abrol IP (1992) Soil erosion rates in India. J Soil Water Conserv 47(1):97–99

Young RA, Onstad CA, Bosch DD, Anderson WP (1989) AGNPS: a nonpoint source pollution model for evaluating agricultural watersheds. J Soil Water Conserv 44(2):168–173

Wischmeier WH, Smith DD (1978). Predicting rainfall erosion losses: a guide to conservation planning. In: Agriculture handbook 282. USDA-ARS, USA

Chapter 8
Geospatial Assessment of Turbidity Along the Ganga River

N. R. Shankar Ram, Anshuman Bhatt, V. M. Chowdary, Khushboo Mirza, Chandra Shekhar Jha, and Chiranjivi Jayaram

Abstract The Ganga River basin is a lifeline to the millions inhabiting the Indian subcontinent. Pollution and deteriorating water quality in this ecosystem have been linked to various anthropogenic activities such as habitation, industrialization, agriculture, etc. The estimation and evaluation of water quality levels are essential for societal and economic development. In recent times, satellite imaging approach is widely used in diverse environmental applications, including water quality monitoring. Turbidity is an indicator of water transparency that is associated with total suspended sediment concentration and other impurities in the water through the process of light attenuation. The present study envisaged surface reflectance values to estimate the water turbidity across the Ganga River system, which is spatially classified into four different river sections. The Modified Normalized Difference Water Index (MNDWI) was used to delineate water pixels from the multispectral satellite datasets, while the turbidity was assessed spatially for different river sections using widely used Turbidity retrieval algorithms. The relative consistency among the selected algorithms was evaluated using collocated *in-situ* measurements during the period 2013–2016. Analysis of turbidity values showed a steady decrease from upstream to downstream, with turbidity values of >115 NTU and 60–85 NTU in

N. R. Shankar Ram (✉) · K. Mirza
Regional Remote Sensing Centre-North, National Remote Sensing Center, Indian Space Research Organisation, Delhi, India
e-mail: shankarramnr@gmail.com

A. Bhatt
Center for Disaster Management Studies, Jamia Milia Islamia University, New Delhi, India

V. M. Chowdary
Department of Agriculture, Cooperation and Farmers Welfare, Ministry of Agriculture and Farmers Welfare, Government of India, Mahalanobis National Crop Forecast Centre, Delhi, India

C. S. Jha
National Remote Sensing Center, Indian Space Research Organisation, Hyderabad, India

C. Jayaram
Regional Remote Sensing Centre-East, National Remote Sensing Center, Indian Space Research Organisation, Kolkata, India

C. S. Jha et al. (eds.), *Geospatial Technologies for Resources Planning and Management*, Water Science and Technology Library 115,
https://doi.org/10.1007/978-3-030-98981-1_8

the upper and lower sections, respectively. The results indicated that remote sensing provides a robust alternative for monitoring surface water turbidity.

Keywords Ganga River · Turbidity · Empirical model · MNDWI · NTU

8.1 Introduction

Climate change has adversely affected the Ganga River basin and its fragile environment in the recent decades. Increased rate of glacier melting and accelerated soil erosion affect the basinwide ecosystem (Ramakrishnan and Rajawat, 2012). Being one of the main water resources for the northern plains of the Indian subcontinent, the Ganga River faces severe challenges due to climate, anthropogenic and environmental changes. Further, increasing population exerts a significant demand for fresh water for consumption and socio-economic development. The key natural factors include contribution from the hydrological, climatic, and geological domains. Changes to the natural hydrology of a region such as the draining of wetlands, the establishment of hydropower units, diversion of river course, etc. disrupt the natural balance in the ecosystem (Du et al. 2010; Manes et al. 2016). Their adverse effects are severe when the water quantities available are low and resources are limited. Human intervention bears serious adversities on the quality of water. In addition to the intensive water usage, activities such as the discharge of industrial, domestic, urban, or other wastes, abundant bottom feeders that stir up bottom sediments or algal growth; the chemical loadings from agricultural lands, either accidental or intentional, result in pollution of water sources (Dietrich et al. 2014; Das 2011, Guttler et al. 2013; Zhou et al. 2006). Thus, to check the rampant deterioration, it is crucial to initially assess the levels of such pollution and further establish a system that monitors its dynamic changes, to plan mitigation or development activities.

Among the various properties of water, turbidity is an important indicator that may be used to investigate river water quality. Turbidity, as a factor of water transparency, provides information about the attenuation of light that is associated with the concentration of total suspended sediments and other impurities present in the water (Devlin et al. 2008; Mishra and Kumar, 2021; Tian et al. 2009). Turbidity can also be understood as a presence of different inorganic and organic materials (particulate or dissolved) in the water. It can also be considered as a measurement of the relative clarity of water, where higher turbidity levels result in increased murkiness of water. Diffusion of light into the water also decreases with the increase of suspended matter, thereby obstructing the amount of light available for photosynthesis. This decreases the extent of vegetative growth, adversely impacting the food chain and also resulting in decreased oxygen levels. Increased turbidity levels also make it difficult for predators that use visual ques to capture their prey (Christian and Sheng, 2003; Devlin et al. 2008).

The particulate matter that ends up in the water bodies originates from sources like soil, plants, animals, industrial effluents, etc. Clay, silt, minute inorganic and organic

matter, dissolved colored organics, algae, plankton, and other microorganisms are examples of such substances. Turbidity is an optical characteristic of water and is a measurement of the quantity of light that is scattered by material in the water when a light passes through the water sample. It is determined by examining water samples on-site or in the lab with the *in-situ* measurements. The higher the intensity of scattered light, the higher the turbidity. It is usually measured in Nephelometric Turbidity Units (NTU), where the instrument measures scattered light from the sample at an angle of 90° from the incoming light (Kitchener et al. 2017). Turbidity measurements of rivers involve the understanding the regime of discharge. It is crucial for the interpretation of measurements of water quality, which include various other parameters viz., flux of contaminants or sediments, suspended sediment, etc. Globally, parameters such as nature of river catchment, its geology, geography as well as climatology also influence the river discharge. In general, water clarity in the river streams tends to be clearer during lean flows, resulting in lower turbidity values, usually less than 10 NTU. During a rainstorm, when water levels are high, most rivers become muddy (brownish) due to suspended sediments from the enhanced terrestrial runoff.

Turbidity is commonly monitored by field measurements and hydrological station observations, which are typically time-intensive and are limited to discrete sites. With the advantage of broad coverage and low cost, remote sensing data provides an alternative way to monitor turbidity at various spatial and temporal scales. The integration of remote sensing data and *in-situ* measurements allows coherent quantification of turbidity changes. Several studies used multispectral and hyper-spectral remote sensing data for turbidity retrieval (Fraser 1998; Frazier and Page, 2000; Ritchie et al. 2003; Kuhn et al. 2019). These studies envisaged multiple algorithms to assess turbidity in riverine waters using different spectral band combinations along with other variables for turbidity assessment. Liu and Wang (2019) developed a reliable turbidity model based on Landsat-8 satellite imagery, while Shen et al. (2021) carried out regression modeling to derive the turbidity from the Yarlung Zangbo River, Southern Tibetan Plateau.

Zhou et al. (2021) generated turbidity maps of the Wuhan region in China, and focused on the turbidity dynamics of this industrial city, for better decision-making and effective water quality management. The relationships of turbidity and metrological and anthropogenic factors were also examined. The study by Kalele (2019) focused on the utilization of satellite spectral reflectance measurements for turbidity retrieval in the Lower Charles River, USA. Similar studies by Allam et al. (2020), Kapalanga et al. (2021), and Pereira et al. (2018) investigated remote sensing-based validation of the satellite-derived values with *in-situ* data over the Ramganga River in the Ganges Basin, Olushandja Dam, north-central Namibia, and Middle Mississippi and Lower Missouri Rivers of the USA, respectively. Specifically, Landsat-8 satellite data have been widely used to estimate water quality parameters. These datasets have been used to examine the spatial and temporal variation of turbidity with the identification of key issues affecting its patterns in El Guajaro Reservoir, Colombia (González-Márquez et al. 2018) and depth in Cam Ranh Bay and the Thuy Trieu Lagoon, Vietnam (Quang et al. 2017). These authors had developed the algorithms to retrieve the turbidity based on the relationship between *in-situ* observations and

the red spectral band of Landsat 8. The study by Surisetty et al. (2018), focused on utilizing Landsat 8 bands, especially Near Infrared (NIR) and Shortwave Infrared (SWIR) to derive turbidity values in the Chilika lagoon.

Thus, various studies were conducted globally to measure the turbidity in major water bodies and river systems using an array of models. The present study comprehensively evaluated some of these algorithms available in literature and aims to identify the most suitable algorithm to effectively retrieve water turbidity across the river Ganga. The specific objectives of the present study include: (1) Assessment of turbidity from satellite data using multiple retrieval algorithms (2) Evaluation of turbidity algorithms using *in-situ* observations (3) Real-time turbidity mapping across various stretches of Ganga River.

8.2 Materials and Methods

8.2.1 Study Area

Ganga River Basin (Fig. 8.1) is the largest river basin in India, covering a total area of 861,404 km^2, comprising the Ganga River and its tributaries. It is marginally greater

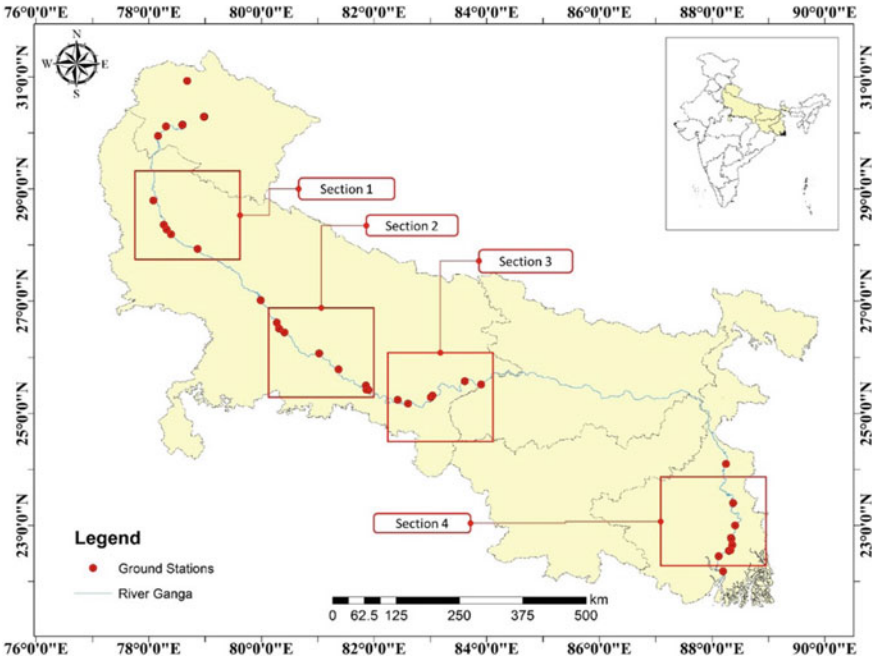

Fig. 8.1 Synoptic view of the study area along with CPCB ground station locations

than a quarter of the total geographical area of the country. This river, considered sacred to billions of Indians, runs along the northern part of India and feeds more than four hundred million people living in the basin area. In total, the Ganga basin is spread in 11 states of the country, namely Bihar, Chhattisgarh, Delhi, Haryana, Himachal Pradesh, Jharkhand, Madhya Pradesh, Rajasthan, Uttar Pradesh, Uttarakhand, and West Bengal. The abundance of water resources, fertile soil, and suitable climatic conditions, across these regions has resulted in an advanced agricultural society with a total cultivated land area of approximately 44 million hectares and a total irrigated area of 23.41 million hectares. It has evolved into one of the most densely inhabited places in the world. The Ganga River has created a basin with extraordinary variations in climatic conditions, altitudes, land use, wildlife, culture, and society. The entire river length was further divided into four river stretches (Fig. 8.1) along the river basin in this study. These stretches were chosen on the basis of availability of *in-situ* datasets and the vicinity of ground station to each other forming a cluster.

8.2.1.1 Climate

The average maximum and minimum temperature across the basin fall in the of range of 30.3 °C–21.5 °C in summer to 21.1 °C–6.4 °C in winter, respectively. The pre-monsoon season (March–May) experiences the hottest temperatures in the basin with an average temperature of ~31.4 °C. The month of January is the coldest across the whole basin. The annual precipitation across the basin is nearly 1000 mm. The monsoon season witnesses the highest amount of rainfall (nearly 84% of the annual total). Of the remainder, 7, 5, and 4% fall during the pre-monsoon, post-monsoon, and winter seasons with some differences in precipitation between the upper and lower Ganges basins. Generally, peak flows occur when melting of snow runoff is reinforced by monsoon rains. The Ganges receives snow-melt from southern flaks of Tibet as well as the Himalayas from the periods from April, extending till June, and subsequently, the flow rate of the river commences to decrease when the July monsoon commences.

8.2.1.2 Topography and Soil Characteristics

The Gangetic plains are generally distributed into the Upper, the Middle, and the Lower Ganga plains, respectively. Approximately 40% of the total Ganga basin area falls under the elevation of 50–200 m. It is confined by the mighty Himalayas in the north, the Vindhyas range and Chotanagpur plateau in the south, the Aravalli range across the west, and the Brahmaputra ridge in the east. The river basin comprises an extensive variety of soils. While the high Himalayan soils in the north face continuous erosion, the Gangetic plain provides a huge depositional platform forming a wide valley plain, where some soils are highly prone to erosion. The montane and alluvial soils cover nearly 60% of the total basin area. Of the remaining area, red soils (12% area) are highly erodible, yellow and red soils, mixed black and red soils (8% area)

have moderate erodibility, and medium and deep black soils (14% area) have low erodibility. Lateritic soils and shallow black soils that cover 6% of the basin area have very low erodibility.

8.2.2 *In-Situ and Satellite Datasets Used in the Study*

The present study investigated the agreement of satellite-based retrieval of turbidity with water quality information collected from the Central Pollution Control Board [CPCB] for the period 2013–2016 (CPCB 2008). A total of 40 ground stations datasets spanning across the study region, i.e., situated between Indian state of Uttarakhand (headwaters) to Sundarbans Delta, West Bengal (mouth of the river) were used in the analysis. The datasets contained turbidity information from *in-situ* instruments placed along the banks of the river. In the present analysis, 17 ground station datasets were selected based on the factors such as concurrent availability with satellite pass and data quality (Fig. 8.1).

Satellite-based imagery from the Landsat-8 satellite in the Landsat series satellites was used in the present study. The satellite payload has two scientific instruments onboard- the Operational Land Imager (OLI) and the Thermal Infrared Sensor (TIRS). These sensors deliver periodic coverage of the landmass with a spatial resolution of 30 m across the NIR, SWIR, and visible bands; 100 m across the Thermal band and 15 m across the Panchromatic band (Table 8.1). An inventory of all available satellite datasets between the year 2013–2016 was generated and concurrent dates

Table 8.1 Spectral bands and resolutions of Landsat 8

Bands	Wavelength (nm)	Type	Spatial resolution (m)
1	430–450	Coastal aerosol	30
2	450–510	Blue	30
3	530–590	Green	30
4	640–670	Red	30
5	850–880	Near Infrared (NIR)	30
6	1570–1650	SWIR 1	30
7	2110–2290	SWIR 2	30
8	500–680	Panchromatic	15
9	1360–1380	Cirrus	30
10	10,600–11,190	Thermal Infrared (TIRS) 1	100
11	11,500–12,510	Thermal Infrared (TIRS) 2	100

Source Hansen and Loveland (2012)

that correspond to CPCB ground station measurement for a satellite overpass were identified. These datasets have been downloaded from the USGS website (Hansen and Loveland 2012) and further processed in this study.

8.2.3 Methodology

Landsat-8 images for the four selected stretches were obtained and further processed by following the methodology as discussed subsequently.

8.2.3.1 Generation of River Mask

The computational intensity to process the satellite datasets was reduced by subsetting the datasets into pixels with only the river course. The Modified Normalized Difference Water Index (MNDWI), which enhances open water features while sufficiently suppressing and removing the built-up land noise as well as soil/vegetation noise was used in the present study (Xu 2006). The index is derived from the modification of the Normalized Difference Water Index (NDWI) (Gao 1996; McFeeters, 1996), by substituting the middle infrared band with the Near Infrared (NIR) band used in the NDWI. The NDWI extracted water area is overestimated as the water mask obtained from satellite imagery is usually mixed up with built-up land noise. Hence, MNDWI, helps in contracting and even eliminating the noise of built-up land and is more suitable for extraction and enhancement of water features with a built-up dominated land area in background. The formula used to compute the MNDWI can be computed as follows:

$$\text{MNDWI} = (\text{Green} - \text{SWIR})/(\text{Green} + \text{SWIR})$$

Where "Green" is the green band and "SWIR" is the Short Wave Infrared band. The water pixels are extracted from the generated MNDWI values by applying a threshold at 0.

8.2.3.2 Extraction of Surface Reflectance for River Mask

The satellite imagery from the four identified river sections was clipped with the water vector polygon. Pixel values from bands 2, 3, 4, and 5 of the clipped satellite imageries are converted to surface reflectance values using a multiplicative factor (0.0000275) as given in the Landsat 8 OLI/TIRS Collection 2 Level 2 Data Format Control Book (USGS 2020).

Table 8.2 Turbidity models evaluated across the river stretch

S. No.	Retrieval model	References
1	$T = -74.26 * B2 - 14.84 * B3 + 267.45 * B4 - 126.89 * B5 + 4.21$ B2 = Band 2, B3 = Band 3, B4 = Band 4, B5 = Band 5	Liu and Wang (2019)
2	$T = -344.784 * B2 + 398.817 * B3 + 1.045$ B2 = Band 2, B3 = Band 3	Kalele (2019)
3	$T = -138.2 - 1718 * (B4/B3) + 695.1 * e(B4/B3)$ e = exponential, B3 = Band 3, B4 = Band 4	Pereira et al. (2018)
4	$T = 380.32 * (B4) - 1.7826$ B4 = Band 4	Quang et al. (2017)
5	Turbidity = $10.26 * (B4 + B5) - 0.18359$ B4 = Band 4, B5 = Band 5	González-Márquez et al. (2018)
6	$T = 15.31856 - 956.806 * (B2) - 747.376 * (B3) + 1742.455 * (B4) + 165.173(B5)$ B2 = Band 2, B3 = Band 3, B4 = Band 4, B5 = Band 5	Kapalanga et al. (2021)
7	$T = 3.896 - 4.186 *$ (Band 2/Band 3)	Allam et al (2020)
8	$T = 23.09 * (r - 0.233/1.28 - r)$ r = broadband reflectance ratio of B4/B3	Surisetty et al. (2018)
9	$T = (1 - \varepsilon) * 2.1170 *$ (red band) $* 2.4880 + \varepsilon * 2.4354 *$ (NIR) $* 2.5673$ ε = (NIR band − 0.028)/0.005	Zhou et al. (2021)
10	$T = 253.884 + (-558.206 * X) + (0 * X2) + (399.496 * X3)$ X = Band 4/Band 3	Li et al (2015)

8.2.3.3 Turbidity Retrieval Algorithms

The widely used strategy to compute turbidity is to establish the relationships between turbidity and image reflectance based on the calibration of *in-situ* measurements from water samples. In this study, we used multiple models from literature to extract the best-suited turbidity model for the Ganga River. Table 8.2 catalogs the 10 turbidity models evaluated in the present study. Each algorithm was implemented over the river sections and the resulting turbidity values were compiled. The results were further evaluated for consistency in their range of values in comparison to *in-situ* datasets and four models were identified.

8.2.3.4 Performance Evaluation of Turbidity Models

Subsequent to obtaining the outputs of all the algorithms, four algorithms were shortlisted based on their value ranges for the validation process. The pixel values

of coordinates falling over the *in-situ* ground stations and model-based extracted turbidity datasets were acquired for all four algorithms, following the nearest neighborhood criteria with the *in-situ* location. The relative performance of these models is evaluated based on the Root Mean Square Error (RMSE) calculation. RMSE is the residual's standard deviation (prediction errors). Residuals measure the distance of the regression line from the data point, showing the spread. This error metric is commonly used in climatology, forecasting, and regression analysis to verify experimental results. The formula to compute RMSE is as follows:

$$\text{RMSE} = \sqrt{\frac{\sum_{i=0}^{N}\left(x_i - \hat{x}_i\right)^2}{N}}$$

N = No. of datasets
x_i = *in-situ* based value
$\hat{x}_i$ = Model-based value.

Subsequent to the validation of the four shortlisted models of turbidity, the most suitable algorithm is selected based on the lowest deviation in the values between *in-situ* data and observed data.

8.2.3.5 Real-Time Turbidity Mapping Across the Ganga River

Cloud-free satellite datasets across the study area were acquired to compute the turbidity across the river. These maps may serve as guiding tools to identify turbidity levels across various stretches of the study area.

8.3 Result and Discussion

Remote sensing and GIS-based technologies were used to retrieve the turbidity of Ganga River. Satellite imagery of the study period from 2013 to 2016 was downloaded and the coordinates of the respective ground stations along with dataset's path and row numbers of the satellite imagery, along with their corresponding dates, are presented in Table 8.3. The description of various intermediate steps and results that were carried across these datasets are as described below.

8.3.1 Extraction of Water Pixels and Generation of River Mask

The MNDWI algorithm was applied onto the Landsat satellite across the identified river stretches. Figure 8.2a, b, show the False-color composite and the MNDWI

Table 8.3 Inventory of satellite data availability corresponding to *in-situ* data with their date of availability

Year	Date	Ground station	Coordinates (latitude, longitude)	Path, row	Landsat 8 Datasets (LC08_L2SP_…)
Section 1					
2013	22-May	G1	28.2731, 78.3182	145, 41	…145041_20130522_20200913_02_T1
2014	17-Nov	G2	28.1897, 78.3959	145, 41	…145041_20141117_20200910_02_T1
Section 2					
2014	09-Apr	G3	25.4192, 81.9005	143, 42	…143042_20140409_20200911_02_T1
2015	23-Feb	G4	25.5023, 81.8554	143, 42	…143042_20150223_20200909_02_T1
		G5	25.4192, 81.9005	143, 42	…143042_20150223_20200909_02_T1
2016	01-Jun	G6	25.4266, 81.8639	143, 42	…143042_20160601_20200906_02_T1
Section 3					
2014	09-Apr	G7	25.244, 82.4183	143, 42	…143042_20140409_20200911_02_T1
2016	25-May	G8	25.1771, 82.6022	142, 43	…142043_20160525_20200906_02_T1
		G9	25.244, 82.4183	142, 43	…142043_20160525_20200906_02_T1
	03-Feb	G10	25.2894, 83.0064	142, 42	…142042_20160203_20200907_02_T1
		G11	25.3199, 83.0366	142, 42	…142042_20160203_20200907_02_T1
Section 4					
2014	02-Dec	G12	22.4535, 88.1153	138, 44	…138044_20141202_20200910_02_T1
	08-May	G13	22.4535, 88.1153	138, 44	…138044_20140508_20200911_02_T1
2015	12-May	G14	23.4001, 88.3734	138, 44	…138044_20151205_20200908_02_T1
		G15	23.0008, 88.4086	138, 44	…138044_20151205_20200908_02_T1
	02-Oct	G16	22.5497, 88.2961	138, 44	…138044_20151002_20200908_02_T1
2016	07-Dec	G17	22.5497, 88.2961	138, 44	…138044_20161207_20200905_02_T1

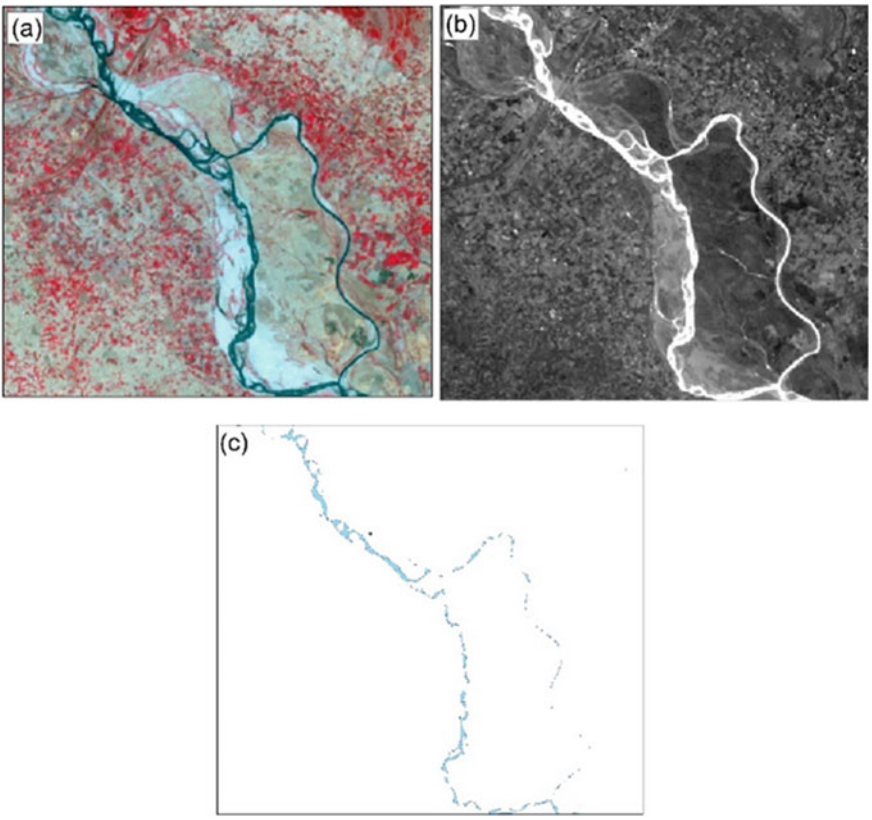

Fig. 8.2 Sample section of the river showing **a** FCC imagery, **b** modified normalized difference water index and **c** river mask

output, respectively across a sample section of the river. The water pixels are extracted by the application of threshold value of 0 onto the MNDWI output. Subsequently, these pixels were converted to vector polygon so as to generate the river mask (Fig. 8.2c).

8.3.2 Estimation of Turbidity Using Multiple Turbidity Retrieval Algorithms

The satellite datasets were clipped and the surface reflectance values were computed for these datasets across the study region as defined in Sect. 8.2.3. The value ranges of all these models were computed and four models with their values lying within the range of values in the *in-situ* datasets were shortlisted. The algorithms from Liu and Wang (2019) (Sr. No. 1), Kalele (2019) (Sr. No. 2), Quang et al. (2017) (Sr. No.

Table 8.4 Shortlisted models for turbidity extraction

Model No	Selected model	References
A	$T = -74.26 * B2 - 14.84 * B3 + 267.45 * B4 - 126.89 * B5 + 4.21$ B2 = Band 2, B3 = Band 3, B4 = Band 4, B5 = Band 5	Liu and Wang (2019)
B	$T = -344.784 * B2 + 398.817 * B3 + 1.045$ B2 = Band 2, B3 = Band 3	Kalele (2019)
C	$T = 380.32 * (B4) - 1.7826$ B4 = Band 4	Quang et al. (2017)
D	$T = 253.884 + (-558.206 * X) + (0 * X2) + (399.496 * X3)$ X = Band 4/Band 3	Li et al (2015)

4), and Li et al. (2015) (Sr. No.10) were taken as Models A, B, C, and D, respectively (Table 8.4).

8.3.3 Estimation of Turbidity Across River Sections Using Different Turbidity Models

The shortlisted turbidity models (Models A, B, C & D) were applied to each section of the river. The values of turbidity across the models over the river Section 1 are shown in Fig. 8.3. Here, the computed turbidity values indicated values ranging from 7 to 39 NTU and 26 NTU to 53 NTU for Model A and Model B, respectively. Model B showed an average turbidity higher than the Model A estimated value. The turbidity estimates from Model C are observed from 99 to 181 NTU which is the highest among all the other algorithms. Although there were only few values greater than 170 NTU, the average values were well over 120 NTU. Turbidity values from Model D also indicated high values with NTU ranging from 65 to 171 NTU.

Figure 8.4 depicts the computed turbidity for various models across Sect. 2 of the study area. The turbidity values ranged from 6 to 38 NTU. The distribution of turbidity was seen to vary with lower values in the upper part of the river and increasing toward the downstream region. Models A and B showed values between 38 and 49 NTU, respectively. Model B showed not only higher turbidity in comparison to Model A, but it also showed greater number of stretches with high values. The output of Model C and D showed turbidity values from 87 to 170 NTU and from 47 to 187 NTU, respectively. Although Model D had the highest maximum value of computed turbidity, Model C showed the highest average value. Low to moderate values of turbidity was observed in the upper part and higher values were computed in the lower part of the river.

The distribution of turbidity across different turbidity models were shown in Fig. 8.5. The output of Model A showed that the turbidity values ranged from 03 to 38 NTU. Few regions where minor tributaries converge showed high turbidity values.

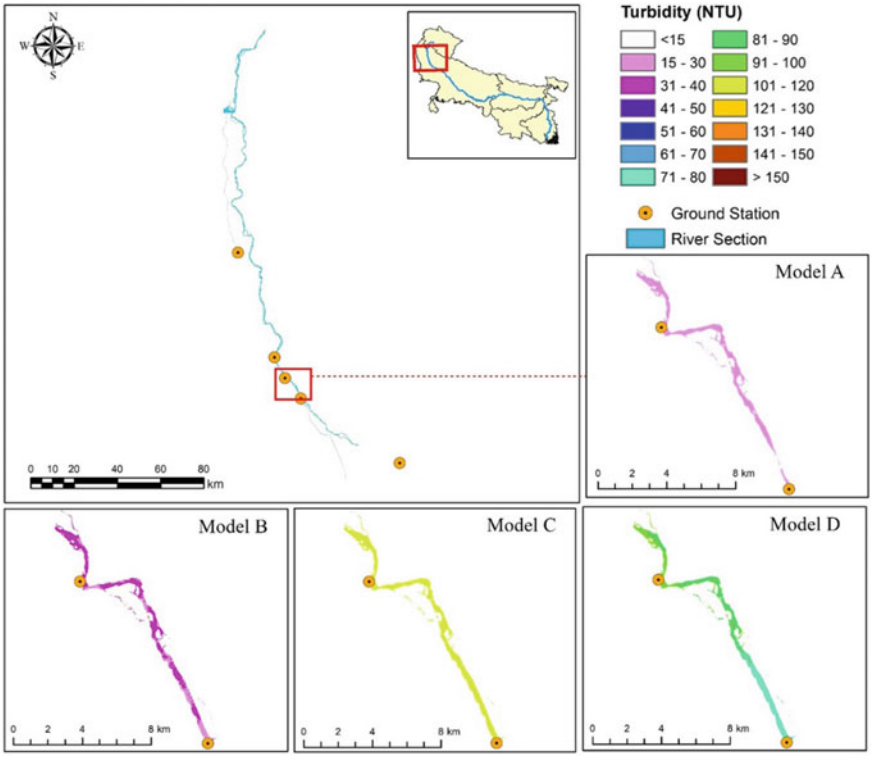

Fig. 8.3 Spatial distribution of turbidity for Models A, B, C & D across Section 1

The turbidity output of Model B (18 NTU to 48 NTU) showed rather low values along the upper and middle part of the river section with higher values in the lower part after the tributaries converge. Model C indicated values ranging from 83 to 149 NTU and 47 NTU to 153 NTU, respectively. They showed the gradual increase in values toward the downstream regions.

Figure 8.6 depicts the turbidity outputs for Models A, B, C, and D across the lowest section (Section 4) of the study region. The output of Model A depicted values that ranged from negligible to 42 NTU. The pixels values for turbidity ranged from low to moderate from the upstream toward downstream regions. The output of Model B (7–70 NTU), showed patterns of the turbidity to be higher in the middle regions of the river while moderate toward the upper and lower reaches of the river. Models C (turbidity between 72 and 248 NTU) showed similar patterns. There were few regions of the river which showed values that exceeded 200 NTU. Model D (turbidity between 16 and 138 NTU) showed low values in the upstream and downstream regions of the river and regions in the middle showed moderate to high turbidity values.

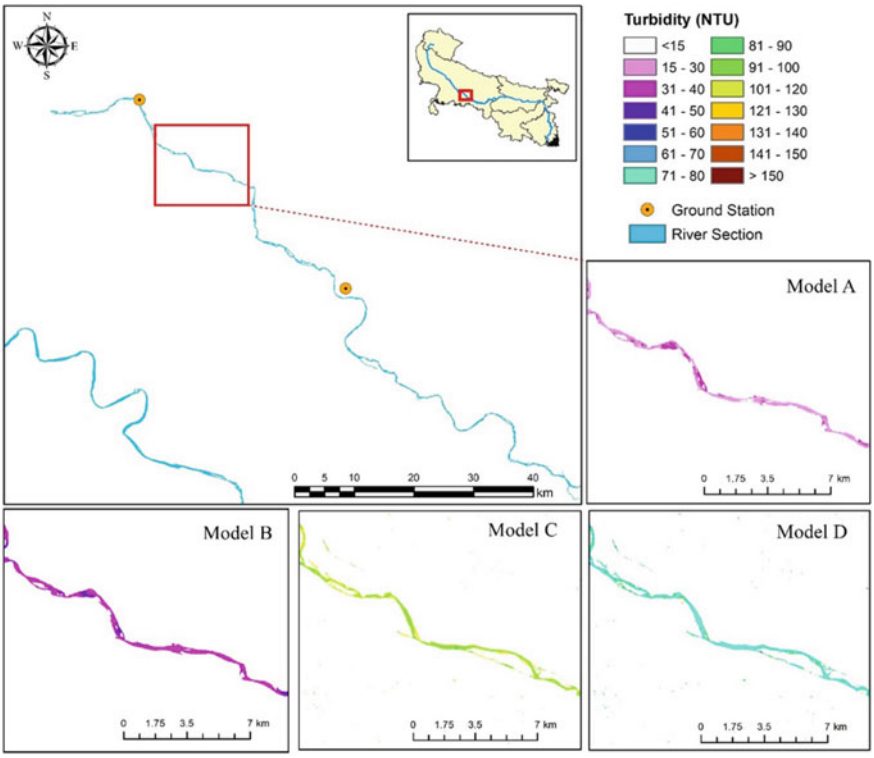

Fig. 8.4 Spatial distribution of turbidity for Models A, B, C & D across Section 2

8.3.4 Evaluation of Turbidity Retrieval Models Using In-Situ Observations

The model outputs for pixels near the spatial vicinity of *in-situ* observation sites were extracted considering the dates and satellite data availability. To extract the model that most accurately represents the *in-situ* datasets, the RMSE matric was computed across various sections of the river. Tables 8.5, 8.6, 8.7 and 8.8 show the RMSE values across various sections of the study area. It was observed that Sections 2, 3, and 4 were best represented by Model D (Li et al. 2015) with the RMSE values of 8.27, 24.18, and 62.65, respectively which indicated that it was a moderately suitable algorithm among these river sections. On the contrary, Model B (Kalele 2019) showed the lowest RMSE error (12.1) for Section 1 of the study area, indicating better performance. In the present study, since Model D depicted the least RMSE value across three different sections, it was selected as the most suitable algorithm among all the other algorithms for estimation of turbidity across the Ganga River.

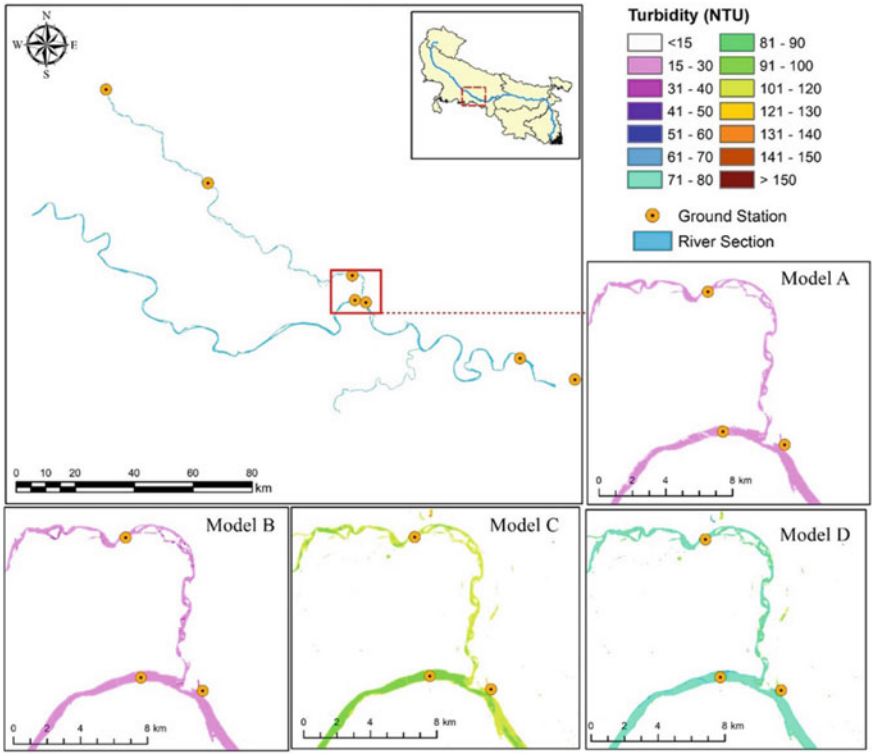

Fig. 8.5 Spatial distribution of turbidity for Models A, B, C & D across Section 3

8.3.5 Real-Time Turbidity Mapping Through the Best Performing Model

Satellite datasets of 13-July-2021 were acquired and the water turbidity across the study area was computed using the most suitable turbidity retrieval algorithm as proposed by Li et al. (2015) (Model D) (Fig. 8.7). The upper reaches of the river exhibited higher turbidity (>115 NTU) values in comparison to the downstream sections (60-85 NTU) after the confluence with its tributaries. During its passage across the middle reaches, the river confluences with many of its tributaries, creating turbid waters. The reduction of turbidity values toward its lower reaches may be attributed to the widening and slowing down of the course of the river, allowing for the settling of particulate matter, thereby reducing water turbidity in the downstream sections. The turbidity values retrieved in the present approach may be operationalized to continually monitor the water quality across the river.

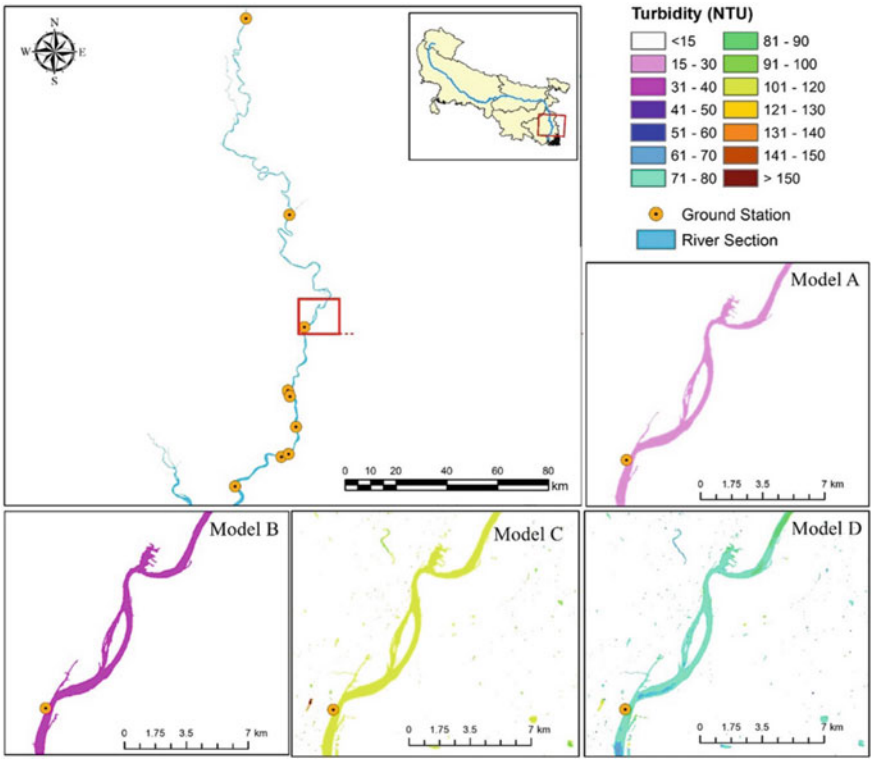

Fig. 8.6 Spatial distribution of turbidity for Models A, B, C & D across Section 4

8.4 Conclusions

Water quality is influenced by a wide range of human and natural factors. Turbidity is an important indicator of water quality and the hydrological conditions of rivers. With the advantage of synoptic coverage and low costs, satellite data and remote sensing techniques have opened up new avenues and provided alternative ways to monitor turbidity at various spatial and temporal scales. The present study investigated the turbidity retrieval from satellite datasets using various retrieval models available across literature. The study further envisaged to identify the most suitable algorithm, that best represented the *in-situ* observations across different sections over the Ganga River. The study indicated that model proposed by Li et al. (2015), best represented the turbidity concentration in the river waters of the Ganga. However, the model was unable to represent the *in-situ* turbidity values across the upstream sections of the river satisfactorily. Thus, a single model may not be adequate to completely model the complete extent of large river systems such as the Ganga. Thus, there is scope for novel models, which may quantitatively best represent different sections of the river course, with is varying agro-climatic and morphological characteristics.

Table 8.5 Relative performance of turbidity model across *in-situ* observations for Section 1

Year	Date	Station no	Observed values	Algorithms							
				Model A		Model B		Model C		Model D	
				Predicted value	RMSE	Predicted value	RMSE	Predicted value	RMSE	Predicted value	RMSE
2013	22/05	G1	42	25	12.10	34	5.65	104	59.07	76	24.30
2014	17/11	G2	30	28		30		86		35	

Table 8.6 Relative performance of turbidity model across *in-situ* observations for Section 2

Year	Date	Station no	Observed Values	Algorithms							
				Model A		Model B		Model C		Model D	
				Predicted value	RMSE	Predicted value	RMSE	Predicted value	RMSE	Predicted value	RMSE
2014	09/04	G3	60	24	35.27	32	27.02	91	32.41	66	8.27
2015	23/02	G4	68	24		33		90		68	
		G5	59	26		34		85		63	
2016	01/06	G6	60	25		36		102		71	

Table 8.7 Relative performance of turbidity model across *in-situ* observations for Section 3

Year	Date	Station no	Observed values	Algorithms							
				Model A		Model B		Model C		Model D	
				Predicted value	RMSE	Predicted value	RMSE	Predicted value	RMSE	Predicted value	RMSE
2014	09/04	G7	72	26	57.14	32	50.12	124	46.65	105	24.18
2016	25/05	G8	108	23		34		108		106	
		G9	108	25		34		109		108	
	03/02	G10	20	20		22		91		54	
		G11	30	20		27		86		56	

Table 8.8 Relative performance of turbidity model across *in-situ* observations for Section 4

Year	Date	Station no	Observed values	Algorithms							
				Model A		Model B		Model C		Model D	
				Predicted value	RMSE	Predicted value	RMSE	Predicted value	RMSE	Predicted value	RMSE
2014	02/12	G12	27	27	108.38	27	103.45	101	67.03	64	62.65
	08/05	G13	51	26		40		100		52	
2015	12/05	G14	186	23		37		126		89	
		G15	99	27		40		100		99	
	02/10	G16	32	23		32		92		34	
2016	07/12	G17	226	31		30		117		113	

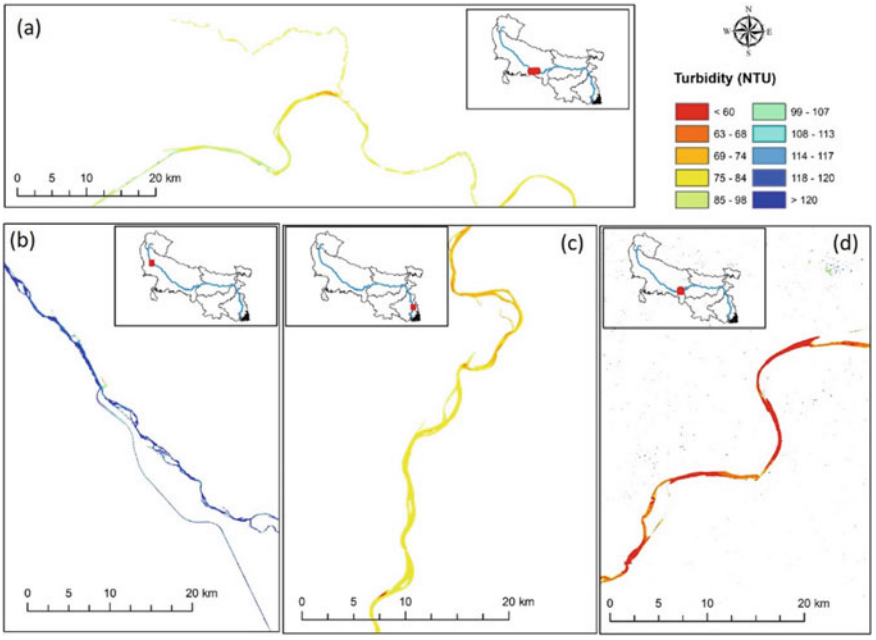

Fig. 8.7 Spatial distribution of turbidity across a) middle (moderate turbidity), b) upper (high turbidity), c) lower (moderate turbidity) and d) middle (high turbidity) river sections using turbidity Model D

References

Allam M, Khan MYA, Meng Q (2020) Retrieval of turbidity on a spatio-temporal scale using Landsat 8 SR: a case study of the Ramganga River in the Ganges Basin, India. Appl Sci 10(11):3702

Christian D, Peter Sheng Y (2003) Relative influence of various water quality parameters on light attenuation in Indian River Lagoon. Estuarine Coast Shelf Sci 57(5–6):961–971

CPCB (2008) Guidelines for water quality monitoring (2007–2008). Central Pollution Control Board CPCB. Ministry of Environment. For. MINARS/27/2007-08. 06-15

Das S (2011) Cleaning of the Ganga. J Geol Soc India 78(2):124–130

Devlin MJ, Barry J, Mills DK, Gowen RJ, Foden J, Sivyer D, Tett P (2008) Relationships between suspended particulate material, light attenuation and Secchi depth in UK marine waters. Estuar Coast Shelf Sci 79(3):429–439

Dietrich AM, Phetxumphou K, Gallagher DL (2014) Systematic tracking, visualizing, and interpreting of consumer feedback for drinking water quality. Water Res 66:63–74

Du N, Ottens H, Sliuzas R (2010) Spatial impact of urban expansion on surface water bodies—a case study of Wuhan, China. Landsc Urban Plan 94(3–4):175–185

Fraser RN (1998) Multispectral remote sensing of turbidity among Nebraska Sand Hills lakes. Int J Remote Sens 19(15):3011–3016

Frazier PS, Page KJ (2000) Water body detection and delineation with Landsat TM data. Photogramm Eng Remote Sens 66(12):1461–1468

Gao B-C (1996) NDWI—A normalized difference water index for remote sensing of vegetation liquid water from space. Remote Sens Environ 58(3):257–266

González-Márquez LC, Torres-Bejarano FM, Torregroza-Espinosa AC, Hansen-Rodríguez IR, Rodríguez-Gallegos HB (2018) Use of LANDSAT 8 images for depth and water quality assessment of El Guájaro reservoir, Colombia. J South Am Earth Sci 82:231–238

Güttler FN, Niculescu S, Gohin F (2013) Turbidity retrieval and monitoring of Danube Delta waters using multi-sensor optical remote sensing data: an integrated view from the delta plain lakes to the western–northwestern Black Sea coastal zone. Remote Sens Environ 132:86–101

Hansen MC, Loveland TR (2012) A review of large area monitoring of land cover change using Landsat data. Remote Sens Environ 122:66–74

Kalele AS (2019) Estimation and mapping of turbidity in the lower Charles River Using Landsat 8 OLI satellite imagery. PhD diss., Northeastern University, 2019

Kapalanga TS, Hoko Z, Gumindoga W, Chikwiramakomo L (2021) Remote-sensing-based algorithms for water quality monitoring in Olushandja Dam, north-central Namibia. Water Supply 21(5):1878–1894

Kitchener BGB, Wainwright J, Parsons AJ (2017) A review of the principles of turbidity measurement. Progress Phys Geogr 41(5):620–642

Kuhn C, de Matos Valerio A, Ward N, Loken L, Sawakuchi HO, Kampel M, Richey J et al (2019) Performance of Landsat-8 and Sentinel-2 surface reflectance products for river remote sensing retrievals of chlorophyll-a and turbidity. Remote Sens Environ 224:104–118

Li H, Li Y, Shen W, Li Y, Lin J, Xiaoyu L, Xia X, Jiang J (2015) Elevation-dependent vegetation greening of the Yarlung Zangbo River basin in the southern Tibetan Plateau, 1999–2013. Remote Sens 7(12):16672–16687

Liu L-W, Wang Y-M (2019) Modelling reservoir turbidity using Landsat 8 satellite imagery by gene expression programming. Water 11(7):1479

Manes F, Marando F, Capotorti G, Blasi C, Salvatori E, Fusaro L, Ciancarella L et al (2016) Regulating ecosystem services of forests in ten Italian metropolitan cities: air quality improvement by PM10 and O3 removal. Ecol Indicators 67:425–440

McFeeters SK (1996) The use of the Normalized Difference Water Index (NDWI) in the delineation of open water features. Int J Remote Sens 17(7):1425–1432

Mishra S, Kumar A (2021) Estimation of physicochemical characteristics and associated metal contamination risk in the Narmada River, India. Environ Eng Res 26(1)

Pereira LSF, Andes LC, Cox AL, Ghulam A (2018) Measuring suspended-sediment concentration and turbidity in the middle Mississippi and lower Missouri rivers using landsat data. JAWRA J Am Water Resour Assoc 54(2):440–450

Quang NH, Sasaki J, Higa H, Huan NH (2017) Spatiotemporal variation of turbidity based on landsat 8 oli in cam ranh bay and thuy trieu lagoon, vietnam. Water 9(8):570

Ramakrishnan R, Rajawat AS (2012) Simulation of suspended sediment transport initialized with satellite derived suspended sediment concentrations. J Earth Syst Sci 121(5):1201–1213

Ritchie JC, Zimba PV, Everitt JH (2003) Remote sensing techniques to assess water quality. Photogramm Eng Remote Sens 69(6):695–704

Shen M, Wang S, Li Y, Tang M, Ma Y (2021) Pattern of turbidity change in the middle reaches of the Yarlung Zangbo River, Southern Tibetan Plateau, from 2007 to 2017. Remote Sens 13(2):182

Surisetty VVAK, Sahay A, Ramakrishnan R, Samal RN, Rajawat AS (2018) Improved turbidity estimates in complex inland waters using combined NIR–SWIR atmospheric correction approach for Landsat 8 OLI data. Int J Remote Sens 39(21):7463–7482

Tian T, Merico A, Jian S, Staneva J, Wiltshire K, Wirtz K (2009) Importance of resuspended sediment dynamics for the phytoplankton spring bloom in a coastal marine ecosystem. J Sea Res 62(4):214–228

USGS/EROS (2020) Landsat 8–9 Operational Land Imager (OLI)-Thermal Infrared Sensor (TIRS) Collection 2 level 2 (L2) Data Format Control Book (DFCB), Department of the interior, U.S. Geological survey

Xu H (2006) Modification of normalised difference water index (NDWI) to enhance open water features in remotely sensed imagery. Int J Remote Sens 27(14):3025–3033

Zhou Q, Wang J, Tian L, Feng L, Li J, Xing Q (2021) Remotely sensed water turbidity dynamics and its potential driving factors in Wuhan, an urbanizing city of China. J Hydrol 593:125893
Zhou W, Wang S, Zhou Y, Troy A (2006) Mapping the concentrations of total suspended matter in Lake Taihu, China, using Landsat-5 TM data. Int J Remote Sens 27(6):1177–1191

Chapter 9
Water Quality Assessment from Medium Resolution Satellite Data Using Machine Learning Methods

R. Ranith, N. Nandini Menon, K. Ajith Joseph, Chiranjivi Jayaram, and Lasse H. Pettersson

Abstract Primary productivity expressed as the abundance of phytoplankton measured by the chlorophyll-*a* concentration (Chl-*a*), and water clarity in terms of suspended particulate matter, are considered as key indicators defining the water quality of any aquatic system. To maintain the good water quality, it is important to continuously monitor the spatio-temporal variability of these key indicators. Optical satellite remote sensing techniques in the visible spectral range are well known for their cost-effectiveness in estimating the water quality features on sufficient spatial and temporal scale with better radiometry. To overcome that, level 1C images from the multi-spectral instrument (MSI) onboard Sentinel 2 (S2), a medium to high resolution satellite sensor, were used in the present study. Even though there has been a radical improvement in the development of semi-analytical optical algorithms especially using band ratio methods, they need accurate spectral and specific absorption characteristics which are challenging to obtain for many inland water bodies. Machine learning algorithms, on the other hand can statistically derive the spatio-temporal distribution of chlorophyll-a and suspended matter from explicit optical relationships without the complexities of conventional empirical or semi-analytical algorithms. In this study, the best suitable machine learning (ML) algorithm using S2-MSI data to retrieve (Chl-*a*) and total suspended matter (TSM) for tropical lakes and inland waters were identified from the available machine learning models. The ML prediction models were trained using the surface reflectance together with the vegetation and water indices that are sensitive to Chl-*a* and TSM obtained from Sentinel-2 data. In situ Chl-*a* values for validation of the machine learning models were obtained from multiple field surveys conducted along the inland water bodies (Vellar river in Tamilnadu, and Paleru and Karedu inland tributaries of Krishna River

R. Ranith · N. N. Menon · K. A. Joseph
Nansen Environmental Research Centre (India), Kerala University of Fisheries and Ocean Studies Amenity Centre, Panangad, Kochi 682506, India

C. Jayaram (✉)
Regional Remote Sensing Centre—East, NRSC/ISRO, New Town, Kolkata 700156, India
e-mail: chvchiranjivi@hotmail.com

L. H. Pettersson
Nansen Environmental Remote Sensing Centre, Bergen, Norway

C. S. Jha et al. (eds.), *Geospatial Technologies for Resources Planning and Management*, Water Science and Technology Library 115,
https://doi.org/10.1007/978-3-030-98981-1_9

in Andhra Pradesh) and a tropical coastal region (Palk Bay) in the south east coast of India (Palk Bay). From the validation analysis it was evident that Support Vector Machine (SVM) performed better in deriving the Chl-*a* (R2 = 0.81; RMSE = 0.19) and Radom Forest (RF) model performed better in modeling TSM distribution along the studied water bodies (R2 = 0.98; RMSE = 1.46). Validation of ML-based models for optically different water bodies proved the efficiency of the SVM and RF models in estimating the optical constituents in inland water bodies and tropical coastal waters with optical complexities from mixed composition of water constituents. The capability of medium resolution satellite like Sentinel 2 can hence provide means to establish tools to monitor the biophysical conditions of small inland water system effectively when coupled with machine learning methods.

Keywords Water quality · Remote sensing · Sentinel-2 · Machine learning · Chlorophyll-*a* · Suspended matter

9.1 Introduction

About 72% of the earth's surface is occupied by water. Inland water bodies, that cover merely 3% of the terrestrial biome have critical role in the existence of life on earth. Global population depends directly or indirectly on these resources as sources of drinking water, food, irrigation, transportation, recreation etc. Aquatic systems and the world oceans also act as major sinks of atmospheric carbon and hence are very important in regional carbon cycle and climate change (Gattuso et al. 1998). Dramatic increase in population and anthropogenic pressures on the aquatic systems have created unprecedented threat to these ecosystems (Schindler 1987; Meyer et al. 1999). Increased demands in food resources for the growing population have led to intensive farming measures with increased use of fertilizers and pesticides (Nonhebel and Kastner 2011). The nutrient run off from terrestrial regions eventually increases the suspended matter load of the aquatic systems causing eutrophication (Waller and Hart 1986; Rathore et al. 2016; Mamum et al. 2018). Deteriorated water quality not only affects the water security, but also impacts the entire aquatic and marine ecosystem. Combined pressure on the aquatic systems from eutrophication and climate change associated warming events has reportedly increased the frequency and intensity of algal blooms (Lin et al. 2021). The increasing frequency of harmful algal blooms (HAB) worldwide is an example of the complex environmental issues from decreased water quality (Pettersson and Pozdnvakov 2012; Berdalet et al. 2016). Intense bloom events can create anoxic conditions by depleting dissolved oxygen in the water body (Liu et al. 2019). Apart from the ecological loss, HAB events also reportedly cause mass mortality of fish and shell fish resulting in huge economic loss (Hoagland et al. 2002; Park et al. 2013; Reis Costa 2016) and at times jeopardize human health, as some of the blooms are toxic (Su et al. 2019). Therefore, regular water quality monitoring is imperative for sustaining a healthy aquatic ecosystem and community. Here, Chlorophyll-*a* (Chl-*a*), total suspended matter (TSM) and turbidity

are commonly used as the key water quality indicators obtained using remote sensing (Chen et al. 2004). In the present situation of climate change, the in situ point-based sampling method to assess water quality is not efficient enough to explain the quality of water body as a whole (Usali and Ismail 2010). The trophic status of a water body can be assessed systematically only by evaluating the variability in chlorophyll-a, turbidity, total suspended matter and other bio-geo-chemical parameters. Systematic assessment requires information on changes in these parameters at definite temporal and spatial scales, which are challenging to be attained though traditional in situ monitoring methods considering the cost of sampling and effort that need to be invested. Satellite remote sensing is proving to be of increased utility here (Sathyendranath et al. 2020). Synoptic scale estimation of change in water quality using earth observation (EO) tools could lead to standardized water quality measures for a larger region and across national/administrative borders. Research works have recognized the efficient use of EO methods in monitoring variables like water color, Chl-*a*, TSM etc. (Danovaro et al. 2016; Tyler et al. 2016).

Water leaving radiance in the optical and infrared wavelengths (400–900 nm) are best suitable to study the water quality parameters like water transparency, Chl-*a*, TSM etc. (Dekker et al. 2002). Optically active components in water body like Chl-*a*, TSM etc. interact with the penetrated solar radiation in the water column by absorption and scattering based on the characteristic behavior of each constituent (Bukata et al. 2018). Quantitative information on the distribution of optically active components in the water like Chl-*a*, TSM, colored dissolved organic material (CDOM) can be extracted from the water leaving radiance. Earlier, empirical models by regressing in situ measurements of studied variables with that of one of multiple sensor bands were commonly used. This also includes usage of in situ validation observations at various spatial and temporal scales. The application of empirical algorithms in retrieving optically active objects is state of art knowledge. However, being based on empirical algorithms, their usage is limited to specific area or for particular sensors (Matthews 2011). Recent advances in data analytics and hardware sophistication resulted with semi-empirical algorithms like neural networks, which is completely data driven and is much generalized in deriving optically active components from an effective training set and statistical relationship irrespective of the sensor (Ceyhun and Yalcin 2010; Matthews 2011).

Monitoring optically complex systems, especially inland water bodies was difficult since the advent of space research due to the lack of satellite sensors with sufficient number of spectral bands to resolve the different optically active water constituents. Also, the radiometric sensitivity of satellite sensors was low with coarse resolution (Matsushita et al. 2016). One of the most research friendly and easily available satellite data was the Landsat series of satellites by the National Aeronautics and Space Administration (NASA), initially designed for terrestrial mapping. However, Landsat series from 1 to 7 suffered from low radiometric resolution that limited their use in water quality monitoring. First instrument available for the measurement of ocean color was the coastal zone color scanner (CZCS) during the year 1978 (Clark 1981). Later in 1997, sea-viewing wide field-of-view sensor (SeaWiFS) was made available to monitor Chl-*a* and water clarity (Hooker and MClain 2000). Ocean color

monitor (OCM) onboard Indian remote sensing satellite and the moderate resolution imaging spectroradiometer (MODIS) by NASA was introduced by the year 1999 (Carder et al. 2003). Low spectral and spatial resolution of MODIS (nine spectral bands in the visible and near infrared) made it less suitable for inland water body monitoring. Recently with the availability of new satellites like Landsat-8, and the European Sentinel-2, water quality monitoring and mapping has been possible to the inland region due to its higher spatial and temporal resolution than their predecessors.

The Multispectral Imager (MSI) sensor onboard Sentinel 2 has a swath width of 209 km with spatial resolution between 10 and 60 m. Features that make Sentinel 2 distinctly better than the Landsat-8 sensor are the availability of red edge bands, better spatial resolution (10 and 20 m depending on the bands) and a comparatively shorter revisit time and hence a higher temporal resolution (Battude et al. 2016; Forkuor et al. 2018). These features make Sentinel 2-MSI data, the best freely available remotely sensed data for inland and coastal water remote sensing (Drusch et al. 2012). Many studies have been using Sentinel-2 images for monitoring water quality parameters like Chl-*a*, water color, CDOM and DOC for inland water bodies (Toming et al. 2016; Ansper and Alikas 2019; Menon et al. 2021). Commonly used method to retrieve water quality information from remote sensing data for water bodies is the band ratio algorithms using either two, three or four spectral bands (Maytsushita et al. 2016). But recent studies showed that optical data modeling using data driven machine learning methods is efficient in retrieving optical components from case 2 optically complex waters (Peterson et al. 2019).

9.1.1 Machine Learning Approaches

9.1.1.1 Artificial Neural Network (ANN)

Artificial Neural Network (ANN) is the most commonly applied classifier/regressor tools for modeling environmental and natural processes, including water quality monitoring etc., (Singh et al. 2009; Maier et al. 2004). The neural networks are made of three basic layers of data and information called input layer, hidden layer and an output layer comprising nodes. These layers are inter-connected by weights and bias. The number of hidden nodes and hidden layers are important as it imparts non-linear transformations of input datasets. This information is vital for choosing the quantity of hidden nodes and layers, as over usage of these layers in ANN may lead to model overfitting. The input layer comprises input variables while the output variable will have the variable of interest. The input data passes through the hidden layer, which forms the internal structure of ANN. The data will be multiplied and added by weight and bias at each layer. A general structure of the ANN is given in Fig. 9.1.

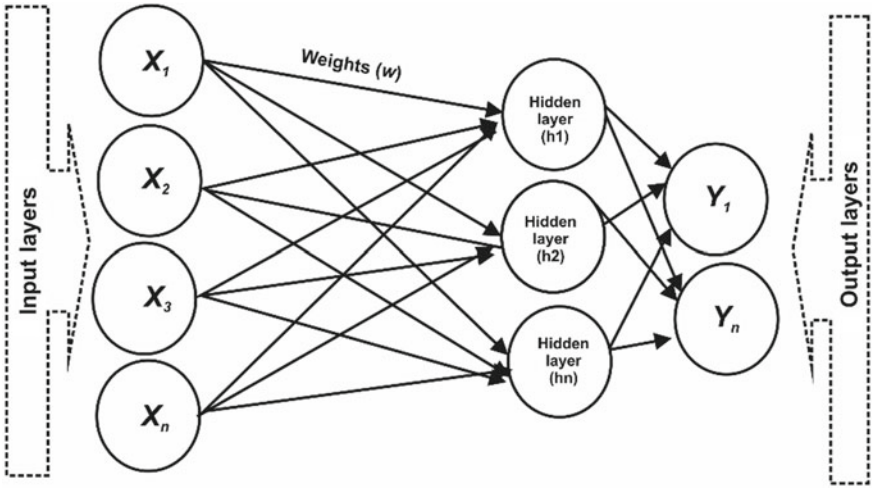

Fig. 9.1 General architecture of ANN adopted in the current study

9.1.1.2 Support Vector Machine Regressor

General applications of support vector machine (SVM) include classification, regression and time series prediction (Thissen et al. 2003; Oomen et al. 2008; Liu et al. 2013). The regression application of SVM is mostly used for continuous variables. The SVR can be expressed through a mathematical equation as:

$$S(Xi) = \sum_{i=1}^{T} Wi\varphi(Xi) + b,$$

where, *Wi* and b are the coefficients obtained after minimizing the error between the network output and target variable. Further, $\varphi(Xi)$ is a non-linear mapping function obtained by the application of a kernel function k (Xi, X) that explains the linear, polynomial and Gaussian radius (Kwon et al. 2018). The SVM regressor will be finally developed using parameters viz., box constraint, epsilon and sigma. Box constraint lets the stringent separation of data by applying a cost to the error. Epsilon adjusts the number of support vectors and sigma is relevant to the model stability. More details on the functioning of support vector machines are detailed by Drucker et al. (1997).

9.1.1.3 XGBOOSTING (Gradient Boosting Algorithm)

Gradient boost belongs to a class of ensemble machine learning models that are applied for classification and regression-based tasks. These ensembles are made out

of decision tree models, where trees are added one at a time to the ensemble and fit, to correct the errors from previous models, called boosting (Chen and Guestrin 2016).

9.1.1.4 Random Forest Model

Random forest model is a multiple decision trees-based ensemble learning method. Random forest regression creates binary splits and multiple regression trees using randomly selected training dataset with a Gini Index. Gini index is calculated by subtracting the sum of squared probabilities of each class from one, that basically explains the degree of probability of wrong variable classification when chosen randomly. Based on which, continuous variables will be predicted in the case of a Random Forest regressor (Breiman 2001). Random Forest regression models are used in multiple studies with satellite derived datasets (Jang et al. 2016).

For illustration of the capability of Sentinel 2 MSI data in retrieving important water quality traits like Chl-*a* and TSM using the machine learning algorithms described above, we present below two case studies:

(a) Water quality traits retrieval from three inland water bodies, viz., Vellar in the state of Tamilnadu, Karedu and Paleru (tributaries of Krishna river) in the state of Andhra Pradesh on the east coast of India.
(b) Water quality traits retrieval from Palk Bay, a coastal waterbody in the state of Tamilnadu on the southeast coast of India.

9.2 Case Studies

9.2.1 Modeling Water Quality Variables Using Machine Learning Methods in the Selected Inland Water Bodies

9.2.1.1 Methodology

In situ sampling was conducted in the Karedu and Paleru waters on January 15th 2020 and in the Vellar waters on May 5th 2020. Corresponding to the field sampling dates, cloud free Sentinel 2 MSI L1C (Level 1 C processed) images were obtained from the ESA Copernicus data hub. If cloud free datasets were not available on our sampling period, satellite images were obtained to the closest days of field survey. The Case-2 Regional Coast Colour processor (C2RCC) package (Doerffer and Schiller, 2007) in the Copernicus SNAP tool box was used to process the ocean optical information from the MSI derived data. The C2RCC processor is based on the radiative transfer modeling of water and the atmospheric vector in the successive order of scattering along with the aerosol optical properties (Lenoble et al. 2007). Water leaving

reflectance after the atmospheric correction from the S2 L1C images is obtained using a set of neural networks for each sensors using band subset. Absorption and scattering coefficients from the water leaving reflectance are obtained from the Inherent Optical properties (IOP) net setup.

For improved computational efficiency, a nearest neighbor re-sampling technique was employed from the 20 m spatial resolution to the 10 m spatial resolution. Vegetation indices and the water indices derived from the water leaving reflectance are reportedly sensitive to chlorophyll-a and TSM respectively, and hence are successful in retrieving the water quality traits (Saberioon et al. 2020). Therefore, to improve the prediction efficiency of the ML models employed in this study, different spectral indices were derived from the C2RCC derived water surface reflectance as shown in Table 9.1. A combination of water reflectance information from eight bands in the visible region (Band 2 to Band 8) of S2 MSI, five spectral indices and three band ratio indices were used in training the four ML models. The spectral indices employed in this study are, NDVI (Normalized Difference Vegetation Index), NDWI (Normalized Difference Water Index), NDTI (Normalized Difference Turbidity Index), SR (Simple Ratio) and SRWC (Simple Ratio Water Colour), Chl-*a* and TSM for random points from the surveyed sites were obtained from the C2RCC processed IOP parameters of S2L1c data as

$\text{Chl} - a = iopapig^{1.04} * 21$ where, iopapig is the pigment absorption.

$\text{TSM} = 1.06 * iopbtot^{0.942}$ where, iopbtot is the total scattering.

Before employing the optical inputs into the ML model training, correlation analysis was done between Chl-*a*, TSM and all 15 optical inputs, in order to understand the significant drivers that could explain the Chl-*a* and TSM distribution. Removal

Table 9.1 Spectral indices derived from the Sentinel 2 MSI bands

Sl. No	Spectral index	Nomenclature in this study	Formula	Definition using sentinel 2 MSI bands
1	NDVI (McFeeters 1996)	NDVI	$\frac{\text{NIR}-\text{Red}}{\text{NIR}+\text{Red}}$	$\frac{B8-B}{B8+B4}$
2	NDWI (McFeeters 1996)	NDWI	$\frac{\text{Green}-\text{NIR}}{\text{Green}+\text{NIR}}$	$\frac{B3-B8}{B3+B8}$
3	NDTI (Lacaux et al. 2007)	NDTI	$\frac{\text{Red}-\text{Green}}{\text{Red}+\text{Green}}$	$\frac{B4-B3}{B4+B3}$
4	SR (Birth and Mc Vey 1968)	SR	$\frac{\text{Red}}{\text{NIR}}$	$\frac{B4}{B8}$
5	SRWC (Zarco-Tejada and Ustin 2001)	SRWC	$\frac{\text{Red}}{\text{Blue}}$	$\frac{B4}{B2}$
6	Band ratio	BR1		$\frac{B3}{B4}$
7	Band ratio	BR2		$\frac{B5}{B4}$
8	Band ratio	BR3		$\frac{B5+B6}{B4}$

Table 9.2 Descriptive statistics of Chl-*a* (mg m^{-3}) from three inland water bodies

Location	Mean	SE	Median	SD	Var	Min	Max	Count	CL (95.0%)
Vellar	0.58	0.006	0.57	0.03	0.001	0.53	0.71	30	0.013
Karedu	0.61	0.003	0.62	0.05	0.002	0.50	0.86	211	0.006
Paleru	0.52	0.004	0.52	0.03	0.001	0.46	0.59	63	0.008

of non-significant optical parameter is presumed to improve the ML models. Correlogram explaining the correlation of Chl-*a* and TSM with S-2 bands, spectral indices, band ratios is shown in Fig. 9.2.

Machine learning models were hence trained for Chl-*a* and TSM prediction using the significant optical inputs alone. While, a total of 15 optical inputs were used in the prediction of Chl-*a* ($p < 0.05$), only 13 optical inputs were found valid for TSM prediction.

Machine learning algorithms were processed using packages neuralnet (Fritsch et al. 2019), random forest (Law and Wiener 2002), XGboost (Chen et al. 2015), caret (Kuhn 2008) and kernlab (Karatzohlou et al. 2004) in the statistical tool R v.4 (R core team 2019). The input data for the model were then randomly grouped into training data (75%) and test data or validation data (25%). All machine learning models were then constructed with the training data and evaluated with the validation datasets.

Cross-validation was used to evaluate the overall performance of each model with the validation data. Chlorophyll-a and TSM concentration were predicted for the validation data using the four constructed ML models. The accuracy of each model was assessed using coefficient of determinant (R2) and RMSE (Root mean squared error). The RMSE value was calculated as, $\mathrm{RMSE} = \sqrt{\frac{1}{n}\sum_{i=1}^{n}(e^2)i}$ where, n is the number of data, *i* represents *i*th Chl-*a*/TSM observation and e_i is the residual observed between modeled and measured Chl-*a*/TSM values.

Descriptive Statistics of Field Recorded Water Quality Traits

Chl-*a* and TSM concentrations obtained from the in-situ sampling, were used to derive the descriptive statistical information like minimum, maximum, mean, standard deviation and coefficient of variation. Inland water bodies as well as the coastal

Fig. 9.2 Correlograms explaining the correlation (r) of Chl-*a* (upper plot) and TSM (lower plot) with S2 MSI bands (8 bands), spectral indices derived from C2RCC processing and band ratios derived (see Table 9.1). Blacked out boxes indicate insignificant correlation at 95% significant level

regions in general have medium to higher chlorophyll and TSM concentration owing to the availability of surplus terrestrial inputs.

9.2.1.2 Results

Since the objective of this case study is to compare the capability of four machine learning methods using sentinel-2/MSI data in deriving Chl-*a* and TSM concentrations efficiently in the optically complex waters, the time series component of the data analysis is not discussed here. Tables 9.2 and 9.3 detail the descriptive statistics of Chl-*a* and TSM from the C2RCC processed datasets. Vellar, Karedu and Paleru water bodies were recorded with mean Chl-*a*; 0.58 ± 0.04 mg m^{-3}, 0.61 ± 0.05 mg m^{-3} and 0.52 ± 0.03 mg m^{-3} and mean TSM values; 28.08 ± 0.22 g m^{-3}, 29.24 ± 0.54 g m^{-3}, 29.47 ± 0.24 g m^{-3}, respectively.

Nine Artificial Neural Networks (ANN) were initially trained using varying configurations of number of nodes and hidden layers. The results of cross validation of the predicted Chl-*a* and TSM values with the validation data are given in Figs. 9.3 and 9.4 respectively.

Match-ups made between the ANN derived predicted Chl-*a* concertation with the validation Chl-*a* data evidenced ANN model 9 configuration (ANN9) to be the best in predicting Chl-*a* with R2 of 0.79. Considering the better performance of ANN9

Table 9.3 Descriptive statistics of TSM (g m^{-3}) from three inland water bodies

Location	Mean	SE	Median	SD	Var	Min	Max	Count	CL (95.0%)
Vellar	28.08	0.07	28.09	0.40	0.16	26.24	28.94	30	0.15
Karedu	29.24	0.04	29.21	0.54	0.30	26.10	31.56	211	0.07
Paleru	29.47	0.03	29.40	0.24	0.06	29.14	30.31	63	0.06

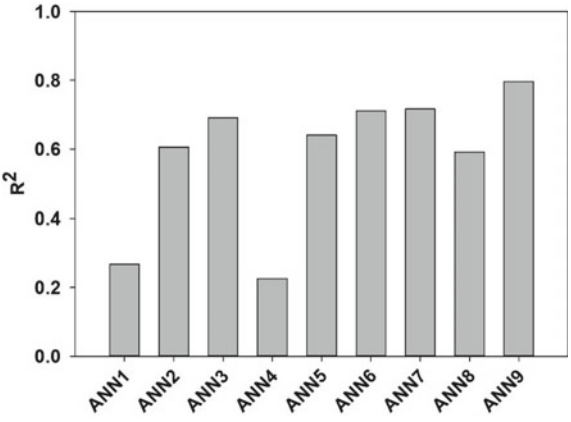

Fig. 9.3 Comparison of multiple Artificial Neural Network (ANN) products to optimize the model with the best prediction capability of Chl-*a*. Bars represent the coefficient of determination (R2) obtained for different ANN models when matched-up between predicted Chl-*a* and Chl-*a* from validation data

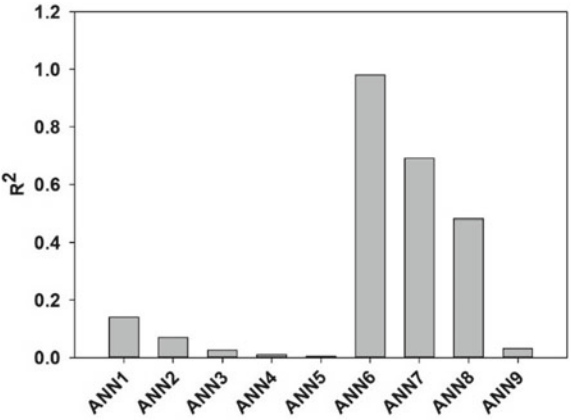

Fig. 9.4 Comparison of multiple ANN products to sort the best model with good prediction capability. Bars represent the coefficient of determination (R2) obtained for different ANN models when matched-up between predicted TSM and TSM from validation data

over other ANN configurations, it was used for the raster prediction and assessment of Chl-*a* parameter.

Similarly, the results from the TSM modeling using nine ANN model configurations showed that the prediction with ANN model 6 (ANN6) gave the best match-up with validation data (R2 = 0.95) as shown in Fig. 9.4. Considering the better performance of ANN6 over other ANN configurations, it was used for the raster prediction and assessment of TSM parameter. It is important to note that the match-up quality of ANN6 in modeling TSM (R2 = 0.95) was better than the that obtained for the Chl-*a* match-up quality of ANN9 (R2 = 0.79). Although both with explained variance of about 80% or above.

Similarly, other ML model methods, SVM, Random Forest and XGboost ML models were also trained to model and assess the concentration of water quality traits. The modeled Chl-*a* and TSM concentrations were then compared with the validation data to assess the performance quality of different ML models evaluated in this study. The performance of different ML models in retrieval of the concentrations of Chl-*a* and TSM as shown in Fig. 9.5.

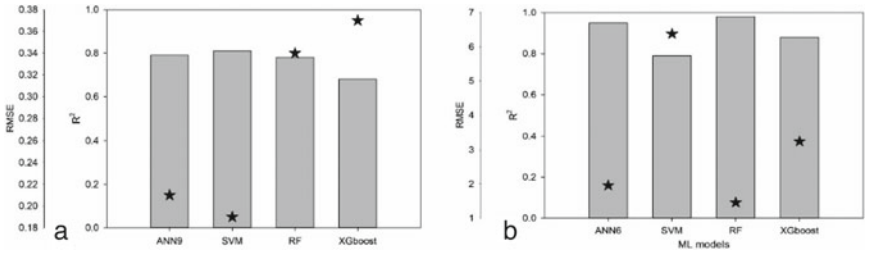

Fig. 9.5 Retrieval capability of different ML models employed for predicting concentrations of Chl-*a* **a** and TSM **b**. Bars represent Coefficient of determination (R2) obtained in the match-up between water quality trait modeled and validation data. '*' represents RMSE obtained

Statistically, the overall performance of SVM model (R2 = 0.81; RMSE = 0.19) and ANN9 model (R2 = 0.79; RMSE = 0.2) were better than RF and XGboost models in predicting Chl-*a*. Whereas, the performance of RF model (R2 = 0.98; RMSE = 1.46) and ANN6 model (R2 = 0.95; RMSE = 1.96) in predicting TSM was better than SVM and XGboost models. Hence, it is evident from the model versus validation data that for optically complex waters of the tropical region like the study area, SVM and ANN9 models outperformed RF and XGboost in modeling Chl-*a*. SVM and XGboost models were outperformed by ANN6 and RF models in predicting TSM concentration.

Spatial Prediction and Validation of Water Quality Traits in Inland Water Bodies with Trained ML Models

The validation done so far has been between the modeled data and the corresponding satellite data retrieval of Chl-*a* and TSM concentrations, respectively. It is also important to compare the performance of the trained ML models to predict the spatial distribution of water quality traits. All the four ML models for Chl-*a* and TSM were applied to the S2 MSI raster images (input spectral variables as given in Table 9.1) of the study areas to derive the spatial distribution of water quality traits. Chl-*a* and TSM concentrations were then extracted from the spatially modeled maps for the corresponding in situ sampling validation locations. Figures 9.6, 9.7 and 9.8 show the Chl-*a* spatial distribution map developed for sampling locations.

For Vellar river, SVM model outperformed statistically the other ML models in accurately predicting Chl-*a* distribution with R2 = 0.9, RMSE = 0.01. The performance was followed by that of RF (R2 = 0.88, RMSE = 0.012), ANN9 (R2 = 0.85, RMSE = 0.019) and XGboost (R2 = 0.67, RMSE = 0.028) models.

For Karedu river, SVM model outperformed other ML models in accurately predicting Chl-*a* distribution with R2 = 0.92, RMSE = 0.013. The modeling quality of SVM was followed by that of ANN9 (R2 = 0.83, RMSE = 0.02), RF (R2 = 0.78, RMSE = 0.023) and XGboost (R2 = 0.63, RMSE = 0.038) models.

For Paleru river, SVM model outperformed other Ml models in accurately predicting Chl-a distribution with R2 = 0.82, RMSE = 0.05. The modeling quality of SVM was followed by ANN9 (R2 = 0.72, RMSE = 0.06), RF (R2 = 0.62, RMSE = 0.06) and XGboost (R2 = 0.16, RMSE = 1.25) models.

Similarly, as discussed above, Figs. 9.9, 9.10 and 9.11 represent the spatial distribution maps of TSM, modeled using the ML models for the three inland water bodies.

For Vellar river, RF model outperformed other ML models in accurately predicting TSM distribution with R2 = 0.84, RMSE = 0.64. The modeling quality of RF was followed by that of SVM (R2 = 0.66, RMSE = 1.4), XGboost (R2 = 0.52, RMSE = 1.85) and ANN6(R2 = 0.52, RMSE = 1.92) models.

For Karedu river, RF model outperformed other ML models in accurately predicting TSM distribution with R2 = 0.98, RMSE = 0.09. The modeling quality

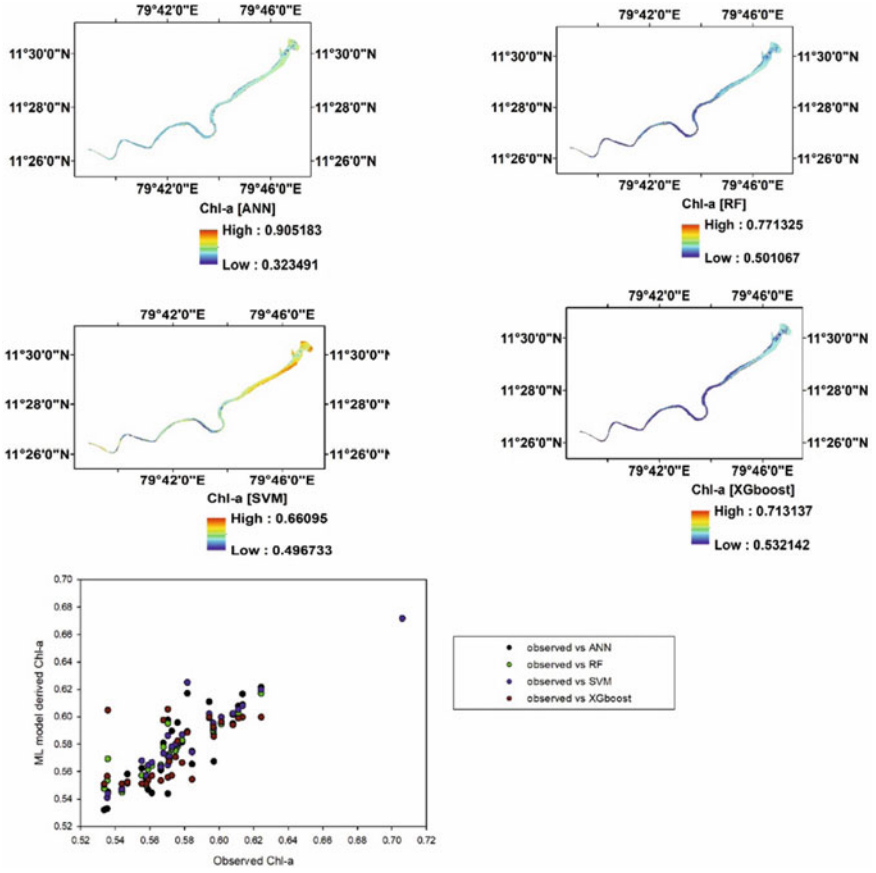

Fig. 9.6 Maps of the Spatial distribution of Chl-*a* using the respective ML models (ANN9, RF, SVM and XGboost from upper left) along Vellar river. The S2 MSI data processed are from date 05.05.2020. Scatter plot represents the matchup between observed Chl-*a* and ML modeled Chl-*a* for the 30 validation points sampled on the same day

of RF was followed by that of ANN6 (R2 = 0.88, RMSE = 0.31), XGboost (R2 = 0.88, RMSE = 0.31) and SVM (R2 = 0.44, RMSE = 1.07) models.

For Paleru river, RF model outperformed other ML models in accurately predicting TSM distribution with R2 = 0.88, RMSE = 0.24. The modeling quality of RF was followed by that of ANN6 (R2 = 0.83, RMSE = 0.31), XGboost (R2 = 0.81, RMSE = 0.35) and SVM (R2 = 0.65, RMSE = 0.67) models.

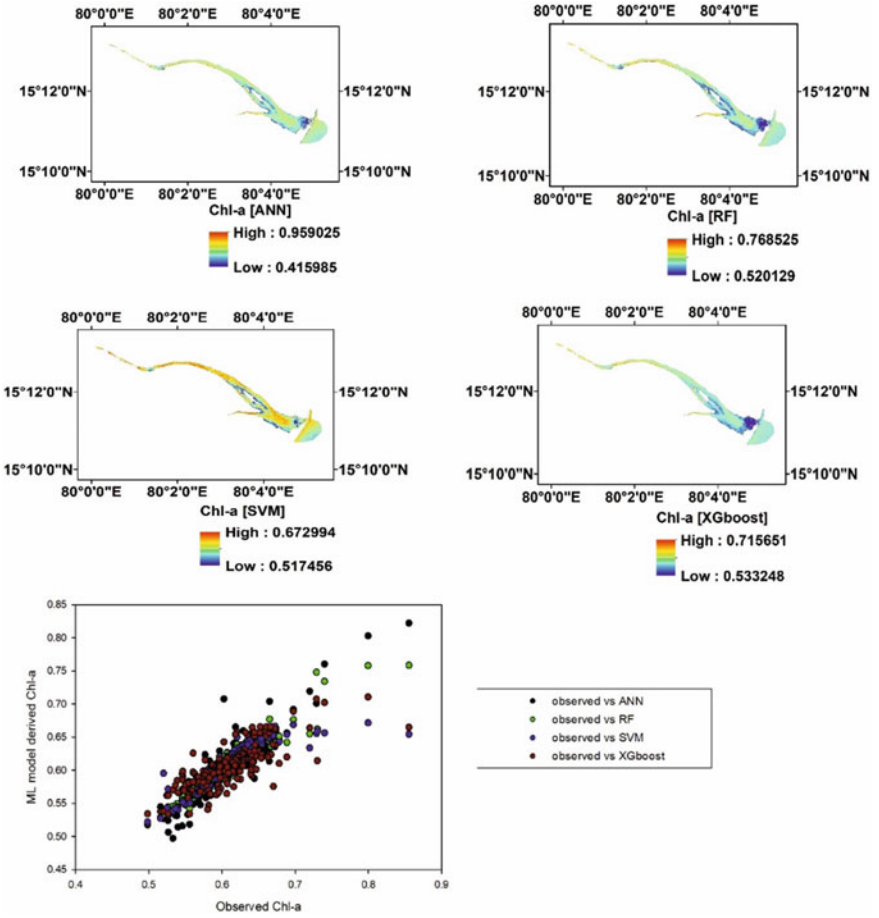

Fig. 9.7 Maps of the Spatial distribution of Chl-*a* using the respective ML models (ANN9, RF, SVM and XGboost from upper left) along Karedu river. The S2 MSI data processed are from date 16.01.2020. Scatter plot represents the matchup between observed Chl-*a* and ML modeled Chl-*a* for the 140 validation points sampled on the same day

9.2.2 Modeling Water Quality Traits Using Machine Learning Methods in the Coastal Waters of Palk Bay

In situ sampling at Palk Bay region was done on May 15th 2020. The modeling and validation approach adopted is described in the Sect. 2.1.1. Based on the results described in Sect. 2.1.2, Artificial Neural Networks (ANN) 9 and 6 were used in the spatial prediction of Chl-*a* and TSM respectively along with the other three ML models; RF, SVM and XG boost.

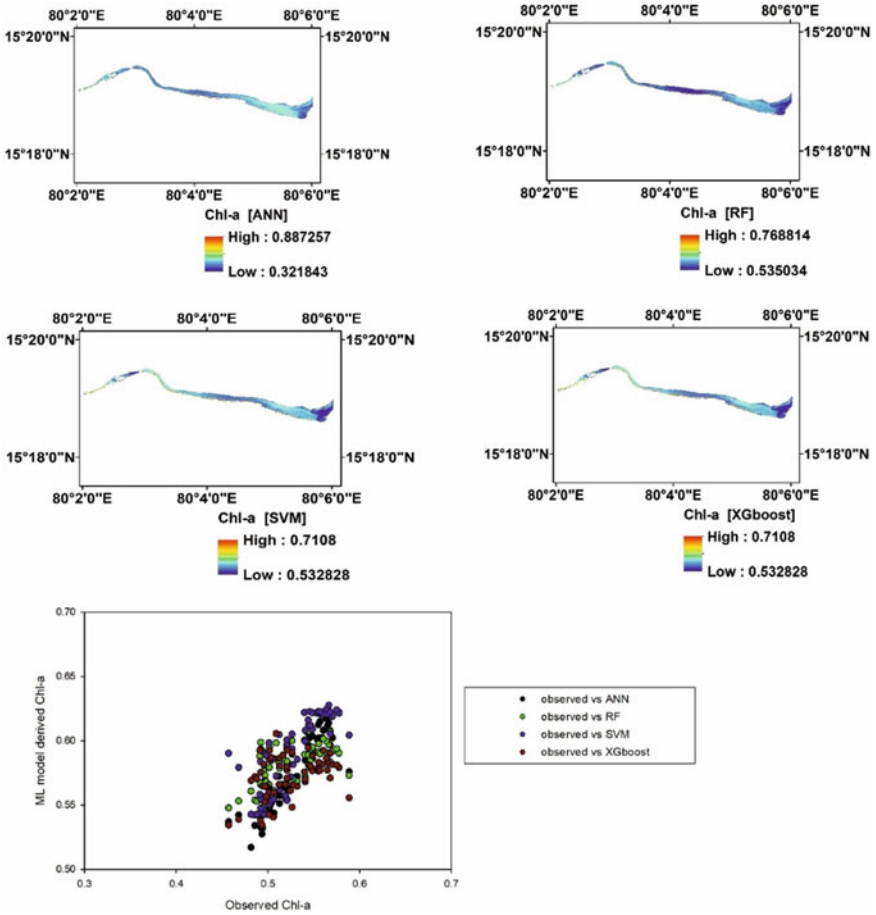

Fig. 9.8 Maps of the Spatial distribution of Chl-*a* using the respective ML models (ANN9, RF, SVM and XGboost from upper left) along Paleru river. The S2 MSI data processed are from date 16.01.2020. Scatter plot represents the matchup between observed Chl-*a* and ML modeled Chl-*a* for the 64 validation points sampled on the same day

9.2.2.1 Results

This section details the description of in situ Chl-*a* and TSM values recorded from the field sampling and the results from the spatial prediction model, assessment and validation of Chl-*a* and TSM from the four ML models trained with spatial spectral inputs as mentioned in Table 9.1.

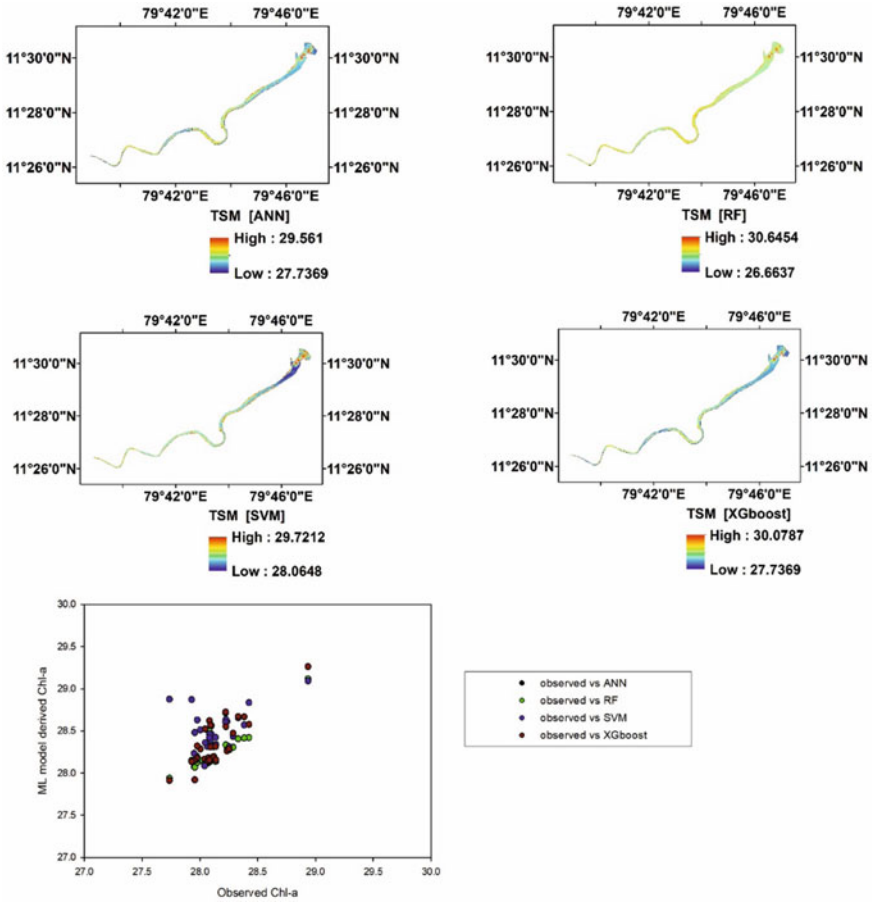

Fig. 9.9 Maps of the Spatial distribution of TSM using the respective ML models (ANN6, RF, SVM and XGboost from upper left) along Vellar river. The S2 MSI data processed are from the date 05.05.2020. Scatter plot represents the matchup between observed TSM and ML modeled TSM for the 30 validation points sampled on the same day

Descriptive Statistics

Palk Bay coastal region was recorded with mean Chl-*a*; 0.54 ± 0.04 mg m^{-3}, mean TSM value; 28.8 ± 0.02 g m^{-3} respectively (Table 9.4).

Spatial Prediction and Validation of Water Quality Traits in Coastal Water Body with Trained ML Models

Figures 9.12 and 9.13 illustrate the Chl-*a* and TSM spatial distribution as modeled using the four selected ML models for Palk Bay region, respectively. For Chl-*a*

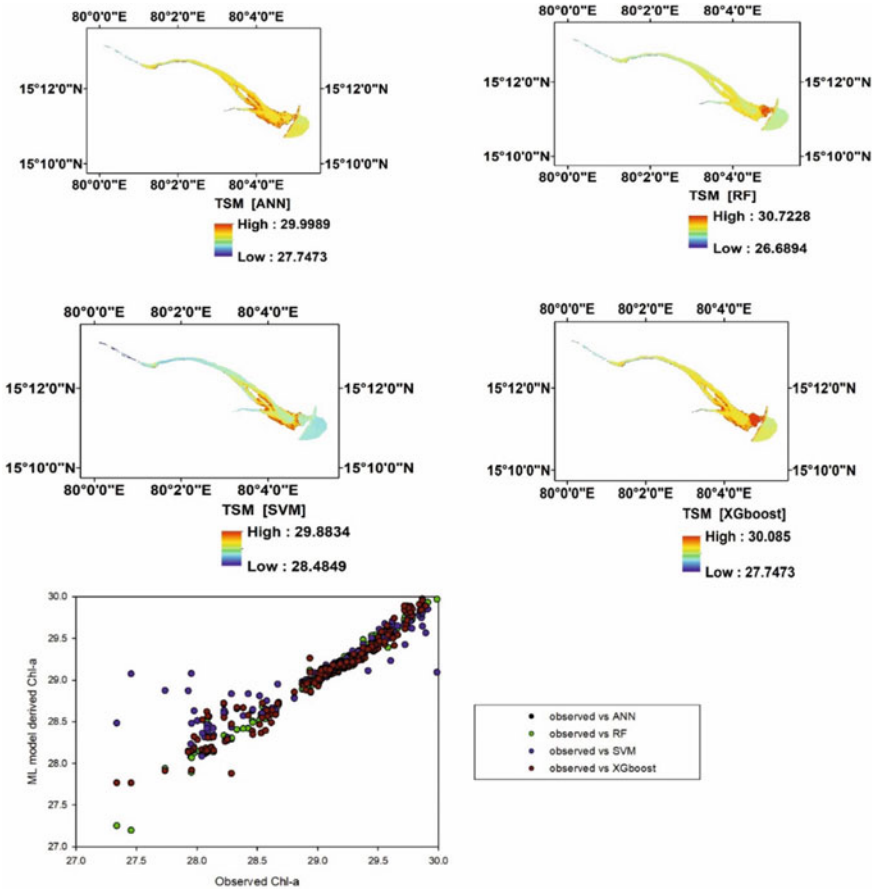

Fig. 9.10 Maps of the Spatial distribution of TSM using the respective ML models (ANN6, RF, SVM and XGboost from upper left) along Karedu river. The S2 MSI data processed are from date 16.01.2020. Scatter plot represents the matchup between observed TSM and ML modeled TSM for the 140 validation points sampled on the same day

prediction, the SVM model outperformed other Ml models in accurately predicting Chl-*a* distribution with R2 = 0.89, RMSE = 0.013. The modeling quality of SVM was followed by that of ANN9 (R2 = 0.83, RMSE = 0.017), RF (R2 = 0.81, RMSE = 0.0) and XGboost (R2 = 0.89, RMSE = 0.302) models.

For TSM prediction, RF model outperformed other ML models in accurately predicting TSM distribution with R2 = 0.92, RMSE = 0.6. The modeling quality of RF was followed by ANN6 (R2 = 0.83, RMSE = 1.2), XGboost (R2 = 0.82, RMSE = 1.2) and SVM (R2 = 0.63, RMSE = 2.41) models.

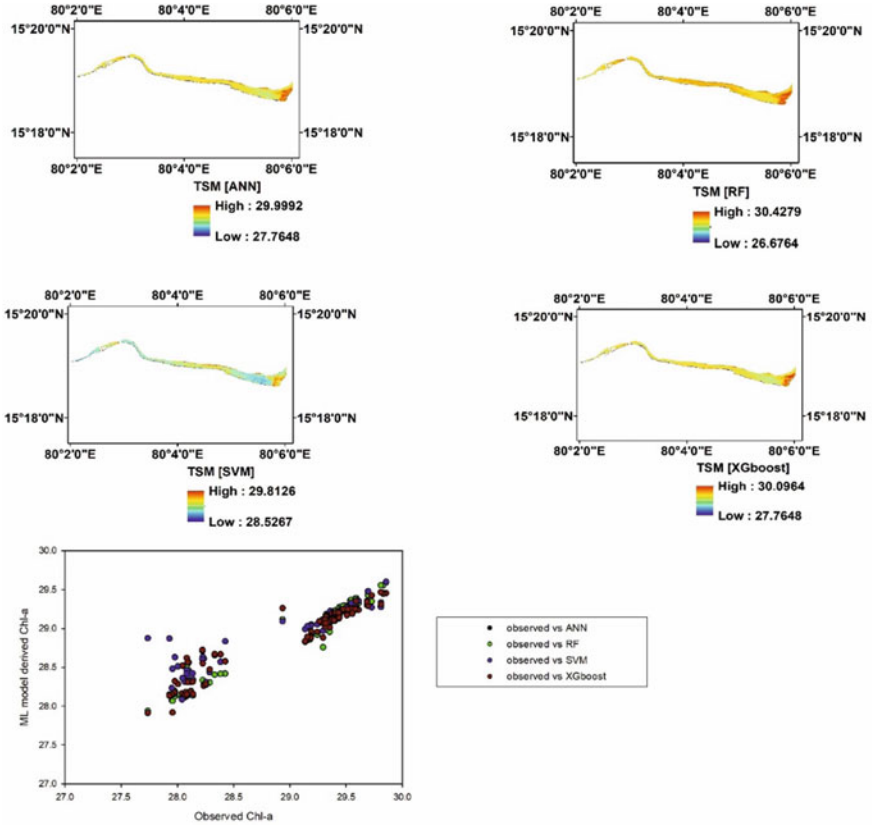

Fig. 9.11 Maps of the Spatial distribution of TSM using the respective ML models (ANN6, RF, SVM and XGboost from upper left) along Paleru river. The S2 MSI data processed are from date 16.01.2020. Scatter plot represents the matchup between observed TSM and ML modeled TSM for the 64 validation points sampled on the same day

Table 9.4 Descriptive statistics of Chl-*a* (mg m^{-3}) from sampling location

Parameter	Location	Mean	SE	Median	SD	Var	Min	Max	Count	CL (95.0%)
Chl-*a*	Palk Bay	0.54	0.004	0.54	0.04	0.002	0.48	0.65	86	0.008
TSM	Palk Bay	28.80	0.02	28.82	0.22	0.05	28.23	29.48	86	0.05

9.3 Discussion

The assessment of the different ML model, spatial mapping and statistical validation results obtained from the present study showed that Sentinel-2 MSI data can efficiently and quantitatively predict the spatial distribution of the water quality traits like

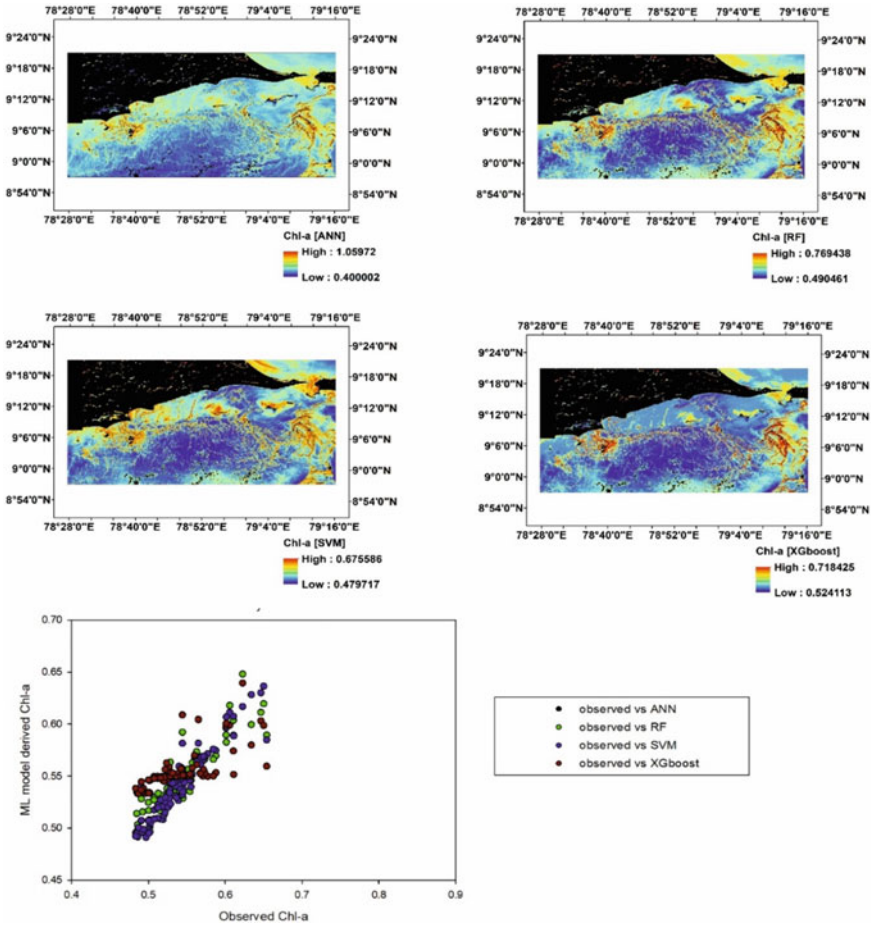

Fig. 9.12 Maps of the Spatial distribution of Chl-*a* using the respective ML models (ANN9, RF, SVM and XGboost from upper left) along Palk Bay. The S2 MSI data processed are from date 15.05.2021. Scatter plot represents the matchup between observed Chl-*a* and ML modeled Chl-*a* for the 87 validation points sampled on the same day

Chl-*a* and TSM in optically complex tropical coastal waters as well as from inland water bodies. The performance of ML algorithms combined with Sentinel-2 MSI data was successful in the spatial modeling of Chl-*a* and TSM with good statistical significance. After an initial statistical screening of nine ANN ML-configurations, the various ML models showed consistent and statistically robust results. Though there are reports on usage of in situ parameters like salinity, pH along with spectral bands in ML modeling (Kupssinsku et al. 2020), our case studies show that ML modeling of Chl-*a* and TSM with better accuracy is possible by considering the interactions of optical properties alone, that can be freely procured from satellites like Sentinel-2 and Landsat-8.

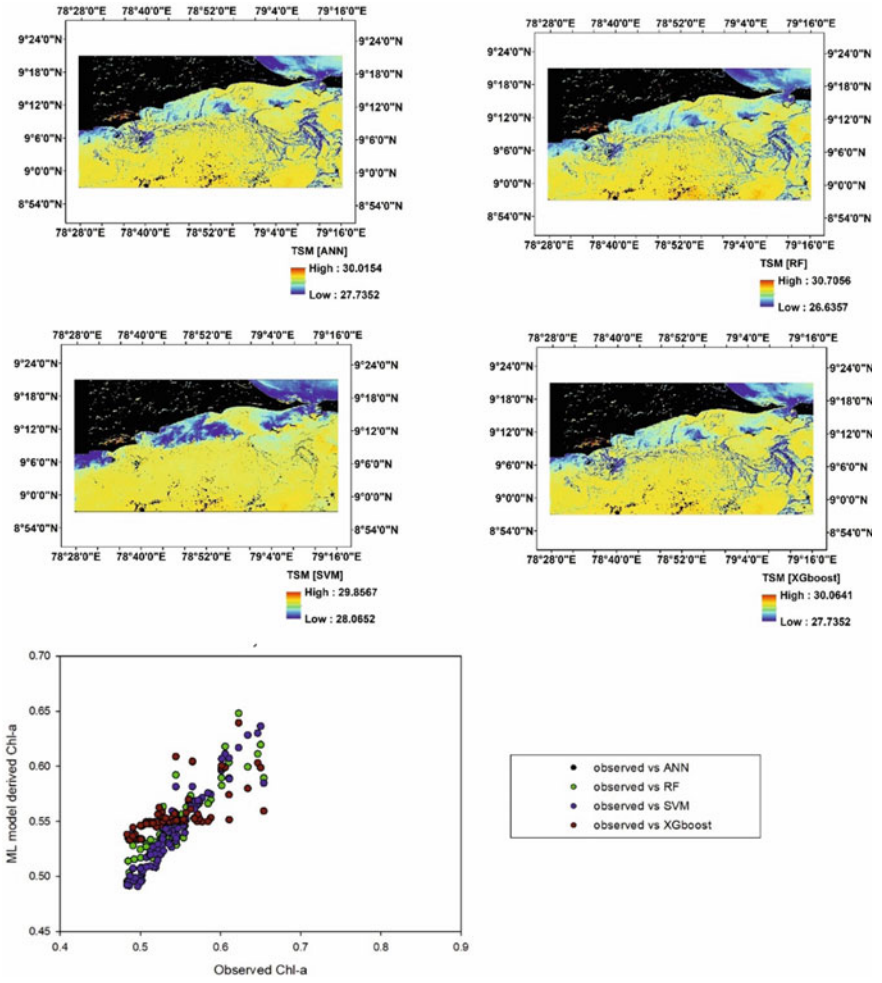

Fig. 9.13 Maps of the Spatial distribution of TSM using the respective ML models (ANN9, RF, SVM and XGboost from upper left) along Palk Bay. The S2 MSI data processed are from date 15.05.2021. Scatter plot represents the matchup between observed TSM and ML modeled TSM for the 87 validation points sampled on the same day

The study has conclusively demonstrated that SVM regressor model shows the best performance in modeling the spatial distribution of Chl-*a* in both the coastal as well as the three inland water bodies. Consistency of SVM in modeling Chl-*a* with better accuracy as observed from the case study suggests the use of SVM model under model conditions from this case study, to retrieve the chl-*a* concentrations of similar optically complex coastal and inland water bodies. Similarly, the consistent performance of RF model in retrieving the spatial distribution of TSM both in inland and coastal waters exhibits the model's capability in predicting TSM across optically

complex and inland waters. No earlier published studies are available from these areas on the same aspect to compare the present results. Quality of ML algorithms, especially for optically complex regions largely depends on the quality of the data, which in turn depends on location, weather, size of sample set, regional optical complexity and environmental conditions (Uudeberg et al. 2019; Kupssinsku et al. 2020). Hence, comparing results from the present study with other ML models from other global regions may not be feasible.

Even though, machine learning models are reportedly susceptible to dimensionality and over fitting errors, selection of most suitable input parameters and cross-validation are reported to be the best practices in ML modeling (Kuhn and Johnson 2013; Domingos 2012). The statistical correlation analysis in the present study was performed to assess the quality of the different ML models for both the studied water quality traits. It is therefore suggested that, adopting this ML scheme for predicting water quality traits in other regions requires an initial validation check for their regional response of input variables with the water quality traits. This is a case study that explains the performance capability of ML models when combined with open access Sentinel 2 MSI data with high spatio-temporal resolution. Machine learning algorithms with remote sensing data are universal prediction models that reportedly will allow to use any spectral bands and any spectral ratios from satellite remote sensing data (Singh et al. 2009; Saberioon et al. 2020). Hence, there are still ways to extend the research activities to improve the water quality trait modeling capability. In our case study, we have assessed the four most commonly used and widely accepted machine learning models and got statistically significant and consistent results. Other machine learning models can also be applied and assessed with the same set of input datasets used in the case study to understand the quality and performance of other ML models in retrieving water quality traits. More spectral indices and band ratio combinations can be modeled and cross-validated for better understanding of water quality retrieval of optically complex water using Sentinel-2 MSI data. As already mentioned, this study does not deal with temporal trend or variability of water quality traits. There is still room for improving the quality of ML algorithms by considering the seasonality and seasonal variability in the relationship between potential input variables and water quality traits. Because the ML algorithms are fully data driven methods to work on complex data, it can be applied to other tropical and inland waters of India or other countries that have similar terrestrial and atmospheric conditions.

With the influence of a changing climate and increased pollution and anthropogenic loads on water quality in inland and coastal waters upon which millions of people depend for their livelihood and drinking water, studies employing high resolution satellite data and ML methods that help to accurately assess the water quality are gaining importance. Such advancements in science are significant in our efforts to address the United Nations Sustainable Development Goals, especially SDG 6 (target 6.3 to improve ambient water quality) and SDG 14 (life below water).

9.4 Conclusion

Machine learning models being fully data driven, turn out to be more suitable for retrievals in optically complex waters (so called case 2 waters) compared to the empirical models, where more a priori knowledge of the optical water complexity is needed. The case study has assessed four commonly accepted ML models (ANN, SVM, RF, XGboost) to retrieve two major water quality traits for three inland rivers and a coastal system in India. In situ data from the locations plus the corresponding Sentinel 2 MSI datasets were respectively used in training and validation of the ML modeling. From the study, it was evident that irrespective of the region (coastal and inland waters), machine learning models could model Chl-*a* and TSM spatial distribution with consistent accuracy, however with some differences in the actual ML model performance for the two studied water quality traits. This type of applications of ML model opens a window to use the many data driven methods available for modeling and assessing water quality conditions and to improve the overall accuracy in complex water bodies. Further research is necessary to improve the knowledge in existing spectral relationship and efficiency of different ML algorithms for various regions with proper validation over longer periods with consecutive available validation data.

Acknowledgements The authors would like to put on record their immense gratitude to the European Space Agency (ESA) for making the Sentinel-2/MSI data freely available. All the participants of the field campaigns are sincerely thanked for their cooperation during the data collection. Authors RR, AJK, NN and LHP acknowledge the financial and infrastructural support provided by Nansen Environmental Remote Sensing Center, Norway and Nansen Environmental Research Centre (India). CJ thanks the General Manager, RRSC-East, Chief General Manager, RCs, NRSC, for their support and encouragement during this work.

References

Ansper A, Alikas K (2019) Retrieval of chlorophyll a from Sentinel-2 MSI data for the European Union water framework directive reporting purposes. Remote Sens 11(1):64

Battude M, Al Bitar A, Morin D, Cros J, Huc M, Sicre (2016) Estimating maize biomass and yield over large areas using high spatial and temporal resolution Sentinel-2 like remote sensing data. Remote Sens Environ 184:668–681

Berdalet E, Fleming LE, Gowen R, Davidson K, Hess P, Backer LC, Enevoldsen H (2016) Marine harmful algal blooms, human health and wellbeing: challenges and opportunities in the 21st century. J Mar Biol Assoc UK 96(1):61–91

Birth GS, McVey GR (1968) Measuring the color of growing turf with a reflectance spectrophotometer. Agron J 60(6):640–643

Breiman L (2001) Random forests. Mach Learn 45(1):5–32

Bukata RP, Jerome JH, Kondratyev KY, Pozdnyakov DV (2018) Optical properties and remote sensing of inland and coastal waters. CRC Press

Carder KL, Chen FR, Lee Z, Hawes SK, Cannizzaro JP (2003) MODIS ocean science team algorithm theoretical basis document. ATBD, 19(Version 7), 7–18

Ceyhun Ö, Yalçın A (2010) Remote sensing of water depths in shallow waters via artificial neural networks. Estuar Coast Shelf Sci 89(1):89–96
Chen T, Guestrin C (2016) Xgboost: a scalable tree boosting system. In; Proceedings of the 22nd acm sigkdd international conference on knowledge discovery and data mining, pp 785–794
Chen T, He T, Benesty M, Khotilovich V, Tang Y, Cho H (2015) Xgboost: extreme gradient boosting. R package version 0.4–2, 1(4):1–4
Chen X, Li YS, Liu Z, Yin K, Li Z, Wai OW, King B (2004) Integration of multi-source data for water quality classification in the Pearl River estuary and its adjacent coastal waters of Hong Kong. Cont Shelf Res 24(16):1827–1843
Clark DK (1981) Phytoplankton pigment algorithms for the Nimbus-7 CZCS. In: Oceanography from space. Springer, Boston, MA, pp 227–237
Danovaro R, Carugati L, Berzano M, Cahill AE, Carvalho S, Chenuil A (2016) Implementing and innovating marine monitoring approaches for assessing marine environmental status. Front Mar Sci 3:213
Dekker AG, Vos RJ, Peters SWM (2002) Analytical algorithms for lake water TSM estimation for retrospective analyses of TM and SPOT sensor data. Int J Remote Sens 23(1):15–35
Doerffer R, Schiller H (2007) The MERIS Case 2 water algorithm. Int J Remote Sens 28(3–4):517–535
Domingos P (2012) A few useful things to know about machine learning. Commun ACM 55(10):78–87
Drucker H, Burges CJ, Kaufman L, Smola A, Vapnik V (1997) Support vector regression machines. Adv Neural Inf Process Syst 9:155–161
Drusch M, Del Bello U, Carlier S, Colin O, Fernandez V, Gascon F (2012) Sentinel-2: ESA's optical high-resolution mission for GMES operational services. Remote Sens Environ 120:25–36
Forkuor G, Dimobe K, Serme I, Tondoh JE (2018) Landsat-8 vs. Sentinel-2: examining the added value of sentinel-2's red-edge bands to land-use and land-cover mapping in Burkina Faso. GISci Remote Sens 55(3):331–354
Fritsch S, Guenther F, Guenther MF (2019) Package 'neuralnet'. Train Neural Netw
Gattuso JP, Frankignoulle M, Wollast R (1998) Carbon and carbonate metabolism in coastal aquatic ecosystems. Annu Rev Ecol Syst 29(1):405–434
Hoagland PADM, Anderson DM, Kaoru Y, White AW (2002) The economic effects of harmful algal blooms in the United States: estimates, assessment issues, and information needs. Estuaries 25(4):819–837
Hooker SB, McClain CR (2000) The calibration and validation of SeaWiFS data. Prog Oceanogr 45(3–4):427–465
Jang E, Im J, Ha S, Lee S, Park YG (2016) Estimation of water quality index for coastal areas in Korea using GOCI satellite data based on machine learning approaches. Korean J Remote Sens 32(3):221–234
Karatzoglou A, Smola A, Hornik K, Zeileis A (2004) kernlab-an S4 package for kernel methods in R. J Stat Softw 11(9):1–20
Kuhn M (2008) Building predictive models in R using the caret package. J Stat Softw 28(1):1–26
Kuhn M, Johnson K (2013) Applied predictive modeling, vol 26. Springer, New York, p 13
Kupssinskü LS, Guimaraes TT, De Souza EM, Zanotta DC, Veronez MR, Gonzaga Jr L, Mauad FF (2020) A method for chlorophyll-a and suspended solids prediction through remote sensing and machine learning. Sensors (Basel, Switzerland) 20(7)
Kwon YS, Baek SH, Lim YK, Pyo J, Ligaray M, Park Y, Cho KH (2018) Monitoring coastal chlorophyll-a concentrations in coastal areas using machine learning models. Water 10(8):1020
Lacaux JP, Tourre YM, Vignolles C, Ndione JA, Lafaye M (2007) Classification of ponds from high-spatial resolution remote sensing: Application to Rift Valley Fever epidemics in Senegal. Remote Sens Environ 106(1):66–74
Lenoble J, Herman M, Deuzé JL, Lafrance B, Santer R, Tanré D (2007) A successive order of scattering code for solving the vector equation of transfer in the earth's atmosphere with aerosols. J Quant Spectrosc Radiat Transfer 107(3):479–507

Liaw A, Wiener M (2002) Classification and regression by randomForest. R News 2(3):18–22
Lin Q, Zhang K, McGowan S, Capo E, Shen J (2021) Synergistic impacts of nutrient enrichment and climate change on long-term water quality and ecological dynamics in contrasting shallow-lake zones. Limnol Oceanogr 66(9):3271–3286
Liu S, Tai H, Ding Q, Li D, Xu L, Wei Y (2013) A hybrid approach of support vector regression with genetic algorithm optimization for aquaculture water quality prediction. Math Comput Model 58(3–4):458–465
Liu XQ, Huang TL, Li N, Yang SY, Li Y, Xu J, Wang HY (2019) Algal bloom and mechanism of hypoxia in the metalimnion of the Lijiahe Reservoir during thermal stratification. Huan jing ke xue= Huanjing kexue 40(5):2258–2264
Maier HR, Morgan N, Chow CW (2004) Use of artificial neural networks for predicting optimal alum doses and treated water quality parameters. Environ Model Softw 19(5):485–494
Mamun M, Lee SJ, An KG (2018) Temporal and spatial variation of nutrients, suspended solids, and chlorophyll in Yeongsan watershed. J Asia-Pacific Biodivers 11(2):206–216
McFeeters SK (1996) The use of the Normalized Difference Water Index (NDWI) in the delineation of open water features. Int J Remote Sens 17(7):1425–1432
Matsushita B, Yang W, Jaelani LM, Setiawan F, Fukushima T (2016) Monitoring water quality with remote sensing image data. Remote Sens Sustain, 163–189
Matthews MW (2011) A current review of empirical procedures of remote sensing in inland and near-coastal transitional waters. Int J Remote Sens 32(21):6855–6899
Menon N, George G, Ranith R, Sajin V, Murali S, Abdulaziz A et al (2021) Citizen science tools reveal changes in estuarine water quality following demolition of buildings. Remote Sens 13(9):1683
Meyer JL, Sale MJ, Mulholland PJ, Poff NL (1999) Impacts of climate change on aquatic ecosystem functioning and health 1. JAWRA J Am Water Resour Assoc 35(6):1373–1386
Nonhebel S, Kastner T (2011) Changing demand for food, livestock feed and biofuels in the past and in the near future. Livest Sci 139(1–2):3–10
Oommen T, Misra D, Twarakavi NK, Prakash A, Sahoo B, Bandopadhyay S (2008) An objective analysis of support vector machine based classification for remote sensing. Math Geosci 40(4):409–424
Park TG, Lim WA, Park YT, Lee CK, Jeong HJ (2013) Economic impact, management and mitigation of red tides in Korea. Harmful Algae 30:S131–S143
Peterson KT, Sagan V, Sidike P, Hasenmueller EA, Sloan JJ, Knouft JH (2019) Machine learning-based ensemble prediction of water-quality variables using feature-level and decision-level fusion with proximal remote sensing. Photogramm Eng Remote Sens 85(4):269–280
Rathore SS, Chandravanshi P, Chandravanshi A, Jaiswal K (2016) Eutrophication: impacts of excess nutrient inputs on aquatic ecosystem. IOSR J Agric Vet Sci 9(10):89–96
Reis Costa P (2016) Impact and effects of paralytic shellfish poisoning toxins derived from harmful algal blooms to marine fish. Fish Fish 17(1):226–248
Saberioon M, Brom J, Nedbal V, Souček P, Císař P (2020) Chlorophyll-a and total suspended solids retrieval and mapping using Sentinel-2A and machine learning for inland waters. Ecol Ind 113:106236
Sathyendranath S, Abdulaziz A, Menon N, George G, Evers-King H, Kulk G et al (2020) Building capacity and resilience against diseases transmitted via water under climate perturbations and extreme weather stress. In: Ferretti S (ed) Space Capacity Building in the XXI Century, pp 281–298
Schindler DW (1987) Detecting ecosystem responses to anthropogenic stress. Can J Fish Aquat Sci 44(S1):s6–s25
Singh KP, Basant A, Malik A, Jain G (2009) Artificial neural network modeling of the river water quality—a case study. Ecol Model 220(6):888–895
Su RC, Blomquist TM, Kleinhenz AL, Khalaf FK, Dube P, Lad A et al (2019) Exposure to the harmful algal bloom (HAB) toxin microcystin-LR (MC-LR) prolongs and increases severity of dextran sulfate sodium (DSS)-induced colitis. Toxins 11(6):371

Thissen UVBR, Van Brakel R, De Weijer AP, Melssen WJ, Buydens LMC (2003) Using support vector machines for time series prediction. Chemom Intell Lab Syst 69(1–2):35–49

Toming K, Kutser T, Laas A, Sepp M, Paavel B, Nõges T (2016) First experiences in mapping lake water quality parameters with Sentinel-2 MSI imagery. Remote Sens 8(8):640

Tyler AN, Hunter PD, Spyrakos E, Groom S, Constantinescu AM, Kitchen J (2016) Developments in Earth observation for the assessment and monitoring of inland, transitional, coastal and shelf-sea waters. Sci Total Environ 572:1307–1321

Usali N, Ismail MH (2010) Use of remote sensing and GIS in monitoring water quality. J Sustain Dev 3(3):228

Uudeberg K, Ansko I, Põru G, Ansper A, Reinart A (2019) Using optical water types to monitor changes in optically complex inland and coastal waters. Remote Sens 11(19):2297

Waller DH, Hart WC (1986) Solids, nutrients, and chlorides in urban runoff. In: Urban runoff pollution. Springer, Berlin, Heidelberg, pp 59–85

Zarco-Tejada PJ, Ustin SL (2001) Modeling canopy water content for carbon estimates from MODIS data at land EOS validation sites. In IGARSS 2001. Scanning the Present and Resolving the Future. Proceedings. IEEE 2001 International Geoscience and Remote Sensing Symposium (Cat. No. 01CH37217) (Vol. 1, pp. 342–344). IEEE.

Chapter 10
Crop Classification in the Mixed Cropping Environment Using SAR Data and Machine Learning Algorithms

Akash Goyal, Mohit Kesarwani, N. Neeti, S. Maity, K. Mukesh, V. M. Chowdary, B. Bimal, and C. S. Jha

Abstract Timely preparation of crop inventory is required to ensure food security in the region. Conventional methods of crop inventory are time-consuming and costly. The state-of-art of remote sensing plays vital role in the generation of pre-harvest crop inventory. Optical remote sensing is typically used for crop mapping. However, optical remote sensors face serious limitations due to cloud cover, especially in tropical regions, where Synthetic Aperture Radar (SAR) remote sensors can overcome this limitation with their cloud penetration capability. Traditionally, crop mapping is carried out using conventional parametric classification approaches that require several assumptions about the dataset. With the advent of advanced non-parametric techniques such as machine learning algorithms, it is possible to model non-linear relationships among variables to identify the pattern in the data. These algorithms are considered to be more powerful and known to have higher accuracy compared to traditional approaches. Specifically, time-series remotely sensed (both optical and SAR) data are used for crop mapping by capturing key phenological crop stages that differ for each crop type. In this study, *kharif* (monsoon) maize crop classification was carried out for a case study area, Kannauj district using time-series Sentinel 1 data, machine learning algorithms (Decision Tree, Support Vector Machine, Random Forest), and traditional classifier, i.e., maximum likelihood approach. Analysis indicated that out of all the three machine learning algorithms, Random Forest performed better for crop mapping during *kharif* season.

A. Goyal (✉)
Regional Remote Sensing Centre-North, New Delhi, India
e-mail: akash_g@nrsc.gov.in

M. Kesarwani · N. Neeti
Department of Natural Resources, TERI School of Advanced Studies, Delhi, India

S. Maity · K. Mukesh · B. Bimal
Space Applications Centre, Ahmedabad, India

V. M. Chowdary
Mahalanobis National Crop Forecast Centre, New Delhi, India

C. S. Jha
National Remote Sensing Centre, Hyderabad, India

C. S. Jha et al. (eds.), *Geospatial Technologies for Resources Planning and Management*, Water Science and Technology Library 115,
https://doi.org/10.1007/978-3-030-98981-1_10

Keywords Crop discrimination · Optical data · SAR data · Multi-temporal data · Machine learning algorithm

10.1 Introduction

Agriculture forms one of the main sectors in the world. Its timely monitoring is required for managing food security in the region. The agriculture sector is a unique sector as fluctuation in crop production is largely controlled by season. Different crops have different growth cycles, some are short-duration crops and some are long duration crops. For example, the most common staple food grain in the world, i.e., rice requires approximately 90–120 days for its growth depending on the crop variety used. Similarly, the largest grown commercial crop, i.e., sugarcane takes about 9–12 months for production. Apart from the season, the other factors that influence crop production are less controlled by climatic variables such as rainfall, temperature, and other important variables viz., evapotranspiration, soil moisture. Different management practices such as the quantity of fertilizers applied and timely irrigation also play an important role. These factors that control crop growth are highly variable, both spatially and temporally. Agricultural production is also influenced by certain unknown factors such as sudden pest or insect attacks or the development of unfavorable environmental/climatic conditions. Given the variability of the above factors, monitoring agricultural production becomes difficult.

In India, agriculture is the sector where 58% of Indian population relies on their livelihood (IBEF 2020). Different crops are grown in India due to the various climatic zones present in the country. The major crops grown in India are Wheat, Rice, Sugarcane, Pulses, etc. Ministry of Finance for the year 2020–21 reported that the estimated contribution of agricultural and allied sectors in the GDP growth was around 20% (Ministry of Finance 2021), an increase of around 2% from the previous year, i.e., 2019–20. Given the importance of India's agricultural sector in the economy, regular monitoring of agricultural activities is essential.

The agriculture sector is spread over a large area and therefore its monitoring using traditional methods such as field surveys is not feasible. Availability and advancements in remote sensing technologies enabled large-scale mapping of landscape due to its synoptic coverage. Over the past few decades, the agricultural monitoring studies using remote sensing data have gained popularity (e.g., Wardlow and Egbert 2008; Kussul et al. 2015; Chen et al. 2018). Earlier studies on agricultural monitoring used freely available optical data such as Landsat series (e.g., Congalton et al. 1998; Turker and Arikan 2005; Devadas et al. 2012). The major problem being faced by these optical sensors is their inability to capture data during cloudy season. The problem of cloud cover has been overcome by the launch of SAR having that all-weather capability. Although SAR satellites such as ERS-1/2, RadarSat-1/2, and TerraSAR-X were launched their utility in agricultural monitoring is limited because of their non-availability in public domain. The launch of Sentinel 1 data has made the SAR data available to public domain at a medium spatial resolution of 10 m.

In the recent past, capabilities of SAR have brought interest among researchers in agricultural monitoring studies using SAR data.

Crop mapping is the most common application of remote sensing in agriculture domain. Earlier crop mapping studies were carried out using conventional parametric such as maximum likelihood, minimum distance to mean, etc. In last decade or so, researchers employed non-parametric approaches such as machine learning algorithms (e.g., Duro et al. 2012; Onojeghuo et al. 2018; Feng et al. 2019). The major advantage of these algorithms is their ability to capture complex patterns in the data and also to handle high-dimensional data. These studies suggest that machine learning algorithms-based classification can give higher accuracy in crop classification compared to traditional techniques.

10.2 Geospatial Data Overview

Geospatial technologies can be simply referred to as the art of acquiring data from space. Optical, SAR, and hyperspectral data captured by different sensors onboard different satellites help in carrying out different agricultural applications in agriculture such as crop mapping, yield assessment, health assessment, damage assessment, etc. The remote sensing data along with ground observations can be highly beneficial in monitoring earth resources with much more precision and accuracy. Remote sensing operates on the property of an object and its interaction within the different wavelengths of electromagnetic spectrum. Optical remote sensing uses the visible (400–700 nm) and infrared (780–1000 nm) regions of the spectrum for object detection, while the Synthetic Aperture Radar (SAR) data uses the microwave (1 mm–1 m) region of the spectrum. The data acquisition process generally involves measuring the reflected radiation that is generated by the interaction of different objects with the incident radiation. The idea is to capture the differential response of different objects to different wavelength regions. For example, in the case of vegetation cover, the highest reflectance can be observed in the near-infrared region of the spectrum while most of the absorption takes place in the visible region. Therefore, maximum reflectance is observed in near-infrared region and minimum reflectance in red region. Similarly, water bodies show maximum reflectance in the blue region and bare soil shows maximum reflectance in the short-wave infrared region. This interaction of different objects to different wavelength regions can help in distinguishing different objects. Thus, to capture these differential responses among different earth features, two types of sensors namely passive and active. Former captures the reflected radiation and the latter is the active sensor that has its own energy source and captures the energy reflected by the object after the interaction. Hence, different satellites sensors have been designed based on this principle over time meant for different applications (Table 10.1).

In general, remote sensing data is characterized in terms of spatial, temporal, spectral, and radiometric resolutions. The first satellite data product available at a medium spatial resolution was Landsat 1 MSS (Multispectral Scanner). The spatial

Table 10.1 List of satellites launched

Satellite	Year launched	Sensor	Agency
Landsat 1	1972	MSS	NASA
Landsat 4	1982	TM	NASA
Landsat 5	1984	TM	NASA
SPOT-1	1986	HRV	CNES
IRS-1A	1988	LISS-1, LISS-2	ISRO
SPOT-2	2009	DORIS, HRV	CNES
RADARSAT-1	1995	SAR	CSA
Landsat-7	1999	ETM+	NASA
Terra	1999	ASTER, CERES, MISR, MODIS, MOPITT	NASA
Aqua	2002	AIRS, AMSR-E, AMSR-A, CERES, HSB, MODIS	NASA
Resourcesat-1	2003	AWiFS, LISS-4, LISS-3	ISRO
ALOS	2006	AVNIR-2, PALSAR, PRISM	JAXA
TerraSAR-X	2007	TOR, SAR-X	DLR
RadarSat-2	2007	SAR	CSA
Landsat 8	2013	OLI, TIRS	NASA
Sentinel 1A	2014	SAR-C	ESA
Sentinel 2A	2015	MSI	ESA
Sentinel 1B	2016	SAR-C	ESA
Sentinel 2B	2017	MSI	ESA
Landsat 9	2021	OLI, TIRS	NASA

NASA national aeronautics and space administration, *ESA* European space agency, *ISRO* Indian space research organization, *CSA* Canadian space agency, *DLR* The German aerospace centre, *JAXA* Japanese aerospace exploration agency, *CNES* national centre for space studies
Source WMO OSCAR (2021)

resolution of the data was 60 m and captures data in four wavelength bands, i.e., Blue, Green, Red, and NIR. Over the time, Landsat program evolved with subsequent launches of Landsat 4-5 TM (Thematic Mapper), Landsat 7 ETM+ (Enhanced Thematic Mapper Plus), and Landsat 8 OLI (Operational Land Imager) since 1977. Landsat 4-5 improved the spatial resolution of Landsat series from 60 to 30 m. Improvements in the spectral resolution with every subsequent launch of Landsat satellite were observed for Landsat 1, Landsat 4-5, Landsat 7, and Landsat 8 with 4, 7, 8, and 8 spectral bands, respectively. These Landsat series are widely used in different applications of agriculture as they provide not only medium-resolution data but also provide a long time-series data essential for long term analysis since 1982.

The Landsat series has a rich source of data record dating from 1972 to present with a spatial resolution as high as 30 m (Hawbaker et al. 2017). Although spatial resolution of Landsat data is 30 m, one of the major limitations with this data is that it may not provide high accuracy for agricultural monitoring studies in heterogeneous cropping environments. In the recent times, European Space Agency (ESA) has

launched its Sentinel series of satellites, where Sentinel 2 is the satellite in this series, that captures the data in the optical and near-infrared region. The Sentinel 2 satellite has finer spatial, temporal, and spectral resolutions as compared to Landsat. The spatial resolution of the satellite is 10 m, which can be considered as good for agricultural applications. In the Landsat series, the data is available at the time interval of 16 days, i.e., two observations per month. In case of Sentinel series, the temporal resolution of the satellite is 10 days allowing three observations per month. The other advantage with Sentinel 2 series is that it includes twin satellites namely Sentinel 2A and 2B, which further improved the temporal resolution to 5 days making six observations per month. These multiple observations within short span help in capturing the crop phenological information of small duration crops with 90–120 days cycle (Cheng et al. 2020). This highlights the capability of Sentinel satellite to provide at least one cloud-free image per month during the cloudy season. Further Sentinel satellite has finer spectral resolution with its ability to capture data in 13 different spectral bands as compared to Landsat 8 having 11 spectral bands. The spectral configuration of both the satellites is similar in terms of visible, near-infrared, and short-wave bands. The main advantage of the Sentinel 2 satellite is that the red band is further divided into three red edge bands. This gives relative advantage to Sentinel satellite over Landsat satellite as these red edge bands can be helpful in vegetation monitoring (Delegido et al. 2011). With the launch of Sentinel mission, the availability of high-resolution multispectral data with high repetivity is possible. Although the repetivity of Sentinel data is very high with repeat cycle of 5 days, there might be issue with the cloud cover.

Over the years, optical data has gained popularity in different applications. The only drawback of multispectral optical data is that they are prone to cloud cover and the reflectance from the surface after interacting with the objects cannot be captured by the sensors during cloudy season. All-weather capability of SAR is possible because the wavelength of the SAR data is high, i.e., in cm. These wavelengths are higher than the radius of the water molecule of cloud cover hence these wavelengths can penetrate the cloud cover and can be easily captured by sensors. SAR data such as ERS-1/2 and Radarsat 1 was not available in the public domain. The Sentinel series has also launched the Sentinel 1 SAR data that acquires data at a high spatial resolution of 10 m with a repeat cycle of 12 days. Similar to Sentinel 2, there are twin satellites, i.e., Sentinel 1A and Sentinel 1B that makes the overall repeat cycle of nearly 6 days.

10.3 Machine Learning Algorithms

The machine learning algorithms capture the pattern in the data from the training datasets in case of supervised learning and further use this pattern recognition for regression or classification (Mahesh 2020). The past decade has seen a rise in the use of machine learning algorithms for different applications in the field of remote sensing (e.g., Friedl and Brodley 1997; DeFries and Chan 2000; Pal and Mather 2005; Cooner

et al. 2016). The major advantage of these algorithms from conventional algorithms is that these methods do not assume linearity in data and can capture complex patterns in the data. Increase in the data availability in the recent past increased the scope for envisaging a greater number of variables for analysis. With the advancement in the sensors, the number of spectral bands increased from eight bands in Landsat 4-5 and 7–11 bands in Landsat 8 and 12 bands in Sentinel 2. Thus, these algorithms prove to be beneficial for analyzing data with such high dimensionality. Different machine learning algorithms classify data using unsupervised supervised, and semi-supervised learning. In unsupervised learning, the training data is not used and the classes in the data are unknown. The model classifies the data by utilizing the pattern in the data into different user-defined classes. In the supervised learning, training data is provided and the model captures the structure of different classes from the input data. These identified structures are then used further for the classification of the data. In semi-supervised learning labeled and unlabelled samples make up the input data. The semi-supervised learning is performed by first classifying the data using unsupervised learning and then using labeled data, the supervised classification is carried out.

The supervised machine learning algorithms that have been widely employed in the field of remote sensing include k-Nearest Neighbor, Artificial Neural Network, Support Vector Machine, Self-Organizing Maps, and Decision Tree. These algorithms have different approaches for their functioning, for example, SVM uses the hyperplane to find the optimum fit for the data, and these hyperplanes are adjusted based on different kernel parameters. In ANN, the data are classified based on different activation functions such as sigmoid, logistic, tanh, etc. The other form of machine learning algorithms is known as ensemble algorithms. An example of a few ensemble machine learning algorithms is Random Forest, AdaBoost, XGBoost, Gradient Tree Boosting. These ensemble algorithms are being developed by using base algorithms. For example, the Random Forest algorithm was developed based on the decision tree algorithms where the majority voting technique is used. A brief description of different machine learning algorithms is described below.

10.3.1 k-Nearest Neighbor

k-Nearest Neighbor (k-NN) is the simplest form of a machine learning algorithm (Laaksonen et al. 1996). The k-NN is a supervised learning technique in machine learning. In k-NN, the datasets are classified based on the distance measure between the training point and sample point. Further, these sample points are classified into a class with which the data has less distance based on the distance measure. It is the simplest machine learning algorithm and requires tuning of only one parameter, i.e., number of neighbors.

10.3.2 Artificial Neural Network

The Artificial Neural Network (ANN) is inspired by the working of biological systems where several neurons assist the brain the decision making (Lek and Guégan 1999). Similar to the biological system, the input and output are connected by different neurons and hidden layers in the ANN algorithm. The ANN is a broad class of algorithms and within ANN, one of the fundamental techniques is feed-forward technique. In this technique, three basic building blocks, i.e., input layer, hidden layer, and output layer exist. The hidden layers present in the algorithm are activated using different activation functions such as sigmoid, tanh function, etc. The data is then classified into different classes based on the input weights. The most commonly used activation function is the sigmoid activation function and is computed using Eq. 10.1.

$$f(n) = \frac{1}{1 - e^{-n}} \tag{10.1}$$

n, weighted sum of input.

10.3.3 Support Vector Machine

The Support Vector Machine (SVM) is the most popular machine learning algorithm that has gained popularity in recent times. The SVM algorithm was developed by Vladimir Vapnik and Alexey Chervonenkis in the year 1963 (Rymarczyk et al. 2019). Later this approach was further modified by Boser et al. (1992) to implement it as classification problem. The SVM algorithms function by creating a hyperplane between the data points in the multidimensional space. This hyperplane is further modified using different kernel functions such as Gaussian, Radial Basis Function (RBF), or linear function (Kavzoglu and Colkesen 2009). The data points lying close to the hyperplane are known as support vectors, which play a crucial role in differentiating one dataset from the other. The most popular kernel used in SVM classifier is the RBF kernel and is computed using Eq. 10.2.

$$K(i, j) = \exp^{-Y|i-j|^2} \tag{10.2}$$

where Y is the gamma function, and $|i - j|$ is the Euclidian distance.

10.3.4 Decision Tree

The Decision Tree (DT) is another easy way to implement machine learning algorithm. DT functions by splitting the data into different nodes. DT name for the algorithm arises due to its tree-like structure where there are roots, nodes, and leaves. The structure of DT can be defined as internal nodes representing characteristics of a dataset, branches representing the rule on which splitting is done, and leaf nodes representing the outcome. The splitting of the nodes is carried out by examining the homogeneity of node which is computed using different methods such as entropy and Gini index (Safavian and Landgrebe 1991). The DT's main structure consists of two components, one is the decision node, where a choice is made on how the data should be split, and the other is the leaf node, where the decision node's final output is not further split.

10.3.5 Random Forest

The Random Forest algorithm is the ensemble classifier where different decision trees are ensembled using majority voting (Breiman 2001). In the DT algorithm, a single tree is constructed whereas in the RF algorithm these trees from different DT are ensembled together. As the name of the algorithm suggests it is a forest consisting of different trees. In the RF algorithm, the outcome is calculated by considering the majority vote from different DTs. The Random Forest works by using random subset of data for splitting of each node which is tuned using variable at each split (*mtry*) variable. Another parameter in the RF algorithm is the total number of trees to be constructed. This parameter is tuned using number of trees (*ntrees*). Generally, it is considered that better classification accuracy can be achieved with increase in the number of trees. However, this has limitation as after certain number of trees the overall accuracy stabilizes (Breiman 2001).

10.4 Remote Sensing Applications in Agriculture

Monitoring agricultural resources is a tedious task as the agricultural fields are spread over a large area and manual surveys can be very time-consuming and costly. The advancement in the field of remote sensing has helped in agricultural monitoring at a large-scale (e.g., Xiao et al. 2005; Liu et al. 2020). The major advantage of remote sensing data is their ability to capture large areas at a fine spatial resolution and also provide the data at a fixed interval of time (multi-temporal). Acreage estimation, crop discrimination, yield estimation, and change detection are the major fields of agricultural application that have received a lot of attention in the past decade. The use of remote sensing data in agricultural monitoring has advantages over other

conventional survey techniques. These advantages include large area mapping, rapid survey, change detection with the available time-series data, low cost with higher accuracy (Ge et al. 2011). With the advancement in the remote sensing data availability, researchers used these data sets for different agricultural studies such as crop mapping (Congalton et al. 1998; Zhong et al. 2014), yield estimation (Rudorff and Batista 1991; Nuarsa et al. 2012) and crop damage assessment (Yamagat and Akiyama 1988; Bentley et al. 2002). The remote sensing data has been widely used in different agricultural-related studies. For example, Skakun et al. (2017) used remote sensing data, i.e., Landsat 8 and Sentinel 2 for crop yield estimation. Pantaleoni et al. (2007) employed Landsat 5 data for crop damage assessment. The study envisaged change detection technique to identify the damage to the crops before and after flood episodes.

The crop classification study is one of the important studies that has been widely explored using remote sensing data. The crop classification study has been widely carried out using optical data such as Landsat, Sentinel, MODIS, etc. The earliest example of remote sensing data utilization in agriculture is by Odenweller and Johnson (1984) where Landsat data was used for identifying different crops in the United States based on the spectral profile. In the Indian context, the field size of agricultural land is not very big and the majority of field sizes are generally below 20 m. There is also heterogeneity in the cropping pattern and different crops are grown in the adjacent fields. The only homogeneity that can be observed is in case of crops such as Rice (*Oryza sativa)* and Wheat (*Triticum aestivum)* that forms the major food grain crop in India. Total area occupied by rice and wheat crop is 44 million ha and 29.5 million ha, respectively indicating the high area under cultivation (Dey et al. 2020). The study of these crops becomes easy as they occupy large areas and are grown mostly in homogenous environments. The problem arises in the mapping of other crops such as Pearl millet (*Pennisetum glaucum),* maize (*Zea mays),* Sorghum (*Sorghum bicolor*), etc. which are grown in the heterogeneous environment. The field size of these crops is very small, i.e., in the range of 10–20 m and sometimes these crops are grown together with other crops. In India, mixed cropping is practiced in majority of the area. Therefore, to monitor the status of these crops, the spatial resolution of Landsat which is 30 m may not be feasible.

Currently, due to the availability of free and medium-resolution SAR data, remote sensing community has explored the utility of SAR data for crop mapping. The SAR has been found to be more effective in mapping crop types as these datasets are sensitive to soil water content and also are affected by the height of the crops (McNairn et al. 2009). The crop mapping requires continuous data to capture different phenological stages of crops such as onset time, peak time, offset time, area under curve, greenness, and senescence slope (Conrad et al. 2011). These characteristics are different for different crops, which can easily help in crop discrimination in a large area. The time-series required for such analysis requires data during the whole growth period, i.e., from sowing to harvesting. If the data gets contaminated by cloud in any way, gap-filling of these data and extracting correct phenological properties may become problematic. Therefore, the newly launched Sentinel 1 series data become handy in crop mapping. The Sentinel 1 data provides data at a high spatial resolution

of 10 m which is ideal for crop type discrimination in the developing countries where the field size is not that large. Secondly, the Sentinel 1 data is available at a repeat time of 6 days which makes it suitable for capturing the phenological information for short-duration crops such as paddy, wheat, maize, pearl millet, sorghum, etc. that are sown and harvested in approximately 3–4 months duration.

In the recent past, different machine learning algorithms viz., RF, SVM, k-NN, ANN, etc. have been widely used in the domain of crop classification studies using Sentinel 1 data. These algorithms have been proved to be more robust in terms of overall accuracy as compared to conventional techniques (Ghimire et al. 2012). Useya and Chen (2019) used the time-series Sentinel 1 data and Random Forest algorithm for crop type classification on different field parcels of Zimbabwe. The study has demonstrated two major aspects. first is the utility of time-series SAR data for crop mapping and second is the robustness of machine learning algorithm. This study indicated the capability of Sentinel 1 data in mapping crop type patterns in the small landholdings. Different studies have used these SAR data in crop mapping studies (e.g., Kenduiywo et al. 2018; Singha et al. 2019; Xu et al. 2019).

10.5 Case Study (*Kharif* Maize Crop Classification)

Maize is one of the most adaptable crops, with the largest genetic yield potential among cereals. It can grow in a variety of agro-climatic situations. It is grown on about 190 million hectares in 165 countries with a vast range of soil, temperature, biodiversity, and management approaches, accounting for 39 percent of global grain production. Maize is primarily a kharif crop in India, with 85 percent of the land under cultivation during the kharif season. After rice and wheat, maize is India's third most important cereal crop. It accounts for about 10% of the country's total food grain production. Thousands of industrial goods use maize as a basic raw material, including oil, alcoholic drinks, food sweeteners, pharmaceutical, cosmetic, textile, package, and paper sectors, among others.

A case study has been presented which utilizes of Sentinel 1 time-series data for discriminating *kharif* maize crop using machine learning and conventional algorithms. Maize crop is generally grown during *kharif* season in India, i.e., June to September month. This season is generally prone to cloud cover most of the time therefore using optical data for crop mapping becomes difficult. The SAR data comes in handy in such seasons as they can easily capture land dynamics without getting affected by cloud. The other advantage of using SAR data is that its availability during entire crop growing season is of great help for classification. The objectives of the study are (i) to in discriminate *kharif* maize crop in the heterogenous growing environment using SAR data (ii) To compare machine learning algorithms and conventional algorithms for *kharif* maize discrimination.

10.5.1 Study Area

This study was carried out in Kannauj district of Uttar Pradesh for *kharif season*, 2020 (Fig. 10.1). The Kannauj district is located between 26° 46′ N and 27° 13′ latitude and 79° 18′ E and 80° 1′ E longitude.

The study district is at an elevation of 143 m above mean sea level with average annual rainfall of 795 mm. The study district is bounded on the north by Farrukhabad district, on the South by Auraiya and Kanpur Dehat, on the East by District Hardoi and Kanpur Nagar, and on the West by Mainpuri and Etawah district. The total reported area of the district is 209300 ha with major crops grown during *kharif* season of 2019–20 are maize (41,129 ha), Rice (20,982 ha), Groundnut (1524 ha),

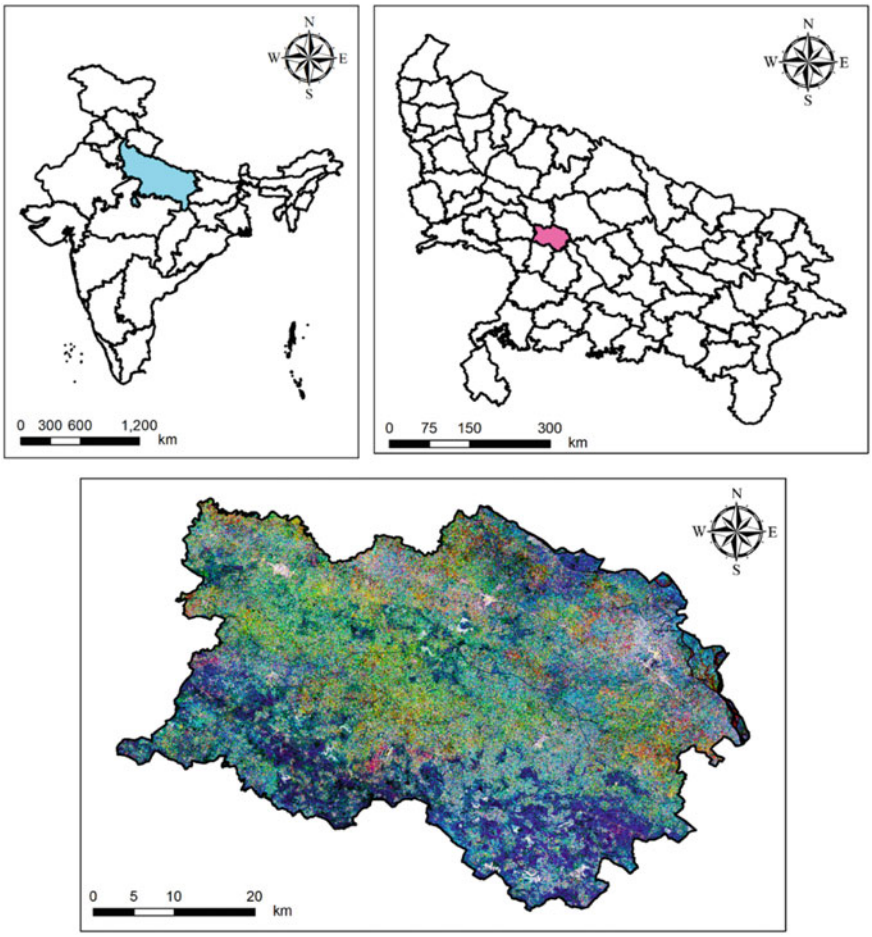

Fig. 10.1 Location map of the study area

Bajra (1188 ha), Jowar (537 ha) (Area Production Statistics, Ministry of Agriculture and Farmers Welfare 2020).

10.5.2 Dataset and Methodology

The current study is carried out using time-series Sentinel 1 SAR data from the June to September 2020. The time-series data is used as it can capture the phenological crop information, which can further assist classifier in discriminating different crops. The SAR data was downloaded and pre-processed using speckle filtering, radiometric calibration, and terrain correction step as highlighted by Filipponi (2019). The time-series stack generated after pre-processing was used for crop classification. The field data were collected for different crops during the peak growing month, i.e., September in the form of polygons. These field data were further analyzed for any error and were then split into training and testing polygons in 70:30 ratio. The crop classification was carried out using three machine learning algorithms namely DT, SVM, and RF and compared with conventional algorithm, i.e., Maximum likelihood classifier (MLC). The validation of the classified maps generated using different algorithms was carried out using different classification accuracy measures. These measures include overall accuracy, kappa, User's accuracy, Producer's accuracy, and F1-score. The F1-score measure was included in the accuracy measure as this gives the overall picture of how well the user and producer accuracy are balanced for a particular class. The F1-score is computed based on the harmonic mean between user and producer accuracies.

10.5.3 Results and Discussion

The crop classification was carried out using DT, SVM, RF, and MLC. The parameters used for RF include 1000 *ntrees* and 2 *mtry,* while radial basis function kernel was used for SVM. Maize and Paddy are the most abundantly grown *kharif* crop in the district. Spatial distribution of these major crops grown in the study district identified using different algorithms was shown in Fig. 10.2. Relative evaluation of these algorithms was carried out using different statistical measures as given in Table 10.2.

Analysis indicated that the overall accuracy achieved was the highest in RF classifier followed by SVM, DT, and MLC (Table 10.2). Parametric classifier, i.e., MLC indicated lower overall accuracy relative to machine learning classifiers. The user and producer accuracies for maize crop were also computed and the result indicated better performance of RF algorithm. The highest F1-score was also observed in RF algorithm.

The result suggested that overall accuracy is much higher with machine learning algorithms is as compared to traditional parametric methods such as MLC. The

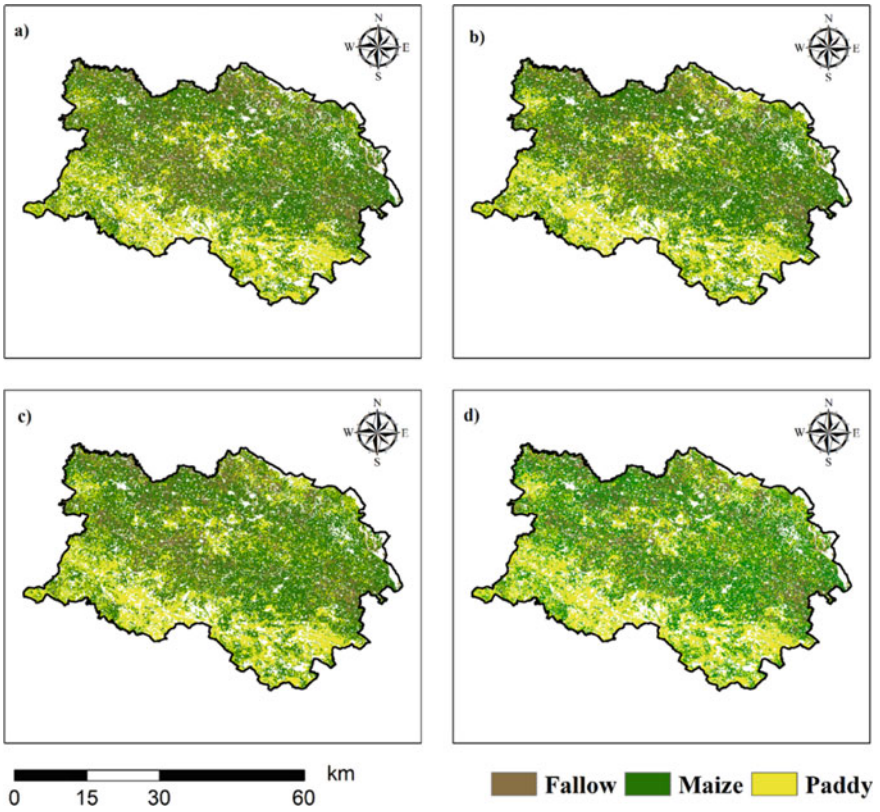

Fig. 10.2 Classified image using **a** Decision tree **b** Random forest **c** Support vector machine **d** Maximum likelihood classifier

Table 10.2 Accuracy measures for crop classification in the study district

Classifier	DT	SVM	RF	MLC
Overall accuracy	89.53	91.37	94.25	71.69
Kappa	0.77	0.82	0.88	0.57
User's accuracy (Maize)	88.71	89.73	92.65	84.34
Producer's accuracy (Maize)	94.72	95.56	97.85	62.56
F1-score (Maize)	0.92	0.92	0.95	0.72

highest accuracy in RF classifier may be due to its ensemble nature, which is constructed based on multiple decision trees. Therefore, the performance of RF algorithm is much superior to any other classifier.

10.6 Conclusions

Agriculture forms the major sector in the world, which is highly volatile to climate change and other local external factors. The accurate and timely study of croplands is important not only for better managing the agricultural activities but also helps in formulating the policy framework regarding the storage, export, and crop management. Given the scale at which agriculture activities are carried out, the manual surveying technique can be time-consuming, costly, and labor intensive. Remote Sensing data has proven to be beneficial in the agricultural sector as this data can cover the large ground area and can also provide observations at a regular time interval. The availability of free medium-resolution satellite data has made agricultural study feasible. Crop mapping studies have been carried out by different researchers by utilizing different satellite products such as Landsat, Radarsat, Sentinel 1, and Sentinel 2. These datasets have evolved over time in terms of their spatial, temporal, and spectral resolution. The earlier launched SAR data such as ERS-1/2 and Radarsat-1 and 2 are not freely available in public domain. With the availability of free Sentinel 1 SAR data at a resolution of 10 m has made the crop mapping study convenient. Several studies have demonstrated that machine learning algorithms are much more powerful than conventional algorithms. This study envisaged Sentinel-1 time-series data and different machine learning algorithms for *kharif* maize crop mapping in the heterogeneous environment.

Different machine learning algorithms such as DT, SVM and RF was compared with traditional technique like MLC. Analysis indicated that machine learning algorithms provided better accuracies compared to traditional parametric classifiers. Out of all the three machine learning algorithms, RF which is an ensemble classifier was shown to be more robust in terms of overall accuracy for crop mapping during *kharif* season.

References

Aps.dac.gov.in (2020) Area production statistics, Ministry of Agriculture and Farmers Welfare. Available at: https://aps.dac.gov.in/Home.aspx?ReturnUrl=%2f. Accessed 19 Mar 2020

Bentley ML, Mote TL, Thebpanya P (2002) Using landsat to identify thunderstorm damage in agricultural regions. Bull Am Meteor Soc 83(3):363–376

Boser BE, Guyon IM, Vapnik VN (1992) A training algorithm for optimal margin classifiers. In: Proceedings of the fifth annual workshop on Computational learning theory, pp 144–152

Breiman L (2001) Random forests. Mach Learn 45(1):5–32

Chen Y, Lu D, Moran E, Batistella M, Dutra LV, Sanches IDA, da Silva RFB, Huang J, Luiz AJB, de Oliveira MAF (2018) Mapping croplands, cropping patterns, and crop types using MODIS time-series data. Int J Appl Earth Obs Geoinf 69:133–147

Cheng Y, Vrieling A, Fava F, Meroni M, Marshall M, Gachoki S (2020) Phenology of short vegetation cycles in a Kenyan rangeland from PlanetScope and Sentinel-2. Remote Sens Environ 248:112004

Conrad C, Colditz RR, Dech S, Klein D, Vlek PL (2011) Temporal segmentation of MODIS time series for improving crop classification in Central Asian irrigation systems. Int J Remote Sens 32(23):8763–8778

Cooner AJ, Shao Y, Campbell JB (2016) Detection of urban damage using remote sensing and machine learning algorithms: revisiting the 2010 Haiti earthquake. Remote Sens 8(10):868

Congalton RG, Balogh M, Bell C, Green K, Milliken JA, Ottman R (1998) Mapping and monitoring agricultural crops and other land cover in the lower Colorado River Basin. Photogram Eng Remote Sens 64(11):1107–1113

DeFries RS, Chan JCW (2000) Multiple criteria for evaluating machine learning algorithms for land cover classification from satellite data. Remote Sens Environ 74(3):503–515

Delegido J, Verrelst J, Alonso L, Moreno J (2011) Evaluation of sentinel-2 red-edge bands for empirical estimation of green LAI and chlorophyll content. Sensors 11(7):7063–7081

Devadas R, Denham RJ, Pringle M (2012) Support vector machine classification of object-based data for crop mapping, using multi-temporal Landsat imagery. Int Arch Photogram Remote Sens Spatial Inform Sci 39(1):185–190

Dey A, Dinesh R (2020) Rice and wheat production in India: an overtime study on growth and instability. J Pharmacognosy Phytochem 9(2):158–161

Duro DC, Franklin SE, Dubé MG (2012) A comparison of pixel-based and object-based image analysis with selected machine learning algorithms for the classification of agricultural landscapes using SPOT-5 HRG imagery. Remote Sens Environ 118:259–272

Feng S, Zhao J, Liu T, Zhang H, Zhang Z, Guo X (2019) Crop type identification and mapping using machine learning algorithms and sentinel-2 time series data. IEEE J Sel Top Appl Earth Observ Remote Sens 12(9):3295–3306

Filipponi F (2019) Sentinel-1 GRD preprocessing workflow. Proceedings 18(1):11

Friedl MA, Brodley CE (1997) Decision tree classification of land cover from remotely sensed data. Remote Sens Environ 61(3):399–409

Ge Y, Thomasson JA, Sui R (2011) Remote sensing of soil properties in precision agriculture: a review. Front Earth Sci 5(3):229–238

Ghimire B, Rogan J, Galiano VR, Panday P, Neeti N (2012) An evaluation of bagging, boosting, and random forests for land-cover classification in Cape Cod, Massachusetts, USA. Gisci Remote Sens 49(5):623–643

Hawbaker TJ, Vanderhoof MK, Beal YJ, Takacs JD, Schmidt GL, Falgout JT, Williams B, Fairaux NM, Caldwell MK, Picotte JJ, Howard SM (2017) Mapping burned areas using dense time-series of Landsat data. Remote Sens Environ 198:504–522

IBEF (2020) Agriculture and Allied Industry report April 2020. https://www.ibef.org/download/Agriculture-and-Allied-Industries-April-2020.pdf

Kavzoglu T, Colkesen I (2009) A kernel functions analysis for support vector machines for land cover classification. Int J Appl Earth Obs Geoinf 11(5):352–359

Kenduiywo BK, Bargiel D, Soergel U (2018) Crop-type mapping from a sequence of Sentinel 1 images. Int J Remote Sens 39(19):6383–6404

Kussul N, Skakun S, Shelestov A, Lavreniuk M, Yailymov B, Kussul O (2015) Regional scale crop mapping using multi-temporal satellite imagery. Int Arch Photogram Remote Sens Spatial Inform Sci 40(7):45

Laaksonen J, Oja E (1996) Classification with learning k-nearest neighbors. In: Proceedings of international conference on neural networks (ICNN'96), vol 3. IEEE, New York, pp 1480–1483

Lek S, Guégan JF (1999) Artificial neural networks as a tool in ecological modelling, an introduction. Ecol Model 120(2–3):65–73

Liu X, Zhai H, Shen Y, Lou B, Jiang C, Li T, Hussain SB, Shen G (2020) Large-scale crop mapping from multisource remote sensing images in google earth engine. IEEE J Sel Top Appl Earth Observ Remote Sens 13:414–427

Mahesh B (2020) Machine learning algorithms—a review. Int J Sci Res (IJSR) [Internet] 9:381–386

McNairn H, Van der Sanden JJ, Brown RJ, Ellis J (2000) The potential of RADARSAT-2 for crop mapping and assessing crop condition. In: Proceedings of the second international conference on geospatial information in agriculture and forestry, vol 2, pp 81–88

McNairn H, Shang J, Jiao X, Champagne C (2009) The contribution of ALOS PALSAR multi-polarization and polarimetric data to crop classification. IEEE Trans Geosci Remote Sens 47(12):3981–3992

Ministry of Finance (2021) Economic survey 2020–21. GoI. https://www.indiabudget.gov.in/economicsurvey/

Nuarsa IW, Nishio F, Hongo C (2012) Rice yield estimation using Landsat ETM+ data and field observation. J Agric Sci 4(3)

Odenweller JB, Johnson KI (1984) Crop identification using Landsat temporal-spectral profiles. Remote Sens Environ 14(1–3):39–54

Onojeghuo AO, Blackburn GA, Wang Q, Atkinson PM, Kindred D, Miao Y (2018) Mapping paddy rice fields by applying machine learning algorithms to multi-temporal Sentinel-1A and Landsat data. Int J Remote Sens 39(4):1042–1067

Pal M, Mather PM (2005) Support vector machines for classification in remote sensing. Int J Remote Sens 26(5):1007–1011

Pantaleoni E, Engel B, Johannsen C (2007) Identifying agricultural flood damage using Landsat imagery. Precision Agric 8:27–36

Rymarczyk T, Kozłowski E, Adamkiewicz P, Sikora J (2019) Application of gaussian kernel with regard to correlations for image reconstruction in electrical tomography. Przegląd Elektrotechniczny 95

Rudorff AF, Batista GT (1991) Wheat yield estimation at the farm level using tm landsat and agrometeorological data. Int J Remote Sens 12(12):2477–2484

Safavian SR, Landgrebe D (1991) A survey of decision tree classifier methodology. IEEE Trans Syst Man Cybern 21(3):660–674

Skakun S, Vermote E, Roger JC, Franch B (2017) Combined use of Landsat-8 and Sentinel-2A images for winter crop mapping and winter wheat yield assessment at regional scale. AIMS Geosci 3(2):163

Saich P, Borgeaud M (2000) Interpreting ERS SAR signatures of agricultural crops in Flevoland, 1993–1996. IEEE Trans Geosci Remote Sens 38(2):651–657

Singha M, Dong J, Zhang G, Xiao X (2019) High resolution paddy rice maps in cloud-prone Bangladesh and Northeast India using Sentinel-1 data. Sci Data 6(1):1–10

Turker M, Arikan M (2005) Sequential masking classification of multi-temporal Landsat7 ETM+ images for field-based crop mapping in Karacabey, Turkey. Int J Remote Sens 26(17):3813–3830

Useya J, Chen S (2019) Exploring the potential of mapping cropping patterns on smallholder scale croplands using Sentinel-1 SAR data. Chin Geogra Sci 29(4):626–639

Wardlow BD, Egbert SL (2008) Large-area crop mapping using time-series MODIS 250 m NDVI data: an assessment for the US Central Great Plains. Remote Sens Environ 112(3):1096–1116

WMO OSCAR (2021) https://space.oscar.wmo.int/satellites/

Xiao X, Boles S, Liu J, Zhuang D, Frolking S, Li C, Salas W, Moore B III (2005) Mapping paddy rice agriculture in southern China using multi-temporal MODIS images. Remote Sens Environ 95(4):480–492

Xu L, Zhang H, Wang C, Zhang B, Liu M (2019) Crop classification based on temporal information using sentinel-1 SAR time-series data. Remote Sens 11(1):53

Yamagata Y, Akiyama T (1988) Flood damage analysis using multitemporal Landsat thematic mapper data. Int J Remote Sens 9(3):503–514

Zhong L, Gong P, Biging GS (2014) Efficient corn and soybean mapping with temporal extendibility: a multi-year experiment using Landsat imagery. Remote Sens Environ 140:1–13

Chapter 11
Soil Penetration Depth of RISAT-1 C-Band and PALSAR-2 L-Band Sensors in Arid Zone of Rajasthan, India

B. K. Bhadra, Ashish K. Jain, Sushilkumar B. Rehpade, Hansraj Meena, and S. Srinivasa Rao

Abstract The moisture content in the soil is an important indicator of agricultural draught, especially in the arid region of India. Microwave data has the capability to estimate the soil moisture and soil penetration depth with different sensors whose sensitivity depends on the frequency and strength of the radar signals. In the present study, multi-frequency microwave satellite data of RISAT-1 C-band (5.3 GHz) and PALSAR-2 L-band (1.2 GHz) is used for calculating soil moisture across the palaeochannel (PC) at Bhimarlai village in Barmer district of Rajasthan. For this purpose, volumetric soil moisture was measured at Pit-1 (inside PC) and Pit-2 (outside PC) up to a depth of 120 cm. Inside the PC (moist zone), depth of soil penetration of L-band is found to be ~11 cm which is higher than that of C-band (~8 cm). However, the penetration depth of L-band in dry soil (outside PC) is found to be more (~16 cm) than the moist soil inside the PC. It has been observed that soil penetration depth with C- and L-bands gradually decreases from surface to a depth of 120 cm in both the pits, which are commensurate with the measured soil moisture and derived dielectric coefficient (ε) or backscattering coefficient (σ°) of the sensors. For cross validation of soil moisture condition in the sub-surface layers, a resistivity survey has been carried out for 240 m traverse length across the PC. 2D tomograms show a thin higher resistivity zone (dry sandy layer) overlying a thick

B. K. Bhadra (✉)
Regional Remote Sensing Centre-North, ISRO/DOS, Antariksh Bhavan, Sadiq Nagar, New Delhi 110049, India
e-mail: bkbhadra63@gmail.com; bhadra_bk@nrsc.gov.in

A. K. Jain · H. Meena
Regional Remote Sensing Centre-West, NRSC, ISRO Complex, Sector-9, Kudi, Jodhpur 342005, India

S. B. Rehpade
Regional Remote Sensing Centre-Central, NRSC/ISRO, N6, Vayusena Nagar, Nagpur 440007, India

S. S. Rao
National Remote Sensing Centre (NRSC), ISRO, Balanagar, Hyderabad, Telengana 500037, India

C. S. Jha et al. (eds.), *Geospatial Technologies for Resources Planning and Management*, Water Science and Technology Library 115,
https://doi.org/10.1007/978-3-030-98981-1_11

zone of low resistivity zone (saturated clayey sand layer) that confirms the presence of the palaeochannel. Thus, a unique method is developed for evaluating sensor penetration depth with variation in soil moisture.

Keywords Microwave data · Soil moisture · Penetration depth · Palaeochannel · Rajasthan

11.1 Introduction

Soil moisture content in the surface and sub-surface layers is of great importance in agriculture, especially crop sowing and cultural practices. It is highly variable in space and time and is governed by the properties like surface roughness, soil texture, soil bulk density, and dielectric constant of the materials (Baghdadi et al. 2006; Das and Paul 2015). In India, soil moisture percentage varied from humid to arid environments and irrigated to non-irrigated regions. Further, this variation is attributed to seasonal and climatic changes and the type of soil material. Thus, the surface soil moisture content in an area is so dynamic that it varies even in day and night conditions. However, soil moisture is assumed to be constant over a season in a particular climatic zone.

Physical properties that control the soil moisture are dielectric constant, soil bulk density, soil roughness, soil texture, and vegetation cover. Each of these parameters is also governed by the frequency and polarization of the active sensors. Dry or wet soil is a mixture of soil particles, air, and water around the particles (Barrett et al. 2009; Zhao and Li 2013). The dielectric constant of any material is represented by the ratio between the electrical permittivity of the material and the electrical permittivity of the vacuum. Land surface roughness is generally measured in the field by calculating the root mean square (RMS) of different surface heights along any transact. Soil texture and roughness mostly affect the backscattering, depending on the look angle of the microwave sensors. Dielectric constant also depends on soil texture (soil-particle size distribution), soil mineralogy, and effective salinity of the soil solution (Dobson and Ulaby 1986; Gharechelou et al. 2015). Due to large surface area, clay soil can hold more bounded water (higher moisture level) than sandy soils. Similarly, vegetation cover (crop, scrub, forest, etc.) also affects the microwave radiation either absorbed or scattered by the vegetation layer over the soil surface. The absorption of incident energy takes place due to the presence of water content in the vegetation. Active sensors like C- and L-bands are more affected by vegetation than passive sensors (Rao et al. 2013; Narvekar et al. 2015; Singh et al. 2019).

Traditionally, soil moisture percentage is measured through field sample collection or in situ measurement through probes which is a laborious and time-consuming exercise to collect data in a limited area. To overcome the situation, satellite image-based soil moisture estimation through empirical to semi-empirical algorithms is a much faster way to cover large areas (Baghdadi and Zribi 2006). Microwave data are sensitive to soil moisture which depends on sensor parameters (frequency, look

angle, and dielectric constant) and field parameters (soil texture, volumetric soil moisture, and bulk density) which are generally used in semi-empirical models. C-band microwave data is generally sensitive to surface soil moisture which have been widely used in different parts of the country and elsewhere in the world (Jackson et al. 2002; Jeu et al. 2008; Rao et al. 2013; Das and Paul 2015).

The penetration depth of any senor depends on the strength of the signal and its interaction with the soil. It is defined as the depth at which the microwave's power is reduced to 37 percent of its value below the surface. Generally, the depth of sensor penetration is a measure of the invasiveness of the radar signal into a soil medium through which the reflections occur due to change in the dielectric constant of the medium (Engman and Chauhan 1995; Owe and Van de Griend 1998; Kafarski et al. 2019). It has been demonstrated that the penetration depth decreases with increasing soil moisture content (Lv et al. 2018; Singh et al. 2019). Most of the previous studies on penetration depth are qualitative in nature. However, references of soil penetration depth of C and L-band data in dry to moist soil are rare. In the present study, an attempt has been made for quantitative estimation of penetration depth using an empirical formula with soil dielectric constant.

11.2 Soil Type of the Study Area

For soil moisture study across the palaeochannel (PC), an area between Bhimarlai and Gira villages has been selected in Barmer district of Rajasthan, India (Fig. 11.1). The average annual rainfall in the study area varies from 141 to 263 mm. Temperature of the area ranges from 46 °C (in summer) to 14 °C (in winter). Surface soil moisture content is generally found to be very low in arid region (1–5%) which varies rapidly with time due to harsh climatic condition. Satellite images show a vast stretch of desertic terrain with undulatory dune features with a few ephemeral drainages. Luni River swerves around the rocky exposures of Siwana Hills in the extreme south-east corner of the study area. The study area covers a small part of Barmer district of Rajasthan which falls under Hyper arid Agro-climatic zone. Soil in the area is deep yellowish-brown with sandy texture and very low in fertility. The hydrological property of these aeolian soil shows high permeability and water retention capacity. Hardpan is also present at varying depths in many places due to gypsiferous layers.

11.3 Soil Moisture Estimation Using Microwave Data

Soil is formed by mixing of soil particles, air with bound and free water (Engman and Chauhan 1995). With increasing soil moisture, water is able to move more freely around the soil particles, which causes a dominant effect on the dielectric constant (ε). Microwave sensors can detect a wide range of soil moisture with large contrast between the dielectric properties of liquid water ($\varepsilon \approx 80$) and dry soil ($\varepsilon \approx 6$).

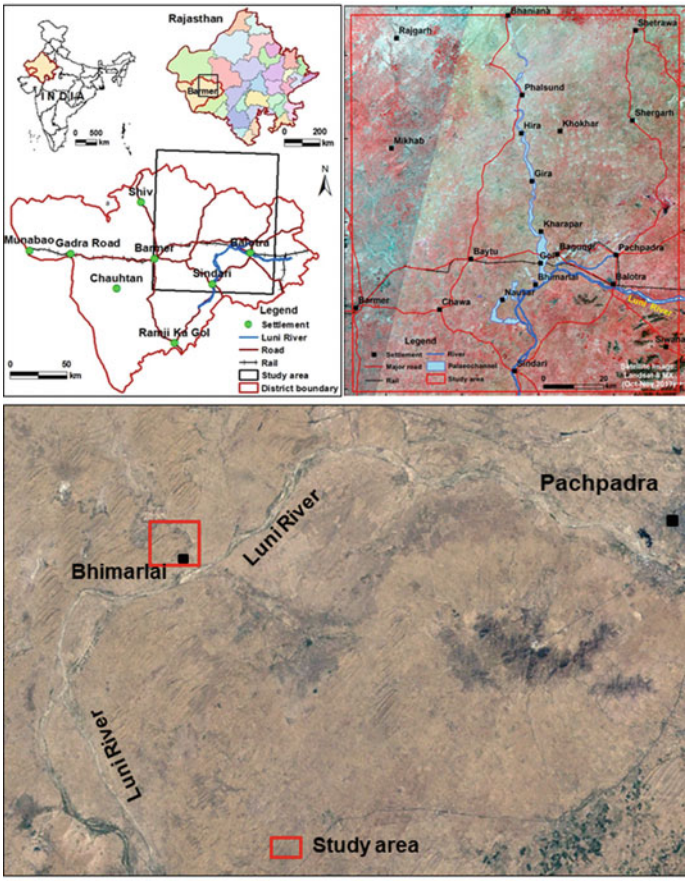

Fig. 11.1 Location map of the study area around Bhimarlai showing anastomosing drainages of Luni River near Pachpadra in Barmer district of Rajasthan

Complex dielectric constant largely depends on the volumetric soil moisture (m_v), which can be used for estimating soil moisture in terms of radar backscattering coefficient.

To take into account of the various sensor configurations and surface parameters, many backscattering models have been developed over the past 30 years (Dubois et al. 1995; Shi et al. 1997; Baghdadi and Zribi 2006). Numerous studies have been carried out in estimating soil moisture by the relationship between the radar signal and certain biophysical parameters like surface roughness and vegetation. These models can be divided into three groups: theoretical, empirical, and semi-empirical.

(a) *Theoretical scattering models*—These models are based on mathematical inversion with known values of surface roughness (rms height), correlation length, and dielectric constant. Integral Equation Method (IEM), Geometrical

optics model (GOM), Physical optics model (POM), Small perturbation model (SPM) are the some of the theoretical models which cannot be reversible. As prior knowledge of surface roughness is required, IEM model for soil moisture retrieval over large areas is time-consuming.

(b) *Empirical scattering models*—The statistical or empirical models are the simplest and most widely used one. It requires a huge amount of ground data. But this model is site-specific and is valid only to the area under investigation. However, due to limitations in observed parameters like frequency, incidence angles, and surface roughness, empirical models are not applicable for data sets other than those used in their development.

(c) *Semi-empirical scattering models*—The semi-empirical model is a combination of empirical and physical approaches. In this model roughness and soil moisture, observations of the target along with the incidence angle and polarization information from radar data are used to retrieve the soil moisture. Semi-empirical backscattering models have been developed by considering the complexity of the theoretical models and simplicity of empirical models. These models are applicable when little or no information about the surface roughness is available. The main advantage of these types of models is that they are not site-dependent, as in the case of empirical backscattering models. The most widely used semi-empirical models are given by Oh et al. (1992), Dubois et al. (1995), Topp et al. (1980), Dobson and Ulaby (1986), and others.

11.4 Materials Used

11.4.1 Satellite Data

In the present study, optical satellite data (Landsat-8 OLI of 30 m resolution and IRS P6 LISS-4 of 5.8 m resolution) and microwave satellite data (RISAT-1 C-band and PALSAR-2 L-band) have been used for geomorphic and palaeochannel mapping. High-resolution satellite images have also been used to interpret large-scale land features and the palaeochannels and to locate the resistivity traverses using Web Map Services of Google Earth. Specifications of the datasets used in the present study are given in Tables 11.1 and 11.2.

11.4.2 Field Survey

Field verification and soil samples were collected during 22–24 Oct., 2017 at Bhimarlai village in Barmer district of Rajasthan. For verification of soil moisture, two pits were dug up to a depth of 1.2 m across the palaeochannels viz. Pit-1 inside the palaeochannel and Pit-2 outside the palaeochannel. Soil samples were collected

Table 11.1 Detailed Specifications of optical satellite data used in the study

Optical satellite data	Band No	Bands	Spectral range (μm)	Resolution (m)	Swath (km)	Date of pass (dd, mm, yyyy)
IRS LISS-4 MX	2	B2	0.52–0.59	5.8	23	03.10.2014
	3	B3	0.62–0.68			
	4	B4	0.77–0.86			
Landsat-8 OLI and TIRS	1	Coastal	0.43–0.45	30	185	26.09.2014 13.10.2014 12.10.2014
	2	Blue	0.45–0.51			
	3	Green	0.53–0.59			
	4	Red	0.63–0.67			
	5	NIR	0.85–0.88			
	6	SWIR-1	1.57–1.65			
	7	SWIR-2	2.11–2.29			
	8	Pan	0.50–0.68	15		
	9	Cirrus	1.36–1.38	30		
	10	TIRS-1	10.6–11.19	30 (100)		
	11	TIRS-2	11.5–12.51			

Table 11.2 Specifications of microwave satellite sensor data used in the study area

Microwave satellite sensor	Band (frequency)	Polarization/incidence angle	Ground resolution (m)	Swath (km)	Date of pass (dd, mm, yyyy)
RISAT-1	C-band (5.3 GHz)	HH, HV, VV, VH 23–49°	25	115	2.10.2014 15.10.2014
PALSAR-2	L-band (1.2 GHz)	HH, HV, VV 8–70°	10	70	2.10.2014

with every 20 cm interval. Physico-chemical analysis like texture, EC, pH and volumetric soil moisture was done in the laboratory. High-resolution Electrical Resistivity Tomography (HERT) survey across the palaeochannels was carried out using IRIS Syscal Pro multi-electrode Resistivity meter on 22 March, 2018.

11.4.3 Methodology

The present study involves palaeochannel mapping using fused satellite data products and penetration depth estimation for C- and L-band sensors using semi-empirical soil moisture modeling. For validation of the subsurface aquifers, resistivity sounding

was done across the palaeochannel. Detailed methodology of the same is explained below:

(a) *Palaeochannel mapping using satellite data*—In this process, fusion techniques have been applied with optical and microwave satellite data (Landsat-8 with RISAT-1 data and LISS-4 with PALSAR-2 data) for palaeochannel mapping. Principal Component Analysis (PCA) fusion technique is found to be useful in highlighting the palaeochannel in the arid region due to having higher soil moisture content than the surrounding. The delineated boundaries have been verified in the field.

(b) *Semi-empirical modeling for soil moisture estimation*—This model involves forward and backward modeling by using field parameters (soil texture, volumetric soil moisture, bulk density, and surface roughness) and sensor parameters (frequency, and look angle).

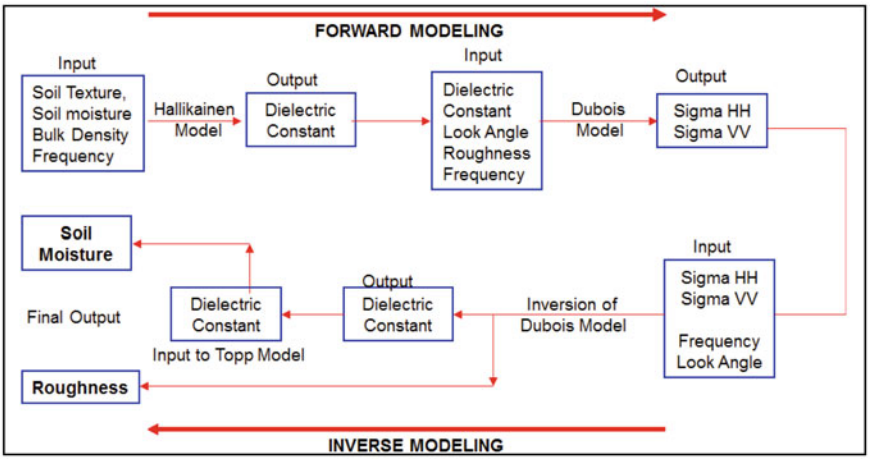

Initially, soil dielectric constant is derived with the help of Hallikaninen model (Hallikaninen et al. 1985):

$$\varepsilon = (a_0 + a_1 S + a_2 C) + (b_0 + b_1 S + b_2 C) m_v + (c_0 + c_1 S + c_2 C) m_v^2 \quad (11.1)$$

Here, ε is observed dielectric constant, m_v is volumetric soil moisture, S&C are volume fraction of sand and clay (% by wt.) in the soil. Derivatives of a, b, and c are constants at different frequency.

Further, the backscattering coefficient (σ^0) is calculated for different polarization (HH and VV) using Dubois equation which is applicable for RMS height (s) of 0.32–3.02 cm, Incidence angle (θ) of 30°–60° and Frequency range from 2.5 to 11 GHz.

$$\sigma^0_{\text{hh}} = 10^{-2.75}\frac{\cos^{1.5}(\Theta)}{\sin^5(\Theta)} \times 10^{0.028\varepsilon\tan(\Theta)}(ks\sin(\Theta))^{1.4}\lambda^{0.7} \tag{11.2}$$

$$\sigma^0_{vv} = 10^{-2.35}\frac{\cos^3(\Theta)}{\sin^3(\Theta)} \times 10^{0.046\varepsilon\tan(\Theta)}(ks\sin(\Theta))^{1.1}\lambda^{0.7} \tag{11.3}$$

Here, $\sigma^0{}_{(\text{HH})}$ **is** Backscattering coefficient, θ is Incidence Angle (rad), ε is Dielectric constant, λ is Wavelength (cm), and s is RMS height (cm). Once the backscattering values of $\sigma_{0(\text{HH})}$ and $\sigma_{0(\text{VV})}$ at selected field samples are correlated with the corresponding values on the actual radar image, then the inversion models (Inverse Dubois model and Topp model) are applied to generate soil moisture and roughness maps of the entire study area.

$$\varepsilon' = \frac{\left(\log 10\left(\frac{(\sigma^0_{\text{HH}})^{0.7857}}{\sigma^0_{\text{VV}}}\right)10^{-0.19}\cos^{1.82}\theta\sin^{0.93}\theta\lambda^{0.15}\right)}{-0.024\tan\theta} \tag{11.4}$$

Here, σ^0 is the backscattering coefficient, θ is incidence angle (rad), ε is dielectric constant, λ is the wavelength (cm), and s is the RMS height (cm).

Roughness (ks) is derived by the equation of

$$ks = \sigma^0_{\text{HH}}{}^{1/1.4}10^{2.75/1.4}\frac{\sin^{2.57}\theta}{\cos^{1.07}\theta}10^{-0.02\cdot\varepsilon'\cdot\tan\theta}\lambda^{-0.5} \tag{11.5}$$

The soil moisture (θ_v) is estimated using Topp's Model

$$\theta_v = -5.3\times10^{-2} + 2.92\times10^{-2}\varepsilon - 5.5\times10^{-4}\varepsilon^2 + 4.3\times10^{-6}\varepsilon^3 \tag{11.6}$$

(c) *Estimation of Penetration Depth*—Penetration depth of microwave sensors is defined as the depth where the power is reduced to 1/e ($e = 2.718$) of the incident radiation. Reduction in power depends on the dielectric properties of the material. Alternately, penetration depth is denoted by the depth at which the power density decreased to 37% (approx. 1/3rd) of its initial value at the surface. Dielectric properties of a material are described by the complex relative permittivity (Von Hippel 1954). Imaginary part of the complex permittivity ($\varepsilon_r{}''$) shows higher loss factor and faster microwave energy absorption in the material. The penetration depth of the electric wave decreases with increasing frequency. The power density will decrease exponentially from the surface to the core region. Penetration depth (PD or d_p) is calculated by the equation

$$d_p = \frac{C}{2\pi f\sqrt{2\varepsilon'\left[\sqrt{1+\left(\frac{\varepsilon''}{\varepsilon'}\right)^2}-1\right]}} \tag{11.7}$$

where, f is the frequency (Hz), c is the speed of light (3×10^{10} cm/s), ε_r' is the real dielectric constant, ε_r'' is the imaginary dielectric constant ε_r', λ is the wavelength ($\lambda = c/f$).

Simplified equation of penetration depth (PD) is represented by real dielectric constant (ε') and imaginary dielectric constants (ε'') for the corresponding wavelength (λ) of radar signal.

$$\mathrm{PD} = \frac{\lambda\sqrt{\varepsilon'}}{2\pi\varepsilon''} \tag{11.8}$$

(d) *Ground Validation using Resistivity Survey*—Electrical resistivity is one of the robust geophysical methods which measures electrical potential difference at any point with subsurface electrical current flow (Dahlin 2001; Loke 2004; Loke et al. 2013). Acquisition of resistivity data is generally done using different electrode configurations (Wenner, Schlumberger, dipole–dipole, pole-pole). Depending on the depth of investigation, 2D tomograms can be generated with advanced IRIS SYSCAL multi-electrode resistivity meter. In the present study, resistivity survey has been carried out using Wenner-Schlumberger (WS) array with 72 electrodes configurations (10 m interval) for a traverse length of 710 m. WS method involves two potential electrodes (P_1 and P_2) at a distance 'a' and two current electrodes (C_1 and C_2) at a distance 'na' from the potential electrodes. Based on the above electrode configuration, apparent resistivity (ρ) is calculated by the following equation:

$$\rho = \pi\, n(n+1)\, a\, (V/I) \tag{11.9}$$

11.5 Results and Discussion

11.5.1 Delineation of Palaeochannels Using Satellite Data

Optical satellite images of Landsat-8 and LISS-4 data show the course of Luni River, which took 90° bending near Bhimarlai village near Pachpadra (Fig. 11.2a). At a number of places, the river has been anastomosed with leaving behind moist zones that possibly indicate old course or palaeochannels. It has been observed that PCA fused images with Landsat-8 and RISAT-1 C-band provide splay of spectacular palaeochannels (cyan tone) in and around the Luni River (Fig. 11.2b). A number of palaeochannels have been marked through online digitization using Arc Map software. Two distinct palaeochannels have been delineated in the north of Luni River such as N-S oriented wide palaeochannel between Dudhawa and Mekarna villages and a narrow curvilinear palaeochannel at Bhimarlai village. On a high-resolution satellite image, Bhimarlai palaeochannel is represented by depressed topography with agricultural land that contains more moisture than the surroundings.

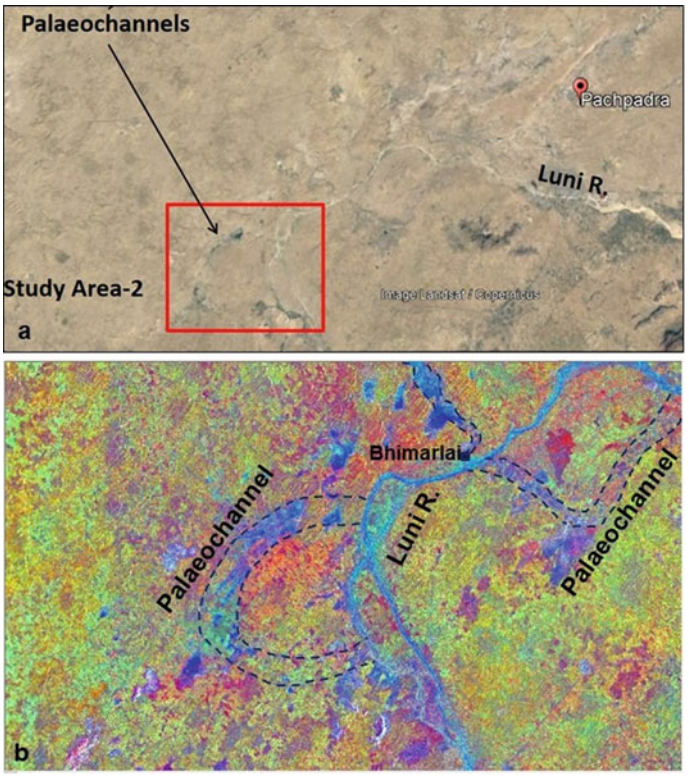

Fig. 11.2 **a**, **b** PCA fused product of RISAT-1 C-band and Landsat-8 MX (October, 2014) showing palaeochannels (blue tone) and the present day Luni River at Pachpadra in Barmer district of Rajasthan

11.5.2 Backscattering Profiles for C and L-bands Across the Palaeochannel

For characterizing the palaeochannels in Bhimarlai area, backscattering profiles have been drawn along C-D traverse (1.2 km) on RISAT-1 C-band and PALSAR-2 L-band images. It has been observed that the magnitude of backscattering coefficient (σ^0) for L-band is much higher (blue line) than that of C-band (red line) sensors across the palaeochannel (Fig. 11.3). The result indicates that penetration capability for L-band into the moist zone is more than the C-band. However, the σ^0 value is much lower in the non-moist zones (dry zone) in the surrounding area of the palaeochannel.

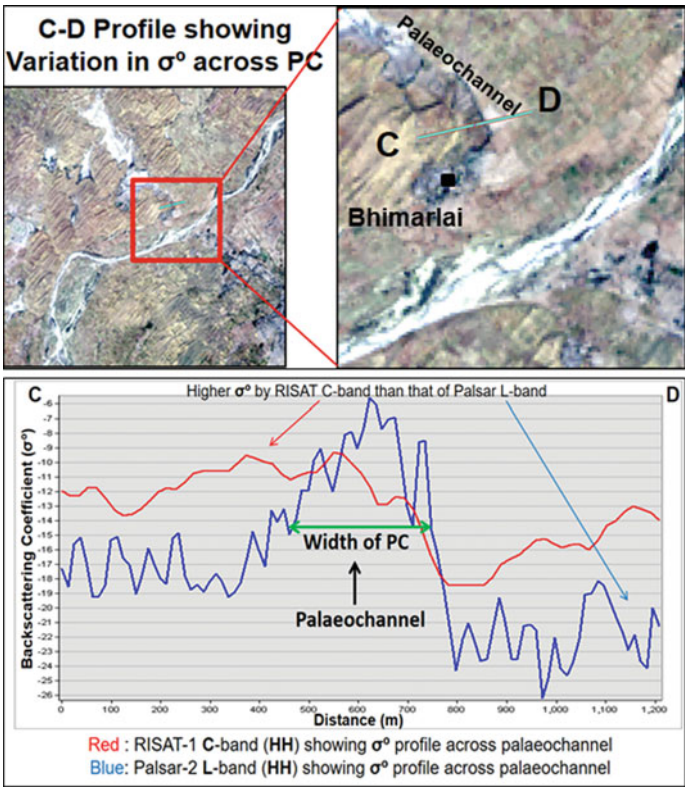

Fig. 11.3 PCA fused product of RISAT-1C and Landsat-8 images highlighting the palaeochannels at Bhimarlai. Spectral profiles show the variation in backscattering coefficient (σ°) with C and L-band data across the palaeochannel

11.5.3 Variation in Field Soil Moisture with Depth

Soil profiles in the study area show increasing soil moisture (3.65–12.29%) from the surface to a depth of 60 cm, followed by gypsiferous soil (impervious layer) with low moisture (1.02% to 0.59%) between 60 and 120 cm. Below this impervious layer, soil moisture again increases (8.39–10.87%) in sandy soil up to a depth of 180 cm. For estimation of volumetric soil moisture, two pits have been dug up to a depth of 1.2 m to collect soil samples at an interval of 20 cm each. Pit-1 was dug in an agricultural field inside the palaeochannel, and Pit-2 dug outside the palaeochannel on a dune field (Fig. 11.4). Soil moisture measurements were done by subtracting weights of wet and dry soil materials in the field. The soil moisture percentage at Pit-1 and Pit-2 are plotted with increasing depth up to 120 cm. It has been observed that soil moisture in Pit-1 (within palaeochannel) increases with depth from 2 to 5% whereas, soil moisture in Pit-2 (outside palaeochannel) is almost constant (1.5%)

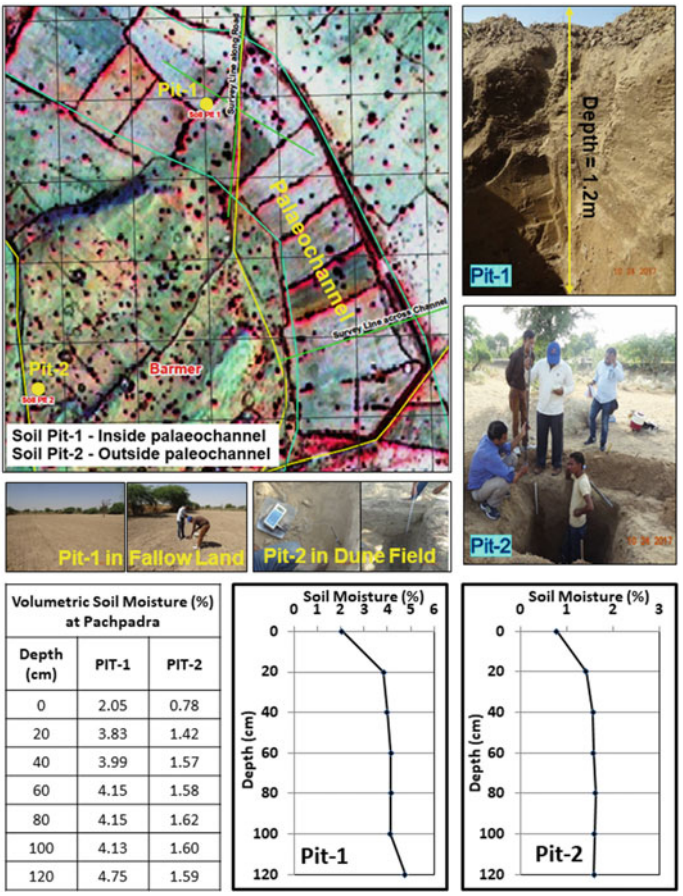

Volumetric Soil Moisture (%) at Pachpadra		
Depth (cm)	PIT-1	PIT-2
0	2.05	0.78
20	3.83	1.42
40	3.99	1.57
60	4.15	1.58
80	4.15	1.62
100	4.13	1.60
120	4.75	1.59

Fig. 11.4 Satellite image shows the delineated palaeochannel (PC) at Bhimarlai. Locations of Pit-1 (inside the PC) and Pit-2 (outside the PC) are shown on the image with field photographs. Soil moisture variation with depth (upto 120 cm) is shown for Pit-1 and Pit-2

throughout the depth. Thus, soil moisture in the palaeochannel is expected to be higher than in the surroundings.

11.5.4 Soil Penetration Depth for C and L-Band Microwave Sensors

As mentioned in the methodology, the soil penetration depth of microwave sensors for C and L-bands can be calculated using derived dielectric constant (ε) using Eq. 11.1 and backscattering coefficient (σ^0) using Eq. 11.2. In the study area, these values are

calculated for corresponding cumulative soil moisture (SM) in different layers viz. surface (0), 0–20, 0–40 cm, etc. Each soil pack's penetration depth (PD) is estimated using real and imaginary parts of dielectric constant for C and L-band sensors (Table 11.3). The extent of penetration of C and L-band sensors in soil is correlated with backscattering coefficient (σ_{ohh}) obtained from the corresponding image pixel. Pit-1 (inside the palaeochannel) shows the least penetration depth for C-band (7.336 cm) and L-band (11.058 cm) respectively (Table 11.3a, b). However, Pit-2 (outside the palaeochannel) shows the least penetration depth for C-band (~0 cm) and L-band (15.240 cm) respectively (Table 11.3c, d). Thus, dry soil shows relatively more penetration depth for L-band sensor. But, C-band sensor shows higher penetration depth in moist soil than that of dry soil due its sensitivity to moisture. Pictorial representation of relative penetration depth for C and L-bands in moist and dry soil is shown in Fig. 11.5a, b.

11.5.5 Validation of Palaeochannels with Resistivity Tomograms

Palaeochannels generally act as the storehouse of sub-surface groundwater. However, these paleochannels need to be validated through HERT survey and drilling data. In the present study, high-resolution resistivity survey has been carried out for 240 m length along the traverse in Bhimarlai area for assessing the groundwater potential of the palaeochannels (Fig. 11.6). After alignment of 48 electrodes with 2.5 m spacing, resistivity data were acquired with Wenner-Schlumberger (WS) method to achieve a depth of investigation up to 50 m. Interpretation of the tomogram was done based on the variation in resistivity of different soil materials. At the same time, this tomogram was validated with the available litholog (drilling) data close to the survey line. It has been observed that the top layer (~6 m) is mostly dry indicating sandy layer having high resistivity. However, the bottom low resistivity layer is relatively moist due to presence of saturated sandy clay layer which may act as brackish to fresh quality groundwater aquifer zone (palaeochannel).

11.6 Conclusions

The above study shows the potential of microwave data (RISAT-1 C-band and PALSAR-2 L-band) for soil moisture estimation based on backscattering coefficient. A unique methodology has been developed to estimate sensor penetration depth across the palaeochannel (PC) in the arid region of Rajasthan. The derived penetration depth for L-band is found to be higher within the palaeochannel than that of C-band. However, penetration depth of L-band is more in dry soil (outside PC) than the moist soil (inside PC). Soil moisture content in the palaeochannel is validated

Table 11.3 Comparison of penetration depth of C and L-band sensors in moist and dry soil across the palaeochannels in western Rajasthan

Pit-1: Inside palaeochannel (moist soil)					Pit-2: Outside palaeochannel (dry soil)				
(a) Field parameters for RISAT-1 C-band (5.3 GHz)					*(c) Field parameters for RISAT-1 C-band (5.3 GHz)*				
Soil depth (cm)	Soil moisture (SM)	Dielectric constant (ε)	Backscattering coefficient σ_{oHH} (dB)	Penetration depth (PD) (cm)	Soil depth (cm)	Soil moisture (SM)	Dielectric constant (ε)	Backscattering coefficient σ_{oHH} (dB)	Penetration depth (PD) (in cm)
0	0.021	2.777	−12.065	– -	0	0.008	2.291	−12.167	~0
0–20	0.038	3.466	−11.919	9.914	0–20	0.014	2.534	−12.116	~0
0–40	0.040	3.526	−11.907	9.341	0–40	0.016	2.591	−12.104	~0
0–60	0.042	3.588	−11.894	8.822	0–60	0.016	2.596	−12.103	~0
0–80	0.041	3.587	−11.894	8.828	0–80	0.016	2.613	**−12.099**	**~0**
0–100	0.041	3.581	−11.895	8.878	0–100	0.016	2.605	−12.101	~0
0–120	0.048	3.823	**−11.844**	**7.336**	0–120	0.016	2.602	−12.102	~0
σ_{ohh} (dB) at Pit-1 on C-band image = **−11.29**					σ_{ohh} (dB) at Pit-2 on C-band image = **−12.06**				
(b) Field parameters for PALSAR-2 L-band (1.2 GHz)					*(d) Field parameters for PALSAR-2 L-band (1.2 GHz)*				
Soil depth (cm)	Soil moisture (SM)	Dielectric constant (ε)	Backscattering coefficient σ_{oHH} (dB)	Penetration depth (PD) (in cm)	Soil depth (cm)	Soil moisture (SM)	Dielectric constant (ε)	Backscattering coefficient σ_{oHH} (dB)	Penetration depth (PD) (in cm)
0	0.021	2.987	−16.536	14.529	0	0.008	2.895	−16.556	16.990
0–20	0.038	3.184	−16.494	12.023	0–20	0.014	2.937	−16.547	15.640
0–40	0.040	3.205	−16.490	11.847	0–40	0.016	2.948	−16.544	15.360
0–60	0.042	3.227	−16.485	11.672	0–60	0.016	2.949	−16.544	15.330
0–80	0.041	3.227	−16.485	11.674	0–80	0.016	2.952	**−16.543**	**15.240**

(continued)

Table 11.3 (continued)

Pit-1: Inside palaeochannel (moist soil)					Pit-2: Outside palaeochannel (dry soil)				
0–100	0.041	3.224	−16.486	11.692	0–100	0.016	2.951	−16.544	15.280
0–120	0.048	3.315	**−16.467**	**11.058**	0–120	0.016	2.95	−16.544	15.300
σ_{ohh} (dB) at Pit-1 on PALSAR-2 Image = **−15.026**					σ_{ohh} (dB) at Pit-2 on PALSAR-2 Image = **−15.740**				

Note Estimation based on surface roughness (s) = 1.5 and volume fraction of sand (S) and clay (C) in soil; $S = 0.72$; $C = 0.15$
Note Estimation based on surface roughness (s) = 1.5 and volume fraction of sand (S) and clay (C) in soil; $S = 0.43$; $C = 0.05$

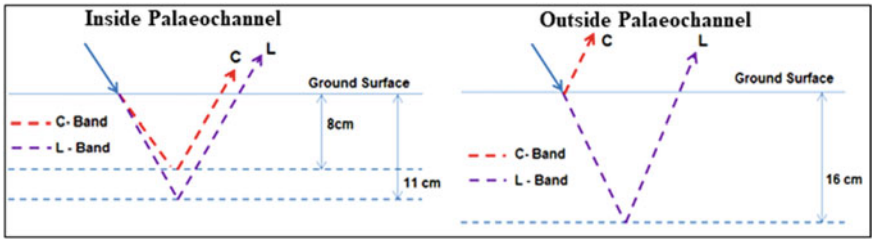

Fig. 11.5 Relative penetration depth for C and L-band sensors in Pit-1 (inside the palaeochannel) and Pit-2 (outside the palaeochannel)

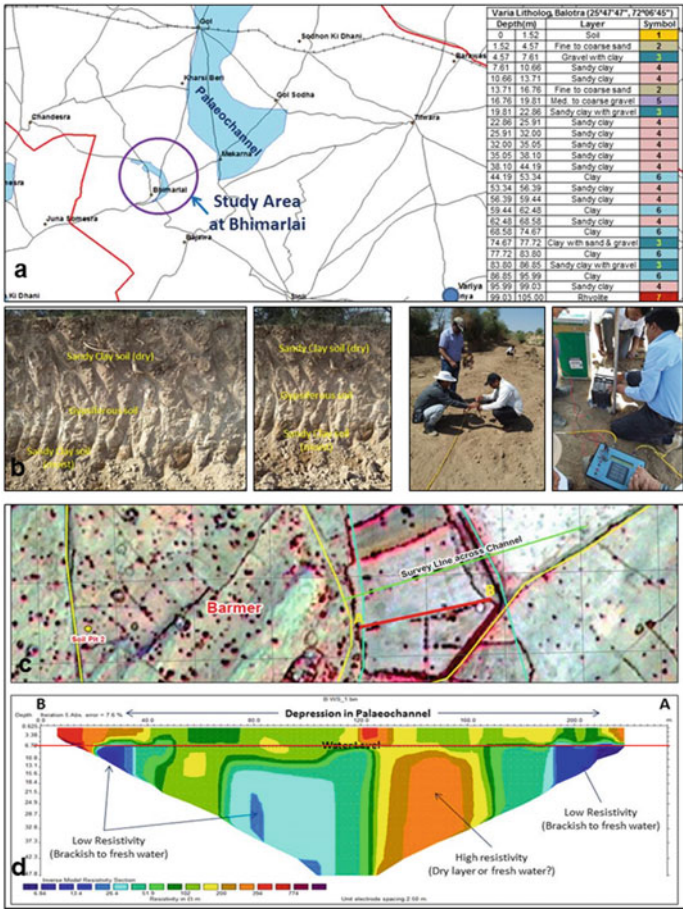

Fig. 11.6 **a** Litholog data at Varia village, SE of Bhimarlai. **b** Soil profile at Bhimarlai showing moist soil at a depth of 5 m from the surface. **c** Resistivity traverse line across the palaeochannel. **d** 2D resistivity tomogram across the palaeochannel at Bhimarlai village

with 2D resistivity tomograms. The low resistivity zone in the sub-surface possibly indicates increasing clay content which is characteristic of the palaeochannel.

Acknowledgements All the authors are grateful to the Director, NRSC, Hyderabad and the Chief General Manager, RCs / NRSC, Hyderabad for their guidance and encouragement. Data provided by the Officials of GWD, Jodhpur and resistivity survey by AiMIL Ltd., New Delhi is duly acknowledged.

References

Baghdadi N, Holah N, Zribi M (2006) Soil moisture estimation using multi-incidence and multi-polarization ASAR data. Int J Remote Sens 27(10):1907–1920. https://doi.org/10.1080/01431160500239032

Baghdadi N, Zribi M (2006) Evaluation of radar backscatter models IEM, OH and Dubois using experimental observations. Int J Remote Sens 27(18):3831–3852. https://doi.org/10.1080/01431160600658123

Barrett BW, Dwyer E, Whelan P (2009) Soil moisture retrieval from active spaceborne microwave observations: an evaluation of current techniques. Remote Sens 1:210–242. https://doi.org/10.3390/rs1030210

Dahlin T (2001) The development of DC resistivity imaging techniques. Comp Geosci 27:1019–1029

Das K, Paul PK (2015) Present status of soil moisture estimation by microwave remote sensing: review article. Cogent Geosci 1(1084669):1–21. https://doi.org/10.1080/23312041.2015.1084669

de Jeu RAM, Wagner W, Holmes TRH, Dolman AJ, van de Giesen NC, Friesen J (2008) Global soil moisture patterns observed by space borne microwave radiometers and scatterometers. Surv Geophys 29:399–420.https://doi.org/10.1007/s10712-008-9044-0

Dobson MC, Ulaby FT (1986) Active microwave soil moisture research. IEEE Trans. Geosci Remote Sens 24(1):23–36. https://doi.org/10.1109/TGRS.1986.289585.

Dubois PC, Van Zyl J, Engman T (1995) Measuring soil moisture with imaging radars. IEEE Trans Geosci Remote Sens 33(4):915–926

Engman ET, Chauhan N (1995) Status of microwave soil moisture measurements with remote sensing. Remote Sens Environ 51:189–198

Gharechelou S, Tateishi R, Tetuko J, Sumantyo S (2015) Interrelationship analysis of L-band backscattering intensity and soil dielectric constant for soil moisture retrieval using PALSAR data. Adv Remote Sens 4:15–24

Hallikainen MT, Ulaby FT, Dobson MC, El-Rayes MA, Wu LK (1985) Microwave dielectric behavior of wet soil part 1: Empirical models and experimental observations. IEEE Trans Geosci Remote Sens 1:25–34

Jackson TJ, Hsu AY, O'Neill PE (2002) Surface soil moisture retrieval and mapping using high-frequency microwave satellite observations in the southern great plains. J Hydrometeorol 3:688–699

Kafarski M, Majcher J, Wilczek A, Szyplowska A, Lewandowski A, Zackiewicz A, Skierucha W (2019) Penetration depth of a soil moisture profile probe working in time-domain transmission mode. Sensors 19(5485):1–13. https://doi.org/10.3390/s19245485

Loke MH (2004) Tutorial: 2D and 3D electrical imaging surveys. University of Alberta, Edmonton, AB, Canada. https://sites.ualberta.ca/~unsworth/UA-classes/223/loke_course_notes.pdf

Loke MH, Chambers JE, Rucker DF, Kuras O, Wilkinson PB (2013) Recent developments in the direct-current geoelectrical imaging method. J Appl Geophy 95:135–156

Lv S, Zeng Y, Wen J, Zhao H, Su Z (2018) Estimation of penetration depth from soil effective temperature in microwave radiometry. Remote Sens 10(519):1–19. https://doi.org/10.3390/rs10040519

Narvekar PS, Entekhabi D, Kim SB, Njoku EG (2015) Soil moisture retrieval using L-band radar observations. IEEE Trans Geosci Remote Sens 53(6):3492–3506. https://doi.org/10.1109/TGRS.2014.2377714

Oh Y, Sarabandi K, Ulaby FT (1992) An empirical model and inversion technique for radar scattering from bare soil surfaces. IEEE Trans Geosci Remote Sens 30(2):370–381

Owe M, Van de Griend AA (1998) Comparison of soil moisture penetration depths for several bare soils at two microwave frequencies and implications for remote sensing. Water Resour Res 34(9):2319–2327

Rao SS, Kumar D, Das SN, Nagaraju MSS, Venugopal MV, Rajankar P, Laghate P, Sivaprasad Reddy M, Joshi AK, Sharma JR (2013) Modified Dubois model for estimating soil moisture with dual polarized SAR data. J Indian Soc Remote Sens 41(4):865–872. https://doi.org/10.1007/s12524-013-0274-3

Shi J, Wang J, Hsu AY, O'Neill PE, Engman ET (1997) (1997) Estimation of bare surface soil moisture and surface roughness parameter using L-band SAR image data. IEEE Trans Geosci Remote Sens 35:1254–1266

Singh A, Meena GK, Kumar S, Gaurav K (2019) Evaluation of the penetration depth of L- and S-band (NISAR mission) microwave SAR signals into ground. URSI AP-RASC 2019, New Delhi, India; 09–15 Mar 2019. https://doi.org/10.23919/URSIAP-RASC.2019.8738217

Topp GC, Davis JL, Annan AP (1980) Electromagnetic determination of soil water content: measurements in coaxial transmission lines. Water Resour Res 16(3):574–582

Von Hippel AR (1954) Dielectric materials and applications. The Technology Press of M.I.T. and Wiley, New York

Zhao W, Li ZL (2013) Sensitivity study of soil moisture on the temporal evolution of surface temperature over bare surfaces. Int J Remote Sens 34(9–10):3314–3331

Chapter 12
Geospatial Applications in Inventory of Horticulture Plantations

H. M. Ravishankar, Shivam Trivedi, S. Rama Subramoniam, J. Mohammed Ahamed, T. R. Nagashree, V. B. Manjula, R. Hebbar, C. S. Jha, and V. K. Dadhwal

Abstract Horticulture is one of India's most important agricultural enterprises, driving the economy's growth. It is a key component for economic development in several states of the country and contributes around 30% to GDP of agriculture, with only about 8.5% of total agricultural area coverage. The lack of an authentic and holistic database on area and production was the major bottleneck limiting perspective planning of horticultural development in India. In this context, to realize the potential use of geospatial technology, several studies were initiated to establish the feasibility of high-resolution satellite data for discrimination of dominant fruit orchards and plantation crops using semi-automated object-oriented image analysis.

H. M. Ravishankar · S. Trivedi (✉) · S. R. Subramoniam · J. M. Ahamed · T. R. Nagashree · V. B. Manjula · R. Hebbar
Regional Remote Sensing Centre-South, NRSC, ISRO, Bengaluru, Karnataka, India
e-mail: shivamtrivedi@nrsc.gov.in

H. M. Ravishankar
e-mail: ravishankar_hm@nrsc.gov.in

S. R. Subramoniam
e-mail: ramasubramoniam_s@nrsc.gov.in

J. M. Ahamed
e-mail: mohammedahamed_j@nrsc.gov.in

T. R. Nagashree
e-mail: nagashree_tr@nrsc.gov.in

V. B. Manjula
e-mail: manjula_vb@nrsc.gov.in

R. Hebbar
e-mail: hebbar_kr@nrsc.gov.in

C. S. Jha
Regional Centres, National Remote Sensing Centre, ISRO, Hyderabad, Telangana, India
e-mail: jha_cs@nrsc.gov.in

V. K. Dadhwal
National Institute of Advanced Studies, Bengaluru, Karnataka, India
e-mail: vkdadhwal@nias.res.in

C. S. Jha et al. (eds.), *Geospatial Technologies for Resources Planning and Management*, Water Science and Technology Library 115,
https://doi.org/10.1007/978-3-030-98981-1_12

The major fruit crops covered were mango, citrus, banana, and grapes, while the nut crops included coconut, arecanut, oil palm, and cashew nut. Multi-resolution and temporal high-resolution data, in conjunction with the GPS-guided ground truth collection, was utilized in these studies. Hybrid semi-automatic classification techniques employing both digital classification and visual image interpretation were employed for spatial delineation of extent of horticultural plantation crops. It was concluded that single date high-resolution data corresponding to month of February–March would be most optimal for delineation of major plantations crops such as mango, citrus, coconut, arecanut, and cashew nut while for banana and grapes multi-temporal data was more suitable for successful inventory. The classification accuracies mostly ranged between 80 and 90%, depending on various factors, viz., age of plantation, extent of heterogeneity, plant spacings canopy cover, agronomic practices, etc. The methodologies for the identification and mapping of various horticultural plantations are established for selected study regions, mainly in peninsular India. Based on the encouraging results and successful completion of pilot projects, these studies were upscaled to regional/national level projects under the auspices of the Ministry of Agriculture. Fruit crops namely Mango, Banana, Citrus & Grapes, and a major nut crop, Coconut were successfully inventoried for major regions of the country. Relevant site-suitability analysis for mango, the king of fruits, has also been carried out by integrating terrain and pedo-climatic parameters under a GIS environment. This chapter summarizes the above efforts and achievements for mapping and monitoring important horticultural crops of India.

Keywords Horticulture · Plantations · Fruits · Semi-automatic classification · Object-oriented image analysis · Hybrid approach · Visual interpretation · Ground truth · Accuracy assessment · Geospatial technology · Deep learning · Site-suitability

12.1 Introduction

12.1.1 Importance of Horticulture

India is bestowed with varied agro-climatic conditions, which are highly favorable for growing many horticultural crops. Globally, India stands second in terms of production of fruits and vegetables (NHRDF 2019). The horticulture crops are an integral part of food and nutritional security and an essential ingredient of economic security. Thus, the horticulture sector in the country has been undergoing a sea change, both in terms of area, production, and productivity. India has emerged as a leading horticultural crop-producing country globally, with a total annual output of 240 million tons of horticulture crops. Areal extent under horticulture in India during 2015–16 was statistics indicate the vital role of horticulture in the Indian economy, in terms of generation of employment, higher farm profitability due to better price realizations, providing

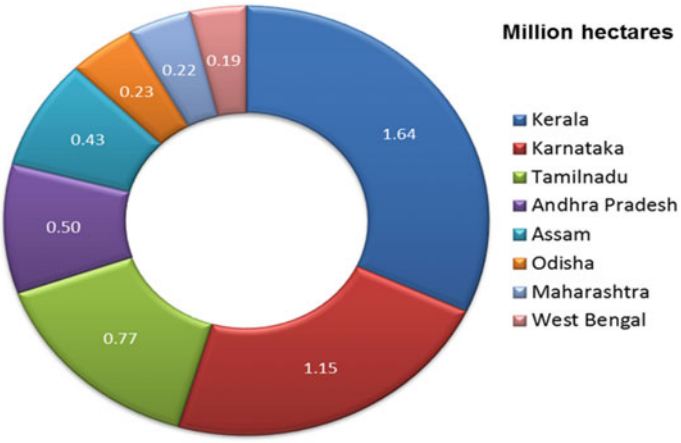

Fig. 12.1 State-wise area distribution under major plantation crops in India

ingredients for several by-products in food-processing industries under value addition chain, and stabilizing the country's balance of trade through export earnings. More than 95% of plantations are cultivated in the eight major states of India, while southern four states, Kerala, Karnataka Tamil Nadu, and Andhra Pradesh (including Telangana), alone contribute more than 75% of the total area and production of plantation crops (Fig. 12.1). Reliable statistical database, both area and production, at different spatial and administrative hierarchies is the fundamental requirement to promote growth of the horticultural sector in the country. In this context, geospatial technology provides an ideal framework for the generation of geodatabase on the spatial extent of horticultural crops at a disaggregated level.

The existing micro-level information base for horticulture plantations is mostly non-spatial or generalized spatial format. Requirement of the database on spatial distribution of major plantations, at large scales, was a felt need during early part of twenty-first century to meet the operational requirements of different segments of horticulture at micro to macro levels. Remote Sensing Satellite data with medium and coarse spatial resolutions have been used operationally for agricultural crop classification and monitoring (Dadhwal et al. 2003; Murthy et al. 2007). However, organized feasibility studies for establishing the use of geospatial technology for inventory/mapping of dominant fruit and plantation crops are, thus far, inadequate. Even though very few discrete studies had been attempted in this direction, a really organized and institutional effort covering multiple fruit and horticulture plantation crops did begin only during 2012. As a first step, pilot studies covering important plantation crops to develop operational methodologies for inventory were attempted. These studies primarily employed a hybrid approach, a combination of semi-automatic object-based classification and limited manual refinement.

As almost 85% of horticulture plantations, in terms of areal extent, are geographically distributed in peninsular India, majority of the pilot studies were carried out

in this region (Fig. 12.1). This chapter summarizes the details of pilot studies for methodology development initially, followed by the operational execution of these techniques or methodologies in inventory of dominant fruit and plantation crops, besides site-suitability analysis, as confined to Karnataka, Tamil Nadu, and Kerala states.

12.1.2 Role of Geospatial Technology

With recent advances in space technology and the availability of high to very high spatial resolution satellite datasets and advanced classification techniques, geospatial technology is expected to play a pivotal role in geospatial database creation on horticulture crops, apart from facilitating the generation of databases on other related components. It has to be specifically mentioned here that such efforts have already covered inventory of commercial plantations, namely tea, rubber, and coffee but were lacking to fruit and plantations crops (RRSSC-B 2001; RRSC-East 2014; RRSC-South 2012, 2019).

Conventional per-pixel classifiers have limited utility for identifying and delineating horticulture crops as large spatial heterogeneity limits the realization of reasonable accuracy (Hebbar and Rao 2002; Srivastava and Gebelein 2007). Object-based image classification technique is a powerful, promising method for classification of high-resolution remote sensing data through the conversion of image pixels into objects using both texture and contextual information. Object-based image classification techniques provide more relevant information at multiple spatial scales than pixel-based classifiers (Gamanya et al. 2007). The main advantage of using object-oriented image analysis is the flexibility in defining various parameters for image objects at intended scales, viz. spectral reflectance, object-textures, feature-shapes, context relationships, apart from integrating both spatial and non-spatial additional collateral information (Bock et al. 2005).

In the Indian context, first-ever operational inventory was carried out for rubber plantations using high-resolution Cartosat-1 and LISS-IV data covering Tripura state, primarily employing onscreen visual interpretation technique. In the same study, site-suitability analysis for identifying suitable wastelands for expansion of rubber cultivation was also carried out (RRSC-South 2012). The utility of a hybrid approach for delineation of banana orchards using a combination of object-based approach and post visual classification editing was demonstrated using high-resolution data (Kasper et al. 2009).

In the background of advancements in space technology, advanced techniques for classification of available indigenous high-resolution satellite data, need for kick-starting the generation of hierarchical (macro to micro levels) geospatial databases on inventory and site-suitability, a series of feasibility studies covering multiple fruits and plantation crops, with the avowed intention of possible operationalization to regional/national levels, were initiated.

12.2 Pilot Studies for Methodology Development

Under ISRO's Earth Observation Applications Mission (EOAM), Regional Remote Sensing Centre-South (Bengaluru), of National Remote Sensing Centre, ISRO made concerted efforts during 2012–15, to study the feasibility of using high-resolution satellite datasets in association with temporal, multispectral datasets for inventory of dominant fruit orchards and plantation crops covering representative regions. Identification and methodology development for inventory of four fruit crops (mango, citrus, banana & grapes) and four plantation crops (coconut, arecanut, oil palm and cashewnut) was carried out under this EOAM project. Specific study areas covered represented diversified agro-climatic regimes of India.

Study area details along with selected horticulture crops are mentioned in Table 12.1: (i) Mango: Malihabad taluka, Uttar Pradesh (ii) Citrus: Sivagiri taluk, Tamil Nadu (iii) Banana: Guntur, Andhra Pradesh (iv) Grapes: Chikaballapura, Karnataka (v) Coconut: Tiptur taluk, Karnataka (vi) Arecanut: Chennagiri, Karnataka (vii) Oil Palm: Rajanagaram mandal, Andhra Pradesh and (viii) Cashewnut: Mandasa mandal, Andhra Pradesh. High-resolution Resourcesat-1 and 2, LISS-IV MX (5.0 m), and Cartosat-1 (2.5 m) data corresponding to 2013–14 were used under the study, along with Resourcesat-1 and 2 LISS-III (24 m) data.

Generalized methodology is depicted in Fig. 12.2. The major steps covered included (i) Satellite data processing (ii) GPS-guided Field data collection (iii) Classification (iv) Post classification refinement. Under all the studies, the collection of relevant ground truth information on crop of interest and competing crops and other classes was conducted in the selected sites/districts for its utilization in digital classification and accuracy assessment (Fig. 12.3). The sample sites were identified based on pre-field interpretation of the satellite data using tone and texture. Information such as sample sites and their locations, crop type, and age of crop, along with geotagged field photos, were organized in a GIS environment for generating a digital library of ground truth. Basically, a semi-automatic classification approach has been employed for the inventory of the majority of the chosen crops, and this approach

Table 12.1 Details of pilot study sites for fruit orchards and plantation crops

S. No.	Plantation crop studied	Taluk/mandal	District	State	Average rainfall (in mm)
1	Mango	Malihabad	Lucknow	UP	963
2	Banana	Guntur region	Krishna	AP	33
3	Citrus	Sivagiri	Tirunelveli	TN	815
4	Grapes	Chikkaballapura	Chikkaballapura	Karnataka	756
5	Coconut	Tiptur	Tumkur	Karnataka	660
6	Cashewnut	Mandasa	Srikakulam	Karnataka	1067
7	Arecanut	Chennagiri	Davanagere	Karnataka	809
8	Oil palm	Rajanagaram	East Godavari	AP	1100

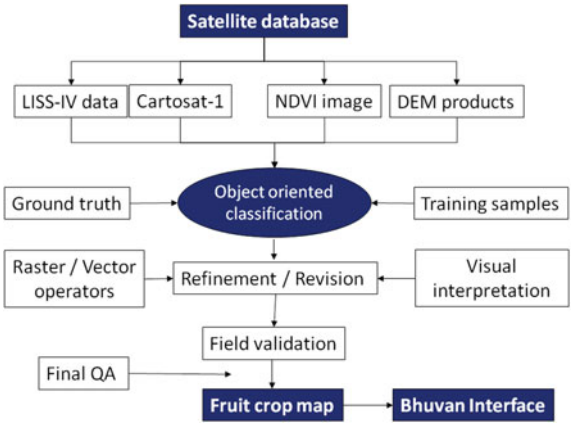

Fig. 12.2 Overall methodology flowchart for inventory of fruit orchards and plantation crops using semi-automatic classification approach

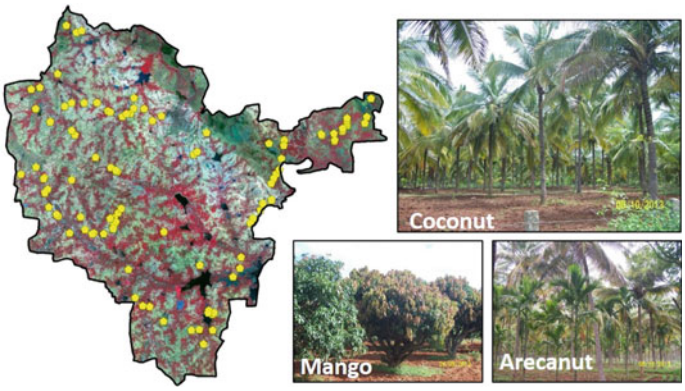

Fig. 12.3 GPS-guided ground truth collection in Tipaturu taluk, Tumakuru district, Karnataka for coconut plantations and other classes

envisaged an appropriate mix of object-oriented classification followed by limited onscreen visual editing.

The details of the pilot studies carried out for individual fruit orchards and plantation crops are discussed below.

12.2.1 Mango Plantations

Mango (*Mangifera indica*) is the king of the fruits with immense economic importance and is generally an alternate bearer (alternatingly yielding high and low during

consecutive years), it is found imperative to generate a scientific spatial database of mango orchards. Toward this end, part of Malihabad taluk (Lucknow district, UP) has been taken up for the study. The mango orchards in Malihabad are densely spaced and contiguously placed, apart from remaining evergreen (despite a dip in NDVI during dry February) althrough the year. In comparison, the surrounding agricultural crops are mostly harvested, post-monsoon, and the fields remain fallow by late Rabi/Summer. Owing to above phenomenon, the temporal NDVI response of mango was distinct from the agricultural crops.

Temporal LISS-IV data (5 dates during 2012–13), covering the study region was used to study NDVI response for discrimination of mango plantations, in order to select optimal window of remote sensing data (Fig. 12.4) February month data was found to be optimal for identification of mango plantations, as most of agricultural crops, barring wheat and paddy, would be harvested by then. Homogeneous, contiguous plantations could be delineated through object-based classification of high-resolution data. Mapping accuracy of 89.2% was achieved which could be further improved to 93.5% through limited onscreen editing by visual interpretation technique. However, a trial exercise was carried out for mango plantations in a contrastingly diverse agro-climatic setup in Southern India viz. Srinivaspura taluka (Kolar district, Karnataka) using temporal LISS-IV data did not achieve satisfactory results. This has necessitated the exploration of further finetuning of semi-automatic

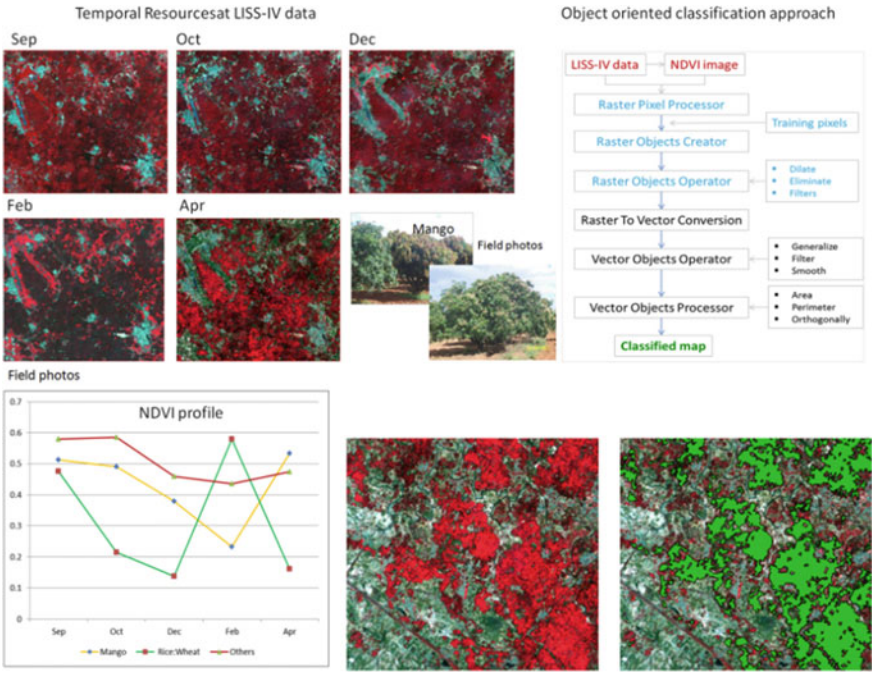

Fig. 12.4 Phenology study and inventory of mango plantations in Malihabad, UP

classification techniques for inventory of these plantations cultivated under diverse agro-horticulture systems, especially with wide inter-tree spacing and for very young orchards.

12.2.2 Banana Orchards

Banana (*Musa* spp.) is widely grown in India with great socio-economic significance; India is the largest producer of bananas in the world. It is well suited for cultivation from humid subtropical to semi-arid sub-tropics up to 2000 m above MSL. The banks of Krishna River in Guntur region have significant presence of banana orchards due to water availability from the river. Heterogeneous cropping pattern in this area also consists of chillies, cotton, citrus, paddy, and tobacco. With minimum soil exposure, banana orchards manifest in bright red tones, owing to dense and lush green canopy. However, a limited conflict with respect to spectral signatures of cotton and chilli crops in satellite data of October–November period. This specific spectral mixing necessitated minimum of two dates' data for classification of banana orchards. The intensive/contiguous cultivation of banana orchards, mostly in near proximity to the river, has favorably limited the temporal datasets to only two dates. Accordingly, multispectral LISS-IV data corresponding to April and June 2013 were chosen for the study, in spite of staggered planting of banana orchards.

Object-based classification has been employed here and the results as compared with field information are satisfactory as the spectral discernability favored improved classification of banana orchards (Fig. 12.5). Mapping accuracy of 91.4% was achieved which could be further improved to 94.6% through limited onscreen editing by visual interpretation technique. However, in places where the banana orchard

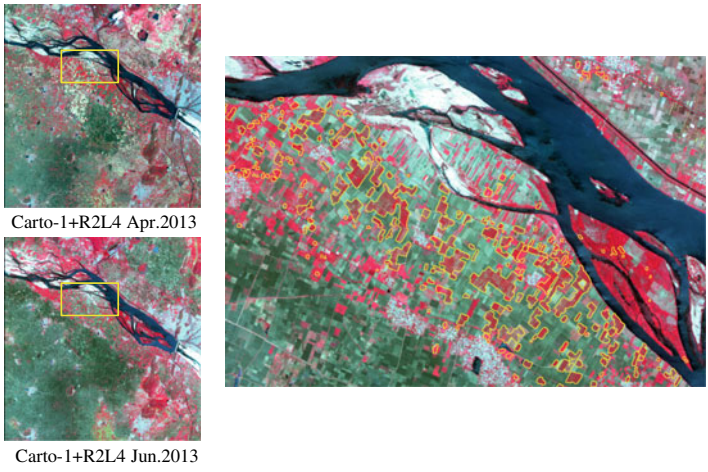

Fig. 12.5 Banana orchards in Guntur, Krishna district, AP

distribution is scattered and cultivation is not so intensive, two dates' data might not suffice. In such scenarios, temporal NDVI profiling might need to be carried out followed by a decision-rule-based hierarchical classification for better classification of banana orchards.

12.2.3 Citrus Orchards

Among the citrus types, Acid-lime (*Citrus aurangifolia)* is the most common type in Karnataka and Tamil Nadu. In Tamil Nadu state, Acid-lime gardens are dominant in Sivagiri taluk, Tirunelveli district, primarily cultivated for exports. The soils are mostly clay loam to sandy clay loam, and these areas fall under rain-fed regions. Temporal LISS-IV data analysis indicated the sufficiency of satellite data of two specific periods (corresponding to October and March–April months) were ideal for identification and delineation of acid-lime (citrus) orchards from other crop and vegetation classes for achieving reasonable classification accuracy (Fig. 12.6).

Based on the NDVI profile, citrus orchards were distinctly identified as compared to surrounding crops. However, it is to be specified that the object-based classification has shown promising results only in dominant citrus areas coupled with well-established and managed citrus orchards. Mapping accuracy of 78.9% was achieved which could be further improved to 90.2% through limited onscreen editing by visual interpretation technique. On the contrary, in regions with scattered as well as young

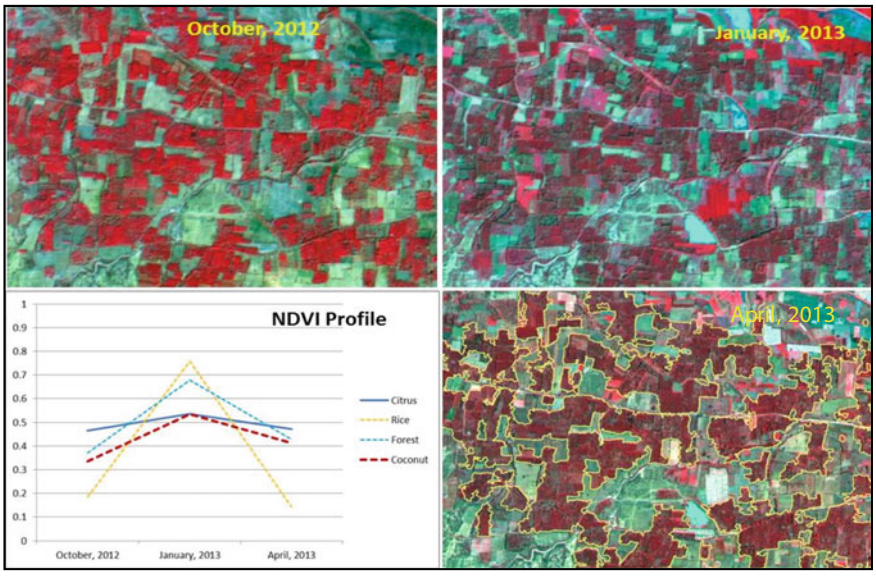

Fig. 12.6 Citrus orchards in Sivagiri taluka, Tirunelveli district, TN

citrus orchards, and also in situations where citrus is inter-planted with coconut, classification tends to be less accurate. Thus, it was concluded that this methodology needed to be deployed for citrus orchard dominant regions only, in similar agro-climatic dispositions.

12.2.4 Grapes Orchards

Grape (*Vitis vinifera*) is a very popular fruit crop cultivated in southern India, especially Karnataka and Maharashtra. It is a deciduous woody vine crop and its natural habitat is temperate and subtropical climate. In Karnataka, the cultivation of grapes is well managed but often restricted to small and medium land holdings, primarily in the districts of Vijayapura and Chikkaballapura. Chikkaballapura taluka is one of the major grape cultivation areas. Grape cultivation involves the unique agronomic practice of biannual pruning during October and April months and lush green leaves emerge after the pruning. Considering this, two date's multispectral datasets (LISS-IV) viz., Nov. and Feb. corresponding to pruning stage and post-pruning lush green stage (fruiting stage), respectively, were used for delineation of grape vineyards.

Object-based classification for delineation of grape orchards was carried out employing a total enumeration approach. In addition to the multispectral merged data corresponding to pre and post-pruning stages, LISS-IV NDVI images of the two dates were also used for classification. LISS-IV and Cartosat-1 merged data covering Chikkaballapura taluka and part of the classified image viz. Figure 12.7 depicts the

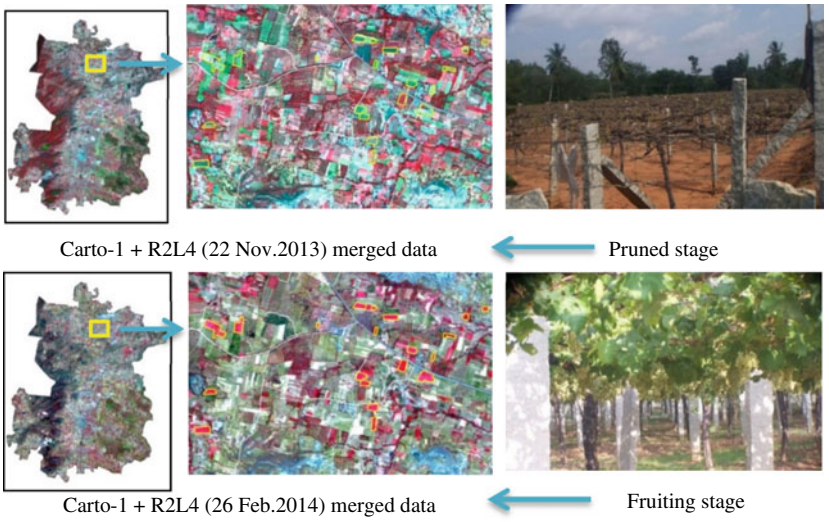

Fig. 12.7 Grape orchards in Chikkaballapura taluk, Karnataka

distribution of grape orchards in the study area. The hectarage of 1321 ha estimated through this technique compared fairly well with reported hectarage of 1705 ha (Dept. of Horticulture), indicating a relative deviation of −29%. This discrepancy is primarily owing to the fact that many of the fields with vegetable crops have spectrally/texturally confused with the greenness pattern of grape orchards during the pre-post pruning periods and thus resulting in underestimation of grape orchards.

Secondly, many of the grape orchards in the study area happen to be the demonstration plots maintained by many agri-business companies and do not strictly adhere to the standard temporal windows for pruning. These problems to a large extent can be overcome using multispectral data corresponding to pre and post-pruning stages of April pruning, in addition to October pruning. A mapping accuracy estimated using limited ground truth observations indicated an accuracy of just around 75%. Most misclassified grape orchard locations happen to be categorized as vegetable fields. It was concluded that the accuracy can be improved through the approach of using a simple NDVI based hierarchical decision rule-based approach using the above four datasets would also help in achieving better statistical and spatial accuracies in addition to object-based classification.

12.2.5 Coconut Plantations

Tipaturu is the cradle of coconut cultivation in Karnataka state and is the major contributor for edible coconut oil production as well as *copra* accounting for almost 35% of the total geographical area of the taluka as per conventional estimates. Coconut plantations in the taluka dot the entire agriculture landscape. As Coconut tree is evergreen, minimal temporal NDVI variations were observed. Figure 12.8 depicts distribution of coconut plantations using LISS-IV and Cartosat-1 data employing object-based classification techniques. As seen, plantations are spatially denser in the southern half of the taluka and the extreme eastern portion. The area estimated through remote sensing-based approach (26,085 ha) compared credibly with that of Dept. of Horticulture, Govt. of Karnataka (28,012 ha). The % relative deviation has worked out to a mere −7.39%. This is basically because the coconut plantations in the taluka are predominantly pure and not mixed with other plantation crops except in selected pockets. Only in the central region of the taluka, arecanut is found to exist as an intercrop in coconut plantations.

Even these regions have been mapped as coconut plantations only. Coconut plantations in certain pockets with shallow gravelly soils and poor groundwater availability lacked sufficient greenness and thus have gone unclassified under this approach. The same may however be accounted for through limited visual interpretation techniques. In a nutshell, results clearly demonstrated the use of February–April months high-resolution data for inventory of coconut plantations. Datasets corresponding to this period coincide with non-agricultural season facilitating better discrimination

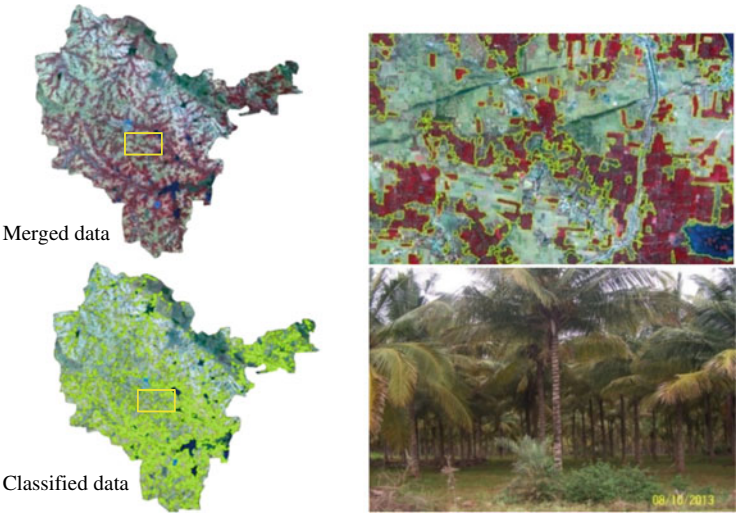

Fig. 12.8 Coconut plantations in Tipaturu taluka, Tumkur district, Karnataka

of coconut. However, due to intrinsic issues associated with poor spectral signatures from young plantations and poor stands of plantations, the same was not accurately classified. It is also to be noted that remote sensing-based approach does not account for the isolated individual rows of coconut trees raised along the field bunds/boundaries. Exclusion of these might slightly influence the extrapolation of area figures to production estimates.

12.2.6 Arecanut Plantations

Single date LISS-IV and Cartosat-1 merged data was used for delineation of arecanut plantations using object-based classification technique. The entire agricultural landscape of taluk has varying degrees of the presence of this plantation. The crop is generally well managed and grown in medium to large holdings.

In general, the crop is grown as monocrop, however, it is also cultivated along with several plantations such as coconut, banana, etc. Spatial expanse of arecanut crop in Chennagiri taluk is depicted in Fig. 12.9. The area estimated through remote sensing-based approach (16,389 ha), again, as in case of coconut in Tipaturu, compares credibly with that of Dept. of Horticulture, Govt. of Karnataka (18,032 ha). The % relative deviation has worked out to −10.02%. The following intricacies have been noticed during the object-based analysis for arecanut plantations:

- Replanting of arecanut is a temporally continuous phenomenon in the context of this crop and the taluk is no exception. Those of the very young fresh and replanted plantations have not been accounted for, during the analysis.

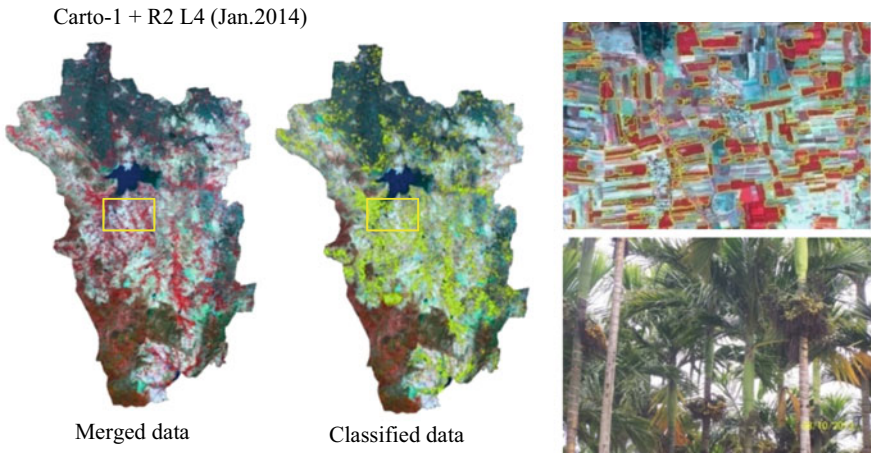

Fig. 12.9 Arecanut plantations in Chennagiri taluk, Davanagere district, Karnataka

- Arecanut being a water-intensive plantation, during the period coinciding with the date of satellite data acquisition, those of the land parcels where groundwater had depleted, the plantations exhibited desiccation and thus were spectrally not discernible.
- Some of the arecanut plantations raised in association with coconut and also having other annuals as intercrops exhibit different spectral signatures. Although a majority of these have been delineated under the approach, the area figures might slightly influence the extrapolation of area figures to production estimates.

12.2.7 Oil Palm Plantations

Our country has been plagued with shortage of edible oil production, ever since independence. Toward mitigation of this perennial problem, the Government of India initiated various measures to augment the oil-seed production adopting a two-pronged approach. On one hand, area under seasonal oil-seed crops was enhanced and on the other, perennial edible oil crops like oil palm were introduced in suitable areas, predominantly in the states of Andhra Pradesh and Karnataka. Oil Palm (*Elaeis guineensis*) is the highest oil-yielding plant among perennial oil-yielding crops, producing palm oil and palm kernel oil.

The West Godavari, East Godavari and Krishna districts of Andhra Pradesh extensively cultivate oil palm and, in this study, Rajanagram Mandal of East Godavari district has been considered for oil palm area estimation. Rajanagram Mandal is also characterized by the presence of two other major horticultural plantation types viz. Cashewnut and Coconut. A unique methodology has been adopted for classification/delineation of oil palm plantations using both object-based techniques as well as visual interpretation approaches. This was basically adopted to evaluate the spatial

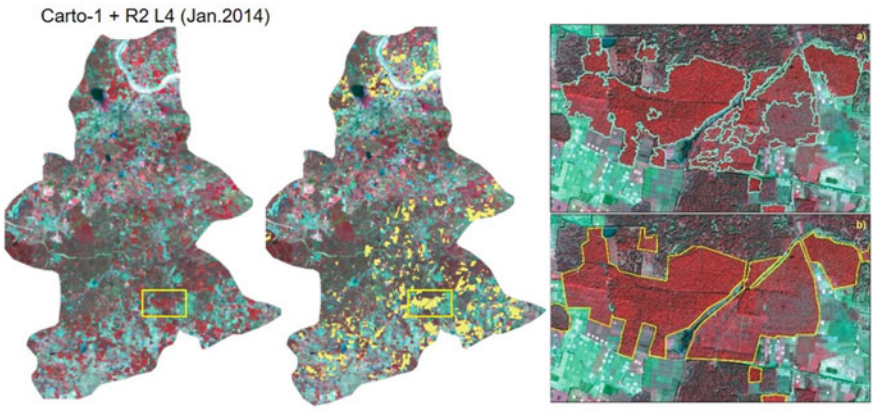

Fig. 12.10 Oil palm plantations in Rajanagaram, Andhra Pradesh **a** object-based classification and **b** visual interpretation approach

mapping accuracy of the semi-automatic approach in comparison to the standard interactive onscreen visual interpretation approach.

The object-based classification carried out using LISS-IV data corresponding to mid-June of 2014 merged with Cartosat-1 data of Nov. 2011 resulting in total oil palm area of 1939 ha (Fig. 12.10). The classification was facilitated with the unique crisscrossing diagonal planting pattern adopted for oil palm in this region as opposed to the normal horizontal-vertical pattern practiced for coconut. Cashew plantations, owing to their contrastingly different textural patterns did not spectrally/texturally confuse with oil palm classification. Onscreen interpretation approach for mapping oil palm plantations resulted in an estimation of the spatial extent of 1886 ha. In comparison of the maps generated using the two approaches, it is evident that semi-automatic classification has classified some of the coconut plantations also as oil palm and missed out on the younger as well as ill-managed oil palm plantations owing to their different spectral/textural characteristics. But the twin issues were obviated by adopting the onscreen approach. The very fact that both the approaches have resulted in near-similar area estimates is a testimony for semi-automatic classification being highly successful for accurately mapping oil palm plantations.

12.2.8 Cashewnut Plantations

Cashew plantations are predominantly found in parts of Srikakulam district, both as pure patches and also in mixed plantations (predominantly with coconut trees). Mandasa taluka, Srikakulam district in Andhra Pradesh was selected as the study area. Cashew plantations do are not planted in regular and defined patterns and manifest as irregular patches with rough texture in darker reddish tones on high-resolution

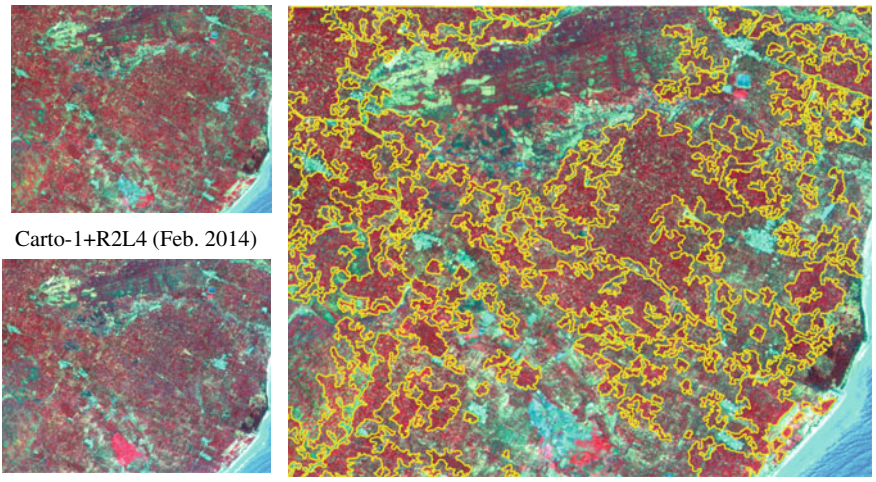

Fig. 12.11 Cashewnut plantations in Mandasa taluka, Srikakulam district, Andhra Pradesh

satellite data (Fig. 12.11). Additionally, the interspersion with coconut trees/small plantation patches makes the application of object-based classifiers further difficult. Thus, the semi-automatic classifier tried out in this region has shown mixed results, better being in patches with cashew nut trees domination and poorer in regions, where other trees co-existed with cashew nut plantations.

Results of the pilot studies covering few crops have been documented earlier (Hebbar et al. 2014).

12.3 Upscaling of Pilot Studies to Regional/National Level

The techniques and methodologies developed during successful conduct of the pilot studies covering inventory of eight different fruit and plantation crops, paved the way for upscaling of the studies to entire peninsular India. This was under a national initiative on "Coordinated program on Horticulture Assessment and Management using GeoiNformatics (CHAMAN)" launched by MNCFC, Department of Agriculture and Cooperation in collaboration with ISRO. The prime objective of CHAMAN was to realize the potential applications of emerging technologies such as remote sensing, GIS, and GPS for an inventory of horticulture crops for overall development of horticultural sector. During Phase-I of this program, RRSC-South, NRSC, and RRSC-Central took the lead role in implementing CHAMAN activities for the Peninsular Indian region with respect to three major fruit crops viz. Mango, Banana and Citrus (Phase-I). As many as 25 districts were covered for inventory, on an operational mode, by RRSC-South. During the Phase-II of the CHAMAN program,

development of techniques for Coconut and Grapes apart from methodology for site-suitability analysis for mango was taken up in nine districts by RRSC-South. Deliverables under Phase-I were also hosted on Bhuvan Geo-platform.

12.3.1 Inventory of Mango Plantations and Banana and Citrus Orchards Under CHAMAN Phase-I

Study areas chosen under CHAMAN Phase-I program for inventory of Mango plantations and Banana and Citrus Orchards are mentioned in Table 12.2.

Satellite Data Used

Multi-resolution datasets were used in the project for mapping of fruit orchards in the selected districts in Karnataka and Tamil Nadu states (Tables 12.3 and 12.4).

Methodology

The general methodology followed for hybrid classification approach employed digital as well as visual interpretation techniques for delineation of spatial extent of horticultural fruit crops. The major steps covered included (i) Satellite data processing

Table 12.2 List of districts selected for inventory of mango plantations and banana and citrus orchards

S. No.	State	Crop	Selected districts
01	Karnataka	Mango	Kolar, Tumkur, Ramanagara, Bengaluru Rural, Chikkaballapur and Dharwad
02		Banana	Chamarajnagar, Mysore, Bellary, Ramanagara, and Tumakuru
03		Citrus	Vijayapura
04	Tamil Nadu	Mango	Krishnagiri, Vellore, Dharmapuri, Dindigul and Thiruvallur
05		Banana	Tirunelveli, Thoothukkudi, Tiruchirapalli, Erode, Coimbatore, Kanniyakumari, and Theni
06		Citrus	Tirunelveli

Table 12.3 Details of satellite data used under the study

Crop	Satellite data used	Purpose/role
Mango	Single date LISS-IV and Cartosat-1 data	Identification and area assessment
Citrus	Single/two dates LISS-IV and one date Carto-1	Identification and area assessment
Banana	3–4 dates LISS-III/Landsat-TM/Sentinel data Single/two date LISS-IV data	Phenology study Identification and area assessment

Table 12.4 Characteristics of remote sensing sensors used under the study

S. No.	Characteristics	Cartosat-1	RS-1		RS-2
			LISS-III	LISS-IV	LISS-IV
1	Spectral resolution (μm)	0.5–0.85	0.52–0.59 0.62–0.068 0.77–0.86 1.55–1.70	0.52–0.59 0.62–0.068 0.77–0.86	0.52–0.59 0.62–0.068 0.77–0.86
2	Spatial resolution (m)	2.5	23.5	5.8	5.8
3	Swath (km)	29/26	141	24	70
4	Radiometry	10	7	10 (7 bits transmitted)	
5	Repetivity (days)	126	24	24	70
6	Revisit (days)	5	24	5	5
7	Stereo	Fore/Aft	–	–	–

(ii) GPS-guided Field data collection (iii) Classification (iv) Post classification refinement (v) Bhuvan Interface.

Classification technique specifically involved the following steps: Hybrid approach using a mix of digital and onscreen visual interpretation techniques for delineation of fruit crops depending upon the suitability and intended accuracy. Object-oriented technique using e-Cognition software was used for classification of horticultural plantations. LISS-IV and Cartosat-1 were used as source data for multi-resolution segmentation. Optimizing segmentation parameters viz., scale, shape, and compactness were carried out iteratively based on visual inspection of the segmented images for their suitability for delineation of fruit crops. Initially, the segmentation was carried out with coarse-scale parameters for creation of cropped area masks using hierarchical classification. Second level segmentation was carried out within the crop mask with a finer scale parameter depending on the heterogeneity. The ground truth information was used for defining training sets for classification. Image features such as spectral mean, standard deviation, textural information like homogeneity, and NDVI were used in Support Vector Machine (SVM) based classification approach for crop inventory. Further refinement was done using geometry-based parameters (area, shape, linearity) followed by smoothening. In case of bananas, object-based classification approach with hierarchical rule sets was used for mapping followed by minimal interactive visual editing for revising the classified map.

Mango Plantations

Mango is the dominant fruit crop in the study districts, occupying large areal extents with marked differences in variety, age group, and management practices. Mango plantations exhibited in dull red color on the merged data with coarse texture due to wider spacing and partial soil exposure. Coconut is the other dominant plantation in some of the regions, manifested as dull red color but in clear-cut rows patterns due to canopy architecture and defined spacing. Typical spectral signature of major

Fig. 12.12 LISS-IV + Cartosat-1 merge data showing spectral signature of various plantations

plantations as manifested on high-resolution LISS-IV + Cartosat-1 merged data is depicted in Fig. 12.12.

Object-based classification was employed for delineating mango plantations using tone, texture, geometry, and vegetation index. Mapping accuracy of about 75–85% could be achieved using object-based classification approach alone. Incremental improvement was achieved through refinement using interactive visual interpretation. The final results demonstrated mapping accuracies of about 90% for most districts using a hybrid classification approach, indicating the potential use of high-resolution data for the inventory of these plantations.

Table 12.5 shows district-wise acreage under mango plantations for 11 major districts of Karnataka and Tamil Nadu states and comparison with the official estimates of State Horticulture Department. Spatial distribution of the crop in Kolar district is provided as Fig. 12.13 Higher deviation in few districts could be attributed to higher proportion of very young plantations which could not be captured using satellite data.

Intricacies observed with respect to inventory of mango plantations are summarized below:

- Spectral signature of young mango plantations (less than 3–5 years old) is not very distinct and discrimination of such plantations using high-resolution data is challenging. Further, at any given period, young plantations of other plantation types like coconut, areca, citrus, etc. are coexisting in the region resulting in spectral confusion to some extent.

Table 12.5 District-wise RS based and conventional acreage estimates under mango

S. No.	District	RS estimates (ha)	Reported area (ha)	Relative deviation (%)
Karnataka				
1	Kolar	41,489	46,772	−12.73
2	Tumkur	16,198	15,110	6.72
3	Ramanagara	26,017	22,131	14.94
4	Bangalore rural	5414	7030	−29.85
5	Chikkaballapura	11,374	14,147	−24.38
6	Dharwad	9520	10,767	−13.09
	Total	1,10,012	1,15,957	−5.40
Tamil Nadu				
7	Krishnagiri	31,118	36,009	−15.72
8	Vellore	14,072	13,979	0.66
9	Dharmapuri	8015	7948	0.84
10	Thiruvallur	10,578	10,603	−0.23
11	Dindigul	Could not be done due to heterogeneity with mixed plantations		
	Total	63,783	68,539	−7.36

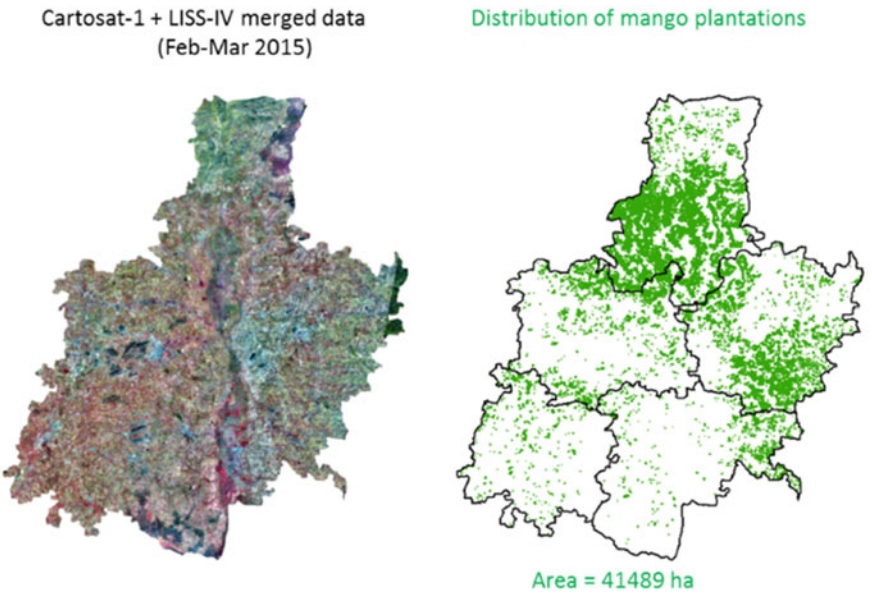

Fig. 12.13 Spatial distribution of mango plantations in Kolar district, Karnataka

- Spacing between mango plantations varies widely in the region with large variations in density, age, variety, etc. Thus, spectral confusion is noticed with the minor plantations such as sapota, tamarind, and guava, which occupy small fields and are scattered in these study districts.
- In some areas, the mango trees are along the bunds and marginal lands and cannot be identified easily on satellite data. Similarly, ill-managed plantations with higher mortality rates were also not identified properly.
- Tree density and age of mango plantations are critical inputs for production estimation and rejuvenation of old plantations. Attempts are being made to analyze the temporal and long-term satellite datasets to establish relative age groups and tree density broadly.

Banana Orchards

Globally, India stands first in production of bananas with diversified cultivation practices (with respect to planting periods, varieties, management practices, crop durations, and crop rotations) across different regions and more specifically between Tamil Nadu and Karnataka states. As opposed to highly staggered planting of bananas in Karnataka, planting within a narrow window of March–May in river flood-plains and irrigated regions of few Tamil Nadu districts, coupled with staggered planting in remaining districts is observed. Crop duration ranges between 10–12 months but will be limited and 6–7 months in case of crop raised for cutting plantain leaves only, for religious significance, and other commercial uses. Banana as monocrop is widely cultivated in selected districts of Tamil Nadu occupying large contiguous patches and growing in the same field for 4–5 years. In Karnataka, RS-based inventory complexities are associated with staggered and mixed planting, periodical cutting of leaves, understory planting, etc. (Table 12.6)

Phenological studies using temporal multispectral data were carried out and concluded that minimum of two date's data of Oct–Nov and Feb–Mar bio-windows, respectively, are best suited for improved discrimination of banana orchards from other coexisting long duration crops like sugarcane. LISS-IV data and other datasets (Tables 12.3 and 12.4) were used to classify banana orchards using a judicious mix of MXL, RGB clustering, and object-based classification techniques. The mapping accuracy ranged from 85.0 to 92.5% with an overall accuracy of 86.20%. District-wise acreages under banana orchards were estimated and compared with the official estimates (Table 12.5). The analysis establishes the potential use of high-resolution data for discrimination of banana orchards with reasonable accuracy for districts having homogenous contiguous areas. The lower RS acreages estimate in few districts are due to mixed and multi-tier cultivation practices, small field size, and staggered planting, especially in Karnataka and two districts of Tamil Nadu. The spatial distribution of banana orchards in Thoothukudi district, Tamil Nadu is shown in Fig. 12.14.

Intricacies observed with respect to mapping/inventory of banana orchards are summarized below:

Table 12.6 District-wise RS based and conventional acreage estimates under banana orchards

S. No.	District	RS estimates (ha)	Reported area (ha)	Relative deviation (%)
Tamil Nadu				
1	Tirunelveli	7015	7176	−2.30
2	Thoothukkudi	7893	8973	−13.68
3	Tiruchirappalli	7214	6913	4.17
4	Erode	7735	9618	−24.34
5	Coimbatore	5530	8115	−46.75
6	Theni	5814	6093	−4.80
7	Kanyakumari	2040	6383	−212.89
	Total	43,241	53,271	−23.20
Karnataka				
8	Bellary	3016	4993	−65.60
9	Ramanagara	3560	4004	−12.47
10	Tumkur	3624	4572	−26.15
11	Mysore	Mapping was not satisfactory due to complex agronomic practices (staggered and mixed planting, periodical cutting of leaves, understory planting, etc.)		
12	Chamarajnagar			
	Total	10,200	13,569	−33.03

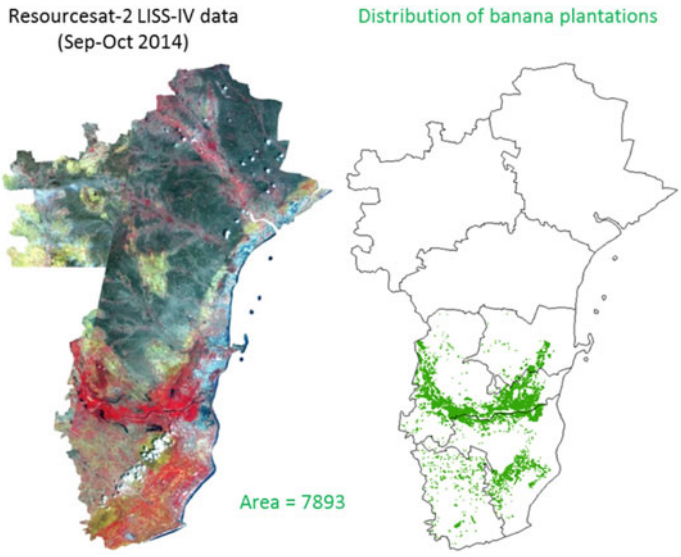

Fig. 12.14 Spatial distribution of banana orchards in Thoothukudi district, Tamil Nadu

- Although single date LISS-IV data is found to be fairly useful for delineating contiguous banana orchards in Tamil Nadu, two date data corresponding to Oct–Nov and Feb–Mar months are ideally suited for improved discrimination in the two states. Availability of optimal cloud-free datasets is a major constraint in some regions.
- Banana orchards in Karnataka are characterized by staggered planting period with peak period from June to December requiring temporal satellite data for identification.
- In general, mixed and two-tier cultivation of banana with coconut/areca plantations is very common, a sustainable farming practice in Karnataka. Mapping mixed plantations using high-resolution data is challenging and needs further detailed studies.

Citrus Orchards

Predominant Citrus category fruits cultivated in Karnataka and Tamil Nadu are lime and lemon. Citrus cultivation in these two states is characterized by small field sizes, sparse distribution with different age group categories, and distribution across the study areas. Besides citrus orchards, grapes, pomegranate, and sugarcane are also cultivated. Identification of citrus orchards is relatively easier in homogenous and large contiguous areas using single date LISS-IV and Cartosat-1 merged data. Object-based classification using spectral and texture information was used for delineation of citrus orchards using Cartosat-1 and LISS-IV merged data. Discrimination of citrus orchards from pomegranate and grape orchards was difficult to a limited extent and required minimal visual editing. The results were reasonably accurate for old and mature orchards with mapping accuracy ranging from 85.0 to 90.5%. The remote sensing-based citrus crop acreage estimates are compared with the official estimates and presented in Table 12.7. The analysis clearly showed that the RS estimates closely match official estimates for all districts. Spatial distribution of citrus orchards in Vijayapura District, Karnataka is shown in Fig. 12.15.

Bhuvan Interface

The output maps depicting the spatial distribution of the three fruit crops in different study districts and geotagged photos (collected during Ground Truth Visits) were hosted on BHUVAN geo-portal for visualization in an exclusive web page for the

Table 12.7 District-wise RS based and conventional acreage estimates under citrus orchards

S. No.	District	RS estimates (ha)	Reported area (ha)	Relative deviation (%)	Mapping accuracy (%)
1	Vijayapura, Karnataka	6936	6499.0	6.3	85.0
2	Tirunelveli, Tamil Nadu	2024	1747.0	13.7	90.5

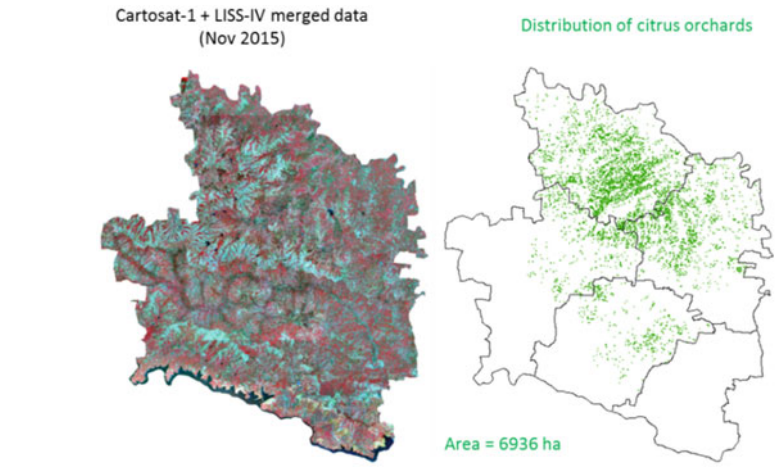

Fig. 12.15 Spatial distribution of citrus plantations in Vijayapura district, Karnataka

CHAMAN program. The same is depicted in Fig. 12.16. (http://bhuvan.nrsc.gov.in/governance/moa_chaman).

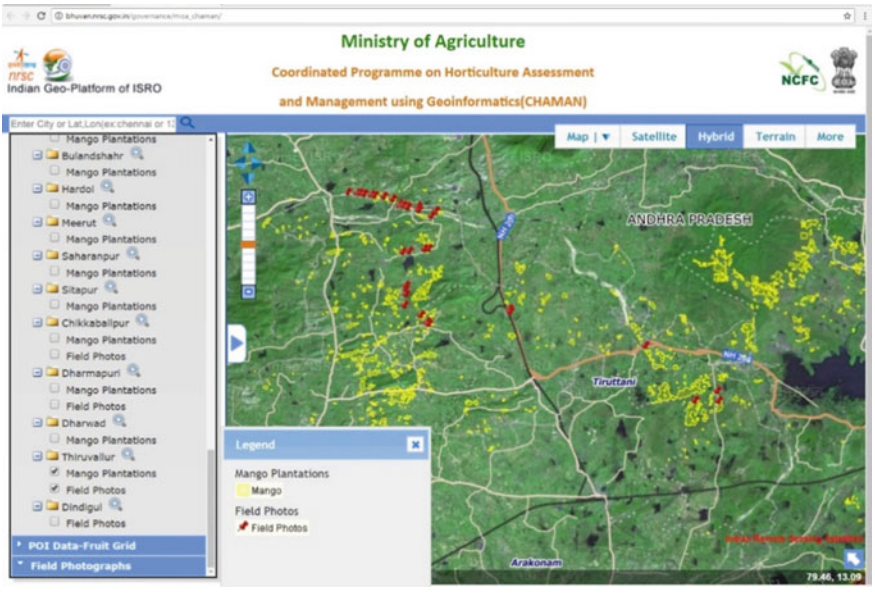

Fig. 12.16 Screenshot of project deliverables in Bhuvan interface

Table 12.8 List of districts covered under CHAMAN Phase-II program for coconut plantations and grapes orchards' mapping

S. No.	Crop	State	District
1	Coconut	Kerala	Kozhikode, Malappuram, Kannur, Kasaragodu
		Karnataka	Tumkur
		Tamil Nadu	Coimbatore
2	Grapes	Karnataka	Chikkaballapura (Chikkaballapura taluk)
		Tamil Nadu	Theni (Uttamapalayam taluk)

12.3.2 Technique Development for Coconut Plantations and Grapes Orchards' Mapping Under CHAMAN Phase-II

With the successful completion of inventory in operational mode for mango, banana, and citrus crops, technique development studies have been carried out during 2018–2020 Coconut Plantations and Grapes Orchards' mapping, at RRSC-South. A total of eight districts have been covered under this program (Table 12.8), predominantly using 2.5 m Cartosat-1 + LISS-IV satellite data.

12.3.3 Coconut Plantations

India is the third-largest coconut-producing nation globally, occupying 21.50 M ha and production of 21,228.2 M nuts with a productivity of 9897 nuts/ha (CDB, 2018–19). The coconut plantation is cultivated across 17 States and 3 UTs covering diverse agro-climatic conditions. The four southern states of Kerala, Tamil Nadu, Karnataka, and Andhra Pradesh are the major coconut-producing states which account for more than 90% of area and production in the country. Coconut plantations being evergreen in nature, variation in temporal NDVI are minimal as a pure crop. February–April months satellite data was found to be best suited for mapping coconut plantations. Coconut plantations in the selected districts occupy large areal extents with marked differences in variety, age group, mixed cropping patterns, and management practices. Coconut plantations are manifested in typical spectral signature with row patterns with coarse texture on the high-resolution satellite data in well managed orchards (Fig. 12.17). However, coconut is cultivated in multi-tier cropping systems with other crops like banana, arecanut, etc. Identification of only coconut trees under such complex cropping systems is quite challenging. Hence, the coconut plantation map and acreage estimates consist of pure coconut stand as well as the mixed plantations.

Object-oriented classification was found to be the appropriate technique for delineating coconut plantations using tone, texture, geometry, texture, and NDVI.

Fig. 12.17 Spectral signature of coconut and other plantations on high-resolution data

Cartosat-1 + LISS-IV merged data and classified maps for few selected districts are depicted in Fig. 12.18. Mapping accuracy was better than 85.0% for Tumakuru, Kasaragod, Kannur, and Coimbatore districts, while Kozhikode and Malappuram showed 81.4 and 78.3%, respectively. Incremental improvement inaccuracies are possible through limited interactive visual interpretation. The district-level acreage estimates coconut plantations along with the reported area is depicted in Table 12.9.

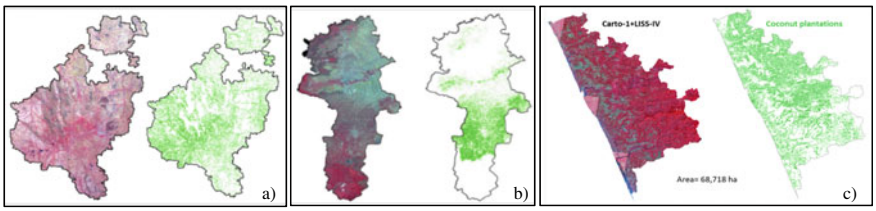

Fig. 12.18 Coconut plantation maps in **a** Tumakuru **b** Coimbatore and **c** Kasaragodu districts

Table 12.9 District-wise RS based and conventional acreage estimates under coconut plantations

State	Districts	RS estimates (ha)	Reported area (ha)	% RD	Mapping accuracy (%)
Karnataka	Tumakuru	207,000	179,000	13.53	>85%
Kerala	Kasaragodu	68,718	67,085	2.38	
	Kannur	76,002	85,972	−13.12	
	Malappuram	98,993	105,090	−6.16	78.3
	Kozhikode	122,878	112,305	8.60	81.4
Tamil Nadu	Coimbatore	81,917	87,000	−6.21	>85%

The table indicates that the relative deviation ranged from −13.12 to 13.53%. The lower accuracy in some of the districts is mainly due to mixed crop patterns and young plantations in the study area. The study indicated the potential of high-resolution data for the inventory of coconut plantations within reasonable accuracy. The use of very high-resolution Cartosat-2 series data and the development of deep learning techniques for mapping coconut plantations are being explored for improvement of classification accuracy and generation of operational procedures.

The intricacies observed in mapping of coconut plantations are as given below:

- Spectral signature of young coconut plantations (less than 3–5 years old) is not very distinct and discrimination of such plantations using high-resolution data is challenging.
- In some areas, the coconut trees are along the bunds and marginal lands and cannot be identified easily on satellite data.
- Spatial resolution used in current analysis may not be sufficient for improved discrimination, especially in heterogeneous and scattered regions and thus very high, sub-meter resolution data where the coconut trees are clearly discernible due to their distinct crown structure would be better suited.

12.3.4 Grapes Orchards

Inventory of grape orchards was carried out for two major taluks viz., Chikkaballapura Taluk Chikkaballapura district, Karnataka, and Uttamapalyam taluk, Theni district of Tamil Nadu using LISS-IV + Cartosat-1 merged data employing object-based classification. Grape orchards showed bright red color on the high-resolution data with smooth texture. It was observed that other plantations of the study area like mango, eucalyptus manifested as deep red color with coarse texture and were spectrally different from grape orchards as depicted in Fig. 12.19 However, spectral signature of short duration vegetable crops was mixing with grape orchards to limited extent.

The temporal Sentinel-2 MX data analysis revealed that two date's data of Nov-Dec and Feb-Mar bio window are best suited for improved discrimination of grape orchards from other coexisting short duration crops. Due to the non-availability of cloud-free high-resolution data, the alternatively available best datasets were used for the study. The mapping accuracy was about 85% for both the study areas. The lower accuracy is attributed to mixing of spectral signature of grape and other competing vegetables crops and accuracy could be improved using two date satellite data. Spatial distribution of grape orchards of Uttamplayam taluk, Theni district is depicted in Fig. 12.20. The crop acreage estimates of grape orchards corresponding to Chikkaballapur and Uttamapalyam taluks are shown in Table 12.10. The results showed that the acreage estimates for both study areas were lower compared to the reported area with a relative deviation of about 11.00%.

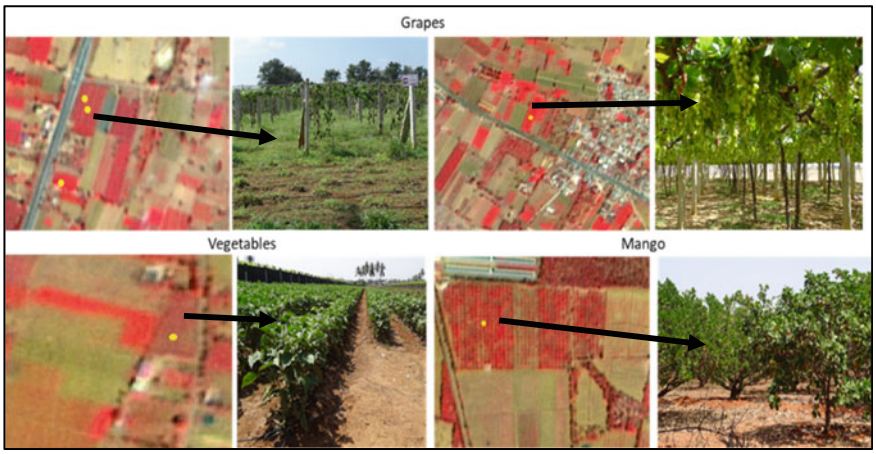

Fig. 12.19 Spectral signature of grape orchards and competing crops

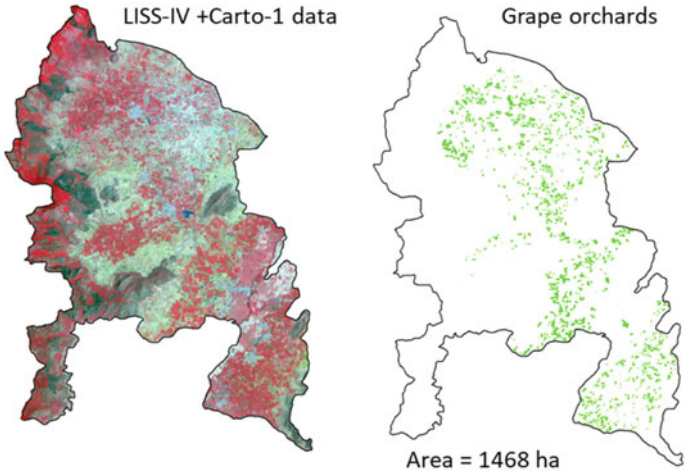

Fig. 12.20 Spatial distribution of grape orchards in Uttamapalyam taluk, Theni, Tamil Nadu

Table 12.10 District-wise RS based and conventional acreage estimates under grape orchards

S. No.	Taluk/district	RS estimates (ha)	Reported area (ha)	Relative deviation (%)
1	Chikkaballapur taluk, Chikkaballapur district, Karnataka	2250	2500	−11.11
2	Uthamapalyam, Theni district, Tamil Nadu	1250	1468	−11.48

12.3.5 Technique Development for Site-Suitability Analysis for Mango Plantations

Mango, being a premium export potential fruit, the scope for expansion of mango cultivation is immense. This has necessitated the current study for site-suitability analysis for mango plantations using pedo-climatic parameters. Ramanagara district of Karnataka state was chosen as the study area. This district also has a significant presence of mango plantations (around 26,000 ha), which facilitates validation of analysis outcomes with an existing scenario. A major part of the district is occupied by red sandy texture soil. Ramanagara district falls under single agro-climatic zone, i.e., Eastern Dry Zone- Zone-5. The maximum and minimum temperature in the district ranges from 29 °C to 36 °C and 15 °C to 20 °C, respectively.

District receives average rainfall of 822 mm. Apart from mango, the important horticultural crops of the district include coconut, areca nut, banana, citrus, beetle vine, and vegetable crops like tomato, brinjal, etc. High-resolution Cartosat-1 and Resourcesat LISS-IV data were used for identification and area assessment of mango plantations as detailed under Sect. 12.3.1. Analysis was carried out using a set of criteria pertaining to pedo-climatic and terrain variables and the list is enclosed in Table 12.11. Carto-DEM was utilized for generation of slope map and soil map at 1:50 K was used for extracting soil parameters like soil texture, pH, organic carbon.

Applying the soil suitability criteria developed by NBSS&LUP, the land site-suitability has been evaluated for soil and climatic parameters. Accordingly, three different categories of suitability under the existing overall land use, exclusively for the existing mango plantation areas as well as specifically under wastelands, have been derived. Results of the spatial analysis carried out study the distribution of existing mango plantations under different suitability regimes are indicated under Fig. 12.21a. The results indicated that about 60.0% of the existing plantations are cultivated in marginally suitable lands while only 13% in highly and moderately

Table 12.11 Pedo-climatic variables used for suitability analysis

S. No	Data used	Parameters	Source
1	Soil Map	• Texture, depth, salinity • pH, OC, salinity	1:50 and 1:250 K
2	Weather	• Temperature • Rainfall	MODIS/IMD
3	Soil MOISTURE	• Soil moisture availability • Length of growing days	MOSDAC/NRSC
4	Groundwater	• Water depth (point data)	Central ground water board
5	LULC map	• Waste lands	1:50 K map, NRSC
6	Crop map	• Mango plantation map	Chaman phase-1
7	Satellite data	• NDVI	LISS-IV and sentinel
8	DEM	• Slope map	Carto-DEM

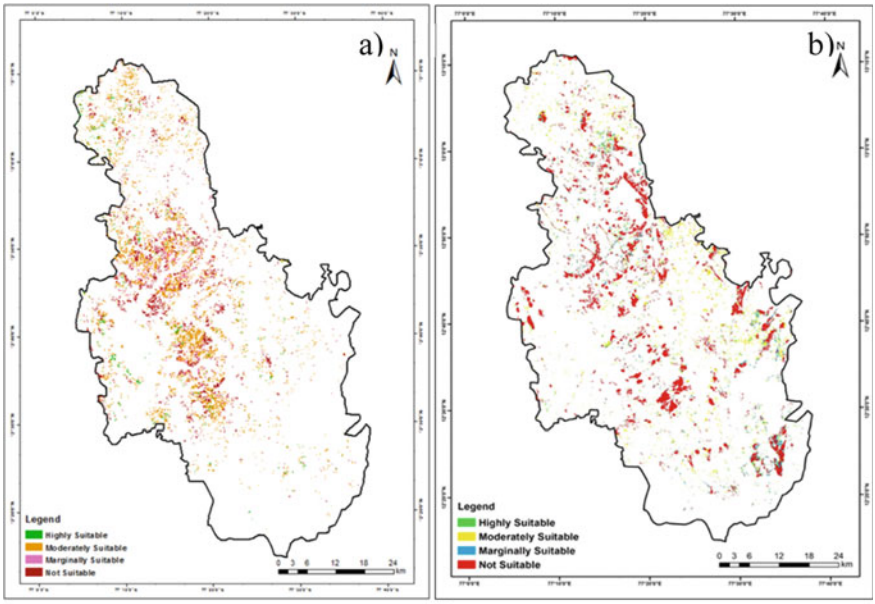

Suitability Regimes	Area of Existing Crop (ha)	Per cent
Highly Suitable	1366	5.3
Moderately suitable	2011	7.7
Marginally Suitable	15604	60.0
Least suitable	7030	27.0
Total	**26011**	

S. N	Class	Area in ha	Per cent
1	Highly Suitable	338	1.04
2	Moderately Suitable	8353	25.8
3	Marginally Suitable	4225	13.1
4	Not Suitable	19359	59.9
		32275	

Fig. 12.21 Site-suitability analysis for mango plantations in Ramanagara **a** proportion of existing mango plantations under different suitability regimes and **b** potential area under wastelands suitable for mango plantations

suitable lands. About 27.0% of the mango plantations have existed in least suitable lands. Similarly, the analysis of wastelands (Open Scrub, Dense Scrub, and grazing lands) for mango plantation suitability has indicated that significant portion of the wastelands are only marginally suitable for mango cultivation, with only about 13% of wastelands being moderate to highly suitable (Fig. 12.21b). The approach adopted under this site-suitability analysis facilitates the identification of suitability regimes under already cultivated fruit crops, apart from identifying additional areas for expansion of crop cultivation. This information is very useful for stratifying crop productivity and production zones.

12.4 Conclusions

This chapter has covered studies under different programs of ISRO, as carried out at RRSC-South, of NRSC/ISRO. Initially, concerted efforts were made during 2012–15, to study the feasibility of using high-resolution satellite datasets in association with temporal, multispectral data in connection with identification and methodology development for inventory of four fruit crops (mango, citrus, banana and grapes) and four plantation crops (coconut, arecanut, oil palm and cashew nut). The techniques and methodologies developed during the pilot studies' successful conduct paved the way for upscaling of the studies to entire peninsular India. This was under a national initiative on "Coordinated program on Horticulture Assessment and MAnagement using GeoiNformatics" (CHAMAN). During Phase-I of this program, three major fruit crops viz. Mango, Banana and Citrus in as many as 25 districts were covered for inventory, on an operational mode. Deliverables under Phase-I were also hosted on ISRO's Bhuvan Geo-platform. During the Phase-II of the CHAMAN program, development of techniques for Coconut and Grapes apart from methodology for site-suitability analysis for mango was taken up in nine districts by RRSC-South.

During the first study on methodology development for 08 fruits and plantation crops, the following have emerged: Multi-resolution, multispectral and at times temporal high-resolution satellite datasets are found to be effective in inventory of the horticulture crops. Phenological studies using temporal LISS-IV data were useful in selecting bio-windows for optimum date/dates' data selection, especially with respect to mango, banana, grapes, and citrus orchards. A hybrid approach involving a judicious mix of semi-automatic object-based classifier and need-based manual editing has been found to be the most effective in achieving better accuracies. Plantations crops viz., coconut, arecanut, and palm oil showed promising results with single date LISS-IV and Carto-1 merged data using object-based classification technique. However, Cashewnut could not be successfully classified using the semi-automatic technique. Out of these, oil palm inventory in Rajanagaram was the most successful showing 92.1% mapping accuracy which further improved to 96.2% through onscreen visual interpretation. Arecanut and Coconut showed lower accuracy levels of 75.2% and 76.5%, which could be further improved to 87.6% and 88.9%, respectively through limited editing of the classified vector layers. Object-based classification technique was unsuitable for cashew nut plantations, and visual interpretation technique was the only feasible alternative for accurate delineation of cashew nut plantations.

However, with the advent of Deep Learning-based classifiers, fresh attempts can be made using very high-resolution satellite datasets, for cashew nut plantations. The fruit crops viz., mango, banana, citrus, and grapes (fruit crops) have exhibited satisfactory results with object-based classifiers. Among the four, mango, in Malihabad has resulted in 89.2% mapping accuracy, improving further to 93.5% (on limited visual-interpretation-based editing). Banana orchards alongside Krishna river in Guntur region have shown corresponding mapping accuracies of 91.4 and 94.6%. In both the above cases, temporal multispectral data has been utilized. Similarly, in

case of citrus plantations in Sivagiri taluka two dates' multispectral LISS-IV data has been employed to achieve mapping accuracies of 78.9 and 90.2%. In case of the fourth fruit crop, grapes the agronomic practice of pruning has been utilized for optimum selection of data corresponding to pre and post pruning stages. This has resulted in 75.8% and 89.0% mapping accuracies, respectively. In all the studies, additional fine-tunings based on visual interpretation have significantly improved mapping accuracy. Thus, this hybrid approach has been adopted during the upscaling of inventory studies to regional/national levels, taking care of the following intricacies observed during the pilot phase. This methodology is most-suited primarily for homogeneous mapping parcels of plantations but is of relatively limited utility in case of heterogeneous parcels, apart from fragmented holdings and multi-cropped regions. Also, mapping of young plantations, plantations under agro-horticultural systems, and mixed cropping systems have also been found to be of lesser amenability. These studies were limited to smaller regions, thus necessitating further finetuning of hybrid approach while scaling up for automation of the classification procedure to regional/state levels for operational applications of high-resolution data.

Under Phase-I of the CHAMAN project during 2015–2018, inventory of three major fruit crops, namely mango, banana, and citrus, has been carried out in 25 major districts of Karnataka and Tamil Nadu. Multi-resolution datasets were used in the study for spatial inventory of fruit crops. Single date LISS-IV and Cartosat-1 data of February–March bio window were used for inventory of mango and two dates' data for citrus plantations. Multi-date LISS-III/TM/Sentinel data was used initially for phenological characterization and for selection of optimum dates of high-resolution data. Best suitable single/two dates' LISS-IV data was used for mapping of banana orchards. As in the pilot phase, in-season ground truth information was carried out in the selected districts for its use in digital classification and accuracy assessment. Hybrid classification techniques with a combination of object-based and visual interpretation techniques were used for delineation of fruit crops. About 75–85% accuracy could be achieved using segmentation-based classification and further improvement in accuracy was achieved using onscreen visual interpretation for updating omitted and committed classes. After quality checking and accuracy assessment, district-wise crop acreages were estimated.

The results indicated that single date LISS-IV and Cartosat-1 data were sufficient to delineate mango plantations with reasonable accuracy. Matured and older plantations could be classified with better accuracy, while the spectral signature of very young plantations (2–5 years) is not quite distinct and could not be mapped. The banana orchards could be mapped with reasonably good accuracy using LISS-IV data in the selected districts of Tamil Nadu since the crop is cultivated as monocrop occupying large contiguous areas. However, banana cultivation in Karnataka is diverse with staggered planting, small field sizes and under mixed agro-horticultural practices (majorly under coconut, arecanut, etc.) and hence, accurate classification of banana orchards is still quite challenging. Identification of citrus orchards is relatively easier in homogenous and large contiguous areas using LISS-IV + Cartosat-1 data. The plantation maps along with geotagged photos were hosted on BHUVAN geo-portal for visualization.

Under Phase-II of CHAMAN project, as many as eight districts from Kerala, Karnataka, and Tamil Nadu have been covered to develop optimum techniques/methodology for inventory of coconut plantations and grapes orchards. The study showed the potential applications of high-resolution satellite data (LISS-IV and Cartosat-1 data) for mapping important horticultural crops like grapes and coconut plantations using an object-based classification approach. In case of coconut, mapping accuracy was better than 85.0% for four districts but slightly lower for Kozhikode (78.3%) and Malappuram (81.4%) districts. The crop acreage estimates were closely matching with the reported area and relative deviations ranged from −13.12 to + 13.53%. Semi-automatic approach has exclusively proven its ability to map coconut plantations with reasonable accuracy. However, it is to be noted that young coconut plantations (less than 3–5 years old), as well as younger plantations of mango, citrus, arecanut and others coexisting in the region, might not be discernible using this technique alone. In case of grapes orchards, as in case of pilot study, minimum of two dates data have been found to be appropriate for improved discrimination from other competing fields and vegetable crops.

Site-suitability analysis was carried out in Ramanagara district, Karnataka, for evaluation of existing mango plantation areas as well as identification of additional areas under wastelands for extension of mango cultivation. About 60.0% of the existing plantations are cultivated in marginally suitable lands instead of a meager 13.0% in highly and moderately suitable lands. Spatial analysis of the cultivable wastelands has identified about 8600 ha of potential land (highly and moderately suitable) as suitable for expanding mango cultivation in the district. Integration of various pedo-climatic parameters showed promising results for suitability analysis for mango plantations, an important input for crop yield modeling and condition assessment.

12.5 Way Forward

Significant strides have been made in the field of utilizing geospatial technology as detailed in this chapter. However, there is still a major scope for covering the gaps in the already conducted studies as well as taking the applications of high to very high-resolution satellite datasets and also additionally utilizing latest ML/DL techniques for the following:

- Better spatial resolution data, preferably at sub-meter level (Cartosat-2 series and other similar sensors) need to be utilized for better discrimination of major fruit and plantation crops in order to achieve better accuracies, obviating the need for incremental editing through visual interpretation.
- Other economically important plantation and fruit crops such as Oil Palm, Pomegranate, Apple, Guava, Sapota, Ber, Litchi, etc. some of which are even grown in smaller and scattered plots also need to be inventoried using semi-automatic classification techniques.

- Advanced Machine Learning/Deep Learning techniques need to be utilized for development of appropriate classification models using training samples. These semantic segmentation models have the proven potential for applicability across different agro-climatic dispositions for various plantation crops. This approach would also, in the long run, facilitate generation of a GT library, in the form of training samples, and can be used periodically for inventory and change mapping.
- All the remaining major areas in the country in which the important fruit & plantation crops are cultivated, also need to be covered in stages. This would facilitate generation of individual crop maps at different administrative hierarchical levels (taluk to national level). This is the pressing need for policy decisions at different levels.
- Individual state and a national level fruit & plantation crop map need to be generated through integration of the outcomes of all above approaches. This shall form a basis for assessment of trees outside forests as part of agro-forestry system, in the country and also frame policies in connection with food and nutritional security in the country.
- Studies for use of geospatial techniques for crop yield estimation also need to be hastened up. Toward this end, the site-suitability evaluation studies in the all the major existing fruit & plantation regions need to be carried out to come out with production/productivity zones. Additionally, site-suitability analysis for necessary non-fruit and plantation regions also needs to be carried out for the possible expansion of cultivation. This is of utmost importance as horticulture produce have an in-built value addition component and thus area income accretive to the farming community.
- Sufficient studies need to be conducted to detect and managed of pests and diseases through the application of ML/DL techniques.
- A national level geospatial database on storage and marketing infrastructure is the need of the hour to supplement the market intelligence, manage demand–supply scenarios, and minimize the post-harvest losses (especially in case of perishable produce).

Acknowledgements The project team expresses its deep sense of gratitude to Director, the National Remote Sensing Centre (NRSC), for his constant encouragement during the studies. We are highly grateful to Shri Uday Raj (Former CGM, Regional Centres, NRSC/ISRO), Dr. K. Ganesha Raj (Former GM, RRSC-South, NRSC/ISRO) for their support, encouragement and valuable guidance during execution of these studies. We thank Shri B. Chandrasekaran and (Late) Shri S. Elango, Scientists, RRSC-South, NRSC, for their contribution in field data collection. We duly acknowledge the efforts of MNCFC Research Analysts Shri Nagoor Kani, Shri Surya Deb Chakraborty, Smt. Mamta Rana and Shri Ghanshyam Shrawankar for their unstinted involvement in different stages of both phases of CHAMAN program.

References

Bock M, Xofis P, Mitchley J, Rossner G, Wissen M (2005) Object-oriented methods for habitat mapping at multiple scales—case studies from Northern Germany and Wye Downs. UK J Nature Conserv 13:75–89

Dadhwal VK, Singh RP, Dutta S, Parihar JS (2003) Remote sensing based crop discrimination and area estimation. A Rev Indian Experience Trop Ecol 43:107–122

Dibyendu D, Amit S, Sunil K (2018) Remote sensing techniques in horticulture. Global Hi-Tech Horticulture, New India Publishing Agency, In book, pp 39–48

Gamanya R, Maeyer PD, Dapper MD (2007) An automated satellite image classification design using object-oriented segmentation algorithms: a move towards standardization. Expert Syst Appl 32:616–624

Hebbar R, Ravishankar HM, Subramoniam STSR, Raj U, Dadhwal VK (2014) Object-oriented classification of high-resolution data for inventory of horticultural crops. In: The international archives of the photogrammetry, remote sensing and spatial information sciences, vol XL-8, 2014 ISPRS technical commission VIII symposium, 09–12 December 2014, Hyderabad, India

Hebbar KR, Krishna Rao MV (2002) Potential of IKONOS data for horticultural crop inventory. Project report, NRSC, Hyderabad

Kasper J, Stuart P, Christian W, Seonaid P, Lisa N (2009) Mapping banana plantations from object-oriented classification of SPOT-5 imagery. Photogram Eng Remote Sens 75. https://doi.org/10.14358/PERS.75.9.1069

Murthy CS, Sesha Sai MVR, Bhanuja Kumari V, Roy PS (2007) Agricultural drought assessment at disaggregated level using AWiFS /WiFS data of Indian remote sensing satellites. Geocarto Int 22:127–140

Naidu LGK, Ramamurthy V, Challa O, Hegde R, Krishnan P (2006). Manual soil-site suitability criteria for major crops. Publication No. 129, NBSS&LUP, Nagpur

NHRDF (2019) Annual report 2018–19. Nat Horticult Res Develop Found New Delhi 110058:104

Pillai KM (1984) A textbook of plantation crops. Vikas Publishing House, New Delhi, p 168p

RRSSC-B (2001) Utilization of satellite remote sensing for coffee inventory in parts of Karnataka, Kerala and Tamil Nadu, Project Report, RRSSC-B/002

RRSC-East (2014) Tea area development and management using RS and GIS. www.nrsc.gov.in/Earth_Observation_Applications_Agriculture_Tea_Management.html

RRSC-South (2012) Geospatial technology for acreage estimation of natural rubber and identification of potential areas for its cultivation in Tripura, Project Report

RRSC-South (2016) Inventory of coffee plantations using geo-spatial technology: pilot study in traditional coffee growing regions of India, NRSC-RC-APR-2016-TR-842, pp 150

RRSC-South (2018) Co-ordinated programme on horticulture assessment and management using geoinformatics (CHAMAN phase-1) technical project report. NRSC-RC-RRSCBANG-JUN-2018-TR-1161-V1.0, p 34

RRSC-South (2019) GeoCUP: geo-spatial inventory of coffee plantations at national level, NRSC-RC-REGBANG-JUL-2019-TR-1325-V1.0, NRSC technical project report, pp 161

RRSC-South (2021) Co-ordinated programme on horticulture assessment and management using geoinformatics (CHAMAN phase-2) technical project report, NRSC-RC-REGBANG-RRSC-BANG-APR2021-TR-0001842-V1.0, p 62

Srivastava RJ, Gebelein JL (2007) Land cover classification and economic assessment of citrus groves using remote sensing. ISPRS J Photogramm Remote Sens 61:341–353

Chapter 13
Management of Citrus Orchards in Central India using Geospatial Technology

Jugal Kishore Mani, A. O. Varghese, G. Sreenivasan, and C. S. Jha

Abstract Citrus fruits rank third in production after banana and mango in India. It is grown in 1.04 million ha covering 26 states. Citrus is grown in subtropical climates of the world though in tropical zones they incline for cyclic growth. Citrus productivity in the country is negatively affected by various biotic and abiotic factors as well as management practices. Citrus farming is overwhelmed with numerous constraints due to restrictive growing conditions, scarcity of water, and frequent pests, and diseases. The geospatial technique is a tool to address the growth limiting factors of citrus orchards, including biotic, abiotic, edaphic stress efficiently. Advanced geospatial technology is being largely used for mapping and area estimation of citrus orchards using object-based classification and machine learning approaches. Another vital area where geospatial technology is being used widely is identifying the health status of the citrus orchards, which greatly impacts the overall productivity of the citrus in the country. Apart from the physiological stress, the biotic stress created due to the disease and pest is yet another significant area where multispectral and hyperspectral RS are being widely used. Expanding the area under horticulture is an important objective under the national horticulture mission. In this respect, identifying new suitable areas for growing citrus is an important requirement. RS technology and GIS play a substantial role in the systematic characterization, assessment of several factors that impact the cultivation of citrus orchards and integrated modeling to finally identify a potential area for citrus orchards. This chapter discusses the implementations of geospatial techniques for managing citrus orchards covering various aspects mentioned above.

Keywords Citrus orchards · Remote sensing · Citrus site suitability · Biotic stress · Abiotic stress

J. K. Mani (✉) · A. O. Varghese · G. Sreenivasan
Regional Remote Sensing Centre—Central, NRSC, Nagpur, India

C. S. Jha
Regional Centers, National Remote Sensing Centre, Hyderabad, India

C. S. Jha et al. (eds.), *Geospatial Technologies for Resources Planning and Management*, Water Science and Technology Library 115,
https://doi.org/10.1007/978-3-030-98981-1_13

13.1 Introduction

Citrus is one of the major varied members of the family *Rutaceae* and is the dominant tree fruit crop globally. It originated in tropical and subtropical Southeast Asia and comprised many species of economic importance. The subtropical climate is utmost appropriate for citrus farming. Availability of most suitable land is important for citrus cultivation and citrus plants are affected by numerous stresses (biotic and abiotic). Citrus is grown more than 140 countries globally. The world's leading countries of citrus fruit production are China, Brazil, the U.S.A., India, Mexico, and Spain, representing close to two-thirds of global production (FAO 2009). Commercially, citrus fruits are sweet orange (*Citrus sinensis* Osbeck), Mandarin (*Citrus reticulata* Blanco), limes (*Citrus aurantifolia* Swingle), lemon (*Citrus limon* (L) Burm.f), grapefruit (*Citrus paradisi* Macf.), and pummel (*Citrus grandis* (L.) Osbeck). In global scenario, the contribution of citrus species is sweet orange (64%) followed by mandarins (20%), limes and lemons (10%), grapefruit and other citrus fruits (6%) (Chaturvedi et al. 2018). In India, citrus acreage is 1.07 million ha whereas production and productivity are 10.48 million tonnes and 9.78 tonnes/ha, respectively. In India, mandarin production is 3.25 million tonnes with a productivity of 10.16 tonnes/ha and cultivated under an area of 0.32 million ha while limes/lemons are grown in 0.21 million ha with production of 2.10 million tonnes and productivity is 9.62 tonnes/ha (De 2017).

In terms of production of fruits, India ranks second in the world and occupies 1st position for mango, banana, sapota, and acid limes (National Horticulture Board 2018). Among several horticultural crops, fruits contributed a major share in area and production, followed by plantation and vegetable crops. Maharashtra is well known for the cultivation of major horticultural fruit crops like citrus and mango. Soil and climatic properties are important natural factors, and a favorable combination is very crucial for the production of horticultural crops. The specific requirement of climate and soil conditions makes the distribution of horticultural crops, especially the plantations, more localized in contrast to other agricultural crops (National Horticulture Board 2018). The diversified climate ranging from temperate to tropical climate is unique important factors that influence the production of horticultural crops and is essential in planning. The fundamental requirements for proper planning in the horticultural sector are the availability of a reliable statistical database regarding area and production at different spatial hierarchies.

In the last four decades, the cultivated area of citrus and production had increased around five-fold with average productivity of 8.8 tonne/ha (National Horticulture Board 2018). In India, citrus is the second principal fruit crop next to mango with respect to area under cultivation (National Horticulture Board 2018). In 2017–18 citrus was cultivated in around 1003 thousand ha with a production of 12,546 thousand metric tonnes (National Horticulture Board 2018). In India, the average citrus fruit yield is very low compared to Brazil, Indonesia, USA, and Turkey (22–35 t/ha) (agricoop.nic.in website). Major producing states of lime are Andhra Pradesh,

Gujarat, Tamil Nadu, Karnataka, Maharashtra, Assam, and Rajasthan with production of 21.08 Lakh Tonnes (National Horticulture Board 2011). In India, the commercial varieties of mandarin are Nagpur mandarin (Central India), Coorg mandarin (South India), Kinnow mandarin (North–West India), and Khasi mandarin (North–East India). While, the traditionally grown sweet orange varieties are *Mosambi* (Maharashtra), *Sathgudi* (Andhra Pradesh), and *Malta and Jaffa* (Punjab) (Srivastava and Kohli 1997). Citrus fruits are sown under diverse agro-ecological environments i.e., arid & semi-arid of the southwest to the humid tropical climate of northeast India. The light soils with good drainage capacity are well suited for citrus orchards. The pH of 5.5–7.5 in deep soils are normally recommended for citrus cultivation. High concentration of $CaCO_3$ in the feeder root zone may be unfavorable for citrus growth (Srivastava and Singh 2001).

Maharashtra occupies the largest area under citrus farming in India, whereas the production is highest in Andhra Pradesh (38.0 lakh tonnes) followed by Madhya Pradesh (11.8 lakh tonnes), Punjab (10.1 lakh tonnes), and Maharashtra (8.61 lakh tonnes) (National Horticulture Board 2011). The discrepancy between acreage and production of citrus in Maharashtra desires attention for enhancing productivity. Nagpur Mandarine (*Citrus reticulata* Blanco) is the principal cultivars of citrus in Central India. Nagpur mandarin is grown in primarily black and red soils in Vidarbha region, Maharashtra; Chindwara and Betul district of Madhya Pradesh. Citrus cultivation has been expanded in last three decades in areas with different type of soils with varying suitability. Reduced longevity of commercially grown citrus because of varying limitations of nutrition is one among the important production linked constraint severely liable for low orchard efficiency (Srivastava and Singh 2008). Initially high fertile soils established nutrient constraints a variability following the non-synchronization of demand & supply for nutrients with the advancement of orchard age. An extensive survey of Nagpur mandarin groves of Central India exhibited huge deficiency of N, P and Zn nutrients, with nearly all sites showing several nutrient deficiencies (Srivastava and Singh 2005).

Citrus farming in the Nagpur district of Maharashtra may be overwhelmed with numerous constraints affected by restrictive growing conditions, scarcity of water, and high prevalence of pests and diseases (Garik 1990). Citrus orchards require sufficient water at critical stage in the initial years. Light irrigation with frequent interval is beneficial and the volume of water and number of irrigations depends on the textural characteristics of soil and growth phase (Das et al. 2009). For the recurrent growth and development, citrus trees usually require more water than most of the other sub-tropical fruits.

Geospatial techniques are an important tool to address the growth limiting factors of citrus orchards, including biotic, abiotic, and edaphic stress. Advanced geospatial technology is mainly used for mapping and area estimation of citrus orchards using object-based classification and machine learning approaches. Further, research is now progressing for yield modeling of citrus adopting integrated multi-parametric approach using moderate-, high- to very high spatial resolution remote sensing (RS) data from satellite and UAV platform. Another vital area where geospatial technology is being used widely is identifying the health status of the citrus orchards,

which greatly impacts the overall productivity of the citrus in the country. Apart from the physiological stress, the biotic stress created due to the disease & pest is yet another significant area where multispectral and hyperspectral RS are being widely used. RS technology and geographic information system (GIS) play a vital role in systematic characterization, assessment of several factors that influence the cultivation of citrus orchards, and integrated modeling to identify a potential area for citrus orchards finally. This chapter discusses the applications of geospatial techniques for the management of citrus orchards covering various aspects mentioned above.

13.2 Acreage Estimation of Citrus Orchards

The citrus orchards require specific monitoring and management to give a good yield. This monitoring starts at the commencement of the agricultural year and continues until the harvest period and concerns several parameters that are vital to get good fruits to yield in terms of quality and quantity. The citrus acreage is assessed by enumeration, whereas the yield is estimated by fruit counting on sample from randomly selected trees in different orchards at the district level. This method is more time intense and more erroneous.

Progressive techniques of RS have great potential in horticulture sector and have opened up new era of enhancing the horticultural database systems in the world. Sharma and Panigrahy (2007) developed the database of apple grove for Himachal Pradesh (India) from LISS III and AWiFS (23 and 55 m spatial resolution, respectively) data and were successfully delineated using relatively low-resolution satellite data. The most suitable sites for passion fruit plantations have been identified and prioritized using the same coarse resolution Indian satellite imageries for the north-eastern states of India.

In recent years, space-borne RS data is being utilized in the assessment of citrus orchards due to less time-consuming and more accurate. Shrivastava and Gebelein (2006) conducted an experiment to demarcate citrus groves from Landsat ETM + (30 m spatial resolution) imagery for economic assessment in Florida. They found a significant correlation between RS imagery between citrus production/income and acreage. Semi-automated classification technique using object-oriented analysis has been verified and evaluated for delineation of horticultural plantations under diverse agro-climatic regions (Hebbar et al. 2014). A combination of digital and visual technique was used for the demarcation of citrus orchards depending on the suitability and classification accuracy. Object-oriented-based classification technique employing both texture and contextual information like shape, size, shadow, and spectral information was used for the generation of citrus crop maps. These maps were fine-tuned, wherever needed, with limited manual on-screen visual interpretation technique. On-screen visual interpretation approach was followed wherever object-oriented classification is not applicable.

In another study for acreage estimation of citrus plantations in Amravati district of Maharashtra, multi-resolution LISS-IV and Cartosat-1 images and their fused

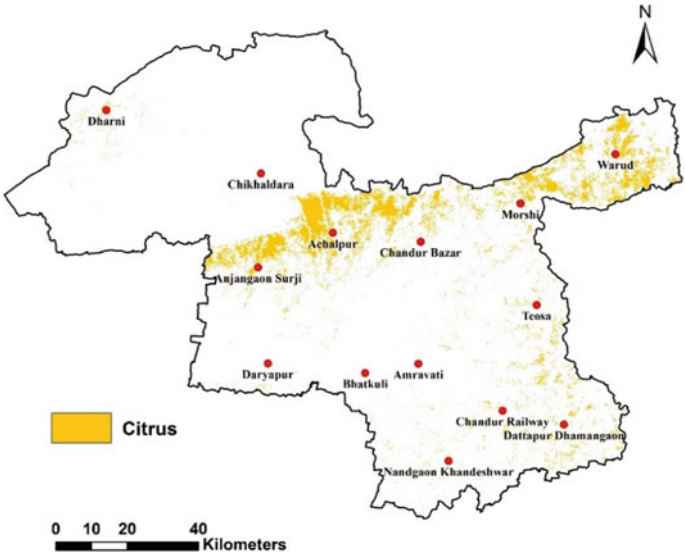

Fig. 13.1 Citrus orchards in Amravati district, Maharashtra, India during 2019

product were used as input in the feature extraction model. LISS-IV derived NDVI, texture from Cartosat-1 image, and spectral characteristics of fused data were taken as input for the creation of Spectral Feature Probability (SFP) layer. The description of the training region for citrus and background pixels is vital for the classification process. To generate the pixel probability layer, the conversion of the SFP layer to raster objects on the basis of threshold and clump function is essential. A group of operators for raster and vector-like probability filter, elimination, size filter and island filter were applied in the successive stages to generate a thematic map of citrus areas in vector format.

An area of 712 square kilometers (5.8%) was found under citrus orchards in the Amravati district out of the 12,235 square kilometers of the total geographical area during 2019 (Fig. 13.1). The validation of citrus orchards delineated by the semi-automated classification technique was validated using ground observations with an accuracy of about 93%.

13.3 Citrus Health Assessment

Citrus trees are affected by several stresses; therefore, it must be taken in all aspects of plant health for citrus production. Stress is a major concern for the agriculture sector, as stress leads to the economic losses of cash crops (Mani and Varghese 2018). The variance in abiotic stress in citrus orchards is mainly responsible for the difference in the health status of the citrus plants.

Vegetation stress is considered as an unfavorable condition that affects or blocks the metabolism, growth, or development of plant. Numerous natural and anthropogenic factors induced vegetation stress (Singh et al. 2003). There is growing attention/awareness among the citrus cultivators to understand the latest technologies for the health condition assessment of citrus. Assessing stress on timely basis is the most effective method to monitor health (Abouatallah et al. 2011). Detection of crop water stress in different growing seasons is necessary to predict yield conditions and plan irrigation scheduling (Payero and Irmak 2006). One of the most efficient methods for stress identification is geospatial technology, which comprises RS technology and GIS (Mani et al. 2016). Geospatial technology is an effective and efficient method for monitoring and analyzing citrus crops under stress using multitemporal satellite images.

A study is carried out for the health condition assessment of citrus groves in Nagpur district using vegetation health index. To estimate the spatial extent of citrus groves in Nagpur district, Sentinel-2 data sets were used (https://scihub.copernicus.eu/, Accessed 16 February 2021) with less than 10% cloud cover in the years of 2018 and 2019. Multitemporal and multispectral data of Landsat-8 OLI (https://earthexplorer.usgs.gov/, Accessed 16 February 2021) were used to assess vegetative health of citrus orchards using the vegetation health index. The total study period considered is 7 years, from 2013 to 2019.

Normalized Difference Vegetation Index (NDVI), Vegetation Condition Index (VCI), Temperature Condition Index (TCI), and Vegetation Health Index (VHI) were used to assess vegetative health and stress conditions. Land Surface Temperature (LST) is calculated using the brightness temperature of two bands of TIR (Rajeshwari and Mani 2014). The VHI is calculated using VCI and TCI as these two indices are more effective for monitoring vegetative stress than other indices (Table 13.1). VHI is categorized into three groups such as poor health condition (VHI 0–40), moderate health condition (VHI 40–60), and excellent health condition (VHI 60–100) as per Owrangi et al. 2011.

Table 13.1 Different vegetation indices used for assessing vegetative health and stress conditions

Indices	Formula	Range
NDVI	(NIR − RED)/(NIR + RED)	−1 to +1
VCI	(NDVIi − NDVImin) * 100/(NDVImax − NDVImin)	0–100
LST	TB10 + C1 (TB10 − TB11) + C2 $(TB10 - TB11)^2$ + C0 + (C3 + C4W) (1-m) + (C5 + C6W)Δm	Kelvin (K)
TCI	(LSTmax − LSTi) * 100/(LSTmax − LSTmin)	0 to 100
VHI	0.5 * VCI + 0.5 * TCI	0 to 100

Where, NIR is near infrared region band, TB10 and TB11 are brightness temperature of band 10 and 11 respectively, W is atmospheric water–vapor content, m is mean land surface emissivity, Δm is difference of land surface emissivity and C0, C1, C2, C3, C4, C5, and C6 are split-window coefficient values (Skokovic et al. 2014)

VHI values derived based on TCI and VCI show large spatial variation of these values in citrus orchards of Nagpur district. Northwest region of the district shows better VHI values for all the years, especially in Kalmeshwar tehsil. Katol tehsil also exhibits very good health condition of citrus orchards. A major part of the citrus groves in the district is classified under the moderate health category as per VHI, and a very less percent of the area was under poor health conditions (Fig. 13.2).

Citrus area under excellent health categories was found to be 47.4% during 2014 whereas it decreased to 2.4% and 1.5% in 2015 and 2018, respectively (Table 13.2). The area of citrus under the 'Excellent' health category drastically reduced from 2014 to 2015 but increased in 2017 to 25.1% and then decreased in the next two consecutive years. About 70.1–91.9% of the citrus area was found under moderate

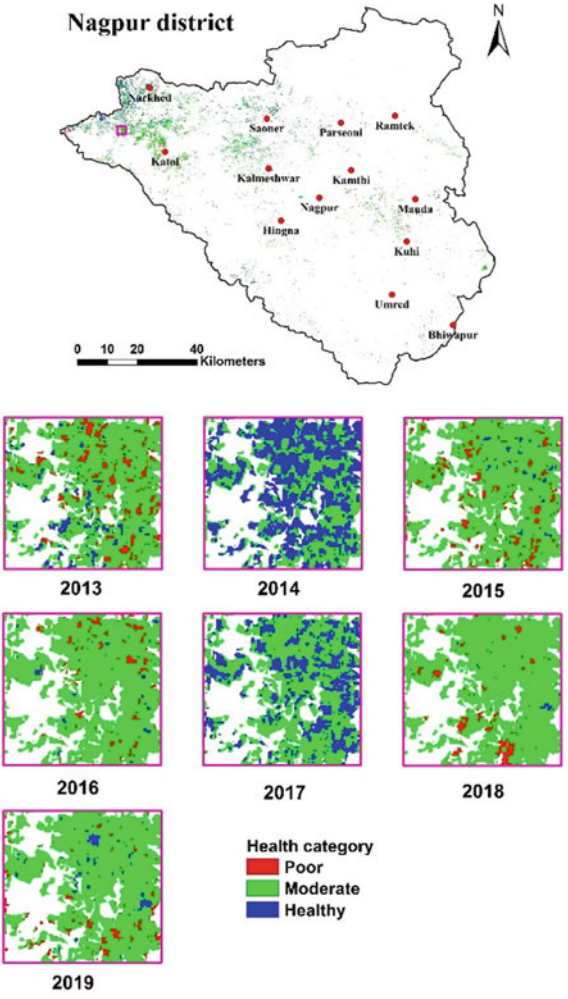

Fig. 13.2 Spatial distribution of VHI of citrus orchards in Nagpur district

Table 13.2 Citrus area (square kilometers) under different health categories of Nagpur district

Year	Health categories		
	Poor	Moderate	Excellent
2013	24.1 (8.5)*	197.8 (70.1)	60.1 (21.3)
2014	4.2 (1.5)	144.0 (51.1)	133.8 (47.4)
2015	30.1 (10.7)	245.2 (87.0)	6.7 (2.4)
2016	13.1 (4.6)	255.8 (90.7)	13.1 (4.6)
2017	2.5 (0.9)	209.0 (74.1)	70.7 (25.1)
2018	18.5 (6.6)	259.2 (91.9)	4.3 (1.5)
2019	12.5 (4.4)	239.7 (85.0)	30.0 (10.6)

*Values in parenthesis indicate percent area under different health categories

health condition across the seven years except in 2014 where the citrus area under moderate health condition was 51.1%. The poor health conditions of citrus plantations were at par in the seven years except during 2014 and 2017. Similarly, Du et al. (2018) also observed that VHI has a high correlation with temperature. Its variability was statistically described by variations in both rainfall & soil moisture in highly dynamic tropical Vu Gia Thu Bon catchment in Vietnam.

13.4 Expansion of Citrus Orchards

The depletion and degradation of natural resources cause water logging, increasing acidity and salinity, decreasing nutrients and productivity. During the last two decades, around 1.68% of total arable land is diminished, and nearly 47% is under degradation (FAO 1976). In recent years, demand for food and industrial use of agricultural products is increasing rapidly whereas agricultural productivity and productive land are decreasing strangely. Land suitability analysis (LSA) is a technique to estimate the grade of suitability of land for certain use (Hopkins 1977; Collins et al. 2001; Malczewski 2004) based upon the qualities and requirements of land (FAO 1976). LSA comprises land capability classification, land irrigability and suitability for crops, plantation, cultivation, industrialization, etc. A wide range of field observations like physiography, soils, vegetation, water, climatic parameters, and socio-eco-cultural aspects are required for these analyses. The conventional way of study, e.g., field work, analysis at laboratory, existing analog maps and data as records, etc., is time intense, costly, laborious, and not enabling to explain holistic information (Tahir et al. 2013).

Land users and planners require basic knowledge of soil, understanding the constraints and potential, and soils suitability for different crops for sustained agricultural production. The information of varied types of soils and their potential to several crop types on the spatial domain is crucial for planners and scientists in agriculture

to encourage farmers to practice cropping systems depending on soil capability to different crop types. Again, sustainable agriculture or farming promotes optimizing crop production. The concept of sustainable agriculture comprises the production of quality products in an ecologically subsisting, socially acceptable, well-organized economy and ensuring optimal utilization of the existing natural resources for effective production in the agriculture sector. To comply with these ideologies in sustainable agriculture, one has to sow the crops in environments where they most suited. This can be obtained by evaluating the suitability of land. Land suitability (LS) is a function of crop needs & land properties. Suitability refers the matching of land properties with crop needs. Evaluation of land suitability has to be done in a way that local requirements and environments are mirrored properly in the final decisions. The information of soil in spatial domain and report is an important component for land suitability analysis. The information of soil and land resource that can be utilized for appropriate land use planning in agriculture was explained by Dumanski et al. 1987.

One of the most efficient ways to assess site suitability and stress identification is geospatial technology, which involves the use of RS Technology and GIS (Mani et al. 2016). RS technology and GIS play an essential role in systematically classifying and evaluating soil resources (Saxena et al. 2000). RS and GIS have the capability to delineate landscape units based on spatial variation of soil characteristics. Classification of land capability (LC) and soil suitability can be done based on the information of landform, soil, land use and land cover in systematically for better utilization and conservation of resources for major crops (Solanke et al. 2005; Shukla et al. 2009). GIS has the potential to achieve a maximum return in the agricultural sector by suggesting a land use strategy for citrus based upon the soil resource information along with LC and site suitability for citrus. With this in view, an effort has been employed to find out potential zone for expansion of orange plantations in Vidarbha region, Maharashtra with RS and GIS-based deductive model (based on expert knowledge) using landscape and soil properties for orange farming explained by Likhar and Prasad (2011) (Table 13.3). Deductive or theoretical approaches use ecological requirements of known species to extrapolate suitable region from the environment and soil variable layers available within the GIS database (Varghese et al. 2010). Roy et al. (2020) compared the established criteria of soil suitability and characteristics of soil for citrus to diminish soil-related constraints using GIS-based inductive modeling approach in Central India.

The soils are categorized based on the parameters that influence the result of pedogenesis, i.e., functionality in terms of crop production is considered. The first step involves identifying broad soil type followed by further classifying the soil types depending on the variations in soil parameters like depth, texture, slope, pH, and organic carbon. The broad soil types and the differentiating soil parameters were classified using geocoded digital LISS-IV and PAN data of Vidarbha region.

The findings of the present study have reported the suitable area for citrus plantations was 35,629 (37.9%) square kilometers followed by 6461 (6.9%) square kilometers of moderate suitable and 22,855 (24.3%) square kilometers of non-suitable in Vidarbha region (Fig. 13.3).

Table 13.3 Landscape and soil properties for orange farming in Vidarbha region

Land use requirement	Class, degree of limitation, and rating scale		
	Suitable	Moderate suitable	Non-suitable
Soil site characteristics			
Slope (%)	0–3	3–5	>5
Drainage	Well	Moderately well	Poor, imperfect
Physical soil characteristics			
Texture/structure	Sandy loam, silty loam, silty clay loam, clay loam, sandy clay loam, loamy sand	sandy clay, fine sand, silty clay	Clay, massive clay, massive silty clay
Soil depth (cm)	>50	50–25	<25
Soil fertility characteristics			
pH	5.5–7.5	7.5–8.5	–
CEC [cmol (p^+) kg^{-1} clay]	>16	<16	–
Organic carbon (%)	>0.8	<0.8	–
Soil salinity and alkalinity			
EC (dS m^{-1})	0–3	3–4	>4
ESP (%)	0–8	8–12	>12

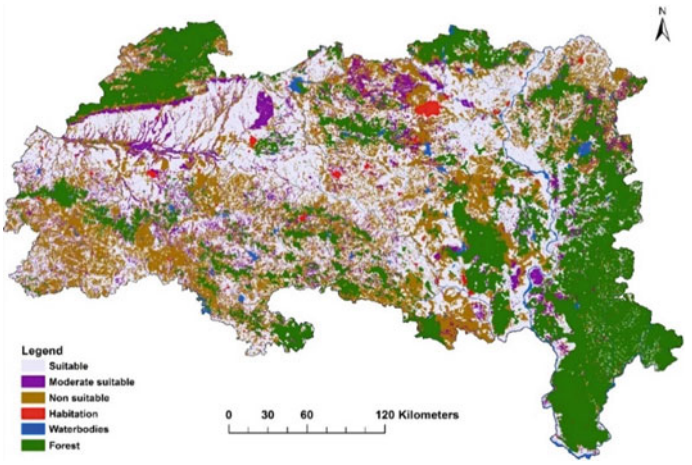

Fig. 13.3 Suitable area for expansion of orange orchards in Vidarbha region, Maharashtra

Table 13.4 Potential area for expansion of orange orchards in Vidarbha region, Maharashtra

District	Potential area (square kilometers)		
	Suitable	Moderate suitable	Non-suitable
Akola	2684 (51.3)*	812 (15.5)	1171 (22.4)
Amravati	5696 (48.4)	856 (7.3)	1722 (14.6)
Bhandara	2001 (50.1)	63 (1.6)	861 (21.6)
Buldhana	4204 (44.7)	739 (7.9)	3176 (33.8)
Chandrapur	3787 (34.5)	465 (4.2)	3123 (28.5)
Gadchiroli	1899 (13.5)	558 (4.0)	519 (3.7)
Gondia	1431 (28.7)	313 (6.3)	1635 (32.8)
Nagpur	3729 (39.1)	977 (10.2)	2777 (29.1)
Wardha	3048 (50.1)	333 (5.5)	1741 (28.6)
Washim	1933 (39.0)	444 (9.0)	2124 (42.8)
Yavatmal	5212 (39.7)	896 (6.8)	4002 (30.5)
Total	35,629 (37.9)	6461 (6.9)	22,855 (24.3)

*Values in parenthesis indicate percent area over total district's area under different suitable categories

Out of 35,629 square kilometers, which was assessed as a suitable area, the largest suitable area is available in Amravati district (5696 square kilometers), followed by Buldhana (4204 square kilometers), Gadchiroli (1899 square kilometers), and Gondia (1431 square kilometers) (Table 13.4). Based on this deductive modeling, the potential area delineated for expansion of orange groves can be utilized for better management of orange farming for increasing the area under the citrus plantations and enhancing overall citrus production from this region.

13.5 Pest and Disease Management

Citrus is grown in subtropical climates of the world though they incline for cyclic growth in tropical zones. The growth of citrus crop is best between the temperature range from 13 to 37 °C. Temperatures below—4 °C are harmful to young plants. High humidity favors the spread of many diseases. Citrus farming is overwhelmed with numerous constraints due to restrictive growing conditions, scarcity of water, and frequent pests, and diseases. Biotic stress interacts with the photosynthesis and physical structure of the plant at several internal and external structural levels and thus disturbs the absorption and reflectance of light energy. The changes of a pattern of light energy can be addressed by the RS technique. Citrus trees are susceptible to a number of destructive pests and diseases that are continuously emerging and can severely limit a country's production.

The changes of structural and physiochemical processes in plants because of pest and disease attacks can be studied scientifically using vegetative spectral reflectance

characteristics. This is required to formulate an effective pest management strategy. Pest management or surveillance operation like field scouting is more expensive, time-intensive, laborious & inclined to enormous error. Timely information on pest infection over a large region with spatial variability can be evaluated using RS technology which is non-destructive and non-invasive. Thus, RS can help to plan for protection advisory in an effective manner. In a recent scenario with the development of space technology, there is a lot of opportunities for RS technology for pests and diseases management.

RS of insect pests of fruit trees was initiated in 1968, detecting sooty mould incidence in citrus. The host medium for sooty mould fungus are citrus mealybugs (*Phenococcus citri)*, citrus blackfly (*Aleurocanthes woglumi)*. Citrus foliage appears black with the occurrence of sooty mould and indicates an evidence for detection of insects through aerial photography (Reisig and Godfrey 2006). Citrus blackfly and brown soft scale occurrence was detected using aerial CIR (color-infrared) photography and multispectral videography of citrus orchards (Hart et al. 1973; Everitt et al. 1996).

To distinguish diseased and healthy trees, vegetation indices are useful and extracted from several bands of multispectral images (Albetis et al. 2017 and Wójtowicz et al. 2016). The mapping of crop diseases has also been evaluated using satellite imagery. The feasibility of RS imagery for the detection of Huanglongbing (HLB) of citrus was examined (Li et al. 2015). In the recent past, unmanned aircraft have been used to detect crop diseases such as citrus greening (Garcia-Ruiz et al. 2013). Phytophthora foot rot infestation was detected and assessed in citrus groves using airborne digital multispectral imagery (Fletcher et al. 2001).

Garcia-Ruiz et al. (2013) evaluated the efficiency of HLB or greening disease of citrus recognition UAV and aircraft-based sensors at different spatial resolutions (5.45 cm and 0.5 m per pixel). Results reported that trees infected by HLB reflect strong light in the VIS region while it was weaker than healthy trees in the NIR region of the electromagnetic spectrum. The classification accuracy was 67–85% and 61–74% for UAV and aircraft-based sensors, respectively. The findings emphasized that UAV could detect the greening disease of citrus efficiently.

Qin et al. (2009) demonstrated the recognition of citrus canker through hyperspectral reflectance imaging technique. The findings reported that the citrus fruit canker and other damages were detected using hyperspectral (Wavelength: 450–930 nm) images with an accuracy of 96.2%. Smith et al. (2005) reported the red-edge position (REP) was strongly correlated with chlorophyll content among all treatments. The collective effects of strong chlorophyll absorption in the red & weak reflectance in the near-infrared (NIR) region of the electromagnetic spectrum because the leaf internal scattering deviates the abrupt reflectance in the red edge (680–740 nm) vegetation spectra. The peak slope point is referred to as REP, which also represents the maximum first derivative reflectance (FDR) of the reflectance spectrum (Collins 1978).

13.6 Citrus Yield Estimation

The alternate bearing is the most common phenomenon for tree crops which causes yield variation of citrus from year to year. The alternate bearing leads to temporal variability of yields as well as quality of the fruit of individual plant because of internal energy reserves dynamics in trees (Isagi et al. 1997; Noguchi et al. 2003; Sakai et al. 2003). Yield estimation of the convectional field-based method mainly depends on the individual's perception, leading to subjective differences among evaluators over a period. Ground-based convectional techniques are laborious and time-consuming. These techniques also unable to enumerate the spatial variation of yield in groves spreading over a large area and might be inaccurate due to the small sample size. The prediction of citrus yield using RS techniques is an effective tool to cover large areas and help citrus cultivators for optimum use of resources.

In India, yield estimation of field crops has been carried out by many researchers using RS techniques. However, yield estimation of horticultural crop using RS techniques has been reported by few researchers. Presently, the yield of citrus is declining in terms of quality and quantity due to biotic, abiotic, edaphic as well as management factors. To improve the fruit quality by alternate bearing though pruning and thinning of fruit of selected tree, development of citrus yield modeling is essentially required using RS techniques.

The successful forecast of crop yield mainly depended on the capability of sensors or imagers for detection of different biophysical parameters like leaf area index (LAI), leaf chlorophyll or leaf nitrogen content, where the individual parameter is closely associated with crop yield (Chang et al. 2005). Earlier investigations of yield estimation and mapping were primarily executed for field crops using RS techniques (Noguchi et al. 2003; Sakai et al. 2003). A scanty of study have been reported on horticultural crops using RS techniques. Fruit yield of citrus is varied with the variation in the count of newly emerged leaf and floral buds during the preceding growing seasons (Noguchi et al. 2003; Sakai et al. 2003).

The potential of reflectance characteristics of various multispectral RS data has capability to estimate biophysiochemical properties at the canopy level (Hall et al. 2003). The development of the yield model, various vegetation indices generated from multispectral RS images were used to assess crop growth conditions in the agricultural field (Zhang et al. 2006). The very high-resolution image from multispectral sensors has also verified the capability to detect fruit yield within an orchard. In the linear calibration model, tree sizes captured by ultrasonically correlated significantly ($R^2 = 0.80$) with fruit yield using half the data. Validation of actual and predicted fruit yield was done using the rest half of the data & the result was also significant ($R^2 = 0.42$). The average prediction accuracy, standard error, and root mean square error was 90.6%, 4.25, and 4.16 Mg/ha, respectively (Zaman et al. 2006). The NDVI has excellent significance for predicting the yield of individual trees of citrus orchards compared to other multiple wavebands (Ye and Sakai 2012).

Biophysiochemical characters of crop are vital for estimating growth and yield (El-Hendawy et al. 2019). For instance, leaf area, crown volume, crown diameter and LAI of plant canopy are significantly associated with an interception of light (Bai et al. 2016), production of biomass (Ribeiro et al. 2008), quality of fruit (Stanley 2016), ecosystem prolificacy (Vyas et al. 2010) and yield (Kucuker et al. 2015). The associations of citrus species and vegetation indices (VIs) fluctuate with season of growing and orchards (Sankaran et al. 2015). The Hyperion and Headwall Micro-Hyperspec (mini-sized and low-cost airborne hyperspectral sensors) have been utilized to retrieve several biophysiochemical characters of fruit trees. For example, characterization of citrus canopies was reported by Tumbo et al. (2002) and citrus yields was estimated by Zaman et al. (2006), Zhuang et al. (2018). Knowledge of yield predictions helped citrus cultivators for optimum use of resources (Dorj et al. 2017). The management and control measure practices of citrus groves is dependent on accurate prediction of potential yields (Bargoti and Underwood 2017). The multiple linear regression models and numerous illustrative variables were not performed well in the neural network to predict yields (Ye et al. 2008).

13.7 Summary

Citrus farming is overwhelmed with numerous constraints due to restrictive growing conditions, scarcity of water, and frequent pests, and diseases in India. Geospatial techniques have been found to have great potential for management of citrus orchards covering various aspects, including estimation of area of existing citrus orchards, identification of health status of the citrus orchards, assessment of pest and disease infections, all of which have a great impact on the overall productivity of the citrus in India. The biotic stress created due to the disease and pest is an important area where multispectral and hyperspectral RS are being widely used. Identifying new potential areas for expansion of citrus orchards is addressed based on physicochemical characteristics of soil and other physiographic parameters using geospatial models. RS technology and GIS play a vital role in the systematic characterization and assessment of various factors that impact the cultivation of citrus orchards. The scientific approach of geospatial techniques can be used to better plan and manage citrus cultivation in India to enhance overall productivity and production.

Acknowledgements Authors express their earnest gratitude to the Director, National Remote Sensing Centre (NRSC) and Chief General Manager, Regional Centers, NRSC, Indian Space Research Organisation (ISRO) for providing valuable suggestion and supervision. Authors are grateful to National Data Centre, NRSC; Sentinel Copernicus Science Hub maintained by the European Space Agency (ESA) and USGS Earth Explorer maintained by the NASA for online accessibility of LISS-IV, Cartosat-1, Sentinel-2, and Landsat data, respectively.

References

Abouatallah A, Salghi R, Hammouti B, El-Fadl A, El-Otmani M, Benismail MC, Eljaouhari N, El EK, Ziani A (2011) Soil moisture monitoring and plant stress measurement of young citrus orchard. Der Pharma Chemica 3(6):341–359

Albetis J, Duthoit S, Guttler F, Jacquin A, Goulard M, Poilvé H, Féret JB, Dedieu G (2017) Detection of flavescence dorée grapevine disease using unmanned aerial vehicle (UAV) multispectral imagery. Remote Sens 9(4):308–327

Bai Z, Mao S, Han Y, Feng L, Wang G, Yang B, Zhi X, Fan Z, Lei Y, Du W (2016) Study on light interception and biomass production of different cotton cultivars. PLoS One 11(5):e0156335

Bargoti S, Underwood J (2017) Deep fruit detection in orchards. In: 2017 IEEE international conference on robotics and automation (ICRA), May 29–June 3, 2017, Singapore, pp 3626–3633

Chang KW, Shen Y, Lo JC (2005) Predicting rice yield using canopy reflectance measured at booting stage. Agron J 97:872–878

Chaturvedi A, Pandey NK, Indu, Tripathi PP, Mishra RC, Tripathi AN (2018) Rejuvenation of Citrus in Arunachal Pradesh. Int J Pure App Biosci 6(4):688–695

Collins MG, Steiner FR, Rushman MJ (2001) Land-use suitability analysis in the United States: historical development and promising technological achievements. Environ Manage 28(5):611–621

Collins W (1978) Remote sensing of crop type and maturity. Photogramm Eng Remote Sens 44:43–55

Das PT, Tajo L, Goswami J (2009) Assessment of citrus crop condition in Umling block of Ri-bhoi district using RS and GIS technique. J Indian Soc Remote Sens 37:317–324

De LC (2017) Citrus rejuvenation in NE region of India. Int J Agric Sci 7(2):325–342

Dorj U-O, Lee M, Yun S-s (2017) An yield estimation in citrus orchards via fruit detection and counting using image processing. Comput Electron Agric 140:103–112

Du TLT, Bui DD, Nguyen MD, Lee H (2018) Satellite-based, multi-indices for evaluation of agricultural droughts in a highly dynamic tropical catchment. Central Vietnam. Water 10(5):659–682

Dumanski J, Phipps M, Huffman E (1987) A study of relationships between soil survey data and agricultural land use using information theory. Can J Soil Sci 67:95–102

El-Hendawy S, Al-Suhaibani N, Elsayed S, Refay Y, Alotaibi M, Dewir YH, Hassan W, Schmidhalter U (2019) Combining biophysical parameters, spectral indices and multivariate hyperspectral models for estimating yield and water productivity of spring wheat across different agronomic practices. PLoS One 14(3):e0212294

Everitt JH, David E, Kenneth S, Mario A, Michael D (1996) Using spatial information technologies for detecting and mapping whitefly and harvester ant infestations in south Texas. Southwest Entomol 21(4):421–432

FAO (1976) A framework for land evaluation. Soils Bulletin 3, FAO, Rome

FAO (2009) FAOSTAT. http://faostat.fao.org/site/567/DesktopDefault.aspx?PageID=567#ancor. Accessed 21 Nov 2021

Fletcher RS, Skaria M, Escobar DE, Everitt JH (2001) Field spectra and airborne digital imagery for detecting Phytophthora foot rot infections in citrus trees. Hortic Sci 36(1):94–97

Garcia-Ruiz F, Sankaran S, Maja JM, Lee WS, Rasmussen J, Ehsani R (2013) Comparison of two aerial imaging platforms for identification of huanglongbing-infected citrus trees. Comput Electron Agric 91:106–115

Garik G (1990) Towards monitoring droughts from space. J Clim 3(2):282–295

Hall A, Louis J, Lamb D (2003) Characterising and mapping vineyard canopy using high-spatial-resolution aerial multi-spectral images. Comput Geosci 29:813–822

Hart WG, Ingle SJ, Davis MR, Mangum C (1973) Aerial photography with infrared color film as a method of surveying for citrus blackfly. J Econ Entomol 66(1):190–194

Hebbar R, Ravishankar HM, Trivedi S, Raj U, Dadhwal VK (2014) Object oriented classification of high-resolution data for inventory of horticulture crops. Int Arch Photogramm Remote Sens Spat Inf Sci XL(8):745–749

Hopkins L (1977) Methods for generating land suitability maps: an evaluation. J American Inst Plann 34(1):19–29

https://earthexplorer.usgs.gov/, Accessed 16 Feb 2021

https://scihub.copernicus.eu/, Accessed 16 Feb 2021

https://www.agricoop.nic.in/sites/default/files/Citrus%20cultivation.pdf, Accessed 18 Nov 2021

Isagi Y, Sugimura K, Sumida A, Ito H (1997) How does masting happen and synchronize? J Theor Biol 187:231–239

Kucuker E, Yildiz K, Ozkan Y (2015) Tree growth yield and fruit quality of different apple cultivars trained as super spindle. Aceh Int J Sci Technol 4:26–31

Li X, Lee WS, Li M, Ehsani R, Mishra AR, Yang C (2015) Feasibility study on huanglongbing (citrus greening) detection based on WorldView-2 satellite imagery. Biosyst Eng 32:28–38

Likhar CK, Prasad J (2011) Characteristics and classification of orange-growing soils developed from different parent materials in Nagpur district, Maharashtra. J Indian Soc Soil Sci 59:209–217

Malczewski J (2004) GIS-based land-use suitability analysis: a critical overview. Prog Plan 62:3–65

Mani JK, Varghese AO (2018) Remote sensing and GIS in agriculture and forest resource monitoring. In: Reddy GPO, Singh SK (eds) Geospatial technologies in land resources mapping, monitoring and management. Springer Nature Switzerland AG, pp 377–400

Mani JK, Varghese AO, Rao SVCK (2016) Suitability analysis for orange orchards in Vidarbha region of Maharashtra using remote sensing and GIS based models, In: Proceedings of international conference on integrated land use planning for smart agriculture—an agenda for sustainable land management (ICILUPSA-2016). November 10–13, 2016, Nagpur

National Horticulture Board (2011) Indian Horticulture Database-2011. http://nhb.gov.in/area-pro/database-2011.pdf, Accessed 15 Nov 2021

National Horticulture Board (2018) Horticultural statistics at a glance 2018. Horticulture Statistics Division, Department of Agriculture, Cooperation & Farmers' Welfare, Ministry of Agriculture & Farmers' Welfare, Government of India

Noguchi Y, Sakai K, Asada S, Garciano L, Sasao A (2003) Modeling of alternate bearing in Satsuma Mandarin-linear dynamic model based on ensemble set for harvested fruits number. Japan J Agric Eng 65:55–61

Owrangi MA, Adamowski J, Rahnemaei M, Mohammadzadeh A, Sharifan RA (2011) Drought monitoring methodology based on AVHRR images and SPOT vegetation maps. J Water Resour Prot 3(5):325–334

Payero JO, Irmak S (2006) Variable upper and lower crop water stress index baselines for corn and soybean. Irrig Sci 25:21–32

Qin J, Burks TF, Ritenour MA, Bonn WG (2009) Detection of citrus canker using hyperspectral reflectance imaging with spectral information divergence. J Food Eng 93:183–191

Rajeshwari A, Mani ND (2014) Estimation of land surface temperature of Dindigul district using Landsat 8 data. Int J Res Eng Technol 3(5):122–126

Reisig D, Godfrey L (2006) Remote sensing for detection of cotton aphid- (Homoptera: Aphididae) and spider mite- (Acari: Tetranychidae) infested cotton in the San Joaquin Valley. Environ Entomol 35(6):1635–1646

Ribeiro NS, Saatchi SS, Shugart HH, Washington-Allen RA (2008) Aboveground biomass and leaf area index (LAI) mapping for Niassa Reserve, northern Mozambique. J Geophys Res 113

Roy PD, Varghese AO, Suryavanshi A, Mani JK, Jangir A, Fagodiya RK, Jena RK, Ray P, Singh S (2020) Characterization of the soil properties of citrus orchards in Central India using remote sensing and GIS. Natl Acad Sci Lett 44:313–316

Sakai K, Noguchi Y, Asada S (2003) Nonlinear dynamics in arable land: alternate bearing of tree crops. Technical report IEICE NLP 2002-132

Sankaran S, Ehsani R, Morgan KT (2015) Detection of anomalies in citrus leaves using laser-induced breakdown spectroscopy (LIBS). Appl Spectrosc 69:913–919

Saxena RK, Verma KS, Chary GR, Srivastava R, Barthwal AK (2000) IRS-1C data application in watershed characterization and management. Int J Remote Sens 21:3197–3208

Sharma A, Panigrahy S (2007) Apple orchard characterization using remote sensing and GIS in Shimla district of Himachal Pradesh. In: Proceedings of remote sensing and photogrammetry annual conference. September 11–14, 2007, Newcastle, UK

Shrivastava RJ, Gebelein JL (2006) Land cover classification and economic assessment of citrus groves using remote sensing. ISPRS J Photogramm 61:341–353

Shukla AE, Prasad J, Nagaraju MSS, Srivastava R, Kauraw DL (2009) Use of remote sensing in characterization and management of Dhamni micro-watershed of Chandrapur district of Maharashtra. J Indian Soc Remote Sens 37:129–137

Singh RP, Roy S, Kogan F (2003) Vegetation and temperature condition indices from NOAA AVHRR data for drought monitoring over India. Int J Remote Sens 24(22):4393–4402

Skokovic D, Sobrino JA, Jimenez-Munoz JC, Soria G, Julien Y, Mattar C, Jordi C (2014) Calibration and validation of land surface temperature for Landsat 8-TIRS sensor. In: Proceeding of the workshop on land product validation and evolution (ESA/ESRIN). January 28–30, 2014, Frascati (Italy)

Smith KL, Steven MD, Colls JJ (2005) Plant spectral responses to gas leaks and other stresses. Int J Remote Sens 26(18):4067–4081

Solanke PC, Srivastava R, Prasad J, Nagaraju MSS, Saxena RK, Barthwal AK (2005) Application of remote sensing and GIS in watershed characterization and management. J Indian Soc Remote Sens 33:239–244

Srivastava AK, Kohli RR (1997) Soil suitability criteria for citrus: an appraisal. Agric Rev 18(3):139–146

Srivastava AK, Singh S (2001) Soil properties influencing yield and quality of Nagpur mandarine. J Indian Soc Soil Sci 49(1):226–229

Srivastava AK, Singh S (2005) Diagnosis of nutrient constraints in citrus orchards of humid tropical India. J Plant Nutr 29(6):1061–1076

Srivastava AK, Singh S (2008) Analysis of citrus orchard efficiency in relation to soil properties. J Plant Nutr 30:2077–2090

Stanley J (2016) Factors affecting fruit set and fruit quality along branch units of different apricot cultivars. N Z J Crop Hortic Sci 44(3):171–191

Tahir M, Imam E, Hussain T (2013) Evaluation of land use/land cover changes in Mekelle city, Ethiopia using remote sensing and GIS. Comput Ecol Softw 3(1):9–16

Tumbo S, Whitney J, Miller W, Wheaton T (2002) Development and testing of a citrus yield monitor. Appl Eng Agric 18(4):399–403

Varghese AO, Joshi AK, Krishna Murthy YVN (2010) Mapping of realized and fundamental Niches of threatened tree species using geoinformatics: a species level approach for sustaining biodiversity. J Indian Soc Remote Sens 38(3):523–534

Vyas D, Mehta N, Dinakaran J, Krishnayya N (2010) Allometric equations for estimating leaf area index (LAI) of two important tropical species (*Tectona grandis* and *Dendrocalamus strictus*). J for Res 21:197–200

Wójtowicz M, Wójtowicz A, Piekarczyk J (2016) Application of remote sensing methods in agriculture. Commun Biometry Crop Sci 11:3–50

Ye X, Sakai K (2012) Fruit yield estimation through multispectral imaging. In: Srivastava AK (ed) Advances in citrus nutrition. Springer, pp 453–473

Ye X, Sakai K, Sasao A, Asada S-i (2008) Potential of airborne hyperspectral imagery to estimate fruit yield in citrus. Chemom Intell Lab Syst 90:132–144

Zaman QU, Schumann AW, Hostler HK (2006) Estimation of citrus fruit yield using ultrasonically-sensed tree size. Appl Eng Agric 22(1):39–44

Zhang J, Wang K, Bailey JS, Wang R (2006) Predicting nitrogen status of rice using multi-spectral data at canopy scale. Pedosphere 16(1):108–117

Zhuang J, Luo S, Hou C, Tang Y, He Y, Xue X (2018) Detection of orchard citrus fruits using a monocular machine vision-based method for automatic fruit picking applications. Comput Electron Agric 152:64–73

Chapter 14
Geospatial Technology for Crop Yield Forecasting-A Case Study of SW Uttarakhand

Kapil Bhoutika, Arvind Kumar, Dhananjay Paswan Das, and Ashish Pandey

Abstract Crop yield forecasting is important for policy decisions at the national and regional levels. In the present study, the yield of rice, Wheat, and Sugarcane crops has been predicted for South-west Uttarakhand. Three major crop-grown districts of SW Uttarakhand, namely Haridwar, Dehradun, and Pauri Garhwal, were taken under the study. MODIS-derived Normalized Difference Vegetation Index (NDVI) and Enhanced Vegetation Index (EVI) parameters were used for crop yield forecasting. Stepwise Regression and Least Absolute Shrinkage and Selection Operator (LASSO) methods were used for forecasting using YIELDCAST-DSS software developed by India Meteorological Department (IMD) with Indian Agricultural Statistics Research Institute (IASRI). The meteorological parameters viz. rainfall, maximum and minimum temperature, the maximum and minimum relative humidity for the last 20 years (2001–2020) were used. The crop yield forecasting has been done for F2 stage (vegetative growth stage) and F3 stages (pre-harvest stage). NDVI helps to provide information about the overall state of vegetation cover and differentiate vegetation from other types of Landcover. EVI is used to quantify the greenness of vegetation, and it is more sensitive to dense vegetation cover. The results revealed a reduction in uncertainties in crop yield forecasting by assimilation of remote sensing data in the crop model. The study shows a good result of yield forecasted by using NDVI and EVI as an independent parameter compared to the other climatic variables without NDVI and EVI. In most models, the EVI outperformed NDVI and climatic variables alone.

Keywords Crop yield forecasting · Remote sensing · Stepwise regression · LASSO · NDVI · EVI

K. Bhoutika (✉) · A. Kumar · D. P. Das · A. Pandey
Department of Water Resources Development and Management, Indian Institute of Technology Roorkee, Roorkee 247667, India
e-mail: kapil_b@wr.iitr.ac.in

C. S. Jha et al. (eds.), *Geospatial Technologies for Resources Planning and Management*, Water Science and Technology Library 115,
https://doi.org/10.1007/978-3-030-98981-1_14

14.1 Introduction

Rice, Wheat, and Sugarcane are the three major crops of India which are the backbone of Indian Agriculture. In 2018, agriculture employed more than half of the total workforce of India and contributed 17–18% of the country's GDP (Ahmed et al. 2021).

Pre-harvest forecast of crop yield is conducive for Government and Planners in taking different arrangement choices identifying with the acquisition, stockpiling, conveyance, promoting, value, trade import, and so on (Agrawal and Mehta 2007). The weather has a significant impact on crop yield. It is expected that the effects of weather factors are not independent as crop yield is influenced by the particular combinations of these factors in which they occur. For example, the impact of rainfall on yield depends not only on the amount of rainfall at the different phenophases of the crop but also on the intensity of weather factors that may be associated with it (Agrawal et al. 1983).

Forecasting Agricultural output using Space, Agro-meteorology, and Land-based observations (FASAL) is a flagship programme of Mahalanobis National Crop Forecast Centre (MNCFC), Ministry of Agriculture and Farmers Welfare, Govt. of India under the guidance of India Meteorological Department sponsored by the Ministry of Earth Sciences, Government of India. FASAL scheme aimed to pre-harvest forecasting of crop yield in various growth stages at block, district, state, and national level (Ray et al. 2014a, 2014b).

There are two fundamental goals in statistical learning—ensuring high prediction accuracy and discovering relevant predictive variables (Zou 2016) applicable in crop yield forecasting. Hence, the relevant predictive variables can be climate variables and the independent remote sensing parameters, which can be used to increase the accuracy of crop yield prediction. The most commonly used techniques for crop yield forecasting are the method of regression analysis. But the major problem in regression analysis is the significance of parameters. No significant parameters lead to less accurate forecasts, which are unreliable. Due to this, various regression methodologies have been used under the study, and the most appropriate regression methods were identified for the study area. Based on significance tests, the stepwise regression method is commonly utilized in the research and medical field (Kutner et al. 2005). However, the fundamental issue with the stepwise regression method is that it searches a wide scale of possibilities, resulting in a high risk of overfitting the data. LASSO (Least Absolute Shrinkage and Selection Operator) method was formulated by Tibshirani (1996). LASSO is a strong method that combines feature selection and regularization to improve the statistical model's interpretability and prediction performance (Kumar et al. 2019).

We can use different remote sensing parameters in regression techniques to decrease the error in crop yield forecasting. MODIS-derived AET (actual evapotranspiration) was used in sugarcane crop yield forecasting, which resulted well (Bhoutika et al. 2022). Time series NDVI has a wide range of applications, including

crop yield, which it gained immense popularity over the years. AVHRR derived time-series data of NDVI used for crop yield forecasting since the 1980s (Kastens et al. 2005). Still, this has an enormous scope of research to use as an independent parameter in different regression models. But recently, MODIS derived NDVI has been used over AVHRR derived NDVI because it has a better spatial resolution (250 m) and radiometric calibration, which helps in more accurate crop yield forecasting (Doraiswamy et al. 2005; Schut et al. 2009; Mkhabela et al. 2011).

EVI was created to improve the vegetation signal's sensitivity in high biomass areas and improve vegetation observation by de-coupling the canopy background signal and reducing atmospheric influences (Huete et al. 2002; Johnson et al. 2016).

Looking at those as mentioned earlier, the study was carried out with the following specific objectives:

I. Yield forecasting of Rice, Wheat, and Sugarcane crops,
II. Comparison of the effectiveness of satellite-derived NDVI and EVI in crop yield forecasting, and
III. Comparison of Stepwise regression and LASSO methods for crop yield forecasting.

14.2 Material and Methods

14.2.1 Study Area

The study area lies between 77°20′–79°20′ E Longitudes and 29°30′ N–31° N Latitudes. It covers Dehradun, Haridwar, and Pauri Garhwal Districts of Uttarakhand State in India (Fig. 14.1). The study area shows four distinct weather seasons viz. summer, monsoon, post-monsoon, and winter seasons. The summer season ranges from March to May; the monsoon season starts from June and continues up to September. The post-monsoon season ranges from October to November. The winter season starts from December to February (Joshi and Sharma 2008). The annual rainfall of the study area varies from 1500 to 2000 mm (Pareek et al. 2019). Rice, Wheat, and Sugarcane are the major crops in Haridwar and Dehradun districts, while Rice and Wheat are the major crops in the Pauri Garhwal district, and sugarcane cultivation was negligible during the recent years.

14.2.2 Data Collection and Preprocessing

14.2.2.1 Weather Data

The historical daily weather data for rainfall, maximum and minimum temperatures, maximum and minimum relative humidity during 2001–2020 of the study

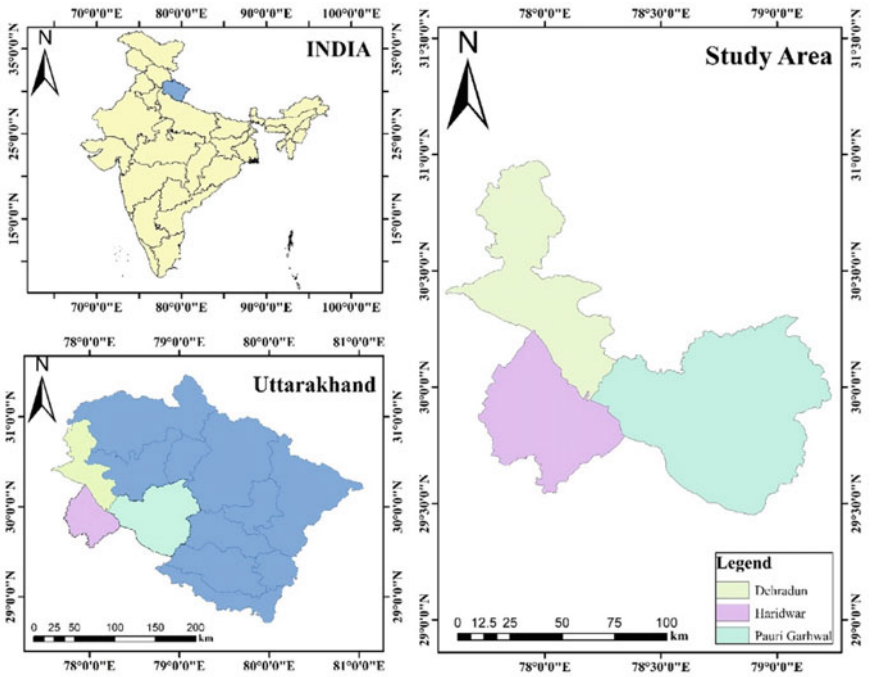

Fig. 14.1 Study area map

area were collected from Agrometeorological Field Unit, IIT Roorkee, and Indian Meteorological Department (IMD), Pune.

14.2.2.2 Crop Yield Data

The district-level annual yield data for Rice, Wheat, and Sugarcane crops were provided by the Directorate of Agriculture, Govt. of Uttarakhand during the period 2001–2020.

14.2.2.3 Land Use Land Cover (LULC) Map

The land use land cover (LULC) map for 2020 of the Haridwar, Dehradun, and Pauri Garhwal districts has been derived from the website https://livingatlas.arcgis.com/landcover/. The LULC map was generated by ESRI impact observatory. The ESA Sentinel 2 imagery, which has 10 m spatial resolution, is used. According to the LULC map, the agriculture area is highest in Haridwar district and least in Pauri Garhwal district (Fig. 14.2).

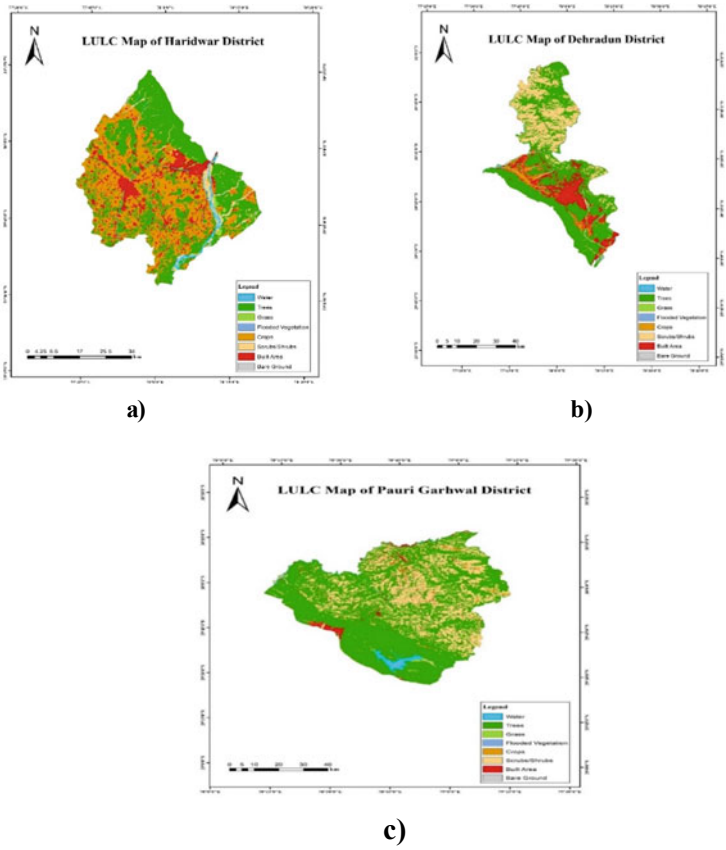

Fig. 14.2 Land use land cover map of **a** Haridwar, **b** Dehradun, and **c** Pauri Garhwal district

14.2.2.4 NDVI and EVI Data Set

MODIS MOD13Q1 V6 16-day interval at 250 m Resolution data for NDVI and EVI was downloaded for the years 2001–2021 from the Google earth engine (Didan 2014). The algorithm chooses the best available pixel value from all the acquisitions from the 16 days. NDVI is alluded to as the continuity index to the existing NOAA, and AVHRR derived NDVI. EVI is the second vegetation layer that minimizes canopy background variations and affects over thick vegetation conditions. The EVI uses the blue band to remove persistent air tainting caused by smoke and sub-pixel thin cloud mists. The MODIS NDVI and EVI items were calculated using atmospherically adjusted bi-directional surface reflectance with clouds, water, cloud shadows, and heavy aerosols masked off.

14.3 Methodology

Yield Cast DSS (Decision Support System) for statistical crop yield forecast developed by ICAR-IASRI has been used for the study. In Yield cast DSS, the Stepwise regression method can be easily compared, and the LASSO method chooses the best model, which gives the slightest error.

The model selection is based on RMSE (Root mean square error) and MAPE (Mean absolute percentage error) values. RMSE is the difference between the values predicted by models and the observed values. In this study, the models are regression models, and observed values are the historical crop yield data. RMSE is always non-negative, and a zero value shows a perfect fit for data that is generally never achieved in practice. A lower RMSE value shows a better model than the higher RMSE model.

$$\text{RMSE} = \sqrt{\frac{\sum_{i=1}^{n}(P_i - O_i)^2}{n}} \tag{14.1}$$

MAPE shows the accuracy of prediction in statistics. It measures the percentage accuracy and is calculated as the average absolute percentage error of observed value minus predicted value divided by observed value. Lower the MAPE value better the forecasted model. MAPE is easy to understand because errors are given in absolute percentage. Also, due to the absolute percentage value in MAPE, the problem of positive and negative values canceling each other is solved.

$$\text{MAPE} = \frac{1}{n}\sum_{i=1}^{n}\left|\frac{O_i - P_i}{O_i}\right| \times 100 \tag{14.2}$$

where,

P_i Predicted value obtained through different regression method.

O_i Observed values of annual crop yield.

n Number of observations in Year.

NDVI and EVI are the two remote sensing parameters used in the study. The NDVI is based on the premise that live plants absorb solar radiation in photosynthetically active radiation (PAR), which they employ as a dynamic energy source throughout the photosynthesis process. Plants scatter sunlight in the near-infrared (NIR) region, which is why they look brighter and darker in the NIR and PAR regions, respectively (Johnson et al. 2016).

$$\text{NDVI} = \frac{\rho_{\text{NIR}} - \rho_{\text{RED}}}{\rho_{\text{NIR}} + \rho_{\text{RED}}} \tag{14.3}$$

ρ_{NIR} and ρ_{RED} represent reflectance at the Near Infrared (0.7–1.1 μm) and red wavelengths (0.6–0.7 μm), respectively (Rouse et al. 1974; Matsushita et al. 2007). The NDVI ranges from − 1 to + 1, a unit less parameter (Mkhabela et al. 2011).

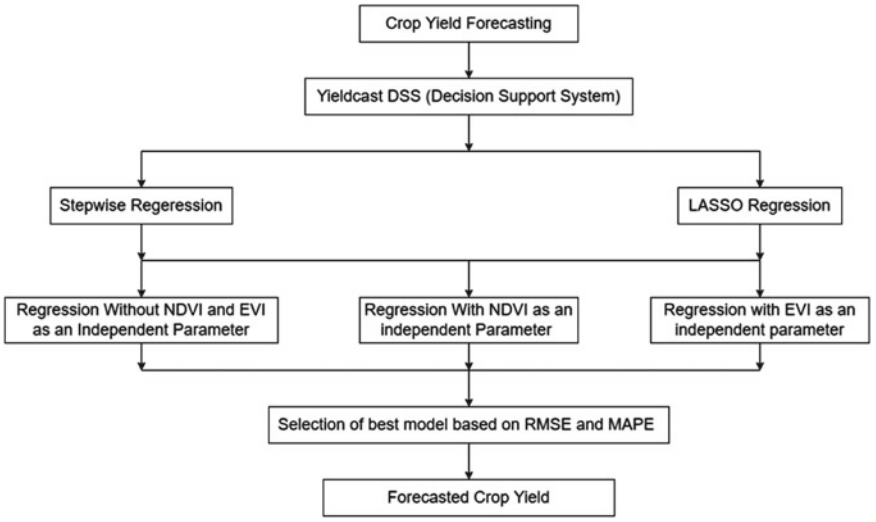

Fig. 14.3 Crop yield forecasting using yieldcast DSS

The second vegetation index used is the EVI, which was developed so that in high biomass regions improve sensitivity to optimize the vegetation signal and improve vegetation monitoring through a reduction in atmospheric influences and de-coupling of the canopy background signal (Huete et al. 2002; Johnson et al. 2016).

$$\mathrm{EVI} = G \times \frac{\rho_{\mathrm{NIR}} - \rho_{\mathrm{RED}}}{\rho_{\mathrm{NIR}} + (C_1 \times \rho_{\mathrm{RED}} - C_2 \times \rho_{\mathrm{BLUE}}) + L} \tag{14.4}$$

Here C_1 and C_2 are coefficients used to correct aerosol scattering in the red band by using the blue band, ρ_{blue} is reflectance at the blue wavelength (0.45–0.52 μm, and L is the Soil adjustment factor. In general, the value G (Gain Factor) = 2.5, L = 1, $C_1 = 6.0$, and $C_2 = 7.5$ (Huete et al. 1997; Matsushita et al. 2007).

A schematic representation of YieldCastDSS has been depicted in Fig. 14.3.

14.3.1 Results and Discussions

The crop Yield forecasting is divided into two stages, i.e., F2 and F3 stages. The models using Stepwise Regression and LASSO methods were identified in which the RMSE and MAPE values were less. For most of the crops and stages, EVI performed well as compared to the refined models with NDVI parameters.

Tables 14.1 and 14.2 show that the performance of LASSO method was better than stepwise regression for Rice crop in Haridwar District. Similarly, the Stepwise regression method was found as a better model than LASSO method for Wheat crop at F2 stage with NDVI parameter. In all other cases, LASSO method was found better than Stepwise regression method. For Sugarcane crop, the Stepwise regression method was better than LASSO method at F2 Stage, and at F3 stage, it was Vice-versa.

Tables 14.3 and 14.4 revealed that the Lasso method was found better than stepwise regression method at all the stages for Dehradun district for Rice crop. For Wheat crop, the Stepwise regression method was found better than the LASSO method at F2 and F3 stages with NDVI parameter. The Stepwise regression method was found better than LASSO method for Sugarcane crop at F2 and F3 stages with EVI parameter. At F3 stage, Stepwise regression method was found better than LASSO method without EVI and NDVI parameters.

Tables 14.5 and 14.6 show that the performance of LASSO method was found better than Stepwise regression method for Pauri Garhwal district at F2 stage while at F3 stage, stepwise regression method was better than LASSO method for all the models. For Wheat crop, LASSO method was better than Stepwise Regression method at both the stages, i.e., F2 and F3 stage.

The deviation percentage from predicted and observed values of yields at F2 and F3 stages with different parameters were depicted in Figs. 14.4, 14.5, and 14.6 for Rice, Wheat, and Sugarcane crops, respectively. The results revealed that the forecasted yield is underestimated than the observed yield, which shows that the observed yield was increased during the recent years, which leads to the variation in the forecasted yield.

14.4 Conclusion

The study reveals that using Remote Sensing Parameters like NDVI and EVI increases the accuracy of crop yield forecasting. In most of the cases in the study area, the performance of EVI was better than NDVI as an independent parameter in crop yield forecasting. Using LASSO with Stepwise regression, increases crop yield forecasting accuracy of Rice, Wheat, and Sugarcane. The models developed reduce inaccuracy in crop yield prediction having a lower RMSE and MAPE values. As a result, we may conclude that crop yield can be forecasted successfully using with remote sensing characteristics like NDVI and EVI. Other remote sensing parameters can be tested to improve the crop yield forecast in future. The study also demonstrates that how geospatial technology can be used to forecast crop yield.

Table 14.1 RMSE and MAPE for Haridwar district using stepwise regression and LASSO methods

Haridwar												
Stages	F2 stage						F3 stage					
	Without NDVI and EVI		With NDVI		With EVI		Without NDVI and EVI		With NDVI		With EVI	
Rice	RMSE	MAPE	RMSE	MAPE	RMSE	MAPE	RMSE	MAPE	RMSE	MAPE	RMSE	MAPE
Stepwise	127.239	5.238	127.238	5.238	123.702	4.953	105.588	4.375	105.591	4.375	100.476	4.132
LASSO	88.441	3.790	137.453	5.294	89.434	3.652	77.355	3.297	88.231	3.774	37.547	1.499
Wheat	RMSE	MAPE	RMSE	MAPE	RMSE	MAPE	RMSE	MAPE	RMSE	MAPE	RMSE	MAPE
Stepwise	35.363	1.061	101.010	3.340	44.482	1.427	99.233	3.274	99.038	2.930	180.534	5.667
LASSO	43.652	1.438	45.354	1.494	37.072	1.204	98.722	3.224	90.493	2.744	93.662	3.005
Sugarcane	RMSE	MAPE	RMSE	MAPE	RMSE	MAPE	RMSE	MAPE	RMSE	MAPE	RMSE	MAPE
Stepwise	728.582	0.991	684.089	0.993	763.457	1.055	634.017	0.871	644.427	0.876	634.017	0.871
LASSO	771.517	1.055	783.707	1.071	848.522	1.164	628.944	0.806	435.593	0.611	609.716	0.787

Table 14.2 Forecasted yield for Haridwar district

Haridwar district						
Stages	F2 stage forecasted yield (Kg/Ha)			F3 stage forecasted yield (Kg/Ha)		
Rice	Without NDVI and EVI (LASSO)	With NDVI (stepwise)	With EVI (LASSO)	Without NDVI and EVI (LASSO)	With NDVI (LASSO)	With EVI (LASSO)
2018–2019	2136	2105	2260	2191	2208	2410
2019–2020	2123	2103	2074	2123	2124	2010
2020–2021	1975	2034	1927	2098	2059	2038
Wheat	Without NDVI and EVI (stepwise)	With NDVI (LASSO)	With EVI (LASSO)	Without NDVI and EVI (LASSO)	With NDVI (LASSO)	With EVI (LASSO)
2018–2019	2774	2924	2932	2913	2961	2967
2019–2020	2798	2951	3036	2879	2895	2930
2020–2021	2571	2775	2780	2904	2893	2948
Sugarcane	Without NDVI and EVI (stepwise)	With NDVI (stepwise)	With EVI (stepwise)	Without NDVI and EVI (LASSO)	With NDVI (LASSO)	With EVI (LASSO)
2018–2019	64,023	62,958	6367	60,923	61,211	60,869
2019–2020	64,182	64,138	64,709	61,408	60,420	61,291
2020–2021	66,590	64,290	65,147	63,463	62,601	63,514

Table 14.3 RMSE and MAPE for Dehradun district using stepwise regression and LASSO methods

Dehradun												
Stages	F2 stage						F3 stage					
	Without NDVI and EVI		With NDVI		With EVI		Without NDVI and EVI		With NDVI		With EVI	
Rice	RMSE	MAPE	RMSE	MAPE	RMSE	MAPE	RMSE	MAPE	RMSE	MAPE	RMSE	MAPE
Stepwise	60.063	2.318	60.090	2.319	36.387	1.519	36.908	1.475	30.011	1.154	36.888	1.474
LASSO	38.936	1.521	39.107	1.467	32.542	1.297	34.737	1.283	11.763	0.475	32.592	1.260
Wheat	RMSE	MAPE	RMSE	MAPE	RMSE	MAPE	RMSE	MAPE	RMSE	MAPE	RMSE	MAPE
Stepwise	127.210	4.920	63.229	2.588	140.696	5.848	155.726	6.097	73.788	2.878	177.179	8.065
LASSO	121.734	4.828	95.141	3.809	115.994	4.563	136.588	5.800	96.054	3.776	124.157	5.219
Sugarcane	RMSE	MAPE	RMSE	MAPE	RMSE	MAPE	RMSE	MAPE	RMSE	MAPE	RMSE	MAPE
Stepwise	1307.582	1.817	1307.582	1.817	1307.582	1.817	578.922	0.723	1058.524	1.415	743.711	0.993
LASSO	745.916	0.865	508.609	0.573	1428.889	1.789	1002.144	1.415	967.293	1.331	913.766	1.222

Table 14.4 Forecasted yield for Dehradun district

Dehradun district						
Stages	F2 stage forecasted yield (Kg/Ha)			F3 stage forecasted yield (Kg/Ha)		
Rice	Without NDVI (LASSO)	With NDVI (LASSO)	With EVI (LASSO)	Without NDVI (LASSO)	With NDVI (LASSO)	With EVI (LASSO)
2018–2019	2007	2007	2006	2030	2082	2032
2019–2020	2048	2048	2070	2041	2091	2064
2020–2021	1977	1990	2012	2010	2103	2034
Wheat	Without NDVI (LASSO)	With NDVI (stepwise)	With EVI (LASSO)	Without NDVI (LASSO)	With NDVI (stepwise)	With EVI (LASSO)
2018–2019	2460	2377	2429	2384	2444	2418
2019–2020	1944	1933	2155	1997	1942	2075
2020–2021	2026	1940	2052	2082	1899	2081
Sugarcane	Without NDVI (LASSO)	With NDVI (LASSO)	With EVI (stepwise)	Without NDVI (stepwise)	With NDVI (LASSO)	With EVI (stepwise)
2018–2019	67,350	68,552	65,991	66,308	66,667	66,237
2019–2020	65,056	64,336	64,680	65,321	66,230	66,412
2020–2021	61,706	55,987	64,614	67,427	66,943	68,548

Table 14.5 RMSE and MAPE for Pauri Garhwal district using stepwise regression and LASSO methods

Pauri Garhwal												
Stages	F2 stage						F3 stage					
	Without NDVI and EVI		With NDVI		With EVI		Without NDVI and EVI		With NDVI		With EVI	
Rice	RMSE	MAPE	RMSE	MAPE	RMSE	MAPE	RMSE	MAPE	RMSE	MAPE	RMSE	MAPE
Stepwise	34.148	2.565	40.543	3.014	34.108	2.564	45.030	3.454	19.332	1.344	45.016	3.453
LASSO	31.947	2.419	27.867	1.982	29.232	2.210	48.764	3.720	19.569	1.328	48.746	3.717
Wheat	RMSE	MAPE	RMSE	MAPE	RMSE	MAPE	RMSE	MAPE	RMSE	MAPE	RMSE	MAPE
Stepwise	137.351	11.599	142.037	11.898	137.351	11.599	114.030	10.735	114.496	10.795	96.297	8.268
LASSO	124.589	11.758	122.105	11.561	126.991	11.974	51.593	4.553	110.335	10.006	73.733	6.695

Table 14.6 Forecasted yield for Pauri Garhwal district

Pauri Garhwal						
Stages	F2 stage forecasted yield (Kg/Ha)			F3 stage forecasted yield (Kg/Ha)		
Rice	Without NDVI (LASSO)	With NDVI (LASSO)	With EVI (LASSO)	Without NDVI (stepwise)	With NDVI (stepwise)	With EVI (stepwise)
2018–2019	1327	1332	1329	1287	1462	1287
2019–2020	1387	1386	1380	1327	1302	1327
2020–2021	1476	1472	1464	1414	1386	1414
Wheat	Without NDVI (stepwise)	With NDVI (LASSO)	With EVI (LASSO)	Without NDVI (LASSO)	With NDVI (LASSO)	With EVI (LASSO)
2018–2019	1277	1232	1263	1392	1356	1476
2019–2020	1394	1340	1373	1346	1474	1657
2020–2021	1350	1295	1308	1625	1392	1577

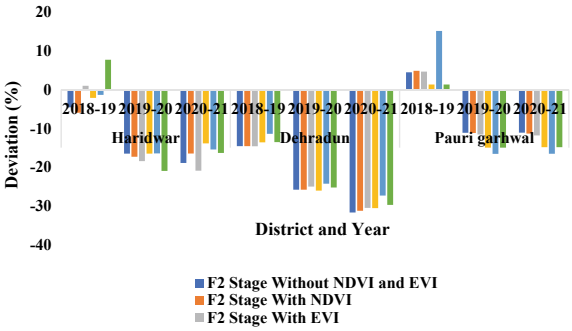

Fig. 14.4 Deviation (%) in yield with observed values for rice crop

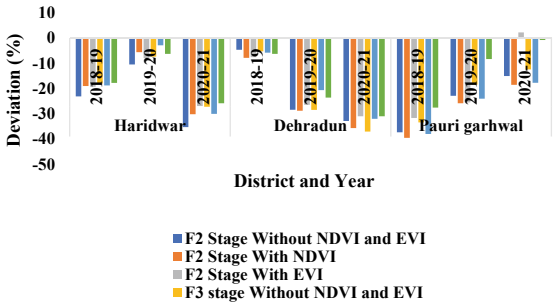

Fig. 14.5 Deviation (%) in yield with observed values for wheat crop

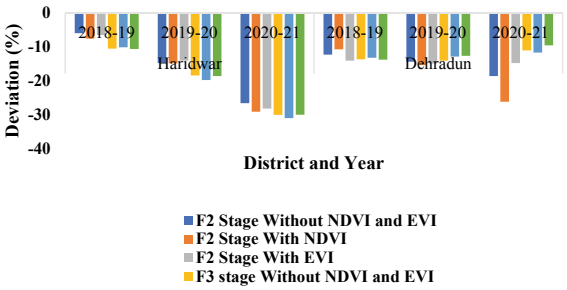

Fig. 14.6 Deviation (%) in yield with observed values for sugarcane crop

Acknowledgements The authors wish to acknowledge the Ministry of Earth Science (MoES), Govt. of India, for funding this study. We are also thankful to the Directorate of Agriculture, Govt. of Uttarakhand. IMD, AMFU, IIT Roorkee, the National Geographic Society, Google World Resources Institute for the Dynamic World Project, Microsoft AI for Earth/Planetary computer program, and ESRI Inc. for supplying historical crop yield statistics, Meteorological data, LULC map, etc.

References

Agrawal R, Jain RC, Jha MP (1983) Joint effects of weather variables on rice yield. Mausam 34(2):189–194

Agrawal R, Mehta SC (2007) Weather based forecasting of crop yields, pests and diseases-IASRI models. J Ind Soc Agril Stat 61(2):255–263

Ahmed A, Qureshi S, Nargis S (2021) Rural agriculture: a mirror to economic sustainable growth in India. Int J Cult Mod 4

Bhoutika K, Das DP, Kumar A, Pandey A (2022) Application of remote sensing and GIS in crop yield forecasting and water productivity. In: Geospatial technologies for land and water resources management, pp 207–222. Springer, Cham

Didan K (2014) MOD13Q1: MODIS/Terra vegetation indices 16-day L3 global 250m grid SIN V006. NASA EOSDIS land processes DAAC. In: Doraiswamy P C et al (eds) Crop condition and yield simulations using Landsat and MODIS. Remote sensing of environment, 2004, vol 92, no 4, pp 548–559

Doraiswamy PC, Sinclair TR, Hollinger S, Akhmedov B, Stern A, Prueger J (2005) Application of MODIS derived parameters for regional crop yield assessment. Remote Sens Environ 97(2):192–202

Huete AR, Liu HQ, Batchily K, YanLeeuwen W. A comparison of vegetation indices global set of TM images for EOS-MODIS. Remote Sens Environ 59:440–451

Huete A, Didan K, Miura T, Rodriguez EP, Gao X, Ferreira LG (2002) Overview of the radiometric and biophysical performance of the MODIS vegetation indices. Remote Sens Environ 83(1–2):195–213

Johnson MD, et al (2016) Crop yield forecasting on the Canadian Prairies by remotely sensed vegetation indices and machine learning methods. Agricult Forest Meteorol 218:74–84

Joshi PC, Sharma PK (2008) First records of coccinellid beetles (Coccinellidae) from the Haridwar (Uttarakhand) India. Trop Nat Hist 8(2):157–167

Kastens JH, Kastens TL, Kastens DL, Price KP, Martinko EA, Lee RY (2005) Image masking for crop yield forecasting using AVHRR NDVI time series imagery. Remote Sens Environ 99(3):341–356

Kumar S, Attri SD, Singh KK (2019) Comparison of Lasso and stepwise regression technique for wheat yield prediction. J Agrometeorol 21(2):188–192

Kutner MH, Nachtsheim CJ, Neter J, Li W (2005) Applied linear statistical models

Matsushita B, Yang W, Chen J, Onda Y, Qiu G (2007) Sensitivity of the enhanced vegetation index (EVI) and normalized difference vegetation index (NDVI) to topographic effects: a case study in high-density cypress forest. Sensors 7(11):2636–2651

Mkhabela MS, Bullock P, Raj S, Wang S, Yang Y (2011) Crop yield forecasting on the Canadian Prairies using MODIS NDVI data. Agricult Forest Meteorol 151(3):385–393

Pareek N, Raverkar KP, Bhatt MK, Kaushik S, Chandra S, Singh G, Joshi HC (2019) Soil nutrient status of Bhabhar and hill areas of Uttarakhand. ENVIS Bull Himalayan Ecol 27

Ray SS, Neetu MS, Gupta S (2014a). Use of remote sensing in crop forecasting and assessment of impact of natural disasters: Operational approaches in India. In: Srivastava MK (ed) Proceedings of the FAO expert meeting on crop monitoring for improved food security, Vientiane, Lao PDR; 17 February 2014. RAP Publication 2014/28. FAO and ADB, 2015. pp 111–112

Ray SS, Sesha Sai MVR, Chattopadhyay N (2014b) Agricultural drought assessment: operational approaches in india with special emphasis on 2012. In: Ray K, Mohapatra M, Bandyopadhyay BK, Rathore LS (eds) High-impact weather events over the SAARC region, 2011, vol 151, no 3, pp. 349–364; 385–393. Springer

Rouse JW, Haas RH, Schell JA, Deering DW (1974) Monitoring vegetation systems in the great plains with ERTS. NASA Spec Publ 351(1974):309

Schut AGT, Stephens DJ, Stovold RGH, Adams M, Craig RL (2009) Improved wheat yield and production forecasting with a moisture stress index, AVHRR and MODIS data. Crop Pasture Sci 60(1):60–70

Srivastava AK, Bajpai PK, Yadav RL, Hasan SS (2007) Weather based sugarcane yield prediction model for the state of Uttar Pradesh. J Indian Soc Agricul Stat 61(3):313–327

Tibshirani R (1996) Regression shrinkage and selection via the lasso. J Royal Stat Soc Ser B (methodol) 58(1):267–288

Zou H (2006) The adaptive lasso and its oracle properties. J Am Stat Assoc 101(476):1418–1429

Chapter 15
Yield Estimation of Rice Crop Using Semi-Physical Approach and Remotely Sensed Data

Mukti Nath Jha, Arvind Kumar, Sunil Dubey, and Ashish Pandey

Abstract Timely and accurate crop yield prediction is vital for agricultural land management and policymaking. With the advent of satellite sensors, the availability of large proxy parameters, advanced computing mechanisms, and strong analytical capability create enormous scope to develop more accurate and reliable crop production estimates. In the present study, an effort has been made to use the multi-sensor, multi-resolution satellite data and crop biophysical parameters to estimate rice crop yield for the Saharanpur district of Uttar Pradesh. A semi-physical approach, also known as light-use efficiency or Production Efficiency Models, has been employed to estimate rice crop productivity using remote sensing and physiological concepts such as the Photosynthetically Active Radiation (PAR) and the fraction of PAR absorbed by the crop. Rice crop map generated using multi-date Sentinel-1 (20 m resolution) microwave data through Sentinel-1 Toolbox "SNAP", the accuracy of crop map was assessed with geotagged ground truth. Pixel level estimates were developed and accumulated at the district level using an area-weighted approach. The estimated yield was compared with the actual estimate obtained from the District Agriculture Department. The result obtained was very encouraging and well within the range of $\pm 10\%$. The study reconfirms that the approach can generate the yield at a lower pixel level aggregated at sub-districts or below administrate units, but percolation at a lower scale requires more ground-specific information such as intensive ground truth and other yield proxies.

Keywords Monteith efficiency model · Kharif rice · Microwave data · Yield · Radiation-use efficiency · NDVI · Harvest index

M. N. Jha · A. Kumar · A. Pandey (✉)
Department of Water Resources Development & Management, IIT Roorkee, Roorkee, India
e-mail: ashish.pandey@wr.iitr.ac.in

S. Dubey
Mahalanobis National Crop Forecast Centre, New Delhi, India

C. S. Jha et al. (eds.), *Geospatial Technologies for Resources Planning and Management*, Water Science and Technology Library 115,
https://doi.org/10.1007/978-3-030-98981-1_15

15.1 Introduction

Rice is the primary food source in India and one of the most important crops. Before harvesting crop yield, forecasting is very important in climate uncertain regions. Crop yield forecasting helps the government plan the import in case of surplus or export in shortfall. Crop yield forecasting also helps strategic plans for food supply in a famine-like situation. So crop yield forecasting in crop growth and crop development is very important (Huang et al. 2013).

Crop yield prediction in India was based on ground-based field visits and reports, which are conventional data collection methods for crop yield forecasting. These traditional methods have less accuracy in crop yield and area estimation due to cost, time, and incomplete ground data collection. In the past few years, with the advancement of remote sensing platforms, especially satellites (both Low Earth orbit-LEO and Geosynchronous) sensors in optical, thermal, and microwaves domain paved a new dimension to Earth Observation Systems-EOS (Segarra et al. 2020; Lu et al. 2020; Karthikeyan et al. 2020; Khanal et al. 2020). Improvement in analytics mechanism and rapid advances in cloud and high-performance computing equally supported the EOS activity significantly (Gorelick et al. 2017; Campos-Taberner et al. 2018; Shakoor et al. 2019). These advancements have become increasingly valuable for monitoring, evaluation, and adaptive decision making in the agriculture sector, one of the verticals is crop production estimates. Based on informatics on crop production, today's agricultural policies, strategies, price fixation of crop commodities, and global trade shape is being determined. Hence, various policy derivatives, i.e., export/import, price fixation, storage, marketing, etc. can be easily regulated through timely, précised, and reliable forecasting.

Due to largely associated variability in the state of crop and phenology, yield estimation at district/sub-district level is a complex task, especially with point-based mechanistic models (Porwollik et al. 2017; Leng and Hall 2020). Availability of Remote Sensing (RS) derived crop phenological parameters like Leaf Area Index (LAI), Biomass; other biophysical parameters like normalized difference vegetation index (NDVI), Absorbed Photosynthetic Active Radiation (APAR) at dis-aggregated scale in frequent time intervals makes the task of crop production easier at lower administrative scale. Moreover, using RS technologies, crop health status (good, medium, poor) can be monitored easily in the temporal and spatial domain. Furthermore, Yield maps can be generated at different stages of crops, i.e., mid-season, peak vegetative stages, and pre-harvesting stages (Singhal et al. 2018; Shafi et al. 2020). RS derived proxies can be used in various ways to estimate the production; the most common approach is a direct empirical relationship between satellite-based indicators like NDVI, LAI with historical yield records (Singh et al. 1992; Rao et al. 2002; Dadhwal et al. 2003a; Hebbar et al. 2008; Dubey et al. 2018). Various satellite-derived parameters, i.e., LAI, sowing dates, can directly be assimilated into simulation models along with several climatic and physical observations (Dadhwal et al. 2003b; Doraiswamy et al. 2005; Sehgal et al. 2005; Tripathy et al. 2013a, b).

Most of the crop simulation models relate the various information like cultivar practices, weather data, soil data in mathematical equations in a computer language to simulate the crop growth and based on that yield are interrelated with the equation (Hogenboom et al. 2012). However, the majority of crop simulation models are point-based, which may not capture the entire variability within the administrative unit. On the other hand, stress factors are not being considered in empirical approaches. Both Simulation models and empirical methods have their pros and cons (Boote et al. 1996; Porwollik et al. 2017).

Most yield models are based on the assumptions that canopy "parameters are related to the final crop yield". With the given uncertainties in both empirical and simulation approaches, an integrated approach called a semi-physical approach wherein canopy parameters (NDVI), physiological parameters (Photosynthetically Active Radiation-PAR, Radiation-Use Efficiency-RUE) along with physical (harvest index) and stress parameters (Land Surface Wetness Index-LSWI and Temperature) has been combined and extensively used for crop yield estimation. District level estimates of sugarcane crops have been developed by Chaurasiya et al. (2017) using physiological concepts such as the photosynthetically active solar radiation (PAR) and the fraction of PAR absorbed by the crop (fAPAR) using Monteith's radiation-use efficiency equation for 75 districts of Uttar Pradesh. The approach was tested for the wheat crop at the state level (Tripathy et al. 2014) with less than 5% variability, and again, the approach was scaled up to district level for yield estimates in Punjab State of India (Tripathy et al. 2013a, b).

During monsoon, the remote sensing data collection with the multispectral sensor is very difficult due to cloud covers. Therefore, active microwave sensors having all-weather night and day capabilities in areas that suffer from frequent cloud cover are used. Time series data from previous studies show that C and X-band sensors have rice mapping potential, the European Remote Sensing satellites (ERS) 1 and 2, Radarsat, Envisat TerraSAR-X, COSMOSkyMed, and more recently Sentinel-1 (Torbick et al. 2017; Onojeghuo et al. 2018; Nguyen et al. 2015; Son et al. 2014) Therefore, active microwave sensors having all-weather night and day capabilities in areas that suffer from frequent cloud cover are employed data can be used in this study. The main objectives of this study are as follows:

(1) To forecast the yield at the district level using the concept of the Semi-physical approach (Monteith and Moss 1977).
(2) To estimate rice production (crop acreage + crop yield) for the Saharanpur district of Uttar Pradesh.

15.2 Materials and Methods

15.2.1 Dataset Used

The details of the dataset used for the present study have been given in Table 15.1.

Table 15.1 Details of data/products used for the present study

Data/product	Satellite/ground	Sensor	Resolution	Source
Daily insolation	INSAT 3D	Imager	1 km	MOSDAC
8 days composite AFPAR	Terra	MODIS	0.5 km	NASA-RIVERB
8-days composite surface reflectance	Terra	MODIS	0.5 km	NASA-RIVERB
NDVI and LSWSI during maximum vegetative stage	Sentinel 2 Landsat 8	MSI OLI	20 m 30 m	ESA NASA
Crop (rice) mask	Sentinel-1	SAR	20 m	ESA
Crop sowing data	Sentinel 1	SAR	20 m	ESA
Harvest index	Ground data		District level	Literature
Daily T_{min} and T_{max}	Gridded data		5 km Grid	IMD

15.2.2 Data Processing and Computation of Parameters

Multitemporal datasets, MOSDAC (INDSAT 3D), MODIS, SAR (Sentinel 1A) have been used for the analysis. The present study has applied SNAP, ARCGIS, ERDAS IMAGINE, and ENVI + IDL software. The MODIS data were converted to Geo Lat/Long (WGS 1984) from geo-referenced projection. Rice crop mask has been generated using the Sentinel-1 image of 20 m resolution for further processing of yield estimation.

15.2.2.1 Image Acquisition and Processing of MODIS Data Product

The 8-day composites MODIS surface reflectance products have been obtained from https://lpdaac.usgs.gov.the. The images are in HDF format with of 500 m resolution with a sinusoidal projection. The composite image in the visible and infrared region contains seven spectral bands of data.

15.2.2.2 Insolation Data Acquisition and Processing

The daily insolation data was downloaded from MOSDAC data (www.mosdac.gov.in) for the whole cropping season, i.e., from 04 June 2019 to 26 October 2019, with 1 km spatial resolution. The daily data have been converted into the 8-day product (Sum) using ENVI + IDL software and converted into 500 m resolution. From the total insolation value, 50 has been assumed as photosynthetically active radiation (PAR). The 8-day sum of insolation during 14–21 August has been shown in Fig. 15.1.

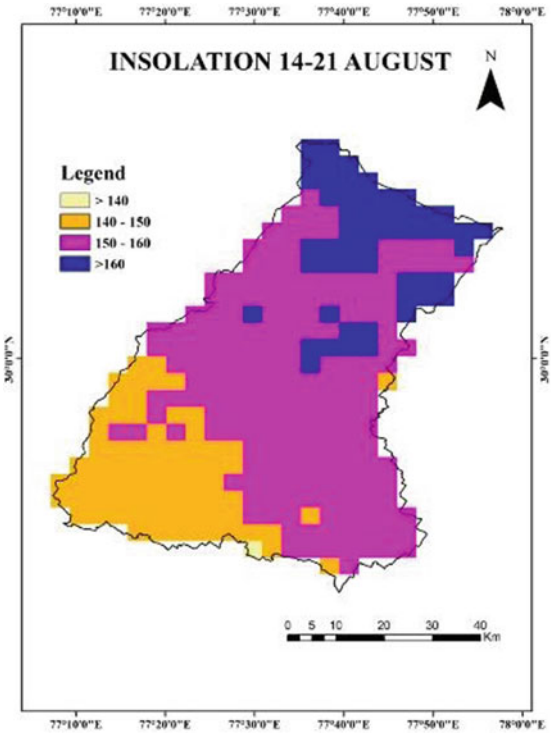

Fig. 15.1 The 8-day sum of insolation (14–21 August 2019)

15.2.2.3 Biophysical Parameter

The MOD15A2H.006 Version 6 MODIS data includes combined Leaf Area Index (LAI) and Fraction of Photosynthetically Active Radiation (FPAR) product have been downloaded from https://lpdaac.usgs.gov**.**

15.2.2.4 Stress Factor

The MOD09A1 product of MODIA has been downloaded from https://lpdaac.usgs.gov and used for determining the surface reflectance, land surface water index (LSWI), and ultimately water stress. The cloud and solar zenith decide the pixel choice. The pixel with the minimum channel 3 (blue) value has been used when several acquisitions meet the criteria. The image was in HDF format and had 13 scene datasets out of which sur_refl_b02: 500 m Surface Reflectance Band 2 (841–876 nm) and sur_refl_b06: 500 m Surface Reflectance Band 6 (1628–1652 nm) has been used for Land Surface Water Index (LSWI).

15.2.2.5 Land Surface Water Index (LSWI)

The Land Surface Water Index (LSWI) utilizes the NIR and shortwave infrared (SWIR) regions of the electromagnetic range. There is strong light retention by liquid water in the SWIR, and the LSWI is known to be delicate to the aggregate sum of liquid water in the soil and its vegetation background. From LSWI, Water-stressed zone is identified. The value of LSWI ranges from −1 to + 1. In the early stage of paddy, the field is saturated, so LSWI may be a significant indicator to map paddy crops. Equation (15.1) has been used for the estimation of LSWI.

$$\text{LSWI} = \frac{(\text{NIR} - \text{SWIR})}{(\text{NIR} + \text{SWIR})} \tag{15.1}$$

15.2.2.6 Computation of Water Stress (WS)

Water stress has been estimated to determine whether the crop is under water-stressed conditions or not. Since paddy is a high water-demanding crop. Water stress has a significant impact on the overall yield. Water stress has been estimated using Eq. (15.2):

$$W_{\text{STRESS}} = \frac{(1 - \text{LSWI})}{(1 + \text{LSWI}_{\text{MAX}})} \tag{15.2}$$

where LSWI_{max} is the maximum LSWI within the plant growing season for individual pixels. The simple formulation of Scalars is a linear scalar with a value range of 0–1.

Tucker (1980) reported that the SWIR band (1.6 μm) was discovered touchy to plant water content. Henceforth, Land Surface Water Index (LSWI) has been inferred as the normalized distinction between the spectral of NIR (0.78–0.89 Am) and SWIR (1.58–1.75 μm) for the evaluation of water stress. This list is sensitive to the aggregate sum of vegetation and soil moisture. The LSWI has been estimated by using Eq. (15.1). The water stress was calculated by using Eq. (15.2).

15.2.2.7 Temperature Data

The maximum, minimum and mean temperature of the cropping season has been used to calculate the temperature stress during the cropping period through the following Eq. (15.3):

$$T_{\text{stress}} = \frac{(T - T_{\text{min}})(T - T_{\text{max}})}{(T - T_{\text{min}})(T - T_{\text{max}}) - \left(T - T_{\text{opt}}\right)^2} \tag{15.3}$$

where,

T_{min} = minimum temperature; T_{max} = maximum temperature; T_{opt} = optimum temperature for photosynthesis (°C); T = the daily mean temperature (°C).

For Rice, T_{min} = 14 °C; T_{max} = 40 °C and T_{opt} = 30 °C and if air temperature falls below T_{min}, T_{stress} is set to be zero.

15.2.3 Estimation of Crop Acreage

15.2.3.1 Ground Truth (GT) Data

The ground truth data were collected at different crop growth stages using cellphones with the geotagging application. Elevation, latitude, and longitude have been recorded for the crosschecking of the identification of the rice field. Total 13 Geotagged ground truths, covering entire districts, along with crop variability have been used for the crop mask generation.

15.2.3.2 Land Use Land Cover Map

The Land Use Land Cover (LULC) map has been prepared to identify agricultural and non-agricultural land using the Landsat eight images. The ground truth data have been validated using these LULC maps. It is freely available and has been downloaded from USGS https://gisgeography.com/usgs-earth-explorer-download-free-landsat-imagery/.

15.2.4 Estimation of Crop Yield

In the present study, the yield estimation is based on the plant biomass from planting to maturity. The equation developed by (Monteith 1977) has been used to quantify the fAPAR. The fAPAR is defined as the ratio of absorbed PAR (APAR) to incident PAR ($0 < \text{fAPAR} < 1$). It ranges from 0 to 1. Where PAR is cumulative intercepted photosynthetically active radiation. The methodology for yield estimation has been shown in Fig. 15.2 through a flow chart. The PAR has been calculated using Eq. (15.4):

$$\text{PAR} = \text{Rs} \times 0.5 \tag{15.4}$$

where Rs = incoming solar radiation (MJm^{-2}).

The Net Primary Productivity is estimated using Eq. (15.5):

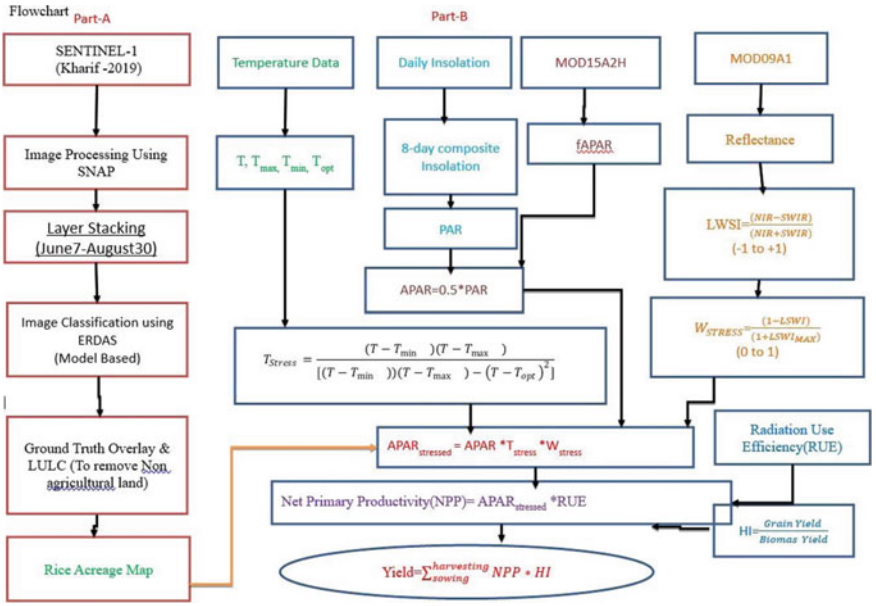

Fig. 15.2 Flow chart for the methodology of yield estimation

$$\text{NPP} = \text{fAPAR} \times \text{PAR} \times \text{RUE} \tag{15.5}$$

where,

NPP = Net Primary Productivity, i.e., accumulated dry matter ($\text{gm}^{-2}\,\text{d}^{-1}$)).

PAR = photosynthetic active radiation ($\text{MJm}^{-2}\,\text{d}^{-1}$);

fAPAR = Ratio of incident PAR to absorbed PAR by the canopy (dimensionless);

RUE = Radiation-use efficiency (g/MJ).

Radiation-use efficiency (RUE) is estimated using Eq. (15.6):

$$\text{RUE}\left(\text{gMJ}^{-1}\right) = \text{Biomass}\left(\text{g/m}^2\right)/\text{PAR}\left(\text{M J/m}^2/\text{day}\right) \tag{15.6}$$

Equation (15.5) can be remodified using water stress (W_{STRESS}) and temperature stress (T_{STRESS}) as Eq. (15.7)

$$\text{NPP} = \text{fAPAR} \times \text{PAR} \times \text{RUE} \times W_{\text{STRESS}} \times T_{\text{STRESS}} \tag{15.7}$$

The final grain yield is calculated by combining NPP and the Harvest index and modified as Eq. (15.8)

$$\text{Grain Yield} = \sum_{\text{sowing}}^{\text{harvesting}} \text{NPP} \times \text{HI} \tag{15.8}$$

where,

Harvest Index (H.I) is calculated from Crop Cut Experiment data using Eq. (15.9):

$$\text{H.I.} = \text{Grain Yield(Kg/ha)} / \text{Biomass Yield (Kg/ha)} \tag{15.9}$$

15.2.5 Microwave Data Acquisition and Processing

Sentinel-1 Microwave data (Spatial Resolution 20 m, Temporal Resolution 12 days) VV polarization mode was used for acreage estimation. Data about seven successive dates from 07 June 2019 to 30 August 2019 (i.e., the area of rice transplantation till that date) covering the entire district has been used for crop acreage estimation. The remote sensing data acquisition dates were as- 07-June-2019, 19-June-2019, 01-July-2019, 13-July-2019, 25-July-2019, 06-August-2019, and 30-August-2019. These images were layer stacked in the Sentinel application platform (SNAP), and batch processing was done before the analysis (Fig. 15.3).

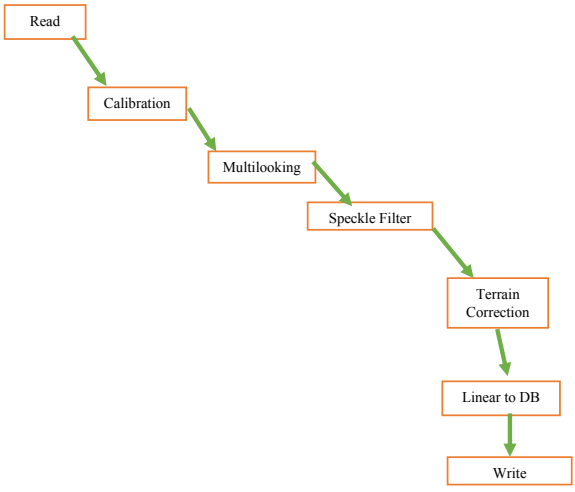

Fig. 15.3 Preprocessing steps of the images in SNAP

15.2.5.1 Calibration

In this procedure, digital pixel values are converted to radiometrically calibrated synthetic aperture radar (SAR) backscatter. Sentinel-1 data information is required to apply the calibration equation; specifically, for simple conversion of image intensity values into sigma nought values. Calibration involves a constant offset, a range-dependent gain, and during level 1 product generation reverses the scaling factor the absolute calibration constant.

In the proposed preprocessing workflow, a LUT to produce sigma nought values is proposed, for the generation of radiometrically calibrated SAR backscatter concerning the nominally horizontal plane. The strength of reflection in terms of the geometric cross-section of a conducting sphere is specified by sigma. It represents the distributed target of a radar cross-section over an expected area of one square meter. The sigma nought significantly changes with the wavelength, incidence angle, and polarization and also with properties of the scattering surface.

15.2.5.2 Multilooking

The process of multilooking improves the SAR image quality by reducing the speckle and allows us to obtain a square pixel on the output image. Subsequent lines are averaged in range or azimuth direction or both the directions to get a better image.

15.2.5.3 Speckle Filter

Speckle in SAR images appeared as granular noise. The reason behind this is the interference of waves which is reflected from the elementary scatterers (Lee et al. 1994). The image quality is increased by reducing speckle through speckle filtering. When such a procedure is done in the SAR data at the early processing stage, speckle is not propagated in ongoing processes (terrain conversion to dB).

Speckle filtering is not advisable when there is an interest in the small spatial structures or image texture identification, since in most cases, it removes such information. The refined Lee filter can preserve edges, point target, linear features, far superior texture information, visual interpretation, and single product speckle filters (Lee et al. 1994). More recently, to reduce speckle, multitemporal speckle filters have been developed, taking advantage of SAR observations multiple times. The proposed preprocessing workflow includes a speckle filtering step, which could be skipped by selecting “None” as the filter type. Currently, one of the following filters is available in the SNAP single product speckle filter operator: “Median”, “Frost”, “Boxcar”, “Gamma Map”, “IDAN” “Lee”, “Refined Lee”, “Lee Sigma”.

15.2.5.4 Terrain Correction

SAR data generally have a varying viewing angle greater than 0 degrees, resulting in images with some side-looking geometry distortion. Terrain corrections are intended to reduce these distortions so that the geometric likeness of the image will be just about as near as conceivable to the present reality. Range-Doppler terrain correction is a method of geometric distortions corrections like foreshortening and shadows caused by topography, utilizing a digital elevation model (DEM) to rectify the location of each pixel. In SNAP, the Range-Doppler terrain correction is accessible from we can easily do the Range-Doppler orthorectification method for geocoding of SAR scenes in radar geometry from images. This utilizes the available radar timing annotations, orbit state vector information in the metadata, and the slant to ground range conversion parameters together with the reference DEM data to find the precise geolocation information (SNAP Software, Help Document 2019).

15.2.5.5 Linear to dB

This is the last step in which logarithmic transformation is used to convert the unitless backscatter coefficient to dB.

15.2.6 Computation of Net Primary Product and Grain Yield

Net primary product (NPP) has been assessed for sowing to harvesting at a time frame of 8 days for each phanophases with a spatial resolution of 500 m utilizing the periodical PAR, Wstress, fAPAR, maximum radiation, and T-stress use efficiency as given in Eq. 15.3. The complete net primary product grain yield per pixel has been computed using Eq. 15.7. The pixel yield has been calculated to estimate district level and average yield at the state level.

15.3 Results and Discussion

The rice acreage map has been generated with model-based classification after preprocessing the images in the SNAP tool. The pre-processed layer stacked image is presented in Fig. 15.4. From classification of satellite data, it was found that the estimated and reported area of rice was found to be 73,286 ha and 60,473 ha, respectively in the Kharif season 2019. Thus, the estimated area is 21% higher than the actual area. The overestimation may be due to the misclassification of the crop as sugarcane is the major standing crop during the acquisition of images. Other factors may be the traditional way of reporting areas under crops at the district level. The estimated

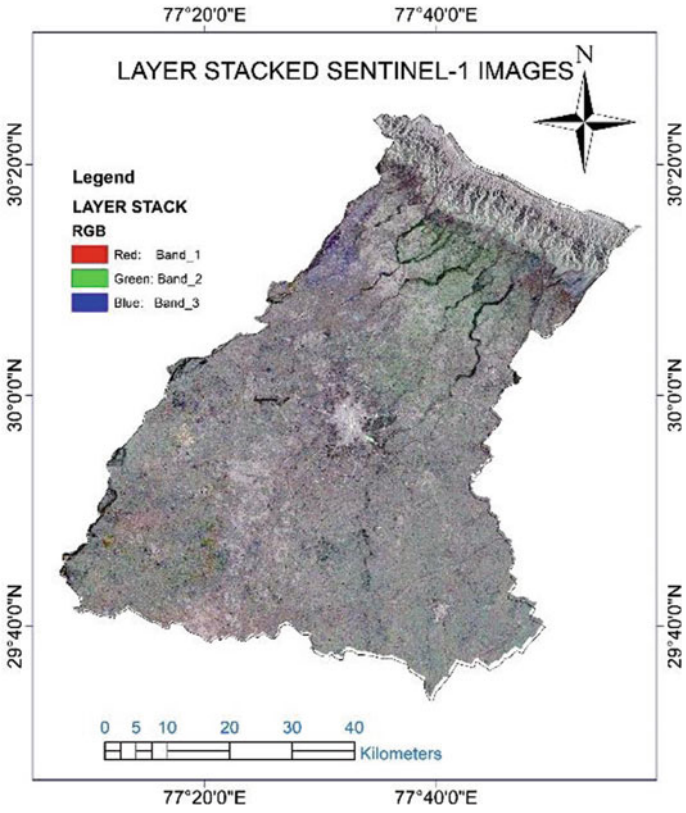

Fig. 15.4 Layer stacked sentinel-1 images

rice acreage map has been shown in Fig. 15.5, where the green color represents the rice crop area while the white color indicates other than the rice crop area.

The date-wise paddy transplanting is mapped by analyzing the crop mask and the layer stacked image. Here, in each step, three dates are considered, and changes in the DN values are recorded, and based on that area of transplanting, between two days is estimated. Analyzing the date of sowing throughout the transplanting season, most transplanting has been completed by the first fortnight of July. Maximum transplanting has been done between June F2–July F1 (Second fortnight of June to first fortnight of July). The date-wise transplanting has been shown in Figs. 15.6 and 15.7.

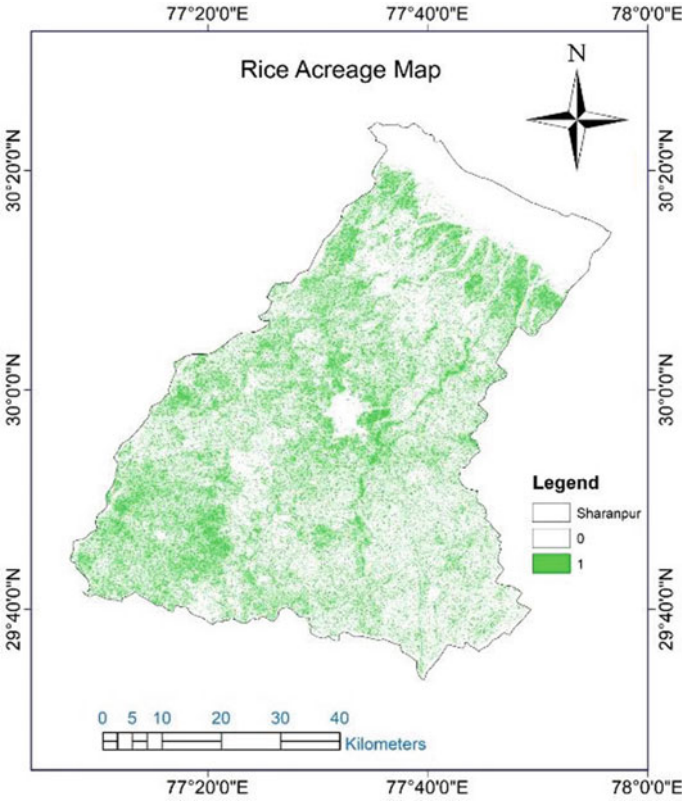

Fig. 15.5 Rice crop mask date-wise transplanting

15.3.1 LSWI and Water Stress Estimation

The Land Surface Water Index (LSWI) was estimated from the MOD09A1 image over the cropping period using Eq. 15.1. Image of LSWI and the corresponding water stress map for 8 days (from 13 to 20 August 2019) has been depicted in Fig. 15.8. A similar map was prepared for every 8 days interval. From Fig. 15.9, it is clear that the LSWI of the study area ranges from −0.15009 to 0.314357 (Range of LSWI −1 to 1) of duration 13–20 August. It indicates that most crops were in normal condition during the period when the crop attained the maximum vegetative growth. The maximum LSWI values of each 8 days starting from 19th June to 24th October during the whole cropping period have been shown in Fig. 15.9.

From the LSWI, water stress was mapped for every consecutive 8 days interval throughout the cropping period. The WS is estimated using the equation. The water stress was applied up to the panicle initiation stage of the crop growth. WS ranged from 0.679 to 1 on the scale of 0–1 (0-maximum stress, 1-No stress) of duration 13–20 August. The water-stressed zone was identified using water stress mapping

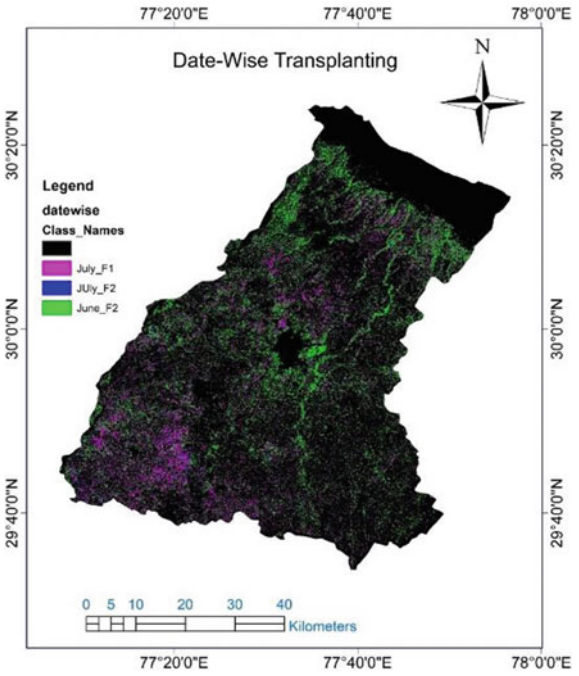

Fig. 15.6 Date-wise transplanting map for rice crop

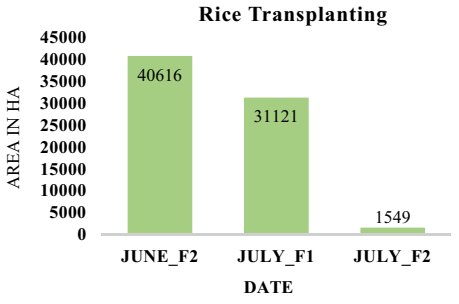

Fig. 15.7 Stage-wise transplanting area of rice crop

as shown in Fig. 15.10. This range of values indicates that the crop was growing smoothly during 13–20 August. The maximum value of water stress obtained in each 8- consecutive days throughout the cropping season has been shown in Fig. 15.11.

Crop yield was computed from the total NPP of the Saharanpur district using the harvest index. The harvest index ranged between 0.35 and 0.40. The estimated rice area was 72,273 ha in 2019, while the reported crop area was 60,473 ha. This method overestimates the rice area by 21.2%. Similarly, the estimated yield is 2.4 ton ha^{-1}, which is 8.7% more than the reported yield. A possible reason for the variability in the yield may have resulted from the error in dates of sowing and harvesting of crops.

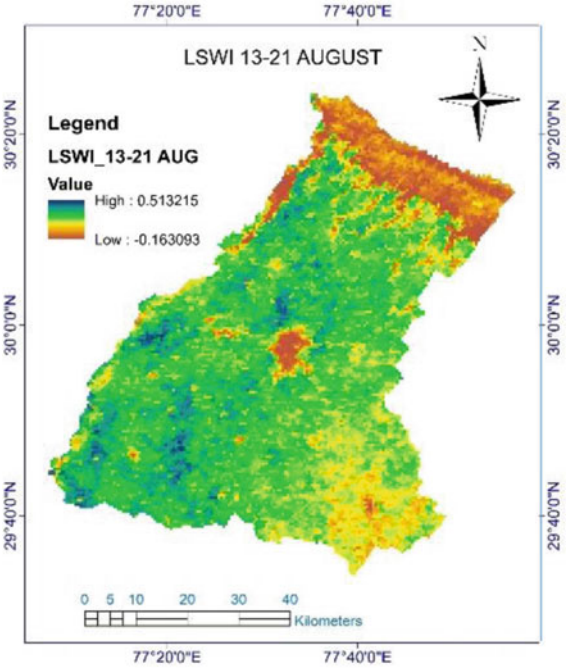

Fig. 15.8 LSWI (13–20 August)

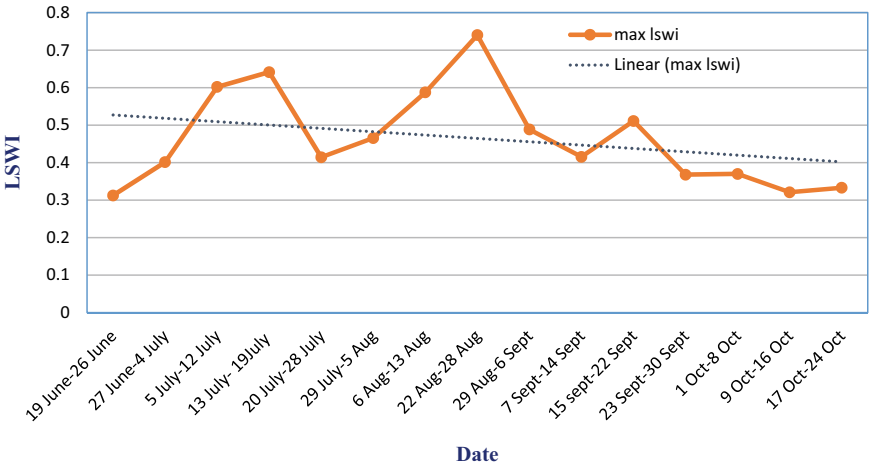

Fig. 15.9 Maximum LSWI

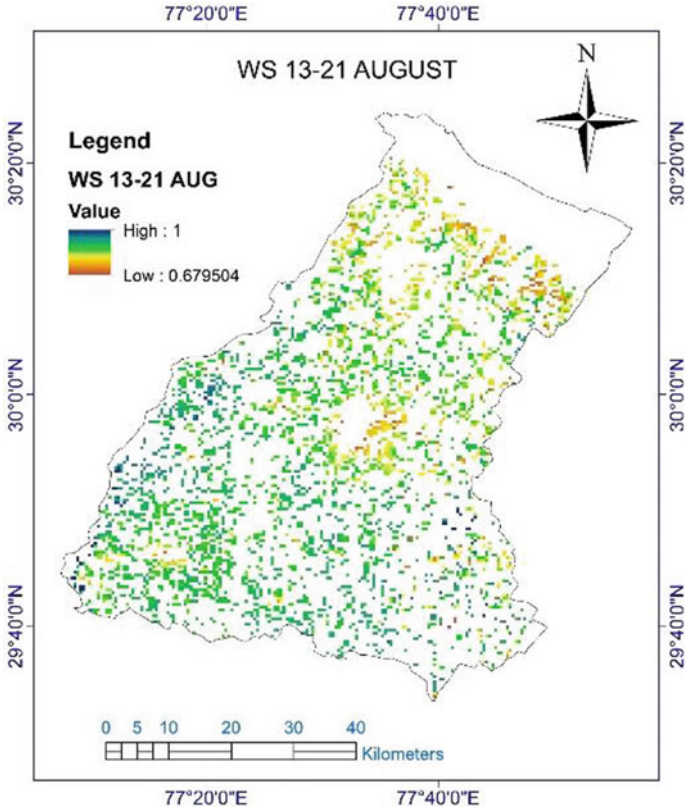

Fig. 15.10 Water stress map

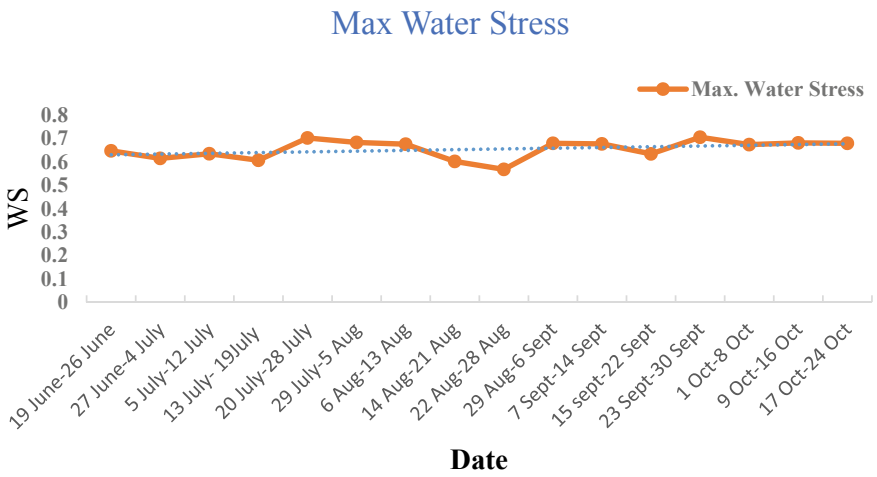

Fig. 15.11 Maximum water stress map

15.4 Conclusion

In this study, rice acreage map has been generated through microwave remote sensing data using the Sentinel-1 image. The result indicates that the estimating area's approach was overestimated by 21%. However, the estimated yield variation using a semi-physical approach was found to be within 10%. The study demonstrates that the crop yield depends on the absorbed photosynthetically active radiation. The product of harvest index (HI) and radiation uses efficiency (RUE) is also an important parameter that helps in estimating the crop's net productivity. The study shows that this model could be used to forecast rice yield at the district and block levels. The study helps in providing the spatial distribution of the Kharif rice yield map and has a broader area of applications. The forecast would help to take timely and effective decisions on a regional scale. The key regulations parameters will include revised estimates of marketable surplus, changes in consumer behaviors, National Food Assistance programs requirements, and the analysis of the domestic and international price transmissions. Accurate crop production forecasting can make informed food policy decisions and allow rapid response to emerging problems. The implication of the current analysis would be many folds, but a check has to be placed in utilizing the methodology in terms of quality. This approach can be further extended to analyze the yield gap due to adverse climate. The study can be extended to develop early warning systems for drought/famine alarms and high-end agrometeorological advisory services at state, district, and block levels.

References

Boote KJ, Jones JW, Pickering NB (1996) Potential uses and limitations of crop models. Agron J 88(5):704–716

Campos-Taberner M, Moreno-Martínez Á, García-Haro FJ, Camps-Valls G, Robinson NP, Kattge J, Running SW (2018) Global estimation of biophysical variables from google earth engine platform. Remote Sens 10(8):1167

Chaurasiya G, Saxena S, Tripathy R, Chaudhary KN, Ray SS (2017) Semi physical approach for sugarcane yield modelling with remotely sensed inputs. Vayumandal 43(1):11–22

Dadhwal VK, Sehgal VK, Singh RP, Rajak DR (2003) Wheat yield modelling using satellite remote sensing with weather data: recent Indian experience. Mausam 54(1):253–262

Dadhwal VK (2003b) Crop growth and productivity monitoring and simulation using remote sensing and GIS. Satell Remote Sens GIS Appl Agric Meteorol 263–289

Doraiswamy PC, Sinclair TR, Hollinger S, Akhmedov B, Stern A, Prueger J (2005) Application of MODIS derived parameters for regional crop yield assessment. Remote Sens Environ 97(2):192–202

Dubey SK, Gavli AS, Yadav SK, Sehgal S, Ray SS (2018) Remote sensing-based yield forecasting for sugarcane (Saccharum officinarum L.) Crop in India. J Indian Soc Remote Sens 46(11):1823–1833

Gorelick N, Hancher M, Dixon M, Ilyushchenko S, Thau D, Moore R (2017) Google earth engine: planetary-scale geospatial analysis for everyone. Remote Sens Environ 202:18–27

Hebbar KB, Venugopalan MV, Seshasai MVR, Rao KV, Patil BC, Prakash AH, Kumar V, Hebbar KR, Jeyakumar P, Bandhopadhyay KK, Rao MRK, Khadi BM, Aggarwal PK (2008) Predicting

cotton production using Infocrop-cotton simulation model, remote sensing and spatial agro-climatic data. Curr Sci 95(11):1570–1579
Hoogenboom G, Jones JW, Traore PC, Boote KJ (2012) Experiments and data for model evaluation and application. In: Improving soil fertility recommendations in Africa using the decision support system for agrotechnology transfer (DSSAT), pp 9–18. Springer, Dordrecht
Huang J, Wang X, Li X, Tian H, Pan Z (2013) Remotely sensed rice yield prediction using multi-temporal NDVI data derived from NOAA's-AVHRR. PloS One 8(8):e70816
Karthikeyan L, Chawla I, Mishra AK (2020) A review of remote sensing applications in agriculture for food security: crop growth and yield, irrigation, and crop losses. J Hydrol 124905
Khanal S, Kushal KC, Fulton JP, Shearer S, Ozkan E (2020) Remote sensing in agriculture—accomplishments, limitations, and opportunities. Remote Sens 12(22):3783
Lee JS, Jurkevich L, Dewaele P, Wambacq P, Oosterlinck A (1994) Speckle filtering of synthetic aperture radar images: a review. Remote Sens Rev 1994(8):313–340.6. Small D, Schubert A (2008) Guide to ASAR geocoding. ESA-ESRIN Technical Note RSL-ASAR-GC-AD, University of Zurich: Zurich, Switzerland, 2008; vol 1, p 36
Leng G, Hall JW (2020) Predicting spatial and temporal variability in crop yields: an inter-comparison of machine learning, regression and process-based models. Environ Res Lett 15(4):044027
Lu B, Dao PD, Liu J, He Y, Shang J (2020) Recent advances of hyperspectral imaging technology and applications in agriculture. Remote Sens 12(16):2659
Monteith JL, Moss CJ (1977) Climate and the efficiency of crop production in Britain [and discussion]. Philos Trans R Soc Lond B Biol Sci 281:277–294
Nguyen DB, Clauss K, Cao S, Naeimi V, Kuenzer C, Wagner W (2015) Mapping rice seasonality in the Mekong Delta with multi-year Envisat ASAR WSM data. Remote Sens 7:15868–15893. https://doi.org/10.3390/rs71215808
Nuarsa IW, Nishio F, Hongo C (2012) Rice yield estimation using Landsat ETM+ data and field observation. J Agric Sci 4(3):45
Onojeghuo AO, Blackburn GA, Wang Q, Atkinson PM, Kindred D, Miao Y (2018) Mapping paddy rice fields by applying machine learning algorithms to multi-temporal Sentinel-1A and Landsat data. Int J Remote Sens 39:1042–1067. https://doi.org/10.1080/01431161.2017.1395969.
Porwollik V, Müller C, Elliott J, Chryssanthacopoulos J, Iizumi T, Ray DK, Deryng D (2017) Spatial and temporal uncertainty of crop yield aggregations. Eur J Agron 88:10–21
Rao PK, Rao VV, Venkataratnam L (2002) Remote sensing: a technology for assessment of sugarcane crop acreage and yield. Sugar Tech 4(3–4):97–101
Segarra J, Buchaillot ML, Araus JL, Kefauver SC (2020) Remote sensing for precision agriculture: sentinel-2 improved features and applications. Agronomy 10(5):641
Sehgal VK, Sastri CVS, Kalra N, Dadhwal VK (2005) Farm-level yield mapping for precision crop management by linking remote sensing inputs and a crop simulation model. J Indian Soc Remote Sens 33(1):131–136
Shafi U, Mumtaz R, Iqbal N, Zaidi SMH, Zaidi SAR, Hussain I, Mahmood Z (2020) A multi-modal approach for crop health mapping using low altitude remote sensing, internet of things (IoT) and machine learning. IEEE Access 8:112708–112724
Shakoor N, Northrup D, Murray S, Mockler TC (2019) Big data driven agriculture: big data analytics in plant breeding, genomics, and the use of remote sensing technologies to advance crop productivity. Plant Phenome J 2(1):1–8
Singh R, Goyal RC, Saha SK, Chhikara RS (1992) Use of satellite spectral data in crop yield estimation surveys. Int J Remote Sens 13(14):2583–2592
Singhal G, Bansod B, Mathew L (2018) Real time crop health monitoring using remote sensing and ancillary information using GIS
SNAP Software, Help Document (2019) Available online: https://step.esa.int/main/toolboxes/snap. Accessed 1 May 2018

Son NT, Chen CF, Chen CR, Duc HN, Chang LY (2014) A phenology-based classification of time-series MODIS data for rice crop monitoring in Mekong Delta Vietnam. Remote Sens 6:135–156. https://doi.org/10.3390/rs6010135

Torbick N, Chowdhury D, Salas W, Qi J (2017) Monitoring rice agriculture across Myanmar using time series Sentinel-1 assisted by Landsat-8 and PALSAR-2. Remote Sens 9:119. https://doi.org/10.3390/rs9020119

Tripathy R, Chaudhari KN, Mukherjee J, Ray SS, Patel NK, Panigrahy S, Parihar JS (2013a) Forecasting wheat yield in Punjab state of India by combining crop simulation model WOFOST and remotely sensed inputs. Remote Sens Lett 4(1):19–28

Tripathy R, Chaudhary KN, Nigam R, Manjunath KR, Chauhan P, Ray SS, Parihar JS (2014) Operational semi-physical spectral-spatial wheat yield model development. Int Arch Photogramm Remote Sens Spat Inf Sci ISPRS Arch 40(8):977–982. https://doi.org/10.5194/isprsarchives-XL-8-977-2014

Tripathy R, Chaudhari KN, Mukherjee J, Ray SS, Patel NK, Panigrahy S, Singh Parihar J (2013b) Forecasting wheat yield in Punjab state of India by combining crop simulation model WOFOST and remotely sensed inputs. Remote Sens Lett 4(1):19–28. https://doi.org/10.1080/2150704X.2012.683117

Tucker CJ (1980) Remote sensing of leaf water content in the near infrared. Remote Sens Environ 10(1):23–32

Chapter 16
Major Natural Disasters in Deserts: Interventions Using Geospatial Technologies

Dandabathula Giribabu, Bera Apurba Kumar, Paliwal Rakesh, Verma Manish Kumar, Gaurav Kumar, Sitiraju Srinivasa Rao, and Jha Chandra Shekhar

Abstract Desert ecosystems cover One-third of Earth's land surface; although the living conditions in the deserts and desert margin regions are hostile but provide adaptability and life support systems to numerous species, including humans. Desert regions are dominated by the cycle of actions resulting due to wind action, erosion, deposition, water/moisture action (or absence), and salt accumulations. The extreme weather settings of the Deserts provoke disaster situations like droughts, flash floods, salt weathering, and strong dust storm events; these events create a dent in the economy of the region. Similarly, the menace created by the native desert locust (*Schistocerca gregaria*) will have devastating effects on food security issues during the phases of upsurge and plagues. A synergy due to the integration of advancements in Earth Observation systems and numerically computed climate variables provides effective management to assess the risk, simulation models, forecasting/early warning, monitoring, damage assessment, and prevention/planning during the aforementioned disasters. This chapter emphasizes the usage of geospatial technologies to manage desert locusts and dust storms.

Keywords Desert locust · Dust storms · Disasters · Arid · Semi-arid · Earth Observation systems

D. Giribabu (✉) · B. A. Kumar · P. Rakesh · V. M. Kumar · G. Kumar
Regional Remote Sensing Centre–West, National Remote Sensing Centre, Indian Space Research Organization, Jodhpur 342005, India
e-mail: dgb.isro@gmail.com

S. S. Rao
Bhuvan Geoportal & Web Services Area, National Remote Sensing Centre, Indian Space Research Organization, Hyderabad 500037, India

J. Chandra Shekhar
Regional Centres Head Quarters, National Remote Sensing Centre, Indian Space Research Organization, Hyderabad 500037, India

C. S. Jha et al. (eds.), *Geospatial Technologies for Resources Planning and Management*, Water Science and Technology Library 115,
https://doi.org/10.1007/978-3-030-98981-1_16

16.1 Introduction

One-third of Earth's land surface is covered by desert ecosystems; although the living conditions in the deserts and desert margin regions are hostile but provide adoptability and life support systems to numerous species, including humans (Ezcurra 2006). Deserts exist in all the continents, including Antarctica and usually, these are the areas where a severe shortage of moisture persists, predominantly because precipitation levels are low (Goudie and Seely 2011); however, the majority of world's deserts like the Sahara, Arabian, Kalahari, Mojave, Sonoran, Chihuahuan, Thar, and some parts of Australian deserts are found within the subtropics (near 30 degrees latitudes) due to the phenomenon of Hadley cell circulations (Whitford and Duval 2019). Desert regions are dominated by a cycle of actions resulting due to wind action, erosion, deposition, water/moisture action (or absence), and salt accumulations. A common factor of deserts is aridity which is defined by the relationship between precipitation (P) and evapotranspiration (ET) and is expressed as P/ET; the lesser the value of P/ET, the more the severity of aridity.

A disaster situation causes a community or society-level functional disruption, which may involve impacts on the human at large, environment, economy, and infrastructure, during which the ability of the affected region may not able to cope with the consequences (UNDRR 2021). The extreme weather settings of desert regions provoke various natural disaster situations like droughts, flash floods, salt weathering, and strong dust storm events (Warner 2008; Mirzabaev et al. 2019; Vaghefi et al. 2019). Similarly, the arid and semi-arid regions tend to naturally host wide varieties of locust; during favorable conditions of environmental and climatic situations, certain variants like desert locust—the planet's most dangerous migratable pest can raze the croplands leading to food security concerns and affecting the livelihoods of village communities (FAO 2021).

The process of desertification is itself a disaster leading to persistent negative trend in land conditions causing long term reduction or loss of biological productivity in arid, semi-arid, and dry sub-humid areas; the adverse consequences of desertification lead to drought, famine, and loss of biodiversity among others (Lambin et al. 2002; Mirzabaev et al. 2019). D'Odorico et al. (2013) mentioned the associated drivers and major mechanisms of desertification in different areas around the world. Salunkhe et al. (2018) suggested a set of indicators that can act as inputs for an early warning system for desertification to identify the areas prone to desertification. Earlier, Albalawi and Kumar (2013) reviewed various remote sensing-based methods to detect, model, and map the desertification process. Masoudi et al. (2018) suggested a novel approach for desertification assessment using geospatial techniques.

During a drought—a prolonged period of water shortage that is below the statistical need of a region's land use will escalate the ecological challenges to the dependent communities, this phenomenon causes a dent in the economy and sustains socio-environmental losses in many countries (Gupta et al. 2011). The climatic conditions in the desert region will highly influence the probability of drought periods (Jodha 1969; Olsson 1993) albeit efforts are in progress to develop drought-resistant crops

(Narain et al. 2000; Bhatt and Sharma 2017). Thenkabail et al. (2004), Khosravi et al. (2017), Bilal et al. (2018), and Zhao et al. (2021) harnessed the utility of remote sensing methods to monitor and assess the drought phenomenon by emphasizing desert regions.

Flash floods in desert regions are unpredictable, infrequent, and short-lived, resulting in heavy sediment transportation (Reid et al. 1994; House and Baker 2001; Cohen and Laronne 2005; Moharana and Kar 2013). Flash floods play a vital role in replenishing the aquifers and groundwater reservoirs but destroys the infrastructure. Also, the new deposit accumulations in topsoil will change the regions' geomorphology (Schepanski et al. 2012). Schepanski et al. (2012), Mashaly and Ghoneim (2018), Attwa et al. (2021), and Ding et al. (2021) elaborated on the usage of remote sensing techniques for mitigating and assessing the impact of flash floods in desert regions.

The climatic conditions of arid and semi-arid regions are pre-eminently supportive of the salt weathering process. The daytime relative humidity is usually low, and temperatures and evaporation rates are significantly high, leading to saline solutions subjected to evaporation and temperature changes promoting crystal growth (Cooke 1981). Salt occurs fairly ubiquitously in desert environments and damages porous materials due to various chemical reactions (Doehne 2002). The process of salt weathering leads to deteriorating heritage buildings, cavern development, aeolian abrasion, and at certain times the aeolian displacement of salt materials leads to damaged crops.

In this chapter, two major disasters associated with desert ecosystems, one being desert locust and the other being dust storms, are envisaged along with their background information and applicability of geospatial technologies toward their monitoring and mapping.

16.2 Geospatial Technologies for Desert Locust Management: Surveillance, Early Warning and Timely Response

Locusts belong to the family *Acrididae*, which includes most short-horned grasshoppers, and in that, a dozen species pose a threat to global food security (Latchininsky 2013). The primary difference between locusts and grasshoppers is that the former will change its behavior, physiology, and movement pattern in sync with the changes in their associated density during certain conditions of the environment and climate situations. As a coherent unit, swarm formation will take place containing millions or billions of individual adult locusts, which requires significant control operations to combat their menace (WMO-FAO 2016). The desert locust, *Schistocerca gregaria* Forsk, a species belonging to the African continent, is considered a dangerous insect and has its natural presence in approximately 30 countries, primarily found in arid and semi-arid regions (Symmons and Cressman 2001; Dandabathula et al. 2020a).

Symmons and Cressman (2001) and Latchininsky (2013) elaborated on the aspects of biology and behavior of locusts in which they will live in two different phases termed as solitarious and gregarious. During the solitarious phase, they tend to have less social interactions, exhibit a sedentary lifestyle, and try to hide themselves using its camouflage appearance, whereas, in the gregarious phase, their color changes, marching happens as cohesive hopper bands (during non-adult stage), and swarm formation occurs during the adult stage. The behavioral changes will occur in a high rapid phase, usually in hours.

The life cycle of the desert locust primarily consists of three stages, viz., egg, nymph to hopper, and adult; the environment and climatic variables highly influence all these stages of the life cycles. Initially, the female locust will probe the soil for required moisture conditions, on successfully determining the favorable conditions the egg production in a clustered fashion called egg-pods will be started and a single egg-pod may contain up to 100 eggs (Symmons and Cressman 2001; Latchininsky 2013). Moist-bare sandy soils permitting the female locusts' oviposition up to a depth of 2–15 cm is a conducive condition for egg-laying (Piou et al. 2019; Ellenburg et al. 2021). Figure 16.1 shows the oviposition and typical clustered egg-pods. The availability of moisture at the root-zone and soil temperature will influence the egg development rate. Egg development may not take place if the temperature is below 15 °C. Successful incubation may happen in 10–12 days if the temperature is between 32 and 35 °C. Thus, availability of spatial data with respect to soil type, soil moisture at the surface and root-zone, air and soil/land surface temperature data are synthesized

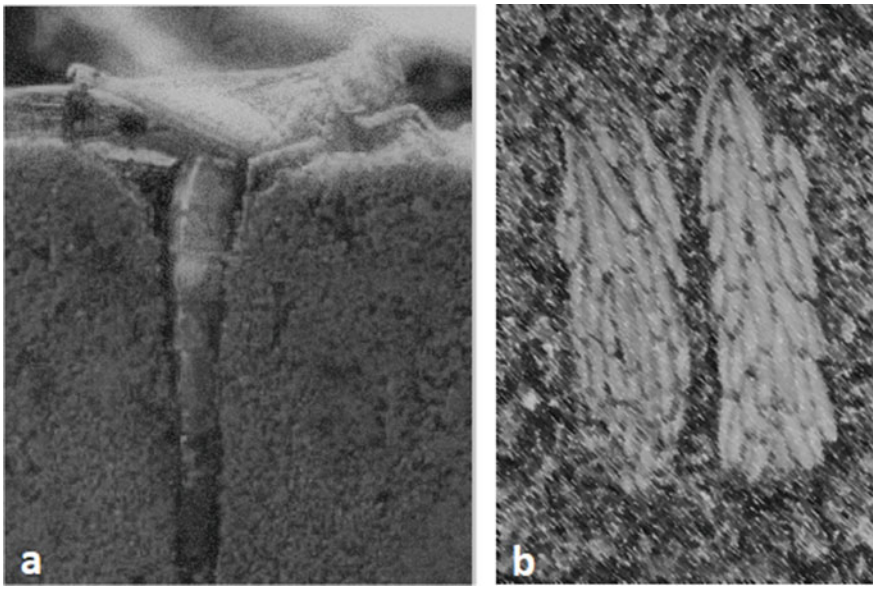

Fig. 16.1 **a** Illustration of ovipositon by desert locust. **b** A typically clustered egg-pods by desert locust

to detect the egg-laying and hatching conditions in a given geographical extent; however, the field data acts as a guide in performing this mapping.

Emerging nymphs (hoppers) will occur post-incubation period through the froth plug to the soil surface and thereafter molt to the first instar rapidly. At later stages, hoppers pass through five to six instar stages by shedding their skin (molting) between each instar stage. During various stages of instar, development hoppers control their body temperature by basking (during early morning sunshine) or under shade of plants (during late afternoon). Hoppers usually have limited mobility, usually in the order 100 m, and their movement depends on locally originated wind direction, patterns of vegetation, and landscape morphology (Culmsee 2002). Thus, toward mapping and monitoring hoppers, knowledge of air temperature, vegetation availability, and wind conditions plays a pivotal role. Occasional rainfalls influence the region's vegetation cover and soil moisture conditions, which impacts the duration of various instar stages of locusts.

Hopper band formation starts while there is an increase in concentrated accumulation of their density where they will get attracted by others; this can happen during vegetation shelter, early morning basking, feeding, or late evening roosting phase (Symmons and Cressman 2001). Toward completion of various instar stages, young adults will emerge with fresh wings during which they will be capable of flying and reproducing. Figures 16.2, 16.3, and 16.4 show the dominant occurrence of hoppers at optimal vegetation, soil moisture, and land surface temperature, respectively.

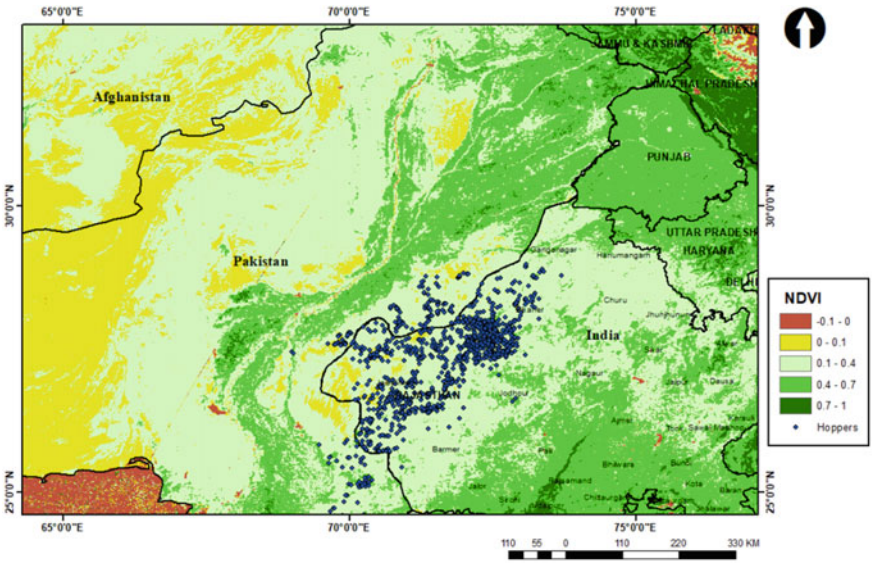

Fig. 16.2 Map showing locations of hoppers between 01-10-2019 and 15-10-2019 overlaid on 8-day composite NDVI data (10–10-2019) in scheduled Thar desert region. Note the occurrence of hoppers dominated at areas with sparse vegetation. Source of hopper's location is from Locust-Hub (2021)

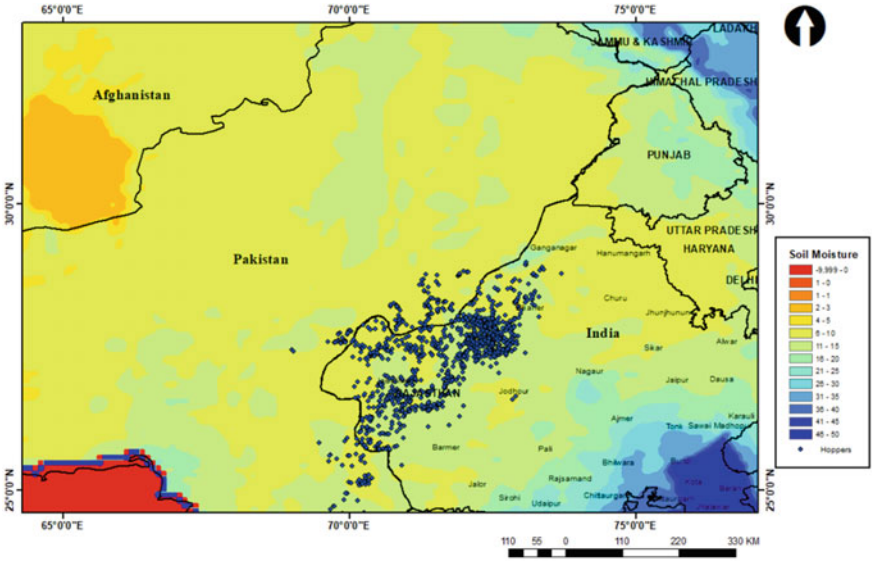

Fig. 16.3 Map showing locations of hoppers between 01-10-2019 and 15-10-2019 in scheduled Thar desert region overlaid on soil moisture product of 10-10-2019 from Soil Moisture Active Passive (SMAP) mission. Note the dominated occurrence of hoppers at the areas with soil moisture in the range of 11–15. Source of hopper's location is from Locust-Hub (2021)

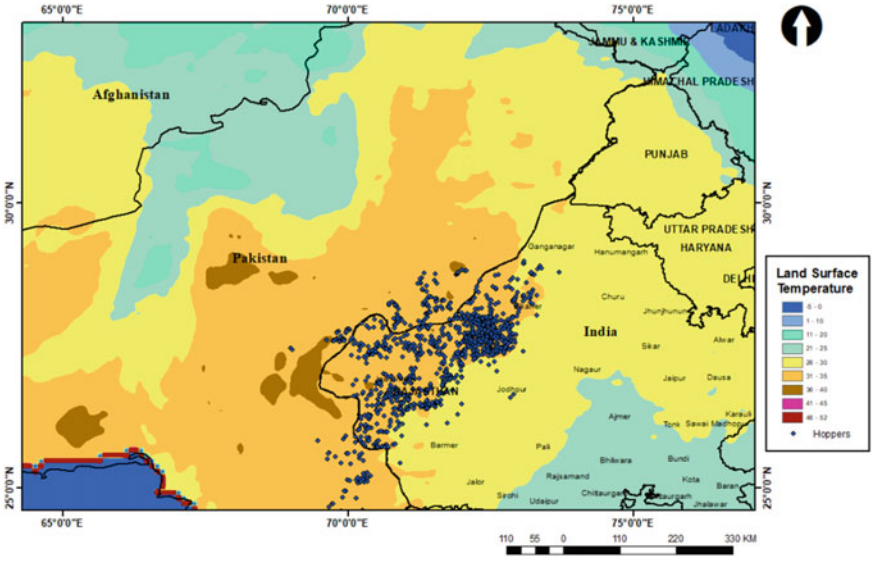

Fig. 16.4 Map showing locations of hoppers between 01-10-2019 and 15-10-2019 in scheduled Thar desert region overlaid on Land Surface Temperature (LST) (on 10-10-2019). Note the dominated occurrence of hoppers at the areas with LST in the range of 31–35. Source of hopper's location is from Locust-Hub (2021)

After fledging, adult wings harden within ten days but remain immature until maturation is stimulated by rainfall and other habitat conditions. However, the hardened wings enable the adult locust to migrate to another area where favorable conditions exist. Thus, patterns of recent rainfall data are a critical parameter to determine the start of maturation (Cressman and Stefanski 2016). Moreover, areas with lush green vegetation with a maximum day temperature of 35^0c or more can amplify the provision of providing habitat to the locust and its survival; adults may not survive long under hot, dry conditions with little to eat, thus the migration process may continue toward searching the vegetation in which for modeling their migration, there is a need of wind data (Dandabathula et al. 2020a).

The gregarization process occurs at a rapid phase (usually in hours) once the aggregation of locusts is brought together; the aggregation process stimulates serotonin at the thoracic-gangalia which is a subsection of central nervous systems and is responsible for triggering the mechanical sensors associated with the hind femur (Anstey et al. 2009). Early morning temperature acts as a catalyst to the process of swarm migration; Gunn et al. (1948), Kennedy (1951), and Weis-Fogh (1956) emphasized the relationship between locust's body temperature and air temperature, which stands to be the main reason for provoking an urge to take-off. Once take-off starts, they can drift away, and wind parameters will completely orient the drifting. However, the sustained flight of swarms depends on the wind speed and direction at 850 hPa atmospheric pressure level, and if any intermediate landing is required, they prefer vegetated areas (Dandabathula et al. 2020a). Desert locusts are highly polyphagous, and the list of preferred plant species contains nearly 500, where most of them are agriculture crops (Latchininsky 2013). A single square kilometer of the dense swarm may have a population of 50 million adults, and this mass gathering, if settled on ground can consume a significant amount of fresh vegetation. Symmons and Cressman (2001) elaborated the details of the locust migration process and its associated environmental and climate patterns that trigger various migration stages, including take-off, sustained flights, and landing/roosting at night time. The primary reason for the long-range swarm migration process is attributed to the winds originating with cyclones. Richardson and Nemeth (1991) and Lorenz (2009) attributed the long-range trans-Atlantic swarm migration in 1988 with the Hurricane Joan. Similarly, unexpected swarm migration of desert locust in the year 2020 from Indo-Pakistan region border region to various parts of India was attributed to cyclone Amphan by Dandabathula et al. (2020a). Figure 16.5 shows the number of sightings about swarm oscillations before and after cycle Amphan originated in the Bay of Bengal during mid-May 2020.

Currently, an early warning system for desert locust plagues namely Desert Locust Information Service (DLIS) was developed and is maintained by Food and Agriculture Organization (FAO); DLIS acts a resourceful web portal for retrieving locust related information at a global level. Monthly bulletins released under the aegis of DLIS contains country-wise prevailing situation of locusts along with their location data, forecast information, and spatial maps depicting the potential habitats/or other significant developments (FAO-DLIS 2021); toward this, field data

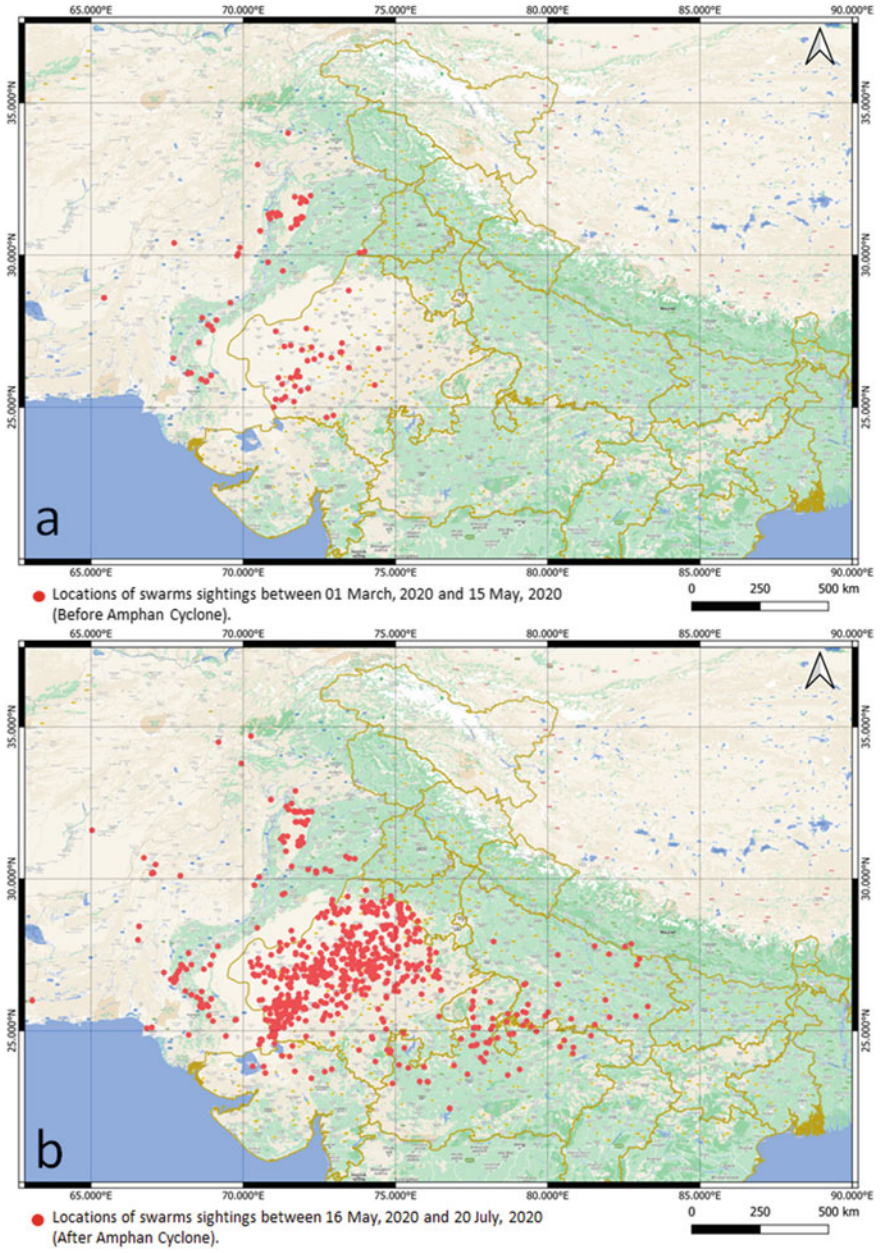

Fig. 16.5 Impact on Swarm oscillations by winds originated due to Amphan Cyclone. **a** Locations of swarms were sighted between 01-March-2020 and 15-May-2020 (before Amphan Cyclone) in scheduled Thar desert region. **b** Locations of swarms that are sighted between 16-May-2020 and 30-July-2020 (during and after Amphan Cyclone). Note the trajectory of swarm migration has extended from scheduled Thar Desert region to Indo-Nepal boundary. Source of sighting pertaining to swarm oscillations is from Locust-Hub (2021)

from country-specific locust and allied centers will be ingested to DLIS. A dedicated web portal titled FAO Locust-Hub disseminates location-based information in a variety of formats that can be ported to Geographic Information Systems (GIS) for further analysis/research; primarily, records of point location (latitude and longitude) details containing various attributes related to various stages of locust's life cycle viz., hoppers, bands, adults, swarms, ecological conditions, and control operations taken up by different countries are made available (Locust-Hub 2021).

Country-specific research activities on locusts can be performed with the help of regional locust warning organizations. Thar Desert region extends Indo-Pakistan border is predominately spread over Rajasthan state of India. Even though the Thar Desert is one of the most miniature deserts of the world, it hosts a wide variety of habitats and biodiversity (Sivaperuman 2009). The Thar Desert, credited as a densely populated desert, exhibits strong variations in its landscape characters (Chouhan and Sharma 2009; Kar 2018). The weather settings of the Thar Desert naturally host the desert locust population and act as summer breeding site (Uvarov 1934; Ramchandra 1942). Locust Warning Organization (LWO), working under the Ministry of Agriculture and Farmers Welfare, Government of India is entrusted to monitoring, forewarn and control the locust in scheduled desert areas of India (LWO 2021).

Table 16.1 shows the summary of optimal environment and climatic conditions that are favorable to various life cycle events of desert locust along with their associated Earth Observation (EO) or modeled data that can be associated to use for locust monitoring or surveillance; this list has been prepared after synthesizing the results from earlier works done by Symmons and Cressman (2001), Latchininsky (2013), and Cressman and Stefanski (2016). Table 16.2 shows the corresponding sources of EO/modeled data at the global level and specific to the Thar Desert region available from current space sensors/agencies. Most of the specified EO/modeled data are freely distributed by the concerned agencies through their web portals.

The relationship between soil type and its associated properties with respect to various life cycle events of desert locust were explored by Hunter-Jones (1964), McCaffery et al. (1998), Van Der Werf et al. (2005), and Ellenburg et al. (2021). Importantly, the oviposition and egg development conditions are depended on the soil features like texture, structure, porosity, or permeability, along with the ability to retain moisture to a depth of 15 cm. Soil resources in the spatial form at global extent are available as Harmonized World Soil Database with 1 km spatial resolution (FAO-Soil 2021) and SoilGrids250m data set with 250 m resolution (SoilGrids250m 2017); moreover, for detailed soil context, one can use respective country-specific data, like for the case of Thar Desert region, ICAR-NBSSLUP (2021) will provide soil information at various scales. Earlier, Ellenburg et al. (2021) used the SoilGrids250m database to detect desert locust breeding grounds in Eastern Africa.

The role of rainfall at various stages of locust life cycles was explored by Holt and Cheke (1996), Symmons and Cressman (2001), Cressman (2016), and Kimathi et al. (2020) wherein the process like breeding, changes in hopper's instar stages, maturation process, adult development, and locust survival are directly related to the accumulated rainfall. Indirectly, the accumulated precipitation is responsible for both the variations of vegetation growth and soil moisture conditions; these variables have

Table 16.1 Favorable environmental and climatic conditions for various life cycles events of desert locust and associated earth observation data

Phase of Locust's life cycle	Favorable environmental conditions	Earth observation-based/modeled data: environment and climatic data associated with the events of locust life cycle
Egg-laying	Bare patches of sandy soils with sufficient moisture especially at root-zone Warm temperature Areas with vegetation availability Areas with previous rainfall (>25 mm/month)	Soil type data along with its moisture information at root-zone Air temperature data Vegetation status Previous two months accumulated rainfall
Egg development (10–20 days in summer and up to 2 months in other seasons)	Soil moisture at the root-zone (nearly 5–12 cm) should be moist; dry soil makes eggs desiccate The optimal range of screen (air) temperature is 20–35 °C The optimal range of soil temperature is 15–35°C; high mortality occurs if soil temperature exceeds 35 °C	Soil moisture at surface and root-zone Screen (air) temperature data Land surface temperature data
Hopper (25–95 days)	Sporadic rainfall supports vegetation growth in arid and semi-arid regions; it also, retains moisture in soil Optimal range of daily air temperature is between 24 and 32 °C Hoppers prefer basking in early morning. And, during midday, they prefer taking shelter under plants Hoppers usually exhibit restricted movement during overcast days The movement of bands is usually downwind	Rainfall data Air temperature data Vegetation status Land surface temperature data and cloud data Wind direction maps

(continued)

their role in supporting the locust habitation as described in Table 16.1. The variance of locust abundance is increased by rainfall (Holt and Cheke 1996; Cressman 2016). Heavy rainfall over vast areas can lead to locust upsurge and further can lead to plagues affecting a continent (Kimathi et al. 2020). The Global Precipitation Measurement (GPM) is an international network of satellites that provide the observations of rainfall at the global level (GPM 2021) can be used to model the locust

Table 16.1 (continued)

Phase of Locust's life cycle	Favorable environmental conditions	Earth observation-based/modeled data: environment and climatic data associated with the events of locust life cycle
Adult (2.5–5 months)	It takes 2 to 4 months for adult locusts to mature. Rapid maturation takes place in the areas where there are significant rains. (Also, adults mature slowly in low temperature or dry habitats) Prefers high screen (air) temperature Take-off 20 min after sunrise above 20–22 °C and wind speed nearly 7 m/s The movement of the adult locust is driven by wind direction Prefers warm temperatures during day time Needs vegetation for survival	Rainfall data Air temperature data Wind speed and wind direction Land surface temperature data and cloud data Vegetation status
Swarm	Early morning radiation from Sun provides the necessary warm-up (basking) Usually, take-off may happen 2–3 h after sunrise; the preferred direction is Sun-facing. Screen (air) temperature needed during take-off of the range 23–26 °C Fly preferences: Downwind at heights up to 1700 m with ground speed of 1.5 to 16 km/h until 2 h before sunset or 0.5 h after sunset Vegetation Cool and overcast weather favors stratiform swarms, while convective updrafts on hot afternoons promote cumuliform swarms	Cloud data to detect bask-able conditions and overshadow regions Air temperature data Wind speed and direction data Vegetation status

Source Symmons and Cressman (2001), Latchininsky (2013), Cressman and Stefanski (2016), Dandabathula et al. (2020b)

Table 16.2 Sources of Earth observation/modeled based environmental and climatic conditions for locust monitoring; for global scenario and specific for Thar Desert region

Environment and climatic data associated with the events of locust life cycle	Sources for earth observation data (global level)	Sources for earth observation data (specific to scheduled Thar Desert region)
Soil data	Harmonized World Soil Database @ 1 km raster database (FAO-Soil 2021) and SoilGrids system at 250 m resolution (SoilGrids250m 2017)	ICAR-National Bureau of Soil Survey and Land Use Planning (ICAR-NBSSLUP 2021)
Precipitation data	Global precipitation measurement (GPM 2021)	India Meteorological Department (IMD 2021) Meteorological and Oceanographic Satellite Data Archival Centre (MOSDAC 2021)
Soil Moisture data and Root-zone soil moisture	NASA-USDA Global Soil moisture data at 0.250*0.250 spatial resolution and Level 4 products from (SMAP 2021) at 9 km spatial resolution	National Information System for Climate and Environmental Studies (NICES 2021)
Temperature data	CPC Global Daily Temperature (PSL-CPS 2021)	Meteorological and Oceanographic Satellite Data Archival Centre (MOSDAC 2021)
Land surface temperature data	Copernicus Global Land Service—Land Surface Temperature (CGLS-LST 2021)	Meteorological and Oceanographic Satellite Data Archival Centre (MOSDAC 2021)
Vegetation status	Copernicus Global Land Service—Normalized Difference Vegetation Index (CGLS-NDVI 2021) or alternative derivable from MODIS, NASA/USGS Landsat program, and Sentinel 2A/B	(MOSDAC-NDVI 2021) and (Bhuvan 2021) or NDVI derivable from AWiFS, LiSS III, LiSS IV
Wind speed and direction data	ECMWF Reanalysis 5th Generation data (ERA5 2021)	Meteorological and Oceanographic Satellite Data Archival Centre (MOSDAC 2021)

habitat locations or aid in the locust early warning systems. However, for large-scale measurements, one can utilize country-specific rainfall measurements. In the case of countries like India, services pertaining to rainfall information can be requested from Indian Meteorological Department (IMD 2021), or alternatively, web services

from Meteorological Oceanographic Satellite Data Archival Center (MOSDAC) can be harnessed (MOSDAC 2021).

Soil moisture at the surface and root-zone is a key indicator while studying the locust habitats from egg-laying activity, egg development, breeding, and survival (Escorihuela et al. 2018; Piou et al. 2019; Gómez et al. 2020). Currently, the soil moisture data products available at a global scale have a spatial resolution of 9 km for every 3 h, which are disseminated as Level 4 products from Soil Moisture Active Passive (SMAP) satellites. Gómez et al. (2019) successfully demonstrated the applicability of soil moisture and its associated data variables from SMAP could aid in locust detection. Similarly, data related to air temperature and land surface temperature (LST) can be retrieved from (PSL-CPS 2021) and (CGLS-LST 2021).

Vegetation status in a region plays a pivotal role during the locust life cycle in hopper and adult stages. Currently, Normalized Difference Vegetation Index (NDVI) and Leaf Area Index (LAI) are the indices generated from optical remote sensing sensors that can indicate vegetation. To a global extent, one can utilize the services from Copernicus Global Land Service to download a 300 m NDVI product (CGLS-NDVI 2021). An 8 or 10 day composited NDVI product at 240 m spatial resolution is available from eMODIS collection (eMODIS 2018). Alternatively, high-resolution NDVI can be derived from optical multispectral data containing red and near-infrared bands for estimating photosynthetically active vegetation coverage (Yang et al. 2017). To assess the crop damage caused by the locust, differences from time-series NDVI can give quantitative information on crop loss (Shao et al. 2021).

A climate reanalysis data gives a numerical portrayal of recent climate states by synthesizing modeled and observation data. European Centre for Medium-Range Weather Forecasts (ECMWF) is computing and disseminating the ECMWF Reanalysis 5th generation (ERA5) data at a $0.25° \times 0.25°$ spatial resolution containing atmospheric parameters at 37 pressure levels (Hersback et al. 2020). Earlier, Ramon et al. (2019) validated the wind parameters from ERA5 and confirmed that the accuracies correlate with real-time data. Wind vectors (speed and direction) at surface level and nearly at 1500 m from the surface (corresponds to at a pressure level of 850 hPa) are of high importance to trace the adult locust movement and swarm flight trajectories, respectively (Rosenberg and Burt 1999; Cressman and Stefanski 2016; Dandabathula et al. 2020a). Heuristic swarm migration prediction can be performed using the ERA5 data by coupling with the early morning basking conditions. Dandabathula et al. (2020a) successfully utilized wind speed and direction data from ERA5 data to assess the migration path of swarms during and post-Amphan cyclones.

The potential of geospatial technology for locust surveillance and early warning system was discussed earlier by Hielkema (1981), Tucker et al. (1985), Voss and Dreiser (1997), Latchininsky (2013), Cressman (2013). The current availability of satellite imagery and numerically computed weather data enables monitoring and prediction of the desert locust outbreaks and plagues efficiently (Dandabathula et al. 2020b; Klein et al. 2021; Schwarzenbacher 2021); Advancements for applying machine learning techniques toward locust detection and early warning systems is well in progress (Gómez et al. 2021; Rhodes and Sagan 2021; Kumar and Rahman 2021; Klein et al. 2021).

However, the lack of very high spatial resolution data in terms of soil moisture critical environmental and climatic variables is one limiting factor for precise mapping and monitoring of desert locusts (Adams et al. 2021). To compensate for these limiting factors, one can use mobile-based apps and the Internet of Things (IoT) to ingest the field level data to the early warning systems (Dandabathula et al. 2020b; Salim et al. 2021; Cressman 2021). The recent advancements in the unmanned aerial vehicles (UAVs) or drones might help survey the areas with locust concentrations (to acquire high-resolution images) and also to aid in control operations like spraying pesticides (Cressman 2021; Mathews 2021).

Technical innovations, especially in EO systems, numerical weather prediction, machine learning, and drones, can play an essential role in the effective management of transboundary pests like a desert locust. Along with the FAO's successful DLIS, country-specific initiatives to combat the menace of desert locusts are imminent due to food security concerns. Mitigating the transboundary disasters originating due to high mobile desert locusts will be possible with cooperation between locust-prone countries in their surveillance activities and control operations. Cressman (2021) has argued that the impact of climate change will induce faster breeding periods, allow desert locust eggs and hoppers to develop rapidly; consequently, the impact of desert locusts on food security and livelihood will be at increased stake if it is not controlled at initial level. For successful mitigation of locust menace and plague dynamics, country-specific early warning systems coupled with EO systems and scientific models with machine learning are needed for timely response. Toward this, the currently available variables from EO sensors and numerically computed weather parameters will be enhanced in terms of improved spatial resolution.

Considerable progress is made in using Entomological Radars for understanding flight altitude, population density, displacement direction, displace rate, head orientation, body mass, and wing-beat frequency of migratory insects (Long et al. 2020). Amarjyothi et al. (2021) has successfully demonstrated the application of Doppler Weather Radar for the identification and tracking of locust swarms.

16.3 Geospatial Technologies for Dust Storm Monitoring: Toward Operational Monitoring of Dust Storms Using Imagery from Geostationary Satellites

Dust/Sand storms are a common meteorological phenomenon in arid and semi-arid regions, where the loose sediments subsist (Kok et al. 2012). The regional characteristic includes the reversal of mean wind direction during a change of season. Dust storms occur principally during the dry season months of spring and summer (Middleton 1986). The negative impact of dust storms includes the reduced activity of photosynthesis, road traffic, human settlements can become shrouded with sand, and at a regional level, there will impact the overall radiation budget (Natsagdorj et al. 2003). The major dust sources are deserts, fallow lands, recently tilled lands,

Table 16.3 Thresholds of wind speeds in various environments containing different types of sand that can lift suspended sediments into the atmosphere

Type of sandy environment	Threshold of wind speed (km/h)
Areas with sand dunes composed of fine to medium sand	16–24
Poorly developed desert pavements with high sand content	>32.2
Flat areas in desert containing fine material	32–40
Lake beds (dried) and/or areas covered with crusted salt flats	48–56
Desert pavements (well-developed conditions)	>64

Source UNEP-WMO-UNCCD (2016)

river flood plains, coastal areas, glacial deposits, ocean sediments, and dry lake beds (Nicholson 2011). The strong and turbulent winds inject the dust into the atmosphere from source regions and are subject to transport. The transportation mode of particles depends predominantly on their size and wind speed. It includes saltation (0.1–0.5 mm), suspension (<0.1 mm) and creeping (>0.5 mm).

A dust storm has the potential to occur when strong and turbulent winds blow over the areas with sparse vegetation cover, surfaces that lack moisture content, or the areas with top soils vulnerable to surface disturbances (Wilcox 2012). Sand storm phenomenon takes place relatively close to the land surface (10–50 feet), but fine dust particles are usually lifted to the atmosphere up to several kilometers; certain times they even cross continents due to strong winds (UNEP-WMO-UNCCD 2016). Table 16.3 shows the wind speed thresholds in various environments containing diffident types of sand that can lift suspended sediments into the atmosphere.

Usually, desert soils form a thin cohesive surface crust due to which they are intact with the ground; thus, they are naturally resistant to wind erosion. This cohesive surface crust is more prevalent in the regions with high vegetation as it helps to stabilize and trap the suspended soil particles. Hence soils with vegetative ecosystems get protection from the wind (Urban et al. 2009; Steenburgh et al. 2012; Wilcox 2012). When this cohesive surface crust gets disturbed due to a reduction in vegetation cover, loosed sediments tend to get carried away through aeolian transport mechanisms.

A soil with high erodible factors influences the susceptibility of soil to erosion. Regions in deserts with a high erodible factor are primary dust producers. Most deserts in subtropical regions contain sandy soils with high erodible factors and provide mobilization of dust due to strong winds (Washington et al. 2003). Deserts of the United States may provoke dust storms for less than 40 days in a year. In contrast, in parts of Mongolia, seasons with more than 100 days a year evoke dust storms (Dagvadorj et al. 2009; NCDC-NOAA 2012). Earlier, Goudie (2009) estimated worldwide dust emission to be in the range of 1000–3000 teragrams per year, in which the Sahara desert itself is the largest contributor.

The interaction of dust with other components of earth system has numerous consequences on the environment, including reduced visibility, loss of nutrient-rich soil, modifying local climate conditions, and biological and chemical changes in oceans (Goudie 2009; Santra et al. 2013). Societal impacts include transportation disruptions, communication line interruption, damage of property, and public health consequences. Dust also constitutes a significant key parameter in climate-aerosol forcing studies. Further, these airlifted aerosols act as airborne bacteria carriers (Hua et al. 2007; Goudarzi et al. 2014). Therefore, a system for comprehensive monitoring of dust storms is needed to understand the dusting process and enhance the dust prediction capabilities (UNEP-WMO-UNCCD 2016).

Monitoring dust storms using EO-based images is a feasible solution since implementing and maintaining in situ sensors pose challenges in the harsh conditions of the deserts. Due to the dynamic nature of the mineral aerosol in emission/reflection, the ability of space-borne sensors to detect plumes associated with dust storms is highly reliant. Different algorithms, sensors, spectral bands, and thresholds are to be identified based on underlying land/ocean surface, presence of water clouds, the thickness of dust clouds, date and time of image acquisition, and geographic extent of the event.

Understanding the extent of dust storms' spread, its timing, and components of aerosols is a complex phenomenon, and within this, the components of the aerosols will influence the dust particles to scatter and absorb the radiation (Satheesh and Moorthy 2005). Chiefly, the aerosol components are sulfates, nitrates, and sea salt (Parungo 1987; Chandra et al. 2004; Seinfeld 2004; Deepshikha and Satheesh 2005).

Atmospheric aerosol can directly alter solar radiation and earth's emitted radiation through absorption and scattering processes; this will alter the radiance obtained using visible (0.4–0.7 μm), middle infrared (1.3–3 μm), and thermal infrared (3–14 μm) regions (Satheesh and Moorthy 2005). Therefore, the magnitude of differences in observations between various spectral regions can assist in providing the signature of dust. Ackerman (1989) investigated that the wavelength region 3.7, 11, and 12 μm are sensitive to dust. Hence, remote sensing techniques associated with both the spectral regions, viz., visible and thermal, are appropriate to detect aerosols in the atmosphere.

Researchers have described various methods to detect dust storms using polar-orbiting satellites (Roskovensky and Lion 2005; Hong et al. 2006; Hao and Qu 2007; Huang et al. 2007; Prasad and Singh 2007; Zhao et al. 2010; Zhao 2012) and geostationary satellites (Hu et al. 2008; Mishra et al. 2015). Li et al. (2021) reviewed the available algorithms that can detect dust storms based on various space-borne sensors.

Most commonly used dust detection methods include the split-window technique, mid-infrared technique, Normalized Difference Dust Index (NDDI), and Infrared Difference Dust Index (IDDI). The major challenges in detecting dust using the imagery are segregation of cloud, snow, bright surface, and water. The Brightness Temperature Difference (BTD) between various bands is useful for detecting dust from background pixels (Ackerman 1989). Mehta and Kunte (2014) suggested that the combination of NDDI and BTD effectively detects dust over land and ocean.

Table 16.4 Specifications of various bands in INSAT-3D/3DR imaging channels along with their applicability for dust storm monitoring

INSAT-3D/3DR imager bands and spectral range (μm)	Resolution (km)	Applicability for dust storm monitoring
1. Visible (0.55–0.75)	1	Cloud detection and masking
2. Shortwave Infrared (1.55–1.70)	1	
3. Middle infrared (3.80–4.00)	4	Dust detection using brightness difference with other bands
4. Water vapor (6.50–7.10)	8	
5. Thermal infrared 1 (10.3–11.3)	4	Dust load detection and dust detection using brightness difference with other bands
6. Thermal infrared 2 (11.5–12.5)	4	Dust detection using brightness difference with other bands

Source Mishra et al. (2015)

Atmospheric observations on both the land and ocean area are required for various applications. INSAT-3D/3DR, the geosynchronous duo-satellites with six imager channels and 19-channel infrared sounder, helps in the identification and setting-up early warning systems for natural disasters like floods, tropical cyclones, forest fires, and dust/sand storms. Multispectral images from INSAT-3D and INSAT-3DR will be acquired every half an hour, respectively (combining both will yield one data set for every 15-min interval) that cover the entire Indian sub-continent through which accurate and timely processing of weather parameters can do. Split-window algorithms can be applied on INSAT-3D/3DR acquired thermal infrared bands for estimating the temperature profiles similarly, information about various cloud types can be understood from visible bands (ISRO 2016). The product is available at various levels of processing such as L1 (basic data products), L2 (geophysical parameters), and L3 (binned geophysical products) (MOSDAC 2021). Table 16.4 shows the INSAT-3D/3DR data specifications and their usage in dust storms monitoring. Figure 16.6 shows a dust storm that lived from 27–28 May 2018 spreading Baluchistan regions and parts of western Afghanistan as seen in MODIS Terra and INSAT-3DR images.

The refractive index of various species leads to the spectral signature that impact radiance observed using satellite in various ways (DeSouza-Machado et al. 2006). The major constituents of dust storms are quartz, illite, kaolinite, iron oxides, and fossil diatoms. Various studies stated that light attenuation for clay minerals and quartz occurs around wavenumber 1000 cm^{-1} and 1100 cm^{-1}, respectively.

The Brightness Temperature Difference (BTD) between ~11.0 and 12.0 μm regions of the electromagnetic spectrum yields specific values that can help in identifying the plumes of volcanic ash in the atmosphere (Prata 1989a, b). Studies done by Ackerman (1997) concluded that the spectral absorption properties of desert dust particles and volcanic silicates in the thermal region of the spectrum are similar. Mishra et al. (2015), while assessing the feasibility of dust detection using INSAT-3D data highlighted that the major constituent of the sand is silica which in the form

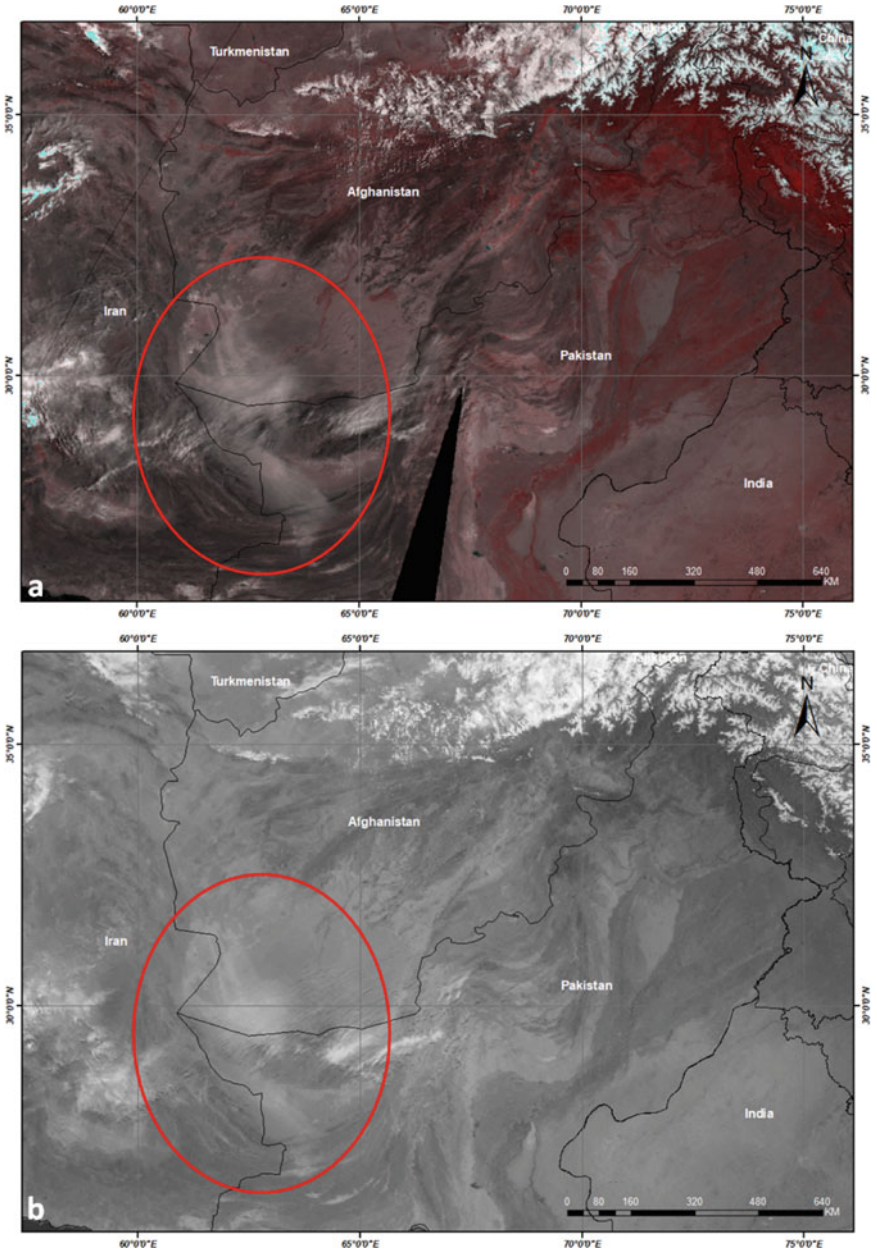

Fig. 16.6 Sistan dust storm (spread across the Baluchistan region and south-western parts of Afghanistan as seen in **a** MODIS Terra and **b** INSAT-3DR. Both the datasets were acquired on 28th May 2018 at 13:30 and 15:15 h, respectively. The dust plume was born on 27th May 2018 and lived up to 28th May 2018

of quartz shows very strong spectral dependency; this feature enables us to detect dust pixels in the images of thermal infrared region. Usually, for dust pixels, the differences between brightness temperatures recorded in 10.8 and 12 μm region will yield nearly negative values, i.e., BTD [10.8, 12.0] < 0.

Legrand et al. (2001) proposed an index, namely Infrared Difference Dust Index (IDDI) while working with Metosat-IR imagery to identify dust load in the arid zones. Categorically, the impact of dust load on the radiance emitted in the thermal infrared region is being considered for detecting dust storms. During dust-free days, the radiance emitted by the surface over days may remain almost constant. As the dust load infuses mineral aerosol content in the atmosphere, it traps the outgoing radiation. Thus, IDDI effectively computes the difference between radiance emitted during dust-free days and dust load periods. Mishra et al. (2015) successfully demonstrated the applicability of IDDI from INSAT-3D to detect dust storms. IDDI can be computed using Eq. 16.1 using various brightness temperatures (BT).

$$\mathrm{IDDI} = \mathrm{BT}_{\mathrm{max}} - \mathrm{BT}_{\mathrm{ob}} \tag{16.1}$$

where $\mathrm{BT}_{\mathrm{ob}}$ is the BT obtained from thermal infrared band at 10.8 μm during the dust load period and $\mathrm{BT}_{\mathrm{max}}$ is the maximum BT recorded from the previous course of days (say for 12 days) at the same thermal infrared band. Figure 16.7

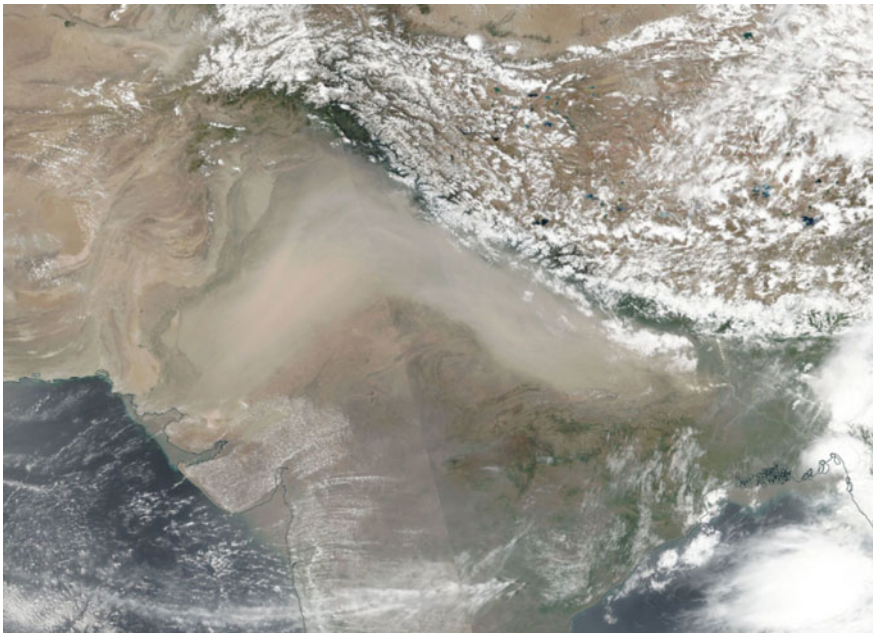

Fig. 16.7 Massive dust storm that lived between 12 and 17 June 2018 and as seen in Suomi NPP/VIIRS acquired on 14 June 2018. The dust storm spread from Western Thar Desert region to Indo-Gangetic Plain has deteriorated the air quality beyond the critical levels in the region

shows a massive dust storm that lived from 12 to 17 June 2018 spanning western India and Indo-Gangetic Plain and is captured by Suomi NPP/VIIRS sensor on 14th June 2018; during such type of situations, there will be the reduction of outgoing long-wave radiation in comparison with dust-free days.

The dust reflects solar radiation at 3.9 μm; therefore, the BT is higher than 11 μm during daytime. Computing the differences in BT at these two bands (i.e., BTD [3.9, 10.8]) results in large differences during the dust load sessions, which can act as an indicator to trace the dust pixels in the satellite imagery. At 3.9 μm the observed radiance is the result of both solar radiation and earth emission during daytime. During night time the observed radiance is a consequence of earth emitted radiation only. Hence, the threshold identified for extracting dust storms during daytime is not valid for night time.

During the process of dust pixel detection, the process of cloud masking is desirable. Toward this, one can take advantage of high reflectance by clouds in the visible channel. Similarly, the BT values will be less than 273 K at 10.8 μm thermal infrared channels for clouds.

Figure 16.8 shows the detectability of dust storms from INSAT-3D/3DR sensors using BTD indices from the thermal and mid-infrared region; the examples shown here are the massive dust storm lived from 12 to 17 June 2018 in the Indian sub-continent.

There exist limitations in dust detection algorithms. Primarily the determination of the threshold values depends on the event's time (day or night) and the region; to overcome these limitations, researchers proposed threshold-free dust storm detection index (Jebali et al. 2021) still they are dependent on sensor specifications. The effectiveness of the dust detection indices can be validated using Aerosol Optical Depth (AOD) information obtained from other space-borne sensors. Alternatively, one can validate the efficacy of dust detection algorithms using the aerosols vertical profiles obtained from space-borne CALIPSO LiDAR data (Chhabra et al. 2021; Li et al. 2021; Wang et al. 2021).

Researchers have harnessed MODIS data to detect dust storm studies because of its higher spatial and spectral resolution, but due to the shorter lifetime of dust storm event (of course due to their large spatial coverage), geostationary satellites with high temporal resolution that acquires synoptic view of Earth are proven to be capture variations of dust storms (Li et al. 2021).

For the Indian sub-continent, a combination of data sets from INSAT-3D/3DR yields to detect variations of dust storms for every 15 min; this enables to detect of the directionality of dust storms and helps predict the course of dust storms using related meteorological parameters like wind vectors. Recently, there has been a thrust to adopt machine learning techniques coupled with space-borne sensors to detect dust storms (Boroughani et al. 2020; Shi et al. 2020; Ebrahimi-Khusfi et al. 2021). Similarly, as the first step toward informing the community about the occurrence of a dust storm, it is important to identify the source of dust storm origin; in this direction, there exists scope for further research to effectively perform numerical weather predictions in sync with the EO systems.

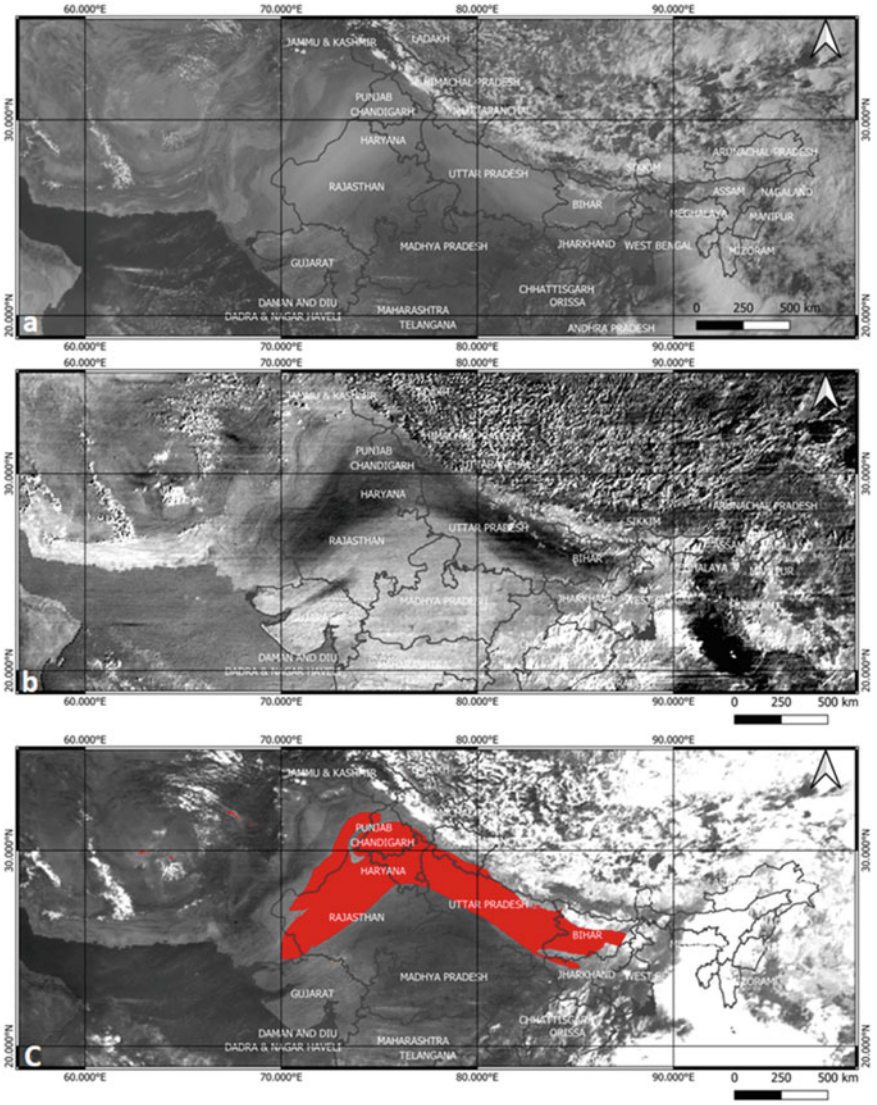

Fig. 16.8 Massive dust storm that lived between 12 and 17 June 2018 and its detection using INSAT-3D/3DR data by computing various Brightness Temperature Differences (BTD) techniques. **a** Dust storm as seen in visible band of INSAT-3D acquired on 14 June 2018 at 11:30 h. **b** BTD [10.8, 12.0] showing blackish pixel values corresponding to dust pixels indicating negative values. **c** Successful detection of dust pixels using indices generated from BTD [10.8, 12.0], BTD [3.9, 10.8], and Infrared Difference Dust Index (IDDI) with its previous 12 days period

16.4 Summary

Disasters associated with deserts pose a major threat not only to the dependent inhabitants but also affect flora and fauna associated with the arid and semi-arid regions. As such, the process of desertification removes the top layers of soil so that the usual rangeland species cannot regenerate. The harsh environment and climatic conditions of arid and semi-arid regions provoke various disasters associated with aeolian mechanisms, chemical and biological phenomena. Chiefly, the disasters associated with the deserts are droughts, flash floods (rarely), salt weathering, dust storms, and insect migrations. Most of the disasters originating from deserts result in transboundary hazards risks. This chapter discussed two disasters associated with the desert ecosystems in which the geospatial technologies can take the lead for implementing successful interventions.

Crop and rangeland damage due to desert locusts with voracious appetites is a great threat to regional and global food security. Stages of desert locust's life cycle include egg, nymph to hopper, and adult; usually spent in two different phases termed solitarious and gregarious. Understanding the environment and climatic variables associated with the life cycles stages of desert locusts enables us to map and monitor the habitat locations, their development, and movement. The availability of these associated environmental and climatic variables from EO systems and numerically computed algorithms enables to establishment of early warning systems through which one can successfully perform control operations to eradicate locusts. Chiefly, the data associated with soil type, precipitation, temperature, vegetation, wind parameters, and soil moisture conditions are highly useful during the monitoring of desert locusts. Similarly, wind parameters like wind speed and wind direction are highly useful to perform heuristic prediction of swarm migration and thus, regional level threat maps can be generated. However, for high precision of desert locust mapping and monitoring, there is need for high-resolution data in terms of soil moisture and climatic variables. Technical innovations in EO systems, numerical weather prediction algorithms, machine learning, drones, and entomological radars can advance the predictability of locust habitats and their development.

Dust storms originating from desert regions have several impacts on the environment, including radiative forcing and biogeochemical cycling by transporting material over thousands of kilometers through aeolian-associated processes. Satellite-based monitoring of dust storms is feasible since ground-based observations are restricted in space and time. Indices based on brightness temperature differences are effective in detecting dust pixels. Data from EO systems with high temporal resolution can help us operational monitor dust storms and accordingly disseminate the information on the directionality of dust storms to the community. Further understanding on detecting the origin of dust storms and toward this research activity based on numerical weather computing and machine learning algorithms has to be emphasized.

Acknowledgements The works described in this chapter would not have been possible without the exceptional support and guidance provided by Director, National Remote Sensing Centre, Hyderabad, India. The authors are grateful for the support provided by the staff members of Regional Remote Sensing Centre—West (RRSC-W), Jodhpur, Standing Committee for Locust Surveillance, Alerts and Monitoring, and officials of EDPO, ISRO Hq. The various organizations and data providers like FAO Locust team, Locust Warning Organisation—Jodhpur, Bhuvan/NICES, MOSDAC, MODIS, SMAP, ERA5, Sentinel, and USGS are gratefully acknowledged for providing free access to various data sets. Sujitha P.R., Koushik Ghosh, and Rohit Hari have provided technical inputs in this work. All literature cited in the text has been fully referenced.

References

Ackerman SA (1997) Remote sensing aerosols using satellite infrared observations. J Geophys Res Atmos 102(D14):17069–17079

Ackerman SA (1989) Using the radiative temperature difference at 3.7 and 11 μm to tract dust outbreaks. Remote Sens of Environ 27(2):129–133

Adams EC, Parache HB, Cherrington E, Ellenburg WL, Mishra V, Lucey R, Nakalembe C (2021) Limitations of remote sensing in assessing vegetation damage due to the 2019–2021 Desert Locust Upsurge. Front Clim 3:714273. https://doi.org/10.3389/fclim.2021.714273

Albalawi EK, Kumar L (2013) Using remote sensing technology to detect, model and map desertification: a review. J Food Agric Environ 11(2):791–797

Amarjyothi K, Kumar DP, Saikrishnan KC (2021) Identification and tracking of locust swarms by Indian Doppler weather radar. IEEE Geosci Remote Sens. https://doi.org/10.1109/LGRS.2021.3086587

Anstey ML, Rogers SM, Ott SR, Burrows M, Simpson SJ (2009) Serotonin mediates behavioral gregarization underlying swarm formation in desert locusts. Science 323(5914):627–630

Attwa M, El Bastawesy M, Ragab D, Othman A, Assaggaf HM, Abotalib AZ (2021) Toward an integrated and sustainable water resources management in structurally-controlled water-sheds in desert environments using geophysical and remote sensing methods. Sustainability 13(7):4004

Bhatt RK, Sharma R (2017) Development of drought tolerant crop varieties. In: Kumar S, Tanwar SPS, Singh A (eds) Drought mitigation and management. Scientific Publishers. Jodhpur, India

Bhuvan (2021) Bhuvan-Indian geo-platform of ISRO. https://bhuvan.nrsc.gov.in

Bilal M, Liaqat MU, Cheema MJM, Mahmood T, Khan Q (2018) Spatial drought monitoring in Thar Desert using satellite-based drought indices and geo-informatics techniques. Proceedings 2(5):179. https://doi.org/10.3390/ecws-2-04948

Boroughani M, Pourhashemi S, Hashemi H, Salehi M, Amirahmadi A, Asadi MAZ, Berndts-son R (2020) Application of remote sensing techniques and machine learning algorithms in dust source detection and dust source susceptibility mapping. Ecol Inform 56:101059. https://doi.org/10.1016/j.ecoinf.2020.101059

CGLS-LST (2021) Copernicus global land service—land surface temperature. https://land.copernicus.eu/global/products/lst

CGLS-NDVI (2021) Copernicus global land service. https://land.copernicus.eu/global/products/ndvi

Chandra S, Satheesh SK, Srinivasan J (2004) Can the state of mixing of black carbon aerosols explain the mystery of 'excess' atmospheric absorption? Geophys Res Lett 31. https://doi.org/10.1029/2004GL020662

Chhabra A, Turakhia T, Chauhan P (2021) Impacts of a Mesoscale dust storm on aerosols characteristics, optical and radiative properties over a semiarid region, Western India. J Indian Soc Remote Sens 1-9. https://doi.org/10.1007/s12524-021-01313-w

Chouhan TS, Sharma UK (2009) Desert ecosystems in India. In: Del Claro K, Oliveira PS, Rico-Gray V (eds) Tropical biology and conservation management-Volume X: Savanna Ecosystems. EOLSS Publications. Oxford, United Kingdom

Cohen H, Laronne JB (2005) High rates of sediment transport by flashfloods in the Southern Judean Desert, Israel. Hydrol Process 19(8):1687–1702

Cooke RU (1981) Salt weathering in deserts. Proc Geol Assoc 92(1):1–16. https://doi.org/10.1016/S0016-7878(81)80015-6

Cressman K (2016) Desert locust. In: Shroder JF, Sivanpillai R (eds) Biological and environmental hazards, risks, and disasters. Elsevier, pp 87–105

Cressman K, Stefanski R (2016) Weather and desert locusts. FAO, Rome, UN

Cressman K (2013) Role of remote sensing in desert locust early warning. J Appl Remote Sens 7(1):075098

Cressman K (2021) Technical innovations in global early warning in support of desert locust area-wide management. In: Hendrichs J, Pereira R, Vreysen MJ (eds) Area-wide integrated pest management: development and field application. CRC Press. Oxon, United Kingdom

Culmsee H (2002) The habitat functions of vegetation in relation to the behaviour of the desert locust Schistocerca gregaria (Forskal) (Acrididae: Orthoptera)-a study in Mauritania (West Africa) Phytocoenologia 32(4):645–664

D'Odorico P, Bhattachan A, Davis KF, Ravi S, Runyan CW (2013) Global desertification: drivers and feedbacks. Adv Water Resour 51:326–344

Dagvadorj D, Natsagdorj L, Dorjpurev J, Namkhainyam B, Gomboluudev P, Batimaa P, Jugder D, Mijiddorj R, Davaa G, Erdenetsetseg B, Khaulenbek (2009) Climate Change Observation and Research in Mongolia, In: Dagvadorj D, Khuldorj B, Aldover R (eds) Mongolia assessment report on climate change 2009. Ministry of Environment, Nature and Tourism, Mongolia, Ulaanbaatar, pp 32–57

Dandabathula G, Verma M, Sitiraju SR, Jha CS (2020) Geospatial opinion on unusual locust swarm invasions during Amphan cyclone. J Geosci Environ Prot 8(12):144–161. https://doi.org/10.4236/gep.2020.812009

Dandabathula G, Bera AK, Rao SS, Jha CS (2020b) Earth observation satellites for locust surveillance. Geography and you. https://geographyandyou.com/earth-observation-satellites-for-locust-surveillance/

Deepshika S, Satheesh SK (2005) Regional distribution of absorbing efficiency of dust aerosols over India and adjacent continents inferred using satellite remote sensing. Geophys Res Lett 32(3). https://doi.org/10.1029/2004GL022091

DeSouza-Machado SG, Strow LL, Hannon SE, Motteler HE (2006) Infrared dust spectral signatures from AIRS. Geophys Res Lett 33(3). https://doi.org/10.1029/2005GL024364

Ding L, Ma L, Li L, Liu C, Li N, Yang Z, Yao Y, Lu H (2021) A survey of remote sensing and geo-graphic information system applications for flash floods. Remote Sens 13(9):1818. https://doi.org/10.3390/rs13091818

Doehne E (2002) Salt weathering: a selective review. In: Siegesmund S, Weiss T, Vollbrecht A (eds) Natural stones, weathering phenomena, conservation strategies and case studies. Geol Soc Spec Publ 205:43–56

Ebrahimi-Khusfi Z, Taghizadeh-Mehrjardi R, Mirakbari M (2021) Evaluation of machine learning models for predicting the temporal variations of dust storm index in arid regions of Iran. Atmos Pollut Res 12(1):134–147. https://doi.org/10.1016/j.apr.2020.08.029

Ellenburg WL, Mishra V, Roberts JB, Limaye AS, Case JL, Blankenship CB, Cressman K (2021) Detecting desert locust breeding grounds: a satellite-assisted modeling approach. Remote Sens 13(7):1276

eMODIS (2018) USGS EROS archive—vegetation monitoring—EROS Moderate Resolution Imaging Spectrometer (eMODIS). https://www.usgs.gov/centers/eros/science/usgs-eros-archive-vegetation-monitoring-eros-moderate-resolution-imaging

ERA5 (2021) ECMWF reanalysis 5th generation. https://www.ecmwf.int/en/forecasts/datasets/reanalysis-datasets/era5

Escorihuela MJ, Merlin O, Stefan V, Moyano G, Eweys OA, Zribi M, Kamara S, Benahi AS, Ebbe MA, Chihrane J, Ghaout S (2018) SMOS based high resolution soil moisture estimates for desert locust preventive management. Remote Sens Appl Soc Environ 1(11):140–150

Ezcurra E (ed) (2006) Global deserts outlook. UNEP/Earthprint, Nairobi, Kenya, p 148

FAO (2021) The impact of disasters and crises on agriculture and food security: 2021. Rome. https://doi.org/10.4060/cb3673en

FAO-DLIS (2021) Food and agriculture organization of the United States—locust watch: desert locust INFORMATION service. Available at https://www.fao.org/ag/locusts/en/activ/DLIS/dailyphotos/index.html

FAO-Soil (2021) Harmonized world soil database v 1.2. https://www.fao.org/soils-portal/data-hub/soil-maps-and-databases/harmonized-world-soil-database-v12/en/

Gómez D, Salvador P, Sanz J, Casanova C, Taratiel D, Casanova JL (2019) Desert locust detection using earth observation satellite data in Mauritania. J Arid Environ 164:29–37

Gómez D, Salvador P, Sanz J, Casanova JL (2020) Modelling desert locust presences using 32-year soil moisture data on a large-scale. Ecol Indic 117:106655

Gómez D, Salvador P, Sanz J, Rodrigo JF, Gil J, Casanova JL (2021) Prediction of desert locust breeding areas using machine learning methods and SMOS (MIR_SMNRT2) near real time product. J Arid Environ 194:104599

Goudarzi G, Shirmardi M, Khodarahmi F, Hashemi-Shahraki A, Alavi N, Ankali KA, Babaei AA, Soleimani Z, Marzouni MB (2014) Particulate matter and bacteria characteristics of the Middle East Dust (MED) storms over Ahvaz, Iran. Aerobiologia (bologna) 30(4):345–356

Goudie AS (2009) Dust storms: recent developments. J Environ Manage 90(1):89–94

Goudie A, Seely M. (2011) World heritage desert landscapes: potential priorities for the recognition of desert landscapes and geomorphological sites on the World Heritage List. International Union for Conservation of Nature (IUCN), Gland

GPM (2021) Global precipitation measurement. https://gpm.nasa.gov/data

Gunn DL, Perry FC, Seymour WG, Telford TM, Wright EN, Yeo D (1948) Behaviour of the desert locust in Kenya in Relation to aircraft spraying. Anti-Locust Bulletin 3, London

Gupta AK, Tyagi P, Sehgal VK (2011) Drought disaster challenges and mitigation in India: strategic appraisal. Curr Sci 25:1795–1806

Hao X, Qu JJ (2007) Saharan dust storm detection using moderate resolution imaging spectroradiometer thermal infrared bands. J Appl Remote Sens 1(1):013510

Hersbach H, Bell B, Berrisford P, Hirahara S, Horányi A, Muñoz-Sabater J, Simmons A (2020) The ERA5 global reanalysis. Q J R Meteorol Soc 146(730):1999–2049

Hielkema JU (1981) Desert locust habitat monitoring with satellite remote sensing. ITC J (Netherlands)

Holt J, Cheke RA (1996) Models of desert locust phase changes. Ecol Modell 91(1–3):131–137

Hong G, Yang P, Huang HL, Ackerman SA, Sokolik IN (2006) Simulation of high-spectral-resolution infrared signature of overlapping cirrus clouds and mineral dust. Geophys Res Lett 33(4)

House PK, Baker VR (2001) Paleohydrology of flash floods in small desert watersheds in Western Arizona. Water Resour Res 37(6):1825–1839

Hu XQ, Lu NM, Niu T, Zhang P (2008) Operational retrieval of Asian sand and dust storm from FY-2C geostationary meteorological satellite and its application to real time forecast in Asia. Atmos Chem Phys 8(6):1649–1659

Hua NP, Kobayashi F, Iwasaka Y, Shi GY, Naganuma T (2007) Detailed identification of desert-originated bacteria carried by Asian dust storms to Japan. Aerobiologia (Bologna) 23(4):291–298

Huang J, Minnis P, Yi Y, Tang Q, Wang X, Hu Y, Liu Z, Ayers K, Trepte C, Winker D (2007) Summer dust aerosols detected from CALIPSO over the Tibetan Plateau. Geophys Res Lett 34(18)

Hunter-Jones P (1964) Egg development in the desert locust (Schistocerca gregaria Forsk.) in relation to the availability of water. In: Proceedings of the royal entomological society of London. Series A, general entomology, vol 39, issue (1–3), pp 25–33. Blackwell Publishing Ltd, Oxford, UK

ICAR-NBSSLUP (2021) Indian council of agricultural research—National bureau of soil survey and land use planning. https://www.nbsslup.in/publications.html
IMD (2021) India Meteorological Department. https://mausam.imd.gov.in/imd_latest/contents/index_rainfall_state_new.php
ISRO (2016) INSAT-3DR Augments INSAT-3D for Improved Weather Monitoring and Prediction. https://www.isro.gov.in/insat-3dr-augments-insat-3d-improved-weather-monitoring-and-prediction
Jebali A, Zare M, Ekhtesasi MR, Jafari R (2021) A new threshold free dust storm detection index based on MODIS reflectance and thermal bands. Gisci Remote Sens 13:1–26
Jodha NS (1969) Drought and scarcity in the Rajasthan desert: some basic issues. Econ Polit Wkly 19:699–703
Kar A (2018) Desertification: causes and effects. In: Bartlett D, Singh R (eds) Exploring natural hazards—a case study approach. Chapman and Hall/CRC, pp 159–206
Kennedy JS (1951) The migration of the desert locust (Schistocerca gregaria Forsk.). I. The behaviour of swarms. II. A theory of long-range migrations. Philos Trans R Soc Lond, B Biol Sci 31:163–290
Khosravi H, Haydari E, Shekoohizadegan S, Zareie S (2017) Assessment the effect of drought on vegetation in desert area using landsat data. Egypt J Remote Sens Space Sci 1(20):S3-12
Kimathi E, Tonnang HE, Subramanian S, Cressman K, Abdel-Rahman EM, Tesfayohannes M, Niassy S, Torto B, Dubois T, Tanga CM, Kassie M (2020) Prediction of breeding regions for the desert locust Schistocerca gregaria in East Africa. Sci Rep 10(1):1–0
Klein I, Oppelt N, Kuenzer C (2021) Application of remote sensing data for locust research and management—a review. Insects 12(3):233
Kok JF, Parteli EJ, Michaels TI, Karam DB (2012) The physics of wind-blown sand and dust. Rep Prog Phys 75(10):106901
Kumar KS, Rahman AA (2021) Early detection of locust swarms using deep learning. In: Patnaik S, Yang XS, Sethi IK (eds) Advances in machine learning and computational intelligence: proceedings of ICMLCI 2019. Springer Nature. Singapore, pp 303–310
Lambin E, Chasek P, Downing T, Kerven C, Kleidon A, Leemans R, Lüdeke M, Prince S, Xue Y (2002) The interplay between international and local processes affecting desertification. In: Reynolds JF, Stafford Smith DM (eds) Do humans cause deserts. Global desertification: do humans cause deserts. Dahlem University Press, Berlin, Germany, pp 387–401
Latchininsky AV (2013) Locusts and remote sensing: a review. J Appl Remote Sens 7(1):075099
Legrand M, Plana-Fattori A, N'doumé C (2001) Satellite detection of dust using the IR imagery of Meteosat: 1. Infrared difference dust index. J Geophys Res Atmos 106(D16):18251–18274
Li J, Wong MS, Lee KH, Nichol J, Chan PW (2021) Review of dust storm detection algorithms for multispectral satellite sensors. Atmos Res 250:105398
Locust-Hub (2021) FAO locust hub. https://locust-hub-hqfao.hub.arcgis.com/
Long T, Hu C, Wang R, Zhang T, Kong S, Li W, Cai J, Tian W, Zeng T (2020) Entomological radar overview: system and signal processing. IEEE Aerosp Electron 35(1):20–32
Lorenz MW (2009) Migration and trans-Atlantic flight of locusts. Quat Int 196(1–2):4–12
LWO (2021) Locust Warning Organization. http://ppqs.gov.in/contactus/locust-warning-organizationlwo
Mashaly J, Ghoneim E (2018) Flash flood hazard using optical, radar, and stereo-pair derived dem: Eastern desert. Egypt Remote Sens 10(8):1204
Masoudi M, Jokar P, Pradhan B (2018) A new approach for land degradation and desertification assessment using geospatial techniques. Nat Hazards Earth Syst Sci 18(4):1133–1140
Matthews GA (2021) New technology for desert locust control. Agronomy 11(6):1052
McCaffery AR, Simpson SJ, Islam MS, Roessingh PE (1998) A gregarizing factor present in the egg pod foam of the desert locust Schistocerca gregaria. J Exp Biol 201(3):347–363
Mehta PS, Kunte PD (2014) Detection and monitoring of two dust storm events by multispectral modis images. Jerad Publ. http://drs.nio.org/drs/handle/2264/4568
Middleton NJ (1986) A geography of dust storms in South-West Asia. J Climatol 6(2):183–196

Mirzabaev A, Wu J, Evans J, García-Oliva F, Hussein IA, Iqbal MH, Kimutai J, Knowles T, Meza F, Nedjroaoui D, Tena F (2019) Desertification. In: Shukla PR, Skea J, Calvo Buendia E, Masson-Delmotte V, Pörtner HO, Roberts DC, Zhai P, Slade R, Connors S, Van Diemen R, Ferrat M (eds) IPCC, 2019: Climate Change and Land: an IPCC special report on climate change, desertification, land degradation, sustainable land management, food security, and greenhouse gas fluxes in terrestrial ecosystems 3. Geneva, Switzerland. pp 249–343

Mishra MK, Chauhan P, Sahay A (2015) Detection of Asian dust storms from geostationary satellite observations of the INSAT-3D imager. Int J Remote Sens 36(18):4668–4682

Moharana PC, Kar A (2013) Fluvial process measurement of arid ephemeral channels in western Rajasthan. In: Gaur M (ed) Remote sensing applications in dryland natural resource management. New India Publishing Agency, New Delhi, India, pp 37–51

MOSDAC (2021) Meteorological and Oceanographic Satellite Data Archival Centre. https://www.mosdac.gov.in/

MOSDAC-NDVI (2021) 10 day composite-normalized difference vegetation index. https://mosdac.gov.in/catalog/doi/13

Narain P, Sharma KD, Rao AS, Singh DV, Mathur BK, Ahuja UR (2000) Strategy to combat drought and famine in the Indian arid zone. CAZRI, Jodhpur, India

Natsagdorj L, Jugder D, Chung YS (2003) Analysis of dust storms observed in Mongolia during 1937–1999. Atmos Environ 37(9–10):1401–1411

NCDC-NOAA (2012) Storm events database. National oceanic and atmospheric administration. National Climatic Data Center. http://www.ncdc.noaa.gov/

NICES (2021) National information system for climate and environment studies. https://www.nrsc.gov.in/EO_Earth_Objective

Nicholson SE (2011) Dryland climatology. Cambridge University Press. https://doi.org/10.1017/CBO9780511973840

Olsson L (1993) On the causes of famine: drought, desertification and market failure in the Sudan. Ambio 22(6):395–403

Parungo FP (1987) Marine aerosols in the marine aerosols in the marine upwelling regions. J Aerosol Sci 18:277–290

Piou C, Gay PE, Benahi AS, Babah Ebbe MA, Chihrane J, Ghaout S, Cisse S, Diakite F, Lazar M, Cressman K, Merlin O (2019) Soil moisture from remote sensing to forecast desert locust presence. J Appl Ecol 56(4):966–975

Prasad AK, Singh RP (2007) Changes in aerosol parameters during major dust storm events (2001–2005) over the Indo-Gangetic Plains using AERONET and MODIS data. J Geophys Res Atmos 112(D9). https://doi.org/10.1029/2006JD007778

Prata AJ (1989) Infrared radiative transfer calculations for volcanic ash clouds. Geophys Res Lett 16(11):1293–1296

Prata AJ (1989) Observations of volcanic ash clouds in the 10–12 μm window using AVHRR/2 data. Int J Remote Sens 10(4–5):751–761

PSL-CPS (2021) CPC global daily temperature. https://psl.noaa.gov/data/gridded/data.cpc.globaltemp.html

Ramchandra Rao RBY (1942) Some results of studies on the desert locust (Schistocerca gregaria, Forsk.) in India. Bull Entomol Res 33:241–265

Ramon J, Lledó L, Torralba V, Soret A, Doblas-Reyes FJ (2019) What global reanalysis best represents near-surface winds? Q J R Meteorol Soc 145(724):3236–3251

Reid I, Powell DM, Laronne JB, Garcia C (1994) Flash floods in desert rivers: studying the unexpected. EOS Trans Am Geophys Union 75:452

Rhodes K, Sagan V (2021) Integrating remote sensing and machine learning for regional-scale habitat mapping: advances and future challenges for desert locust monitoring. IEEE Trans Geosci Remote Sens. https://doi.org/10.1109/MGRS.2021.3097280

Richardson CH, Nemeth DJ (1991) Hurricane-borne African locusts (Schistocerca gregaria) on the Windward Islands. GeoJournal 23(4):349–357

Rosenberg J, Burt PJA (1999) Windborne displacements of desert locusts from Africa to the Caribbean and South America. Aerobiologia (bologna) 15:167–175
Roskovensky JK, Liou KN (2005) Differentiating airborne dust from cirrus clouds using MODIS data. Geophys Res Lett 32(12). https://doi.org/10.1029/2005GL022798
Salim SA, Amin MR, Rahman MS, Arafat MY, Khan R (2021) An IoT-based smart agriculture system with locust prevention and data prediction. In: 8th International conference on information technology, computer and electrical engineering (ICITACEE). IEEE, pp 201–206
Salunkhe SS, Bera AK, Rao SS, Venkataraman VR, Raj U, Murthy YK (2018) Evaluation of indicators for desertification risk assessment in part of Thar Desert Region of Rajasthan using geospatial techniques. J Earth Syst Sci 127(8):1–24
Santra P, Mertia RS, Kumawat RN, Sinha NK, Mahla HR (2013) Loss of soil carbon and nitrogen through wind erosion in the Indian Thar Desert. J Agric Phys 13(1):13–21
Satheesh SK, Moorthy K (2005) Radiative effects of natural aerosols: a review. Atmos Environ 39:2089–2110
Schepanski K, Wright TJ, Knippertz P (2012) Evidence for flash floods over deserts from loss of coherence in InSAR imagery. J Geophys Res Atmos 117(D20). https://doi.org/10.1029/2012JD017580
Schwarzenbacher F (2021) Habitat suitability modeling for Desert Locust in the Awash River basin: Estimation of the breeding probability based on remote sensing, climatology and environment data. Doctoral dissertation. University of Wuerzburg
Seinfeld JH (2004) Regional climatic and atmospheric chemical effects of Asian dust and pollution. Bull Am Meteorol Soc 85:367–380. https://doi.org/10.1175/BAMS-85-3-367
Shao Z, Feng X, Bai L, Jiao H, Zhang Y, Li D, Fan H, Huang X, Ding Y, Altan O, Saleem N (2021) Monitoring and predicting desert locust plague severity in Asia-Africa using multisource remote sensing time-series data. IEEE J Sel Top Appl Earth Obs Remote Sens 14:8638–8652
Shi L, Zhang J, Zhang D, Igbawua T, Liu Y (2020) Developing a dust storm detection method combining Support Vector Machine and satellite data in typical dust regions of Asia. Adv Space Res 65(4):1263–1278
Sivaperuman C, Baqri QH, Ramaswamy G, Naseema M (eds) (2009) Faunal ecology and conservation of the Great Indian Desert. Springer, Berlin Heidelberg
SMAP (2021) Soil moisture active passive. https://smap.jpl.nasa.gov./data/
SoilGrids250m (2017) SoilGrids and WoSIS. https://soilgrids.org/
Steenburgh WJ, Massey JD, Painter T (2012) Episodic dust events of Utah's Wasatch front and adjoining region. Appl Meteorol Climatol 5(9):1654–1669
Symmons PM, Cressman K (2001) Desert locust guidelines: biology and behaviour. FAO, Rome
Thenkabail PS, Gamage MSDN, Smakhtin VU (2004). The use of remote sensing data for drought assessment and monitoring in Southwest Asia. Reserch Report 85. IWMI, Colombo, Sri Lanka
Tucker CJ, Hielkema JU, Roffey J (1985) The potential of satellite remote sensing of ecological conditions for survey and forecasting desert-locust activity. Int J Remote Sens 6(1):127–138
UNDRR (2021) United Nations office for disaster risk reduction. https://www.undrr.org
UNEP-WMO-UNCCD (2016) Global assessment of sand and dust storms. United Nations Environment Programme, Nairobi
Urban FE, Reynolds RL, Fulton R (2009) The dynamic interaction of climate, vegetation, and dust emission, Mojave Desert, USA. In: Fernandez-Bernal A, De La Rosa MA (eds) Arid environments and wind erosion. Nova Science Publishers Inc., New York, pp 1–25
Uvarov BP (1934) The locust outbreak in Africa and Western Asian in 1933. Publication No. 63-80-3, London: His Majesty's Stationery Office
Vaghefi SA, Keykhai M, Jahanbakhshi F, Sheikholeslami J, Ahmadi A, Yang H, Abbaspour KC (2019) The future of extreme climate in Iran. Sci Rep 9(1):1–11
Van Der Werf W, Woldewahid G, Van Huis A, Butrous M, Sykora K (2005) Plant communities can predict the distribution of solitarious desert locust Schistocerca gregaria. J App Ecol 42(5):989–997

Voss F, Dreiser U (1997) Mapping of desert locust habitats using remote sensing techniques. In: Krall S, Peveling R, Diallo BD (eds) New strategies in locust control. Birkhäuser Basel

Wang Z, Liu C, Hu Q, Dong Y, Liu H, Xing C, Tan W (2021) Quantify the Contribution of Dust and Anthropogenic Sources to Aerosols in North China by Lidar and Validated with CALIPSO. Remote Sens 13(9):1811

Warner T (2008) Weather-related disasters in arid lands. In: Gad-el-Hak M (ed) Large-scale disasters: prediction, control, and mitigation. Cambridge University Press, pp 377–426

Washington R, Todd M, Middleton NJ, Goudie AS (2003) Dust-storm source areas determined by the total ozone monitoring spectrometer and surface observations. Ann Am Assoc Geogr 93(2):297–313

Weis-Fogh T (1956) Biology and physics of locust flight II. Flight performance of the desert locust (Schistocerca gregaria). Philos Trans R Soc Lond 239:459–510

Whitford WG, Duval BD (2019) Ecology of desert systems. Academic Press, Oxford, United Kingdom

Wilcox B (2012) Dust storms roll across America. United States Geological Survey Science Features. http://www.usgs.gov/blogs/features/usgs_top_story/dust-storms-roll-across-arizona-2/

WMO-FAO (2016) Weather and desert locusts, WMO-No. 1175. World Meteorological Organization (WMO)—Food and Agriculture Organization of the United Nations, Rome

Yang H, Yang X, Heskel M, Sun S, Tang J (2017) Seasonal variations of leaf and canopy properties tracked by ground-based NDVI imagery in a temperate forest. Sci Rep 7(1):1–10

Zhao X (2012) Asian dust detection from the satellite observations of moderate resolution imaging spectroradiometer (MODIS). Aerosol Air Qual Res 12(6):1073–1080

Zhao TXP, Ackerman S, Guo W (2010) Dust and smoke detection for multi-channel imagers. Remote Sens 2(10):2347–2368

Zhao X, Xia H, Pan L, Song H, Niu W, Wang R, Li R, Bian X, Guo Y, Qin Y (2021) Drought monitoring over Yellow River basin from 2003–2019 using reconstructed MODIS land surface temperature in Google Earth Engine. Remote Sens 13(18):3748

Chapter 17
Satellite-Based Terrestrial Evapotranspiration Product for India

K. Chandrasekar, Nidhi Misra, J. Mohammed Ahamed, Anurag Mishra, P. Madhavi, K. Abdul Hakeem, P. V. Raju, V. V. Rao, and C. S. Jha

Abstract Evapotranspiration (ET) is the major component of the terrestrial water cycle. Information on ET will help monitor crop water requirement, crop phenology & production, and better irrigation water management. Despite its importance, ET's near-real-time estimation at a varied spatial and temporal scale is not available. Different types of instruments are used to measure ET, which includes simple Lysimeter to more complex eddy covariance flux towers. However, for operational estimation of ET at a regional scale, methods like crop models or remote sensing-based techniques provide a reliable alternative. Estimation of ET using the remote sensing technique uses the various geophysical and biophysical parameters collected from the satellite platform. The satellite platform enables to estimate ET over a large area at a frequent time interval with reliable accuracy levels acceptable for several applications. This chapter discusses the different methods of deriving the

K. Chandrasekar (✉) · N. Misra · A. Mishra · P. Madhavi · K. Abdul Hakeem · P. V. Raju · V. V. Rao · C. S. Jha
National Remote Sensing Centre, Hyderabad, India
e-mail: chandrasekar_k@nrsc.gov.in

N. Misra
e-mail: nidhi_misra@nrsc.gov.in

A. Mishra
e-mail: anurag_mishra@nrsc.gov.in

P. Madhavi
e-mail: madhavi_p@nrsc.gov.in

K. Abdul Hakeem
e-mail: abdulhakeem_k@nrsc.gov.in

P. V. Raju
e-mail: raju_pv@nrsc.gov.in

V. V. Rao
e-mail: vvrao@nrsc.gov.in

J. Mohammed Ahamed
National Remote Sensing Centre, Bangaluru, India
e-mail: mohammedahamed_j@nrsc.gov.in

C. S. Jha et al. (eds.), *Geospatial Technologies for Resources Planning and Management*, Water Science and Technology Library 115,
https://doi.org/10.1007/978-3-030-98981-1_17

ET and the justification for adopting the Priestley Taylor algorithm. It also describes the methodology of deriving the terrestrial ET in a near real-time basis and discusses the intra-seasonal dynamics and comparison with the field ET data.

Keywords Evapotranspiration · Priestley Taylor algorithm · Net radiation · Land surface temperature · Vegetation index

17.1 Introduction

Water is a very important constituent for the existence of life on earth. It is very dynamic by changing its forms from solid, liquid, and vapor during the hydrologic cycle. Net radiation from the Sun is the major driver of this phase transformation (Allen et al. 2007). The major components of the hydrological cycle are Precipitation and Evapotranspiration (ET). While precipitation is the downward flux of water, ET is the upward flux of which is the major and important component of the terrestrial hydrological cycle (Penman 1948). The flow of energy and water exchange between hydrosphere, atmosphere, and biosphere is enabled through evapotranspiration process (Priestley and Taylor 1972; Monteith 1973; Sellers et al. 1996). ET thus becomes quantitatively the second-largest component of the hydrological cycle after precipitation (Mu et al. 2013; Korzoun et al. 1978; L'vovich and White 1990). ET is defined as an integrated term involving processes during which surface water and soil moisture get converted into atmospheric water vapor (Dingman 2002).

Agriculture and forests, which consume most of the global freshwater are the major contributors of terrestrial evapotranspiration (Biggset al. 2015; Hoekstra and Mekonnen 2012; Shiklomanov 2000). To monitor crop water requirement, improved irrigation water management, crop phenology, and production estimation require information on ET (Glenn et al. 2011). Despite its importance, ET's near-real-time estimation at a varied spatial and temporal scale is not available. Different types of instruments are used to measure ET, which includes Lysimeter, which estimates ET over a spatial scale from ~1 m and up to ~10–1000 m using eddy covariance flux towers (Biggs et al. 2015). However, for operational estimation of ET at a regional scale, methodologies like the crop models or the remote sensing-based technology provide a reliable alternative. Estimation of ET using the remote sensing technique uses the various geophysical and biophysical parameters collected from the satellite platform. The satellite platform enables estimation ET over a large area, at frequent time intervals with reliable accuracy levels acceptable for several applications (Biggs et al. 2015; Glenn et al. 2007; Melesse et al. 2008). This chapter describes India's derivation of the operational satellite-based terrestrial ET at a spatial resolution of 5.5×5.5 km^2 on a daily time interval.

17.2 Theoretical Background

Evapotranspiration is the process by which the water from the soil and vegetation gets transported from the earth to atmosphere. In this process, the energy also gets transported from land to the atmosphere. The main drivers for this process are (i) solar energy, (ii) vapor pressure gradient between the evaporating surface and the atmosphere, and (iii) the resistance that the land cover offers to the process. The entire process of evapotranspiration can be defined as the residual of the energy balance model for the land surfaces

$$\lambda E = R_n - G - H \tag{17.1}$$

where

λE is the latent heat flux (W/m^2),

R_n is the net radiation (W/m^2),

G is the soil heat flux (W/m^2) and

H is the sensible heat flux (W/m^2).

Theoretically, estimation of ET can be carried out using

- Mass balance methods
- Energy balance methods
- Combination of mass and energy balance methods.

The ET assessment can be derived using field instruments like the Lysimeter, eddy covariance flux tower, and Scintillometer (French et al. 2012; Petropoulos et al. 2013; Swinbank 1951). These instruments provide direct measurements of ET. However, these measurements represent a spatial scale from a few meters in Lysimeter to a few hundred meters in case of eddy covariance flux towers. The major constraint with this method is that it is prohibitively costly, requires continuous maintenance, and may not bring out the spatial variability of ET (Ershadi et al. 2013). To assess ET at a regional scale, empirical/statistical methods can be used to upscale the point measured ET to large scales with earth observation proxies (Glenn et al. 2008a, b; Jung et al. 2011; Nagler et al. 2009). ET estimated using empirical models uses minimal weather parameters to compute ET (Shahidian et al. 2012). Blaney-Criddle method (Blaney and Criddle 1950; Brooks et al. 2012; Hargreaves-Samani 1985) uses just the temperature to estimate the ET. Another way to assess ET at a regional scale are the physical models which estimates ET as a residual of the energy balance components (Bastiaanssen et al. 1998a, b, 2005; Overgaard et al. 2006; Ma et al. 2002; Allen et al. 2007). Physical models use the meteorological parameters and remotely sensed inputs to estimate the energy fluxes. The energy balance approach is based on the principle that the net energy exchange is considered constant between water, earth, and atmosphere (Brooks et al. 2013).

The three coupled equation that governs the energy partitions at the earth's surface are

$$H = \rho c_p \frac{T_s - T_a}{r_a} \tag{17.2}$$

$$\lambda E = \frac{\rho c_p}{\gamma} \frac{e_{\text{sat}} - e}{r_a + r_s} \tag{17.3}$$

$$A' = R_n - \Delta S - G = H + \lambda E \tag{17.4}$$

where,

H is the sensible heat flux (W/m^2),

λE is the latent heat flux (W/m^2),

A' is the available energy (W/m^2),

R_n is the net radiation (W/m^2),

G is the soil heat flux (W/m^2),

ΔS is the heat storage flux (W/m^2),

ρ is air density (kg/m3),

c_p is the specific heat capacity of air (~1.013 kJ/kg/K),

T_s, T_a is the aerodynamic surface and air temperatures (K),

r_a is the aerodynamic resistance (s/m),

e_{sat}, e is the water vapor pressure at the evaporating surface and in the air (kPa),

r_s is the surface resistance to evapotranspiration, which is an effective resistance to evaporation from land surface and transpiration from the plant canopy.

The psychrometric constant γ is given by

$$\gamma = c_p \times P_a \times M_a / (\lambda \times M_w) \tag{17.5}$$

where

M_a and M_w are the molecular masses of dry air and wet air and

P_a is atmospheric pressure (kPa).

Several operational energy balance-based ET or λE retrieval algorithms have been developed in the last four decades. The Surface Energy Balance Algorithm for Land (SEBAL), (Bastiaanssen et al. 1998a), Surface Energy Balance System (SEBS) (Su et al. 2002), Mapping Evapotranspiration at high Resolution with Internalized Calibration (METRIC) (Allen et al. 2007), Atmosphere-Land Exchange Inversion Model (ALEXI) (Norman 1995)and Two Source Model (TSM) (Kustas and Norman

1999) models are used to estimate ET using the surface energy balance principle. The basis of these models is either the Penman–Monteith equation or the Priestley-Taylor (P–T) equations with different assumptions associated with the respective model.

17.3 Study Area and Data Used

17.3.1 Study Area

The entire Indian sub-continent enveloped between 5° and 38° latitude and 66°–104° longitude is considered for this study. The study area has diverse agro-climatic conditions providing a wide range of precipitation and temperature regimes. The varied agroecosystem across the country will help us assess the unique evapotranspiration cycles of a region.

17.3.2 Data Used

The major input data used in this study can be categorized as meteorological data and satellite data.

17.3.2.1 Meteorological Data

The two main meteorological data required for resolving the energy balance technique adopted in this study (Priestley-Taylor method) are the air temperature and the dew point temperature. The temperature data used in this study is from the Automatic Weather Station (AWS) network of the India Meteorological Department (IMD).

The temperature data measured across the country by the AWS is then pushed to the Climate Data Analysis System (CDAS) at the National Remote Sensing Centre where it is processed, archived, and disseminated. If the IMD stations, which are the primary source, are non-functional within the Indian boundary, the meteorological data from the National Centers for Environmental Prediction (NCEP) reanalysis daily average data is used. The temperature data is lapse rate corrected using the CARTODEM data. The lapse rate fixed temperature data are interpolated, and the spatial air temperature and dew point temperature maps are derived. Table 17.1 shows the details of the meteorological data used in this study.

Table 17.1 Details of the air and dew point temperature

Weather data for ET estimation		Primary source	Temporal resolution	Spatial resolution	Data availability
Air temperature	Primary Input	IMD station point data	Hourly	Point data	April 2012 onwards
	Secondary Input	NOAA Gridded data (CPC)	Daily	0.5 decimal degree	1979 onwards
Dew point temperature/relative humidity	Primary Input	IMD station point data	Hourly	Point data	April 2012 onwards
	Secondary Input	NOAA Gridded data (NCEP reanalysis)	Daily	2.5 decimal degree	1948 onwards

17.3.2.2 Satellite Data

The satellite data products that are used in the implementation of the P–T algorithm are

- Insolation (INSAT 3D & 3DR)
- Outgoing Longwave Radiation (INSAT 3D & 3DR)
- Normalized Vegetation Difference Index (NDVI) (Soumi-NPP)
- Land Surface Temperature (LST) (Soumi-NPP)
- Albedo (Soumi-NPP)
- Cloud Mask (Soumi-NPP).

17.3.2.3 Insolation

Solar insolation can be defined as the amount of solar radiation that reaches the earth's surface. The solar radiation which reaches the earth's surface after being attenuated by different constituents of the atmosphere is the primary form of solar insolation. The second form of solar insolation is diffused insolation, where the solar radiation reaches earth after scattering. In this study, the insolation product of the Indian National Satellite System (INSAT) 3D satellite system is being used. The insolation data is downloaded from the Meteorological & Oceanographic Satellite Data Archival Centre web portal (https://mosdac.gov.in) of Space Application Centre, ISRO. The insolation product is available at a daily time interval with a spatial resolution of 4 × 4 km with an accuracy of 90%. The detail of the INSAT 3D Insolation product is discussed in detail in the ATBD (http://www.mosdac.gov.in).

17.3.2.4 Outgoing Longwave Radiation

The Outgoing Longwave Radiation (OLR) is one of the important components of the net radiation budget. A considerable amount of energy is dissipated through the longwave radiation from the earth's surface which is responsible for the temperature of the atmosphere and earth (Singh 2013). The OLR can be defined as the thermal radiation ranging from 4 to 100 μ which are emitted through the earth-atmosphere to outer space (Singh 2013). An algorithm to estimate the OLR from the INSAT-3Dimager has been developed under the framework of the INSAT Meteorological Data Processing System (IMDPS). The detailed methodology on the derivation of OLR product is described in the ATBD document (https://mosdac.gov.in). The algorithm uses the INSAT 3D data to derive the 4 × 4 km OLR products operationally over the Indian Sub-continent (Singh 2013). The pixel value of OLR product values ranges from 50 to 400 W/m^2 with an accuracy of 3%.

17.3.2.5 Normalized Difference Vegetation Index

The Soumi-NPP's (S-NPP) Visible Infrared Imaging Radiometer Suite (VIIRS) instrument daily Vegetation Index (VI) product is used in the analysis. The top of the canopy reflectance data in the red region (0.6–0.68 μm) and Near-Infrared Region (NIR) (0.85–0.88 μm) from the Visible Infrared Imaging Radiometer Suite (VIIRS) onboard S-NPP are used in the derivation of NDVI. The NDVI products for VIIRS are defined by:

$$\mathrm{NDVI} = \frac{\rho_{\mathrm{nir}} - \rho_{\mathrm{red}}}{\rho_{\mathrm{nir}} + \rho_{\mathrm{red}}} \tag{17.6}$$

where ρ_{nir} and ρ_{red} are the directional reflectance in the near-infrared and red region, respectively (Godin, 2014).

17.3.2.6 Land Surface Temperature

The S-NPP VIIRS Land Surface Temperature (LST) gives the skin surface temperature of the land surface. The brightness temperature of the two thermal bands (10.8, 12 μm), are used in the split-window algorithm to derive LST for each land cover type. Under most optimal conditions, another dual split-window algorithm that uses four thermal brightness temperatures bands (10.8, 12, 3.75, and 4.005 μm) is used to retrieve LST. Under clear-sky conditions, the dynamic range of LST extends from 213 to 343 °K with an accuracy of 1.4 °K (Baker, 2013).

Table 17.2 Input satellite data for the Priestley-Taylor algorithm

Parameter	Source	Temporal resolution	Spatial resolution
Land surface temperature	NPP Suomi	Daily	750 m
Outgoing longwave radiation	INSAT 3D/3DR	30 min	4 km
Insolation	INSAT 3D/3DR	30 min	4 km
Cloud mask	NPP Suomi	Daily	750 m
NDVI	NPP Suomi	Daily	375 m
Albedo	NPP Suomi	Daily	750 m

17.3.2.7 Cloud Mask

Most optical remote sensing application requires accurate cloud pixel information. The VIIRS Cloud Mask (VCM) Intermediate Product (IP) has been developed for use with S-NPP, VIIRS Environmental Data Record (EDR) products. A number of cloud detection algorithms to determine the cloud pixel are implemented to provide information on cloud confidence of (i) confidently cloudy, (ii) probably cloudy, (iii) probably clear, and (iv) confidently clear. It also includes information on the phase of the cloud, such as (i) water, (ii) supercooled water or mixed phase, (iii) opaque ice, (iv) non-opaque ice or overlapping cloud (Pavolonis and Heidinger 2004).

17.3.2.8 Albedo

Albedo is defined as the ratio of the reflected radiant energy to the incoming solar irradiation generally expressed in percentage. It is an important parameter in the net radiation budget, weather prediction models, and climate change studies. The net short wave incoming radiation is a function of albedo, and hence it is an important parameter in the estimation of ET. In this study, the Land surface albedo (LSA), derived from VIIRS using the dark pixel sub-algorithm (DPSA) and the bright pixel sub-algorithm (BPSA), was used to retrieve the LSA.

Table 17.2 gives the consolidated details of the satellite-based input parameters used in the derivation of ET.

17.4 Methodology

Priestley Taylor's algorithm is a simplification of the Penman–Monteith equation (Priestley and Taylor 1972). The P–T method reduces the parameterization of aerodynamic and surface resistance and only uses the air temperature and dew point temperature without decreasing the accuracy of the AET estimates (Fisher 2008; Jin 2011; Priestley and Taylor 1972; Yao et al. 2015).

17.4.1 Priestley-Taylor Algorithm

In this study, the Priestley-Taylor algorithm has been used. The Priestley-Taylor algorithm for estimating the latent heat flux under saturated surface under conditions of minimal advection (λE_{PT}) is given by

$$\lambda E_{\mathrm{PT}} = \alpha \left[\frac{\Delta}{(\Delta + \gamma)} \right] (R_n - G) \tag{17.7}$$

Under the saturated soil moisture conditions, the Priestley-Taylor coefficient (α) takes a value of 1.26 (Ai and Yang 2016; Priestley and Taylor 1972; Parlange and Katul 1992). However, several studies have indicated α varies over the whole growing season for different crops and soil moisture conditions (Castellvi et al. 2001; Diaz-Espejo et al. 2005; Kustas et al. 1996; Lei and Yang 2010; Zhang et al. 2004). Under dry & hot weather and strong wind conditions, advection is common (Brutsaert 1982). Under such conditions, α is expected to increase from 1.6 to 1.8 (Castellvi et al. 2001; Flint and Childs 1991; Pereira 2004). Although 1.26 has been reported universally for open water surface, those values have not been necessarily obtained over bare soil or vegetated surface with unlimited soil water supply (Priestley and Taylor 1972).

Several studies, however, have used the thermal region of the electromagnetic spectrum to assess the crop stress, ET, and soil moisture deficiency (Carlson et al. 1994; Jackson et al. 1981; Jiang and Islam 2001, 2003, 1999; Moran et al. 1994; Price 1990). If the area under study is large enough to accommodate variability in the soil moisture and vegetation cover condition, the Surface Temperature (T_s) and Vegetation Index (VI) triangle space could provide better information on surface soil moisture status and crop water stress (Gillies et al. 1997; Nemani and Running 1989; Price 1990).

In the LST—VI triangle space given in Fig. 17.1, the LST is negatively correlated to VI along the upper boundary of the triangle space, which is called the dry edge, while the lower boundary is parallel to x-axis, which is called the cold edge (Sun et al. 2012). The LST—NDVI space interpretations elaborately dealt in (Sandholt et al. 2002). The triangle shape of the LST—NDVI space is influenced by Fractional vegetation cover, Evapotranspiration, Thermal properties of the surface, Net

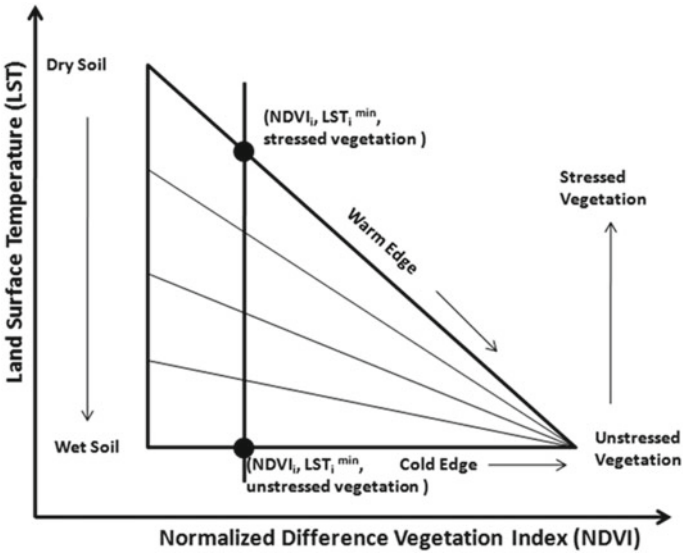

Fig. 17.1 Conceptual plot of LST-NDVI triangle

radiation, Atmospheric forcing, and surface roughness and interaction among these factors (Sandholt et al. 2002). The cold edge represents that there are potential evapotranspiration conditions with unlimited water supply while the warm upper edge represents that there is a limitation in water supply resulting in lesser evapotranspiration and more energy is available as sensible heat (Sandholt et al. 2002; Sun et al. 2012).

The Priestley-Taylor coefficient α is replaced by a coefficient α_e which accounts for a wide range of aerodynamic and crop resistance (Jiang and Islam 2001; Kalma et al. 2008). Using the scatter of LST and NDVI, under the full ranges of soil moisture availability and varied vegetation cover, α_e is derived. Here α_e overcomes the parameterizations of aerodynamic and surface resistance without decreasing the accuracy of the AET estimates (Fisher 2008; Jin 2011; Priestley and Taylor 1972; Yao et al. 2015). The LST-NDVI scatter plot is used to derive the αe value using simple linear interpolation between the warm and cold edge of the triangular distribution. The parameterization of α_e in this study has the same assumption of Jiang and Islam (2001), which is (Kalma et al. 2008):

$$\alpha_{e\,\max} = 1.26 \text{ for the densely vegetated and well - watered pixel and}$$
$$\alpha_{e\,\min} = 0 \text{ for the driest bare soil.}$$

Hence the estimation of actual α_e value for each pixel using a NDVI image and its corresponding LST image is given by

$$\alpha_e = \alpha_e \max[\,\mathrm{LST}_{\max} - \mathrm{LST}_i\,]/[\mathrm{LST}_{\max} - \mathrm{LST}_{\min}] \tag{17.8}$$

where the LST_{max} and LST_{min} are the value of LST in the warm and cold edge for the corresponding NDVI which corresponds to the lowest and highest evaporation rates, respectively.

$$LST_{max} = a + b\ NDVI_{max} \tag{17.9}$$

$$LST_{min} = a' + b'\ NDVI_{min} \tag{17.10}$$

where NDVI is the normalized difference vegetation index, a and b are the intercept and slope of the linear warm edge and a' and b' are the intercept and slope of the linear cold edge. The values of a, b, a', and b' are estimated over the study area with soil moisture ranging from field capacity to wilting point and vegetation density ranging from sparse vegetation to dense vegetation.

17.4.2 Net Radiation

Earth's net radiation is the sum of the net shortwave radiation and the net longwave radiation and is given by Eq. 17.11.

$$R_n = R_{S\downarrow} - R_{S\uparrow} + R_{L\downarrow} - R_{L\uparrow} \tag{17.11}$$

where, $R_S\downarrow$ denotes the incoming shortwave radiation (W/m^2), $R_{S\uparrow}$ denotes the reflected shortwave radiation (W/m^2), and $R_{L\downarrow}$ and $R_{L\uparrow}$ are the incoming and outgoing longwave radiations (W/m^2), respectively. These are the four components of net radiation. Net radiation can also be defined as the difference between the total upward and downward radiation fluxes. The net energy available at the earth's surface can be termed net radiation.

The four components of net radiations are explained in the following sections.

17.4.3 Net Shortwave Radiation

The net shortwave radiation is defined as the difference between the incoming and outgoing shortwave radiation ($R_{NS} = R_{S\downarrow} - R_{S\uparrow}$).

$$R_{NS} = R_{si}(1 - \alpha) \tag{17.12}$$

where R_{NS} is the net shortwave radiation, α is the shortwave band albedo estimated from the reflectance data of NPP-Suomi data as given in Liang (2001). R_{si} is the solar insolation which is solar radiation that reaches the earth's surface directly without being attenuated by different constituents of the atmosphere like water vapor,

ozone gas, aerosol particles, other air molecules, cloud, and fog. This study uses the insolation product derived from the Indian National Satellite System (INSAT) satellite system. The detail of the data and the algorithm used to derive the insolation product is given in the ATBD document (Bhattacharya 2015).

17.4.4 Net Longwave Radiation

The difference between incoming and outgoing longwave radiation is net longwave radiation, and it is expressed as:

$$L^* = L_{\downarrow} - L_{\uparrow} \tag{17.13}$$

17.4.5 Incoming Longwave Radiation

The downward longwave radiation is influenced by the atmospheric condition. The major atmospheric parameters that influence the downward longwave radiations are atmospheric temperature, atmospheric humidity, and the presence of other gases. Longwave radiation occurs due to water vapor, aerosol particles in the 3–100 μm bands. Prata (1996) developed a parameterization scheme for downward longwave radiation using vapor pressure and air temperature. The procedure for estimating net longwave radiation is given in Eqs. 17.14–17.20. This approach is valid for clear-sky conditions only.

$$R_L \downarrow = \varepsilon_a . \sigma . T_a^4 \tag{17.14}$$

where,

$$\varepsilon_a = (1 - (1 + \in) \exp(-(1.2 + 3\varepsilon)^{0.5} \tag{17.15}$$

$$\varepsilon = 46.5 * \frac{e_0}{T_a} \tag{17.16}$$

$\in_a$—Air emissivity

T_a—Air temperature

σ—Stefan-Boltzmann Constant,$5.67 \times 10^{-8} \frac{\mathrm{W}}{\mathrm{m^2 K^4}}$.

The screen level vapor pressure is estimated from Clausis-Clapeyron equation for vapor pressure given in Eq. 17.17.

$$e_0 = 6.11 \exp\left(\frac{L_v}{R_v}\left(\frac{1}{T_0} - \frac{1}{T_d}\right)\right). \tag{17.17}$$

Latent heat of vaporization, $L_v = 2.5 \times 10^6$ J/Kg
Gas constant for water vapor, $R_v = 461$ J/Kg K

T_0—Mean air temperature

T_d—Mean dew point temperature.

Air temperate and dew point temperature data is corrected with lapse rate data as given in Eq. 17.18.

$$\theta_a = T_a(P_o/P_z)^{R/mC_P} \tag{17.18}$$

where,

$$P_z = P_o[T_b/(T_b + \lambda z)]^{(mg/\lambda R)} \tag{17.19}$$

θ_a—Sea Level Potential Temperature (°K)

T_a—Air Temperature (°K)

P_o—Sea level pressure (1.0 × 105 (Pa))

P_z—Air pressure at elevation z (m)

R—Gas constant (8.3143 J/mol°K)

m—Molecular weight of dry air (0.02897 kg/mol)

C_p—Specific Heat of dry air at constant pressure (1005 J/Kg °K)

T_b—Sea level temperature (300 °K)

Z—Station elevation (m)

λ—Assumed temperature lapse rate (−0.0065 °K/m)

g—Acceleration due to gravity (9.80616 m/s^2).

The air temperature and the dew point temperature were used from the Climate Date Analysis System which processes and archives the weather data received from the IMD automatic weather station network across the country.

17.4.6 Outgoing Longwave Radiation

The emitted thermal radiation between 4 and 100 μm from the earth's surface and atmosphere into outer space is defined as the Outgoing Longwave Radiation (OLR). The outgoing longwave radiation is also estimated using Stefan-Boltzmann

law considering earth emissivity and land surface temperature (Singh 2013). The energy absorbed by the earth's surface during daytime is radiated back to the atmosphere in the form of longwave radiation ($L_{\uparrow}$). The OLR radiated back to the atmosphere depending on the temperature of the radiating surface. The OLR is defined in Eq. 17.20.

$$L_{\uparrow} = \sigma \varepsilon_s T_s^4 \tag{17.20}$$

where,

$L_{\uparrow}$—Outgoing Longwave Radiation (OLR) W/m^2

σ—Stefan-Boltzmann constant

ε_s—Calculated surface emissivity

T_s—Land Surface Temperature (LST), Kelvin.

The OLR data product from Meteorological Oceanographic Satellite Data Archival Centre (MOSDAC) was used in this study. The net radiation is estimated for the clear-sky condition. Instantaneous radiation for each satellite time pass is estimated, and daily average net radiation product is derived for each pass. A daily average net radiation value varies across the country and mainly depends on the season and latitude.

17.4.7 Soil Heat Flux

Several empirical models have been proposed which estimate soil heat flux from biophysical parameters like NDVI, albedo, and LST (Sun et al. 2013). The different empirical methods are used to estimate the soil heat flux iteratively. Soil Heat flux is empirically estimated using as a function of LST, albedo, and NDVI (Sun et al. 2013). Different iterative methods are studied to determine the soil heat flux over Indian region and the methodology adopted by Bastiaanssen et al. (1998a) is used for the estimation of soil heat flux in this study.

$$\frac{G}{R_n} = \frac{T_{\mathrm{LST}}}{\alpha}\left[0.0032\alpha + 0.0064\alpha^2\right]\left[1 - 0.98\mathrm{NDVI}^4\right] \tag{17.21}$$

where,

G—Soil heat flux

R_n—Net radiation

T_{LST}—Land surface temperature (°C)

α—Land surface albedo

NDVI—Normalized Difference Vegetation Index.

17.4.8 Slope of Saturated Vapor Pressure Curve

The saturation vapor pressure ($e°$(T)) is the pressure at which equilibrium is reached between the water molecules escaping and returning to the liquid phase. The slope of the saturated vapor pressure curve is a function of the temperature. At low temperatures, the slope is milder while at higher temperatures, the slope is large for a small change in temperature. The saturation vapor pressure curve slope is an important parameter in describing vaporization and is given in Eq. 17.22 (Allen et al. 1994).

$$\Delta = \frac{2503.058}{(237.3 + T)} \exp\left\{\frac{17.27T}{T + 237.3}\right\} \tag{17.22}$$

where

Δ—Slope of saturated vapor pressure at a certain air temperature T.

17.4.9 Psychrometric Constant

Psychrometric constant is the ratio of specific heat of moist air at constant pressure, C_p to Latent heat of vaporization (Campbell 1977). When atmospheric pressure is expressed in terms of elevation, γ can be estimated as a function of elevation and air temperature (Kotoda 1986). The psychrometric constant, γ is estimated by Eq. 17.23.

$$\gamma = \frac{C_p P}{\varepsilon \lambda} = 0.665 \times 10^{-3} P \tag{17.23}$$

where,

γ—Psychrometric constant (kPa/°C)

P—Atmospheric pressure (kPa)

L—Latent heat of vaporization, 2.45 (MJ/Kg)

c_p—specific heat at constant pressure, 1.013×10^{-3} (MJ/Kg °C)

ε—Ratio molecular weight of water vapor/dry air = 0.622.

When atmospheric pressure is expressed in terms of elevation, γ can be calculated as given in the equation (Kotoda 1986)

$$\gamma = \frac{\left[1005\left(1013.25 - 0.11986E + 0.000005356E^2\right)\right]}{[622(2501 - 2.3T)]} \tag{17.24}$$

where

γ—Psychrometric constant

T—Air temperature.

17.4.9.1 Estimation of Latent Heat Flux

After incorporation of the Priestley-Taylor parameter (α_e) Eq. 17.25 will be

$$\lambda ET_{\mathrm{PT}} = \alpha_e \left(\frac{\Delta}{(\Delta + \gamma)} \right) (R_n - G) \tag{17.25}$$

where

λET_{PT} is the latent heat flux,

α_e is the Priestley-Taylor parameter,

Δ is the slope of the saturation vapor pressure curve,

γ is the psychrometric constant,
R_n is the net radiation and.

G is the surface soil heat flux.

While determining the dry edge and cold edge in the NDVI-LST triangle space, care should be taken to satisfy the following condition in selecting points for the triangle space. A complete range of surface conditions (extreme dry to extreme wet) is ensured on the selected domain. Contaminations of clouds and atmospheric effects have to be removed. Figure 17.2 shows the overview of the Priestley-Taylor algorithm for deriving the operational ET product.

17.4.9.2 Instantaneous Values to Daily Average Flux Value Estimation

The instantaneous values of the latent heat flux estimated from the satellite platform are integrated into the daily average values for the estimated fluxes. For the daily estimation of instantaneous fluxes, the sinusoidal model is used (Bisht et al. 2005) as given in Eq. 17.26.

$$\mathrm{DAV} = \frac{2\mathrm{INV}}{\pi \sin\left(\left(\frac{t_{\mathrm{overpass}} - t_{\mathrm{rise}}}{t_{\mathrm{set}} - t_{\mathrm{rise}}} \right) \pi \right)} \tag{17.26}$$

where,

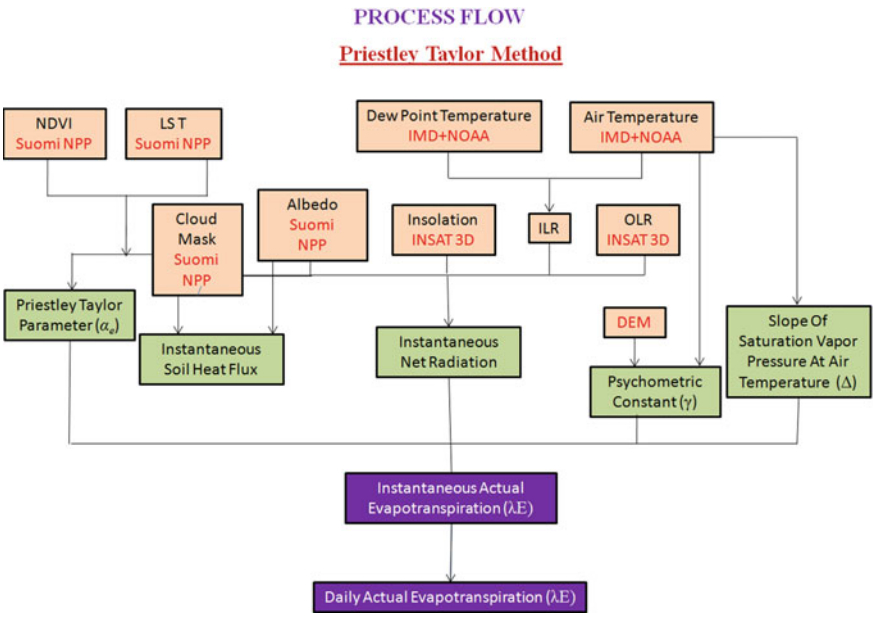

Fig. 17.2 Process flow diagram for operational ET product generation

DAV—Daily Average Variable

INV—Instantaneous variable

$t_{overpass}$—Satellite overpass time

t_{rise}—1 h after local sunrise time

t_{set}—1 h before local sunset time.

For operational product generation, sunset and sunrise time for each pixel is estimated from the procedure given in NOAA manual (GML 2020).

17.5 Results and Discussions

From the methodology presented in Sect. 17.4, P–T parameter (α) and energy balance components are estimated over the Indian region at a grid resolution of 5.5 km^2. An automated NDVI and LST scatter plot was used to define the warm and cold edge to estimate the α_e. Latent heat flux and other surface energy balance components are estimated for the daily satellite passes.

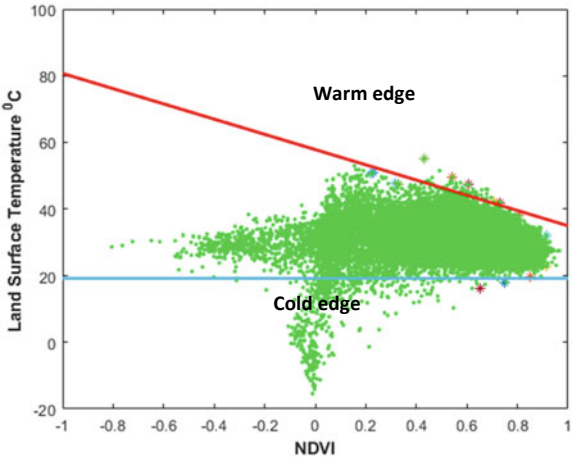

Fig. 17.3 Warm and cold edge derived from Suomi NPP NDVI and LST data

17.5.1 Intra-Seasonal Variations of Warm and Cold Edge

The P–T parameter (α) is sensitive to the warm and cold edge, and hence the accurate estimation of the warm and cold edge is essential. The warm and cold edge derived for a different time period of the year was used to derive the P–T parameter and evaluated. The warm edge is determined with best fit line of maximum LST values, and cold edge is determined with mean of minimum LST values in the given NDVI range in Fig. 17.3. The NDVI greater than 0.2 is considered for fitting the cold edge as values below 0.2 NDVI indicates non-vegetative features. Figure 17.4 shows the one-year intra-seasonal dynamics of warm edge (slope & intercept) and cold edge. The warm edge slopes are negative and have a higher degree of slope during the summer months from March to June and a milder slope during the cooler months. The intercepts also have higher values during the summer and lower values during the winter. The dynamics of the cold edge indicate that the cold edge values increase during the summer months and decrease during the cooler months of the year.

17.5.2 Seasonal Variation of AET Over India

Figure 17.5 shows the monthly AET over India during the year 2019. The derived products observe seasonal transitions in AET values throughout the year. The AET values of the northern plains of India are higher during January to March. These regions grow the rabi (winter) crop, and hence the AET was higher in these regions. During the months of April, May, and June the AET was elevated in North-East India and the Western coast of India. These are due to the many thundershowers received over the forested regions of these parts of the country. From July to October, the AET

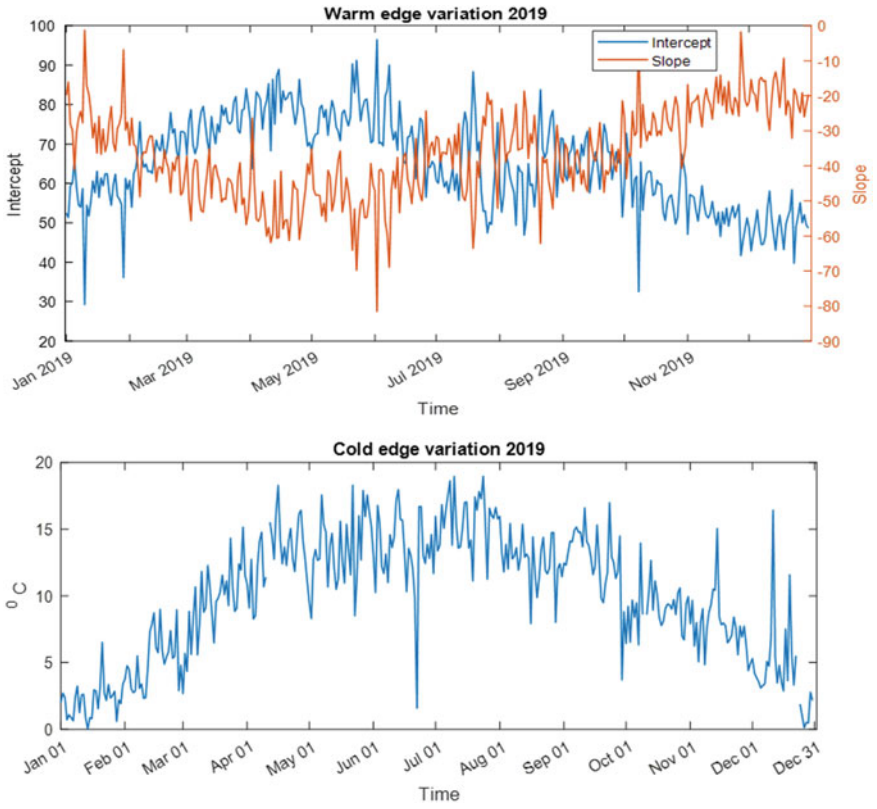

Fig. 17.4 Intra-seasonal variation of warm edge (slope & intercept) and cold edge

is observed to be higher throughout the country due to the Kharif (summer) cropping season. During November and December, the southern peninsular of India, which receives North-East monsoon and its coinciding unique cropping season, results in higher AET in this region. The low level of AET is consistently observed in the Western Rajasthan and parts of Maharashtra due to the sparse vegetation there. The analysis shows that the derived AET follows the country's established cropping seasons and rainfall pattern (Fig. 17.6).

To analyze the dynamics of AET with different Land Use Land Cover (LULC) classes, the mean and standard deviation of the AET for each of the LULC classes was derived. The 1:250 K LULC map derived under NR Census program of NRSC, ISRO was used in this analysis. The major LULC classes considered for this analysis are (i) Kharif crop, (ii) Rabi crop, (iii) Double/triple crop, (iv) Plantation, (v) Evergreen forest, (vi) Deciduous forest, (vii) Degraded/scrub forest, (viii) Grassland and (ix) Shifting cultivation. Figure 17.6 shows the box plot of the monthly average AET for each LULC class of India. It can be observed that during kharif cropping season, the AET increased from June and peaked during the month of August/September.

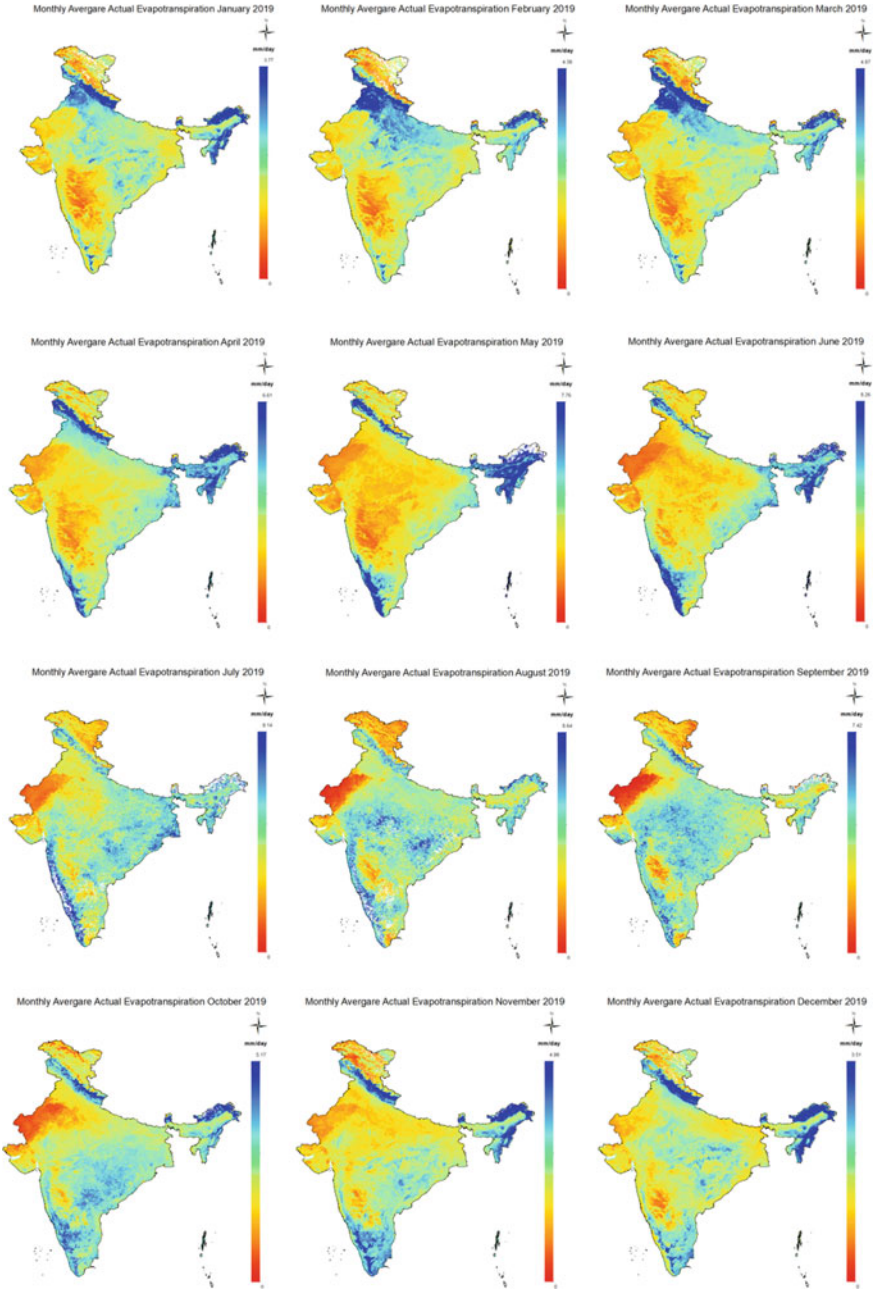

Fig. 17.5 Monthly dynamics of AET over the Indian region during 2019

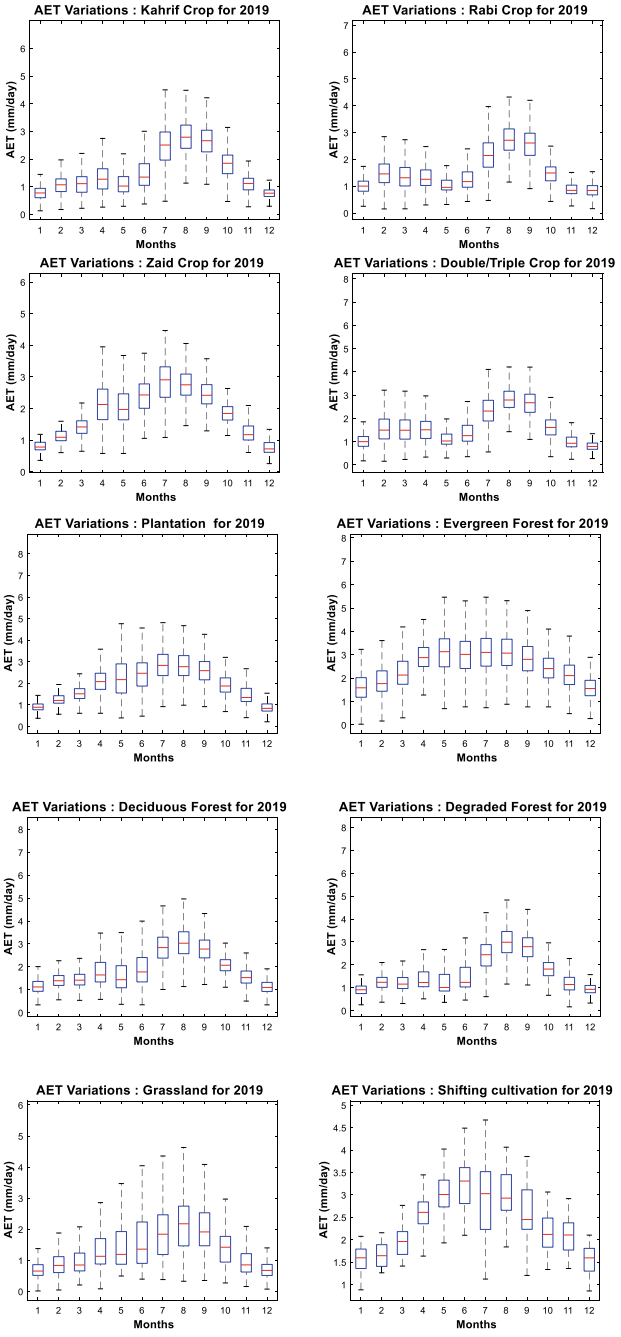

Fig. 17.6 Box plot of monthly average AET for different LULC classes over India

The yearly AET profile of kharif cropping season exhibited unimodal curve. The AET profile of Rabi/double-cropped area exhibited two peaks, the first one during February/March and the second peak during August/September. Zaid land cover shows maximum AET obtained in summer and monsoon months. Over plantation land cover, AET gradually increases from winter to monsoon and decreases gradually until winter. Evergreen forest AET is less in winter while other seasons are almost constant. Deciduous forest and scrubland AET values show an increase during the monsoon months only. While the deciduous forest AET decreases from the peak are more gradual, the scrubland AET decreases sharply. Grassland and shifting cultivation shows a gradual increase in AET values from winter, reach a peak in monsoon season, and gradually decrease again. Data shows minimum AET values are obtained in the winter months, while AET estimates are higher in monsoon and post-monsoon season. The seasonal dynamics of satellite-based AET estimates are in line with the seasonal rainfall and vegetative phenological changes experienced over India.

17.5.3 Statistical Comparison of Spatial Estimates for Crop-Specific Land Covers in India

To assess the accuracy of satellite-derived P–T AET estimation, the results are validated using open-path eddy covariance measurements of the Central Institute for Cotton Research (CICR), Nagpur. It has a cotton-jowar cropping system under a hot sub-humid climate system. CICR is situated at 303 m above sea level and has a hot sub-humid climate system with an average height of canopy of 1–1.25 m.

For comparison with model estimates, half-hourly measurements from Eddy Covariance (EC) tower are integrated over day length. Model estimates are compared with ground measurements for cloud-free days between April 2019 to March 2020. Figure 17.7 shows the time series plot of EC measured AET and the P–T estimated

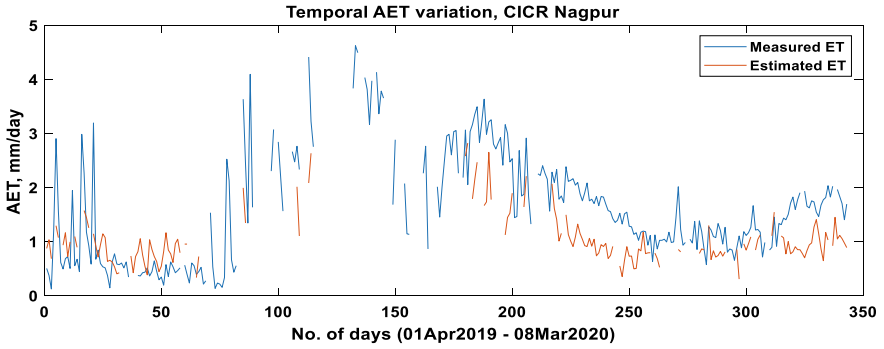

Fig. 17.7 Temporal variation of measured and estimated AET at CICR Nagpur

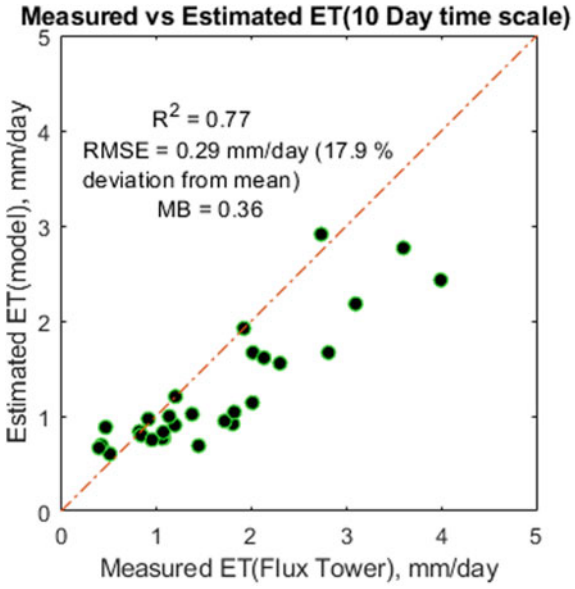

Fig. 17.8 Scatter plot between 10 days average EC and P–T estimated AET

AET. It can be observed that the P–T AET is closely following EC AET except during the senescence phase of Kharif crop.

Figure 17.8 shows the regression analysis was carried out between the P–T AET is closely following EC AET. There is an excellent linear agreement between EC AET and P–T AET values. There is a marginal underestimation of P–T AET values when compared to EC AET. This may be due to larger footprint of the satellite-derived AET. There are also uncertainties associated with the eddy covariance measurements due to instrument calibration, post-processing of data, and confined fetch area of the instrument. It is planned to validate P–T AET with more flux tower observations spread across different agro-ecosystems in the future.

17.6 Summary

Actual ET estimates are required for many water resource and agricultural sector applications. Although it is a critical parameter, the availability of regional level estimation over a daily time scale is very limited. The surface energy balance-based Priestley Taylor method is used to estimate the daily AET for India. The major advantage of this methodology is that it avoids the parameterizations of aerodynamic and surface resistance without decreasing the accuracy of the AET estimates. The P–T model-derived AET captured the seasonal dynamics of the cropping season across the country. Comparison of the model-derived AET with the EC tower data shows a close match. The 10-day average P–T AET shows a strong relation ($R^2 =$

0.77) with the field observation. In this study, though the AET was estimated at 5.5 km^2, efforts are being made to derive AET at the S-NPP resolution of 750 m by deriving the insolation and OLR at 750 m instead of using coarser INSAT products. To overcome the contextual nature of the triangle method, attempts will be made to parameterize the EF or model the LST-VI triangle to improve the warm and cold edge estimation. The current model results are valid for clear-sky conditions with minimal advection and terrestrial features, excluding water and snow. All-sky AET will address the cloud parameters to retrieve the radiation. It is planned to improve model parameterization and address the complex areas where the deviations between the estimated and ground measurements are large.

Acknowledgements This work is carried out under National Hydrology Project at National Remote Sensing Centre, ISRO Hyderabad. The authors thank SAC-ISRO and IMD for providing data for the project. The authors thank Data Processing group and agriculture group of NRSC Hyderabad for providing data support for this project. The authors would like to thank Director NRSC for providing guidance and support.

References

Ai Z, Yang Y (2016) Modification and validation of Priestley–Taylor model for estimating cotton evapotranspiration under plastic mulch condition. J Hydrometeorol 17(4):1281–1293

Allen R, Smith M, Pereira L, Perrier A (1994) An update for the calculation of reference evapotranspiration. ICID Bull 43(2):35–92

Allen RG, Tasumi M, Trezza R (2007) Satellite-based energy balance for mapping evapotranspiration with internalized calibration (METRIC)—model. J Irrig Drain Eng 133(4):380–394

Baker N (2013) Joint Polar Satellite System (JPSS) VIIRS land surface temperature algorithm theoretical basis document (ATBD). NASA, Goddard Space Flight CenterGreenbelt, Maryland

Bastiaanssen W, Menenti M, Feddes R, Holtslag A (1998a) A remote sensing surface energy balance algorithm for land (SEBAL). 1. Formulation. J Hydrol 212–213:198–212

Bastiaanssen W, Menenti M, Feddes R, Holtslag A (1998b) A remote sensing surface energy balance algorithm for land (SEBAL).: Part 2: Validation. J Hydrol 213–229

Bastiaanssen WG, Noordman EJ, Pelgrum H, Davids G (2005) SEBAL model with remotely sensed data to improve water-resources management under actual field conditions. J Irrig Drainage Eng 131(1):85–93

Bhattacharya, BK, Rahul N (2015) Surface Insolation over Land from INSAT-3D, INSAT-3D Algorithm Theoretical Basis Document, pp. 335–360, https://mosdac.gov.in/data/doc/INSAT_3D_ATBD_MAY_2015.pdf

Biggs T, Petropoulos G, Velpuri N, Marshall M (2015) Remote sensing of evapotranspiration from croplands. In: Thenkabail P (ed) Remote sensing handbook: remote sensing of water resources, disasters, and urban studies. CRC Press, pp 59–99

Bisht G, Venturini V, Islam S, Jiang L (2005) Estimation of the net radiation using MODIS (Moderate Resolution Imaging Spectroradiometer) data for clear sky days. Remote Sens Environ 97(1):52–67

Blaney HF, Criddle WD (1950) Determining water requirements in irrigated areas from climatological and irrigation data. U.S. Soil Conservation Service, Pap. No. 96, 48 pp

Brooks KN, Ffolliott PF, Magner JA (2013) Hydrology and the management of watersheds, 4th edn. John Wiley & Sons Inc.

Brooks KN, Ffolliott PF, Magner JA (2012) Hydrology and the management of watersheds, 4th edn. Wiley & Sons, Inc

Brutsaert W (1982) Evaporation into the atmosphere—theory, history and applications. Springer Netherlands

Campbell GS (1977) An introduction to environmental biophysics. Springer, New York

Carlson TN, Gillies RR, Perry EM (1994) Method to make use of thermal infrared temperature and NDVI measurements to infer surface soil water content and fractional vegetation cover. Remote Sens Rev 9(1–2):161–173

Castellvi F, Stockle CO, Perez PJ, Ibañez M (2001) Comparison of methods for applying the Priestley–Taylor equation at a regional scale. Hydrological Process 15(9):1609–1620

Diaz-Espejo A, Verhoef A, Knight R (2005) Illustration of micro-scale advection using grid-pattern mini-lysimeters. Agric for Meteorol 129(1–2):39–52

Dingman SL (2002) Physical hydrology, 2nd edn. Prentice Hall

Ershadi A, McCabea M, Evans J, Walker J (2013) Effects of spatial aggregation on the multi-scale estimation of evapotranspiration. Remote Sens Environ 131:51–62

Fisher BT (2008) Ecosystem services and economic theory: integration for policy relevant research. Ecol Appl 18:2050–2067

Flint AL, Childs SW (1991) Use of the Priestley-Taylor evaporation equation for soil water limited conditions in a small forest clearcut. Agric For Meteorol 56(3–4):247–260

French AN, Alfieri JG, Kustas WP, Prueger JH, Hipps LE, Chávez JL, Evett SR, Howell TA, Gowda PH, Hunsaker DJ, Thorp KR (2012) Estimation of surface energy fluxes using surface renewal and flux variance techniques over an advective irrigated agricultural site. Adv Water Resour 50:91–105

Gillies RR, Kustas WP, Humes KS (1997) A verification of the "triangle" method for obtaining surface soil water content and energy fluxes from remote measurements of the Normalized Difference Vegetation Index (NDVI) and surface e. Int J Remote Sens 18(15):3145–3166

Glenn EP, Huete AR, Nagler PL, Hirschboeck KK, Brown P (2007) Integrating remote sensing and ground methods to estimate evapotranspiration. Crit Rev Plant Sci 26(3):139–168

Glenn EP, Morino K, Didan K, Jordan F, Carroll KC, Nagler PL, Hultine K, Sheader L, Waugh J (2008a). Scaling sap flux measurements of grazed and ungrazed shrub communities with fine and coarse-resolution remote sensing. Ecohydrol Ecosyst Land Water Process Interact Ecohydrogeomorphol 1(4):316–329

Glenn E, Huete A, Nagler P, Nelson S (2008b) Relationship between remotely-sensed vegetation indices, canopy attributes and plant physiological processes: what vegetation indices can and cannot tell us about the landscape. Sensors 8(4):2136–2160

Glenn EP, Doody TM, Guerschman JP, Huete AR, King EA, McVicar TR, Van Dijk AI, Van Niel TG, Yebra M, Zhang Y (2011) Actual evapotranspiration estimation by ground and remote sensing methods: the Australian experience. Hydrol Process 25(26):4103–4116

GML E (2020) Solar calculation details. Retrieved 28 Apr 2020, from Global Monitoring Laboratory, Earth System Research Laboratories: https://www.esrl.noaa.gov/gmd/grad/solcalc/calcdetails.html

Godin R (2014) Joint polar satellite system (JPSS) VIIRS vegetation index (VVI) algorithm theoretical basis document. NASA, Goddard Space Flight CenterGreenbelt, Maryland

Hargreaves GH, Samani ZA (1985) Reference crop evapotranspiration from ambient air temperature. In: Winter meeting of american society of agricultural engineers. American Society of Agricultural Engineers, Chicago

Hoekstra AY, Mekonnen MM (2012) The water footprint of humanity. Proc Natl Acad Sci 109(9):3232–3237

Jackson RD, Idso SB, Reginato RJ, Pinter Jr PJ (1981) Canopy temperature as a crop water stress indicator. Water Resour Res 17(4):1133–1138

Jiang L, Islam S (1999) A methodology for estimation of surface evapotranspiration over large areas using remote sensing observations. Geophys Res Lett 26(17):2773–2776

Jiang L, Islam S (2001) Estimation of surface evaporation map over southern Great Plains using remote sensing data. Water Resour Res 37(2):329–340

Jiang L, Islam S (2003) An intercomparison of regional latent heat flux estimation using remote sensing data. Int J Remote Sens 24(11):2221–2236

Jin ZY (2011) A new parameterization of spectral and broadband ocean surface albedo. Opt Express 19(27):26429–26443. https://doi.org/10.1364/OE.19.026429

Jung M, Reichstein M, Margolis HA, Cescatti A, Richardson AD, Arain MA, Arneth A, Bernhofer C, Bonal D, Chen J, Gianelle D, Gobron N, Kiely G, Kutsch W, Lasslop G, Law BE, Lindroth A, Merbold L, Montagnani L, Moors EJ, Papale D, Sottocornola M, Vaccari F, Williams C (2011) Global patterns of land-atmosphere fluxes of carbon dioxide, latent heat, and sensible heat derived from eddy covariance, satellite, and meteorological observation. J Geophys Res 116(G3).

Kalma JD, McVicar TR, McCabe MF (2008) Estimating land surface evaporation: a review of methods using remotely sensed surface temperature data. Surv Geophys 29:421–469

Korzoun VI, Sokolov AA, Budyko MI, Voskresensky KP, Kalinin GP (1978) World water balance and water resources of the earth. In: National Committee for the IHD (USSR), Studies and Reports in Hydrology (UNESCO), No. 25. United Nations Educational, Scientific and Cultural Organization, Paris, p 638

Kotoda K (1986) Estimation of river basin evapotranspiration. Environmental research center papers, no 8, pp 1–66

Kustas WP, Norman JM (1999) Evaluation of soil and vegetation heat flux predictions using a simple two-source model with radiometric temperatures for partial canopy cover. Agric For Meteorol 94(1):13–29

Kustas WP, Stannard DI, Allwine KJ (1996) Variability in surface energy flux partitioning during Washita '92: Resulting effects on Penman-Monteith and Priestley-Taylor parameters. Agric For Meteorol 82(1–4):171–193

Lei H, Yang D (2010) Interannual and seasonal variability in evapotranspiration and energy partitioning over an irrigated cropland in the North China Plain. Agric For Meteorol 150(4):581–589

Liang S (2001) Narrowband to broadband conversions of land surface albedo I: Algorithms. Remote Sens Environ 76(2):213–238

L'vovich MI, White GF (1990) Use and transformation of terrestrial water systems. In: Turner II BL, Clark WC, Kates RW, Mathews JT, Richards JF, Meyer WB (eds) The earth as transformed by human action: global and regional changes in the biosphere over the past 300 years. Cambridge University Press, Cambridge, UK, p 713

Ma Y, Su Z, Li Z, Koike T, Menenti M (2002) Determination of regional net radiation and soil heat flux over a heterogeneous landscape of the Tibetan Plateau. Hydrol Process 16(15):2963–2971

Melesse AM, Frank A, Nangia V, Hanson J (2008) Analysis of energy fluxes and land surface parameters in a grassland ecosystem: a remote sensing perspective. Int J Remote Sens 29(11), 3325–3341

Monteith JL (1973) Principles of Environmental Physics. Edward Arnold Limited, London

Moran M, Clarke T, Inoue Y, Vidal A (1994) Estimating crop water deficit using the relation between surface-air temperature and spectral vegetation index. Remote Sens Environ 49(3):246–263

Mu Q, Zhao M, Kimball JS, McDowell NG, Running SW (2013) A remotely sensed global terrestrial drought severity index. Bull Am Meteorol Soc 94(1):83–98

Nagler P, Morino K, Murray R, Osterberg J, Glenn E (2009) An empirical algorithm for estimating agricultural and riparian evapotranspiration using MODIS enhanced vegetation index and ground measurements of ET. I. Description of method. Remote Sens 1(4):1273–1297

Nemani RR, Running SW (1989) Estimation of regional surface resistance to evapotranspiration from NDVI and thermal-IR AVHRR data. J Appl Meteorol 28:276–284

Norman JM (1995) Source approach for estimating soil 695 and vegetation energy fluxes in observations of directional radiometric surface temperature. Agric for Meteorol 77:263–293

Overgaard J, Rosbjerg D, Butts MB (2006) Land-surface modelling in hydrological perspective—a review. Biogeosciences 3(2):229–241

Parlange MB, Katul GG (1992) Estimation of the diurnal variation of potential evaporation from a wet bare soil surface. J Hydrol 132(1–4):71–89
Pavolonis MJ and Heidinger AK (2004) Daytime cloud overlap detection from AVHRR and VIIRS, J Appl Meteorol 43:762–778
Penman HL (1948) Natural evaporation from open water, bare soil and grass. Proc R Soc London Ser A Math Phys Sci 193(1032):120–145
Pereira AR (2004) The Priestley–Taylor parameter and the decoupling factor for estimating reference evapotranspiration. Agric For Meteorol 125(3–4):305–313
Petropoulos GP, Carlson TN, Griffiths HM (2013) Turbulent fluxes of heat and moisture at the earth's land surface: importance, controlling parameters, and conventional measurement techniques. In: Petropoulos GP, Petropoulos GP (ed) Remote sensing of energy fluxes and soil moisture content. CRC Press, Taylor & Francis Group, p 562
Prata AJ (1996) A new long-wave formula for estimating downward clear-sky radiation at the surface. Quar J R Meteorol Soc 122(533):1127–1151
Price J (1990) Using spatial context in satellite data to infer regional scale evapotranspiration. IEEE Trans Geosci Remote Sens 28(5):940–948
Priestley C, Taylor R (1972) On the assessment of surface heat flux and evaporation using large-scale parameters. Monthly Weather Rev 100(2):81–92
Sandholt I, Rasmussen K, Andersen J (2002) A simple interpretation of the surface temperature/vegetation index space for assessment of surface moisture status. Remote Sens Environ 79(2–3):213–224
Sellers PJ, Tucker CJ, Collatz GJ, Los SO, Justice CO, Dazlich DA, Randall DA (1996) A revised land surface parameterization (SiB2) for atmospheric GCMS. Part II: The generation of global fields of terrestrial biophysical parameters from satellite data. J Clim 9:706–737
Shahidian S, Serralheiro R, Serrano J, Teixeira J, Haie N, Santos F (2012) Hargreaves and other reduced-set methods for calculating evapotranspiration. In: Irmak A (ed) Evapotranspiration—remote sensing and modeling, pp 59–80
Shiklomanov IA (2000) Appraisal and assessment of world water resources. Water Int 25(1):11–32
Singh RT (2013). Outgoing Longwave Radiation Product ATBD. https://doi.org/10.19038/SAC/10/3DIMG_L2B_OLR
Su, Z. (2002). The Surface Energy Balance System (SEBS) for estimation of turbulent heat fluxes, Hydrol. Earth Syst Sci 6:85–100. https://doi.org/10.5194/hess-6-85-2002
Sun Q, Wu Z, Tan J (2012) The relationship between land surface temperature and land use/land cover in Guangzhou, China. Environ Earth Sci 65:1687–1694
Sun Z, Gebremichael M, Wang Q (2013) Evaluation of empirical remote sensing-based equations for estimating soil heat flux. J Meteorol Soc Jpn 91(5):627–638
Swinbank WC (1951) The measurement of vertical transfer of heat and water vapor by eddies in the lower atmosphere. J Meteorol 8(3):135–145
Yao Y, Liang S, Li X, Chen J, Wang K, Jia K, Cheng J, Jiang B, Fisher JB, Mu Q, Gruenwald T (2015) A satellite-based hybrid algorithm to determine the Priestley–Taylor parameter for global terrestrial latent heat flux estimation across multiple biomes. Remote Sens Environ 165:216–233
Zhang L, Hickel K, Dawes WR, Chiew FH, Western AW, Briggs PR (2004) A rational function approach for estimating mean annual evapotranspiration. Water Resour Res 40(W02502)

Chapter 18
Improving Quality of Digital Elevation Models Derived from Satellite Stereo Images Using Geospatial Techniques

D. S. Prakasa Rao, Ashish Jain, G. Sreenivasan, S. Srinivasa Rao, and C. S. Jha

Abstract Deriving Digital Elevation Models (DEMs) from satellite stereo images are the standard in geospatial studies world over, as it is pragmatic, practically feasible, economically viable and technically sound. Specific satellite missions were put and stereo data has been acquired in these missions. Techniques have been developed globally by many institutes for the utilization of this data for image matching and DEM generation. During the last couple of decades, automatic DEM generation has been taken up at global and regional levels, SRTM global DEM, ASTER GDEM and CartoDEM being some examples. The quality of a DEM measures how accurate the elevation is at each pixel (absolute accuracy) and how accurately the morphology is presented (relative accuracy). However, the DEMs produced automatically from satellite stereo images suffer from the problems of sinks/spikes, non-uniformity of elevation over water bodies, ill-conditioned along streams and rivers. The quality of DEM could be improved either at the process level or at the product level. There, will not be any manual intervention in the automatic DEM production chain and hence has to be dealt with at the product level. The quality of such DEMs can be improved interactively by applying custom tools/methods/algorithms. Multi-temporal satellite stereo data comes in handy to improve absolute accuracy and produce DEMs at super resolutions (which may not be feasible with single-date data). This article discusses methods of spike/sinks correction, hydrological conditioning, combining multi-temporal DEMs into a single DEM, and also DEM production at super resolutions.

Keywords Digital elevation model · Stereo image · SRTM · ASTER GDEM · CartoDEM

D. S. Prakasa Rao (✉) · G. Sreenivasan
Regional Remote Sensing Centre—Central, NRSC, ISRO, Nagpur, India
e-mail: prakashngp@gmail.com

A. Jain
Regional Remote Sensing Centre—West, NRSC, ISRO, Jodhpur, India

S. Srinivasa Rao · C. S. Jha
National Remote Sensing Centre, ISRO, Hyderabad, India

C. S. Jha et al. (eds.), *Geospatial Technologies for Resources Planning and Management*, Water Science and Technology Library 115,
https://doi.org/10.1007/978-3-030-98981-1_18

18.1 Introduction

A digital elevation model is a digital representation of the Earth's relief consisting of an ordered array of elevations. The term DEM is used here to describe a raster data set, representing the elevation of the terrain surface as a two-dimensional array or matrix of height values (Wood 1996). The terms DEM and DTM are used interchangeably. Some use DTM for any model of the elevation of the terrain surface (Carrara et al. 1997; Heywood et al. 1998). Another term, Digital Surface Model (DSM), is more commonly used to describe a model of an upper surface that includes vegetation and buildings. Numerous ways of representing terrain in digital form are explained by Li et al. (2005), as shown in Fig. 18.1.

18.1.1 Data Sources for DEM Generation

Several techniques are suitable for DEM extraction like digital aerial and terrestrial Photogrammetry, airborne and terrestrial laser scanning, Global Positioning System (GPS) and active and passive remote sensing, with optical and microwave satellite imagery (Fraser et al. 2002). A digital photogrammetry is a powerful tool in elevation model generation extracting high-resolution DEMs using automated image matching techniques (Farrow and Murray 1992; Heipke 1995; Mitchell and Chadwick 1999; Schenk 1999). Different techniques are in vogue for DEM extraction using the topographic data obtained from Ground surveys, Topographical maps, Global Positioning Systems (GPS), Remote Sensing (Aerial Images/Spaceborne images: Optical and Microwave), InSAR, and LIDAR.

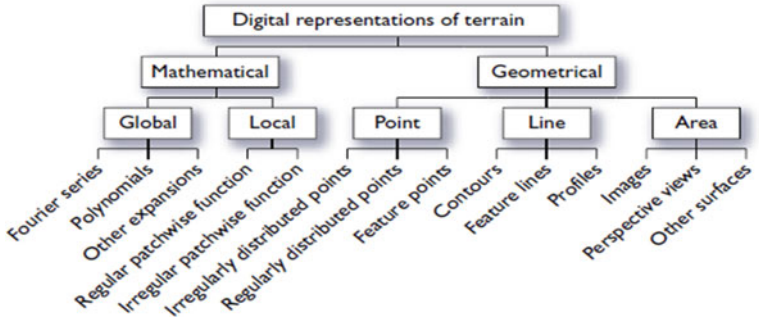

Fig. 18.1 Digital representation of Terrain (Adopted from Li et al. 2005)

Table 18.1 Available global DEM datasets

Dataset	Coverage	Horizontal Posting
GTOPO30	Global	1 km
US LEVEL 2 DTED	Global	30 m
SRTM	60° N to 54° S	30 m
ASTER GDEM	83° N to 83° S	30 m
ALOS WORLD 3D (AW3D & AW3D30)	Global	5 m and 30 m

18.1.2 DEM Generation: Global Scenario

For decades, conventional surveying and aerial images were the only sources of generating DEM. The emergence of GPS facilitated conventional techniques. However, limitations such as large time required, reach to inaccessible areas, high expenses were still remaining. Finally, the possibility of using satellite stereoscopic images for global digital elevation data was commenced with the first SPOT series satellites in 1986. Details of available Global DEM datasets are presented in Table 18.1.

18.1.3 DEM Generation: Indian Scenario

With the launch of IRS 1C and 1D satellites, which have across-track stereoscopic capability, attempts have been made to generate medium to coarse resolution DEM. With the launch of Cartosat-1, an along-track stereoscopic imaging mission of the Indian Space Research Organisation (ISRO), possibilities for operational availability of high-resolution stereo-imagery from space for remote sensing and cartography user communities have emerged (Srivastava et al. 2007). The high-resolution stereo data beamed from twin cameras onboard Cartosat-1 mission facilitates topographic mapping up to 1:25,000 scale (Srivastava et al. 2006). An initiative to generate a database of seamless, homogeneous DEM, named CartoDEM and associated ortho-image tiles at the country level, has been undertaken by ISRO (Srivastava et al. 2007).

18.2 DEM from Satellite Stereoscopy

As already stated, DEMs can be based on a ground survey, aerial images, airborne laser scanning, space images, and interferometric synthetic aperture radar (InSAR) from air and space. The ground survey is time-consuming and economically not viable for large areas. Stereoscopic aerial and satellite images are a standard method

for the generation of height models along with airborne laser scanning. In a number of countries, aerial images and laser scanner data are unavailable, expensive, or not available at the national level. Because of these problems, space-borne remote sensing techniques provide a viable alternative to DEM generation for many applications (Sefercik et al. 2010). Many experiments have been conducted to evaluate remote sensing data as a new alternative for generating DEM (Jacobsen 2002; Toutin and Cheng 2002; Fraser and Hanley 2003; Amato et al. 2004). The base-height (B/H) ratio of 0.6 or greater that is possible with the present-day sensor configurations make them significant alternatives for generating DEMs and 3D views (Sadeghian et al. 2001; Nikolakopoulos 2020).

18.2.1 Satellite Stereoscopy

For 3-D mapping, stereo pairs are required. To obtain stereoscopy with images from satellite scanners, three solutions are possible (Toutin 2001):

- Adjacent-track stereoscopy from two different orbits;
- Across-track stereoscopy from two different orbits; and
- Along-track stereoscopy from the same orbit using fore and aft images.

In recent years, a large amount of research has been devoted to efficient utilization of these high spatial resolution imagery data, involving different sensor modeling and image orientation (Baltsavias et al. 2001; Fraser et al. 2002; Fraser and Hanley 2003; Grodecki and Dial 2003; Jacobsen 2003; Eisenbeiss et al. 2004; Poli 2005). Several researchers have worked on automatic DTM/DSM generation using satellite stereoscopy (Jacobsen 2004; Poli et al. 2004; Toutin 2004; Toutin et al. 2004; Zhang and Gruen 2004).

18.2.2 DEM Generation

DEM generation from stereo satellite imagery involves the following steps (Gopala Krishna et al. 1998; Jacobsen 2004; Poli et al. 2004; Toutin 2004; Toutin et al. 2004; Deilami and Hashim 2011). A DEM generation workflow is depicted in Fig. 18.2.

- GCP collection (for determination/refinement of satellite orientation parameters)
- Image matching (Identification of conjugate points)
- Filtering and interpolation (surface fitting)
- Three-dimensional coordinate determination by space intersection method
- Height interpolation to compute heights of regularly spaced grid points.
- Checking and editing of the DEM (quality control and quality assessment).

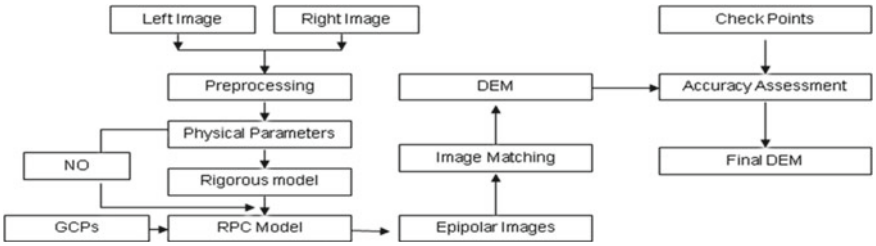

Fig. 18.2 DEM generation workflow (after Deilami and Hashim 2011)

18.3 DEM Quality Assessment

The literature reveals two broad approaches to assessing DEM quality—Qualitative and Quantitative. Qualitative methods include visual quality assessment, DEM walk throughs, Studying the elevation profiles drawn across different features, orthographic displays, etc. Quantitative involves measurements with respect to higher accuracy reference data and computation of statistical measures like RMSE, LE90 and CE90 etc. to ascertain the quality of the product in question. Additionally, a second variable or data set can be draped over the surface to assess the quality of a DEM (Fig. 18.3). The realism of a hillshade map or aerial photograph draped over an orthographic DEM display can take advantage of the ability of the viewer to make visual sense of images and therefore reveal parts of the surfaces that differ from the

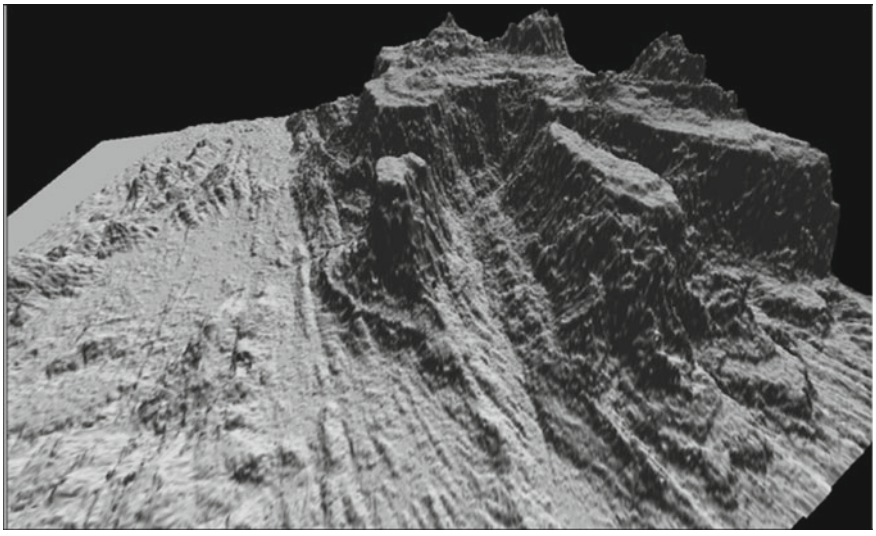

Fig. 18.3 Satellite image draped over an orthographic DEM, example of Nashik area, Maharashtra

expected (Wood 1994). Additionally, rendering DEM derivatives can also give useful information on the quality of the product.

One of the standard procedures to assess the quality of a DEM is to compare with a reference DEM. A differential DEM to the reference DEM could be prepared, which gives locations of DEM inaccuracies for refinement. The color-coded differential DEM has been proposed by many authors, including Krishna Murthy et al. (2008).

18.3.1 Quality Issues of Automatic DEMs

Using the methodology mentioned in Sect. 18.2.2, DEM could be generated manually or fully automatic methods. In manual methods of generating a DEM, a photogrammetric operator can place the floating mark to the requested location and can collect elevation points and a continuous image can be produced using interpolation techniques. This is not possible by the automatic functions widely in use now for economic reasons (Jacobsen 2001).

To generate error-free DEM from stereo imagery, there is a requirement of post-processing techniques like solutions for filling gaps in DEMs, filtering process or manual editing such as adding breaklines and editing mass points in 3D stereo editing environment (Toutin 2002; Reinartz et al. 2010). Manual editing of the DEM consumes time (Wild and Krzystek 1996; Lee et al. 2003; Yuan et al. 2011), and the resultant quality of the DEM depends on the human operators' efficiency.

Key attributes of good DEM data are its homogeneity and consistency. Automatic DEM extraction procedures may induce certain inconsistencies; the challenge is to remove these inconsistencies and preserve the quality of DEM through the post-processing/finishing process. Accordingly, quality improvement has to be an iterative and interactive process.

18.4 Geospatial Solutions

After a closer look at some of the DEMs produced using automatic techniques, it has been observed that there are certain discrepancies over water body regions, and the water body is not homogeneous in terms of elevation values. The automatic techniques also produce certain artifacts like sinks/spikes and mosaic-related distortions at certain places. In the subsequent sections, geospatial solutions to address these issues are discussed.

18.4.1 Waterbody Flattening

It is often noticed that the DEM over large water bodies looks uneven. This is due to non-availability of match points over water bodies or wrongly correlated match points. Such cases are detected visually by a simultaneous display of ortho-image and DEM during Quality verification. DEMs are viewed on interactive editing systems to identify and correct blunders and systematic errors. DEMs are verified for physical format and logical consistency at the production centers before archiving.

Hydro-flattening of DEMs is predominantly accomplished through the use of breaklines, and this method is considered standard. Maune (2007) provide the definitions related to the adjustment of DEM surfaces for hydrologic analyses. 'Hydro-Conditioned' and 'Hydro-Enforced' are important and valuable modifications, which result in surfaces that differ significantly from a traditional DEM. A 'hydro-conditioned' surface has had its sinks filled and may have had its water bodies flattened (NGP 2010).

A color-coded version of the DEM over the regions of water bodies is presented in Fig. 18.4a. The boundary of the water body delineated from the corresponding ortho-image is overlaid on this DEM. The variations in the color shades indicate the non-homogeneity of elevation values over these regions. The same is confirmed by the elevation profile drawn across the water body, as shown in the inset of Fig. 18.4a.

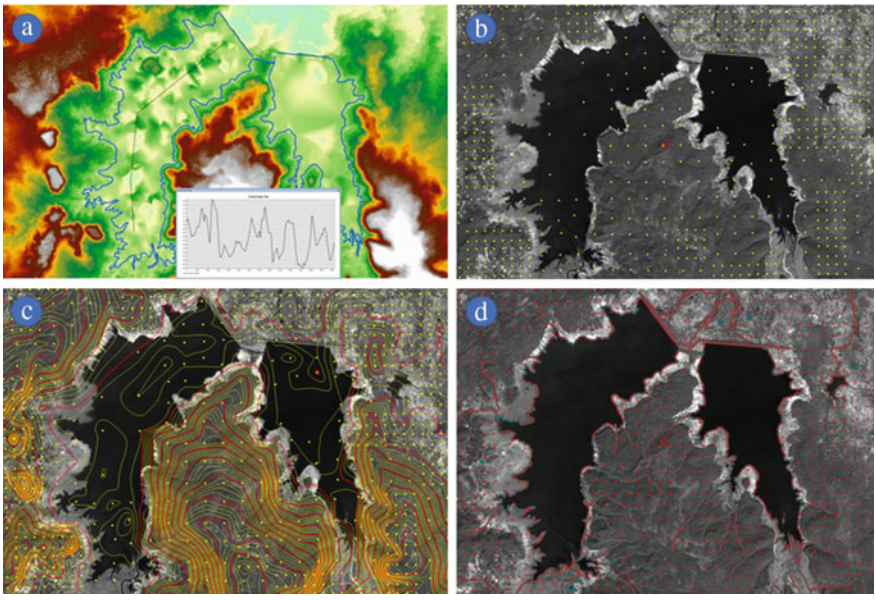

Fig. 18.4 DEM over the regions of water bodies **a** Color-coded DEM over water body regions; **b** Mass points overlaid on the stereo model; **c** Interpolated mass points on the stereo model with contours; **d** Editing of mass points and breaklines

COTS software like Leica Photogrammetry Suite can be used for preparing DEM in an automatic manner. This software has a sub-system for interactively editing DTMs. This interactive system operates on a data structure called LTF (Leica TIN Format), which is an enhanced version of TIN. An LTF is a type of TIN that can serve elevation data from hundreds of millions of irregularly spaced points.

A snapshot of the stereo model from the terrain editing system of LPS software showing mass points is depicted in Fig. 18.4b. As it is seen, a number of points with varying elevation values are present over the water body regions. This is further verified by the interpolation of these mass points depicted as contours overlaid on the stereo model, as illustrated in Fig. 18.4c. The ideal solution to flatten the water bodies is to manually delete all the points present over the water body regions and draw breaklines demarcating the water bodies' boundaries, keeping intact other points present on the regular terrain. A sample of this exercise is shown in Fig. 18.4d indicating the editing requirements in such areas.

The approach implemented in this case is delineating water body regions assigning suitable elevation values to the regions. Haibo et al. (2011) analyzed multiple methods, including unsupervised classification, supervised classification, single-band threshold, inter spectrum relation method, decision tree method; and water index methods such as normalized difference water index (NDWI), modified normalized difference water index, new water index, and assessed their relative performance for extracting water information.

Region Growing Approach: This approach is implemented to delineate waterbody regions in this study. Region growing algorithms cluster pixels starting from a limited number of single seed points (Adams and Bischof 1994). Region growing is a simple region-based image segmentation method. It is also classified as a pixel-based image segmentation method since it involves the selection of initial seed points. Region growing is a procedure that groups pixels or sub-regions into larger regions. The simplest of these approaches is pixel aggregation, which starts with a set of seed points and grows regions by appending to each seed point those neighboring pixels with similar properties, such as gray level, texture or color (Gonzalez 2002). For delineating each water body, a seed point is marked; further, in an interactive editing environment, the seed point is used to delineate the water body.

Flattening Process: After delineating the water body using region growing or any other approach, then the height values of the pixels covered by the region are examined in the DEM image, and appropriate value is decided, and this height value is assigned to all the pixels in the DEM covered by the water body region.

Customized open source software makes the process automatic, fast, and simple, especially when the study area is very large or when improving the quality of a National level DEM. One such software is developed for water body flattening to improve the quality of CartoDEM, a national DEM developed by ISRO using CARTOSAT-1 stereo pair data. The custom software that is developed implement the region growing process and subsequent flattening process automatically in the process chain of DEM generation. The software operates on the input image based on the user options and output image contains the region of the water body. The water

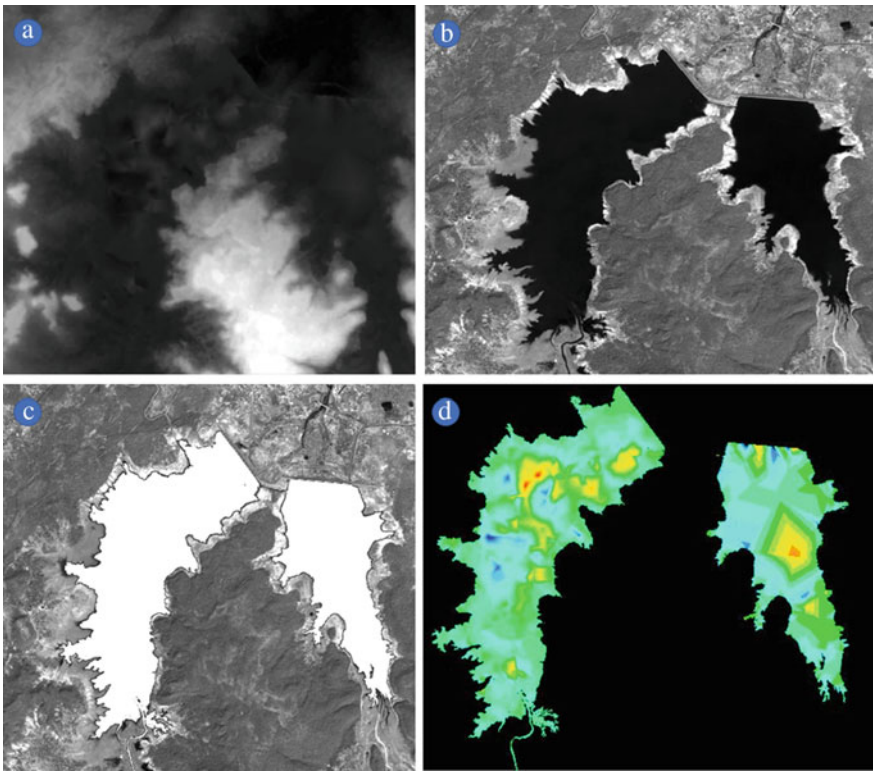

Fig. 18.5 Delineation of water body region using automatic open-source software. **a** DEM over water bodies; **b** ortho-image of the corresponding region; **c** water body mask overlaid on ortho-image; **d** color-coded DEM showing variation of elevation values in the water body

body thus extracted will be used for flattening the water body region in the DEM. Figure 18.5a shows DEM over a water body, and Fig. 18.5b shows the corresponding ortho-image. Figure 18.5c shows the waterbody extracted using this approach and Fig. 18.5d shows the extracted color-coded image of the waterbody, which clearly shows the non-uniformity of elevation values over the region. The DEM before water body flattening and after water body flattening is presented in Fig. 18.6a, b, respectively. The effect of flattening is very clearly seen in Fig. 18.6b. A profile drawn across the water body region depicting the effect of flattening is presented in Fig. 18.6c. As it is seen from Fig. 18.6c, the undulations in the water body are removed, and a uniform height value is assigned to the region of the water body.

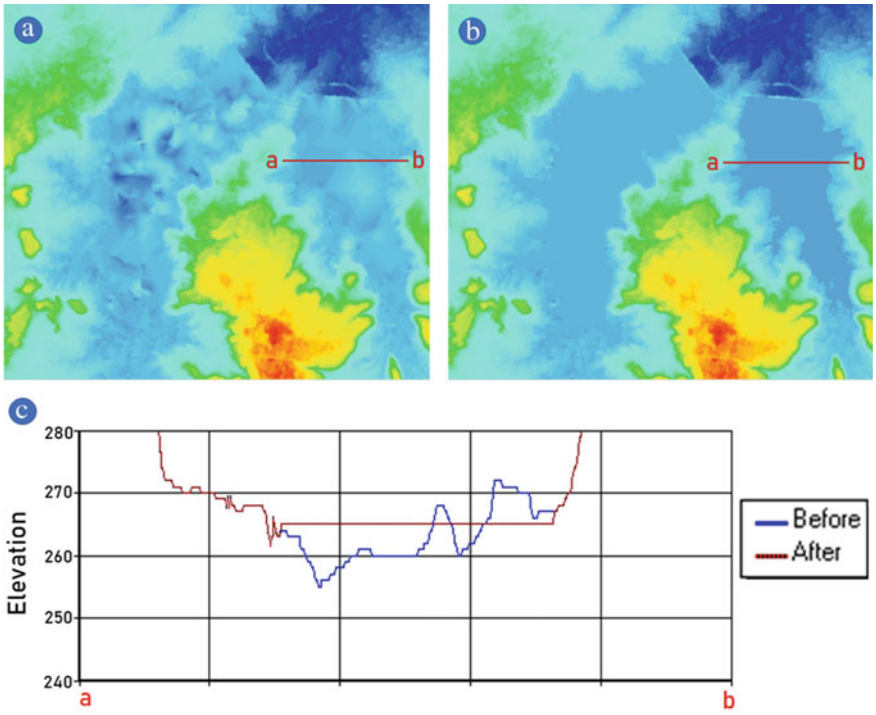

Fig. 18.6 Quality improved DEM before and after water body flattening developed using automatic open-source software. **a** DEM before waterbody flattening; **b** DEM after waterbody flattening; **c** profile drawn across the water body region

18.4.2 Sink/Spike Correction

Automatically derived DEMs often contain depressions that result in areas referred to as sinks or pits. Sinks are identified by noting impediments to a flow direction surface derived from a DEM. A number of methods have been described for identifying sinks (Lindsay and Creed 2006). Several methods have been described for eliminating such sinks, or depressions in DEMs (O'Callaghan and Mark 1984; Jenson and Domingue 1988; Hutchinson 1989; Jenson 1991; Rieger 1998; Martz and Garbrecht 1999; Lindsay and Creed 2005; Zhu et al. 2013). Commercial software like ESRI ArcGIS uses an algorithm based on the D8 single flow direction flow routing method.

One of the most widely used DEM data sources is the elevation information provided by the Shuttle Radar Topography Mission (SRTM) (Coltelli et al. 1996; Farr and Kobrick 2000), and has been one of the most important publicly available spatial data sets in recent years. Earlier versions of this data suffered from the artifacts like spikes, pits, and voids. Different methods that addressed solutions to these issues can be found in Reuter et al. (2007).

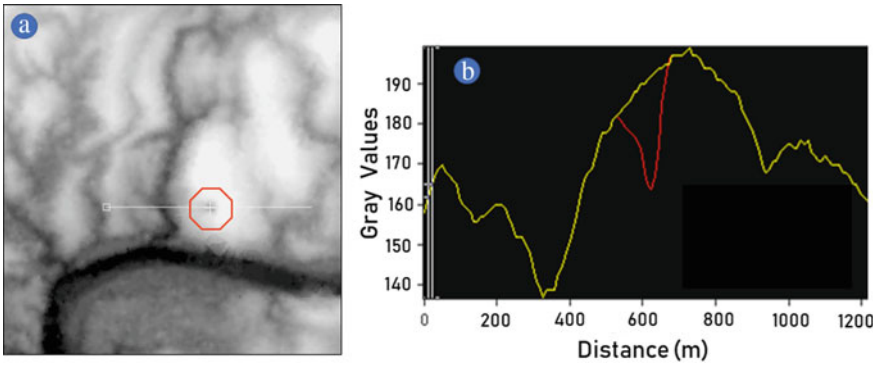

Fig. 18.7 DEM with sink region and corresponding elevation profile. **a** DEM with sink region; **b** elevation profile across the sink

Some of the solutions implemented by commercial software packages assume that all depressions are due to underestimating elevation in the sink, rather than overestimating surrounding cells. Applying these algorithms to the area of the entire DEM may produce spurious results. The best way to address this issue is to view the DEM in an interactive editing system and solve the problem. The area of a DEM containing a sink is depicted in Fig. 18.7a and the area around the sink is encircled in 'red'. Whether it is really a sink or not can be judged by drawing an elevation profile across the sink. The elevation profile across the corresponding sink area is presented in Fig. 18.7b.

As can be seen from the profile, the region encircled is indeed a sink. The sudden drop in elevation values, indicated in 'red' in the profile, suggests that it is a sink. The ideal solution for solving this problem is stereo viewing and editing at a mass point or TIN level to detect floating/digging of points and adjust them. As described in the previous section, the mass points responsible for this sink have to be removed or adjusted.

In the generation of DEM in an automatic process chain, there is no provision for stereo viewing and hence no provision for editing the mass points in a stereo environment. Local update or enhancement operations (restricted only to some portions of a dataset) or integration of heterogeneous DEMs is a field of research where no definitive solutions have been found yet (Papasaika and Baltsavias 2010). New research and development of tools are, therefore, necessary to address these problems. Accordingly, a solution in 2-D environment has to be arrived at using the data available in the DEM itself. Marking a boundary around a sink and applying an algorithm to replace values in the sink region may be thought of as one solution.

18.4.2.1 Application of Available Algorithms

A walk through the ortho-image and DEM tiles will enable the identification of sink regions. They will appear relatively low in contrast compared to surroundings in the DEM. Sometimes even long triangles can be seen in the region due to interpolation of spurious data. A sample sink region is shown in Fig. 18.8. After spotting a sink, a boundary encompassing the sink region can be drawn, as shown in the figure for processing.

While working on the DEM data, the DEM/pixel values of the boundary drawn are used as input. These values are available as x, y, and z values. In the conventional approach, this coordinate stream is converted as a vector and imported into the commercial software, and then processed through any of the well-known algorithms such as Inverse Distance Weighted, Kriging, Natural Neighbor Interpolator, Thin-Plate Splines or Multi Quadrilateral, for assigning new elevation values for the sink region.

It is observed that there are certain drawbacks of this process. As the pixels constituting the sink boundary are used for interpolation, a new surface is created, not consistent with background. Therefore, after interpolation, the sink boundary is seen very clearly in the output.

These limitations have prompted for development of a new algorithm and software-based solution, which is simple easy to use in an interactive editing environment yet not compromise with the quality of the result. The only operator intervention required would be drawing a sink boundary. The approaches used, the final outcome, and the comparison of the outputs of different interpolation techniques are illustrated in the following sections.

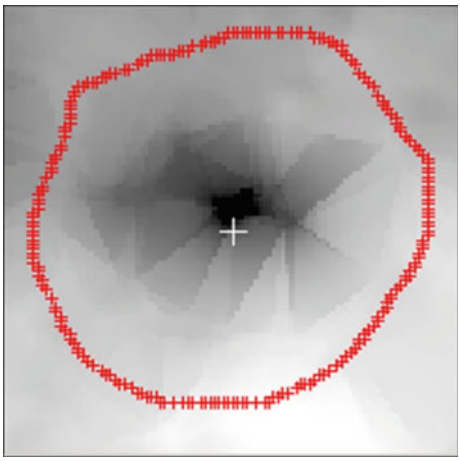

Fig. 18.8 A sink region in DEM, boundary drawn around it

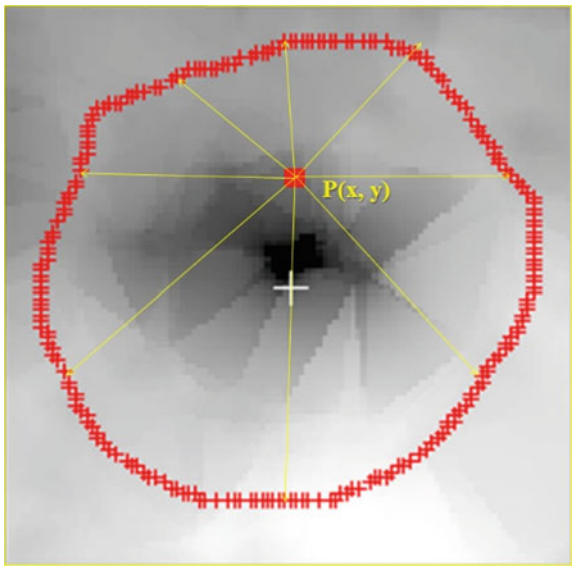

Fig. 18.9 8-connected approaches for deriving the new elevation value of the sink pixels, $P\ (X, Y)$, in a DEM for correction of sinks

18.4.2.2 8-Connected and N-Connected Algorithms

Using the inputs of the sink boundary and underlying elevation values, many configurations have been experimented toward developing an algorithm and the solution.

8-connected: For each pixel $P\ (x, y)$ within the sink region, the line passing through the pixel is extended to touch the boundary of the region, in horizontal vertical and along with diagonal directions, in either direction (total 8 directions) to identify the DEM values on the sink boundary. The corresponding length of the line segments in eight directions is used as weights, and the value at $P\ (x, y)$ is calculated as weighted from the eight boundary pixel values, as shown in Fig. 18.9.

N-connected: For each pixel $P\ (x, y)$ within the sink region, the distance of the pixel in question with respect to all the pixels on the boundary is calculated and used as weights, and the value at that pixel is calculated as a weighted average of the boundary pixel values.

18.4.2.3 Analysis of Results

An analysis of the outputs of different algorithms mentioned in Sect. 18.4.2.2 is carried out. The output of 8-connected distance weighted average and that of other interpolation algorithms explained in Sect. 18.4.2.1, are compared in Fig. 18.10. The outputs are analyzed graphically with the help of profiles. Figure 18.10a compares

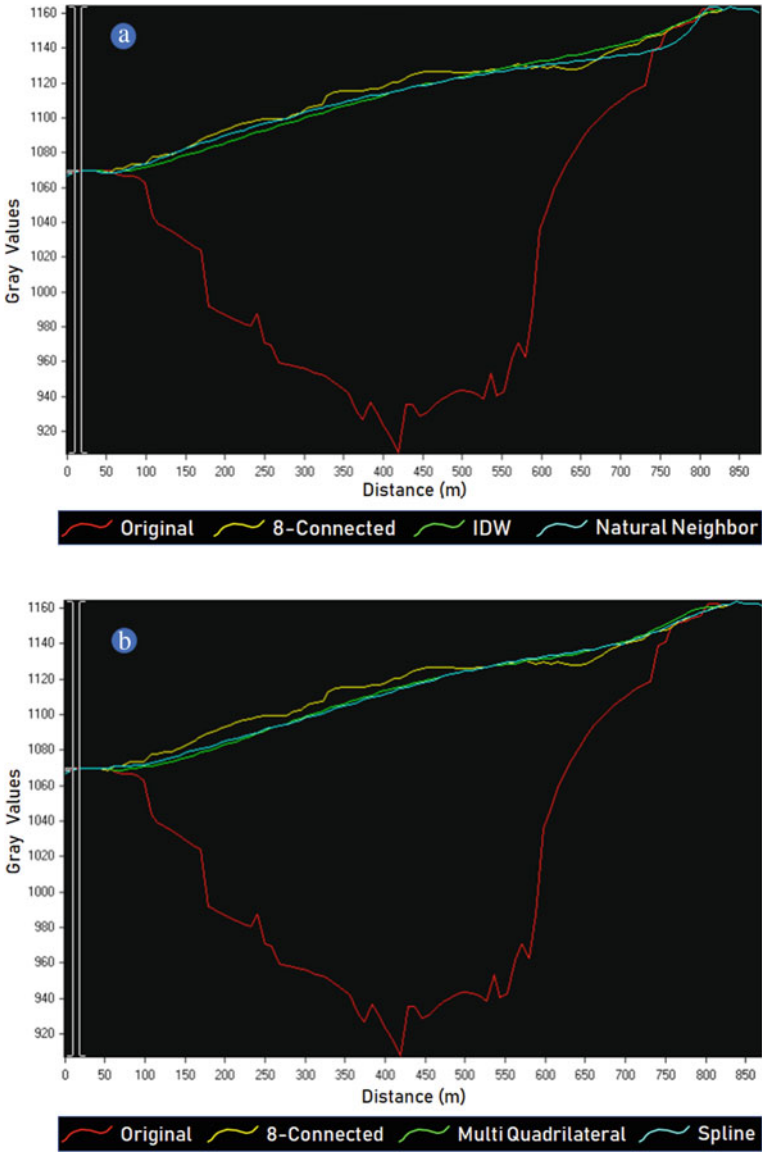

Fig. 18.10 Comparison of 8-connected algorithm with other interpolators. **a** comparison between original DEM and sink corrected DEM generated using 8-connected, IDW and Natural Neighbor algorithms; **b** comparison between original DEM and sink corrected DEM generated using 8-connected, Multi Quadrilateral, and Spline algorithms

the profiles of the original sink, 8-connected, IDW, and Natural Neighbor interpolators. Figure 18.10b compares the profiles of the original sink, 8-connected, Multi Quadrilateral, and Spline interpolators for the same sink region.

As it is evident from these illustrations, the 8-connected algorithm fared well and produced results comparable to that of the established complex interpolation algorithms discussed earlier in Sect. 18.4.2.1. Apart from this, not much difference is observed between the 8-connected and n-connected outputs. Accordingly, the 8-connected algorithm is chosen for implementation into an interactive DEM editing system.

18.4.3 Bias Distortion Correction in Preparation of DEM Mosaics

The availability of free and open-source DEMs at local and global levels has increased their application potential (Nuth and Kaab 2011). To address these applications, the elevation data sets have to be combined to produce regional or global scale products. Mosaicing is the process of combining multiple images into a single seamless composite image (Jensen 2005). It is the process of combining adjacent or overlapping raster layers/images. Papasaika and Baltsavias (2009), Papasaika et al. (2008, 2009, 2011) and Schindler et al. (2011) have used the term 'fusion' while combining DEMs captured with different acquisition techniques or from different times. The fusion of digital surfaces, their optimal combination into a new single dataset, is a crucial topic in the geomatic sciences (Papasaika et al. 2009). The objectives of fusion are fusion of DEMs produced by different technologies, update of existing DEMs and change detection, DEM accuracy improvement, filling of gaps, and preparation of DEM mosaics.

In an automated DEM production chain using satellite stereo imagery, there were two possibilities so far. First, as implemented in ASTER GDEM, all the available stereo pairs are processed, and individual scene-wise DEMs are produced (Fujisada et al. 2012). Second, as implemented in CartoDEM, long stereo strips of 500 km are processed using Stereo Strip Triangulation (Srinivasan et al. 2006), and strip-wise DEMs are produced. In both cases, either we have a scene-wise DEM or a strip-wise DEM. When it comes to producing DEM at regional or even at a map sheet level, the required elevation data sets have to be brought together, mosaiced and a product has to be prepared.

While generating mosaics in an automated way or while fusing DEMs produced from two different sources, there is some bias (offset) present in the DEM in some areas. This is called as 'bias distortion'. An example is shown in Fig. 18.11a, in which a DEM with bias distortion along the mosaic cutline is clearly seen. This is caused due to the bias in elevation values (in this case, relatively less values) compared to the surroundings. The amount of positive or negative bias that has to be added can

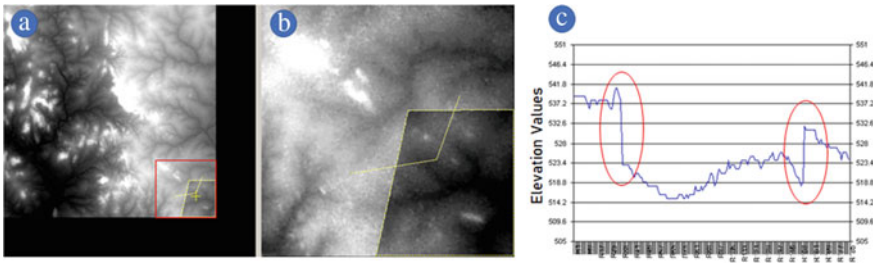

Fig. 18.11 DEM with Bias distortion, **a** showing the DEM image with bias distortion and **b** Zoom of the area shown within red colored box in (**a**); **c** elevation profile drawn across the mosaic cutline, with red circles indicating sudden drop in the elevation values due to the bias distortion

be estimated by drawing a profile across the region, as shown in Fig. 18.11b. The corresponding elevation profile is shown in Fig. 18.11c.

The presence of the bias is confirmed by the sudden drop in elevation values (Fig. 18.11c). It is seen very clearly here that the variations present between the encircled regions of the profile are genuine local variations and have to be maintained/preserved even in the final DEM.

18.4.3.1 Proposed Solution for solving Bias Distortion

The underlying idea of the proposed solution is to estimate the amount of bias present in the region compared to the surroundings in an interactive way by interpreting elevation profile and accounting for it. This idea is implemented in a stand-alone interactive editing software developed in Microsoft Visual Studio environment using Visual C++ Language and GeoTIFF image format libraries. The DEM in TIFF format is the input for this software. The overall process flow for solving this problem involves the following steps.

1. Displaying the DEM image in overview (compressed mode)
2. Identifying the region having mosaic distortion in 1:1 resolution
3. Drawing a line across the distorted region to study the elevation profile
4. Applying the Bresenham's (1965) algorithm to find the pixels covered by the profile line
5. Extracting the DEM values of the pixels under the profile line
6. Displaying the 2-D elevation profile.
7. From the DEM profile, estimating the amount of bias to be added
8. Drawing a region of interest (ROI), where this bias has to be applied
9. Adding the amount of bias to the DEM values in the ROI
10. Feathering to remove the discontinuities
11. Producing another DEM image incorporating these bias adjusted DEM values.

The result of this procedure applied on a DEM is seen in Fig. 18.12a, where the bias is estimated by raising elevation values, and the profile is adjusted, accounting

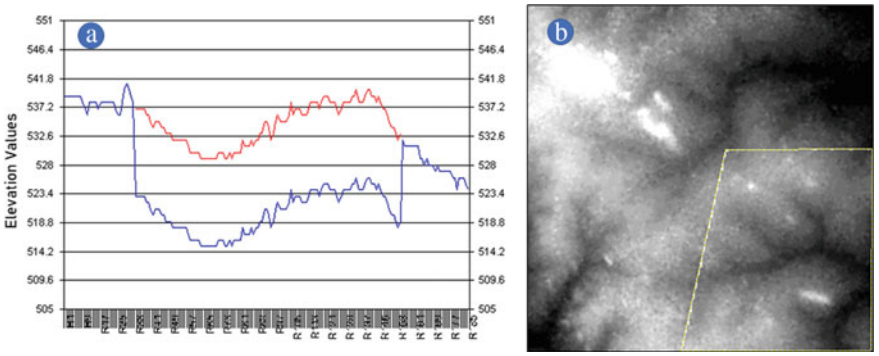

Fig. 18.12 Application of bias correction. **a** Bias estimation by raising of the elevation profile. The original profile is displayed in blue, the profile after applying the estimated bias is shown in red; **b** the resultant DEM after correcting for the bias distortion

for the bias present but still maintaining the genuine local variations in the elevation values between the two abrupt drops in the profile. The resultant output DEM is free of bias distortion, and the elevation value is seamless along the mosaic cutline (Fig. 18.12b).

18.4.4 Hydrological Conditioning of DEM

Hydrologic conditioning refers to modifying topographic data in a raw or 'bare earth' DEM through a series of GIS processing steps to more accurately represent the movement of water across the landscape. Hydrological conditioning, as also called as 'hydro-flattening' of DEMs, is predominantly accomplished through the use of breaklines. Maune (2007) provide the definitions related to the adjustment of DEM surfaces for hydrologic analyses. 'Hydro-Conditioned' and 'Hydro-Enforced' are important and useful modifications, and they both result in surfaces that differ significantly from a traditional DEM. A 'hydro-conditioned' surface has had its sinks filled and may have had its water bodies flattened (NGP 2010).

If the DEM is produced using manual methods, the editing system will have functionality to incorporate breaklines etc. But this process is highly labor-intensive and time-consuming, thereby increasing the cost of production. The DEM generated using fully automatic processes will have issues with hydro-conditioning. One such issue of surface water body flattening is explained in Sect. 18.4.1. This section illustrates how the elevation values can be adjusted in the case of streams/rivers as post-processing operations.

The process includes enforcing drainage connections such as culverts, storm sewers, and known tile drainage. In normal DEM, Flow accumulation lines from DEMs do not match vector stream lines. Reconditioning of the DEM is necessary

so that all cells drain toward the stream and downstream. Drainage enforcement algorithms are implemented in COTS tools using 3 methods, namely,

(a) ANUDEM (Hutchinson 2006)
(b) AGREE (Hellweger and Maidment 1997) and
(c) IDDEA (Inverse Distance Drainage Enforcement Algorithm).

To perform hydrological conditioning along streams and rivers, custom software is built which performs the following steps, and the same is depicted in the flow chart (Fig. 18.13), and elaborated step by step below.

1. Clipping river polygons inside of original DEM extent.
2. Splitting of river line features inside river polygons.

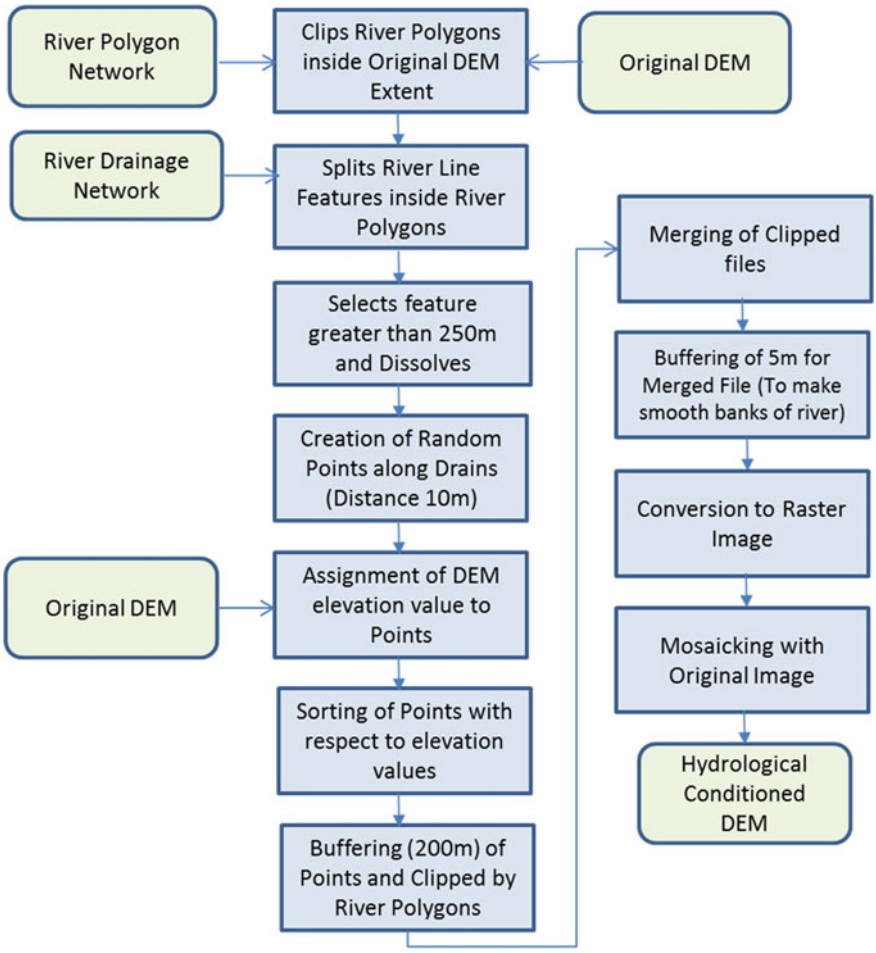

Fig. 18.13 Methodology for Hydrological Conditioning of DEM using river polygon network

3. Dissolving of river line features whose lengths are greater than 250 m into single feature.
4. Generation of a series of random points (intermediate distance 10 m) along with river line features.
5. Assigning value of DEM elevation to these random points.
6. Sorting the elevation points, so that elevation values are in descending order while iterating through points.
7. Buffering of the elevation points with buffer distance of 200 m and clipping using river polygon network.
8. Merging of the clipped shapefile into a single shapefile.
9. Implementing buffering of 5 m to accommodate smoothness to river banks.
10. Conversion of the buffered file into raster image.
11. Mosaicing of the resultant raster image with original image to produce a conditioned DEM.

For evaluation of processed DEM, elevation profiles are generated along and across river polygons to assess the hydrological conditioning of the DEM (Fig. 18.14).

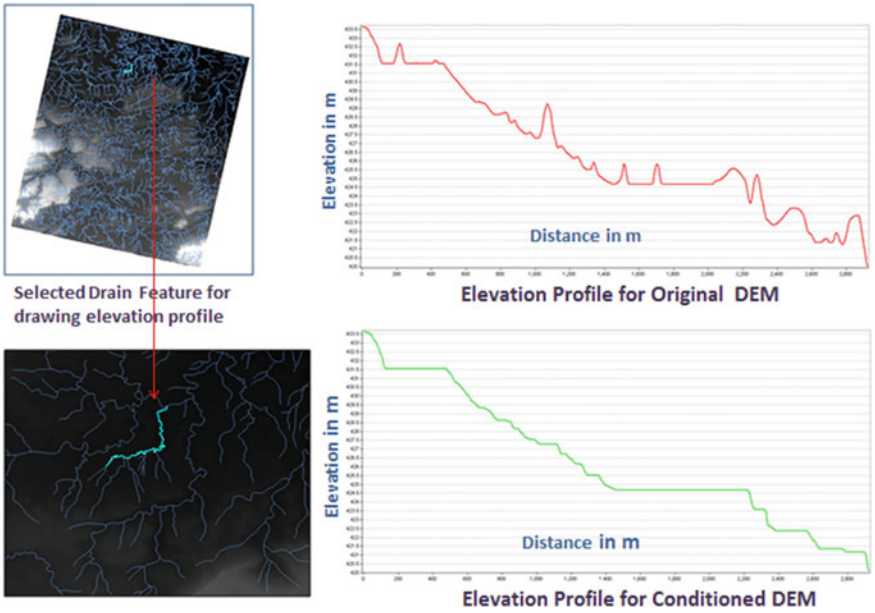

Fig. 18.14 Elevation profile of original and processed DEM for selected river segment

18.4.5 Role of Multi-temporal Stereo Data

18.4.5.1 DEM Accuracy Improvement

Traditionally Photogrammetric data processing has been labor-intensive with lot of manual intervention. However, some amount of automation also has been built into the system for processing voluminous data. As remote sensing stereo data can be acquired many times for the same area, these rich data sets could be put to use for improving the quality of DEM. ASTER has implemented this kind of idea in the preparation of ASTER GDEM by processing millions of stereo pairs (Fujisada et al. 2012).

As more stereo pairs are at our disposal, multiple DEM datasets for the same area can be prepared, these DEM datasets can be used to remove the outliers at each pixel, and appropriate elevation can be assigned at that location. The ASTER methodology has been improved further with the incorporation of more algorithms for outlier removal and fixing candidate elevation value at a pixel.

The improved methodology for the removal of outliers and improving DEM accuracy has been tested in two sites near Mahabaleshwar and Pachmadi. For each site, stereo data pertaining to 11 dates have been processed using the traditional photogrammetric approach using DGPS-based control points without doing any manual editing. All the 11 produced DEMs were stacked to form one single image stack so that at each pixel 11 elevation values are available.

Four different approaches have been implemented to filter the outliers and assigning elevation values at each pixel through a custom-developed open-source software.

1. *Median-based*: outlier elimination and an average of remaining pixels at each pixel (Fujisada et al. 2012).
2. *1-Sigma Based*: at each pixel, the mean and standard deviation (SD) of elevation values are computed. The DEM value at each pixel is computed as average of pixel values falling in the envelope of (mean – SD) to (mean + SD) as shown in the process flow chart (Fig. 18.15).
3. *Median + -:* Median at a pixel value of the stack is computed. The DEM value at each pixel is computed as an average of median value, values above and below the median value.
4. *Average of best DEMs*: This is a two-step process. In the first step, median filtering as applied by Fujisada et al. (2012) is used. In this process, it is important to keep track as to how many times elevation values from a particular DEM channel has contributed to the output and not got eliminated in the median-based outlier elimination process. Based on this count output value at a pixel is produced as an average of the best 'n' channels, 'n' being the value of a number of channels between 1 and the number of channels in that stack.

A sample image produced using one of the above techniques is presented in Fig. 18.16.

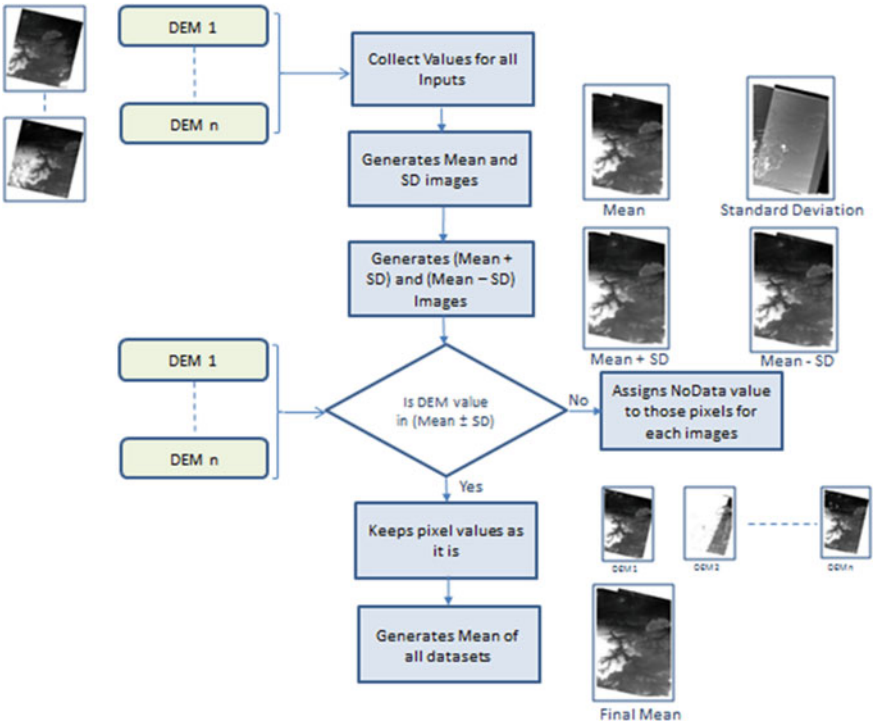

Fig. 18.15 Process flow for implementation of I-sigma-based filtering of outliers for improving DEM accuracy

18.4.5.2 Producing Super Resolution DEM

Generally, the posting interval/grid spacing in a typical DEM that can be produced using a particular stereo dataset is of the order of 3 GSD (Ground Sampling Distance). For instance, if a satellite stereo pair data with 2.5 m spatial resolution data is used to generate a DEM, the best possible posting interval would be 10 m. The process of producing a 'super resolution' DEM considers 4 × 4 pixels of one of the images of the stereo pair, and the typical mass point generation algorithm will pick the best possible pixel (based on a criteria). Then conjugate point in the other image of the pair is found using epi-polar geometry and image matching. If multiple stereo pairs are used, the interesting point and subsequent mass point location may change (Fig. 18.17). By applying this process to multi-temporal stereo datasets will result in elevation samples at better resolution. This idea can be extended to produce a higher/super resolution DEM.

This process is easily automated through a custom-developed software. A blank output image, with the resolution of user's choice is prepared as an input to this software. A resampling process is employed working from the output coordinate system. For each pixel in the output, the candidate input pixel is found, and the

Fig. 18.16 Output of the process of DEM accuracy improvement using I-sigma-based filtering of outliers by using multi-temporal stereo data. Example of Mahabaleshwar area, Maharashtra

stack of pixel values from the input is extracted. The elevation values are filtered for outliers. Suppose there are 'n' channels in the stack, 'k' outliers are eliminated, remaining $(n - k)$ pixel values are used to estimate the elevation at that output position. At every pixel location in the output, $(n - k)$ random numbers between 0.1 and 1.0 are generated, whose sum equals 1.0. These random numbers are used as weights to produce the output elevation value at that location. The advantage of this technique is it uses more sample values to produce elevation value at a particular location, instead of doing simply resolution resampling.

18.5 Conclusion

DEM Quality is a complex issue, and there are many factors to it. The quality of the automatically derived DEMs could be improved by applying Geospatial technology tools and custom-built methodologies/software.

Non-uniformity of elevation values over water bodies is one of the issues in automatically derived DEMs. As a solution, the water body flattening algorithm is developed and successfully implemented in the automatic processing chain of National Level CartoDEM development. Sinks/spikes are commonly seen in automatically created DEMs as a result of improper point matching or result of errors during

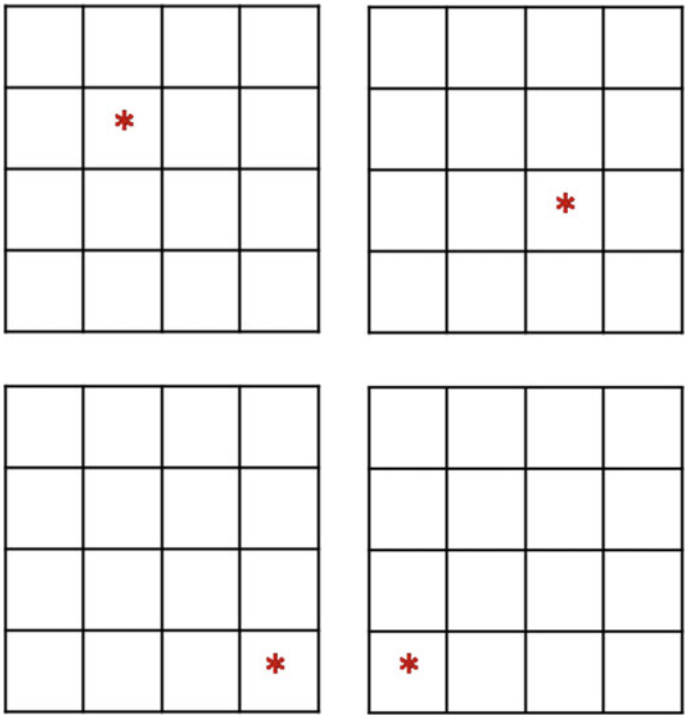

Fig. 18.17 An example of use of multiple stereo pair in generation of a super-resolution DEM, showing the possible location of the interest points

interpolation. Automatic identification of such regions may result in further anomalies. Different candidate algorithms are analyzed to solve this problem. 8-connected distance weighted average algorithm is found more accurate for filling such sink regions in an interactive way and has been successfully implemented in generating national level DEMs such as CartoDEM.

When DEMs are mosaiced, there may be some regions where the elevation is inconsistent with the surrounding region, having bias distortion. A technique suitable for an interactive editing environment is designed and developed, wherein the amount of bias distortion can be estimated based on editing the elevation profile. That bias can be applied, and improved quality DEM mosaics are generated for regional area products. Automatically derived DEMs are generally ill-conditioned along drainage lines and rivers, unfavorable for hydrological applications. Custom solutions have been developed for addressing this issue, and hydrologically corrected improved DEMs are generated. Multi-temporal coarser DEMs datasets-based algorithms have been developed for the generation of super-resolution DEMs, which provides an alternate method of producing DEMs at finer resolutions, which are needed for several developmental planning applications at the micro-level.

References

Adams R, Bischof L (1994) Seeded region growing. IEEE Trans Pattern Anal Machine Intell 16:641–647

Amato R, Dardanelli V, Emmolo D, Franco V, Lo Brutto M, Midulla P, Orlando P, Villa B (2004) Digital orthophotos at a scale of 1:5000 from high resolution satellite images. Int Arch Photogram Remote Sens Spatial Inform Sci 35(B4):593–598

Baltsavias EP, Pateraki M, Zhang L (2001) Radiometric and Geometric Evaluation of IKONOS Geo Images and Their Use for 3D Building Modeling. In: Proceedings of joint ISPRS Workshop on "high resolution mapping from space 2001", 19–21 September, Hannover, Germany, on CD-ROM

Carrara A, Bitelli G, Carla R (1997) Comparison of techniques for generating digital terrain models from contour lines. Int J Geogr Inf Sci 11(5):451–473

Coltelli M, Fornaro G, Franceschetti G, Lanari R, Migliaccio M, Moreira JR, Papathanassiou KP, Puglisi G, Riccio D, Schwabisch M (1996) SIR-C/X-SAR multifrequency multipass interferometry: a new tool for geological interpretation. J Geophys Res 101:23127–23148

Deilami K, Hashim M (2011) Very high-resolution optical satellites for DEM generation: a review. Eur J Sci Res 49(4):542–554

Eisenbeiss H, Baltsavias EP, Pateraki M, Zhang L (2004) Potential of IKONOS and QUICKBIRD imagery for accurate 3D-point positioning, orthoimage and DSM generation. Int Arch Photogram Remote Sens 35(B3):522–528

Farr TG, Kobrick M (2000) Shuttle radar topography mission produces a wealth of data. Am Geophys Union 81:583–585

Farrow J, Murray K (1992) Digital photogrammetry—options and opportunities. Int Arch Photogramm Remote Sens 29(B2):397–403

Fraser C, Hanley HB (2003) Bias compensation in rational functions for IKONOS satellite imagery. Photogramm Eng Remote Sens 69(1):53–57

Fraser CS, Baltsavias EP, Gruen A (2002) Processing of IKONOS imagery for sub-meter 3D positioning and building extraction. ISPRS J Photogramm Remote Sens 56(3):177–194

Fujisada H, Urai M, Iwasaki A (2012) Technical methodology for ASTER global DEM. IEEE Trans Geosci Remote Sens 50(10):3725–3736

Giribabu D, Srinivasa Rao S, Krishna Murthy YVN (2013) Improving Cartosat-1 DEM accuracy using synthetic stereo pair and triplet. ISPRS J Photogramm Remote Sens 77:31–43

Gonzalez RC, Woods RE (2002) Digital image processing, 2nd ed. Prentice Hall, New Jersey, p 460

Gopala Krishna B, Iyer KV, Goswami A, Alurkar M, Rana YP, Srivastava PK, Majumder KL (1998) Approach for generation of digital elevation models (DEM) and orthoimages from IRS-1C stereo data. Int Arch Photogramm Remote Sens XXXII(Part I):164–171

Grodecki J, Dial G (2003) Block adjustment of high-resolution satellite images described by rational polynomials. Photogramm Eng Remote Sens 69(1):59–68

Haibo Y, Zongmin W, Hongling Z, Yu G (2011) Water body extraction methods study based on RS and GIS. In: Proceedings of 3rd international conference on environmental science and information application technology (ESIAT 2011), pp 2619–2624

Hellweger F, Maidment D (1997) AGREE-DEM surface reconditioning system

Heipke C (1995) State-of-the-art of digital photogrammetric workstations for topographic applications. Photogramm Eng Remote Sens 61(1):49–56

Heywood I, Cornelius S, Carver S (1998) An introduction to geographical information systems. Longman, Harlow

Hutchinson MF (1989) A new procedure for gridding elevation and stream line data with automatic removal of spurious pits. J Hydrol 106:211–232

Hutchinson MF (2006) ANUDEM Version 5.2, Centre for Resource and Environmental Studies, The Australian National University

Jacobsen K (2001) New developments in digital elevation modelling, geoinformatics, June 2001, S.18–21. http://www.ipi.uni-hannover.de/uploads/tx_tkpublikationen/jac_DevelopDEM.pdf

Jacobsen K (2002) Comparison of high resolution mapping from space. In: INCA workshop 2002, Ahmedabad
Jacobsen K (2003) Geometric Potential of IKONOS- and QuickBird-Images, In: Fritsch D (ed) Photogrammetric weeks '03, pp 101–110
Jacobsen K (2004) DTM generation by SPOT5 HRS. Int Arch Photogramm Remote Sens 35(B1):439–444
Jenson S (1991) Applications of hydrologic information automatically extracted from digital elevation models. Hydrol Processes 5:31–44
Jensen JR (2005) Introductory digital image processing: a remote sensing perspective, 3rd ed. Prentice Hall, New Jersey, 2005, p 250
Jenson S, Domingue JO (1988) Extracting topographic structure from digital elevation data for geographic information system analysis. Photogramm Eng Remote Sens 54(11):1593–1600
Kelley D, Loecherback T (2006) Challenges and successes in photogrammetric approaches to LIDAR-derived products. In: Proceedings MAPPS/ASPRS 2006 Fall Conference, San Antonio, Texas, 6–10 November, (on CDROM)
Krishna Murthy YVN, Srinivasa Rao S, Prakasa Rao DS, Jayaraman V (2008) Analysis of DEM generated using CARTOSAT-1 stereo data over MAUSANNE LES ALPILES –CARTOSAT scientific APPRAISAL PROGRAMME (CSAP TS – 5). The international archives of the photogrammetry, remote sensing and spatial information sciences Vol.XXXVII. Part B1. Beijing
Lee HY, Kim T, Park W, Lee HK (2003) Extraction of digital elevation models from satellite stereo images through stereo matching based on epipolarity and scene geometry. Image vis Comput 21(9):789–796
Li Z, Zhu Q, Gold C (2005) Digital terrain modeling: principles and methodology. CRC Press, Boca Raton, FL, p 323
Lindsay JB, Creed IF (2005) Removal of artifact depressions from digital elevation models: towards a minimum impact approach. Hydrol Processes 19:3113–3126
Lindsay JB, Creed IF (2006) Distinguishing actual and artifact depressions in digital elevation data. Comput Geosci 32(8):1192–1204
Martz LW, Garbrecht J (1999) An outlet breaching algorithm for the treatment of closed depressions in a raster DEM. Comput Geosci 25:835–844
Maune D (2007) The digital elevation model technologies and applications: the DEM users manual, 2nd ed. ASPRS Publication
Mitchell HL, Chadwick RG (1999) Digital photogrammetric concepts applied to surface deformation studies. GEOMATICA 53(4):405–414
NGP (2010) USGS national geospatial program: lidar guidelines and base specification, ILMF 2010. http://lidar.cr.usgs.gov/USGS-NGPUSGS-NGP Lidar Guidelines and Base Specification v13(ILMF).pdf
Nikolakopoulos KG (2020) Accuracy assessment of ALOS AW3D30 DSM and comparison to ALOS PRISM DSM created with classical photogrammetric techniques. Euro J Remote Sens 53(sup2):39–52. https://doi.org/10.1080/22797254.2020.1774424
Nuth C, Kaab A (2011) Co-registration and bias corrections of satellite elevation data sets for quantifying glacier thickness change. Cryosphere 5:271–290
O'Callaghan JF, Mark DM (1984) The extraction of drainage networks from digital elevation data. Paper presented at Computer Visualization Graph. Image Proceedings of GIS/LIS, GIS/LIS
Papasaika H, Poli D, Baltsavias E (2008) A framework for the fusion of Digital Elevation Models. In: Proceedings of the XXI ISPRS Congress, Beijing, China, July, 2008
Papasaika H, Baltsavias E (2009) Fusion of LiDAR and photogrammetric generated digital elevation models. In: Proceedings of the ISPRS Hannover workshop on high-resolution earth imaging for geospatial information, Hannover, Germany, 2–5 June, 2009
Papasaika H, Poli D, Baltsavias M (2009) Fusion of digital elevation models from various data sources. In: The international conference on advanced geographic information systems and web services, February 1–7, Cancun, Mexico

Papasaika H, Baltsavias E (2010) Quality evaluation of DEMs. In: Proceedings of the Accuracy 2010, Leicester, UK, 20–23 July, 2010, pp 249–252

Papasaika H, Kokiopoulou E, Baltsavias E, Schindler K, Kressner D (2011) Fusion of digital elevation models using sparse representations. In: Proceedings of the photogrammetric image analysis, Munich, Germany, 5–7 October, 2011

Poli D (2005) Modelling of spaceborne linear array sensors, Ph. D. Dissertation, IGP Report No. 85, ISSN 0252-9335 ISBN3-906467-3, Institute of Geodesy and Photogrammetry, ETH Zurich, Switzerland

Poli D, Zhang L, Gruen A (2004) SPOT-5/HRS stereo image orientation and automatic DSM generation. Int Arch Photogramm Remote Sens 35(B1):421–432

Reinartz P, d'Angelo P, Krauss T, Chaabouni-Chouayakh H (2010) DSM generation and filtering from high resolution optical stereo satellite Data. In: Proceedings 30th European association remote sensing laboratories (EARSeL) Symposium, Paris, France, 31 May–3 June, pp 527–536

Reuter HI, Nelson A, Jarvis A (2007) An evaluation of void filling interpolation methods for SRTM data. Int J Geogr Inf Sci 21(9):983–1008

Rieger W (1998) A phenomenon-based approach to upslope contributing area and depressions in DEMs. Hydrol Processes 12:857–872

Sadeghian S, Zoej MJV, Delavarl MR, Abootalebiz A (2001) Precision rectification of high resolution satellite imagery without ephemeris data. JAG 3(4)

Schenk T (1999) Digital photogrammetry (TerraScienze, Laurelville, OH), 1, pp 41–76

Schindler K, Papasaika H, Schütz S, Baltsavias E (2011) Improving wide-area DEMs through data fusion - chances and limits. In: Proceedings of the 53rd Photogrammetric week

Sefercik UG, Alobeid A, Soergel U, Jacobsen K (2010) Generation and analysis of DEMs based on space-borne remote sensing. In: 17th international symposium. Damascus, 2010, CD

Srinivasan TP, Singh S, Neethinathan P, Nain JS, Gupta A, Misra G, Kartikeyan B, Gopala Krishna B, Srivastava PK (2006) Stereo Strip Tringulation for Cartosat-1, Technical Commission IV symposium on "Geospatial Databases for sustainable development", Goa, India

Srivastava PK, Gopala Krishna B, Srinivasan TP, Amitabh Trivedi S, Nandakumar R (2006) Cartosat-1 data products for topographic mapping. In: ISPRS Commission-IV international symposium on "geospatial databases for sustainable development, Goa 27–30 September

Srivastava PK, Srinivasan TP, Gupta A, Singh S, Nain JS, Amitabh Prakash S, Katikeyan B, Gopala Krishna B (2007) Recent advances in Cartosat-1 data processing, ISPRS Hannover Workshop 2007: Hannover, Germany. http://www.isprs.org/proceedings/XXXVI/1-W51/paper/Srivastava_etal.pdf

Toutin Th (2001) Elevation modeling from satellite visible and infrared (VIR) data: a review. Int J Remote Sens 22(6):1097–1125

Toutin T (2002) Three-dimensional topographic mapping with ASTER stereo data in rugged topography. IEEE Trans Geosci Remote Sens 40(10):2241–2247

Toutin Th (2004) Comparison of stereo-extracted DTM from different high-resolution sensors: SPOT-5, EROS-A, IKONOS-II, and QuickBird. IEEE Trans Geosci Remote Sens 42(10):2121–2129

Toutin Th, Cheng P (2002) QuickBird–milestone for high resolution mapping. Earth Observ Maga 11(4):14–18

Toutin Th, Briand P, Chenier R (2004) DTM Generation from SPOT5 HRS In-Track stereo Images. Int Arch Photogramm Remote Sens 35(B1):416-420

Wild D, Krzystek P (1996) Automatic breakline detection using an edge preserving filter. Int Arch Photogramm Remote Sens 31(Part B3):946–952

Wood JD (1994) Visualising contour interpolation accuracy in digital elevation models. In: Hearnshaw HM, Unwin DJ (eds) Visualization in geographical information systems. Wiley, Chichester, pp 168–180

Wood JD (1996) The geomorphological characterisation of digital elevation models. PhD Thesis, University of Leicester. http://www.soi.city.ac.uk/~jwo/phd/

Yuan F, Zhang JX, Zhang L, Gao JX (2011) DEM generation from airborne LIDAR data. Int Arch Photogramm Remote Sens Spatial Inform Sci 38(Part 7/C4):308–312

Zhang L, Gruen A (2004) Automatic DSM generation from linear array imagery data. Int Arch Photogramm Remote Sens 35(B3):128–133

Zhu D, Ren Q, Xuan Y, Chen Y, Cluckie I (2013) An effective depression filling algorithm for DEM-based 2-dimensional surface flow modelling. Hydrol Earth Syst Sci Discuss 17:495–505

Chapter 19
Assessment of Urban Dynamics Using Geospatial Techniques

Sudha Ravindranath, Shivam Trivedi, S. Rama Subramoniam, T. R. Nagashree, V. Poompavai, A. Vidya, H. M. Ravishankar, R. Hebbar, and C. S. Jha

Abstract Bengaluru, the capital of Karnataka state and IT capital of India, is well known globally for its affable weather and greenery. During the last few decades, Bengaluru has witnessed phenomenal growth due to various factors, including rapid urbanization, unprecedented population expansion, and Spatio-temporal changes in vegetation cover and lakes. Reliable quantitative information about urban dynamics, especially in terms of vegetation cover and the lake system, is extremely crucial for preserving the quality of life in cities, suburbs, and periphery of metropolitan areas. A detailed geospatial study was carried out using satellite to understand the decadal changes in the vegetated regions and other land use/land cover classes in Bruhat Bengaluru Mahanagara Palike (BBMP) area to understand the decadal

S. Ravindranath (✉) · S. Trivedi · S. R. Subramoniam · T. R. Nagashree · V. Poompavai · A. Vidya · H. M. Ravishankar · R. Hebbar
Regional Remote Sensing Centre-South, NRSC, ISRO, Bengaluru, Karnataka, India
e-mail: ravindranath_s@nrsc.gov.in

S. Trivedi
e-mail: shivamtrivedi@nrsc.gov.in

S. R. Subramoniam
e-mail: ramasubramoniam_s@nrsc.gov.in

T. R. Nagashree
e-mail: nagashree_tr@nrsc.gov.in

V. Poompavai
e-mail: poompavai_v@nrsc.gov.in

A. Vidya
e-mail: vidya_a@nrsc.gov.in

H. M. Ravishankar
e-mail: ravishankar_hm@nrsc.gov.in

R. Hebbar
e-mail: hebbar_kr@nrsc.gov.in

C. S. Jha
Regional Centres, National Remote Sensing Centre, ISRO, Hyderabad, Telangana, India
e-mail: jha_cs@nrsc.gov.in

C. S. Jha et al. (eds.), *Geospatial Technologies for Resources Planning and Management*, Water Science and Technology Library 115,
https://doi.org/10.1007/978-3-030-98981-1_19

changes in the vegetated regions and ancillary datasets. An overall decrease of 4% area under vegetation cover was observed during 2006 and 2019. However, areas under other classes, mainly buildings, transport networks, and other urban categories, increased from 43.9 to 55.3%. A change map highlighting both positive and negative vegetation change areas and the vegetated areas with nominal changes was prepared for 198 BBMP wards. Karnataka Lake Conservation and Development Authority (KLCDA) requested a systematic spatial–temporal change detection study of drainages and lakes falling within the BDA limits. Under the project, lakes which required to be conserved, preserved, rejuvenated to prevent further deterioration the lakes, were identified using satellite and ancillary data. The study revealed that within the Bengaluru Development Authority (BDA) limits, about 500 lakes existed as per the cadastral map inventory, which decreased to 408 as per the inventory of 2017 satellite image. A prioritization of lakes analysis was carried out using the EMPRI's field support which indicated that 8.0% of lakes required revival and 46.0% of lakes required immediate action. The detailed database of lakes generated under the project is of immense importance to chalk out conservation and lake revival plans for a few lakes aimed at restoring the lake system of Bengaluru. This chapter highlights the findings of the studies undertaken for assessment of urban dynamics of Bengaluru city using geospatial techniques.

Keywords Bengaluru · Urbanization · Vegetation · Lakes · BBMP · BDA · Geospatial

19.1 Introduction

Bengaluru city (earlier known as Bangalore) has witnessed phenomenal population growth, especially during the last few decades. Several factors have contributed to urban sprawl of Bengaluru, primarily its pleasant climate with good infrastructure, presence of large technical manpower and skilled labor, comprehensive scientific and industrial base, and Information Technology (IT) in recent times, being the prime driving force, responsible for further city growth. Bengaluru, also known as 'Garden-city of India', encompassing a large area under tree cover, mainly as large number of small and large parks, over 400 lakes and thick vegetation patches in few forested regions along with good vegetation cover in cantonments and many PSUs, Government and research institutions.

Bengaluru city also experienced a lot of industrial growth during the past few decades with the setting up of factories like Hindustan Machine Tools (HMT), Hindustan Aeronautical Limited (HAL), Indian Telephone Industry (ITI), Bharat Electronics Limited (BEL), etc. Additionally, in recent times, Bengaluru has become major software hub with many software technology parks located in various locations of the city. Economic growth has had a significant impact on ecosystems and biodiversity. The city was once known for its tree-lined wide avenues, historic parks, and expansive water bodies. The influx of growth has led to the encroachment and

pollution of water bodies, the felling of thousands of trees, and large-scale conversion of open areas into commercial, industrial, and residential settlements. According to Census, Bengaluru had a population of 12.07 lakhs in 1941, which increased to 29.22 lakhs in 1981 and 84.26 lakhs in 2011. The current city population is about 128.2 lakhs (BBMP 2019). Some of the ill-effects of this phenomenal growth of population due to natural causes and migration, as well as urban expansion led to deterioration of biodiversity, water scarcity and epidemics, consequent impacts on human health and well-being, decrease in vegetation cover, development of slums, unplanned growth, pressure on the infrastructure for sewerage, water supply, garbage disposal, traffic jams, urban flooding, air, and water pollution, etc. within the city.

Globally, urbanization and urban sprawl are causing rapid changes in the ecosystem (Wratten et al. 2013). Behera et al. (1985) studied Bengaluru city growth from 1912 to 1985 utilizing SOI topo maps, as well as Landsat-MSS (1973) satellite image of 80 m spatial resolution and Landsat-TM satellite image of 30 m spatial resolution (1985). Land use land cover included major classes like built-up, agriculture, plantation/parks, scrub, waterbody, rock outcrop, and non-green area, highlighting that the growth of the built-up area was at the cost of surface water bodies and agricultural land. The urban sprawl and developmental activities happening at a very fast pace in Bengaluru City have taken a toll on both the urban vegetation and urban lake system. World Health Organization has recommended a minimum green space of 9.5 m^2/person, considering the goods and services (oxygen, moderation of microclimate etc.) of an urban environment (Ramachandra et al. 2014). Urban vegetation represents more significant heterogeneity in the form of green spaces, including parks, avenue trees, home gardens, office complexes, plantations, and urban forests. For maintaining a better quality of life in urban regions, tree patches and green lung spaces have been extremely essential as they provide numerous benefits; hence detailed information about urban green cover in the suburbs and the fringes of metropolitan areas is a prerequisite (Dimitrov et al. 2018). Lakes/tanks are an essential part of the urban ecosystem for the conservation of water, recharging groundwater, and maintaining the biodiversity of the region. Due to the rapid urbanization of Bengaluru, many lakes have been slowly altered to layouts, buildings, parks, playgrounds, stadiums, bus stands, industrial sheds etc. and the rest of the surviving lakes have turned into cesspools as a result of indiscriminate discharge of industrial sewages and unrestricted discarding of solid wastes. Further, deterioration of the lakes may lead to water scarcity and reduce groundwater recharge, which would adversely affect the wetlands ecosystem of the city.

In view of the developmental activities in Bengaluru city, such as road-widening, metro-line construction, expansion of built-up areas as new lay-outs and high-rise buildings, increasing population, various integral components of urban dynamics and Spatio-temporal changes needs to be understood. Geospatial techniques provide excellent tools for carrying out these studies due to the multi-temporal and synoptic coverage of satellite imagery and amenability for digital image processing. Thus, an in-house research initiative on assessment of vegetation cover change was carried out (RRSC-South 2019), and the lake inventory was carried out as a user project, titled 'Spatio-Temporal Analysis of Lakes of Bengaluru' (S-TALAB) in collaboration with

KLCDA, Bengaluru (RRSC-South 2018). The present chapter discusses the results of these two studies.

19.2 Study Area

Bengaluru, the capital city of Karnataka state, India, is among the rapidly growing cities of the world and is located in the southern part of the Deccan Plateau. Bruhat Bengaluru Mahanagara Palike (BBMP) limits of Bengaluru is the study area for assessment of temporal changes in vegetation cover, land use, and land cover (Fig. 19.1a). BBMP jurisdiction covers the majority area of the Bengaluru urban district and lies between 77°25′ to 77°48′ E longitude and 12°50′ to 13°10′ N latitude.

Due to its elevation, Bengaluru enjoys a pleasant and equable climate throughout the year. The average minimum temperature range during winter is 10–15 °C, and the maximum summer temperature range is between 30 and 38 °C. Bengaluru receives about 970 mm of rain annually, the wettest months being August, September, and October.

Bengaluru City is drained by two minor rivers Vrishabhavathi River, a tributary of Arkavathi, which flows for a small stretch on the west side, and the other one is Dakshina Pinakini or South Pennar, which flows in the eastern region of the city. Hebbal, Koramangala-Challaghatta, and Vrishabhavathi are the three major valley systems. The city is situated at an elevation of 920 m above Mean Sea Level with undulating topography of hills and valleys. Bengaluru is unique, where the lakes form into a group of reservoirs in each of the three valley systems. It is seen that, the ridge top in each valley gives birth to small streams. Due to the natural flow, the streams merge to form a major stream system. Thus, one finds that all the lakes of Bengaluru are located in the valleys interconnected with a group of series of chains of lakes,

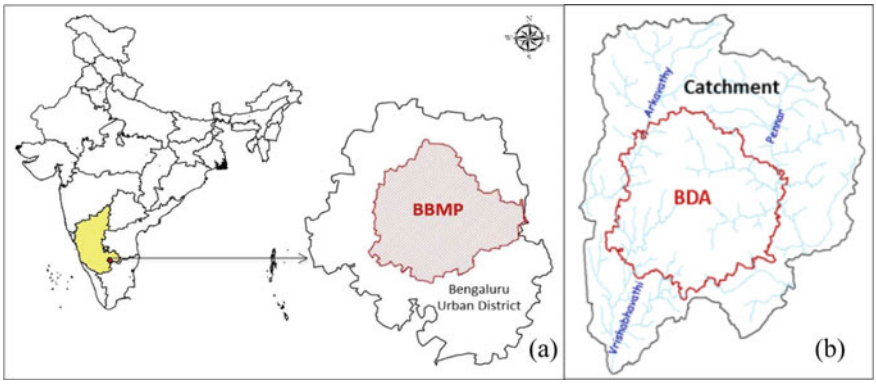

Fig. 19.1 Location of the study areas **a** BBMP region for vegetation cover assessment and **b** BDA region with a catchment area of surrounding watersheds

giving a Cascading effect to the drainage system. For the S-TALAB project, catchment area falling mostly in Bengaluru Urban and Rural districts falling in Cauvery and Dakshinna Pinakini basins has 7 major watersheds. However, the results of the analysis are limited to BDA boundary within the catchment area (Fig. 19.1b).

19.3 Satellite and Ancillary Data Used

For vegetation cover assessment, satellite data of 2006 (IRS-1D PAN + Resourcesat-1 LISS-III merged data), 2019 (Resourcesat-2 LISS-IV, MX) and ancillary datasets were used. Ancillary datasets from different sources, which were utilized directly or as a reference, during the study, include Cartosat-1-based Digital Elevation Model (10 m) for ortho-rectification, legacy data on vector layers on parks, playgrounds, lakes, roads, rail, administrative, and ward boundaries, etc. sourced from BBMP, BBMP ward-wise statistics, Reference Topomaps, Reserved Forest boundary, geo-tagged field photographs and relevant image processing and GIS Software packages, available with the center.

The inventory of lakes within BDA was carried out by using both optical and Synthetic Aperture Radar (SAR) data. Multi-resolution cloud-free optical data viz., merged product of Cartosat-1 + Resourcesat LISSIV (2017) along with Corona Black and White data of 1965 was the primary data for delineating the lake boundary. As when required, Sentinnel-2 optical data was also processed and used, whereas the Sentinel-1 satellite SAR data pertaining to monsoon months corresponding to the non-availability of cloud-free optical data the water spread area. Information collected by EMPRI on various characteristics of the lakes viz., its name, lake code, location details, administrative details etc. has also been incorporated. The existing thematic layers which were created under various national/regional projects were collected and updated using HRS (High-resolution Satellite) data. Collateral information was collected from various related organizations and suitably utilized.

19.4 Methodology

19.4.1 Vegetation Cover Assessment in Bengaluru City

Primarily focussing on the status of vegetation cover, these changes were assessed for the years 2006 and 2019 within the BBMP area. Additionally, all other major Land Use/Land Cover classes have also been classified. Both satellite datasets pertaining to years 2006 and 2019 were digitally classified. Information on 730 Ground Truth locations, along with geo-tagged field photographs, was collected, covering diverse areas of vegetation components with density classes, non-vegetated urban regions

and areas under other major classes. The classified outputs were refined using AOI-based corrections using high-resolution satellite data. Linear features (road, rail) were overlaid after creating appropriate buffers, while the polygon-based features (parks and playgrounds) were overlaid as vegetation and open land suitably. The overall classification scheme was divided into 3 major categories, namely, (a) Vegetation areas comprising of dense vegetation, moderately dense vegetation, and sparse vegetation, (b) Lake areas consisting of water, vegetation in lake, weeds in lake and dry lake/tank area, (c) Others include the non-vegetated part of the study area, viz. built-up, major transport network (road, rail) and other classes (open-land, plot/sites, open area in parks, playgrounds, fallow land, wastelands, etc.).

Area statistics corresponding to different vegetation and other land use land cover classes were generated for both periods (2006 and 2019). These statistics were further analyzed to compute relative deviations and area percentage changes using year 2006 as reference. Ward-wise statistics were also computed for 198 wards of BBMP. Additionally, statistics for 34 prominent areas showing good tree cover were also computed separately and analyzed.

19.4.2 Spatial and Temporal Change Analysis for Lakes of Bengaluru City

Multi-date high-resolution satellite datasets were analyzed along with collateral data like cadastral maps, DEM, toposheets etc., for carrying out spatial and temporal change analysis of lakes for the purpose of generating an inventory as well as monitoring the lakes. Thematic layers were developed for the entire study area (4000 km^2). However, the Spatio-temporal analysis has been carried out for the lakes within BDA limits. The lake jurisdictional boundary as per the survey numbers, was created for lakes greater than 3.0 acres using cadastral maps. The location information of lakes provided by EMPRI served as a reference for lake identification.

19.5 Results and Discussion

The findings and observations of the present study are presented in two sections below, namely (i) Assessment of vegetation and other land use land cover categories (ii) Assessment of spatial and temporal changes in lakes.

19.5.1 Assessment of Vegetation and Other Land Use Land Cover Categories

19.5.1.1 Vegetation Cover Change Analysis

Ortho-rectified IRS-1D PAN merged with Resourcesat-1 LISS-III satellite data was used for classification for the year 2006. It was noticed from the classified output that the vegetation cover was relatively lesser in most of the core urban areas in comparison to the peripheral area. It was also observed that the core city region had a densely built-up area, whereas the peripheral region infrastructure was still developing.

Resourcesat-2 LISS-IV (MX) ortho-rectified satellite dataset was used for classification for 2019. Vegetation cover in Bengaluru was estimated to be 18,572.2 ha (26.1%) in 2019, while in 2006 it was 21,414.9 ha (30.1%), suggesting overall decrease of 4% in vegetation. Similarly, the area under built-up, major transport network, and other urban categories increased from 43.9–55.3% during 2006 and 2019 within BBMP region. Built-up areas were spreading in radial pattern toward the periphery. Numerous high-rise buildings have contributed to vertical growth along with horizontal growth due to new layouts, mostly in the peripheral region of the city.

Increase and densification of vegetation were observed in most government/Public institutions/campuses, Defense lands, and parks. Vegetation cover in some of the forests region viz. Thurahalli, Ibbaluru, Bannerghatta has become denser. Increase of vegetation cover was observed in stabilized residential layouts also. Reduction in vegetation was observed mainly in developing/newly developed lay-outs, areas close to infrastructure development (like ring roads, road-widening, metro rail, etc.) In general, decrease in vegetation cover was noticed in the core city area and peripheral wards. Figure 19.2 gives the status of the vegetation as of 2019 overlaid on ward boundaries and satellite data. Table 19.1 depicts the status of total vegetation cover in 2006 and 2019 with reference to a geographical area. At one hand reduction in vegetation has occurred due to construction activities, while at the other (Figs. 19.4 and 19.6), densification and increase in vegetation cover is conspicuously witnessed (Figs. 19.3 and 19.5). Therefore, the overall impact due to negative changes in vegetation cover at specific locations is minimized due to the positive changes and density improvement in vegetation cover at various other locations, within the city.

19.5.1.2 Vegetation Change Analysis at Ward Level Within Bengaluru

There are about 198 wards within the BBMP region whose geographical areas vary from a minimum of 32 ha to a maximum of 2847 ha (Fig. 19.7). Based on their area, these wards have been divided into five categories for carrying out a detailed analysis of vegetation status during two time periods. It is seen that wards greater

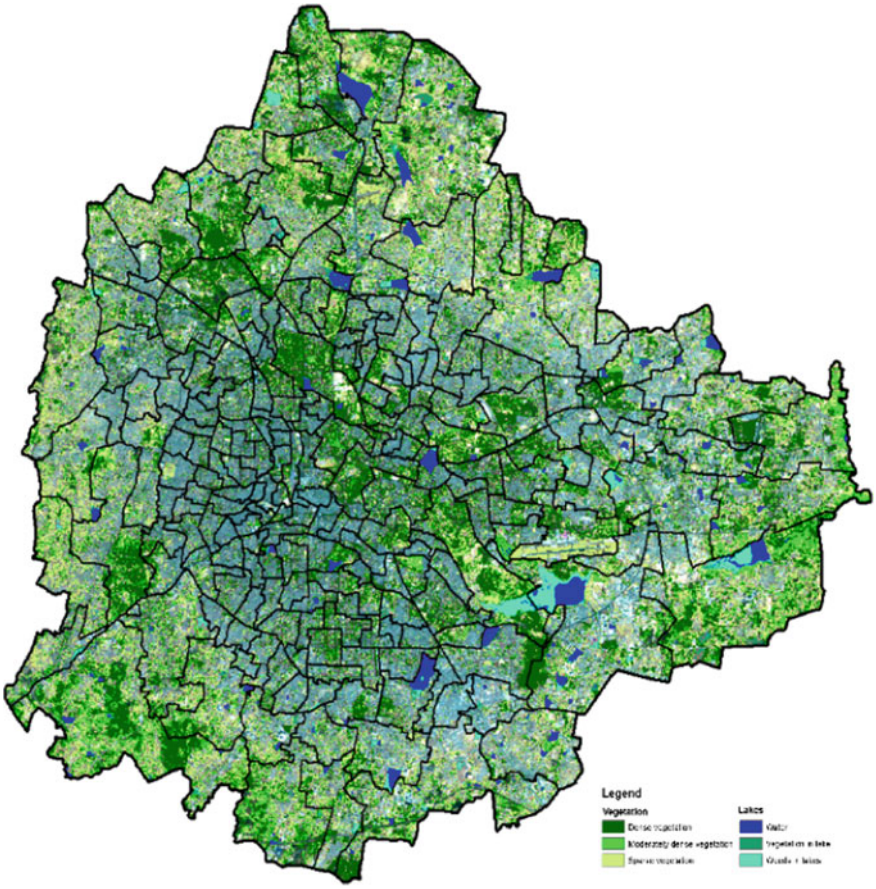

Fig. 19.2 Status of vegetation and lakes of Bengaluru in 2019. (Overlaid on 2019 LISS-IV FCC, with BBMP wards boundaries)

Table 19.1 Vegetation change area estimates across 2006 and 2019

Year	Area under vegetation (Tree cover) in ha	% Contribution wrt total BBMP geographical area
2006	21,414.9	30.1
2019	18,572.2	26.1
	Overall change	− 4.0

than 500 ha or 1000 ha are mostly located in peripheral regions, while the smaller wards are mainly located in the core city area.

Out of the total 198 wards of BBMP, 82 wards exhibited a positive trend with vegetation increase, 54 wards showed a negative trend with a decrease in vegetation

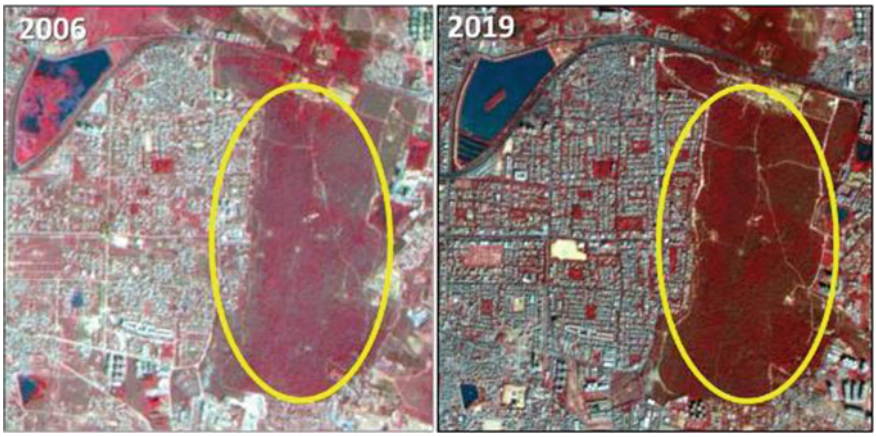

Fig. 19.3 Positive changes—Densification of vegetation in Ibbaluru forest; Agara lake rejuvenation is also seen

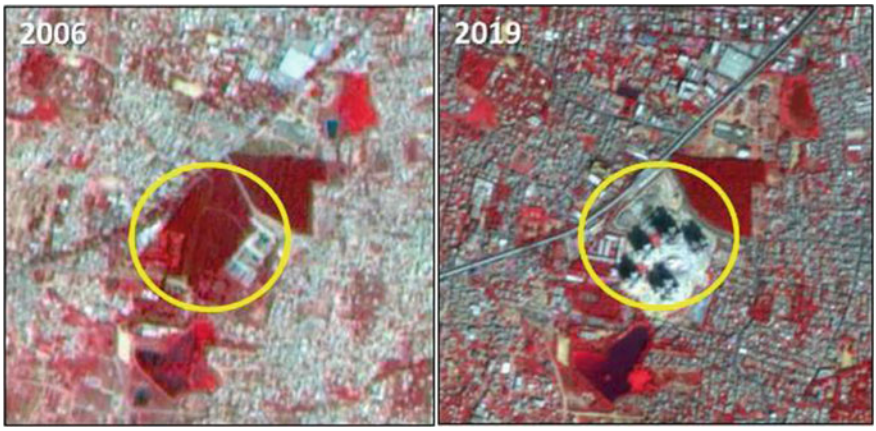

Fig. 19.4 Negative changes—Dense plantation patch converted to construct high-rise buildings in Konanakunte

cover, and 62 wards showed minimal changes in terms of vegetation cover with respect toward area (within 2%).

Urbanization is on the rise inwards located in peripheral region viz. ward numbers 1, 2, 3, and 11 in Yelahanka (toward north), due to location of International Airport and Aerospace zone; ward numbers 53, 54, 55, 81, 83, 84 and 85 in Mahadevapura (eastern side) due to presence of Information Technology Park Limited (ITPL) and other software technology parks and ward numbers 159 and 198 in RR Nagara (south-west toward Mysore road) due to upcoming residential lay-outs and construction of houses. Within wards in the core city, many old buildings have been dismantled to

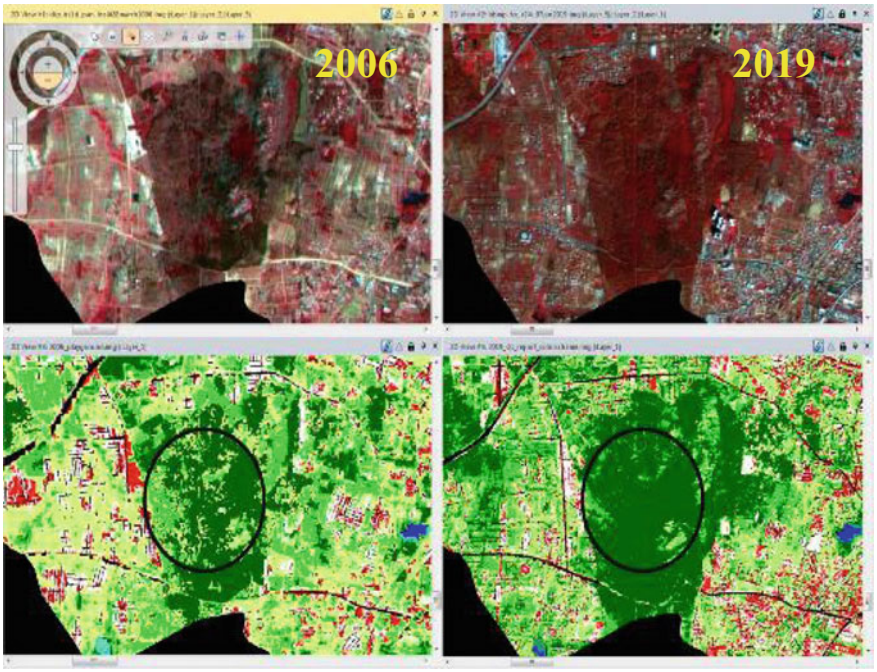

Fig. 19.5 Positive changes in Thurahalli Forest (mainly densification)

build new multi-storey apartments, contributing to vertical growth. Detailed ward-wise vegetation change analysis for these wards reveals trends to significant positive and negative changes in their vegetation cover during 2006 and 2019.

Within the core city, Shivajinagar, Chikpete, and Padarayanapura wards have just about 2% area under vegetation, as these areas are highly congested, with unplanned built-up regions and roads. On the contrary, Jalahalli with defense and public sector establishments has about half the area with vegetation cover. Hagdur, Varthur, and Kuvempu Nagar wards in the periphery have less built-up and more area under vegetation, possibly due to building activities, yet to pick up. Based on assessment of percent vegetation area with reference toward area, it was noticed that Jalahalli, Varthuru, Armane Nagara, Kuvempu Nagar, Hagadur, and Sampangiram Nagar wards have greater than 50% ward area under vegetation cover. A study of the actual vegetated area in 2006 indicates that vegetation cover was as high as about 1200–1400 ha in Varthuru and Hemmigepura wards, whereas in core city wards and commercially dominant wards, it was less than 2 ha viz., Chickpete, Kempapura Agrahara, Padarayanapura, Shivajinagar, Kushal Nagar wards etc. A similar trend was observed in 2019 in core city wards. A significant decrease in vegetation cover was noticed in Varthuru (1447–957 ha), and a slight decrease in Hemmigepura (1247–1218 ha) was observed.

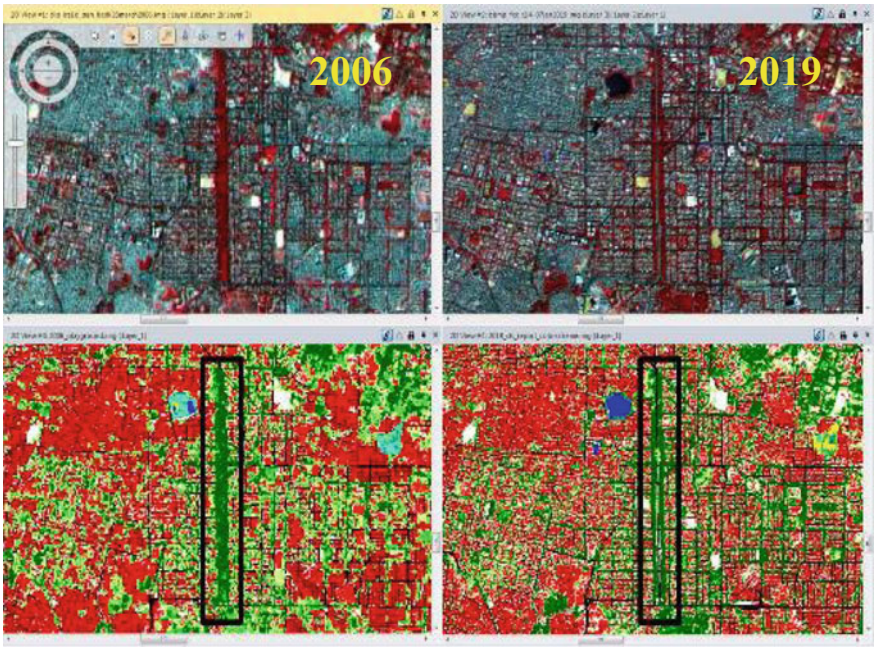

Fig. 19.6 Negative changes in R V Road and surroundings (construction of metro line)

Several wards indicated significant positive changes, while others indicated negative changes, and few others also showed a mixed category of changes within different ward regions. For example, positive changes such as densification of vegetation were very evident in the eastern part of HSR Layout ward (ward no. 174, with 705 ha total area), which contains part of Ibbaluru forest. Additionally, Agara lake rejuvenation is another positive change in the northern part of this ward resulting in the increase of water spread by about 10 ha and clearing of weeds from 25 ha area within the lake (Fig. 19.8).

19.5.1.3 Change Assessment Within Densely Vegetated Areas of City

Several important areas of Bengaluru with dense tree cover have also been analyzed separately to assess the changes in vegetation cover (dense to moderately dense) within these locations for two time periods, viz., 2006 and 2019 (Fig. 19.10). These 34 locations include various vegetation niche areas in parks (Cubbon park and Lalbagh); public sector areas (such as HAL, BEL, ITI, HMT); defense areas (such as CMP, Madras Regiment, BSF); research/academic institutes (such as Bengaluru University, GKVK, IISc, IIM); and forest areas (such as Thurahalli, Ibbaluru, Doresanipalaya forests). The boundaries of these prominently vegetated areas have been interpreted from satellite imagery based on the compound wall and roads and do not necessarily

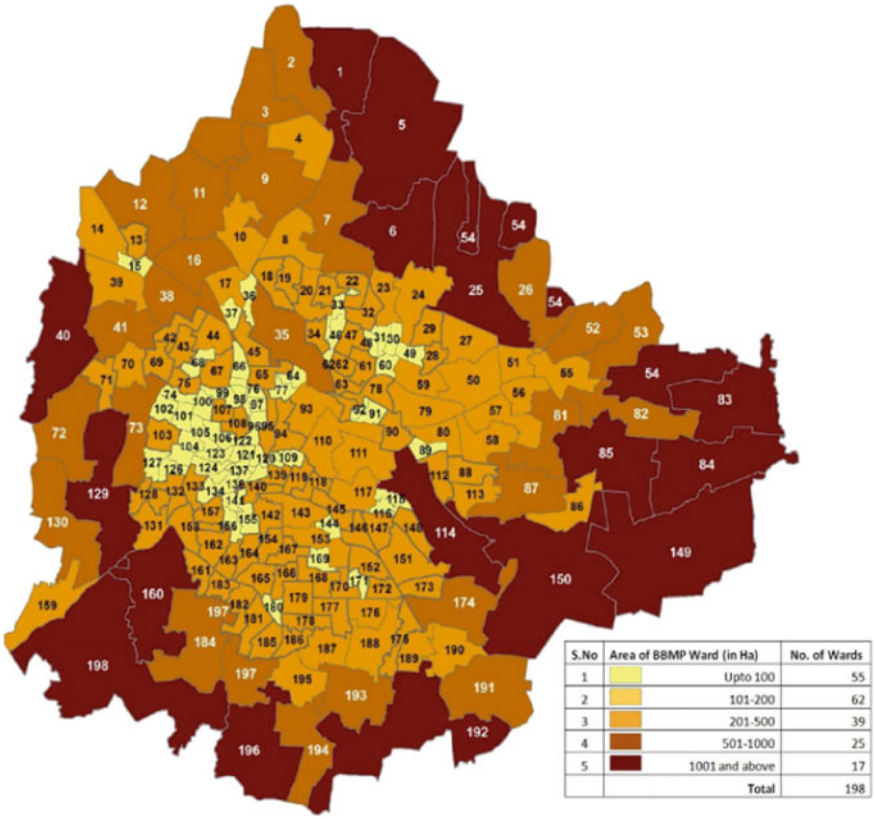

Fig. 19.7 Geographic area-wise distribution of wards

represent the actual administrative boundaries. In many locations, the surrounding areas were also included for assessing the changes in vegetation cover. Locations of these areas are depicted in Fig. 19.9, and the statistical results are presented in Table 19.2. The numerals depicted in Fig. 19.10 and the serial numbers in Table 19.2 are to be referred to together.

It was observed that there was an overall increase of 261.1 ha in the vegetation Cover indicating an increase of 5.4% in dense and moderately dense vegetation cover within these locations. In forest areas alone, there is an increase of 177.3 ha vegetation (Thurahalli and Ibbaluru forest areas mainly). Most public sectors, academic/research institutes, and defense areas have increased their vegetation cover, thereby contributing to an overall positive change in vegetation status. Percentage-wise positive change greater than 50% with respect to 2006 is seen in DRDO and surroundings, HAL-Part 3 and Kadugodi-Part 1, further densification of dense and moderately dense vegetation was noticed.

However, a reduction of about 108 ha of vegetation cover in the GKVK campus contributed to a negative change of 29.4%. It could mainly be attributed to the

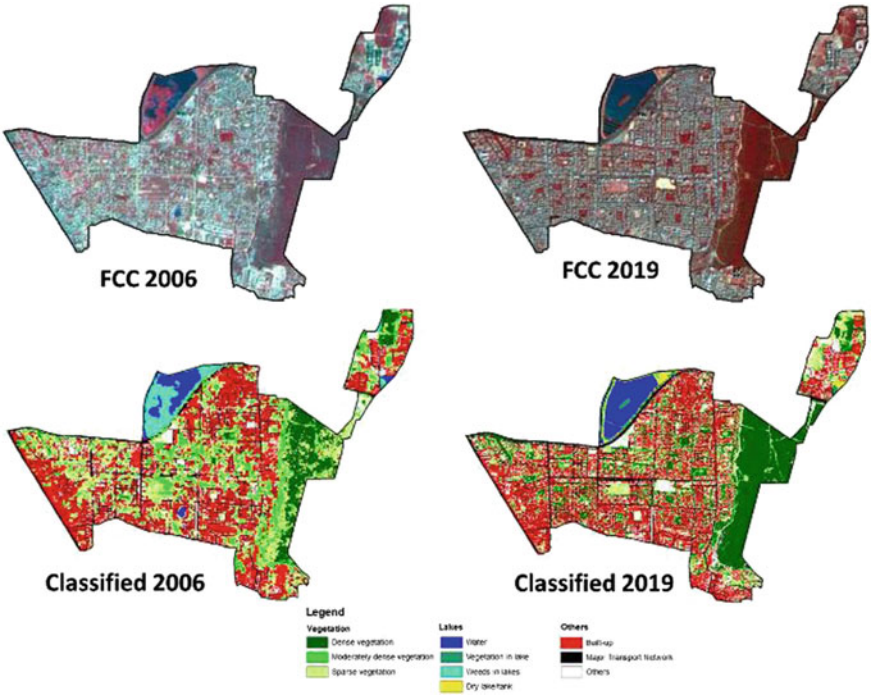

Fig. 19.8 Comparison of vegetation cover and water-spread in HSR Layout (Ward no. 174)

conversion of densely vegetated areas into agricultural research plots, resulting in decreased vegetation. About 12–13% decrease in vegetation cover was also observed in Nallurhalli, Pattandur Lake, and surrounding areas in the eastern part of city, where construction activities have taken place. Also, in both Cubbon and Lalbagh parks, a marginal decrease in vegetation cover was observed due to minor construction activities within the parking area. Therefore, change analysis of prominently vegetated areas of the city gave a good idea about the status of urban vegetation in the city, with an overall increase of 261.1 ha in vegetation cover within these areas.

19.5.2 Spatio-Temporal Assessment of Long-Term Changes: Natural Drainage Systems and Lakes

Using 1965 Corona satellite data and recent 2017, a geospatial database of lakes and drainages was created for a study area falling within BDA bounds. The surface water spread area of lakes was mapped using temporal SAR data. Long-term changes of lakes and drainage pattern in terms of water spread area, inventory, modification of drainages, prioritization of lakes were attempted.

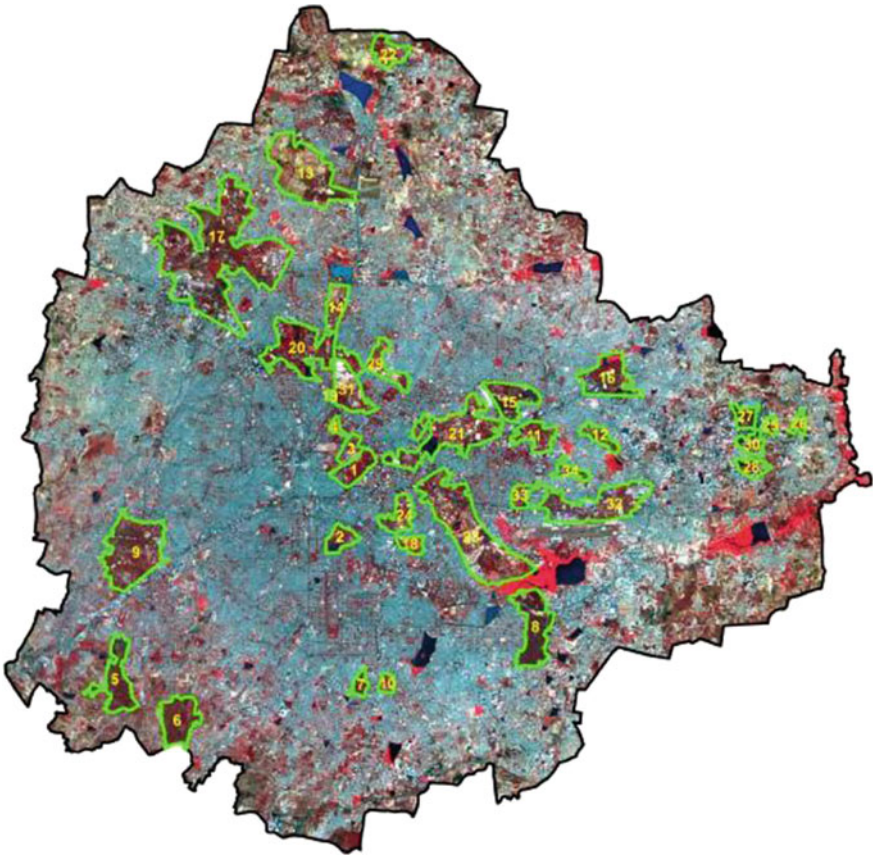

Fig. 19.9 Densely vegetated areas of Bengaluru city (Numerals in the figure represent the serial numbers of locations, refer to Table)

19.5.2.1 Delineation of Watersheds in the Catchment Area

A geospatial database was created for a catchment area of 4000 km^2 surrounding Bengaluru. The catchment area was further divided into 481 micro-watersheds with a geographical area ranging from 2500 to 15,000 ha (approximately). These micro-watersheds were further grouped into 86 urban, 105 semi-urban, along with 290 rural watersheds depending on the percentage of urban areas within them. The micro-watersheds are depicted in Fig. 19.10.

19.5.2.2 Inventory of Lakes and Its Spectral Properties

The urban lakes showed spectral and tonal variations when examined on LISS-IV data. Based on the field knowledge, the status of the lakes could be identified as

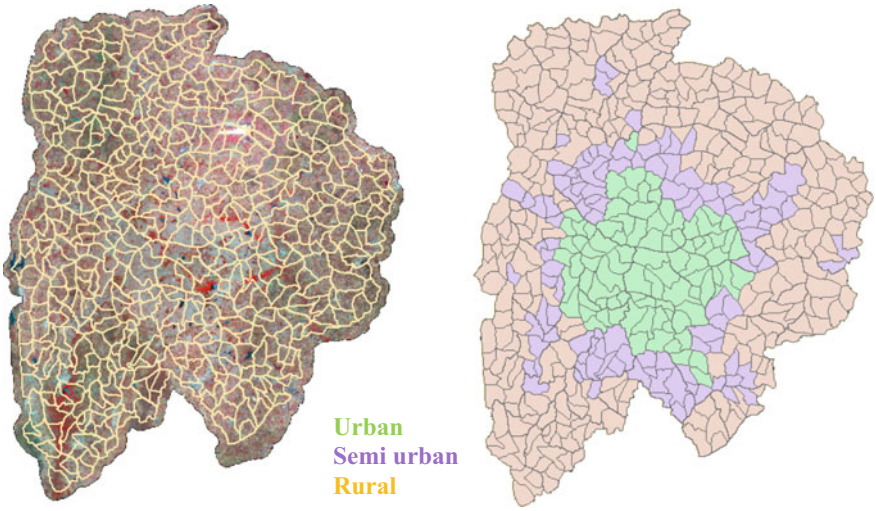

Fig. 19.10 Depicting the Micro watersheds based on its location—urban, semi-urban and rural

whether it is deep, shallow, turbid, polluted or filled with weeds or dry lake bed. The digital number of different lakes was plotted in Fig. 19.11. The figure depicts lesser DN values for clear water when compared across the three bands of LISS-IV data. However, the DN value was higher for turbid water. Similarities were observed between the spectral signature of aquatic weed and vegetation (bright red to pinkish in color) and dry lakes and open land/fallow lands. These spectral characteristics of water and surrounding land use patterns are used to demarcate the lake extent as manifested on HRS data for creating geospatial database on lakes.

The inventory of lakes has been done using both Corona 1965 satellite data and LISS IV satellite data of 2017. It is quite difficult to delineate the actual jurisdictional boundary of the lakes using satellite data alone. The ancillary data viz., cadastral maps, toposheets, drainage system DEM etc. have also been used to interpret lakes and their extent.

The village cadastral maps were used to inventory lakes within the BDA region and attribute information such as lake-ID, name of the lake, geo-location, area, administrative hierarchy (village, hobli, and taluka), and survey numbers were added for the creation of baseline database. Georeferenced cadastral maps covering the BDA region available at Survey and Land Records department were used in the study for the creation of a comprehensive database on lakes. Cadastral maps for 16 villages in the core urban areas were not available; hence the lakes falling in the core urban area were digitized from 1965 satellite data. Collateral data from EMPRI, SSLR ground survey data, toposheets were also used for improving the quality of the database. Figure 19.12 gives the spatial distribution of lakes as in 1965 and 2017.

Table 19.2 Details of change analysis for densely vegetated areas of Bengaluru

S. No.	Location of prominently vegetated area important areas	Vegetation area (ha)		Change Area (ha)	% Change (wrt 2006)
		2006	2019		
1	Cubbon Park	106.7	102.4	− 4.3	− 4.0
2	Lalbagh	62.5	59.7	− 2.8	− 4.5
3	Vidhan Soudha and Surroundings	40.6	59.7	− 3.3	− 8.1
4	Golf Course	24.0	22.5	− 1.5	− 6.3
5	Thurahalli Forest Part 1	174.7	219.9	45.2	25.9
6	Thurahalli Forest Part-2	173.2	225.1	51.9	30
7	Doresanipalaya Forest	42.7	44.5	1.8	4.2
8	Ibbaluru Forest	190.4	268.6	18.2	41.1
9	Bengaluru University and Surroundings	352.2	398.5	46.3	13.1
10	Indian Institute of Management	30.2	32.3	2.1	7.0
11	Defence Research and Development Organisation (DRDO), CV Raman Nagar	93.5	102.2	8.7	9.3
12	DRDO and Surroundings	32.6	53.7	21.1	64.7
13	Gandhi Krishi Vignana Kendra (GKVK) Campus and Surroundings	369.1	260.6	− 108.5	− 29.4
14	University of Agricultural Science (UAS) Campus at Hebbal and Surroundings	70.5	61.0	− 9.5	− 13.5
15	National Government Electrical Factory (NGEF)	124.7	144.5	19.8	15.9
16	Indian Telephone Industry (ITI)	149.1	165.9	16.8	11.3
17	Bharat Electronics limited (BEL), and Hindustan Machine Tools (HMT) Surroundings	1006.2	962.0	− 44.2	− 4.4
18	National Dairy Research Institute (NDRI)	18.9	20.1	1.2	6.3
19	National Tuberculosis Institute	7.3	7.5	0.2	2.7
20	Defence Area and Indian Institute of Science (IISC)	313.4	312.0	-1.4	− 0.4
21	Madras Regiment Area, Halasuru	255.0	300.8	45.8	18.0

(continued)

Table 19.2 (continued)

S. No.	Location of prominently vegetated area important areas	Vegetation area (ha)		Change Area (ha)	% Change (wrt 2006)
		2006	2019		
22	Airforce, Yelahanka	51.1	72.2	21.1	41.3
23	Defence Area Near old airport	406.3	441.7	35.4	8.7
24	Corps of Military Police (CMP)	72.9	78.6	5.7	7.8
25	Kadugodi Part 1	13.3	23.1	9.8	73.7
26	Kadugodi Part 2	29.7	29.5	− 0.2	− 0.7
27	Kadugodi Part 3	57.7	61.5	3.8	6.6
28	Nallurhalli and Surroundings	41.7	36.4	− 5.3	− 12.7
29	TV Tower and Surroundings	121.6	136.2	14.6	12.0
30	Pattandur Lake and Surroundings	44.9	38.8	− 6.1	− 13.6
31	Palace Grounds and surroundings	81.3	96.9	15.6	19.2
32	Hindustan Aeronautics Limited (HAL)—Part 1	228.4	215.4	− 13	− 5.7
33	HAL—Part 2	41.7	42.2	0.5	1.2
34	HAL—Part 3	27.8	43.0	15.2	54.7
Total		4855.7	5116.7	261.1	5.4

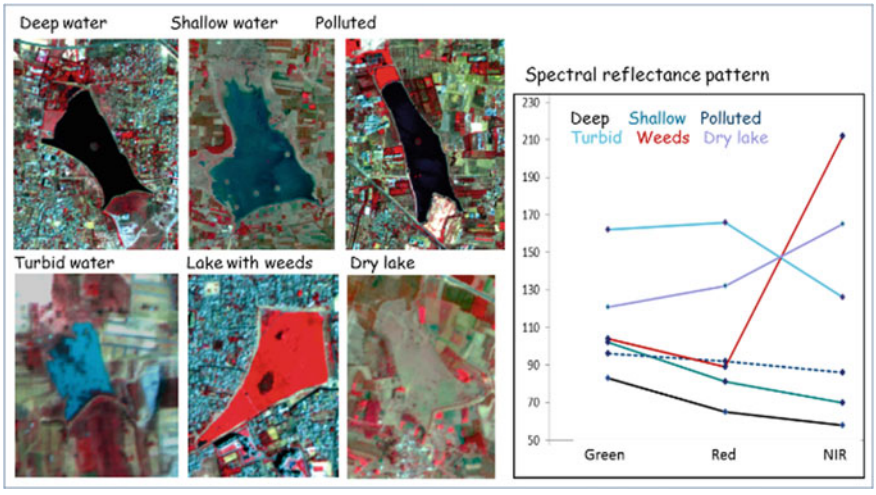

Fig. 19.11 Spectral Pattern of Urban lakes

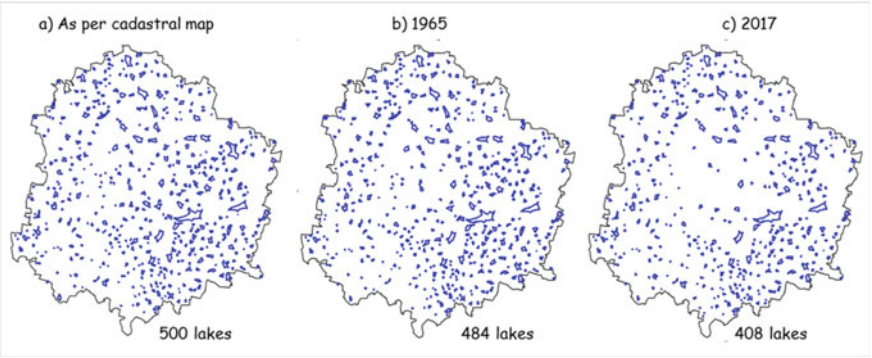

Fig. 19.12 Distribution of Lakes **a** as in 1965 and **b** as in 2017

19.5.2.3 Spatial and Temporal Changes in Lakes

Spatio-temporal changes have been carried out for the lakes falling within BDA limits to understand the changes within the urban area. The details of the lakes with their temporal changes are given in Table 19.3 and spatially represented in Fig. 19.13. A cursory analysis reveals that out of 500 lakes as per cadastral maps within the BDA limits, lakes were present during 1965. This number was further reduced to 408 lakes as per satellite data analysis of 2017. This is an indication of change in land use over the past 50 years. From the statistics, it is evident that about 86 lakes were converted from waterbody to different land uses. A positive indication is that 10 lakes have been newly formed after 1965.

Uncontrolled urbanization and haphazard growth of the city is the main cause for the degradation of lakes within the BDA limits and changes observed within the lakes. Some of the observations about the land use of lakes are given below and represented in Fig. 19.14

- Lake footprint has reduced, which is reflected from the reduction in the geographical area of the lake.
- Partial infestation of lakes with aquatic weeds

Table 19.3 Details of number of lakes within BDA limits

S. No.	Details	No. of lakes
1	Cadastral maps (1850s): lakes delineated	500
2	Corona Space Image: lakes delineated	484
3	L4 + Cartosat-1 image: lakes delineated	407
4	Non-existing lakes prior to 1965	16
5	Converted lakes between 1965 and 2017	86
6	New Lakes constructed after 1965	10

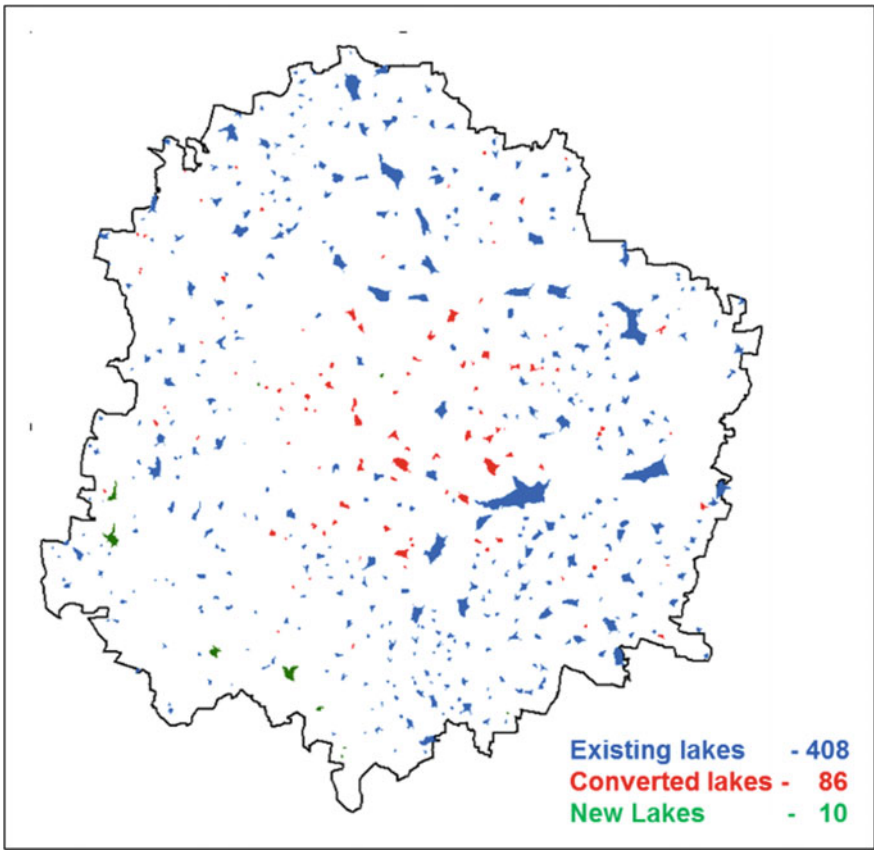

Fig. 19.13 Spatio-temporal changes of lakes within BDA limits

- Land use changes observed where some lakes have been partially transformed to built-up areas or parks or vegetated patches, etc.
- New lakes have been constructed within the Bannerghatta Reserved Forest area

19.5.2.4 Surface Water Spread Area of Lakes Within BDA

Bangalore received an annual rainfall of about 1600 mm (approx.) in 2017, while the average annual rainfall over the last few areas was 859 mm. However, it was observed that maximum rain was observed in 2017 during the monsoon months. The maximum water spread area of the lakes was observed from mid-August to October 2017. Sentinel SAR data in VV and VH polarization corresponding to peak rainfall periods from August to November 2017 was used for delineating the water spread area. The results have been validated using optical data of November 2017.

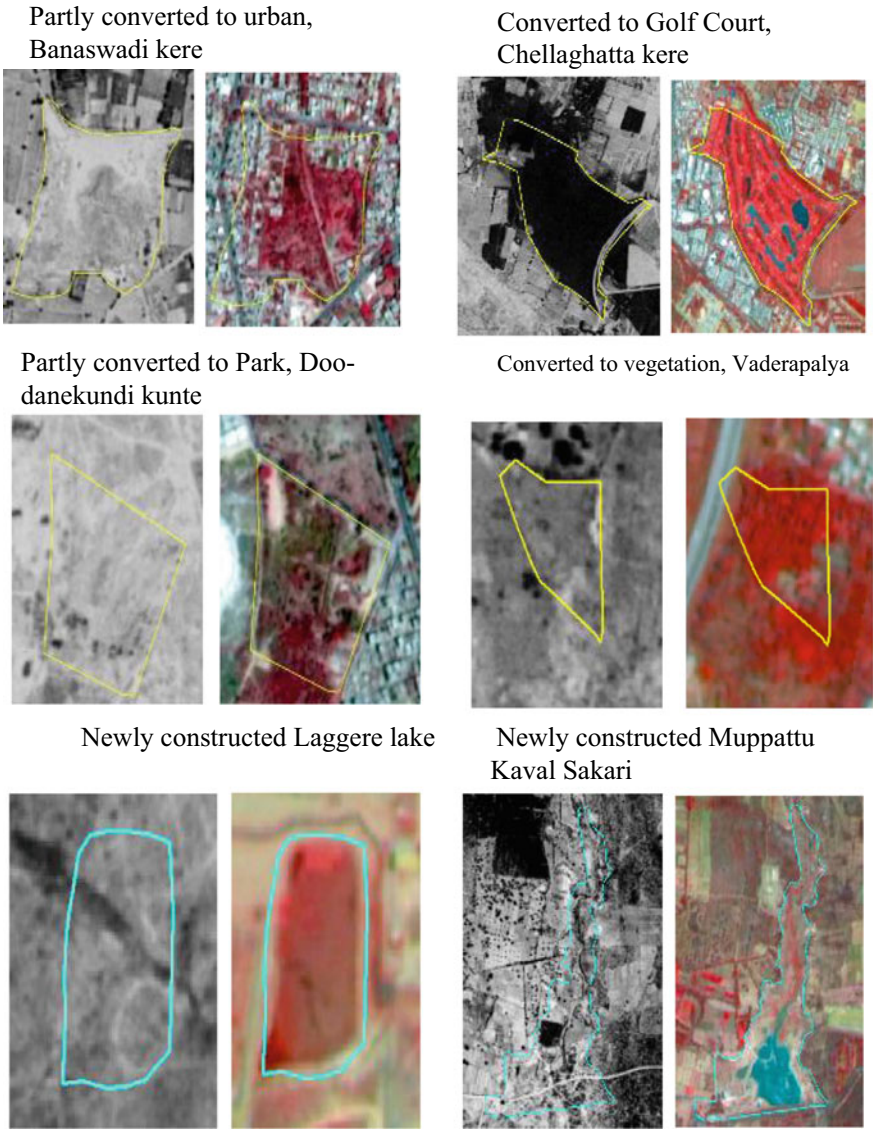

Fig. 19.14 Typical spatio-temporal changes: 1965–2017

From the Sentinel SAR data using thresholding algorithm based on valley emphasis method, water spread area within each lake was extracted using the backscatter values (Fig. 19.15). Weeds and surface vegetation exhibited higher backscatter when compared with water. This trait was used to interpret the spread of water within each lake. The lakes were grouped into five groups based on the percentage of the geographical area covered with the spread of water (Fig. 19.16).

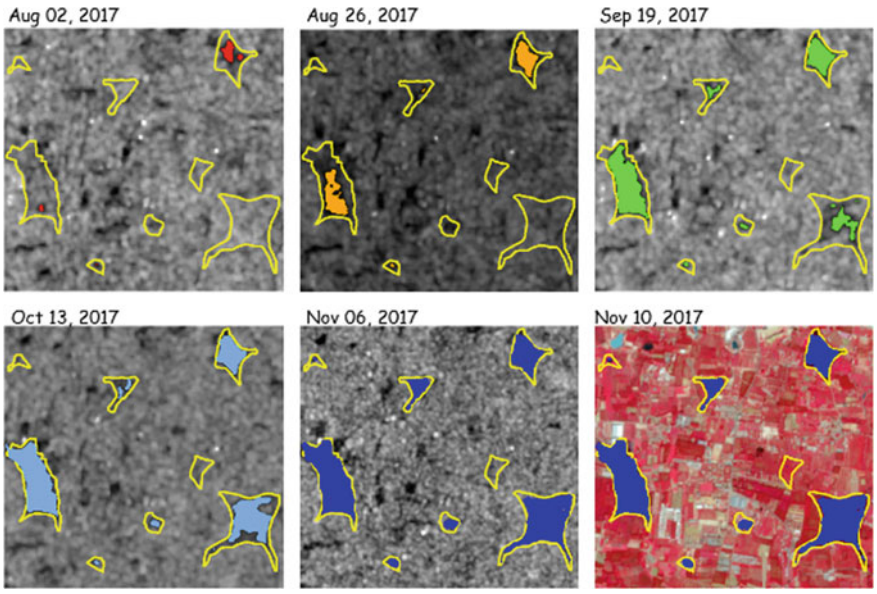

Fig. 19.15 Water spread area extracted for different periods from SAR and optical data

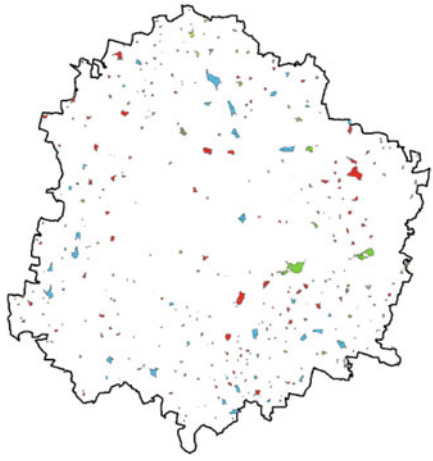

% Water Spread to Geographical Area	No. of Lakes
0 - 15	44
15 - 30	41
30 - 50	86
50 - 75	144
75 - 100	51

Fig. 19.16 SAR Image and Proportion of water spread area to Geographical area of lakes

Even during a very wet monsoon season, nearly 85 lakes were dry or completely covered with weeds/vegetation, and a total of 171 lakes have only about 50% of their geographical area underwater. This reflects the status of the filling up of lakes even during the monsoon.

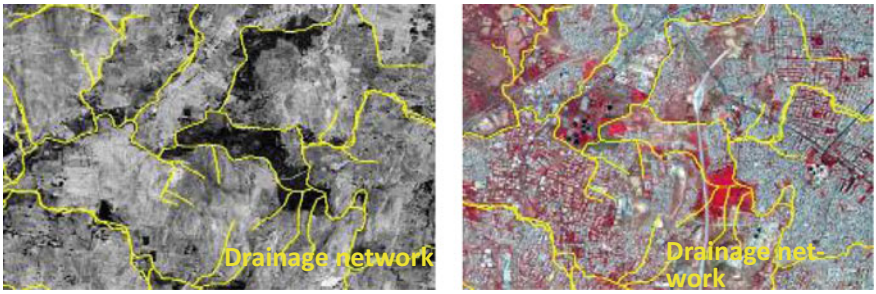

Fig. 19.17 Typical drainage network in urban area as interpreted from satellite data

19.5.2.5 Drainage Network

Visual interpretation methods were adopted for interpreting and generation of drainage network from satellite data on a 1:10,000 scale using collateral data also (Fig. 19.17). The drainage network was delineated as lines from the Corona Space Image of 1965, which was generated and updated using 2017 satellite data.

As drainages were fully or partially covered with weeds/vegetation or lined with trees on both sides or, in some cases, fully covered with concrete, delineating drainage from satellite data was very difficult as it was not clearly interpretable on satellite data. Sometimes, roads were confused as drainages while interpreting drainages due to its similar spectral nature. The drainages, especially first-order streams and drains, which were not clearly seen on the satellite data, have been analyzed from toposheets and DEM. Spatially depiction of the changes in the drainage pattern is given in Fig. 19.18. Due to rapid urban development and construction of many industrial establishments, large apartments, layouts, etc., drains' length has significantly changed from 1965 to 2017. The total drainage length from the interpreted drainage layer showed a loss of 325.4 km of drainage network in Bengaluru city as observed from 1965 to 2017.

19.5.2.6 Characterization and Prioritization of Lakes

Characterization and prioritization of lakes were carried out by EMPRI by a systematic collection of field information of 78 parameters and adopting the Battelle method suitably modified for Indian condition, and lakes have been prioritized based on the importance of action required. From their study it emerged nearly 210 lakes need urgent revival and care for its existence.

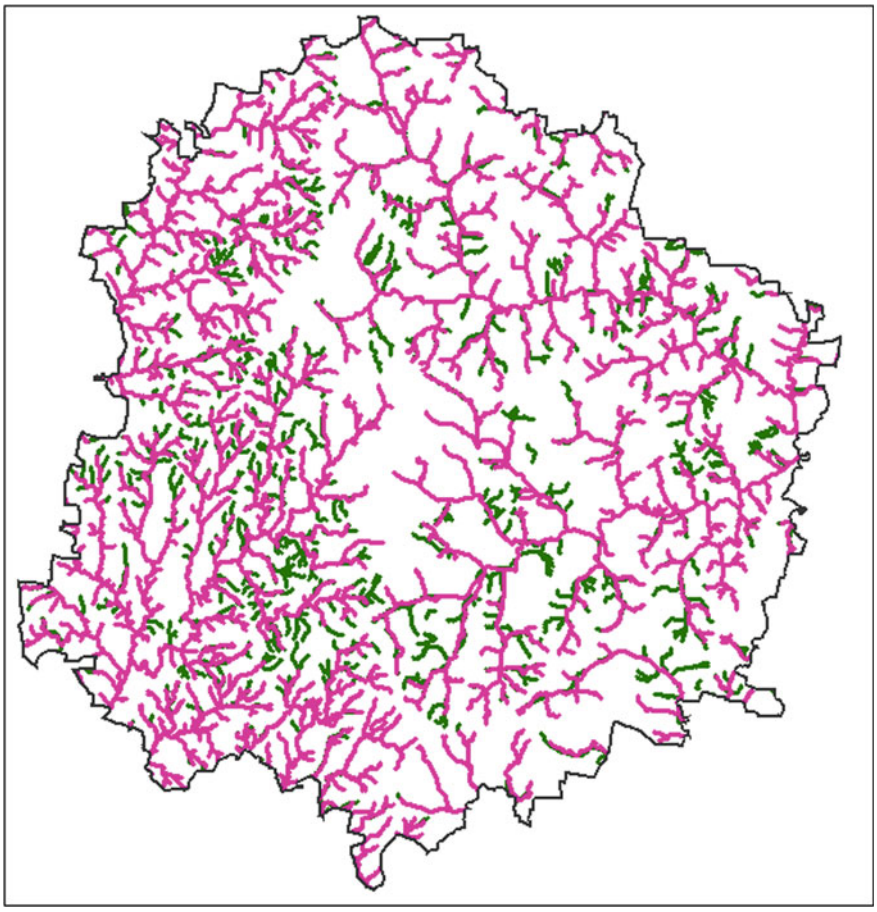

Fig. 19.18 Changes in drainage network between 1965 and 2017

19.6 Conclusion and Recommendations

This chapter presents a summary of two major studies involving assessment of various components of urban dynamics of Bengaluru city viz., vegetation, land use/land cover, and lakes, using geospatial techniques. Based on the total area of BBMP, spread across 711.59 km^2 (consisting of 198 wards), the total change in the vegetation status of Bengaluru city was estimated to be a reduction of about 4% between the years 2006 and 2019 i.e., decrease of vegetation cover in Bengaluru from 30.1% (21,414.9 ha) in 2006 to 26.1% (18,572.2 ha) in 2019. For this estimation, densely vegetated areas and moderately vegetated categories were considered, as they represent the main component of vegetation (consisting of tree cover). Area, representing vegetation of seasonal nature especially the grasses, herbaceous vegetation on vacant sites/plots, fallow land, scrubland etc. grouped under sparse vegetation class was not considered

for change analysis. A detailed vegetation change map was prepared (between 2006 and 2019). Ward-wise detailed analysis of vegetation indicated that out of 198 wards within BBMP area, the vegetated area increased in 82 wards, vegetated area decreased in 54 wards while 62 wards showed nominal changes in vegetated areas or almost similar status. Additionally, an exclusive vegetation change analysis for importantly vegetated 34 areas of Bengaluru city (such as Lalbagh, Cubbon Park, etc.) indicate an increase in vegetation cover by 261.1 ha (accounting to 5.4% increase), suggesting a total positive trend in vegetation cover in terms of area and density under these locations.

Most BBMP wards have numerous green parks, apart from historically present and recently planted avenue plantations. Defense campuses established since the pre-independence era and non-built up spaces in many government institutions/campuses within the city also have a very large presence of intact vegetation cover, undisturbed by the uninhibited pace of urbanization. The greenery in such locations is functioning as real lung spaces for the local populace. Urbanization is observed to be spreading toward the peripheral region in a radial pattern. The negative changes observed in multiple locations have not impacted the overall density of vegetation in a negative manner. To improve the vegetation cover of Bengaluru city, the recommendations/suggestions based on the present study are: (i) protecting the existing vegetation (ii) further densification of vegetated areas (iii) replacement of dead, dying, and diseased trees (iv) compensatory planting at other areas or in the neighborhood for road-widening/metro lines (v) Selection of appropriate plant species (vi) Transplantation of trees (vii) Seeding using seed balls (viii) Vertical/Terrace gardens (ix) Enhancing the existing vegetation by plantation drives (x) Kitchen Gardens/Indoor vegetation (xi) Growing more trees around Lakes/Playgrounds/Open spaces (xii) Densification of Parks and (xiii) Rain Water Harvesting.

The unplanned urban expansion and creation of urban infrastructure have incurred a loss of natural drainage network and the conversion of lakes in Bengaluru. The results of the spatial–temporal analysis of lakes within BDA limits are emphasized.

- Lakes with size > 3.0 acres: The interpretation of cadastral maps, Corona 1965 image, and Cartosat1 + LISS 4 image of 2017 have yielded that from 500 lakes as per cadastral maps have been converted and reduced to 484 during 1965 and further reduced to 408 during 2017. Thus about 86 lakes have been converted from lakes into different land use after 1965. On the positive side, about 10 new lakes were also constructed especially in the Bannerghatta park area of the city.
- Drainage pattern: The total loss 325.24 km drainage length has been observed due to urbanization within BDA Area. Total length of the natural drainage network was estimated as 1647.5 km (in 1965) and 1295.1 km (in 2017).
- Surface water spread area: SAR data analysis has shown that 212 lakes out of the existing 408 lakes depicted more than 50% area under surface water-spread (2017 monsoon season). 113 lakes depicting area under 25% water-spread, though with good monsoon season during 2017, require immediate attention for protection and conservation. The remaining lakes were dry and completely occupied by weeds

in spite of the heavy rains showing a possible loss of drainage connectivity and flow of water into these lakes.

Lake inventory and its present status and loss of drainage network are valuable inputs to prepare an integrated action plan for the conservation of the lakes. Some of the immediate actions required are conservation of lakes which have been covered with aquatic weeds; improve the drainage connectivity between lake series and also the clear the drainages which are covered with vegetation, garbage etc. and ensure smooth flow of water, desilting of lakes, setting up of STPs and treating the drainage water before letting it into the lakes, preventing the various forms of solid, liquid and other bio-medical wastes being dumped into the lakes. Apart from this, integrated development of lakes requires further studies on the impact of urbanization, status of pollution, computing run-off estimation, and flood inundation.

Acknowledgements The project team expresses its deep sense of gratitude to Director, National Remote Sensing Centre (NRSC) for his constant encouragement during the studies. We are highly grateful to Shri Uday Raj (Former CGM, Regional Centres, NRSC/ISRO), Dr. K. Ganesha Raj (Former GM, RRSC-South, NRSC/ISRO), and Dr K.S. Ramesh (Former Head Applications, RRSC-South, NRSC/ISRO) for their support, encouragement, and valuable guidance during execution of these studies. We sincerely acknowledge the continuous support extended from Smt. Seema Garg, IFS (Chief Executive Officer), Shri. G. Vidya Sagar, IFS (Former Chief Executive Officer) and other senior officials and team members of Karnataka Lake Conservation and Development Authority (KLCDA), Bengaluru, in the execution of S-TALAB study. We also place on record our sincere thanks to the officials of Environmental Monitoring and Policy Research Institute (EMPRI), Bengaluru, for sharing field information on lakes, involvement in quality checking, and suggestions provided during project review meetings. We want to thank Dr. Sameena and Shri Akash for their contributions in the S-TALAB project.

References

BBMP (2019). Bruhat Bengaluru Mahanagara Palike website. www.bbmp.gov.in

Behera G, Nageshwara Rao PP, Dutt CBS, Manikiam B,Balakrishna P, Krishnamurthy J, Jagadeesh KM, Ganesha Raj K, Diwakar PG, Padmavathy AS, Parvathy R (1985) Growth of Bangalore city since 1980 based on maps and satellite imagery. ISRO technical report, ISROEOS-TR-55-85, Indian Space Research Organisation, Bangalore

Dimitrov SS, Georgiev GT, Georgieva M, Glushkova M, Chepisheva V, Mirchev P, Miglen AZ (2018) Integrated assessment of urban green infrastructure condition in Karlovo urban area by in situ observations and remote sensing. One Ecosyst 3:e21610. https://doi.org/10.3897/oneeco.3.e21610

EMPRI (2017) Inventorization of water bodies in Bengaluru metropolitan area. Draft Report, Centre for Lake Conservation (CLC), EMPRI

EMPRI (2018) Inventorization of water bodies in Bengaluru Metropolitan Area (BMA), Volume-1, Technical Document, Centre for Lake Conservation (CLC), EMPRI

Nguyen D (2016) Automatic detection of surface water bodies from Sentinel-1 SAR images using Valley-Emphasis method. Vietnam J Earth Sci 37. https://doi.org/10.15625/0866-7187/37/4/8298

Pham-Duc B, Prigent C, Aires F (2017). Surface water monitoring within Cambodia and the Vietnamese Mekong delta over a year, with sentinel-1 SAR observations. Water 9. https://doi.org/10.3390/w9060366

Raj KG, Trivedi S, Ramesh KS, Sudha R, Subramoniam SR, Ravishankar HM, Vidya A (2020) Assessment of vegetation cover of Bengaluru city, India, using geospatial techniques. Published online, Nov 2020, J Indian Soc Rem Sens

Ramachandra TV, Bharath HA, Vinay S, Rao GR, Gouri Kulkarni, Tara NM, Nupur Nagar (2014) Trees of Bengaluru. ENVIS technical report 75, ENVIS, Centre for ecological sciences, IISc, Bangalore 560012, p 75

Ramesh KS, Elango S, Adiga S (2001) Prioritization of sub watersheds of Dakshina Kannada district, Karnataka using remote sensing data. In: Proceedings of IWIWM, Bangalore, 21–23 June 2001, p 10

RRSC-South (2018) Spatio-temporal analysis of lakes of Bengaluru: S-TALAB. Technical project report, NRSC-RC-RRSCBANG-JUL-2018-TR-1176-V2.0, pp1–100

RRSC-South (2019) Assessment of vegetation cover of Bengaluru city using Geospatial techniques, NRSC/ISRO technical report. NRSC-RC-REGBANG-RRSC-BANG-DEC-2019-TR-0001406 - V1.0, pp 1–73

Sharma KD, Singh S, Singh N, Kalla AK (1989) Role of satellite remote sensing for monitoring of surface water resources in an arid environment. Hydrol Sci J 34(5):531–537

Strahler AN (1957) Quantitative analysis of watershed geomorphology. Trans Am Geophys Union 38:913–920

Strahler AN (1964) Quantitative geomorphology of drainage basins and channel networks. In: Chow VT (ed) Handbook, of applied hydrology. McGraw Hill Book Company, New York, pp 4–11

Sudhira HS, Nagendra H (2013) Local assessment of Bangalore: graying and greening in Bangalore-impacts of urbanization on ecosystems, ecosystem services and biodiversity. In: Urbanization, biodiversity and ecosystem services-challenges and opportunities: a global assessment, Springer, pp 75–91

Wratten SH, Cullen R, Costanza R (2013) Ecosystem services in agricultural and urban landscapes. Wiley, New Jersey

Chapter 20
Mobile GIS Applications for Spatial Planning at Grass Root Level

Khushboo Mirza, Vinod K. Sharma, N. R. Shankar Ram, V. M. Chowdary, and C. S. Jha

Abstract Spatial planning in rural areas is crucial in order to have well-designed rural communities, economic progress, sustainable growth, and improved quality of life. Spatial planning activity is traditionally done using High-resolution satellite date along with the thematic datasets on natural resources and infrastructure. The spatial planning activity becomes more meaningful when it is augmented with field survey data collected through mobile GIS applications. This study introduces the implementation and use of real-time field survey data using Smart phone-based GIS applications. Real-time field survey data and ground truth information were made readily available for spatial planners while a survey team was reporting from the field through a mobile device. All these data combined together with high-resolution satellite data and the thematic datasets form the basis for the planning activities at the Gram Panchayat level across the country. Both geographic data and geo-referenced remotely sensed image data are used for the planning exercise. Such applications help to understand the relationship between geo-information and governance. Such data collection aided by mobile GIS applications aims to create more logical planning of land use and the linkages between them and strike a balance between the need for development and the need to safeguard the environment while achieving social and economic objectives. This study brings further awareness about such technologies to spatial planners as they could benefit from using dedicated applications developed for mobile devices. Such applications could enrich workflow, accuracy, and quality of data, which can help to achieve better results for the planning exercise.

K. Mirza (✉) · V. K. Sharma · N. R. S. Ram
Regional Remote Sensing Centre-North, National Remote Sensing Center, Indian Space Research Organisation, New Delhi, India
e-mail: khushboo.mirza@gmail.com

V. M. Chowdary
Department of Agriculture, Cooperation and Farmers Welfare, Ministry of Agriculture and Farmers Welfare, Government of India, Mahalanobis National Crop Forecast Centre (MNCFC), New Delhi, India

C. S. Jha
National Remote Sensing Center, Indian Space Research Organisation, Hyderabad, India

C. S. Jha et al. (eds.), *Geospatial Technologies for Resources Planning and Management*, Water Science and Technology Library 115,
https://doi.org/10.1007/978-3-030-98981-1_20

Keywords Field mapping · Mobile GIS · Mobile apps · Location-based · Governance · Spatial planning

20.1 Introduction

Developmental planning is a multifaceted process of decision-making based on the resource information, socio-economic conditions, and institutional constraints. Development plans for a Gram Panchayat (GP) provide a framework that enables more effective utilization of available resources. Spatial planning in rural areas is essential for economic progress and sustainable growth. Reliability of the spatial and non-spatial databases is therefore crucial for the success of developmental planning. Therefore, understanding several elements of Gram Panchayat and their interrelationship for ecological planning is necessary for spatial planning. The ability of space technology for obtaining systematic, synoptic, swift, and repetitive coverage in different windows of the electromagnetic spectrum, and over large areas has made this technology unique and powerful. Further, local knowledge of the area plays a vital role in the preparation of the development plans. This knowledge, combined together with high-resolution satellite data along with the thematic datasets on natural resources and infrastructure, helps to prepare the spatial development plans. Integration of this information with field survey data aids the development planning process and makes it more meaningful. Non-availability of spatial information at the local level leads to difficulty in prioritization of developmental schemes, and poor decision-making. Field survey of households carried out spatially using a GIS-based mobile app has proven to be an important tool for spatial planning activity. Although, the use of mobile devices and dedicated applications for field surveys has increased in recent times, limited attention was paid in the literature (Nowak et al. 2020). The success of a mobile-based GIS application mostly depends on three factors, viz. spatial functions, user interface design, and system performance (Charland and Leroux 2011; de Abreu Freire and Painho 2014; Roth 2017). Web GIS integrated with data collected from mobile apps and geospatial resources delivers powerful information analysis for end-users through geo-visualization or animation with interactive web portals (Yang et al. 2007).

This chapter highlights the potential of Mobile GIS for spatial analysis of the current household data at GP level which in turn helps for conceptualization and generation of developmental plans that account for the aspirations of Gram Panchayats for the future. The field survey data collected through mobile applications cover a wide range of socio-economic, geographical, and other relevant parameters of the households.

20.2 Mobile GIS Applications

Advancements in technology show no parity between rural and urban India. Rural India is transforming rapidly through interactions with its urban counterparts and the government's creation of amenities and services. However, the growth among the villages in rural areas is not uniform. Villages in urban fringes are developing faster when compared to interior villages. It is also observed that the development in fringe villages is not inclusive. To enable inclusive growth among these fringe Gram Panchayats, an appropriate development plan generation taking into account the current status and the requirements in the future needs to be developed. Spatial development plan facilitates multi-criteria analysis and enables understanding of issues from a spatial perspective. Traditionally manual surveys are carried out to assess the gap in the development of Gram Panchayats. However, traditional surveys are laborious and time consuming. A mobile app-based field survey using GIS capabilities of mobile phones proves to be helpful in such scenarios.

Mobile GIS is a technology framework that allows mobile devices to access geospatial data and location-based services. With the advent and convergence of GPS, Internet, and wireless communication technologies, mobile GIS has a lot of promise to help in the data collection process and validation in the field (Pundt 2002). The field data collected through mobile applications can be visualized and analyzed in a GIS environment. Since spatial planning plays a key role in providing a framework for the development-related activities of a region, Spatial field survey data can be correlated geospatially with other related data available at Gram Panchayat (GP) level for the gap analysis and planning exercise.

20.3 Material and Methods

20.3.1 Study Area

The mobile app-based Household (HH) survey was carried out by thirteen partner institutions (PIs) in 23 GPs spread across 11 states. List of the Gram Panchayats (GPs) identified for HH survey is shown in Table 20.1. The location map of selected GPs in this study is shown Fig. 20.1.

20.3.2 Methodology

Gram Panchayat Spatial Development Plan (GPSDP) generation necessitates the collection of data from households situated in the Gram Panchayat. The data collected through the household survey in this study includes 175 attributes pertaining to land holdings, socio-economic conditions, employment details etc. Collection and

Table 20.1 GPs selected for House hold survey analysis across India

	State name	District name	GP name
1	Haryana	Ambala	Mullana
2	Haryana	Ambala	Patrehri
3	Uttarakhand	Haridwar	Belda
4	Uttar Pradesh	Lucknow	Bakkas
5	Andhra Pradesh	Krishna	Paritala
6	Andhra Pradesh	Krishna	Telaprolu
7	Tamil Nadu	Tiruchirapalli	Navalurkuttapattu
8	Tamil Nadu	Thiruvallur	Sembarambakkam
9	Tamil Nadu	Thiruvallur	Morai
10	Tamil Nadu	Tiruchirapalli	Gundur
11	Karnataka	Udupi	Shankaranarayana
12	Karnataka	Udupi	Uppunda
13	Madhya Pradesh	Sehore	Bilkis ganj
14	Madhya Pradesh	Vidisha	Murvas
15	Maharashtra	Nagpur	Gondkhairi
16	Maharashtra	Nagpur	Mansar
17	Maharashtra	Pune	Belhe
18	Maharashtra	Pune	Rajuri
19	Chhattisgarh	Surguja	Udaipur
20	Chhattisgarh	Durg	Jhit
21	West Bengal	West Medinipur	Aguibani
22	Jharkhand	Bokaro	Kandra
23	Jharkhand	Ranchi	Neuri

analysis of this household data is the starting point for the planning exercise in the Gram Panchayats. A cross-platform mobile application is developed for carrying out the field survey. The app's design is based on the survey questionnaire, which covers a wide range of attributes ranging from household information, family data, land holding details, services availed by the household, health, livestock to energy sources information, etc. The app with a simple GUI was designed in such a way that anyone can use it without the need for formal training.

The methodology involves the integration of geospatial and mobile app-based surveys, household data collection, sampling, and analysis. It also includes cross-referencing through historical data to ascertain environmental concerns such as eco-sensitive zones, brick kilns, quarries for building material, etc. The GPSDP outlays a vision to guide the growth and development of rural areas for the next 20 to 30 years by utilizing the latest geographical information system (GIS) technology. The proper integration of sector planning and productive information resources into the master plan of the GPs not only provides orderly and protective development but also helps

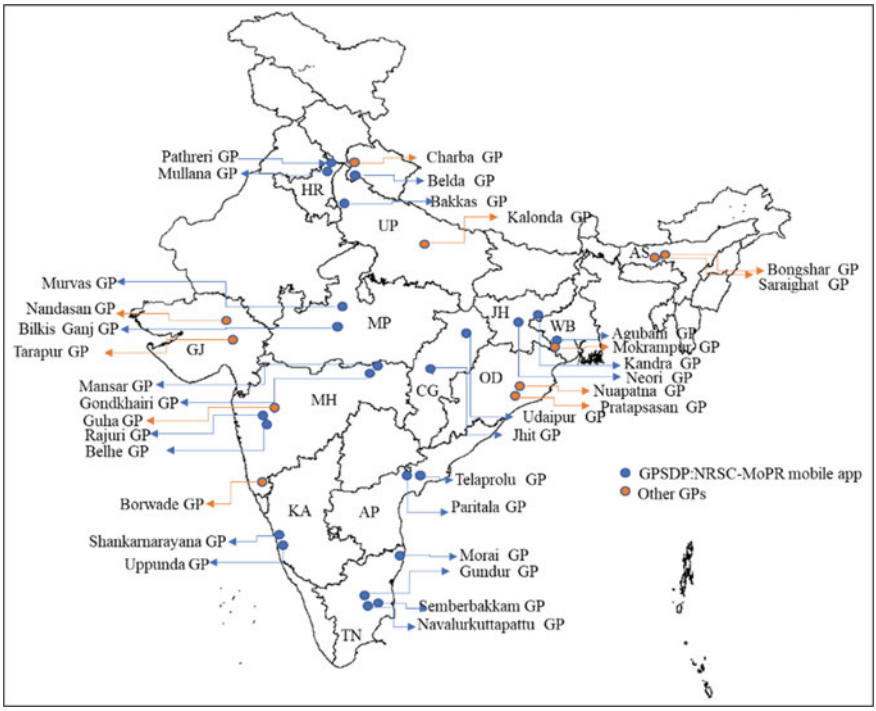

Fig. 20.1 Location map of selected GPs

in the maintenance of infrastructure strengthening the local identity of the Gram Panchayat and its people.

20.4 Architecture of Mobile Application

A mobile application, sometimes known as an app, is a type of software designed to run on a mobile device. It consists of a mobile client where the application is installed, while back-end application and the databases are hosted in the web server. A typical architecture of mobile application is shown in Fig. 20.2.

The Mobile client-side often includes GPS-enabled mobile terminal and software (i.e., a mobile app) deployed on the mobile terminal to access the system features. The mobile terminal could be various mobile devices, e.g., smartphones, pocket PCs, PDAs, tablets, laptops etc. These devices are commonly equipped with display, memory, and central processing units and they can be developed based on different operating systems, such as Android and iOS. Android is the most popular operating system used nowadays. A cross-platform mobile app can work on different operating systems like android or iOS, and offers the similar kind of interface and features

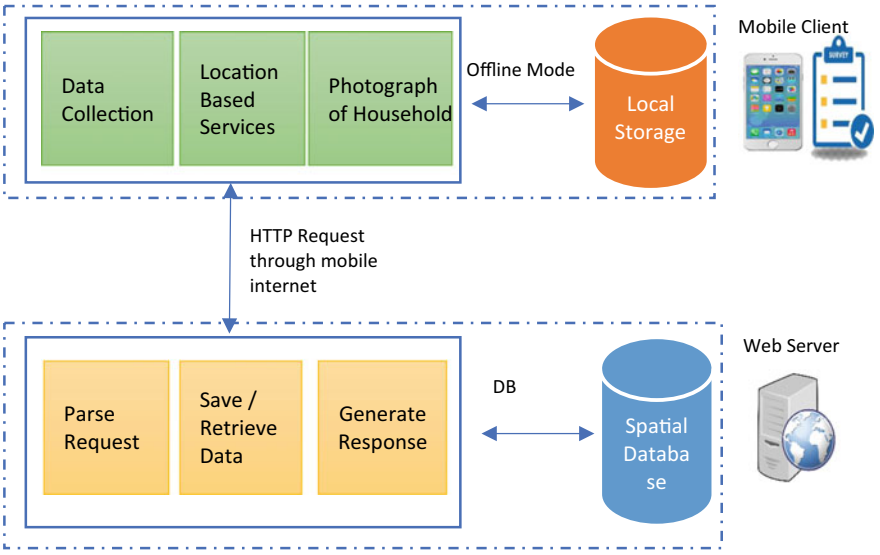

Fig. 20.2 Architecture of mobile GIS application

irrespective of the OS used in the mobile phone. A mobile app with offline mode allows users to do crucial tasks even when they are not connected to the Internet by accessing locally stored datasets on the mobile device's storage.

The server side typically consists of server-side applications and the database engine. The server-side script parses the request received from the mobile app and queries the database. The database processes the query and in turn, returns a response. This response is sent back to the mobile client after the request processing. The data transfer happens over the internet provided by mobile network and uses HTTP protocol, which specifies the format of response and requests.

20.5 Cross-Platform Mobile App for Household Survey

A cross-platform mobile application is developed to facilitate the household (HH) survey in various Gram Panchayats across the country. Mobile app (Fig. 20.3) is compatible with android & iOS Operating systems and was developed using the react-native framework. It has 12 different forms (Table 20.2) for data collection with information on 175 attributes. The mobile app was envisaged for conducting household surveys in the 23 g Panchayats (GPs) in the country. Data collected through mobile app can be sent to the server in real time. The app also has the facility to store the survey data in case network connectivity is not available. Provision is also made for a secure login access that ensures authorized use of app. The data collected through the mobile app is uploaded to the GIS portal through mobile internet services. This

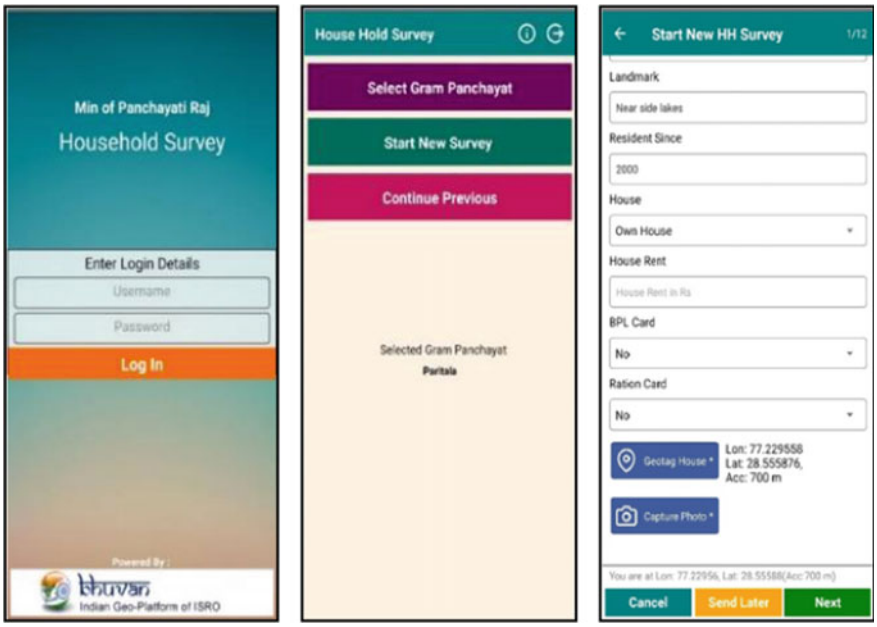

Fig. 20.3 Mobile app for household survey

Table 20.2 Categories under which data collection is done through mobile app

12 category of forms for data Collection	
1	Household
2	Family
3	Land holding
4	Built up
5	Services
6	Toilet
7	Monthly expenditure
8	Health
9	Livestock
10	Other assets
11	Energy source
12	Other (suggestions, feedback etc.)

data is organized in a relational database for query and retrieval purpose. This data helps planners in the preparation of the spatial plans for the Gram Panchayats.

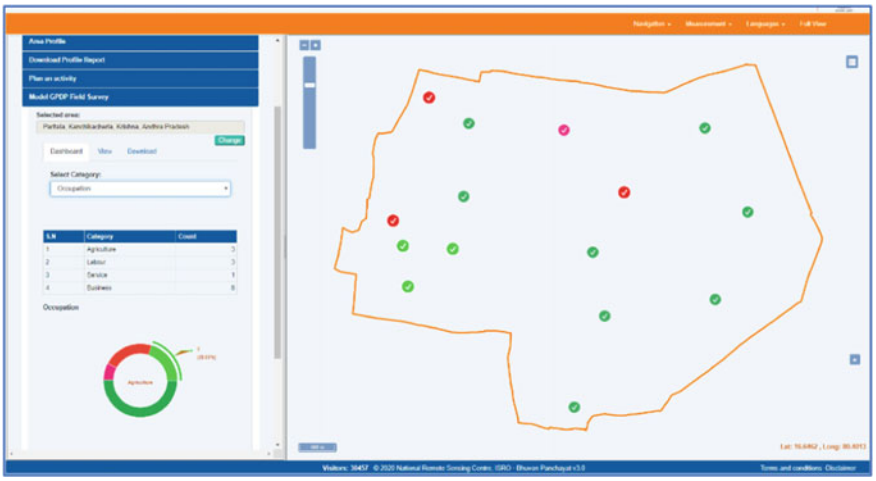

Fig. 20.4 Dashboard for visualization and analysis of household survey data

20.6 Analysis of Household Survey Data Collected Through the Mobile App

A dashboard was developed to visualize and analyze the survey data collected through the Mobile App (Fig. 20.4). The dashboard has 3 components integrated with a spatial viewer for visualization of the survey data onto a 2D map viewer. The components of HH dashboard are View, Analyze, Download, and prepare GP plan.

Dashboard facilitates visualization and query of survey data based on user-defined queries such as ownership status, poverty status, education level, occupation, and facilities like toilet, drinking water etc. Results of queries can be visualized in graphical form on the map viewer. The results can be easily visualized using different colors indicating the category type. Individual HH records can also be viewed under the view tab. The facility to download the HH data (.csv format) for a date range is provided under the download tab (Fig. 20.5).

20.7 Case Study-House Hold Survey Data Analysis for Mullana GP, Haryana

Mullana GP is situated in Saha Mandal of Ambala district of Haryana, with population of ~4956 (census 2011). Geographically it covers an area of 12.96 km^2. GP has good road connectivity with district head quarter. Agriculture is the main source of income in this GP. HH survey was successfully carried out by Chandigarh College of Architecture using the mobile app. The survey was carried out for 15% of the population. The data was submitted from the ground and hosted geospatially on GIS

Fig. 20.5 Facility to download survey data on the dashboard

portal for further analysis. Surveyed data overlaid on very high-resolution satellite data is shown in Fig. 20.6. Data was analyzed based on several socio-economic parameters, and the maps were generated.

20.7.1 Distribution of House Types in Mullana GP

Distribution of house types such as kachcha, pucca, semi pucca houses, and others in the Gram Panchayat was spatially analyzed and represented graphically (Fig. 20.7). Majority of the houses (79%) in GP are pucca houses.

20.7.2 Residents of Kachcha Houses with BPL Cards in Mullana GP

Availability of BPL card among the residents staying in Kachcha house was analyzed (Fig. 20.8). The houses were categorized as BPL card available, non-available and no input provided. The majority of residents of kaccha houses (68%) doesn't have BPL card.

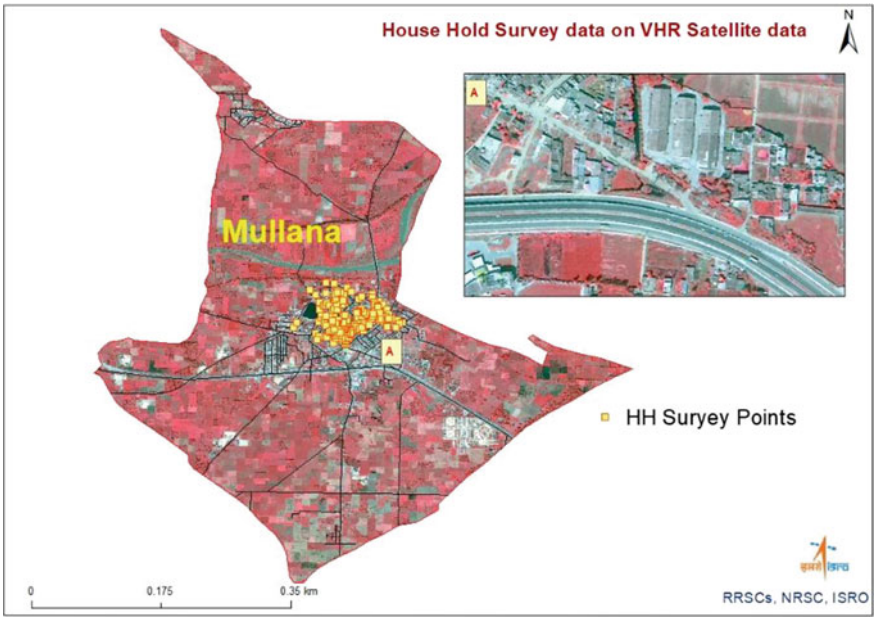

Fig. 20.6 House hold surveyed locations on very high-resolution satellite data

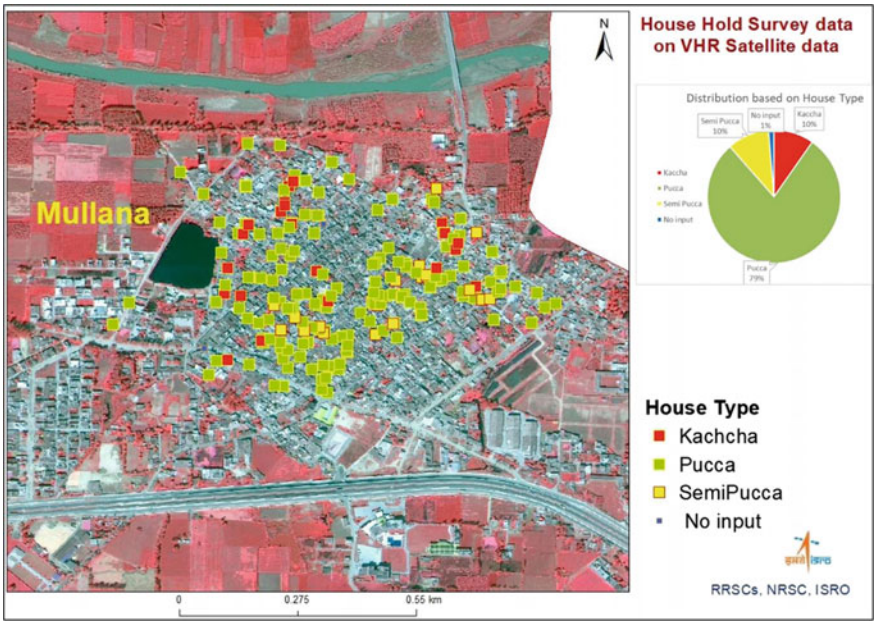

Fig. 20.7 House Hold data distribution of Mullana GP based on house types on very high-resolution satellite data

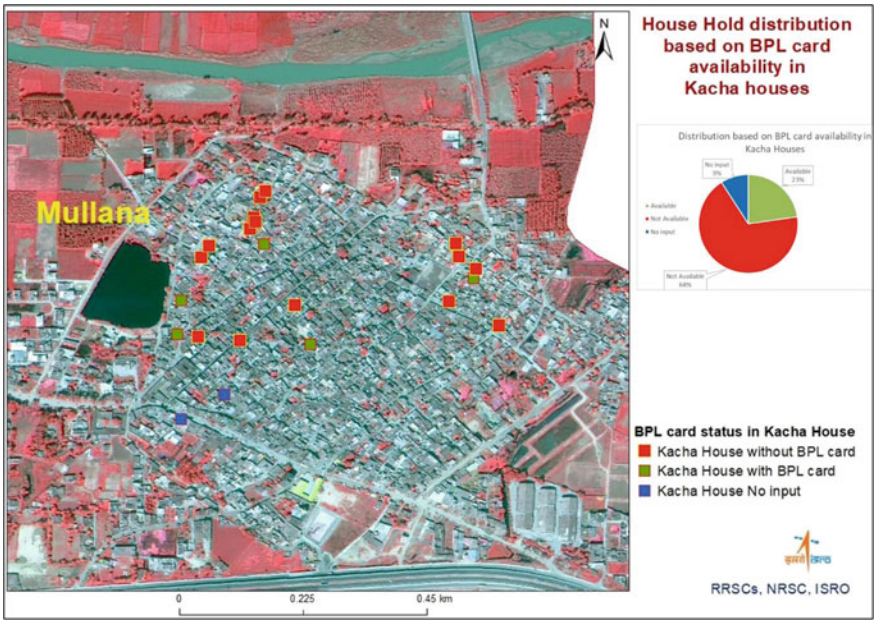

Fig. 20.8 House Hold data distribution of Mullana GP based on BPL card availability in kachcha houses

20.7.3 Water Availability and Their Sources in Mullana GP

Water supply sources in the GP were analyzed and categorized as a hand pump, borewell, well, public tap, private tap, submersible, and no water available. Spatial distribution based on the water availability is shown in Fig. 20.9. Private tap is the source of water in the majority of houses (69%).

20.7.4 Distribution Based on Residency Period of Habitants in Mullana GP

HH data is analyzed to derive the information of residents based on their length of stay in GP. HH data based on field 'resident since' is categorized in different time frames as shown in Fig. 20.10. The majority of residents are staying for more than 3 decades in the GP.

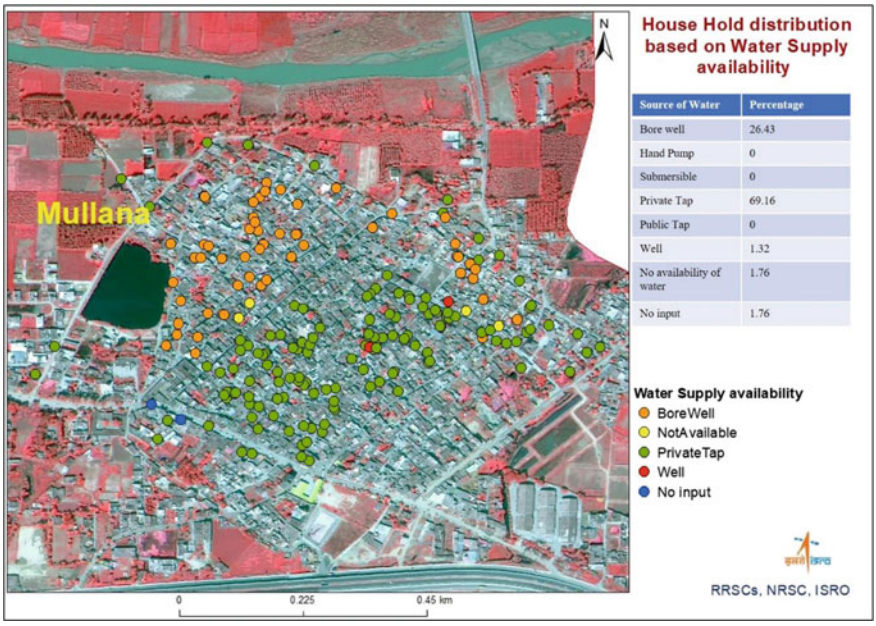

Fig. 20.9 House Hold data distribution of Mullana GP based on the water supply source

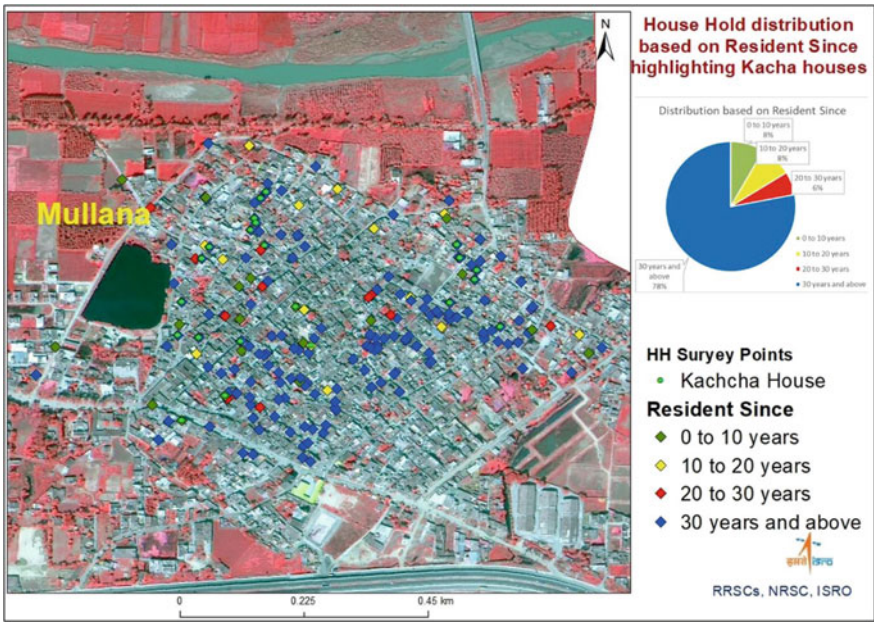

Fig. 20.10 House Hold data distribution of Mullana GP based on 'resident since' highlighting kachcha houses

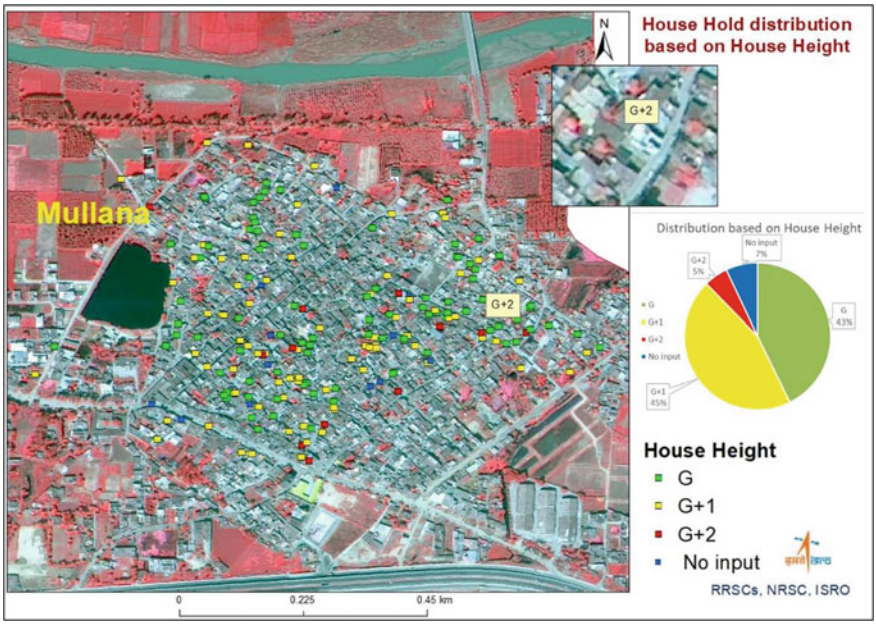

Fig. 20.11 House Hold data distribution of Mullana GP based on house height

20.7.5 Analysis Based on House Height/floor in Mullana GP

Distribution of house types such as kachcha, pucca, semi pucca houses, and others in the Gram Panchayat was spatially analyzed and represented graphically (Fig. 20.11). Half of the houses in the GP are multi-story, where 45% of the places have G + 1 floor, and 5% have G + 2.

20.7.6 Distribution of Houses Based on Liveable Conditions in Mullana GP

The distribution of houses based on house conditions is categorized into good, liveable, and dilapidated and is shown in Fig. 20.12. The majority of homes in GP are either in good (67%) or liveable (24%) condition.

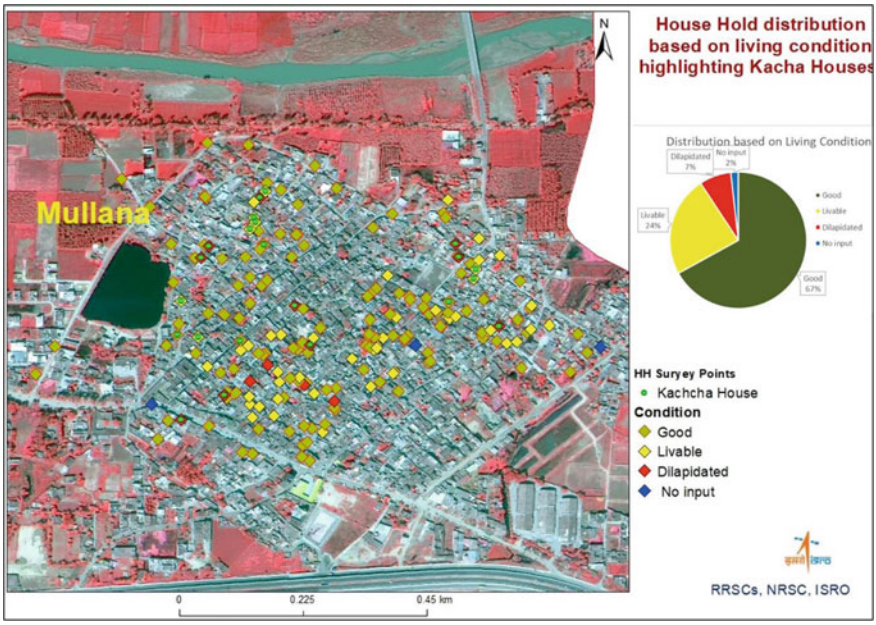

Fig. 20.12 House Hold data distribution based on house condition of residents of Mullana GP

20.7.7 Solid Waste Disposal Facility in Mullana GP

Analysis of facilities available in GP for solid waste disposals was carried out. The facilities are categorized into collection cart, composite, open disposal, and not available. Detailed distribution of solid waste facility is shown in Fig. 20.13. The majority of residents (82%) use collection cart for solid waste disposal.

20.7.8 Toilet Availability and Type in Mullana GP

The houses based on toilet type are categorized into a private toilet, public toilet, community toilet, open defection, and not available. Spatial distribution is shown in Fig. 20.14. The majority of houses (97%) have private toilets in the GP.

20.7.9 Spending Pattern of Residents of Mullana GP

Spending patterns for the residents were analyzed by preferences of expenditure during the survey. Details on spending on food, education, health, transport, rent,

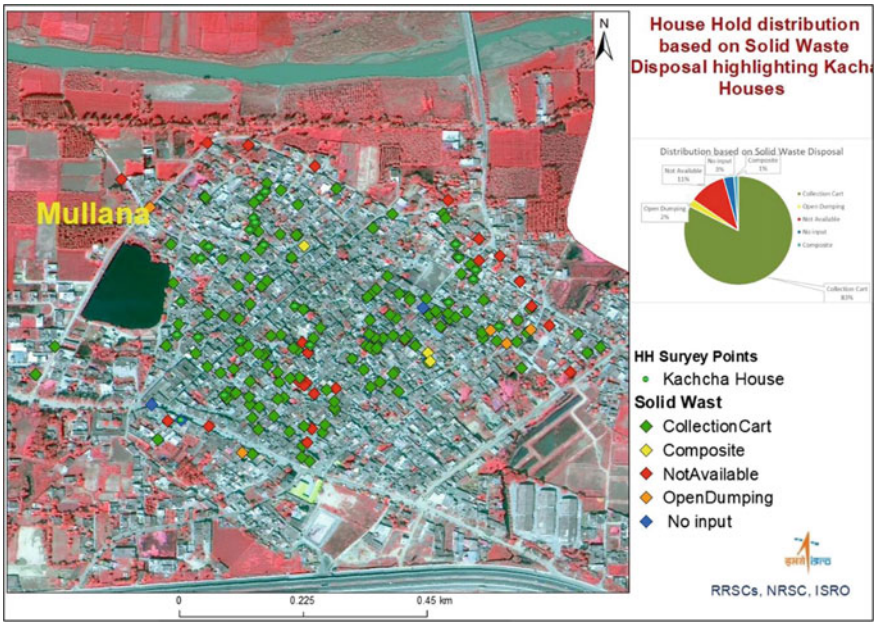

Fig. 20.13 House Hold data distribution based on solid waste disposal highlighting kachcha houses in Mullana GP

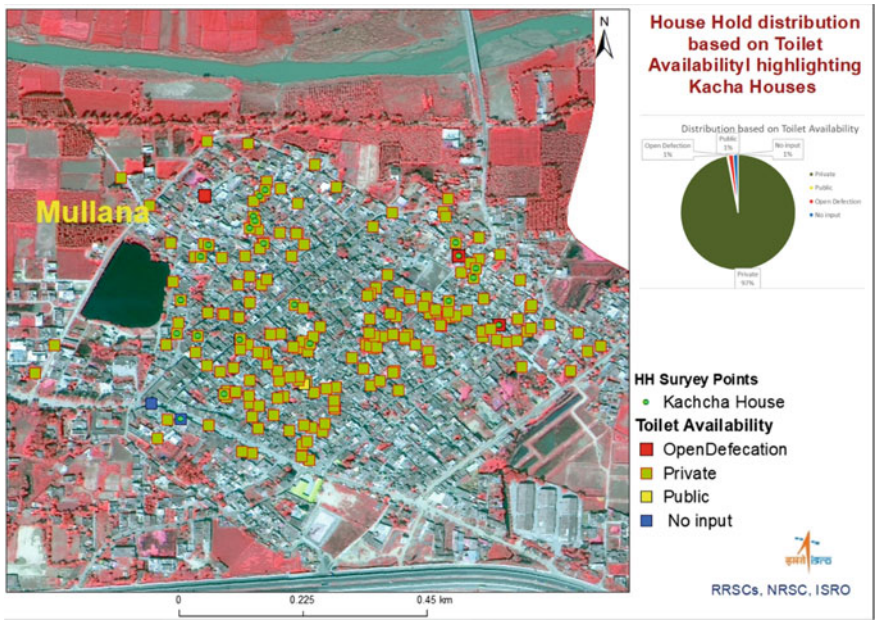

Fig. 20.14 House Hold data distribution based on toilet availability to residents of Mullana GP

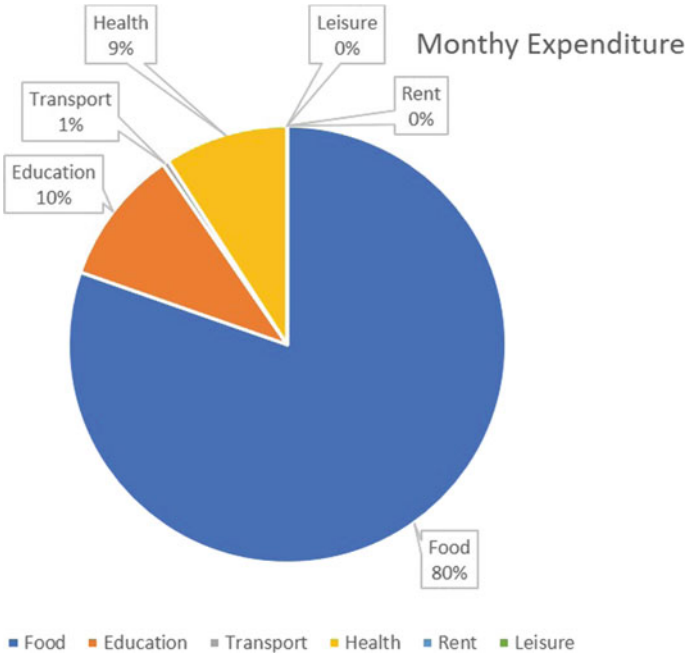

Fig. 20.15 Expenditure analysis of residents of Mullana GP

and leisure as a first priority were collected and analyzed (Fig. 20.15). A major portion of earning is spent on education by the majority of residents (36%) in GP.

20.8 Results and Discussion

Household survey data collected through the mobile application for 23 GPs was analyzed based on the socio-economic parameters such as house height, availability of BPL card, ration card, toilet availability etc. Relative distribution of Kaccha, Pucca, and Semi Pucca houses among all GPs is given in Fig. 20.16.

Morai GP of Tamil Nadu, Bilkis Ganj of Madhya Pradesh & Mullana GP of Haryana shown the highest percent of Kaccha, Semi-Pucca, and Pucca housing, respectively.

Height of houses in all GPs in terms of Ground (G), One storey (G + 1), and more than one storey is shown in Fig. 20.17. Paritala GP of Andhra Pradesh, Gundur GP of Tamil Nadu, and Jhit GP of Chhattisgarh show the highest percentages of G type house with values of 95%, 94.5%, and 94%, respectively, while Aguibani (52%) and Shankaranarayana (57%) GPs show the highest percentages of G + 1 and more than G + 1 type house height, respectively.

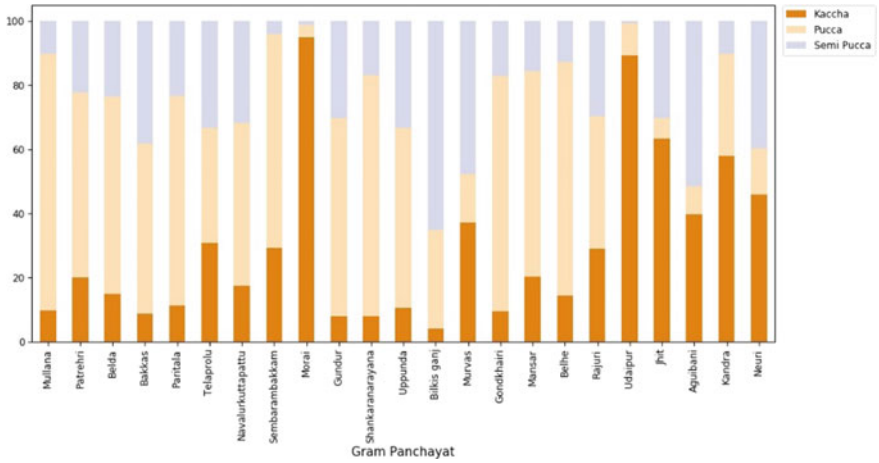

Fig. 20.16 Comparison of GPs based on house type

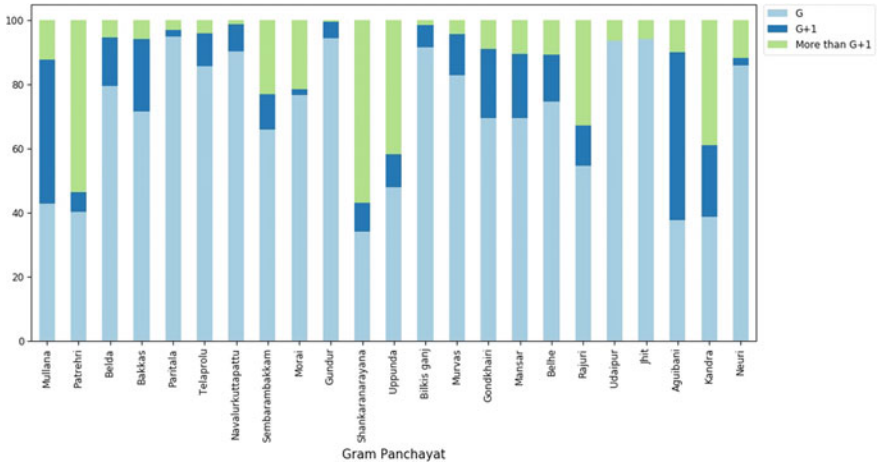

Fig. 20.17 Comparison of GPs based on houses height

Comparative analysis of GPs based on the BPL card and ration card availability was represented for all GPs in Figs. 20.18 and 20.19. Morai GP of Thiruvallur district and Navalurkuttapattu GP of Tiruchirapalli district in Tamil Nadu have the highest and the lowest percentage of BPL cardholders, respectively. The distribution of availability of ration cards across the GPs indicated that all GPs have greater than 73% of its household.

Biogas availability drastically varied among the households where Shankaranarayana GP of Karnataka indicated the highest value of 85.8%, while Paritala GP of Andhra Pradesh indicated the lowest value of 1% (Fig. 20.20).

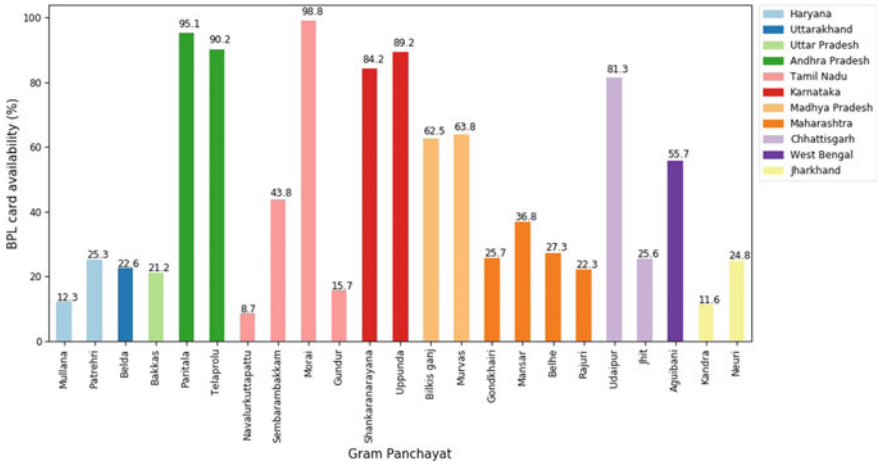

Fig. 20.18 Comparison of GPs based on availability of BPL card

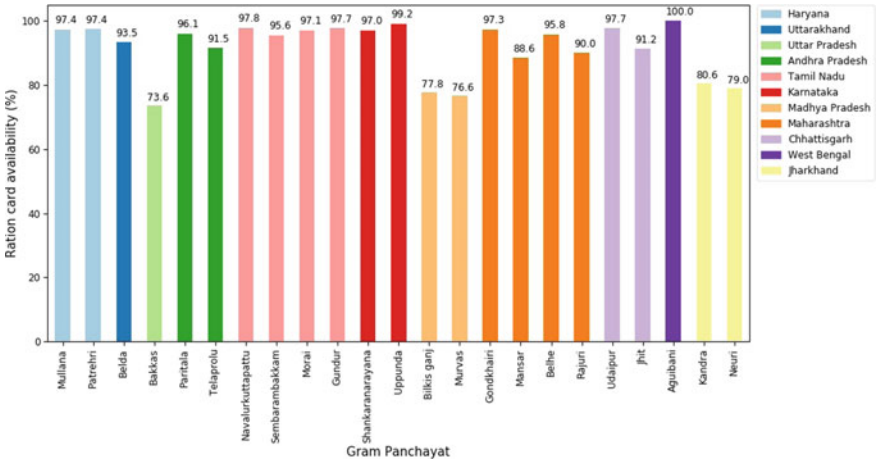

Fig. 20.19 Comparison of GPs based on availability of ration card

The distribution of solar equipment among the households in GPs was analyzed, and large variations exist among all GPs. 87% of Households in Shankaranarayana GP of Karnataka had this facility, while Paritala & Telaprolu GPs of Andhra Pradesh showed the lowest value of 1.5% and 1%, respectively (Fig. 20.21).

Residents' health among GPs in terms of vaccination (Fig. 20.22) and prominent diseases (Fig. 20.23) were analyzed. Jhit GP (5.1%) of Durg, Chattishgarh & Kandra GP (5.7%) of Bokaro, Jharkhand indicated the lowest percentage of vaccination whereas Morai GP (95.7%) of Thiruvallur, Tamilnadu, and Agubani GP (91.8%)

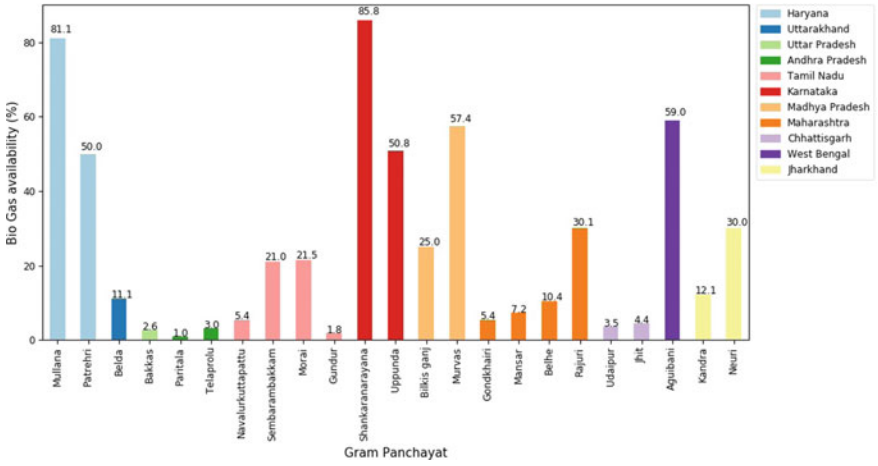

Fig. 20.20 Comparison of GPs based on the availability of biogas in houses

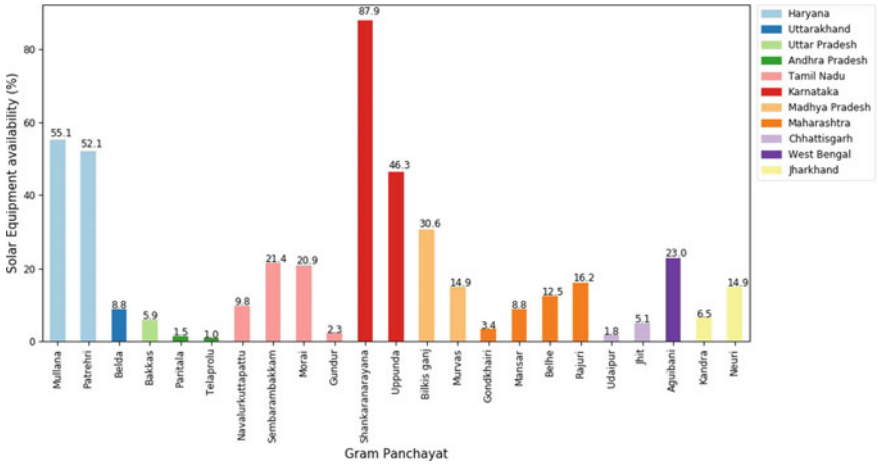

Fig. 20.21 Comparison of GPs based on the availability of solar equipment's in houses

of West Medinipur, West Bengal showed the highest percentage of vaccinated households.

Expenditure by households among all GPs toward food, education, transportation, and health were analyzed (Fig. 20.24). The Jhit GP & the Udaipur GP of Chhattisgarh showed the highest (98.5%) and lowest (8.2%) expenditure toward food. The Bilkis Ganj GP (48.6%) of Madhya Pradesh and Morai GP (0.3%) of Tamil Nadu reported the highest and lowest expenditure toward education, respectively. Udaipur GP (14.6%) of Chhattisgarh and Navalurkuttapattu GP (27%) have reported the highest expenditure toward transportation and health, respectively.

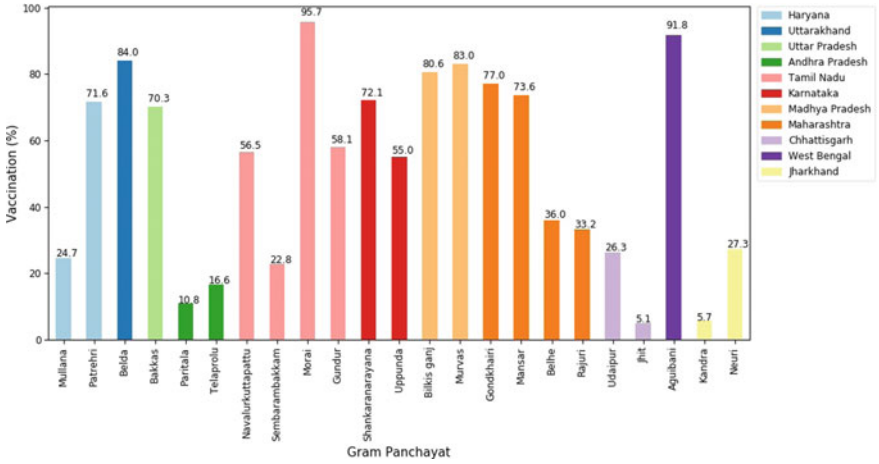

Fig. 20.22 Comparison of GPs based on vaccinated households

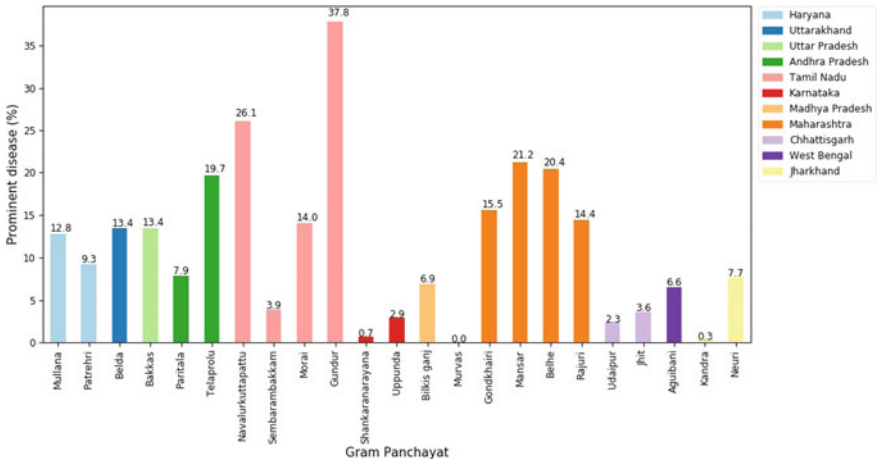

Fig. 20.23 Comparison of GPs based on the presence of prominent disease to residents

20.9 Conclusions

Gram Panchayats prepare annual plans to develop their region and more effective utilization of available resources. Particularly integration of geospatial technologies such as remote sensing and GIS with mobile-based field survey data can help to achieve sustainable development goals. The use of spatial planning for self-governance at the grass-root level, aided with technology can ensure transparency and accountability in the functioning of GPs. With the aid of GIS, satellite imagery, and mobile technology, a detailed record of the available resources and facilities can

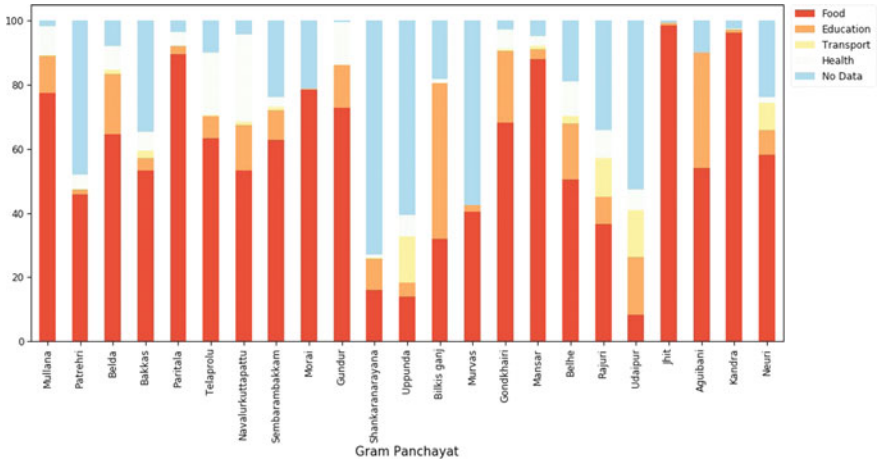

Fig. 20.24 Comparison of GPs based on their relative expenditure toward food, education, Transport, and Health

be visualized in a simple and cost-effective manner. This information becomes a backbone for planning different activities in the Gram Panchayat. The analysis of other GPs based on available resources compares GPs in the field of various domains like; health, education, infrastructure, etc. Thus the planners can identify and prioritize the development activities in the Gram Panchayat based on the data. It enables the user to make better decisions based on geographical data. There is a need to have objectivity in the planning process by acquiring relevant data and performing planning at the GP level using geographic data for sustainable development. Mobile GIS-based field data can increase the credibility and acceptability of the Panchayat Raj Institutes among its stakeholders.

References

Charland A, Leroux B (2011) Mobile application development: web vs. native. Queue 9(4):20

de Abreu Freire C, Painho M (2014) Development of a mobile mapping solution for spatial data collection using opensource technologies. Procedia Technol 16:481–490

Huang Q (2019) Programming of mobile GIS applications. In: Wilson JP (ed) The geographic information science & technology body of knowledge (1st Quarter 2020 ed). https://doi.org/10.22224/gistbok/2020.1.2

Nowak MM, Dziób K, Ludwisiak Ł, Chmiel J (2020) Mobile GIS applications for environmental field surveys: a state of the art. Glob Ecol Conserv 23:e01089

Pundt H (2002) Field data collection with mobile GIS: dependencies between semantics and data quality. GeoInformatica 6(4):363–380

Roth R (2017) User interface and user experience (UI/UX) design. In: Wilson JP (ed) The geographic information science & technology body of knowledge (2nd Quarter 2017 ed)
Yang P, Evans J, Cole M, Marley S, Alameh N, Bambacus M (2007) The emerging concepts and applications of the spatial web portal. Photogramm Eng Remote Sens 73(6):691–698

Chapter 21
Geospatial Technologies for Development of Cadastral Information System and its Applications for Developmental Planning and e-Governance

Subrata N. Das, G. Sreenivasan, S. Srinivasa Rao, A. K. Joshi, A. O. Varghese, D. S. Prakasa Rao, K. Chandrasekar, and C. S. Jha

Abstract Space-based geospatial technology, because of timely availability of information derived from remote sensing data on the desired scale, along with the Information and Communication Technology (ICT) including Geographical Information System (GIS), has accelerated the process of developmental planning and e-Governance initiatives in the country. With the advancements in satellite remote sensing technology, which is providing data with the best spatial resolutions, mapping has been possible at larger scales, progressing to the cadastral level (~ 1:4000). This rightly caters to the requirement of current Government programs to provide planning at village and gram panchayat levels. High-resolution satellite data is considered the ideal operational source for georeferencing the village cadastral maps. Overlay of the georeferenced cadastral maps on the high-resolution satellite data helps in carrying out detailed natural resource mapping to characterize each land parcel to understand their potential and limitations in terms of various natural resources and terrain characteristics. These include surface and groundwater availability, soil and land capability, geology, lineaments, and rock formations, geomorphology and the terrain characteristics, present land use including agriculture, forest, wastelands, water bodies, and the available infrastructure. Integration and geospatial modeling of these parameters facilitate cadastral level planning, development, and management for several applications. These include management of agricultural and horticulture, forest, land resources, surface water conservation, groundwater development and recharge, reclamation of wastelands, planning industrial corridors, planning for new and self-sustained townships, and several other infrastructure and amenities planning. Information and planning maps derived through the Remote Sensing data at the

S. N. Das · G. Sreenivasan (✉) · A. O. Varghese · D. S. Prakasa Rao
Regional Remote Sensing Centre—Central, NRSC, ISRO, Nagpur, India
e-mail: sreenu_v@yahoo.com

S. Srinivasa Rao · A. K. Joshi · K. Chandrasekar · C. S. Jha
National Remote Sensing Centre, ISRO, Hyderabad, India

A. K. Joshi
MRSAC, Nagpur, India

C. S. Jha et al. (eds.), *Geospatial Technologies for Resources Planning and Management*, Water Science and Technology Library 115,
https://doi.org/10.1007/978-3-030-98981-1_21

cadastral level, along with the ICT including GIS, are used in various e-Governance services in the country. Apart from providing online village-level services, it caters to the use of ICT for strategic village-level development planning, thus reaching the development goals of the government. This chapter discusses the geospatial techniques and methodologies for the generation of georeferenced village cadastral systems and presents some of the main applications of georeferenced cadastral maps for developmental planning and e-Governance with case studies from Chhattisgarh and Maharashtra.

Keywords Cadastral · *Cadastre* · *Gaothan* · *Chak* · *Tippan* · Village maps · Remote sensing · GIS · ICT · Cadastral georeferencing · Cadastral level planning · Developmental planning · e-Governance · Mobile applications

21.1 Introduction

For integrated developmental planning, the timely and reliable inflow of information is a prerequisite. Satellite remote sensing, with large synoptic coverage, timely, accurate, and cost-effective data with Geographical Information System (GIS), an ideal tool for managing spatial data, forms a spatial information base. The pragmatic action plans for land resource and water resource development are prepared with due consideration of conservation and development of natural resources (Rao et al. 1995; Krishna Murthy and Adiga 2000; Sreenivasan and Krishna Murthy 2018). Further, to meet the people's requirements and imbibe local wisdom in the action plans, integration of the information available at the parcel level with spatial information base is a prerequisite (Sreenivasan and Krishna Murthy 2018).

The main thrust is to accurately generate the largest scale land database which is efficient, reliable, cost-effective, scale-independent, capable of adopting information from various sources, and compatible with the other information systems. The Land Information System (LIS) system should address an individual farmer with a parcel number as the unique identity. The parcel number and the information on the record of location, extent, value, and ownership of land are derived from the "*Cadastre*" or the Cadastral Information System (CIS), which is integrated with the natural resources information using Geographical Information Systems (GIS) to develop a LIS. The planning system thus based on the LIS should act as a planning and developmental tool addressing all the issues faced during local level planning, implementation, and subsequent monitoring of the impact of developmental activities (Gopala Rao 2000; Williamson et al. 2000).

Developing an efficient LIS requires accurate, up-to-date, and standardized CIS comprising the cadastral maps in the digital environment, with a proper geodetic control framework for linking the cadastral data to GIS, high-resolution satellite data, and the thematic maps (Sreenivasan and Krishna Murthy 2018).

21.2 Geospatial Technology

Geospatial Technology, commonly known as geomatics/geo-informatics, refers to the technology used for capture, measurement, visualization, and analysis of features or phenomena that occur on the earth (surface, underground and aboveground). Geospatial technology includes three different technologies that are all related to mapping features on the surface of the earth. These three technology systems are Remote Sensing (RS), Geographical Information Systems (GIS), and Global Navigation Satellite Systems (GNSS).

21.2.1 Remote Sensing

Remote Sensing technology is the technics of identifying an object by exploring and measuring its reflecting and transmitting characteristics in the electromagnetic spectrum either in passive or active mode. Satellite remote sensing is used mostly to sense the surface object characteristics in various electromagnetic bands as images. The images come in various resolutions (special, spectral, radiometric, and temporal) and are georeferenced with the earth referencing system (projection, datum, and coordinates) for ingestion into various national importance projects using GIS.

In recent times, high-resolution (usually considered from 30 cm to 2.5 m) satellite images to very high-resolution (usually considered from 1 to 10 cm) (https://www.satimagingcorp.com/) earth images (Fig. 21.1) are acquired and processed using the photogrammetry techniques. Using this geoprocessing a planimetric accurate base earth image is generated which is commonly known as orthoimage or ortho-corrected image. These types of data form the base for any cadastral level mapping and generation of the action plan for development.

Fig. 21.1 **a** Satellite data (50 **cm**), **b** UAV data (5 cm)—high-resolution data form the base of all land property records and their uses

21.2.2 Global Navigation Satellite System (GNSS)

GNSS generally constitutes a constellation of medium earth orbiting (MEO—5000–20,000 km) satellites to provide autonomous geospatial earth surface positioning. The GNSS device receives the electronic radio signals from multiple satellites to determine their location (longitude, latitude, and altitude/elevation) to high precision (sometimes within a few centimeters to meters depending upon the observation time). The system is used for providing position and navigation (track shifting receiver location).

A satellite navigation system with global coverage may be termed a global navigation satellite system (GNSS). As of September 2020, the US Global Positioning System (GPS), Russia's Global Navigation Satellite System (GLONASS), China's BeiDou Navigation Satellite System (BDS), are some of the existing GNSS systems. The Indian Regional Navigation Satellite System (IRNSS) is for the Indian subcontinent and plans to expand to a global version in the long term.

The GNSS receivers are used in various applications viz. military, satellite and air navigation, automotive navigation, survey and mapping, and for all location-based services (LBS).

The mapping grade GNSS receivers use the carrier wave data from only the L1 frequency but have a precise crystal oscillator that reduces errors related to receiver clock jitter. This allows positioning errors on the order of a few meters or less in real-time. With a differential GNSS signal received using a separate radio receiver. By using the carrier phase measurements and then differentially post-processing the data, the positioning errors can be reduced to the order of 10 cm. Thus, the GNSS receivers used for surveying land and land-based objects use the signal from both the L1 and L2 GPS frequencies (dual frequency). These receivers are mostly used for the cadastral level survey where a high level of accuracy is needed. The mapping grade GNSS receivers are used for various mobile-based instruments for various applications within the GIS environment.

21.2.3 Geographic Information System (GIS)

GIS is a tool (software) that facilitates the collection and management of spatial (thematic) and non-spatial (attributes) information having spatially referenced coordinates.

GIS is utilized in multiple technologies, processes, techniques, and methods. GIS and location intelligence applications are at the foundation of location-enabled/location-based services, that rely on geographic analysis and visualization. Locations and extents that are found in the earth's spacetime, can be recorded through the date and time of occurrence, along with x, y, and z coordinates; representing, longitude (x), latitude (y), and elevation (z) on the earth. All earth-based, spatial–temporal,

location and extent references, should be relatable to one another, and ultimately, to a real physical location or extent.

Geoprocessing is a GIS operation used to manipulate spatial data. Common geoprocessing operations include geographic feature overlay, feature selection and analysis, topology processing, raster processing, and data conversion. Geoprocessing allows for definition, management, and analysis of information used to form decisions (Wade and Sommer 2006).

GIS-based analysis in e-governance is the most popularly used analysis considering the importance of location-based services requirements in GIS-based applications. All spatial-based analytical tools use the GIS tools as the back-office management for bringing in the new authority and transparency in the business of governance, sometimes also termed as "spatial intelligence". New internet-based methods and procedures are being developed along with the encapsulated database to encourage the use of more geographic information with better social objectives. Geospatial intelligence, based on GIS spatial analysis, has also become a key element for security. Cadastral geodatabase today uses most of the advanced geospatial technologies with advanced geodatabase type, structure, and encryption procedures.

For dissemination and e-governance of cadastral-based information, geoportal is used. A geoportal is a type of web portal used to find and access geographic information (geospatial information) and associated geographic services (display, editing, analysis, etc.) via the internet. An effective geoportal has a GIS running in the background. Geographic information providers, including government agencies and commercial sources, use geoportals to publish their geographic information descriptions (geospatial metadata). Geographic information consumers, professional or casual, use geoportals to search and access the information they need. Thus, geoportals serve an increasingly important role in the sharing of geographic information and can avoid duplicated efforts, inconsistencies, delays, confusion, and wasted resources. Geoportals access data from multiple sources and provide easy-to-use operational applications.

21.3 *Cadastre* or Cadastral Information System

The dynamically changing relationship of humankind to land has a great influence on the development of land administration systems (Gopala Rao 2000). The relationship in short is depicted in a system called a "*cadastre*". The *cadastre* is a public record of location, extent, value, and ownership of land in a district for taxation. The *cadastre* evolved in response to the demands from society (Ting and Williamson 1999a). The evolution of cadastral maps is described in different phases of society's evolution, i.e., agricultural, feudal, industrial, and information revolution which has defined the *cadastre* in content and meaning. A typical cadastral map of a village and city cadastral map is shown in Fig. 21.2.

The *cadastre* or the cadastral information resides with two departments viz. Land Record Department (LRD) and the Inspector General of Registration (IGR). One

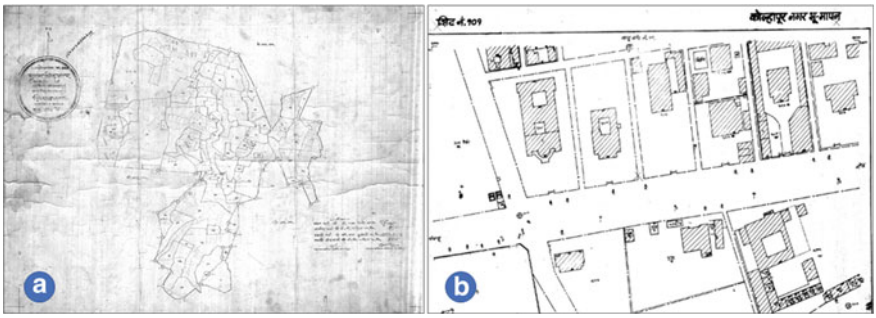

Fig. 21.2 A typical cadastral map: **A** village cadastral map, example of Hodnar village from Chhattisgarh state, **B** city cadastral map or city survey map, an example of Kolhapur, Maharashtra

department maintains the land record in physical map form and the other manages the land ownership and transactional details. There is a global trend over the last two decades to migrate from paper-based information systems to digital information systems to improve efficiency and accessibility of information (Borzacchiello and Craglia 2012). This is realized in the modernization of cadastral, land information, and land administration systems.

Land information refers to physical, legal, economic, or environmental information or characteristics concerning land, water, and sub-surface resources. The International Federation of Surveyors (FIG 1996) defines Land Information System as: "a tool for legal, administrative and economic decision-making and aid for planning and development. A land information system consists, on the one hand, of a database containing spatially referenced land-related data for a defined area and, on the other, of procedures and techniques for the systematic collection, updating, processing, and distribution of the data". The information has been used in a variety of systems over the years, from the register of the deed, tract indexes to surveyors' tie sheets or soil surveys (Holstein 1990). Today, many organizations are moving land information into Geographic Information Systems (GIS) and encrypted complex and intelligent digital geodatabase. Land Information System (LIS) is mainly focused on land records information. Land information becomes an integral part of government and private sector development activities. The LIS techniques advance broader social purposes by helping to make more effective decisions for using natural resources in a more optimal way (Barnes 1990).

The emphasis shifted from the physical ownership of land to the wealth for the mobility of assets. Cadastral records, including deeds, served as documents of ownership that establish the owner of the piece of land and provide the authority and trust to transact the sale of land (Dhal et al. 1994; Ting and Williamson 1999a).

The Torrens System of registration of ownership suited 19th-century paradigms of countries such as India and Australia with large tracts of un-surveyed and untitled land (Ting and Williamson 1999a; Raja Rao and Rajsekhar 2000). In short, *cadastre* then existed to facilitate land transfers, as it is a record of ownership and land taxation.

As today's society faces continuing resource scarcity, the imperative to better planning of land use gained urgency. The information revolution has a great potential to support the complex decision-making demands of sustainable development (Williamson 1986; Ting and Williamson 1999b; Dhal 1999). Multipurpose cadastres are expected to increase the interoperability of data sources to fulfill their fiscal, land transfer, and land management roles.

The growth of adjacent towns and villages with higher-density of populations and housing has increased the importance of the infrastructure to sustain the population with better urban planning. Reservation of land use by the urban planner with the community is aimed at providing public amenities, minimizing spillover effects on contiguous land, and increasing efficiency by guiding the development of land (Ting and Williamson 1999a; Raja Rao and Rajsekhar 2000). The *cadastre*, as the record of land parcels and registry of ownership, acts as useful information for the city planning and allotment of the various functional land use for utilities as prescribed in the URDPFI guidelines, 2014. The cadastral data also provide the legal reservation under different notifications of the government from time to time.

Also, the Government of India has brought in 73rd and 74th amendments to strengthen decentralized planning and to enhance the participation of local people in the planning process (GOI 1985; Behar and Kumar 2002). The 73rd Constitutional Amendment Act strengthened the role of the Panchayati Raj Institutions (PRI), the rural local bodies as institutions of self-governance responsible to plan and manage rural development (GOI 1985). Thus, institutions of local self-governance can become the basis for the elaboration and strengthening of civil society in the country (GOI 1985; Planning Commission 1989). For such grassroots level planning and development, georeferenced cadastral maps and the Cadastral Information System (CIS) form the base.

The CIS addresses each parcel at 1:8000–1:4000 scales. The GIS addresses the developmental plans generated at 1:50,000–1:10,000. The LIS developed based on cadastral maps and high-resolution satellite data bridges the gap between the planning and subsequent implementation and monitoring activities (Krishna Murthy et al. 1996a, b, 2000). LIS is visualized as a tool that facilitates pragmatic developmental planning at the micro-level (Sreenivasan and Krishna Murthy 2018), implementation of developmental plans through stakeholders and individual farmers participation, monitoring the impact at parcel level and implementation and linking the various government schemes and the beneficiaries.

Broadly, there are two ways in which spatial data has been organized in the country. In certain States/UTs, village maps with parcel boundaries are used, whereas, in certain other states, ladder data on individual land parcels or *tippans* or field measurement books (FMBs) or gat maps are used. In most parts of the country, the land parcels depicted in cadastral village maps are covered in one or more sheets, depending upon the scale of mapping and area of the village. These cadastral village maps/sheets will be considered as the basic input for digitization and mosaicing of the cadastral maps in these States/UTs. However, in the other States/UTs, where ladder data or gat maps/*tippans*/FMBs are used, the same will be taken for digitization and further mosaicing of the map. The cadastral map for each village is available on larger

scales like 1:4000–1:8000. These maps depict the survey boundaries with survey numbers, cultural features like transport networks, and natural features like drainage, etc. These cadastral maps have been prepared using plane table surveying and chain surveying. These maps have to be brought under a standard projection/coordinate system for effective linkage of the plans generated in the G1S environment.

In the development of CIS, a comprehensive data design provides a robust architecture for the database to be viewed in its entirety and evaluated how the various aspects of it need to interact. A good design results in a well-constructed, functionally and operationally efficient database. Database standards are an important element of database design. Standards enable applications and technology to work together, they encourage efficiency and effectiveness, help reduce costs, protect investments in data against technological change and lead to the availability of accurate, complete, and current data. Tools, applications, and data affect each other, and standards are established with this condition.

21.4 Development of Cadastral Information System (CIS)

The basic requirements for the creation of CIS are to have accurate, up-to-date, and standardized cadastral maps in a GIS environment with a geodetic control framework. The digital database prepared under such conversion forms the base for all future planning and development processes of the authority. The Revenue Department is the state government authority that maintains and manages all land information and its present status. The department manages the land and revenue data (Record of Rights—RoR), its spatial dimensions and geometry, maintain the history of the transaction, its values, and updation. For maintaining such records (both spatial and no-spatial) a strong nation/state standards need to exist that are based on the latest geospatial technologies, to facilitate future operation and maintenance of the records. Robust database management technology is adopted and across the board, a national standard is formulated. Broadly, the database construction for the development of a CIS can be divided into four major components. These components of CIS development are described in more detail in the following sections.

21.4.1 Digitization of Cadastral Maps

Different entities of the database are generated as the approved database standards. The institute/vendors/agency/service provider must ascertain that the digitization is per the prescribed standards. The outputs of each stage are put through stringent tests, scrutiny, and quality checking procedure to achieve maximum accuracy and correctness.

The reconstruction of an immaculate digital database with correct geometric and topology is the prime and the complex task upon which the usefulness of the database

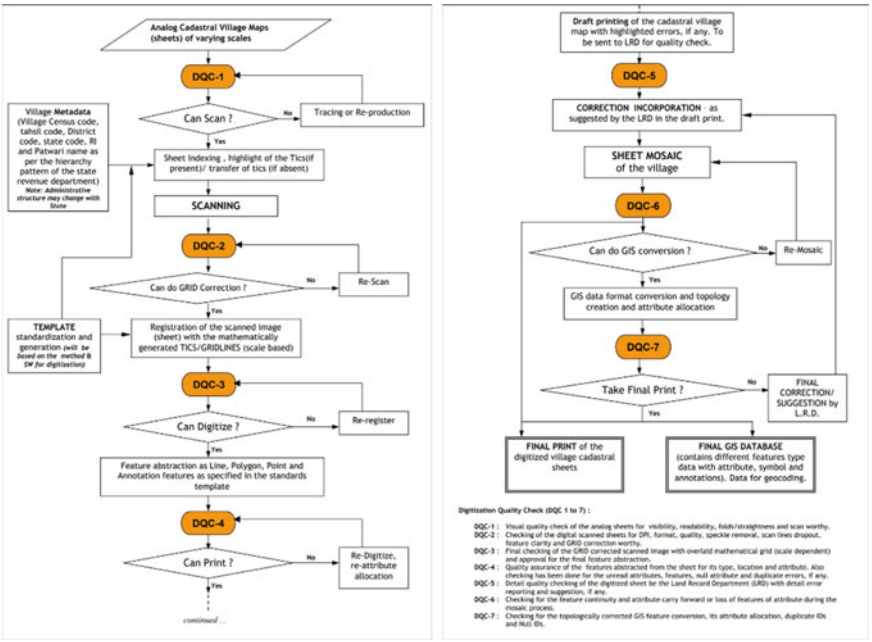

Fig. 21.3 Flowchart depicting the digitization of the cadastral village map and quality assurance

lies. Two important aspects need to be considered which creation of the digital database they are (a) the actual geographic standard data to define the physical piece of land or the shape and size of the land with its location, and (b) the unique identifier to link the attribute and transaction data of the land. The digitization process is the technical process of conversion of analog or tabular data (khata data) into spatial and non-spatial digital data. The process has to follow systematic steps of conversion, quality evaluation, and correction as depicted in the flowchart (Fig. 21.3), and described in the following sections.

21.4.1.1 Collection of the Cadastral Village Maps and Tracing of the Analog Maps

The first step of the digitization process is the procurement of the paper cadastral village map sheets. The physical condition of the map needs to be ascertained to facilitate the proper scanning procedure. The map should be clear, readable, and up-to-date concerning the mutation.

During the quality checking process (DQC-1) one needs to check the condition of the map with no folds or no tear or cloth mount behind it. The control tics or the grid of SOI should be visible, if not, need to be highlighted. The features of the map viz. line, symbols, the text should be clear and easily distinguishable. The parcel number

(khasra number) should be inked and all field control points (stone symbols) should be properly visible with a distinct symbol. Once all the basic parameters are found appropriate, the sheet is indexed with the unique number (preferable to the village code with other administrative codes) and set aside for the next procedure—scanning.

In case the sheet is found not fit for scanning, it is sent back to the land record department (LRD) for redrawing or tracing on mylar film (75–100 GSM) with all features and proper dimensions.

21.4.1.2 Converting Analog to Raster Cadastral Images

The cadastral maps, passing the DQC-1, are converted into digital data by the process called scanning using an A0 size wide format scanner either a drum scanner or a flatbed scanner. The selection of a proper scanner is an important step while considering its stability, repeatability, linearity, resolution, and skew adjustment. The scanning resolution is an important parameter and should be scanned at an appropriate DPI (Dots per inch). The recommended resolution is around 100–200 DPI for black and white sheets (8-bit gray tone) considering the density and quality of the map. Sometimes, for the denser and the colored features, the scanning resolution is set to 400 DPI. The scanning is done by allowing the map to roll on the drum slowly, or if the flatbed scanner is used it is flattened, pressed with the glass to remove the wrinkles/bulging, and scan.

Once the scanning of the analog map is completed the quality checking (DQC-2) of the scanned (*.tiff) file is performed. The digital file is cleaned and made noise-free (removing speckles, if any) by applying the de-speckling in the image processing software. The file is then checked for the relative distance between the tic points or the grid lines against any skewing or wrapping. If the grid size or the tic locations vary in the scanned and original document by $\pm$ 0.1% of the distance, then the map is rejected and sent for rescanning. Also, it needs to be ascertained that all the texts, lines, and symbols are properly visible in the scanned document.

21.4.1.3 GRID Correction of Scanned Cadastral Map

Even after performing the quality check of the scanned document, there can be some inherent error that may creep in due to the instrument specification and scanning techniques. There can be some manuscript (raw map) internal distortion due to wear and tear and shrinkage/expansion. If these errors are not corrected at this stage, then the error will be carried forward and beyond repair.

To remove these irregular errors and make the map planimetrically accurate, the digital scanned map is registered to the predefined mathematically accurate vector grid. The grid is prepared based on the defined scale and the distance as depicted on the map. Generally, the old maps of 16 in. = 1 (one) mile, i.e., 1:3960 scale, the grids are generally of 10 zaribs (= 50.8 cm or 2.00000008 in.); whereas, the SOI grid (1:4000 scale) has a grid system of 25 mm apart. The old maps have 10

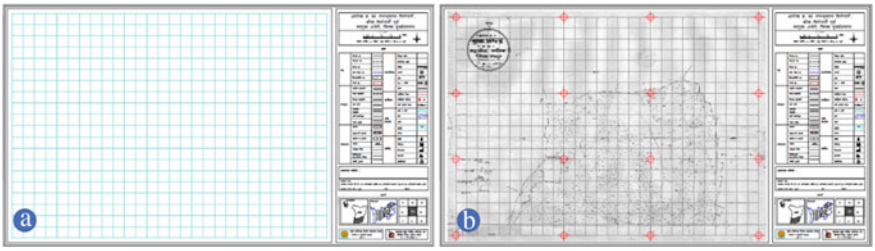

Fig. 21.4 **a** Standard cadastral sheet prototype and **b** the grid rectified cadastral raw sheet

× 14 grid blocks and the SOI maps have 20 × 28 grid blocks. The scanned sheet is registered with these grid blocks and then rectified to match the grid (Fig. 21.4). High accuracy with low RMS error is expected in this registration to remove any warping effect in the sheet. The quality check is performed on the rectified scanned image by overlaying the grid and seeing the matching of the grid tics at the intersection. This process is defined as DQC-3, and if the errors are within the expected level of shifts, the scanned sheet is sent for the process of feature extraction.

21.4.1.4 Feature Extraction From the Grid Corrected Scanned Cadastral Images

Feature abstraction process may be defined as the process of capturing the geometric entities of the map by drawing and storing them as GIS entities of point, line, and polygon features. These are captured and stored as vectors; the text as an annotation. The grid corrected raster image is either opened in the CAD or GIS environment and one by one the features are drawn in the same environment. The environment of the software is pre-set before the extraction process concerning the various tolerances (snap, grain, etc.). The attributes about the feature are also captured and are attributed to the respective features. During vectorization, care should be taken to follow the centerline with appropriate zooming; auto-vectorization should be avoided. The output should be within the permissible limit of the digitization errors viz. coordinate movement tolerance, weed tolerance, coordinate unit, fuzzy tolerance, etc. Feature connectivity and adjacency should be ensured. The features concerning their topological relationship should be ascertained. Sliver polygon tolerance should be set and cleaned if any.

Included in the standard document prepared for the digitization process, a predefined template is prepared with the standard names and symbols. The names and the symbol refer to the various features on the ground like bunds as parcels, roads, canals, rivers, etc. The location of point features that are shown as symbols is defined as it is in the form of digital points symbols. The template maintains uniformity among all digitized maps for future integration. The templates will have all the major map elements viz. headings, legend, index map, grids, north arrow, etc. and are approved by the competent authority. The texts are generally written in the local state language

in the UNICODE system. The template may vary from state to state, as the different states may follow a different map depicting and approval procedures.

The feature extraction or the feature digitization process will create GIS/CAD entity layers and resemble the paper map with all features in it. The layers are all topological corrected and checked for the attributes. The map will be a part of the template and will be printed on the template map, with all standardized components and elements, for physical checking with the original map. (Fig. 21.5).

The DQC-4 is performed at this stage. The digitized features are overlaid on the rectified scanned sheet and are checked for extraction of all features and annotation (text). This will ensure that features are true to-its-type, accurate in location and attributes. The features/ attributes which are not extractable are sent for clarification to the LRD and are incorporated after duly resolved.

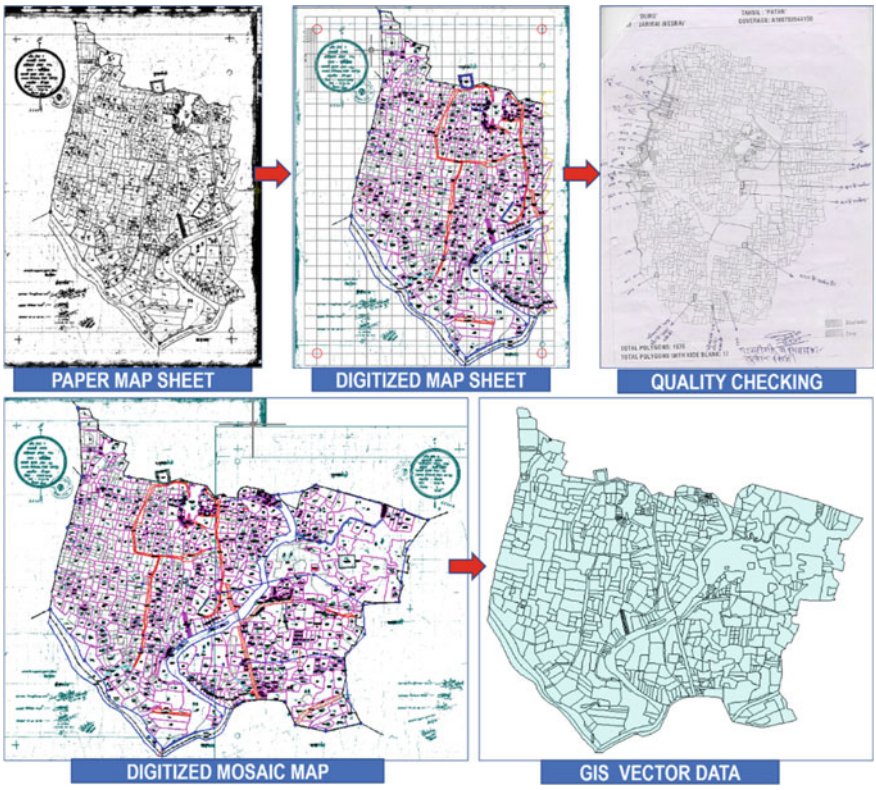

Fig. 21.5 Cadastral map grid referencing, vectorization, mosaicking, and GIS format conversion

21.4.1.5 Hard Copy Printing for Evaluation

The digital features extracted from the rectified scanned raw cadastral maps are organized on the predefined and approved sheet template with all map elements. The template with the digitized features is converted into a Portable Document Format (PDF) file and then printed true to the inherent scale. Good quality paper should be used (75–100 GSM) for printing. This is named as the first draft copy of the sheet and is sent to the land record department for verification. At this stage, 100% validation is performed by the department and is assigned as DQC-5 in the process flow of digitization of land records. The outputs first checked for village name, patwari name/number, revenue inspector circle, and taluka name along with the adjacent villages on the map. The features inside the map are checked for the physical location of the parcel, orientation, dimension, adjacency, and attributes. All symbols with their attributes are thoroughly checked. All parcel numbers are checked and the missed-out numbers are assigned with the number at this stage. Any bifurcation/updates in the parcel are also incorporated at this stage. The corrected draft copy is duly signed by the authority and sent for the digital alteration and incorporation if any.

21.4.1.6 Incorporation of Correction Suggested by LRD

The corrected and signed draft hard copy once received by the agency incorporates the necessary correction in the digital file layer-wise. The data once incorporated is run for the topological errors and clean and accurate data is generated. Likewise, if there are multiple sheets for a village, in each sheet the corrections are incorporated and sent for the mosaic at the village level.

21.4.1.7 Sheet Mosaicing of a Village

On most occasions, the village area is divided into sheets with overlaps or joining controls. The features are extracted and corrected sheet-wise. Since the village is a single entity having the features and parcel numbers in continuity, the sheets need to be mosaiced. The sheets are mosaiced by matching the feature edges with the reference grid control. The continuity of the features is seen and merged in the GIS/CAD environment. The duplicate annotation/attributes are also merged and fresh topology is run. The topology will ensure the completeness, contiguity of the features. Duplicate features, especially the sheet control symbols, should be deleted and cleaned. Finally, a topologically corrected single GIS/CAD layer will be generated with all features for the entire village for further quality checking and approval. This process is termed DQC-6 to ascertain the feature continuity and attribute carry forward.

21.4.1.8 Conversion of the Digitized Data into a Topologically Correct GIS Data Format

Once the DQC-6 is performed, the digitized and sheet mosaiced village cadastral data is rechecked for the topology and converted into topologically corrected GIS data. This can be a propriety data format (ESRI geodatabase) or an open data format (shapefiles). The GIS data has separate point, line, polygon, and annotation layers, and together they are topologically linked and spatially related. The annotation or the attribute are related to the spatial layers through spatial relationships. The basic objective of bringing all features under the GIS environment is for the establishment of the spatial relationships between various layers/features concerning the shape, size, containment, location, proximity, contiguity, adjacency, and intersection. The relational database standard and structure is being followed to generate the primary and foreign key for integration with the external database system for linking and querying. At this stage, the uniqueness of the primary key and the foreign key is checked, the completeness or redundancy in the data concerning the other attributes is checked and error files are generated. This forms part of the DQC-7 procedure. The error report concerning the duplicate or null values are generated and sent to the land record for validation. As suggested by the land record department the errors are checked and incorporated. The data, both spatial and attribute, are again checked and evaluated. Wherever the errors could not be incorporated, a flag in the database is generated. The data, thus generated is finally ready for the georeferencing with the ortho-corrected high-resolution satellite data.

21.4.1.9 Final Deliverables (Hard Copy Print and GIS Data for Geocoding)

The final GIS data, correct in all aspects, is converted into village-wise PDF files with all feature symbols and overlays in the prescribed format. Also, sheet-wise outputs are generated in PDF format. For archival, the hard copy output may be printed on a relatively good quality thick paper (150 GSM). The GIS data are maintained in one directory as the unrectified village cadastral mosaic file which will be used for georeferencing with the high-resolution satellite data for adding the geographic coordinates.

The georeferenced cadastral matches with the satellite data and have a reference to the earth's location. These data are useful for identifying the beneficiary (farmers/owners) related to various e-governance procedures of the government. The georeferenced cadastral maps help in demarking the planning and developing areas, finding out the affected areas during the disaster, prioritizing the constraint area, and using the cadastral information for achieving the various sustainable development goals (SDGs) efficiently. The geocoded cadastral data, being digitally integrated, can be disseminated on the web geoportal and used for development activities by the Ministry of Panchayat and Rural Development through different government-recognized schemes.

21.4.1.10 Metadata Preparation

The cadastral data are one of the largest scale data and are generally in volumes. These are the legal documents and describe the ownership of a piece of land. Often, searching for such data from the database consumes a lot of time. Metadata is the information about such voluminous data and helps in quick searching of the data. It represents the who, what, when, where, why, and how of the resource data (FGDC 2016). So, for speedy access and retrieval of the data, good metadata is essential with well-defined standards. Well-maintained metadata allows the organization to maintain the data with all required information of the database creation, alteration, and updation. It defines the access procedures and the security of the data, provides data catalogs, format, currentness, and procedures of the data handling and manipulation.

The metadata standards of the cadastral map will facilitate understanding the availability of the data, its access protocol, how it can be used, and its transfer protocol. The metadata has the identification information describing the data with keywords definitions. It also describes the GIS data entity format and the attributes information in it. Metadata reveals the information about the data quality, spatial data referencing (coordinates system and projection), and its database organization. Metadata also describes the period (time) and contact information. Thus, all information regarding the cadastral data can be accessed without actually calling the data from the system. It is designed to store information about the cadastral village layer, and in the future, it should be designed to store the updation rate, history, and time of the land transaction.

21.4.1.11 Linkage of the Spatial Data with RoR

Through the title deed, every citizen attains rightful ownership over a particular property or land. All legal transaction and other transaction of the government is based on this deed. The RoR (Record of Rights) is the primary record of land that is mentioned in the title deed and holds information of property transactions. Though, the property under consideration, finds a mention of location and sketch map in the deed and the RoR, the actual integration with the georeferenced cadastral is not always available. Thus, textual information of the land is integrated with the geospatial data of the property.

The linkage of the spatial georeferenced cadastral will facilitate the online updation of the records, both in terms of records and spatial data. The spatial data is either bifurcated or amalgamated or reconstructed. In all the cases, the procedure of integration will help the process of geospatial changes and the registration of records at the same time. This will facilitate to access online information of the property regarding its status. Integration of the spatial data with the government records improves the credential of the maps and provides all types of online queries. Linkage also helps in the management of the various government activities/projects, helps in understanding the ownership and the status of the land in question.

21.4.1.12 Quality Assurance

Data quality is one of the prime concerns in database creation and transfer. The quality control standards should be well-defined and strictly followed at each step. The measurement of the accuracy is based on the allowable limits either as a physical or logical accuracy.

In the process of data conversion, many errors can creep in due to the instrument, drawing procedure, projection, transformation, and sometimes software accuracy. Which the software, used to extract the feature, the tolerance setting plays a major role. This decides how the feature are located on the map with respect to each other. The GIS entities of points, lines, and polygons are affected by the tolerance setting and are maintained within the spatial data structure. In other words, it describes how the feature is constructed. For point feature, how best it is located within the prescribed distance limits; the line is represented by the vertices length segment, its direction, and overall length, whereas in polygon the number of the lines that make the polygon, its perimeter, and area confined. On the other hand, logical accuracy is described by the correctness and completeness of the data concerning their attributes. Logical accuracy comes into play with the spatial and attribute query for the selection of the right entity in the data. Thus, maintaining the proper quality data will help in better data fidelity and help in taking the right decision at the right time.

21.4.2 Preparation of Reference Satellite Image Base

The cadastral map at the village level is available on larger scales of 16 in. = 1 mile (1:3960) in the older FPS system and 1:4000 in the new metric system of measurement. The cadastral maps are generally prepared using plane table surveying and chain surveying. These maps are drawn to a true area projection or Cassini projection. For using such maps for development purposes, the maps need to be brought under a proper referencing system that describes the coordinates, projection, and datum of the data under the GIS environment. The following methodology has been developed for establishing a one-to-one correspondence with the ground coordinates through the satellite data.

The early phase of the digitization and georeferencing of the cadastral maps initiated with the use of the IRS 1C/1D satellite data, available in four spectral windows of 23.5 m resolution and panchromatic data of 5.8 m resolution with stereo capability. With the advancement in satellite-sensor technology, currently, better resolution satellite data are available and the meter to sub-meter resolution satellite data are more appropriate for generating the ortho-corrected mosaic satellite base data for the state. A list of a few satellites' sensors providing sub-meter spatial resolution data is given in Table 21.1.

The satellite images depict many natural features such as the field with bunds, roads, and tracks, streams, and nullahs besides the settlement, tanks, and other transport features like rails and roads, which are advantageous in identifying ground

Table 21.1 List of satellites' sensors providing sub-meter spatial resolution for CIS

Satellite	Sensor	Spatial resolution (in m)
IRS CARTOSAT-3	PAN	0.65
GeoEye-1	PAN	0.46
GeoEye-2	PAN	0.34
WorldView-1	PAN	0.46
WorldView-2	PAN	0.46
WorldView-3	PAN	0.31
Pleiades-1A	PAN	0.50
Pleiades-1B	PAN	0.50
KOMPSAT-3	PAN	0.70
QuickBird	PAN	0.65
IKONOS	PAN	0.82
Planet Lab SkySat-C	PAN	0.50
SkySat-2	PAN	0.90

control points (GCP) for developing transformation model for an image-vector tie-down.

The digital image processing algorithms are used for merging of high spatial resolution data of panchromatic and moderate to low spatial resolution multispectral data. The panchromatic data is registered with available GCP acquired through the process of survey and triangulation or GPS survey. Sometimes Survey of India (SOI) toposheet is used for an image-to-map transformation model. The multispectral band data is enhanced to the panchromatic pixel size and then merged with the panchromatic image to generate a high-resolution multispectral image base with all the sharpness and resolution of PAN and the color/hue of the multispectral bands. The panchromatic image is merged with the multispectral bands to bring more information into the satellite data. The techniques used often are the high pass filtering technique, IHS transform-based image fusion, Wavelet transform image fusion, etc. The cadastral features match the features of the satellite data.

With the high-resolution stereo data, aerial photographs, or UAV data, the photogrammetry technique is used for registering the stereo data with GCPs and Tie-points, thus generating the Digital Elevation Model (DEM). The DEM is used to perform the terrain correction of the satellite data generating ortho-corrected merged satellite data.

The satellite data of the late rabi season or summer season (generally during the months from February to June) are found suitable for satellite data acquisition and generating the merged product. The images should not have any clouds and are corrected from the atmospheric haze. The sequence of steps for preparing the satellite data for georeferencing of cadastral maps is described in the following sections.

21.4.2.1 Coordinate System Definition

The cadastral maps at the village level are generated on paper without any projection or in some places used Cassini projection. The area of the village is small and hence the curvature of the earth has little or no impact in assuming that the earth is flat in a single village area. Mathematically this assumption causes very little or no significant error in dimensions of the plotted area. However, when a mosaic of several villages at taluk or district is being created, the assumption that the earth is flat will fall wayward. This assumption will induce errors when the study area is large. In turn, the process of making a mosaic of several villages will face several shortcomings. To avoid the shortcomings, the coordinate system is required with proper projection to project the curved surface onto a two-dimensional flat surface (ESRI 1995). The projection designed at the state level facilitates a seamless mosaic of databases originating from different scales and area extents (Snyder 1987; Srivastava 2001; Srinivasa Rao et al. 2002). The reference system may be a transformation of the geodetic coordinates (latitude and longitude) or it may be a mathematically related rectangular system as that of SOI (Polyconic projection-based system). The type of map projection applied depends upon the location, size, and shape of the study area and acceptable tolerance limits in terms of angular, linear, and area distortions (Snyder 1987; Srivastava 2001).

The projections relevant to India are Polyconic, Lambert Conformal Conic, Mercator, Transverse Mercator, Universal Transverse Mercator, and Cassini (Agrawal 1998; Rajak et al. 2002; Srinivasa Rao et al. 2002). Srinivasa Rao et al. (2002) have carried out extensive studies on coordinate systems for generating seamless databases and have developed the "Indian State Plane Coordinate System". This coordinate system is validated by geodesy experts across India and adopted for the generation of a digital database for all the projects at the state level including LIS.

21.4.2.2 Gridbase Generation

Construction of image-to-map transformation model is a time-consuming and tedious job, and the accuracy of the registration is dependent upon the GCP characteristics and their distribution. To facilitate better GCP acquisition and to maintain satisfactory GCP distribution, a technique is used to generate referencing scheme for the entire State, i.e., gridbase. The regional referencing scheme, i.e., gridbase is generated consisting of latitude and longitude of 5 min intervals (depending upon the scale of the satellite data). The gridbase is generated to register the scanned maps with high accuracy. The inputs needed to generate gridbase are upper left corner coordinate (dd-mm-ss), lower right corner coordinate (dd-mm-ss), grid interval (dd-mm-ss), and pixel resolution. The gridbase is generated in the form of the raster image, with the vector grid contained in the file.

21.4.2.3 MAPGRID Generation

In this approach, the maps, containing information of cultural features, notified forest boundaries, elevation contours, and drainage on 1:50,000 scale or 1:10,000 scale are scanned and registered with already generated gridbase. This output facilitates the accurate collection of GCPs. The MAPGRID will become a standard database of topographic information and this information is readily available for GCP acquisition.

21.4.2.4 GCP Network Generation

Generally, it is advised to generate a network of well-controlled surveyed GCPs for any area. Geodetic GPS surveys are the best-recommended technique for establishing GCPs. These GCPs are surveyed under a set plan and controlled environment constituting iconic, primary, secondary, and tertiary GCP points. Different levels of points have different accuracy levels and control the next level points in the network.

All GCP points must be identifiable on the imagery. GCPs used must meet certain distribution and quantity requirements. Ground control points must be well-identifiable on the image as well as the ground. Sharp intersections or corners of features are selected for planimetric control (e.g., the sharp corner of road/track/field bund junctions are selected instead of the center of road intersection). Well, identifiable points on a flat surface and preferably at ground level are selected as vertical control.

GPS observations are made by the approved network plan. Use of well-conditioned figures in the network plan is essential. The network should contain figures of braced quadrilaterals or simple triangles. If more than 4 GPS receivers are used for observations in nearby locations simultaneously, it is important to use only the vectors as per the approved network plan during computation. A sketch relating to the identification of the GCP on the image with a proper format is required for the official record. This is sufficient to correctly access the GCP later on by some other person to identify the GCP on the field.

The density (GCP grid distance and level) of the GCPs will be dependent on the strip size of the satellite data. It is recommended to have more than 3 (Three) GCPs per image for registration. The GCPs, if monumented, can be stored as GCP image chips and can be used for any future geo-registration of the images.

21.4.2.5 Georeferencing of High-Resolution Image or Ortho Registration of Stereo Data

The high-resolution image is rectified using the GCPs from the satellite data and the corresponding ground coordinates are derived from the MAPGRID image or GCPs. A second-order transformation model is established between the image and the GCPs. The threshold set for the transformation model are (a) the residual error at each GCP is less than two pixels in each direction and (b) the RMS error for the

entire model is less than one pixel in either direction. These thresholds will ensure good planimetric accuracy of the rectified satellite data.

High to very high-resolution stereo satellite data are used to generate a terrain corrected image base. The photogrammetry process increases the accuracy through state-of-the-art photogrammetric and image processing algorithms for automatic point measurement, triangulation, and orthophoto generation. This maximizes productivity with automated algorithms, fast processing, and a tight focus on workflow. The workflow generally consists of the creation of block files, measurement of GCPs/Tie-points, block adjustment, generation of DTM/DEM/DSM, feature and edge matching, and generation of orthophoto. Various such orthophotos are edge matched and a single ortho-corrected image is generated. Sometimes, the merged product (as raw processed image) is used to generate the orthoimage, and the subsequent procedures of multispectral data registration and merging are not required.

21.4.2.6 Registration of Multispectral Data of Coarse Resolution

The multispectral data is registered using rectified panchromatic data or orthoimage as the reference image. A second-order transformation model is established and the thresholds are set as per the standards depending upon the image resolution.

21.4.2.7 Merged Product Generation

The multispectral satellite data is registered with rectified high-resolution satellite data using the image-to-image transformation model. The multispectral data is digitally enlarged by a factor of 4 (four) in both directions to generate a pixel size similar to the high-resolution data (this may vary depending upon the data used for merging). These results are smoothened with a 3 by 3 low pass filter to eliminate the blockiness introduced by the four times enlargement. The Hue-Intensity-Saturation method is used to merge the information contents of both data sets. The resultant output is a high-resolution, edge enhanced, a color composite image depicting the natural and manmade boundaries like river/stream/nullah, transport network, canals, tanks, field bunds, and notified forest boundaries. The survey boundaries on the cadastral maps perfectly match these features.

21.4.2.8 Assessment of Geometric Accuracy

Geospatially referenced ortho-rectified imagery offers photographic information combined with accurate geodetic models to support the compilation of scaled mapping themes. In general, the accuracy of fewer than two pixels of residual error and standard deviation, and RMS error of less than one pixel for the entire model is achieved during the process of ortho-rectification of satellite data when the study

area is generally flat and good control points are available on the satellite data with a rational polynomial coefficient (RPC) at acquisition. In extreme circumstances like highly undulating terrain and lack of good control points, an error of 2–3 pixels is tolerable with CE90 less than 2 m. For example, if high-resolution satellite data of 0.5 m is used as a reference dataset for georeferencing, then high accuracy GCPs (having accuracy of 50 cm) is required to derive a residual error of less than 0.5 m, however, an overall accuracy of less than one (1 m) will be acceptable. Wherever possible, better resolution reference maps may be used for achieving better geometric accuracy.

21.4.3 Georeferencing of Cadastral Maps

21.4.3.1 Need for Georeferencing of Cadastral Maps

Since in most states of India, the cadastral map does not have the earth referencing system (i.e., geodetic coordinates), the use of these maps becomes limited to reference only and cannot be used in conjunction with Geographical Information System (GIS). Large volumes of information are generated by many organizations using conventional techniques and/or remote sensing techniques in a GIS environment. Lack of geodetic coordinates information refrains the use of cadastral maps for use in development activities.

Once a cadastral map is georeferenced, it can be linked to district and state-level maps to finally establish a micro and/or macro level LIS. The georeferencing process enables deriving geodetic coordinates for each map and in turn for each node of the cadastral map. The georeferencing will help the Revenue Department to update and standardize the cadastral database by using state-of-art technologies like Remote Sensing, GIS, and Global Navigation Satellite System (GNSS/GPS) and facilitates linking of cadastral maps to the National Natural Resources Information System (NRIS), National Spatial Data Infrastructure (NSDI), Natural Resources Data Management System (NRDMS), Bhuvan and other spatial databases (Dhal 1999; Gopala Rao 2000; Krishna Murthy and Adiga 2000; Srinivasa Rao et al. 2003).

21.4.3.2 What Is Georeferencing?

"The process of defining the position of geographical objects relative to a standard reference grid is known as georeferencing" (Bernstein 1983). It is performed to assign the geographic coordinates to the lines and column image data for making the data amenable to GIS analysis and to facilitate viewing in conjunction with other maps.

Rectification can be defined as the process of transforming the data from one grid system (image row and column or cartesian coordinates) into another (map coordinate system) using an nth order polynomial (Bernstein 1983). The pixels of the new grid may not align perfectly with the pixels of the original grid, so resampling

is needed. Resampling is the process of extrapolating data values for the pixels on the new grid from the values of the source pixels (Lillesand and Keifer 1987; Mather 1987; Jensen 2000). The geometry of an image area is made planimetric by rectification (Haralick 1973; Castleman 1978; Davidson 1986), relating Ground Control Point (GCP) pixel coordinates (row and column) with their corresponding map coordinates. This is the most precise geometric correction since each pixel can be referenced not only by its row and column in a matrix after rectification is completed, but it is also rigorously referenced in degrees, feet, or meters in a standard map projection. Geometric rectification is essential for the accurate area, direction, and distance measurements (Bernstein 1983; Friedman et al. 1983). This is often referred to as image-to-map rectification.

There are two techniques to correct the various types of geometric distortions in digital data. One is to model the nature and magnitude of the sources of distortion and use these models to establish correction formulas (Richards 1994). This technique is effective when the types of distortion are caused by systematic errors (Jacobsen 1998; ERDAS 2003). The second approach is creating a mathematical coordinate relationship model between the pixels of the image and the coordinates of the geodetic maps (resembling coordinates of the ground). These relationships generate the coefficients and are used to correct the image concerning its geometry and location on the earth irrespective of the analyst's knowledge of the source and types of distortion (Bernstein 1983). The second approach is used for georeferencing of the cadastral maps (Krishna Murthy et al. 2000; Srinivasa Rao et al. 2003). The georeferencing process can be divided into two processes viz. registration and rectification. Image registration is a mathematic algorithm transformation model that is used to relate the target image space to the reference image space, and the rectification process is the application of the transformation model to rewrite/resample the image into a new coordinate system. An example of georeferencing of the city cadastral maps with land use development plan rectified on the high-resolution panchromatic satellite data is shown in Fig. 21.6.

Fig. 21.6 A sample digitized city survey cadastral map with land use attributes and satellite data overlay

21.4.3.3 Data Sources for Georeferencing

The process of georeferencing requires location information as Ground Control Points (GCPs). These GCPs should be in the real-world coordinates with high accuracy as prescribed. The geographic coordinates of the GCPs are obtained through an on-field survey using the DGPS instrument as iconic, primary, secondary, and sometimes tertiary points. The source of GCPs can be from the ground control survey, topographical maps, and coordinates of GNSS (Srinivasa Rao et al. 2003). The secondary sources consist of aerial images or high-resolution satellite images as described in Sect. 21.4.1 of this chapter.

The lack of compatibility between the scales and currency of available topographical maps and the cadastral maps may influence the error budget in the locational accuracy of the georeferenced cadastral maps. The other source of deriving real-world coordinates directly is through the Global Navigation Satellite System (GNSS) as described in Sect. 21.2.2.

21.4.3.4 Approaches for Georeferencing of Cadastral Maps

There are six major approaches for georeferencing of cadastral maps depending upon the primary source of geodetic control (Topographical Maps or GPS) and the secondary sources, i.e., via media used for better identification of parcel boundaries (aerial photos or very high-resolution satellite data or direct method). The six approaches are as follows.

(a) Topographical Maps (1:50,000/1:25,000 scale) and cadastral maps (Direct Approach)
(b) Topographical Maps (1:50,000/1:25,000 scale), aerial photos and cadastral maps
(c) GNSS GCPs and cadastral maps (Direct Approach)
(d) GNSS GCPs, aerial photos and cadastral maps
(e) GNSS GCPs, very high-resolution satellite data, and cadastral maps
(f) Topographical Maps (1:50,000/1:25,000 scale), very high-resolution satellite data and cadastral maps.

Of the above methods, to increase the accuracy of georeferencing of the cadastral map, the method of deriving the real-world coordinates from the GCPs using GNSS/GPS is followed first. Using these geodetic coordinates, the high to very high-resolution satellite data are rectified. This forms the base for georeferencing of the cadastral maps which are generally in cartesian coordinates. The cadastral maps are georeferenced using the feature-based GCPs of the rectified high-resolution satellite data. The high to very high-resolution satellite/aerial data has the potential to collect a well-defined large number of feature-based GCPs for achieving good accuracy (Srinivasa Rao et al. 2003).

21.4.3.5 Methodology

The methodology mainly comprises of two broad steps—First, is the vectorization of the cadastral maps, and second, is GCP Collection, Georeferencing, and Validation of Model Accuracy and Product Accuracy.

Cadastral Maps Generation in Vector Mode

The process of generation of cadastral maps in vector mode is explained in Sect. 21.4.1. The main tasks involved in this process are the acquisition of cadastral maps, scanning, and digitization of cadastral maps, and generation of vector data about the parcel's entity and its related attributes.

Georeferencing of Cadastral Maps

The georeferencing of digital cadastral maps consists of the following steps.

Acquisition of ground control points: Sufficient numbers of GCPs are identified on the vector cadastral map and the merged product, for generating the transformation model. The spatial and radiometric resolutions of the satellite data play a major role in identifying the GCP with good geometric definition. The characteristics of the GCPs are corners of water tanks, the intersection of parcel boundaries, intersections of river/stream with parcel boundary, the intersection of roads with parcel boundaries, and the intersection of roads and rivers. The GCPs should spread uniformly in the entire map and be of good quality to generate an accurate transformation model. The GCPs are labeled uniquely for identification in similar coordinate-based surveys.

Transformation model assessment: Usually a second-order polynomial model or affine transformation model has applied for georeferencing the cadastral map for obtaining the best results. The area of the village, number of sheets covered in a single village, condition of the cadastral map sheets, number and characteristics of GCPs collected and terrain conditions influence the order of the polynomial model. The transformation model is assessed by the values arrived for residual error at each GCP and root mean square error for the entire model. The RMS error contribution is ensured to less than one pixel in either direction. The threshold value for the residual error at each GCP is 2–3 pixels in either direction (Srinivasa Rao et al. 2003). The transformation model is accepted when the actual rms and residual errors arrived are less than the threshold values.

Georeferencing of cadastral maps: Once the transformation model is accepted, the vector cadastral map is georeferenced in the GIS environment using a rectification tool, and the output georeferenced cadastral map is generated (Fig. 21.7). New vector files are generated for the polygon, line, and point features. The outputs are further validated both visually and mathematically.

Validation of Georeferenced map, in isolation: Output product validation is an essential element in the development of CIS. The georeferenced vector file of each

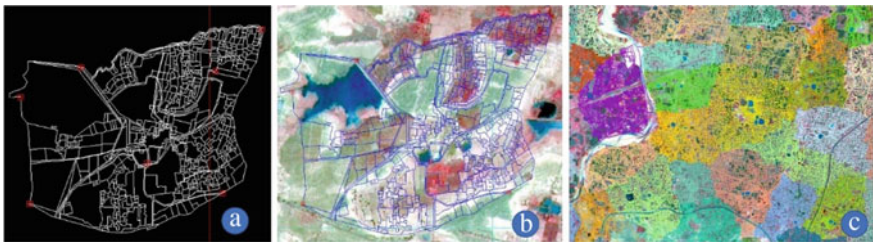

Fig. 21.7 Georeferencing of cadastral map—**a** Vectorized and attributed village map with tie-points, **b** georeferenced village on the satellite data, and **c** mosaiced multiple villages cadastral maps on satellite data

village is validated with reference to the high-resolution satellite image (reference image). The georeferenced vector file is overlaid on the reference image and initial validation is carried out through visual checking. If the parcel boundaries coincide with the image features and deviations/displacements are not observed, the georeferencing is successful. The displacement is measured as the distance between the image point and the vector point. If the shift is more than allowable limits, georeferencing is carried out once again. Feature matching is checked in the following order of priority; tanks, water bodies, tank bunds, ponds; road, rail, canal; stream, nala, river; field bunds; forest boundary/vegetation boundary; abadi (village settlement), for matching in all eight directions within tolerance. The feature matching error tolerance in the controlled region is one pixel and in the uncontrolled region it is around two pixels, it may be considered as successful georeferencing.

Validation of Georeferenced map, with the neighborhood: This validation is carried out to ensure that the village boundary is matching with all adjoining village boundaries. The following precautions are taken for the purpose.

- Ensuring continuity of feature as well as attributes
- Preservation of all parcels in the area of overlap
- Ensuring feature matching as well as boundary matching within tolerance.

The boundary should match perfectly. However, following the terrain conditions, the boundary (overlap/underlap) error tolerance in undulating terrains is kept around 2–3 pixels and 3–4 pixels in hilly areas (Srinivasa Rao et al. 2003). In case of boundary mismatch beyond error tolerance, the concerned village file is rejected, and once again GCPs are taken for georeferencing to ensure the quality of the product.

Georeferencing of Tippans/FMBs

In a few states, individual land parcels or *tippans* or field measurement books (FMBs) or gat maps are available. These maps are generally on a 1:1000 scale showing the vertices length and angle of all field and subdivision boundaries. The measurements are solved to generate a graphic sketch of the parcel geometry. The individual parcel

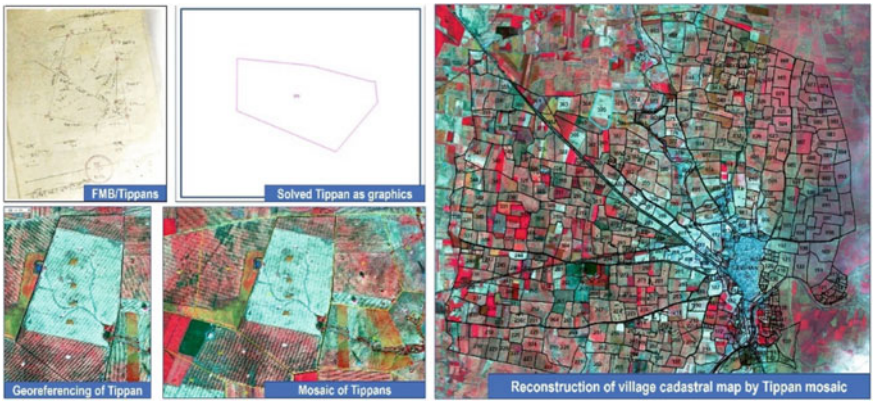

Fig. 21.8 Tippan/FMB solving, vectorization, georeferencing, and mosaic to create a village cadastral map

is then georeferenced with the high-resolution satellite base. Likewise, all individual parcels with their subdivisions are converted and georeferenced. The parcels are later mosaiced to form a village cadastral map (Fig. 21.8).

21.4.4 State-Level Cadastral Database

After georeferencing the cadastral maps to the required accuracy standards, several maps are mosaiced at the next higher administrative level. Mosaics of polygon, line, and point features of cadastral maps are generated at the Halka, RI, and taluk levels. The village boundary maps are generated up to taluk, district, and state levels. While mosaicing, feature continuity as well as attribute accuracy is maintained. These are the final products of georeferencing of cadastral maps and the development of CIS. These products are directly linked to LIS and GIS databases.

Important guidelines and accuracy standards are considered for the generation of state-level cadastral databases. The high-resolution satellite image is displayed in the backdrop during the edge matching process. The boundary feature that best fits the image is taken as a reference. The boundary feature that is underlapping, or overlapping on the fitting feature is adjusted using the background image as the reference. If the displacement is more than the upper limit of the tolerable locational accuracy of 2–3 pixels then that feature is not edge matched and an entry of the same is made in the comment section of metadata for that village. After edge matching, the duplicate boundary is eliminated to keep only one single boundary. The features that meet this boundary are adjusted and cleaned so that dangles, overshoots, or slivers are eliminated and feature geometry and unique coding scheme are maintained. Along the boundary of the tehsil, the edge matching is done with a reference tehsil boundary cover, which is provided by District/State administration. If the village

boundary overlaps or underlaps the tehsil boundary by more than the upper limit of the tolerable locational accuracy of 2–3 pixels then the boundary is not adjusted and an entry of the same is made in the metadata comments section. In the edge matching process, the shapes of the features are maintained. The relative position of features on both sides of the boundary should be the same. Care is taken where the boundary is a river/road feature so that the double line is edge matched without any slivers or gaps. The edge matching is carefully tracked and recorded in the metadata for each village for solving the edge matching problems.

21.4.4.1 Mosaics at Taluk, District, and State Level

After the edge matching process at taluka, the taluk maps are mosaiced into one single district layer. Another GIS layer containing only the village outer boundaries along with a label of the village code is created separately by extracting the outer boundaries of villages from the mosaiced layer. The feature ids for this layer are maintained for further linking. Thus, an accurate district-level village boundary is generated with is very accurate both with respect to its extent and area.

The district-level maps may be further mosaiced to generate a state-level cadastral map. However, the database is mostly maintained and managed at the taluka level for linking with LIS and utilization in developmental planning.

21.4.5 Dissemination of the Cadastral Database

In the digital world, it is often discussed that who is authorized to view and download the data, especially the spatial data. Cadastral data, being the largest scale spatial government data, falls under the restricted category, especially when it is geocoded/georeferenced. On the other hand, the cadastral maps are supposed to be public data and the information should be available in the public domain, without restriction. Sometimes, the digital copy (PDF format) of the data is available in a saleable form for the public. However, the digital format of the data is always available with the government organization for various development plan generation and e-governance programs of the government.

The new technologies of web geoportal dissemination of the data have enhanced the utility of the cadastral database on the web. There is a growing trend of private companies processing government data and at times partnering with the city and other governments agencies for development and governance activities.

The digital data forms the base of various mapping projects at the cadastral level. The online available data can be now be analyzed on the fly to derive various statistical views and maps. This helps in making a quick decision and the implementation of the project is also expedited. The dissemination techniques should be such that people may feel it convenient to operate and use by browsing the website. The application should be people-centric and achieve e-governance goals. The dissemination

procedure "will make the citizens more powerful and the authorities more accountable" (Jeremy et al. 2018). It brings transparency and the currentness of information in the system.

The data dissemination is a useful starting point to answering the various FAQs. They employ user-friendly interfaces that require little knowledge of technology and no mapping expertise. But the digital divide still exists; not everyone has access to computers or smart devices, and not everyone knows how to productively search the internet, what to search for, and how to use the results. However, the government is making all efforts to go digital and encouraging digital transactions with various initiatives.

Metadata creation (as explained in Sect. 21.4.1.10) is an absolute necessity for the data which are going to be distributed (open/freely accessed) because they provide valuable information necessary for their evaluation. Good metadata of the spatial digital cadastral data will stimulate fast search and retrieval of the information, thus driving the system to efficiently.

21.4.6 Government Initiatives

The Digital India Land Record Modernization Program (DILRMP), previously known as the National Land Record Modernization Program (NLRMP), was launched in 2008 by the Government of India with the purpose to digitize and modernize land records and develop a centralized land record management system. The official land records information will enable the owner and the government to have quick and authenticated access to the information for various development purposes. The DILRMP is the amalgamation of two projects: Computerization of Land Records (CLR) and Strengthening of Revenue Administration and Updating of Land Records (SRA and ULR).

The main aim was to adopt the latest ITC technologies to digitize the various form of cadastral maps and FMBs and to georeferenced the same to make it GIS-ready and usable over the web. The digital georeferenced cadastral will modernize the land record management system of the country. Up-to-date land data will provide the status of the land, information about the disputes, if any, ad facilitate transparency in the transaction and deal of the land property.

The four basic principles of NLRMP is to provide (i) a single window to manage, monitor, transact and update all form of land records and their textual records, (ii) to maintain a mirror of the cadastral data and record with the ground reality, (iii) to ensure that the record of title is a true representation of the land on the ground and the ownership status, and when mutated following the process of registration automatically maintains the history of the transaction, and (iv) insurance of title deed, thus guarantee the maintenance of digital record in the event of loss arising from calamities.

Major components of the NLRMP Program are (i) digitalization of all forms of land records with periodic mutations, (ii) digitization of cadastral analog maps and

integration of textual with spatial data, (iii) facilitate the department in survey/re-survey and updation of the original land information using latest ITC technologies, wherever needed, (iv) Integrate and link the computerized registration process with the spatial land record data, and (v) build a web-based geospatial information system with knowledgeable manpower.

Once the system is in place the benefits of the NLRMP Project are:

- Build a modern, comprehensive, and transparent land records management system in each state.
- Provide a one-stop solution for access of land records, including maintenance and updating of textual records, maps, survey and settlement operation, and registration of immovable property.
- Maintains currency of land data—up-to-date land records information, and provide them in government geoportal for people to have quick access at ease.
- Development of integrated land records information system and land administration.
- Land value assessment by Inspector General of Registration (IGR).
- Preparation of field-level soil health cards.
- Land-based smart cards for farmers to facilitate e-governance and e-banking.
- Project base land acquisition and rehabilitation.
- Field crop assessment and insurance.
- Grant of agricultural damage and drought subsidies.

21.5 Applications of Cadastral Database

"The vocation of the *cadastre* for all countries has become multipurpose: serving administrative mandates, maintaining an up-to-date database, assigning values for taxation, calculating subsidies, addressing rural development and agrarian management, and providing products and services to citizens and companies" (ESRI 2005). The GIS-based cadastral information system extends more benefit by extending its purposes. The central, state, and local governments can use the land valuation models applied to the *cadastre* database to support land market values and assess taxation fees. Cadastral data forms the base of any planning, detailed project report (DPR) preparation, development, management, and monitoring of most of the land-related projects. In cities and towns, the city survey cadastral map forms the basis of all location-based services, property management, taxation, and facility and utility mapping and management. Some applications of the cadastral database utilized in various projects and e-governance services are mentioned in the subsequent sections.

21.5.1 Cadastral Thematic Database

The development of any country depends upon the efficient utilization of natural resources. Often the exploitation and non-utilization of resources in a sustainable way cause the resources to degrade, thus causing erratic and unbalanced growth in the society. Knowledge of the natural resources with details and accuracy will pave the way for achieving sustainable development goals and bring overall growth to the country. This can be achieved by creating effective thematic maps at a very large-scale using modern geospatial technologies.

In India, major initiatives have been taken to generate the various thematic maps at different scales under the IMSD, NRIS, NNRMS, NSDI, NR Census, and SIS-DP projects of the government. The thematic maps were generated by interpretation of the satellite data directly, or in some themes, the in-situ information need to be added to arrive at the desired thematic maps. The maps which are directly generated from the satellite data are land use/cover, transport, drainage and water body, etc. The layers like soil, geology, groundwater, etc. require exhaustive ground truth and ancillary information to prepare the thematic maps. The preparation of the thematic maps at the level of cadastral scale needs very high-resolution satellite data and the legacy data is updated for the project. An example of thematic layer generation at the cadastral scales is depicted in Fig. 21.9.

21.5.2 Cadastral Level Development Planning

The advent of new technologies like high-resolution remote sensing, GIS, GNSS/GPS, etc. has led to an overall change in the planning process. Information about the natural resources such as soil, hydrogeomorphology, slope, groundwater, and land use-land cover is generated at regular intervals using remote sensing techniques. Based on this information, the prevailing socio-economic conditions, and the government developmental policies/priorities, the management plans for natural resources development are generated.

The prime concern of the planners is that when plans are generated over a large area, i.e., across district or state it ignores the locale-specific problems and potentials. It is because the planning point and the candidate site are not connected in a spatial context. The second concern is the level of planning. If the planning is considered for a large area, the scale of the thematic maps is generally at 1:50 K/25 K which does not address the micro-level problems, thus, the resultant planning does not always effectively address the local issues. These limitations are overcome by decentralized planning in many projects (Planning Commission 1989; NRSA 2002). For decentralized planning at a gram panchayat level, a cadastral map forms the base of all developmental plans.

Action plans for sustainable natural resource development essentially deal with area-specific and locale-specific measures. Watersheds of about 500–4000 ha with

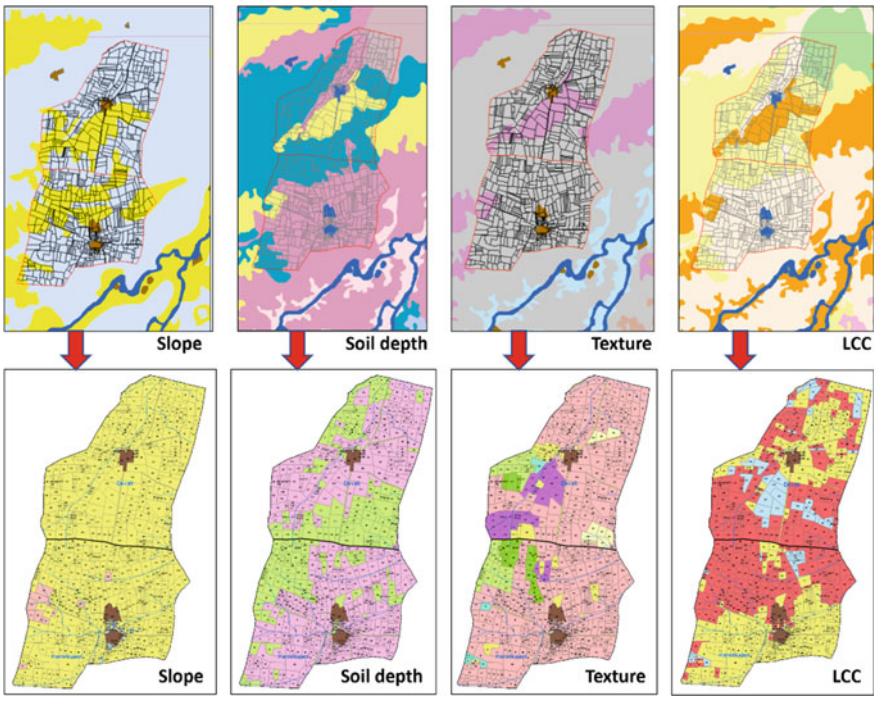

Fig. 21.9 Cadastral level thematic map generation—propagation from 1:50 K/10 K to 4 K

village cadastral boundary overlay facilitate the easier location of the field boundary, thus the beneficiaries, for generation of an implementable action plan. The maps help to plan sustainable agricultural growth with appropriate soil and water conservation measures at the micro-watershed or village level depending upon the land conditions and needs of the area (Jeyaram et al. 1996; NRSA 1995, 2002; Sreenivasan and Krishna Murthy 2018). Cadastral data plays an important information resource in this management planning—it provides information about the beneficiary.

Apart from the preparation of plans for land and water resources development, the cadastral database is being utilized currently for developmental planning in many other fields such as forest and wildlife management, crop assessment for cess collection, micro-irrigation management, crop insurance disbursement, infrastructure planning like delineation of suitable electrical transmission lines, railway lines and roads, management of specific ecosystems, etc. A few use cases of cadastral database applications are illustrated in the following sections.

21.5.3 Case Studies/Use Cases of Cadastral Database Applications

21.5.3.1 Decentralized Planning Using Georeferenced Cadastral Maps and High-Resolution Satellite Data—A Case Study of Holistic Watershed Development Program

Decentralized planning requires planning at grass-root levels—either a watershed/micro-watershed, gram panchayat, or village levels at a very large-scale. Decentralized planning benefits from upscaling the natural resources' thematic information into large-scale and integration into Cadastral Information System (CIS). Watershed management is an important endeavor for agricultural and rural development in rainfed areas of India. Holistic watershed development and management is an effective means for the conservation and development of land and water resources and enhancing the socio-economic status of the constituent villages. Holistic watershed development and management, is an interdisciplinary approach, integrating the biophysical and technological as well as the socio-cultural and economic aspects of development. Watershed supports a holistic framework which means the combined application of technologies on soil and water conservation with improved crop varieties, farming systems, and agronomic management, taking into account both arable and non-farm land.

The technological innovations over the last few decades, especially the advances in remote sensing technology in terms of the availability of very high spatial resolution sensors, had an impact on watershed development, especially in the planning and implementation process. The current availability of high- to very high spatial resolution remote sensing data, from the satellite platform or UAV platform, has enabled the generation of cadastral level databases on land use, geomorphology, hydrology, soils, groundwater, etc. This helps in understanding the potential and limitation of natural resources at the parcel level, modeling various natural processes occurring in the watershed, toward scientific planning, and suggesting alternate strategies for land and water resources development at the micro-level (Sreenivasan and Krishna Murthy 2018).

Holistic watershed interventions combined with livelihood support activities have been taken up in Maharashtra for 36 village clusters/watersheds covering 90,000 ha in the districts of Akola, Amravati, Buldhana, Yeotmal, Washim, and Wardha. This initiative is with the support of the National Bank for Agriculture and Rural Development (NABARD). Under this program, it was proposed to treat 15,000 ha per district on a cluster basis, covering 2500 ha per cluster consisting of 2–3 mini watersheds encompassing 6–7 villages. Four Resource Support Organizations (RSOs) supervised and guided the 27 Project Implementing Agencies (PIAs) selected for the field implementation of the program. NABARD decided to use advanced geospatial techniques for the planning and development of these clusters. With ISRO's help the baseline natural resources database for these watersheds at the cadastral level, including the action plans, was generated with cadastral overlay.

The thematic maps on land use-land cover, soil texture, soil depth, land capability, geomorphology, and groundwater prospects of 1:50 K were updated to 1:10,000 scale using high-resolution satellite data and field inventory data on the cadastral map (Fig. 21.10). The land and water resources action plans were generated using the thematic knowledge and the local needs of the cluster by the PIAs (Fig. 21.11). The entire program was envisaged to enhance the capabilities of RSOs/PIAs in utilizing the satellite data and related GIS output and information for watershed development projects.

21.5.3.2 Rationalization of Great India Bustard (GIB) Sanctuary Boundary

The Great Indian Bustard (GIB), a threatened and endemic species to the Indian subcontinent, is under tremendous threat in its last strongholds and sliding inextricably toward extinction. It is listed in Schedule-1 of the Indian Wildlife Protection Act (WPA) and considered Globally Endangered by BirdLife International (2021) and IUCN (2014).

Formerly, GIB was widely distributed in Indian semi-arid grassy plains and open scrubs but presently is restricted to a few pockets with fragmented and decreasing population, attributed to the destruction of its habitat.

The GIB sanctuary in Maharashtra is one of the last refuges of the bird constituting an area of 8496 km^2 spread over in seven taluks of Solapur and Ahmednagar districts. GIB boundary is not based on species and their habitat requirements; the major portion of the sanctuary (94.3%) consists of privately owned lands under a variety of economic vocations and a large number of villages and townships. Given the legal restrictions relating to Protected Area under the Wildlife (Protection) Act 1972, the inhabitants of villages and townships faced a very difficult situation regarding the use of their lands, the development of properties, and deriving benefits from planned local and regional development. This entailed the intervention of the Honorable Supreme court and it constituted an Expert Committee to rationalize the boundary.

Geospatial technology has been used in a binary deductive habitat suitability assessment and derived areas that are important for the GIB and excluded areas that are not important in the sanctuary (Varghese et al. 2016). Habit and habitat of GIB, slope, minimum patch size, and disturbance sources are the main parameters considered for the assessment (Rahmani 1986). Based on ecological and realistic management criteria (fragmentation, contagion, patch size, and juxtaposition) the rationalized GIB wildlife sanctuary was demarcated on the georeferenced cadastral data (Fig. 21.12).

Out of necessity, the new sanctuary is a patchwork of isolated blocks of important habitats scattered through portions of two tehsils of Ahmednagar District and four tehsils of Solapur District. Although the area may be in patches with dendritic shapes, the boundaries can easily be identified and demarcated in the field by parcel gat or cadastral numbers. The realigned boundary derived using georeferenced cadastral data, remote sensing image and GIS tool have been accepted by Honorable Supreme

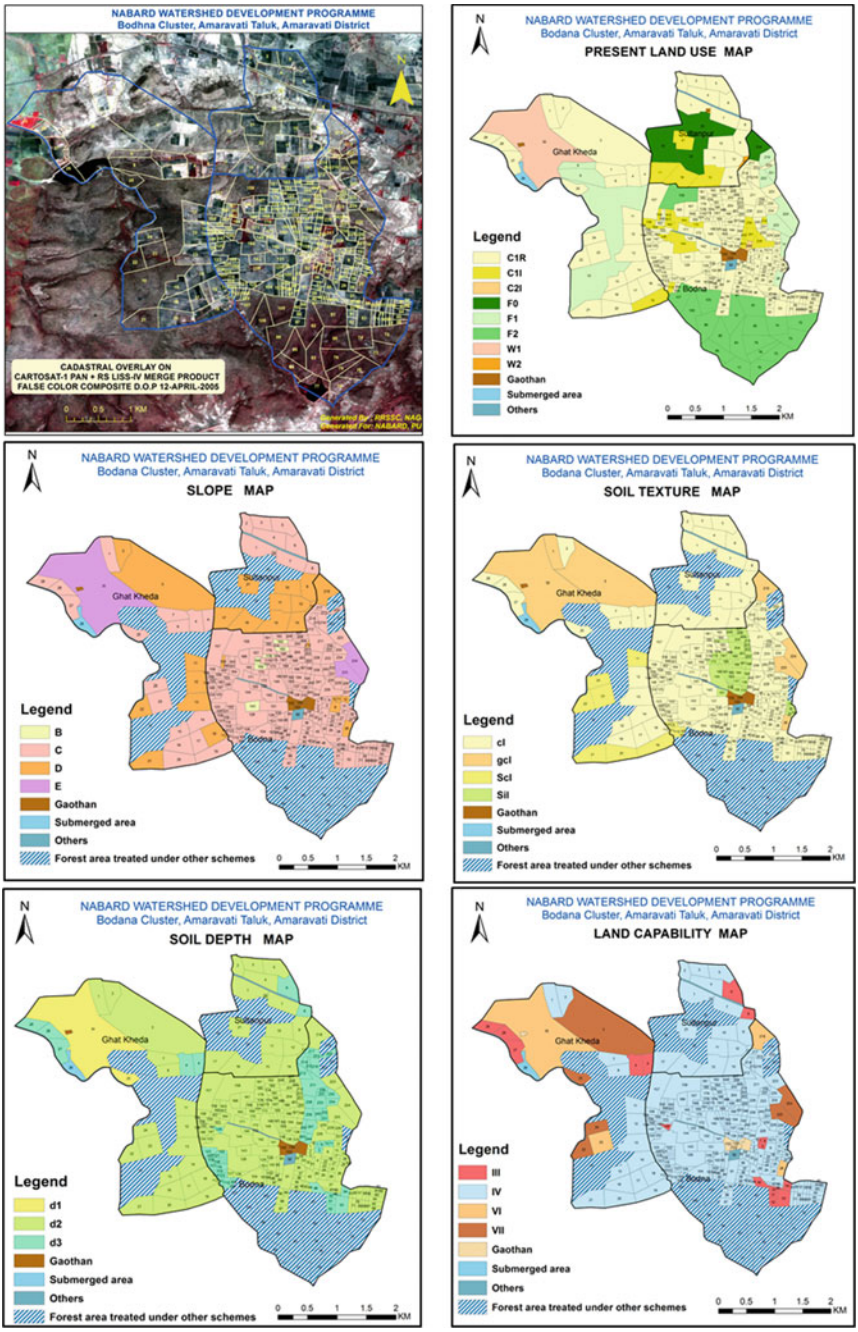

Fig. 21.10 High-resolution satellite (HRS) image and the cadastral level thematic database for a few themes generated using HRS image for a village cluster under NABARD supported holistic watershed development program

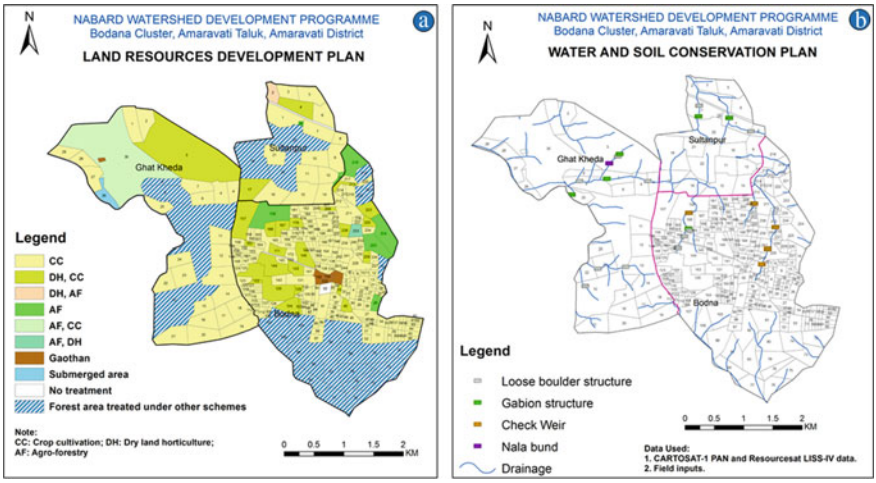

Fig. 21.11 Cadastral level land resources development plan (**a**), and water and soil conservation plan (**b**) for a village cluster under NABARD supported holistic watershed development program

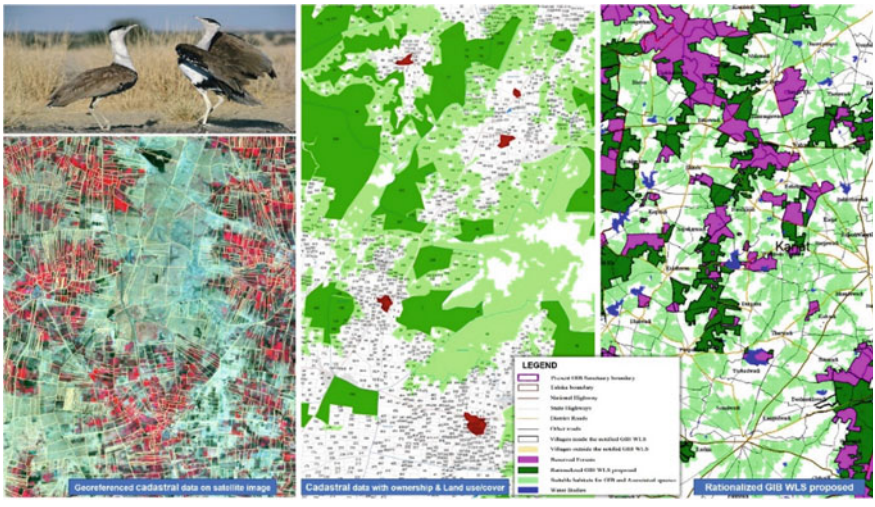

Fig. 21.12 Use of cadastral and satellite data, GIS tool to demarcate rationalized GIB WLS area

Court of India after referring to The Committee on Rationalization of boundaries of National Parks and Sanctuaries and National Board for Wildlife (NBWL—18th meeting of the standing committee).

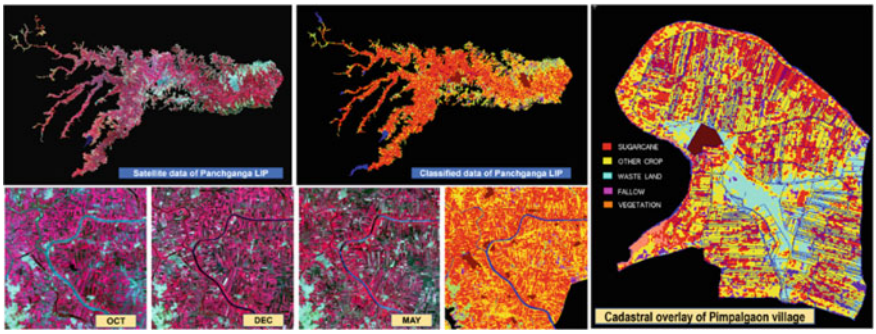

Fig. 21.13 Sugarcane mapping and use of cadastral data for irrigation cess collection

21.5.3.3 Crop Assessment and Cess Collection in Western Maharashtra

Sugarcane is a cash crop in the irrigated areas of western Maharashtra, especially controlled by the sugar factory in the area. Since the irrigation is provided by the Water Resource Department (WRD), Government of Maharashtra (GoM), it needs to assess the actual area under the crop and who is growing how much area.

Remote sensing techniques of multi-temporal data are used to identify the crop. The georeferenced cadastral data is overlaid on the sugarcane classified data to assess the area of the crop under each cadastral khasra. Accordingly, the cess is calculated for each cadastral and collected from the landowner (Fig. 21.13). This technique has increased the revenue collection of WRD, GoM through water cess by three folds.

21.5.3.4 Crop Disaster and Insurance

Often it is noticed that due to climate change lots of disasters such as floods, drought, hail storms, cyclones, etc. are frequently happening. After the disaster, it becomes difficult to quickly assess the damage and find out the affected people. The technologies of remote sensing, crowdsourcing, GIS, and the georeferenced cadastral map help in quickly and accurately locating the disaster-affected area and finding out the disaster-affected beneficiaries.

For the disaster-related analysis, pre and post-disaster satellite data are procured and analyzed. The output is overlaid with the georeferenced cadastral data. The changes about each cadastral are carefully noted and the disaster-affected lands and areas are reported. Thus, with the georeferenced digital cadastral map, a quick assessment is made to find out the extent and severity of the damage. Hence, for providing compensation at the right time to the right person, geospatial technology, and the CIS generated using this technology can be a great help. An example of hail storm damage in the Chichondi village in the Latur district of Maharashtra is shown in Fig. 21.14. Crops like grapes, chili, tomato, banana, sugarcane are damaged due to the storm, and compensation has been paid to the affected farmers.

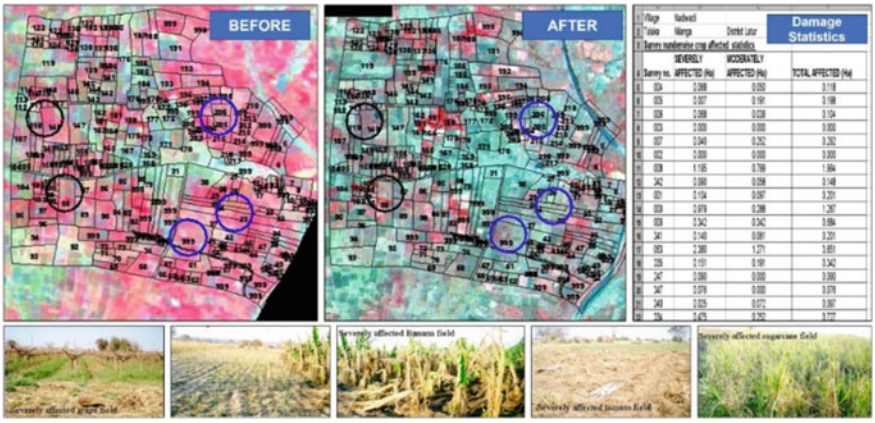

Fig. 21.14 Hail storm damage in the Chichondi village, Latur district—satellite data shows cadastral area devoid of vegetation post the storm

21.5.3.5 Demarcation of Corridor and Erection of New Transmission Line in Chhattisgarh

Chhattisgarh state has immense potential for thermal power generation and has surplus power in the state. To move the excess power a network of the high-power transmission line was laid for connecting the power grid. Also, to develop the Naxal affected areas, redundant power supply line construction was envisaged. For suggesting the suitable corridor for the transmission line, without doing the reconnaissance field survey, the available GIS database was used along with the cadastral maps for finalization of the transmission line route. The following criteria, prescribed by the government, was used for the demarcation of new transmission line:

- Minimum of forest area is disturbed.
- Nearer to the road for easy maintenance.
- Away from the settlement/abadi (populated area).
- The transmission line should have minimum bends (maximum of 60°).
- Minimum crossings over major rivers and crossing of the river should be at the minimum span.
- Transmission line should cross the road, rail, and river/stream in a more or less perpendicular position.
- Should be at least 5 km away from the airport, Reserve Park/National Park boundary.
- Avoid mining areas (active mining, dumps, etc.).

After performing the GIS analysis, suitable transmission line routes, with alternate options, were delineated and submitted to the department (CSEB—Chhattisgarh State Electricity Board) for finalization. The department after doing the detailed survey finalized the route with minor changes and the pillion/tower location was

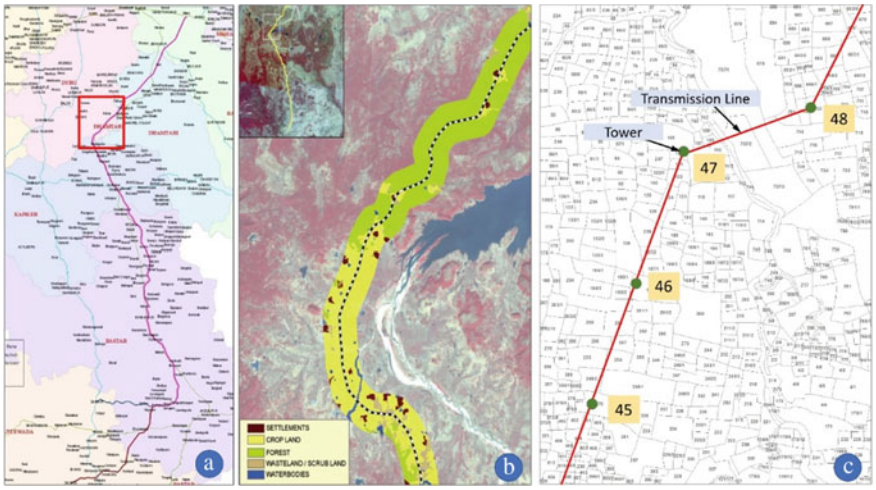

Fig. 21.15 **a** Demarcation of the high-voltage transmission line in Chhattisgarh state using thematic criteria, **b** extraction of land use/cover along the transmission line, **c** use of cadastral data for tower construction and execution after due permission and approval

marked. The line along with the tower was overlaid on the cadastral map. The land on which the tower will be constructed was marked for land acquisition/compensation (Fig. 21.15). The path cadastral maps and report were then generated with the line, tower, and land detail, and submitted to the department for approval and further implementation.

21.5.3.6 Coastal Mangroves Management in Maharashtra

Mangrove forests form one of the primary coastal ecosystems in the tropical and subtropical regions of the world. However, mangrove ecosystems are very sensitive and fragile, and have great importance as a source of carbon storage, apart from other benefits like protection against floods, acting as a natural barrier against violent storm and coastal erosion, providing a livelihood for coastal people, a breeding ground for fish and marine fauna, etc. In recent years, the pressures of increasing population, and the resulting expansion of agricultural land and industrial and urban development, have caused a significant reduction of the mangrove resource. For the coastal mangroves management and monitoring, the mapping of the mangroves using high-resolution satellite data for coastal areas of Maharashtra on a 1:4000 cadastral map was taken up by the Chief Conservator of Forest, Mangrove Cell, Maharashtra Forest Department.

21.5.3.7 Coastal Mangroves Management in Maharashtra

Mangrove forests form one of the primary coastal ecosystems in the tropical and subtropical regions of the world. However, mangrove ecosystems are very sensitive and fragile, and have great importance as a source of carbon storage, apart from other benefits like protection against floods, acting as a natural barrier against violent storm and coastal erosion, providing a livelihood for coastal people, a breeding ground for fish and marine fauna, etc. In recent years, the pressures of increasing population, and the resulting expansion of agricultural land and industrial and urban development, have caused a significant reduction of the mangrove resource. For the coastal mangroves management and monitoring, the mapping of the mangroves using high-resolution satellite data for coastal areas of Maharashtra on a 1:4000 cadastral map was taken up by the Chief Conservator of Forest, Mangrove Cell, Maharashtra Forest Department.

Information regarding the spatial distribution of mangroves is crucial to assess mangrove deforestation, monitor the state of the remaining mangrove forests, and ensure their sustainable management. In mangrove areas, the task of collecting information by ground inventory is extremely difficult, time-consuming, and, therefore, expensive. For this reason, remote sensing is an authentic means of obtaining information and defining the status of the mangrove area within the cadastral framework, and updating the management plans. The major objectives of the initiative were to map the mangroves along with coastal Maharashtra, overlay the village cadastral database and provide the database for conservation and management strategies.

In the present study, mangroves cover has been categorized into dense mangroves (crown density more than 40%) and sparse mangroves (crown density from 10 to 40%). The various mangrove categories and other features that have been delineated are labeled uniquely along with a description. These features are overlaid on the georeferenced cadastral map. Base map details such as road, rail, creeks, waterbody, settlement, and other features are transferred on the mangrove map. The mangrove details are validated on the ground at places by selective ground truth verification.

Cadastre-wise statistics are generated and the parcels having mangrove and their different categories are noted in tables (Table 21.2). The statistics are further aggregated village/Mouza wise and taluka-wise (Table 21.3) concerning the mangrove-based land use/land cover. Finally, the mangrove areas with different categories have been defined within each cadastral parcel. For the mangrove areas outside the mouza limit (on the coast side), a new polygon boundary has been created as per the satellite image with a new parcel number. Each village-wise map is prepared with standard legend and symbology for archival (Fig. 21.16).

21.5.3.8 Chak-Wise Data for Micro Water Irrigation Management System in Maharashtra

The Water Resources Department (WRD), Government of Maharashtra (GoM), provides irrigation of the fields through the canals. The actual distribution of the

Table 21.2 Cadastral parcel-wise mangrove statistics for Mouza-Awas, taluka—Alibag, district—Raigarh (*Source* MRSAC 2015)

Parcel/gat no.	Categories	Area (m^2)
183	Mangrove dense	34.53
183	Mangrove dense	1.44
539	Mangrove dense	3142.19
539	Mangrove dense	41,115.90
539	Mudflat	29,272.99
540	Mangrove dense	879.74
540	Mangrove dense	299.54
540	Mudflat	168.11
540	Creek	7.93
541	Mangrove dense	4443.34
541	Mangrove dense	10,878.38
541	Mudflat	3229.88

Table 21.3 Taluk wise mangrove statistics for district Raigad, Maharashtra (*Source* MRSAC 2015)

Taluka	Categories area (ha)						Area (ha)
	Creek	Mangrove dense	Mangrove sparse	Mudflat	Saltpan	Water bodies	
Alibag	1847.13	2325.62	1201.14	947.47	3.75	0.00	6325.11
Mahad	371.73	68.85	60.88	21.84	0.00	0.00	523.30
Mhasla	2140.21	981.07	605.02	387.72	0.00	0.12	4114.14
Murud	2171.70	396.64	377.01	111.92	78.68	0.00	3135.95
Panvel	976.24	721.23	678.03	219.43	0.00	0.12	2595.05
Pen	1331.36	875.44	583.50	689.70	179.21	0.29	3659.50
Roha	368.27	210.87	151.92	133.36	58.75	0.00	923.17
Shivardhan	1334.18	536.26	126.17	64.46	157.52	0.00	2218.59
Tala	1193.44	298.12	201.21	301.44	7.62	0.00	2001.83
Uran	413.24	1432.45	915.16	1011.78	171.08	0.33	3944.04
Total	12,147.50	7846.56	4900.04	3889.12	656.61	0.86	29,440.68

irrigation is done through the field canals and is managed by the Water Users' Association (WUA). Each cadastral is earmarked with the irrigation facilities and the field canals are provided to that location or nearby.

Few groups of cadastral or farmers which is serviced by the same outlet are assigned as one chak. The farmer of a few "chaks" are statutory elected to form a Water Users' Association. In the Purna Medium Irrigation Project, there are 19 WUAs and the number of chaks per WUA varies from 9 to 44 chaks. Here the cadastral maps of the villages play a very important role in deciding the irrigated area, the layout

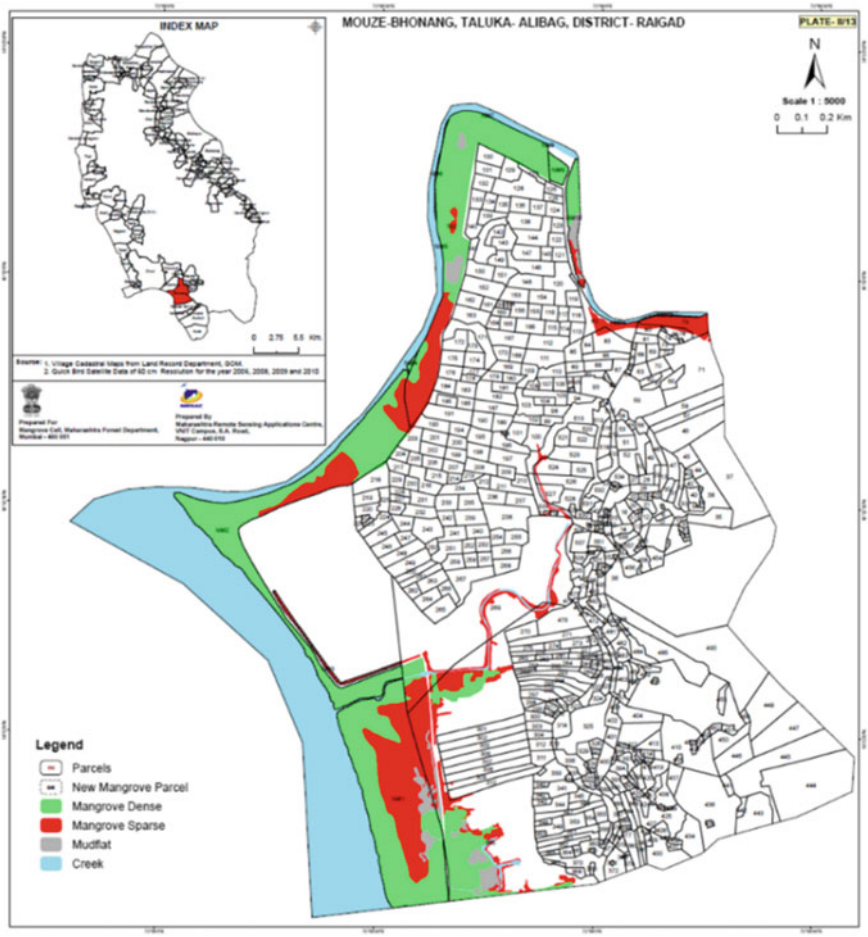

Fig. 21.16 Sample final map of a village with mangrove status depiction and spread with cadastral

of the field outlets and turnouts, and in the scheduling of the irrigation by WUA. A detailed depiction of the field canal/pipeline layout in the Purna Irrigation project along with the attribute data of each cadastral (farmer) is given in Fig. 21.17.

Thus, the cadastral map along with other thematic data and GIS comes as a handy tool in envisaging the micro water irrigation distribution system and its management. The data is integrated with the Water Resources Department (WRD) web portal (URL: https://mrsac.maharashtra.gov.in/.wrd) for easy access.

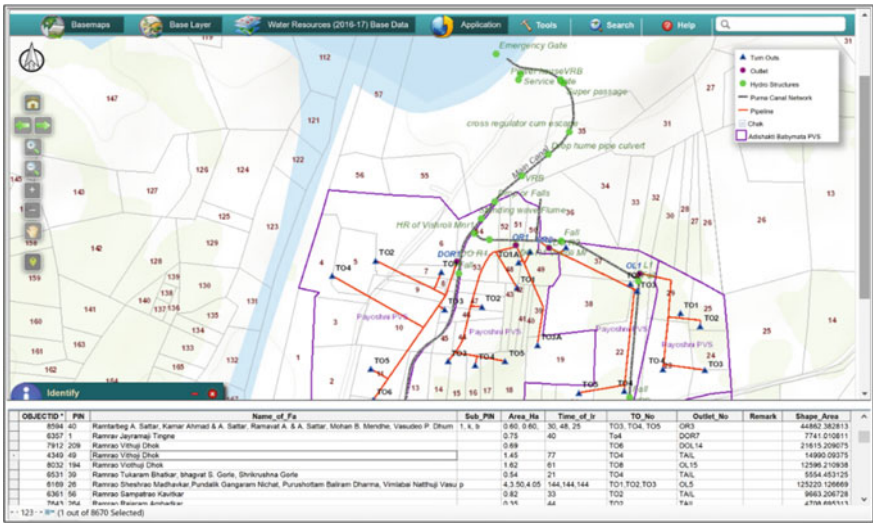

Fig. 21.17 Web portal showing the canals, outlets, turnouts, and pipeline with Chak boundary overlaid on cadastral data. The table at the bottom displays the attribute information of each cadastral/farmer

21.6 e-Governance Applications of Cadastral Database

The government at the center (National Government) and the State Governments are adapting more digital technologies, especially the Information and Communication Technologies (ICT) for dissipating the citizen-centric services and governance. The geospatial technologies and information have further enhanced the capability of the government to reach the needy and the poor. The location-based services along with the inherent land potential/constraints information have helped the citizens, especially farmers, to adopt an integrated information-based farming system and management. All development planning and implementation require the cadastral as their base and the digital cadastral maps/records provide quick and amicable solutions during the execution of the project.

21.6.1 Mobile Applications for e-Governance

Governance through mobile devices is called mobile-governance or m-governance and is a sub-domain of e-governance. It ensures that electronic services are available to people via mobile technologies and applications using devices such as mobile phones or similar devices. Mobile services are now extensive, cheaper, and well accessible in most of rural India.

Increasing the mobile phone accessibility, adaptability and with the millions of subscription base, governments are promoting and using the mobile phone in delivering the e-Governance services. In the last few years, governments have seen in what way mobile phones can empower citizens and affect the way citizens interact with each other and with society at large. Mobile phones are also considered to be an effective tool in strengthening democracy through better citizen-government interaction, thus influencing the political decision-making process and making governments accountable for their activities. The services which were once available on the web are now accessible on mobile through various mobile applications. Today's smartphones are equipped with most ICT devices and are easy to operate with security.

The MSDG (Mobile Services Delivery Network) empowers the government to deliver citizen-centric services over the cheaper communication devices—smart mobile phones through various mobile-based technologies, such as Short Message Service (SMS), Interactive Voice Response System (IVRS), Unstructured Supplementary Service Data (USSD), Cell Broadcasting Services (CBS), Location-Based Services (LBS), Mobile Payment Service and mobile applications. Such technologies, in combination with geospatial technologies, enhance interoperability among the various public service which reduces duplication of the data generation cost and the overall cost of operation of m-Governance services. The web-based and cloud technologies pull the data from the common pool of resources aggregating the demand for communication and e-Governance services. The mobile-based integrated application allows the various Government Departments and Agencies to test, rapidly deploy, and reach the citizens. It is very easy to maintain m-Governance services across the country with frequent updates. Most of the infrastructure is based on open standards and can be developed as a cloud-based service.

21.6.2 Web Applications for e-Governance

Often it is presumed that the government citizen-centric services are mostly time-consuming and sometimes less responsive. There has always been a high demand for good government services and attempts are made to not compromise on the quality and speed by adopting the new available technologies (Alotaibi 2020). It is to say that more citizens are now possessing electronic gadgets with ICT-enabled technologies. Thus, the demand to provide information and services online and in real-time is growing day by day. The infrastructure required for providing such services, both in terms of data in digital format and architecture, is now in place. The geospatial infrastructure has increased both in the government and private sector, to facilitate the use of online applications for various services.

The e-governance mechanism can be attributed to government-to-government (G2G), government-to-business (G2B), and government-to-citizen (G2C). The main objectives are to support and simplify governance for government, citizens, and businesses. It makes the government administration more transparent and accountable while addressing society's needs and expectations through efficient public services

and effective interaction. Thus, it reduces corruption and ensures speedy administration of services and information. E-governance facilitates "ease of doing business" and "ease to doing work" in the system.

Digital India was launched in 2015 to empower the country digitally, developing a secure and stable digital infrastructure, delivering government services digitally, and achieving overall digital literacy. The e-governance citizen-centric applications which are related to agriculture or non-agriculture activities has a direct link to the parcel of landholding of individual farmers or individual beneficiary. Therefore, most of the e-governance applications have a direct relation to the Cadastral Information, as the cadastre gives all required information about the beneficiaries.

A few examples of government initiatives to use geospatial data, cadastral information, and ICT for development activities, their monitoring, and management as a part of healthy e-governance are mentioned in the subsequent sections.

21.6.3 Case Studies

21.6.3.1 Jalyukt Shivar Abhiyaan—Web and Mobile-Based Online Reporting System

Jalyukt Shivar is a flagship program of the Government of Maharashtra to tackle water scarcity in Maharashtra. Under this program, a mission is taken up to provide water to everyone and make Maharashtra villages water scarcity-free (Water Neutral). Various kinds of Water conservation works are undertaken in all villages with multi-departmental activities viz. recharge and augment groundwater level, conserve water for agriculture and increase the availability of drinking water, rejuvenate water supply schemes by strengthening water sources, improve the storage capacity of existing water sources, remove silt from exiting storages, conserve soil erosion, take afforestation program and sensitize people for water conservation.

In this endeavor, the water conservation department, under agriculture decided to take advantage of the latest ICT in mobile communication and GIS for mapping all works and monitoring the future work with cadastral maps in GIS and with the latest satellite data. The work of designing and developing mobile and web-based applications for mapping and monitoring the work was executed by MRSAC, Government of Maharashtra.

The Jalyukt Shivar web portal has many modules of data entry, mobile application downloads, training, training and instruction, mapping monitoring, statistics, and reporting and validation for the entire operation of the project implementation (Fig. 21.18).

The department is first facilitated online (web services) to select the villages and prepare its profile, water budget, and water utilization plan. Based on the requirements and the recommendation of the experts, the water resources plans are selected and the work code is generated with the location on the cadastral map. The work code is then approved by the line department online and sanctioned by the Agriculture

Fig. 21.18 Sample home page of Jalyukt Shivar with various module and dashboard

Water Conservation Department. Once, the work is sanctioned, the work code with its details is transferred to the mobile application for work monitoring and management (Fig. 21.19). The user (maybe an officer/vendor) goes to the appropriate spot, takes the location information (latitude/longitude) of the workplace and the photograph of the position before the work starts. Subsequently, during the work progress, the user takes photographs of the same location showing the progress of the work. Once the work is completed and the photographs are received properly in the web portal, the user with other details will submit the bill online for processing and payments release. This completes the cycle of single work. Similarly, the other works are also

Fig. 21.19 Mobile application to capture the location, progress photographs, and field information of the work

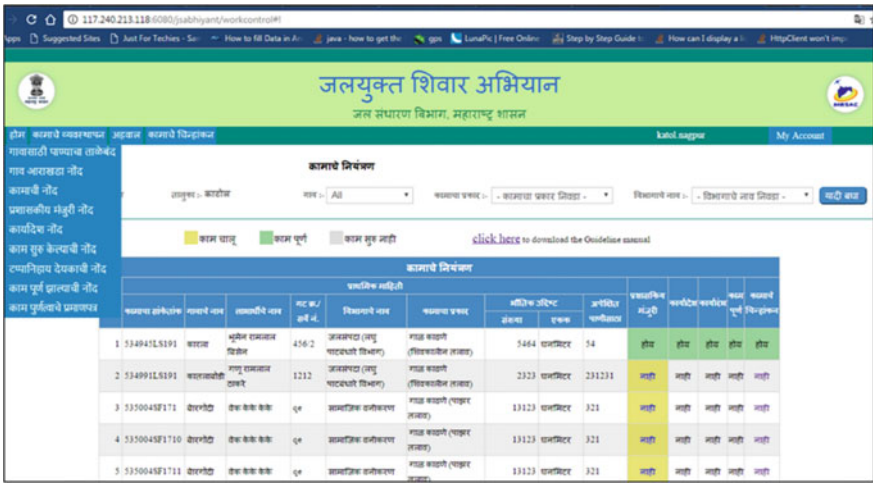

Fig. 21.20 Work progress monitoring dashboard and decision-making screen for administrator

monitored and a GIS data of the initiated, progress, and completed work are visible in the GIS web portal with on satellite and cadastral data backdrop.

The Jalyukt Shivar web portal activity provides an overall e-governance implementation of the government project using geospatial technologies. All the activities/works are captured and stored in the GIS environment and are available for spatial query. Various types of statistics and reports are generated on the fly. The statistics of the query are also visible on the dashboard. Facilities have been provided for the administrator to visualize the project progress and provide comments from time to time before final approval for billing (Fig. 21.20).

21.6.3.2 District Administration Support System: Non-agriculture (NA) Permission

The development rate is very high and quick around the big cities. A lot of agricultural lands are brought under the purview of the town planning and city corporation for expansion and development. For any greenfield development, the agricultural land needs to be converted into non-agriculture land, and for this one has to seek a No Objection Certificate (NOC) from the district administration. The provision is called NA and cadastral data information along with the other thematic maps are utilized to provide the NOC. This is an e-governance application of the district administration which provides information on the various thematic constraints of a particular cadastre and guides the administration from which department the NOC needs to be taken. The application aims at providing vital information with decision support on the web portal for the district administrator and planners for providing non-agriculture permission to the applicant. The application is developed by the

Maharashtra Remote Sensing Application Centre (MRSAC), the Government of Maharashtra.

The spatial database (base layers) includes the state administrative layer, Cadastral Boundary, *gaothan* (settlement) boundary, road network, railway network, canal network, transmission lines, and parcel-wise regional planning status.

To achieve this task, a web application has been developed by integrating the latest situation of natural resources in the district along with the status of the various land parcels information in the records of the district administration. The spatial inputs (maps) are provided by MRSAC and the non-spatial inputs (attributes/tables) are provided by the Collectorate office. The authorities of the district administration have certified the inputs.

The various departments which play a role in granting non-agriculture permission include the Indian Railways, MIDC, PWD, MSETCL, Land Acquisition officers, Irrigation Department, Urban Land Ceiling Department, etc. Unlike the traditional system, where the application moves from one department to another for getting the No Objection Certifications (NOC), the application for non-agriculture permission is validated by the system. The limitations/restrictions/objections of the various department are fed into the system. On request, the parcel is then checked for the restriction violation and pops up the result with departmental details (Fig. 21.21).

If the parcel is having some objection, then permission is not provided, and a detailed list is provided. The permission is sought from only those departments against which the objection is raised. The parcel with no objection from any department can be granted permission and the certificate. This is in tune with the approach of business process re-engineering adopted under the head of E-governance.

Systematic efforts are required to bring the databases of different departments (involved in giving NOC) to a common reference system with cadastral maps. Validations and cross verifications are undertaken to ascertain the correctness of the

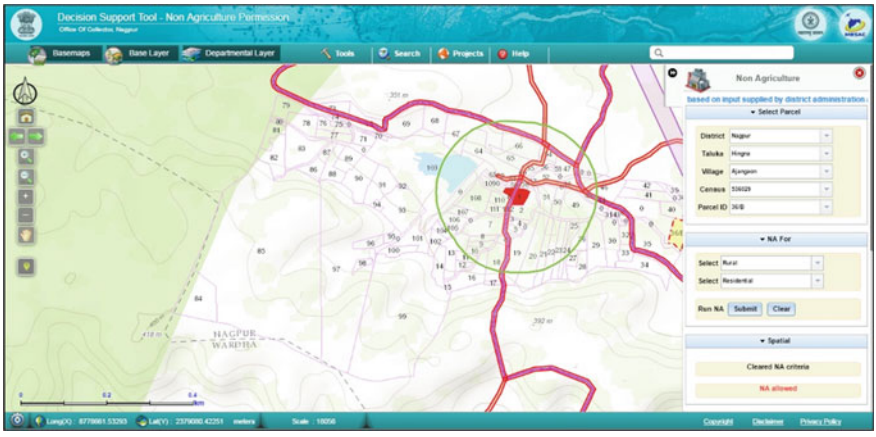

Fig. 21.21 Application screenshot, query builder, and analysis result of NA application

information. The latest maps generated from the satellite images are used and the hitherto available information is refined with this latest technology input.

The application is validated for three checks namely the spatial criteria checking, the non-spatial criteria checking, and the *gaothan* expansion rules.

Under the spatial criteria, checking is done for the various buffers of railway lines, roads, high tension lines, irrigation canals, according to the prescribed standards. These buffers are the restricted zones where the NA permission cannot be automatically provided or need to be sought. Under the non-spatial criteria, checking is done for the various prohibited and already identified prohibited areas viz. lands acquired for mining, lands under the submergence zones, lands reserved by the town planning department, regional planning zone, and also the urban land ceiling areas. The lands other than these lands can be provided for NA permission. Also, to prevent haphazard development, there are rules for *gaothan* expansion. The NA permission for residential purposes is allowed in the zones around *gaothan* based on the population. Various buffers/zones are derived through the system and the parcels/parts of the parcels inside these buffers are granted permission.

When the application is received from the citizen, the operator has to select the district, taluka, village, and parcel number from the predefined list available in the system and run the analysis module. All three criteria are checked and immediately the result is provided by the system in a graphical and textual format (Fig. 21.22). This makes the decision-making unbiased, fast, efficient, and saves time.

The system is developed in the Geographical Information System (GIS) environment using APIs in the JavaScript domain. The database is stored in RDBMS format. The database is accessed in the web application as a web service that uses an ArcGIS server at the backend. Geoprocessing tools based on proximity relationships such as buffering, union, and overlay are being used to come out with the final NA result.

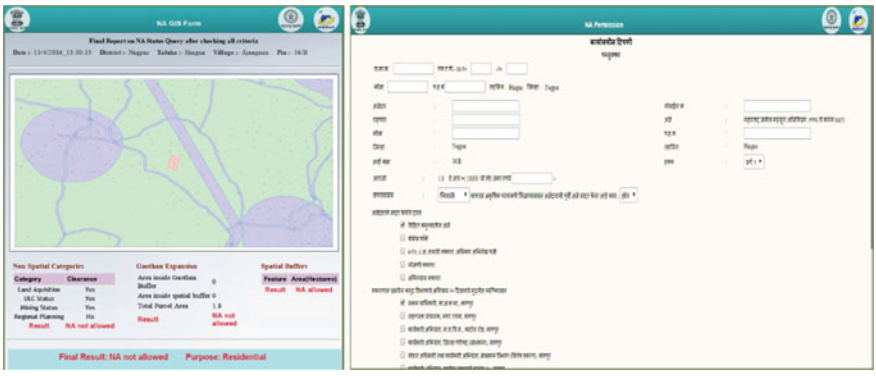

Fig. 21.22 NOC output generation and report format of NA application

21.6.3.3 Land Valuation Zone Mapping

In Maharashtra, the market value of the land to be acquired will be determined by the "Ready Reckoner" (RR) value fixed under Maharashtra Stamp Act, 1958. The Inspector General of Registration (IGR) fixes the monitory values of land on 1st January every year considering the location and development index for urban and rural areas. The RR is prepared by the office of the Joint Director, Town Planning (Valuation), Department for IGR. Since the georeferenced digital cadastral maps are available for the entire state, the IGR, Maharashtra decided to use the geospatial techniques for deciding the rates of each parcel.

The application is a GIS-based analysis run on the entire state based on the cadastral maps, the definition of the *gaothan* (settlement) area, and roads with the definition of national and state highways. The requirement was initiated by the Inspector General of Registration (IGR) and Town Planning (Valuation) and was developed by Maharashtra Remote Sensing Application Centre (MRSAC), Government of Maharashtra.

The procedure for valuation of each parcel is:

(a) Listing the national and state highways fronting the parcels (S. No./G. No.) in the villages having a population less than 1000 as per Census 2011,
(b) Listing the parcels (S. No./G. No.) within the *gaothan* buffer for the villages having a population greater than 1000 as per Census 2011,
(c) Listing the parcels (S. No./G. No.) within the *gaothan* Buffer for the villages having a population greater than 1000 as per Census 2011 and list of Parcels (S. No./G. No.) linked to the highways,
(d) Generate the Buffer Zone and Highway Maps of Nagar Panchayat and *Prabhav Kshetra* Villages identified by Town Planning (Valuation) Dept.

The Georeferenced Village Map data and the updated road network of PWD Road Development Plan 2001–2021 data are used for this project. Georeferenced Village Map data contains district-wise cadastral mosaic with Survey Nos. and Gat Nos. of all the parcels in the state. The PWD Road Development Plan 2001–2021 is having all planned roads including National Highways and State Highways.

The following steps were used for geoprocessing of data to derive the required outputs for submission to IGR for RR purposes.

- Creation of Village *gaothan* layer from cadastral data.
- Generation of *gaothan* Buffers based on population and distance criteria specified by Town Planning (Valuation).
- Extraction of Survey Nos./*Gat* Nos. in buffer area by intersection method.
- Selection of Highway fronting parcels by spatial join method followed by spatial editing for addition and deletion of parcels concerning roads in cadastral data.
- Generation of Tables according to the objectives defined.

- Composition of maps in GIS and creation of "Value Zone Maps" in PDF format (Fig. 21.23).
- Data validation by the officials of Town Planning (Valuation).
- Final data submission after appropriate corrections.

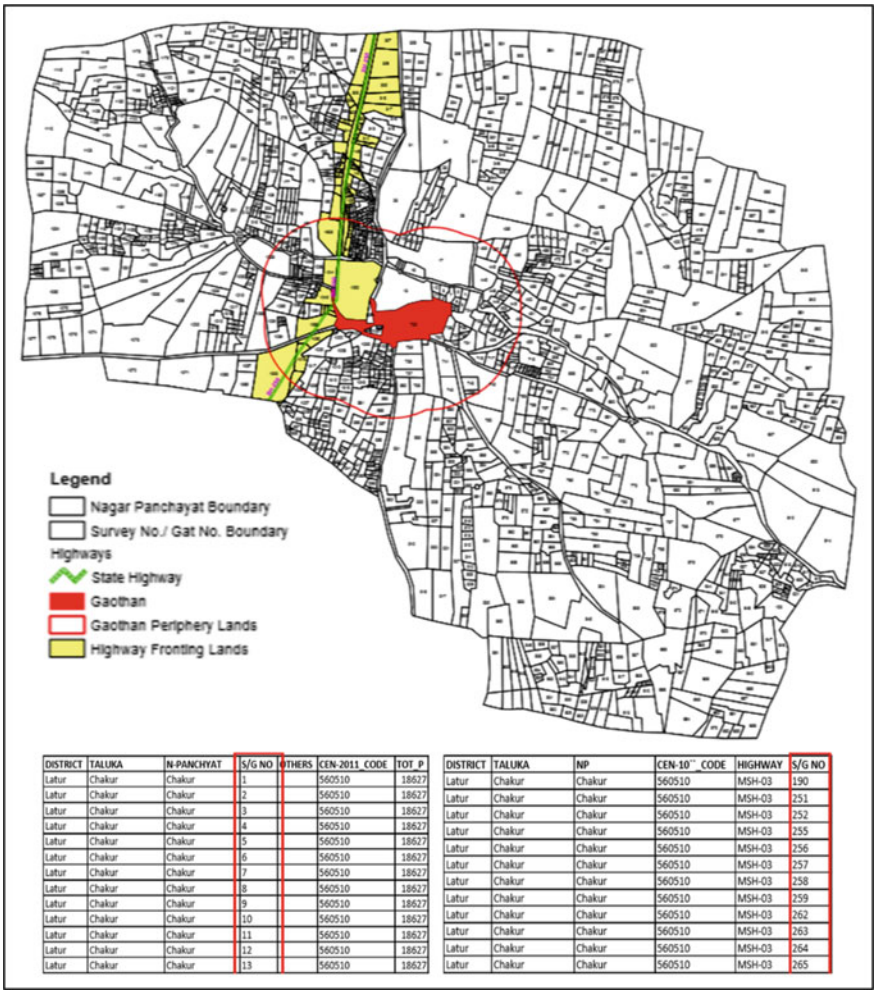

DISTRICT	TALUKA	N-PANCHYAT	S/G NO	OTHERS	CEN-2011_CODE	TOT_P
Latur	Chakur	Chakur	1		560510	18627
Latur	Chakur	Chakur	2		560510	18627
Latur	Chakur	Chakur	3		560510	18627
Latur	Chakur	Chakur	4		560510	18627
Latur	Chakur	Chakur	5		560510	18627
Latur	Chakur	Chakur	6		560510	18627
Latur	Chakur	Chakur	7		560510	18627
Latur	Chakur	Chakur	8		560510	18627
Latur	Chakur	Chakur	9		560510	18627
Latur	Chakur	Chakur	10		560510	18627
Latur	Chakur	Chakur	11		560510	18627
Latur	Chakur	Chakur	12		560510	18627
Latur	Chakur	Chakur	13		560510	18627

DISTRICT	TALUKA	NP	CEN-10th_CODE	HIGHWAY	S/G NO
Latur	Chakur	Chakur	560510	MSH-03	190
Latur	Chakur	Chakur	560510	MSH-03	251
Latur	Chakur	Chakur	560510	MSH-03	252
Latur	Chakur	Chakur	560510	MSH-03	255
Latur	Chakur	Chakur	560510	MSH-03	256
Latur	Chakur	Chakur	560510	MSH-03	257
Latur	Chakur	Chakur	560510	MSH-03	258
Latur	Chakur	Chakur	560510	MSH-03	259
Latur	Chakur	Chakur	560510	MSH-03	262
Latur	Chakur	Chakur	560510	MSH-03	263
Latur	Chakur	Chakur	560510	MSH-03	264
Latur	Chakur	Chakur	560510	MSH-03	265

Fig. 21.23 Land value zone map with a tabular display of parcel's zone value along with the settlement and parcel's value along major state highway (MSH-03) in Chakurnagar panchayat

21.7 Conclusion

Geospatial techniques and tools consisting of remote sensing, GIS, and GNSS (GPS) technologies play a pivotal role in gathering and enhancing the vital land (spatial) parameters on natural resources and ownership. Further, the geospatial techniques facilitate the integration of the various location-based services and information under one platform. The ITC technologies have enabled the information to be available on the online website or web portals. The cadastral maps, which are the largest scale available land information in terms of dimension and ownership, play an important role in all development, management, and monitoring activities of the region efficiently. The digital georeferenced cadastral maps act as the base for all geospatial-related programs of the government/private/NGOs/etc. The inclusion of cadastral maps in all micro-level planning is well known for achieving the sustainable development of natural resources, their management, and conservation (Sreenivasan and Krishna Murthy 2018).

Digitalization of the cadastral or land records is one of the prime priorities of the Central Government of India. Though the land record is a state subject and there are various methods and procedures to maintain the land record, the fact remains that once the records are geodetically converted, they can be used for all development activities. Today's geospatial technologies provide better resolution of satellite data and options, better techniques and accuracy of database creation, and its integration with the GIS and other operational systems.

Today, more development emphasis is given at the grass-root level, i.e., at the gram panchayat level, and cadastral data is finding a place in the planning and implementation of all the development projects of the State. With citizens becoming more tech-savvy—availability of affordable communication technologies in a rural area; the need to provide the citizens with real-time information and advisories on the mobile device is becoming an initiative of the government of the day.

The use of *cadastre* data has become multipurpose: serving the administrative mandates, maintaining an up-to-date database, assigning values for taxation, monitoring disaster, calculating subsidies, addressing rural development and agrarian management, and providing products and services under e-governance mechanism of G2G, G2B, and G2C. This makes the government administration more transparent and accountable while addressing the societal needs and expectations through efficient public services and effective interaction, reducing corruption and ensuring speedy administration of services and information. E-governance facilitates "ease of doing business" and "easy to doing work" in the system.

Acknowledgements The authors thank the teams of scientists from the Regional Remote Sensing Centre-Central, Nagpur (RRSC-C), who have contributed to developing methodologies and carrying out the georeferenced cadastral mapping and its applications of different states, the examples of which have been quoted in this work. The authors thankfully acknowledge Director, Maharashtra Remote Sensing Application Centre (MRSAC), Nagpur to allow to cite of some of the applications that were carried out in the state of Maharashtra and the team of scientists from MRSAC who have contributed to the works cited in this chapter.

References

Agrawal NK (1998) Abandon polyconic projection. GIS India 7(1)
Alotaibi SJ (2020) internet application and technology for e-government public services. Int J Dig Soc (IJDS) 11(1):1579–1582
Behar A, Kumar Y (2002) Decentralization in Madhya Pradesh, India: from Panchayati Raj to Gram Swaraj (1995–2001). Working paper 170. Overseas Development Institute, 111 Westminster Bridge Road, London, SE1 7JD, UK
Barnes G (1990) The evolution of the modern cadastre: from domes day book to LIS/GIS network. Surv Land Inf Syst 50(1):5–9
Bernstein R (1983) Image geometry and rectification. In: Colwell RN (ed) Chapter 21 in the manual of remote sensing, vol 1. Falls Church, VA, American Society of Photogrammetry and Remote Sensing, pp 875–881
BirdLife International (2021) Species factsheet: *Ardeotis nigriceps*. Downloaded from http://www.birdlife.org on 02/12/2021
Borzacchiello MT, Craglia M (2012) Estimating benefits of spatial data infrastructures: a case study on e-cadastres. computers, environment, and urban systems. Elsevier Ltd. viewed Feb 28, 2013
Castleman KE (1978) Geometric operations. In: Chapter 8 in digital image processing. Prentice-Hall, Inc., Englewood Cliffs, N.J., pp 111–112
Davidson GJ (1986) Ground control pointing and geometric transformation of imagery. Int J Remote Sens 71:65–74
Dhal N, Madame RS, Krishna Murthy YVN (1994) Cadastral mapping and LIS. In: 14th INCA congress on proceedings, Bangalore
Dhal N (1999) Angul-Nalco project. Training notes. Survey Training Institute, Survey of India, Hyderabad, 78 p
ERDAS (2003) Imagine 8.4: field guide. ERDAS, Inc. Atlanta, Georgia
ESRI (1995) Map projections. Environmental Systems Research Institute, Redlands, California, USA
ESRI (2005) https://www.esri.com/content/dam/esrisites/sitecore-archive/Files/Pdfs/library/brochures/pdfs/gis-for-cad-mgmt.pdf
FGDC (2016) www.fgdc.gov. Retrieved 1 Apr 2016
FIG (1996) Bogor declaration on cadastral reform. Report from United Nations Interregional Meeting of Experts on the Cadastre, Bogor, Indonesia
Friedman DE, Friedel JP, Magnussen KL, Kwok R, Richardson S (1983) Multiple scene precision rectification of space-borne imagery with very few ground control points. Photogramm Eng Remote Sens 49:1657–1667
GOI (1985) 73rd and 74th amendment acts. Govt. of India
Gopala Rao M (2000) LIS in India—perspective, and retrospective. In: Proceedings, national conference on land information system, New Delhi
Haralick RM (1973) Glossary and index to remote sensed image pattern recognition concepts. Pattern Recogn 5:39–46
Holstein L (1990) The cadastre as a tool of resource management in developing countries. In: Proceedings, sixth general assembly and technical seminar. London
IUCN (2014) The IUCN red list of threatened species. Version 2014.3. http://www.iucnredlist.org/. Downloaded on 17 Nov 2014
Jacobsen K (1998) Requirements and accuracy of topographic maps produced from space imagery. In: Proceedings, workshop on mapping from space, Ho-Chi-Minh-City
Jensen JR (2000) Remote sensing of the environment—an earth resource perspective. Prentice-Hall, Upper Saddle River, New Jersey
Jeremy WC, Eric MH, Emily CK (2018) Book comprehensive geographic information system volume 1—public GIS: social impact and ethics of GIS, pp 398–414
Jeyaram A, Krishna Murthy YVN, Sinha AK, Srinivasa Rao S, Ravindran KV, Radhakrishnan K, Goyal S (1996) Water resources conservation using remote sensing and geographical information

system. In: Proceedings, Indo-US symposium-workshop on remote sensing and its application, Mumbai, pp 175–183
Krishna Murthy YVN, Adiga S (2000) Integrated sustainable development of land and water resources using space technology inputs. SPACE FORUM, special issue on Indian space program
Krishna Murthy YVN, Srinivasa Rao S, Srinivasan DS, Radhakrishnan K (1996a) Land information systems (LIS) for rural development. In: IX INCA conference, New Delhi
Krishna Murthy YVN, Srinivasa Rao S, Srinivasan DS, Sinha AK, Jeyaram A, Radhakrishnan K (1996b) Village level development planning using IRS-1C data. In: Proceedings, national symposium on remote sensing for natural resources, Pune
Krishna Murthy YVN, Srinivasa Rao S, Srinivasan DS, Adiga S (2000) Land information system (LIS) for rural development. In: Technical proceedings, geomatics
Lillesand TM, Keifer RW (1987) Remote sensing and image interpretation, 2nd edn. Wiley, New York, USA
Mather PM (1987) Computer processing of remotely sensed images—an introduction. Wiley, New York, USA
MRSAC (2015) Annual Report. Maharashtra Remote Sensing Application Centre, Govt. of Maharashtra, 2015
NRSA (1995) Integrated mission for sustainable development—technical guideline. National Remote Sensing Agency, Department of Space, Hyderabad
NRSA (2002) integrated mission for sustainable development—path to progress. Technical report. National Remote Sensing Agency, Department of Space, Hyderabad
Planning Commission (1989) Information gap. Report of the committee of the study group on information gap, Govt. of India, New Delhi
Rahmani AR (1986) Study of ecology of certain endangered species of wildlife and their habitats: the great Indian bustard (1985–86), BNHS, p 50
Raja Rao T, Rajsekhar P (2000) Vision LIS 2000—A total technology solution for land records. In: Proceedings, national conference on land information system, New Delhi
Rajak DR, Oza SR, Oza MP, Dadhwal VK (2002) Selection of map projections for crop monitoring spatial database. Scientific note, RSAM/SAC/RSDB/SN/01/2002, SAC, Ahmedabad, Dec 2002
Rao UR, Chandrasekhar MG, Jayaraman V (1995) Caring for the planet earth, space and agenda 21. Prism Books Pvt. Ltd., India
Richards John A (1994) Remote sensing digital image analysis, an analysis. Springer-Verlag, p 56
Snyder JP (1987) Map projections—a working manual. U.S. Geological survey professional paper 1395, US Government Printing Office, Washington
Srinivasa Rao S, Krishna Murthy YVN, Prakasa Rao DS (2002) Map projections and datum for NSDI. In: Proceedings, 2nd workshop on national spatial data infrastructure, Ooty, Tamil Nadu
Srinivasa Rao S, Krishna Murthy YVN, Joshi AK, Shantanu B, Das SN, Pandit DS (2003) Computerization and geo-referencing of cadastral maps in Chhattisgarh State. Technical document. Regional Remote Sensing Service Centre/ISRO, Nagpur
Sreenivasan G, Krishna Murthy YVN (2018) Remote sensing and GIS applications in micro level planning. In: Reddy GPO, Singh SK (eds) Geospatial Technologies in land resources mapping, monitoring and management, geotechnologies and the environment, vol 21. Springer International Publishing AG. Part of Springer Nature 2018. https://doi.org/10.1007/978-3-319-78711-4_29
Srivastava PK (2001) Report of the committee on map projections and datum for future IRS data products. Technical Report. Space Application Centre, Ahmedabad
Ting L, Williamson I (1999a) Cadastral trends: a synthesis. Austr Surveyor 4(1):46–54
Ting L, Williamson I (1999b) Land administration and cadastral trends: the impact of the changing humankind-land relationship and major global drivers. In: Proceedings, UN-FIG conference on land tenure and cadastral infrastructures for sustainable development, Melbourne, Australia, 25–27 Oct 1999
Varghese AO, Sawarkar VB, Rao YLP, Joshi AK (2016) Habitat suitability assessment of *Ardeotis nigriceps* (Vigors) in great Indian bustard sanctuary, Maharashtra (India) using remote sensing and GIS. J Indian Soc Remote Sens 44(1):49–57. https://doi.org/10.1007/s12524-015-0486-9

Wade T, Sommer S (2006) A to Z GIS: an illustrated dictionary of geographic information systems. ESRI Press, Redlands, CA, p 288

Williamson IP (1986) Cadastral and land information systems in developing countries. Austr Surv 33(1):27–43

Williamson IP, Ting L, Grant DM (2000) The evolving role of land administration in support of sustainable development—a review of the United Nations. Austr Surv 44(2):126–135

Chapter 22
System Dynamics and Geospatial Technology-Based Approach for Sustainable Development in Mining Dominant Area

Paliwal Rakesh, V. Pavithra, S. Srinivasa Rao, and C. S. Jha

Abstract The sustainable development approach for the utilization of natural resources for the areas undergoing intense anthropogenic activities is very essential. The assessment of assimilative and carrying capacity of the region plays the major and crucial role for sustainable development. The sustainable development encompasses the environment, economy and societal aspects in an interrelated manner. In order to assess the impact of environment, the three major components—air, water and land and their interactions need to analyzed. The comprehensive planning for sustainable environmental conditions depends on the quality of air, water and land and their long-term dynamics. Hence, an integrated environmental modeling and simulation approach is needed to encompass interactions among these three components (air, water and land) along with anthropogenic activities for sustainable resource management. The system dynamics modeling and simulation approach provides a platform to build an integrated environmental modeling of a region with various policy options to achieve the sustainable resource management. The temporal land resources monitoring and assessment using geospatial technology viz.; remote sensing (RS), geographical information system (GIS) and other collateral environmental data, pertaining to air and water and integrating them using system dynamic modeling and simulation gives the overall insight for past, present and future of the system. A study around the mining area in Rajasthan State, India for the same has been illustrated in the chapter.

P. Rakesh (✉)
Regional Remote Sensing Centre-West, National Remote Sensing Centre, Indian Space Research Organization, Jodhpur 342005, India
e-mail: paliwalrakesh@gmail.com

V. Pavithra
Indian Institute of Management, Ahmedabad 380015, India

S. S. Rao
Bhuvan Geoportal and Web Services Area, National Remote Sensing Centre, Indian Space Research Organization, Hyderabad 500037, India

C. S. Jha
Regional Centres Head Quarters, National Remote Sensing Centre, Indian Space Research Organization, Hyderabad 500037, India

C. S. Jha et al. (eds.), *Geospatial Technologies for Resources Planning and Management*, Water Science and Technology Library 115,
https://doi.org/10.1007/978-3-030-98981-1_22

Keywords System dynamics (SD) · Remote sensing (RS) · GIS · Air · Water · Land · Environment · Simulation and modeling · Geospatial technology

22.1 Introduction

The anthropogenic activities like industrialization and urbanization and further industrial and urban expansion/sprawl in the country give rise to the economic growth but adversely affect the environment by over utilizing and depleting the natural resources (viz., forest, lakes, rivers etc.) and deteriorate the health of the living mankind and organisms as well. The occurrence of different environmental problems and degradation depends on overexploitation/improper management/depletion of natural resources. Regeneration and degeneration of natural resources depends on the assimilative capacity and carrying capacity of the region. The natural resources or environment of the region encompass air, water and land and they are interactive in nature in space and time. The sustainable development of the region depends on the supportive and assimilative capacity and in total the carrying capacity of the region, economic development and the society in an interactive manner over a period of time. Hence, to capture these aspects, an environmental modeling approach is needed. Moreover, the interrelationship between air, water, land as well economic development and society as variables in time domain is not only direct and linear in nature but the relationship of these variables can be direct/indirect, linear/non-linear and to a further extent, it can be primary, secondary, tertiary etc. in temporal domain.

So, to address and imitate such behavioral phenomenon in the temporal domain, the system dynamics modeling and simulation approach is advisable. The approach accommodates the past and current status of variables as well as envisages the future by simulation technique with some proactive policy options for sustainable development of the region as a whole or specific to any problem oriented environmental component. The mining activity (majorly for cement industry) of a small area of Rajasthan State of India as economic activity is considered as an illustration for understanding. The mining activity affects the surrounding air, water and land resources by pollutants and residuals. At the same time mining activity supports the economic and societal development in the region. In India, the contribution of greenhouse gases emissions from the cement industries is approximately 8% of the total national emission (CII 2010). The pollutants of toxic property have fatal effects on ecosystem and environment. These pollutants contaminate agricultural soil, surface and ground water resources, air and affect living beings and may result in imbalance in natural ecosystem (Dolgner et al. 1983; Sai et al. 1987; Mishra 1991; Murugesan et al. 2004; Shukla et al. 2008). Hence, these alarming phenomena caution us that the developmental activities should be carried out in harmony with the environment, within the carrying capacity of the ecosystem through sustainable developmental planning. In this context geospatial technology have been widely used. Choi et al. (2020) reviewed the utility of GIS-based mine environmental management as well time series remote sensing images for monitoring of variation in the mining environment. The role

of spatial databases for prediction and management of mine induced disasters and hazards on human health as well on mining environment has been also emphasized. A model has been developed by Moomen et al. (2017) to quantify the relationship between biophysical conditions and mining areas using geospatial impact assessment among land degradation and mine developmental activities. Kopeć et al. (2020) demonstrated the synergistic use of SAR (Sentinel-1A/B) and optical multispectral data (Sentinel-2A/B) as well as geological and meteorological data with machine learning and GIS analysis to assess the impact of mining activities on the state of surrounding environment. In addition, geographically weighted regression (GWR) analysis has been carried out to investigate the factors responsible for occurrence of flooding/wetlands due to mining activities in the region. The recent advances in RS and increasing availability of open source tools have enhanced the observation strategy for improvement of monitoring the mine environment (Dlamini et al. 2019), however RS data has not been utilized in full extend for land rehabilitation at mining areas and mainly restricted to field-based approaches which are unable to reveal seamless patterns of disturbance and restoration activities (Kariyawasam et al. 2014). Apart from use of geospatial technology, the system dynamics approach in conjunction with geospatial technology also promises the sustainable decision-making for anthropogenic activities viz.; urbanization, mining etc. Wanhui et al. (2011) have attempted the systems dynamics and geospatial technology approach for analyzing the land use/land cover changes due to urbanization anthropogenic activity. Xu et al. (2012) have developed GISSD system by integrating the GIS, SD and 3D visualization for understanding the interaction and variation of the sustainability indicators for residential development.

In the present study air, water and land environmental components of dominated mine areas have been considered. The mine areas and other land resources viz.; forest cover, water bodies, agricultural area etc. are obtained using geospatial analysis in temporal domain. The temporal data of air and water environmental component have been obtained from concern government departments and analyzed. The steps for development of an integrated system dynamic model viz., casual loop diagram, feedback loop diagram, stock flow diagram, model coupling etc. are described in the chapter.

22.2 Sustainable Development

The concept of sustainable development was first introduced by "World Commission on Environment and Development (WCED)" in the publication—"Our Common Future" and also known as "The Brundtland Report", in which first time wider attention was drawn to the possibilities of linking the economy with the environmental considerations. The sustainable development is "a development that fulfils the needs of the present generation without endangering the needs of future generations" (WCED 1987).

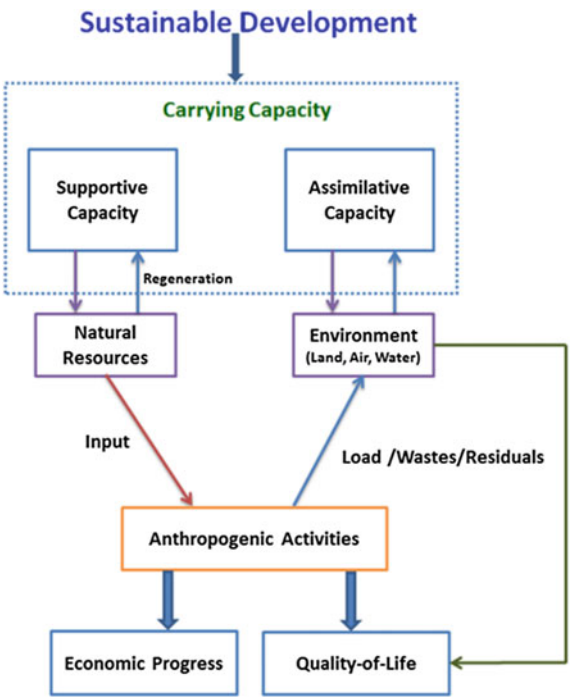

Fig. 22.1 Basis of the sustainable development

Further to assess the sustainable development, the carrying capacity in terms of supportive capacity and assimilative capacity needs to be considered while accounting the anthropogenic activities. The anthropogenic activities on one side provide economic progress and helping toward ease of quality of life. On the other side the anthropogenic activities impact the natural resources. As supportive capacity of a region, the natural resources are regenerative by nature, if it is used within limits and if they are overexploited then natural resources lead to depletion. During anthropogenic activities, generated waste/load/residuals again will be assimilated by the ecosystem if it is within limits and that is called assimilative capacity of the region. Figure 22.1 depicts the basis for the sustainable development assessment based on various capacities explained above.

22.3 Concept of System Dynamics Modeling and Simulation

In mid-1950s, Jay W. Forrester of the Massachusetts Institute of Technology, has introduced the "System Dynamics", a computer simulation technique (Maani et al. 2000). Since 1960s, system dynamics (SD) methodology has been widely used in

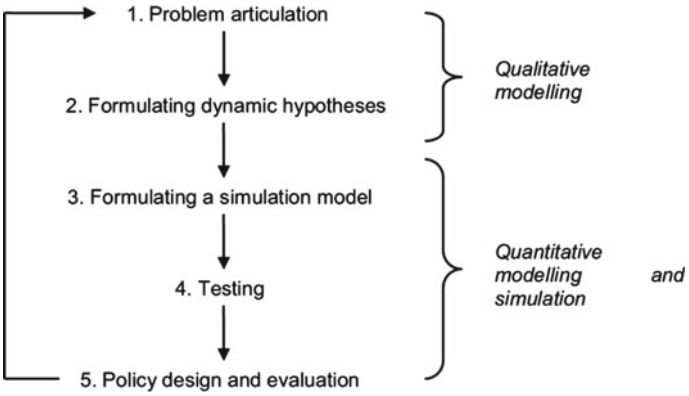

Fig. 22.2 Strategies for system dynamics modeling (Sterman 2000)

many areas like industry, inventory, finance, economics, health sector, biology, environmental studies, information technology etc. Sapiri et al (2017) stated that "The history of system dynamics as a methodology to study non-linear system and feedback control in engineering sciences background dated back in the mid-1950. Later in the late 1950s, the application of system dynamics was extended to non-corporate fields".

According to Forrester (1961) "SD methodology has four key principles: feedback control theory, understanding the decision-making process, use of mathematical models to simulate complex processes, and the use of computer-based technologies to develop simulation models". Figure 22.2 depicts the strategy for system dynamics modeling process suggested by Sterman (2000).

The system dynamics approach can be applied to any real-world system. The system contains elements which are interactive in nature and the interaction or impact of each element on the other elements could be linear/non-linear, could be positive/negative and could be primary/secondary etc. in a temporal dimension. Therefore, in the sequence of system formulation, dynamic hypothesis of a system and with set of its elements, system simulation with model calibration and validation need to be carried out to imitate the real complex system for precisely predicting the future scenario. In case of policy options further the model can be simulated to analyze the effects of the policies for future behavior of the system. In order to proceed further, Stephanie (1997) defined the following stages/key elements for designing the system dynamic modeling:

i. Conceptualization involves
- Define the model purpose
- Model boundary definition and key variable identification
- Describe the behavior or draw the reference modes of the key variables
- Diagram the basic mechanisms, the feedback loops, of the system

ii. Formulation
- Conversion of feedback diagrams to level and rate equations

- Estimation and selection of parameter values

iii. Testing

- Model simulation and testing the dynamic hypothesis
- Test the model's assumptions
- Test model behavior and sensitivity to perturbations

iv. Implementation

- Test the model's response to different policies
- Translate study insights to an accessible form.

Forrester (1969) elaborated that "In system dynamics, the fundamental premise is that the dynamic behavior over time (BoT) is endogenously generated from the 'systemic structure' or the network of interactions that bind system components together. Therefore, understanding this causal structure is prerequisite for understanding and managing the system. A system dynamics model represents the cause-effect relationships, feedback loops, delays, physical/information links, and decision rules that are thought to generate the system behavior".

Meadows (2008) explained about the causal loop diagram and stated that "A causal loop diagram is a simple map of a system with all its constituent components and their interactions. By capturing interactions and consequently the feedback loops, a causal loop diagram reveals the structure of a system; by understanding the structure of a system, it becomes possible to ascertain a system's behavior over a certain time period".

The causal loop diagram visualizes the structure and behavior of the system qualitatively. Further, to perform the detailed quantitative analysis, the casual loop diagram needs to be transformed into stock (level of accumulation and depletion over time) and flow (rate of change of level/stock) diagram with the help of equations development of a system's model. Then the built system model can be simulated through computer software. The equation development can be done by examining the pattern of behavior (exponential, S-shaped, oscillation etc.) between the system parameters/variables.

22.4 System Dynamics Modeling and Geospatial Technique-Based Approach to Assess the Impact of Mining Activity in the Surrounding Area and Environment

Rajasthan is one of the largest states in India in terms of mineral wealth and the mining industry forms a major revenue sector for the state. Mining activity is the second predominant activity in Rajasthan state of India after agriculture. As per Maps of India (2022), "there are about 42 major and 28 minor minerals available in the state. This sector provides employment to about two million mine workers throughout the state". Environmental impact due to mining activities inevitably represents an alteration on environment by affecting in its area of influence. The impact and its magnitude of the mining activities depends upon mining operations, size/area of

mining, technology of mining, surface and sub-surface mining, climate, assimilative capacity of surrounding environment and other interrelated factors. The surrounding environment encompasses land, water and air. The sustainable resource management of the region needs the assessment and monitoring of the environment (land, water and air), society and mining as economic growth activity. The system dynamic modeling using inputs from geospatial technology (remote sensing, geographical information system etc.) and other ancillary data sources deal with the challenges and complex issues involved for above-mentioned assessment and monitoring. Table 22.1 illustrates the various probable data sources for the land, water, air and population as a part of socio-economy of the region.

Table 22.1 Data sources for system dynamics modeling

Monitoring component	Parameters/variables	Source of data/agency
Land component	Kharif crop area	Satellite data
	Rabi crop area	
	Wastelands area	
	Fallow land area	
	Mining area	
	Type of geology (in terms of mining prospects)	District resources map
Water component	Rainfall	Indian meteorological department (IMD)
	Surface water spread area	Satellite data
	Ground water—pre and post monsoon ground water level	Central/state groundwater department
	Irrigation infrastructure	Satellite data/field data
	Water quality—chloride, fluoride, nitrate, pH, TDS	Central/state pollution control board, state ground water department
Air component	Suspended particulate matter (SPM) $PM_{2.5}$ and PM_{10}	Central/state pollution control board
	Carbon monoxide and carbon dioxide	
	Sulphur dioxide	
	Nitrous oxide	
Socio-economic	Population (birth rate and death rate), worker/non-worker, economic activity, literacy, amenities, etc.	Census of India - Decadal census data

22.4.1 Mining Dominant Study Area

There are many locations of various mining exist in the Rajasthan state. A small area about 90,000 hectares near Chittorgarh city of Rajasthan in India has been considered for illustration of the conceptual approach which consists of four major cement industries with their limestone mine pits, red ocher mine pits and other mine pits. The study area location is presented in the Index Fig. 22.3a and satellite image in Natural Color Composite (NCC) of the same area is shown in Fig. 22.3b. Major study area comprises of agriculture land, forest cover and sufficient water resources in terms of ground water (GW), surface (SW). There exists Ghosunda Dam and Gambhiri Reservoir as surface water sources. The area surrounding to the mine areas is generally more or less undulating plain with gentle slope. The area observes maximum temperature of 45 °C in May–June months and minimum temperature of 3 °C in December–January months. Average annual rainfall recorded in the area is about 760 mm.

22.4.2 Causal Loop Diagramming

Further, based on the available datasets from the various sources, the factors/parameters viz.; quality of life, employment opportunity, agriculture production, infrastructure amenities etc. are derived. Figure 22.4 depicts the casual loop diagram for primary parameters and secondary derived parameters with positive (+ve) and negative (−ve) polarity feedback loop. As mentioned in the Table 22.1 the land environment component consisting of kharif/rabi crop area and fallow land area depends on rainfall, surface and ground water availability and their linkage is shown with +ve feedback loop. Whereas mining activity or increase in mining area impacts the other lands negatively thereby decreasing the cropland and wastelands area. The richness of limestone reserves geologically, enhances the mining lease areas with + ve polarity. In case of water environment component, the good rainfall in the region with positive polarity increases the surface waterbody spread area and recharge of groundwater level which in turn on secondary level with positive polarity affects the kharif/rabi crop area and with negative polarity the fallow land area. The air environment component may also get affected by spread of mining area and mining activities with negative polarity depending on the techniques of mining whereas mining activity supports the economic growth of the region with +ve polarity which in turn at secondary level enhances the quality of life/living of the society with +ve polarity.

But again, air quality deterioration in the region affects the quality of life/living with −ve polarity due to health issues in the population residing in the region. Both +ve and −ve polarity factors in total are driving the population level of the society by birth rate and death rate. Hence, the causal loop diagram visualizes qualitatively the

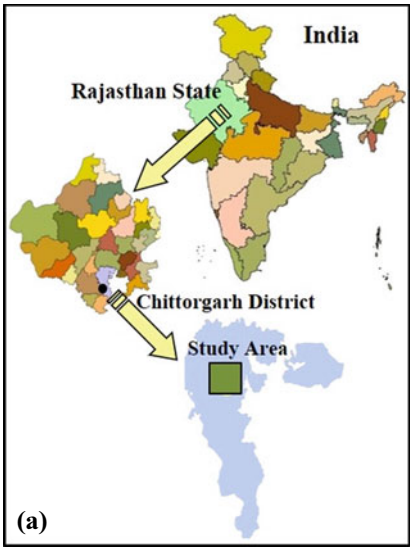

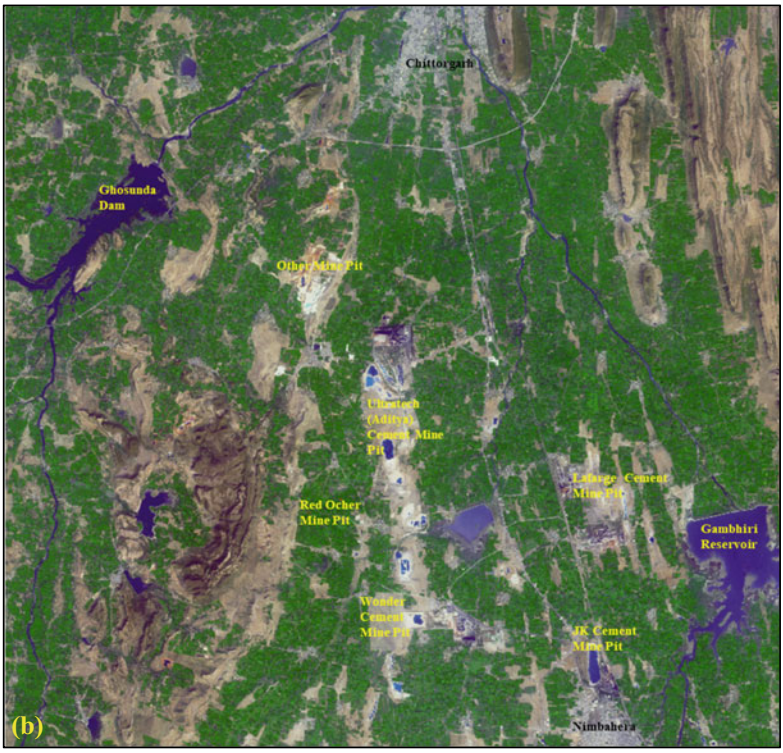

Fig. 22.3 **a** Study area situated in Chittorgarh district, Rajasthan, India. **b** Satellite image (NCC) of mining dominant area near Chittorgarh city, Rajasthan, India *Source data* Bhuvan (2022)

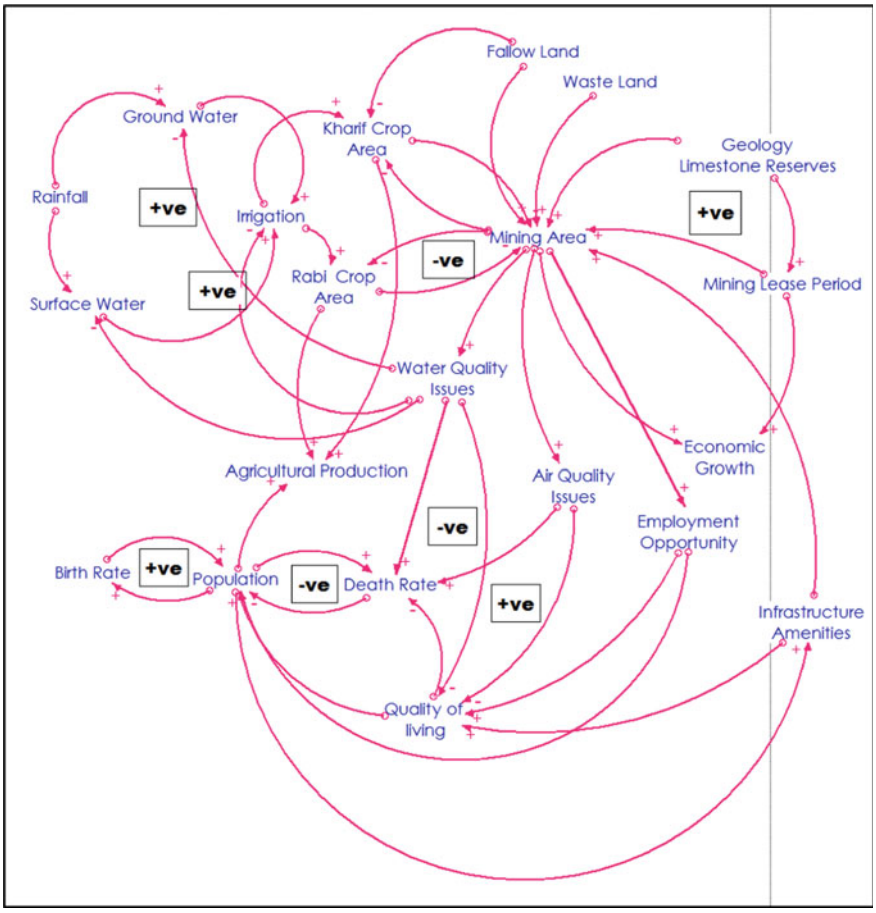

Fig. 22.4 System dynamics causal loop diagram

interaction of system parameters with its behavioral polarity with primary, secondary and tertiary impact with each other.

22.4.3 Stock-Flow Diagramming

In the sequence of development of the system dynamics model, the casual loop is transformed to stock flow diagram for quantitative analysis and simulation over a period of time. The stock flow diagram of an integrated system dynamics model for surrounding environment of mine areas is shown in Fig. 22.5. As procedural steps, individual land, water and air environmental component sub-models have been developed and afterwards through appropriate model coupling parameters, an

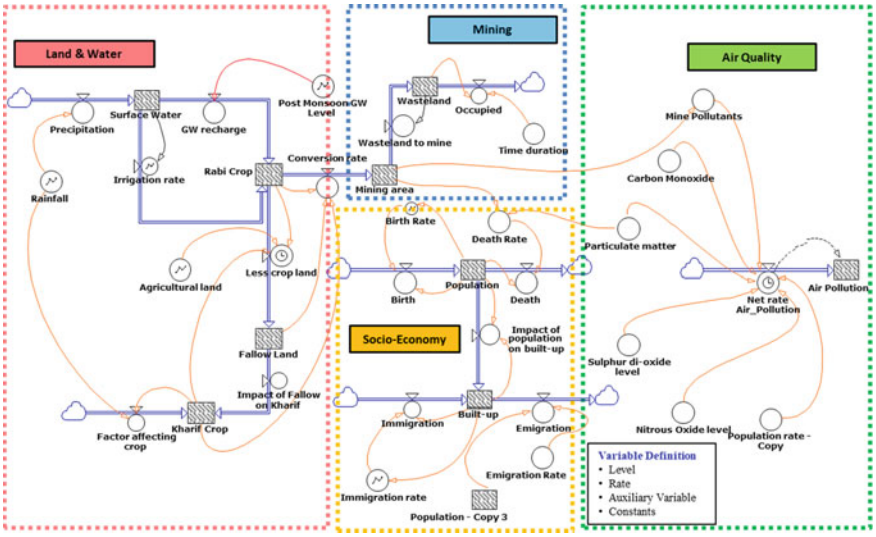

Fig. 22.5 Stock-flow diagram of an integrated system dynamics model for surrounding environment of mine areas

integrated system dynamics model has been developed and simulated over a period of time.

22.4.4 Land Use/Land Cover Analysis for Land Sub Model

In the Land sub model, the major inputs are derived from land use/land cover (LU/LC) analysis. LU/LC have been categorized into different classes as per LU/LC classification system given in Table 22.2 (NRSC 2006). The area under major LU/LC categories has been calculated from temporal LU/LC geospatial layers and percentage area of important major classes are represented in Fig. 22.6, which shows the increasing trend of agriculture, mining and built-up area and reduction in wastelands area over period of time. The temporal LU/LC geospatial layers have been prepared from periodic satellite RS data in the GIS environment. The LU/LC thematic map for the year 2017–18 is shown in Fig. 22.7 as an example.

22.4.5 Data Inputs for Air and Water Sub Model

The inputs for air and water sub model considered in terms of pollutant concentrations based on the Air Quality Index (AQI) and Water Quality Index (WQI) of the surrounding area of mines. In air quality index, pollutants such as Nitrogen

Table 22.2 Land use/land cover classification system

S. No.	Level-I	Level-II	Level-III
1	Built-up land	Built-up land	Rural Urban
2	Agricultural land	Cropland Fallow land	Kharif Rabi Double (Kharif + Rabi) Fallow
3	Forest	Dense forest Open forest Scrub forest	Dense forest Open forest Scrub forest
4	Wasteland	Land with or without scrub Rocky Outcrop	Land with scrub Land without scrub Rocky outcrop
5	Water bodies	River/stream Tanks/ponds	River/stream/Nala Tanks/ponds
6	Others	Stone quarries Mining Plantation	Stone quarries Mining Plantation

Source NRSC (2006)

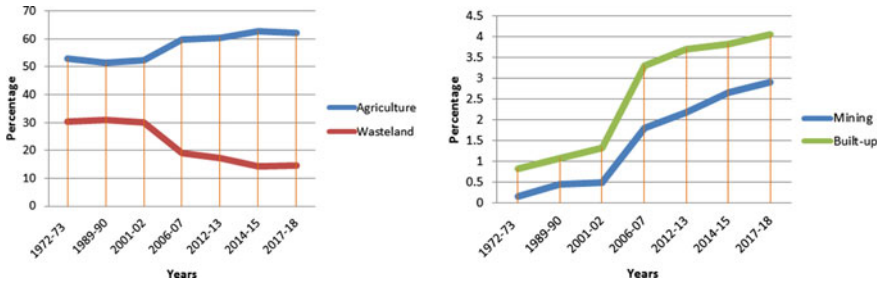

Fig. 22.6 LU/LC classes behavior over period of time

oxides, Sulphur di-oxide and Suspended Particulate Matter and Respirable Particulate Matter have been considered. The data has been collected from Rajasthan State Pollution Control Board (RSPCB), Jaipur, Rajasthan, India and shown in Fig. 22.8. Figure 22.8b represents that the air quality data is within permission limit in the current time period, when it is compared with National Ambient Air Quality data.

Similarly, for development of WQI, water quality data viz.; pH, total dissolved solids, total hardness, chloride and ground water level (pre and post monsoon) have been collected from Rajasthan State Ground Water Department, Jodhpur, Rajasthan, India. The rainfall data has been collected from Indian Meteorological Department (IMD). The rainfall versus post monsoon groundwater water level behavior of the region is shown in Fig. 22.9 based on the temporal data availability.

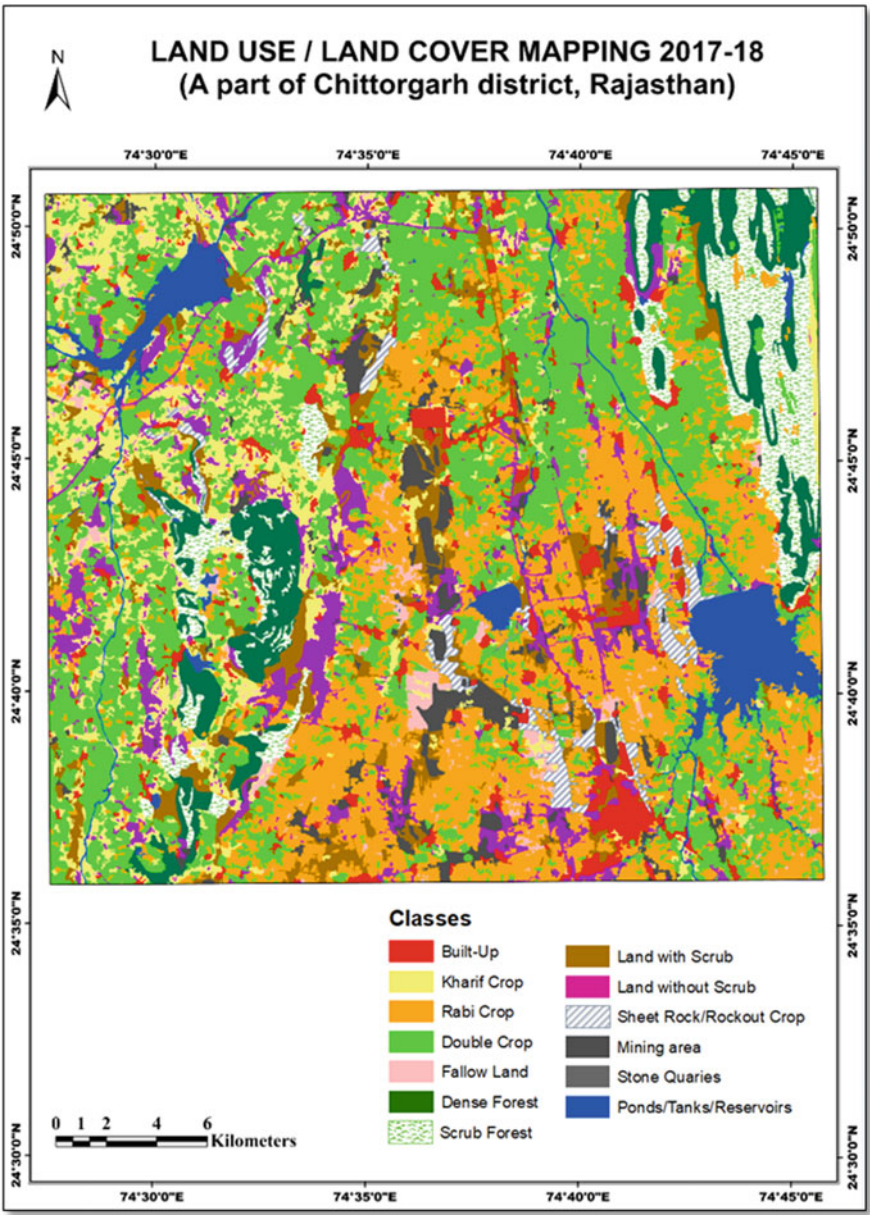

Fig. 22.7 Thematic map showing different LU/LC classes of the study area

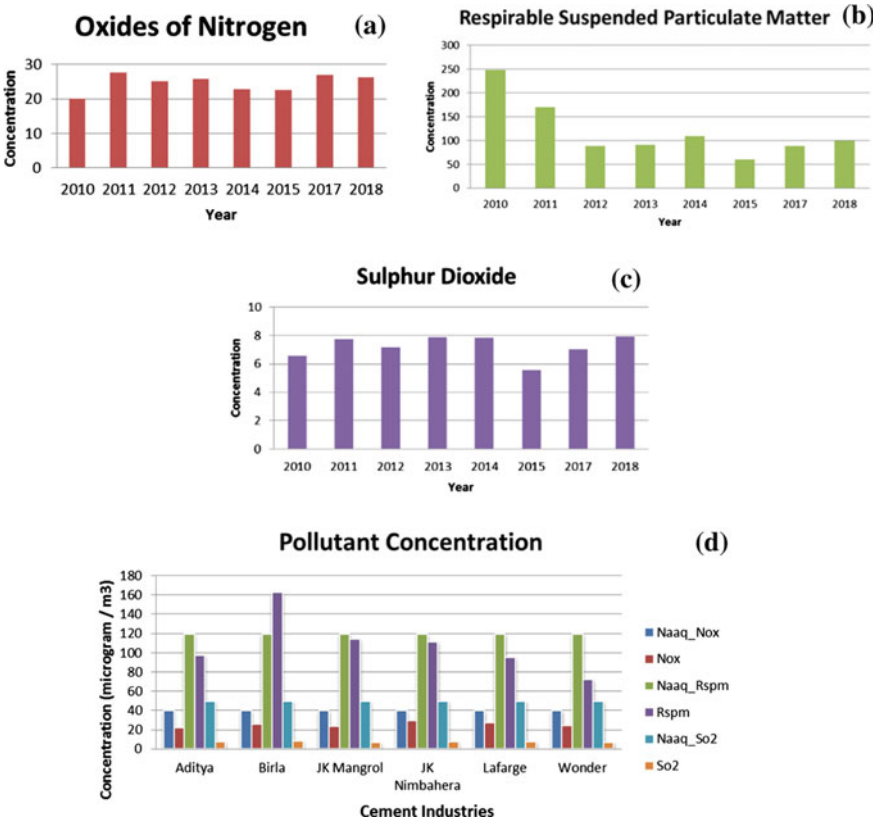

Fig. 22.8 **a**, **b** and **c** Average point source data (microgram/m3 concentration) of air quality. **d** Comparison of air quality data of each cement industries with national ambient air quality (NAAQ) data (*source* RSPCB, Jaipur)

22.5 Model Simulation, Calibration and Validation

It is a multi-test process based on real model-behavioral pattern. All datasets of from 2006 to 2018 year duration have been taken in the integrated model. The model has been initialized from year 2006 and simulated for about 40-year time span through system dynamics Stella computer software (other software viz.; Vensim, Powersim etc. can be used). The model simulation shows the interaction between agricultural land, mining area, wastelands, rainfall and groundwater level/fluctuation, air quality, water quality individually. The various interactions among the parameters/variable and their direct or indirect impacts on one another can also be observed in terms of pattern of behavior. After model simulation is performed, results of the simulated model can be generated in the form of tables and graphs for each parameters/variables of the system. The model has been calibrated and validated using intermittent datasets

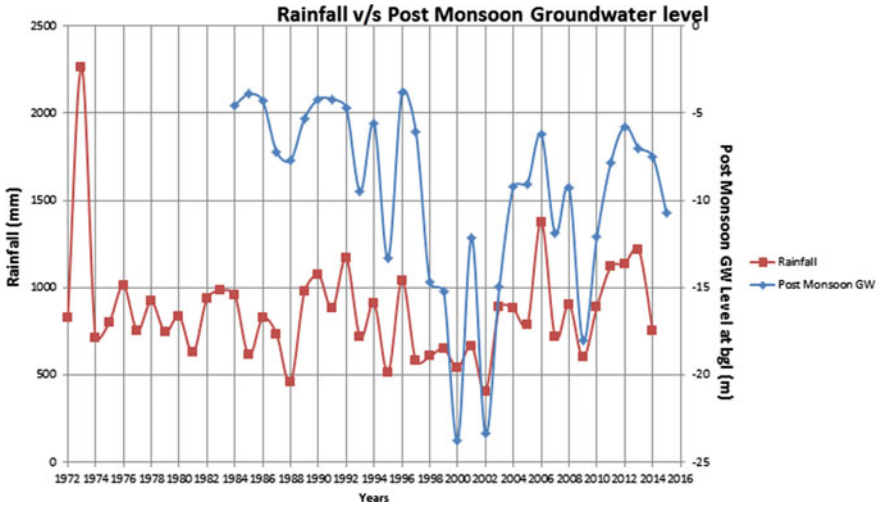

Fig. 22.9 Depiction of behavior of post monsoon ground water level with rainfall

standard procedure. The integrated model simulation graphs for major parameters are shown in Figs. 22.10, 22.11 and 22.12.

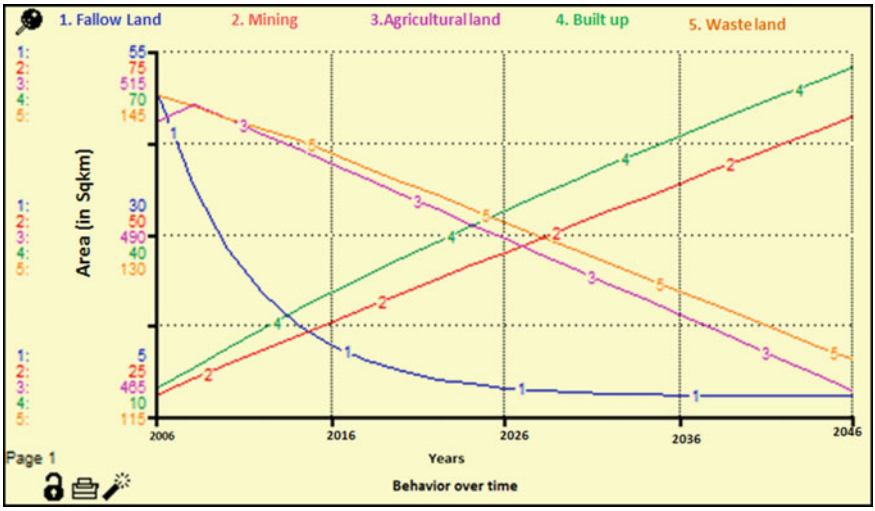

Fig. 22.10 Depiction of behavior of major LU/LC classes through model simulation

Fig. 22.11 Depiction of behavior of AQI, WQI and mining area through model simulation

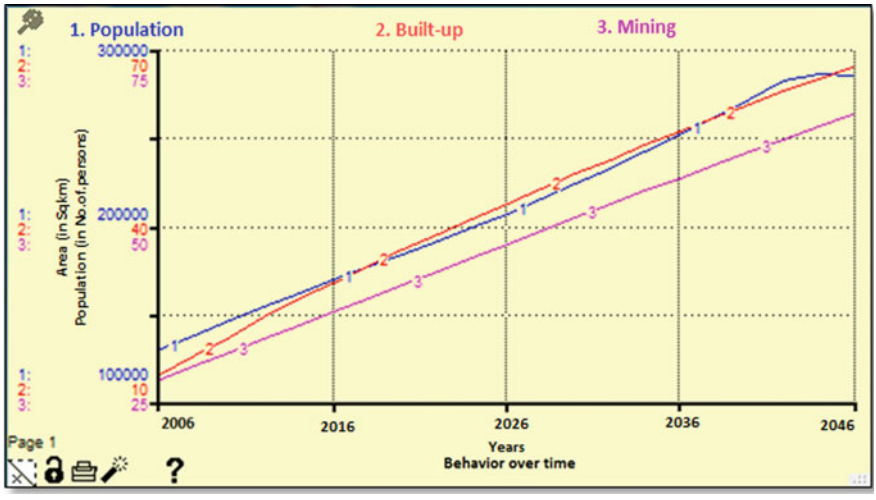

Fig. 22.12 Depiction of behavior of population, built-up area and mining area through model simulation

22.6 Summary

Usually environmental components like land, air, water etc. are studied as impact of mining activity individually, but the present approach has catered the holistic modeling approach considering air, land and water to analyze the linkages between various impacts linearly/non-linearly, directly/across, over a period of time span. In

the land module, remote sensing data provides reliable information due to its synoptic and temporal dimension and as well time and cost effective. Hence, the synoptic and temporal characteristics of remote sensing data provide better monitoring of LU/LC changes and its distribution in the surroundings of mining area. LU/LC analysis of temporal remote sensing data and the modeling of various individuals LU/LC classes with other collateral data provide the overall insight for past, present and future status of land environment or natural resources and anthropogenic activities. Thus, RS and GIS techniques are useful tools to assess the delicate areas like mining area vicinity for periodical monitoring, planning and for policy development. In case of air and water quality secondary data sources have been used for analysis and also used as input for the integrated model. From the model simulation, it is inferred that air and water quality index has improved over the period of time; but within the permissible limit of Central Pollution Control Board (CPCB) guidelines. System dynamics approach provides the whole view of the inter-connection of various factors capturing the linear and non-linear behavior of the system variables. Here, the integrated model has been simulated with the base run of 2006 year and projected up to a period of 40 years assuming that existing conditions will prevail in the future. This modeling approach would help the decision-makers to explore the changes in the surrounding area of mining or any other anthropogenic activities more comprehensively and it can be used as an aid to define policy actions for sustainable natural resources planning and management in the region. Therefore, the combination of system dynamics modeling and geospatial technology delivers the solutions for sustainable development based on the past, present and future scenarios.

Acknowledgements Authors are thankful to Director, National Remote Sensing Centre (NRSC), Hyderabad, India for encouraging and providing all sort of support for carrying out the described work. Authors are also grateful for the support provided by the staff members of Regional Remote Sensing Centre—West (RRSC-W), NRSC, Jodhpur. The various organizations and data providers like Rajasthan State Pollution Control Board (RSPCB) Jaipur, Rajasthan State Ground Water Department (RSGWD), Jodhpur, IMD, Bhuvan are gratefully acknowledged for providing various data sets.

References

Bhuvan (2022) Bhuvan-Indian geo-platform of ISRO. Available at https://bhuvan.nrsc.gov.in

Choi Y, Baek J, Park S (2020) Review of GIS-based applications for mining: planning, operation, and environmental management. Appl Sci 10(7):2266

CII (2010) Low carbon roadmap for indian cement industry. Confederation of Indian Industry, CII-Sohrabji Green Business Centre

Dlamini LZ, Xulu S (2019) Monitoring mining disturbance and resto-ration over RBM site in South Africa using landtrendr algorithm and landsat data. Sustainability 11(24):6916

Dolgner R, Brockhaus A, Ewers U, Wiegand H, Majewski F, Soddemann H (1983) Repeated surveillance of exposure to thallium in a population living in the vicinity of a cement plant emitting dust containing thallium. Int Arch Occup Environ Health 52(1):79–94

Forrester JW (1961) Industrial dynamics. MIT Press, Cambridge, Mass

Forrester JW (1969) Urban dynamics. The Massachusetts Institute of Technology press
Kariyawasam N, Raval S and Shamsoddini A (2014) Incorporating remote sensing as a tool to assist rehabilitation monitoring in a dolomite mining operation in South Australia. In: Proceedings of the xxv fig International Congress, Kuala Lumpur, Malaysia, pp 16–21
Kopeć A, Trybała P, Głąbicki D, Buczyńska A, Owczarz K, Bugajska N, Kozińska P, Chojwa M, Gattner A (2020) Application of remote sensing, GIS and machine learning with geographically weighted regression in assessing the impact of hard coal mining on the natural environment. Sustainability 12(22):9338
Maani KE, Cavana RY (2000) Systems thinking and modelling: understanding change and complexity. Prentice Hall, Auckland
Maps of India (2022) Map of India. https://www.mapsofindia.com/maps/rajasthan/rajasthanminerals.htm
Meadows D (2008) Thinking in systems: a primer. Earthscan
Mishra GP (1991) Impact of industrial pollution from a cement factory on water quality parameters at Kymore. Ecol Environ 9(4):876–880
Moomen AW, Dewan A (2017) Assessing the spatial relationships between mining and land degradation: evidence from Ghana. Int J Min Reclam Environ 31:505–518
Murugesan M, Sivakumar A, Jayanthi N, Manonmani K (2004) Effect of cement dust pollution on physiological and biochemical activities of certain plants. Pollut Res 23(2):375–378
NRSC (2006) Manual for national land use land cover mapping using multi-temporal satellite data. Report No. RCJ 04.9/PR/2008/AC1. Land Use Division, RS and GIS Application Area, NRSC, Dept. of Space, Govt. of India, Hyderabad
Sai VS, Mishra MP, Mishra GP (1987) Effect of cement dust pollution on trees and agricultural crops. Asian Environ 9(1):11–14
Sapiri H, Zulkepli J, Ahmad N, Zainal AN, Hawari NN (2017) Introduction system dynamic modelling and Vensim software. UUM Press, Malaysia
Shukla SK, Nagpure AS, Kumar V, Baby S, Shrivastava P, Singh D, Shukla RN (2008) Impact of dust emission on plant vegetation in the vicinity of cement plant. Environ Eng Manag J 7(1):31–35
Stephanie A (1997) Building a system dynamics model part 1: conceptualization. D-4597 Massachusetts Institute of Technology
Sterman JD (2000) Business dynamics: systems thinking and modeling for a complex world. Irwin McGraw-Hill, Boston, MA
Wanhui Y, Shuying Z, Changshan W, Wen L, Xiaodong N (2011) Analyzing and modeling land use land cover change (LUCC) in the Daqing City, China. Appl Geogr 31:600–608
World Commission on Environment and Development (1987) Our common future. Oxford University Press, Oxford
Xu Z, Coors V (2012) Combining system dynamics model, GIS and 3D visualization in sustainability assessment of urban residential development. Build Environ 1(47):272–287

Chapter 23
Geospatial Techniques for Archaeological Applications

Sudha Ravindranath, V. M. Chowdary, G. Sreenivasan, S. Pathak, Y. K. Srivastava, A. Vidya, K. Nagajothi, P. V. Vinod, B. Chandrasekaran, T. R. Nagashree, V. B. Manjula, and M. Arulraj

Abstract India is a culturally rich country with around 3700 monuments and heritage sites which are nationally important and few thousands of monuments of state importance. These heritage sites are cultural resource which is non-renewable needing conservation and protection. Generation of geospatial information and action

S. Ravindranath (✉) · A. Vidya · K. Nagajothi · P. V. Vinod · B. Chandrasekaran · T. R. Nagashree · V. B. Manjula
Regional Remote Sensing Centre-South, NRSC, ISRO, Bengaluru, Karnataka, India
e-mail: ravindranath-s@nrsc.gov.in

A. Vidya
e-mail: vidya_a@nrsc.gov.in

K. Nagajothi
e-mail: nagajothi_k@nrsc.gov.in

P. V. Vinod
e-mail: vinod_pv@nrsc.gov.in

B. Chandrasekaran
e-mail: chandrasekaran_b@nrsc.gov.in

T. R. Nagashree
e-mail: nagashree_tr@nrsc.gov.in

V. B. Manjula
e-mail: manjula_vb@nrsc.gov.in

V. M. Chowdary
Mahalanobis National Crop Forecast Centre, New Delhi, India

G. Sreenivasan
Regional Remote Sensing Centre-Central, NRSC, ISRO, Nagpur, Maharashtra, India
e-mail: sreenivasan_g@nrsc.gov.in

S. Pathak
Regional Remote Sensing Centre-West, NRSC, ISRO, Jodhpur, Rajasthan, India
e-mail: s_pathak@nrsc.gov.in

Y. K. Srivastava
Regional Remote Sensing Centre-East, NRSC, ISRO, Kolkata, West Bengal, India
e-mail: srivastava_yk@nrsc.gov.in

C. S. Jha et al. (eds.), *Geospatial Technologies for Resources Planning and Management*, Water Science and Technology Library 115,
https://doi.org/10.1007/978-3-030-98981-1_23

plans of the monuments requires the conjunctional use of both conventional and high-resolution satellite images, GIS and Global Positioning Systems and other geo-spatial techniques. To demonstrate the effective use of geospatial techniques, a project was taken up by Ministry of Culture, Government of India (GOI) and Indian Space Research Organization (ISRO), Department of Space (DOS) for Inventory and site management plans of national importance in the country (SMARAC). The project has been implemented by Regional Centres, National Remote Sensing Centre (NRSC) in collaboration with Archaeological Survey of India (ASI) and National Monument Authority (NMA). A systematic geodatabase of the inventory of heritage sites and monuments which comprises geo-coordinates, temporal high-resolution satellite images, field photos, total station survey data, sketch maps and other ancillary has been completed. An online Decision Support System (DSS) has been developed to improve the operational efficiency of inventory and generation of Site Management Plan (SMP) and other scientific activities of ASI and other stake holders. Webservices are exchanged between NRSC BHUVAN Geo-portal and NIC server for automatic geoprocessing/proximity analysis and help in decision making as a part of DSS. Customized mobile apps viz., SMARAC G2G and SMARAC CITIZEN have been developed exclusively for empowering the stake holders in augmenting geospatial database as well as the common public in obtaining online approvals for building construction. At present, most of the urban/town corporations across the country are using SMARAC CITIZEN App for processing their online NOC applications within a week's time. The book chapter discusses in detail the SMARAC project.

Keywords Monuments · Heritage sites · DSS · SMARAC G2G · SMARAC citizen

23.1 Introduction

Geospatial techniques play an important role in carrying out multitude of application projects for mapping and monitoring of natural resources. Remote sensing data has been used for archaeological studies as early as 1907 when Stonehenge was photographed from a balloon for understanding of the archaeological feature (Capper 1907). Remote sensing tools have been considered as a non-destructive as well as non-invasive tool preserving the monuments intact. (Sanger and Barnett 2021). Advancements in remote sensing especially different platforms viz., ground, balloon, air, space and the improvements in the cameras with better spatial resolutions has resulted in enormous collection and processing of archeological data that too from the twenty-first century (Cooper and Green 2016; Huggett 2020; Luo et al. 2019). Use of Airborne and Space borne remote sensing for cultural heritage applications has been dealt by (Osiciki 2000; Luo et al. 2019), in their works. Deodato

M. Arulraj
Bhuvan Geoportal & Web Services Area, NRSC, ISRO, Hyderabad, Telangana, India
e-mail: arulraj_m@nrsc.gov.in

et al. (2018) has opined that the increased use of digital techniques in archaeology is due to the improved sensors with high spatial resolutions for data capture and ease of accessibility of data and also the advancements in the integration and fusion of extracted information. Deroin et al. (2017) have synthetically mapped archaeological site and its environment using remote sensing techniques and advocated the use of very high-resolution imagery as vital tool for monitoring archaeological site in its widest context. Pappu et al. (2011) have extensively used geospatial techniques for prehistoric studies in Tamil Nadu and predictive location modeling aspects.

India is known for its culturally diversity from historic times. These is evident from innumerable art forms, traditions, practices, languages, sculptures, monuments, folk lore, structural designs etc. that exist in different parts of our country and are popularly known as monuments/heritage sites. These sites have attracted both national and international attention and acclaim and in turn has contributed significantly in the increase of tourism sector also. It is well known fact that these heritage sites face numerous risks mainly due to the urban growth, infrastructure development, policy changes of the government and ignorance of the public about the value of the sites which pose significant challenges for its conservation, preservation and management. Generation of a systematic geospatial database with development of management strategies are a must for conservation and preserving of archaeological sites/monuments. These SMPs need to be integrated with respective Master Plans of towns/cities which will ensure a balance between development and preservation of the archaeological sites, which in turn would ensure a balanced development of urban areas. The emergence of new digital technologies and Internet access together provide possibility for web-based information systems for preparing the catalogue of immovable monuments and its effective management.

Remote Sensing and GIS offer excellent tools for the mapping and monitoring of sites, particularly sites which are spread across large tracts/areas, provide synoptic views with their present status. These help in planning proper management strategies for its conservation and protection. A combination of conventional techniques along with advanced geospatial techniques are essential to monitor and map these heritage sites and monuments in an efficient manner.

23.1.1 Background

Generation of Inventory and management plan for heritage sites and monuments of national importance in the country is an unprecedented initiative backed by Ministry of Culture, GOI and ISRO, DOS. The project is implemented by NRSC in collaboration with ASI and NMA. Effective use of space technology for generating inputs for the following three broad areas under the purview of Ministry of Culture has been discussed in detail (Raj et al. 2017).

- Inventory and Geospatial database of heritage sites and monuments
- Geospatial visual tour of world heritage sites

- Predictive Locational Modelling in exploration archaeology in siting prospective archaeological locations.

Out of the above three broad areas, the first two are important operational activities and require urgent implementation due to rapid urbanization and economic development in the country which may pose serious threat of encroachment and damage to the invaluable monuments. A generic operational guideline is required to prepare the geodatabase and plans for the management of heritage sites for conservation, preservation and development. The present project was conceived with a scope to develop an operational methodology using satellite data with very high spatial resolution and geospatial technology to assist the ASI in developing a geospatial database of all nationally important archaeological sites and monuments. The major focus is to empower NMA with a decision support system to regulate the buffer zones around the monuments and heritage sites and with appropriate development.

23.2 Scope and Objectives

Under the project, an exhaustive inventory of the monuments has been undertaken. The geospatial database contains the following: Latitude and longitude coordinates of locations, temporal high-resolution satellite images, field photos, drawings, sketches, survey data, and other ancillary information.

The site management plan is an integrated planning concept which provides rules and procedures to be followed for conserving and protecting the site and developing the area around the site. The management plan should be modular, scalable, flexible and more thorough and complete with time. Depending on the usage at different levels, appropriate scale maps will be the part of management plan.

The massive job of generating the huge database and management plans of sites by conventional techniques is tedious, laborious and time consuming with lot of subjectivity. In the project, new digital technologies, open source Software tools, Web-based information systems have been used for generating the geodatabase of the monuments as well as preparation of management plans of immovable monuments, which can be scalable, adaptable and extendable to meet the needs of specific requirements of Culture and Archaeology. These geospatial databases on heritage sites can be used by concerned authorities like ASI, NMA and planning organizations for taking up effective management practices.

The major work component carried out as part of the project include the following:

Inventory of all the monuments and heritage sites under the authority of ASI using Remote Sensing, GIS and other techniques.

Preparation of Site Management plans for all the heritage sites and monuments based on ASI's Ancient Monuments and Archaeological Sites and Remains AMSAR 2010 act and GIS techniques

Development of tools web based and mobile based for effective utilization of the geodatabase

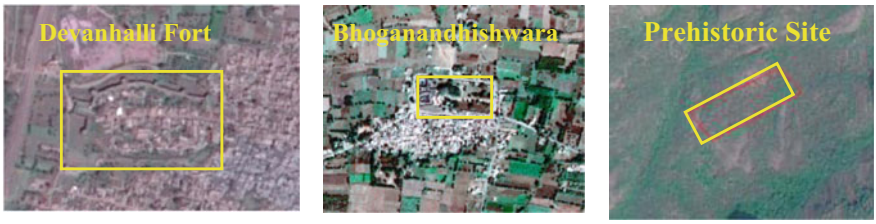

Fig. 23.1 Examples depicting a fort, monument and a prehistoric site in Karnataka

Using Bhuvan Geo-platform for hosting the ASI's heritage database for providing an access to numerous stakeholders.

The inventory has broadly three categories of objects viz. Monuments, Forts/group of building and Sites.

Monuments: They are works of art, architecture buildings/structures, inscriptions, caves, or combination of all the features, with heritage values from historical, artistic and scientific perspective.

Forts/Group of Buildings: Group of separate blocks or connected buildings with in a fort which have architecture and heritage value, homogeneity.

Sites: They are works of human and nature with immense value in terms of historic, aesthetics, ethnological or anthropological perspective.

Figure 23.1 depicts examples of fort, temple and a prehistoric site falling in Bengaluru ASI circle, Karnataka.

23.3 Database Preparation

As per ASI records, about 40 world heritage sites and around 3700 heritage sites and monuments having national importance are present across the country (Fig. 23.2). These monuments belonging from the prehistoric times to the colonial period to the modern times are spatially present in diverse topographical surroundings. These monuments can be temples, mosques, tombs, cemeteries, forts, architectural marvels, etc.

High resolution ortho-corrected satellite data forms the primary input data source for carrying out the inventory of monuments and delineation of the protected boundary of the monuments and heritage sites (Fig. 23.3) Other supplementary data available with ASI circle offices like the survey data (Fig. 23.4), the site maps (Fig. 23.5), gazette notifications, village cadastral maps, city survey maps, local planning area maps, the ASI officials field knowledge, GPS based surveys etc. also form the ancillary data sources.

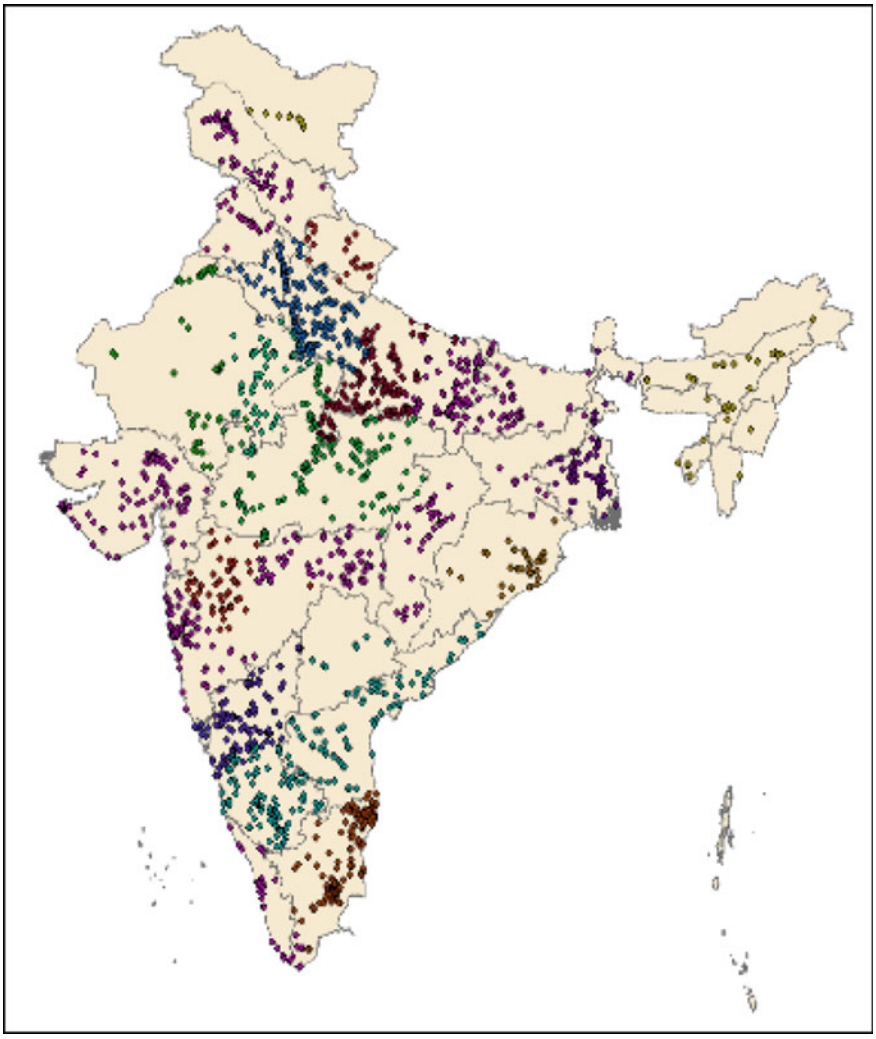

Fig. 23.2 Inventory of ASI Monuments across the country

23.4 Methodology

The high-resolution satellite database preparation included orthorectification, image enhancement and data fusion. The satellite data has been used for visualization, value addition and identification of monuments. Supplementary data viz., field survey, sketches, architectural plans etc. have been referenced and assigned real world coordinates. These collateral data along with satellite data of very high spatial resolution has been used for listing and identification of the protected boundaries of the monuments using visual interpretation techniques. Incorporating standard projection and

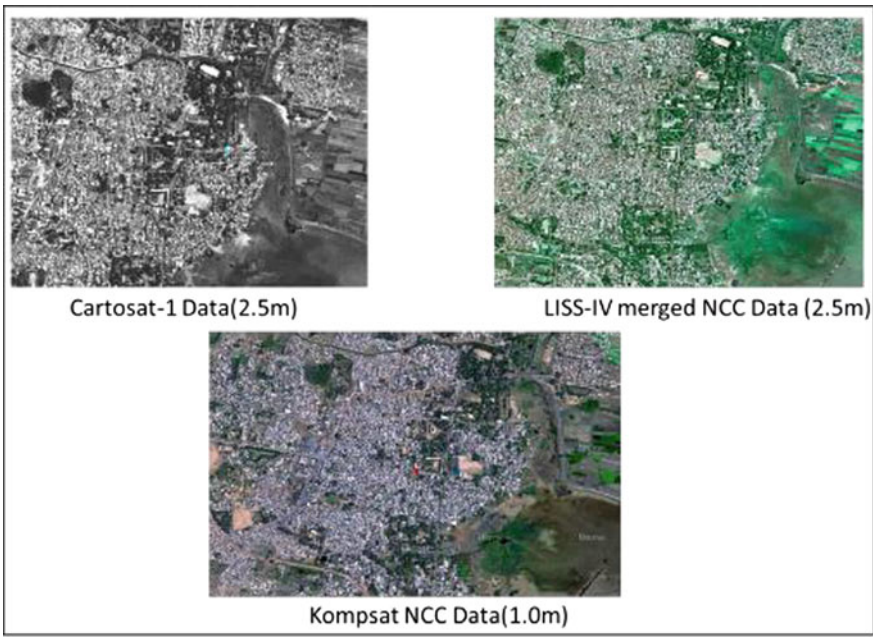

Fig. 23.3 High resolution satellite data of Kolaramma Temple, Karnataka

datum parameters the geospatial database has been created with a unique naming convention for both vector and raster files for each ASI circle. A unique monument number (10 characters) has been assigned to each monument which highlights the ASI circle, district and a continuous number. Thus, the geospatial database design supports a wide variety of spatial and aspatial which includes raster data, vector, autocad drawing files, image chips, and multi-user access for editing of the database. It is scalable as well as agile to address concept of ease of doing business and developmental activities without compromising the objective of conservation, preservation and sustainable management of heritage sites. A specific flag field is designed to know, if the monument is representing a single or multiple monument enclosed by a protected boundary.

23.5 Highlights of the Project

23.5.1 Inventory

To make a systemic and scientific listing of all the nationally important monuments falling under the jurisdiction of ASI in the country, identification and determining the accurate latitude and longitude of the monuments is essential. Such systematic

Fig. 23.4 Total station survey data Tippu palace, Karnataka

geodatabase has its use in various applications including preparation of the site management plans. The geo-coordinates of the heritage sites monuments are obtained by two methods.

1) By identifying a monument on orthorectified satellite image and logging the latitude and longitudes of the image (Fig. 23.6).
2) By customized GPS enabled mobile apps for determining the geo-coordinates of the monuments directly from the field either online or off line.

Under the project SMARAC G2G, a mobile APP using either internal GPS or GAGAN dongle integrated with smartphone was developed exclusively for ASI with many features for capturing coordinates, mapping management boundaries etc. When the app is installed on a smartphone, the coordinates of the locations are automatically captured as point data from a determined location of the monument along with a provision to capture the photographs of the monument.

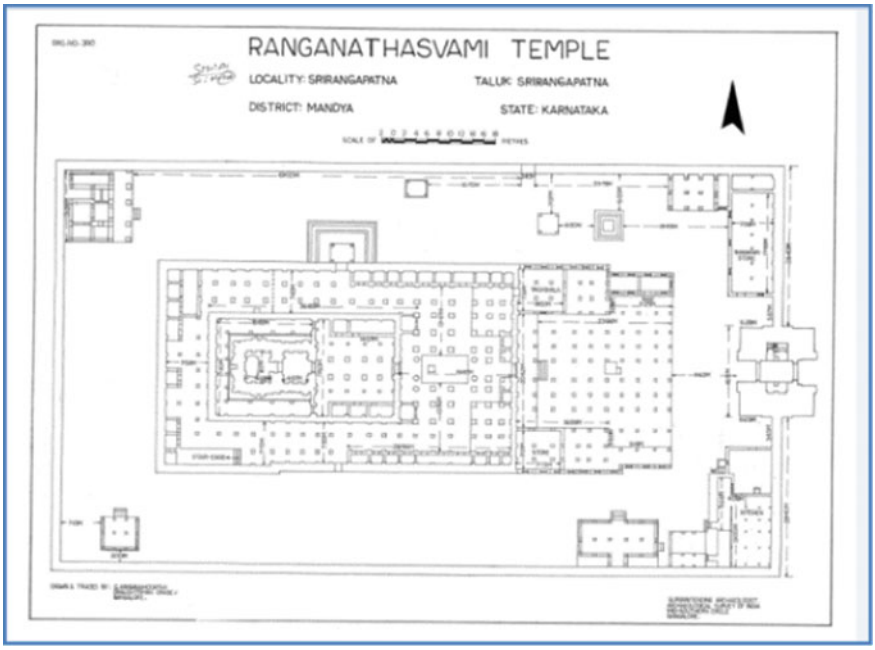

Fig. 23.5 Site sketch map: Ranganathaswami Temple, Karnataka

Fig. 23.6 Typical Monument inventory information Gomateswara statue, Sravanabelgola, Karnataka

23.5.2 Site Management Plans (SMP)

A heritage site/monument is a fragile and non-renewable cultural resource which requires protection of the environment and sustainable management around it. The protection of heritage sites in an area should be integrated in the planning process at national, regional or local levels depending on the importance of the heritage site

with reference to its physical dimensions and historic importance, popularity, tourist influx etc. Land use around a heritage site must be therefore controlled and developed to minimize the destruction of the heritage site. Management Plan of the sites (SMP) is essentially required to protect the monuments from the pressure of unregulated growth and development. Generally, SMPs are prepared using ground surveys, but with availability of very high resolution, it is possible to delineate SMP of monuments with ground knowledge. Three management/buffer areas are delineated around every monument/heritage site using GIS tools. These areas have been defined as per the AMASR 2010 Act of the Government. The management zones and their significance with respect to heritage bye laws are explained below.

23.5.2.1 Protected Area and Its Delineation

It is the main zone enclosing the monument with its various components. This is directly under the full administrative control and ownership of ASI. Every feature/object falling in this zone is fully protected and preserved exclusively by ASI.

This is very important and critical boundary which has to be precisely delineated with the aid of high-resolution satellite data (Fig. 23.7) and spatial and aspatial collateral data with the full field knowledge of ASI officials. Delineation of other two management boundaries viz., prohibited and regulated boundaries solely depend on the accuracy of protected boundary. Any error in the protected boundary would carry forward to these two boundaries also. Hence, it is extremely important to delineate the protected boundary as accurately as possible with the assistance of all the available data sources and techniques. The heritage site area foot print synonyms with protected area which can be identified by adopting any of the three methods suggested or in combination.

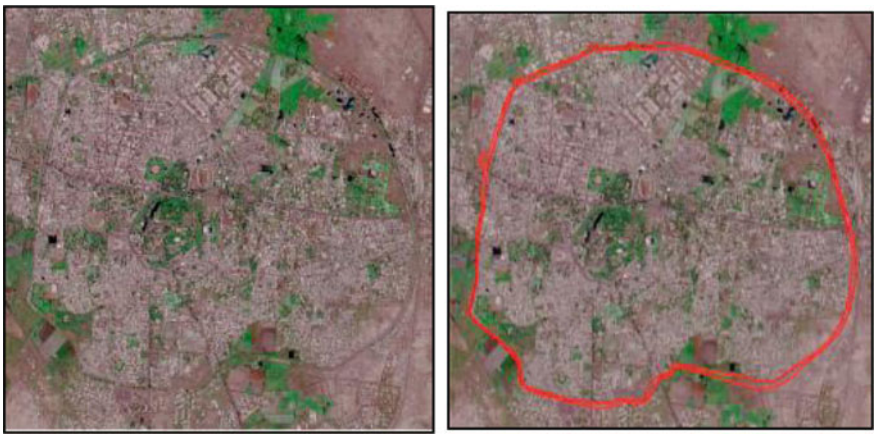

Fig. 23.7 Protected boundary of Bijapur fort walls delineated using high resolution satellite data

Fig. 23.8 Protected boundary delineation using total station data: Praneshvara temple, Shimoga

SMARAC G2G APP: It is mobile app based on GPS is established for this project. The geocoordinates of the polygon nodes of the protected boundary are captured in the ground while traversing around the heritage site/monument and on fly, the vector is generated on the mobile phone display as well as on the central server with the high-resolution image in the background to assess the correctness and to validate the boundary.

To effectively use the app in delineating the protected boundary, a prior knowledge of the ASI official of the boundary based on the land marks on ground and interpretation of high-resolution satellite data are required.

It is also possible to superimpose the protected boundary vector derived from the georeferenced total station data or the site maps of the concerned monument (Fig. 23.8) and edit based on the high-resolution image base to fix the boundary as accurately as possible.

23.5.2.2 Prohibited Area and Its Delineation

A 100 m buffer area around the protected area of a heritage site/monument is termed as prohibited area. Any kind of development or modification in conflict with the heritage site/monument ambiance is not allowed or permitted. Only repair works to maintain the existing structures/features are allowed as per the heritage by laws.

Prohibited area is designated as area near or adjoining a protected as per the heritage by laws and is declared to be a prohibited area for purposes of excavation or construction. An area up to 100 m from the limits of protected area boundary around a heritage site is declared as prohibited area. The prohibited area boundary is delineated by creating a buffer of 100 m from the protected boundary of the monument/heritage site using GIS functionality.

23.5.2.3 Regulated Area and Its Delineation

An area of 300 m buffer around the protected area is defined as regulated area. The development in this zone is regulated as per the heritage by laws.

Regulated area is designated as an area near or adjoining a prohibited area as per the heritage by laws. It is an area declared as regulated zone for the purpose of excavation or construction. As per the bylaws, it is declared as 200 m beyond the prohibited area. The regulated area boundary is delineated by creating a buffer of 200 m from the prohibited boundary of the monument/heritage site using GIS functionality.

The protected, prohibited and regulated boundaries for a monument are shown below in red, yellow and green vectors burned on the image as vectors. As shown in Fig. 23.9

23.5.3 Geo-Tagging

Geotagging is a method of adding geographical identification metadata for various features located inside the management zones for a monument/heritage site such as a geotagged photograph or video. Geotagged features are nothing but features which have geographical latitude and longitude information. Apart from this they will have information on the altitude, direction, accuracy of data, place names of the features such as public buildings. The houses located inside the prohibited and regulated zones were geotagged using Bhuvan POI App. Figure 23.10 depicts the

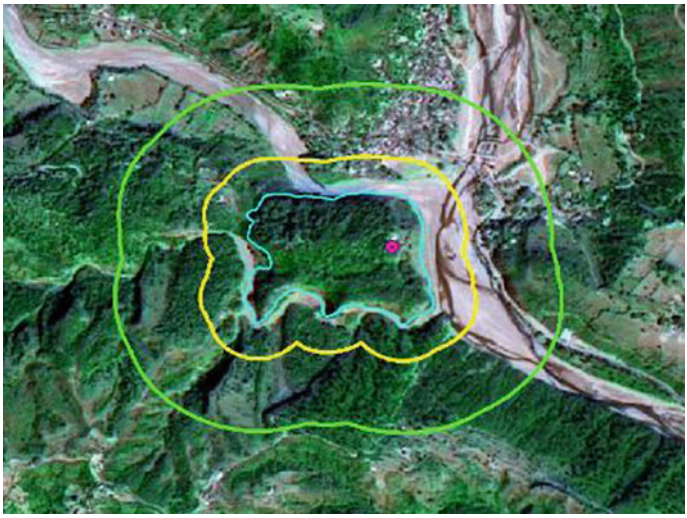

Fig. 23.9 Protected, prohibited and regulated boundaries for Fort Kotla, Kotla, Shimla circle

Fig. 23.10 Geotagging of features inside regulated boundary for Srirangapatna, Bangalore ASI circle, Karnataka

geotagging of features within regulated boundary of Srirangapatna, Bangalore ASI circle, Karnataka.

23.5.4 Outputs

Geospatial database has been generated for all the 30 ASI circles of nearly 3700 monuments within the country with inventory, site management plans, field photographs, and the location details. Typical geospatial outputs generated for Hampi monuments are shown in Fig. 23.11

For a few monuments, 3D models have been constructed from the field photographs collected of the temple to give a realistic view of the temple. Figure 23.12 gives a 3D model of Tippu Palace of Bangalore ASI Circle and Fig. 23.13 gives a 3D model of the buildings within the SMP of Someshwara temple in Bangalore ASI circle.

23.5.5 Geospatial Database of Monuments in BHUVAN Geoportal

The geodatabase of monuments has been ported onto BHUVAN platform of Indian Space Research Organization (ISRO) (Fig. 23.14). BHUVAN hosts at present through its URL http://bhuvan.nrsc.gov.in, a variety of applications and services that caters to seeing of multi-dates and multi-platform, different sensor satellite data, various thematic maps, tools for querying and analysis, free satellite services for disaster applications, data downloads and products, mobile based apps for variety of geospatial applications. The raster datasets are stored as part of BHUVAN database and

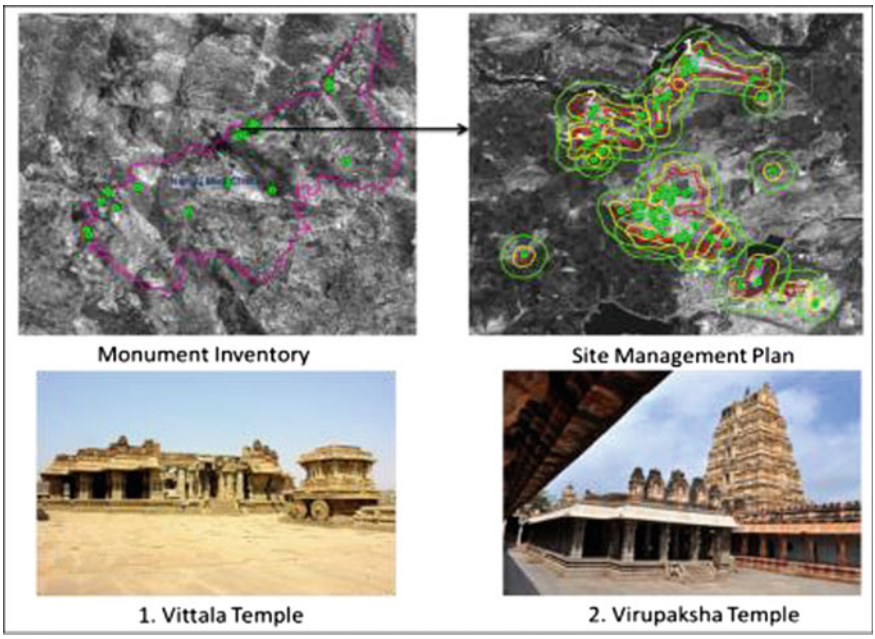

Fig. 23.11 Geo-spatial outputs of world heritage site at Hampi, Hampi mini circle

Fig. 23.12 3D model of Tippu palace, Bangalore ASI circle

served through web Services of BHUVAN. The vector datasets of the heritage sites are stored in BHUVAN Server and in Postgres SQL RDBMS using an Add-on module PostGIS. This facilitates the geoprocessing, identify and querying database. The advantage of storing the datasets in RDBMS is to maintain data security and

Fig. 23.13 3D building models within site management area of Someshwara Temple, Kolar, Bangalore ASI circle

Fig. 23.14 Monuments webpage in BHUVAN

integrity and in addition, indexing facilitates for fast retrieval of information from large database.

23.6 Applications of Geodatabase

The geodatabase on monuments of ASI is an important milestone database of ASI hosting both inventory and Site Management Plans information of the monuments. The database is now being regularly used for Decision Support Service for National Monument Authority.

23.6.1 Decision Support Services

To enhance the operational efficiency and improve the turnaround time of building plan approval process within the vicinity of heritage sites as per the heritage by laws, geospatial decision support system is conceived using the inventory database and mobile based applications. This has been specifically designed for National Monument Authority, NMA whose mandated task is to evaluate the effect of huge infrastructure development projects both private and public which might be proposed in the regulated area/prohibited area. Based on their evaluation, NMA has to recommend the Competent Authority for giving permission grant of NOC for any constructional activities.

To arrive at a single window clearance for building/construction purpose, a common application form is designed and available on the portals of NMA integrated with the online portal of planning bodies of Delhi, viz., National Delhi Municipal Corporation. NMA checks the location of applicant's property with respect to the SMP of the monument. The applicant needs to fill up a single form which will be sent online to the concerned departments from where No Objection Certificate (NOC) is to be obtained. NMA will inform its decision to the planning body within six working days. This has drastically reduced the time limit from 90 days which has been prescribed according to (AMASR) governmental Act. The progress of the application can be tracked by the applicant online and there is no requirement for any physical presence or visit to any office in this regard. However, Single Window Clearance System does not consider large projects involving construction of building beyond 2000 m^2. Figure 23.15 gives the working of the NOC application process. Online NOC application processing system consists of three major sub systems viz; SMARAC Citizen App, NMA NIC server and BHUVAN Geoprocessing module.

23.6.1.1 SMARAC CITIZEN Mobile App

SMARAC CITIZEN mobile application is developed to enable 'Ease of doing Business'. Any citizen/user desiring to get the building plan approved within the vicinity of a heritage site can use the mobile app to get the approval. It uses the database that will be created through the Smart SMARAC app or by other procedures and facilitate online NOC application processing for construction activities around the protected national monuments by individuals or companies/organizations in a transparent and efficient way.

SMARAC CITIZEN app consumes web services provided by the NMA NIC server for user authentication and GPS data uploading. NMA NIC server uses the web services provided by the BHUVAN Geoprocessing module and sends the GPS data received from the citizens by the SMARAC CITIZEN app to the BHUVAN server for further geoprocessing (Fig. 23.16).

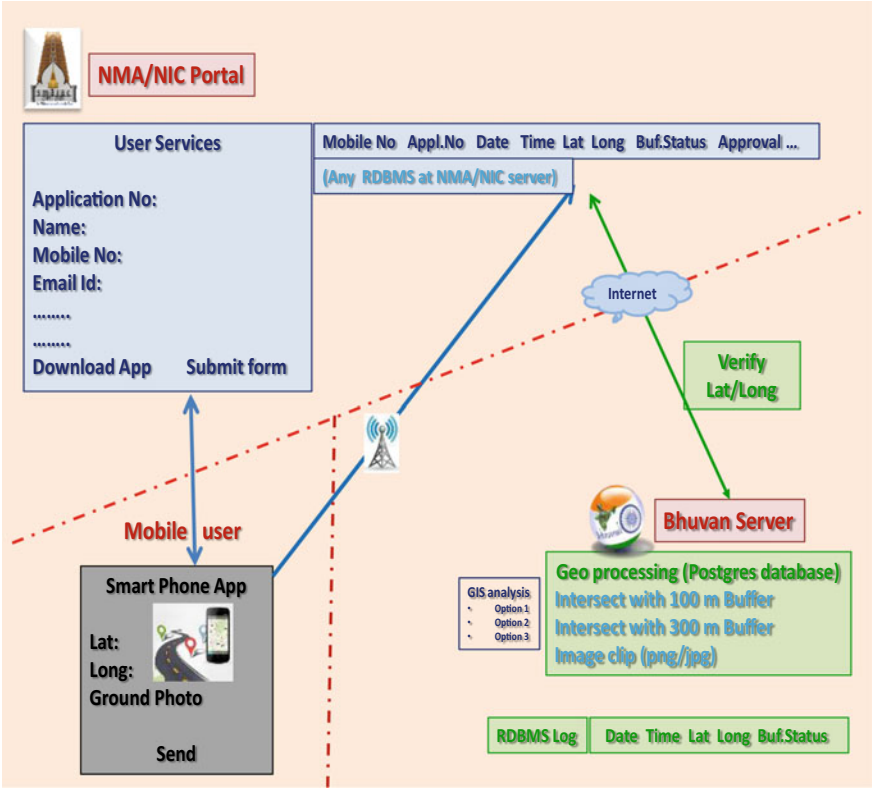

Fig. 23.15 Design concept of NOC clearance by NMA, BHUVAN and SMARAC CITIZEN (Raj et al. 2017)

23.6.1.2 Auto Geo-Processor

This is the core of the DSS whose process flow is explained below. When the user or a citizen accesses the NMA portal and register to identify himself to obtaining permission/guideline, the mobile number will act as a link for further common communication.

After registration, user is advised to download the mobile application, using which he can capture and send the geographic co-ordinates of the location (for which the permission is sought), along with ground photograph (optional). The co-ordinates and the user details are stored in a database at NMA portal. Authorized NMA official can access this database to VERIFY the proximity of the location with the monuments/archaeological sites around. The software application, at NMA server, connects to the spatial database generated and stored at BHUVAN portal to obtain the proximity result by automatic geoprocessing.

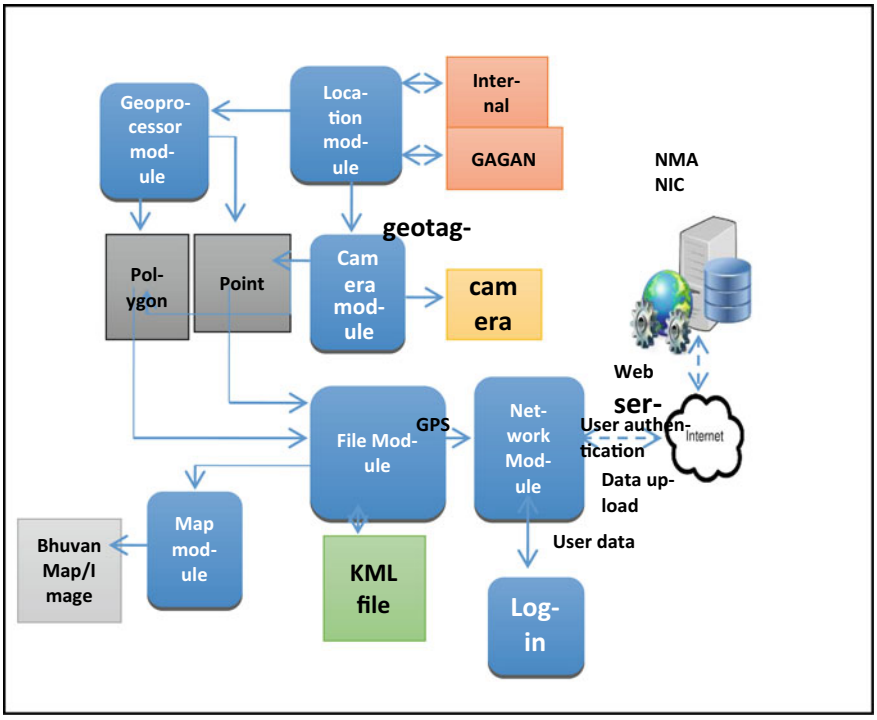

Fig. 23.16 SMARAC CITIZEN app architecture

Based on the proximity status flagged by the automatic geoprocessing result, ASI officials take appropriate decision and send back the permission/guideline to the respective user. The log is stored in the database with date/time/decision taken, etc.

23.6.2 Landuse/Landcover Within SMP

The geodatabase of the monuments when integrated with thematic databases available in BHUVAN viz., Landuse/Landcover, Transportation, water bodies, etc. generated under various national application projects offers wealth of information about the site location, its land use/land cover within the site management plan area (300 m buffer). The temporal changes in landuse/landcover offers a direct or indirect indication about the possible impacts faced by the monuments in terms of urban growth/sprawl (Elfadaly 2018) flooding hazard (if it is located on the banks of river/water body), pollution if it is located close to an industrial area, etc. Transportation network and other ground information about the amenities etc. also helps in improving the tourist potential of the sites.

Fig. 23.17 SMP of Amruteswara temple, Annigere in Dharwad ASI circle, Karnataka along with the LULC

A study was carried out for six ASI monuments located in Dehradun ASI circle where the landuse/landcover changes were studied over time to assess the impact of urbanization. The tourism potential of the sites have been evaluated based on physical, social, and environmental parameters using weighted ranking method, a popular multi-criteria decision making tool and suitable measures have been suggested to enhance the tourism potential of the sites (Ravindranath et al. 2017) Fig. 23.17 depicts the LULC of the SMP area around Amruteswara temple, in Dharwad ASI circle. The LULC data helps in characterizing the monument as facing urban growth pressure.

23.6.3 Predictive Locational Modeling

From the generated geodatabase, the sites are being characterized with reference to its geographical location, architecture, historical significance, thematic resources in the surrounding, and other parameters to identify relevant patterns in association with the help of ASI field teams. Predictive location modeling studies Pappu et al. (2010a, 2010b), Nsanziyera et al. (2018), is being planned to identify other culturally important areas based on the known patterns.

23.7 Way Forward

Disaster Risk Management (DRM) for cultural heritage is a complex task that requires multiple inputs (Agapiou 2020; Gainullin 2016). Remote sensing plays a vital role in generating critical inputs for DRM. A heritage risk assessment of all the monuments under ASI Hampi Mini circle was undertaken using geospatial techniques. (Aishwarya et al. 2019). Efforts are underway for studying the vulnerability of the

monuments ASI circle wise and also possible disaster mitigation plans of a few major monuments spread across diverse landforms and historical setting.

Cultural heritage sites in this project has been mapped mostly using visual interpretation techniques. From the project it is seen that, cultural heritage sites are of diverse form and nature viz., buildings/structures, prehistoric sites, forts, mounds, pillars etc. The size of the monuments varies from few m^2 to few hundred m^2. Tapping the fact that heritage sites have typical patterns in terms of its building architecture, size, extent, shape, geographical setting and other characteristics, it is being planned to take up Object Based Image Analysis (OBIA) and Deep Learning based techniques for mapping the cultural heritage sites of considerable dimension with set patterns and geographical setting. This will automatize the process of inventory of the monuments in our country, where there are thousands of unprotected monuments which do not have any documentation at all and is being lost over the years due to unplanned urban growth. For mapping of unprotected monuments in rural and semi-urban landscapes, plans are underway for the use of multi-source data from satellite, aerial, and UAV platforms (Valenti et al. 2021), along with LiDAR data for spectral and spatial characterization of heritage sites. The use of LIDAR for constructing the 3D models (Erenoglu 2017), is also being explored for a few architecturally important monuments.

Acknowledgements It is our privilege to thank Former Chairman ISRO, Dr. Kiran Kumar, Sri. N. K. Sinha, Secretary, Ministry of Culture and Dr. Rakesh Tewari, Director General, ASI for providing constant encouragement and support for the project's initiation and execution. The guidance provided by Dr. Y. V. N. Krishna Murthy, former director of NRSC is duly acknowledged. We are highly grateful to Shri Uday Raj (Former CGM, Regional Centres, NRSC/ISRO) for the project formulation and execution of the project across all RCs and continued support of Dr. K. Ganesha Raj (Former GM, RRSC-South, NRSC/ISRO), during the entire project execution. The support offered by BHUVAN team for hosting the database in BHUVAN is duly recognized and acknowledged. The multimedia support provided by Shri. M. L. Ramachanadra (retired scientist, RC-South) is gratefully acknowledged. With a deep sense of gratitude, the support provided by Member, NMA and the officials from NIC in implementing the modules for issuing the NOCs is acknowledged. We acknowledge the support provided by the SMARAC team members from 4 RCs viz., Smt. Anju Bajpai, Shri. Arun Suryavanshi, Shri. Hansraj Meena, Shri. M. B. Rana, Smt. Sadhana Jain and Shri. Shambu Singh Tak. We offer our sincere thanks to all the General Managers and Dy. General Managers of RCs viz. RC-South, RC-East, RC-West, RC-Central and RC-North for their constant support in the smooth project execution. The efforts of Regional Directors, Superintending Archaeologists, Dr. Aloni and other officials from 30 ASI Circle Offices, is gratefully acknowledged for their constant cooperation throughout the project execution and in successful completion of the project.

References

Abdelaziz E, Attia W, Qelichi MM, Murgante B, Lasaponara R (2018) Management of cultural heritage sites using remote sensing indices and spatial analysis techniques. Surv Geophys 39:1347–1377. https://doi.org/10.1007/s10712-018-9489-8

Aishwarya P, Sudha R, Vidya A, Raj G (2019) Risk assessment of heritage sites and monuments of Hampi World Heritage site using geospatial techniques. In: Proceedings of 38th international congress, conference on INCA, https://www.researchgate.net/publication/338095852_38_th_inca_international_congress

Ancient Monuments and Archaeological Sites and Remains AMSAR 2010 ACT, www.nma.gov.in

Agapiou A, Lysandrou V, Hadjimitsis DG (2020) Earth observation contribution to cultural heritage disaster risk management: case study of Eastern Mediterranean open air archaeological monuments and sites. Remote Sens 12:1330. doi: https://doi.org/10.3390/rs12081330, www.mdpi.com/journal/remotesensing

Capper J (1907) Photographs of Stonehenge as seen from a war Balloon. Archaeologia 60:571, Plates 69–70, cited in Fowler (1996)

Cooper A, Green C (2016) Embracing the complexities of 'big data' in archaeology: the case of the english landscape and identities project. J Archaeol Method Theor 23(1):271–304. https://doi.org/10.1007/s10816-015-9240-4

Deiana R, Leucci G, Martorana R (2018) New perspectives on geophysics for archaeology: a special issue. Surv Geophys 39:1035–1038. https://doi.org/10.1007/s10712-018-9500-4

Deodato T (2018) Remote sensing and geosciences for archaeology. Geosciences 8:41. doi: https://doi.org/10.3390/geosciences8020041, www.mdpi.com/journal/geosciences

Deroin JP, Kheir RB, Abdallah C (2017) Geoarchaeological remote sensing survey for cultural heritage management. Case study from Byblos (Jbail, Lebanon). J Cult Heritage 23:37–43

Erenoglu RC, Akcay O, Erenoglu O (2017) An UAS-assisted multi-sensor approach for 3D modeling andreconstruction of cultural heritage site. J Cult Heritage 26:79–90

Gainullin II, Khomyakov PV, Sitdikov AG, Usmanov BM (2016) Study of anthropogenic and natural impacts on archaeological sites of the Volga Bulgaria period (Republic of Tatarstan) using remote sensing data. In: Proceedings volume SPIE 9688, fourth international conference on remote sensing and geoinformation of the environment (RSCy2016); 96880Z, https://doi.org/10.1117/12.2240728

Huggett J (2020) Is big digital data different? towards a new archaeological paradigm. J Field Archaeol 45(sup1):S8–S17. https://doi.org/10.1080/00934690.2020.1713281

Luo L, Wang X, Guo H, Lasaponara R, Zong X, Masini N, Wang G, Shi P, Khatteli H, Chen F, Tariq S, Shao J, Bachagha N, Yang R, Yao Y (2019) Airborne and spaceborne remote sensing for archaeological and cultural heritage applications: a review of the century (1907–2017). Remote Sens Environ 232:111280. https://doi.org/10.1016/j.rse.2019.111280

Nsanziyera AF, Rhinane H, Oujaa A, Mubea K (2018) GIS and remote-sensing application in archaeological site mapping in the Awsard area (Morocco). Geosciences 8:207. doi:https://doi.org/10.3390/geosciences8060207. www.mdpi.com/journal/geosciences

Osicki A (2000) A review of remote sensing application in archaeological research geography, vol 795, no 28(333). Accessed at www.yumpu.com/en/document/read/27431073/a-review-of-remote-sensing-application-in-archaeological-research. Accessed on 21 Nov 2021

Pappu S, Akhilesh K, Ravindranath S, Raj U (2011) From stone tools to satellites: recent research into the prehistory of Tamil, Ancient India, bulletin of the archaeological survey of India. New Series 1:87–100

Pappu S, Kumar A, Ravindranath S, Raj U (2010a) Applications of satellite remote sensing for research and heritage management in Indian prehistory. J Archaeol Sci. doi:10.https://doi.org/10.1016/j.jas.2010.4.005

Pappu S, Kumar A, Ravindranath S, Raj U, Gunnell Y (2010b) Research and management of paleolithic resources in Tamil Nadu, South India, Antiquity Project Gallery online, 2010, http://antiquity.ac.uk/projgall/pappu325/

Raj U, Sinha NK, Tewari R (2017) National scale inventory and management of heritage sites and monuments: advantages and challenges of using geospatial technology. Curr Sci 113(10). Accessed 25 Nov 2017

Sanger M, Barnett K (2021) Remote sensing and indigenous communities: challenges and opportunities. Adv Archaeol Pract

Sudha R, Vidya A, Bukadia P, Raj U (2017) Geospatial techniques for heritage site monitoring and evaluation of tourism potential in Uttarakhand. https://a-a-r-s.org/proceeding/ACRS2017/ID_753_1652/1012.pdf

Valenti R, Paternò E (2021) 3D integrated survey for the study of archaeological sites: the case study of Euryalus Castle in Siracusa. IOP Conf Ser Earth Environ Sci 767:012015. IOP Publishing doi: https://doi.org/10.1088/1755-1315/767/1/012015

Chapter 24
Site Suitability for Sewage Treatment Plant and Routing Using Geospatial Technology—A Case Study for Two Indian Towns

Dibyendu Dutta, Tanumi Kumar, Chiranjivi Jayaram, Debasish Chakraborty, Arati Paul, Niraj Priyadarshi, Wasim Akram, and C. S. Jha

Abstract Siting wastewater treatment systems is one of the vital components that need spatially-referenced and up-to-date data for effective planning, management and environmental protection. Most commonly used geo-indicators for siting sewage treatment plants (STP) are landuse, surface slope, soil hydrology, ground water table, river/streams, water bodies, sensitive features, urban sprawl and its direction along with the prevailing wind pattern. In the present study, surface hydrological, topological and landuse parameters were generated from high resolution satellite data and multi-criteria analysis was implemented for site suitability. The candidate STP locations were further constrained by the regulatory norms, in the form of buffer zones and examined with respect to the annual wind condition. In the first step, a well-defined spatial criterion was used while in the second step, prioritization was done on already finalized candidate sites so as to address conflicts and ambiguity in a rational manner. In both Rayagada and Siddipet towns, the identified location lies in the south-west of the town, outside the urban perimeter, dominated by wastelands but the slope varies from 1% in Rayagada to 1–3% in Siddipet. For both the towns, prevailing wind is from west and 'calm' prevails less than 3% of time on annual basis. As the urban sprawl is mostly in the north-east direction with respect to the proposed STP site, the harmful gases or foul odor are presumed to have less impact on urban settlement. Besides site suitability, network analysis was also performed for sewage collection and transport to the pre-defined STP site. Shortest path algorithm was used to obtain the optimal route that has least distance between source and destination

D. Dutta (✉) · T. Kumar · C. Jayaram · D. Chakraborty · A. Paul · N. Priyadarshi
Regional Remote Sensing Centre—East, NRSC/ISRO, Kolkata 700156, India
e-mail: ddisro@gmail.com

W. Akram
Vidya Sagar University, Midnapore, West Bengal, India

C. S. Jha
National Remote Sensing Centre, ISRO, Balanagar, Hyderabad, India

C. S. Jha et al. (eds.), *Geospatial Technologies for Resources Planning and Management*, Water Science and Technology Library 115,
https://doi.org/10.1007/978-3-030-98981-1_24

nodes. The ideal locations for STP, along with sewage routing are presented in the form of a map with supporting themes for decision support.

Keywords Sewage treatment plant · Site suitability · Satellite data · Remote sensing · GIS · Multi-criteria · Network analysis

24.1 Introduction

Wastewater treatment is a process of removing the contaminants from wastewater to produce treated effluent and solid waste or sludge that is suitable for discharge to the surrounding environment or an intended reuse application. This process helps to prevent water pollution from raw sewage discharges (Khopkar 2004). The sewage contains a mixture of domestic waste matter, effluents discharged from industries and urban runoff. In general, all the sewage treatment plants (STP) include physical, chemical and biological processes to remove physical, chemical and biological contaminants, respectively. A recent study estimated that globally, about 52% of sewage is being treated (Jones et al. 2021). However, dismal scenario is observed for different countries around the world. For instance, while high-income countries treat approximately 74% of their sewage, developing countries treat an average of just 4.2% (Jones et al. 2021). Data of 2020 for 128 countries showed that only 66% of all domestic wastewater flows were collected at treatment facilities (UN-Water 2021). As per population in 2001 Census, all Class I cities and Class II towns together produce an estimated 29,129 million liters per day (MLD) of sewage. In contrast, the existing sewage treatment capacity is only 6190 MLD, with an additional 1742.6 MLD is anticipated. Still there is a gap of 21,196 MLD (72.7%) between sewage generation and existing sewage treatment capacity. Assuming 30% decadal growth in urban population, the sewage production will be 33,212 MLD in 2020. In addition, considering the actual capacity utilization of STPs as 72.2%, only 13.5% of the sewage is being treated in India. The above discussion clearly indicates that the inappropriate location of STPs is the main cause of pollution in the rivers and lakes. There is an urgent requirement for increasing the sewage treatment capacity and its optimal use for improving the quality of water in the rivers and lakes. United Nations agenda for Sustainable Development (2015) adopted resolution with a set of goals to end poverty, protect the environment and ensure prosperity for all. The agenda includes 17 Sustainable Development Goals (SDGs), each with specific targets to be achieved over a 15-year period (UNGA 2015). SDG 6.3 recommends improving water quality by decreasing pollution, eradicating dumping and reducing discharge of harmful chemicals and materials, thereby, halving the amount of unprocessed wastewater and considerably increasing recycling and safe reuse worldwide by 2030 (Ritchie et al. 2018). In India Atal Mission for Rejuvenation and Urban Transformation (AMRUT) has earmarked the policy guidelines for implementation of wastewater reuse infrastructure solutions in selected towns and cities. Hence, keeping in view the long-term population growth and the broadening gap between sewage generation

and treatment capacity as well as the UN agenda, the decision makers are required to make a very thoughtful action plan in a limited time frame. In the context of the above-mentioned challenges, a new paradigm for waste management has arisen, changing attention to resources' efficacy and reduction of environmental impacts throughout the life cycle of waste management (Chalkias and Lasaridi 2011).

Siting wastewater treatment systems is one of the vital components that needs spatially-referenced and up-to-date data for effective wastewater planning, management and environmental protection. Most commonly used geo-indicators are landuse, surface slope, soil hydraulics, ground water table, river/streams, water bodies, sensitive features, urban sprawl and its direction as well as the prevailing wind pattern. A Geographic Information System (GIS)-based decision support system will aid in identifying key socioeconomic and environmental factors, and find a more comprehensive and suitable way to optimize the locations for STPs that are appropriate for different local conditions.

The objective of this study is to optimize the location of STPs by integrating GIS with local factors by adopting selection criteria based on technical, environmental and topographic factors. In the first step a well-defined spatial criteria was used while in the second step prioritization was done on already finalized candidate sites so as to address conflicts and ambiguity in a rational manner. GIS-based multi-criteria analysis was used as decision model to finalization of site suitability. Besides site suitability a network analysis was also performed for sewage collection and transport to pre-defined STP site.

24.2 Type of Wastewater Treatment Plants

There are several types of wastewater treatment processes viz., (i) Effluent Treatment Plants (ETP) (ii) Sewage Treatment Plants (STP) and (iii) Common and Combined Effluent Treatment Plants (CETP). ETPs are meant for purifying pharmaceutical and industrial waste water from high amounts of organics, debris, dirt, grid, pollution, toxic and non-toxic materials, polymers, etc. STP unit removes contaminants from municipal or domestic sewage. Precisely, ETP is employed in industrial areas whereas STP cleanses household water. CETP's are set up in the industrial estates where there are clusters of small-scale industrial units that host many polluting industries. The Ministry of Environment, Forest and Climate Change, Govt. of India, has launched the centrally sponsored scheme, namely, Common Effluent Treatment Plant (CETP) in order to make a cooperative movement of pollution control specially to treat the effluent, emanating from the clusters of compatible small-scale industries.

24.3 Sewage Water Quality

In designing a STP, one of the key factors to be considered is, the per person organic matter load (alternatively known as population equivalent, PE), the values of which differ from country to country. In general, 1 PE is equivalent to 60 g of Biological Oxygen Demand (BOD) per person per day, and it also equals 200 L of sewage per day (Henze et al. 2008). Typically, a domestic sewage would contain approximately 300–450 mg/liter of BOD and Chemical Oxygen Demand (COD). Sewage also contains coliform bacteria (*Escherichia coli*), which is harmful to human beings if water containing such bacteria is consumed. Another feature of sewage is the presence of Total Suspended Solids (TSS) in high quantities. In general, the physico-chemical characteristics of untreated sewage in developing countries are given as: 180 g/person/d for total solids (or 1100 mg/L when expressed as a concentration), 50 g/person/d for BOD (300 mg/L), 100 g/person/d for COD (600 mg/L), 8 g/person/d for total nitrogen (45 mg/L), 4.5 g/person/d for ammonia-N (25 mg/L) and 1.0 g/person/d for total phosphorus (7 mg/L) (CPCB). Typical values for nutrient loads per person and nutrient concentrations in raw sewage are given as: 8 g/person/d for total nitrogen (45 mg/L), 4.5 g/person/d for ammonia-N (25 mg/L) and 1.0 g/person/d for total phosphorus (7 mg/L). The typical ranges for these values are: 6–10 g/person/d for total nitrogen (35–60 mg/L), 3.5–6 g/person/d for ammonia (20–35 mg/L) and 0.7–2.5 g/person/d for total phosphorus (4–15 mg/L) (Von Sperling, 2015). The treated water should have pH of 6.5–8.5, BOD on 5th day < 10 mg/L, COD < 50 mg/L, suspended solids < 10 mg/L, ammoniacal nitrogen < 5 mg/L, total nitrogen < 5 mg/L, fecal coliform < 100MPN/100 ml.

24.4 Different Stages of Sewage Treatment

Sewage treatment mostly involve two main stages viz., (i) primary treatment and (ii) secondary treatment. In addition, advanced treatment involves a tertiary treatment also which mostly does polish and nutrient removal.

(i) Primary treatment: In this stage, raw sewage is partitioned to remove floating debris/insoluble impurities such as plastic bags, papers, leaves, twigs, etc. This ensures minimum damage or clogging of the pumps and sewage lines. The hydraulic retention time is about 1.5–2.5 h (Tchobanoglous et al. 2014). The primary sedimentation tanks are expected to remove 50–70% of the suspended solids and 25–40% of the biological oxygen demand (BOD) (Tchobanoglous et al. 2014). The remaining liquid is subjected to secondary treatment.

(ii) Secondary treatment: The main processes involved in the secondary sewage treatment are designed to remove as much of the solid material as possible (Henze et al. 2008). They use biological processes to digest and remove the remaining soluble material, especially the organic fraction. These processes are performed by micro-organisms in a managed aerobic or anaerobic process

depending on the treatment technology. Secondary treatment can reduce organic matter (measured as BOD) from sewage, using aerobic or anaerobic biological processes. In this stage, air is mixed into the sewage to stimulate the microbes which consume the pollution load and which then becomes sludge. The sludge can be used as compost. The purpose is to achieve a certain degree of effluent quality in a STP suitable for the intended disposal or reuse option.

(iii) Tertiary treatment: The purpose of tertiary treatment (also called 'advanced treatment') is to provide a final treatment stage to further improve the effluent quality before it is discharged to the receiving water body or reused. It is also called 'effluent polishing'. Tertiary treatment may include biological nutrient removal (alternatively, this can be classified as secondary treatment), disinfection and removal of micro-pollutants, such as environmental persistent pharmaceutical pollutants.

(iv) Technique for elimination of micro-pollutants is a fourth treatment stage mainly consisting of activated carbon filters that adsorb the micro-pollutants. The combination of advanced oxidation with ozone followed by granular activated carbon (GAC) has been suggested as a cost-effective treatment combination for pharmaceutical residues.

Besides sewage, sludge treatment aims at reducing the volume for easy transportation, decreasing the costs and potential health hazards of disposal choices. Water removal is the primary means of weight and volume reduction, while pathogen destruction is normally achieved through heating during thermophilic digestion, composting, or through burning. The choice of a sludge treatment method depends on the volume of sludge produced, and assessment of treatment costs required for available disposal options.

STPs can have significant effects on the biotic status of receiving waters and can cause some water pollution, especially if only the basic treatment process is used. Water pollution reduces the ability of the body of water to provide the ecosystem services that it would otherwise provide. In addition to damage to many species, water pollution can also lead to water-borne diseases for people (Water Pollution 2013). This process can lead to algal blooms, a rapid growth, and later decay, in the population of algae. In addition to causing de-oxygenation, some algal species produce toxins that contaminate drinking water supplies.

24.5 Guidelines for STP/CETP Site Selection

Before proposing a new STP/CETP, various processes that need to be considered are described below (Handbook of Forest Conservation Act 1980).

24.5.1 Wastewater Checklist

(i) Finding out the potential users of CETP, their type and number of industries in the geographic area.
(ii) Identifying the type (organic/inorganic/toxic) and volume of wastewater probably to generate (concentrated/dilute, etc.).
(iii) Calculating the future waste load on CETP—aids in designing the plant capacity on a modular basis.
(iv) Investigating the compatibility and identifying the appropriate treatment options.
(v) Assessing cleaner technologies—recommending changes in the raw material, manufacturing process, reducing waste generation, etc., in an individual member.

24.5.2 CETP/STP Sizing

(i) Quality of effluent and projected growth rate of the specific industries in the region.
(ii) Flow rate: Minimum and maximum flow rate for hydraulic computations and size of pipe distribution. Anticipated future increase also has to be added.
(iii) Effluent characteristics: They can be grouped into physical and chemical characteristics.

24.5.3 Mode of Disposal of Sewage and Sludge

(i) Surface water bodies
(ii) On land- for irrigation
(iii) Marine outfall
(iv) Public sewers
(v) Agricultural use, if free from hazardous constituents.

24.5.4 Distance Criteria for Sitting STP

While siting STPs, care should be taken to reduce the adverse effect of the industries on the surrounding neighborhood as well as distant locations. With regards to site selection environmental impacts of odors, air, soil, subsoil ground water, surface water contamination, sludge transportation, vector attraction and devaluation of nearby areas are also to be considered (Von Sperling 2015). The wastewater treatment pond location must be downhill of ground water supply source to avoid

chemical or bacterial pollution. The pond site should not be liable to flooding and the site elevation should permit the pond to discharge the effluent by gravity to the receiving streams. The site should preferably allow an unobstructed sweep of wind across the pond and open to the sun. Advantages should be taken of natural depressions while locating the ponds. In order to protect sensitive locations, the industries may maintain the distances as given below.

(i) Ecologically and/or otherwise sensitive areas: 5 km (preferably); depending on the geo-climatic conditions the required distance need to be increased by the appropriate agency.
(ii) Coastal areas: 500 m from the high tide line (preferably).
(iii) Flood plain of the riverine system: 500 m (preferably) from the flood plain or modified flood plain affected by dam in the upstream or by flood control systems.
(iv) Transporter communication system: 500 m from the railway and highway.
(v) Major settlements: Non obligatory pond sites should be at least 200 m away from inhabitations or from planned built up area in future. The pond should be located such that the prevailing wind blows toward unpopulated areas.

24.6 GIS Modeling for the Optimization of STP Location and Sewage Transport

Remote sensing and Geographic Information System (GIS) are the twin technologies for data collection, processing, integration, visualization, management and analyses which are widely used for geo-locational studies. Besides, GIS has powerful graphical representation, along with efficient data organization and mass spatial data analysis. In geo-spatial sense, the data is presented as thematic layers or as digital maps. The main objective of using GIS technology is to overlay various thematic layers in order to identify the most suitable locations based on complex project requirement. GIS, powered with other tools like Global Positioning System and satellite remote sensing can provide most updated, location specific information at very high spatial resolution. Brimicombe (2003) have mentioned how GIS is being used is various fields such as natural resources management, forestry, geology, disaster management, utility planning and environmental planning.

GIS-based spatial analysis for site suitability evaluation (Zhao et al. 2009) followed by multi-criteria analysis (MCA) for optimal evaluation of alternatives form a very powerful tool that supports complex decision-making process (Anagnostopoulos et al. 2007). The GIS with MCA has been proven as one of the best methods for decision makers to make a systematic and scientific decision after considering multiple factors derived from geospatial data (Yang and Lee 1997; Agarwal 2019). GIS, powered by spatial analysis tools, geostatistics, AHP and artificial intelligence has significant advantage. The actionable output map is a convergence of expert and stakeholders opinion (Geneletti 2010). GIS based decision support system provides

a number of alternatives to choose from, for siting sewage treatment plant, based on some well-defined spatial criteria.

Siting waste management site using GIS has been a popular technique, from the early onset of the technology (Esmaili 1972; Ghose et al. 2006; Golden et al. 1983; Karadimas et al. 2007; Sonesson 2000). This technique has been recognized as one of the most pragmatic approaches in the process of waste planning and management (Karadimas and Loumos 2008). In the last decade several attempts have been made to use GIS and multi-criteria analysis for landfill site evaluation (Geneletti 2010; Nas et al. 2010), use of AHP in the backdrop of GIS (Saaty 1980; Vuppala et al. 2006; Wang et al. 2009), GIS and fuzzy systems (Chang et al. 2008; Gemitzi et al. 2007; Lotfi et al. 2007), GIS and factor spatial analysis (Biotto et al. 2009; Kao and Lin 1996), as well as integrated GIS-based methods (Hatzichristos and Giaoutzi 2006; Gómez-Delgado and Tarantola 2006; Kontos et al. 2003, 2005; Zamorano et al. 2008). In general, selection criteria are based on six major stages viz., (i) creation of spatial database (primary variables) (ii) construction of criteria (iii) reclassification of the layers (iv) estimation of the relative weights for the criteria (pairwise comparison between variables) (v) calculation of suitability index and (iv) site suitability zonation.

The efficient route planning for collection and transport of municipal solid wastes from urban clusters to STP location is a crucial factor and must ensure public health safety, downsizing the travel time and cost, fuel consumption, CO_2 emission and least possible human intervention. GIS network analysis evaluates the man-made and natural network to understand the flow behavior in and around the analysis zone. It focuses on edge-node topology to represent real life networks of information. Its function is based on the mathematical sub-disciplines of graph theory and topology (Jenson 2013). A network is represented as a graph that contains a set of vertices (i.e., intersections or junctions) connected by edges. These edges (or lines) are used in GIS to depict roads, waterlines, pipelines, streams, railways and communications lines, among other things. The edges and vertices contain attributes, for example, a road network may have speed limits attached to its edges while a junction may restrict right turns. Additionally, a network can have directed/undirected edges depending upon the situations. These networks are used to perform analyses such as shortest distance, fastest route, closest facility, allocation, service regions, vehicle rouging and so on. In this process commonly used properties include length, direction, connectivity and pattern. GIS have the potential to simplify the development of spatial analytical network functions through different types of network model viz., transportation network, utility network, stream network etc. Transportation (or road network model) is utilized in transportation planning, measurements of accessibility, allocation of service, human mobility behavior and many more. Utility networks are generally directed and includes water pipes, sewage lines, electrical circuits etc. Stream network is a directed network that represents the direction of natural flow of stream in catchment and helps in understanding the dynamic behavior of river flow for assessment of flood impact.

In the present study ideal routing for waste collection was performed using ArcGIS Network Analyst modelling tool. To achieve this Dijkstra's shortest path algorithm

(Dijkstra 1959) is used that has least distance between source and destination nodes. Layers namely road network, settlement locations and proposed STP location are used for finding the optimal route. Settlement points and STP location are used as source and destination locations respectively in the network analysis. Road network is considered for connecting source to destination assuming that the sewerage route generally follows the road network. Route optimization in terms of waste collection and transport minimization has been investigated by several authors (Adamides et al. 2009; Zsigraiova et al. 2009).

All the studies have used GIS and spatial modeling for optimization and economic savings by reducing travel distance, time, fuel consumption and environmental pollution (Johansson 2006; Kim et al. 2006; Sahoo et al. 2005; Tavares et al. 2008; Apaydin and Gonullu 2007; Lopez Alvarez et al. 2008; Nuortio et al. 2006; Chalkias and Lasaridi 2009). However, this model can be improved further using effective data structures such as d-heaps (ESRI 2006). This algorithm can be adapted in order to accommodate the real-world constraints. This will help generating a cost structure between source and destinations (Chalkias and Lasaridi 2011).

24.7 Wind Data Analysis

The purpose of wind data analysis is of paramount importance if the STP/CETP produces hazardous air pollutions (HAPs) which may have adverse health impacts in animals and human beings respectively. The meteorological conditions at the STP site regulate the transport and diffusion of air pollutants released into the atmosphere. The STP should be ideally located keeping in view that the odor emanating from the plant must not be carried toward the neighboring population by the winds (CPHEEO). Similarly, the plant should be oriented in such a way to minimize the odor and misting issues. Therefore, the plant should be located in a suitable site where the dominant wind direction is away from the habitation. Likewise, a wind mast needs to be located by the plant operators at a distance of 100 m in the upwind side and downwind side to monitor the prevailing wind conditions in the location for optimized operation of the plant (Butler et al. 2017). The site should be devoid of any obstructions that could block the wind blowing across the pond. Hence, the facultative ponds should be ideally oriented with their longest dimension in the direction of the prevailing wind so that the vertical mixing and the subsequent distribution of dissolved oxygen, algae, BOD leads to a good quality effluent (FAO; Butler et al. 2017). Wind facilitates re-aeration within the treatment pond through surface circulation in the upper layers (Ukpong 2013). The prevailing wind pattern is significant for the facultative ponds as the wind induced mixing of warmer and cooler layers in the ponds is vital for subverting the thermal stratification of the water column that could lead to anaerobiosis and the subsequent failure of the reactor (USEPA 2011; Butler et al. 2017). This further establishes that the significant role of wind pattern in velocity distribution over the treatment pond and determining the surface re-aeration (Ukpong 2013).

24.8 Study Areas

Two of the emerging towns in Odisha and Telangana states of India were selected for the study. Brief description of both the cities is given in the following sub-sections.

Rayagada: The Rayagada town is located in the Odisha state and lies between the coordinates 19° 09′ N–19° 11′ N latitude and 83° 23′ E–83° 25′ E longitude. The mean elevation is ~ 220 m and the slope direction is from north-west to south-east. The Rayagada town is located in an apparent valley like geographical setting that is bounded by a north to south aligned hill complex and scattered hillocks in the west thereby constraining the city sprawl. Besides the hill complex the Nagavali River (flow in N–S direction) and a local stream flowing from west to east and draining to Nagavali River restricts the growth of the city in all the directions except the north. The area under municipal boundary is about 18.32 km^2. The city is lying in the plain area but there are hillocks along the eastern, western and south-western boundary (Fig. 24.1a). In general, the drainage direction is toward the southeast at the confluence of both the rivers. As per 2011 census, total population of the town is 71,208 out of which male population is 36,036 and female population is 35,172 with decennial population growth of 1347 per year (15.74%) from 2001 to 2011. Considering the present growth rate, the estimated population as of 2020 would be 83,331. The population density is 136 inhabitants per square kilometer. The average literacy rate of the district is 64%, higher than the national average of 59.5%: male literacy is 72%, and female literacy is 56%.

The climate of the district is typically tropical and sub-tropical with three distinct seasons e.g., summer, winter and rainy. December is the coldest month with mean daily average temperature of 20 °C which reaches a maximum of 42 °C during May. The rainfall in the area is mostly from the south west monsoon that lasts from

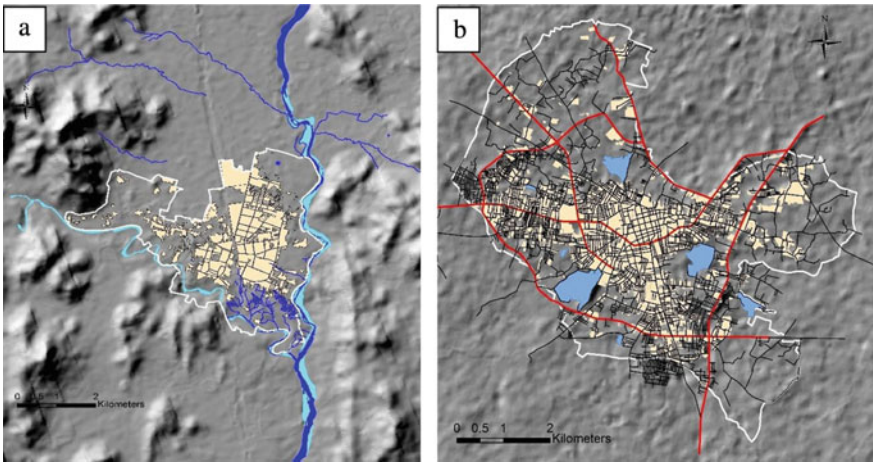

Fig. 24.1 Location of the **a** Rayagada town and **b** Siddipet town at the backdrop of hill shade view

Table 24.1 Month-wise weather parameters of Rayagada

Variables	Jan	Feb	Mar	Apr	May	Jun	Jul	Aug	Sep	Oct	Nov	Dec
T_{av} (°C)	21.5	24.2	27.3	30.1	31.8	30.2	27.3	27.3	27.4	26.6	23.1	21.1
T_{min} (°C)	15.2	17.9	21.2	24.7	26.9	26.3	24.6	24.5	24.3	22.6	17.7	14.9
T_{max} (°C)	27.9	30.5	33.5	35.6	36.7	34.1	30.1	30.1	30.6	30.6	28.6	27.3
RF (mm)	10	10	20	37	82	186	278	295	225	133	29	7

the middle of June to October. The average annual rainfall varies from 1030.21 to 1569.50 mm. Rainfall is the highest in the July–August and minimum during winter months. The average annual temperature in Rayagada is 26.5 °C. Monthly averages of different weather parameters of Rayagada district are presented in Table 24.1.

The Rayagada district has varied geomorphological features including Lateritic uplands, Pediplane, Denuded hills, Flood plain, Structural hills, Inselberg, Mesa and Butte, Residual hills, Intermontane valley and Bazada. Quaternary formations are mostly confined to the Nagavali and Vamsadhara river basins and catchment area. Hydro-geologically the major water bearing formations are weathered and fractured crystalline rocks. Based on physical and chemical characteristics, mode of origin and occurrence, soils of the district may be classified into two groups namely Alfisols and Entisols. The red loamy soils of Alfisols group occur throughout the district. These are light textured, porous and friable. There is absence of lime kankar, free carbonates and very less soluble salts are present. These soils are suitable for cultivation of paddy. The Entisols are restricted to the flood plains of Vamsadhara and Nagavali rivers in the blocks of Ramanguda, Gudari, Padampur, Rayagada and Kolnara. These soils are alkaline and deficient in nitrogen and humus. The Vamsadhara and Nagavali rivers are the most prominent rivers in the district. Nagavali originates in the Kalahandi district, flows through Nawarangpur and Koraput districts and enters in Baster district Chattisgarh state and sustains perennial flow. The Nagavali River originated from a hill near Lakhbahal village in Thuamul Rampur block of Kalahandi district. It touches Nakrundi, Kerpai areas of Kalahandi, Kalyansinghpur and Rayagada of Rayagada district of Odisha and merges in Bay of Bengal near Kallepalli village near Srikakulam district of Andhra Pradesh. The Tel and Bhaskel are the other rivers flowing through the district.

Out of total geographical area of the district about 4785 km^2 (67.65%) is under forest of which 777 km^2 is reserve forest. Other land utilization patterns include permanent pasture (260 km^2), culturable wasteland (220 km^2), barren and unculturable land (380 km^2) and net sown area of 1740 km^2. About 94% of the population of the district live in the rural areas and depend on agriculture for their livelihood. Paddy, wheat, ragi, green and black gram, groundnut, sweet potato and maize are the district's major crops.

Siddipet: Siddipet district is carved out of erstwhile Medak district with annexation of some parts of Karimnagar and Warangal districts. District is located in the central portion of the state surrounded by Karimnagar district on the north, Warangal and Yadadri districts on the East, Medchal district on South and Medak

and Kamareddy districts on the West (Fig. 24.1b). The district forms a part of table land of the Deccan plateau with an area of 3842 km^2. The Siddipet town is confined between 18° 03′ 41″–18° 08′ 49″ N latitude and 78° 48′ 34″–78° 53′ 46″ E longitude with an area of 36.03 km^2 and mean elevation is 675 m. The city has several lakes distributed all around viz., Komati Cheruvu, Narsapur Cheruvu and the Yerra Cheruvu. The total length of the drainage network is 49 km. According to the 2011 census of India, the town has a population of 111,358 of which male and female populations are almost similar (male 56,769 and female 57,322). The population density is 3100 persons per km^2. The overall literacy of the district is 61.61% but in the city the literacy is very high to the order of 90.73%.

The district has semi-arid climate. The average annual rainfall is 839.5 mm but varies between 800 and 1000 mm. May and June are the hottest months during which the mean maximum temperature reaches to 42 °C and minimum of 30 °C. Overall, the temperature typically varies from 15 to 39 °C and is rarely below 12 °C or above 43 °C. The rainy season starts in June and ends in September. January is the coldest month having mean maximum temperature of 21 °C and minimum of 9 °C. During summer the town's mean daily maximum temperature is about 43 °C and a mean daily minimum temperature of 16 °C. The days are intensively very hot. Monthly averages of different weather parameters of nearby weather station (Ramagundam) is given in Table 24.2.

There are broadly 19 types of soils in the region including shallow gravelly red soils to clayey to gravelly clayey moderately deep dark brown soils. Red type soils occupy more than 50% of the area and followed by calcareous soils, colluvial soils and black soils. The red soils have sandy to loamy texture. They are occurring in the uplands. The black soils are clayey in texture and are prevalent in the low-lying area along stream courses. The depth of the soil varies from a few cm to meters. Red sandy soils are generally less deep than the black soils. Alluvial soils are developed to areas of rivers and stream beds. The district mostly falls in the Godavari basin. The topography of the district can be characterized by plains as well as upland, plateau, with significant areas of stony waste and boulder rocks along with dry channels. The district has an average height between 500 and 600 m above mean sea level. Isolated peaks and rocky clusters lie scattered. The hilly areas are covered under reserved forests. The district is composed of oldest rock formations, i.e., Archaean gneisses and those consisting principally of peninsular granite. The drainage pattern developed over granite/gneiss is sub-dendritic to dendritic.

Most of the area in the district is under agriculture, interspersed with forested lands and wastelands. Agricultural land constitutes 57.23% of geographic area. Forest land occupies in 6.76% (260 km^2) of the district, of which 0.83% is protected and 5.62% is reserved categories. Permanent pasture occupies 103 km^2 (2.68%). Other landuse classes prevalent in the district include open scrub, dry channels and ponds. Major crops grown are paddy, maize, castor, jowar and pulses. Rabi crops include jowar, bengal gram, sunflower and chilli.

Table 24.2 Month-wise weather parameters of Ramagundam

Variables	Jan	Feb	Mar	Apr	May	Jun	Jul	Aug	Sep	Oct	Nov	Dec
T_{av} (°C)	22.75	24.2	27.6	32.1	33.5	33.6	29.05	29.3	28.4	27.95	24.75	21.6
T_{min} (°C)	15.3	16.6	21.4	24.8	26.7	28.3	25.3	25.2	24.3	22.5	17.7	14.0
T_{max} (°C)	30.2	31.8	33.8	39.4	40.3	38.9	32.8	33.4	32.5	33.4	31.8	29.2
RF (mm)	18.1	32.4	109.18	189.52	115.86	193.64	81.1	22.8	2.04	18.1	32.4	109.18

24.9 Data Used and Preparation of the Input Layers

Four types of data were used in this study, DEM (digital elevation model), satellite image, vector data digitized at 1:500 scale and wind data from published literature. The DEM data used in this study is from Advanced Spaceborne Thermal Emission and Reflection Radiometer (ASTER, 30 m spatial resolution). High resolution Satellite data (Kompsat, K3, data of 18 February, 2019) was used for digitization of roads, river/streams, ponds, built up areas and other landuse. Municipal boundary of the towns was collected from district administration. The hardcopy maps were registered with respect to high resolution satellite data using 35 control points so that the Root Mean Square Error (RMSE) value is less than a pixel. Different regulatory norms, laid down by the Ministry of Environment, Forest and Climate Change, Government of India were used in the form of buffer distance. The annual trend of wind data was obtained from www.indianclimate.com/wind-data.php.

24.9.1 Surface Hydrology Layers Using DEM

ASTER DEM was first filled for sinks, which is an iterative process to generate a depression less DEM. This DEM is then used for generation of 'flow direction' and 'flow accumulation' raster. The 'flow direction' function creates a raster from each cell to its steepest downslope neighbor. The output is an integer raster whose values range from 1 to 255, representing various directions. The 'Flow accumulation' raster is a product in which each pixel contains the information on how many neighboring pixels are contributing to the surface flow. Output cells with a high flow accumulation are areas of concentrated flow and can be used to identify stream channels. The input for calculation of flow accumulation is 'flow direction' raster. All the surface analyses were carried out using ArcGIS (ver.10.4.1) tool.

From the flow accumulation raster, the highest cell values were reselected. Care was taken to have a greater number of accumulation raster distributed across the urban boundary. In some cases, to have better spatial representation some of the relatively low valued accumulation rasters were also considered. However, preference is always given to high value pixels.

24.9.2 Altitude

The average altitudes of Rayagada and Siddipet are 220 and 675 m above mean sea level. The STP location should be above the highest flow peak and at the same time should not be too high to extract the sewage from the city pipe network. Hence the altitude was selected accordingly between 200–300 m and 450–500 for Rayagada and Siddipet, respectively.

24.9.3 Slope

STP should be constructed in less sloppy areas to get natural gradient for wastewater flow and also to avoid overland urban runoff during rainy season. Different authors have put forward different slope types for locating STP. Mansouri et al. (2013) suggested for 0–2% slope is ideal for STP location, whereas Agarwal et al. (2019) suggested 5–10% of land slope ideal for STP. In the context of STP location slight to moderate slope (1–3%) is preferred to facilitate gravity flow of wastewater through treatment units.

24.9.4 Generation of Constraint Maps

In reality regulatory norms are translated into distance constraints with respect to land use, slope and road network for siting optimum location for STP. Some criteria have buffer, so assigning the constraint area and its buffer area to 0 and the pixels out of the buffer to 1.

Slope constraint map: Sewage treatment plant needs to be located in a little sloppy area for drainage. In the present study 1–3% slope was considered optimum.

Built-up constraint map: The sewage treatment plant should be away from the urban area and ideally in the wastelands, to avoid any harmful gas emission and foul odor. Agarwal et al. (2019) and Taghilou et al. (2019) suggested a distance of 500 m from the urban built-up area whereas Abdalla (2017) suggested for 1000 m distance. It was set to 500 m for the present study.

Road's constraint map: Distance from roads increases the cost of infrastructure development and also maintenance. At the same time, presence of an effluent treatment plant close to the roads also affects the landscape, city climate and public health. Some of the given criteria include 500 m from major road and 50 m from minor road (Mansouri et al. 2013); 200 m from road to have easy access (Agarwal et al. 2019). A distance of 200 m buffer from road is applied in the study.

Water body constraint map: To avoid contamination to nearby river/streams, 500 m and 200 m buffer distance was maintained for major rivers and small streams respectively.

Rivers and water body constraint map: River and drainage buffer was generated wherein 500 m was set for major river and 200 m for minor drains. Ponds are sensitive from environment point of view and hence a buffer distance of 200 m was set based upon the research of Agrawal et al. (2019).

24.9.5 Multi-Criteria Analysis (MCA) Model

Multi-criteria analysis (MCA) is a technique that is used to consider various criteria when making a decision. MCA gives a logical, well-structured process to follow, so different factors can be clearly identified and prioritized. It allows the alternative solutions being considered to be ranked in the order of suitability. The efforts to integrate GIS and MCDA (Multi-criteria Decision Analysis) was initiated during late 1980s and early 1990s. This development can be associated with the proliferation stage of the GIS development (Waters 1998; Malczewski 2004). Researchers have often applied GIS-MCDA for mostly 'Spatial Decision Support Systems (SDSS)', 'Collaborative Spatial Decision Making' and 'GIS and Society' projects. GIS-MCDA is defined as a collection of methods and tools for transforming and combining geographical data and preferences (value judgments) to obtain information for decision making (Malczewski et al. 2015). The MCA model was implemented in three phases. First the land suitability in terms of slope, landuse, surface hydrology was determined. In the second phase the regulatory norms were implemented using integrated constraint maps. In the second phase all the buffers were integrated to generate a single buffer area for exclusion of any 'flow accumulation (FAC)' point falling within the buffer areas. After exclusion of the accumulation raster points falling within the buffer area the FAC points were further examined for underneath slope and landuse pattern. For suitability the slope was kept 1–3% and landuse preferably wasteland, otherwise agricultural land. In the third and final phase network analysis was considered for final selection of the candidate locations.

24.9.6 Sewage Accumulation Points and Routing

Initially the road network layer is converted into a network dataset in a geo-database to solve length-dependent route. Subsequently a new route analysis layer is added in the map. This layer includes classes like 'Stop' locations, 'Routes', etc. Settlement locations are imported as stop location, where the STP location is added into it as the destination. After solving the network based on the given inputs the optimal sewerage route is estimated. The above procedure is followed for generating optimal sewerage route of the study sites Rayagada, and Siddipet, separately.

24.9.7 Wind Data Analysis

Wind data was analyzed for its annual trends in terms of direction and speed. For Rayagada and Siddipet, nearest meteorological station's data of Koraput and Karimnagar have been used. Average wind speed has been classified into 7 categories viz. < 0.5, 0.5–1.0, 1.0–2.0, 2.0–3.0, 3.0–4.0, 4.0–5.0 and > 5.0 m/s. The wind directions

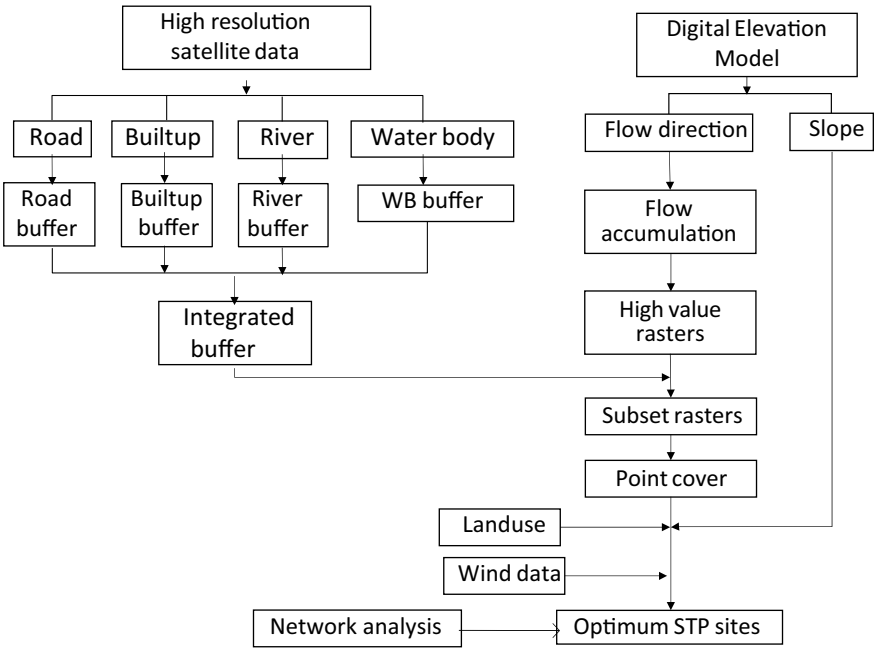

Fig. 24.2 Overall methodology

were grouped into 16 classes. Figure 24.2 shows the schematic of the procedure followed in the present study.

24.10 Results and Discussion

24.10.1 Land Use

The town of Rayagada is located at the confluence of two rivers and the sprawl is mostly centralized. The rivers flowing from north to south and north-west to south-east delimits the expansion of the urban limit (Fig. 24.3a). Several open/vacant lands are available across the urban boundary but very less ponds except the located one in the north. There are no built-up areas in the north-west, north and south-east of the urban boundary. Considerable area is under agriculture in those areas, except in the south where the land is mostly ravenous. Unlike Rayagada, the Siddipet town is mostly located on the plain area. Significant sprawl is noted along north and eastern side of the urban boundary (Fig. 24.3b). The city has several lakes distributed all around viz., Komati Cheruvu, Narsapur Cheruvu and the Yerra Cheruvu. Open lands are limited to the north-east and some parts in the western periphery. Northern and eastern half are dominated by agricultural practices.

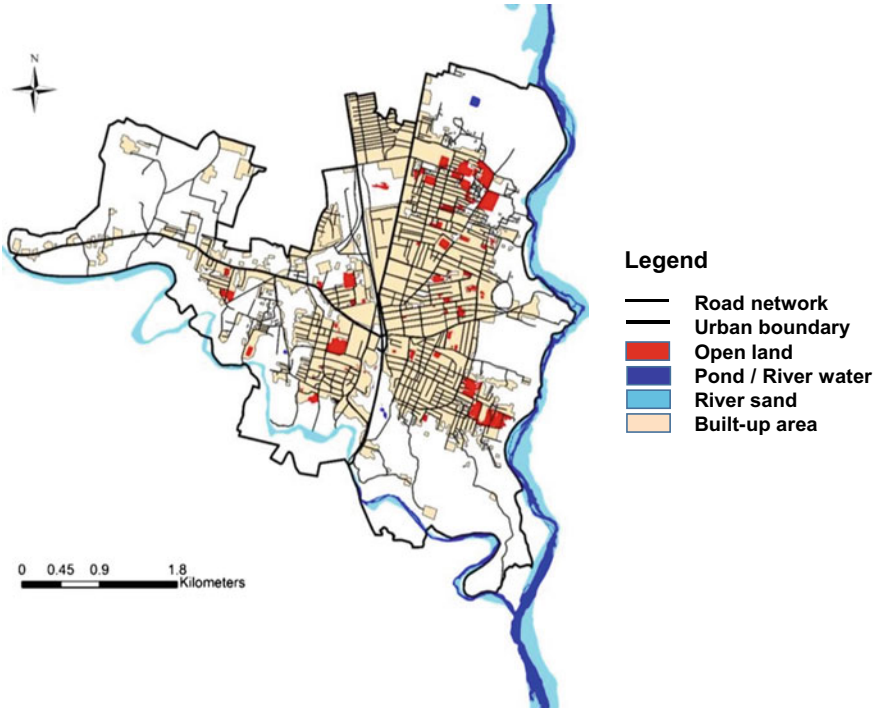

Fig. 24.3 **a** Vector layers including road, river, pond, open land, and build up area of the Rayagada town. **b** Vector layers including road, river, pond, open land and build up area of the Siddipet town

24.10.2 Surface Topography

From Fig. 24.4a, it is apparent that the major part of the urban areas of Rayagada are nearly plain. The north-west and some portion of the south-west has an elevation ranging between 600 and 800 m. As the slope (Fig. 24.4b) in the south-west region outside the urban limit is having higher, the location may not be suitable for siting an STP.

In Siddipet, the eastern side is having lower elevation whereas north, west and south has higher elevations, however, the slope is minimal and varies between 0 and 1%. Figure 24.5 depicts the spatial distribution of elevation (Fig. 24.5a) and the percentage of slope (Fig. 24.5b); hence, slope is not a constraint for construction of STP.

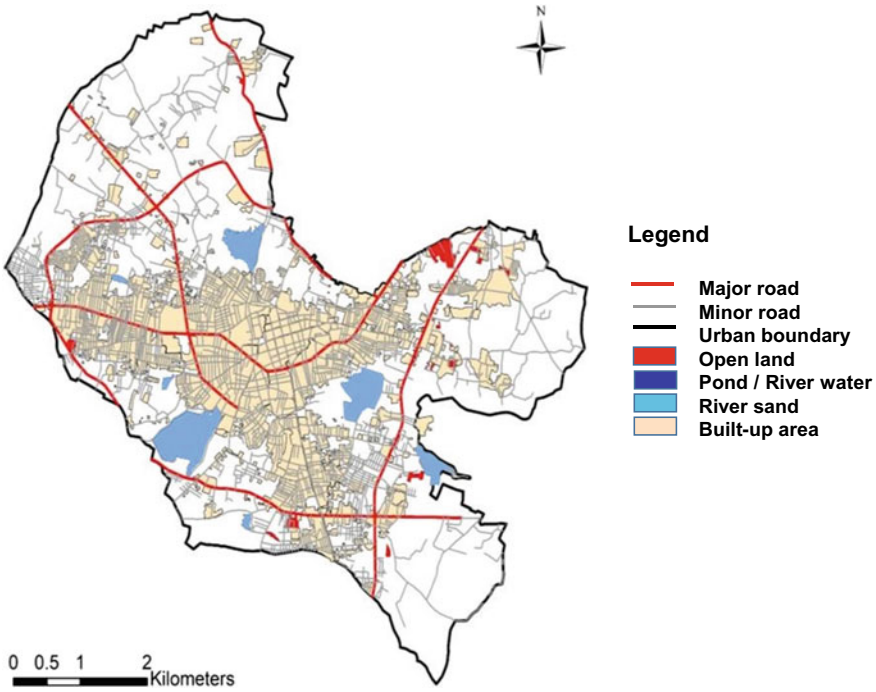

Fig. 24.3 (continued)

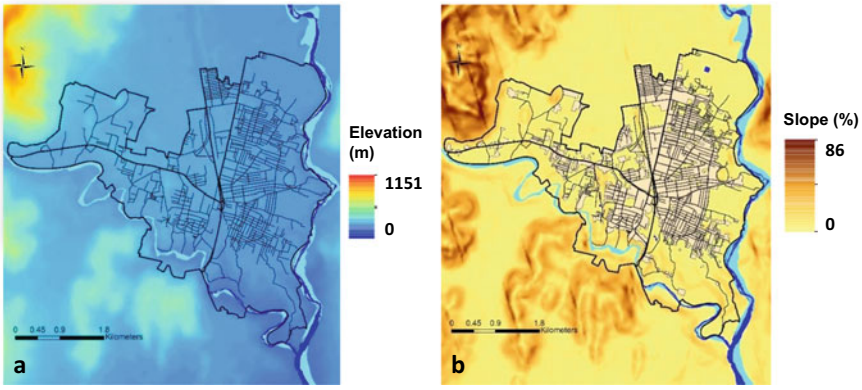

Fig. 24.4 Surface topography of the Rayagada town **a** digital elevation model, **b** slope (%)

24.10.3 Surface Hydrology

From Fig. 24.6a it is apparent that the direction of surface flow is mostly undefined in the urban boundary of Rayagada town with general tendency toward east and south.

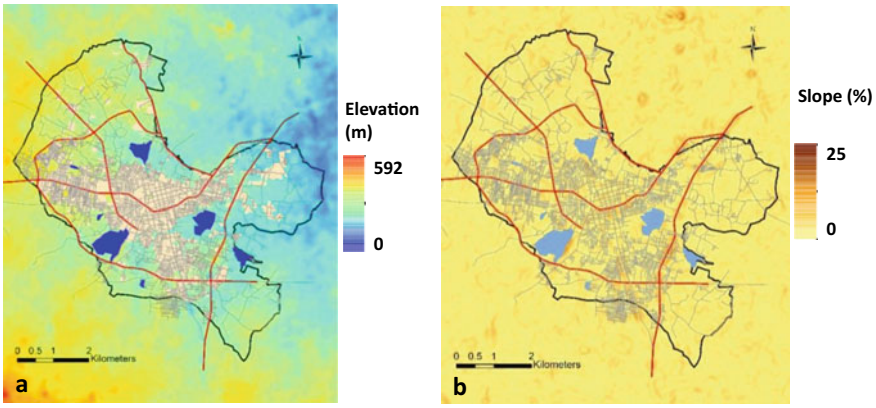

Fig. 24.5 Surface topography of the Siddipet town **a** digital elevation model, **b** slope (%)

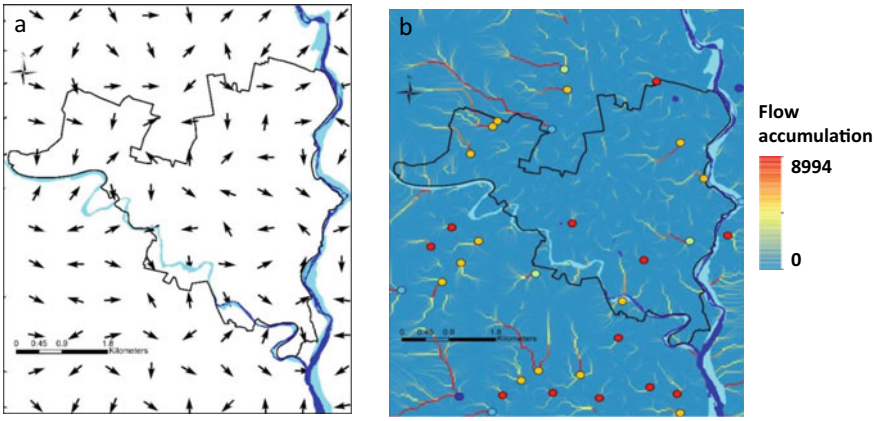

Fig. 24.6 Surface hydrological properties of Rayagada town **a** flow direction and **b** flow accumulation

Some of the locations within the urban boundary and outside its limit represent high flow accumulation values. The blue circles in the Fig. 24.6b depicts the high accumulation values, followed by cyan, yellow and red circles (least accumulation) in decreasing order. This helps in identifying the natural gradient and capacity to store the surface runoff. High accumulation values were found one in the south-west corner of the study area and another in the north-east across the Nagavali River.

The dominant flow direction in Siddipet is toward the north, however, in the urban core it is random (Fig. 24.7a) and indicates the local sink. The flow accumulation (Fig. 24.7b) is highly localized and divided into several micro-basins.

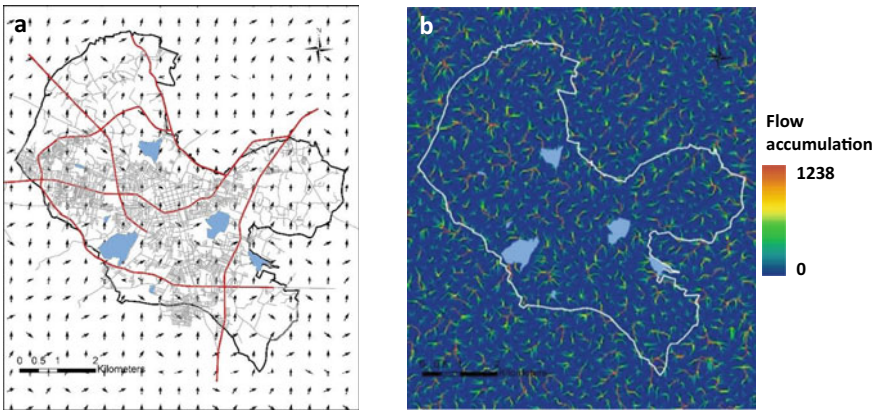

Fig. 24.7 Surface hydrological properties of Siddipet town **a** flow direction and **b** flow accumulation

24.10.4 Setting up Buffer Distance Based on Regulatory Norms and Exclusion of Areas

Several buffers were generated based on the regulatory guidelines and an all-inclusive buffer layer was generated (Fig. 24.8). The buffer distances for pond, road, built-up and river were taken as 200 m, 200 m, 500 m and 300 m respectively as mentioned earlier. Once constrained by the buffers the candidate STP sites falling within the urban boundary are mostly eliminated. For Rayagada (Fig. 24.8), 15 points qualify for establishing STP after elimination using the integrated buffer layer. Out of these 15 locations, only 3 (location no 1, 8 and 15) falls in the wasteland and having slope value between 1 and 3%. However, the location no.1 has natural constraint as it is on the other side of the Nagavali River, although having better hydrological suitability. The location ID 8 is away from the urban limit which will be the transportation cost but the location no. 15 is close to the urban limit and appears to most feasible among the 3 locations shortlisted. The selection criteria of all the 15 locations can be seen in Table 24.3.

In case of Siddipet, following suitability criteria and exclusion of the locations falling within the regulatory zones (buffers), a total of 6 candidate locations were selected in the first phase. The landuse and slope characteristics of those points, which are well distributed in the east, south and west of urban boundary are provided in Table 24.4. The slope of all the locations is within 2% and the landuse type is wasteland. Among all the locations ID 22, 23, 31 are shortlisted which have slope little higher than the rest but the distance from the urban boundary varies from 0.3 to 1.7 km. The location ID 31 is close to the urban limit and appears to most feasible in terms of transport requirement among the 3 locations shortlisted. The spatial distribution of candidate STP locations is given in Fig. 24.9.

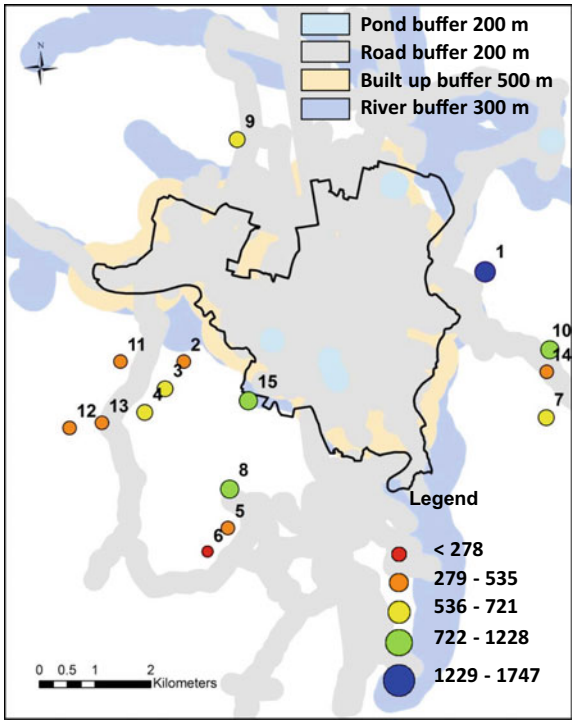

Fig. 24.8 Candidate STP locations for Rayagada town. The circles with different colors indicate the flow accumulation values and the number associated with each circle is the location ID

Table 24.3 Criteria for suitability of STP locations for Rayagada town

Location ID	Elevation (m)	Slope (%)	Landuse	Location ID	Elevation (m)	Slope (%)	Landuse
1	234	0.469	Wasteland	9	236	2.096	Plantation
2	225	1.048	Agril. land	10	359	4.916	Wasteland
3	235	0.994	Agril. land	11	269	10.453	Wasteland
4	239	0.994	Agril. land	12	280	3.774	Wasteland
5	202	1.40	Agril. land	13	254	0.741	Agril land
6	205	0.469	Agril. land	14	235	2.343	Wasteland
7	263	5.982	Agril. land	15	218	0.741	Wasteland
8	222	1.048	Wasteland				

24.10.5 Network Analysis

Analytical tools of GIS are used to optimize the vehicle route based on the travel time and distance. Shortest path algorithm given by Dijkstra (1959) and Cormen et al

Table 24.4 Criteria for suitability of STP locations for Siddipet town

Location ID	Elevation (m)	Slope (%)	Landuse	Location ID	Elevation (m)	Slope (%)	Landuse
2	498	0.99	Wasteland	30	497	0.99	Wasteland
22	455	1.20	Wasteland	31	482	1.05	Wasteland
23	454	1.66	Wasteland	33	491	1.05	Wasteland

FAC flow accumulation, *WL* wasteland

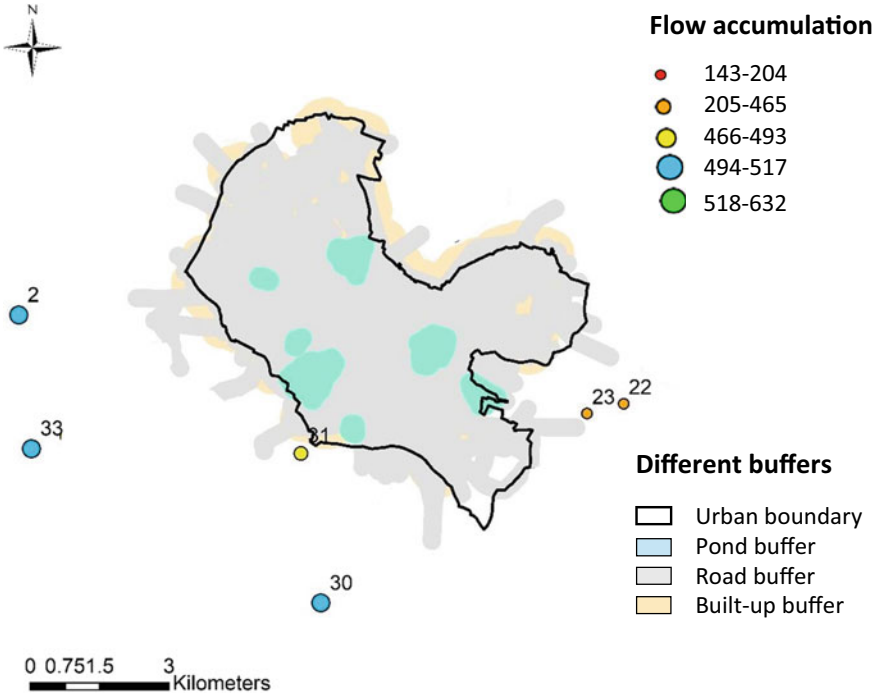

Fig. 24.9 Candidate STP locations for Siddipet town. The circles with different colors indicate the flow accumulation values and the number associated with each circle is the location ID

(2001) was used for finding optimal route between source and the destination. Built-up clusters have been used as source, road network as a proxy to sewage network because the bins are usually allocated on the road intersections and proposed STP site as destination. After solving the network based on the given inputs, the optimal sewerage route is estimated. The output of network analysis is given in Fig. 24.10. In the figure built-up cluster centroids are given in solid black circles and sewage network as brown lines. The network ends near the proposed STP location (solid red circle), based upon site suitability criteria. The proposed network does not connect the STP location as there is no road available near the proposed site. In both the towns the proposed location falls in the south-west of the urban limit.

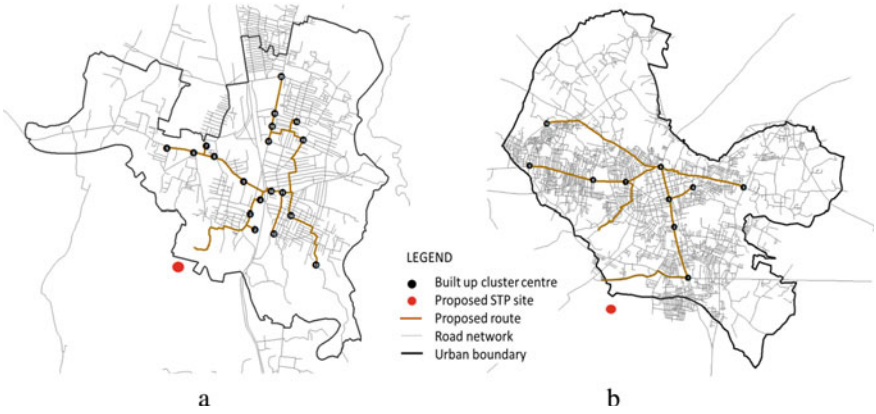

Fig. 24.10 Proposed route for sewage flow towards STP site in **a** Rayagada and **b** Siddipet

24.10.6 Wind Data Analysis

In absence of the wind data of Rayagada, the data of nearby meteorological station (Koraput) has been used. Like any region in the Indian sub-continent, the wind conditions over the Rayagada are generally governed by the monsoons with the average wind speed of approximately 3–4 m/s for most part of the year. From Table 24.5, 14.43% of the time in a year wind blows from west direction in Rayagada. The wind direction from SW and WSW is almost equal and constitutes less than 12%. Further, most of the time winds blow at speeds between 2 and 3 m/s, which is 36.85% of the time. About 2.89% of time winds were 'calm' i.e., wind speeds less than 0.5 m/s. As the dominant direction is W (14.4%) and calm is 2.89%, the chances of wind pollution in the urban settlement is very less. Orography plays a vital role here in modulating the distribution of winds in the region as the town is bounded by a string of hillocks on the western side (> 700 m) that are punctuated in between by two gaps, while the eastern side of the town is completely bounded by a hill extending in the north-south direction thereby curtailing the wind flow in West–East direction. The windrose diagram showing the distribution of wind direction for Koraput is given in Fig. 24.11.

For Siddipet, the wind data of nearby meteorological station (Karimnagar) was used. Light to moderate winds prevail in general all through the year with slightly stronger winds in the early monsoon period. Winds are light and variable in the post-monsoon and winter seasons particularly during the morning hours, while during the afternoon hours the winds are slightly stronger and normally blow from directions between northwest and north. The winds change gradually in the pre-monsoon months and by May they are predominantly from directions between northwest and southwest. In the southwest monsoon season, the winds are south-westerly or predominantly westerly (NTPC 2015). The strength of wind in turn dictates the distance of occurrence of maximum ground level concentration (Rao and Pasha

Table 24.5 Wind pattern (m/s) in Koraput, Odisha

Direction	< 0.5	0.5–1.0	1.0–2.0	2.0–3.0	3.0–4.0	4.0–5.0	> 5.0	Total
N	0.14	0.50	2.10	2.47	0.55	0.14	0.23	6.13
NNE	0.14	0.50	2.05	3.47	0.82	0.09	0.27	7.34
NE	0.18	0.46	1.69	2.51	0.59	0.41	0.14	5.98
ENE	0.23	0.55	1.96	1.46	0.27	0.05	0	4.52
E	0.14	0.41	1.64	1.23	0	0	0	3.42
ESE	0.05	0.23	1.64	0.68	0	0	0	2.60
SE	0.14	0.41	1.51	0.82	0	0	0	2.88
SSE	0.05	0.27	1.69	1.28	0.05	0	0	3.34
S	0.32	0.41	1.74	2.01	0.18	0.09	0.09	4.84
SSW	0.14	0.27	2.74	3.70	0.91	0.23	0.09	8.08
SW	0.27	0.68	3.01	5.30	1.87	0.41	0.05	11.59
WSW	0.18	0.55	3.97	4.34	1.55	0.87	0.09	11.55
W	0.27	0.50	5.07	4.25	2.56	1.10	0.68	14.43
WNW	0.23	1.00	2.24	2.01	1.19	0.55	0.27	7.49
NW	0.32	0.46	1.14	0.41	0.14	0.14	0.14	2.75
NNW	0.09	0.18	1.69	0.91	0.05	0.05	0.09	3.06
Total	2.89	7.38	35.88	36.85	10.73	4.13	2.14	100

Source https://www.indianclimate.com/wind-data.php

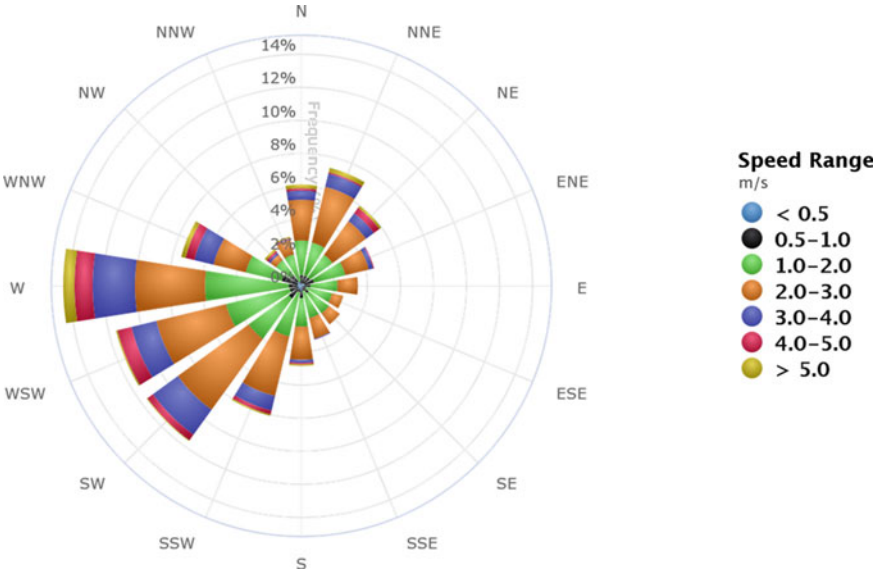

Fig. 24.11 Annual Windrose diagram of Koraput (https://www.indianclimate.com/wind-data.php)

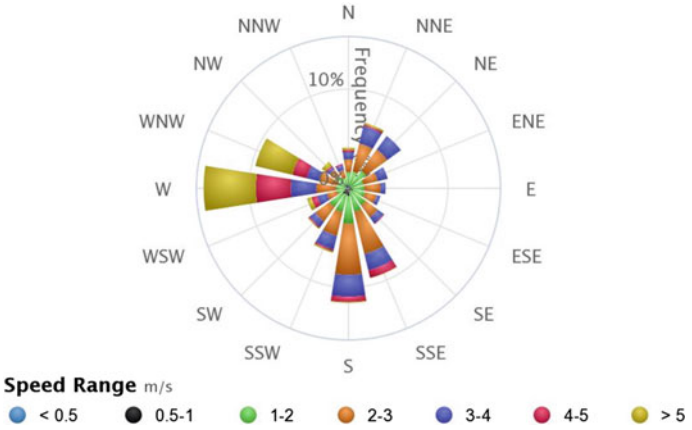

Fig. 24.12 Annual Windrose diagram of Karimnagar

1993). The Windrose of Karimnagar (Fig. 24.12) shows that dominant wind blow from the west much of the time—about 14.57% of all hourly wind directions, followed by south (S) that accounts 11.56% (Table 24.6). Further, at Karimnagar most of the time windspeed ranges from 2 to 3 m/s—which is 32.83% of the time. About 1.61% of time winds were 'calm' i.e., wind speeds less than 0.5 m/s, which may not be a concern for dispersal of foul odor and gases. The proposed STP location is in between dominant wind direction i.e., W and S and hence expected to be relatively safer for the urban inhabitants.

24.11 Conclusion

Geospatial modeling and multi-criteria analysis are powerful tools for STP site suitability. In GIS environment various thematic layers were integrated and criteria-based selection is made for candidate STP sites. Undoubtedly the Geospatial technology can help taking decisions in complex geo-physical environment and regulatory protocols entrusted by different enforcing agencies. In the present study surface hydrological, topological and landuse parameters were generated from high resolution satellite data and multi-criteria analysis was implemented for site suitability. The candidate STP locations were further constrained by the laid down regulatory norms, in the form of buffer zones, and examined in respect to the annual wind condition. After meeting all the exclusion criteria, three locations each were identified for Rayagada and Siddipet town. In Rayagada one of the candidate locations is located in the east across the Nagavali River, which is technically infeasible, although had better hydrological suitability. The other two locations are in the south-west direction outside the urban boundary and occurring on the wastelands. The slope of these two locations is also within 1%. But, one of the probable locations is close to urban limit and

Table 24.6 Wind pattern (m/s) in Karimnagar, Telangana

Direction	< 0.5	0.5–1.0	1.0–2.0	2.0–3.0	3.0–4.0	4.0–5.0	> 5.0	Total
N	0.18	0.18	1.28	1.28	0.73	0.23	0.23	4.11
NNE	0.05	0.23	1.46	2.92	1.78	0.18	0.18	6.80
NE	0.00	0.23	1.96	2.65	1.69	0.00	0.00	6.53
ENE	0.14	0.18	1.23	1.51	1.00	0.00	0.00	4.06
E	0.09	0.23	1.28	1.64	0.50	0.00	0.00	3.74
ESE	0.05	0.41	1.28	1.19	0.37	0.00	0.00	3.30
SE	0.09	0.18	1.87	1.51	0.73	0.09	0.00	4.47
SSE	0.09	0.23	2.15	4.34	1.69	0.78	0.05	9.33
S	0.23	0.55	2.79	5.16	2.19	0.55	0.09	11.56
SSW	0.05	0.59	1.87	2.42	1.42	0.18	0.14	6.67
SW	0.14	0.59	1.64	1.78	0.68	0.14	0.09	5.06
WSW	0.23	0.18	0.78	1.05	1.00	0.59	0.46	4.29
W	0.09	0.09	1.10	1.96	2.56	3.52	5.25	14.57
WNW	0.00	0.32	0.87	1.87	1.28	1.46	3.84	9.64
NW	0.09	0.37	1.19	0.73	0.27	0.18	0.50	3.33
NNW	0.09	0.27	0.73	0.82	0.50	0.14	0.00	2.55
Total	1.61	4.83	23.48	32.83	18.39	8.04	10.83	100

Source https://www.indianclimate.com/wind-data.php

hence, may be considered the best location. In case of Siddipet, all the three short-listed locations are on wasteland with slope ranging between 1 and 3% but only one among them is close to the urban boundary and hence decided as the best location among all the candidate sites. For both the towns prevailing wind is from west and 'calm' prevails less than 3% of time on annual basis. As the urban sprawl is mostly in the north-east direction with respect to the proposed STP site, the harmful gases or foul odor are presumed to have less impact on urban settlement. Based upon the network of roads and the settlement clusters sewage route optimization was done to minimize the time and distance by the garbage collecting vehicles. Shortest path algorithm was used to obtain the optimal route that has least distance between source and destination nodes. The route optimization would positively impact the cost by saving the fuel and maintenance. Also, this will contribute toward lessening the sound and environmental pollution in the urban habitats. The ideal locations for STP, along with sewage routing were presented in the form of a map with supporting themes for decision support.

Acknowledgements Authors are thankful to the Director, NRSC for assigning this task to the Regional Remote Sensing Centre—East. The satellite data downloaded from earthexplorer.usgs.gov is gratefully acknowledged. The authors thank the urban authorities of Siddipet and Rayagada for making the urban boundary available and 'www.indiaclimate.com' for wind data.

References

Abdalla OO, Khidir SOHE (2017) Site selection of wastewater treatment plant using RS/GIS data and multi-criteria analysis (MCA): case study Omdurman city, Khartoum state, Sudan Alneelain. J Geosci 01:94–107

Adamides ED, Mitropoulos P, Giannikos I, Mitropoulos I (2009) A multi-methodological approach to the development of a regional solid waste management system. J Oper Res Soc 60(6):758–770. https://doi.org/10.1057/palgrave.jors.2602592

Agarwal R, Srivastava AK, Nigam AK (2019) GIS and AHP based site suitability for sewage treatment plant in Sultanpur District, India. Int J Innov Technol Explor Eng 8(6S4):961–964. https://doi.org/10.35940/ijitee.F1196.0486S419

Anagnostopoulos KP, Gratziou M, Vavatsikos AP (2007) Using the fuzzy analytic hierarchy process for selecting wastewater facilities at prefecture level. Euro Water 19(20):15–24

Apaydin O, Gonullu MT (2007) Route optimization for solid waste collection: Trabzon (Turkey) case study. Global NEST J 9(1):6–11

Biotto G, Silvestri S, Gobbo L, Furlan E, Valenti S, Rosselli R (2009) GIS, multi-criteria and multi-factor spatial analysis for the probability assessment of the existence of illegal landfills. Int J Geogr Inf Sci 23(10):1233–1244. https://doi.org/10.1080/13658810802112128

Brimicombe AJ (2003) A variable resolution approach to cluster discovery in spatial data mining. In: Kumar V, Gavrilova ML, Tan CJK, L'Ecuyer P (eds) Computational science and its applications—ICCSA 2003. Lecture notes in computer science, vol 2669. https://doi.org/10.1007/3-540-44842-X_1

Butler E, Hung YT, Al Ahmad MS, Yeh RYL, Liu RLH, Fu YP (2017) Oxidation pond for municipal waste water treatment. Appl Water Sci 7:31–51.https://doi.org/10.1007/s13201-015-0285-z

Chalkias C, Lasaridi K (2009) A GIS based model for the optimization of municipal solid waste collection: the case study of Nikea, Athens, Greece. WSEAS Trans Environ Dev 5(10):640–650. http://www.wseas.us/e-library/transactions/environment/2009/29-809.pdf

Chalkias C, Lasaridi K (2011) Benefits from GIS based modelling for municipal solid waste management. In: Kumar S (ed) Integrated waste management, vol I. IntechOpen. https://doi.org/10.5772/17087

Chang NB, Parvathinathan G, Breeden JB (2008) Combining GIS with fuzzy multicriteria decision-making for landfill siting in a fast-growing urban region. J Environ Manage 87(1):139–153. https://doi.org/10.1016/j.jenvman.2007.01.011

Cormen TH, Leiserson CE, Rivest RL, Clifford S (2001) Section 24.3: Dijkstra's algorithm in Introduction to algorithms, 2nd edn. MIT Press and McGraw-Hill, pp 595–601. ISBN 0-262-03293-7

Dijkstra EW (1959) A note on two problems in connexion with graphs. Numer Math 1:269–271. https://doi.org/10.1007/BF01386390

Esmaili H (1972) Facility selection and haul optimization model. J Sanitary Eng Div 98(2). https://doi.org/10.1061/JSEDAI.0001482

ESRI (2006) ArcGIS network analyst tutorial. ESRI press, 36 pages

Gemitzi A, Tsihrintzis VA, Voudrias E, Petalas C, Stravodimos G (2007) Combining geographic information system, multicriteria evaluation techniques and fuzzy logic in siting MSW landfills. Environ Geol 51:797–811. https://doi.org/10.1007/s00254-006-0359-1

Geneletti D (2010) Combining stakeholder analysis and spatial multicriteria evaluation to select and rank inert landfill sites. Waste Manage 30(2):328–337. https://doi.org/10.1016/j.wasman.2009.09.039

Ghose MK, Dikshit AK, Sharma SK (2006) A GIS based transportation model for solid waste disposal—a case study of Asansol municipality. Waste Manage 26(11):1287–1293. https://doi.org/10.1016/j.wasman.2005.09.022

Golden BL, Dearrmon JS, Baker EK (1983) Computational experiments with algorithms for a class of routing problems. Comput Oper Res 10(1):47–59. https://doi.org/10.1016/0305-0548(83)90026-6

Gómez-Delgado M, Tarantola S (2006) GLOBAL sensitivity analysis, GIS and multi-criteria evaluation for a sustainable planning of a hazardous waste disposal site in Spain. Int J Geogr Inf Sci 20(4):449–466. https://doi.org/10.1080/13658810600607709

Handbook of Forest (Conservation) Act (1980) Forest (conservation) rules, 2003 (guidelines and clarifications). Ministry of Environment, Forest and Climate Change, Government of India, 2019

Hatzichristos T, Giaoutzi M (2006) Landfill siting using GIS, fuzzy logic and the Delphi method. Int J Environ Technol Manage 6(1–2):218–231. https://doi.org/10.1504/IJETM.2006.008263

Henze M, van Loosdrecht MCM, Ekama GA, Brdjanovic D (2008) Biological wastewater treatment: principles, modelling and design. IWA Publishing. https://doi.org/10.2166/9781780401867. ISBN 978-1-78040-186-7

Jensen JR, Ryan R (2013) Introductory geographic information systems. Pearson, Boston

Johansson OM (2006) The effect of dynamic scheduling and routing in a solid waste management system. Waste Manage 26(8):875–885. https://doi.org/10.1016/j.wasman.2005.09.004

Jones ER, van Vliet MTH, Qadir M, Bierkens MFP (2021) Country-level and gridded estimates of wastewater production, collection, treatment and reuse. Earth Syst Sci Data 13(2):237–254. https://doi.org/10.5194/essd-13-237-2021

Kao JJ, Lin HY (1996) Multifactor spatial analysis for landfill siting. J Environ Eng 122(10):1943–7870. https://doi.org/10.1061/(ASCE)0733-9372(1996)122:10(902)

Karadimas NV, Loumos VG (2008) GIS-based modeling for the estimation of municipal solid waste generation and collection. Waste Manage Res 26(4):337–346. https://doi.org/10.1177/0734242X07081484

Karadimas NV, Papatzelou K, Loumos VG (2007) Optimal solid waste collection routes identified by the ant colony system algorithm. Waste Manage Res 25(2):139–147. https://doi.org/10.1177/0734242X07071312

Khopkar SM (2004) Environmental pollution monitoring and control. New Age International (P) Ltd., New Delhi, p 299. ISBN 978-81-224-1507-0

Kim BI, Kim S, Sahoo S (2006) Waste collection vehicle routing problem with time windows. Comput Oper Res 33(12):3624–3642. https://doi.org/10.1016/j.cor.2005.02.045

Kontos TD, Komillis DP, Halvadakis CP (2003) Siting MSW landfills in Lesvos Island with a GIS based methodology. Waste Manage Res 21(3):262–277. https://doi.org/10.1177/0734242X0302100310

Kontos TD, Komilis DP, Halvadakis CP (2005) Siting MSW landfills with a spatial multiple criteria analysis methodology. Waste Manage 25(8):818–832. https://doi.org/10.1016/j.wasman.2005.04.002

Lopez Alvarez JV, Aguilar Larrucea M, Fernandez-Carrion Quero S, Jimenez del Valle A (2008) Optimizing the collection of used paper from small businesses through GIS techniques: the Leganés case (Madrid, Spain). Waste Manage 28(2):282–293. https://doi.org/10.1016/j.wasman.2007.02.036

Lotfi S, Habibi K, Koohsari MJ (2007) Integrating GIS and fuzzy logic for urban solid waste management (a case study of Sanandaj city, Iran). Pak J Biol Sci 10(22):4000–4007. https://doi.org/10.3923/pjbs.2007.4000.4007

Malczewski J (2004) GIS-based land-use suitability analysis: a critical overview. Prog Plan 62:3–65

Malczewski J, Rinner C (2015) Multi-criteria decision analysis in geographic information science. Springer, New York, NY, USA

Mansouri Z, Moghaddas NH, Dahrazma B (2013) Wastewater treatment plant site selection using AHP and GIS: a case study in Falavarjan, Esfahan. Jgeope 3(2):63–72

Nas B, Cay T, Iscan F, Berktay A (2010) Selection of MSW landfill site for Konya, Turkey using GIS and multi-criteria evaluation. Environ Monit Assess 160(1–4):491–500. https://doi.org/10.1007/s10661-008-0713-8

NTPC (2015) Executive summary of draft environmental impact assessment report for Telangana super thermal power project, stage-I, doc no. 9591/999/GEG/S/001, p 16

Nuortio T, Kytöjokib J, Niska H, Bräysy O (2006) Improved route planning and scheduling of waste collection and transport. Expert Syst Appl 30(2):223–232. https://doi.org/10.1016/j.eswa.2005.07.009

Rao IN, Pasha K (1993) Determination of critical wind velocities for thermal power plants—a Gaussian plume model approach. Indian J Environ Prot 14(1):53–56

Ritchie R, Mispy O-O (2018) Measuring progress towards the sustainable development goals (SDG 1). SDG-Tracker.org

Saaty TL (1980) The analytic hierarchy process. McGraw-Hill, New York, p 287. ISBN: ISBN 0-07-054371-2

Sahoo S, Kim S, Kim B-I, Kraas B, Popov A (2005) Interfaces routing optimization for waste management 35(1):24–36.https://doi.org/10.1287/inte.1040.0109

Sonesson U (2000) Modeling of waste collection—a general approach to calculate fuel consumption and time. Waste Manage Res 18(2):115–123. https://doi.org/10.1034/j.1399-3070.2000.00099.x

Taghilou S, Peyda M, Khosravi Y, Mehrasbi MR (2019) Site selection for wastewater treatment plants in rural areas using the analytical hierarchy process and geographical information system. J Human Environ Health Prom 5(3):137–144

Tavares G, Zsigraiova Z, Semiao V, Carvalho M (2008) A case study of fuel savings through optimization of MSW transportation routes. Manag Environ Qual 19(4):444–454

Tchobanoglous GH, David Stensel HD, Tsuchihashi R, Burton FL, Abu-Orf M, Bowden G (2014) Wastewater engineering: treatment and resource recovery, 5th edn. New York, NY. ISBN 978-0-07-340118-8. OCLC 858915999

Ukpong EC (2013) Modeling wind effect on waste stabilization pond performance. Int J Appl Sci Technol 3:13–26

UNGA (2015) Transforming our world: the 2030 agenda for sustainable development. Resolution adopted by the general assembly on 25 Sept 2015. A/70/L.1. UNGA, New York. www.un.org/ga/search/view_doc.asp?

UN-Water (2021) Summary progress update 2021—SDG 6—water and sanitation for all. Version: July 2021. Geneva, Switzerland

USEPA (United States Environmental Protection Agency) (2011) Principles of design and operations of waste water treatment pond systems of plant operators, engineers and managers. EPA 600-R-11-088. Office of Research and Development, Cincinnati. http://www.epa.gov/ordntrnt/ORD/NRMRL/lrpcd/projects/ponds.htm

Von Sperling M (2015) Wastewater characteristics, treatment and disposal. Water Intell Online 6:9781780402086. https://doi.org/10.2166/9781780402086.ISSN1476-1777

Vuppala P, Asadi SS, Reddy MA (2006) Solid waste disposal site selection using analytical hierarchy process and geographical information system. Pollut Res 25(1):73–76

Wang G, Qin L, Li G, Chen L (2009) Landfill site selection using spatial information technologies and AHP: a case study in Beijing, China. J Environ Manage 90(8):2414–2421. https://doi.org/10.1016/j.jenvman.2008.12.008

Water Pollution (2013) Environmental health education program. Harvard T.H. Chan School of Public Health, Cambridge, MA, July 23. Retrieved 2021-09-18

Waters NM (1998) Geographic information systems. In: Kent A, Hall CM (eds) Encyclopedia of library and information science. Marcel Dekker, New York, NY

Yang JQ, Lee H (1997) An AHP decision model for facility location selection. Facilities 15:241–254

Zamorano M, Molero E, Hurtado A, Grindlay A, Ramos A (2008) Evaluation of a municipal landfill site in Southern Spain with GIS-aided methodology. J Hazard Mater 160(2–3):473–481. https://doi.org/10.1016/j.jhazmat.2008.03.023

Zhao YW, Qin Y, Chen B, Zhao X, Li Y, Yin XA, Chen GQ (2009) GIS-based optimization for the locations of sewage treatment plants and sewage outfalls – a case study of Nansha district in Guangzhou City, China. Commun Nonlinear Sci Numer Simul 14(4):1746–1757. https://doi.org/10.1016/j.cnsns.2007.12.016

Zsigraiova Z, Tavares G, Semiao V, Carvalho MG (2009) Integrated waste-to-energy conversion and waste transportation within island communities. Energy 34(5):623–635. https://doi.org/10.1016/j.energy.2008.10.015

Chapter 25
Remote Sensing and Deep Learning for Traffic Density Assessment

Debasish Chakraborty, Dibyendu Dutta, and Chandra Shekhar Jha

Abstract With the advent of high resolution (HR) remote sensing (RS) techniques, RS image can now be used to quickly obtain traffic data. When compared to the traditional technique of traffic density assessment, which depends on surveillance or aerial data, traffic density assessment utilizing remote sensing satellite data has many advantages, including convenience, cheap cost, and high safety. Apart from that, the resolution of RS satellite data has significantly improved; for example, many HR remote sensing satellites now provide images with a resolution of 0.5–1 m. Although satellite data resolution is not yet comparable to aerial or surveillance data, it is sufficient for traffic density estimation. In this chapter, traffic density is estimated using HR satellite data and a deep convolution neural network (DCNN). To recognize vehicles in HR images, a DCNN architecture with one convolution layer, two pooling layers, and a five-layer fully connected neural network are used. To mask and measure the area of vehicles, a simple mathematical method is used to change the scale and orientation of the movable window. A formula is used to compute the traffic density using the estimated vehicles and road areas. The approach is validated using WorldView-2 images with a spatial resolution of 0.46 m. The proposed method for assessing traffic density in HR images achieves a high level of accuracy (99%) while requiring less training and processing time than CNN and ResNet-18.

Keywords Remote sensing · High resolution image · Vehicle · Road · Deep learning · Traffic density

D. Chakraborty (✉) · D. Dutta
Regional Remote Sensing Centre-East, National Remote Sensing Centre, ISRO, New Town, Kolkata, West Bengal, India
e-mail: deba.isro@gmail.com

C. S. Jha
Regional Centres, National Remote Sensing Centre, Hyderabad, India

C. S. Jha et al. (eds.), *Geospatial Technologies for Resources Planning and Management*, Water Science and Technology Library 115,
https://doi.org/10.1007/978-3-030-98981-1_25

25.1 Introduction

Satellite images can now be used to quickly obtain traffic data due to the advent of satellites and high-resolution imaging techniques. Compared to traditional traffic density assessment methods that rely on surveillance or aerial images (Bethke et al. 2007; Reinartz et al. 2006; Ernst et al. 2003), traffic density assessment using remote sensing satellite images offers a number of benefits, including convenience, low cost, and high safety. The resolution of satellite imagery has significantly improved; for example, many high-resolution satellites, such as IKONOS (1 m), CARTOSAT-2 (1 m), QuickBird (0.61 m), WorldView (0.46 m), and others, provide 0.5 to 1 m resolution images. Satellite images have a resolution that is sufficient for traffic density assessment, though it is still not comparable to aerial or surveillance images. As a result, in recent years, traffic density estimation using HR satellite images has become a focus for research.

Larsen et al. (2009) identified vehicles on the road from high resolution (HR) satellite images for traffic density analysis using hand-crafted features such as mean intensity, mean gradient, and standard deviation of the intensity within the object. However, in high-resolution imageries, it frequently misinterpreted other small objects as vehicles. This is due to the fact that the features generated by this method are not always sufficient to distinguish vehicles from other small objects. To detect traffic density in optical remote sensing data, Palubinskas et al. (2010) used the Multivariate Alteration Detection (MAD) method (Nielsen 2007) and image processing techniques. Despite the fact that the method is effective at detecting traffic density on highways, it is reliant on the geo-referencing of overlapping images and the road data base. For measuring the state of traffic, Eikvil et al. (2009) used QuickBird satellite images and road network data. Leitloff et al. (2006) employed Haar-like features to detect vehicles and estimate traffic status in satellite images. He et al. (2011) used supervised classification and thresholding to extract traffic information from HR satellite images. Mantrawadi et al. (2013) suggested a data mining and knowledge extraction approach for detecting traffic condition in HR satellite images. For obtaining traffic information, Chen et al. (2013) proposed an ANN-based vehicle detector. Cao et al. (2016b) introduced a vehicle detection algorithm for assessing traffic state utilizing lower resolution satellite data, which overcomes constraints such as low resolution and a lack of training samples. For traffic monitoring, Eslami and Faez (2010) used satellite images and image processing techniques.

Deep convolution neural network (DCNN) algorithms, are being used to detect objects in natural images acquired by digital cameras (Jiao et al. 2019). When it comes to recognizing objects in natural images, these algorithms show promising result (Galvez et al. 2018; Ou et al. 2019; Mane and Mangale 2018; Pathaka et al. 2018; Ren et al. 2015). Deep Learning (DL) is a subfield of machine learning that deals with artificial neural networks, inspired by the structure and function of the brain. It is composed of multiple layers and can learn from data. Currently, DCNN-based methods are being used to detect vehicles in high resolution images automatically (Cao et al. 2016a; Tang et al. 2017). The benefit of this technique is that it

automatically extracts detail features of the object of interest from the image in order to distinguish it from other objects. The convolutional neural network (CNN) is a type of ANN capable of detecting and classifying objects in images. The DNN (Deep Neural Network) is a type of ANN that has several layers between the input and output layers. An ANN is a network of nodes that was inspired by a brain simplification. For detecting vehicles in HR arial imagery, Tang et al. (2017) used Deep CNN and SVM algorithms. Deep CNN is used to extract features from data, and SVM is used to detect and obtain the object's bounding box using these feature vectors as input. Though this technique provided a good detection result, it took longer.

A sufficient number of training datasets is required to prepare a DCNN-based model. Obtaining enough vehicle training datasets from HR remote sensing images is a difficult and time-consuming task. Currently, there are several publicly available areal datasets that cover the vehicles inhabited region. The goal of this study is to prepare a DCNN model for identifying and measuring the area of vehicles in HR images using freely available areal datasets and HR remote sensing satellite datasets as a training dataset. However, using these multisource training datasets to train the DCNN is difficult and time consuming. The texture feature is useful when using multisource satellite data for analysis. As a result, texture features in areal and high-resolution remote sensing datasets are measured using a convolution operation, allowing texture values to be used as input to fully connected neural networks (FCNN) instead of intensity values. To reduce the spatial size of the transformed datasets, two pooling operations are used. The FCNN is trained using the texture representation sets after an L-layer FCNN architecture is designed. Following that, the FCNN model is used to identify vehicles in HR images. The movable window's scale and orientation are adjusted to best mask the vehicles and measure their area in the HR input images. Following that, the estimated vehicle and road areas are used to determine the current state of traffic density. The proposed approaches, CNN (Galvez et al. 2018) and ResNet-18 (Ou et al. 2019), were used to measure vehicle area and assess traffic density using WorldView-2 pan-sharpened multispectral images with spatial resolution 0.46 m covering road sections. When it comes to assessing vehicle area in HR images and interpreting traffic density, the suggested algorithm surpasses CNN and ResNet-18, according to the findings.

25.2 Study Area and Data Used

The study area is the EM Bypass in Kolkata, West Bengal, India. Buildings, water bodies, roads, and green space make up the region, which is located between 22° 33′ 10.35″ and 22° 30′ 52.80″ North latitude and 88° 25′ 23.63″ and 88° 27′ 50.62″ East longitude. The WorldView-2 pan-sharpened multispectral images with a spatial resolution of 0.46 m that were obtained on October 26th, 2019, were used in this study. The free datasets Cars Overhead with Context (COWC) (Nathan et al. 2016), DLR 3 K Munich (Liu et al. 2015), and Vehicle Detection in Aerial Imagery (VEDAI) (Razakarivony et al. 2016) were also used in this study.

25.3 Preparation of Datasets

The datasets for training and validating the DCNN architecture have been prepared. The dataset is prepared using freely available COWC, DLR 3 K Munich, VEDAI, and WorldView-2 pan-sharpened multispectral satellite images. Because preparing a large number of vehicle training datasets from satellite images is difficult, we used publicly available areal datasets.

The COWC dataset is a large collection of high-quality overhead imagery collected from aerial platforms at a nadir view angle, similar to satellite imagery. This data has a spatial resolution of (0.15 m $\times$ 0.15 m). For the area of Munich, Germany, the DLR3K Munich vehicle dataset is available. This information was provided by the German Aerospace Center's Remote Sensing Technology Institute. This data has a spatial resolution of (0.13 m $\times$ 0.13 m). The VEDAI dataset was collected in Utah, USA, and includes a variety of backgrounds, including agrarian, rural, and urban areas. The VEDAI images are available in spatial resolutions of (0.125 m $\times$ 0.125 m) and (0.25 m $\times$ 0.25 m). These areal images are taken into account because they only capture areas where vehicles are present and freely available. Before being used as a training dataset, areal images are downscaled to the spatial resolution (0.46 m $\times$ 0.46 m) of WorldView-2 satellite images. Figure 25.1a, b show a few trainings and validation areal datasets, whereas Fig. 25.2a, b show a few trainings and validation Worview-2 datasets, respectively. Four-wheelers and heavy vehicles are clearly visible in WorldView-2 pan-sharpened multispectral images with a spatial resolution of 0.46 m, so these vehicles are labelled in these images.

To demarcate the vehicle in areal and satellite images, the VIA (Visual Geometry Group Image Annotator) tool is used. It was chosen because it is an image annotation software that is both simple and standalone. Furthermore, VIA is a web-based application that does not require any installation or configuration. More than 2700 vehicles visible in the images, mostly four-wheelers and buses, have been labelled. The DCNN architecture is trained and tested using these labelled data. Out of 2700 labelled datasets, 2160 (or 80%) are randomly selected for training the DCNN, while the remaining 540 (or 20%) are kept for validating the DCNN model.

25.4 Methodology

In the proposed approach, there are four major steps. The first step is to use a road mask to extract road regions from HR images. The DCNN architecture is configured and trained with the training and validating datasets in the second step. In the third step, the trained model is used to detect vehicles and measure their area in extracted HR images. The final step is to assess traffic density. The method's flow diagram is shown in Fig. 25.3.

Fig. 25.1 **a** Areal datasets with labels were used to train the CNN architecture. **b** Areal datasets with labels were used to validate the CNN model

25.4.1 Extraction of Road Region from High Resolution Image

The GPS points in each road turn around the selected part of the road are collected using handheld GPS equipment. The GPS points are imported into the Erdas-Imagine tools to create a road mask, which is then used to extract the road region from the original HR image and calculate the road area using Eq. 25.1. The pixel values of the road regions are represented as actual values in the extracted image, while the pixel values of the other regions are defined as zero. To detect vehicles, the proposed CNN

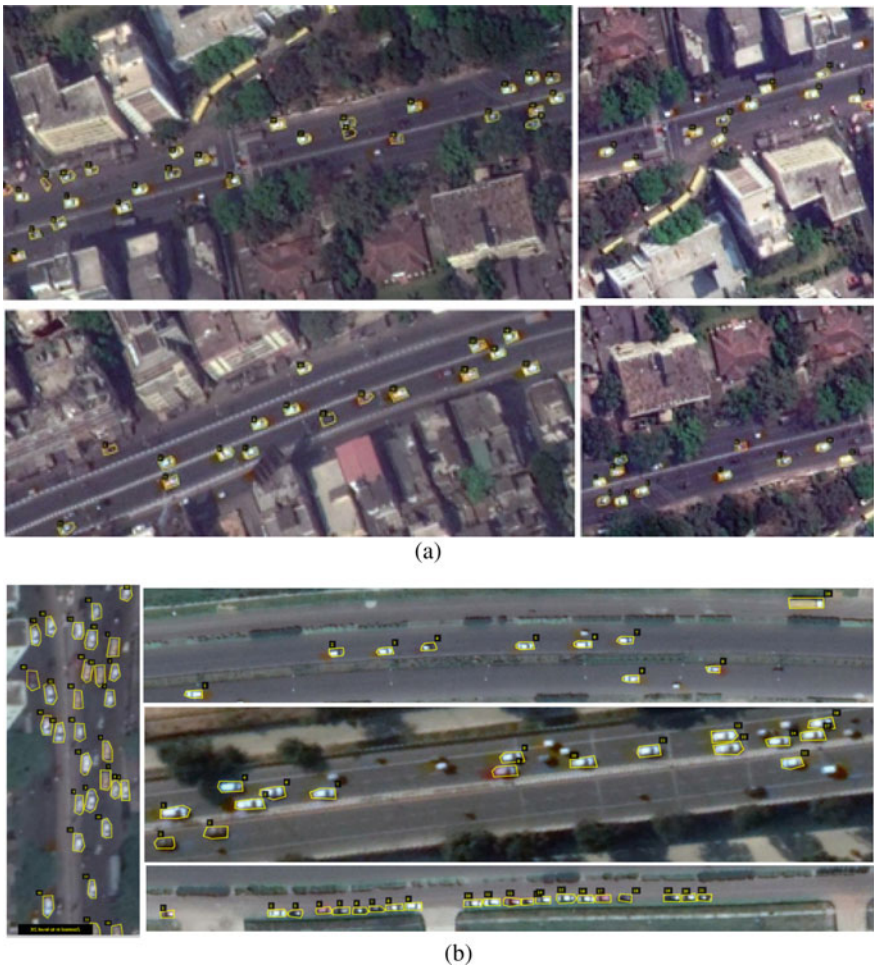

Fig. 25.2 **a** Satellite datasets with labels were used for training the CNN architecture. **b** Labelled satellite datasets used for validating the CNN model

model is only applied to the extracted image's non-zero region (i.e. the road region). If W is a region of interest (ROI) and $f(W)$ is a function, then the proposed CNN model will only be applied to W if $f(W) = 1$. Equation 25.2 is used to formulate $f(W)$. As a result, the computation time is reduced. The benefits of using the extracted road area include a reduction in process time and false positives, as the extracted road area is largely populated by vehicles.

$$R_{\text{Area}} = p \times r^2 \tag{25.1}$$

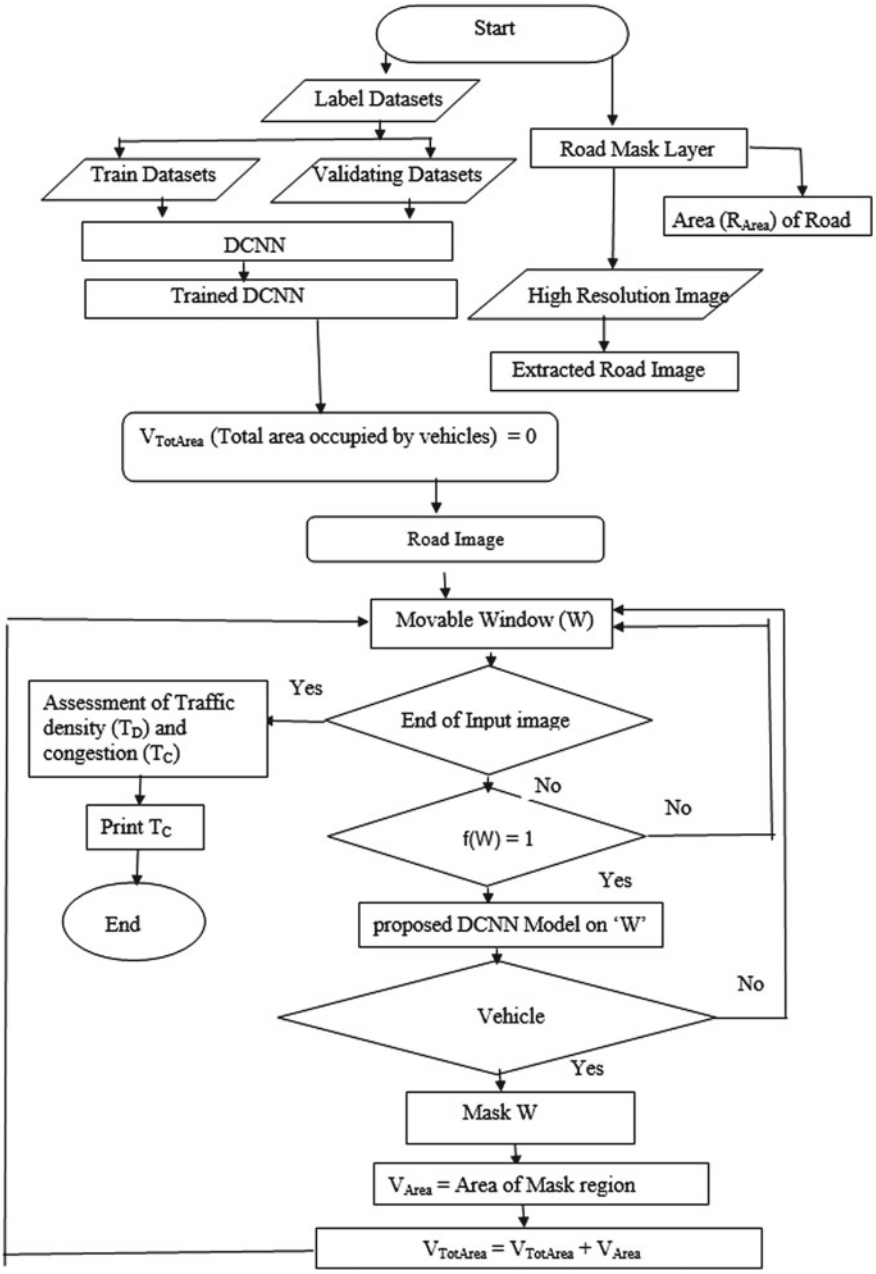

Fig. 25.3 Flow diagram of proposed method

where, $\mathrm{ROAD}_{\mathrm{Area}}$ represents area of road, p represents number of pixels in mask region, and r represents resolution of the satellite image

$$f(W) = \begin{cases} 0, & \sum_{i=1}^{m} \sum_{i=1}^{n} W(i, j) = 0 \\ 1, & \text{Otherwise} \end{cases} \tag{25.2}$$

where, W represents ROI (i.e. road region), m and n are length and width of the ROI respectively.

25.4.2 Preparation of Deep Convolutional Neural Network (DCNN) Architecture

The proposed DCNN architecture includes convolution layer, pooling layers, and fully connected layer (FCL) to model complex relationships between inputs and outputs. The model helps in identifying, masking, and measuring the area occupied by vehicles in a road image. The convolution layer is a kernel with a smaller dimension than the input image. It conducts a convolution operation on a small area of the input image. Due to a lack of satellite images covering vehicle regions, we used publicly available areal datasets in addition to satellite images covering vehicles to train the fully connected layer. Because the training datasets come from a variety of sources and use different sensors, the intensity values of similar objects will differ. Directly training the DCNN architecture with these multisource training datasets is difficult and time consuming. As a result, in this study, a convolution is used to measure the texture around each pixel of the training datasets, so that the texture value of the dataset can be used as input to FCL instead of the intensity value. Each pixel value is represented by the pixel value of the output convolution layer. This layer is then used for farther processing. When using multisource satellite data for analysis, the texture feature becomes useful. Through pooling, the size of the convolved features is minimized. To create a simple FCL with one-fourth the spatial size of the convolution layers, we used two max pooling operations with filters of size 2×2 and stride of 2. Max pooling is employed here since it summarizes the highest activated presence of a feature. The FCL is the final layer of a CNN and is a feed forward neural network. The FCL considered here has L hidden layers, one input layer, and one output layer. The last pooling layer's output is flattened and fed into the FCL as the input to the FCL. Before being used to train the CNN architecture, the labelled datasets were transformed to a fixed size so that the fully connected layer had the same number of input nodes. The average vehicle length (m) and width (n) from the labelled training datasets are evaluated and treated as a fixed size. After that, all of the labelled datasets are transformed into ($m \times n$) sizes. Interpolation is used to scale down or up labelled datasets that are larger or smaller than the fixed size to the target fixed size. The Nearest Neighbor resampling method is used for interpolation in this study. It was chosen because it is the most straightforward method and does

not change the original values (Baboo and Devi 2010). Equation 25.3 is used to compute the number of neurons in the hidden layer (Hinton et al. 2006; Kurt 1991), whereas the output layer only has one neuron. The sigmoid activation function was used in the input, hidden layers, and output layers. The sigmoid activation function is a type of activation function that has a range of output between 0 and 1. The following neuron receives this output as an input. Equation 25.4 is used to calculate the sigmoid activation function.

$$N_h = \frac{2}{3}N_i + N_o \tag{25.3}$$

where, N_i, N_o, and N_h represents the number of neurons in input, output, and hidden layers respectively.

$$S(x) = \frac{1}{1 + e^{-x}} \tag{25.4}$$

where, $S(x)$ is the output value of the activation function and x represents the input value.

During the learning phase, the structure of the fully connected layer is altered. The process of learning patterns by FCL is called training. FCLs are trained using Back Propagation (BP) depending upon which the connecting weights among the layers are updated. The FCL is adaptively updated until the performance goal is achieved. The FCL is trained in two broad passes: forward and backward, with Mean Square Error (MSE) calculation and connection weight updating in between. The batch training method is used because it increases the speed of training and the rate of converges of MSE to the desired value (Haykin 2003). An epoch is a complete cycle of the training set. The procedure is repeated until MSE meets the performance requirements. The DCNN architecture is trained and validated using the labelled datasets shown in Figs. 25.1a, b and 25.2a, b.

In order to clarify the significance of texture value, which is necessary for the identification of vehicles in high resolution images, the model is also prepared with intensity value instead of texture value and applied in Fig. 25.7a, e and i, respectively, and the results are compared to the proposed method's outcomes.

To determine the optimal number of hidden layers (L), the proposed method is applied to a WorldView-2 image having resolution 0.46 m × 0.46 m (Fig. 25.7a), with different numbers of hidden layers for identification and computing area of vehicles.

25.4.2.1 Convolution Operation

Convolution is used to assess the texture around each pixel in the ROI. It's a three-step procedure. The homogeneous and non-homogeneous patterns appearing within

the movable kernel of size $s \times s$ were quantized in the first step; these patterns are essential properties of high-resolution image texture. All pixel intensities in the moving window are compared to the central pixel during the quantization stage. Let's say 'K' is a $s \times s$ convolution kernel, and $K(p, p)$ represents the intensity value of the central pixel of 'K'. The intensity values in the range $K(p, p) \pm t$ are then categorized into 1, while intensity values outside of this range are labelled as 2. Equation 25.5 is used to formulate this quantization process.

$$L(i, j) = \begin{cases} 1, (K(p, p) - t) \leq K(i, j) \leq (K(p, p) + t) \\ 2, (K(i, j) > (K(p, p) + t)) \text{ or } (K(i, j) < (K(p, p) - t)) \end{cases} \tag{25.5}$$

where $K(i, j)$ is the intensity value of pixel (i, j) in kernel 'K', L is a window of size $s \times s$ holding quantized value, and $L(i, j)$ is the quantized value of corresponding $K(i, j)$, 't' is the threshold value, and Eq. 25.6 is used to compute it.

$$t = \frac{\text{PV}_{\text{Max}} - \text{PV}_{\text{Min}}}{N} \tag{25.6}$$

where, $N = s \times s$, PV_{Max} and PV_{Min} denotes maximum and minimum pixel values respectively in widow 'K'.

The intensity value of the moving kernel 'K' is replaced by the quantized value in the second step. As a result, the quantized kernel 'L' is obtained. Pixels are labelled 1 and 2 in the quantized kernel 'L' having $s \times s$ pixels. Non-homogeneous patterns, i.e. points or regions that are much brighter or darker than the center pixel, are labelled as 2. The numeral 1 specifies homogeneous patterns with points or regions that are moderately equal to the central pixel.

In the third step, the original and quantized windows are used together to assess texture around the pixel. The texture around each pixel is evaluated in three steps. Equation 25.7 is used to compute the occurrence of 1 and 2 in quantized window 'L' in the first step. The 'L' labelled mask window and Eq. 25.8 are used in the second step to extract homogeneous and non-homogeneous regions from 'K'. As a result, we have 'F1' and 'F2' of size $s \times s$. F1 contains only intensity value of homogeneous pattern, whereas 'F2' contains only non-homogeneous pattern intensity values. In the third stage, the texture surrounding $K(p, p)$ is measured using Eq. 25.9. As a result, the convolved image is created, with each pixel representing the texture measure around it.

$$O_T = \sum_{i=1}^{s} \sum_{j=1}^{s} u(L(i, j)), \quad T = 1, 2 \tag{25.7}$$

where,

$u(z) = \begin{cases} 1, L(i,j) = T \\ 0, L(i,j) \neq T \end{cases}$ and O_T denote the occurrence of Tth pattern and $T = 1, 2$ represents the homogeneous and non-homogeneous patterns in 'L' respectively.

$$F_T(i,j) = r(K(i,j)),\ (i = 1, \ldots, s),\ (j = 1, \ldots, s),\ (T = 1, 2) \tag{25.8}$$

where,

$r(g) = \begin{cases} K(i,j), L(i,j) = T \\ 0, L(i,j) \neq T \end{cases}$ and F_T is the extracted Tth region of size $s \times s$.

$$D = \left| \frac{V_1}{O_1} - \frac{V_2}{O_2} \right| \tag{25.9}$$

where D is the texture measure around $K(p, p)$, O_1, O_2 denotes the occurrence of homogeneous and non-homogeneous patterns in L, computed using Eq. 25.7, and V_1, V_2 denotes the total intensity values of homogeneous and non-homogeneous regions in 'K', computed using Eq. 25.10.

$$V_T = \sum_{i=1}^{s} \sum_{j=1}^{s} F_T(i,j), \quad T = 1, 2 \tag{25.10}$$

where, V_T is the total intensity value of pixels appearing in Tth region.

V_1/O_1 and V_2/O_2 represents average intensity values in homogeneous and non-homogeneous region respectively and D is the measure of degree of texture around $K(p, p)$.

Because basic mathematical formulae are utilized to measure the texture around each pixel in a HR image, this convolution technique has the advantage of being computationally simple. Furthermore, it is noise-resistant, as the texture assessment measure V_2/O_2 minimizes the effect of noise, and the combination of bright and dark patterns substantially eliminates noise interference.

25.4.3 Detection of Vehicles and Measurement of Its Area

The size of the movable window is determined by the average length (m) and breadth (n) of the vehicles as determined by the training labelled datasets (W). This window (W) moves in the input HR road image to detect and measure the area occupied by vehicles. The model created in Sect. 25.3.2 is extended to those windows (W) for which $f(W) = 1$ to find the probable cars within the window (W) (Fig. 25.3). When a vehicle is identified within the window, the window is masked, and the masked area is computed using Eq. 25.11, and then the area counts are incremented to measure

the overall area occupied by vehicles on the road. As illustrated in Fig. 25.3, this method is followed until the end of the input image. Thus, vehicles are masked in the input image, and the total area (V_{TotArea}) occupied by vehicles on that road is measured.

$$V_{\text{Area}} = (m \times n) \times r^2 \tag{25.11}$$

where, V_{Area} represents area covered by individual vehicle, m and n represents length and width of the vehicle respectively and r represents resolution of the satellite image.

Following the model's identification of a prospective vehicle within the kernel, the vehicle's probable boundary is defined. To do this, the kernel scale is changed to $(\frac{1}{2}m, \frac{1}{2}n)$,$(\frac{1}{2}m, n))$, $(m, \frac{1}{2}n)$,(m, n),$(2m, n)$,$(m, 2n)$,$(2m, 2n)$ respectively to find the probable size of the vehicles. The kernel is then rotated in π/6, π/3, π/2, 2π/3 orientations for each scale to determine the vehicle's orientation, including longitudinal and transverse positions. Here, m and n represent the average length and width of the vehicles assessed from training labelled datasets to consider the size of the movable window. Equation 25.12 is used to rotate the window (W) in angle 'θ' about the origin (Rafael et al. 1992; William 1992). Subsequently, the proposed DCNN model is extended to find vehicles in all varied scales and oriented windows (W), the highest scoring kernel is considered as the potential vehicle boundary. All pixels inside the potential vehicle boundary are then filled with 1 to mask the probable vehicle.

$$\begin{bmatrix} u \\ v \end{bmatrix} = \begin{bmatrix} \cos\theta & -\sin\theta \\ \sin\theta & \cos\theta \end{bmatrix} \begin{bmatrix} x \\ y \end{bmatrix} \tag{25.12}$$

where, (x, y) be the co-ordinate of a point in the window and (u, v) be the new position of that point after rotating the window anticlockwise in 'θ' about the origin.

25.4.4 Measurement of Traffic Density

Road area (R_{Area}) computed using Eq. 25.1 and total area (V_{TotArea}) of all vehicles occupied in the same road computed using Eq. 25.13 are used here for measuring the traffic density. Mathematically, traffic density is formulated in this study using Eq. 25.14.

$$V_{\text{TotArea}} = \sum_{r=1}^{K} V_{\text{Area}}^{r} \tag{25.13}$$

where, K is number vehicles are masked, V_{Area}^{r} is the area of rth vehicle in the same road.

$$d = \frac{V_{\text{TotArea}}}{R_{\text{Area}}} \times 100 \tag{25.14}$$

where, d is the traffic density.

The traffic density tells how significant is the congestion of vehicles on the selected portion of the road. The traffic considered as congested only when the density reaches more than the threshold value 't'. The same is represented by Eq. 25.15. In this study, $t = 50\%$ is considered as a threshold. Thus, will be considered as congested only if $t \geq 50\%$. It's a criterion for determining the level of congestion on a particular road. This applies to main roads, with the exception of highways, where the t can be increased to 60%.

$$c = \begin{cases} 1, & d \geq t \\ 0, & d < t \end{cases} \tag{25.15}$$

where, c represents traffic congestion and t represents threshold value.

25.5 Results and Discussion

The suggested vehicle masking method is tested in WorldView-2 data with a spatial resolution of 0.46 m using different 'L' values of 1, 2, 3, 4, 5, 6, 7, 8, 9, 10, 11, 12, 13, 14, and 15 accordingly. For various 'L' values, the F1 score is evaluated. Figure 25.4 depicts the F1 score with various 'L'. Figure 25.4 shows that 'L' has a significant impact on the F1 score when masking cars in high-resolution images. As a result, choosing the right 'L' for masking vehicles in high-resolution images is crucial. The model's complexity rises as the number of hidden layers rises, resulting in overfitting. In this research, $L = 5$ achieved the best performance (Fig. 25.4) for masking vehicles in WorldView-2 images having resolution of 0.46 m.

To create a road mask, GPS points are collected in each road turn around the road. As a result, for Fig. 25.7a, e, and i, we acquired 25, 23, and 18 GPS points, respectively, to create road masks. Only GPS points with a precision of less than one

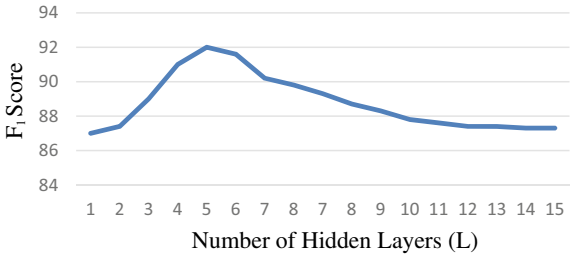

Fig. 25.4 Accuracy with different number of hidden layers 'L'

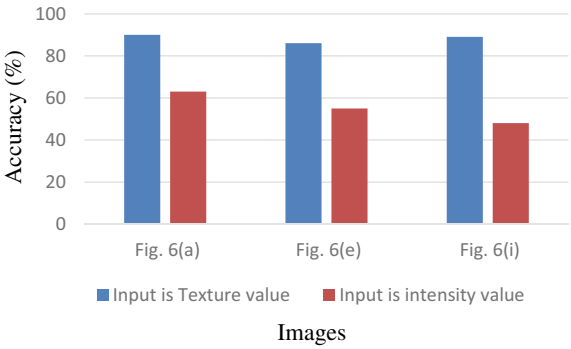

Fig. 25.5 Results of the model based on intensity and texture value respectively

meter are accepted. This helped create a clear road mask, which was then used to extract the road region from the original high-resolution image.

We used publicly available areal datasets because preparing a large number of vehicle training datasets from satellite images is difficult. It's difficult and time consuming to train the DCNN architecture directly with these multisource training datasets. As a result, instead of using the intensity value as an input to FCL, the texture value of the dataset is used. The model is also prepared with intensity value instead of texture value and applied in Fig. 25.7a, e and i, respectively, to explain the significance of texture value, which is important for the identification of vehicles in HR images, and the results are presented in Fig. 25.5. Figure 25.5 shows that texture has an impact on masking vehicles in HR images.

For evaluating the performance of the proposed architecture, CNN (Faster-RCNN with InceptionV2) (Galvez et al. 2018), ResNet-18 (Ou et al. 2019), and the Proposed methods are applied individually to WorldView-2 pan-sharpened multi-spectral images with a spatial resolution of 0.46 m. Galvez et al. (2018) used a twenty-two-layer CNN (Faster-RCNN with InceptionV2) architecture, whereas ResNet-18 (Ou et al. 2019) used an eighteen-layer convolutional neural network.

Figure 25.6a, b and c show the number of epochs vs MSE to determine the optimal number of epochs for the CNN, ResNet-18, and proposed DCNN, respectively. The MSE value is represented on the y-axis, and the number of epochs is represented on the x-axis in these graphs. When the slope of the line drops dramatically, that point is known as the optimal point (to almost zero). Increasing the number of epochs in the MSE at this point only makes a minor difference. As shown in Fig. 25.6a, b and c, the optimal number of epochs for CNN, ResNet-18, and the proposed approach during training are 78,975, 58,857, and 24,201, respectively.

The three architectures applied independently on three different WorldView-2 images as shown in Fig. 25.7a, e and i respectively. The results of applying CNN, ResNet-18, and the proposed technique to (Fig. 25.7a, e and i) separately are shown in (Fig. 25.7b, f and j), (Fig. 25.7c, g and k), and (Fig. 25.7d, h and l), respectively.

Tables 25.1, 25.2, and 25.3 show the accuracy of CNN, ResNet-18, and the proposed technique in masking vehicles in Fig. 25.7a, e and i, respectively. The area of the road is represented by the first column, the number of vehicles visible in

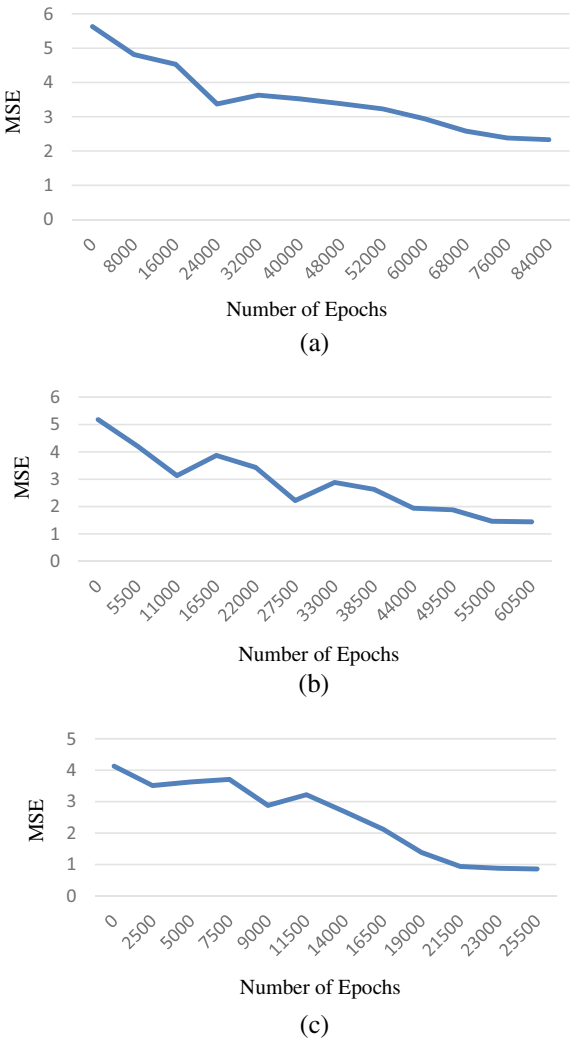

Fig. 25.6 **a–c** shows the MSE versus number of epochs during training of CNN, Resnet 18 and Proposed method respectively

the road image is represented by the second column, and the total area covered by these vehicles is represented by the third column. The fourth, fifth, sixth, seventh, and eighth columns, respectively, represent the number of masked vehicles, the area of masked vehicles, the accuracy in computing the area of vehicles, the measured traffic density, and the ascertained congestion using a specific technique.

Because CNN was unable to mask vehicles well in Fig. 25.7a, as shown in Fig. 25.7b, accuracy in measuring vehicle area in Fig. 25.7a is 43%, as shown in Table 25.1. As a result, traffic density is measured as 30%, and congestion is denoted by the letter 'n' in Fig. 25.7a, as shown in Table 25.1. This model also struggled to compute vehicle area in Fig. 25.7e, i, as seen in Fig. 25.7f, j, respectively. As a

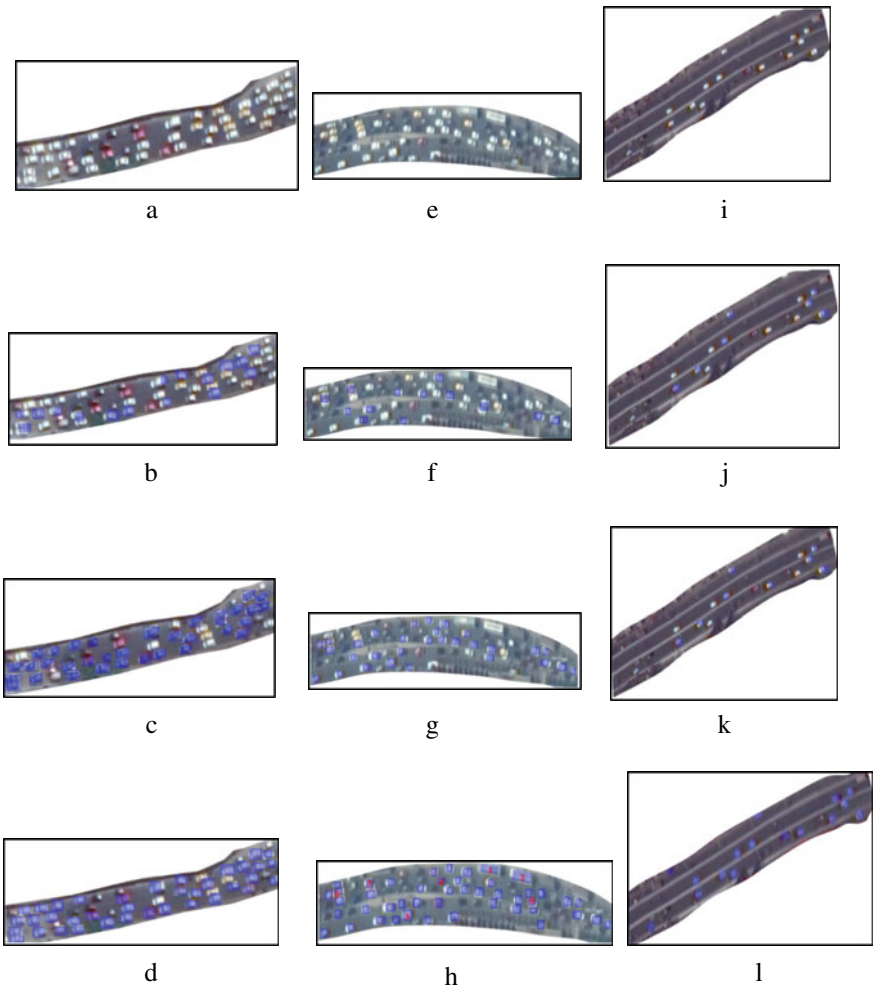

Fig. 25.7 **a**, **e**, **i** input images covering buildings, vacant land, trees, and water bodies, **b**, **f**, **j** output images obtained after applying ResNet-18 on figure a, e, and i respectively, **c**, **g**, **k** output images obtained after applying CNN on figure a, e, and i respectively, **d**, **h**, **l** output images obtained after applying proposed method on figure a, e, and i respectively,

result, CNN's accuracy in computing vehicle area is 31% and 39%, respectively, as shown in Table 25.1. As a result, in Fig. 25.7e, i, traffic density and congestion are interpreted as (20% and 'n') and (7% and 'n') respectively.

Figure 25.7a shows how ResNet-18 moderately masks vehicles, as seen in Fig. 25.7c. As a result, as shown in Table 25.2, the accuracy in measuring the area of vehicles in Fig. 25.7a is 76%. Despite performing better than CNN in Fig. 25.7e, i, as seen in Fig. 25.7g, k, as well as in Table 25.2, ResNet-18 was unable to achieve an average accuracy of more than 60% when measuring the area of vehicles on the

Table 25.1 Measurement of area of vehicles and traffic density and congestion by CNN

Figure	Area of road (m^2)	Vehicle number	Area covered by vehicles (m^2)	No of vehicles masked	Area of masked vehicle (m^2)	Accuracy in computing area of vehicles (%)	Traffic density (%)	Congested (Y/N)
25.7b	480	42	336	18	144	43.00	30.00	N
25.7f	627	51	408	16	128	31.00	20.41	N
25.7j	632	18	126	7	49	39.00	07.00	N

Table 25.2 Measurement of area of vehicles and traffic density and congestion by ResNet-18

Figure	Area of road (m^2)	Vehicle number	Area of occupied vehicles (m^2)	No of vehicles masked	Area of masked vehicles (m^2)	Accuracy in computing area of vehicles (%)	Traffic density (%)	Congested (Y/N)
25.7c	480	42	336	32	256	76.00	53.33	Y
25.7g	627	51	408	30	240	59.00	38.27	N
25.7k	632	18	126	8	56	44.0	09.00	N

Table 25.3 Measurement of area of vehicles and traffic density and congestion by proposed method

Figure	Area of road (m^2)	Vehicle number	Area of occupied vehicles (m^2)	No of vehicles masked	Area of masked vehicles (m^2)	Accuracy in computing area of vehicles (%)	Traffic density (%)	Congested (Y/N)
25.7d	480	42	336	38	304	90.00	63.3	Y
25.7h	627	53	408	44	352	86.00	56.14	Y
25.7l	632	18	126	16	112	89.00	17.72	N

road. Traffic density and congestion are therefore interpreted in Fig. 25.7a, e and i as (53% and 'y'), (38% and 'n'), and (9% and 'n') respectively as visible in Table 25.2.

The proposed architecture outperformed ResNet-18 and masked the majority of the vehicle in Fig. 25.7a, e and i, as seen in Fig. 25.7d, h and i. As a result, the proposed method's average accuracy has increased to 89%, as shown in Table 25.3. Traffic density and congestion are therefore interpreted in Fig. 25.7a, e, and i as (63% and 'y'), (56% and 'y'), and (18% and 'n') respectively as visible in Table 25.3.

The proposed technique clearly identified scale variant vehicles marked as 1, 2, 3 & 4 in Fig. 25.7h, with 1 and 2 representing buses and 3 and 4 representing four-wheelers, respectively. Individual vehicles from densely located regions marked as

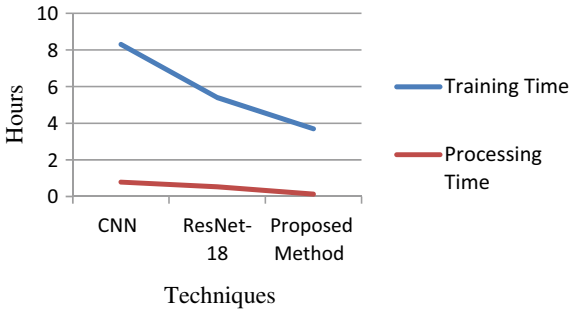

Fig. 25.8 Training and processing time consumed by ResNet-18, CNN, and proposed method respectively

5 & 6 in Fig. 25.7h were effectively masked using this method. Two vehicles are masked with a single bounding box in the region '7' in Fig. 25.7h. This is due to the fact that the gap between adjacent vehicles in this area is very small, as shown in Fig. 25.7e. As shown in Fig. 25.7h, the method detected large vehicles marked 1 and 2.

The same labelled datasets were used to train CNN, ResNet-18, and the proposed method on the same machine in the current study. The trained CNN, ResNet-18, and proposed method are then applied to three images (Fig. 25.7a, e, and i) with sizes of (300 × 400), (300 × 250), and (400 × 400) pixels respectively. The machine time consumed individually by these three techniques to train is shown in Fig. 25.8. The average process time consumed individually by these three techniques to mask vehicles in Fig. 25.7a, e, and i is also shown in Fig. 25.8. As shown in Fig. 25.8, the proposed approach took less time to train the architecture than CNN and ResNet-18. Figure 25.8 also shows that when masking and measuring the area of vehicles in HR images, the trained proposed method takes less time than CNN and ResNet-18. CNN and ResNet-18 employ a large number of convolution layers and pooling layers before constructing the ANN architecture, but the suggested technique requires just one convolution layer and two pooling layers. As a result, the proposed approach takes less time to train the architecture than CNN and ResNet-18.

The proposed method performed well in three different regions, with an average accuracy of 89%. In addition to the study area, the proposed approach can be used to measure traffic density and congestion in high resolution satellite images covering other urban areas. The accuracy of the method's outcome in other areas may not always be the same as in the study area. Because of the scarcity of high-resolution images, we only used a small number of training datasets. The method can be improved by training the architecture with a larger number of variant training datasets. Using high-resolution satellite images, the method can be used to measure traffic density as well as traffic congestion.

The method's main flaw is that it requires training datasets from different regions to keep the model stable. To overcome this limitation, a variety of high-resolution satellite images from various urban regions must be gathered and labelled for the preparation of training datasets.

25.6 Conclusion

The traffic density and congestion were assessed using remote sensing satellite images in this study. To do so, a simple DCNN architecture was first created and trained to detect vehicles in high-resolution images with movable windows. The scale and orientation of the movable window were then adjusted to best mask the vehicles and measure their area in the input high-resolution images. Following that, the estimated vehicle and road areas were used to assess traffic density. To detect and mask vehicles in HR images, the proposed method uses less training and processing time than ResNet-18 and CNN. Using remote sensing data and a simple DCNN architecture, this study discovered that traffic density and congestion can be assessed with minimal computation time and 99% accuracy. The method's limitation is that it can only be used to assess traffic density on highways and main roads, because four-wheelers, buses, and heavy vehicles that can be seen in high-resolution images are frequently seen on these types of roads.

References

Baboo SS, Devi MR (2010) An analysis of different resampling methods in Coimbatore, District. Global J Comp Sci Technol 10(15):61–66

Bethke K-H, Baumgartner SV, Gabele M (2007) Airborne road traffic monitoring with RADAR. In: World congress on intelligent transport systems (ITS), Beijing, China, pp 1–6

Cao Y, Niu X, Dou Y (2016a) Regional-based convolutional neural networks for object detection in vey high resolution remote sensing images. In: 12th international conference on natural computation, Fuzzy systems and knowledge discovery, pp 548–554

Cao L, Wang C, Li J (2016b) Vehicle detection from highway satellite images via transfer learning. Inf Sci

Chen X, Xiang S, Liu C-L, Pan CH (2013) Vehicle detection in satellite images by parallel deep convolutional neural networks. In: IAPR Asian conference on pattern recognition, pp 181–185

Eikvil L, Aurdal L, Koren H (2009) Classification-based vehicle detection in high resolution satellite images. ISPRS J Photogramm Remote Sens 64:65–72

Ernst I, Sujew S, Thiessenhusen KU, Hetscher M, Raßmann S, Ruhé M (2003) LUMOS—airborne traffic monitoring system. In: Proceedings of 6th IEEE international conference on intelligent transportation systems, Shanghai, China

Eslami M, Faez K (2010) Automatic traffic monitoring from satellite images using artificial immune system. In: Hancock structural, syntactic, and statistical pattern recognition. SSPR. vol 6218. Springer, Berlin, Heidelberg

Galvez RL, Bandala AA, Dadios EP, Vicerra RRP, Maningo JMZ (2018) Object detection using convolutional neural networks. In: IEEE region 10 conference, Jeju, Korea (South), pp 2023–2027

Haykin S (2003) Neural networks a comprehensive foundation, 2nd edn. Pearson Education, New Delhi

He XF, Zhou LQ, Li J (2011) Extraction of traffic information in high resolution satellite images. Urban Geotechn Invest Survey 3:49–51

Jiao L, Zhang F, Liu F, Li L, Feng Z, Qu R (2019) A survey of deep learning-based object detection. arXiv preprint arXiv:1907.09408.

Larsen SO, Koren H, Solberg R (2009) Traffic monitoring using very high-resolution satellite imagery. Photogramm Eng Remote Sens 75(7):1–12

Leitloff J, Hinz S, Stilla U (2006) Vehicle detection in very high-resolution satellite images of city areas. IEEE Trans Geosci Remote Sens 48:2795–2806

Mane S, Mangale PS (2018) Moving object detection and tracking using convolutional neural networks. In: Second international conference on intelligent computing and control systems (ICICCS)

Mantrawadi AN, Nijim M, Lee Y (2013) Object identification and classification in a high-resolution satellite data using data mining techniques for knowledge extraction. In: IEEE international systems conference, pp 750–755

Nielsen AA (2007) The regularized iteratively reweighted MAD method for change detection in multi- and hyperspectral data. IEEE Trans Image Process 16(2):463–478

Ou X, Yan P, Zhang Y, Tu B, Zhang G, Wu J, Li W (2019) Moving object detection method via ResNet-18 with encoder–decoder structure in complex scenes. IEEE Access 7:108152–108160

Palubinskas G, Kurz F, Reinartz P (2010) Model based traffic congestion detection in optical remote sensing imagery. Eur Transp Res Rev 2:85–92

Pathaka AR, Pandeya M, Rautaraya S (2018) Application of deep learning for object detection. In: International conference on computational intelligence and data science, vol 132, pp 1706–1717

Reinartz P, Lachaise M, Schmeer E, Kraub T, Runge H (2006) Traffic monitoring with serial images from airborne cameras. ISPRS J Photogrammetry Remote Sens 61:149–158

Ren S, He K, Girshick R, Sun J (2015) Faster R-CNN: towards real-time object detection with region proposal networks. IEEE Trans Pattern Anal Mach Intell 39(6):1137–1149

Tang T, Zhou S, Deng Z, Zou H, Lei L (2017) Vechile detection in arieal images based on regional convolutional neural networks and hard negative example minning. Sensors 17(2):E336

Chapter 26
Geospatial Technology for Geographical Indications of India

V. Poompavai, V. B. Manjula, B. Prashanth Kumar, J. Sai Ramakrishna, and M. Arulraj

Abstract A Geographical Indication (GI) is an indication which identifies products with a particular geographical region, because of unique characteristics of the product belonging to that specific locality (e.g., Darjeeling Tea of West Bengal, Madhubani Paintings of Bihar). The present work provides a "Spatial Dimension" to the inventory of registered Geographical Indication products under different categories of goods: Agricultural, Textile, Handicrafts, Food Stuff, Manufactured, and, Natural Goods, using Geographic Information System (GIS). Thematic maps have been generated using open source GIS software to spatially visualize the origin of GI products as geographic co-ordinate points with the corresponding state/districts of production as polygons. Attributes for each GI include photograph, logo, type of goods, classification, registration details etc. The Geospatial Database has been customized for web-based spatial visualization on Satellite Imagery and Map in ISRO's BHUVAN Geoportal. Query tools for display of geographical indications by GI Name, State and Type of Goods are added as modules in the portal. The spatial tagging of Geographical Indications creates consumer awareness, helps in protecting indigenous goods and supports the stakeholders of local community who are involved in the production of Geographical Indications.

V. Poompavai (✉) · V. B. Manjula
Regional Remote Sensing Centre – South, NRSC, ISRO, Bengaluru, Karnataka, India
e-mail: poompavai_v@nrsc.gov.in

V. B. Manjula
e-mail: manjula_vb@nrsc.gov.in

B. P. Kumar
Geographical Indications Registry, Intellectual Property Office, Chennai, India
e-mail: prashanth.ipo@nic.in

J. S. Ramakrishna · M. Arulraj
National Remote Sensing Centre, ISRO, Hyderabad, Telangana, India
e-mail: sairamakrishna_j@nrsc.gov.in

M. Arulraj
e-mail: arulraj_m@nrsc.gov.in

C. S. Jha et al. (eds.), *Geospatial Technologies for Resources Planning and Management*, Water Science and Technology Library 115,
https://doi.org/10.1007/978-3-030-98981-1_26

Keywords Geographical indications · Geospatial database · Web-GIS · BHUVAN

26.1 Introduction

Geographical Indication (GI), according to the Article 22.1 of the TRIPS (Trade-Related Aspects of Intellectual Property Rights) Agreement, is an indication which identifies products having unique qualities from a specific geographical region. The agro-climatic conditions and traditional methods of manufacturing give rise to unique qualities and characteristics of the GI goods (WIPO 2021). The distinctive nature and uniqueness of Geographical Indication, is the amalgamation of natural factors such as climatic conditions, landform, soil, temperature, rainfall, methods of plantation, in addition to the indigenous methods of production followed since generations.

The Geographical Indication name consists of the location from which the goods are produced, such as ***Madurai*** Malli, ***Udupi*** Mattu Gulla Brinjal, Kathputlis of ***Rajasthan***, ***Agra*** Durrie, ***Tezpur*** Litchi, ***Bandar*** Laddu and ***Kashmir*** Pashmina Shawl. Non-geographical names such as Basmati Rice and Feni also constitute GI. Geographical indications are typically grouped under different types of goods: agricultural products, food stuff, handicrafts, textile goods, meat/poultry, natural and manufactured goods. Each GI is further assigned a class number as per Nice Classification (WIPO 2017). For e.g. Tea and Coffee belong to Class 30.

Darjeeling tea, known as "The Champagne of Teas" is the first Indian product to receive a Geographical Indication tag in 2004–2005 via the Office of Controller General of Patents, Designs and Trade Marks, India. Due to the agro-climatic conditions prevailing in the region, Darjeeling Tea is produced and grown exclusively in

Fig. 26.1 Few GI products in handicrafts category

87 gardens of the hilly regions of Darjeeling district, West Bengal, India (GI Journal 2004). Some of the ancient metal handicraft styles registered as GI (Fig. 26.1) are made of Zinc, Copper, Brass, Silver and Gold (e.g. Bidriware, Pembarthi Metal Craft and Bastar Dhokra, Budithi Bell and Brass Craft). The GI products comprising traditional crafts and textile products of each State are centuries old and handmade, (e.g. Kashmir Paper Machie, Channapatna dolls of Karnataka, Surat Zari Craft, Aranmula Kannadi of Kerala, Blue Pottery of Jaipur, Lucknow Chikan Craft, Thanjavur Paintings), and, are usually produced by local (rural) communities.

There is always a connection or relationship between the product identified as Geographical Indication and its geographical origin (WIPO 2021). For example, Bangalore Rose Onion, locally called Gulabi Eerulli, is a variety of onion grown in the districts of Kolar, Chikkaballapur, and Bengaluru (Urban and Rural) districts of Karnataka. These districts are rich in two types of soil namely, sand mix of red soil as well as deep fertile mekklu soil, which are both very suitable for growing this variety, which has a deep scarlet red colour and spherical shape with flat base bulbs. In addition, the region has an average temperature of 25–35 °C and relative humidity of 70–75%. The soil in these regions have pH ranging between 6.5 and 7.0. The Bangalore Rose Onion has high pungency with less moisture content making it suitable for prolonged storage. (GI Journal 2014). Similarly, GI Kancheepuram Silk is made from pure mulberry silk using the legendary Korvai weaving technique which is exclusive to the artisans of Kancheepuram region in Tamil Nadu, India, whereas GI Muga Silk is produced by the Garo community in Assam, from a native species of silkworm called Antheraea assamensis. GI Dharwad Pedha is a sweet food stuff prepared from the milk of Dharwadi buffaloes raised by the Gavali community in and around Dharwad, Karnataka, India. Hence, as observed, the geographical and climatic conditions prevalent in the region, or the production techniques inherited by farmers and artisans from their ancestors, contribute to the unique qualities of any Geographical Indication.

26.1.1 Registration Process of GI

The Geographical Indications of Goods (Registration and Protection) Act, 1999 aims to provide registration and better protection of geographical indications relating to goods in India under the administration of Controller General of Patents, Designs and Trade Marks (Registrar of Geographical Indications). The process of registering a product as Geographical Indication is carried out by Geographical Indications Registry located at Chennai, India. There are a set of guidelines for a product to be registered as Geographical Indication. Each registered GI has a validity period of 10 years from the date of registration, which is renewable. The application and registration process for GI, Details of registered GIs, Authorized Users and Application Status are provided in IPIndia website (https://ipindia.gov.in/). The Geographical Indications journals published by GI Registry have been made online since Issue No. 56 dated 22/01/2014. The Geographical Indication journal consists of details

on Official Notices, Registered GIs, Justification for Registration including maps of production region submitted by applicant, New GI Applications for Registration, GI Authorized Users, General Information and Registration Process.

26.1.2 Benefits of GI

Geographical Indication protects the producers and consumers of GI goods, in addition to giving boost to exports and rural development, by conferring legal protection and preventing unauthorized use of the products. The growing awareness among consumers about the potential benefits of spatial origin-labelled products due to factors such as food safety and typical qualities of the product has increased the reputation of GI (WIPO 2021; Cerkia Bramley et al. 2009). But, fierce competition in the global market and ever-increasing demand for popular products leads to imitation and fake goods. Hence, GI protects consumers from counterfeit and deception, since a genuine product could be easily identified with the Geographical Indication tag.

A decision support system for application and registration of potential GIs encourages automation of registration process and provides efficient management process (Ray and Samaddar 2011). A geospatial database of Geographical Indications if integrated with such type of decision support system, would bring spatial awareness for promoting the GI and complement the registration process, which is crucial for achieving the vision of AtmaNirbharBharat, by implementation of region-specific social and environmental schemes and development programmes.

26.2 Geospatial Database of GI

Geospatial database provides well-organized platform for geographical data display and helps in handling complex spatial analysis and queries. Spatial representations are organized in GIS as a series of thematic layers. In the present work, Geographical Indications are organized in a spatial database form and represented on Map and Satellite Imagery, using Open Source GIS software (QGIS). The **geographical origin** of the Geographical Indications is displayed as points in WGS 1984 Geographic (longitude/latitude) coordinate system. In addition, **Attribute** information giving details about Type of Goods, Classification, Applicant Name and Address, Registration Validity, Photograph and Logo of Product are added and displayed in the GIS database (Poompavai et al. 2020). To distinguish between the type of goods (agricultural, handicrafts, textile etc.), the GI points are represented with a typical point symbology (Colour and shape) (Fig. 26.2a). Label field is displayed using single attribute or multi-attribute. Every spatial point is associated with the corresponding attributes and appears when clicked on that point (Fig. 26.2b).

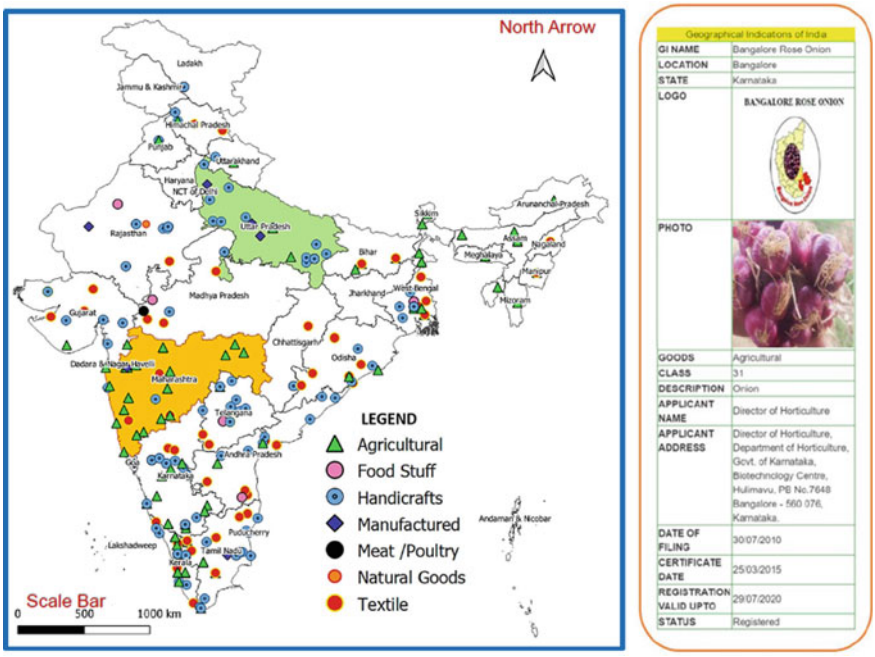

Fig. 26.2 **a** Spatial representation and **b** attribute information of GI

26.2.1 Spatial Visualization of Production Region

A map displaying production region of hand-knotted carpet called Bhotia Dann from the State of Uttarakhand is generated using GIS software. The Bhotia Dann carpets are woven by the Bhotia tribe of Uttarakhand, mainly in the districts of Uttarkashi, Chamoli, Pithoragarh and Bageshwar (GI Journal 2020). The state and districts of production of GI Bhotia Dann are represented spatially in map form (Fig. 26.3). Similar maps could be generated in GIS for all the GI products following a uniform layout. The regions corresponding to GI Gulbarga Tur Dal produced in the Kalburgi and Yadgir districts of Karnataka (GI Journal 2019) (Fig. 26.4) are represented with reference to Satellite Imagery. The layouts have been generated using GIS software. (Poompavai et al. 2019).

26.2.2 Spatial Visualisation of GIs of Karnataka

Geographical Indication Products belonging to the State of Karnataka are depicted in the form of a map (Fig. 26.5). The point and polygon layers have been referenced using geographic co-ordinate system. Map symbols are used for representing

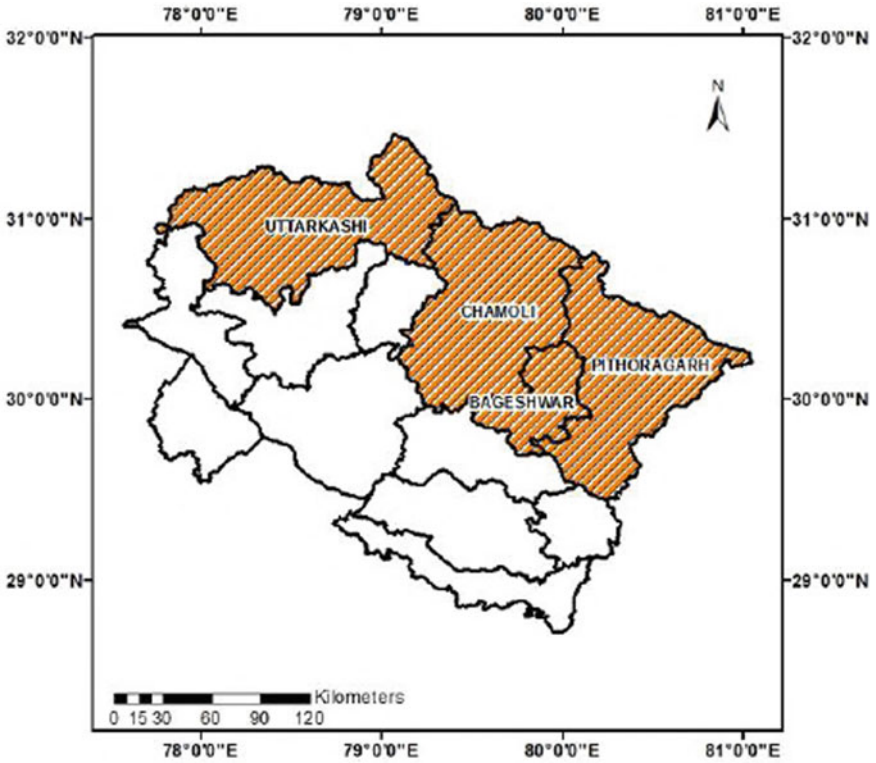

Fig. 26.3 Map of state and districts associated with GI Bhotia Dann

geographic features using visual variables such as colour, size, and shape. Each vector layer follows user-defined symbology and labelling properties for clear and creative display of map contents. The points are classified according to the type of goods and symbology has been assigned accordingly (Poompavai et al. 2019).

26.3 Web GIS—Spatial Visualization in BHUVAN

Bhuvan is a Web GIS platform that provides spatial data visualization in 2D, 2.5D, 3D, free data download, and various geoprocessing analytical tools on vector and raster data sets. More than 195 applications have been hosted on Bhuvan catering to various State, Central Ministries, and Citizen-Centric applications. Bhuvan also showcases near real-time disaster management support services like a flood, cyclone, drought, etc. Geographic Information System (GIS) has provided the great capability of interpreting various categories/types of data in the form of visualization and better spatial analytical purpose. There are many open-source tools and software where one

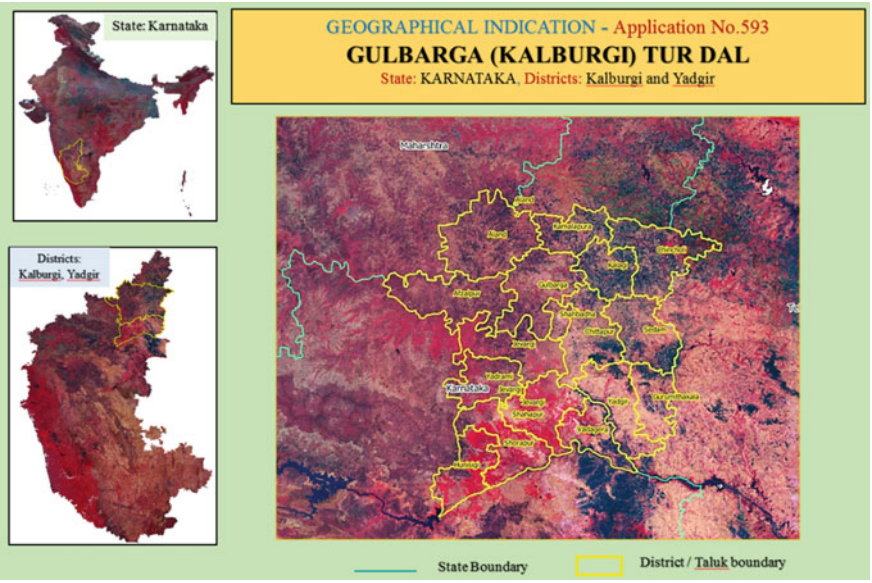

Fig. 26.4 Satellite imagery (false color composite) with state, districts and taluks corresponding to production of GI Gulbarga Tur Dal

can bring data to life. The GI database is brought to the Web GIS platform including various analytics options like filtering and query shell analysis.

The URL (Uniform Resource Locator) of ISRO Bhuvan Geoportal for Geographical Indications is https://bhuvan-app1.nrsc.gov.in/geographicalindication/. The default view of the web page displays all the GI goods of India as points spatially on Satellite Image and Map. The following section provides the details of the implementation of web-based spatial visualization and query of Geographical Indications (Fig. 26.6).

- Bhuvan Framework and software stack (WMS, WFS).
- Data preparation.
- GI Modules.

26.3.1 Bhuvan Framework and Software Stack

Generally, any web application has client and server-side scripts/components. The client-side scripts/ modules consist of User Interface (UI) and corresponding actions that can be performed on the web page, while the server-side scripts/modules mainly consist of Data/Service retrieval/Processing in the form of Application Programming Interface (API) either from the database, file retrieval from storage or data rendering like map server, geo-server or from Postgres/PostGIS.

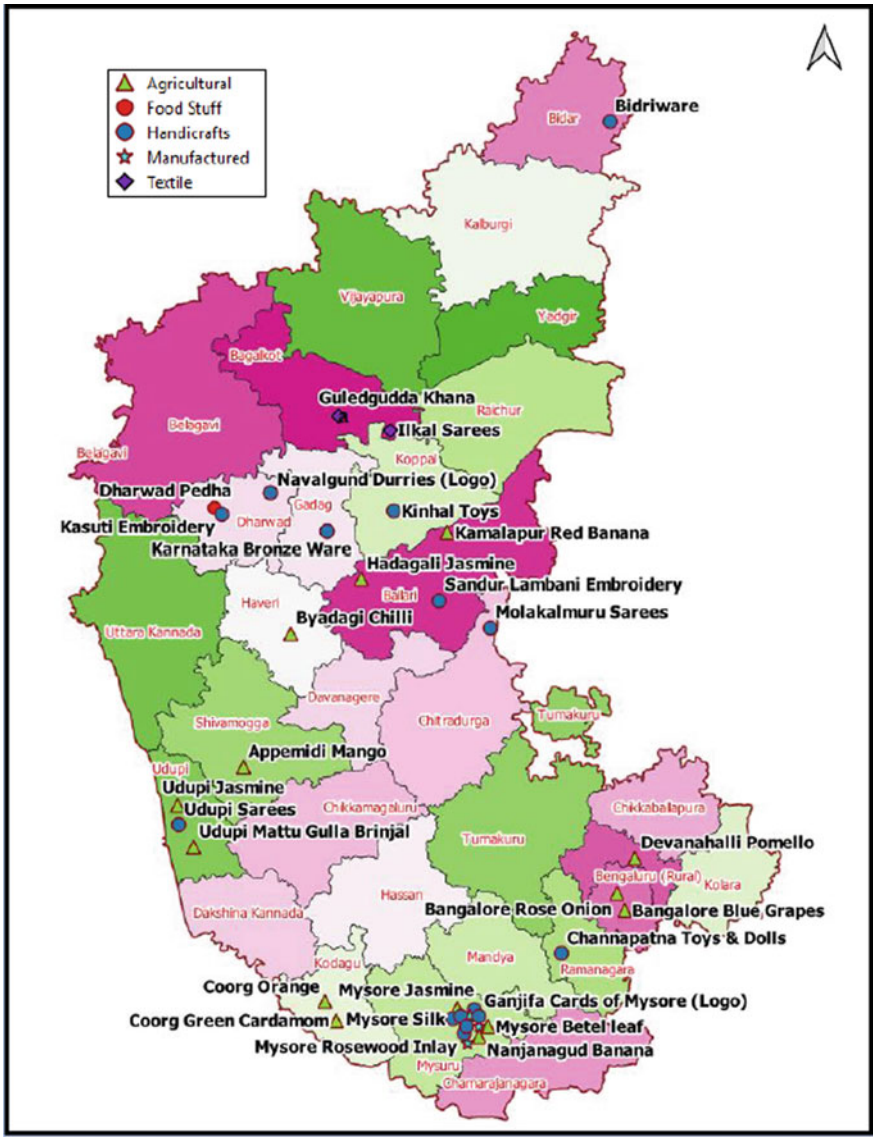

Fig. 26.5 Points of geographic origin associated with GIs of Karnataka

In the current framework, the following open source libraries and software stack have been used.

- Web application hosting: Apache-HTTP(Hypertext Transfer Protocol).

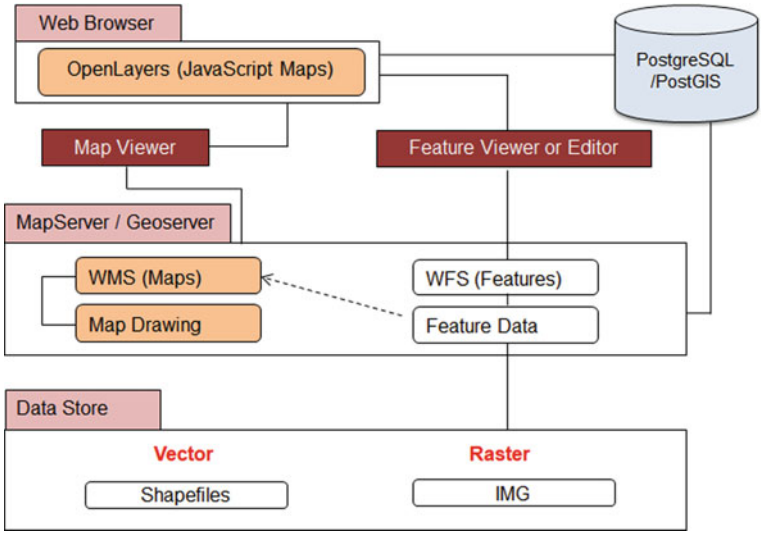

Fig. 26.6 Flow diagram of Bhuvan framework

- Client-side libraries: Open layers for map requests and actions that can be performed on the map, jQuery, Bootstrap (for Responsive Web Design), HTML (Hyper Text Markup Language), CSS (Cascading Style Sheets), and JavaScript.
- Map Rendering Software.
- GeoServer for Vector data.
- MapServer for Raster data.
- Database for data retrieval: Postgres along with PostGIS (PostGIS enables spatial capabilities on the database).
- SSD(Solid-State Drive) Storage for image storing and retrieval using apache.

26.3.2 Data Preparation and Workflow

Web GIS helps in providing visualization and analysis of data to various users asynchronously while compared to Desktop GIS software which will be limited to the single user and physical data availability. Map-rendering software such as GeoServer and MapServer provides web map services in Open Geospatial Consortium (OGC) standards which can be consumed by map libraries like Leaflet or OpenLayers. This enables GIS platform in web environment and also provides capabilities such as filtering, getting feature data on the map, styling of features, etc.

The shapefiles are ported to Postgres and the layers are published in GeoServer using the PostGIS plugin which is available in GeoServer. Then these layers have been integrated in Bhuvan framework to bring out the GI application (Fig. 26.7). The shapefile has been ported to Postgres with the help of PostGIS commands as

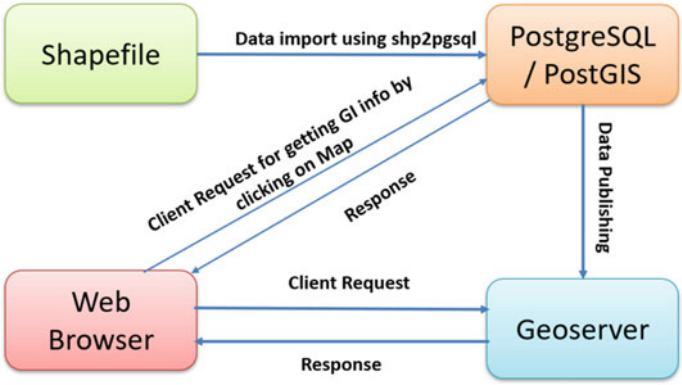

Fig. 26.7 Bhuvan data integration and workflow

follows: "*shp2pgsql-c-s 4326-**I file location of shp** |psql-h **server-ip**-p **server-port**-U **database-username**-d **database-name***".

26.3.2.1 Geographical Indication Visualization Module

The current GI application has components like visualization of GI, along with details on click of GI, query shell analysis, visualization based on type, and highlighting of district boundary from which the GI has originated is displayed. In this module, the user can view the GI of a specific category or all types of categories based on checkbox selection as shown in the below figures. The GI name is represented using multi-lingual labels corresponding to native language of the State (Tamil, Kannada, Hindi, Malayalam, Telugu, Assamese, Kashmiri, Gujarati, Assamese, Bengali, Odia etc.) based on the origin of GI goods. e.g. Kodaikanal Malai Poondu (கொடைக்கானல் மலை பூண்டு), Coorg Arabica Coffee (ಕೂರ್ಗ್ ಅರೇಬಿಕಾ ಕಾಫಿ), Malda Laxman Bhog Mango (মালদা লক্ষ্মণ ভোগআম), Srikalahasthi Kalamkari (శ్రీకాళహస్తి కాలంకారీ), Rajkot Patola (રાજકોટપટોળા), Boka Chaul (বোকা চাউল), Alleppey Green Cardamom (ആലപ്പുഴഗ്രീൻ ഏലക്ക). The default labelling displays the GI name in English and native language. The point symbology is displayed in the form of GI logo in different colours, such as Agricultural goods in green, Handicrafts in red colour etc. (Figs. 26.8 and 26.9).

Feature Selection can be made to choose a subset of features by clicking on checkbox or by using SQL statements to select features based on attributes. A selection module in the webpage provides options to choose the type of goods. When "Agricultural" is checked in the selection box, all the agricultural type of GI goods are displayed on Image (Fig. 26.10) or Map. On clicking any GI point on the map, all the districts associated with the GI are highlighted and detailed information on the GI will be shown in the attribute pop-up window. In the backend, on-click on

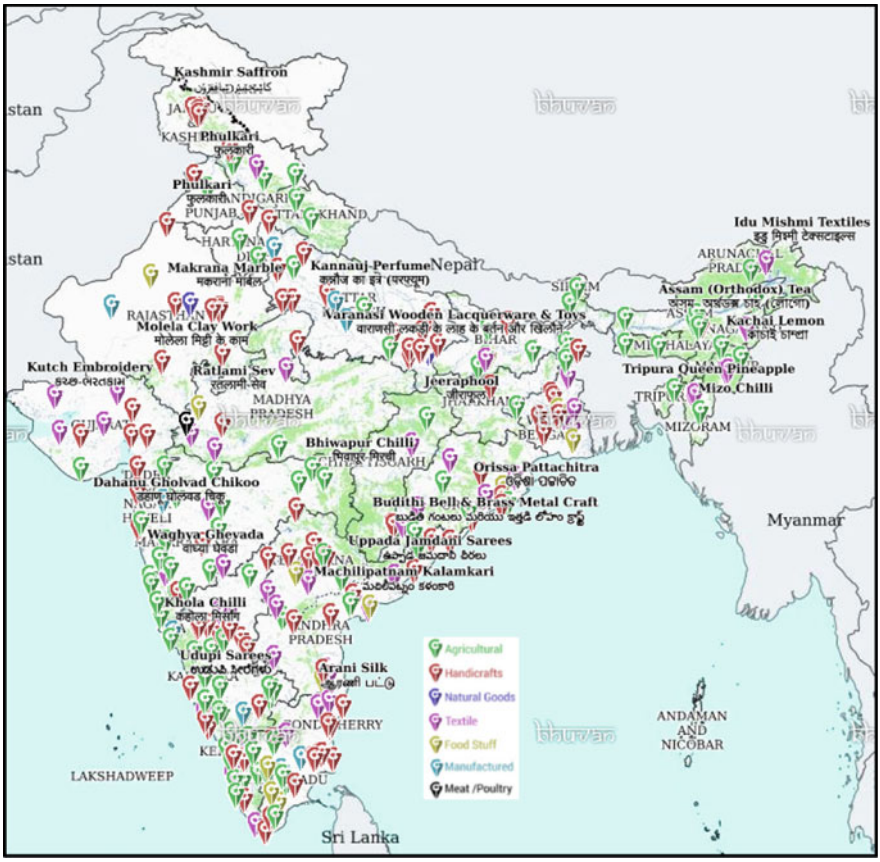

Fig. 26.8 GI goods displayed in Bhuvan geoportal on map

the map, the client map library will put a getfeatureinfo request (a method to get details associated with the point) to the map on the GI layer and the information will be shown on the map or satellite image, for example on clicking GI "Chikmagalur Arabica Coffee" point, the corresponding production district is highlighted in red colour and attribute box appears as pop-up window (Fig. 26.11).

26.3.2.2 Query Shell Analysis

Spatial query is used in Geographic Information System for deriving spatial relationship between the features. Spatial queries are statements in the form of a set of commands called Structured Query Language (SQL). Spatial analysis in GIS involves two types of operations: Spatial Query and Attribute Query (non-spatial query). Proximity, Adjacency, Containment and Buffering are some of the examples

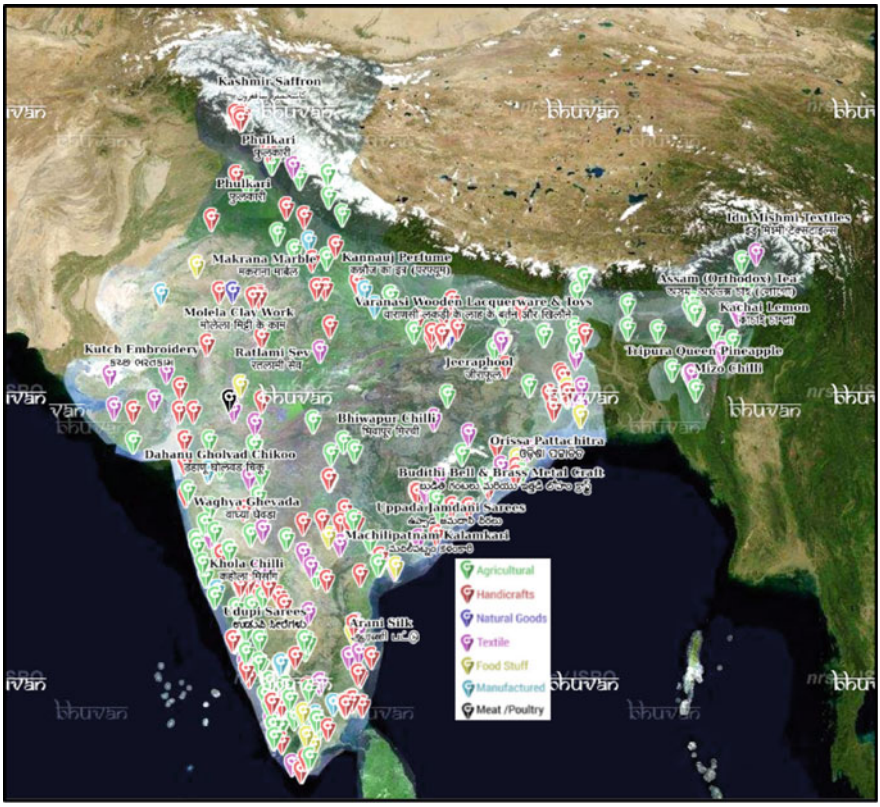

Fig. 26.9 GI goods displayed in Bhuvan geoportal on satellite image

of Spatial Query. Attribute query is used to derive information from the attribute tables which contain fields and data values related to each spatial feature. The query results are displayed in GIS both in spatial and attribute form.

Attribute query requires the processing of Attribute information. For example as shown in Fig. 26.12, feature selection is made using two attributes, i.e. Handicraft goods belonging to the State of Karnataka. The selected features are highlighted after the function is executed in Bhuvan Query Shell: "Goods" = "Handicrafts" AND "State" = "Karnataka". New datasets or maps are generated based on the results of spatial queries. Spatial queries are useful to extract spatial relationships between features and layers. The results of such analysis could be effectively used in decision making.

Query shell analysis is a module where the user specifies data filters based on goods, GI, or state and can visualize the results based on operations like AND, OR, NOT. Based on user selection the query expression will be added to the panel and results will be displayed on the map with the corresponding GI goods getting highlighted. For example, when the user selects a specific Geographical Indication

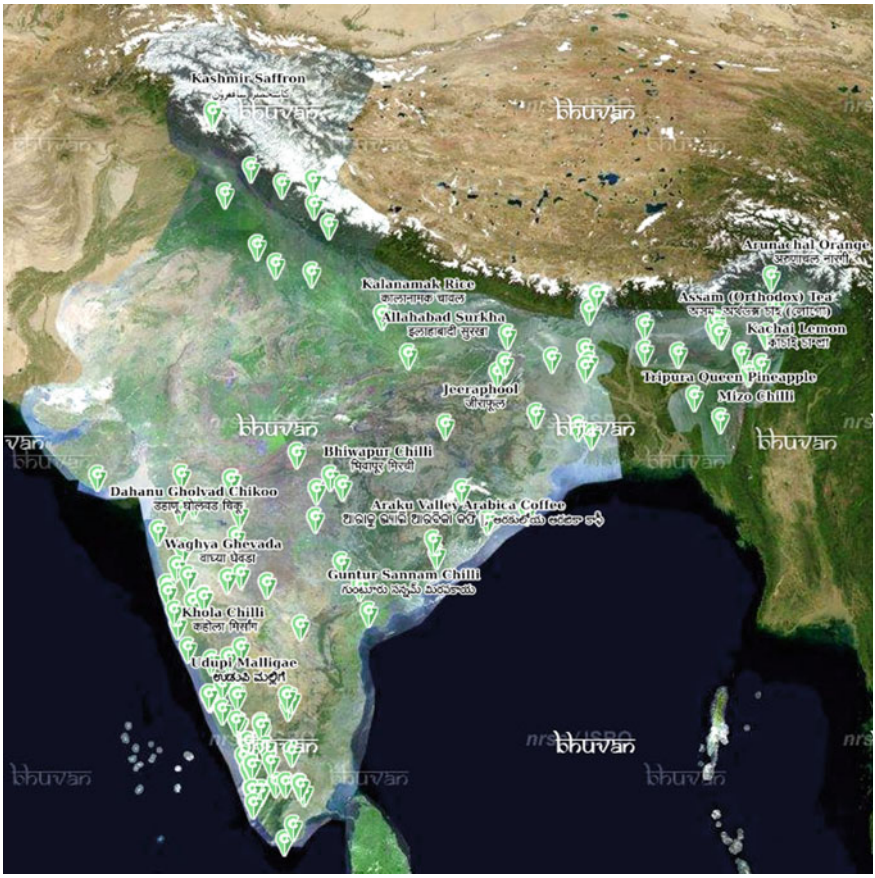

Fig. 26.10 Agricultural GI goods displayed in BHUVAN

"Andhra Pradesh Leather Puppetry" using the Query Shell Module, the GI point gets displayed on Satellite Image. On clicking the point, the attribute pop-up box is displayed, along with the corresponding districts being highlighted in red polygon (Fig. 26.13). The attribute pop-up box consists of a link "For More Info" which redirects to the GI Registry in IPIndia portal (https://search.ipindia.gov.in/GIRPublic) showing all the Registered goods and their details.

26.4 Conclusion and Way Forward

A spatial framework is essential for representing the Geographical Indications in a common platform and to provide easy access to up-to-date digital geospatial data. The GI points indicate the actual geographical origin of the goods which further leads to

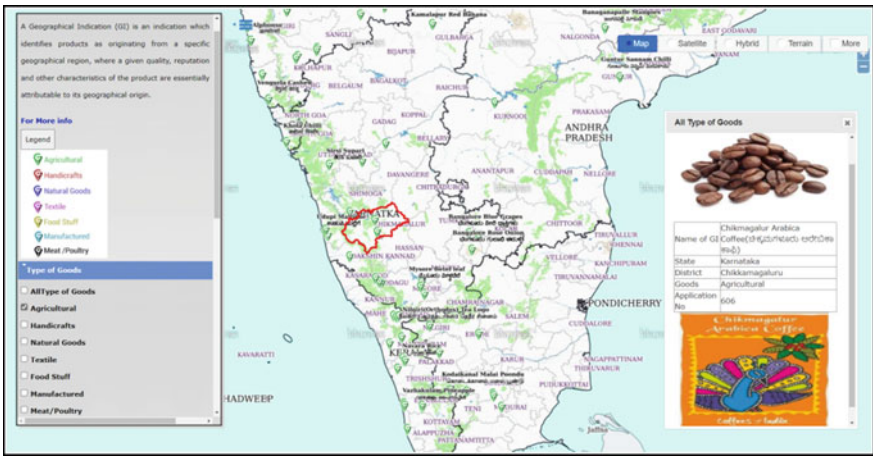

Fig. 26.11 Production region and attributes of GI Chikmagalur Arabica coffee

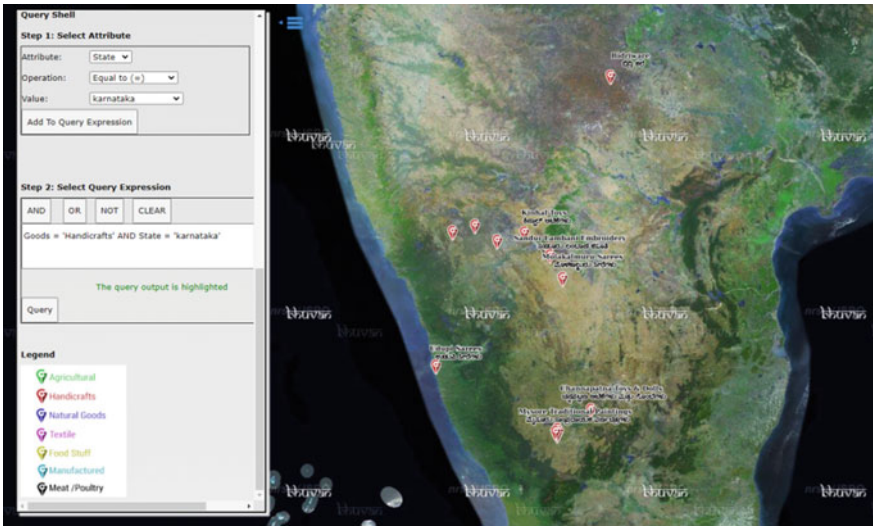

Fig. 26.12 GI Handicrafts of Karnataka highlighted using query expression

monitoring and management of natural resources in that region. The adverse impacts of climatic conditions on the production of agricultural goods and availability of raw material for certain products could be studied spatially. Geographical Indications showcase the spatial diversity of agricultural and horticultural crops in India. The present work encourages research community to make effective approaches of remote sensing studies for identification and discrimination of agricultural and horticultural crop varieties.

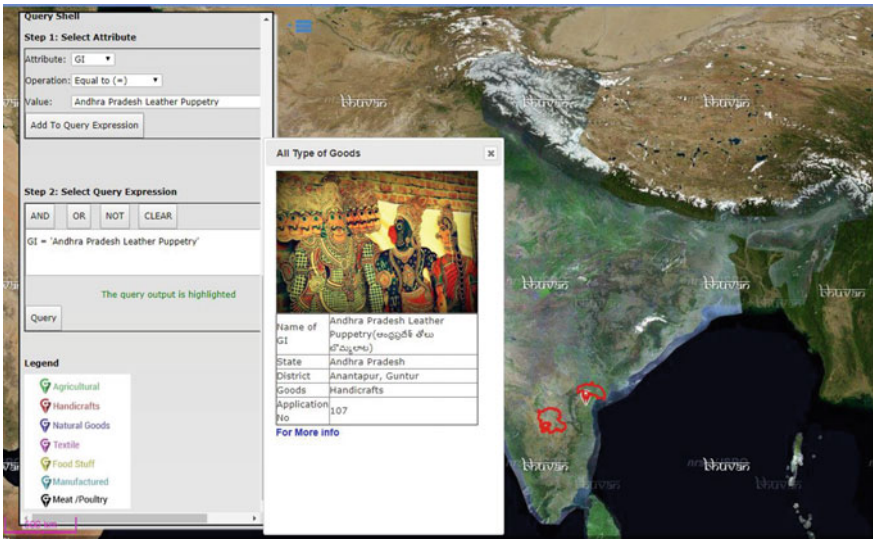

Fig. 26.13 Query shell analysis in Bhuvan geoportal

Complementary use of Microwave and Hyperspectral Satellite data along with multispectral data would certainly help in crop yield modelling and forecast studies. Development of spectral libraries in visible, NIR (Near Infrared) and SWIR (Short-wave Infrared) wavelength regions, using spaceborne hyperspectral imagers and ground-borne spectroradiometers, for various crop varieties and soil types associated with Geographical Indications, would be useful for further agricultural and vegetation studies and development. The geoportal, in general, helps to create geospatial awareness, among decision makers, general public, and especially farmers, weavers and artisans, on the importance of Geographical Indication for economic prosperity, rural development and protection of indigenous goods, while fostering cultural and traditional values.

Acknowledgements The Geographical Indications Registry (Chennai) organization, is gratefully acknowledged for free accessibility to the various data sets forming part of the work. All literature cited in the text have been duly referenced. The authors are thankful for the support and encouragement provided by Director, CGM-RCs and DGM-RRSC (South) of NRSC, ISRO. The authors give special thanks to Dr. K. Ganesha Raj, Shri. K. Nagajothi and Shri. Chinnaraja G Naidu for their valuable support and guidance.

References

Bramley C, Biénabe E, Kirsten J F(2009) The economics of Geographical Indications: Towards a conceptual framework for Geographical Indication research in developing countries. In: The Economics of Intellectual Property. Suggestions for Further Research in Developing Countries and Countries with Economies in Transition, ed. WIPO, 109–141. Geneva: WIPO

Document on Geographical Indications of Goods (Registration and Protection) Act (1999) Manual of Geographical Indications: Practice and procedure, version 01.11; Document on Classification of goods; Document on list of registered Geographical Indications of India. Accessed online from https://ipindia.gov.in

Geographical Indications Journal (2004) No. 1, GI registry. Intellect Prop India 1–6

Geographical Indications Journal (2014) No. 60, GI registry. Intellect Prop India 7–11

Geographical Indications Journal (2019) No. 120, GI registry. Intellect Prop India 37–43

Geographical Indications Journal (2020) No. 131, GI registry. Intellect Prop India 22–29

Poompavai V, Manjula VB, Nagajothi K and Ganesha Raj K (2019) Geospatial database of Geographical Indications of India. Project Report Document, NRSC-RC-REGBANG-NOV-2019-TR-1383-V1.0, p. 68

Poompavai V, Manjula VB, Nagajothi K, Ganesha Raj K, Prashanth Kumar B, Chinnaraja Naidu G (2020) Geospatial database of Geographical Indications of India. In: Proceedings of 107th Indian Science Congress 2020, Earth System Sciences, p 121

Ray S, Samaddar SG (2011) GI-GIS: A methodology of DSS for potential Geographical Indication in India. In: Proceedings of Geospatial World Forum, p 15

WIPO (2017) NICE classification, 11th edn, Version 2017, p 319

WIPO (2021) Geographical indications—an introduction, 2nd edn, p 44

Chapter 27
Generation of Geospatial Database for Notified Forest Lands of Karnataka

T. R. Nagashree, A. Vidya, R. Hebbar, Eregowda, K. Muhyiddin, Bishwajit Mishra, K. Ganesha Raj, and C. S. Jha

Abstract Forest ecosystems are very important and complex ecological units which are vulnerable to degradation and encroachment. Therefore, geospatial maps indicating jurisdiction boundaries and ownership of parcel boundaries are very critical for enforcing forest conservation and protection measures. All State Forest Departments are primarily responsible to create reliable spatial database of all parcels of land which may be defined as forest for the purpose of the FCA 1980. Karnataka has adopted geospatial approach for creation of a robust database indicating the notified forest land boundaries and to provide various institutional mechanisms for dissemination of information to various stakeholders. In this direction, Regional Remote Sensing Centre-South, in collaboration with Karnataka Forest Department, initiated a pilot study to make best use of available technology and information with the different departments to finish the task within a reasonable accuracy, time frame, and cost-effective manner. In the pilot phase, a Standard Operating Procedure (SOP) was prepared for creation of geospatial database of notified forest lands at cadastral level. On success of the pilot study, a state-level project is initiated to generate GIS database for all Notified Forest lands of Karnataka using high-resolution satellite data, village cadastral maps, GAGAN-based GCPs collected in field survey, and to publish the same georeferenced forest maps for easy reference for general public.The major contribution of this initiative includes generation of ortho-products of HRS data and collection of precise GCPs in field using the GAGAN-based GPS device,

T. R. Nagashree (✉) · A. Vidya · R. Hebbar · K. Ganesha Raj
Regional Remote Sensing Centre-South, NRSC, ISRO, Bengaluru, Karnataka, India
e-mail: nagashree_tr@nrsc.gov.in

A. Vidya
e-mail: vidya_a@nrsc.gov.in

R. Hebbar
e-mail: hebbar_kr@nrsc.gov.in

Eregowda · K. Muhyiddin · B. Mishra
Karnataka Forest Department, Aranya Bhavan, Malleswaram, Bengaluru, Karnataka, India

C. S. Jha
National Remote Sensing Centre, ISRO, Hyderabad, Telangana, India

C. S. Jha et al. (eds.), *Geospatial Technologies for Resources Planning and Management*, Water Science and Technology Library 115,
https://doi.org/10.1007/978-3-030-98981-1_27

georeferencing and edge matching of cadastral maps, and generation of seamless mosaic of these maps at various administrative hierarchies. Remotes sensing data from Cartosat-1 (2.5 m) and Resourcesat LISS-IV (5.0 m) sensors for time frame of February-April months were orthorectified using photogrammetric techniques to generate seamless ortho-products for the state. For each village, corresponding notified forest lands boundary is transferred to cadastral maps and verified by respective Range Forest Officer for generation of notified forestland maps for each village. Cadastral maps along with notified forest maps have been georeferenced using GAGAN-based GCPs and few tie points from the orthoimage. Subsequently, quality checking of cadastral maps, edge matching of adjacent village maps has been carried out using additional GCPs collected along the village boundary and *hissa* boundary (specific to Karnataka state). After verification of the georeferenced notified forest land maps by respective Forest Range Officer, georeferenced maps were mosaicked at Forest range/division level to generate seamless GIS database for all notified forest lands of Karnataka state. This is the first exercise in the country toward creation of reliable GIS database on notified forest lands which would serve as baseline database for management and conservation of forest lands.

Keywords Notified forest lands · Geospatial technology · Remote sensing · GIS · GAGAN · Cadastral maps · Orthorectification · Georeferencing

27.1 Introduction

Forests are the predominant terrestrial ecosystems that are major contributors to gross primary productivity and biodiversity. Administratively, forest exists based primarily upon land ownership, and lands that are legally designated as a forest even without tree canopy. Forest ecosystems provide fresh air, water resources, organic matter, control erosion, sustenance of agriculture, biodiversity, climate change mitigation, and many ecosystem services. Majority of rural and tribal populations are directly dependent on forests for their livelihood. In India, primary responsibility of State Forest Departments is to protect the forests and wildlife, conserving the rich biodiversity while maintaining ecological balance of the forest ecosystems, as they are very vulnerable to degradation and encroachment which may result in loss of forest biodiversity. Hence, creation of geospatial database of natural resources is very critical for protection, conservation, and management of these critical natural resources.

Reliable geospatial maps are essential for establishing accurate boundaries and adopting proper planning and conservation strategy. The forest boundary defines ownership of any parcel of land for legal purposes. The land ownership along with its boundaries relating to possession and control of land is clearly documented and notified in historical records and gazette notifications. Map featuring land ownership and jurisdiction boundaries are very important to protect and conserve forest. Most of this information is available as documents and maps in hard copies and some

of them have been prepared during British rule. Survey of India (SOI) maps at 1:50,000 and 1:250,000 scale are the earliest spatial maps indicating forest lands as greenwash areas. However, ownership details are not mentioned in these maps and forest boundaries are indicative, and significant land cover changes have occurred in the last 3–4 decades. In this context, there is urgent need for generation of reliable spatial maps depicting every parcel of forest land along with its ownership details.

Honorable Supreme Court of India has mandated the following: "Creation and regular updating of GIS-based decision support database, tentatively containing inter-alia the district-wise details of the location and boundary of

- Each plot of land that may be defined as forest for the purpose of the FCA (Forest Conservation Act) 1980,
- The core area buffer and eco-sensitive zone of the protected areas constituted as per the provisions of the Wildlife (Protection) Act, 1972;
- Important migratory corridors for wildlife;
- The forest land was diverted for non-forest purposes in the past in the district.

The Survey of India (SOI) toposheets in digital format, the forest cover maps prepared by Forest Survey of India (FSI) in preparation of successive "India Status of Forest Report (ISFR)" and the conditions stipulated in the approvals accorded under the FCA for each case of diversion of forest land in decision support database. Therefore, the State Forest Departments are now having a mandate to create a robust and reliable geospatial database of all parcels of land (such as Notified forest, diverted forest Lands Compensatory forestation lands, and area under Joint Forest Planning and Management (JFPM) that may be defined as forest for the purpose of the FCA 1980. Recent advances in geospatial technology have the requisite potential for mapping and monitoring of natural resources at different spatial hierarchies and generation of GIS database of the forest lands for visualization, easy accessibility, and periodic updation in the future.

27.2 Geospatial Technology

The main thrust of any Land resources Information System (LIS) is the creation of comprehensive database for planning and implementation of developmental activities which is efficient, reliable, cost-effective, scalable, capable of assimilating information from various sources, and compatible with the other information systems. The cadaster is a public record of location, extent, value, and ownership of land in each village for the purpose of taxation. The LIS address an individual stakeholder with parcel number as the unique identity derived from the cadastral map integrated with thematic information and action plans generated in other information systems. The cadastral information system basically consists of cadastral maps as the base layer over which various thematic maps are built upon. Thematic maps generated in GIS are linked to LIS. The basic requirements for creation of such information system are (a) Accurate, up-to-date and standardized maps in digital format and (b) Geodetic

control framework for georeferencing of maps. In general, standards of these cadastral maps differ from state to state and scale varies from 1:5000 to 1:7500 scale. The accuracy standards also differ from state to state and are not adequate for present-day requirements of large-scale geodatabase of a state/region.

Karnataka State Forest Department has vast stretches of forestlands occupying about 0.43 lakh km^2. It is very essential to protect and conserve these forest lands using suitable modern tools and techniques. Thus, it is very important to have a reliable GIS database of forest lands which should be brought to same level as that of revenue records. In general, the cadastral maps were prepared about a century ago and there are significant land use changes. The available forest land records with KFD include hard copies of forest maps of different scales and shapefiles of greenwash area of Survey of India toposheets. However, the respective Revenue Department units like village and survey number records are not depicted or reliably placed on these maps. The primary records for the land are Revenue records and thus, it is very essential to bring all the forest land records as per Revenue records for creation of uniform centralized GIS database. The cadastral maps in digital format generated through the geospatial approach need to be verified by State Revenue Department to make it as certified document for any legal evidence.

Modern surveying techniques such as total station and DGPS techniques are very accurate but very expensive, cumbersome, and time-consuming. Few State Forest Departments have attempted total station survey for mapping of forestlands in their respective states, but, ran into problems and full survey could not be completed. In view of the shortcoming of the above surveying tools, remote sensing, GIS and GPS tools can provide cheaper, efficient, and faster solutions in more objective manner for creating GIS database of forestlands and reconciliation of boundaries.

Remote Sensing (RS), Geographical Information System (GIS), and Global Positing System (GPS) are the new generation information systems constituting the field of geospatial technology. Remote Sensing refers to the science of identification of earth surface features and estimation of their geo-biophysical properties using electromagnetic radiation as a medium of interaction. RS data, capability for a synoptic view with repetitive coverage and calibrated sensors to detect changes at various resolutions, provides an alternate solution for natural resources management compared to traditional surveying.

In India, remotely sensed data has been extensively used in some of the major application themes such as agriculture, forestry, water resources, land use, urban sprawl, geology, environment, coastal zone, marine resources, snow and glacier, disaster monitoring and mitigation, infrastructure development, and biodiversity characterization. Currently, high-resolution ortho-database is being generated under various national and regional missions using Resourcesat LISS-4 and Cartosat-1 data at a spatial resolution of 2.5 m as a part of Bhuvan geoportal which can be used for creation of georeferenced cadastral maps which can serve as inputs for planning and development purposes.

GIS helps in handling voluminous data, updation of information on geographic features, which is helpful for infrastructure development and natural resource management. GIS is collection of computer hardware, software, and geographic data,

organized effectively to capture, store, retrieve, manipulate and analyze all forms of geographically referenced data and is an important additional tool in monitoring and management of natural resources.

For forestry-related applications, medium resolution satellite datasets are being routinely used for forest cover mapping, biodiversity characterization, biomass estimation, habitat monitoring, etc. (Reddy et al. 2015; Roy et al. 2015; Jha et al. 2015). Decadal changes in the vegetation cover of Bengaluru city were assessed between 2006 and 2019 utilizing IRS multispectral imagery (5.0 m) by unsupervised classification technique which showed overall reduction of vegetation (Ganesh Raj et al. 2020). Forest Survey of India (FSI) adopted geospatial technology for National Forest Cover mapping and evolved methodology over the last decade for improving the mapping accuracy. Recently, the 16th cycle of biennial assessment of India's forests indicated that total forest and tree cover increased to 24.56% of the total geographical area of the Country (FSI 2019).

Recent advances in GPS technology have shown considerable improvements in positional accuracy and reduced both time and cost of the ground surveys (Eugene, 2005). GPS Aided Geo Augmented Navigation (GAGAN) system is a Satellite-Based Augmentation System (SBAS) jointly developed by ISRO and Airports Authority of India (AAI) to render GPS signal for navigation over the Indian airspace and its surroundings. GAGAN system improves accuracy, integrity, availability, and continuity of GPS solution by providing corrected signals for ionospheric interference, clock and ephemeris errors. The location accuracy from GAGAN system after 15 min of observation is found to be sub-meter in planimetry and 5.0 m in elevation. Thus, GAGAN-derived GCPs can replace existing practice of relative positioning GPS surveys in quicker and efficient manner. The GCPs collected have been used for georeferencing of cadastral and notified forest maps of the villages pertaining to each forest range.

Regional Remote Sensing Centre-South, NRSC, ISRO has taken up a collaborative pilot study in association with Karnataka Forest Department for creation of reliable geospatial database. The comprehensive Standard Operating Procedure (SOP) was an outcome of the collaborative pilot project carried out by Information and Communication Centre (ICT), Karnataka Forest Department, GoK, Bengaluru, and Regional Remote Sensing Centre, National Remote Sensing Center under Indian Space Research Organization, Bengaluru. The focus of the study was to generate a uniform centralized GIS database for all notified forest lands of the state using high-resolution sensing satellite data, village cadastral maps, GAGAN-based GPS coordinates. Based on the encouraging results with acceptable accuracy as per the user requirement, the project was extended to cover entire Karnataka State. The scope of the project was also to make these georeferenced forest maps available in the public domain for easy access for general public and use the database in various operational and developmental projects related to forestry. The digital database, thus prepared, shall form the base data for any further activities viz. revenue data management (RoR), spatial data management, development, and updating of land records including forest land boundaries.

The chapter discusses the standard operating procedure developed in the pilot phase for generation of geospatial database for notified forest lands of Karnataka using high-resolution satellite data, village cadastral maps and GAGAN-based GCPs. After the success of the pilot study with encouraging results, the standard methodology was adopted for generation of geospatial database for all the notified forestlands of Karnataka covering 10,250 village cadastral maps.

27.3 Study Area

In the first phase, a pilot study was undertaken in order to develop and evaluate the geospatial approach for generation of GIS database on notified forest lands in four forest ranges namely Bidar, Shimoga, Bhadravati, and Hassan regions of Karnataka state covering about 212 villages which represented the overall diversity in terms of terrain, forest types and cadastral maps. After the successful conclusion, state-level project was initiated to cover all the notified forest lands of Karnataka state covering about 10,200 villages. Karnataka state is divided into 58 forest divisions for administrative purposes and the selected villages are located within these forest divisions. The location details of the study area for the pilot and state-level project are depicted in Fig. 27.1.

Karnataka state is located between 11° 30′ and 18° 30′ N latitudes and 74° 10″ and 78° 30″ E longitudes with geographical area of 1.92 lakh km^2. The Western Ghats, cover about 60% of forests in Karnataka which is recognized among the 18 mega biodiversity hotspots of the world. The total notified forestlands of the state occupy an area of approximately about 0.34 lakh km^2 constituting 17.5% of the geographical area. The Western Ghats forests are very rich source of fauna and floral diverseness

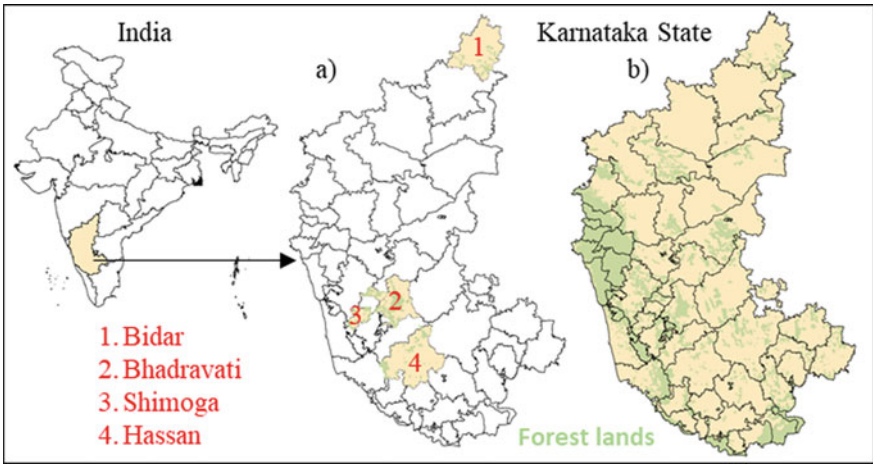

Fig. 27.1 Location map of the study area for **a** pilot study and **b** state-level study

and are very precious as they are genetic and natural resources. Many plant and animal species are native to forests in the State. Many plant species like sandalwood (*Santalum album*), rosewood (*Dalbergia latifolia*), teak (*Tectona grandis*), honne (*Pterocarpus marsupium*), white cedar (*Dysoxylon malabaricum*), and many other wild species belonging to non-timbers and fruit and medicinal plants are also native to forests of Karnataka.

The state is bestowed with most beautiful forests of the country which include magnificent evergreen forests of the Western Ghats, scrub forests in plains, and classic flora and fauna. The evergreen/semi evergreen forests of Western Ghats are characterized by evergreen canopy mixed with deciduous trees. The regions with moderate rainfall and temperature with cold winters are known for moist deciduous forests which mostly occur in the eastern slopes of the Western Ghats, North-Eastern region of the Peninsula. The deciduous forests generally shed their leaves during winter months of December due to scarce water resources. This type of forest is considered as degraded version of the moist deciduous forest occupying large tracts between moist deciduous of the east to tropical thorn in the western part. The low rainfall regions are dominated by scrub and thorny forests. The trees in this region are stunted due to lack of sufficient water. The abundant tree species in the region area include Acacias, Euphorbias along with typical spiny and thorny varieties and wild palms.

27.4 Satellite and Ancillary Data

In view of the large variability in the forest types of Karnataka, high-resolution satellite data was used in the project. Cartosat-1 stereo data corresponding to 2008–2009 was utilized for generation of DEM with photogrammetric block file. The remote sensing data used in the study are provided in Table 27.1. Cartosat-1 image of 2.5 m spatial resolution and Resourcesat-2 LISS-IV multispectral data of 5.0 m resolution have been utilized. Cartosat-1 Mono and LISS-IV data of latest years were used for generation of satellite ortho-database. About 500 Cartosat-1 mono data of 2017–2019 period covering the study area with not greater than 5.0° roll tilt angles

Table 27.1 Satellite data used

Satellite/sensor	Resolution (m)	Swath (km)	Acquisition period
Cartosat-1 stereo	2.5	28	2008–2009
Cartosat-1 mono	2.5	70	2017–2019
Resourcesat LISS-IV	5.0	70	2017–2019

were used. Latest Resourcesat-2 LISS-IV images corresponding to two seasons were procured for generation of merged data for interpretation of forest lands.

Following ancillary data, image processing and GIS software packages were used

- 1:50,000 scale SOI toposheets
- Relevant administrative, reserved forest boundary
- Digital village cadastral maps along with notified forestlands
- Parishud GAGAN-based GPS instrument for collection of GCPs
- Geo-tagged field photographs
- Relevant attribute Information
- ERDAS Imagine Image processing package
- ARCMAP GIS package.

27.5 Geospatial Products

The study was executed jointly by RRSC-South, NRSC/ISRO, and Information and Communication Centre (ICT), Karnataka Forest Department within the broad framework of the Operating Procedure developed during pilot study as depicted in Fig. 27.2. High-resolution satellite data (HRS) of Cartosat-1 and LISS-IV data were processed and analyzed using image processing and Geographic Information System (GIS). Village Cadastral maps along with notified forestland boundary in digital format were made available by Karnataka Forest Department for georeferencing.

The project work was divided into six major work components as given below.

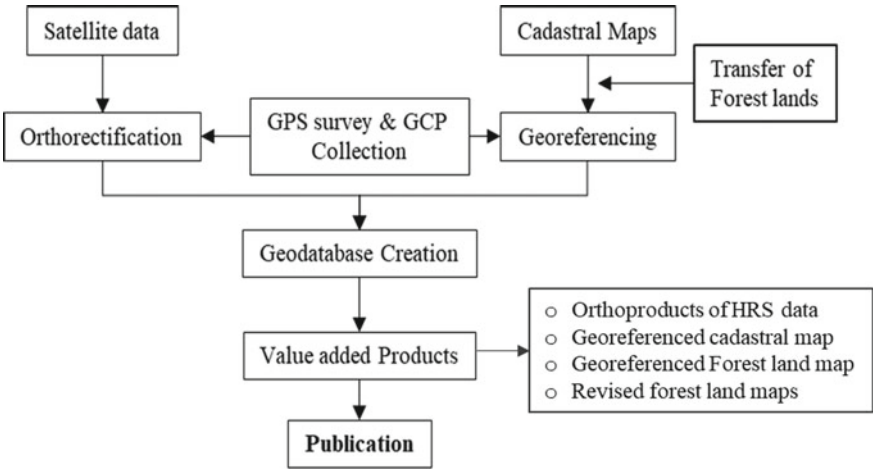

Fig. 27.2 Flowchart showing overall methodology adopted in the study

27.5.1 Creation of Orthoimage Database

The existing Cartosat-1 ortho-database corresponding to 2008–2009 periods was used for planning the field itinerary for GPS survey and collection of Ground Control Points (GCPs). Generation of ortho-database involved creation of photogrammetric block file, generation DEM, orthorectification, and fusion of Cartosat-1 PAN and LISS-IV multispectral data.

The photogrammetric block file was created using 500 Cartosat-1 stereo pairs and processed using ERDAS Photogrammetric suite through bundle block adjustment techniques. Adequate number of well-distributed GCPs of sub-meter accuracy and image tie points were added to the block file. Additionally, 2–3 tie points per image were identified as to checkpoints in order to verify the block adjustment. The triangulation results were verified using Root Mean Square Error (RMSE) and the block file was refined iteratively till the triangulation error was within acceptable limit (better than 0.5). Further, quality assessment of the block file was carried out by taking stereo measurements in terms X, Y and Z coordinate in the overlapping regions. After convergence of the block within acceptable triangulation error, Digital Elevation Model for each scene was generated from the block file. The DEM was validated using ground points in terms of LE 90 and RMSE using accurate reference points.

DEM was generated in LTF format and post-processing of DEM was carried out in order to remove any artifacts. Minimum DEM editing was carried out for correcting the floating/digging points. Depending on the requirement, DEM editing for major features such as water bodies, drainage, transport network, steep hills was taken up by adding hard/soft break lines so that the subsequent contours/slope derived are more realistic and follow the real-world terrain as closely as possible. Finally, the DEM with 10.0 m posting was generated in raster format and subsequently mosaicked for creation of seamless DEM for the study area which was used in orthorectification of satellite data.

Orthorectification is the process to improve the planimetric and positional accuracy of the satellite data by reducing the sensor and terrain-related distortions in a high-resolution imagery. DEM was used for generation of 500 ortho-products of Cartosat-1 stereo images using bundle block adjustment and mosaicked for creation of state-level reference ortho-database. These ortho-products and DEM served as reference data for subsequent orthorectification of recent years Cartosat-1 mono and LISS-IV data. Cartosat-1 mono and multispectral LISS-IV images were fused using Brovey transform technique to generate high-resolution images for generation of seamless mosaic of the fused data for the state as given in Fig. 27.3.

Validation of DEM and orthoimage using the photogrammetry technique was tested using accurate reference ground control points. About 36 well-distributed points representing diversity and clearly identifiable features were chosen and at each point planimetric and height accuracies were checked. The results indicated that the RMSE in X direction and Y direction has been found to be 4.19 m and 3.75 m, respectively, for the orthoimage. RMSE and LE90 for the DEM were 3.16 m

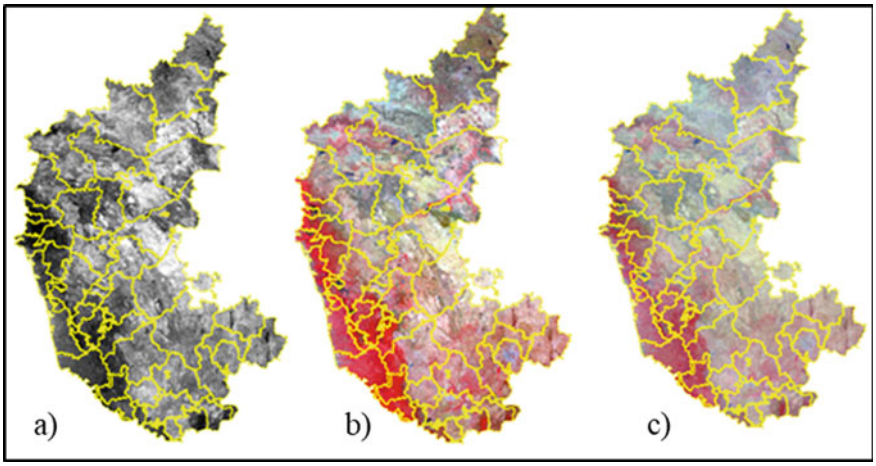

Fig. 27.3 Seamless mosaic of satellite data **a** cartosat-1 images, **b** LISS-IV images and **c** merged data for Karnataka state

and 6.2 m, respectively. As per the design of CartoDEM, the DEM accuracy is 8.0 m at LE90 and 15.0 m at CE90 for ortho data (Muralikrishnan et al. 2011). The accuracy obtained in our study is well within the specifications of Cartosat-1 Stereo indicating the suitability of the ortho-products in the study.

27.5.2 Preparation of Cadastral Maps

Village cadastral maps are the primary input for generation of geospatial database for the forestlands and identification ownership of each parcel of forest lands. Karnataka Forest Department was responsible for procurement and preparation of good quality cadastral maps as per the specification. Converting the cadastral maps in digital format was done through scanning of these maps as per standard resolution (DPI) of better than 200. Quality checking of each village cadastral map in terms, of village name, scanning resolution, folding/distortion in maps was verified by quality assessment team. Redrawing of the cadastral maps was taken up, whenever necessary, especially for the folded and poor-quality maps. About 10,200 village cadastral maps were scanned for this purpose. The parcel boundaries in each village were digitized for preparation of village cadastral maps in vector format. These raster and vector maps were used for preparation of notified forest land maps (Govind Kumar et al. 2013)

27.5.3 Preparation of Notified Forest Land Maps

A massive exercise was carried out by Karnataka Forest Department for preparation of hard copies of notified forestland maps through collection of relevant documents, forest maps, and ancillary information. The forest land boundary on cadastral maps was identified by referring to C-statement or boundary description and other relevant ancillary information. Further, the notified forest lands were transferred on the hard copy of cadastral maps and verified by respective forest range officers as depicted in Fig. 27.4. These maps were scanned for preparation of notified forest land maps in digital format.

27.5.3.1 GAGAN-Based GPS Surveys

Exclusive field survey was carried out in each village by survey team for collection of Ground Control Points (GCPs) using GAGAN-based GPS device. Commercially available Parishud GPS receiver uses SBAS signal for correcting the coordinates and thus, providing very accurate geo-coordinates as compared to normal GPS devices. About 10–15 well-distributed GCPs were required for georeferencing of each cadastral map. Figure 27.5 depicts typical example of GCPs collected for georeferencing of cadastral maps. In total, about 185,000 GCPs have been collected for georeferencing cadastral maps. GCPs were mainly collected in bi-junction, tri junction, field bunds, and few points along the adjacent village boundary for edge matching. GCPs

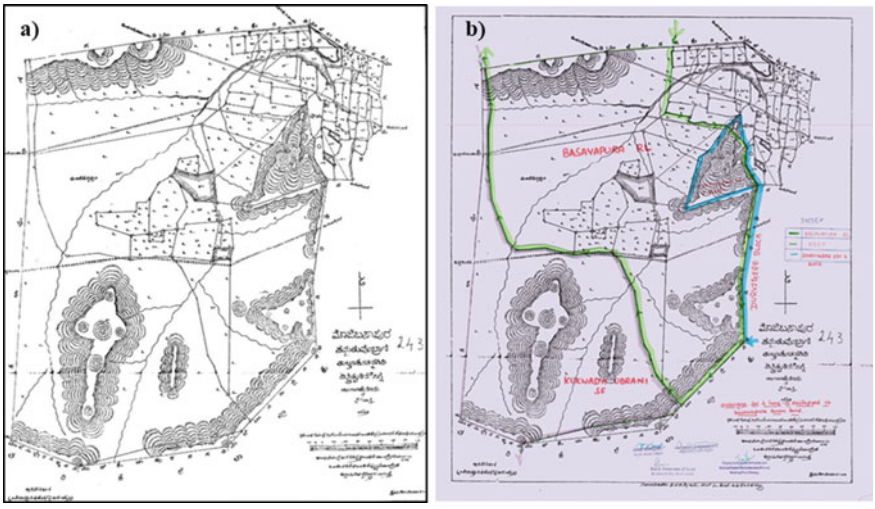

Fig. 27.4 Scanned maps in digital format **a** village cadastral map, **b** notified forest land map (*depicted in green color*)

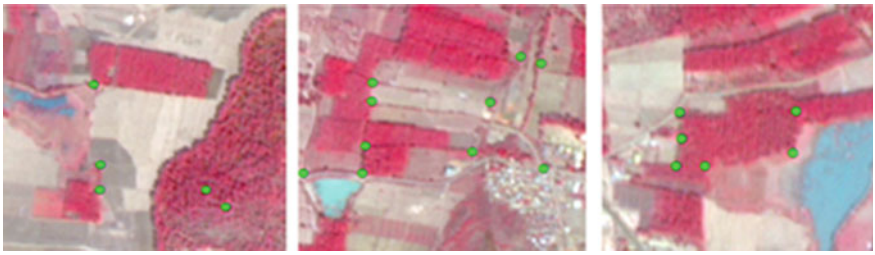

Fig. 27.5 Location GAGAN-based GCPs (*green color*) used for georeferencing of cadastral maps

have been used for georeferencing cadastral maps for generating digital libraries and generation of seamless mosaic as per forest range and division.

27.5.4 Georeferencing of Cadastral and Notified Forest Maps

The village cadastral maps were georeferenced using GAGAN-based GCPs using first-order polynomial transformation and nearest neighbor resampling technique. Initially, georeferencing of cadastral maps was carried out using X and Y locations of few well-distributed GCPs and refined subsequently using additional GCPs until cadastral maps had the best fit with the ortho data. These maps have been overlaid on the orthorectified data to check the extent of matching between cadastral maps and orthoimages (Fig. 27.6). It was observed that georeferenced village cadastral maps

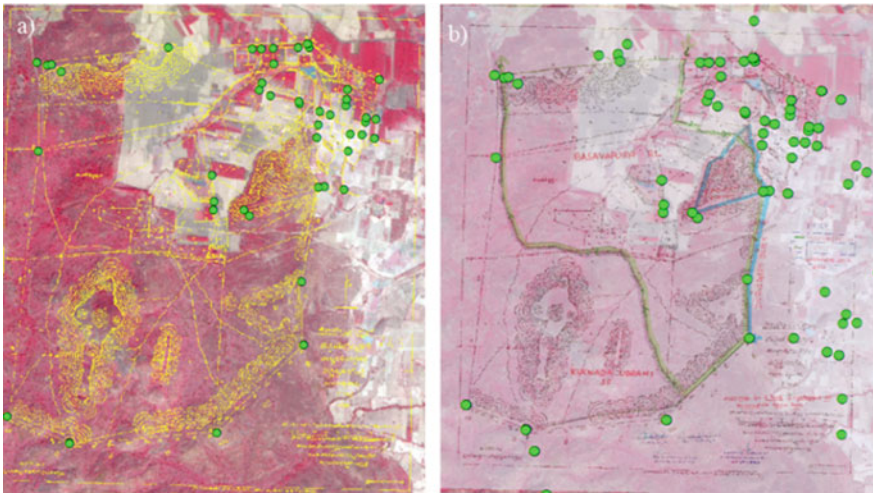

Fig. 27.6 Georeferenced maps using GAGAN-based GCPs (*green color*) overlaid on satellite data **a** cadastral map and **b** notified forest land map

matched closely with ortho-products with better than 7.5 m accuracy for 85% of the cadastral maps meeting the standards envisaged in the project. Further, the spatial integrity of georeferenced cadastral was validated using the survey number-wise land record details available on Bhoomi website, Government of Karnataka. The portal hosts survey number-wise land records and holdings along with area for all the parcels for the entire state. About 26 georeferenced village maps were randomly selected covering all diversity in terms of terrain and slope to validate the maps with reference to actual ground area collected from Bhoomi Website. The validation exercise indicated that the deviation in area of parcels was with acceptable deviations up to ± 3% for majority of parcels while in extreme cases up to 5% deviation was observed especially in the hilly and undulating regions.

Depending on the requirement, additional GCP points were identified from orthoimage or field surveys for edge matching. Edge matching is one of the important activities of the project for seamless mosaicking of the cadastral maps covering a forest range/division using GCPs collected along with village boundaries as well as hissa information provided by Survey Settlements and Land Records (SSLR) department. Figure 27.7 presents typical example of notified forest land maps at cadastral level after seamless edge matching of the maps.

The methodology has been tested for establishing and updating the standard operating procedure for generation of geospatial products and GIS maps of forest lands. It was observed that about 85% of village cadastral maps were within acceptable

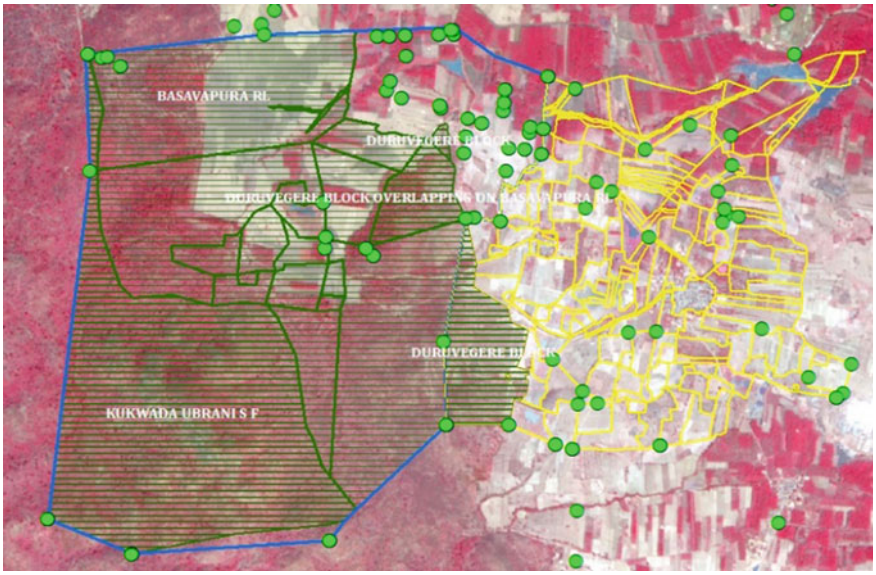

Fig. 27.7 Edge matched cadastral map (Basavapura and Duruvigere villages) in vector format overlaid on satellite data showing notified forest boundary (*in green color*)

accuracy. About 10–15% of village cadastral maps could not be properly georeferenced due to lack of adequate number of GCPs, distortions associated with scanning, large village, misalignment. Some of issues and challenges have been addressed and recommended for collection of additional GCPs, use of hiss boundaries and in extreme cases resurvey.

27.5.5 Notified Forest Land Boundary

Notified Forest boundaries as marked on the georeferenced notified forest land maps were vectorized for creation of forest boundary in vector format for each village and mosaicked at range/division level in order to create baseline geospatial database. Multispectral datasets for the period of November–December and March–April LISS-IV have been used for delineating forest land cover from non-forest land use/land cover categories. This was very much essential for identification of current forest land boundaries within the notified forest regions. The land use changes were analyzed by visual interpretation of forest and other categories using parameters like tone, texture, pattern, composition, and terrain conditions. Multispectral 2.5 m merged data was displayed at approximately 1:5000 scales and based on the spectral signature as seen on the merged data, forest land and other non-forest categories have been delineated. This comparison has been carried out at cadastral level for each parcel of land and it has been observed that significant changes have occurred in the fringe of the forest lands as depicted in typical example for Basavanapura village. Figure 27.8 indicates significant land use changes in Basavapura village. The area of forest lands as per the notification was 1552.1 ha which was reduced to 793.2 ha as per the latest image. The major change observed was transformation of noticed forest land cover to agriculture and some extent toward plantations and built-up.

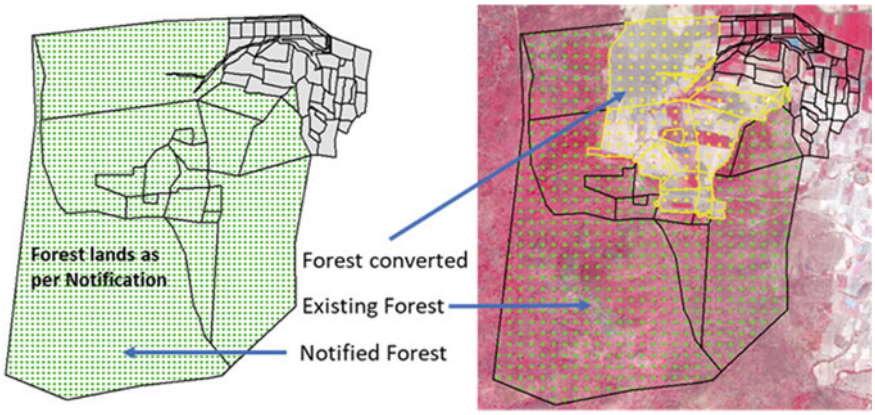

Fig. 27.8 Reconciliation of notified forest land boundary—Basavanapura village, Karnataka

27.6 Summary

In the present study, multi-resolution satellite datasets and cadastral maps were used for creation of geospatial database for notified forest lands of Karnataka State. Initially, a pilot study was conducted to evaluate the potential use of geospatial approach for this purpose. Based on the experience gained from the pilot study; a Standard Operating Procedure (SOP) was developed for extending the study to state/regional level (RRSC-South' 2016). After the successful execution of the pilot study, the scope of the study extended to cover all the forest lands of Karnataka state. Cartosat-1 and LISS-IV data have been used to generate ortho-database for the forest ranges. GAGAN-based GCPs were used for georeferencing of cadastral and notified forest land maps. It was found that about 85% of the cadastral maps showed accuracy better than 7.5 m with respect to the field boundaries. Reconciliation of notified forest land boundaries was done using two seasons Cartosat-1 and LISS-IV satellite database. A comparative study was carried out to analyze the land use changes within notified forest lands which indicated significant diversion of forest lands to agriculture and other developmental activities. The project involved large number of databases in raster, vector, tables, and map formats which need to be stored systematically for easy accessibility and retrieval. Hence, geodatabase was used for storing of large volume of datasets which included ortho-products, cadastral maps, and notified forestlands along with attribute data. The outcome of the project has clearly indicated the utility of high-resolution data for generation geospatial database for notified forestlands and reconciliation of boundaries at cadastral level. These geospatial databases would form important input for forest departments for managing and conserving these vast tracks of natural resources for maintaining ecological balance.

Acknowledgements Regional Remote Sensing Centre (RRSC-South), NRSC/ISRO, acknowledges with great appreciation, the initiative taken by Karnataka Forest Department (KFD), Govt. of Karnataka for carrying out this study and funding. The project team acknowledges the keen interest and support provided by Principal Chief Conservator of Forests and the senior management team at KFD. The project team is thankful for the support extended by the technical and administrative staff of RRSC-South and Karnataka Forest Department during different stages of implementation of the project.

References

FSI (2019) India state of forest report, IFSR, 16th edn., vols 1 and 2. Forest Survey of India, Ministry of Environment Forest and Climate Change, Kaulagarh road, Dehradun

Ganesha Raj K, Trivedi S, Ramesh KS, Sudha R, Rama Subramoniam S, Ravishankar HM, and Vidya A (2020) Assessment of vegetation cover of Bengaluru City, India, using geospatial techniques. J Indian Soc Remote Sens. https://doi.org/10.1007/s12524-020-01259-5

Govind Kumar VV, Venkata Reddy K, Deva P (2013) Updation of cadastral maps using high resolution remotely sensed data. IJET 2(4):50–54

Jha CS, Fararoda R, Rajasekar G, Singh S, Dadhwal VK (2015) Spatial distribution of biomass in Indian forests using spectral modelling. In: Geospatial information systems for multi-scale forest biomass assessment and monitoring in Hindu Kush Himalayan region. Special Science Publication, ICIMOD, Nepal

LeLong C, Thong-Chane A (2003) Application of textural analysis on very high-resolution panchromatic images to map coffee orchards in Uganda. Geoscience and remote sensing symposium, 2003. IGARSS'03. Proc IEEE Int 2:1007–1009

Muralikrishnan S, Narender B, Reddy S, Pillai A (2011) Evaluation of Indian national DEM from cartosat-1 data. Summary report v1.0. https://bhuvan-app3.nrsc.gov.in/data/download/tools/document/CartoDEM-Readme_v1_u1_23082011.pdf, pp 1–19

Raju KNP, Kumar S, Mohan K (2008) Urban cadastral mapping using very high-resolution remote sensing data. J Indian Soc Remote Sens 36:283–288

Reddy CS, Jha CS, Diwakar PG, Dadhwal VK (2015) Nation-wide classification of forest types of India using remote sensing and GIS. Environ Monit Assess 187(12):1–30

Roy PS et al (2015) New vegetation type map of India prepared using satellite remote sensing: comparison with global vegetation maps and utilities. Int J Appl Earth Observ Geoinf 39:142–159

Chapter 28
Applications of Geospatial Technology in Forest Resource Assessment, Management, and Monitoring

A. O. Varghese, Jugal Kishore Mani, and Chandra Shekhar Jha

Abstract Forests impact human lives and livelihood in several ways because of their vital role in the global and regional ecosystems. However, our forests are deteriorating both qualitatively and quantitatively. Sustainable management of the forests with application of geospatial technologies can be useful for the conservation and monitoring of this renewable resource. Geospatial technology can be successfully used for the assessment of the extent of the forests, forest density and types, plantation, grasslands and for monitoring of these for change and damage assessment. Change monitoring includes afforestation and reforestation, forest cover transformation, and damages like forest degradation, encroachment, shifting cultivation, forest fire, pest, and disease. Advancements in autecological and synecological studies by means of geospatial technology are beneficial for the identification of hotspot areas in relation to biodiversity, endemicity, and threatened species; species habitat-relationship modeling, and deriving niche metrics. These inputs may play an important role in prioritizing areas for conservation and addressing biotic pressure to these areas for mitigation purposes. Geospatial technology is an ideal tool to quantify the forest as the major sink of atmospheric carbon, so as to assess forest biomass carbon, gross primary productivity, leaf area index and carbon sequestration rate, etc. Similarly, hyperspectral remote sensing is used for forest leaf biochemistry, spectral species identification, and forest health assessment. Advanced geospatial technologies like microwave and lidar are being effectively used nowadays for forest density, height, and volume estimation, which are indispensable for working plan preparation. All these inputs are very key for policymakers for strategic planning and preparation of management plans, working plans, and planning social forestry activities. In this chapter, we provide a review of the various geospatial technologies mentioned above that can be utilized effectively for forest resource assessment, management, and monitoring.

A. O. Varghese (✉) · J. K. Mani
Regional Remote Sensing Centre—Central, NRSC, Nagpur 440033, India
e-mail: vargheseao@rediffmail.com

C. S. Jha
National Remote Sensing Centre, Hyderabad, India

C. S. Jha et al. (eds.), *Geospatial Technologies for Resources Planning and Management*, Water Science and Technology Library 115,
https://doi.org/10.1007/978-3-030-98981-1_28

Keywords Geospatial technology · Forest cover mapping · Forest type mapping · Social forestry · Agroforestry · Forest working plans · Encroachment assessment · Forest right act—2006 · Forest fire · Biodiversity · Niches · LAI · GPP · Carbon sequestration · Forest biomass · Forest volume

28.1 Forest Cover Mapping, Density Assessment, and Monitoring

Monitoring the forest cover involves its changes during the course of time either in density or cover transformation. Multi-temporal remotely sensed (RS) dataset is an ideal tool to discriminate areas of land cover change between dates of imaging (Dalmiya et al. 2019; Stehman and Foody 2019). RS data has been widely used to inventory forests, wherever up-to-date information about its spatial occurrence is not available. Early effort to map Indian forests at national level was attempted on 1:1 million or 1:250,000 scale using visual interpretation of false-color images of Landsat MSS data based on canopy closure during 1972–75 and 1980–82. Forests were mapped into three classes closed (above 40%), open (10–30%) and mangrove based on canopy closure (NRSA 1985). Forest Survey of India (FSI) also used a comparable method for forest mapping during 1981–83 on 1:250,000 scale subsequently, in which, below ten percent canopy cover is classified as scrub contrary to NRSA's nonforest category (FSI 2003). Experiences gained from these studies have evolved into a national program to monitor vegetation cover biennially by means of satellite RS data by FSI. Arrival of better RS resolutions satellite-like Resourcesat 1 and 2 data facilitates the new classification scheme at FSI into three forest canopy classes as open, moderately dense (40–70%) and very dense (canopy density more than 70%) (FSI 2019). A new category of Tree Outside Forest (TOF) is also included in the census to cover the trees lying outside the notified area. Methodologies for FSI's forest cover mapping are in continuous process of improvement keeping in pace with the technology and total inventory of every cycle is enhanced by delineating the difference from the previous cycle. As per the latest FSI (2019) census, the total forest and tree cover is 24.56% of the total geographical area of India, of which forest cover is 21.67% and the TOF is 2.89%. FSI's biannual mapping of national forest cover is an efficient way to monitor forest cover and its changes. Recently the availability of very high-resolution satellite imagery (WorldView-2, WorldView-3, GeoEye-1, IKONOS, and Quickbird-2) in panchromatic (0.3–1 m) and multispectral mode (1–3 m) is being used for detailed forest cover mapping with more than five density classes. Varghese and Suryavanshi (2017) carried out forest cover change analysis study in Melghat Tiger Reserve (MTR), Maharashtra (India) between 1999 and 2016 to understand the effect of the translocation of settlement from the reserve area to outside. Forest cover change in MTR shows that nearly 69.31% of the area i.e., 1429.27 km^2 area falls under no change category. In 27% of the sanctuary area (27.83%) vegetation cover is improved and in 2.85% of area it is decreased. Positive

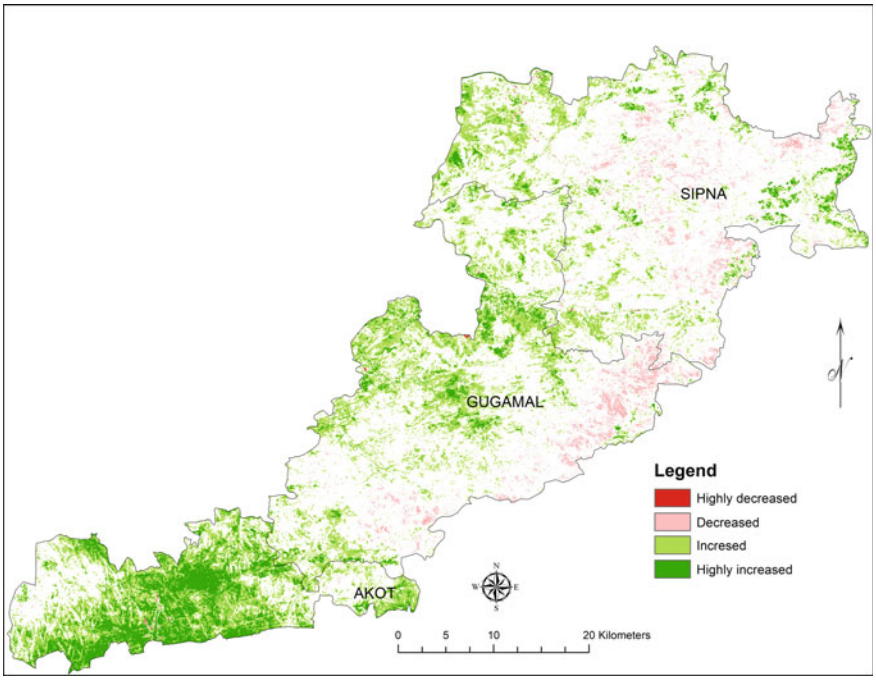

Fig. 28.1 Forest cover change analysis in Melghat tiger reserve during 2001–2016

changes were observed in MTR with respect to increase in vegetation cover mainly because of the translocation of settlement from the reserve area to outside (Fig. 28.1).

Optical or SAR (Synthetic Aperture Radar) sensor is appropriate for deriving details regarding forest cover, but the cloud cover limits optical sensors usage during rainy days where SAR data can be utilized (Sinha et al. 2015). The capability of SAR to penetrate inside forest canopy makes it possible to collect more structural information about the forest density than that of optical data and provides a better accuracy (Varghese and Joshi 2015).

Varghese et al. (2016) analyzed the possibility of employing various radar polarimetry decomposition methods in forest density slicing along with other land cover features. Among the various target decomposition theorems employed, Yamaguchi4 component decomposition provided a better accuracy of 92. 86% tailed by Vanzyl decomposition (92. 57%) by using support vector classifier (SVM). Similar results were obtained for decompositions based on Risat one hybrid pseudo polarimetric data for Yamaguchi 4-component decomposition (Fig. 28.2) and Van Zyl decomposition (72.43% each) (Varghese and Suryavanshi (2014). This study infers that SAR data has substantial potential for assessing forest canopy density in tropical forests.

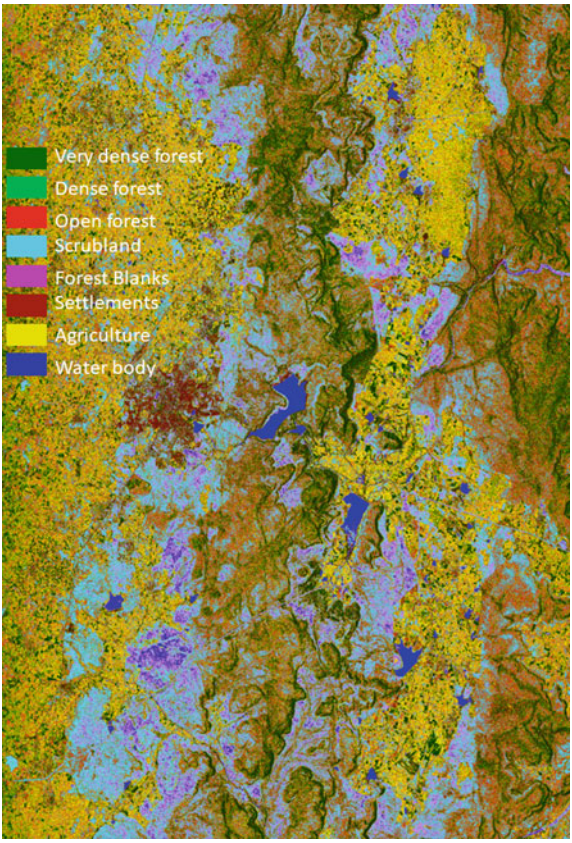

Fig. 28.2 Forest density classification of Madav NP generated from Risat-1 pseudo-polarimetric Yamaguchi4 decomposition method using SVM classifier

28.2 Forest Type Mapping and Monitoring

To prepare a plan for conservation of species or population, one of the important steps is to categorize all distinguishable ecosystems occurring within the area (Varghese 1997). One way of doing it is through identifying all distinct vegetation types in the area since the plants being the primary producers' influence and choose the fauna (consumers) of the region (Nair 1991). Champion and Seth's (1968) revised forest type classification is the generally followed scheme in India, which categorized forest into five main groups on climatic factors. These main groups are again separated into sixteen type groups and these type groups are further classified into numerous subgroups and finally into 202 forest types and subtypes.

Initial forest type map of India on 1:1 M scale using IRS-1C WiFS was generated by Indian Institute of Remote Sensing (IIRS) with 22 vegetation classes (IIRS 2004). A forest type map of India was brought out by FSI in the year 2009 (FSI 2009) based on IRS 1D LISS III data of 2002 on 1:1 M scale. NRSC generated a very detailed vegetation type map of India (1: 50,000) from IRS LISS-III data based on visual

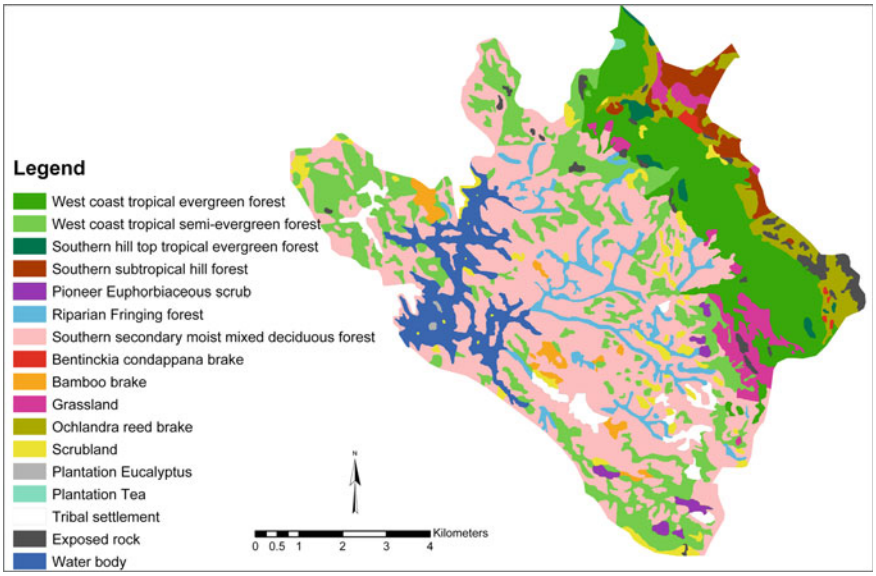

Fig. 28.3 Very detailed vegetation type map of Peppara WLS prepared from IRS P6 LISS IV data

interpretation method and this map is the most comprehensive one developed for India so far with a precision of 90% (Roy et al. 2012; Roy et al. 2015). Reddy et al. (2015) delineated forest types of India by using IRS Resourcesat-2 AWiFS data based on elevation, climate, phenology, and floristic to match with prevailing global and national classification legends. Varghese et al. (2010) prepared a very detailed vegetation type map of Peppara wildlife sanctuary (WLS) based on IRS Resorcesat-1 LISS IV imagery for niche level mapping of threatened tree species (Fig. 28.3). With the advent of very high-resolution satellite imagery in panchromatic and multispectral mode, a very detailed forest type maps can be prepared nowadays (Hościło and Lewandowska 2019).

28.3 Social Forestry and Agroforestry

The main objective of the social forestry is promoting plantations in rural areas to supply the rising needs of wood, firewood, cattle feed, etc. for rural populations, thus reducing their dependence on the protected forest land. The main problem in implementing the social forestry activity in India is the absence of data on where to implement and what to implement or their suitability location. Latest data about the roads, canals, and railway lines and their length and breadth in conjunction with the anthropogenic pressure and nearness of notified forest land, etc. are the

important information needed for the application. The availability of very high-resolution satellite data of IRS Cartosat series, the generation of the above parameters nowadays can be prepared easily. The suitability for social forestry plantations in the form of linear or block can be modeled successfully using geospatial technology with the relevant thematic database like soil, slope, land use/land cover, etc. (Suryavanshi et al. 2015). Varghese and Suryavanshi (2016) conducted a study to identify suitable areas for social forestry activities in Maharashtra. Suitable sites for linear (road, rail, canal side) and block plantation were derived by using criteria-based modeling in GIS (Fig. 28.4). Criteria involve road, rail, canals (for linear plantations), land use/land cover (site identification for block plantation using wasteland category) soil texture, depth (for species selection), slope (below 15°), distance to notified forest, and village wise socio-economic data (population and no. of job cards holders to prioritize the areas). By integrating the database a customized standalone software, SOFIS (Social Forestry Information System), is developed for identification and management of social forestry activities.

Agroforestry is the planned incorporation of woody perennials (trees, shrubs, palms, bamboos, etc.) into cropland and animal farming schemes to generate ecological, financial, and societal profits (ICRAF 1993). Geospatial technology can be applied to site suitability assessment for various agroforestry activities as well as for the inventory and monitoring of the existing agroforestry classes (Ahmad and

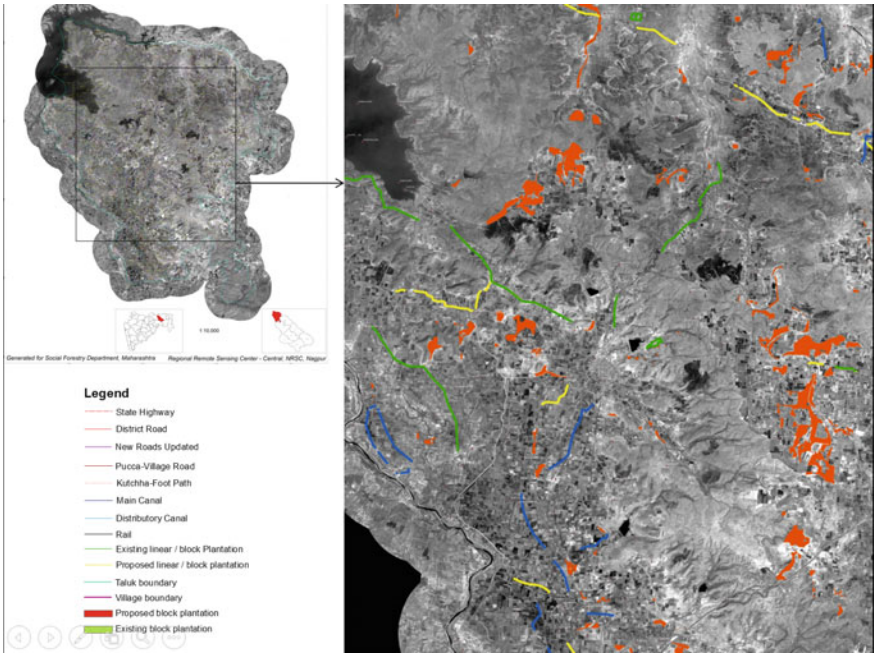

Fig. 28.4 Suitable areas for social forestry plantations in Ashti taluk of Wardha district, Maharashtra

Goparaju 2017). In one of the studies (Ahmad et al. 2020), geospatial technology is utilized for the tree cover estimation, agroforestry suitability analysis, present and future (2050) climatic agriculture susceptibility, proportion of people living below poverty line to recognize potentiality, and the critical multidimensional relationship among them. One of the major problems facing agroforestry mapping is the lack of adequate procedures for demarcating the area in a mixed farm where a tree mixing varies significantly with crops. To tackle this problem, NRSC/ISRO in collaboration with FAO is carrying out a collaborative project to map the different agroforestry classes of Indian region using high-resolution satellite images with machine learning techniques (Jha et al. 2022).

28.4 Forest Working Plan Preparations/Revision

Forest working plans (WP) are the tools for technical forest conservation and administration, which are prepared/revised every ten years in India. They are valuable in appraising the current position of natural resources, evaluating the effect of past management activities, and determining the future actions to realize the purposes of the working plan. The WPs are revised for every forest division with five to ten percent sampling from the field. This sampling from the field may take more than two years, hence generating inputs for WP is tiresome, time-consuming, and are based on ocular estimation (Rao et al. 2006). The aforesaid work is allocated to various officials with different skill sets, so the outcome may be highly scientific. Some of the primary inputs for WP preparation like forest type, density, stand height, stand volume, fire frequency slope, soil, etc. can be realized rapidly and precisely through geospatial technology (Rao et al. 2007). Based on these primary inputs secondary inputs like treatment types and suitability for various silviculture operations can be derived with limited ground-based information. First requirement of WP revision is the demarcation of treatment classes. All the compartments need to be separated into different treatment types based on the capability of that land unit for the purpose of explicit silvicultural activity. Delineation of working circles (WC), felling series, and coupes can be generated based on the majority and continuity of treatment classes in the division. WC is defined as a forest area planned with a specific objective, and function for one silvicultural scheme of working plan treatment. In some situations, WC may overlap with more than one silvicultural system. So, the generation of management map for afforestation WC, Selection-cum-Improvement WC, Non-wood Forest Produce WC, protection WC, teak plantation WC, Plantation WC (Rao et al. 2007), etc. can be delineated using geospatial technology. The poor correlation between stand tree height and stand volume with optical data can be overcome by the use of SAR and lidar technology. The examination of DLR SAR data of L band exhibited comparatively good sensitivity and correlation of radar backscattering coefficient with tree stand density and stand volume for HH (r^2 0.75) and HV (r^2 0.71) polarizations (Varghese et al. 2011). Varghese and Suryavanshi (2018) demonstrated that geospatial technologies in combination with forest ground measurement data

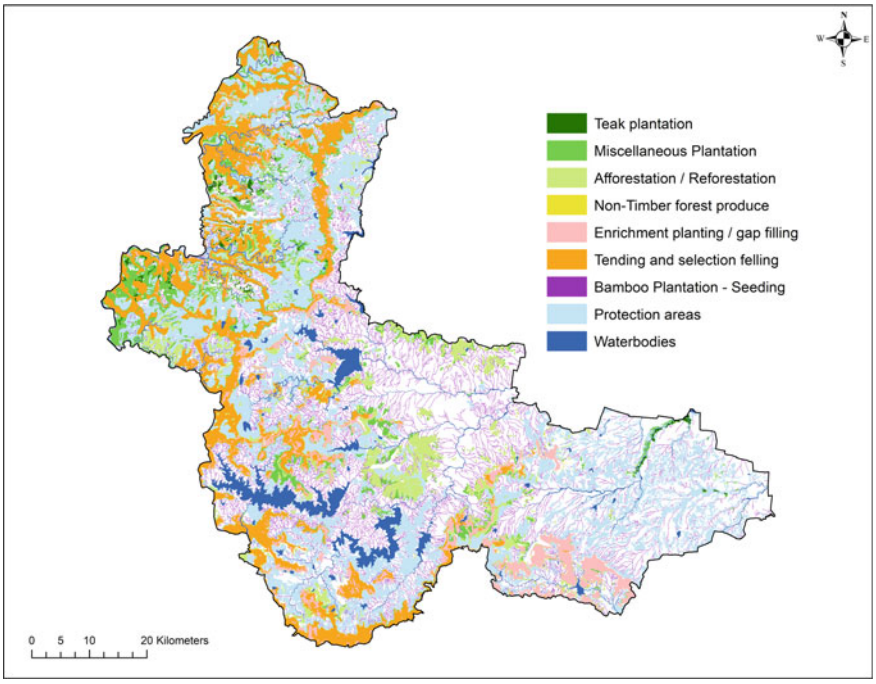

Fig. 28.5 Suitable areas derived for the zonation of different working circles, felling series, and coupes in West Nashik forest division, Maharashtra

can be effectively used for the preparation of different inputs for the WPs (Fig. 28.5). Generation of treatment types; separation of WC for various silvicultural operations, etc. can be generated with a better precision, timeliness, and cost-effectiveness with geospatial technology than the conventional method (Varghese and Suryavanshi 2018). The usage of SAR and lidar technologies further reduce the dependence of ground-level measurements in WP preparation.

28.5 Monitoring of Afforestation/Deforestation and Encroachment

Forests deliver numerous environmentally, economically and societal tangential and non-tangential benefits to the humans like species and genetic diversity, water supplies, nutrient cycling, soil conservation, and greenhouse gas balancing (Rao and Pand 2001). RS gives a systematic synoptic view of earth surfaces at regular time intervals which are useful for analyzing rate of deforestation or reforestation and drivers of change at global as well as regional scales. Intergovernmental Panel on Climate Change recommends the usage RS data in combination with ground truth

data to evaluate the forest, carbon stocks, and its variations (Zhu and Woodcock 2014; Sirro et al. 2018). Earlier works mapped forest mainly based on low-resolution RS data (300–1 km) (Coppin et al. 2004; Hansen 2000), this has limited utility at regional scale (Coppin et al. 2004). Subsequently, with the arrival of Landsat 30 m resolution and 25 m resolution PALSAR-based datasets (Chen 2015; Gong 2013; Shimada 2014), a number of time sequence forest change analysis methods and outputs have been established by the use of automated/semi-automated procedures (Banskota 2014; Mitchell 2017). In time series and large scales analysis, supervised classifiers like SVM, boosting tree (SGB), decision tree, and random forest (RF) (Huang 2002; Pandya and Pandya 2015) are better than unsupervised and object-oriented techniques. L-band SAR data exhibits better capability in monitoring forest cover changes because of its penetration capabilities to distinguish woody vegetation and insensitivity to cloud coverage (Reiche et al. 2013). Reddy et al. (2016) assessed nationwide change in natural forest cover for last eight decades and showed that the current rate of gross forest loss in India is very low at 0.05% owing to effectiveness of conservation measures taken at national level.

28.6 Forest Right Act (2006) Implementation

Indian Forest Rights Act—2006 (FRA-2006) is to identify and legalize the rights of forest-dwelling people who are staying in forest for generations. In this context, FRA-2006 envisages legalizing the rights of these forest-dwelling people in their land who have been residing in forest before 13 December 2005. In many of the states, the dependable data concerning the occupancy details of land previous to the cutoff date are not available thereby creating a major problem in ascertaining the claims for rights over the land. In this context, the real qualified persons are facing difficulties in claiming the rights, and on the other hand lot of false claims are also coming up. Remote sensing technology with its wealth of time-stamped archival data sets in high-resolution will provide good solution for this problem. To tackle this problem, Mani et al. (2020) developed standalone software integrated with IRS Cartosat1 and LISS IV data of the dates before 13th December 2005 and thereafter to understand the status of the forest cover. Notified forest boundary, village boundary, and cadastral maps were also integrated into the software with facilities like locating place with geographic coordinates, area estimation, toggling the images between dates for FRA dispute analysis and implementation (Fig. 28.6).

28.7 Forest Fire and Risks Mapping

One of the most complex problems that the tropical forests face, particularly in deciduous forests, is the recurrent incidence of fire. It is a well-known fact that fire caused extensive damage in the forest ecosystem quantitatively and qualitatively

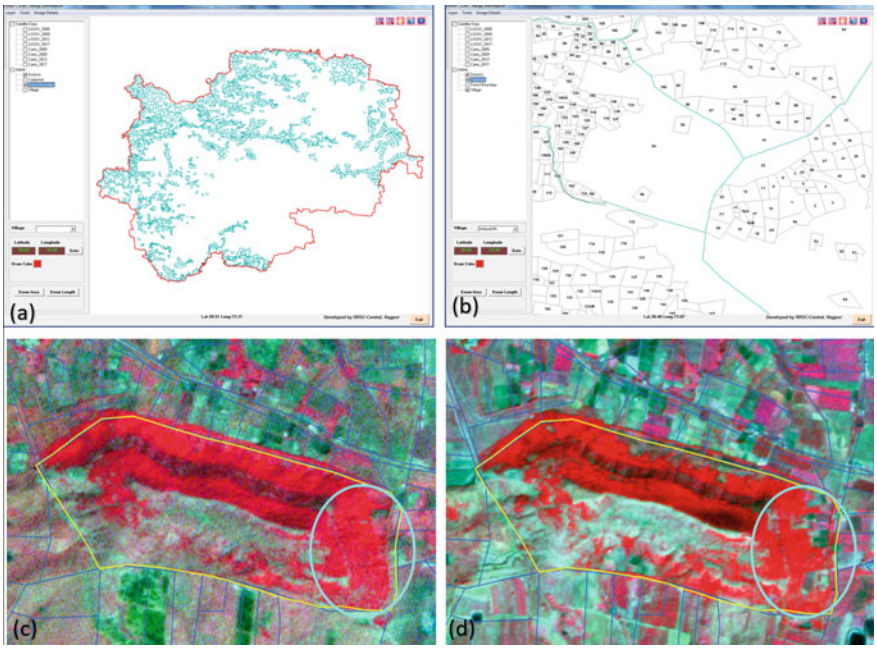

Fig. 28.6 Software developed for FRA-2006 implementation **a** console with forest boundary **b** cadastral boundary **c** LISS IV data of 2004 **d** LISS IV data of 2017

(Bright et al. 2019; Reddy 2020; Halofsky 2020). Indian National working plan code (2014) specifies to carry out fire frequency and burned area mapping for fire vulnerability identification for working plan preparation/revision. Geospatial technology is an effective tool in pre, active, and post-fire ecology management through various applications. Generation of fire-prone areas, fuel mapping, monitoring active fire locations, assessment of burn scar & its severity, and monitoring of the impact of fire & its recovery on flora are some of the applications (Varghese and Suryavanshi 2017; Axel 2018; Szpakowski and Jensen 2019) in this regard. Planning for employing preventive measures for fire necessitate fire risk prioritization based on scientific data. Fire-prone area can be prepared to forecast the area of fire initiation, its propagation, and the potential damages of fire occurrence. Fire-inducing factors like vegetation density, slope, aspect, elevation, weather conditions, proximity to village & road, NWFP collection areas, etc. are the inputs needed for modeling fire risk zones and their prioritization (Prasanth et al. 2009). Generally employed model for fire progression simulation is FARSITE (Finney 1998) in which the inputs are surface fuel conditions, elevation, aspect, slope, crown base height and bulk density, cover density and height, crown bulk density, and meteorological parameters.

Another method to identify fire-prone areas is the fire frequency analysis based on mapping of fire scars from satellite data, which can be derived through visual interpretation or digital classification. Various spectral indices (SI) are developed

for the detection of burn scar and fire severity analysis based on the combination of visible, near-infrared, and shortwave infrared domains of the electromagnetic spectrum. Burned Area Index (Martin et al. 1998), Normalized Burn Ratio (Key et al. 2006), Normalized Difference Moisture Index (Wilson et al. 2002), Burned Area Index Modified–LSWIR (Martin et al. 2006), Burned Area Index Modified-SWIR (Martin et al. 2006), Mid Infrared Burn Index (Trigg and Flasse 2001), Tass Cap Brightness, Tass Cap Greenness, Tass Cap Wetness WET index (Crist and Cicone 1884; Crist 1984) and Global Environmental Monitoring Index (Pinty et al. 1992) are some of the commonly used SIs. Figure 28.7 shows the BAI image derived from

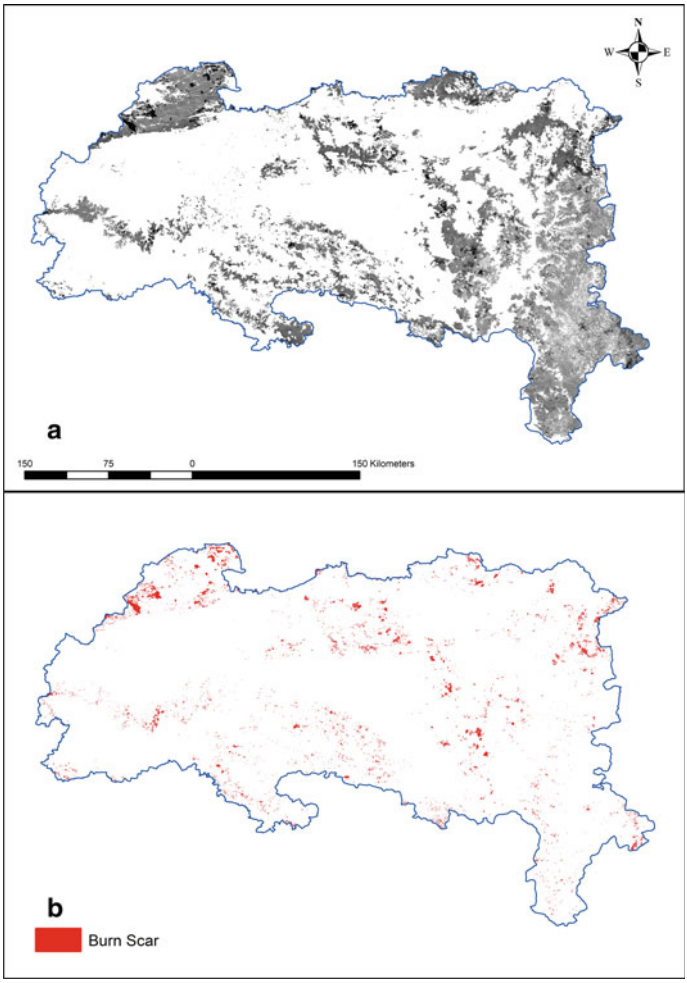

Fig. 28.7 **a** BAI image of Landsat-8 OLI **b** Burned area extracted from BAI image in Vidarbha region of Maharashtra, India

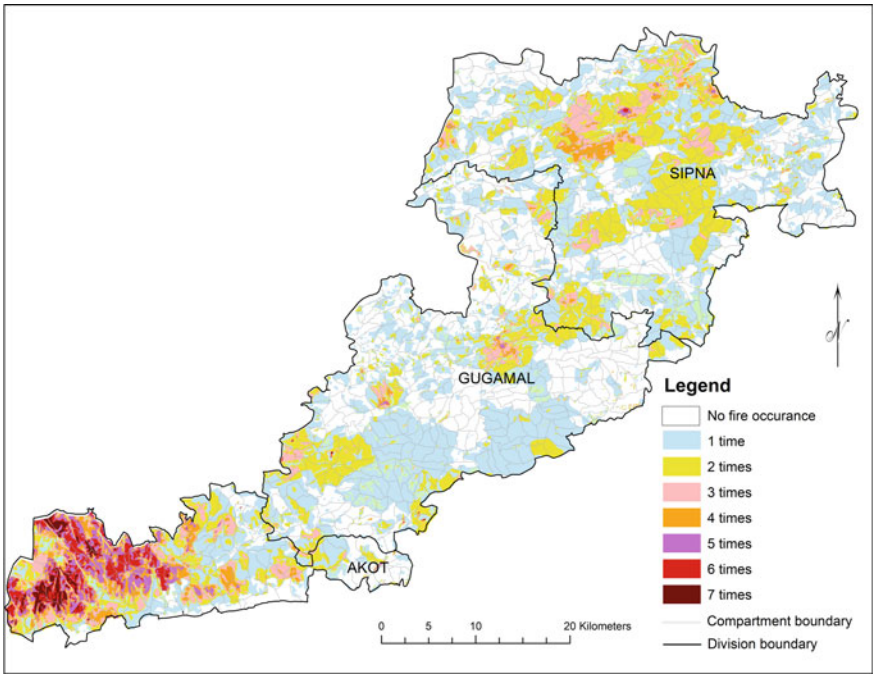

Fig. 28.8 Fire frequency map of MTR prepared by fire scar mapping of 7 years Landsat series data

Landsat 8-OLI satellite data (2018 April) and the fire scar discriminated from the BAI image by thresholding method (Fig. 28.7) in Vidarbha region of Maharashtra.

Varghese and Suryavanshi (2017) derived fire frequency map of MTR based on the fire scar mapping of the temporal Landsat data during fire sessions (January–June) for seven years (Fig. 28.8). Fire frequency analysis shows that an area of 0.52% of the reserve was burned all seven years followed by 1.49% for six times, 1.88% for five times, 2.70% for four times, 5.80% for three times, 18.03% for two times, 34.31% for once and 35.27% remains unburned all these seven years (Fig. 28.8). To reduce occurrences of forest fire, proper management of fire is highly important which entails identification of suitable areas for watchtowers, fire closure areas, grazing closure areas, and fire lines (Varghese and Krishnamurthy 2006). Forest fire watchtowers at vital points provide a better view, efficient communication system, and flexibility to arrive at the fire locations in faster way, etc. are the significant factors for successful fire protection and management. Existing fire watchtowers do not cover the entire area of MTR for monitoring the incidence of fire. Identification of suitable sites for locating new watchtowers has been done by integrating and modeling of forest fire frequency map, existing watchtowers, and viewshed analysis in GIS. Based on these results watchtowers were divided into three categories—newly suggested, retainable, and removable (Varghese and Suryavanshi (2017) (Fig. 28.9).

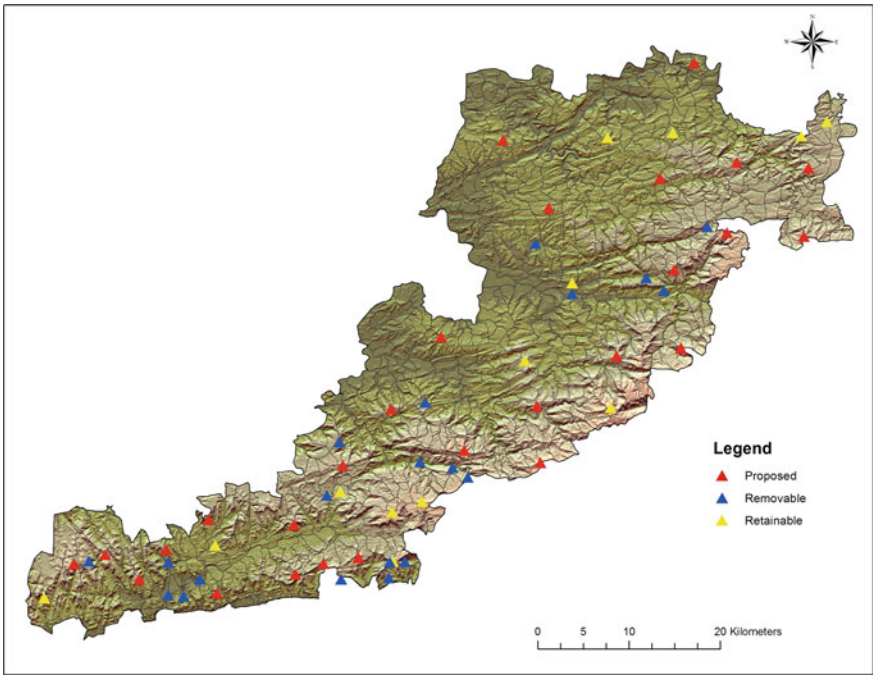

Fig. 28.9 Proposed Forest fire watchtowers of MTR derived from fire frequency, fire-prone areas, and viewshed analysis

Active fire detection needs a high temporal resolution RS data to monitor ongoing fires and the remote sensing systems used for this purposes are Environmental Satellite (GOES), Geostationary Operational Advanced Very High-Resolution Radiometer (AVHRR), Visible Infrared Imaging Radiometer Suite (VIIRS), and MODIS (Schroeder 2014, 2016; Giglio 2006). Data from MODIS Terra and Aqua sensors are the main source of inputs for the identification of active fire locations over the past two decades because of their customized channels for fire monitoring and high temporality. Indian Forest Fire Response and Assessment System (Inffras) established at NRSC is based on MODIS and DMSP-OLS sensors (Kiran et al. 2006). Inffras alerts contain all thermal anomalies noticed by the sensors regardless of the administrative boundaries where it falls. FSI, making use of this facility, broadcasting the fire alerts within the forest area. Since 2017, FSI initiated the broadcasting warnings gained from SNPP-VIIRS sensor, which has a good resolution (375 m × 375 m) in relation to MODIS (1 km × 1 km). FSI's Forest Fire Alert System (FAST 3.0) broadcasting the warning within the notified forest area and filters out all other fires (FSI 2017).

28.8 Biodiversity Assessment and Monitoring

RS platforms with their advanced sensors can assess the various signatures of ecosystem health called essential biodiversity variables (EBV). EBV is categorized into six classes species population, species trait, community composition, ecosystem structure, ecosystem function, and genetic composition. Of these six EBVs, remote sensing can address five classes and genetic composition requires ground-level studies. Biodiversity can be quantified in multiple dimensions like taxonomic, functional, phylogenetic, and spectral diversities. Of these, spectral diversity can be directly generated using RS data in many different ways. Whittaker (1960, 1972) classified biodiversity across space in community ecology as α diversity (species diversity within communities) and β diversity (variation in species composition among communities). Gamma diversity is the diversity of a whole area contributed by α- and β-diversities. Spectral diversity is the spatial variation in spectral reflectance (Rocchini et al. 2010; Gholizadeh et al. 2018a, 2018b; Wang et al. 2019). To derive spectral diversity, the pixels of an RS imagery must be almost equivalent or lesser than the plant canopies in the area of measurement (Wang et al. 2018) to gather straight, spatially clear approximations of α, β, and γ-diversity (Féret and Asner 2014). Theoretically, spectral diversity metrics can be related to taxonomic or phylogenetic components by mean spectra of the species concerned. The same way functional diversity can be discerned by absorption features for specific chemical traits or other pant features that can be identified in the spectral bands. Jha et al. (2019) used Airborne Visible and Infrared Imaging Spectrometer (AVIRIS) hyperspectral data in the discrimination of species and α-diversity at community level with a moderate accuracy (60%). Derivation of biodiversity to the species level is very tough because its accuracy depends upon different factors as well as RS resolutions (Diamond 1988). Hence, the alternative methods are the assessment of the indicators or other surrogate components, according to the spatial scale or grain, which have direct influence on biodiversity (Menon and Varghese 2000). A national-level assessment of biodiversity richness was undertaken for the first time in India using spatial data on 1:50,000 scale to identify and map potential biodiversity-rich areas in the country (Roy et al. 2015). This study has documented the vegetation type, landscape metrics relevant to biodiversity, disturbance sources, and richness (biological) for the Indian region. In another ongoing study, Reddy et al. (2021) used satellite-derived descriptions on vegetative composition, phenology, plant functional types, spatial patterns of vegetation to identify a set of variables that are significant to answer both spatial and ecological questions on the compositional, structural, and functional aspects of biodiversity at the community level.

28.9 Species-Niche Relationship Modeling

Each species needs a set of biotic and abiotic settings for its survival and reproduction and these necessities describe its 'niche' (Goodall 1970). The fundamental niche is the optimum conditions of these requirements and the realized niche is typically a more limited region of this space without other biotic competitions (Hutchinson 1957). Species with wide niche breadth is called a generalist and narrow niche breadth is called a specialist. A lot is known about the general necessities of several species but no species niche has been entirely described. Commonly two GIS modeling approaches are in use for niche modeling: inductive and deductive methods. Deductive approach uses known species ecological requirements, from literature or expert opinion, to extrapolate suitable areas from the environmental variable layers in the GIS database (Corsi et al. 2000). In inductive approach, the ecological necessities of the taxa will be derived from the areas in which it occurs based on the presence-absence data or abundance data and extrapolate to a wider area (Skidmore 2002). Generalized linear or additive models (logistic or Poisson regression), artificial neural networks, classification and regression trees (CARTs), and genetic algorithms are some of the inductive methods used for the suitability assessment. Biomapper, openModeller, Maxent, DesktopGARP, etc. are some of the standalone modeling packages useful for this purpose. Inductive models are possibly more precise than rule-based or literature-review-based models but they necessitate gathering of lot of field observations of the species concerned. Varghese et al. (2010) classified the fundamental and realized niches of threatened trees of Peppara WLS based on inductive modeling using the locational data of the species and the thematic database like forest type, altitude, slope, aspect, soil, mesic and riparian conditions, disturbance regime (Fig. 28.10).

The ecological requirements of each threatened tree species were derived along with the hotspots of threatened species (Fig. 28.11) and critical habitats to be conserved. Habitat specialists and generalists were also derived from the study from the phytosociological data collected along with threatened species.

28.10 Leaf Area Index (LAI) Measurement

LAI is an important biophysical parameter affecting the biological process of an ecosystem like photosynthesis, transpiration, and energy balance and is an essential input for numerous ecological models (Bonan 1993). There are two main types of methods to derive LAI using RS data, empirical and physical methods, of these the first one is based on the association between LAI and RS data, and second one is based on canopy radioactive transfer (RT) models (Atzberger et al. 2015). Empirical approaches are specific to location, time, vegetation, and RS sensors (Tillack et al. 2014). Physics-based methods depend on the radiative transfer (RT) models which abridge the information of the physical progressions that happened to the photon

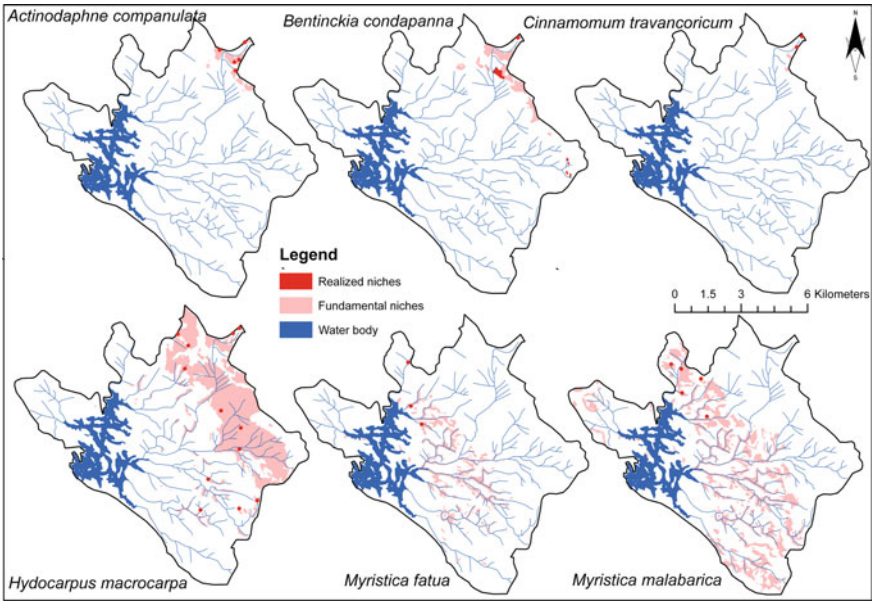

Fig. 28.10 Niches of threatened tree species of Peppara WLS

transference in forest structure (Strahler 1997), hence, this method can be used for different circumstances (Myneni et al. 2002; Deng et al. 2006). RT models are classified into one-dimensional and three-dimensional models based on its capability to discern canopy layer as such or individual tree canopies separately. The canopy architecture of each forest type differs depending upon the biome to which they belong, hence no single RT model suits to cover all forest canopies. So, each vegetation type requires its own RT model to estimate the LAI (Yao et al. 2008). Empirical models are easier to implement and an ideal tool for relating field-measured LAI to spectral vegetation indices or remote sensing data channels. Mani et al (2017) developed empirical models for Landsat-8 OLI and IRS Resourcesat Awifs sensors using stepwise multiple linear regression of the monthly LAI measured from the field (Teak forest *Tectona grandis*) and spectral vegetation indices derived from the satellite data. The field-derived LAI of *Tectona grandis* ranges from 0.19 (April) to a maximum of 5.01 (October). These models provided comparatively good r^2 values with Landsat-8 OLI (0.85) and AWiFS sensors derived LAIs for teak forests of Central India (Fig. 28.12). In another study, Padalia and Varghese (2010) derived LAI of tropical dry deciduous *Shorea robusta* forest of India using the spectral vegetation indices of narrow spectral bands of Hyperion hyperspectral data. The field-derived LAI of *Shorea robusta* ranges from 1.9 to a maximum of 4.3. Optical band ratios selected for LAI estimation from cross-correlation analysis from this study are 518 − 671/518 + 671 (r^2 0.84) followed by 528 − 671/528 $^+$ 671 (r^2 0.82) and 538 − 671/538 $^+$ 671 (r^2 0.82).

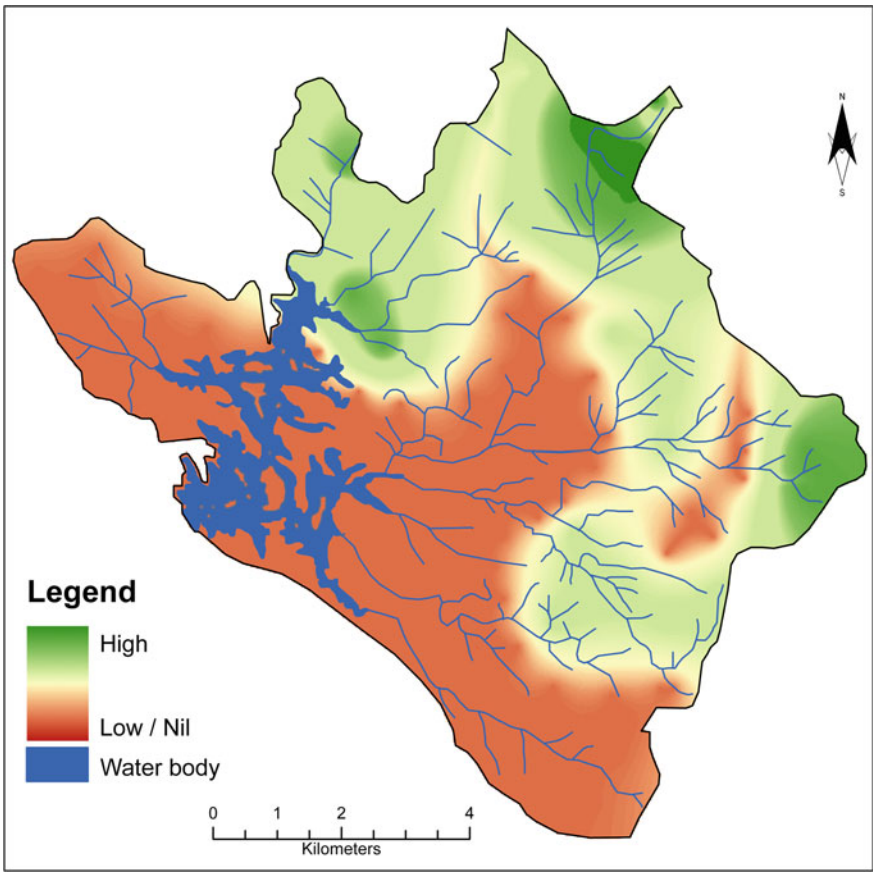

Fig. 28.11 Hotspots of threatened tree species in Peppara WLS

28.11 Primary Productivity

Forest vegetation sequester carbon dioxide from the atmosphere, use it in its physiologic system, subsequently store it as biomass, and ultimately release it into the soil as organic carbon. So, carbon management in the forest ecosystem is one of the most important factors in the context of increasing greenhouse gases emission and mitigation of global climate change. For this, one of the vital parameters to assess forest ecosystems is their primary productivity. Mainly two categories of models are used to derive gross primary productivity (GPP) using remote sensing techniques, first, one employs models based on the maximum light use efficiency. Some of the examples are VPM (Xiao et al. 2004) MODIS-GPP algorithms (Running et al. 2000), CASA model (Potter et al. 1993), GLOPEM (Prince and Goward 1995). The second category GPP models are TG, VI (Wu et al. 2010), GR (Gitelson et al. 2008), etc. The bottleneck of first category models is the requirement of many ground meteorological

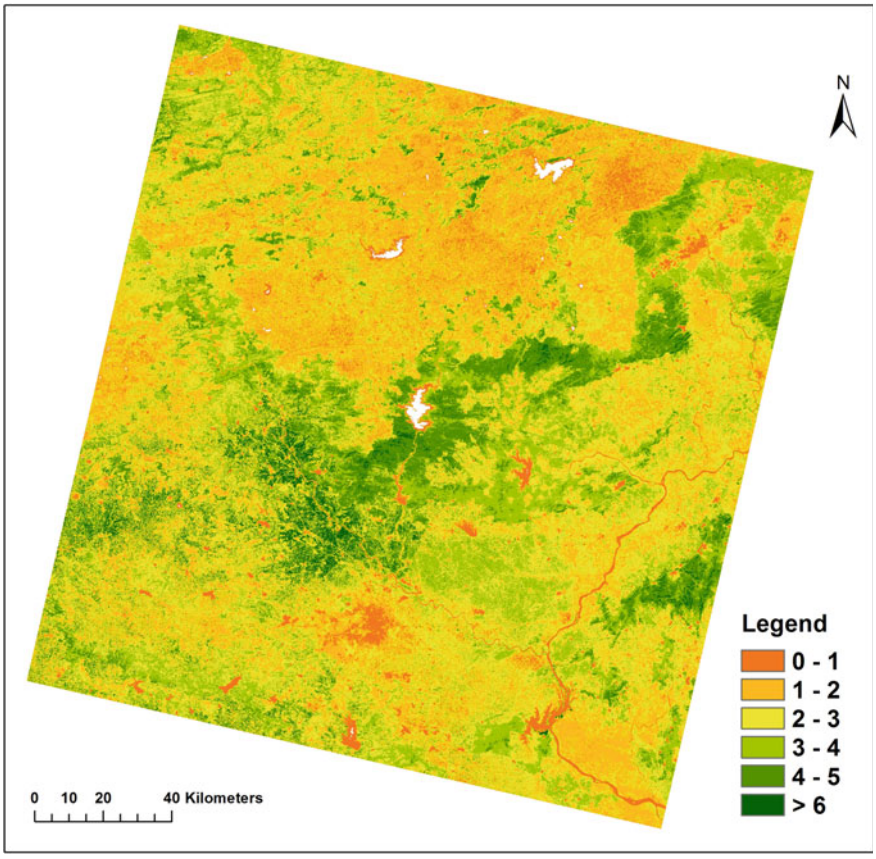

Fig. 28.12 LAI of teak forest of Central India derived from stepwise multiple linear regression of Landsat-8 OLI satellite data and ground-based LAI measurement

observations but provides a better accuracy. The main problem of the second category models is the relationship between GPP and the used model parameters could not be explained explicitly and the estimates give less accuracy. Varghese et al. (2015) analyzed the GPP of Central Indian deciduous forests using MODIS-GPP algorithm, VPM and TG models, and derived seasonal patterns of GPP, analysis of the variation of GPP in different forest types and densities. Estimated GPP for Central Indian forests using different RS models are 914.47, 2.50 gC/m^2 (Annual sum and mean, respectively), 638.44, 1.75 gC/m^2, and (161.74, 0.44 gC/m^2) for MODIS, VPM, and TG models, respectively. This study found out that VPM model gives a better accuracy in GPP estimation when compared with eddy covariance tower derived GPP (Fig. 28.13).

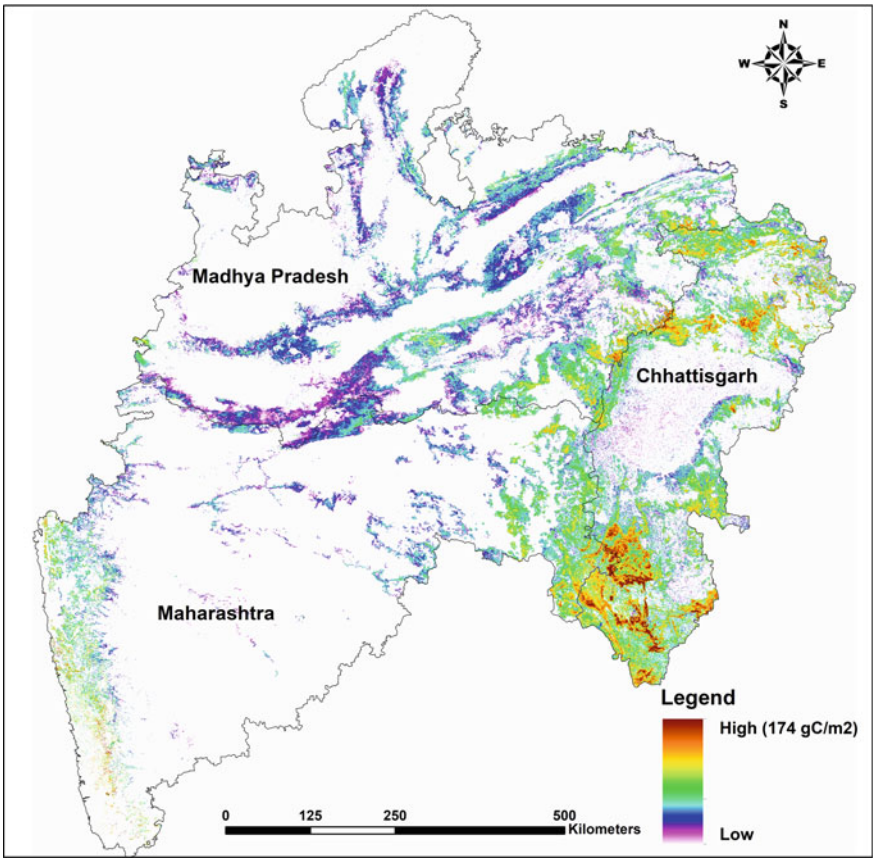

Fig. 28.13 GPP of central Indian states derived using vegetation photosynthesis model

28.12 Biomass and Volume Assessment

Forest biomass comes around 45% of the terrestrial carbon stock and 31% of total carbon sink (Le Quéré 2017) and plays a vital part in balancing the global carbon cycle. Above-ground biomass is mainly estimated by traditional field measurements (West 2015) or remote sensing methods (Lu 2006) using optical/microwave regions. Radar has the capability to enter into the forest canopy and interact with the main biomass components such as trunks and branches and its backscattering strength increases as forest biomass increases according to its wavelength. Mainly statistical regression models are using the inventory sample data and remote sensing parameters to derive biomass or volume. A comprehensive documentation of the relationship between SAR C and L bands backscattering coefficients and forest stand parameters has been given by Varghese et al. (2011). Linear correlation of the single-channel SAR derived backscattering coefficient with the field measured means registered a

good correlation between L HV withstand volume ($r^2 = 0.71$) (Fig. 28.14) and L HH with stand density ($r^2 = 0.75$).

Nowadays to describe the complex nonlinear relationship between forest biomass and RS inputs, machine learning methods like decision tree, K-nearest neighbor, artificial neural network, and support vector machine are used (Li et al. 2020). Tushar et al. (2009) documented the present carbon stock, rate of carbon sequestration, potential sites for carbon sequestration in Nagpur District of Maharashtra using stratified random sampling of the vegetation, optical remote sensing data, and eddy

Fig. 28.14 Forest stand volume estimated for parts of Tadoba National Park using DLR-SAR data

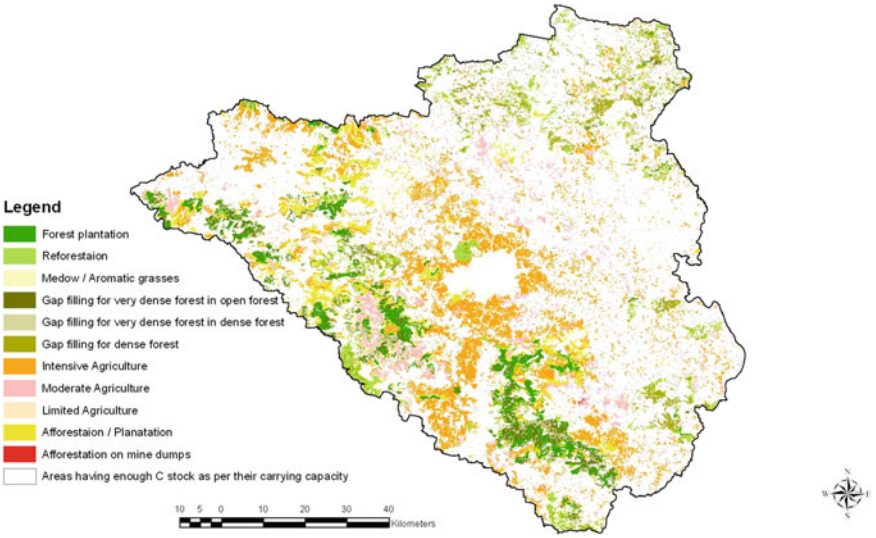

Fig. 28.15 Potential areas for carbon sequestration in nagpur district using afforestation, forestry and agricultural models

covariance tower. The potential area for up-scaling carbon sequestration by various forestry, afforestation, and agricultural practices is also explored in this study by integrating soil, land capability, and modeling in GIS (Fig. 28.15). LiDAR is the recent technology and pragmatic substitute to conventional field method for stand density, volume, and above-ground biomass estimation apart from optical and SAR data for production forestry. LiDAR's capability to deliver detailed three-dimensional vegetation structure is valuable to derive biomass, volume, and height-related parameters (Chan 2021) in a much better way.

28.13 Summary

Last few decades show that geospatial tools are indispensable in forest inventory, management, and monitoring at global or regional scale. The emergence of very high-resolution, high temporal, and spectral remote sensing sensor datasets provides very detailed information about the forest to its species level for management. Radar and lidar technologies usher the foresters to a new path for forest mensuration which revolutionized the silviculture and management practices in forestry. The freely available temporal satellite data catalogs made the geospatial applications more user-friendly, affordable and to better manage the environmental challenges of the next few decades. The development of new analytic methods in remote sensing data processing using artificial intelligence and deep learning techniques enhanced the

capabilities of geospatial technology in understanding forest structure, function, and ecological processes.

References

Ahmad F, Goparaju L (2017) Land evaluation in terms of agroforestry suitability, an approach to improve livelihood and reduce poverty: a FAO based methodology a geospatial solution: a case study of Palamu district, Jharkhand, India. Ecol Ques 25:67–84. https://doi.org/10.12775/EQ.2017.006

Ahmad F, Uddin M, Goparaju L, Rizvi J, Biradar C (2020). Quantification of the Land Potential for Scaling Agroforestry in South Asia. Kartographische Nachrichten. 70:71–89. https://doi.org/10.1007/s42489-020-00045-0

Atzberger C, Darvishzadeh R, Immitzer M, Schlerf M, Skidmore A, le Maire G (2015) Comparative analysis of different retrieval methods for mapping grassland leaf area index using airborne imaging spectroscopy. Int J Appl Earth Obs Geoinform 43:19–31. https://doi.org/10.1016/j.jag.2015.01.009

Axel AC (2018) Burned area mapping of an escaped fire into tropical dry forest in Western Madagascar using multi-season landsat OLI data. Remote Sens 10(3):371. https://doi.org/10.3390/rs10030371

Banskota A, Kayastha N, Falkowski MJ, Wulder MA, Froese RE, White JC (2014) Forest monitoring using Landsat time series data: a review. Can J Remote Sens 40:362–384

Bonan GB (1993) Importance of leaf area index and forest type when estimating photosynthesis in boreal forests. Rem Sen Environ 43(3):303–314. https://doi.org/10.1016/0034-4257(93)90072-6

Bright BC, Hudak AT, Kennedy RE, Braaten JD, Henareh Khalyani A (2019) Examining post-fire vegetation recovery with landsat time series analysis in three Western North American forest types. Fire Ecol 15(1):8

Champion HG, Seth SK (1968) A revised survey of forest types of India. Delhi, India

Chan EPY, Fung T, Wong FKK (2021) Estimating above-ground biomass of subtropical forest using airborne LiDAR in Hong Kong. Sci Rep 11:1751. https://doi.org/10.1038/s41598-021-81267-8

Chen J, Chen J, Liao A, Cao X, Chen L, Chen X, He C, Han G, Peng S, Lu M et al (2015) Global landcover mapping at 30m resolution: a pok-based operational approach. ISPRS J Photogramm 103:7–27

Coppin P, Jonckheere I, Nackaerts K, Muys B, Lambin E (2004) Digital change detection methods in ecosystem monitoring: a review. Int J Remote Sens 25:1565–1596

Corsi F, De Leeuw J, Skidmore AK (2000) Modeling species distribution with GIS. In: Boitani L, Fuller TK (eds) Research techniques in animal ecology; controversies and consequences 2000, Columbia University Press, pp 389–434, ISBN0231501390

Crist EP (1985) A TM Tasseled Cap equivalent transformation for reflectance factor data. Remote Sens Environ 17:301–306

Crist EP, Cicone RC (1984) A physically-based transformation of thematic mapper data—The TM Tasseled Cap. IEEE Trans Geosci Remote Sens GE-22:256–263

Dalmiya CP, Santhi N, Sathyabama B (2019) A novel feature descriptions for automatic change detection in remote sensing images. Egypt J Remote Sens Space Sci 22(2):183–192

Deng F, Chen M, Plummer S, Pisek J (2006) Algorithm for global leaf area index retrieval using satellite imagery. IEEE Trans Geosci Rem Sen 44(8):2219–2229. https://doi.org/10.1109/TGRS.2006.872100

Diamond J (1988) Factors controlling species diversity: overview and synthesis. Ann Missouri Bot Gard 75:117–129. https://doi.org/10.2307/1218190

Feret JB, Asner GP (2014) Mapping tropical forest canopy diversity using high-fidelity imaging spectroscopy. Ecol Appl 24(6):1289–1296. https://doi.org/10.1890/13-1824.1 PMID: 29160652

Finney, Mark A (1998) FARSITE: fire area simulator-model development and evaluation. Research Paper RMRS-RP-4, Revised 2004, Ogden, UT: U.S. Department of Agriculture, Forest Service, Rocky Mountain Research Station, pp 47

FSI (2017) India state of forest report, 2017 forest survey of India. Minist Environ For Clim Change Govern India Dehradun 2017:294

FSI (2003) India State of Forest Report, 2003 Forest Survey of India. Ministry of Environment Forest & Climate Change, Government of India, Dehradun, 2003:185

FSI (2009) India State of Forest Report 2009 Forest Survey of India. Ministry of Environment, Forest & Climate Change, Government of India, Dehradun, 2009:199

FSI (2019) India state of forest report, 2019 forest survey of India. Minist Environ For Clim Change Govern India, Dehradun 2019:294

Gholizadeh H, Gamon JA, Zygielbaum AI, Wang R, Schweiger AK, Cavender-Bares J (2018) Remote sensing of biodiversity: soil correction and data dimension reduction methods improve assessment of alpha-diversity (species richness) in prairie ecosystems. Remote Sens Environ 206:240–253. https://doi.org/10.1016/j.rse.2017.12.014

Gholizadeh H, Gamon JA, Zygielbaum AI, Wang R, Schweiger AK, Cavender-Bares J (2018) Remote sensing of biodiversity: soil correction and data dimension reduction methods improve assessment of α-diversity (species richness) in prairie ecosystems. Remote Sens Environ 206:240–253. https://doi.org/10.1016/j.rse.2017.12.014

Giglio L, Justice SWCO (2006) The collection 6 MODIS active fire detection algorithm and fire products. Remote Sens Environ 178:31–41

Gitelson AA, Peng Y, Masek JG, Rundquist DC, Verma S, Suyker A, Baker JM, Goldstein A, Hollinger D, Misson L (2008) A new model of gross primary productivity for North American ecosystems based solely on the enhanced vegetation index and land surface temperature from MODIS. Remote Sens Environ 112:1633–1646

Gong P, Wang J, Yu L, Zhao YC, Zhao YY, Liang L, Niu ZG, Huang XM, Fu HH, Liu S (2013) Finer resolution observation and monitoring of global land cover: first mapping results with landsat TM and ETM+ data. Int J Remote Sens 34:2607–2654

Goodall DW (1970) Statistical plant ecology. Ann Rev Ecol Syst 1:99–124

Halofsky JE, Peterson DL, Harvey BJ (2020) Changing wildfire, changing forests: the effects of climate change on fire regimes and vegetation in the Pacific Northwest, USA. Fire Ecol 16:4. https://doi.org/10.1186/s42408-019-0062-8

Hansen MC, Defries RS, Townshend JRG, Sohlberg R (2000) Global land cover classification at 1 km spatial resolution using a classification tree approach. Int J Remote Sens 21:1331–1364

Hatfield JL, Meyers T (2012) Remote estimation of crop gross primary production with Landsat data. Remote Sens Environ 121:404–414

Hościło A, Lewandowska A (2019) Mapping forest type and tree species on a regional scale using multi-temporal sentinel-2 data. Remote Sens 11:929. https://doi.org/10.3390/rs11080929

Huang C, Davis LS, Townshend JRG (2002) An assessment of support vector machines for land cover classification. Int J Remote Sens 23:725–749

Hutchinson GE (1957) Concluding remarks population studies: animal ecology and demography. Cold Spring Harb Symp Quant Biol 22:415–427

IIRS (2004) Biome level characterization of Indian vegetation using IRS WiFS data. Indian Institute of Remote Sensing, Dehradun pp: 166

IPCC (2006) IPCC guidelines for national greenhouse gas inventories—a primer. In: Eggleston HS, Miwa K, Srivastava N, Tanabe K (eds) Prepared by the national greenhouse gas inventories programme published. IGES, Japan

ICRAF (1993) A Global Agenda by Helen Van Houten, International Centre for Research in Agroforestry. International Centre for Research in Agroforestry Nairobi Kenya pp: 20

Jha CS, Rakesh JS, Reddy CS, Rajashekar G, Maity S, Patnaik C et al (2019) Characterization of species diversity and forest health using AVIRIS-NG hyperspectral remote sensing data. Current Sci 116(7):1124–1135

Jha CS, Hebbar R, Ravishankar HM, Varghese AO, Bera AK, Chakraborthy D, Chandrashekar K et al. (2022) Spatial inventory of agroforestry resources using geospatial technology and AI with very high-resolution images, Food and Agriculture Organization of the United Nations (FAO) and National Remote Sensing Centre, ISRO, Govt. of India, NRSC-RRSC-BANG-APR 2022-TR-0001999-V1.0 Technical Report pp 118.

Key CH, Benson NC (2006) Landscape assessment: ground measure of severity, the composite burn index; and remote sensing of severity, the normalized burn ratio USDA forest service, Rocky Mountain Research Station: Ogden. UT, USA

Kiran Chand TR, Badarinath KVS, Prasad VK, Murthy MSR, Elvidge C, Tuttle BT (2006) Monitoring forest fires over the Indian region using DMSP-OLS nighttime satellite data. Remote Sens Environ 103(2):165–178

Le Quéré C**,** Andrew RM, Friedlingstein P, Sitch S, Pongratz J, Manning AC, Korsbakken JI, Peters GP, Canadell JG et al. (2018) Global carbon budget 2017. Earth Syst Sci Data 10:405–448 (2018) https://doi.org/10.5194/essd-10-405-2018

Li Y, Li M, Li M, Li C, Liu Z (2020) Forest aboveground biomass estimation using Landsat 8 and Sentinel-1A data with machine learning algorithms. Sci Rep 10:9952. https://doi.org/10.1038/s41598-020-67024-3

Lu D (2006) The potential and challenge of remote sensing-based biomass estimation. Int J Remote Sens 27:1297–1328

Luoto KM, Nagendra H, Oldel J, Ricotta C, Southworth J, Neteler M (2010) Remotely sensed spectral heterogeneity as a proxy of species diversity: recent advances and open challenges. Ecol Inform 5(5):318–329

Mani JK, Varghese AO (2018) Remote sensing and GIS in agriculture and forest resource monitoring. In: Reddy GPO, Singh SK (eds) Geospatial technologies in land resources mapping, monitoring and management, geotechnologies and the environment. Springer International Publishing AG, part of Springer Nature 2018, pp 377–400

Mani JK, Gangwar S, Jain S, Suryavanshi A, Wadodkar M, Varghese AO (2020) Applications of geospatial technologies to aid developmental work in Nashik District, Maharashtra. NRSC Report NRSC-RC-REGNAGP-RRSC-NAGP-FEB2021-TR0001800-V1.0

Mani JK, Varghese AO, Kameshwara Rao SVC (2017) Estimation of leaf area index of teak forests of central India using satellite remote sensing. In: Proceedings of 38th international Asian conference on remote sensing at New Delhi, October 2017

Martín MP, Gómez I, Chuvieco E (2006) Burnt Area Index (BAIM) for burned area discrimination at regional scale using MODIS data. For Ecol Manag 234

Martin Pilar M, Chuvieco E, De Grandes C (1998) Incendios Forestales En La Península Ibérica a Partir De Imágenes Noaa-Avhrr. Ser Geogr 7:109–128

Menon ARR, Varghese AO (2000) Biodiversity monitoring. In: Sivadasan M, Mohanan KV (eds) Biodiversity and ecology—concepts and facts. University of Calicut, pp 102–116

Menon ARR, Varghese AO, Martin Lowel KJ (1999) Impact of fire on Moist deciduous forest ecosystem of southern tropical forests of India. In: Impacts of fire and human activities on forest ecosystems in the tropics proc. International symposium on asian tropical forest management III, pp 52–61

Mitchell AL, Rosenqvist A, Mora B (2017) Current remote sensing approaches to monitoring forest degradation in support of countries measurement, reporting and verification (MRV) systems for REDD+. Carbon Balance Manage 12:9. https://doi.org/10.1186/s13021-017-0078-9

Myneni R, Hoffman S, Knyazikhin Y, Privette J, Glassy J, Tian Y, Wang Y, Song X, Zhang Y, Smith G (2002) Global products of vegetation leaf area and fraction absorbed PAR from year one of MODIS data. Rem Sen Environ 83(1–2):214–231. https://doi.org/10.1016/S0034-4257(02)00074-3

Nair SC (1991) The Southern Western Ghats: a biodiversity conservation plan studies in ecology and sustainable development, INTACH, New Delhi

National Working Plan Code (India) – (2014) National working plan code—2014 for sustainable management of forests and biodiversity in India. Forest Research Institute, Dehradun, Ministry of Environment and Forests Government of India

NRSA (1985) Forest cover assessment of India using satellite remote sensing data during 1972–1975 and 1980–1982 periods. National Remote Sensing Agency Hyderabad India: Technical Report

Pandya R, Pandya J (2015) C5.0 algorithm to improved decision tree with feature selection and reduced errorpruning. Int J Comput Appl 117:18–21

Padalia Hitendra, Varghese AO (2010) Evaluating sensitivity of hyper spectral remote sensing satellite data based indices to in-situ measured biophysical characteristics of dry deciduous forests NRSC Report number: NRSC-RC-Mar-2010-TR-619

Pinty B, Verstraete MM (1992) GEMI: a non-linear index to monitor global vegetation from satellites. Vegetatio 101:15–20

Prince SD, Goward, SN (1995). Global primary production: a remote sensing approach. Journal of Biogeog. 22:815–835

Potter C, Randerson J, Field C, Matson P, Vitousek P, Mooney H, Klooster S (1993). Terrestrial Ecosystem Production: A Process Model Based on Global Satellite and Surface Data. Global Biogeochemical Cycles 7:811–841. https://doi.org/10.1029/93GB02725

Potter C, Randerson J, Field C, Matson P, Vitousek P, Mooney H, Klooster S (1993). Terrestrial Ecosystem Production: A Process Model Based on Global Satellite and Surface Data. Global Biogeochemical Cycles 7:811–841. https://doi.org/10.1029/93GB02725

Prasanth DK, Ashwini SP, Varghese AO, Joshi AK (2009) Mapping of forest fire risk zones and identification of suitable sites for fire watchtowers using remote sensing and GIS. In: Proceedings of the ISRS symposium on advances in geo-spatial technologies with special emphasis on sustainable rainfed agriculture, 17–19 September 2009, Nagpur

Rao MK, Varghese AO, Krishna Murthy YVN (2007) Remote sensing and GIS inputs for working plan preparation. Indian Forester 133(1a):65–76

Rao MK, Varghese AO, Krishna Murthy YVN (2006) Use of geospatial database in sustainable forest management. In: Proceedings of ISPRS international symposium on geospatial database for sustainable development, 27–30 September 2006, Goa, India, WG-IV-3-12

Rao KS, R Pand (2001) Land use dynamics and landscape change pattern in a typical micro watershed in the mid elevation zone of central Himalay, India. Agric. Ecosyst Environ 86:113–124

Reddy CS, Jha CS, Diwakar PG, Dadwal VK (2015) Nationwide classification of forest types of India using remote sensing and GIS. Environ Monit Assess 187(12):777. https://doi.org/10.1007/s10661-015-4990-8

Reddy CS, Satish KV, Prasada Rao PVV (2018) Significant decline of forest fires in Nilgiri biosphere reserve India. Remote Sens Appl Soc Environ 11:172–185

Reddy CS, Varghese AO, Padalia H, Saran S, Ayyappan N, Srivastava G, Sreejith KA et al (2021) Manual. Biodiversity characterization at community level in India using earth observation data. DBT-DOS Project Document. National Remote Sensing Centre, Hyderabad

Reddy C S, Saranya Kotturu, Shaik Vazeed, Satish K, Jha Chandra, Diwakar P, Dadhwal Vinay, Rao PS, Murthy et al. (2018). Assessment and monitoring of deforestation and forest fragmentation in South Asia since the 1930s. Global and Planetary Change 161:132–148. https://doi.org/10.1016/j.gloplacha.2017.10.007

Reddy CS, Bird, NG, Sreelakshmi S, Manikandan TM, Asra M, Krishna PH, Jha C, Rao P, Diwakar PG (2020). Identification and characterization of spatio-temporal hotspots of forest fires in South Asia. Environmental Monitoring and Assessment 191, 791 https://doi.org/10.1007/s10661-019-7695-6

Reiche J, Souza C M, Hoekman DH, Verbesselt J, Persaud H, Herold M (2013) Feature level fusion of multi-temporal ALOS PALSAR and Landsat data for mapping and monitoring of tropical deforestation and forest degradation. IEEE Journal of Selected Topics in Applied Earth Observations and Remote Sensing, 6(5):2159–2173. https://doi.org/10.1109/JSTARS.2013.2245101

Reiche J, Souzax CM, Hoekman DH, Verbesselt J, Persaud H, Herold M (2018) Feature level fusion of multi-temporal alos palsar and landsat data for mapping and monitoring of tropical deforestation and forestdegradation. IEEE J Sel Top Appl Earth Obs Remote Sens 6:2159–2173

Rocchini D, Balkenhol N, Carter GA, Foody GM, Gillespie TW, He KS, Kark S, Levin N, Lucas K, Luoto M, Nagendra H, Oldeland J, Ricotta C, Southworth J, Neteler M (2010) Remotely sensed spectral heterogeneity as a proxy of species diversity: recent advances and open challenges. Ecol Inform 5(5):318–329. ISSN 1574–9541, https://doi.org/10.1016/j.ecoinf.2010.06.001

Roy PS, Behera MD, Murthy MSR, Roy A, Singh S, Kushwaha SPS, Jha CS, Sudhakar S, Joshi PK, Reddy CS et al (2015) New vegetation type map of India prepared using satellite remote sensing: comparison with global vegetation maps and utilities. Int J Appl Earth Obs Geoinf 39:142–159

Roy Parth, Kushwaha Satya, Murthy MSR, Roy Arijit, Kushwaha Deepak C, Sudhakar Reddy, Behera Mukunda, Mathur Vinod, Padalia Hitendra, Saran Sameer, Singh J S, Jha Chandra, Porwal MC (2012) Biodiversity Characterisation at Landscape Level: National Assessment. Indian Institute of Remote Sensing Dehradun India pp: 140, ISBN: 81-901418-8-0

Running S W, Thornton P E, Nemani R, Glassy J M (2000) Global terrestrial gross and net primary productivity from the Earth observing system. In: O Sala, RB Jackson, HA.Mooney, R W Howarth (Eds.). Methods in ecosystem science. New York' Springer Verlag pp 443–57

Schroeder W, Oliva P, Giglio L, Csiszar IA (2014) The new VIIRS 375m active fire detection data product: algorithm description and initial assessment. Remote Sens Environ 143:85–96

Schroeder W, Oliva P, Giglio L, Quayle B, Lorenz E, Morelli F (2016) Active fire detection using Landsat-8/OLIdata. Remote Sens Environ 185:210–220

Shimada M, Itoh T, Motooka T, Watanabe M, Shiraishi T, Thapa R, Lucas R (2014) New global forest/non-forest maps from alos palsar data (2007–2010). Remote Sens Environ 155:13–31

Sirro L, Häme T, Rauste Y, Kilpi J, Hämäläinen J, Gunia K, Jong B, Paz PF (2018) Potential of Different Optical and SAR Data in Forest and Land Cover Classification to Support REDD+ MRV. Remote Sensing 2018 10(6):942. https://doi.org/10.3390/rs10060942

Sinha S, Jeganathan C, Sharma LK et al. (2015) A review of radar remote sensing for biomass estimation. International Journal Environ Sci Technol 12: 1779–1792. https://doi.org/10.1007/s13762-015-0750-0

Skidmore AK (2002) Taxonomy of environmental models in the spatial sciences. In: Skidmore A (ed) Environmental modelling with GIS and remote sensing, Taylor & Francis, pp 8–24. https://doi.org/10.1201/9780203302217.ch2

Stehman SV, Foody GM (2019) Key issues in rigorous accuracy assessment of land cover products. Remote Sens Environ 231:111199

Strahler AH (1997) Vegetation canopy reflectance modeling-recent developments and remote sensing perspectives. Rem Sen Rev 15:179–194. https://doi.org/10.1080/02757259709532337

Suryavanshi AS, AO Varghese**,** AK Jha, J.R. Shrama (2015) Social forestry information system (SOFIS): a standalone software for holistic planning of social forestry activities. In: Proceedings of open source geospatial tools in climate change research and natural resource management, (FOSS4G-India 2015), second national conference on free and open source software for geospatial, 8–10, June, Dehradun

Szpakowski DM, Jensen JLR (2019) A review of the applications of remote sensing in fire ecology. Remote Sens 11(22):2638. https://doi.org/10.3390/rs11222638

Tillack A, Clasen A, Kleinschmit B, Förster M (2014) Estimation of the seasonal leaf area index in an alluvial forest using high-resolution satellite-based vegetation indices. Rem Sen Environ 141:52–63. https://doi.org/10.1016/j.rse.2013.10.018

Trigg S, Flasse S (2001) An evaluation of different bi-spectral spaces for discriminating burned shrub-savannah. Int J Remote Sens 22:2641–2647

Tushar W, Varghese AO, Tawale P, Nair R, Singh SK, Juwarkar AA (2009) Assessment of the potential for carbon sequestration through afforestation, forestry and agriculture models using remote sensing and GIS. In: Proceedings of the ISRS symposium on advances in geo-spatial technologies with special emphasis on sustainable rainfed agriculture, 17–19 September 2009, Nagpur

Varghese AO, Krishna Murthy YVN (2006) Remote sensing and GIS inputs for Working Plan preparation of East Melghat Forest Division, Maharashtra. RRSSC Technical Report Number RRSSC/7-30-2006. doi: https://doi.org/10.13140/RG.2.1.2382.3847

Varghese AO (1997) Ecological studies of the forests of Peppara Wildlife Sanctuary using remote sensing techniques. PhD Thesis Forest Research Institute Dehradun, pp 286

Varghese AO, Suryavanshi A (2016) Generation of perspective plan for social forestry in Nagpur social forestry circle using remote sensing and GIS. NRSC Report: NRSC-RC-REGNAGP-RRSC-NAGP-OCT2020-TR0001692-V1.0

Varghese AO, Suryavanshi A (2017) Forest cover transformation analysis and management of Melghat Tiger Reserve using RS and GIS, NRSC Report: NRSC-RC-REGNAGP-RRSC-NAGP-OCT2020-TR0001690-V1.0. doi: https://doi.org/10.13140/RG.2.2.27068.49280

Varghese AO, Suryavanshi A (2018) Generation of geo-spatial inputs for working plan preparation of West Nashik Forest Division, Maharashtra. NRSC Report number: NRSC-RC-REGNAGP-RRSC-NAGP-OCT2020-TR0001691-V1.0

Varghese AO, Suryavanshi A (2014) Assessment of the information content of C-band SAR data to develop methods for characterizing forests in terms of density, NRSC Report Number REGNAGP-RRSC-NAGP-NOV2020-TD-0001714-V1.0

Varghese AO, Joshi AK, Krishna Murthy YVN (2010) Mapping of realized and fundamental niches of threatened tree species using geoinformatics: a species level approach for sustaining biodiversity. Spec Issue Biodiv Landscape Ecol J Indian Soc Remote Sens 38(3):523–534

Varghese AO, Joshi AK, Krishna Murthy YVN (2011) Tropical dry deciduous forest stand variable estimation using SAR data. J Indian Soc Remote Sens 39(4):583–589

Varghese AO, Suryavanshi A, Joshi AK (2016) Analysis of different polarimetric target decomposition methods in forest density classification using C band SAR data. Int J Remote Sens 37(3):694–709

Varghese AO, Mathew DC, Mani JK (2015) Estimation of biomass and seasonal dynamics of GPP of the deciduous forests in central India using RS based models. NRSC Report No. NRSC-RC-Jan-2016-TR-823

Varghese AO, Joshi AK (2015) Polarimetric classification of C-band SAR data for forest density characterization. Curr Sci 108(1):100–106

Wang R, Gamon JA, Cavender-Bares J, Townsend PA, Zygielbaum AI (2018) The spatial sensitivity of the spectral diversity–biodiversity relationship: an experimental test in a prairie grassland. Ecol Appl 28:541–556

Wang Z, Townsend PA, Schweiger AK, Couture JJ, Singh A, Hobbie SE, Cavender-Bares J (2019) Mapping foliar functional traits and their uncertainties across three years in a grassland experiment. Remote Sens Environ 221:405–416

West PW (2015) Tree and forest measurement. Springer. https://doi.org/10.1007/978-3-319-14708-6

Whittaker RH (1960) Vegetation of the Siskiyou mountains, Oregon and California. Ecol Monogr 30(3):280–338

Whittaker RH (1972) Evolution and measurement of species diversity. Taxon 21(2/3):213–251

Wilson EH, Sader SA (2002) Detection of forest harvest type using multiple dates of Landsat TM imagery. Remote Sens Environ 80:385–396

Wu C, Munger JW, Niu Z, Kuang D (2010) Comparison of multiple models for estimating gross primary production using MODIS and eddy covariance data in Harvard Forest. Remote Sens Environ 114(12):2925–2939. https://doiorg/https://doi.org/10.1016/j.rse.2010.07.012

Xiao X, Zhang Q, Braswell B, Urbanski S, Boles S, Wofsy S, Moore B, Ojima D (2004). Modeling gross primary production of temperate deciduous broadleaf forest using satellite images and climate data. Remote Sensing of Environment 91:256–270. https://doi.org/10.1016/j.rse.2004.03.010

Yao Y, Liu Q, Liu Q, Li X (2008) LAI retrieval and uncertainty evaluations for typical row-planted crops at different growth stages. Rem Sen Environ 112(1):94–106. https://doi.org/10.1016/j.rse.2006.09.037

Zhu Z, Woodcock CE (2014) Continuous change detection and classification of land cover using all available Landsat data. Remote Sens Environ 144:152–171

Chapter 29
Earth Observation Data for Spatio-Temporal Analysis of Land Cover Changes Within Notified Forest Areas

Niraj Priyadarshi, Dibyendu Dutta, V. M. Chowdary, and Chandra Shekhar Jha

Abstract Time-series satellite data provide vital input for effective and accurately monitoring land cover change and assessment of vegetation condition on the land surface. Land cover change can be easily detected by any changes in temporal profile and pattern in long-term EVI data. Snapshot satellite image-based (two-date or multi-date) land cover change detection approach is in existence for quite a long time and is successful, though, snapshot image-based approaches have limitation such as temporal resolution, cloud cover etc. Therefore, in recent time, availability of huge dataset especially long-term satellite data provides the opportunity to study vegetation dynamics and accurately observing natural resources. In this study, analysis of temporal pattern to identify change in land cover based on Wavelet transform (WT) technique and statistical approaches (Mann–Kendall test and Sen slope's method) in time-series Moderate Resolution Imaging Spectroradiometer (MODIS) Enhanced Vegetation Index (EVI) data for the period of 2005–2014. The Mann–Kendall (MK) test is used to detect monotonic trends and the Sen's slope estimate the magnitude of existing trend in long-term EVI data. Multi-temporal MODIS EVI time-series of the MOD13Q1 global products with 250-m spatial resolution was used for the period 2005–2014 and temporal pattern was analyzed to identify change on Earth surface. The results from this study can serve guideline for accurately monitoring and sustainable strategies for conservation of green cover in study area.

N. Priyadarshi (✉) · D. Dutta
Regional Remote Sensing Centre—East (RRSC-East), NRSC/ISRO, Plot No: BG-2, A1B, Newtown, Kolkata 700156, India
e-mail: nirajpriyadarshi@yahoo.com

D. Dutta
e-mail: dutta_d@nrsc.gov.in

V. M. Chowdary
Regional Remote Sensing Centre—North (RRSC-North), NRSC/ISRO, Loknayak Bhawan, Khan Market, New Delhi, India

C. S. Jha
National Remote Sensing Centre (NRSC), Balanagar, Hyderabad 500037, India

C. S. Jha et al. (eds.), *Geospatial Technologies for Resources Planning and Management*, Water Science and Technology Library 115,
https://doi.org/10.1007/978-3-030-98981-1_29

Keywords Time series · EVI · Wavelet · Land cover change · Mann–Kendall test · Sen slope

29.1 Introduction

Time-series satellite data provide vital input to monitor land cover change and assessment of vegetation condition on the ground (Jung and Chang 2015). Land use land cover change directly influence ecosystem processes, biodiversity and climate change (Fung 1990; Lambin and Strahler 1994). Ecosystem prediction models utilized historical climate data along with land cover change to predict change in temporal profile/path (Priyadarshi et al. 2020; Quaye Ballard et al. 2020). Continuous anthropogenic changes on Earth surface may influence the global properties with unidentified impact on the environment (Boriah et al. 2008; Kayet et al. 2016; Quaye Ballard et al. 2020; Li et al. 2018). Evidences shown by researchers about the influence of deforestation, degradation, mining, urbanization and conversion are mainly farmland to build up, forest to agriculture on local to regional vegetation over central India (Priyadarshi et al. 2020; Singh and Jeganathan 2016; Srivastava et al. 2013; SFR 2019; Ahmad and Gopraju 2017). Hence, there is requirement to study land cover change detection problem to address the dynamics of climatic condition and ecosystem.

The change detection problem is widely used in various areas mainly signal processing, control theory and statistics (Inclan and Tiao 1994; Gustafsson 2000; Lai 1995). There is available huge archive of remote sensing satellite data where these techniques fail to handle high dimensional satellite time-series data (Boriah et al. 2008). Hence, it provides opportunities to develop robust and efficient algorithm to handle these long-term datasets. Time-series is one of the class in spatio-temporal data which play very crucial role in various applications such as electrocardiogram (ECG), climate studies and stocks price (Fu 2011). Time-series data is numeral (numerical and continuous nature) of series of observation in due course of time organized in sequential manner. Time-series data has large volume, high dimensionality and keep growing the data size continuously. It has property to measure as a whole of series data instead of in discrete value. Recently, increasing use of time-series data provide us ample opportunities in data mining.

Time-series vegetation indices includes Normalized Difference Vegetation Index (NDVI) and Enhanced Vegetation Index (EVI) can be obtained by satellite's sensors such as Thematic Mapper (Landsat TM), AVHRR (NOAA), MODIS (TERRA/AQUA) etc. These vegetation index (VI) used to measure green vegetation over land surface and widely used in various remote sensing applications such as vegetation phenology, LULC, monitoring of natural resource etc. (Beck et al. 2006; Boriah et al. 2008; Gu et al. 2009; Priyadarshi et al. 2020). MODIS vegetation index data is useful for land cover change detection study because it has high revisit ability and extensive spectral range particularly over tropical region where cloud and atmospheric contamination is more.

Satellite observation is cost effective and has larger coverage that consists land, ocean and atmosphere which provide tremendous scope to study the dynamics of land cover change (Lunetta et al. 2006). Time-series satellite data provides us many imageries which perform as monitoring schema for repeatable vegetation index and help to detect changes that takes place over the ground surface (Jong et al. 2012). Previously, various change detection methods/approaches such as Principal Component Analysis (PCA), Tasselled Cap Transformation (TCT), Change Vector Analysis (CVA) etc. were applied to analyze land cover change detection problem but selecting most suitable method is very difficult task (Lambin and Strahlers 1994; Lu et al. 2004; Singh and Talwar 2014; Deng et al. 2008). Time-series analysis has advantage to study temporal profile to detect changes in land cover over the ground surface (Boriah et al. 2008).

The inherent noise and missing information are present in MODIS NDVI/EVI due to clouds and poor atmospheric conditions (Priyadarshi et al. 2018; Lu at el. 2007). These noises reduce quality of data, introduce ambiguity, not compatible with gradual process of vegetation and finally complicate/mislead the analysis of temporal profile. Hence, it is compulsory to eliminate the noise from the time-series vegetation index data for more accurate investigation of remote sensing application such as land cover change studies (Abbes et al. 2018; Priyadarshi et al. 2018). There are several techniques available to remove noise from time-series vegetation index that includes threshold based, least-squares linear regression, Fourier based fitting and Savitzky-Golay filtering methods (Priyadarshi et al. 2018).

In this study, Savitzky-Golay approach was used to eliminate/reduce noise in time-series EVI data by preserving features and temporal pattern of the data set such as relative maxima, minima and width (Chen et al. 2004). Further, analysis of temporal pattern was to identify change in land cover based on Wavelet transform (WT) technique along with Mann–Kendall test and Sen slope's method in time EVI data (MOD13Q1 global products with 250-m spatial resolution) for the period of 2005–2014. The Mann–Kendall method was performed to authenticate the significance of trends whereas the Sen slope's was used to estimate magnitude of the trend. The results from this study can also serve as a guideline for effective monitoring and management by the natural resource policy makers.

29.2 Data Used and Study Area

The Earth Observing System (EOS) provide us the platform to investigate how the various vegetation covers are distributed globally and also to understand how vegetation contributes to the functions of Earth as a system (Didan et al. 2015). Vegetation Indices (VI) provide vegetation information on the ground and MODIS MOD13 product of VI provides global vegetation data at different Vegetation Indices, (VI) represents vegetation. MODIS provides vegetation index product at various time interval such as 8 day, 16 day and monthly with different spatial resolution such as 250, 500 m, 1 and 5 km (Didan et al. 2015; Web Ref 5). These vegetation indices are

widely used and analyzed by various researchers in remote sensing applications for precise and regular observation of natural resource on land surface. The vegetation index (NDVI and EVI) was obtained from MODIS VI data products where EVI is considered better due to its enhanced sensitivity over high biomass on the ground surface of Earth. MODIS sensor (TERRA/AQUA) is considered as enhanced sensor compared to the AVHRR sensor (NOAA) due to its performance and has higher spectral and spatial resolution (Neteler 2004). In this study, MODIS (MOD13Q1) EVI data product with spatial resolution of 250 m at 16 day time stamp was used for the period 2005–2014 for this study.

The highly undulating West Singhbhum district of Jharkhand state is the study area covering nearly 100 × 110 km^2 area (Fig. 29.1). The study area is having dense forest and major land cover classes includes agriculture, barren land, build up, scrub forest and deciduous forest. The study area has mining area with large deposit of iron ore and has minerals such as Chromite, Magnetite, Kainite etc. It has a hilly area with many hills along with rivers flowing through (Web Reference 6). The elevation of study area has a mean altitude of approximately 244 m above mean sea level and nearly 1400 mm is the average annual rainfall (Web Reference 1, 2, 3, 4).

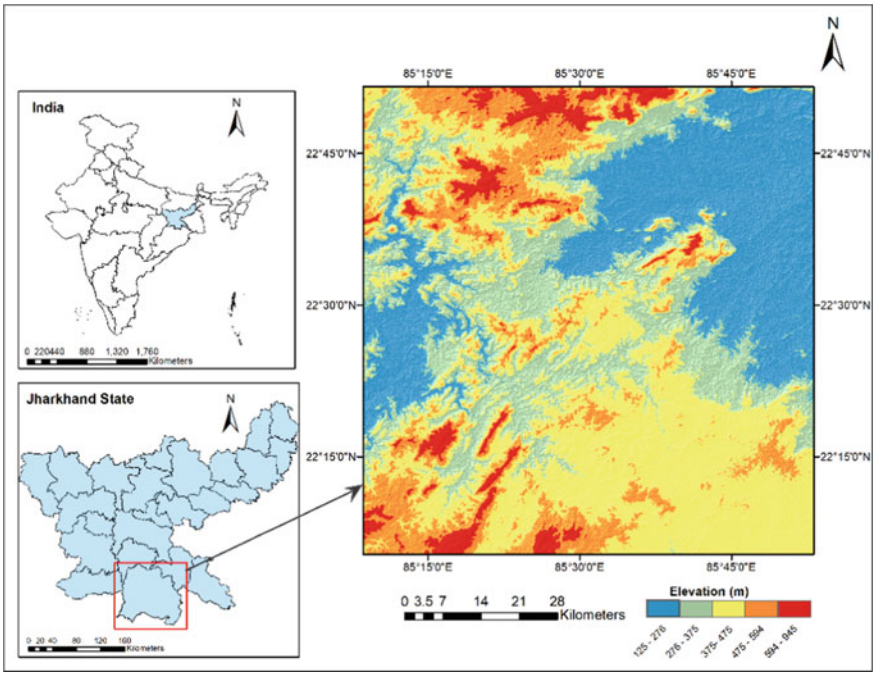

Fig. 29.1 Map of West Singhbhum district of Jharkhand state (study area)

29.3 Methodology

MODIS vegetation index provides EVI/NDVI time-series data to measure vegetation over the ground surface. EVI data has utilized under this study since EVI has enhanced sensitivity in the high biomass area. EVI has advantage of not getting saturated during the process of observing Earth surface with high concentration of chlorophyll (Priyadarshi et al. 2020; Abera et al. 2018; Abbes et al. 2018). Time-series EVI data was utilized for this study and computed as follow,

$$\text{EVI} = g * \frac{\text{nir} - \text{red}}{\text{nir} + c1 * \text{red} - c2 * \text{blue} + l} \tag{29.1}$$

where nir, red and blue surface reflectance after atmospheric correction, $g = 2.5$ (gain factor), $\text{l} = 1$ (soil adjustment factor) and $c1 = 6$ and $c2 = 7.5$ are coefficients that help in atmospheric correction condition to compute EVI value (Setiawan and Yoshino 2010; Priyadarshi et al. 2020). The flowchart of land cover change detection of proposed approach is shown in Fig. 29.2.

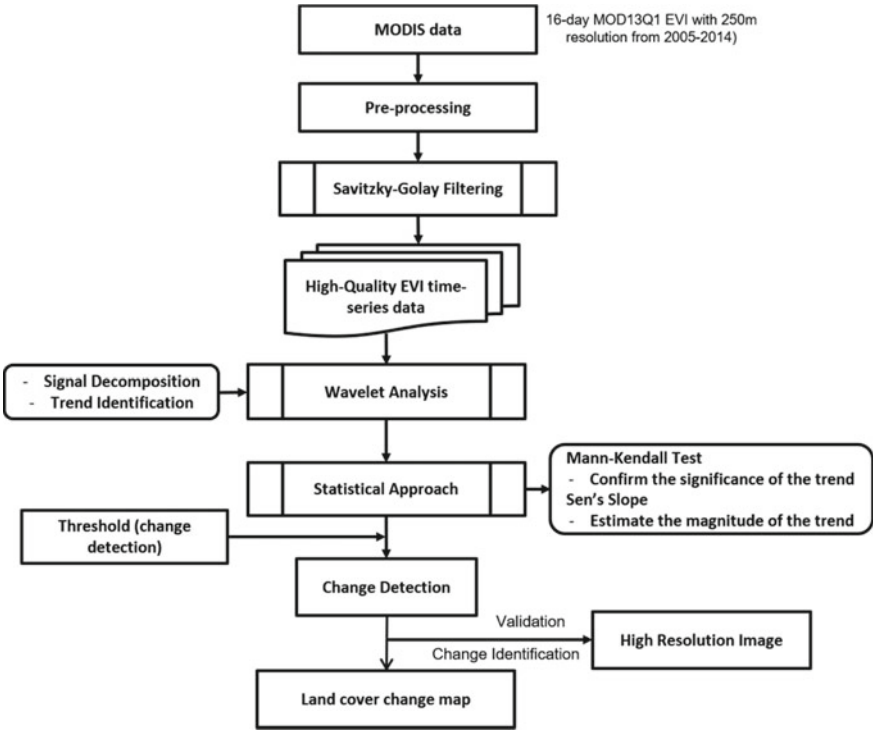

Fig. 29.2 Flowchart of land cover change analysis

29.3.1 Reconstruction of EVI Data Using Savitzky–Golay Filter

MODIS VI was generated by considering higher percentage of clear sky data to minimize noise and also included Maximum Value Composited (MVC) method (Holben et al. 1986). Still, low quality pixels and some noise occurred in time-series EVI dataset (Lu et al. 2007; Setiawan and Yoshino 2010). The inherent noise and missing information are also present in MODIS NDVI/EVI due to clouds and poor atmospheric conditions. The Savitzky-Golay (SG) filtering method (Savitzky and Golay 1964) was used for noise reduction and to generate a good quality vegetation index i.e., EVI data. The SG filtering method uses polynomial function technique to suppress disturbance, while preserves features of the data set such as relative maxima, minima and width (Kim et al. 2014; Priyadarshi et al. 2018). The SG filter method was used to reconstruct raw vegetation index to smoothen long-term vegetation index data and the equation shown in Eq. 29.2,

$$d_j^* = \frac{\sum_{k=-m}^{k=m} f_k d_{l+1}}{n} \tag{29.2}$$

where f_k is the filter coefficient at the kth vegetation data, d^* is noiseless vegetation data, m is the filter interval, d_{l+1} is the vegetation value at position l + 1 and n is the number of convoluting integers with filtering window size ($2m = 1$) (Priyadarshi et al. 2018).

29.3.2 Change Detection Analysis

Investigation of changes on Earth surface is performed in non-agricultural areas using reconstructed high quality long-term EVI data for the period 2005–2014 in this study. Land use land cover (LULC) map on 1:50,000 scale generated by National Remote Sensing Centre (NRSC) was used to generate mask of water bodies and agriculture areas. The water bodies were masked as due variation on water bodies, fluctuation in water level and presence of turbidity may induce errors in investigation of change detection (Priyadarshi et al. 2020; Quaye Ballard et al. 2020). Subsequently, agriculture areas were also masked, as crop rotation and its seasonal variability may also induce false change detection.

Long-term vegetation data is a sequential multiple real observations value at specific time with equal time interval (timestamp) and was used for analysis of variability of any data variable for various remote sensing applications (Quaye Ballard et al. 2020; Priyadarshi et al. 2020). The non-stational nature inherent property present in time-series data and to handle non-stationary nature, various approaches

and techniques were established to analyze for remote sensing applications (Rhif et al. 2019). The Spatio-temporal method in frequency variations can be a possible solution for characterization of non-stationary. In recent years, wavelet analysis in time frequency domain is utilized for the characterization of non-stationary data where it decomposes the signal into sub-signals as per frequency. The wavelet analysis is very efficient transformation since it has ability to retain the time–frequency information of long-term data.

29.3.2.1 Wavelet Analysis

Wavelet Transform (WT) was performed in time-series analysis for studying vegetation variability, phenological information, LULC, monitoring of natural resource (Quaye Ballard et al. 2020; Rhif et al. 2019; Priyadarshi et al. 2020). Wavelet transform is utilized to decompose the signal into component sub-signal and represents signal distribution in time frequency domain. It regulates scaling and shifting factor of the mother wavelet while decomposition of signal is very effective to analyze stationary and non-stationary long-term EVI data. Wavelet analysis does not assume any incorrect distribution of long-term vegetation index data. The approximation components (higher scale with lower frequency) eliminate the fluctuation and noise variation present in time-series data and hence, provides the stable pattern such as seasonal, annual and monthly means (Priyadarshi et al. 2020). The detail components (low-scale and high-frequency) showed the localized, abrupt changes in the long-term data (Quaye Ballard et al. 2020; Rhif et al. 2019; Priyadarshi et al. 2020). In this study, smoother db5 Daubechies wavelet is utilized to analyze non-stationary long-term vegetation index data for 2005–2014 period.

A wavelet is a mathematical function $\psi_{s,t}(x)$ which decomposes a signal into sub-signal at different scales and it is obtained from mother wavelet $\psi(x)$ using shifting factor and dilations as shown in Eq. 29.3,

$$\psi_{s,t}(x) = \frac{1}{\sqrt{|s|}}\psi\left(\frac{x-t}{s}\right), s, t \epsilon R, s0 \tag{29.3}$$

where, 't' is the shifting factor, 's' is the scaling factor and $\frac{1}{\sqrt{|s|}}$ is the normalization. The scaling factor utilized to estimate compression, shifting parameter of wavelet utilized to estimate time location and normalization utilized to confirm the same energy at every scale of wavelet (Quaye Ballard et al. 2020; Rhif et al. 2019; Priyadarshi et al. 2020). The wavelet transform has the ability to accurately identify local characteristics in the non-stationary signal since duration of mother wavelet $\psi(x)$ function is very limited (Martinez and Gilabert 2009; Nalley et al. 2012; Abbes et al. 2018). The wavelet transforms $f(x)$ shown as follows,

$$wf(s,t) = \int_{-\alpha}^{+\alpha} f(x)\psi_{s,t}(x)\mathrm{d}x \tag{29.4}$$

A wavelet function decomposes long-term vegetation index data into sub-signal at different scales and levels using Eq. 29.5 and equation is shown as follows

$$\psi_{j,k}(x) = 2^{\frac{j}{2}}\psi\left(2^j x - m\right) \tag{29.5}$$

where m is the *m*th coefficient of wavelet and *j* is the *j*th level after decomposition.

Trend Analysis of Long-Term Vegetation Index Data

The Mann–Kendall (MK) test (Mann 1945; Kendall 1975) is used to detect monotonic trends in long-term vegetation index data. It is non-parametric in nature and works well for all distributions. MK test has the ability to automatically detect trend (negative or positive) present in long-term EVI data. MK test has major advantage that it is easy to estimate, robust and is able to handle noisy or missing data (George and Athira 2020; Priyadarshi et al. 2020). The MK test statistic T is shown in Eq. 29.6,

$$T = \sum_{i=1}^{m-1}\sum_{j=i+1}^{m} \mathrm{sign}\left(y_j - y_i\right) \tag{29.6}$$

where m is length of the dataset, j is time after time I, y_j is observed value at j and y_i is observed value at i.

The Sen's slope (Sen 1968) was performed to estimate the magnitude of the trend in long-term data. It is non-parametric in nature and widely used due to its robustness and able to handle noisy/error dataset. The Slope Q_i is defined as (George and Athira 2020; Priyadarshi et al. 2020)

$$Q_i = \frac{y_j - y_i}{(j-k)}, i = 1, 2, \ldots M, j > k \tag{29.7}$$

For m values y in the long-term $M = m(m-1)/2$ slope calculates Q_i.

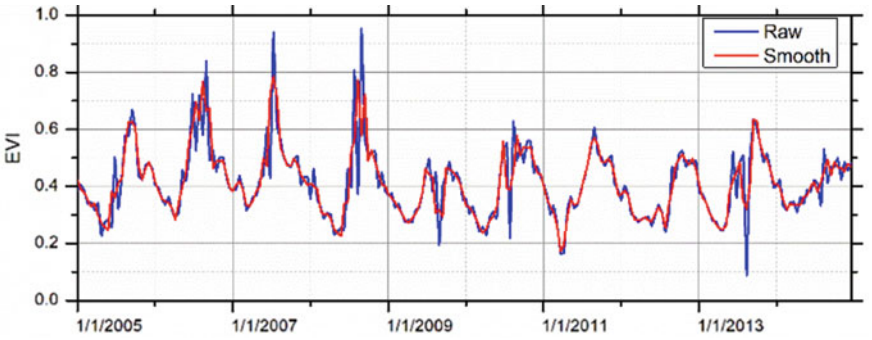

Fig. 29.3 Profile of raw and smooth time-series EVI data for forest pixel

29.4 Results

29.4.1 De-noising Time-Series EVI Data

Long-term MODIS 16-day raw vegetation data has significant presence of noise. These noisy pixels can directly affect and even greatly change the resultant output and may also provide incorrect result. Hence, to avoid such anomalies, it required to filter and reconstruct the time-series dataset for accurate analysis. The Savitzky-Golay filter was performed to reconstruct good quality of time-series EVI data (noise free) by suppressing the disturbance and preserving profile of a signal i.e., time-series EVI data. Temporal profile of raw and smoothened data obtained after passing the original EVI data through the SG filter is shown in Fig. 29.3. It can be observed that reconstructed EVI data has high quality and it has also eliminated the noise and deviation from the normal value (fluctuation such as peaks and drops) present in long-term EVI data.

29.4.2 Wavelet Transform to Detect Land Cover Change

Daubechies wavelet (db5) was performed to examine the long-term 16-day EVI data to recognize land cover change locations during 2005–2014 period for the study area. The wavelet (db5) was selected for the analysis to detect all the approximation and to compute the coefficients of variability existing in long-term EVI data. The wavelet decomposition level of signal was identified and the trend analysis of the signal using smoother wavelet (db5) was carried out. The Daubechies wavelet family is widely used due to its ability to orthogonal and compact support for pattern analysis. The a1–a6 indicates approximation components and the d1–d6 indicates detailed components (Fig. 29.4). The approximation coefficient (a1–a6) represents inter-annual variability while detailed components (d1–d6) present the abnormalities in the signal on 16-day

Fig. 29.4 Wavelet decomposition representing negative trend in long-term EVI data (2005–2014) where a and d indicated approximation and detailed components respectively

scale. The approximation and detailed components together provide the signatures of inter-annual abnormality and seasonality and fluctuation present in dataset. The smoother mother wavelet (db5) is easy to implement and preferred to carry out the analysis since trend in long-term data is changing slowly and gradually over the time.

The trend analysis was performed over the approximation component a6 since it is not affected by noise, abnormality and seasonality which are present in the data. The noise and seasonality get eliminated by detail components (d1–d6) and therefore, higher approximation series a6 has been selected form analysis (Fig. 29.4). The wavelet transform has the ability to detect trend and does the analysis for land cover change using time-series EVI data. The approximation components a6 was considered for analysis of long-term EVI data and identified existing trend present in data.

The Sen's slope is performed to accurately estimate the magnitude of the identified trend and slope Q is computed for either positive or negative trend in EVI data.

The Mann–Kendall test was performed on the approximation components (a6) to detect significant trend in long-term EVI data. The confirmation of significance (MK test) at 95% confidence level having conditions that if significant than hypothesis H coefficients $= 1$; otherwise $H = 0$ and p-value (two sided) is less than 0.05. The MK test can automatically identify the monotonic trend but is unable to provide trend magnitude (slope). Hence, the Sen's slope method was performed to estimate magnitude of the trend which is identified by the MK test in long-term vegetation index data. The slope Q accurately estimated the net change occurred over study area during 2005–2014. Figure 29.6 shows the magnitudes distribution over study area either positive or negative slope computed using Sen's slope method. A systematic and repeated investigation was performed to identify optimal threshold by different value of slope and determined that when slope (Q) extend across threshold value -5 represent change on the ground surface. Figures 29.5 and 29.6 represents map of change locations on the land surface (red color) with negative trends of study area for the period of 2005–2014.

The results (change locations) come out using proposed methods were validated using Google Earth images for analysis of land cover change studies (Fig. 29.6). Figure 29.7 shows validation using Google images for various change locations on the land surface detected using proposed method over study area during 2005–2014. The six locations (box a–f in Fig. 29.6) in study area were shown using high resolution of Google Earth images (Fig. 29.7). In Fig. 29.7, locations a1–a2 represents the box 'a' shown in Fig. 29.6 (a). Similarly, locations b1–b2, c1–c2, d1–d2; e1–e2 and f1–f2 (Fig. 29.7) represents the boxes 'b'–'f' respectively in Fig. 29.6. The proposed method depicted about 363 pixels (locations) where about 289 (79.61%) were actual change and about 74 (20.38%) were wrong change on the ground surface through visual interpretation on the high-resolution image Google images. Hence, the methodology developed under this study has the ability to reduce noise and to identify change locations on land surface using long-term EVI data at regional scale.

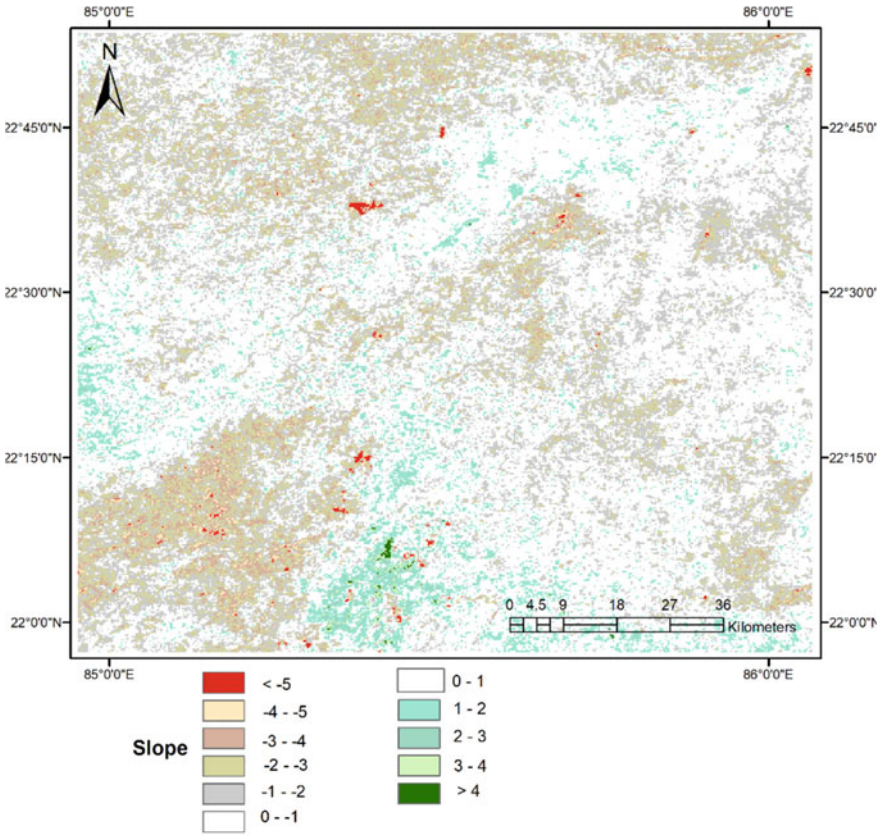

Fig. 29.5 The magnitudes distribution over study area either positive or negative slope. Negative trend represent change on land surface

29.5 Conclusion

Wavelet analysis was performed to study inter-annual vegetation variations and to detect land cover change in long-term EVI data at various temporal scale. Wavelet based proposed approach has the ability to easily detect change in temporal profile in long-term EVI data. Inherent noise present in the EVI data was reduced by Savitzky–Golay filtering method and the regeneration of good quality long-term EVI data which is required for accurate and better analysis. The trend analysis was performed over the approximation component a6 since it is not affected by noise, abnormality and seasonality which are present in the data. The MK test was used to confirm the significance of automatic identification of monotonic trend which is present in the long-term vegetation index data. The Sen's slope method was performed to estimate magnitude of the trend identified by the MK test in long-term vegetation index data. The proposed method depicted about 363 pixels (locations) where about 289 (79.61%)

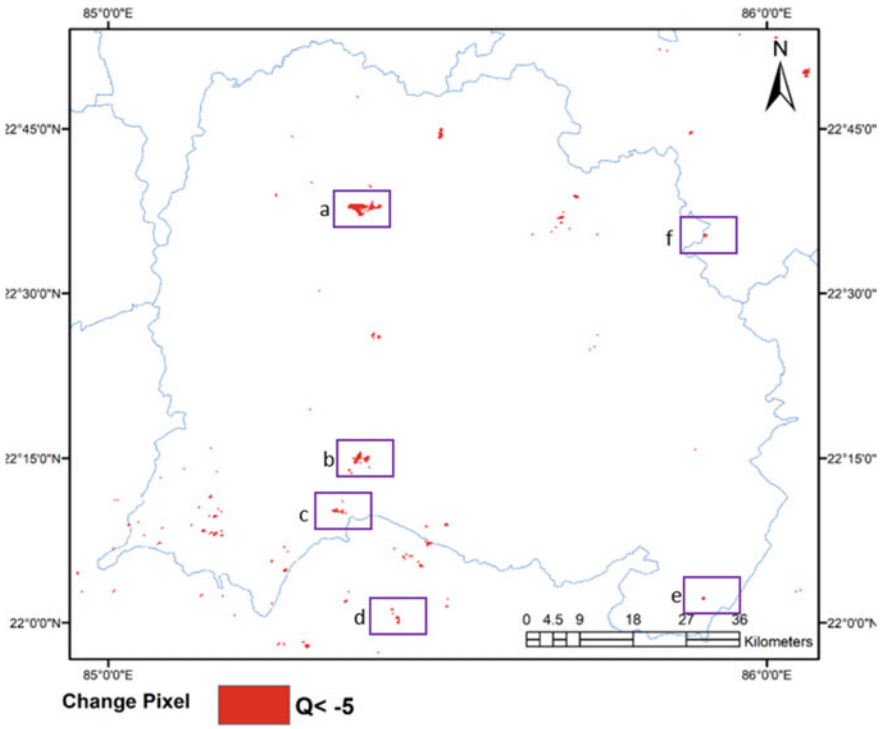

Fig. 29.6 Change pixel locations of land cover of study area detected by proposed method

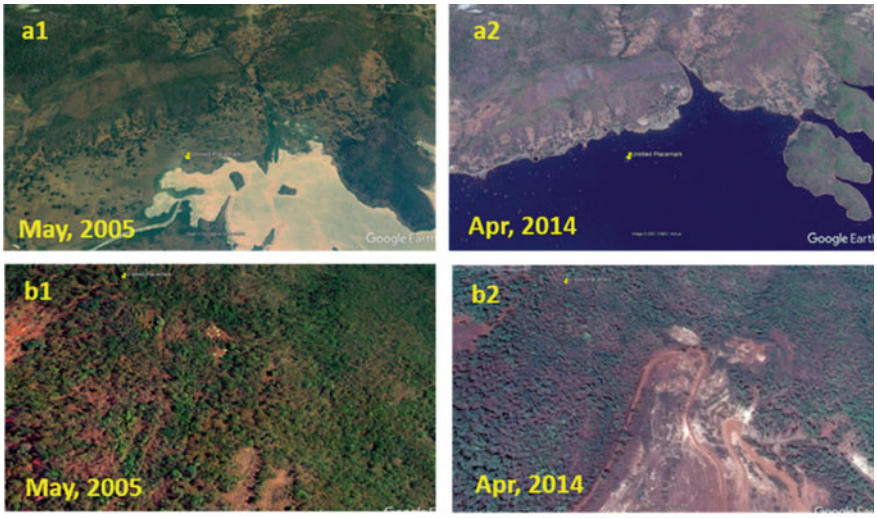

Fig. 29.7 Validation of change pixels (locations) a1–a2, b1–b3, c1–c2, d1–d2, e1–e2 and f1–f2 represents the boxes 'a'–'f' shown in Fig. 29.6 respectively marked on Google Image

Fig. 29.7 (continued)

were actual change and about 74 (20.38%) were false change identified through visual interpretation on the high-resolution image Google images. The proposed method allows us to identify changes in temporal profile and pattern whether it is gradual and abrupt changes on land surface in long-term EVI data.

Acknowledgements The authors thank Director, NRSC for encouraging this work. We acknowledge NASA Earth observing system (http://e4ftl01.cr.usgs.gov/MOLT/MOD13Q1.005/) for providing free MOD13Q1 products.

References

Abera TA, Heiskanen J, Pellikka P, Maeda EE (2018) Rainfall vegetation interaction regulates temperature anomalies during extreme dry events in the Horn of Africa. Glob Planet Change 167(2018):35–45. https://doi.org/10.1016/j.gloplacha.2018.05.002

Abbes AB, Bounouh O, Farah IR, Jong RD, Martínez B (2018) Comparative study of three satellite image time-series decomposition methods for vegetation change detection. Euro J Remote Sens 51(1):607–615. https://doi.org/10.1080/22797254.2018.1465360

Ahmad F, Goparaju L (2017) Long term deforestation assessment in Jharkhand state, India: a grid based geospatial approach. Biolog Forum Int J 9(1):183–188

Beck PS, Atzberger C, Høgda KA, Johansen B, Skidmore AK (2006) Improved monitoring of vegetation dynamics at very high latitudes: a new method using MODISNDVI. Remote Sens Environ 100:321–334

Boriah S, Kumar V, Steinbach M, Potter C, Klooster S (2008) Land cover change detection: a case study. In: Proceedings of the 14th ACM SIGKDD international conference on knowledge discovery and data mining, pp 857–865

Chen J, Jönsson P, Tamura M, Gu Z, Matsushita B, Eklundh B (2004) A simple method for reconstructing a high-quality NDVI time-series data set based on the Savitzky-Golay filter. Remote Sens Environ 91(3–4):332–344

Deng JS, Wang K, Deng YH, Qi GJ (2008) PCA-based land-use change detection and analysis using multitemporal and multisensory satellite data. Int J Remote Sens 29:4823–4838

Didan K, Munoz AB, Solano R, Huete A (2015) MODIS vegetation index user's guide (MOD13 series). Version 3.00, June 2015

Fu TC (2011) A review on time series data mining. Eng Appl Artif Intell 24(2011):164–181

Fung T (1990) An assessment of TM imagery for land-cover change detection. IEEE Trans Geosci Remote Sens 28:681–684

Forest Survey of India's State of Forest Report (SFR, 2019) Ministry of Environment, Forest and Climate Change, Dehradun, India

George J, Athira P (2020) Long-term changes in climatic variables over the Bharathapuzha river basin, Kerala, India. Theor Appl Climatol. https://doi.org/10.1007/s00704-020-03255-8

MODIS Data Rem Sens Environ 104:283–296

Gu J, Li X, Huang C, Okin GS (2009) A simplified data assimilation method for reconstructing time-series MODIS NDVI data. Adv Space Res 44:501–509

Gustafsson F (2000) Adaptive filtering and change detection. Wiley

Holben BN (1986) Characteristic of maximum value composite images for temporal AVHRR data. Int J Remote Sens 7(11):1417–1434

Inclan C, Tiao GC (1994) Use of cumulative sums of squares for retrospective detection of changes of variance. J Am Stat Assoc 89(427):913–923. ISSN 0162-1459

Jong RE, Verbesselt J, Schaepman ME, Bruin SD (2012) Trend changes in global greening and browning: contribution of short-term trends to longer-term change. Glob Change Biol 2012(18):642–655

Jung M, Chang E (2015) NDVI-based land-cover change detection using harmonic analysis. Int J Remote Sens 36(4):1097–1113

Kayet N, Pathak K, Chakrabarty A, Sahoo S (2016) Spatial impact of land use/land cover change on surface temperature distribution in Saranda Forest, Jharkhand. Model Earth Syst Environ 2:127. https://doi.org/10.1007/s40808-016-0159-x

Kim S-R, Prasad AK, El-Askary H, Lee W-K, Kwak D-A, Lee S-H, Kafatos M (2014) Application of the Savitzky-Golay filter to land cover classification using temporal MODIS vegetation indices. Photogramm Eng Remote Sens 80(7):675–685

Kendall MG (1975) Rank correlation methods, 4th edn. Charles Griffin, London, UK

Lambin EF, Strahler AH (1994) Change vector analysis in multitemporal space: a tool to detect and categorize land cover change processes using hight temporal resolution satellite data. Remote Sens Environ 48(2):231–244

Li J, Wang Z, Lai C, Wu X, Zeng Z, Chen X, Lian Y (2018) Response of net primary production to land use and land cover change in mainland China since the late 1980s. Sci Total Environ 639(2018):237–247. https://doi.org/10.1016/j.scitotenv.2018.05.155

Lai TL (1995) Sequential change point detection in quality control and dynamical systems. J R Stat Soc Ser B (Methodol) 57(4):613–658

Lunetta RS, Joseph FK, Ediriwickrema J, Lyon JG, Worthy LD (2006) Land cover change detection using multi-temporal MODIS NDVI data. Remote Sens Environ 105:142–154

Lu X, Liu R, Liang S (2007) Removal of noise by wavelet method to generate high quality temporal data of terrestrial MODIS products. Photogramm Eng Remote Sens 73(10):1129–1139

Lu D, Mausel P, Brondizio E, Moran E (2004) Change detection techniques. Int J Remote Sens 25:2365–2401

Mann HB (1945) Non-parametric tests against trend. Econometrica 13:245–259

Martinez B, Gilabert MA (2009) Vegetation dynamics from NDVI time series analysis using the wavelet transform. Remote Sens Environ 113(2009):1823–1842. https://doi.org/10.1016/j.rse.2009.04.016

Neteler M (2004) MODIS time series remote sensing for epidemiological modelling. In: International symposium on geoinformatics for spatial infrastructure development in earth and allied sciences

Nalley D, Adamowski J, Khalil B (2012) Using discrete wavelet transforms to analyze trends in streamflow and precipitation in Quebec and Ontario (1954–2008). J Hydrol 475(2012):204–228

Priyadarshi N, Chowdary VM, Srivastava YK, Das IC, Jha CS (2018) Reconstruction of time series MODIS EVI data using de-noising algorithms. Geocarto Int 33(10):1095–1113. https://doi.org/10.1080/10106049.2017.1333535

Priyadarshi N, Chowdary VM, Das IC, Jeganathan C, Srivastava YK, Rao GS, Raj U, Jha CS (2020a) Wavelet and non-parametric statistical based approach for long term land cover trend analysis using time series EVI data. Geocarto Int 35(5):512–534. https://doi.org/10.1080/10106049.2018.1520925

Quaye-Ballard JA, Okrah TM, Andam-Akorful SA, Awotwi A, Osei-Wusu W, Antwi T, Tang X (2020) Assessment of vegetation dynamics in upper east region of Ghana based on wavelet multi-resolution analysis. Model Earth Syst Environ.https://doi.org/10.1007/s40808-020-00789-8

Rhif M, Abbes AB, Farah IR, Martínez B, Sang Y (2019) Wavelet transform application for/in non-stationary time-series analysis: a review. Appl Sci 9:1345. https://doi.org/10.3390/app9071345

Savitzky A, Golay MJE (1964) Smoothing and differentiation of data by simplified least squares procedures. Anal Chem 36(8):1627–1639

Setiawan Y, Yoshino K (2010) Temporal pattern analysis of wavelet-filtered MODIS EVI to detect land use change in JAVA island, Indonesia. Int Arch Photogramm Remote Sens Spat Inf Sci XXXVIII, 8

Sen PK (1968) Estimation of regression coefficients based on Kendall's tau. J Am Stat Assoc 63:1379–1389

Singh B, Jeganathan C (2016) Spatio-temporal forest change assessment using time series satellite data in Palamu district of Jharkhand, India. J Indian Soc Remote Sens 44(4):573–581. https://doi.org/10.1007/s12524-015-0538-1

Singh S, Talwar R (2014) A comparative study on change vector analysis based change detection techniques. Indian Acad Sci 39(6):1311–1331

Srivastava DS, Easa PS, Jauher JB (2013) Integrated wildlife management plan for west Singhbhum, Jharkhand. Department of Forest and Environment, Government of Jharkhand

Web References

http://en.wikipedia.org/wiki/West_Singhbhum_district. Accessed on 17 June 2020
http://www.pacsindia.org/west-singhbhum. Accessed on 17 June 2020
http://en.wikipedia.org/wiki/Jharkhand. Accessed on 18 June 2020
http://earthobservatory.nasa.gov/Features/MeasuringVegetation/measuring_vegetation_4.php. Accessed on 05-Aug-2020.
https://modis-land.gsfc.nasa.gov/vi.html. Accessed on 18 Aug 2020
http://www.jharkhand.gov.in/web/west-singhbhum/district-profile. Accessed on 28 Aug 2020

Chapter 30
Impact of Land Use Land Cover on Land Surface Temperature Over Alaknanda River Basin Using Geospatial Techniques

Sachchidanand Singh, Lingaraj Dhal, Alka Yadav, and Mitthan Lal Kansal

Abstract Growing demand to satisfy human needs has been creating pressure on natural resources. Natural Earth cover is also rapidly changing with human interventions. Land use and land cover (LULC) change and greenhouse gas emissions influence the regional climatic conditions and, ultimately, the global climate system. Land surface temperature (LST) has been considered as a key physical parameter for studying regional and global climate change and its influence on different ecosystems. In this study, the Moderate Resolution Imaging Spectroradiometer (MODIS) satellite-derived products have been used to estimate the LST Day and Night, LULC, NDSI (Normalized Difference Snow Index), NDWI (Normalized Difference Water Index), and NDVI (Normalized Difference Vegetation Index) over the Alaknanda River Basin for the year 2001 and 2020. The results showed that in the last 20 years, the Savanna region has grown by 352 km^2 (3.4%), while croplands have shrunk by approximately 231 km^2 (2.3%). The mean day surface temperature was observed to be 10.7°C in the year 2001 which decreased to 10.3°C in the year 2020. The mean night surface temperature was observed to be -2.2°C in the year 2001 which increased to -1.4°C in the year 2020. The NDSI forms a good correlation (− 0.92) among all other remote sensing indices, demonstrating that LST has a significant impact on the snow-covered region of the basin. Thus, incessant monitoring of LULC dynamics is essential to guide supportable land-use strategies in this region that promote environmental protection and economic development.

S. Singh (✉) · L. Dhal · A. Yadav · M. L. Kansal
Department of Water Resources Development & Management, Indian Institute of Technology Roorkee, Roorkee, India
e-mail: ssingh1@wr.iitr.ac.in

L. Dhal
e-mail: ldhal@wr.iitr.ac.in

A. Yadav
e-mail: ayadav@wr.iitr.ac.in

M. L. Kansal
e-mail: mlk@wr.iitr.ac.in

C. S. Jha et al. (eds.), *Geospatial Technologies for Resources Planning and Management*, Water Science and Technology Library 115,
https://doi.org/10.1007/978-3-030-98981-1_30

Keywords Land use land cover change · Land surface temperature · NDVI · NDSI · NDWI · MODIS

30.1 Introduction

Growing anthropogenic activities to meet the demand of the burgeoning population creates pressure on the natural resources of the Earth and causes an imbalance in terrestrial ecosystems at a different spatial scale (Hua and Ping 2018; Zhanga et al. 2013). Land cover is the interface where the interaction of energy and matter between the atmosphere and Earth system occurs (Tan et al. 2020). Land Surface Temperature (LST) reflects the energy flow interaction between the atmosphere and the Earth system. The LST has a connection with the regional climate change and global climate responses with an imperative influence in agriculture, hydrology, ecology, and environment (Vancutsem et al. 2010; Zhao et al. 2016). In general, land use and land cover (LULC) are used synonymously. However, the biophysical ground surface is referred to as land cover, and the land cover modified by humans is referred to as land use for the political, and socioeconomic conditions (Aldhshan and Shafri 2019). The LULC change is one of the key approaches for natural resources managers, particularly in developing nations to understand the surface resources dynamics (Li and Wang 2019). The study of land-use and land cover change (LU/LCC) is an environmental change study that is strongly connected to socioeconomic development.

Different studies have been carried out to determine the influence of LULC change on regional climate through different processes e.g. heat and water fluxes (Anderson-Teixeira et al. 2012), wind speed (Xia et al. 2016), and boundary layer turbulences (Takata et al. 2009). To explore the underlying science between LULC change and local climate has become a hot research topic among environmental and climate researchers (Mahmood et al. 2014; Pitman et al. 2012). The land surface physical characteristics such as radiation, heat absorption, and water vapor exchange with the atmosphere are directly linked with the LULC change and which ultimately influence the regional climate. Further LULC changes alter the vegetation type, density (Singh et al. 2020), and chemical composition of the land surface (Chuai et al. 2018). Thus, the LULC changes alter the terrestrial carbon stocks and their fluxes (Brovkin et al. 2013; Xiong et al. 2014), resulting increase in the level of atmospheric greenhouse gases (Ramdani and Hino 2013). Land surface temperature is proved to be one of the key physical properties to study the Earth system's surface energy equilibrium (Chen et al. 2020). Changes in LST causes urban heat island (Choudhury et al. 2019; Jaiswal and Jhariya 2020), heat waves (Zou et al. 2021), ecosystem alternation (Opelele Omeno et al. 2021; Tan et al. 2020), and reduction in agricultural yield (Majumder et al. 2020). Therefore, investigating LULC change and its impact on LST is necessary to address regional environmental problems and manage the natural resources sustainably (Tan et al. 2020).

Mountainous places have a climate system that differs from lower elevations, any change in land use in the higher altitudes would have a profound impact on the total

climate of the region (Kansal and Thakur 2017; Rittger et al. 2013). Mountainous locations can store and filter different energies, as well as provide habitat for a wide variety of creatures due to their terrain variation. However, due to the inaccessibility to every location, the monitoring of the natural resources in the mountain ecosystem becomes difficult. In addition, land expansion is often poorly managed, with little or no input prior to the start of projects. Satellite data can be used through remote sensing techniques to meet the basic needs of sustainable resource management, planning, and conservation. (Meer and Mishra 2020; Vijith et al. 2018). Remote sensing allows for a large range of observation and strong spatial continuity as compared to traditional ways of monitoring LST. This relationship between regional and global climate and LULC and LST has been studied extensively using remote sensing data (Chen et al. 2020; Ding and Shi 2013). It is helpful in land resource management and for global climate change studies. Remote sensing data has been extensively used for LULC monitoring regarding its spatio-temporal dynamics. For instance, several indices derived from remote sensing are utilized for the classification of various LULC classes. For example, vegetation features in terms of water content and greenness can be differentiated using the NDWI, NDVI, respectively (Aldhshan and Shafri 2019; Edan et al. 2021) and snow-covered surface areas with the help of normalized difference snow index (NDSI).

In this study, an attempt has been made to evaluate the land-use dynamics of the Alaknanda river basin and to further estimate the changes in the land cover with the land surface temperatures for the years 2001 and 2020. Investigation of regional LU/LC and temperature change patterns and processes can serve as a model for a broader spectrum of global change research.

30.2 Study Area

The Alaknanda, a Himalayan River flowing in Uttarakhand, is a significant headstream of the Holy River Ganga. It originates from the confluence of Sathopanth and Bhagirath Kharak glaciers, flows downstream to meet River Saraswati tributary at Mana village India, 21 km from Tibet. After flowing 200 km from its origin, the Alaknanda River confluences with the Bhagirathi River (another headstream of Ganga) at Devprayag and continues as River Ganga (Remya et al. 2020). The total area of the Alaknanda basin taken in this study is about 10,278 km^2, keeping the outlet at Rudraprayag lies in between 78° 45′ E and 80° 15′ E longitudes and 30° 10′ N to 31° 5′ N latitudes. The elevation of the basin ranges between 609 and 7804 m (Singh and Kansal 2020). The basin observes sub-tropical, humid, and alpine types of climate. Every year, more than 75% of the total annual rainfall is delivered during the monsoon period i.e., from June to September. The physiography of the basin results from immense tectonic movements, and heavy downfall comprised of high relief, elevated steep hilly terrains, v-shaped valleys, river terraces, and high drainage density (Panwar et al. 2017). Microclimatic conditions predominate in the basin due to hilly terrain and temperature changes spatio-temporally. Due to this, the region

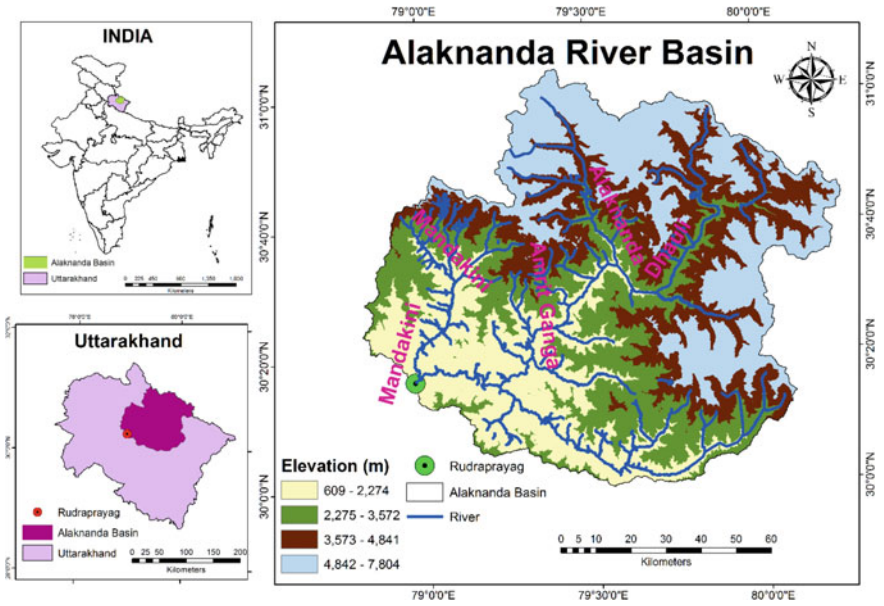

Fig. 30.1 The study area map of the Alaknanda river basin

is susceptible to numerous natural disasters in the form of cloudbursts, flash floods, landslides, and earthquakes (Kansal et al. 2014; Singh and Kansal 2022). The study area map of the river basin is displayed in Fig. 30.1.

30.3 Materials and Methodology

The method used in this study has been broken down into three main parts to investigate the relationship between the LULC and the LST in the area. In the first step, natural resources of the region such as water, snow, vegetation, and other LULC features were extracted. In the second phase, the LST for both day and night were obtained. Finally, in the third phase, the statistical analysis by estimating correlation as well as the variation of LST with different features was studied. The overall methodology to assess the resources in the Alaknanda river basin and their variation with LST is shown in Fig. 30.2.

The study utilizes numerous satellite datasets provided by Moderate Resolution Imaging Spectroradiometer (MODIS) to assess the resources on the surface of the Earth, the details of which are as follows:

a. MODIS Yearly Land Use Land Cover—MCD12Q1.006, at 500 m spatial resolution.

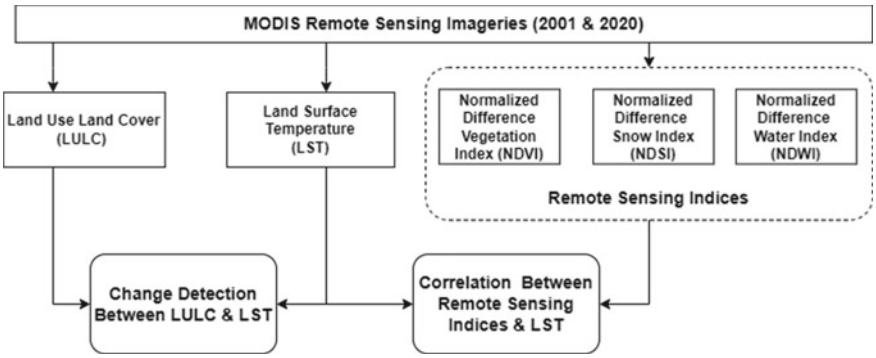

Fig. 30.2 The methodology used in the study

b. MODIS Terra Daily Land Surface Temperature (both Day and Night)—MOD11A1.006, at 1000 m spatial resolution.
c. MODIS Terra Daily Normalized Difference Water Index (NDWI)—MOD09GA_006_NDWI, at 1000 m spatial resolution. This product was generated from MODIS Surface reflectance composites (MODIS/006/MOD09GA).
d. MODIS Terra Daily Normalized Difference Snow Index (NDSI)—MOD09GA_006_NDSI, at 1000 m spatial resolution. This product was also generated from MODIS Surface reflectance composites (MODIS/006 /MOD09GA).
e. MODIS 16 Daily Normalized Difference Vegetation Index (NDVI)—MOD13A1.006, at 500 m spatial resolution.

All the datasets were obtained from the cloud-based Google Earth Engine (GEE) (Gorelick et al. 2017; Sidhu et al. 2018; Singh et al. 2018) platform using different image retrieving algorithms for the years 2001 and 2020. The details of each image and its algorithm could be obtained from https://developers.google.com/earth-engine/datasets/catalog/modis?hl=en.

MODIS NDVI

NDVI is a commonly used vegetation index based on the observation that different surfaces reflect or absorb different portions of the electromagnetic spectrum (Carrasco et al. 2020; Kafy et al. 2021; Mushore et al. 2017). Using the difference in reflectance between the near-infrared and red wavelengths of the electromagnetic spectrum, this indicator measures the amount and vigor of vegetation on the surface of the Earth. NDVI is highly sensitive to changes, and therefore, alterations in NDVI may result in changes in LST (Ding and Shi 2013; Tran et al. 2017). The equations used to determine the NDVI is given by Eq. 30.1:

$$\mathrm{NDVI} = \frac{\mathrm{MODIS}_{B(\mathrm{NIR})} - \mathrm{MODIS}_{B(\mathrm{RED})}}{\mathrm{MODIS}_{B(\mathrm{NIR})} + \mathrm{MODIS}_{B(\mathrm{RED})}} \tag{30.1}$$

where, $\text{MODIS}_{B(\text{NIR})}$ = Near infra-red band of MODIS imagery, and $\text{MODIS}_{B(\text{RED})}$ = Red band of MODIS imagery.

MODIS NDSI

Snow is a valuable fresh water source and an important part of the hydrological cycle (Rittger et al. 2013; Thakur et al. 2018). NDSI is satellite derived index which is used to prepare snow cover maps. The decrease in snow cover could indirectly indicate the increase in the LST value. The NDSI could be estimated by Eq. 30.2 given by:

$$\text{NDSI} = \frac{\text{MODIS}_{B(\text{GREEN})} - \text{MODIS}_{B(\text{SWIR})}}{\text{MODIS}_{B(\text{GREEN})} + \text{MODIS}_{B(\text{SWIR})}} \tag{30.2}$$

where, $\text{MODIS}_{B(\text{GREEN})}$ = Green band of MODIS imagery, and $\text{MODIS}_{B(\text{SWIR})}$ = Short-wave Infra-red band of MODIS imagery.

MODIS NDWI

Water is a major component of Earth ecosystem balance that maintains the carbon cycle, climatic variabilities, etc. for the sustainability of life. The NDWI is the most important and widely used remote sensing-based indicator that measures water or moisture on the ground (Choudhury et al. 2019; McFeeters 1996; Xu 2006). For the measurement of NDWI, Green and NIR bands of any multispectral images are used as per Eq. 30.3:

$$\text{NDWI} = \frac{\text{MODIS}_{B(\text{GREEN})} - \text{MODIS}_{B(\text{NIR})}}{\text{MODIS}_{B(\text{GREEN})} + \text{MODIS}_{B(\text{NIR})}} \tag{30.3}$$

Statistical Analysis Using Pearson's Correlation Coefficient

Linear regression was used to make scatter plots for the years 2001 and 2020. These plots show how the environmental variables (NDVI/NDWI/NDSI) affect LST intensification. The values of LST, NDWI, NDVI, and NDSI pixels were extracted over 500 points on the study region using GEE algorithms. To figure out the relationship between LST and NDVI, NDSI, and NDWI, Pearson's correlation coefficient ('r') was used. The dependent variable was LST, and the independent variables were NDVI/NDWI/NDSI. Pearson's 'r' was found out through the Eq. 30.4:

$$r = \frac{\sum_{i=1}^{n}(x_i - \overline{x})(y_i - \overline{y})}{\sqrt{\sum_{i=1}^{n}(x_i - \overline{x})^2}\sqrt{\sum_{i=1}^{n}(y_i - \overline{y})^2}} \tag{30.4}$$

where, x denotes the value of NDVI, NDWI, and NDSI, and y denotes LST values. x_i and y_i are single samples that are indexed with i. $\overline{x}$ and $\overline{y}$ represent the mean values. 'n' represents the number of samples.

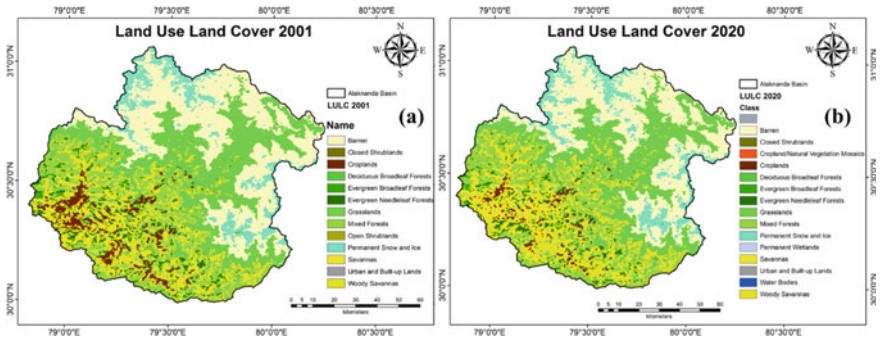

Fig. 30.3 The land use land cover map of the Alaknanda river basin for the years **a)** 2001, **b)** 2020

30.4 Results and Discussions

30.4.1 Land Use Land Cover Change (2001 and 2020)

A total of 16 land use land cover classes, namely, Deciduous Broadleaf Forests (DBF), Evergreen Broadleaf Forests (EBF), Mixed Forests (MF), Closed Shrublands (CS), Evergreen Needleleaf Forests (ENF), Open Shrublands (OS), Woody Savannas (WS), Savannas (S), Grasslands (G), Permanent Wetlands (PW), Croplands (C), Urban and Built-up Lands (BU), Cropland/Natural Vegetation Mosaics (CNV), Permanent Snow and Ice (PS), Barren (B), and Water Bodies (WB) were identified, covering 10,278 km^2 as shown in Fig. 30.3.

The areal distribution of each land cover class for the years 2001 and 2020 is shown in Table 30.1. It is observed that in the year 2001, 28.1% of total area was occupied by the B, followed by G (26.1%), WS (17.6%), MF (12%), PS (6.3%), C (4.5%), ENF (2.5%), S(1.9%), EBF (0.6%) DBF(0.3), OS(0.02%), BU(0.004%) and CS(0.002%). On comparing LULC of 2001 and 2020, the increase in the area was observed in S by 3.42%, PS by 0.79%, MF by 0.49%, WB and CNV by 0.02% each. While the decrease in the area was observed in the C by 2.26%, B by 1.1%, G by 0.6%, WS by 0.3%, ENF, DBF, and EBF each by 0.2%, and OS by 0.02%.

30.4.2 LST (Day and Night)

In the year 2001, the value of LST Day (Fig. 30.4a) ranged from − 14.9 to 26.5 ℃, having a mean value of 10.7 ℃, and the LST Night (Fig. 30.4c) ranged from − 28.3 to 14.4 ℃ having mean value of − 2.2 ℃. In 2020, the value of LST Day (Fig. 30.4b) ranged from − 13.3 to 25.4 ℃, having a mean value of 10.3 ℃, and the LST Night (Fig. 30.4d) ranged from − 23.1 to 14.4 ℃ having a mean value of − 1.4 ℃. It is observed that the LST has the minimum values in the northern and eastern region,

Table 30.1 The areal distribution and area change of each LULC feature for the years 2001 and 2020

Class	Area 2001 (km^2)	Area 2020 (km^2)	Area change between 2001 and 2020 (km^2)
Evergreen needleleaf forests (ENF)	257.00	236.41	− 20.59
Evergreen broadleaf forests (EBF)	59.38	41.259	− 18.13
Deciduous broadleaf forests (DBF)	34.345	14.815	− 19.53
Mixed forests (MF)	1,234.71	1,285.44	50.73
Closed shrublands (CS)	0.214	0.429	0.22
Open shrublands (OS)	2.15	-	− 2.15
Woody savannas (WS)	1,804.64	1,776.10	− 28.54
Savannas (S)	197.55	549.114	351.56
Grasslands (G)	2,686.00	2,629.88	− 56.12
Permanent wetlands (PW)	-	0.645	0.65
Croplands (C)	466.442	234.66	− 231.78
Urban and built-up lands (BU)	0.43	0.43	0.00
Cropland/natural vegetation (CNV)	-	1.72	1.72
Permanent snow and ice (PS)	650.205	730.948	80.74
Barren (B)	2,885.10	2,774.37	− 110.73
Water bodies (WB)	-	1.933	1.93

while the western and southern region shows a high value of LST in all of the years. On comparing the LST Day of 2020 with 2001, it is found that the values of mean LST have decreased by 0.4 ℃, which could be due to the increase in the forest cover. However, the value of LST Night has increased by 0.8 ℃, which might indicate the increase in the construction and mining activities during the night-time.

30.4.3 LULC Versus LST

In the year 2001, out of all the classes, the maximum and minimum value of mean LST Day is observed for the class C (23.1 ℃) and the class OS (− 10.1), respectively, and, the maximum and minimum value of mean LST Night is also obtained for class C (10.9 ℃) and class OS (− 19.2 ℃), respectively. In the year 2020, the maximum and minimum value of mean LST Day is observed for the class CNV (22.9 ℃) and the class PS (− 3.42), respectively, while the maximum and minimum value of mean

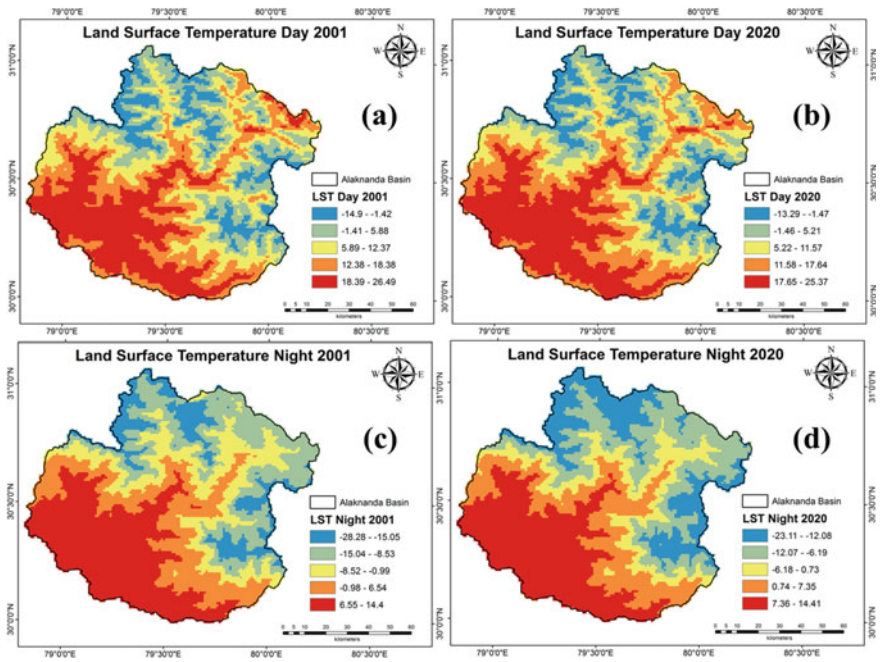

Fig. 30.4 The spatial pattern of land surface temperature for the Alaknanda river basin for **a)** day 2001, **b)** day 2020, **c)** night 2001, **d)** night 2020

LST Night is obtained for class CNV (11.6 ℃) and class PS (− 14.9 ℃), respectively. The different values of LST day and night obtained for the year 2001 and 2020 for every LULC class is displayed in Table 30.2.

Table 30.3 denotes the changes in the LST values over each LULC class for the year 2001 and 2020. It is observed that maximum and minimum increase in the mean LST day is obtained for the DBF (0.91 ℃) and S (0.6 ℃) class, respectively, while the maximum and minimum decrease in the mean LST day is obtained for the CS (− 4.98 ℃) and B (− 0.21 ℃) class, respectively. The increase in the mean LST over DBF and S could indicate deforestation in the region. Moreover, the maximum and minimum increase in the mean LST night is obtained for the PS (2.82 ℃) and WS (0.06 ℃) classes, respectively. In contrast, the maximum and minimum decrease in the mean LST night is obtained for the CS (− 1.39 ℃) and C (− 0.18 ℃) classes, respectively.

30.4.4 NDVI Versus LST

The NDVI value of more than 0.6 represents the forest cover, while very low value (0.1 and less) represents barren/sand/snow area, moderate values (0.2–0.3) represent

Table 30.2 The value of LST day and night obtained for each class for the year 2001 and 2020

CLASS		BU	ENF	EBF	DBF	MF	CS	OS	WS	S	G	PW	C	CNV	PS	B	WB
LST day for 2001	Min	9.2	11.1	12.2	8.3	5.7	12.1	− 10.1	6.5	11.8	− 2.1	–	16.7	–	− 13.3	− 14.9	–
	Max	19.8	24.8	20.9	20.1	23.5	12.1	− 10.1	25.6	26.4	25.7	–	26.5	–	9.6	19.6	–
	Mean	14.5	17.6	16.1	13.6	15.5	12.1	− 10.1	18.3	21.2	12.0	–	23.1	–	− 2.9	2.7	–
	Std.	5.3	3.5	1.9	3.0	3.2	0.0	0.0	3.9	2.7	5.8	–	1.7	–	4.3	5.7	–
LST night for 2001	Min	− 3.3	2.3	2.7	− 2.2	− 2.0	− 0.8	− 19.2	− 5.1	− 0.4	− 13.4	–	5.2	–	− 27.1	− 26.8	–
	Max	9.8	14.4	10.9	7.9	13.1	− 0.8	− 19.2	14.4	14.4	14.1	–	14.4	–	− 6.4	− 1.4	–
	Mean	3.3	8.2	7.3	2.7	6.2	− 0.8	− 19.2	7.8	10.4	− 1.8	–	10.9	–	− 17.7	− 12.3	–
	Std.	6.6	3.4	1.6	2.6	2.7	0.0	0.0	3.6	2.5	6.1	–	1.9	–	3.5	3.6	–
LST day for 2020	Min	8.08	11.39	13.08	8.88	7.75	7.14	–	6.02	7.51	− 2.25	19.58	16.00	22.52	− 13.29	− 11.01	− 5.47
	Max	19.39	24.20	20.32	19.66	23.21	7.14	–	24.44	25.37	24.26	19.58	25.31	23.43	8.16	20.58	2.00
	Mean	13.74	17.89	16.15	14.49	15.76	7.14	–	17.66	21.26	11.13	19.58	22.34	22.95	− 3.42	2.51	− 2.91
	Std.	5.66	2.97	1.54	2.57	2.87	0.00	–	3.90	2.44	5.41	0.00	1.57	0.37	3.70	5.04	3.48
LST night for 2020	Min	− 2.42	2.45	4.75	− 0.32	− 2.26	− 2.18	–	− 4.19	− 1.25	− 13.26	10.20	5.57	10.68	− 23.11	− 19.81	− 13.13
	Max	9.98	14.07	11.03	7.02	13.64	− 2.18	–	14.41	14.19	14.30	10.20	14.10	12.79	− 2.53	− 0.12	− 12.31
	Mean	3.78	9.21	7.97	4.25	7.00	− 2.18	–	7.90	10.69	− 1.77	10.20	10.72	11.67	− 14.91	− 11.00	− 12.67
	Std.	6.20	3.05	1.20	2.03	2.49	0.00	–	3.58	2.22	5.68	0.00	1.62	0.87	2.60	2.78	0.35

Table 30.3 The change in the values of LST day and night over each class

	LST day change between 2001 and 2020				LST night change between 2001 and 2020			
	Min	Max	Mean	Std.	Min	Max	Mean	Std.
DBF	0.56	− 0.42	0.91	− 0.44	1.89	− 0.84	1.57	− 0.53
ENF	0.26	− 0.57	0.34	− 0.49	0.19	− 0.30	0.96	− 0.33
MF	2.03	− 0.30	0.22	− 0.32	− 0.28	0.50	0.82	− 0.20
S	− 4.27	− 0.99	0.06	− 0.25	− 0.90	− 0.19	0.29	− 0.25
EBF	0.92	− 0.56	0.00	− 0.37	2.03	0.11	0.71	− 0.36
B	3.89	0.95	− 0.21	− 0.70	7.02	1.28	1.26	− 0.79
PS	− 0.02	− 1.44	− 0.51	− 0.59	3.94	3.89	2.82	− 0.95
WS	− 0.44	− 1.16	− 0.64	− 0.01	0.91	0.03	0.06	− 0.07
C	− 0.67	− 1.16	− 0.72	− 0.17	0.32	− 0.31	− 0.18	− 0.23
BU	− 1.12	− 0.39	− 0.76	0.36	0.88	0.14	0.51	− 0.37
G	− 0.17	− 1.46	− 0.91	− 0.40	0.15	0.24	0.06	− 0.39
CS	− 4.98	− 4.98	− 4.98	0.00	− 1.39	− 1.39	− 1.39	0.00

grasslands and shrubs. The value of NDVI ranged from − 0.1 to 0.83, having a mean value of 0.3 in the year 2001, while it ranged from − 0.09 to 0.86 with a mean value of 0.32 in the year 2020, as shown in Fig. 30.5. The overall high NDVI values in both the images are in the southwestern and central regions of the basin. The low NDVI values denoting water/snow are predominant in the eastern and northern parts of the basin. The increase in the mean NDVI is mainly due to the expansion of the forest cover in the central part of the basin.

A scatter plot between high NDVI (representing forest) and LST is displayed in Fig. 30.6. It is observed that the NDVI varies negatively with the LST, indicating lesser temperature at higher NDVI values. These correlations between NDVI and LST Day were negative all the time, declining from − 0.21 to − 0.14. The correlations between NDVI and LST Night were also negative, declining from − 0.15 to − 0.06.

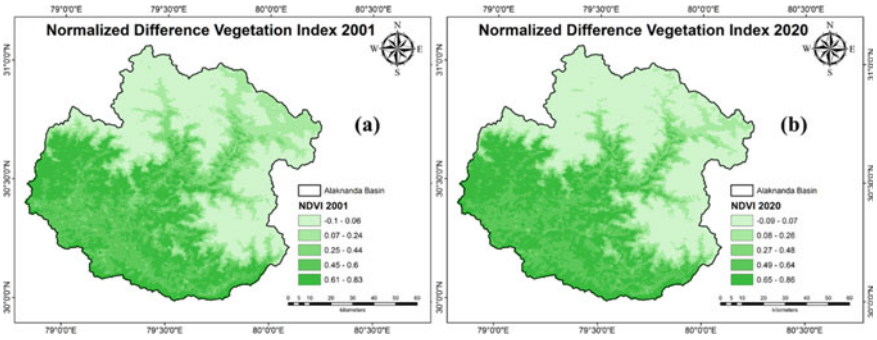

Fig. 30.5 The NDVI map for the year **a)** 2001 and **b)** 2020

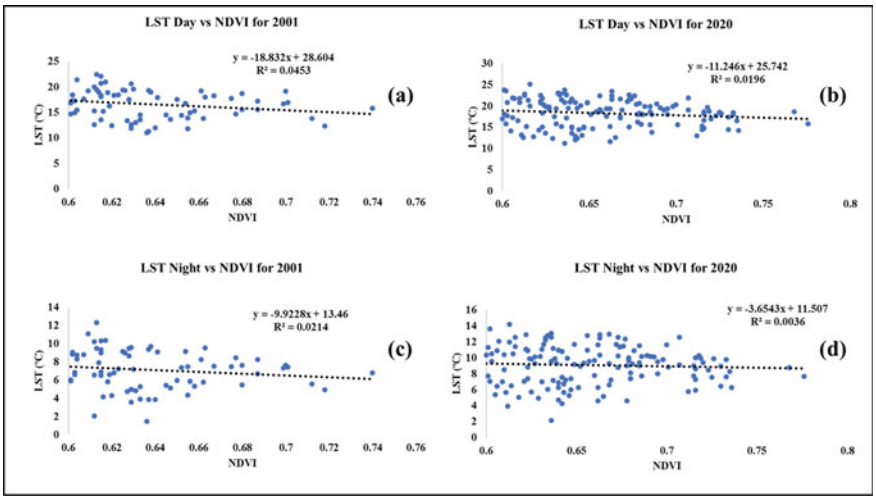

Fig. 30.6 The scatter plot between LST and NDVI **a)** LST Day vs NDVI 2001, **b)** LST Day vs NDVI 2020, **c)** LST Night vs NDVI 2001, **d)** LST Night vs NDVI 2020

30.4.5 NDSI Versus LST

The value of NDSI ranged from − 0.6 to 0.77, having a mean value of − 0.02 and standard deviation of 0.38 in the year 2001, while it ranged from − 0.6 to 0.76 with a mean value of 0.06 and standard deviation of 0.38 in the year 2020, as shown in Fig. 30.7. The overall high NDSI values, denoting snow area, in both the images are in the eastern and northern regions of the basin. The low NDSI values are predominant in the southwestern part of the basin. The increase in the mean NDSI indicates the increase in the overall snow area in the basin.

A scatter plot between NDSI > 0 (representing snow) and LST is displayed in Fig. 30.8. It is observed that the NDSI varies negatively with the LST, indicating

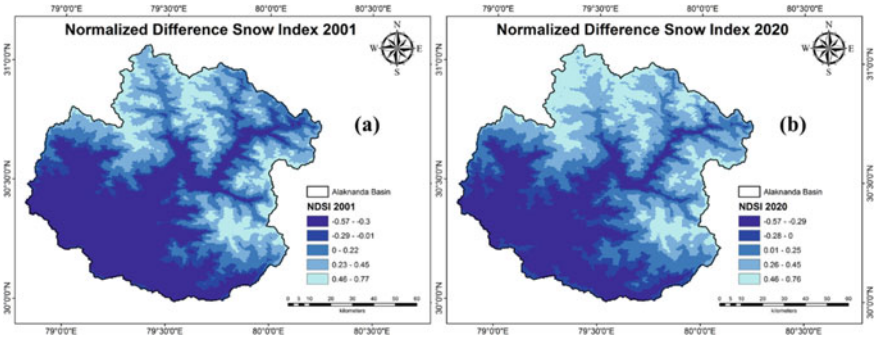

Fig. 30.7 The NDSI map for the year **a)** 2001 and **b)** 2020

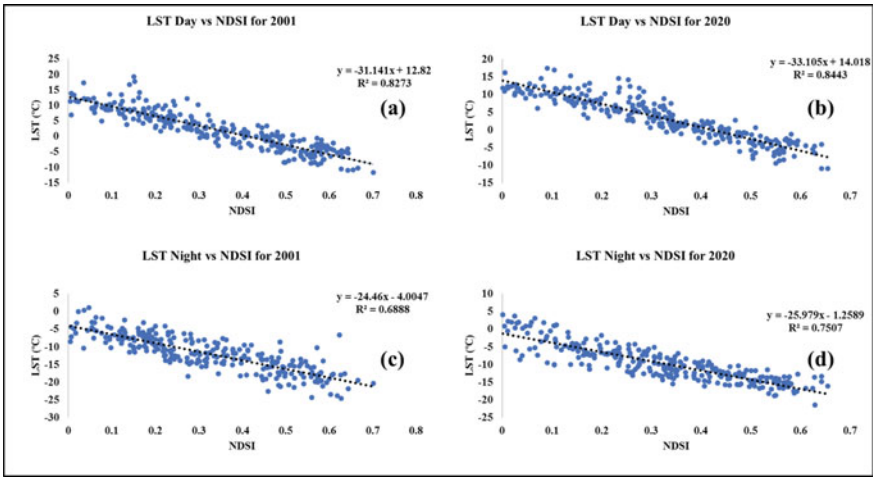

Fig. 30.8 The scatter plot between LST and NDSI **a)** LST Day vs NDSI 2001, **b)** LST Day vs NDSI 2020, **c)** LST Night vs NDSI 2001, **d)** LST Night vs NDSI 2020

lesser temperature at higher NDSI values. These correlations between NDSI and LST Day were significantly negative all the time, rising from − 0.91 to − 0.92. The correlations between NDVI and LST Night were also negative all the time, rising from − 0.83 to − 0.87.

30.4.6 NDWI Versus LST

The value of NDWI ranged from − 0.35 to 0.53, having a mean value of 0.03 and standard deviation of 0.17 in the year 2001, while it ranged from − 0.21 to 0.55 with a mean value of 0.08 and standard deviation of 0.16 in the year 2020, as shown in Fig. 30.9. The overall high NDWI values, denoting snow/water area, in both the images are in the eastern and northern regions of the basin. The low NDWI values are predominant in the southwestern part of the basin. The increase in the mean NDSI indicates the increase in the overall snow/water area in the basin.

A scatter plot between NDWI > 0 (representing water/snow) and LST is displayed in Fig. 30.10. It is observed that the NDWI varies negatively with the LST, indicating lesser temperature at higher NDWI values. These correlations between NDWI and LST Day were significantly negative for all the time, rising from − 0.81 to − 0.89. The correlations between NDVI and LST Night were also negative for all the time rising from − 0.74 to − 0.82.

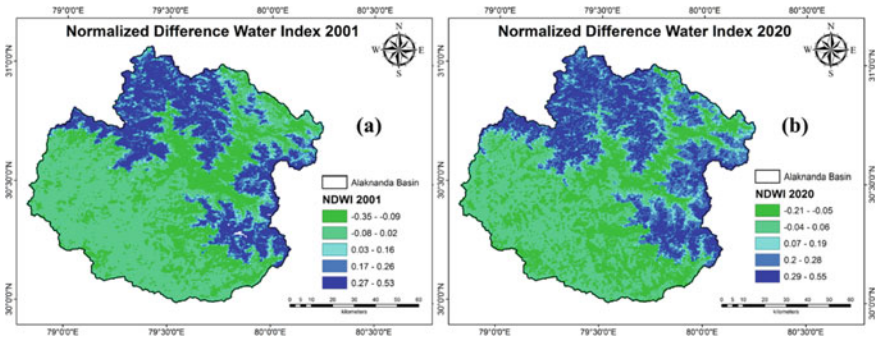

Fig. 30.9 The NDWI map for the year **a)** 2001 and **b)** 2020

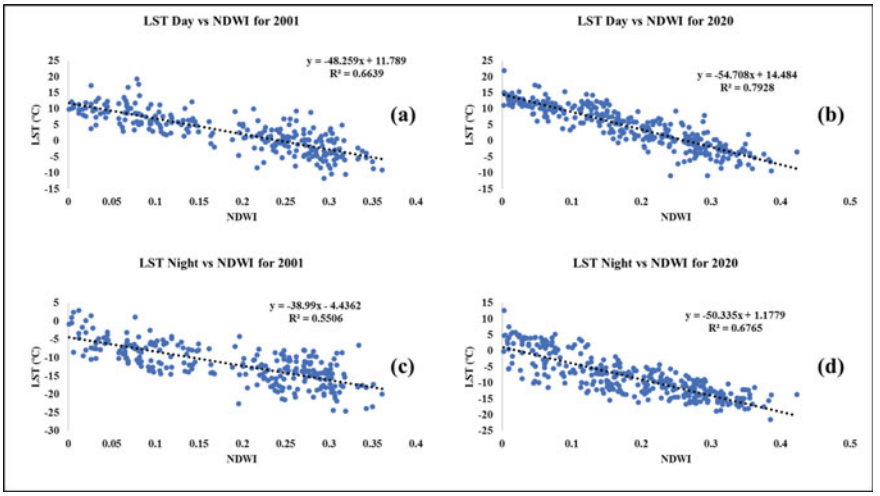

Fig. 30.10 The scatter plot between LST and NDWI **a)** LST Day vs NDWI 2001, **b)** LST Day vs NDWI 2020, **c)** LST Night vs NDWI 2001, **d)** LST Night vs NDWI 2020

30.5 Conclusion

In this study, multi-temporal and multi-spectral MODIS satellite imageries were utilized to study the influence of land use the land cover on land surface temperature for the year 2001 and 2020. The study demonstrates the effectiveness of remote sensing techniques in conjunction with geographic information systems (GIS) in extracting land use information and estimating landscape changes of the Alaknanda river basin. The results showed that in the last 20 years, the Savanna region has grown by 352 km^2 (3.4%), while croplands have shrunk by approximately 231 km^2 (2.3%). The mean daily temperature of the surface in the year 2001 is observed to be 10.7 ºC which decreased to 10.3 ºC in the year 2020. The mean night temperature

of the surface has increased from − 2.2 ℃ in year 2001 to − 1.4 ℃ in the year 2020. The increase in the mixed forest areas and decrease in the barren region could have contributed to the fall of LST day. The MODIS NDSI highly correlates (− 0.92) among all the remote sensing indices, indicating the strong impact of LST over snow-covered regions. This knowledge is essential for expanding operations involving environmental planning and landscape monitoring. Several studies addressing the monitoring of current natural resources could benefit from this research. Furthermore, it is deduced that ongoing monitoring of LULC dynamics is essential to lead supportable land-use strategies in this region that promote environmental conservation and economic development.

Acknowledgements We are grateful to the Indian Institute of Technology, Roorkee, for providing the necessary infrastructure and assistance for completing this research. We also acknowledge the efforts of scientists associated with Environmental Systems Research Institute (ESRI), Google Earth Engine, and Google Earth for providing datasets, and high-resolution base layers.

Conflict of interests The authors declare that they have no known conflict of interests that could have appeared to influence the work reported in this paper.

References

Aldhshan SRS, Shafri HZM (2019) Change detection on land use/land cover and land surface temperature using spatiotemporal data of landsat: a case study of gaza strip. Arab J Geosci 12(14). https://doi.org/10.1007/s12517-019-4597-4

Anderson-Teixeira KJ, Snyder PK, Twine TE, Cuadra SV, Costa MH, Delucia EH (2012) Climate-regulation services of natural and agricultural ecoregions of the Americas. Nat Clim Chang 2(3):177–181. https://doi.org/10.1038/nclimate1346

Brovkin V, Boysen L, Arora VK, Boisier JP, Cadule P, Chini L, Claussen M, Friedlingstein P, Gayler V, Van den Hurk BJJM, Hurtt GC, Jones CD, Kato E, De Noblet-Ducoudre N, Pacifico F, Pongratz J, Weiss M (2013) Effect of anthropogenic land-use and land-cover changes on climate and land carbon storage in CMIP5 projections for the twenty-first century. J Clim 26(18):6859–6881. https://doi.org/10.1175/JCLI-D-12-00623.1

Carrasco RA, Pinheiro MMF, Junior JM, Cicerelli RE, Silva PA, Osco LP, Ramos APM (2020) Land use/land cover change dynamics and their effects on land surface temperature in the western region of the state of São Paulo, Brazil. Region Environ Change 20(3). https://doi.org/10.1007/s10113-020-01664-z

Chen C, Wang L, Myneni RB, Li D (2020) Attribution of land-use/land-cover change induced surface temperature anomaly: how accurate is the first-order taylor series expansion? J Geophys Res Biogeosci 125(9):1–19. https://doi.org/10.1029/2020JG005787

Choudhury D, Das K, Das A (2019) Assessment of land use land cover changes and its impact on variations of land surface temperature in Asansol-Durgapur development region. Egypt J Remote Sens Space Sci 22(2):203–218. https://doi.org/10.1016/j.ejrs.2018.05.004

Chuai X, Qi X, Zhang X, Li J, Yuan Y, Guo X, Huang X, Park S, Zhao R, Xie X, Feng J, Tang S, Zuo T, Lu J, Li J, Lv X (2018) Land degradation monitoring using terrestrial ecosystem carbon sinks/sources and their response to climate change in China. Land Degrad Dev 29(10):3489–3502. https://doi.org/10.1002/ldr.3117

Ding H, Shi W (2013) Land-use/land-cover change and its influence on surface temperature: a case study in Beijing City. Int J Remote Sens 34(15):5503–5517. https://doi.org/10.1080/01431161.2013.792966

Edan MH, Maarouf RM, Hasson J (2021) Predicting the impacts of land use/land cover change on land surface temperature using remote sensing approach in Al Kut, Iraq. Phys Chem Earth Parts A/B/C 123(1474–7065):103012. https://doi.org/10.1016/j.pce.2021.103012

Gorelick N, Hancher M, Dixon M, Ilyushchenko S, Thau D, Moore R (2017) Google earth engine: planetary-scale geospatial analysis for everyone. Remote Sens Environ 202:18–27. https://doi.org/10.1016/j.rse.2017.06.031

Hua AK, Ping OW (2018) The influence of land-use/land-cover changes on land surface temperature: a case study of Kuala Lumpur metropolitan city. Euro J Remote Sens 51(1):1049–1069. https://doi.org/10.1080/22797254.2018.1542976

Jaiswal T, Jhariya DC (2020) Impacts of land use land cover change on surface temperature and groundwater fluctuation in Raipur district. J Geol Soc India 95(4):393–402. https://doi.org/10.1007/s12594-020-1448-6

Kafy AA, Faisal AA, Al Rakib A, Roy S, Ferdousi J, Raikwar V, Kona MA, Fatin SMAA (2021) Predicting changes in land use/land cover and seasonal land surface temperature using multi-temporal landsat images in the northwest region of Bangladesh. Heliyon 7(7). https://doi.org/10.1016/j.heliyon.2021.e07623

Kansal ML, Shukla S, Tyagi A (2014) Probable role of anthropogenic activities in 2013 flood disaster in Uttarakhand, India. In: World environmental and water resources congress 2014: water without borders—proceedings of the 2014 world environmental and water resources congress, May, pp 924–937. https://doi.org/10.1061/9780784413548.095

Kansal ML, Thakur A (2017) Flood estimation for a cloudburst event in an ungauged western himalayan catchment. Int J Hydrol 1(6):163–168. https://doi.org/10.15406/ijh.2017.01.00030

Li D, Wang L (2019) Sensitivity of surface temperature to land use and land cover change-induced biophysical changes: the scale issue. Geophys Res Lett 46(16):9678–9689. https://doi.org/10.1029/2019GL084861

Mahmood R, Pielke RA, Hubbard KG, Niyogi D, Dirmeyer PA, Mcalpine C, Carleton AM, Hale R, Gameda S, Beltrán-Przekurat A, Baker B, Mcnider R, Legates DR, Shepherd M, Du J, Blanken PD, Frauenfeld OW, Nair US, Fall S (2014) Land cover changes and their biogeophysical effects on climate. Int J Climatol 34(4):929–953. https://doi.org/10.1002/joc.3736

Majumder A, Kingra PK, Setia R, Singh SP, Pateriya B (2020) Influence of land use/land cover changes on surface temperature and its effect on crop yield in different agro-climatic regions of Indian Punjab. Geocarto Int 35(6):663–686. https://doi.org/10.1080/10106049.2018.1520927

McFeeters SK (1996) The use of the normalized difference water index (NDWI) in the delineation of open water features. Int J Remote Sens 17(7):1425–1432. https://doi.org/10.1080/01431169608948714

Meer MS, Mishra AK (2020) Land use/land cover changes over a district in northern India using remote sensing and gis and their impact on society and environment. J Geol Soc India 95(2):179–182. https://doi.org/10.1007/s12594-020-1407-2

Mushore TD, Mutanga O, Odindi J, Dube T (2017) Linking major shifts in land surface temperatures to long term land use and land cover changes: a case of harare, Zimbabwe. Urban Clim 20:120–134. https://doi.org/10.1016/j.uclim.2017.04.005

Opelele Omeno M, Yu Y, Fan W, Lubalega T, Chen C, Kachaka Sudi Kaiko C (2021) Analysis of the impact of land-use/land-cover change on land-surface temperature in the villages within the luki biosphere reserve. Sustain (Switzerland) 13(20). https://doi.org/10.3390/su132011242

Panwar S, Agarwal V, Chakrapani GJ (2017) Morphometric and sediment source characterization of the Alaknanda river basin, headwaters of river Ganga. Nat Hazards 87(3):1649–1671. https://doi.org/10.1007/s11069-017-2838-y

Pitman AJ, Arneth A, Ganzeveld L (2012) Regionalizing global climate models. Int J Climatol 32(3):321–337. https://doi.org/10.1002/joc.2279

Ramdani F, Hino M (2013) Land use changes and ghg emissions from tropical forest conversion by oil palm plantations in riau province, Indonesia. PLoS ONE 8(7):1–6. https://doi.org/10.1371/journal.pone.0070323

Remya SN, Kulkarni AV, Hassan Syed T, Nainwal HC (2020) Glacier mass loss in the Alaknanda basin, Garhwal Himalaya on a decadal scale. Geocarto Int:1–19.https://doi.org/10.1080/10106049.2020.1844309

Rittger K, Painter TH, Dozier J (2013) Assessment of methods for mapping snow cover from MODIS. Adv Water Resour 51:367–380. https://doi.org/10.1016/j.advwatres.2012.03.002

Sidhu N, Pebesma E, Câmara G (2018) Using google earth engine to detect land cover change: Singapore as a use case. Euro J Remote Sens 51(1):486–500. https://doi.org/10.1080/22797254.2018.1451782

Singh S, Dhasmana MK, Shrivastava V, Sharma V, Pokhriyal N, Thakur PK, Aggarwal SP, Nikam BR, Garg V, Chouksey A, Dhote PR (2018) Estimation of revised capacity in gobind sagar reservoir using google earth engine and gis. In: The international archives of the photogrammetry, remote sensing and spatial information sciences XLII–5:589–595. https://doi.org/10.5194/isprs-archives-xlii-5-589-2018

Singh S, Dhote PR, Thakur PK, Chouksey A, Aggarwal SP (2020) Identification of flash-floods-prone river reaches in Beas river basin using GIS-based multi-criteria technique: validation using field and satellite observations. Nat Hazards 105(3):2431–2453. https://doi.org/10.1007/s11069-020-04406-w

Singh S, Kansal ML (2020) Flash flood hazard mapping using satellite images and GIS: a case study of Alaknanda river basin. In: Flash floods: challenges and its management. The Institution of Engineers Centenary Publication, pp 77–83

Singh S, Kansal ML (2022) Cloudburst—a major disaster in the Indian Himalayan states. In: Kolathayar S, Pal I, Chian SC, Mondal A (eds) Civil engineering for disaster risk reduction. Springer Singapore, pp 115–126. https://doi.org/10.1007/978-981-16-5312-4_9

Takata K, Saito K, Yasunari T (2009) Changes in the Asian monsoon climate during 1700–1850 induced by preindustrial cultivation. Proc Natl Acad Sci USA 106(24):9586–9589. https://doi.org/10.1073/pnas.0807346106

Tan J, Yu D, Li Q, Tan X, Zhou W (2020) Spatial relationship between land-use/land-cover change and land surface temperature in the Dongting Lake area, China. Sci Rep 10(1):1–9. https://doi.org/10.1038/s41598-020-66168-6

Thakur PK, Garg V, Nikam BR, Singh S, Jasmine Chouksey A, Dhote PR, Aggarwal SP, Chauhan P, Senthil Kumar A (2018) Snow cover and glacier dynamics study using C-AND L-BAND SAR datasets in parts of North West Himalaya. Int Arch Photogramm Remote Sens Spatial Inf Sci ISPRS Arch 42(5):375–382.https://doi.org/10.5194/isprs-archives-XLII-5-375-2018

Tran DX, Pla F, Latorre-Carmona P, Myint SW, Caetano M, Kieu HV (2017) Characterizing the relationship between land use land cover change and land surface temperature. ISPRS J Photogramm Remote Sens 124:119–132. https://doi.org/10.1016/j.isprsjprs.2017.01.001

Vancutsem C, Ceccato P, Dinku T, Connor SJ (2010) Evaluation of MODIS land surface temperature data to estimate air temperature in different ecosystems over Africa. Remote Sens Environ 114(2):449–465. https://doi.org/10.1016/j.rse.2009.10.002

Vijith H, Hurmain A, Dodge-Wan D (2018) Impacts of land use changes and land cover alteration on soil erosion rates and vulnerability of tropical mountain ranges in Borneo. Remote Sensing Appl Soc Environ 12:57–69. https://doi.org/10.1016/j.rsase.2018.09.003

Xia G, Zhou L, Freedman JM, Roy SB, Harris RA, Cervarich MC (2016) A case study of effects of atmospheric boundary layer turbulence, wind speed, and stability on wind farm induced temperature changes using observations from a field campaign. Clim Dyn 46(7–8):2179–2196. https://doi.org/10.1007/s00382-015-2696-9

Xiong X, Grunwald S, Myers DB, Ross CW, Harris WG, Comerford NB (2014) Interaction effects of climate and land use/land cover change on soil organic carbon sequestration. Sci Total Environ 493:974–982. https://doi.org/10.1016/j.scitotenv.2014.06.088

Xu H (2006) Modification of normalised difference water index (NDWI) to enhance open water features in remotely sensed imagery. Int J Remote Sens 27(14):3025–3033. https://doi.org/10.1080/01431160600589179

Zhanga Y, Odeh IOA, Ramadan E (2013) Assessment of land surface temperature in relation to landscape metrics and fractional vegetation cover in an urban/peri-urban region using landsat data. Int J Remote Sens 34(1):168–189. https://doi.org/10.1080/01431161.2012.712227

Zhao N, Han S, Xu D, Wang J, Yu H (2016) Cooling and wetting effects of agricultural development on near-surface atmosphere over Northeast China. Adv Meteorol 2016.https://doi.org/10.1155/2016/6439276

Zou Z, Yan C, Yu L, Jiang X, Ding J, Qin L, Wang B, Qiu G (2021) Impacts of land use/land cover types on interactions between urban heat island effects and heat waves. Build Environ 204(0360–1323):108138. https://doi.org/10.1016/j.buildenv.2021.108138

Chapter 31
Geospatial Applications in Wildlife Conservation and Management

A. O. Varghese, Arun S. Suryavanshi, and Chandra Shekhar Jha

Abstract Wildlife, which is one of the integral parts of our ecosystem, nowadays facing a severe threat from anthropogenic actions, like forest obliteration, wildlife poaching and trade, introduction of invasive species, pest and diseases, etc. Moreover, the anthropogenic influence on the Earth's environment and climate is altering the nature of wildlife habitats and which in turn is accelerating the process of wildlife extinction in a faster way. Advancement in geospatial technology gives conservationists the benefit to improved understanding of the wildlife, their habitats, and the danger that they are facing, in a scientific way to simplify the process of planning, implementing, and tracking wildlife for conservation and management activities. This chapter provides an appraisal of various geospatial technologies in wildlife conservation and management that can be utilized effectively. One of the major applications of geospatial technology in wildlife management is habitat assessment. Wildlife habitat can be assessed for risk assessment, suitability assessment, habitat utilization pattern, and habitat restoration program or protecting threatened habitats. Bio-logging or bio-telemetry, one of the geospatial technologies, provides meaningful information about the movement ecology of individual species which can be used to understand the behavioral pattern of wildlife in relation to its environment. Another use of geospatial technology is the assessment of home ranges, territories, corridors, and connectivity metrics with the aid of bio-telemetry/camera traps/pug marks/visual observations. Assessment of human–wildlife conflicts for conflicts mitigation efforts is yet another application that offers a wide variety of solutions to the managers to mitigate conflicts. Nowadays geospatial technology is being used for wildlife census, wildlife crime investigation, and Management Effectiveness Evaluation (MEE) of protected areas. This chapter briefly explains the methodologies and utilities of various applications mentioned above with some examples to demonstrate the utility of geospatial technology for wildlife conservation and management.

A. O. Varghese (✉) · A. S. Suryavanshi
Regional Remote Sensing Centre—Central, NRSC, Nagpur 440033, India
e-mail: vargheseao@rediffmail.com

C. S. Jha
National Remote Sensing Centre, Hyderabad, India

C. S. Jha et al. (eds.), *Geospatial Technologies for Resources Planning and Management*, Water Science and Technology Library 115,
https://doi.org/10.1007/978-3-030-98981-1_31

Keywords Wildlife · Geospatial technology · Movement ecology · Home range · Territory analysis · Corridors · Habitat suitability assessment · Habitat risk assessment · Habitat utilization pattern · Wildlife census · Human–wildlife conflicts

31.1 Introduction

Wildlife conservation and management denotes preserving wildlife and their surroundings to sustain healthy species or populations and to protect or improve and reinstate the natural ecosystems in which they live. Geospatial technology can efficiently simplify the process of evaluation, monitoring, planning, and management of wildlife species/population and their habitat for conservation in an accurate, timely, and cost effective way. Current development in wildlife biotelemetry techniques enhanced the gathering of positional data at an increasing rate and precision ushered the path for development of new methods of analysis of movement ecology, home ranges, territories, corridors, migration, and dispersal of the wildlife species. Availability of submeter VHS satellite imagery and centimeter-scale images captured from manned aerial and UAV surveys have enhanced the potential for wildlife census. These advancements in biotelemetry and remote sensing data availability (multifrequency, multitemporal and multiscale) with the arrival of new image processing and GIS techniques open a new scenario in geospatial applications for wildlife conservation and management. This leads to the improvement in species–habitat relationship modeling, habitat quality and risk assessment, habitat utilization pattern and space use, human–wildlife conflict assessment and mitigation efforts more precisely and effectively. This chapter examines the utility of various geospatial technologies in wildlife conservation and management under the following themes.

- Study of movement ecology and behavioral pattern
- Home Range and Territory analysis
- Species—habitat relationship modeling/habitat suitability assessment
- Wildlife Corridors and Connectivity metrics
- Habitat quality, Risk assessment, and maintenance
- Habitat utilization pattern/space use
- Wildlife Census
- Human–Wildlife conflicts assessment and mitigation efforts.

31.2 Study of Movement Ecology and Behavioral Pattern

A spatial variation in the location of wildlife with reference to time, determined by processes which act across its habitat in numerous spatial and sequential scales is a fundamental characteristic of wildlife. This movement of wildlife in relation to its environment is called movement ecology (Nathan 2008). Food accessibility,

predator evasion, and ecological settings, that will increase its capacity to survive and reproduce, are some of the factors affecting the movement of wildlife (Morales 2010). Being sedentary in annual ranges, migration, nomadism, and dispersal are the four major population-level distribution strategies of animal movement (Mueller and Fagan 2008; Matthysen 2012). Along with the types of movement, characteristics of movement like trails, distance and timing, dimension of home ranges or territories, habitat choice, habit of layover locations by migratory species are some of the important components to be incorporated in species conservation and management (Allen and Sigh 2016).

One of the geospatial technology, bio-logging or bio-telemetry, gives positional information of collared wildlife in terms of latitude and longitude of a particular place. Wildlife tracking initially trusted on Very High Frequency (VHF) methods, i.e., wildlife fixed with transmitters releasing radio frequencies received by conservationist through the radio receivers they are holding (Craighead 1998). This technique necessitates receivers to be near to the wildlife species to triangulate their locations; hence the conservationists need to be in the field. The disadvantage of this traditional method is the presence of the conservationist in the field which may disturb the wildlife behavior (Cooke et al. 2004). The advent of satellite telemetry allows remote tracking of animal positions and movements without affecting animal behavior. Argos and Iridium satellites systems have emerged as the predominant satellite-based system for tracking wildlife (Herbert 2002). Argos system which uses Doppler-based positioning (Tomkiewicz et al. 2010) is less accurate and because of this it can be used for migration and dispersion patterns of wildlife species. Iridium satellites provide pole-to-pole coverage and are overhead for ten minutes at a time. In Xeos Iridium products the GPS position accuracy is up to 1.5 m, while in Argos positions it is generally up to 50 m (Argos 2016). Collared animals' locations can be mapped by using its time stamped graticules in near real-time mode based on the frequency of the locational information gathered or can be analyzed by means of GIS software (Turner et al. 2000). There is much evidence that shows that radio telemetry has provided increased opportunities to examine activity patterns, habitat use, and behavior of wildlife species (Samuel 1994), and its reliability and remote detection of the collared animal's position are other advantages. Satellite telemetry provides a lot of useful information about animal migration (Fronczak et al. 2017; Hoodless and Heward 2019; Moore et al. 2021), temporal and spatial patterns of movement during migration, identification of the staging areas, critical stopover sites, wintering grounds and energy requirements (Kenow et al. 2000). GPS-based spatial positions with high frequency, time stamped data, gathered systematically can be represented as movement tracks (Nathan et al. 2008), and the higher the frequency of positions, the more trustworthy the movement paths. Varghese et al. (2020) used radio-collared data of four elephants representing four different herds in Central Indian forests to study the movement ecology of the pachyderms. The distance covered by each elephant per hour is calculated based on the hourly GPS fixes. Using the distance between successive graticules, the movement path of each elephant (Fig. 31.1) is created for hourly, daily, seasonal, and annual basis in the geodatabase (Fig. 31.2). As per the path analysis, elephants in the study area are moving at an average speed

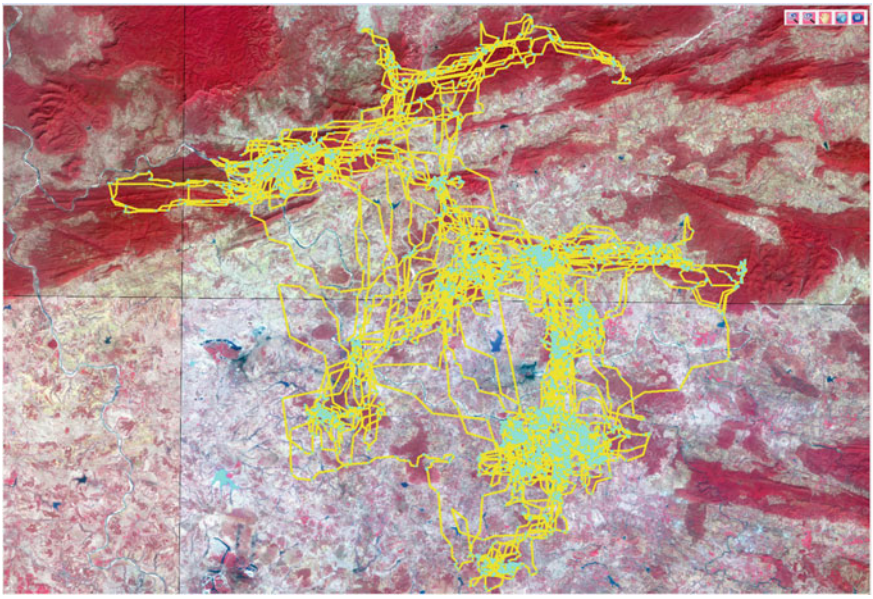

Fig. 31.1 Trail path of the elephant Dev constructed using successive graticules of the collared data

of 394 m/h and much of their activity is in between 16:00 and 06:00 h. The average distance covered per day is 8.7 km and the maximum speed registered is 726 m/h. As per the activity level observed, elephants sleep from 10:00 to 12:00 AM h, the polyphasic sleeping habit of the elephants is not evidenced. Evelyn et al. (2010) quantified the kill rates and bases of difference in kill rates of predators to their prey using GPS-based movement data for quantifying key predation components of large carnivores. They showed the utility of geospatial models in the study of wildlife as well as landscape features on handling time or killing competence of predators.

31.3 Home Range and Territory Analysis

A home range of an animal is the zone in which it survives and moves on a regular basis and the territory is the area that is actively defended from other individuals or species within home range. The notion of the home range was presented originally by Burt (1943) by plotting charts displaying the animal presence registered at various times. Information for drawing a home range can be obtained from bio-telemetry/camera traps/pug marks/careful visual observations of the species. Currently, the wildlife tied or implanted with a collar is the most common method to observe its movement and then its home range or territory. The geographical scale of wildlife's space usage, its home range extent, is an important feature for conservation

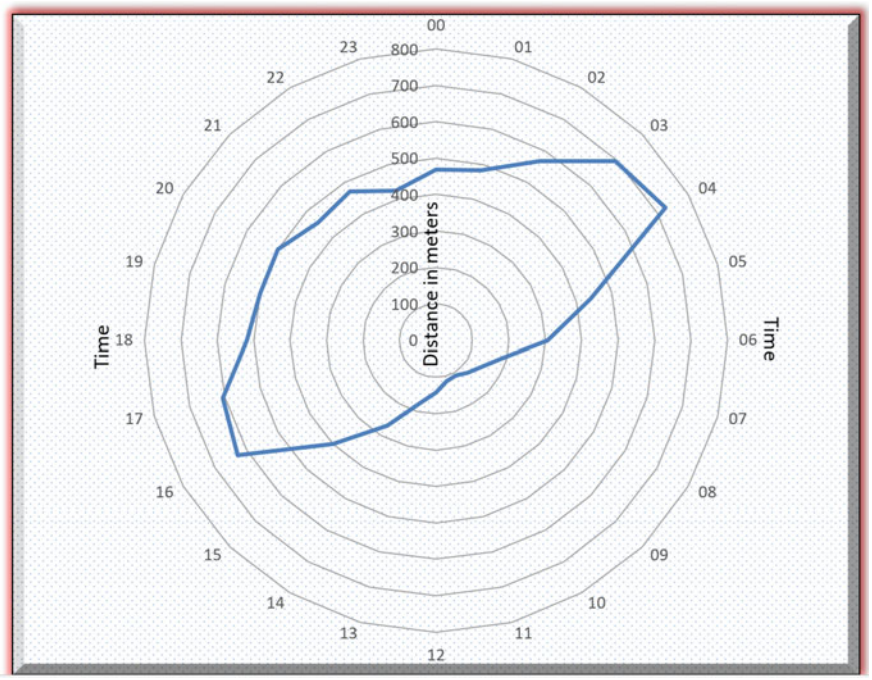

Fig. 31.2 Diurnal variation in the movement of the elephants (averaged from four collared elephants)

and management of that species as well as its individuals and thus by ecosystems in which they live (Ofstad et al. 2016). Geoinformatics is an ideal tool for analyzing the home ranges of wildlife species spatially and temporally. Constructing the minimum convex polygon (MCP) round the presence data is the easiest method of estimating the home range but this tends to overestimate the range. Several approaches are there nowadays to assess the home range apart from MCP and the commonly used are the grid cell method, kernel density estimators (KDE) (Worton 1989), and low convex hull (LoCoH) (Getz and Wilmers 2004). The Brownian bridge movement model (BBMM), a trajectory-based estimation approach, introduced by Horne et al. (2007), has developed as better substitutes to conventional KDE (Downs and Horner 2012). BBMM incorporated animal's movement trail, with distance and time lag, into the model contrary to discrete locational points of the KDE model, which delivers an approximation of the wildlife's mobility denoted as the Brownian motion variance. KDE is the most statistically efficient non-parametric method for probability density estimation (Silverman 1986; Izenman 1991; Tsurlach 1999). KDE uses positional information of an animal to generate a utilization distribution pattern, which defines the likelihood of finding that animal in an assumed site (Worton 1989). In KDE, a kernel distribution (i.e., a three-dimensional hill or kernel) is placed on each telemetry location and the height of the hill is determined by the bandwidth of the distribution

(Worton 1989; Seaman and Powell 1996). Home Range Extension in ArcView GIS, the Home Range Tools in ArcGIS, Open JUMPHoRAE (a free GIS and toolbox) are some of the tools applicable for this purpose. In a study conducted by Varghese et al. (2020) in central Indian forests, the home ranges of four collared elephants were derived using KDE method with 0.95% probability of occurrences contours. KDE with fixed biweight kernel using automated rule-based ad hoc bandwidth was employed to derive the home ranges (Fig. 31.3). In Chhattisgarh the average size of the home ranges of the elephants including buffer areas is 2898 km^2. This is mainly because Asian elephants are long ranging species with extensive habitat and nutritional requirements. If core area alone is considered as home range the average size of the home range is 1221 km^2. Using the camera trap locations of four years, Varghese and Suryavanshi (2017) derived the home ranges of some of the tigers in Melghat Tiger Reserve in Maharashtra, India by MCP method (Fig. 31.4). This study also documented the annual fluctuation of the home ranges and dispersal pattern of tiger cubs in the study area using camera trap locations.

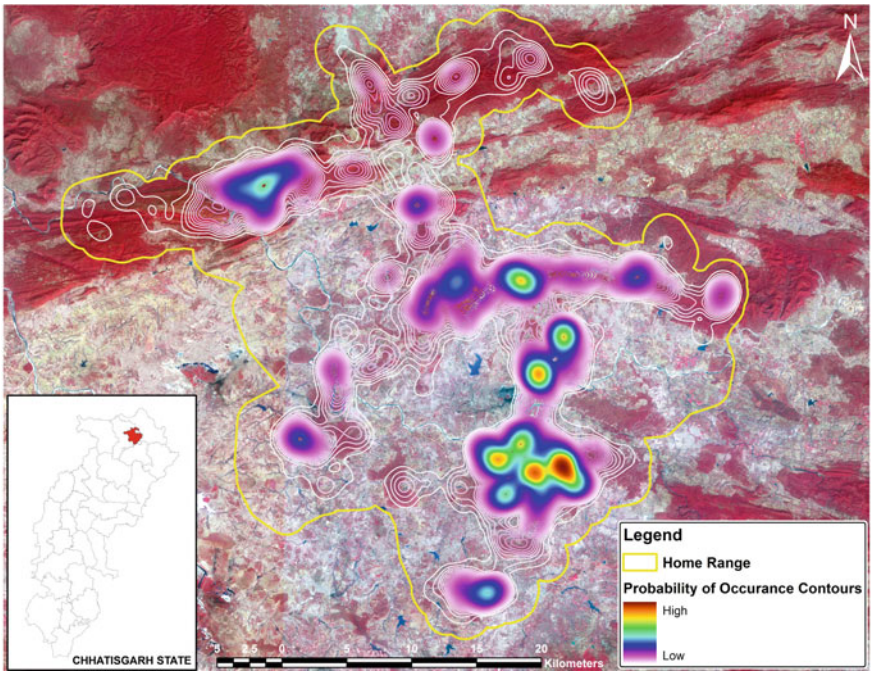

Fig. 31.3 The home range and the probability of occurrence of the elephant Dev derived using KDE method

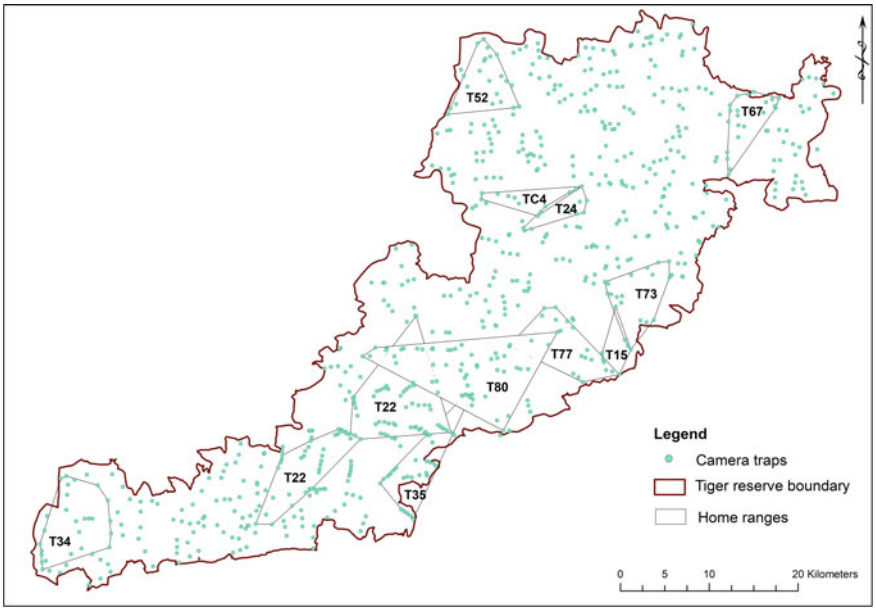

Fig. 31.4 Home ranges of some of the tigers in Melghat tiger reserve derived using minimum convex polygon method

31.4 Species–Habitat Relationship Modeling/Habitat Suitability Assessment.

A habitat of a species is an ecological or environmental setup and zone that is occupied by a specific species (Hall et al. 1997). Each species requires a set of necessities of resources and environmental conditions to live and replicate and the way a species uses its habitat is called its niche (Hutchinson 1957). Some species occupy a very narrow niche, means that they have very strict habitat necessities and can only live under certain habitat settings, and they are called habitat specialists. Other species occupy a broad niche, means that they are very flexible in their habitat wants and can live in a variety of habitat circumstances, called habitat generalists (Pandit 2009). General habitat necessities of numerous wildlife species are known, but no species habitat requirement are fully described or understood. In general, vertebrate's habitat requirements are well recognized than that of invertebrates species. Geospatial technology can successfully be used for habitat suitability assessment. Main components considered for habitat assessment are habit of the species, dietary requirements, water, shelter for prey from predators or ambush cover for predators, temperature cover, nest sites, etc. (Krausman 1999). In habitat association modeling the fitness can be classified into a binary (suitable and unsuitable), ordinal (high, medium, low) or ratio (an index score) values as per the requirement of the conservation biologist. The species' habitat can be derived by biotic and environmental features associated with it and

its distribution can be predicted from the model used to a wider area. Commonly two GIS modeling approaches are in use for habitat suitability: inductive and deductive methods (Corset et al. 2000). Deductive technique uses known species ecological requirements, from literature or expert opinion, to extrapolate suitable areas from the environmental variable/thematic layers in the GIS database. In inductive approach, the ecological requirements of the species will be derived from the localities in which the species occur based on the presence–absence data or abundance and extrapolate to a wider area (Skidmore 2002; Varghese et al. 2010). Generalized linear or additive models (logistic or poisson regression), artificial neural networks, classification and regression trees (CARTs), and genetic algorithms are some of the methods which use inductive suitability assessment (Fallah et al. 2009; Gobeyn et al. 2017). Biomapper, open Modeller, Maxent, or DesktopGARP etc. are some of the stand-alone modeling packages useful for the purpose. Inductive models are possibly better than deductive models but they necessitate collection of lot of field data, which requires more time and effort. Based on a binary deductive method Varghese et al. (2016) separated out suitable habitat of Great Indian Bustard (GIB) in GIB Wildlife Sanctuary for the realignment of the GIB Sanctuary. Habit and habitat of GIB (obtained from the literature and experts) gradient, patch size and disturbance sources are the main parameters considered for the assessment. Based on these criteria, suitable habitats of GIB are derived using geospatial technology with an area of 1222 km^2 and 95% overall accuracy. The rationalized GIB wildlife sanctuary was demarcated on the suitable habitats based on ecological and realistic management criteria like fragmentation, contagion, patch size, and Juxtaposition by the committee set by Honorable Supreme Court of India (Fig. 31.5).

31.5 Wildlife Corridors and Connectivity Metrics

The linear paths in a landscape, which connect two or more suitable habitats, used by wildlife for migration or dispersal are called corridors. Corridors of wildlife provide the connecting link from one patch of suitable habitat to another and thus by decreasing the isolation of species (Daniel et al. 1997) or inbreeding depression. Wildlife corridors can be classified into several categories based on the amount of the linear feature is fragmented or the number of linear features used by the concerned species or its function and the species which it uses. So elephant corridors can be arbitrarily classified into the following types as per their spatial context; (a) Standard corridor (b) multiple corridor (c) Foothill corridor (d) Stepping-stone corridor (e) Fragmented forest corridor and (f) community corridor, etc. (Venketaraman et al. 2017). Corridor is one of the three landscape elements in ecological literature, the other two being ‘patch’ and ‘matrix’ (Forman and Godron 1986). A number of connectivity metrics are developed for conservation planning and monitoring based on structural and functional connectivity, species–non-specific and species-specific population sizes, spatial and dispersal functions (Keely et al. 2021). An ideal method to identify the corridor of a species in GIS is founded on

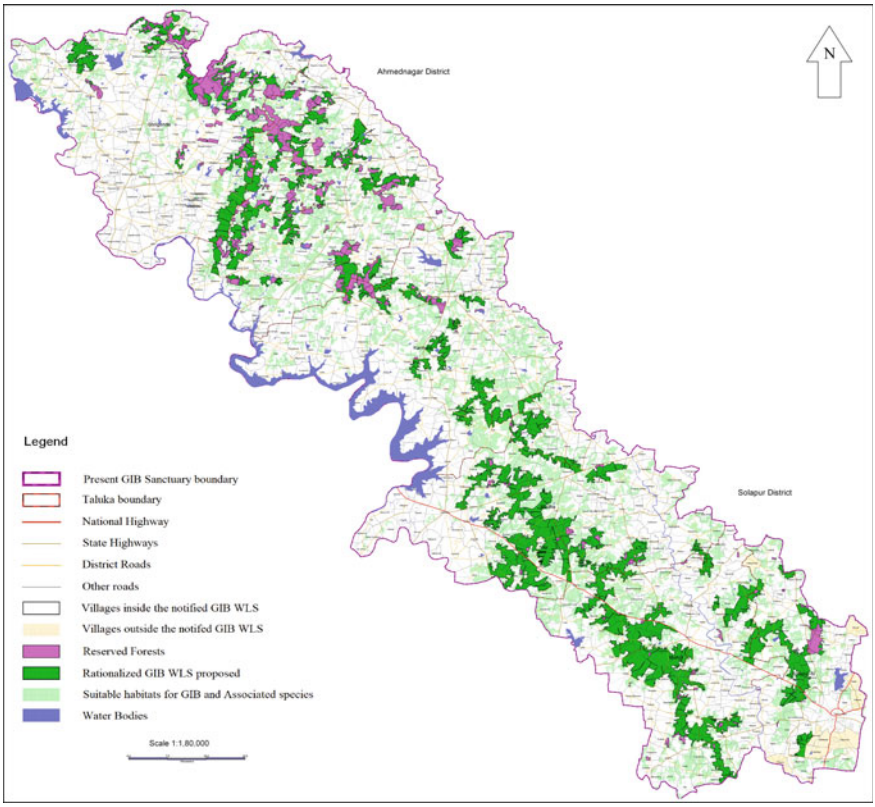

Fig. 31.5 Suitable habitat of GIB and associated species derived using deductive modeling

empirical observations of the trail path of that species (Graves et al. 2007) and the common methods are least-cost path approach (Sawyer et al. 2011; Cushman et al. 2013; Correa et al. 2016; Rudnick et al. 2012) and circuit theory (McRae et al. 2008; Rudnick et al. 2012). Apart from these other approaches are graph theory (Urban et al. 2001; Carroll et al. 2011), resistant kernel models (Compton et al. 2007), and individual-based movement models (Cushman et al. 2013). All these approaches are based on landscape resistance functions (RSFs), the cost of movement of a species across a site in the landscape (Zeller et al. 2012; Boyce et al. 2002). Many of these corridor models do not include the species behavior, even though they are meaning to forecast animal travel (Sawyer et al. 2011; Zeller et al. 2012). Nowadays, wildlife species trails which are obtainable with better GPS temporality and resolutions (Brown et al. 2012) enabled the incorporation of step (Fortin et al. 2005; Thurfjell et al. 2014) and path (Cushman and Lewis 2010) selection functions in corridor modeling. The inclusion of step and path in the corridor modeling will enrich our knowledge of animal space usage, behavior, and their survival in the changing ecosystem (Barton et al. 2012; Buchmann et al. 2012). Varghese et al. (2020) used

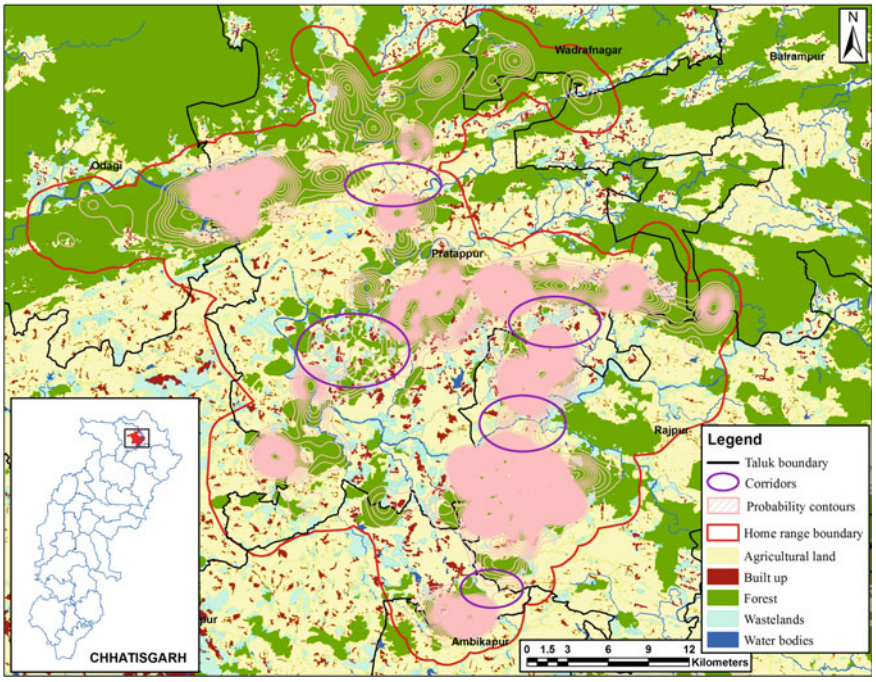

Fig. 31.6 Multiple corridors of the elephant Dev

GPS-derived movement data as an analytical tool for identifying behaviors of the collared elephants and for discerning elephant corridors in Chhattisgarh. Movements of linear parallel (form), rapid, and frequent trails (function) were considered as corridors (Fig. 31.6). This study considered the efficiency and pattern of movement to differentiate corridors from foraging movements in the habitats because corridors are mainly used for traveling. These corridors can be called as realized or animal defined corridors against the functional corridors mentioned above. This corridor characterization is including function as well as form in corridor delineation than cost-based models. In Chhattisgarh, elephants are using multiple, stepping-stone and foothill corridors because of the highly fragmented nature of the forest. The average width and length of the multiple corridors are 5.28 and 4.60 km (order of). In order to ameliorate the human–elephant conflict in this study are, sensitive corridors, where infrastructure can be deployed to broadcast the presence of the elephants to the nearest settlements or vulnerable areas like railway crossings or roads were identified. Crego et al. (2021) conducted a study for recognizing pivotal corridors for large herbivores, like African elephant (*Loxodonta africana*), reticulated giraffe (*Giraffa reticulata*), plains zebra (*Equus quagga*), and Grevy's zebra (*Equus grevyi*)) across a multiple land use landscape in Kenya.

31.6 Habitat Quality and Risk Assessment and Management

Geospatial technology is being successfully used for wildlife habitat assessment and monitoring (Varghese 1997). Identification of the drivers for habitat degradation and its significances, and initiation of preventive measures for appropriate maintenance and conservation are some of the applied usage in geospatial technology (Varghese and Menon 1999). Frequent occurrences of fire, forest fragmentation, forest degradation, habitat loss, depletion of the prey base/predators etc. are some of the reasons for habitat quality loss of the wildlife (Varghese and Suryavanshi 2017). Cover is one of the basic needs of wildlife in its habitat which helps them to hide from heat, cold, rain, snow, wind, and predators (Suraj et al. 1997). Wildlife sometimes need more than one type of cover (interspersion) in an area or for different seasons. Hence, monitoring the cover depletion or transformation is one of the foremost requirements of wildlife conservation. Multiscale and high temporal natures of satellite images make it possible to map forest cover successfully over a period of time both in large scale to small scale over the last few decades (Ashutosh and Roy 2021).

One of the most complex problems forests faces, particularly in deciduous forests, is the recurrent incidence of fire. It is well known that fire caused extensive damage in the wildlife habitat quantitatively and qualitatively (Menon et al. 1999). Geospatial technology is an efficient and apt tool for forest fire management by generating fire prone areas or fire risk areas (Prasanth et al. 2009), monitoring fires on a real-time basis (Chand et al. 2006; Dwyer et al. 1998), and estimation of burnt scars (Mani and Varghese 2018; Axel 2018). High temporality of the satellite data helps in analyzing the frequency of forest fires of a particular area. Another problem which can address successfully using remote sensing is the analysis of forest fragmentation. Forest fragmentation is breaking of large, contiguous forested areas into smaller patches due to anthropological development activities like roads, agriculture, utility corridors or because of other natural calamities (Fahrig 2019). Forest fragmentation changes the physical and biological properties of habitats, interrupts the movement (corridors) and dispersal of the animals, and disrupts the microenvironment at the fragment edges (Magnago et al. 2015). Wildlife species which are sensitive to these changes can be wiped out from these fragments. Remote sensing combined with GIS provides an ideal tool to assess forest fragmentation both qualitatively and quantitatively (Reddy et al. 2013). Fragstats, a computer software program designed to compute a wide variety of landscape metrics for categorical map patterns, is an ideal tool to understand the effect of fragmentation in landscape variations (Cushman 2006; Saikia et al. 2013; Millington et al. 2003).

As tertiary consumers' predators play a significant part in checking prey species such as herbivores. Likewise, the availability of the prey base for predators is also an important factor. This equilibrium between prey and predator plays a pivotal role in maintaining robustness of the ecosystem. Unsustainable anthropogenic activities disturb this equilibrium and ultimately lead to the degradation of the wildlife habitats and endanger the species which uses it (Fardell et al. 2020). Wildlife census data

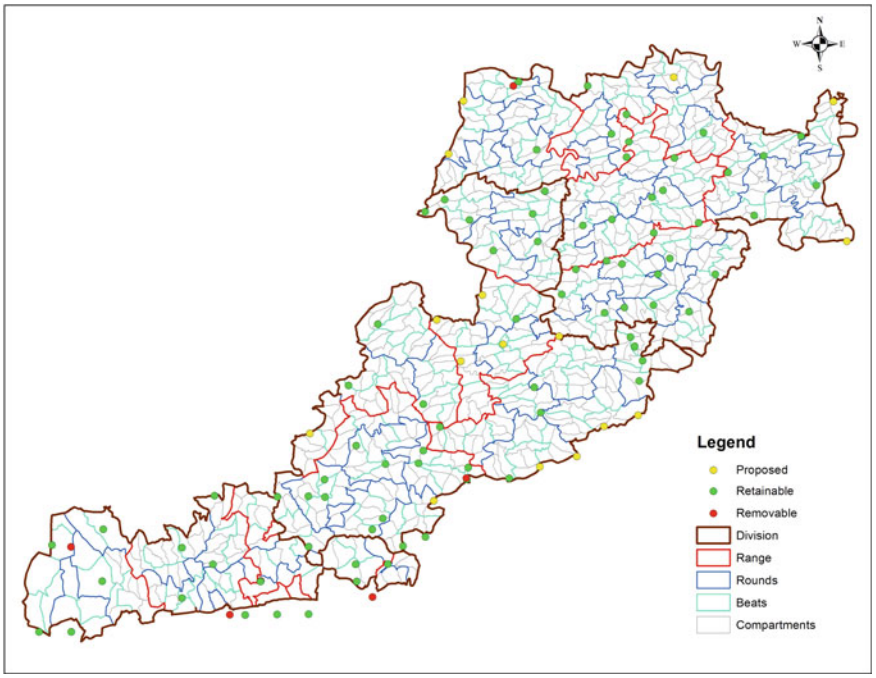

Fig. 31.7 Proposed areas for protection huts in MTR derived using wildlife census, wildlife crime, and existing protection huts

obtained from the field along with GIS provides an excellent tool to study prey–predator association; analysis of herbivore or ungulates density in an area (prey base), carnivores and their territories/home range analysis, suitability analysis for infrastructure development for forest fire watch towers, protection huts (Fig. 31.7), salt licks, and waterholes (Fig. 31.8) (Ashwini et al. 2009).

31.7 Habitat Utilization Pattern/Space Use

Habitat utilization is the mode of an animal's usage of the biotic and abiotic resources of the habitat for survival and reproduction. This usage involves hunting, browsing, cover from predator or cover for predator, nesting, roosting, courtship display, escape, denning, or other behaviors of a species (Krausman 1999). A species may use one habitat in summer and another in winter so seasonal or yearly basis activities of an animal need to be studied with specific biotic and abiotic components. Combination of radio telemetry, remote sensing, and GIS can be used as an excellent platform to understand the habitat utilization pattern of wildlife. The distance between successive graticules obtained by radio telemetry can be represented as a single movement path

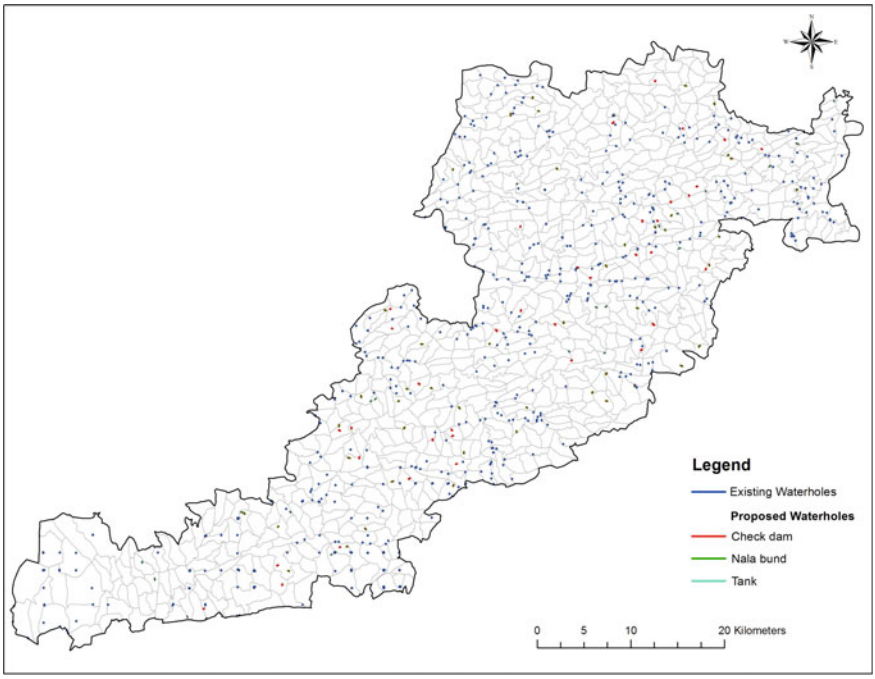

Fig. 31.8 Proposed areas for water holes in MTR derived from wildlife census data and existing waterholes

of the individual as step selection (Fortin et al. 2005; Thurfjell et al. 2014) and path selection (Cushman and Lewis 2010). Using GPS recorded information on the date, time, and latitude and longitude of the collared animal, a trail path can be created in geodatabase collectively for all historic positions recorded. This can be utilized for getting trail path for a specified duration with the length and the direction of travel, daily activity levels, analysis of spatial and temporal variations in the behavior of the species under consideration (Varghese et al. 2020). High resolution land use / land cover map of the habitat under consideration along with slope, edaphic and climatic variable can be used as inputs for habitat variables. These inputs and trail paths can be used for habitat utilization study by feature overlay analysis using identify operation in GIS. Overlay operation in GIS superimposes numerous features of datasets that represent diverse thematic information composed for examining or classifying the relationship of each layer by the combination of different attributes and geometry of datasets or entities. Identify overlay operation provides tabular information regarding habitat utilization patterns based on the attribute and geometry of datasets used.

Varghese et al. (2020) analyzed the habitat utilization pattern of Asian elephants in Central India using geospatial technology. Percentage of occurrence of the collared elephants in different land units derived from path analysis shows that elephants spend nearly 69.79% of their time inside the forest, 23.24% of time raids into the

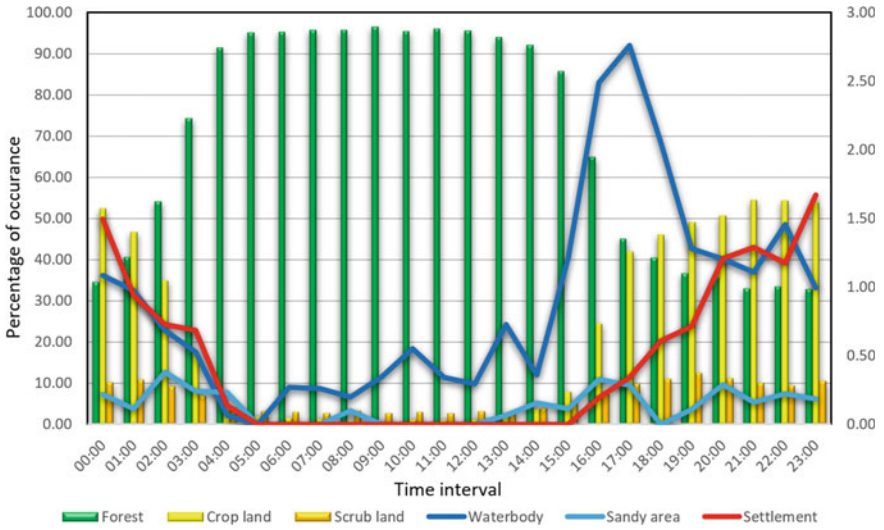

Fig. 31.9 Habitat utilization pattern of the elephants in Chhattisgarh derived from LULC map and collared data of four elephants

agricultural land, 5.49% in scrublands, 0.6% break-in to the settlements. Figure 31.9 represents the average hourly activity level of four collared elephants in each land use/land cover class. It is observed that elephants prefer to stay in the forest during most of the day time, especially 03:00–16:00 h (almost 90% of occurrence), and occasionally start to raid in agricultural land in between 18:00 and 01:00 h with a peak in between 21:00 and 24:00 h (1.60% of occurrence). Elephants sometimes break into settlement (built-up) areas rarely from 17:00 to 03:00 h with a peak at 23:00 h (1.60% of occurrence). As can be perceived from Fig. 31.9, elephants quench their thirst after the daytime rests in the evening with a peak at around 17:00 h (2.80% of occurrence). Month wise occurrence of elephants in different land units shows that because of summer, elephants occur in forest areas nearly 80% of time and less time in forest during September–October (65%). Likewise, elephants raid in to the agriculture land is more during October–January (nearly 30%) when the *kharif* and *rabi* crops seasons and less in summer months (April–May, 15%).

31.8 Wildlife Census

One of the major problem in employing space borne remote sensing data in wildlife census is the low spatial resolution relative to that of the surveyed animals or clusters of animals (LaRue et al. 2017). Submeter very-high-resolution imageries (VHS) taken by aerospace RS techniques are employed for wildlife census for the last few years. Even though the VHS have the ability to map the individuals of large (above

0.6 m) wildlife species; it is very difficult for small (below 0.6 m) species (Wang et al. 2019). Panchromatic images with spatial resolutions below 0.31 m have the capability in wildlife census in open forest and savannahs (Wang et al. 2019). Centimeter-scale images captured from manned aerial surveys have long been employed for animal census over large areas, however because of their noise, such aerial surveys cause significant disturbances to wild animals and are costly to implement in small areas. These problems can overcome by using unmanned aircraft system (UAS) surveys but with a tradeoff in coverage (Wang et al. 2019).

Recently, submeter VHS satellite imagery of WorldView-2, WorldView-3, GeoEye-1, IKONOS, and Quickbird-2 are using to recognize wildlife species with the size above 0.6 m like zebras (*Equus quagga*) (Yang et al. 2014), southern right whales (*Eubalaena australis*) (Fretwell et al. 2014; Cubaynes et al. 2018),wildebeests (*Connochaetes gnou*), albatrosses (Fretwell et al. 2017), polar bears (*Ursus maritimus*) (Stapleton et al. 2014; Platonov et al. 2013), and weddell seals (*Leptonychotes weddellii*) (LaRue et al. 2011). Infrared thermography has been tested based on the temperature variance in the case of some wildlife species (Goodenough et al. 2018; Burn et al. 2006; Garner et al. 1995; Franke et al. 2012). Manual enumeration of animals from the imagery collected from satellites (Stapleton et al. 2014; Cubaynes et al. 2018), manned aircraft (Li 1985; Wiig and Bakken 1990, Andriolo et al. 2006), and UASs (Vermeulen et al. 2013) has been performed for over a half century with reasonable precision (LaRue et al. 2011), but these methods are time consuming and subjective (Linchant et al. 2015; Smyser et al. 2016). Two main classification techniques used in general for discriminating animals are pixel-based and object-based techniques, of these object-based image analysis can be done in detailed manner making use of the capability of various RS resolutions (Wang et al. 2019). Nowadays various automatic and semi-automated algorithms are developed by researchers for identification and enumeration of wildlife species (Rey et al. 2017) for its census form RS data. India carried out its tiger census during 2018–2019 years in three phases. Geotagged mobile photo-evidences considered as preliminary data for the first phase. RS data were used to obtain the dispersal and richness of tigers based on habitat features and anthropogenic factors in the second phase. Ultimately in the third phase, camera trap photographs spread all over the Indian forest areas were used to count the tigers based on its stripe patterns. As per the latest census 2019, India's tiger population now stands at 2967, which is 70 percent of the global tiger population (Jhala et al. 2019).

31.9 Human–Wildlife Conflicts (HWC) Assessment and Mitigation Efforts

Necessity for more land for agriculture, roads, dams, mines, railways, and housing as per the world's exponential population growth caused the degradation, fragmentation, and decrease of wildlife's habitats (Acharya et al. 2016). This reduction and

degradation of wildlife habitat resulted in various types of conflicts between humans and wildlife (Acharya et al. 2016). The livelihood of the local people is affected by the HWC due to the loss of human life, crops, property, and livestock (Barua et al. 2013). The revengeful killing of wildlife endangers the wildlife species and equilibrium of the ecosystem in which they live (Nyhus 2016).

Geospatial analysis can provide a better understanding of the spatial interactions between humans and wildlife. Identification of conflict hotspots, spatial analysis of HWC patterns, spatial risk models (conflict risk mapping) (Prashanti et al. 2020), prediction and risk zonation (Ruda et al. 2018) etc. are some of the promising application in HWC using geospatial technology. Correlation modeling based on animal resource use, spatial association, and spatial interpolation are the frequent used approaches in HWC analysis. These approaches use the event data gathered from the field and identifying the specific land use/land cover category or environment that are associated with it. KDE and Getis-Ord Gi* are two commonly used geospatial hot spot analysis method (Rosenshein, 2018). Behavior pattern of the wildlife derived from collared data with land use/land cover map can be taken as input to analyze HWC. Varghese et al. (2020) analyzed the hourly activity level of the collared elephants in each land use/land cover class and identified crop raiding period and settlement break time in Chhattisgarh on daily (Figs. 31.10 and 31.11) and seasonal basis. The study also resulted in identifying sensitive corridors, where infrastructure

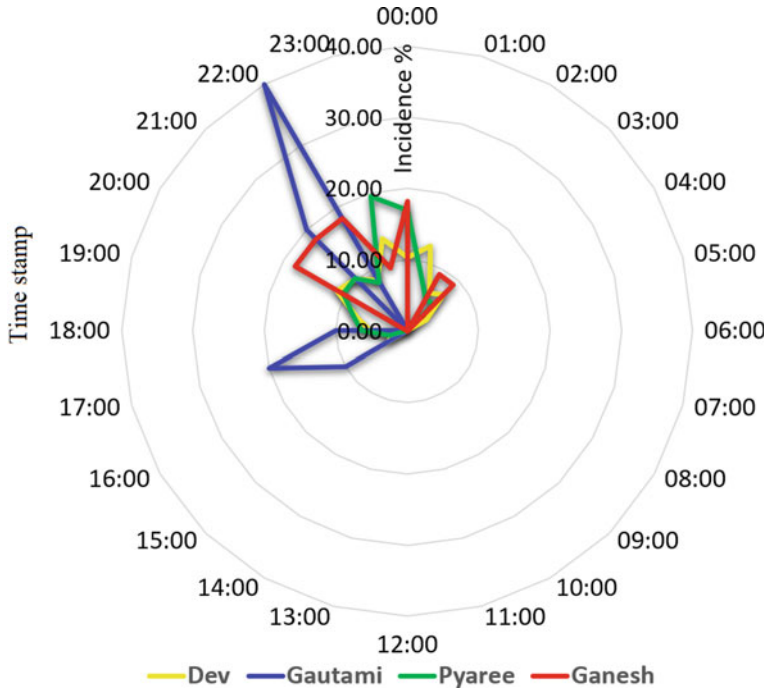

Fig. 31.10 Diurnal pattern of the elephant break-in to the settlement areas in Chhattisgarh

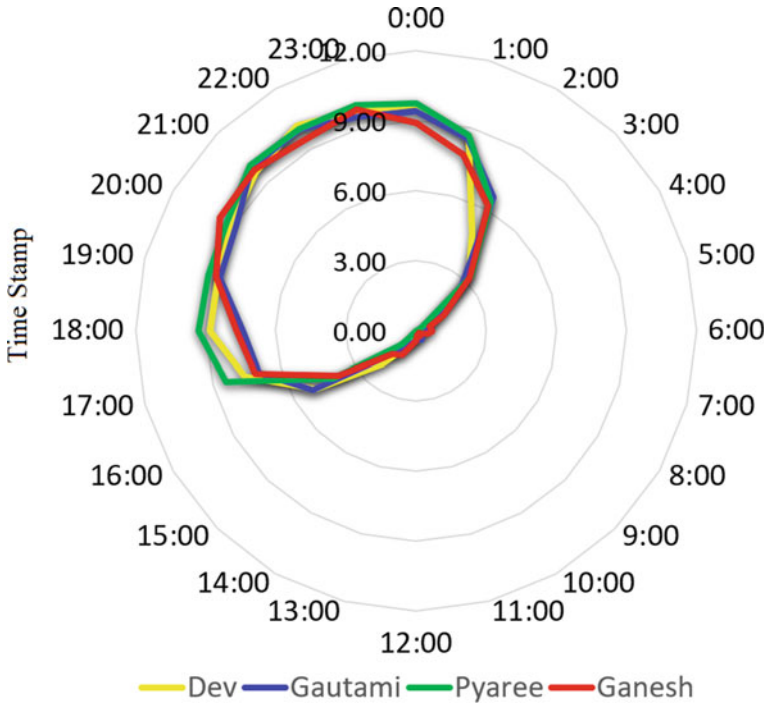

Fig. 31.11 Diurnal pattern of the crop-raid of the elephants in Chhattisgarh

can be deployed to broadcast the presence of the elephants to the nearest settlements, and vulnerable areas like railway crossings or roads to ameliorate human–elephant conflict. Likewise, areas were identified for habitat restoration and improvement needs and hot spots of conflicts for mitigation measures (Fig. 31.12).

31.10 Summary

Advancement in animal tracking and biotelemetry ushered the path for development of new methods of analysis of movement ecology, home ranges, territories, corridors, migration, and dispersal of the wildlife species. Availability of submeter VHS satellite imagery and centimeter-scale images captured from manned aerial and UAV surveys have enhanced the potential for wildlife census. These advancements in biotelemetry and remote sensing data availability (multifrequency, multitemporal and multiscale) with the arrival of new image processing and GIS techniques open a new scenario in geospatial applications for wildlife conservation and management. This leads to the improvement in species–habitat relationship modeling, habitat quality and

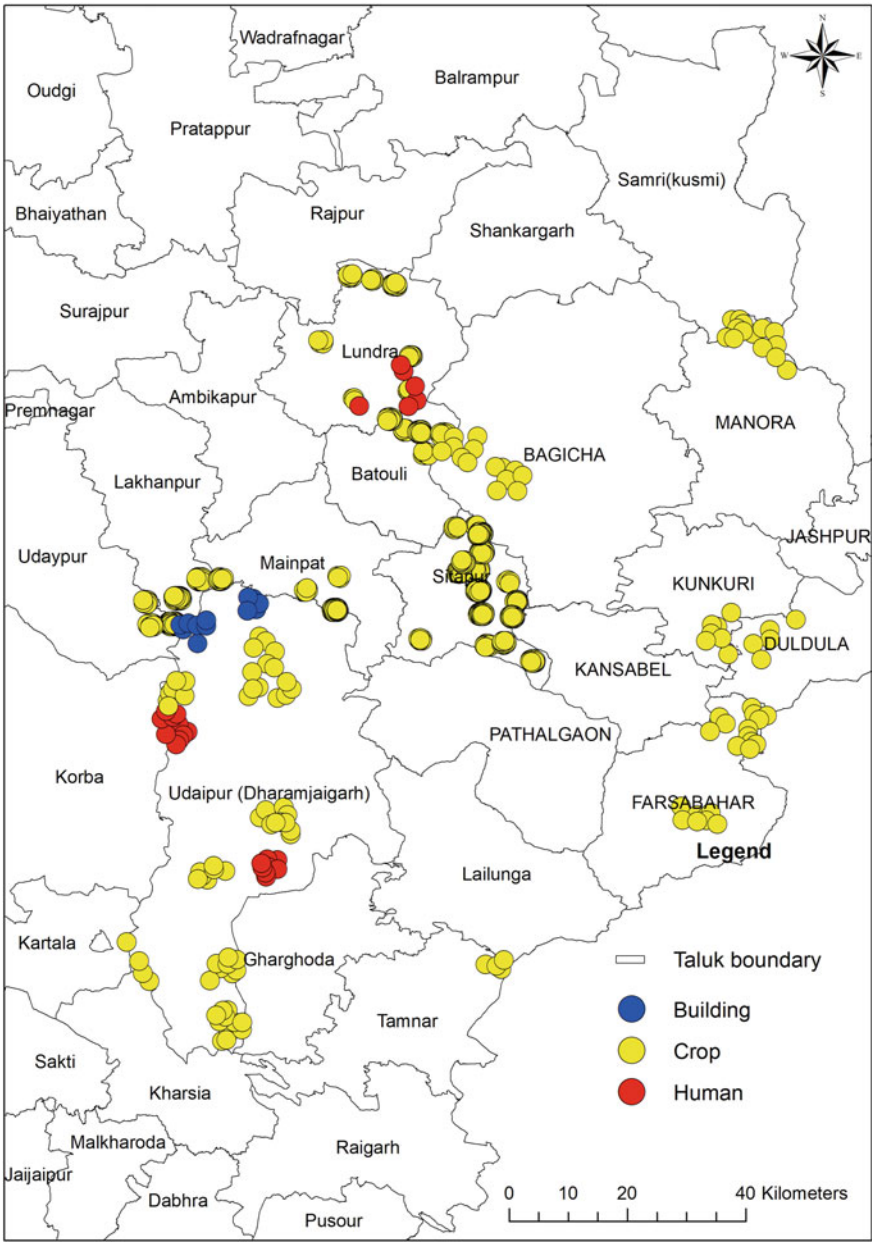

Fig. 31.12 Spatial representation of human–elephant conflicts types in Chhattisgarh

risk assessment, habitat utilization pattern and space use, human–wildlife conflicts assessment and mitigation efforts more precisely and effectively.

References

Acharya KP, Paudel PK, Neupane PR (2016) Human-wildlife conflicts in Nepal: patterns of human fatalities and injuries caused by large mammals. PLoS ONE 11(9):e0161717. https://doi.org/10.1371/journal.pone.0161717

Allen Andrew M, Singh NJL (2016) Movement Ecology with Wildlife Management and Conservation. Frontiers in Ecology and Evolution 3: 155 https://www.frontiersin.org/ article/https://doi.org/10.3389/fevo.2015.00155

Andriolo A, Martins C, Engel MH, Pizzorno JL, Más-Rosa S, Freitas AC, Morete ME, Kinas PG (2006) The first aerial survey to estimate abundance of humpback whales (Megaptera movaeangliae) in the breeding ground of brazil (breeding stock). J Cetacean Res Manag 8:307–311

Argos (2016) Argos user's manual. www.argos-system.org/manual/. Accessed 13 May 2016

Ashutosh S, Roy PS (2021) Three decades of nationwide forest cover mapping using Indian remote sensing satellite data: a success story of monitoring forests for conservation in India. J Indian Soc Remote Sens 49:61–70. https://doi.org/10.1007/s12524-020-01279-1

Ashwini SP, DK Prasanth, AO Varghese, AK Joshi (2009) Sensitivity categorization and management of forest protection huts using Geoinformatics. In: Proceeding of the ISRS Symposium on Advances in Geo-spatial technologies with special emphasis on sustainable rainfed Agriculture. 17–19 September 2009 Nagpur India

Axel AC (2018) Burned area mapping of an escaped fire into tropical dry forest in Western Madagascar using multi-season landsat OLI Data. Remote Sens 10(3):371. https://doi.org/10.3390/rs10030371

Bartoń KA, Hovestadt T, Phillips BL, Travis JMJ (2012) Risky movement increases the rate of range expansion. Proc R Soc B Biol Sci 279:1194–1202

Barua M, Bhagwat SA, Jadhav S (2013) The hidden dimensions of humane wildlife conflict: health impacts, opportunity and transaction costs. Biol Conserv 157:309e316

Boyce MS, Vernier PR, Nielsen SE, Schmiegelow FKA (2002) Evaluating resource selection functions. Ecol Model 157:281–300. https://doi.org/10.1016/s0304-3800(02)00200-4

Buchmann CM, Schurr FM, Nathan R, Jeltsch F (2012) Movement upscaled—the importance of individual foraging movement for community response to habitat loss. Ecography 35:436–445

Burn DM, Webber MA (2006) Udevitz, MS (2006) Application of airborne thermal imagery to surveys of pacific walrus. Wildl Soc Bull 34:51–58

Burt WH (1943) Territoriality and home range concepts as applied to mammals. J Mammal 24(3):346–352

Carroll C, McRae BH, Brookes A (2011) Use of linkage mapping and centrality analysis across habitat gradients to conserve connectivity of Gray Wolf populations in Western North America. Conserv Biol 26(1):78–87. https://doi.org/10.1111/j.1523-1739.2011.01753.x PMID: 22010832

Chand Kiran T, Badarinath KVS, Krishna Prasad V, Murthy MSR (2006) Monitoring forest fires over the Indian region using DMSP-OLS nighttime satellite data. Remote Sens Environ 103:165–168

Compton B, McGarigal K, Cushman SA, Gamble L (2007) A resistant kernel model of connectivity for vernal pool breeding amphibians. Conserv Biol 21:788–799. https://doi.org/10.1111/j.1523-1739.2007.00674.x PMID: 17531056

Cooke SJ, Hinch SG, Wikelski M, Andrews RD, Kuchel LJ, Wolcott TG, Butler PJ (2004) Biotelemetry: a mechanistic approach to ecology. Trends Ecol Evol 19(6):334–343. https://doi.org/10.1016/j.tree.2004.04.003 PMID: 16701280

Correa Ayram CA, Mendoza ME, Etter A, Salicrup DRP (2016) Habitat connectivity in biodiversity conservation: a review of recent studies and applications. Prog Phys Geogr 40(1):7–37

Corset F, De Leeuw J, Skidmore AK (2000) Modeling species distribution with GIS. In: Boitani L, Fuller TK (eds) Research techniques in animal ecology, controversies and consequences. Columbia University Press, pp 389–434. ISBN0231501390

Craighead DJ (1998) An integrated satellite technique to evaluate grizzly bear habitat use. Ursus 10:187–201. http://www.jstor.org/stable/3873127

Crego RD, Wells HBM, Ndung'u KS, Evans L, Njeri Nduguta R, Chege MA, Brown MB, Ogutu JO et al (2021) Moving through the mosaic: identifying critical linkage zones for large herbivores across a multiple use African landscape. Landscape Ecol 36:1325–1340. https://doi.org/10.1007/s10980-021-01232-8

Cubaynes HC, Fretwell PT, Bamford C, Gerrish L, Jackson JA (2018) Whales from space: four mysticete species described using new VHR satellite imagery. Mar Mamm Sci 1:1–26

Cushman SA (2006) Effects of habitat loss and fragmentation on amphibians: a review and prospectus. Biol Cons 128(2):231–240. https://doi.org/10.1016/j.biocon.2005.09.031

Cushman SA, Lewis JS (2010) Movement behavior explains genetic differentiation in American black bears. Landscape Ecol 25:1613–1625. https://doi.org/10.1007/s10980-010-9534-6

Cushman SA, McRae B, Adriaensen F, Beier P, Shirley M, Zeller K (2013) Biological corridors and connectivity. In: Macdonald DW, Willis KJ (eds) Key topics in conservation biology 2 First edn. John Willey & Sons, Ltd., pp 384–405

Danielle DB, LaPoint S, Kays R, Heidrich W, Kümmeth F, Wikelski M (2012) Accelerometer-informed GPS telemetry: reducing the trade-off between resolution and longevity 36(1):139–146, https://doi.org/10.1002/wsb.111

Downs JA, Horner MW (2012) Analysing infrequently sampled animal tracking data by incorporating generalized movement trajectories with kernel density estimation. Comput Environ Urban Syst Elsevier Ltd 36:302–310

Dwyer E, Gregoire J-M, Malingreau J-P (1998) A global analysis of vegetation fires using satellite images: spatial and temporal dynamics. Ambio 27:175–181

Fahrig L (2019) Habitat fragmentation: a long and tangled tale. Glob Ecol Biogeogr 28(1):33–41. https://doi.org/10.1111/geb.12839

Fallah N, Gu H, Mohammad K, Seyyedsalehi SA, Nourijelyani K, Eshraghian MR (2009) Nonlinear Poisson regression using neural networks: a simulation study. Neural Comput Applic 18:939–943. https://doi.org/10.1007/s00521-009-0277-8

Fardell LL, Pavey CR, Dickman CR (2020) Fear and stressing in predator-prey ecology: considering the twin stressors of predators and people on mammals. Peer J 8:e9104. https://doi.org/10.7717/peerj.9104

Forman RTT, Godron M (1986) Landscape ecology. John Wiley and sons, New York

Fortin D, Beyer HL, Boyce MS, Smith DW, Duchesne T, Mao JS (2005) Wolves influence elk movements: behaviour shapes a trophic cascade in Yellowstone National Park. Ecology 86:1320–1330

Franke U, Goll B, Hohmann U, Heurich M (2012) Aerial ungulate surveys with a combination of infrared and high–resolution natural colour images. Anim Biodivers Conserv 35:285–293

Fretwell PT, Scofield P, Phillips RA (2017) Using super-high resolution satellite imagery to census threatened albatrosses. Ibis 159:481–490

Fretwell PT, Staniland IJ, Forcada J (2014) Whales from space: counting southern right whales by satellite. PLoS ONE 9:e88655

Fronczak DL, Andersen DE, Hanna EE, Cooper TR (2017) Distribution and migration chronology of eastern population sandhill cranes. J Wildl Manage 81:1021–1032

Garner DL, Underwood HB, Porter WF (1995) Use of modern infrared thermography for wildlife population surveys. Environ Manag 19:233–238

Getz WM, Wilmers CC (2004) A local nearest-neighbor convex-hull construction of home ranges and utilization distributions. Ecography 27:489–505

Gobeyn S, Volk M, Dominguez-Granda L, Peter LM (2017) Goethals, input variable selection with a simple genetic algorithm for conceptual species distribution models: a case study of river

pollution in Ecuador. Environ Model Softw 92:269–316. https://doi.org/10.1016/j.envsoft.2017.02.012
Goodenough AE, C63arpenter WS, MacTavish L, MacTavish D, Theron C, Hart AG (2018) Empirically testing the effectiveness of thermal imaging as a tool for identification of large mammals in the African bushveldt. Afr J Ecol 56:51–62
Graves TA, Michael SF, Goldstein I, Servheen C (2007) Identification of functional corridors with movement characteristics of brown bears on the Kenai Peninsula, Alaska. Landscape Ecol 22:765–772
Hall LS, Krausman PR, Morrison ML (1997) The habitat concept and a plea for standard terminology. Wildl Soc Bull 25(1):173–182
Herbert JK (2002) Observation of the earth and its environment: survey of missions and sensors. Springer Verlag
Hodgson A, Kelly N, Peel D (2013) Unmanned aerial vehicles (UAVS) for surveying marine fauna: a dugong case study. PLoS ONE 8:e79556
Hodgson A, Peel D, Kelly N (2017) Unmanned aerial vehicles for surveying marine fauna: assessing detection probability. Ecol Appl 27:1253–1267
Hoodless AN, Heward CJ (2019) Migration timing, routes and connectivity of Eurasian woodcock wintering in Britain and Ireland In: Krementz DG et al (eds) Proceeding 11th American woodcock symposium, pp 136–145
Horne JS, Garton EO, Krone SM, Lewis JS (2007) Analyzing animal movements using Brownian bridges. Ecology 88:2354–2363 PMID: 17918412
Hutchinson GE (1957) Concluding remarks. Cold Spring Harbor Symp 22:415–427
IUCN (2020) The IUCN red list of threatened species. Version 2020-2. https://www.iucnredlist.org
Izenman AJ (1991) Recent developments in nonparametric density estimation. J Am Stat Assoc 86(413):205–224
Jha CS, Goparaju L, Tripathi A, Gharai B, Raghubanshi AS, Singh JS (2005) Forest fragmentation and its impact on species diversity: an analysis using remote sensing and GIS. Biodivers Conserv 14(7):1681–1698. https://doi.org/10.1007/s10531-004-0695-y
Jhala YV, Qureshi Q, Nayak AK (eds) (2019) Status of tigers, co-predators and prey in India 2018 Summary Report National Tiger Conservation Authority, Government of India, New Delhi & Wildlife Institute of India, DehradunTR No./2019/05
Kenow KP, Meyer MW, Reaman PS, Evers DC, Douglas DC, Hines J (2000) Effectiveness of abdominally implanted satellite transmitters to identify Common Loon migration routes, staging areas, and wintering range, pp 69–77 in Loons: Old history and new findings. In: McIntyre JW, Evers DC (eds) Proceedings of a symposium from the 1997 meeting, American Ornithologists' Union, North American Loon Fund, Holderness, NH
Kessel ST, Gruber SH, Gledhill KS, Bond ME, Perkins RG (2013) Aerial survey as a tool to estimate abundance and describe distribution of a carcharhinid species, the lemon shark, Negaprion brevirostris. J Mar Biol 597383
Keeley ATH, Beier P, Jenness JS (2021) Connectivity metrics for conservation planning and monitoring. Biol Conserv 255:109008
Krausman PR (1999) Some basic principles of habitat use. In: Launchbaugh KL, Sanders KD, Mosley JL (eds) Grazing behaviour of livestock and wildlife, Idaho Forest, Wildlife and Range Exp Sta. Bull. No. 70, University of Idaho, Moscow, ID, pp 85–90
LaRue MA, Rotella JJ, Garrott RA, Sini DB, Ainley DG, Stauer GE, Porter CC, Morin PJ (2011) Satellite imagery can be used to detect variation in abundance of weddell seals (Leptonychotes weddellii) inerebus bay, Antarctica. Polar Biol 34:1727–1737
LaRue MA, Stapleton S, Anderson M (2017) Feasibility of using high-resolution satellite imagery to assess vertebrate wildlife populations. Conserv Biol 31:213–220
Li S (1985) Aerial surveys of wildlife resources. Jilin for Sci Tech 1:50–51
Linchant J, Lisein J, Semeki J, Lejeune P, Vermeulen C (2015) Are unmanned aircraft systems (UASS) the future of wildlife monitoring? A Rev Accomplishments Challenges Mamm Rev 45:239–252

Magnago LFS, Rocha MF, Meyer L, Martins SV, Meira-Neto JAA (2015) Microclimatic conditions at forest edges have significant impacts on vegetation structure in large Atlantic forest fragments. Biodiv Conserv 24(9):2305–2318. doi: https://doi.org/10.1007/s10531-015-0961-1

Mani JK, Varghese AO (2018) Remote sensing and GIS in agriculture and forest resource monitoring In: Obi Reddy GP, Singh SK (eds) Geospatial technologies in land resources mapping, monitoring and management. Springer, Switzerland, pp 377–400

Matthysen E (2012) Multicausality of dispersal In dispersal ecology and evolution. In: Baguette M, Benton TG, Bullock JM (eds) J Clobert. Oxford University Press, Oxford, pp 3–18

McRae BH, Dickson BG, Keitt TH, Shah VB (2008) Using circuit theory to model connectivity in ecology and conservation. Ecology 10:2712–2724

Mekonen S (2020) Coexistence between human and wildlife: the nature, causes and mitigations of human wildlife conflict around Bale Mountains National Park Southeast Ethiopia. BMC Ecol 20:51. https://doi.org/10.1186/s12898-020-00319-1

Merrill E, Sand H, Zimmermann B, McPhee H, Webb N, Hebblewhite M, Wabakken P, Frair JL (2010) Building a mechanistic understanding of predation with GPS-based movement data. Philosophical transactions of the Royal Society of London Series B: Biological sciences 365:2279–88. https://doi.org/10.1098/rstb.2010.0077

Menon ARR, Varghese AO, Martin Lowel KJ (1999) Impact of fire on Moist deciduous forest ecosystem of southern tropical forests of India In: Impacts of fire and human activities on forest ecosystems in the tropics proc international symposium on Asian Tropical Forest Management III, pp 52–61

Millington AC, Velez-Liendo XM, Bradley AV (2003) Scale dependence in multitemporal mapping of forest fragmentation in Bolivia: implications for explaining temporal trends in landscape ecology and applications to biodiversity conservation. ISPRS J Photogramm Remote Sens 57(4):289–299. https://doi.org/10.1016/S0924-2716(02)00154-5

Moore JD, Andersen DE, Cooper T, Duguay JP, Oldenburger SL, Al Stewart C, Krementz DG (2021) Migration phenology and patterns of American woodcock in central North America derived using satellite telemetry. Wildlife Biol 1:wlb.00816

Morales JM, Moorcroft PR, Matthiopoulos J, Frair JL, Kie JG, Powell RA et al (2010) Building the bridge between animal movement and population dynamics. Philos Trans R Soc Lond B Biol Sci 365:2289–2301. https://doi.org/10.1098/rstb.2010.0082

Mueller T, Fagan WF (2008) Search and navigation in dynamic environments—from individual behaviours to population distributions. Oikos 117:654–664. https://doi.org/10.1111/j.0030-1299.2008.16291.x

Nathan R, Getz WM, Revilla E, Holyoak M, Kadmon R, Saltz D, Smouse PE (2008) A movement ecology paradigm for unifying organismal movement research. Proc Natl Acad Sci USA 105(49):19052–19059. https://doi.org/10.1073/pnas.0800375105

Nyhus PJ (2016) Humane wildlife conflict and coexistence. Annu Rev Environ Resour 41:143e171. https://doi.org/10.1146/annurev-environ-110615-085634

Ofstad EG, Herfindal I, Solberg EJ, Sæther BE (2016) Home ranges, habitat and body mass: Simple correlates of home range size in ungulates. Proc Biol sci vol. 283(1845):20161234. https://doi.org/10.1098/rspb.2016.1234

Pandit Shubha N, Jurek Kolasa, Karl Cottenie (2009) Contrasts between Habitat generalists and specialists: an empirical extension to the basic metacommunity framework. Ecology 90(8):2253–62. http://www.jstor.org/stable/25592741

Peterson CJ, Mitchell MS, DeCesare NJ, Bishop CJ, Sells SS (2021) Habitat selection by wolves and mountain lions during summer in Western Montana. PLoS ONE 16(7):e0254827. https://doi.org/10.1371/journal.pone.0254827

Platonov NG, Mordvintsev IN, Rozhnov VV (2013) The possibility of using high resolution satellite images for detection of marine mammals. Biol Bull 40:197–205

Prasanth DK, Ashwini SP, Varghese AO, Joshi AK (2009) Mapping of forest fire risk zones and identification of suitable sites for fire watch towers using remote sensing and GIS In: Proceeding of

the ISRS symposium on advances in geo-spatial technologies with special emphasis on sustainable rainfed Agriculture, 17–19 September 2009, Nagpur, India, pp 17–19
Prashanti S, Chettri N, Uddin K, Wangchuk K, Joshi R, Tandin T, Pandey A, Gaira KS, Basnet K, Wangdi S, Dorji T, Wangchuk N, Sudhir Chitale V, Uprety Y, Sharma E (2020) Mapping human–wildlife conflict hotspots in a transboundary landscape. Eastern Himalaya Glob Ecol Conserv 24:e01284
Reddy CS, Sreelekshmi S, Jha CS, Dadhwal VK (2013) National assessment of forest fragmentation in India: landscape indices as measures of the effects of fragmentation and forest cover change. Ecol Eng 60:453–464
Rey N, Volpi M, Joost S, Tuia D (2017) Detecting animals in African savanna with UAVs and the crowds. Remote Sens Environ 200:341–351
Rosenberg DK, Noon BR, Charles Meslow E (1997) Biological corridors: form, function, and efficacy. Bioscience 47(10):677–687. https://doi.org/10.2307/1313208
Rosenshein L (2018) Spatial statistics. Available online: https://geonet.esri.com/thread/12214. Accessed 4 Jan 2018
Ruda A, Kolejka J, Silwal T (2018) GIS-assisted prediction and risk zonation of wildlife attacks in the Chitwan National Park in Nepal. ISPRS Int J Geo Inf 7(9):369. https://doi.org/10.3390/ijgi7090369
Rudnick D, Beier P, Cushman S, Dieffenbach F, Epps CW, Gerber L, Hartter J, Jenness J, Kintsch J, Merenlender AM, Perkle RM, Preziosi DV, Ryan SJ, SC Trombulak (2012) The role of landscape connectivity in planning and implementing conservation and restoration priorities. Issues in Ecology. Report No. 16. Ecological Society of America. Washington, DC
Saikia A, Hazarika R, Sahariah D (2013) Land-use/land-cover change and fragmentation in the Nameri tiger reserve. India. Geografisk Tidsskrift-Danish Journal of Geography 113(1):1–10. https://doi.org/10.1080/00167223.2013.782991
Samuel MD, Fuller MR (1994) Wildlife radiotelemetry. In: Bookhout TA (ed) Research and management techniques for wildlife and habitats, 5th edn. The Wildlife Society, Bethesda, MD, pp 370–418
Sawyer SC, Epps CW, Brashares JS (2011) Placing linkages among fragmented habitats: do least-cost models reflect how animals use landscapes? J Appl Ecol 48:668–678
Seaman DE, Powell RP (1996) An evaluation of the accuracy of Kernel Density Estimation for home range analysis. Ecology 77(7):2075–2085
Silverman BW (1986) Density estimation for statistics and data analysis. Chapman and Hall, London
Skidmore AK (2002) Introduction: environmental modelling with GIS and remote sensing. In: Skidmore A (ed) Environmental modelling with GIS and remote sensing. Taylor & Francis, pp 2–7
Smyser TJ, Guenzel RJ, Jacques CN, Garton EO (2016) Double-observer evaluation of pronghorn aerial line-transect surveys. Wildl Res 43:474–481
Stapleton S, Larue M, Lecomte N, Atkinson S, Garshelis D, Porter C, Atwood T (2014) Polar bears from space: assessing satellite imagery as a tool to track arctic wildlife. PLoS ONE 9:e101513
Suraj MA, Menon ARR, Varghese AO, Suresh Babu PK, Pradeep Kumar M (1997) Land cover mapping using remote sensing data: a case study of Chimmony Wildlife Sanctuary. Indian Forester 123(1):53–60
Thurfjell H, Ciuti S, Boyce MS (2014) Applications of step-selection functions in ecology and conservation. Mov Ecol 2:1–12
Tomkiewicz Stanley M, Fuller Mark R, Kie John G, Bates KK (2010) Global positioning system and associated technologies in animal behaviour and ecological research Phil. Trans R Soc B 365:2163–2176. https://doi.org/10.1098/rstb.2010.0090
Turlach BA (1999) Bandwidth selection in Kernel Density estimation: a review. Handbook of Systemic Autoimmune Diseases CiteSeer
Turner LW, Udal MC, Larson BT, Shearer SA (2000) Monitoring cattle behavior and pasture use with GPS and GIS. Can J Anim Sci 80(3):405–413

Urban D, Keitt T (2001) Landscape connectivity: a graph-theoretic perspective. Ecology 82:1205–1218

Varghese AO (1997) Ecological studies of the forests of Peppara Wildlife Sanctuary using remote sensing techniques. PhD Thesis Forest Research Institute Dehradun pp 286

Varghese AO, Joshi AK (2013) Mapping the expansion and habitat restoration need of Great Indian Bustard (GIB) in GIB Sanctuary using RS&GIS. NRSC Technical Report: NRSC-RC-Jan-2010-TR-621

Varghese AO, Suryavanshi A, Jha CS (2020) Monitoring elephant movements& human conflict for conservation and conflict mitigation efforts using geospatial technologies. NRSC Report: NRSC-RC-REGNAGP-RRSC-NAGP-FEB2021-TR0001799-V1.0

Varghese AO, Joshi AK, Krishna Murthy YVN (2010) Mapping of realized and fundamental niches of threatened tree species using geoinformatics: a species level approach for sustaining biodiversity. Spec Issue Biodiv Lands Ecol J Indian Soc Remote Sens 38(3):523–534

Varghese AO, Menon ARR (1999) Floristic composition, dynamics and diversity of Myristica swamp forests of Southern Western Ghats. Kerala. Indian Forester 125(8):775–783

Varghese AO, Arun Suryavanshi (2017) Forest cover transformation analysis and management of Melghat tiger reserve using remote sensing and GIS, NRSC Technical report number: NRSC-RC-REGNAGP-RRSC-NAGP-OCT2020-TR0001690-V1.0. doi: https://doi.org/10.13140/RG.2.2.27068.49280

Varghese AO, Sawarkar VB, Rao YLP, Joshi AK (2016) Habitat suitability assessment of ardeotis nigriceps (Vigors) in great Indian Bustard Sanctuary, Maharashtra (India) Using Remote Sensing and GIS. J Indian Soc Remote Sens 44(1):49–57. https://doi.org/10.1007/s12524-015-0486-9

Venketaraman V, Sandeep KT, K Ramkumar (2017) What is an Asian elephant corridor In: Menon V, Tiwari SK, Ramkumar K, Kyarong S, Ganguly U, Sukumar R (eds) Right of passage: elephant corridors of India (2nd edn). Conservation Reference Series No. 3. Wildlife Trust of India, New Delhi

Vermeulen C, Lejeune P, Lisein J, Sawadogo P, Bouche P (2013) Unmanned aerial survey of elephants. PLoS ONE 8:e54700

Wang D, Shao Q, Yue H (2019) Surveying wild animals from satellites, manned aircraft and unmanned aerial systems (UASs): a review. Remote Sens 11(11):1308. https://doi.org/10.3390/rs11111308

Wiig Ø, Bakken V (2019) Aerial strip surveys of polar bears in the Barents sea. Polar Res 8:309–311

Witczuk J, Pagacz S, Zmarz A, Cypel M (2017) Exploring the feasibility of unmanned aerial vehicles and thermal imaging for ungulate surveys in forests—preliminary results. Int J Remote Sens 39(15–16):5504–5521. https://doi.org/10.1080/01431161.2017.1390621

Witmer GW (2005) Wildlife population monitoring: some practical considerations. Wildl Res 32:259–263

Worton BJ (1989) Kernel methods for estimating the utilization distribution in home-range studies. Ecology 70(1):164–168. https://doi.org/10.2307/1938423

Yang Z, Wang T, Skidmore, AK, De LJ, Said, MY, Freer J (2014) Spotting East African mammals in open savannah from space. PLoS ONE 9:e115989

Zeller KA, McGarigal K, Whiteley AR (2012) Estimating landscape resistance to movement: a review. Landscape Ecol 27(6):777–797. https://doi.org/10.1007/s10980-012-9737-0